K.A. Gschneidner, Jr. and L. Eyring
Editors

HANDBOOK ON THE PHYSICS AND CHEMISTRY OF RARE EARTHS

Volume 2

Alloys and Intermetallics

North-Holland

PREFACE

Karl A. GSCHNEIDNER, Jr., and LeRoy EYRING

These elements perplex us in our rearches [sic], *baffle us in our speculations, and haunt us in our very dreams. They stretch like an unknown sea before us – mocking, mystifying, and murmuring strange revelations and possibilities.*

Sir William Crookes (February 16, 1887)

Today, about a decade short of two centuries after Lt. C.A. Arrhenius discovered the rare earths, we are witnessing a rapid growth in our knowledge of this family of 17 elements. In the five years, 1971 through 1975, we have learned as much about the rare earths as in the previous 25 years. In an attempt to assess the current state of the art (1976) the editors, with the encouragement of the publishers and other fellow scientists, have invited experts in various areas to write comprehensive, broad, up-to-date, and critical reviews. Some of the subjects were chosen because they are mature and still quite active; others because they are essential as background information and for reference; and some topics because they are relatively new and exciting areas of research. Unfortunately there are a few areas which have not been included in the four volumes either because they could not be covered adequately at present or because the appropriate authors were unavailable. Perhaps a future volume could remedy this and bring other rapidly expanding topics up-to-date.

A goal of these volumes is to attempt to combine and integrate as far as practical the physics and the chemistry of these elements. The strategy has been to divide the work into four volumes, the first two dealing primarily with metallic materials and the other two with non-metallic substances. The interaction of these disciplines is important if our knowledge and understanding is to advance quickly and broadly. Historically there are several important instances where one discipline had a great influence on the advancement of the science of rare earths. From the time of Arrhenius' discovery in Ytterby, Sweden until the last naturally occurring rare earth was discovered (lutetium in 1907) the chemistry of the rare earths was hopelessly confused, but the theoretical work of Niels Bohr and the experimental studies of H.G.J. Moseley (both physicists) in 1913–1914 showed that there were 15 lanthanide elements to be expected plus the two closely related metals scandium and yttrium. The discovery of ferromagnetism in gadolinium by G. Urbain,

P. Weiss and F. Trombe in 1935 stirred much excitement and was a foreshadow of the activities of the past twenty years. All of this, however, might not have been were it not for the efforts of two groups of chemists headed by G.E. Boyd at the Oak Ridge National Laboratory and F.H. Spedding at the Ames Laboratory who in the late 1940's developed the ion exchange techniques for separating rare earths. The method developed by the latter group is still being utilized by many industrial firms for preparing high purity rare earth materials. In the 1960's and 1970's several important discoveries—rare earth phosphors, cracking catalysts, rare earth-cobalt permanent magnets, etc. have made significant practical impacts and stimulated much research, but the extent of these are difficult to judge and put into their proper perspective at this time. Hopefully, these four volumes, and any which may follow will make a major contribution to our progress in understanding these exotic and fascinating elements.

In writing these chapters the authors have been asked to use the term "rare earths" to include Sc, Y and the elements La through Lu, and the term "lanthanides" when referring to only the elements La through Lu. The editors have attempted to enforce this usage rigorously when editing the various chapters. Furthermore, we have encouraged the authors to use the SI units as far as practicable to bring the subject matter into accord with current scientific and technical practice.

CONTENTS

VOLUME 1: METALS

VOLUME 2: ALLOYS AND INTERMETALLICS

VOLUME 3: NON-METALLIC COMPOUNDS – I

VOLUME 4: NON-METALLIC COMPOUNDS - II

Handbook on the Physics and Chemistry of Rare Earths, edited by K.A. Gschneidner, Jr. and L. Eyring

Chapter 13

CRYSTAL CHEMISTRY OF INTERMETALLIC COMPOUNDS

A. IANDELLI and A. PALENZONA
Institute of Physical Chemistry, University of Genoa, C.so Europa, Palazzo delle Scienze, 16132 Genoa, Italy

Contents

Symbols

a = crystallographic axis
A = coefficient in heat of formation equation
b = crystallographic axis
B = coefficient in heat of formation equation
c = crystallographic axis
H = enthalpy
r = ionic radius
R = rare earth
S = entropy
T = temperature
V = volume
V_m = mean atomic volume
V_u = unit volume
X = partner element
Z = nuclear charge
Δ = difference

1. Introduction

The existence of intermetallic compounds and the reason for their formation represent for chemistry and metal science an old problem, which has not been completely resolved. Intermetallic compounds are formed according to the thermodynamic stability of certain types of crystal structures, but quantum chemistry is unable to predict their existence.

The realization of a certain crystal structure can be related to several factors: geometric, electronic, electrochemical and chemical bonds, which, in limiting cases, correspond to ionic, covalent or metallic-type bonds. Only in a few cases, when one of these types of bonds is enhanced, is it possible to explain the composition and the crystal structure of a given compound, e.g. for phases with prevalent ionic character or for covalent compounds where the bond directionality must be fulfilled by the structure.

Lacking dominant factors, the structures of intermetallic compounds tend to reach the highest symmetry, the highest space filling and the highest number of connections among atoms. A more quantitative factor is represented by the dimensions of the constituent atoms and by the interatomic distances realized after the formation of the compound.

The space filling is determined by the ratio of the atomic radii, which is also a controlling factor for the existence ranges of the crystal structures. Both atomic radii ratios and interatomic distances have been utilized by Pearson (1972) in drawing "near-neighbor diagrams", which can be used to analyze the type of interaction among atoms and to derive some indications of the bond type.

It must be pointed out that the several factors can produce two principal effects. The first concerns the short-range order around one atom and the second concerns the long-range arrangement which leads to the formation of a certain structure. According to the available thermodynamic data, the possible structures for a given composition do not show appreciable stability differences, so that the final choice of the structure often depends on second-order effects.

The measure of the stability of an intermetallic phase is determined by the difference between its free energy with respect to that of the starting elements. The most important contribution to its value is given by the heat of formation, since the term $T\Delta S$ can be neglected, at least at low temperatures. Evaluation of the heat of formation appears important even though the results represent only a first approximation. Actually two different methods can be used: the first due to Kubaschewski (1959) and the second to Miedema (1973). Following Kubaschewski, a crystal structure is analyzed in terms of atomic dimensions and interatomic distances to derive a new "effective" coordination number for both of the atoms. The heat of formation is obtained on the basis of the difference of the coordination numbers and the heats of sublimation of the two metals. In the method due to Miedema, the crystal structure is disregarded and the difference in the electronegativities of the two metals, defined through the work function, is taken into account, along with the difference in the electron densities at the boundary of the Wigner–Seitz cells. Despite the use of such different factors, the results obtained by both methods are in fairly good agreement with the experimental data.

The study of the rare earth intermetallic compounds represents an important part of the more general problem of the metallic phases. As is well known, the rare earths, due to their particular electronic structure, show a regular change of their properties, especially of atomic dimensions and electronegativities.

Moreover, some of them exhibit different valence states in compounds with metallic character, which give rise to interesting structural, electronic and magnetic properties.

The number of binary intermetallic compounds of rare earths for which the crystal structures have been determined is about 1800 and this number will increase in the future. In the early years of these studies the simplest structures were resolved and only the more complex structures await complete determinations.

After examining the large number of available experimental data, some precautions must be pointed out regarding their utilization. A lot of old data are probably incorrect in terms of structure type, composition and numerical values of the lattice constants, and their revision is most desirable. Discrepancies and incompleteness are often met with in recent data, and can be ascribed to several factors, which are summarized as follows: 1) different methods of preparation and heat treatments; 2) lack of analytical and metallographic controls of the samples; 3) different purities of the starting materials which can lead to the stabilization of certain crystal structures or alter the physical properties of these phases; 4) different methods of crystallographic examination; 5) incomplete determinations of complex structures, which usually result in less accurate values for the atomic positional parameters; 6) possible existence of solid solutions; and 7) "structural" formula different from the stoichiometric one. Furthermore, from a thermodynamic point of view, the stability of most of the compounds is not known and the possible existence of sluggish solid state transformations, which can mislead the structural analysis, must be considered. For these reasons, lattice constant data for the most favorable cases (cubic structures) must be considered reliable with some uncertainty at least in the third decimal figure.

Considerable difficulty was encountered in the collection and judgement of the available data. The number of works in this field has grown in recent years (about 1200 documents in 1975) so that it is possible that a number of data have been missed for several reasons, including the difficulty in obtaining the original papers. A second point concerns the confusion arising from the existence of different data for the same compound or a series of compounds. When possible, results from the same investigator, which at least tends to hold the reasons for discrepancies constant, were weighed more strongly. Otherwise, we have utilized a weighted mean value following a criterion of reliability as imposed by the above mentioned reasons.

Owing to the limited number of pages of this work, we have focused our attention on binary compounds between rare earths and other metals, disregarding hydrogen, metalloids and the elements on the left of group VIIB of the periodic system, but including Be and Mg. No description of the different structure types has been included since they are reported in detail in monographs, like those of Gschneidner (1961), Schubert (1964), Pearson (1967) and Savitskii et al. (1975), while new structure types can be found in current literature, and are cited in the

text. Lattice constants are reported only for the series of compounds which are discussed in detail.

This paper is concerned with the following points: compound formation in binary systems, compositions and structure types, metallic and ionic radii, mean atomic volumes and volume contractions, discussion of the most frequently occurring compositions (R_5X_3, RX, RX_2, RX_3), and intermetallic compounds with anomalous lanthanide valence states.

2. Compound formation in binary systems

In fig. 13.1 are shown the binary systems for which the phase diagram, complete or partial, has been determined, excluding those systems which contain no intermediate phases. Actually about 200 diagrams with the above mentioned elements are known and represent 40% of the 496 possible cases. As can be seen the most investigated R–X systems correspond to X = Mn, Fe, Co, Ni, Al and Mg for their applicative interest, or those for which fewer experimental difficulties are encountered (low melting points, low reactivity with the containers, low oxidation rates of the alloys). From a scientific point of view, many other systems would be interesting, for example, involving the group VIII elements and especially the rare earths with variable valency.

For the rare earths, the more studied systems are those with La, Ce, Pr, Sm, Gd, Er, Y and Yb, while for Tm and Lu, perhaps for economic reasons, only a few systems have been examined.

Many of the known phase diagrams have been studied or revised recently, after 1950–1955, and can be considered sufficiently reliable, but for a certain

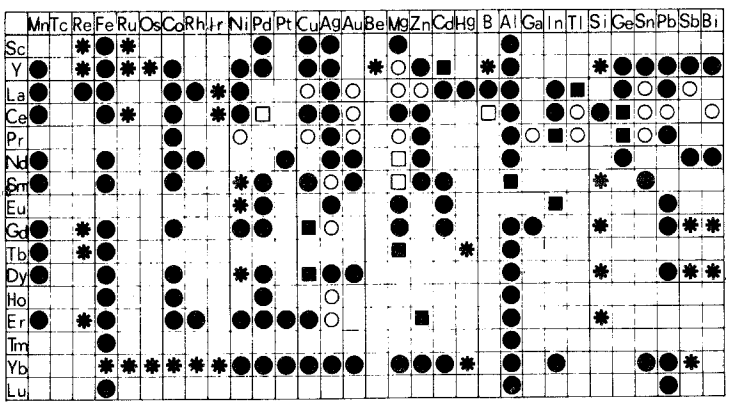

Fig. 13.1. Known phase diagrams for binary R–X systems. ● = Complete, recent phase diagram; ○ = Complete, old phase diagram; ■ = Incomplete, recent phase diagram; □ = Incomplete, old phase diagram; * = Proposed phase diagram. Groups A and B are indicated, according to the most common form of the periodic system.

TABLE 13.1
Sign of the heat of formation in the R–X systems.

								Mg	Al	Si	
								–	–	–	
Ti	V	Cr	Mn	Fe	Co	Ni	Cu	Zn	Ga	Ge	
+	+	+	±	±	–	–	–	–	–	–	
Zr	Nb	Mo	Tc	Ru	Rh	Pd	Ag	Cd	In	Sn	Sb
+	+	+	–	–	–	–	–	–	–	–	–
Hf	Ta	W	Re	Os	Ir	Pt	Au	Hg	Tl	Pb	Bi
+	+	+	–	–	–	–	–	–	–	–	–

number of old diagrams a careful revision is needed.

In fig. 13.1 we have not reported systems between R and elements for which no intermediate phases exist. These elements are those lying on the left of group VIIB of the periodic system, with the exception of Be and Mg. For the metals of the preceding groups the known systems show only eutectic points or immiscibility regions in the liquid state or, sometimes, solid solubilities. This behavior, namely the non-existence of intermediate phases with the transition elements preceding those of group VIIB, can be predicted from the relationship proposed by Miedema (1973). By evaluating the sign of the heats of formation of the phases in the R–X systems, when X is an element of IV, V and VIB groups, a positive sign is obtained, while a negative sign is obtained for the others. For R mean values for the parameters were used in the cited equation and these were adjusted for the systems with Mn and Fe to explain the difference of alloying behavior in the series from La to Lu where compounds of the light rare earths do not exist. These results are summarized in table 13.1.

It is possible to obtain intermetallic compounds of the rare earths with transition metals before those of group VIIB if ternary compounds are considered. In the known cases, however, R atoms are never in contact with those of the transition metal, as is observed for example in the compounds RCr_4Al_8 (Zarechnyuk, 1966) and RMo_2Al_4 (Fornasini and Palenzona, 1976), for which R atoms are bounded only with Al atoms. An analogous behavior is observed for Th compounds, like $ThCr_2Si_2$ (Ban and Sikirica, 1965).

The formation of compounds with the first elements of group VII seems to depend on the dimensions of R: La and Ce do not form compounds with Mn, while Pr gives $PrMn_2$ and the same situation is found with Re and Tc. No compounds are formed in the La–Fe system.

3. Composition and structure types

In figs. 13.2–13.16 are reported graphically all the data concerning the compositions and the structure types of the intermetallic compounds which are formed in the known systems. As footnotes to the figures we have reported

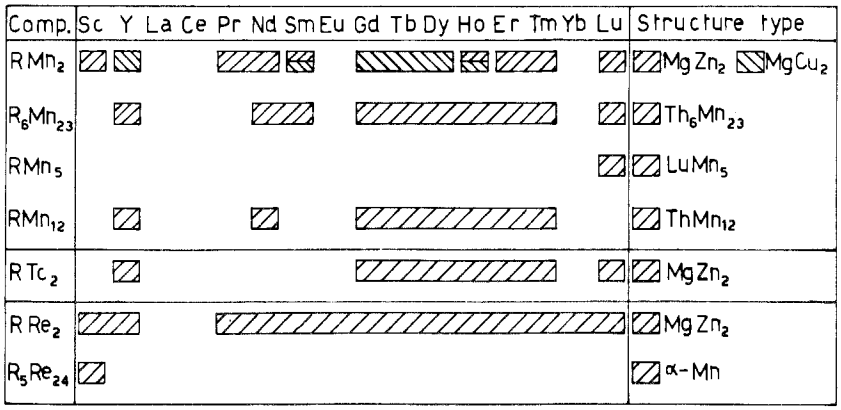

Fig. 13.2. Compound formation in the *R*–Mn, *R*–Tc, *R*–Re systems. Notes: 1) (Y, Sm, Gd, Tb, Dy, Ho, Er, Yb)Mn_2 synthesized under pressure, crystallize with the $MgZn_2$ type of structure. 2) $PrRe_2$ at high temperature crystallizes with the $MgCu_2$ structure type.

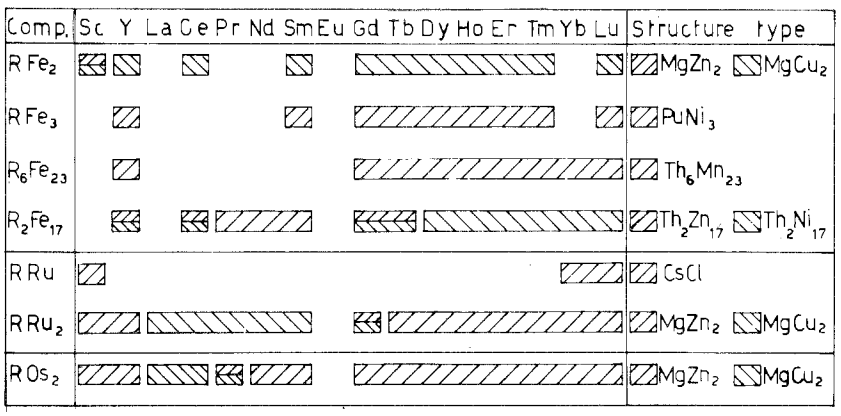

Fig. 13.3. Compound formation in the *R*–Fe, *R*–Ru, *R*–Os systems. Notes: 1) $TbFe_2$ also crystallizes with a rhombohedral modification derived from the $MgCu_2$ type. 2) (Pr, Nd, Yb)Fe_2 synthesized under pressure, crystallize with the $MgCu_2$ type structure. 3) (Nd, Sm)Ru_2 and (La, Ce)Os_2 under pressure transform to the $MgZn_2$ structure type. 4) The following compounds have been claimed to exist but no structural details are available: (Sc, Y, La, Ce)$_3$Ru and (Y, La, Ce)$_3$Os.

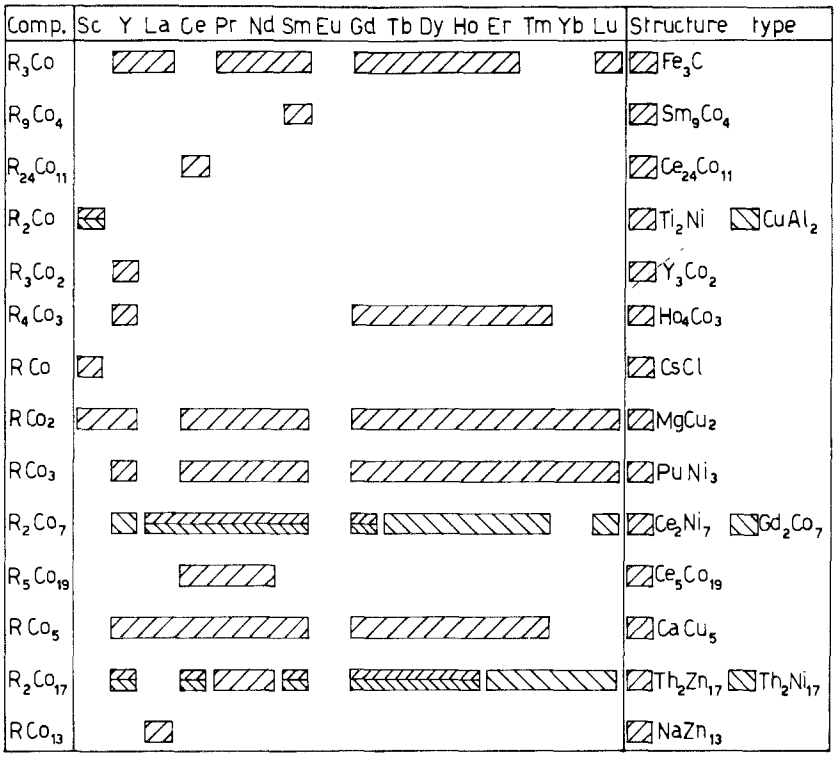

Fig. 13.4. Compound formation in the R–Co systems. Notes: The following compounds have been claimed to exist but no structural details are available: Eu_3Co; $(Pr, Nd)_7Co_3$; $(Gd, Dy, Ho, Er)_5Co_3$; La_4Co_3; $(Pr, Nd)_2Co_{17}$; $(Y, La)_2Co_3$.

some observations on the possible existence of compounds, for which the compositions and the crystal structures have not yet been determined and have indicated pressure or temperature induced structural changes.

All of these data are further summarized with respect to the existence of the various phases in fig. 13.17 where the composition ranges for which intermetallic compounds exist are represented by vertical lines and the phases are marked with horizontal segments. This representation reflects a unique behavior of the rare earths, in that it corresponds to the widest range of compounds in existence. The partner X elements are arranged according to the groups of the periodic system and the following observations are made. In no system do we observe compounds richer in R than R_3X. The reported R_4X phases with X = Rh and Ir must be considered to have the R_3X composition, since their structure is of the Fe_3C type. This behavior is surely related to the large dimensions of R atoms and likewise occurs with Ca and Th. The appearance of the first phase in the different systems changes regularly along the periodic system. For the group VIIB

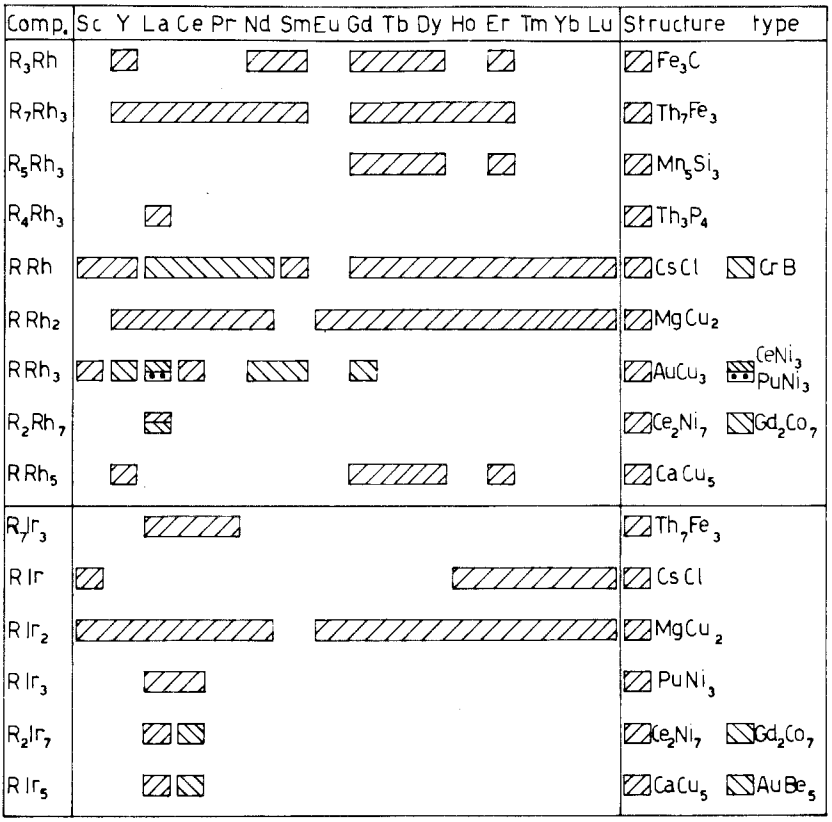

Fig. 13.5. (*See opposite*)

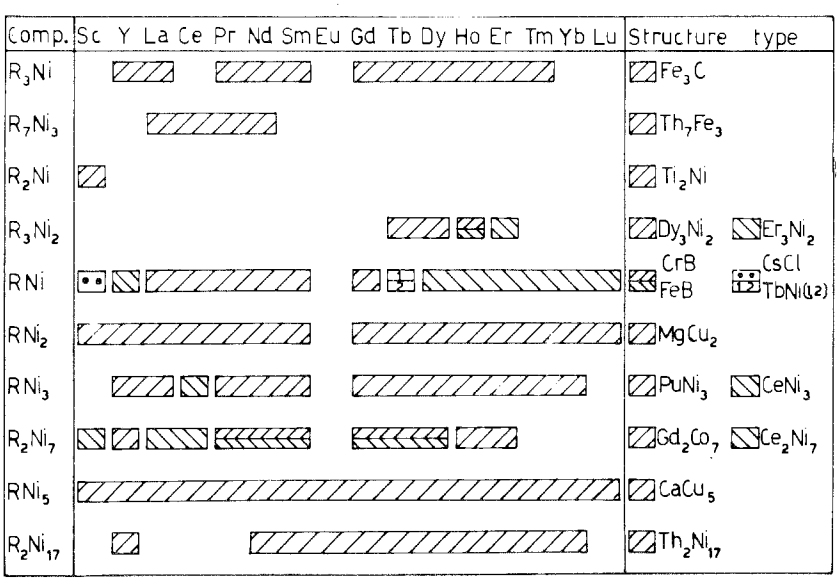

Fig. 13.6. (*See opposite*)

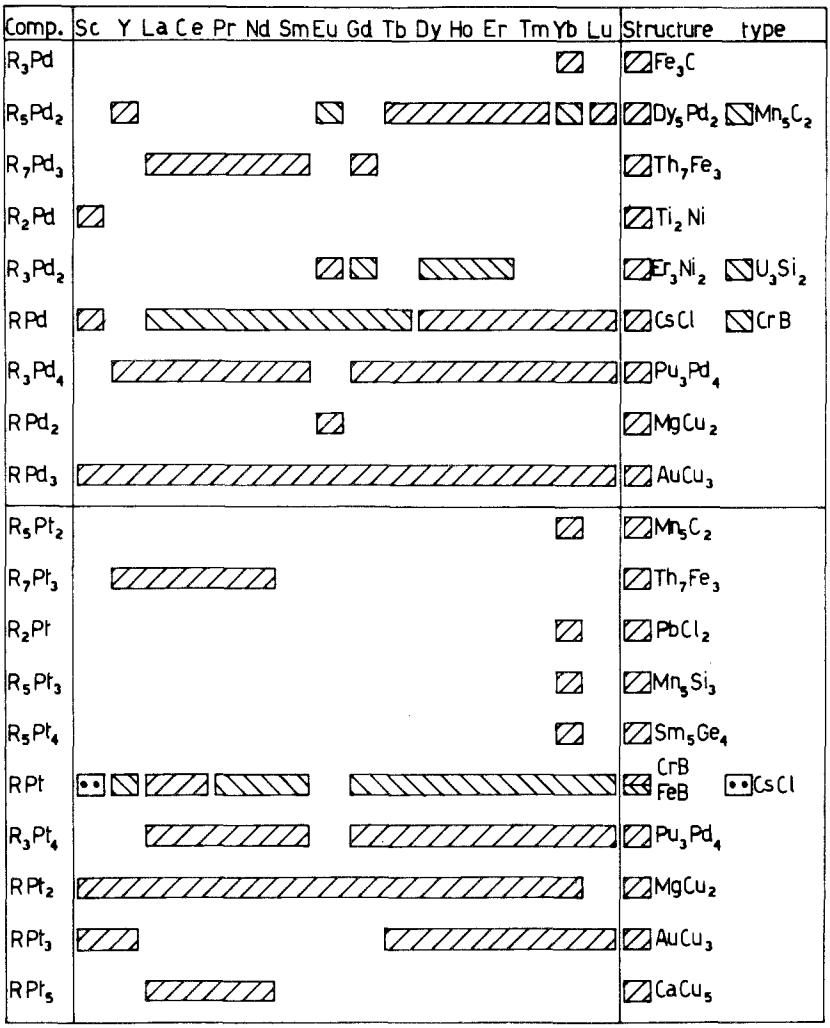

Fig. 13.7. Compound formation in the *R*–Pd and *R*–Pt systems. Notes: 1) (Y, Sm, Eu, Gd, Tb, Dy, Ho, Er, Tm)Pt_5 crystallize with various orthorhombic structures derived from the $CaCu_5$ type. 2) The following compounds have been claimed to exist but no structural details are available: (La, Ce)$_3$Pd; (Y, Sm)$_3Pd_2$; YPd; (Y, Gd, Dy, Ho, Er)$_2Pd_3$; (Y, Sm, Gd, Dy, Ho, Er, Yb)Pd_2; (Sm, Eu)Pd_5; $YbPd_{1.63}$; $YbPd_{2.13}$; (La, Ce, Er)$_3$Pt; Er_2Pt; (Y, Nd, Gd, Tb, Dy, Ho)$_5Pt_2$; Ce_3Pt_5; (Sm, Eu)$_2Pt_7$.

Fig. 13.5. Compound formation in the *R*–Rh and *R*–Ir systems. Notes: 1) (La, Ce, Nd, Sm, Gd, Y, Dy, Er)$_5Rh_3$ crystallize with various crystal structures but not with the Mn_5Si_3 type. 2) (La, Nd)$_3$Rh crystallize with the La_3Rh type. 3) The following compounds have been claimed to exist but no structural details are available: La_5Rh_4; $LaRh_2$ (h.T.); (Ce, Nd, Sm, Gd)$_4Rh_3$; Ce_4Ir; La_3Ir; Er_5Ir_3; (La, Ce)Ir; La_2Ir_{17}.

Fig. 13.6. Compound formation in the *R*–Ni systems. Notes: 1) YNi also crystallizes with a monoclinic structure related to the FeB type. 2) Er_5Ni_{22} and Er_4Ni_{17} crystallize with structures derived from the $CaCu_5$ type. 3) The following compounds have been claimed to exist but no structural details are available: Eu_3Ni; (Y, Gd)$_3Ni_2$; (Y, Gd)Ni_4.

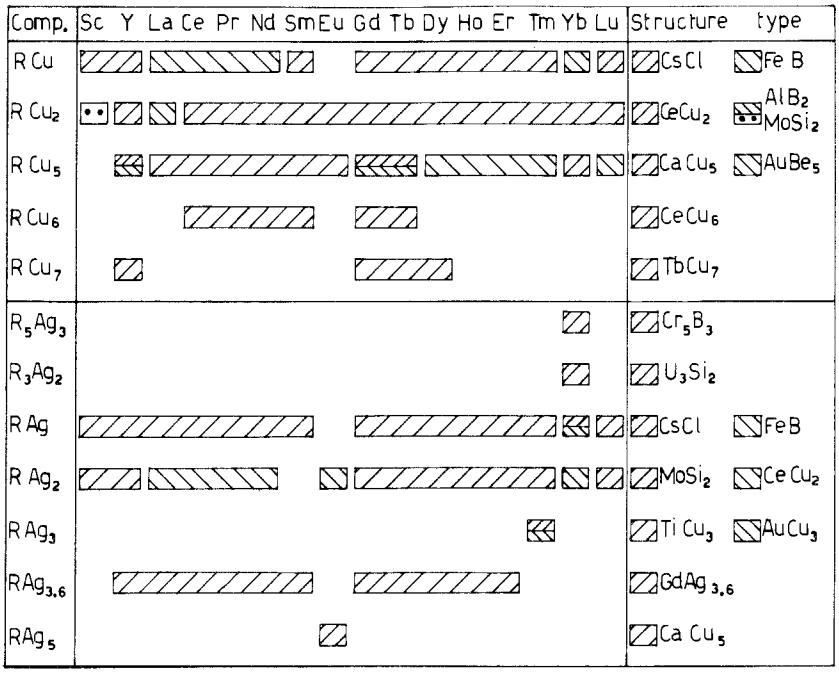

Fig. 13.8. (*See opposite*)

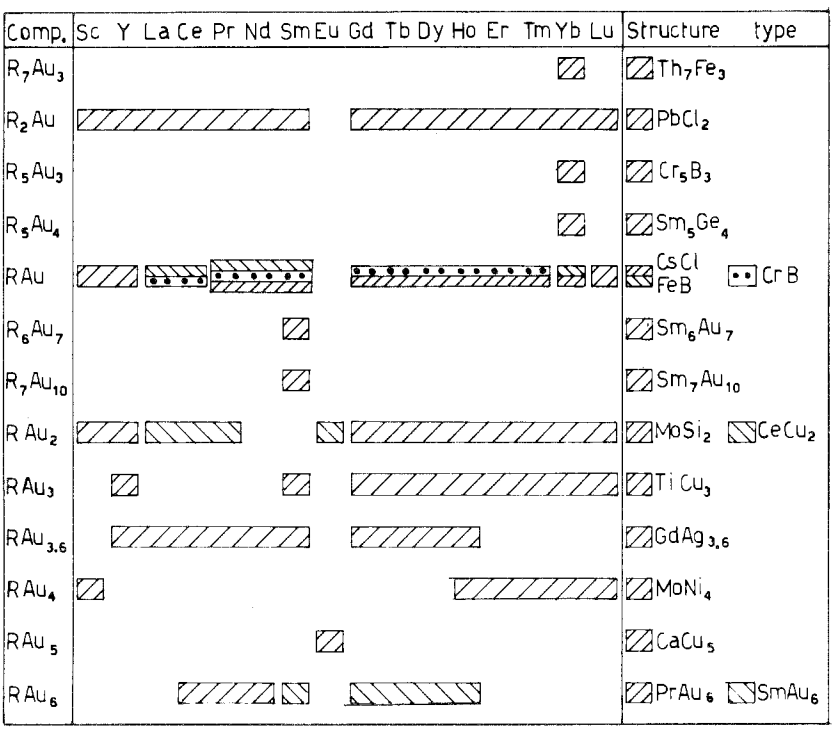

Fig. 13.9. (*See opposite*)

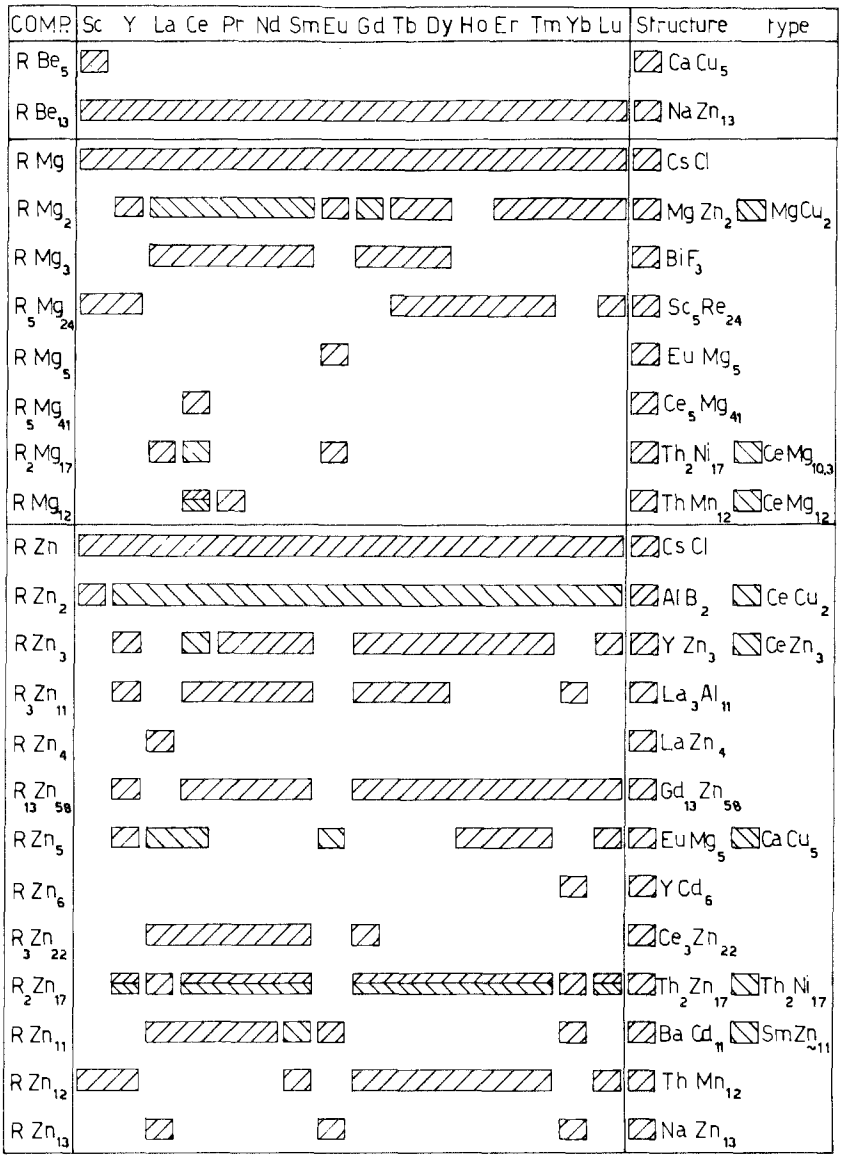

Fig. 13.10. Compound formation in the *R*–Be, *R*–Mg, *R*–Zn systems. Notes: The following compounds have been claimed to exist but no structural details are available: $(Pr, Nd)_5Mg_{41}$; Gd_2Mg_{17}; $ScZn_3$; Sc_2Zn_7.

Fig. 13.8. Compound formation in the *R*–Cu and *R*–Ag systems. Notes: 1) $LaAg_5$ (l.T.) crystallizes with a structure derivable from the $MgZn_2$ type. 2) The following compounds have been claimed to exist but no structural details are available: Yb_2Cu_7; $CeCu_4$; (Sc, Y, La, Pr, Nd, Gd)Cu_4; Yb_2Cu_9; (Y, La)Cu_6; Eu_5Ag_3; EuAg; $EuAg_4$; Yb_2Ag_9; $LaAg_5$ (h.T.); (Ce, Pr)Ag_5. 3) Yb_2Ag_7 is isomorphous with Ca_2Ag_7.

Fig. 13.9. Compound formation in the *R*–Au systems. Notes: The following compounds have been claimed to exist but no structural details are available: $EuAu_3$; $(Sc, Y)_2Au$; $YAu_{3.6}$; (Pr, Nd, Sm)Au_2; $NdAu_4$.

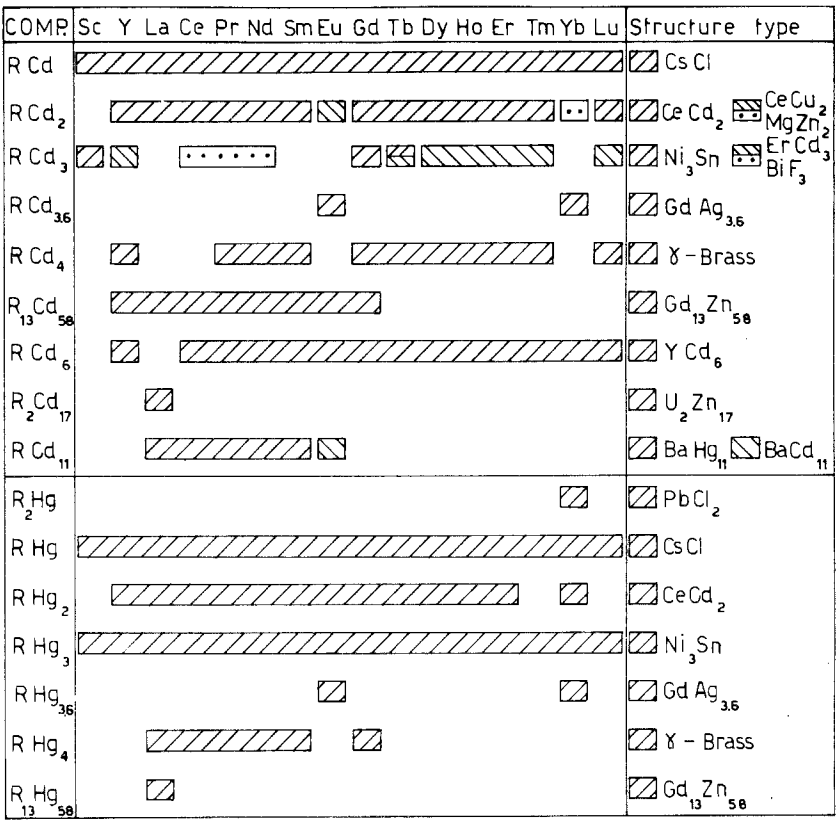

Fig. 13.11. Compound formation in the R–Cd and R–Hg systems. Notes: The following compounds have been claimed to exist but no structural details are available: (Eu, Yb)$_3$Cd$_8$; Yb$_3$Cd$_{17}$; (Y, Tb, Dy, Ho, Er, Yb)Hg$_4$; (La, Ce, Pr, Nd, Sm)Hg$_{6.5}$.

elements and Fe, the first compound is RX_2, while with the other transition metals it is R_3X. With the IB and IIB elements, except for Au, the first compound is RX, while again R_3X is found with group III, IV and V A elements.

The upper limit for the existence of compounds is more irregular. The richest X compositions are observed with the IIB group element, while from Al to Bi they are limited to RX_3. A singular behavior is represented by B which gives the richest known X composition: RB_{66}.

Besides consideration of the dimensions of the R and X atoms, which is a dominant factor for Be and B, the existence ranges represented in fig. 13.17 correspond to a division of the X elements into three classes, namely: transition elements, IB and IIB elements (with the only exception of Au) and those of the other groups. The determining factor appears to be the electronic structure of the X atoms, which contain d or s or sp electrons in the three cases. The same

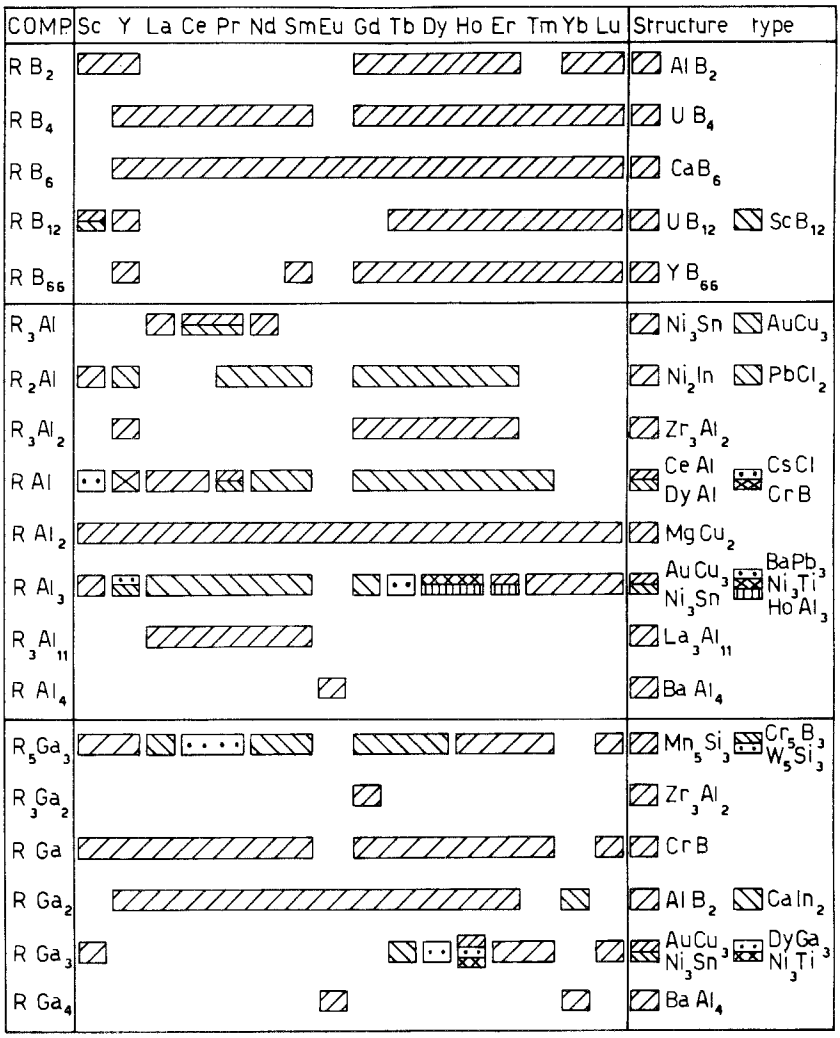

Fig. 13.12. Compound formation in the *R*–B, *R*–Al, *R*–Ga systems. Notes: 1) R_3Al_{11} at high temperature transform to the $BaAl_4$ structure type. 2) RAl_3 obtained by "splat cooling" crystallize in the various structure types observed in the RAl_3 series. 3) (Gd, Tb)Al_4 at high temperature crystallize with the UAl_4 type of structure. 4) The following compounds have been claimed to exist but no structural details are available: SmB_2; ScB_6; Y_3Al; Tm_3Al_2; Pr_3Ga; Dy_3Ga_2; Eu_2Ga_3; $EuGa_3$.

division can be applied to other properties of these intermetallic phases.

Figure 13.17 shows that some compositions are common to almost all systems, while others correspond to single cases. The frequency of the various stoichiometries is represented in fig. 13.18, where the relative percentage of each composition is shown. From this histogram we can observe that four stoi-

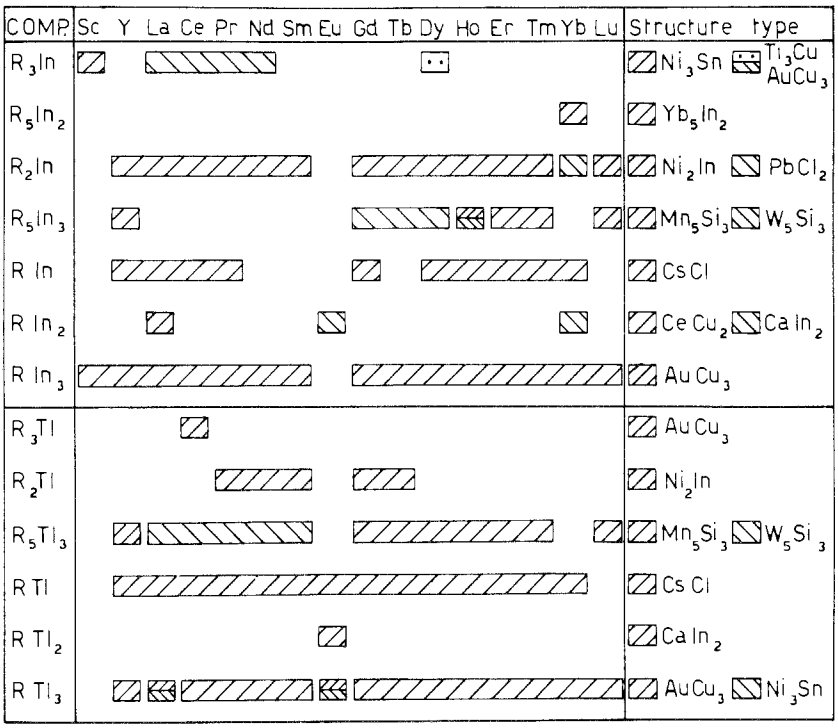

Fig. 13.13. Compound formation in the *R*–In and *R*–Tl systems. Notes: The following compounds have been claimed to exist but no structural details are available: (La, Ce, Pr)$In_{1.5}$; La_3In_5; $CeIn_2$; $EuIn_4$; $(La, Pr)_3Tl$; $(La, Ce)_2Tl$.

chiometries are by far the most frequent and correspond to R_5X_3, RX, RX_2 and RX_3. These families will be examined in detail later.

Table 13.2 contains the statistical data for each composition which includes the structure types, the number of compounds for each structure type and the partner elements with which this structure is realized.

4. Metallic and ionic radii

Generally the structural data for a given phase are discussed by comparing the observed interatomic distances with the dimensions of the starting atoms. This can be done only if, for the considered structure, the atomic positional parameters are known with sufficient reliability. If so, a lot of information may be derived: shape of the coordination polyhedron around each atomic kind and coordination number, contraction in the interatomic distances and indications concerning the type of bond. Atomic radii for the starting elements are derived from their metallic structures. These values refer to a given coordination number, which can be corrected to correspond to different coordination numbers

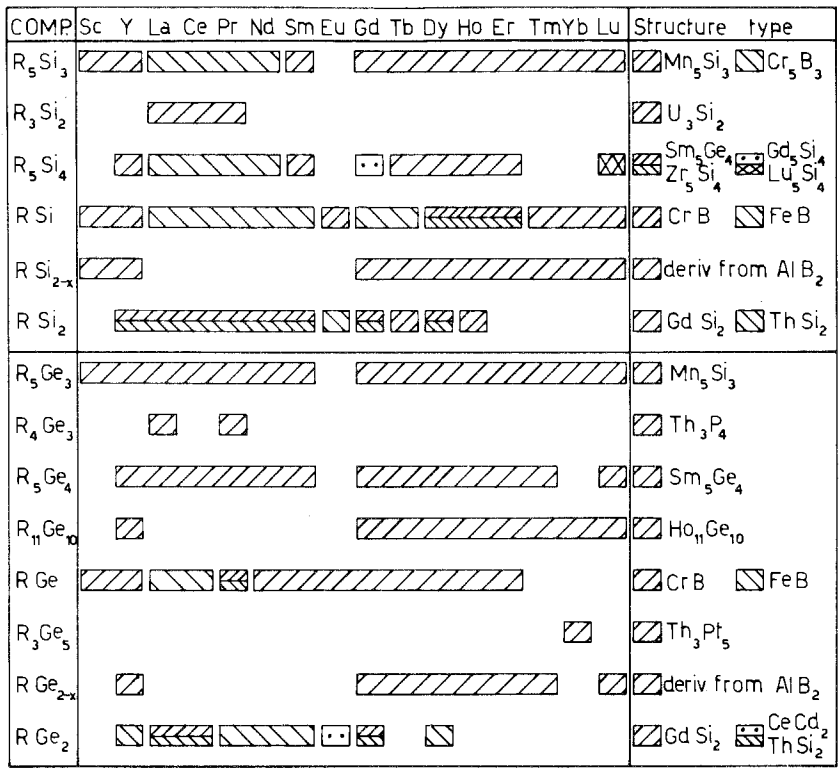

Fig. 13.14. Compound formation in the *R*–Si and *R*–Ge systems. Notes: 1) Compounds $RSi_{\sim 2}$ and $RGe_{\sim 2}$ should probably be replaced by R_3Si_5 and R_3Ge_5 and the related structure could be the Th_3Pt_5 type. 2) Around the $YGe_{1.6}$ composition there exist several compounds with structures derived from the AlB_2 and $ThSi_2$ types. 3) The following compounds have been claimed to exist but no structural details are available: La_3Ge (tetragonal); Ce_2Ge_3; (Y, Gd, Tb, Dy, Ho)Ge_2 (orthorhombic); Y_2Ge_7.

if necessary. The values considered in the following are for C.N.12.

For the rare earths some observations must be made. The atomic radius of Ce (1.824_7 Å) appears anomalous with respect to that of the following element Pr which is greater (1.827_9 Å). This is a well known situation which derives from the valence of Ce in the metal itself (3.1 instead of 3, see ch. 4, section 2.3). The radius corresponding to trivalent Ce has been evaluated by different methods which give values between 1.846 and 1.848 Å. For tetravalent Ce a radius of 1.672 Å has been derived, see ch. 4, section 2.3 and table 4.3.

For Eu two radii must be considered to correspond to the valences 2 and 3, These values are 2.041_6 Å and 1.798 Å, respectively. For Yb the corresponding values are 1.939_2 Å and 1.741 Å.

The metallic radius of Gd (1.801 Å) is close to that of Sm (1.804_1 Å) and does not follow the regular decrease for the lanthanides. This could be ascribed to its

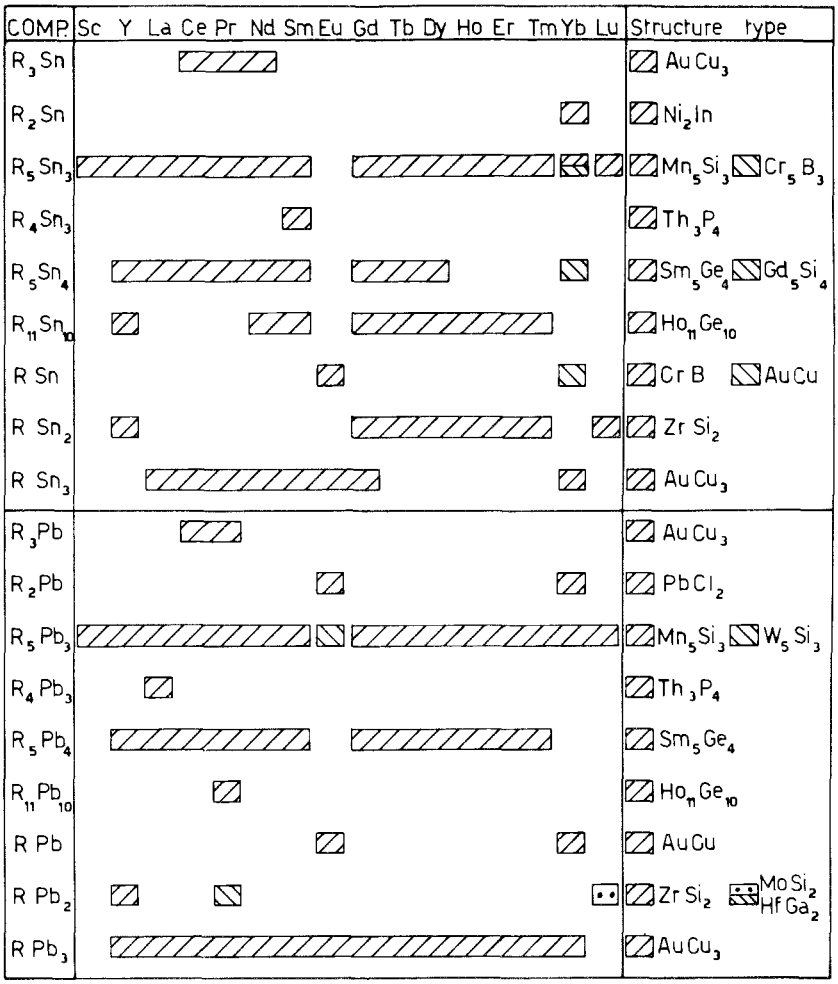

Fig. 13.15. Compound formation in the *R*–Sn and *R*–Pb systems. Notes: 1) (Y, Tb, Dy, Ho, Er)Sn_3 synthesized under pressure, crystallize with the $AuCu_3$ type of structure. 2) (La, Ce, Pr)$_5Pb_3$ at high temperature crystallize with the W_5Si_3 type of structure. 3) $LuPb_3$ synthesized under pressure is $AuCu_3$ type. 4) The following compounds have been claimed to exist but no structural details are available: (Ce, Pr)$_{11}Sn_{10}$; (La, Ce, Pr)$_2Sn_3$; Sm_2Sn_3 (tetragonal); Lu_5Pb_4 (Pnma); Lu_6Pb_5 (Ibam); (La, Gd)$_{11}Pb_{10}$; DyPb; Gd_6Pb_7; La_3Pb_4; (La, Nd, Sm, Gd, Dy, Ho, Er, Tm)Pb_2.

particular electronic configuration (4f shell half filled). Based on different arguments, some authors have derived a radius of 1.794 Å for Gd.

The atomic dimensions of these cited anomalous elements can vary in their different intermetallic compounds and each time the valency state should be determined to assure the use of the correct atomic radius.

Another dimensional parameter, which appears to change with a more regular

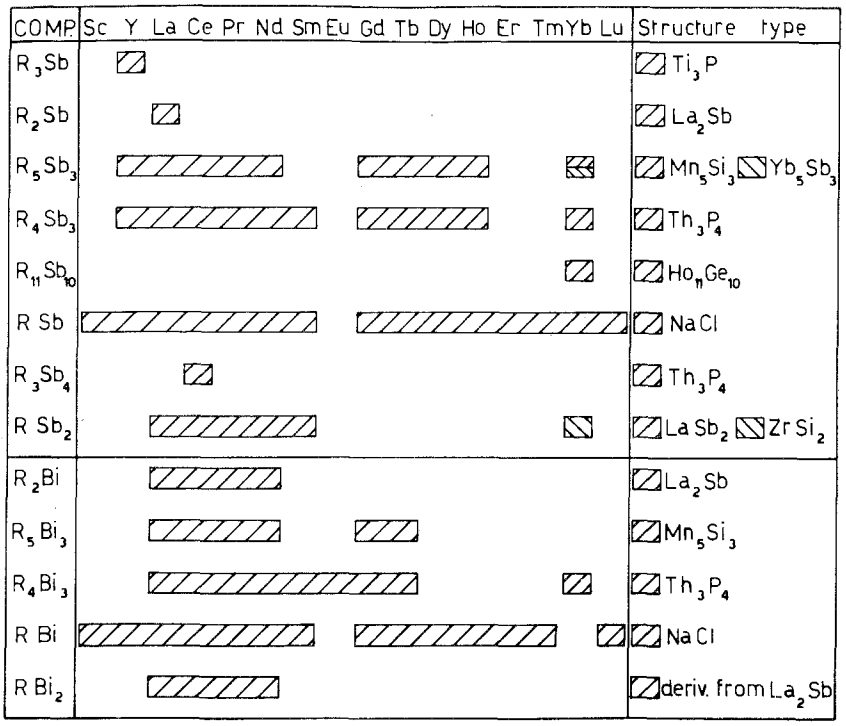

Fig. 13.16. Compound formation in the *R*–Sb and *R*–Bi systems. Notes: 1) (Y, Dy, Ho, Er, Tm, Lu)Sb_2 synthesized under pressure, crystallize with the $LaSb_2$ structure type. 2) The following compounds have been claimed to exist but no structural details are available: Yb_2Sb (two modifications); Yb_5Sb_2; Y_4Sb_3 (tetragonal); Yb_5Sb_4; $(Ce, Nd)_3Bi$; Gd_2Bi; Dy_4Bi_3; Nd_5Bi_4; $(Y, Gd, Tb, Dy, Ho, Er, Tm)_{5+x}Bi_3$ (orthorhombic).

trend, is represented by the ionic radii which have been derived from ionic compounds. We have used the values of Templeton and Dauben (1954), with the exception of La^{3+}, for which the value of 1.061 Å has been changed to 1.071 Å. This latter value generally produces for all the series of compounds a linear trend for the lattice dimensions and related data. The values for divalent and tetravalent ionic radii, evaluated by the authors, are based on the NaCl-type compounds with S, Se, Te and the RO_2 oxides with the CaF_2-type structure. The best and most recent values for the metallic radii and atomic volumes are found in table 2.13, and the ionic radii in table 13.3.

Following Pauling (1960) the radii of isoelectronic ions are related linearly to the reciprocal of the effective nuclear charge; fig. 13.19 shows that such a correlation also holds for the lanthanide ions in the different valence states.

By using the values of the ionic radii, linear correlations can be obtained with lattice constants and interatomic distances, with the exception of a few cases, which will be examined in the following. The ionic radii appear more useful

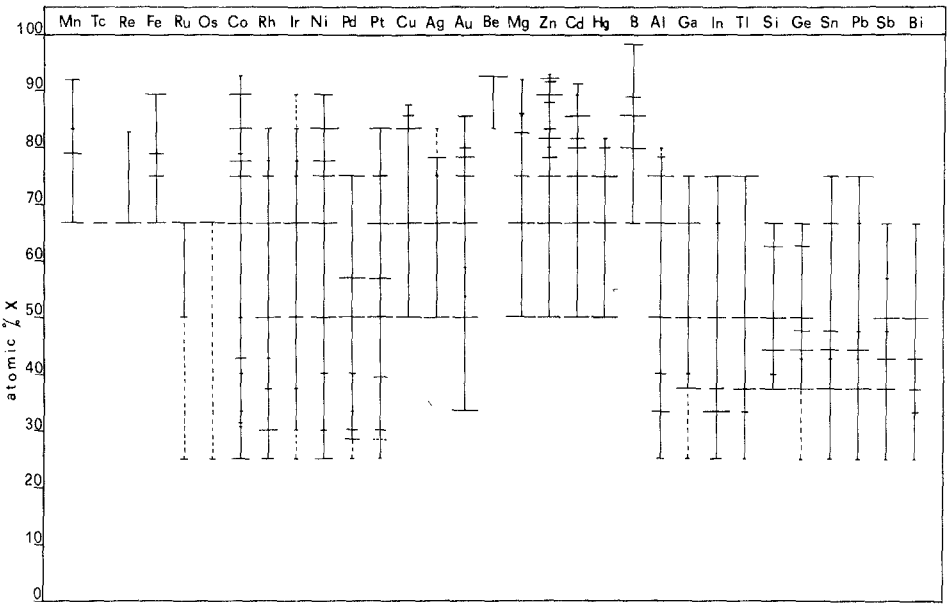

Fig. 13.17. Composition ranges for compound formation in the R–X systems.

than the atomic radii or atomic number for comparison of the structural properties of series of either isostoichiometric or isomorphous compounds. Ionic radii can also be employed to correlate other properties, particularly the thermodynamic data. The heats of formation of particular series of isomorphous compounds can be correlated with the ionic radii ratios of the involved elements and such correlations can be used to predict some of these values, which cannot be determined experimentally. Such correlations hold for both trivalent and divalent rare earths by taking the corresponding ionic radii (Palenzona and Cirafici, 1974a).

The above mentioned linear correlations with the ionic radii are particularly simple for the lattice constants and for the interatomic distances if the positional atomic parameters are known. In any case, it is possible to utilize as dimensional data, the cube root of the unit formula volume (V_u), which, in the case of a cubic substance, corresponds to the lattice constant. This procedure gives an average value that is less sensitive to experimental errors.

While it is possible to find a linear trend for ionic or partially ionic compounds, the same also holds for intermetallic phases for each composition. The few exceptions are represented by the series: RCd_4, RFe_5, RCo_5, RCu_5, RCd_6, RZn_{13} and RX_3 compounds, with X = In, Tl, Sn, Pb. These irregularities can be attributed to either stoichiometry differences or solid solutions or the dimensions of the X partners, as in the case of the RX_3 phases.

The plots of the cube roots of V_u show the cases in which the rare earths exhibit a valence different from three, particularly for Ce, Eu and Yb, which as

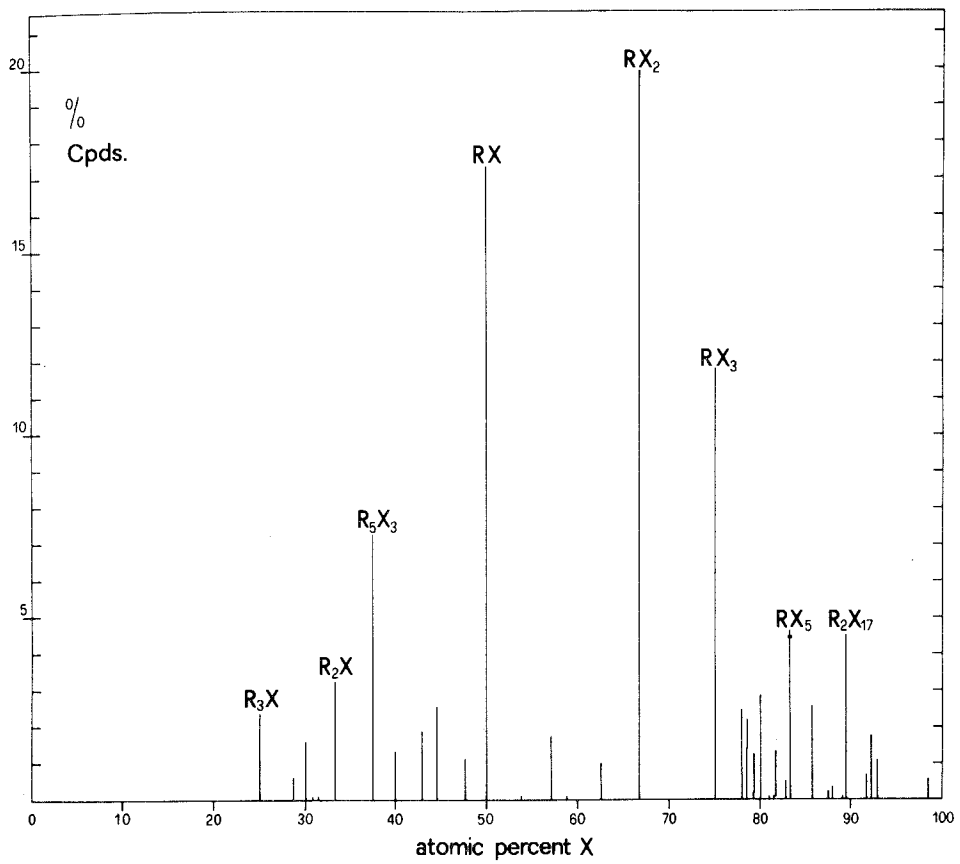

Fig. 13.18. Percentages of compounds occurring in R–X systems.

tetra- or divalent elements, have smaller or larger values. In the following figures the points for these three lanthanides are included only if they are mostly in the trivalent state.

The slopes of the straight lines change slightly for the same composition, if there are changes of structure but are much more sensitive to changes of the stoichiometry. Examining, for example, the case of an X (Au, Zn or Cd), which forms many phases of different compositions, and plotting the slopes of the straight lines obtained for the different phases, starting from a common origin (Lu), for scaling, the situation is like that shown in fig. 13.20. When the percentage of the X partner is increased the slopes decrease which shows that the larger contraction is to be ascribed to the R atoms, in accordance with their higher compressibility.

TABLE 13.2
Statistical data on intermetallic compounds.

Comp.	at.% X	N (compds.)	Structure types, partner elements and frequency of occurrence.
R_3X	25.0	42	23 Fe_3C[Co(11), Ni(11), Pd(1)];
			12 $AuCu_3$[Al(2), In(4), Tl(1), Sn(3), Pb(2)];
			5 Ni_3Sn[Al(4), In(1)];
			1 Ti_3Cu[In(1)];
			1 Ti_3P[Sb(1)];
R_5X_2	28.6	11	7 Dy_5Pd_2[Pd(7)];
			3 Mn_5C_2[Pd(2), Pt(1)];
			1 Yb_5In_2[In(1)];
R_7X_3	30.0	28	28 Th_7Fe_3[Ni(4), Rh(11), Pd(4), Ir(3), Pt(5), Au(1)];
R_9X_4	30.8	1	1 Sm_9Co_4[Co(1)];
$R_{24}X_{11}$	31.4	1	1 $Ce_{24}Co_{11}$[Co(1)]
R_2X	33.3	58	29 $PbCl_2$[Pt(1), Au(15), Hg(1), Al(9), In(1), Pb(2)];
			20 Ni_2In[Al(1), In(13), Tl(5), Sn(1)];
			5 La_2Sb[Sb(1), Bi(4)];
			3 Ti_2Ni[Co(1), Ni(1), Pd(1)];
			1 $CuAl_2$[Co(1)]
R_5X_3	37.5	129	96 Mn_5Si_3[Rh(4), Pt(1), Ga(6), In(5), Tl(8), Si(11), Ge(15), Sn(15), Pb(15), Sb(10), Bi(6)];
			13 Cr_5B_3[Ag(1), Au(1), Ga(6), Si(4), Sn(1)];
			12 W_5Si_3[Ga(2), In(4), Tl(5), Pb(1)];
			7 Y_5Bi_3[Bi(7)];
			1 Yb_5Sb_3[Sb(1)]
R_3X_2	40	23	8 U_3Si_2[Pd(4), Ag(1), Si(3)];
			7 Zr_3Al_2[Al(6), Ga(1)];
			3 Dy_3Ni_2[Ni(3)];
			3 Er_3Ni_2[Ni(2), Pd(1)];
			1 Gd_3Ni_2[Ni(1)];
			1 Y_3Co_2[Co(1)]
R_4X_3	42.9	33	25 Th_3P_4[Rh(1), Ge(2), Sn(1), Pb(1), Sb(11), Bi(9)];
			8 Ho_4Co_3[Co(8)]
R_5X_4	44.4	46	42 Sm_5Ge_4[Pt(1), Au(1), Si(6), Ge(13), Sn(9), Pb(12)];
			2 Gd_5Si_4[Si(1), Sn(1)];
			1 Lu_5Si_4[Si(1)];
			1 Lu_5Pb_4[Pb(1)]
$R_{11}X_{10}$	47.6	20	20 $Ho_{11}Ge_{10}$[Ge(9), Sn(9), Sb(1), Pb(1)]
RX	50.0	310	155 CsCl[Co(1), Ni(1), Ru(3), Rh(11), Pd(7), Ir(6), Pt(1), Cu(9), Ag(15), Au(13), Mg(15), Zn(16), Cd(16), Hg(16), Al(1), In(10), Tl(14)];
			67 CrB[Ni(6), Rh(4), Pd(8), Pt(2), Au(11), Al(1), Ga(14), Si(9), Ge(11), Sn(1)];
			44 FeB[Ni(7), Pt(12), Cu(5), Ag(1), Au(6), Si(10), Ge(3)];
			29 NaCl[Sb(15), Bi(14)];
			9 DyAl[Al(9)];
			3 AuCuI[Sn(1), Pb(2)];
			3 CeAl[Al(3)];
			1 TbNi[Ni(1)]
R_6X_7	53.8	1	1 Sm_6Au_7[Au(1)]
R_3X_4	57.1	31	28 Pu_3Pd_4[Pd(14), Pt(14)];
			3 Th_3P_4[Ge(2), Sb(1)]
R_7X_{10}	58.8	1	1 Sm_7Au_{10}[Au(1)]
R_3X_5	62.5	18	18 Th_3Pt_5[Si(10), Ge(8)]
RX_2	66.7	359	122 $MgCu_2$[Mn(6), Re(1), Fe(11), Co(14), Ni(15), Ru(6), Rh(14), Os(3), Ir(15), Pt(14), Mg(6), Al(16)];
			65 $MgZn_2$[Mn(8), Tc(8), Re(14), Fe(1), Ru(10), Os(15), Mg(8), Cd(1)];
			40 $CeCu_2$[Cu(14), Ag(6), Au(4), Zn(15), Cd(1)];
			26 $CeCd_2$[Cd(13), Hg(12), Ge(1)];
			24 AlB_2[Cu(1), Zn(1), B(10), Ga(12)];
			21 $MoSi_2$[Cu(1), Ag(9), Au(10), Pb(1)];
			18 $ThSi_2$[Si(10), Ge(8)];
			13 $GdSi_2$[Si(10), Ge(3)];
			11 $ZrSi_2$[Ge(1), Sn(8), Pb(1), Sb(1)];

TABLE 13.2 (*Continued*)

Comp.	at.% X	N (compds.)	Structure types, partner elements and frequency of occurrence.
			7 $LaSb_2$[Sb(7)];
			4 $CaIn_2$[Ga(1), In(2), Tl(1)];
			4 La_2Sb[Bi(4)];
			3 $NdAu_2$[Au(3)];
			1 $HfGa_2$[Pb(1)]
RX_3	75.0	211	89 $AuCu_3$[Rh(2), Pd(16), Pt(9), In(15), Al(5), Ga(5), Tl(15), Sn(8), Pb(14)];
			36 $PuNi_3$[Fe(8), Co(13), Ni(12), Rh(1), Ir(2)];
			29 Ni_3Sn[Cd(3), Hg(16), Al(7), Ga(1), Tl(2)];
			11 BiF_3[Mg(8), Cd(3)];
			11 YZn_3[Zn(11)];
			10 $TiCu_3$[Au(10)];
			7 $CeNi_3$[Fe(1), Ni(1), Rh(5)];
			7 $ErCd_3$[Cd(7)];
			3 $HoAl_3$[Al(3)];
			3 $TiNi_3$[Al(2), Ga(1)];
			2 $DyGa_3$[Ga(2)];
			2 $BaPb_3$[Al(2)];
			1 $CeZn_3$[Zn(1)]
R_2X_7	77.8	44	24 Gd_2Co_7[Co(13), Ni(9), Rh(1), Ir(1)];
			18 Ce_2Ni_7[Co(7), Ni(9), Rh(1), Ir(1)];
			1 Ca_2Ag_7[Ag(1)];
			1 Y_2Ge_7[Ge(1)]
$R_{14}X_{51}$	78.5	25	25 $Gd_{14}Ag_{51}$[Ag(11), Au(10), Cd(2), Hg(2)]
R_3X_{11}	78.6	14	14 La_3Al_{11}[Zn(9), Al(5)]
R_5X_{19}	79.2	3	3 Ce_5Co_{19}[Co(3)]
R_6X_{23}	79.3	19	19 Th_6Mn_{23}[Mn(10), Fe(9)]
RX_4	80.0	50	17 γ-Brass[Cd(11), Hg(6)];
			14 UB_4[B(14)];
			8 $MoNi_4$[Ag(2), Au(6)];
			8 $BaAl_4$[Al(6), Ga(2)];
			2 UAl_4[Al(2)];
			1 YMn_4[Mn(1)]
R_4X_{17}	81	1	1 Er_4Ni_{17}[Ni(1)]
R_5X_{22}	81.5	1	1 Er_5Ni_{22}[Ni(1)]
$R_{13}X_{58}$	81.7	22	22 $Gd_{13}Zn_{58}$[Zn(13), Cd(8), Hg(1)]
R_5X_{24}	82.8	9	9 Ti_5Re_{24}[Re(1), Mg(8)]
RX_5	83.3	83	54 $CaZn_5$[Co(12), Ni(16), Rh(5), Ir(1), Pt(4), Cu(10), Ag(1), Au(1), Be(1), Zn(3)];
			9 $AuBe_5$[Cu(8), Ir(1)];
			6 $EuMg_5$[Mg(1),Zn(5)];
			9 RPt_5[Pt(3 + 4 + 2)];
			4 RAg_5[Ag(3 + 1)];
			1 $LuMn_5$[Mn(1)]
RX_6	85.7	46	15 YCd_6[Zn(1), Cd(14)];
			7 $CeCu_6$[Cu(7)];
			5 $SmAu_6$[Au(5)];
			3 $PrAu_6$[Au(3)];
			16 CaB_6[B(16)]
RX_7	87.5	4	4 $TbCu_7$[Cu(4)]
R_3X_{22}	88	6	6 Ce_3Zn_{22}[Zn(6)]
R_5X_{41}	89.1	1	1 Ce_5Mg_{41}[Mg(1)]
R_2X_{17}	89.5	81	48 Th_2Ni_{17}[Fe(10), Co(11), Ni(11), Mg(3), Be(1), Zn(12)];
			31 Th_2Zn_{17}[Fe(7), Co(9), Be(1), Zn(14)];
			2 U_2Zn_{17}[Be(1), Cd(1)]
RX_{11}	91.7	12	7 $BaCd_{11}$[Zn(6), Cd(1)];
			5 $BaHg_{11}$[Cd(5)]
RX_{12}	92.3	31	21 $ThMn_{12}$[Mn(8), Mg(3), Zn(10)];
			9 UB_{12}[B(9)];
			1 $CeMg_{12}$[Mg(1)]
RX_{13}	92.9	19	19 $NaZn_{13}$[Be(16), Zn(3)]
RX_{66}	98.5	10	10 YB_{66}[B(10)]

TABLE 13.3
Ionic radii for the rare earths.

R	Ionic radii (Å) r^{2+}	r^{3+}	r^{4+}	R	Ionic radii (Å) r^{2+}	r^{3+}	r^{4+}
La		1.071		Tb		0.923	0.86
Ce		1.034	0.94	Dy		0.908	
Pr		1.013	0.93	Ho		0.894	
Nd		0.995		Er		0.881	
Pm		0.979		Tm	1.01	0.869	
Sm	1.13	0.964		Yb	1.00	0.858	
Eu	1.12	0.950		Lu		0.848	
Gd		0.938		Sc		0.730	
				Y		0.905	

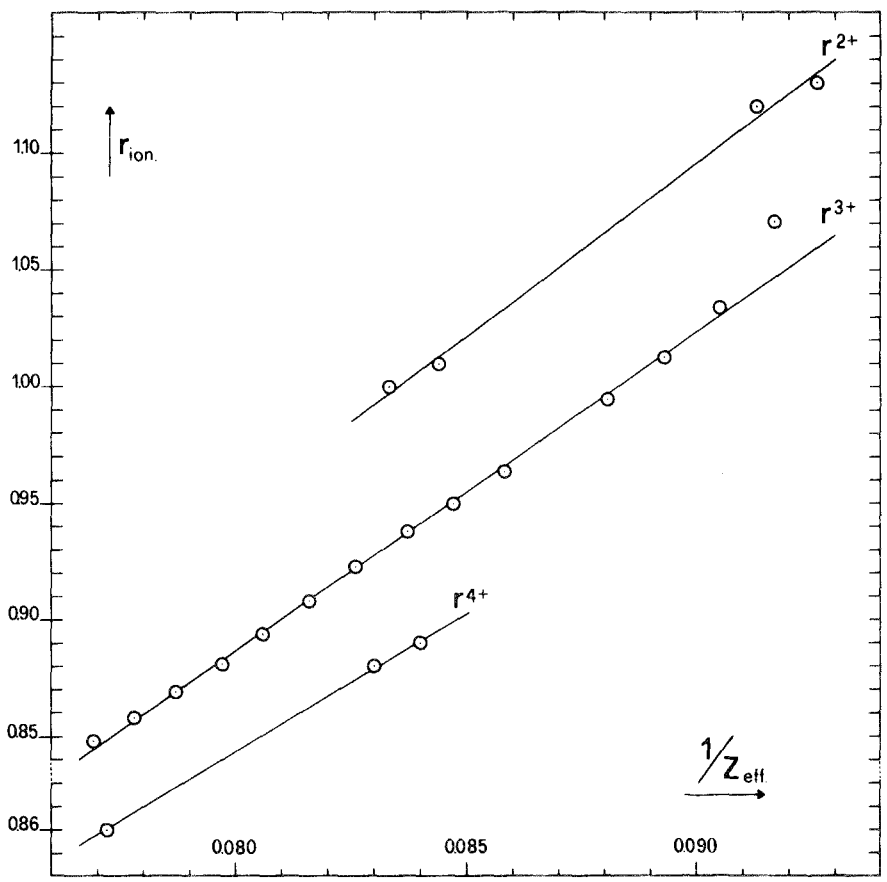

Fig. 13.19. Lanthanide ionic radii vs. reciprocal effective nuclear charge (Z_{eff}).

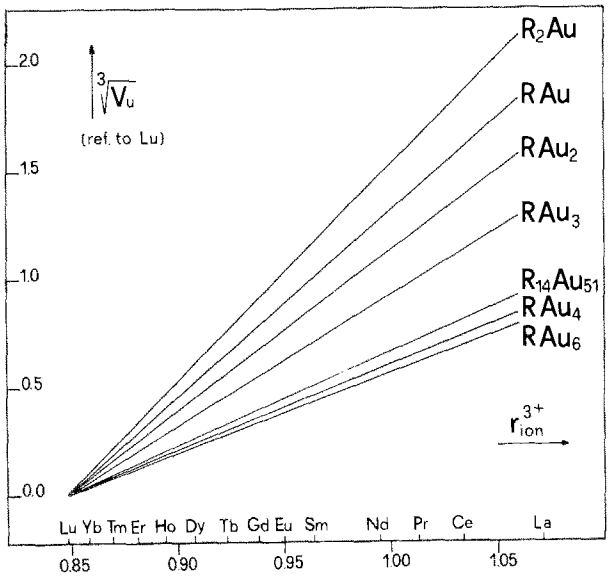

Fig. 13.20. Slopes of the cube roots of the unit formula volume $(V_u)^{1/3}$ relative to Lu or R–Au phases vs. ionic radii.

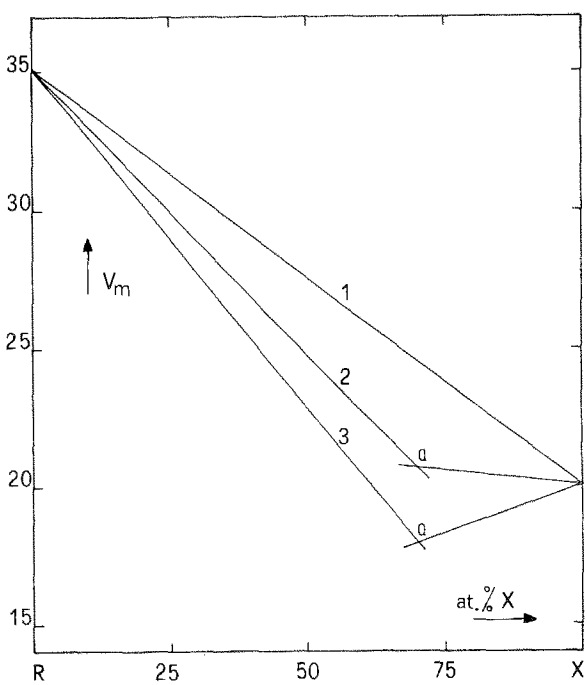

Fig. 13.21. Mean atomic volumes (V_m) vs. composition for R–X systems.

5. Mean atomic volumes and volume contractions

The properties of intermetallic compounds of the rare earths R with an element X can be examined by following their variations for a given composition by changing R along the series, or by studying the variations with the composition for a fixed R. In the second case, a useful parameter is represented by the mean atomic volume (V_m), which is obtained by dividing the volume of the unit cell by the number of atoms contained in the cell. The ideal behavior would correspond to straight lines joining the volumes of the starting elements. For the rare earth compounds three types of behavior are obtained as shown in fig. 13.21. If the experimental points lie on the straight line, type 1, compound formation occurs without volume change, points above and below the straight line correspond, respectively, to expansion and contraction of the volume. The difference between ideal and experimental values gives the relative volume changes.

Type 1 behavior has been found in the systems with Mn, and with Cu, Ag, Mg, Al for lighter lanthanides. Type 2 is the most frequent and is common to the systems with Fe, Co, Rh, Ni, Pd, Pt, Cu, Ag, Au, Mg, Zn, Cd, Al, B, Ga. Finally, type 3 has been found with Hg, In, Tl, Si, Ge, Sn, Pb. The intersection point of the two straight lines Q always corresponds to composition between 65 and 75 at.% X with the exception of Zn (90–95 at.% X) and of Mg and Cu (50–60 at.% X). Examining the behavior of all the rare earths with a given partner X, the Q point lowers progressively and it is possible to change from type 1 to types 2 and 3, in going from La to Lu.

As has already been observed, the volume contraction based on lattice constants is independent of the positional parameters and therefore gives useful information. A large contraction is related to a large decrease in the free energy of formation and corresponds to a high stability of the compound. The values of

TABLE 13.4
Mean volume contractions ($\Delta V\%$) for R_mX_n series along the periodic table of the elements.

R_mX_n						Mg	Al	Si	
R_5X_3						—	—	11.3	
RX						0.1	2.6	16.2	
RX_2						0.4	6.4	23.5	
RX_3						3.8	4.7	—	
R_mX_n	Mn	Fe	Co	Ni	Cu	Zn	Ga	Ge	
R_5X_3	—	—	—	—	—	—	4.7	12.3	
RX	—	—	—	5.5	3.5	2.6	6.1	16.4	
RX_2	2.0	10.5	13.2	14.0	2.8	1.8	11.2	25.2	
RX_3	—	6.9	13.0	10.3	—	3.0	15.0	—	
R_mX_n	Tc	Ru	Rh	Pd	Ag	Cd	In	Sn	Sb
R_5X_3	—	—	9.0	—	—	—	2.0	5.6	12.1
RX	—	14.0	12.3	6.7	2.4	3.2	4.5	—	4.4
RX_2	9.0	9.9	11.5	—	4.0	3.4	—	10.3	11.7
RX_3	—	—	7.0	10.7	—	5.0	11.9	10.0	—
R_mX_n	Re	Os	Ir	Pt	Au	Hg	Tl	Pb	Bi
R_5X_3	—	—	—	7.6	—	—	5.7	6.9	12.4
RX	—	—	14.7	6.4	3.7	8.6	11.5	—	7.7
RX_2	12.0	10.3	11.8	11.1	6.3	10.4	—	—	8.2
RX_3	—	—	—	12.0	5.5	10.6	12.7	9.2	—

$|\Delta V|\%$ in the various series of compounds with the same X always show, in accordance with the trend in the mean atomic volumes, an increase in proceeding from La to Lu. In table 13.4 the average contractions for the four series of compounds which will be discussed later are listed. The smallest contractions are observed with Mg, and the largest with Si and Ge. Fixing one of the four compositions and going along the periodic system, the smallest contractions are found with the IB and IIB elements, which corresponds again to the above mentioned classification of X elements according to their electronic structure (section 13.3).

In section 6.4 concerning the RX_3 phases a correlation which exists between the volume contractions and heats of formation is discussed.

6. Discussion of the most frequent compositions

In the following subsections the most frequent compositions R_5X_3, RX, RX_2 and RX_3 are discussed primarily from a structural point of view, by considering the structure types, their distribution in the periodic system and the correlation of the cube root of V_u with the ionic radii (figs. 13.22–13.27). For these 4 series of compounds, we have also listed the values of the lattice constants (tables 13.5–13.44).

TABLE 13.5
Crystallographic data for R_5X_3 compounds with the hexagonal Mn_5Si_3 type structure (Å).

Compd.	a	c	Compd.	a	c	Compd.	a	c
Gd_5Rh_3	8.244	6.455	Lu_5Si_3	8.21	6.14	Y_5Sn_3	8.878	6.516
Tb_5Rh_3	8.176	6.385	Sc_5Si_3	7.861	5.812	La_5Pb_3	9.526	6.994
Dy_5Rh_3	8.152	6.288	Y_5Si_3	8.403	6.303	Ce_5Pb_3	9.473	6.825
Er_5Rh_3	8.084	6.306	La_5Ge_3	8.930	6.874	Pr_5Pb_3	9.345	6.818
Yb_5Pt_3	8.337	6.251	Ce_5Ge_3	8.832	6.653	Nd_5Pb_3	9.278	6.778
Ho_5Ga_3	8.533	6.398	Pr_5Ge_3	8.818	6.686	Sm_5Pb_3	9.166	6.693
Er_5Ga_3	8.495	6.389	Nd_5Ge_3	8.772	6.636	Gd_5Pb_3	9.083	6.644
Tm_5Ga_3	8.446	6.368	Sm_5Ge_3	8.653	6.471	Tb_5Pb_3	9.022	6.602
Lu_5Ga_3	8.382	6.347	Gd_5Ge_3	8.548	6.437	Dy_5Pb_3	8.961	6.560
Sc_5Ga_3	8.074	5.951	Tb_5Ge_3	8.495	6.351	Ho_5Pb_3	8.918	6.536
Y_5Ga_3	8.576	6.479	Dy_5Ge_3	8.425	6.327	Er_5Pb_3	8.868	6.506
Ho_5In_3	8.939	6.595	Ho_5Ge_3	8.387	6.284	Tm_5Pb_3	8.837	6.489
Er_5In_3	8.889	6.558	Er_5Ge_3	8.346	6.268	Yb_5Pb_3	9.325	6.929
Tm_5In_3	8.856	6.533	Tm_5Ge_3	8.31	6.23	Lu_5Pb_3	8.768	6.441
Lu_5In_3	8.800	6.486	Yb_5Ge_3	8.360	6.421	Sc_5Pb_3	8.467	6.158
Y_5In_3	8.971	6.745	Lu_5Ge_3	8.24	6.17	Y_5Pb_3	8.971	6.614
Gd_5Tl_3	9.042	6.664	Sc_5Ge_3	7.939	5.883	La_5Sb_3	9.42	6.62
Tb_5Tl_3	8.978	6.596	Y_5Ge_3	8.472	6.348	Ce_5Sb_3	9.302	6.514
Dy_5Tl_3	8.921	6.584	La_5Sn_3	9.425	6.943	Pr_5Sb_3	9.233	6.510
Ho_5Tl_3	8.883	6.553	Ce_5Sn_3	9.328	6.788	Nd_5Sb_3	9.180	6.463
Er_5Tl_3	8.842	6.524	Pr_5Sn_3	9.283	6.765	Gd_5Sb_3	8.975	6.343
Tm_5Tl_3	8.798	6.495	Nd_5Sn_3	9.202	6.721	Tb_5Sb_3	8.920	6.304
Lu_5Tl_3	8.726	6.446	Sm_5Sn_3	9.097	6.630	Dy_5Sb_3	8.870	6.266
Y_5Tl_3	8.912	6.705	Gd_5Sn_3	9.026	6.581	Ho_5Sb_3	8.851	6.234
Sm_5Si_3	8.56	6.45	Tb_5Sn_3	8.949	6.535	Yb_5Sb_3	8.995	6.870
Gd_5Si_3	8.510	6.390	Dy_5Sn_3	8.886	6.487	Y_5Sb_3	8.911	6.296
Tb_5Si_3	8.42	6.29	Ho_5Sn_3	8.848	6.460	La_5Bi_3	9.659	6.697
Dy_5Si_3	8.37	6.26	Er_5Sn_3	8.804	6.442	Ce_5Bi_3	9.531	6.587
Ho_5Si_3	8.34	6.22	Tm_5Sn_3	8.774	6.409	Pr_5Bi_3	9.449	6.555
Er_5Si_3	8.293	6.207	Yb_5Sn_3	9.47	6.90	Nd_5Bi_3	9.370	6.513
Tm_5Si_3	8.25	6.18	Lu_5Sn_3	8.689	6.352	Gd_5Bi_3	9.158	6.419
Yb_5Si_3	8.23	6.19	Sc_5Sn_3	8.408	6.081	Tb_5Bi_3	9.101	6.365

TABLE 13.6
Crystallographic data for R_5X_3 compounds with the tetragonal Cr_5B_3 type structure (Å).

Compd.	*a*	*c*
Yb_5Ag_3	7.942	14.881
Yb_5Au_3	7.793	14.260
La_5Ga_3	8.066	14.733
Nd_5Ga_3	7.881	14.395
Sm_5Ga_3	7.796	14.280
Gd_5Ga_3	7.726	14.170
Tb_5Ga_3	7.681	14.108
Dy_5Ga_3	7.635	14.035
La_5Si_3	7.953	14.04
Ce_5Si_3	7.89	13.78
Pr_5Si_3	7.812	13.75
Nd_5Si_3	7.81	13.91
Yb_5Sn_3	7.939	14.686

TABLE 13.7
Crystallographic data for R_5X_3 compounds with the tetragonal W_5Si_3 type structure (Å).

Compd.	*a*	*c*
Ce_5Ga_3	12.44	5.571
Pr_5Ga_3	12.48	5.488
Gd_5In_3	12.340	6.048
Tb_5In_3	12.238	6.010
Dy_5In_3	12.170	5.988
Ho_5In_3	12.092	6.010
La_5Tl_3	12.799	6.347
Ce_5Tl_3	12.642	6.192
Pr_5Tl_3	12.553	6.172
Nd_5Tl_3	12.480	6.184
Sm_5Tl_3	12.346	6.140
Eu_5Pb_3	13.190	6.214

TABLE 13.8
Crystallographic data for $R_{5+x}Bi_3$ compounds with the orthorhombic Y_5Bi_3 type structure (Å).

Compd.	*a*	*b*	*c*
Gd_5Bi_3	8.227	9.531	12.081
Tb_5Bi_3	8.199	9.476	11.999
Dy_5Bi_3	8.160	9.421	11.934
Ho_5Bi_3	8.133	9.382	11.874
Er_5Bi_3	8.093	9.340	11.813
Tm_5Bi_3	8.065	9.306	11.758
Y_5Bi_3	8.190	9.420	11.975

TABLE 13.9
Crystallographic data for orthorhombic Yb_5Sb_3 (Å).

Compd.	*a*	*b*	*c*
Yb_5Sb_3	12.398	9.562	8.246

6.1. *R_5X_3 compounds*

In the periodic system the R_5X_3 phases are formed particularly with the III A IV A and V A elements, with the exception of B and Al. Recently they have also been found in the systems with Rh, Pd, Ir, while being absent for the other elements of group VIII as well as for the IB and IIB groups. These phases, however, can be formed with Ag and Au, but with divalent rare earth elements, analogous to the behavior of the alkaline earth elements. The Cr_5B_3 type structure in such cases is the preferred one.

The R_5X_3 compounds represent 7% of the examined phases and crystallize in the following 5 structure types: Mn_5Si_3(74%), table 13.5; Cr_5B_3(10%), table 13.6; W_5Si_3(9%), table 13.7; Y_5Bi_3(5%), table 13.8 (Schmidt et al., 1969); and Yb_5Sb_3, table 13.9 (Brunton and Steinfink, 1971). After Schubert (1964), the first three types can be considered to be derived from structural elements of the $CuAl_2$ and β-W types. The near-neighbor diagram of Pearson (1972) shows that the Mn_5Si_3 structure forms mainly for geometric reasons and tends to realize high coordination numbers. The Mn_5Si_3 structure contains octahedral holes, which can be filled and stabilized by small atoms such as O, C, B and N.

When a structure change occurs in a series of R_5X_3 compounds, the Mn_5Si_3

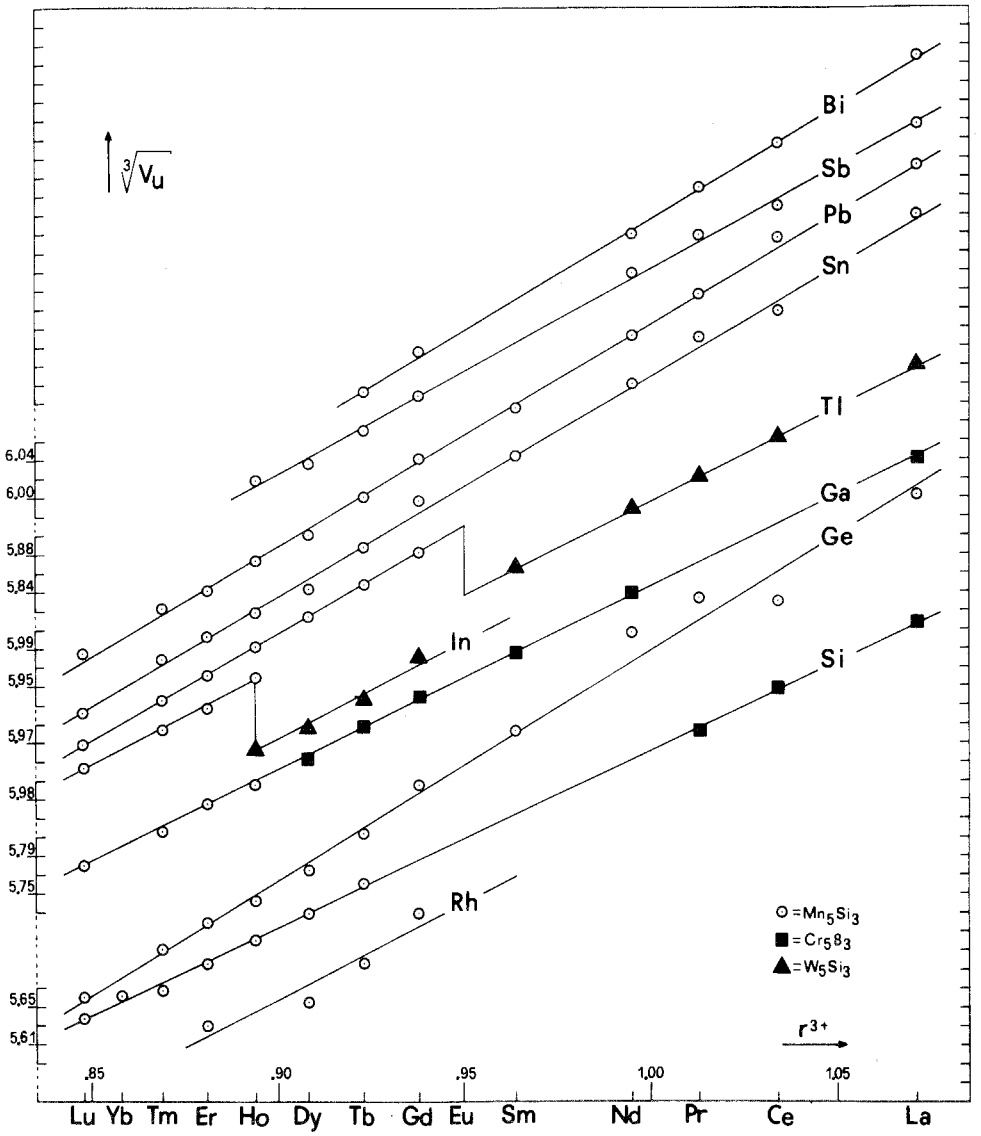

Fig. 13.22. Cubic root of V_u vs. ionic radius for R_5X_3 compounds.

type is formed for the lowest radius ratios (r_R/r_X), followed by the W_5Si_3 or Cr_5B_3 types. The change of structure can occur with (W_5Si_3–Mn_5Si_3) or without (Cr_5B_3–Mn_5Si_3) volume change, as can be seen in fig. 13.22, where the cube root of V_u is plotted vs. ionic radii. For the compound Ho_5In_3 which exists in two modifications, the high temperature form has the Mn_5Si_3 type structure and the low temperature form the W_5Si_3 one. The transformation occurs with a volume increase of 4%.

TABLE 13.10
Crystallographic data for RX compounds with the cubic CsCl type structure (Å).

Compd.	a	Compd.	a	Compd.	a	Compd.	a
YbRu	3.360	YCu	3.476	ErMg	3.737	PrHg	3.799
LuRu	3.329	LaAg	3.798	TmMg	3.746	NdHg	3.780
ScRu	3.203	CeAg	3.756	LuMg	3.727	SmHg	3.744
ScCo	3.16	PrAg	3.736	ScMg	3.595	EuHg	3.880
SmRh	3.464	NdAg	3.716	YMg	3.796	GdHg	3.719
GdRh	3.440	SmAg	3.677	LaZn	3.760	TbHg	3.690
TbRh	3.417	GdAg	3.650	CeZn	3.713	DyHg	3.676
DyRh	3.403	TbAg	3.625	PrZn	3.678	HoHg	3.660
HoRh	3.388	DyAg	3.608	NdZn	3.667	ErHg	3.645
ErRh	3.372	HoAg	3.593	SmZn	3.625	TmHg	3.632
TmRh	3.358	ErAg	3.577	EuZn	3.812	YbHg	3.731
YbRh	3.347	TmAg	3.562	GdZn	3.601	LuHg	3.607
LuRh	3.332	YbAg	3.680	TbZn	3.576	ScHg	3.487
ScRh	3.205	LuAg	3.541	DyZn	3.562	YHg	3.684
YRh	3.407	ScAg	3.416	HoZn	3.546	ScAl	3.450
HoIr	3.383	YAg	3.617	ErZn	3.533	LaIn	3.985
ErIr	3.368	PrAu	3.68	TmZn	3.515	PrIn	3.955
TmIr	3.352	NdAu	3.659	YbZn	3.629	GdIn	3.830
YbIr	3.346	SmAu	3.621	LuZn	3.491	DyIn	3.787
LuIr	3.332	GdAu	3.601	ScZn	3.354	HoIn	3.774
ScIr	3.206	TbAu	3.576	YZn	3.578	ErIn	3.745
ScNi	3.165	DyAu	3.555	LaCd	3.905	TmIn	3.739
DyPd	3.486	HoAu	3.541	CeCd	3.865	YbIn	3.807
HoPd	3.468	ErAu	3.535	PrCd	3.830	YIn	3.806
ErPd	3.458	TmAu	3.520	NdCd	3.811	LaTl	3.936
TmPd	3.440	YbAu	3.584	SmCd	3.771	CeTl	3.893
YbPd	3.447	LuAu	3.496	EuCd	3.960	PrTl	3.869
LuPd	3.417	ScAu	3.373	GdCd	3.748	NdIn	3.848
ScPd	3.283	YAu	3.559	TbCd	3.734	SmTl	3.813
ScPt	3.270	LaMg	3.962	DyCd	3.716	EuTl	3.970
SmCu	3.528	CeMg	3.901	HoCd	3.695	GdTl	3.780
GdCu	3.503	PrMg	3.877	ErCd	3.677	TbTl	3.760
TbCu	3.479	NdMg	3.860	TmCd	3.665	DyTl	3.743
DyCu	3.461	SmMg	3.832	YbCd	3.808	HoTl	3.735
HoCu	3.447	EuMg	4.102	LuCd	3.640	ErTl	3.715
ErCu	3.431	GdMg	3.808	ScCd	3.514	TmTl	3.711
TmCu	3.415	TbMg	3.778	YCd	3.719	YbTl	3.826
LuCu	3.390	DyMg	3.759	LaHg	3.864	YTl	3.751
ScCu	3.256	HoMg	3.755	CdHg	3.816		

By examining the values of the axial ratio c/a for Mn_5Si_3 phases, it can be seen that along a period or a group of the periodic system, with increasing X atomic numbers, the c/a ratio decreases from 0.76 for R_5Ga_3 to 0.69 for R_5Bi_3. Volume contractions reported in table 13.4 increase rapidly to the right of the periodic system.

Except for the series of R_5Ge_3 compounds, the plots in fig. 13.22 show a linear almost parallel trend for all the series, and the slopes are the largest of the four examined compositions.

6.2. *RX compounds*

Second only to the RX_2 phases in number, the RX compounds constitute 17% of all those examined and are represented by the eight structure types given in

TABLE 13.11
Crystallographic data for *RX* compounds with the orthorhombic CrB type structure (Å).

Compd.	*a*	*b*	*c*	Compd.	*a*	*b*	*c*
LaRh	3.986	11.144	4.249	PrGa	4.446	11.334	4.197
CeRh	3.852	10.986	4.152	NdGa	4.426	11.253	4.183
PrRh	3.905	10.910	4.210	SmGa	4.383	11.121	4.146
NdRh	3.883	10.835	4.240	GdGa	4.337	11.032	4.111
LaNi	3.907	10.810	4.396	TbGa	4.311	10.939	4.085
CeNi	3.788	10.556	4.366	DyGa	4.291	10.874	4.067
PrNi	3.816	10.503	4.354	HoGa	4.277	10.787	4.050
NdNi	3.803	10.461	4.339	ErGa	4.258	10.732	4.039
SmNi	3.776	10.358	4.291	TmGa	4.244	10.679	4.019
GdNi	3.766	10.316	4.244	LuGa	4.208	10.583	4.003
LaPd	3.945	11.032	4.660	ScGa	4.022	10.204	3.895
CePd	3.890	10.910	4.635	YGa	4.299	10.868	4.074
PrPd	3.850	10.826	4.614	EuSi	4.694	11.14	3.981
NdPd	3.832	10.776	4.609	DySi	4.237	10.494	3.818
SmPd	3.771	10.666	4.574	HoSi	4.228	10.429	3.801
EuPd	4.097	11.121	4.447	ErSi	4.193	10.39	3.790
GdPd	3.745	10.597	4.558	TmSi	4.18	10.35	3.78
TbPd	3.722	10.523	4.554	YbSi	4.178	10.31	3.768
LaPt	3.974	11.037	4.558	LuSi	4.15	10.24	3.75
CePt	3.921	10.920	4.524	ScSi	3.989	9.87	3.672
LaAu	3.95	11.20	4.78	YSi	4.260	10.528	3.84
CeAu	3.90	11.14	4.75	PrGe	4.478	11.091	4.058
PrAu	3.87	11.10	4.72	NdGe	4.449	11.020	4.032
NdAu	3.84	11.07	4.70	SmGe	4.373	10.877	4.001
SmAu	3.80	11.00	4.66	EuGe	4.725	11.202	4.112
GdAu	3.76	10.94	4.64	GdGe	4.333	10.779	3.963
TbAu	3.73	10.90	4.62	TbGe	4.295	10.705	3.944
DyAu	3.71	10.87	4.61	DyGe	4.267	10.677	3.927
HoAu	3.69	10.84	4.60	HoGe	4.244	10.620	3.913
ErAu	3.65	10.81	4.58	ErGe	4.207	10.573	3.910
TmAu	3.62	10.78	4.57	ScGe	4.007	10.06	3.762
YAl	3.884	11.522	4.385	YGe	4.270	10.693	3.940
LaGa	4.511	11.49	4.24	EuSn	4.976	11.90	4.456
CeGa	4.467	11.380	4.212				

TABLE 13.12
Crystallographic data for *RX* compounds with the orthorhombic FeB type structure (Å).

Compd.	*a*	*b*	*c*	Compd.	*a*	*b*	*c*
DyNi	7.043	4.164	5.451	NdCu	7.32	4.55	5.59
HoNi	7.022	4.140	5.435	YbCu	7.568	4.260	5.771
ErNi	6.991	4.114	5.418	YbAg	7.590	4.670	6.013
TmNi	6.959	4.099	5.398	LaAu	7.52	4.69	5.96
YbNi	6.936	4.080	5.388	CeAu	7.43	4.66	5.93
LuNi	6.912	4.073	5.366	PrAu	7.38	4.63	5.90
YNi	7.151	4.124	5.513	NdAu	7.32	4.61	5.89
PrPt	7.294	4.560	5.698	SmAu	7.25	4.57	5.85
NdPt	7.256	4.551	5.675	YbAu	7.430	4.590	5.849
SmPt	7.152	4.525	5.626	LaSi	8.44	4.015	6.049
GdPt	7.088	4.502	5.590	CeSi	8.303	3.965	5.971
TbPt	7.018	4.494	5.561	PrSi	8.265	3.940	5.930
DyPt	6.983	4.478	5.544	NdSi	8.18	3.925	5.886
HoPt	6.951	4.470	5.532	SmSi	8.093	3.894	5.817
ErPt	6.904	4.453	5.512	GdSi	7.998	3.855	5.727
TmPt	6.855	4.446	5.496	TbSi	7.944	3.826	5.696
YbPt	6.814	4.429	5.480	DySi	7.857	3.81	5.659
LuPt	6.810	4.417	5.479	HoSi	7.809	3.795	5.631
YPt	7.010	4.471	5.552	ErSi	7.772	3.785	5.599
LaCu	7.532	4.625	5.711	LaGe	8.468	4.132	6.109
CeCu	7.370	4.623	5.648	CeGe	8.354	4.082	6.033
PrCu	7.343	4.584	5.604	PrGe	8.288	4.050	5.987

TABLE 13.13
Crystallographic data for *RX* compounds with the cubic NaCl type structure (Å).

Compd.	*a*	Compd.	*a*	Compd.	*a*	Compd.	*a*
LaSb	6.488	HoSb	6.130	LaBi	6.580	DyBi	6.250
CeSb	6.429	ErSb	6.106	CeBi	6.506	HoBi	6.229
PrSb	6.366	TmSb	6.087	PrBi	6.463	ErBi	6.203
NdSb	6.322	YbSb	6.079	NdBi	6.422	TmBi	6.188
SmSb	6.271	LuSb	6.056	SmBi	6.358	LuBi	6.156
GdSb	6.217	ScSb	5.838	GdBi	6.310	ScBi	5.954
TbSb	6.179	YSb	6.155	TbBi	6.276	YBi	6.260
DySb	6.156						

TABLE 13.14
Crystallographic data for *RX* compounds with the orthorhombic DyAl type structure (Å).

Compd.	*a*	*b*	*c*
PrAl	5.967	11.773	5.738
NdAl	5.940	11.728	5.729
SmAl	5.899	11.622	5.678
GdAl	5.888	11.527	5.656
TbAl	5.834	11.370	5.621
DyAl	5.811	11.390	5.610
HoAl	5.801	11.339	5.621
ErAl	5.801	11.272	5.570
TmAl	5.77	11.24	5.56

TABLE 13.15
Crystallographic data for *RX* compounds with the orthorhombic CeAl type structure (Å).

Compd.	*a*	*b*	*c*
LaAl	9.531	7.734	5.809
CeAl	9.279	7.680	5.760
PrAl	9.221	7.635	5.706

TABLE 13.16
Crystallographic data for *RX* compounds with the tetragonal AuCu I type structure (Å).

Compd.	*a*	*c*
YbSn	4.960	4.400
EuPb	5.226	4.586
YbPb	5.085	4.443

TABLE 13.17
Crystallographic data for TbNi (Å).

Compd.	Structure	*a*	*b*	*c*	*β*
TbNi (h.T.)	Orthorhombic	21.09	4.22	5.45	—
TbNi (l.T.)	Monoclinic	21.26	4.21	5.45	97.25°

TABLE 13.18
Crystallographic data for RX_2 compounds with the cubic $MgCu_2$ type structure (Å).

Compd.	a	Compd.	a	Compd.	a	Compd.	a
$SmMn_2$	7.79	$PrCo_2$	7.306	$EuIr_2$	7.566	$EuPt_2$	7.68
$GdMn_2$	7.732	$NdCo_2$	7.298	$GdIr_2$	7.550	$GdPt_2$	7.637
$TbMn_2$	7.620	$SmCo_2$	7.262	$TbIr_2$	7.533	$TbPt_2$	7.615
$DyMn_2$	7.573	$GdCo_2$	7.257	$DyIr_2$	7.517	$DyPt_2$	7.602
$HoMn_2$	7.507	$TbCo_2$	7.210	$HoIr_2$	7.496	$HoPt_2$	7.588
YMn_2	7.692	$DyCo_2$	7.190	$ErIr_2$	7.473	$ErPt_2$	7.573
$PrRe_2$	7.572	$HoCo_2$	7.173	$TmIr_2$	7.478	$TmPt_2$	7.556
$CeFe_2$	7.302	$ErCo_2$	7.154	$YbIr_2$	7.473	$YbPt_2$	7.545
$PrFe_2$	7.467	$TmCo_2$	7.135	$LuIr_2$	7.461	YPt_2	7.590
$NdFe_2$	7.452	$YbCo_2$	7.121	$ScIr_2$	7.348	$LaMg_2$	8.787
$SmFe_2$	7.416	$LuCo_2$	7.106	YIr_2	7.500	$CeMg_2$	8.733
$GdFe_2$	7.390	$ScCo_2$	6.89	$LaNi_2$	7.365	$PrMg_2$	8.689
$TbFe_2$	7.348	YCo_2	7.216	$CeNi_2$	7.224	$NdMg_2$	8.662
$DyFe_2$	7.324	$LaRh_2$	7.646	$PrNi_2$	7.289	$SmMg_2$	8.622
$HoFe_2$	7.306	$CeRh_2$	7.546	$NdNi_2$	7.271	$GdMg_2$	8.59
$ErFe_2$	7.280	$PrRh_2$	7.575	$SmNi_2$	7.233	$LaAl_2$	8.147
$TmFe_2$	7.247	$NdRh_2$	7.564	$GdNi_2$	7.208	$CeAl_2$	8.063
$YbFe_2$	7.239	$EuRh_2$	7.500	$TbNi_2$	7.178	$PrAl_2$	8.031
$LuFe_2$	7.217	$GdRh_2$	7.514	$DyNi_2$	7.163	$NdAl_2$	8.003
$ScFe_2$	7.09	$TbRh_2$	7.492	$HoNi_2$	7.146	$SmAl_2$	7.942
YFe_2	7.358	$DyRh_2$	7.483	$ErNi_2$	7.132	$EuAl_2$	8.126
$LaRu_2$	7.703	$HoRh_2$	7.462	$TmNi_2$	7.109	$GdAl_2$	7.903
$CeRu_2$	7.538	$ErRh_2$	7.444	$YbNi_2$	7.096	$TbAl_2$	7.865
$PrRu_2$	7.623	$TmRh_2$	7.417	$LuNi_2$	7.075	$DyAl_2$	7.837
$NdRu_2$	7.613	$YbRh_2$	7.432	$ScNi_2$	6.926	$HoAl_2$	7.818
$SmRu_2$	7.577	$LuRh_2$	7.418	YNi_2	7.181	$ErAl_2$	7.796
$GdRu_2$	7.56	YRh_2	7.459	$LaPt_2$	7.777	$TmAl_2$	7.776
$LaOs_2$	7.737	$LaIr_2$	7.686	$CePt_2$	7.741	$YbAl_2$	7.881
$CeOs_2$	7.594	$CeIr_2$	7.573	$PrPt_2$	7.711	$LuAl_2$	7.742
$PrOs_2$	7.663	$PrIr_2$	7.621	$NdPt_2$	7.692	$ScAl_2$	7.579
$CeCo_2$	7.161	$NdIr_2$	7.605	$SmPt_2$	7.661	YAl_2	7.855

TABLE 13.19
Crystallographic data for RX_2 compounds with the hexagonal $MgZn_2$ type structure (Å).

Compd.	a	c	Compd.	a	c	Compd.	a	c
$PrMn_2$	5.61	9.16	$DyRe_2$	5.391	8.804	$SmOs_2$	5.336	8.879
$NdMn_2$	5.545	9.037	$HoRe_2$	5.378	8.753	$GdOs_2$	5.325	8.837
$SmMn_2$	5.511	8.976	$ErRe_2$	5.381	8.788	$TbOs_2$	5.316	8.814
$ErMn_2$	5.281	8.621	$TmRe_2$	5.359	8.761	$DyOs_2$	5.306	8.790
$TmMn_2$	5.241	8.565	$YbRe_2$	5.340	8.685	$HoOs_2$	5.296	8.760
$LuMn_2$	5.215	8.55	$LuRe_2$	5.33	8.72	$ErOs_2$	5.288	8.743
$ScMn_2$	5.033	8.19	$ScRe_2$	5.270	8.590	$TmOs_2$	5.27	8.72
$GdTc_2$	5.397	8.883	YRe_2	5.397	8.824	$YbOs_2$	5.268	8.690
$TbTc_2$	5.375	8.843	$GdRu_2$	5.274	8.904	$LuOs_2$	5.258	8.663
$DyTc_2$	5.365	8.830	$TbRu_2$	5.264	8.860	$ScOs_2$	5.183	8.495
$HoTc_2$	5.353	8.813	$DyRu_2$	5.255	8.845	YOs_2	5.307	8.786
$ErTc_2$	5.340	8.792	$HoRu_2$	5.245	8.815	$EuMg_2$	6.382	10.316
$TmTc_2$	5.334	8.775	$ErRu_2$	5.232	8.780	$TbMg_2$	6.09	9.81
$LuTc_2$	5.309	8.739	$TmRu_2$	5.238	8.765	$DyMg_2$	6.02	9.76
YTc_2	5.373	8.847	$YbRu_2$	5.221	8.746	$ErMg_2$	6.00	9.74
$PrRe_2$	5.34	8.81	$LuRu_2$	5.210	8.728	$TmMg_2$	5.97	9.74
$NdRe_2$	5.364	8.772	$ScRu_2$	5.119	8.542	$YbMg_2$	6.231	10.10
$SmRe_2$	5.303	8.804	YRu_2	5.256	8.792	$LuMg_2$	5.96	9.71
$EuRe_2$	5.316	8.742	$PrOs_2$	5.369	8.953	YMg_2	6.02	9.74
$GdRe_2$	5.455	8.841	$NdOs_2$	5.368	8.926	$YbCd_2$	5.989	9.597
$TbRe_2$	5.272	8.648						

TABLE 13.20
Crystallographic data for RX_2 compounds with the orthorhombic $CeCu_2$ type structure (Å).

Compd.	*a*	*b*	*c*
$CeCu_2$	4.425	7.057	7.475
$PrCu_2$	4.400	7.024	7.435
$NdCu_2$	4.387	7.000	7.420
$SmCu_2$	4.360	6.925	7.375
$EuCu_2$	4.434	7.250	7.553
$GdCu_2$	4.320	6.858	7.330
$TbCu_2$	4.310	6.825	7.320
$DyCu_2$	4.300	6.792	7.300
$HoCu_2$	4.280	6.759	7.290
$ErCu_2$	4.275	6.726	7.265
$TmCu_2$	4.266	6.695	7.247
$YbCu_2$	4.291	6.899	7.386
$LuCu_2$	4.245	6.627	7.220
YCu_2	4.308	6.891	7.303
$LaAg_2$	4.825	7.287	8.196
$CeAg_2$	4.800	7.090	8.205
$PrAg_2$	4.781	7.084	8.196
$NdAg_2$	4.772	7.027	8.153
$EuAg_2$	4.785	7.534	8.215
$YbAg_2$	4.671	7.204	8.178
$LaAu_2$	4.700	7.295	8.155
$CeAu_2$	4.528	7.203	8.068
$PrAu_2$	4.672	7.040	8.178
$EuAu_2$	4.67	7.33	8.14
$LaZn_2$	4.689	7.638	7.593
$CeZn_2$	4.635	7.540	7.501
$PrZn_2$	4.619	7.474	7.533
$NdZn_2$	4.599	7.409	7.566
$SmZn_2$	4.552	7.299	7.590
$EuZn_2$	4.728	7.650	7.655
$GdZn_2$	4.513	7.214	7.606
$TbZn_2$	4.492	7.142	7.595
$DyZn_2$	4.477	7.090	7.600
$HoZn_2$	4.460	7.042	7.612
$ErZn_2$	4.448	6.984	7.610
$TmZn_2$	4.433	6.944	7.604
$YbZn_2$	4.573	7.325	7.569
$LuZn_2$	4.416	6.866	7.600
YZn_2	4.504	7.143	7.664
$EuCd_2$	5.053	7.920	8.447
$LaIn_2$	4.759	7.695	9.092

TABLE 13.21
Crystallographic data for RX_2 compounds with the trigonal $CeCd_2$ type structure (Å).

Compd.	*a*	*c*
$LaCd_2$	5.074	3.565
$CeCd_2$	5.074	3.447
$PrCd_2$	5.043	3.445
$NdCd_2$	5.023	3.451
$SmCd_2$	4.979	3.458
$GdCd_2$	4.942	3.469
$TbCd_2$	4.914	3.451
$DyCd_2$	4.906	3.446
$HoCd_2$	4.897	3.431
$ErCd_2$	4.886	3.421
$TmCd_2$	4.880	3.413
$LuCd_2$	4.865	3.382
YCd_2	4.882	3.501
$LaHg_2$	4.960	3.650
$CeHg_2$	4.942	3.540
$PrHg_2$	4.918	3.539
$NdHg_2$	4.904	3.520
$SmHg_2$	4.877	3.515
$EuHg_2$	4.978	3.710
$GdHg_2$	4.854	3.496
$TbHg_2$	4.833	3.487
$DyHg_2$	4.816	3.466
$HoHg_2$	4.798	3.470
$ErHg_2$	4.790	3.442
$YbHg_2$	4.896	3.534
YHg_2	4.771	3.536
$EuGe_2$	4.102	4.995

TABLE 13.22
Crystallographic data for RX_2 compounds with the hexagonal AlB_2 type structure (Å).

Compd.	*a*	*c*
$LaCu_2$	4.347	3.812
$ScZn_2$	4.363	3.196
GdB_2	3.31	3.94
TbB_2	3.28	3.86
DyB_2	3.285	3.835
HoB_2	3.27	3.81
ErB_2	3.28	3.79
TmB_2	3.25	3.74
YbB_2	3.250	3.731
LuB_2	3.246	3.704
ScB_2	3.146	3.517
YB_2	3.298	3.843
$LaGa_2$	4.320	4.416
$CeGa_2$	4.321	4.320
$PrGa_2$	4.272	4.298
$NdGa_2$	4.27	4.27
$SmGa_2$	4.238	4.187
$EuGa_2$	4.348	4.513
$GdGa_2$	4.220	4.138
$TbGa_2$	4.209	4.095
$DyGa_2$	4.200	4.066
$HoGa_2$	4.192	4.044
$ErGa_2$	4.186	4.018
YGa_2	4.198	4.095

TABLE 13.23
Crystallographic data for RX_2 compounds with the tetragonal $MoSi_2$ type structure (Å).

Compd.	*a*	*c*
$ScCu_2$	3.290	8.388
$GdAg_2$	3.728	9.292
$TbAg_2$	3.710	9.250
$DyAg_2$	3.697	9.215
$HoAg_2$	3.683	9.183
$ErAg_2$	3.669	9.155
$TmAg_2$	3.650	9.135
$LuAg_2$	3.632	9.105
$ScAg_2$	3.524	8.941
YAg_2	3.691	9.241
$GdAu_2$	3.730	9.020
$TbAu_2$	3.707	8.989
$DyAu_2$	3.693	8.963
$HoAu_2$	3.677	8.941
$ErAu_2$	3.663	8.923
$TmAu_2$	3.647	8.900
$YbAu_2$	3.632	8.886
$LuAu_2$	3.623	8.876
$ScAu_2$	3.509	8.728
YAu_2	3.685	8.965
$LuPb_2$	3.706	13.120

TABLE 13.24
Crystallographic data for RX_2 compounds with the tetragonal $ThSi_2$ type structure (Å).

Compd.	*a*	*c*
$LaSi_2$	4.295	13.775
$CeSi_2$	4.192	13.86
$PrSi_2$	4.22	13.71
$NdSi_2$	4.111	13.56
$SmSi_2$	4.08	13.51
$EuSi_2$	4.29	13.66
$GdSi_2$	4.10	13.61
$DySi_2$	4.03	13.38
YSi_2	4.04	13.42
$LaGe_2$	4.330	14.245
$CeGe_2$	4.275	14.06
$PrGe_2$	4.255	13.94
$NdGe_2$	4.240	13.89
$SmGe_2$	4.175	13.81
$GdGe_2$	4.11	13.74
$DyGe_2$	4.05	13.65
YGe_2	4.060	13.683

TABLE 13.25
Crystallographic data for RX_2 compounds with the orthorhombic $GdSi_2$ type structure (Å).

Compd.	*a*	*b*	*c*
$LaSi_2$	4.271	4.182	14.035
$CeSi_2$	4.19	4.13	13.92
$PrSi_2$	4.20	4.16	13.76
$NdSi_2$	4.155	4.125	13.67
$SmSi_2$	4.105	4.035	13.46
$GdSi_2$	4.09	4.01	13.44
$TbSi_2$	4.057	3.97	13.375
$DySi_2$	4.04	3.945	13.34
$HoSi_2$	4.03	3.944	13.30
YSi_2	4.048	3.95	13.36
$LaGe_2$	4.405	4.305	14.165
$CeGe_2$	4.35	4.25	14.07
$GdGe_2$	4.130	4.096	13.76

TABLE 13.26
Crystallographic data for RX_2 compounds with the orthorhombic $ZrSi_2$ type structure (Å).

Compd.	*a*	*b*	*c*
$ScGe_2$	3.888	14.873	3.793
$GdSn_2$	4.428	16.410	4.322
$TbSn_2$	4.404	16.301	4.307
$DySn_2$	4.391	16.233	4.300
$HoSn_2$	4.377	16.185	4.292
$ErSn_2$	4.365	16.132	4.285
$TmSn_2$	4.357	16.062	4.285
$LuSn_2$	4.343	15.997	4.273
YSn_2	4.394	16.340	4.305
YPb_2	4.550	16.46	4.450
$YbSb_2$	4.54	16.63	4.26

TABLE 13.27
Crystallographic data for RX_2 compounds with the orthorhombic $LaSb_2$ type structure (Å).

Compd.	*a*	*b*	*c*
$LaSb_2$	6.314	6.175	18.56
$CeSb_2$	6.295	6.124	18.21
$PrSb_2$	6.230	6.063	17.89
$NdSb_2$	6.207	6.098	18.08
$SmSb_2$	6.171	6.051	17.89
$GdSb_2$	6.157	5.986	17.83
$TbSb_2$	6.123	5.969	17.72

TABLE 13.28
Crystallographic data for RX_2 compounds with the hexagonal $CaIn_2$ type structure (Å).

Compd.	*a*	*c*
$YbGa_2$	4.456	7.187
$EuIn_2$	4.975	7.869
$YbIn_2$	4.889	7.630
$EuTl_2$	5.035	7.964

TABLE 13.29
Crystallographic data for RX_2 compounds with the triclinic La_2Sb type structure (Å).

Compd.	a	b	c	α	β	γ
$LaBi_2$	6.575	13.140	11.970	91.724°	102.620°	91.998°
$CeBi_2$	6.528	13.056	11.852	91.515°	103.020°	92.199°
$PrBi_2$	6.510	13.017	11.822	91.480°	102.920°	92.305°
$NdBi_2$	6.468	12.980	11.858	91.723°	104.013°	92.361°

TABLE 13.30
Crystallographic data for RX_2 compounds with the tetragonal $NdAu_2$ type structure (Å).

Compd.	a	c
$PrAu_2$	16.0	9.36
$NdAu_2$	15.93	9.33
$SmAu_2$	15.70	9.28

TABLE 13.31
Crystallographic data for $PrPb_2$ with the tetragonal $HfGa_2$ type structure (Å).

Compd.	a	c
$PrPb_2$	4.66	32.0

TABLE 13.32
Crystallographic data for RX_3 compounds with the cubic $AuCu_3$ type structure (Å).

Compd.	a	Compd.	a	Compd.	a	Compd.	a
$CeRh_3$	4.022	$YbPt_3$	4.047	$HoIn_3$	4.573	$LaSn_3$	4.769
$ScRh_3$	3.909	$LuPt_3$	4.029	$ErIn_3$	4.564	$CeSn_3$	4.721
$LaPd_3$	4.235	$ScPt_3$	3.954	$TmIn_3$	4.558	$PrSn_3$	4.716
$CePd_3$	4.132	YPt_3	4.069	$YbIn_3$	4.615	$NdSn_3$	4.706
$PrPd_3$	4.138	$ErAl_3$	4.213	$LuIn_3$	4.553	$SmSn_3$	4.687
$NdPd_3$	4.128	$TmAl_3$	4.202	$ScIn_3$	4.477	$EuSn_3$	4.744
$SmPd_3$	4.105	$YbAl_3$	4.202	YIn_3	4.593	$GdSn_3$	4.678
$EuPd_3$	4.091	$LuAl_2$	4.186	$LaTl_3$	4.806	$YbSn_3$	4.681
$GdPd_3$	4.092	$ScAl_3$	4.103	$CeTl_3$	4.767	$LaPb_3$	4.904
$TbPd_3$	4.077	$HoGa_3$	4.226	$PrTl_3$	4.747	$CePb_3$	4.874
$DyPd_3$	4.068	$ErGa_3$	4.212	$NdTl_3$	4.733	$PrPb_3$	4.863
$HoPd_3$	4.063	$TmGa_3$	4.196	$SmTl_3$	4.708	$NdPb_3$	4.852
$ErPd_3$	4.055	$LuGa_3$	4.180	$EuTl_3$	4.718	$SmPb_3$	4.835
$TmPd_3$	4.040	$ScGa_3$	4.096	$GdTl_3$	4.690	$EuPb_3$	4.917
$YbPd_3$	4.054	$LaIn_3$	4.735	$TbTl_3$	4.680	$GdPb_3$	4.824
$LuPd_3$	4.029	$CeIn_3$	4.689	$DyTl_3$	4.672	$TbPb_3$	4.810
$ScPd_3$	3.981	$PrIn_3$	4.672	$HoTl_3$	4.666	$DyPb_3$	4.806
YPd_3	4.074	$NdIn_3$	4.655	$ErTl_3$	4.661	$HoPb_3$	4.800
$TbPt_3$	4.083	$SmIn_3$	4.626	$TmTl_3$	4.657	$ErPb_3$	4.797
$DyPt_3$	4.073	$GdIn_3$	4.607	$YbTl_3$	4.770	$TmPb_3$	4.794
$HoPt_3$	4.064	$TbIn_3$	4.590	$LuTl_3$	4.653	$YbPb_3$	4.863
$ErPt_3$	4.053	$DyIn_3$	4.579	YTl_3	4.680	YPb_3	4.818
$TmPt_3$	4.042						

TABLE 13.33
Crystallographic data for RX_3 compounds with the rhombohedral $PuNi_3$ type structure (hexagonal lattice parameters, Å).

Compd.	a	c	Compd.	a	c	Compd.	a	c
$SmFe_3$	5.187	24.91	$GdCo_3$	5.038	24.51	$LaNi_3$	5.084	25.05
$GdFe_3$	5.166	24.71	$TbCo_3$	5.018	24.40	$PrNi_3$	5.035	24.92
$TbFe_3$	5.145	24.60	$DyCo_3$	5.000	24.36	$NdNi_3$	5.027	24.72
$DyFe_3$	5.120	24.57	$HoCo_3$	4.989	24.29	$SmNi_3$	5.004	24.60
$HoFe_3$	5.097	24.49	$ErCo_3$	4.976	24.23	$GdNi_3$	4.990	24.49
$ErFe_3$	5.090	24.47	$TmCo_3$	4.968	24.17	$TbNi_3$	4.973	24.44
$TmFe_3$	5.075	24.43	$YbCo_3$	4.946	24.18	$DyNi_3$	4.965	24.35
$LuFe_3$	5.052	24.33	$LuCo_3$	4.950	24.09	$HoNi_3$	4.953	24.31
YFe_3	5.137	24.61	YCo_3	5.010	24.31	$ErNi_3$	4.942	24.24
$CeCo_3$	4.965	24.72	$LaRh_3$	5.326	26.46	$TmNi_3$	4.937	24.21
$PrCo_3$	5.066	24.77	$LaIr_3$	5.370	26.34	$YbNi_3$	4.919	24.15
$NdCo_3$	5.068	24.76	$CeIr_3$	5.288	26.18	YNi_3	4.974	24.41
$SmCo_3$	5.053	24.59						

TABLE 13.34
Crystallographic data for RX_3 compounds with the hexagonal Ni_3Sn type structure (Å).

Compd.	a	c	Compd.	a	c	Compd.	a	c
$GdCd_3$	6.621	4.933	$TbHg_3$	6.565	4.887	$CeAl_3$	6.545	4.609
$TbCd_3$	6.585	4.925	$DyHg_3$	6.543	4.880	$PrAl_3$	6.504	4.604
$ScCd_3$	6.330	4.853	$HoHg_3$	6.526	4.872	$NdAl_3$	6.472	4.606
$LaHg_3$	6.808	4.951	$ErHg_3$	6.505	4.866	$SmAl_3$	6.381	4.598
$CeHg_3$	6.755	4.957	$TmHg_3$	6.491	4.856	$GdAl_3$	6.328	4.595
$PrHg_3$	6.724	4.937	$YbHg_3$	6.596	5.021	YAl_3	6.276	4.582
$NdHg_3$	6.695	4.929	$LuHg_3$	6.467	4.851	$TbGa_3$	6.273	4.507
$SmHg_3$	6.632	4.900	$ScHg_3$	6.369	4.762	$LaTl_3$	6.92	5.53
$EuHg_3$	6.794	5.074	YHg_3	6.541	4.870	$EuTl_3$	7.018	5.313
$GdHg_3$	6.591	4.889	$LaAl_3$	6.662	4.609			

TABLE 13.35
Crystallographic data for RX_3 compounds with the cubic BiF_3 type structure (Å).

Compd.	a	Compd.	a
$LaMg_3$	7.509	$GdMg_3$	7.31
$CeMg_3$	7.436	$TbMg_3$	7.32
$PrMg_3$	7.430	$CeCd_3$	7.228
$NdMg_3$	7.410	$PrCd_3$	7.200
$SmMg_3$	7.327	$NdCd_3$	7.182

TABLE 13.36
Crystallographic data for RX_3 compounds with the orthorhombic YZn_3 type structure (Å).

Compd.	a	b	c
$PrZn_3$	6.655	4.590	10.380
$NdZn_3$	6.713	4.547	10.288
$SmZn_3$	6.725	4.489	10.199
$GdZn_3$	6.718	4.439	10.158
$TbZn_3$	6.690	4.411	10.104
$DyZn_3$	6.700	4.398	10.06
$HoZn_3$	6.697	4.366	10.099
$ErZn_3$	6.678	4.350	10.024
$TmZn_3$	6.661	4.330	9.997
$LuZn_3$	6.650	4.300	9.974
YZn_3	6.690	4.405	10.111

TABLE 13.37
Crystallographic data for RX_3 compounds with the orthorhombic $TiCu_3$ type structure (Å).

Compd.	*a*	*b*	*c*
$SmAu_3$	6.397	4.966	5.068
$GdAu_3$	6.170	5.004	5.098
$TbAu_3$	6.115	4.992	5.096
$DyAu_3$	6.091	4.977	5.088
$HoAu_3$	6.059	4.965	5.079
$ErAu_3$	6.030	4.952	5.082
$TmAu_3$	6.016	4.942	5.074
$YbAu_3$	5.982	4.926	5.075
$LuAu_3$	5.962	4.921	5.072
YAu_3	6.096	5.084	4.968

TABLE 13.38
Crystallographic data for RX_3 compounds with the hexagonal $CeNi_3$ type structure (Å).

Compd.	*a*	*c*
$LaRh_3$	5.305	17.59
$NdRh_3$	5.282	17.52
$SmRh_3$	5.255	17.46
$GdRh_3$	5.235	17.40
YRh_3	5.230	17.38
$CeNi_3$	4.97	16.55

TABLE 13.39
Crystallographic data for RX_3 compounds with the orthorhombic $ErCd_3$ type structure (Å).

Compd.	*a*	*b*	*c*
$TbCd_3$	6.963	10.97	4.851
$DyCd_3$	7.052	10.828	4.833
$HoCd_3$	7.077	10.765	4.818
$ErCd_3$	7.094	10.678	4.804
$TmCd_3$	7.104	10.617	4.795
$LuCd_3$	7.140	10.517	4.771
YCd_3	7.044	10.864	4.837

TABLE 13.40
Crystallographic data for RX_3 compounds with the rhombohedral $HoAl_3$ type structure (hexagonal lattice parameters, Å).

Compd.	*a*	*c*
$DyAl_3$	6.073	35.89
$HoAl_3$	6.056	35.83
$ErAl_3$	6.025	35.65

TABLE 13.41
Crystallographic data for RX_3 compounds with the hexagonal $TiNi_3$ type structure (Å).

Compd.	*a*	*c*
$DyAl_3$	6.090	9.533
$HoAl_3$	6.06	9.53
$HoGa_3$	6.078	9.417

TABLE 13.42
Crystallographic data for RX_3 compounds with the hexagonal $DyGa_3$ type structure (Å).

Compd.	*a*	*c*
$DyGa_3$	6.157	22.93
$HoGa_3$	6.161	23.04

TABLE 13.43
Crystallographic data for RX_3 compounds with the rhombohedral $BaPb_3$ type structure (hexagonal lattice parameters, Å).

Compd.	*a*	*c*
$TbAl_3$	6.175	21.172
YAl_3	6.195	21.137

TABLE 13.44
Crystallographic data for orthorhombic $CeZn_3$ (Å).

Compd.	*a*	*b*	*c*
$CeZn_3$	6.644	4.627	10.437

table 13.2. The NaCl type (9%), table 13.13, is found only with the non-metallic elements of the VA and VIA groups and the partial ionic character of these elements is undoubtedly responsible for the formation of these phases. The remaining 7 types are more metallic in character. The AuCu I type, table 13.16, has been observed only for divalent lanthanides (and alkaline earth elements)

with Sn and Pb (Palenzona and Cirafici, 1976). Two other types are proper of the *R*Al compounds, tables 13.14 and 13.15; while CsCl (50%), table 13.10; CrB (22%), table 13.11; and FeB (14%), table 13.12 are spread throughout the periodic system. Finally, the two modifications of TbNi, table 13.17 (Lemaire and Paccard, 1970), represent intermediate modifications between CrB and FeB.

Structural interrelations between CrB and FeB types have been discussed by Hohnke and Parthé (1966) and those for CeAl and DyAl by Bècle and Lemaire (1967). In all these types there are present structural units characterized by trigonal prisms formed by *R* atoms and centered by zigzag *X* chains. The different packing of these prisms gives rise to the different structure types. For the CsCl type it is also possible to find trigonal prisms obtained by dividing the unit cell with a diagonal plane (110) and compressing along the direction (001) (Bècle and Lemaire, 1967). From this point of view, the compounds with these structure types can be distinguished from the compounds with other compositions. Therefore it is reasonable that these three types, CsCl, CrB and FeB, often appear together as modifications of the same compound or as structural changes along a *RX* series.

In a series of *RX* compounds the CsCl type is found generally for the rare earths with the smallest atomic radius, while the other types are more dependent on the *X* element. With the group VIII metals, in going from Lu to La, the sequence CsCl–FeB–CrB is found, in other cases the sequence is CsCl–CrB–FeB.

For the FeB and CrB types a further division can be made by considering the dimensions of the trigonal prisms which build up the structure. With both the group VIII and Cu-group elements, prisms are shortened (type II), in other cases they are elongated (type I) (Hohnke and Parthé, 1966). The relative prism dimensions remain unaltered in the change from FeB to CrB and vice versa. The two types differ only in the packing of the prisms.

When an *RX* compound exists in two or three modifications, the order of occurrence depends on the *X* element. For example, with decreasing temperature, the sequence for the *R*Pd compounds is CsCl–FeB–CrB, while for the *R*Au compounds the sequence is CsCl–CrB–FeB. In all cases the high temperature stable form is the CsCl type. At high temperatures the transformations are sufficiently fast and easily detected. At low temperatures the transition points show large differences between heating and cooling determinations and the heats of transformation are generally low (Palenzona and Cirafici, 1975a).

Following Pearson (1972) these three types are mainly determined by *R*–*X* contacts and the final choice in some cases can be related to an *X*–*X* bond factor, like for *R*Ge and *R*Si.

The trend of the cube root of V_u is reported in figs. 13.23 and 13.24. For CsCl type compounds the straight lines have slopes near $\frac{1}{2}\sqrt{3}$, which corresponds to the additivity of the interatomic *R*–*X* distances, as in a hard sphere model. Lattice constants of these compounds can therefore be estimated by summing the rare earth ionic radius with an "apparent" radius for the partner element and multiplying this sum by $2\sqrt{3}$ (table 13.45).

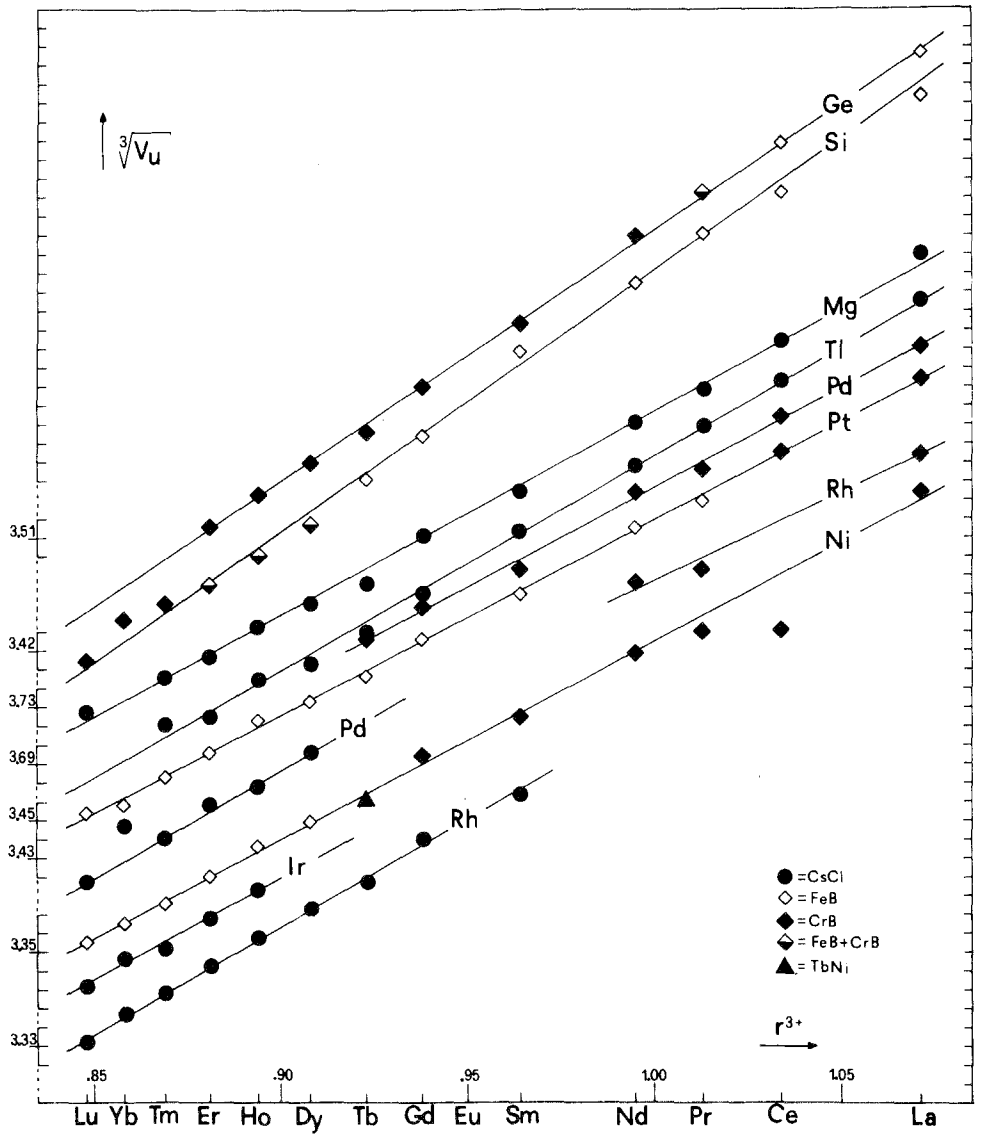

Fig. 13.23. Cubic root of V_u vs. ionic radius for RX compounds, where X = Mg, Si, Ni, Ge, Rh, Pd, Ir, Pt or Tl.

TABLE 13.45
Apparent radii for X elements in RX compounds, CsCl-type.

Rh	2.039	Ag	2.219	Hg	2.275
Pd	2.111	Au	2.174	Tl	2.337
Ru	2.035	Mg	2.369	In	2.373
Ir	2.036	Zn	2.177		
Cu	2.090	Cd	2.307		

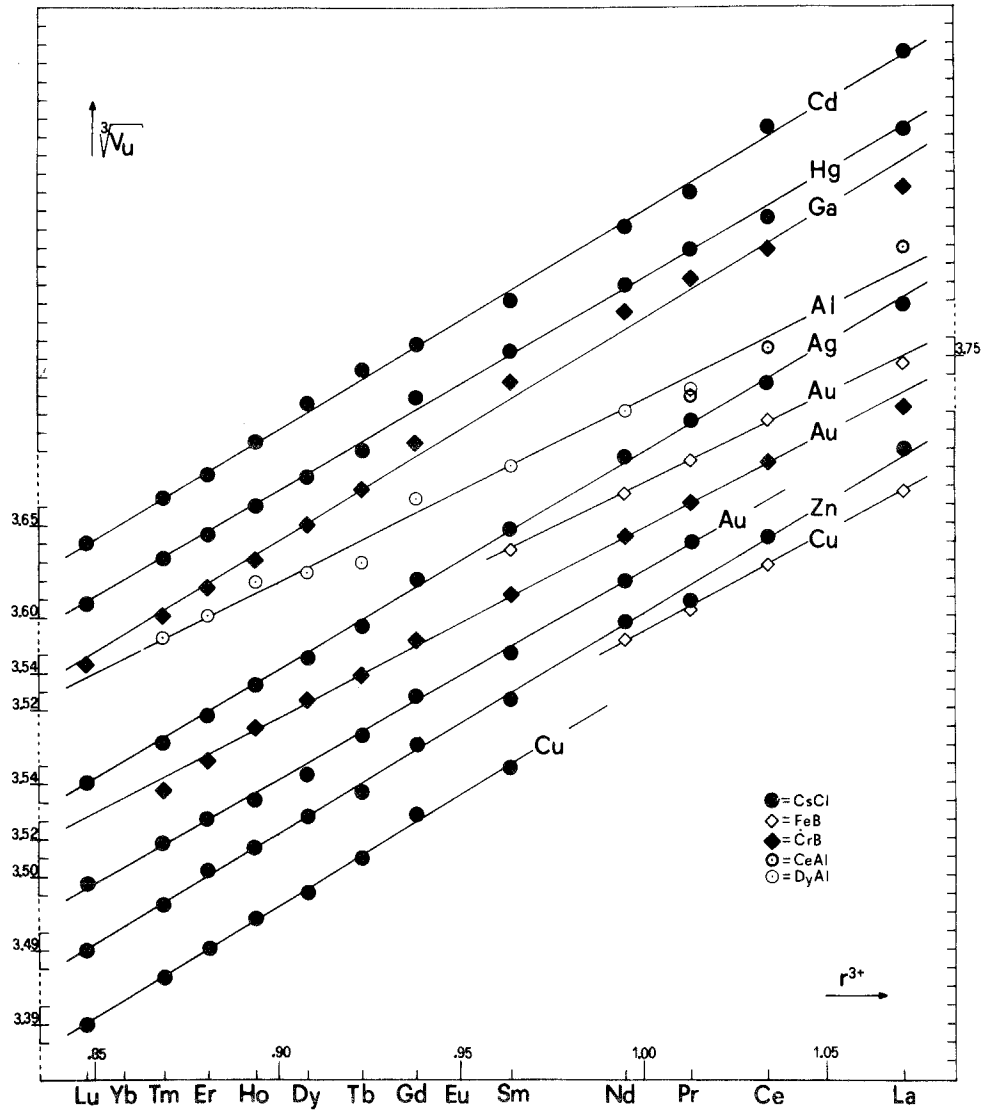

Fig. 13.24. Cubic root of V_u vs. ionic radius for RX compounds, where X = Al, Cu, Zn, Ga, Ag, Cd, Au or Hg.

For the other types the points lie again on straight lines, but with different slopes. CrB and FeB compounds characterized by type I prisms (X = Ga, Ge, Si) give slopes greater than $\frac{1}{2}\sqrt{3}$, while those of type II prisms give slopes less than $\frac{1}{2}\sqrt{3}$.

6.3. RX_2 compounds

The RX_2 compounds are the largest family, are unique because this composition is found to be common to all examined R–X systems (except R–Be and perhaps R–Pd), see fig. 13.17, and represent 20% of all rare earth compounds. They crystallize with 14 structure types (table 13.2) which, excluding those with only a few representatives, tables 13.27 and 13.29, correspond to five principal families: 1) Laves phases (52%), tables 13.18 and 13.19; 2) AlB_2, table 13.22, and derivable types ($CeCd_2$, table 13.21 and $CaIn_2$, table 13.28) (15%); 3) $CeCu_2$, table 13.20 and $NdAu_2$, table 13.30, deformations of AlB_2 (12%); 4) $ThSi_2$, table 13.24, and $GdSi_2$, table 13.25, related to AlB_2 (9%); 5) $MoSi_2$, table 13.23, and derivable types ($ZrSi_2$, table 13.26, and $HfGa_2$, table 13.31 (9%)).

The structural relations among AlB_2, $CeCd_2$ and $CaIn_2$ are evident from their crystallographic description. The $CeCu_2$ type can be derived from AlB_2 by describing the latter as an ideal orthorhombic unit cell with $a' = a(AlB_2)$, $b' = 2c$, $c' = a\sqrt{3}$ and by slightly changing the atomic positions(**Larson and Cromer**, 1961). The resemblance between AlB_2 and $ThSi_2$ (transposition structures) has been pointed out by Brown (1961), and by Parthé (1965), and that between $ThSi_2$ and $GdSi_2$ by Pearson (1972). A structure type not easily derivable from the preceeding ones is $MoSi_2$, which, however, is related to the $ZrSi_2$ and $HfGa_2$ types (Schubert, 1964).

All of the preceeding structures are spread along the periodic system following a sequence formed by: Laves phases with group VIII elements; $CeCu_2$, $MoSi_2$ with IB group metals; AlB_2, $CeCu_2$ with IIB metals and Ga; $ThSi_2$, $ZrSi_2$ and their derivable types with IV A group. A particular situation is found for Mg and Al, which again form Laves phases. The Si and Ge compounds can be defect compounds, with compositions RSi_{2-x} and RGe_{2-x}, and with AlB_2. $ThSi_2$ or derived structures (Parthé, 1965; Schmidt et al., 1972).

It has been observed by Raman (1967) that increasing the valence electron concentration (VEC) the structural sequence should be: $MgCu_2$–$MgZn_2$–AlB_2–$ThSi_2$–$GdSi_2$–$ZrSi_2$–$MoSi_2$. This sequence is only partially verified for RX_2 compounds, primarily because it is difficult to define a VEC, especially for transition metals. With all B group elements, the above sequence seems to agree with the increasing of VEC, except for the $MoSi_2$ type, which is realized only with Ag and Au.

The influence of VEC can be examined by comparing the behavior of the lanthanides with Ca and Th, which have similar atomic radii, but different valences. The situation for the structures of Ca compounds is similar to that of La, with some exceptions which are also found with the divalent Eu and Yb. Therefore VEC is not a determining factor for Ca with respect to La. With Th the situation is different, because the structural sequence, which is similar to that for the rare earths, is shifted leftward in the periodic system. The AlB_2 type already appears for $ThNi_2$ and continues with Cu, Ag and Au. The $ThSi_2$ type is found in the III A group for $ThGa_2$. For the rare earths the AlB_2 and $ThSi_2$ types are found to begin at Cu and Si, respectively.

Hexagonal Laves phases exhibit c/a values near to the ideal 1.63 value in compounds with Mn and Re and slightly higher values for $R\mathrm{Tc}_2$ (1.65). These values for $R\mathrm{Ru}_2$ (1.69–1.67) and for $R\mathrm{Os}_2$ (1.67–1.65) are high, but decrease with increasing lanthanide atomic number.

The variations of the cube roots of V_u are reported in figs. 13.25 and 13.26 and show a regular, linear decrease from La to Lu. In this case it is impossible to obtain the lattice constants by assuming the same hard spheres model as for

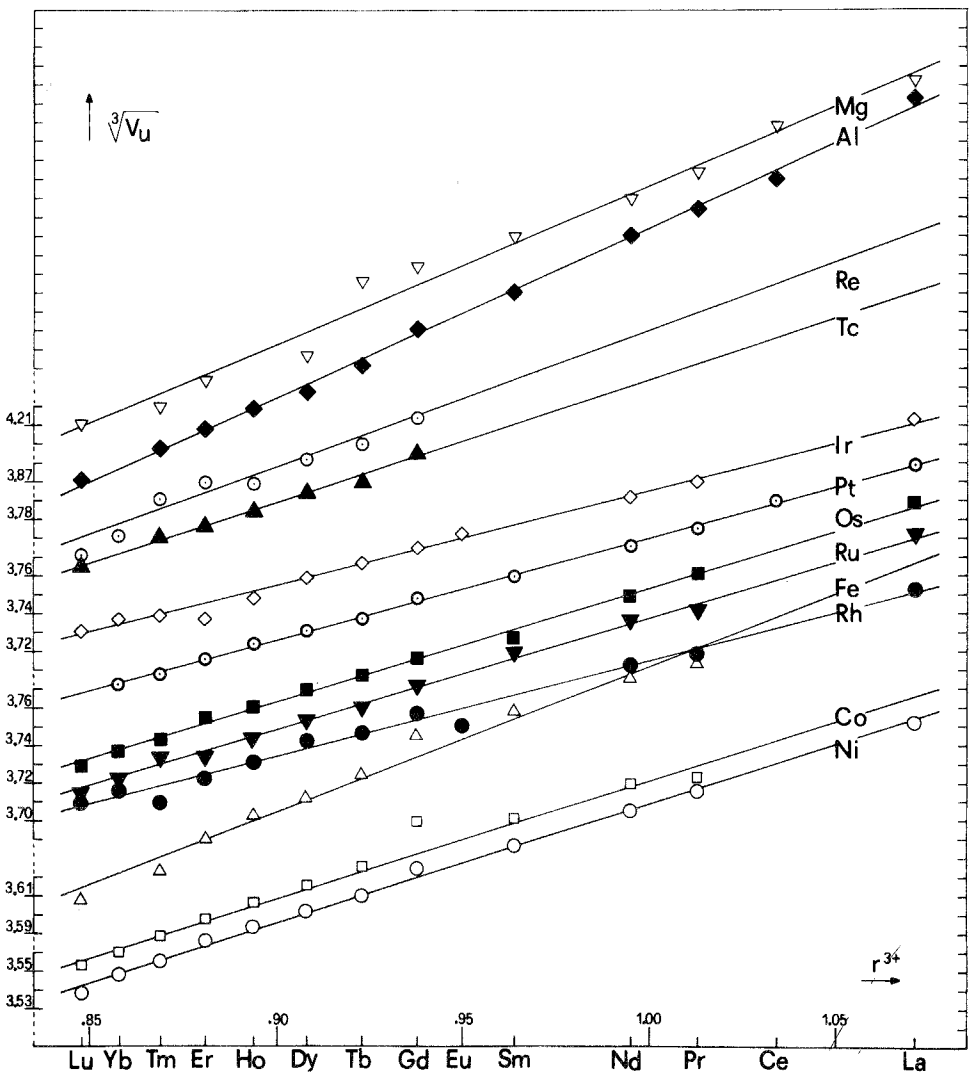

Fig. 13.25. Cubic root of V_u vs. ionic radius for the RX_2 Laves-phase compounds. where X = Mg, Al, Fe, Co, Ni, Tc, Ru, Rh, Re, Os, Ir or Pt.

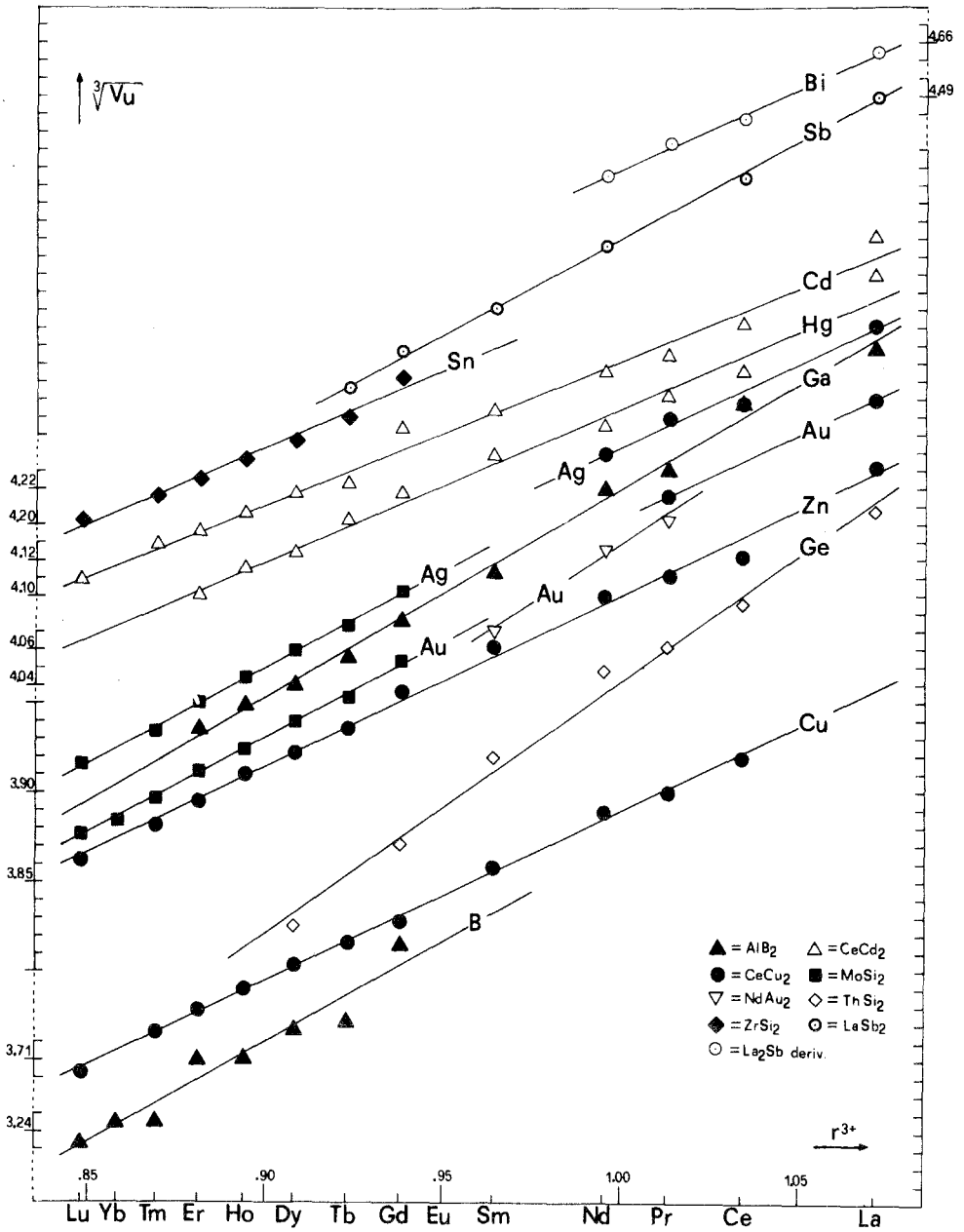

Fig. 13.26. Cubic root of V_u vs. ionic radius for RX_2 compounds, where X = B, Cu, Zn, Ga, Ge, Ag, Cd, Sn, Sb, Au, Hg or Bi.

CsCl type compounds, because the X–X distances decrease from La to Lu compounds. The variations in this decrease of lattice constants indicate a higher or lower deformability of the structure, which is dependent upon changing rare earth ionic radius. Comparing the slopes of the straight lines of figs 13.25 and 13.26, a regular behavior can be found. The RX_2 phases with group VIII elements have the smallest slopes (0.5–0.8); those with elements of IB and IIB groups change from 0.8 to 1.1; those with IIIA metals go from 0.9 to 1.2 and, finally, with IVA elements this value rises to 1.4. Such trends correspond again to the division of the X elements according to their electronic structure, in d, s and sp, which yields the classification presented in section 13.3. The behavior of the ΔV_m shown in table 13.4 is in agreement with the same division of X elements. The smallest contractions occur in the cases of the IB and IIB metals.

6.4. *RX_3 compounds*

The 13 structure types observed for RX_3 compounds (11% of the total) can be grouped into four families: 1) Ni_3Sn, table 13.34, and derivable types – $BaPb_3$, table 13.43, $DyGa_3$, table 13.42, Ni_3Ti, table 13.41, $HoAl_3$, table 13.40, $AuCu_3$, table 13.32 (60%); $TiCu_3$, table 13.37 (5%) and $ErCd_3$, table 13.39 (3%), obtainable by deformation; 2) $CeNi_3$, table 13.38, and $PuNi_3$, table 13.33 (20%); 3) $CeZn_3$, table 13.44, and YZn_3, table 13.36 (6%); 4) BiF_3, table 13.35 (5%). The RX_3 composition is formed by almost all the elements, with the exception of the group VIIB metals, Ru, Os, Cu, Be, B, Si, Ge, Sb, and Bi, see fig. 13.17.

Ni_3Sn and $AuCu_3$ represent the extreme types of an interesting series of structures characterized by the presence of hexagonal layers with 1:3 composition which can be packed in several ways as has been shown by Van Vucht and Buschow (1965). The derivable structures can be described with a hexagonal or rhombohedrical unit cell, in which the a_{hex} persists while the c-axis varies according to the arrangement and hence the number of layers. The simplest unit cell corresponds to the Ni_3Sn type and is formed by two layers with hcp packing (100% hexagonal character). The last type is formed by three layers, with a rhombohedral sequence and the cubic symmetry of the $AuCu_3$ type (100% cubic character). The other possible sequences correspond to intermediate percentages of hexagonal or cubic character. Only a limited number of these possibilities are realized: 5 for RAl_3 compounds and 4 for RGa_3. The sequence of these structures is regular: by decreasing the dimensions of R, the structures change from the hexagonal Ni_3Sn type to the cubic $AuCu_3$ (Ni_3Sn(100% hex.) – $BaPb_3$(67%) – $DyGa_3$(60%) – Ni_3Ti(50%) – $HoAl_3$(40%) – $AuCu_3$(0%)). High pressure induced polymorphic changes are in the direction of structures with increased cubic character (Cannon and Hall, 1975).

A different sequence is observed for RCd_3 compounds, where with decreasing R dimensions are found the types: BiF_3, Ni_3Sn and an orthorhombic deformation of this last type represented by the $ErCd_3$ type (Fornasini and Merlo, 1972). $CeZn_3$ and YZn_3 represent nearly the same structure type, with slight shifts in the atomic position parameters, and are limited to the RZn_3 compounds (Bruzzone et al., 1970).

$CeNi_3$ and $PuNi_3$ types contain the same structural units, formed by stacking single layers of the RNi_5($CaCu_5$-type) structure and double layers of the RNi_2($MgCu_2$-type). These structural units are packed two by two hexagonally in the $CeNi_3$ type and three by three rhombohedrally in the $PuNi_3$ type.

The majority of the RX_3 compounds crystallize with the $AuCu_3$ type, which is widespread in the periodic system. The $PuNi_3$ and $CeNi_3$ structures are characteristic of the compounds with the group VIII elements, while the RAu_3 compounds crystallize with the $TiCu_3$ type which is a deformation of the Ni_3Sn type (Schubert, 1964).

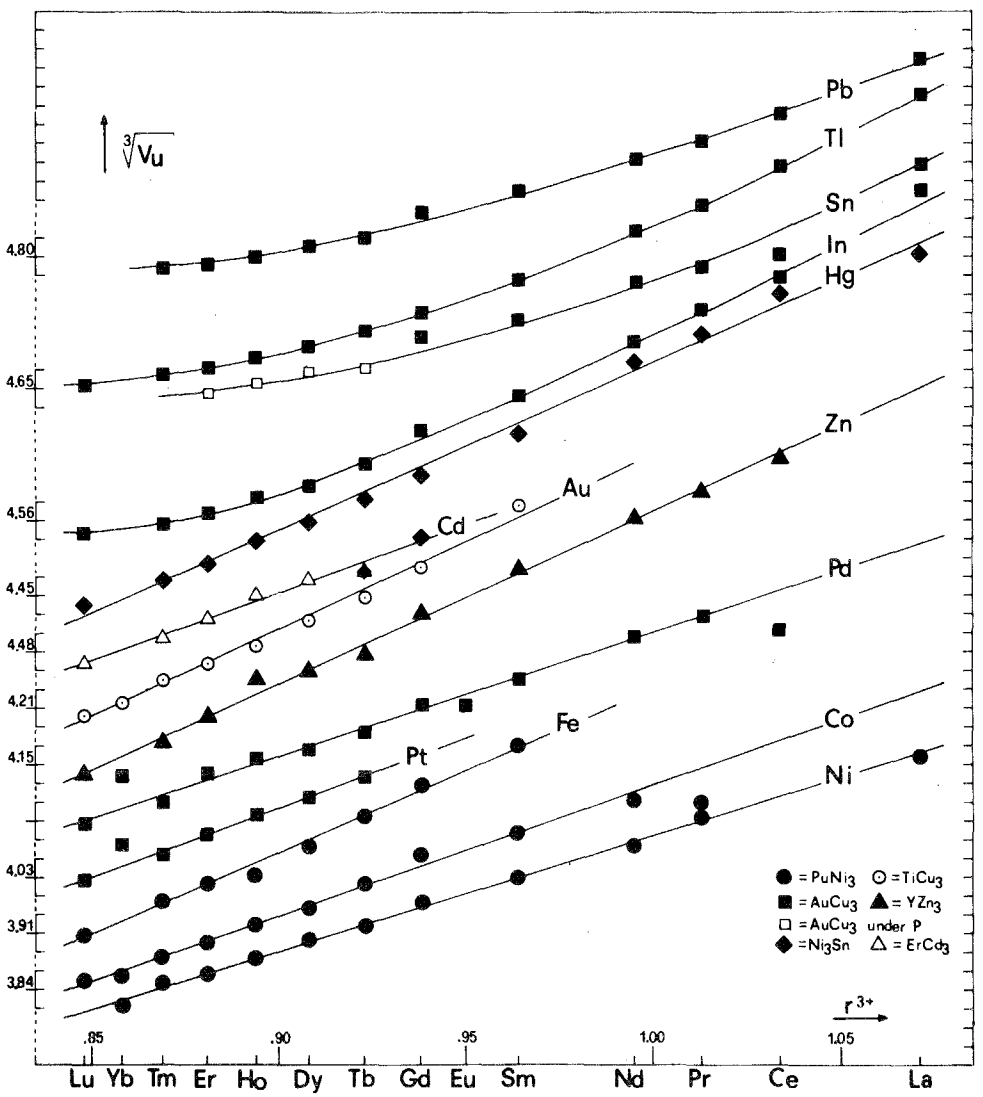

Fig. 13.27. Cubic root of V_u vs. ionic radius for RX_3 compounds.

Figure 13.27 shows the values of the cube roots of V_u for some of the RX_3 series. The general trend corresponds again to linearity with slightly smaller slopes for compounds with the group VIII metals. An exception is noted in the RX_3 compounds with X = In, Tl, Sn, Pb, which do not follow a linear trend. This behavior is evidently due to the dimensional factor, since these X atoms have the largest atomic radii among all elements forming $AuCu_3$ type compounds. From interatomic distances the X atoms appear to be in contact with a strong contraction which prevents their further approach on decreasing R dimensions.

For the RX_3 compounds (X = In, Tl, Sn, Pb) the thermodynamic data (heats of formation) are completely known (Palenzona and Cirafici, 1974a, 1974b) and can be related to the structural data. The simplest correlation between volume contractions and heats of formation does not seem to be valid in these cases. Volume contractions increase rather rapidly, while heats of formation decrease from La to Lu in accordance with the lowering of the melting points. As suggested by Gschneidner (1969a) the correlation can be found by taking into account the lanthanide contraction in these compounds in proportion to that existent in the pure metals. The unit cell volumes of the RX_3 phases are divided by the atomic volumes of the pure metals (R) and these volume ratios are divided by the volume ratio relative to the La compound, giving a scale relative to La (1.000). The resultant values increase with the R atomic number, i.e. the lanthanide contraction in the compound is less severe than in the pure metals and a decrease in the heats of formation can be expected in going from La to Lu. In fig. 13.28 this behavior for $R\text{In}_3$ and $R\text{Tl}_3$ is shown as an example. This same correlation is also found with the divalent R elements, considering Ba, Eu and Yb as members of a "baride" series and using Ba as the reference (fig. 13.29).

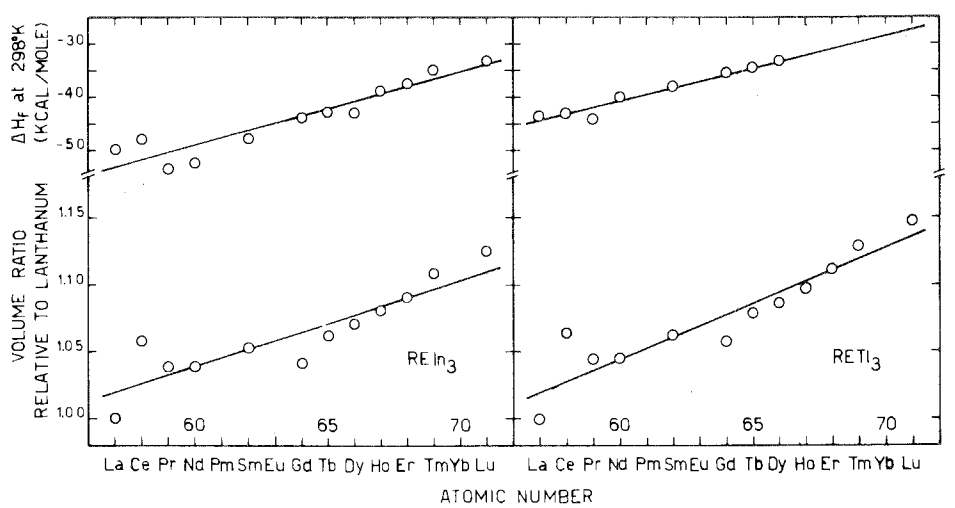

Fig. 13.28. Heats of formation and relative volume ratios for $R\text{In}_3$ and $R\text{Tl}_3$ compounds vs. the atomic number of R.

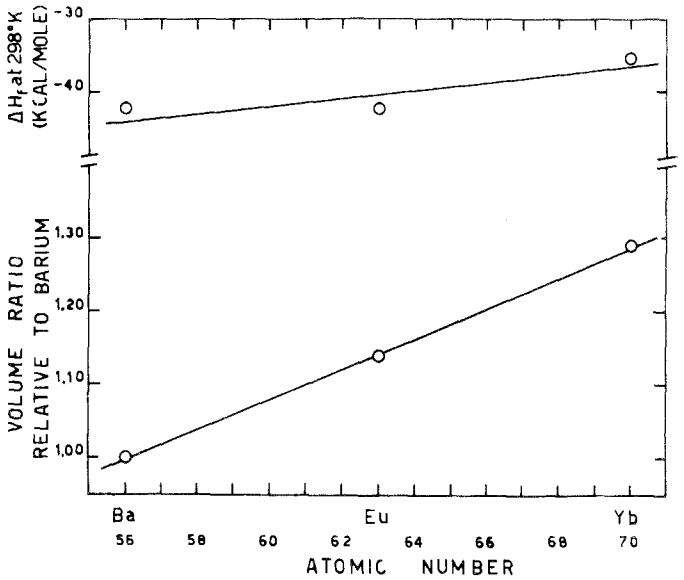

Fig. 13.29. Heats of formation and relative volume ratios for $BaPb_3$, $EuPb_3$, $YbPb_3$ vs. the atomic number. ($BaPb_3$ = rhombohedral, $R\bar{3}m$, $a = 9.565$ Å, $\beta = 44°47'$, $Z = 3$).

TABLE 13.46
A and *B* coefficients for eq. (13.1).

	A	*B*
R^{2+}	−11.11	4.44
R^{3+}	−11.10	2.27
Th	−9.94	4.40
U	−3.56	0.03

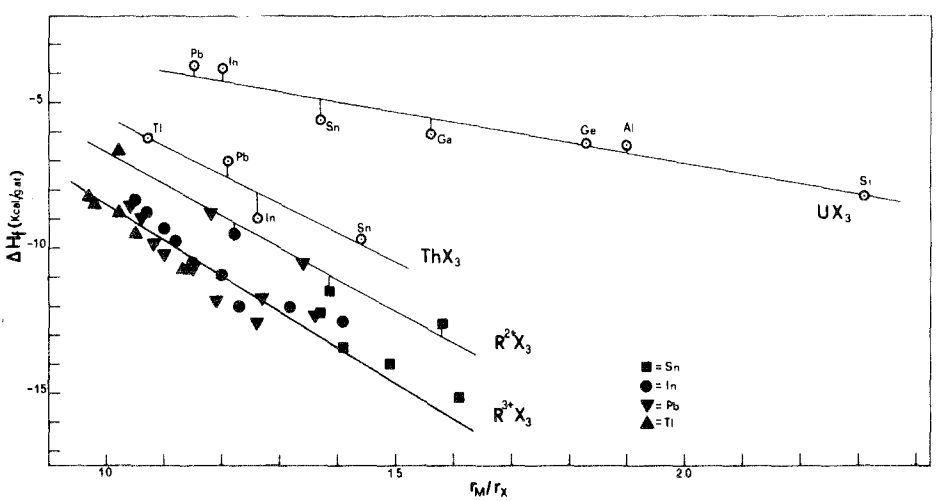

Fig. 13.30. Heats of formation vs. ionic radius ratio.

As observed in section 13.4, a quantitative correlation can be found by using the ionic radii of R and of X corresponding to their higher valence state and plotting the values of ΔH_f vs. the ratio r_R/r_X. In all cases a linear trend is obtained for the trivalent and divalent lanthanides and also for the isomorphous RX_3 phases of Th and U (fig. 13.30) (Palenzona and Cirafici, 1975b). In fig. 13.30 some data relative to the trivalent lanthanides were omitted when overlapping occurred. Generally, the heats of formation are given by:

$$\Delta H_f = A(r_R/r_X) + B \qquad \text{(kcal/g-at.)} \tag{13.1}$$

with different A and B values for each straight line (table 13.46).

7. Intermetallic compounds with anomalous valency states

The last problem is represented by the intermetallic compounds in which the R atoms show a valency different from the usual three.

Ionic compounds which contain lanthanides with a valence 2 or 4 have been known for a long time. These anomalous valence states are due to the stability of certain 4f electronic configurations, namely those of $4f^0$, $4f^7$ and $4f^{14}$. Compounds containing tetravalent Ce, Pr and Tb and divalent Sm, Eu, Tm and Yb can be prepared. Their abundance and stability are greater for those of Ce, Eu and Yb. Some semimetallic compounds of Sm(II), Tm(II) and perhaps Pr(IV) are known, but the most studied semimetallic and intermetallic compounds are those of Ce, Eu and Yb, which are described in the following.

The lanthanides with valences other than three produce differences from trivalent lanthanides in the systematic studies of binary phase diagrams. The effect is most noticeable in compound formation. The same crystal structure can exist, but the cell dimensions are usually not in the correct proportion relative to those of the neighboring lanthanides. Furthermore, compounds present in the trivalent systems may either be of different structure types or may not exist at all for the other valence states. Physical properties such as magnetic susceptibility, electrical conductivity, specific heat, heat of formation, etc., also show remarkable changes. Therefore, the valency changes can be detected by studying both crystallographic and other physical properties of these compounds.

The behavior can be summarized as follows: 1) compounds containing lanthanides with a normal fixed valency corresponding to 3 for Ce, 2 for Eu and Yb; 2) compounds containing lanthanides with an anomalous fixed valency: 4 for Ce and 3 for Eu and Yb; 3) compounds containing lanthanides with intermediate valency, fixed or variable with temperature and pressure. The last case represents the most interesting one and when valency changes with T and P a different behavior is found for Ce compared to Eu and Yb. A pressure increase always produces a transition to the higher valency; a temperature increase gives the same transition for Yb, while for Ce the tetravalency is reached by decreasing the temperature. For Eu, sufficient data are not available and only cases 1 and 2 are realized in binary compounds.

The behavior with temperature for Eu and Yb can be understood by assuming that the states corresponding to the trivalency have an energy higher than those for divalency. Following Gschneidner (1969b), the promotion energy to trivalency is about 9 kcal/g-at. for Yb and 23 kcal/g-at. for Eu. These values have been obtained from thermochemical data for ionic compounds. For intermetallics they are probably lower and different from case to case. On the assumption of Sales (1974) that the Ce^{4+} configuration lies lower in energy than Ce^{3+}, the effect of temperature on compounds like CeN and CeB_4 can also be explained. The hypothetical model accepted for this case corresponds to the assumption of interconfigurational fluctuations of valency. In some cases the lifetime of each configuration has been evaluated from different measurements and seems to be of the order of 10^{-13} sec (Borsa et al., 1973).

7.1. *Compounds of cerium*

The various modifications of cerium metal exhibit the phenomenon of intermediate valences under various conditions of pressure and temperature, see ch. 4, section 2.3.

The atomic radius of Ce(IV) (1.672 Å) is intermediate between those of Hf (1.580 Å) and of Th (1.798 Å) and the same is true of the tetravalent ionic radius. However, compared to its trivalent lanthanide neighbors, La and Pr, Ce does not show great differences in compound formation even if it is completely in the tetravalent state. The compounds are usually isomorphous with those of La and Pr, with relatively smaller lattice dimensions.

Along the periodic system, the different elements give rise to the behavior mentioned above and this is shown schematically in fig. 13.31.

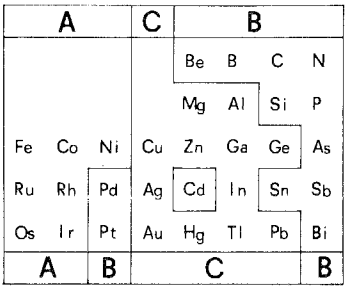

Fig. 13.31. Schematic diagram to explain the properties of Ce compounds.

A-elements form compounds containing Ce with a valence greater than 3, and for the *A*-richest compositions, tetravalent Ce can be realized. *B*-elements form compounds with Ce in intermediate valence states and finally, with *C*-elements the valence of Ce is 3. $CeCd_2$ is the only compound in the *C*-element area that contains Ce in the intermediate valency state.

7.2. *Compounds of europium and ytterbium*

In the metallic state, Eu and Yb give physico-chemical properties similar to those of the divalent alkaline-earth metals and do not change their valence with either temperature or pressure. With respect to their neighboring lanthanides they therefore have remarkably different properties, such as melting point, compressibility, density, etc. They form very limited solid solutions with the other *R* elements, but do form extensive solid solutions with the alkaline-earth metals.

In the divalent state, their binary phase diagrams are clearly different from those of the lanthanides, and if isostructural compounds are formed the lattice dimensions are much larger. In the trivalent state their behavior is quite similar to that of their neighboring lanthanides.

Of the two elements, Eu shows the lower tendency to acquire trivalency, which corresponds to a higher promotion energy and in fact only a few cases of compounds containing Eu(III) are known to exist. On the basis of the scarce available data, Eu seems to be able to form compounds containing only Eu(II) or Eu(III). Recently it has been shown that $EuCu_2Si_2$ belongs to the kind of compound with an intermediate valence which decreases with increasing temperature (Sales, 1974). The behavior of Eu with the other elements of the periodic system can be summarized as follows: compounds with Eu(III) have been found in the systems with Re, Rh, Ir, Ni, Pd, Pt, Be and with the metalloids N and P; in the Eu–Pd and Eu–Pt systems compounds can exist containing either Eu(III) or Eu(II); in all other systems, compounds of Eu(II) are formed; no compounds, and probably liquid immiscibility, occur in the systems with Mn, Fe and with the elements preceding group VII.

The behavior of ytterbium has been studied in a large number of binary systems, for which the corresponding phase diagrams have been determined and the structural and physical properties of several additional intermetallic compounds have been investigated. Figure 13.32 summarizes the known data obtained in the different binary systems which contain Yb.

The systems formed with *C*-elements, in which Yb is divalent, as shown by magnetic susceptibility measurements, are considerably different from those of the corresponding trivalent lanthanides (melting points, composition and struc-

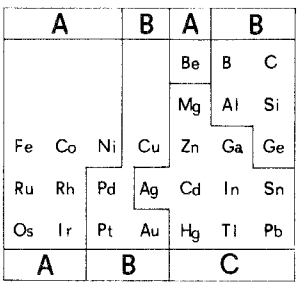

Fig. 13.32. Summary of binary systems containing Yb.

ture of the intermediate phases) and are remarkably similar to those of the alkaline-earth elements, particularly of Ca which has the same valence and an atomic radius close to that of Yb.

In the systems formed with *A*-elements – all transition metals, except for Be (in the Yb–Be system only $YbBe_{13}$ is known to exist) – as long as the concentration of the *X* element does not reach a certain value, Yb maintains its divalency and correspondingly does not alloy with *X*, giving rise to wide liquid immiscibility ranges. Above this critical concentration, which depends on *X*, Yb becomes trivalent and forms compounds isomorphous with those of the neighboring lanthanides (Iandelli and Palenzona, 1976). This critical concentration increases regularly from left to right and down in the periodic system.

In the systems with *B* elements: Cu (Iandelli and Palenzona, 1971), Pd (Iandelli and Palenzona, 1973), Pt (Iandelli and Palenzona, 1975), Au (Iandelli and Palenzona, 1969), the intermediate phases show a valence variable with *X* concentration. First appear compounds with Yb(II); then increasing *X*, compounds with intermediate valency and finally, with high *X* concentrations, Yb becomes completely trivalent. Only one exception occurs in the Yb–Cu system, where after Yb_2Cu_9, containing Yb(III), another compound richer in Cu is formed with Yb(II). Another group of *B* elements is found among those with a metalloid character and Al. Only the Yb–Al system is completely known (Palenzona, 1972), and the two existing compounds $YbAl_2$ and $YbAl_3$ have been thoroughly studied for their anomalous properties. $YbAl_3$ contains mainly Yb(III), while for $YbAl_2$ measurements of the magnetic susceptibility and of the lattice constant at different temperatures show that the valence of Yb increases with increasing temperature reaching a value of about 50% of Yb(III) at 600°C (Iandelli and Palenzona, 1972). The corresponding promotion energy of the 4f electron, evaluated by different methods, is of the order of about 3000 cal/g-at.Yb.

8. Recent developments

The data reported and discussed in the previous pages correspond, apart for possible forgetfulness, to works which have appeared in current literature up to the end of 1975; in the meantime other data have been published and we have collected them in the three following additional tables.

A systematic study on the intermetallic compounds of *R*'s with VIII group metals, concerning their existence and crystal structures, is actually in progress by a Geneva (Switzerland) research group (Parthé, Moreau, Paccard, Le Roy). Some of their results have been published (Parthé et al., 1977) while others will appear in Acta Crystallographica.

In the field of thermochemical research a comprehensive article of Bayanov (1975) contains together with those referred to valence compounds, the data of a number of intermetallic compounds, divided in groups with d, s and p elements. The heats of formation in the whole range of compositions of the following systems: Y–Bi (Ferro et al., 1974); Nd–Bi (Borsese et al., 1974); Pr–Bi (Borsese et al., 1975a);

Y–Pb (Borsese et al., 1975b); La–Pb (Ferro et al., 1975); La–In (Borsese et al., 1977a); Nd–Sb (Borsese et al., 1977b); Dy–Bi (Borsese et al., 1977c), have been determined by means of high temperature calorimetry. The authors have tried to verify the validity of the formula of Miedema, finding a reasonable agreement in most cases, only with small changes of the parameters involved. By means of DDC, the heats of formation of the series *R*Pd and *R*Pt compounds have been measured (Palenzona et al., 1975, 1978), finding analogous regularities as for the series of RX_3 compounds.

Many works have been devoted to the study of compounds with fluctuating valency states (ICF systems), especially for semimetallic compounds. An international Colloquium on the metal–non-metal transitions in rare earth compounds, was held in 1976 and the results have been published in the Journal de Physique (Colloque C4, supplement au No. 10, Tome 37, October 1976). Theory and experiments concerning intermetallic ICF systems have not so far received an analogous development.

Additional data to figure 13.1

The following systems correspond to a complete or almost complete phase diagram.

Gd–Ru (Loebich Jr. et al., 1976a)
Dy–Ru (Loebich Jr: et al., 1976a)
Gd–Rh (Loebich Jr. et al., 1976b)
La–Cu (Cirafici et al., 1977)
Tb–Ag (Delfino et al., 1976)
Dy–B (Speer, 1974)
Yb–Ga (Palenzona et al., 1978)
Nd–Tl (Delfino et al., 1978)
La–Bi (Nomura et al., 1976)

Notes: The following compounds have been claimed to exist, but no structural details are available: Gd_3Ru, $Gd_{73}Ru_{27}$, Gd_2Ru; Dy_3Ru, $Dy_{73}Ru_{27}$, Dy_2Ru; Gd_3Rh_2, Gd_4Rh_3.

Additional data to table 13.2

Comp.	at.% *X*	*N* (compds.)	Structures types, partner elements and frequency of occurrence
R_3X	25.0	20	19 Fe_3C[Ir(11), Rh(8)] 1 $AuCu_3$[Tl(1)]
R_5X_2	28.6	3	3 Mn_5C_2[Co(3)]
R_7X_3	30.0	4	4 Th_7Fe_3[Pd(2), Pt(2)]
R_2X	33.3	9	9 $PbCl_2$[Pt(8), Ga(1)]
$R_{12}X_7$	36.8	5	5 $Ho_{12}Co_7$[Co(5)]
R_5X_3	37.5	16	12 Mn_5Si_3[Rh(4), Pt(8)] 4 Er_5Ir_3[Rh(3), Ir(1)]

Additional data to table 13.2 (contd.)

Comp.	at.% X	N (compds.)	Structures types, partner elements and frequency of occurrence
R_8X_5	38.5	1	1 Y_8Co_5[Co(1)]
R_3X_2	40.0	21	9 Er_3Ni_2[Rh(4), Pd(1), Pt(4)] 11 Y_3Rh_2[Rh(6), Ir(5)] 1 Y_3Ni_2[Ni(1)]
R_5X_4	44.4	8	1 Sm_5Ge_4[Pt(1)] 7 Gd_5Si_4[Rh(6),Ir(1)]
RX	50.0	3	2 CrB[Pt(2)] 1 AuCu[Ga(1)]
R_2X_3	60.0	2	2 La_2Ni_3[Ni(1), Co(1)]
R_3X_5	62.5	1	1 Pu_3Pd_5[Tl(1)]
$R_{11}X_{45}$	80.4	11	11 $Sm_{11}Cd_{45}$[Cd(11)]
RX_6	85.7	1	1 $CeCu_6$[Cu(1)]

Additional data to tables 13.5–13.44

Crystallographic data for R_5X_3, RX and RX_3 compounds.

Compound	Structure type	Lattice constants (Å) a	b	c
Dy_5Rh_3	Mn_5Si_3	8.153	–	6.365
Ho_5Rh_3		8.100	–	6.335
Tm_5Rh_3		8.058	–	6.252
Lu_5Rh_3		8.002	–	6.213
Y_5Rh_3		8.161	–	6.398
Gd_5Pt_3		8.479	–	6.275
Tb_5Pt_3		8.415	–	6.230
Dy_5Pt_3		8.367	–	6.210
Ho_5Pt_3		8.319	–	6.191
Er_5Pt_3		8.298	–	6.181
Tm_5Pt_3		8.252	–	6.128
Lu_5Pt_3		8.183	–	6.155
Y_5Pt_3		8.370	–	6.276
PrPt	CrB	3.891	10.899	4.569
NdPt		3.846	10.769	4.542
YNi	YNi	4.114	7.14 $\beta = 90.0°$	5.501
YbGa	AuCu	4.82	–	3.94
$LaMg_3$	BiF_3	7.467	–	–
$CeMg_3$		7.424	–	–
$PrMg_3$		7.411	–	–
$NdMg_3$		7.397	–	–
$SmMg_3$		7.360	–	–
$GdMg_3$		7.326	–	–
$TbMg_3$		7.296	–	–

References

Ban, Z. and M. Sikirica, 1965, Acta Cryst. **18**, 594.

Becle, C. and R. Lemaire, 1967, Acta Cryst. **23**, 840.

Borsa, F., G. Olcese and G.B. Silbernagel, 1973, XVII Congress Ampere, Turku, North-Holland Publ. Co., V. Hovi (ed.), p. 326.

Brown, A., 1961, Acta Cryst. **14**, 860.

Brunton, G.D. and H. Steinfink, 1971, Inorg. Chem. **10**, 2301.

Bruzzone, G., M.L. Fornasini and F. Merlo, 1970, J. Less-Common Met. **22**, 253.

Cannon, J.F. and H. Tracy Hall, 1975, J. Less-Common Met. **40**, 313.

Fornasini, M.L. and F. Merlo, 1972, Acta Cryst. **B28**, 3094.

Fornasini, M.L. and A. Palenzona, 1976, J. Less-Common Met. **45**, 137.

Gschneidner, K.A. Jr., 1961, Rare Earth Alloys, Van Nostrand.

Gschneidner, K.A. Jr., 1969a, J. Less-Common Met. **17**, 1.

Gschneidner, K.A. Jr., 1969b, J. Less-Common Met. **17**, 13.

Hohnke, D. and E. Parthé, 1966, Acta Cryst. **20**, 572.

Iandelli, A. and A. Palenzona, 1969, J. Less-Common Met. **18**, 221.

Iandelli, A. and A. Palenzona, 1971, J. Less-Common Met. **25**, 333.

Iandelli, A. and A. Palenzona, 1972, J. Less-Common Met. **29**, 293.

Iandelli, A. and A. Palenzona, 1973, Rev. Chim. Minerale **10**, 303.

Iandelli, A. and A. Palenzona, 1975, J. Less-Common Met. **43**, 205.

Iandelli, A. and A. Palenzona, 1976, Rev. Chim. Minerale **13**, 55.

Kubaschewski, O., 1959, The Physical Chemistry of Metallic Solutions and Intermetallic Compounds, Vol. 1, Sec. 3C, p. 2, Her Majesty's Stationary Office, London.

Larson, A.C. and D.T. Cromer, 1961, Acta Cryst. **14**, 73.

Lemaire, R. and D. Paccard, 1970, J. Less-Common Met. **21**, 403.

Miedema, A.B., 1973, J. Less-Common Met. **32**, 117.

Palenzona, A., 1972, J. Less-Common Met. **29**, 289.

Palenzona, A. and S. Cirafici, 1974a, Thermochim. Acta, **9**, 419.

Palenzona, A. and S. Cirafici, 1974b, Analytical Calorimetry, Vol. 3, R.S. Porter and J.F. Johnson (ed.), Plenum Press, p. 743.

Palenzona, A. and S. Cirafici, 1975a, Thermochim. Acta **12**, 267.

Palenzona, A. and S. Cirafici, 1975b, Thermochim. Acta **13**, 357.

Palenzona, A. and S. Cirafici, 1976, J. Less-Common Met. **46**, 321.

Parthé, E., 1965, Colloques Internationaux du CNRS, n°157, Paris-Orsay, p. 195.

Pauling, L., 1960, The Nature of the Chemical Bond, Cornell University Press.

Pearson, W.B., 1967, A Handbook of Lattice Spacings and Structures of Metals and Alloys, Vol. 2, Pergamon Press.

Pearson, W.B., 1972, The Crystal Chemistry and Physics of Metals and Alloys, Wiley-Interscience.

Raman, A., 1967, Z. Metallk. **58**, 179.

Sales, B., 1974, Valence Fluctuations on Rare Earth Ions, (Thesis), University Microfilms, Ann-Arbor Michigan.

Savitskii, E.M. and V.F. Terekhova, 1975, Metallovedenie Redkozemelnikh Metallov, Ed. Nauka, Moscow.

Schmidt, F.A., O.D. McMasters and R.R. Lichtenberg, 1969, J. Less-Common Met. **18**, 215.

Schmidt, F.A., O.D. McMasters and O.N. Carlson, 1972, J. Less-Common Met. **26**, 53.

Schubert, K., 1964, Kristallstrukturen zweikomponentiger Phasen, Springer-Verlag.

Templeton, D.H. and C.H. Dauben, 1954, J. Am. Chem. Soc. **76**, 5237.

VanVucht, J.H.N. and K.H.J. Buschow, 1965, J. Less-Common Met. **10**, 98.

Zarechnyuk, O.S., 1966; Dopov. Akad. Nauk. Ukr. RSR, **6**, 767.

References to section 8

Bayanov, A.P., 1975, Russian Chem. Rev. **44**, 122.

Borsese, A., R. Capelli, S. Delfino and R. Ferro, 1974, Thermochim. Acta **8**, 393.

Borsese, A., R. Ferro, R. Capelli and S. Delfino, 1975a, Thermochim. Acta **11**, 205.

Borsese, A., R. Ferro, R. Capelli and S. Delfino, 1975b, J. Less-Common Met. **42**, 179.

Borsese, A., A. Calabretta, S. Delfino and R. Ferro, 1977a, J. Less-Common Met. **51**, 45.

Borsese, A., R. Ferro, R. Capelli and S. Delfino, 1977b, J. Less-Common Met. **55**, 77.

Borsese, A., G. Borzone, R. Ferro and S. Delfino, 1977c, J. Less-Common Met. **55**, 115.

Cirafici, S. and A. Palenzona, 1977, J. Less-Common Met. **53**, 199.

Delfino, S., A. Saccone, A. Borsese and R. Ferro, 1976, Z. Metallkde **67**, 392.

Delfino, S., A. Saccone, G. Borzone and R. Ferro, 1978, J. Less-Common Met., in press.

Ferro, R., A. Borsese, R. Capelli and S. Delfino, 1974, Thermochim. Acta **8**, 387.
Ferro, R., A. Borsese, R. Capelli and S. Delfino, 1975, Z. anorg. allg. Chem. **413**, 279.
Loebich, Jr., O. and E. Raub, 1976a, J. Less-Common Met. **46**, 7.
Loebich, Jr., O. and E. Raub, 1976b, J. Less-Common Met. **46**, 1.
Nomura, K., H. Hayakawa and S. Ono, 1977, J. Less-Common Met. **52**, 259.
Palenzona, A. and S. Cirafici, 1978, J. Less-Common Met., in press.
Palenzona, A. and S. Cirafici, 1975, Thermochim. Acta **12**, 267.
Palenzona, A. and S. Cirafici, 1978, Thermochim. Acta, in press.
Parthé, E. and J.M. Moreau, 1977, J. Less-Common Met. **53**, 1.
Speer, K.E., 1974, 4th Intern. Symp. on Boron, Tbilisi URSS, Izdatel'stvo Nauka, Moscow.

Handbook on the Physics and Chemistry of Rare Earths, edited by K.A. Gschneidner, Jr. and L. Eyring

Chapter 14

MAGNETIC PROPERTIES OF INTERMETALLIC COMPOUNDS OF RARE EARTH METALS

Hans R. KIRCHMAYR and Carl A. POLDY
(in cooperation with R. GROESSINGER, R. HAFERL, G. HILSCHER, W. STEINER and G. WIESINGER)
Institut für Experimentalphysik der Technischen Universität Wien, A-1040 Wien, Karlsplatz 13, Austria

Contents

Symbols

A_n^m = crystal field parameter
a = lattice parameter
B = magnetic induction
B = chemical symbol for non-rare earth partner element
B_n^m = crystal field parameter
$B(T)$ = Landau parameter
b = lattice parameter
C = Curie constant
C' = magnetoelastic coupling constant
c = lattice parameter
E_A = anisotropy energy
E_F = Fermi energy

e = electronic charge
F = free energy
G = s–f exchange integral
g = Landé g-factor
H_A = anisotropy field
H_c = critical field (metamagnetic)
${}_BH_c$, ${}_MH_c$ = coercivities for B vs H and M vs H demagnetization curves, respectively
H_M = molecular field
$\mathscr{H}$ = hamiltonian
h = Planck's constant
I = exchange integral (itinerant electrons)
J = total angular momentum quantum number
$\mathscr{J}$ = exchange integral
K = anisotropy constant
k_B = Boltzmann's constant
$\boldsymbol{k}_F$ = Fermi wave vector
k_F^0 = theoretical k_F value of free conduction electrons
L = orbital angular momentum quantum number
M = magnetization
m_0 = rest mass of electron
m^* = effective electronic mass
N = number of magnetic ions per unit volume
$N(E_F)$ = density of states at Fermi level
n = electron density
n_{ij} = molecular field coefficients between magnetic sublattices i, j
$\hat{O}_n^m$ = crystal field operator equivalents
p = pressure
p_{eff} = effective paramagnetic moment in μ_B
$\boldsymbol{q}$ = wave vector of sinusoidal spin structure
q_i = charge on ion i
R = universal gas constant
R = chemical symbol for rare earth
$\boldsymbol{R}_{ij}$ = vector connecting lattice site i to site j
$\boldsymbol{r}$ = position vector
S = spin quantum number
s = spin polarization of conduction electrons
T_c = superconducting transition temperature
T_C = Curie temperature (ferromagnetic or ferrimagnetic ordering temperature)
T_N = antiferromagnetic ordering temperature
T_k = compensation temperature
t = time
W = exchange energy
x_F = critical concentration of mixed crystal series where ferromagnetism appears
Z = thermodynamic state sum
α_J = Steven's crystal field multiplicative factor
Γ_n = crystal field level
γ = specific heat
ϵ_i = energy eigenvalue of ith crystal field level
θ = angle
θ_p = paramagnetic Curie temperature
κ = compressibility
λ = mean free path
μ = magnetic moment
μ_B = Bohr magneton
μ_0 = permeability of free space
ρ_{spd} = spin disorder resistivity
σ = itinerant electron spin density
τ = relaxation time
Φ = wave function
φ = angle
χ = susceptibility
ω = volume strain

1. Introduction and scope

In this chapter about the magnetic properties of intermetallic compounds involving "rare earth metals" we are concerned with three different concepts, namely "Magnetism", "Intermetallic Compounds" and "Rare Earth Metals". In other chapters of this book the development of the science of Rare Earth Metals has been described. Magnetism in itself is an old concept, while the term

"Intermetallic Compounds" is fairly new (see Westbrook, 1967). The seemingly small area "Magnetic Properties of Intermetallic Compounds involving Rare Earth Metals" is in fact a vast field of hectic scientific activities. This fact is based on one hand on the rise of magnetism in general in recent years, and on the other hand on the fact that some of these intermetallic compounds, because of specific magnetic properties, have recently found technical applications and will find more applications in the near future. In this chapter we therefore can only try to give an overview of this field, because a complete coverage would not be possible even in a far longer article. What we wish to attempt, however, is to show the basic concepts and the central ideas which are connected with the magnetic properties of R_nB_m intermetallic compounds of rare earth metals R with other metals B. We will not follow the most simple and clear-cut division of this material, this would be a division based on the elements which are present in the different intermetallic compounds. Rather we wish to follow as closely as possible basic physical concepts and we shall treat different intermetallic compounds in one section if we believe that because of their physical properties and not because of their composition they belong to a distinct group.

Section 2 will therefore involve intermetallic compounds for which the B-moment is zero. Typical compounds belonging to this group are for instance R–Al compounds. Section 3 will be concerned with intermetallic compounds where the second component has a moment which is distinctly non-zero. Typical compounds are for instance iron or cobalt compounds. Section 4 will be concerned with boundary cases which do not fit into the two preceding sections. A typical "boundary case" will be for instance a system based on YCo_2 in which a 3d moment appears when a third component is substituted. Section 5 will cover some striking phenomena which can be summarized by the term "time dependence". In sections 2–4 only static or pseudostatic properties are discussed, but in section 5 the additional dimension of time plays an important role. The sub-divisions of the sections are organized to a large extent according to crystal structure and stoichiometry. Some specific hard magnetic materials, which are of great technical significance, are discussed in section 6. The leading compound is $SmCo_5$ and a general discussion of the significance of this compound with respect to technical applications is given.

We have tried to write a chapter which is self-consistent. We had naturally to leave out as much material as possible, which is covered in other chapters of this book. This refers especially to ch. 13 by Iandelli and Palenzona which is concerned with the many fascinating problems in the crystal chemistry of intermetallic compounds. Naturally, the crystal structure is the basis for the understanding of nearly all the physical properties of crystalline materials. In our case, namely in the case of the magnetic properties, the problem is still more complicated. In this case not only the boundary condition of the crystal lattice is essential for understanding the electrical and transport properties, but the crystal structure is also the basis for the understanding of any ordered magnetic state. Since the magnetic properties of magnetically ordered materials are of more interest than just the diamagnetic or paramagnetic properties, we will concen-

trate more on magnetically ordered systems. In this connection we naturally have to refer to the crystal structure of each compound, which may be discussed in more detail in other chapters. We also had to leave out as much as possible of the magnetostrictive properties, which are especially interesting in compounds with the formula RFe_2. These and related properties will be discussed in ch. 15 by Clark. Also the details of electrical crystal fields, of NMR, ESR and the Mössbauer effect and the properties of specific rare earth compounds such as e.g. the chalcogenides or the pnictides are left out of this chapter. Nevertheless the material to be covered or at least to be mentioned in this chapter is overwhelming. Therefore we have tried to make a selection which is naturally subjective. Where possible we have tried not only to give just the data, but to make a confrontation between data of different authors and to compare these data and their interpretation; naturally, also with our own experience. The reader is also referred to the books by Taylor and Darby (1972), Wallace (1973) and Nesbitt and Wernick (1973) as well as review articles (Taylor, 1971a; Buschow, 1971).

If one really tried to treat the given subject of magnetic properties of intermetallic compounds in a rigorous manner, one should start from first principles with the behaviour of electrons within a crystal lattice. This would mean one should try to discuss the band structure and deduce from this the electrical and magnetic properties. This is possible in the case of elemental rare earth metals and has been discussed in ch. 3 by Liu. In the case of intermetallic compounds, however, this treatment is rarely possible, because of the scarcity of accurate band structure or Fermi surface information available at present for most of these intermetallic compounds. Therefore at the present moment we are confined to a semi-empirical treatment of the magnetic properties. We are naturally aware of the fact that these magnetic properties are related and should be related to the basic properties of electrons in a periodic lattice. However such a rigorous treatment is, as mentioned above, not generally possible today. We therefore take the magnetic moment of a rare earth metal and also of the second component as a given entity. Starting from this value we consider the influence of the electrical crystal field and other fields, such as exchange fields, which may change the magnetic moment. The crystal field is of essential importance for intermetallic compounds, and especially its connection with the magnetic anisotropy.

Many recent developments in the investigation of rare earth intermetallic compounds have only been made possible either by the availability of pure rare earth metals, or of possibilities to prepare single phased intermetallic compounds. Also developments with respect to the determination of crystal structures etc. and new scientific and experimental techniques for investigations of magnetic properties, which are essential to our present knowledge of the magnetic properties of intermetallic compounds will not be mentioned explicitly.

The fairly new scientific field of intermetallic compounds is characterized by the fact that usually only simple stoichiometric ratios between two or more components are possible. This is closely related to the fact that usually very

complicated crystal structures with narrow homogeneity ranges are observed. On the other hand naturally a group of very similar elements as especially the rare earths can usually replace each other in a compound without changing the crystal structure. The same is frequently the case for the series of elements such as Mn, Fe, Co, Ni etc. In some cases much more detailed and more systematic information can be obtained if one rare earth element is replaced by other rare earth elements on one side and if on the other side the non-rare earth element partner is replaced by another non-rare earth element. Therefore, these so-called "pseudobinary compounds" have been treated extensively in this chapter. One must, however, be aware of the fact that the possible number of these combinations is enormous. For practical reasons and because we think that just the pseudobinary systems give particularly valuable information, we mainly concentrate on simple pseudobinary systems of the type $R_n(B^1B^2)_m$ or $(R^1R^2)_nB_m$ rather than on quaternary and similar systems of the type $(R^1_xR^2_{1-x})_n(B^1_yB^2_{1-y})_m$.

Because of the large number of possible and already investigated intermetallic compounds of rare earth metals and because the sometimes strange and unique magnetic properties of these compounds have been in the focus of interest, we are convinced that by still more detailed investigations of these compounds, especially with respect to the magnetic properties, more possible applications of these properties in science and technology will appear within the near future. Nevertheless only a few really large scale technical applications are seen on the horizon today, especially in future oriented fields like the computer industry, electronics, design of intricate devices etc. Some possible applications of these hard and soft magnetic materials are based on very specific properties of rare earth intermetallic compounds which are unique for the rare earths.

2. Intermetallics with zero B-moment

2.1. *Theoretical concepts*

2.1.1. *Free lanthanide ions*

Although the details of the properties of the free atoms of the lanthanides are dealt with in ch. 1, it is not out of place to give here a brief survey of the ionic properties, since they can be regarded as being the foundation upon which the contents of this chapter are based.

The free ions of the lanthanides occur usually in the trivalent state, and this can also be said of them in the solid state. Exceptions often occur for Ce, Eu, Yb due to the tendency to adopt a state with either empty, half-full or full 4f shells.

The magnetically important 4f electrons couple together according to the Russell–Saunders coupling and Hund's rules. Thus the total angular momentum $\boldsymbol{J}$ is built up of the vectors $\boldsymbol{L}$ and $\boldsymbol{S}$. The vector $\boldsymbol{L}$ is the total orbital angular momentum vector resulting from the magnetic coupling of angular momenta of the individual 4f electrons ($l = 3$). $\boldsymbol{S}$ is the total spin vector, due to the

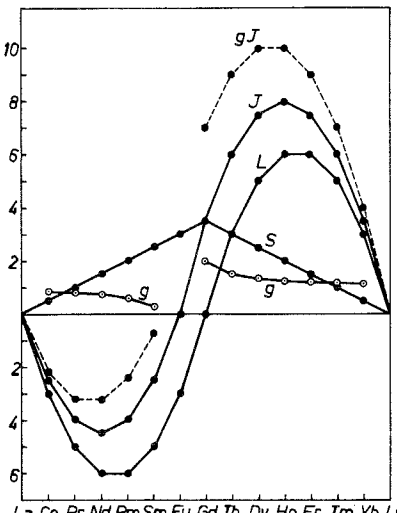

Fig. 14.1. The theoretical construction of the gJ values of the trivalent lanthanides.

intra-atomic exchange coupling of the individual spins. In turn we have an additional magnetic interaction which couples the $\boldsymbol{L}$ and $\boldsymbol{S}$ vectors to give a resultant $\boldsymbol{J}$ vector. Hund's rules state the conditions of the coupling: The lowest energy state of the system is such that firstly the total $\boldsymbol{S}$ vector is as large as possible and secondly the total $\boldsymbol{L}$ vector is as large as possible within the constraints of the Pauli exclusion principle. The coupling between $\boldsymbol{L}$ and $\boldsymbol{S}$ then occurs such that $\boldsymbol{L}$ couples against $\boldsymbol{S}$ for the light lanthanides and parallel to $\boldsymbol{S}$ for the heavy lanthanides. This can be seen to follow naturally as depicted in fig. 14.1. In this figure are also shown the Landé g-factors and gJ which gives the maximum measurable component of magnetic moment in Bohr magnetons.

The magnetic moment magnitude of the free ions in units of Bohr magnetons is given by $g[J(J+1)]^{1/2}$. For paramagnetic lanthanide ions occurring in the tripositive state in solids this quantity should be equal to the effective moment p_{eff} obtainable from paramagnetic susceptibility measurements if the ions occur as free ions. Table 14.1 summarizes some of the most important ionic properties of the free tripositive lanthanide ions.

2.1.2. *The exchange interaction*

In this work, interactions between magnetic ions in solids are of primary importance. The magnitudes of the possible magnetic dipole forces between the ionic moments are too small to account for the large ordering temperatures observed in many cases, e.g. GdZn $T_C = 268$ K. Thus we have to turn to some other mechanism, though not necessarily purely magnetic in origin, which may be instrumental in aligning the magnetic moments. This can be found in the exchange interaction. The exchange interaction is of purely quantum mechanical origin since it results from the need to anti-symmetrize the wave functions of

TABLE 14.1.
Some theoretical ionic properties of the trivalent lanthanides.

	La^{3+}	Ce^{3+}	Pr^{3+}	Nd^{3+}	Pm^{3+}	Sm^{3+}	Eu^{3+}	Gd^{3+}	Tb^{3+}	Dy^{3+}	Ho^{3+}	Er^{3+}	Tm^{3+}	Yb^{3+}	Lu^{3+}
Ground state	$^1S_0$	$^2F_{5/2}$	$^3H_4$	$^4I_{9/2}$	$^5I_4$	$^6H_{5/2}$	$^7F_0$	$^8S_{7/2}$	$^7F_6$	$^6H_{15/2}$	$^5I_8$	$^4I_{15/2}$	$^3H_6$	$^2F_{7/2}$	$^1S_0$
J	0	$\frac{5}{2}$	4	$\frac{9}{2}$	4	$\frac{5}{2}$	0	$\frac{7}{2}$	6	$\frac{15}{2}$	8	$\frac{15}{2}$	6	$\frac{7}{2}$	0
g	–	$\frac{6}{7}$	$\frac{4}{5}$	$\frac{8}{11}$	$\frac{3}{5}$	$\frac{2}{7}$	–	2	$\frac{3}{2}$	$\frac{4}{3}$	$\frac{5}{4}$	$\frac{6}{5}$	$\frac{7}{6}$	$\frac{8}{7}$	–
$(g-1)^2J(J+1)$	–	0.18	0.8	1.84	3.2	4.46	–	15.75	10.5	7.08	4.5	2.55	1.17	0.32	–
$p_{\text{eff}} = g^2J(J+1)$	–	2.54	3.58	3.62	2.68	0.84	–	7.94	9.72	10.63	10.58	9.59	7.55	4.54	–

identical fermions. When this is performed it is found that the Coulomb energy of a system of electrons is affected by the relative orientation of their spins. This is because the orbital part of the collective wave function of a system of fermions must be symmetrical if the spin part is antisymmetric and vice versa. Thus there is a different spacial distribution of the charge clouds depending upon whether the spins are parallel or antiparallel. This energy of interaction between spins can be expressed in the Heisenberg form by

$$E = -\mathcal{J}\boldsymbol{S}_1 \cdot \boldsymbol{S}_2, \tag{14.1}$$

where $\mathcal{J}$ is the exchange integral and $\boldsymbol{S}_1$ and $\boldsymbol{S}_2$ are the spin vectors of the interacting electrons. Since each spin $\frac{1}{2}$ is automatically associated with a magnetic moment $1\,\mu_B$ we can regard such an interaction as an interaction between magnetic moments. In addition, due to intra-atomic L–S coupling, the spin is not only associated with its own $1\,\mu_B$, but also with the orbital moment. Thus the basically electrostatic spin interactions result in an effective interaction between magnetic moments. This is not of magnetic origin and it will be noticed from eq. (14.1) that it is isotropic since nothing was said about the angle between the line joining the two interacting spins and the direction of the spins.

We can thus express the isotropic exchange interaction between two magnetic moments μ by $E = -A\mu_1\mu_2$. From this we can obtain the concept of a molecular field $H_M = A\mu_1$ so that $E = -H_M\mu_2$. This is just the form of the energy E of a dipole moment μ_2 in the field H_M. Though this field can be expressed in A/m or Oe, it must be borne in mind that this is not a real magnetic field and should not be confused with the hyperfine field at the nucleus. Since exchange occurs only between identical particles (e.g. electron–electron) the nucleus will be blind to the molecular field produced on its own atom by neighbouring electronic spins. On the other hand the effects of exchange can be felt indirectly by the nucleus but there need not be a 1 : 1 ratio between the molecular and hyperfine fields.

The molecular field model assumes the existence of some sort of exchange between magnetic ions possessing spin without requiring explicit knowledge of the type of exchange. Using this model one obtains expressions for the ordering temperature T_C, T_N and paramagnetic Curie temperatures θ_p. These are in the case of ferromagnetism

$$T_C = \theta_p = [2J(J+1)/3k] \sum_{i<j} \mathcal{J}'_{ij}(r). \tag{14.2}$$

Since J is a good quantum number, and not S, we must project S onto J and consider the effects of exchange between the projected $\boldsymbol{S}$ vectors. Using the projection theorem, the projected S value is $(g-1)J$. Within the molecular field model $T_C = \theta_p$ for a ferromagnetic material and $T_N > \theta_p$ for an antiferromagnet. In the case of only nearest neighbour interactions $\theta_p = -T_N$ (Van Vleck, 1941). Information may be obtained from the slope of $1/\chi$ vs T curves in paramagnetic regions. If the curve is linear, as expected for well-behaved materials, the value p_{eff} of the paramagnetic moment can be calculated and compared with the expected value according to a free rare earth ion. This gives information about

the state of the ionic moments, e.g. whether they are trivalent or not, whether or not they are localized and behaving like isolated free ions.

2.1.3. *Indirect exchange*

Usually R moments in metals are treated as trivalent localized moments R^{3+} in a sea of conduction electrons. This is justified in many cases since the spatial extent of 4f wave functions is small. However this now raises the problem as to how we shall account for the presence of exchange interactions, since exchange requires overlap of some kind. Thus, since direct exchange of 4f wave functions is precluded, we must resort to an indirect exchange via the conduction electrons. We require a total wave function derived from 4f electron and conduction electron wave functions in order to describe the electrons in the whole system. The nature of the free localized ions is certainly distorted to some extent, but this may be minimal since no direct overlap of 4f wave functions prevails. (It is, of course, conceptually difficult to see how rigorously localized 4f electrons of a free lanthanide ion can interact by exchange with those of another identical ion without losing part of their localized character, since exchange automatically implies overlap [whether direct or indirect], and overlap implies at least some degree of itineracy!)

2.1.4. *The* RKKY *model*

In order to calculate T_N, T_c or θ_p we require a value for the exchange energy in eq. (14.2), and its variation with distance between the interacting ions. The possibility of performing this is provided by the RKKY model of interacting localized moments in metals. The model contains a number of simplifying assumptions about the nature of the conduction electrons which are, unfortunately, not usually justified. Very little progress has been made, however, in refining the model in order to make it more realistic. One of the simplifying assumptions is that the Fermi surface is spherical (that is, that the conduction electrons are free). The dropping of the simplifying assumptions raises enormous difficulties in computation.

We shall give here a brief outline of the RKKY model without dwelling on the details. For this the reader is referred to de Gennes (1962), Mattis (1965) to mention only two of the numerous works available on this subject, also see ch. 3, subsection 4.1. The essential form of the indirect interaction between localized moments was introduced by Ruderman and Kittel (1954) to describe the hyperfine interactions between nuclear moments. This was then applied to the exchange interaction between localized electronic moments (Kasuya, 1956; Yosida, 1957).

The conduction electrons are representable by the wave functions $U_{\boldsymbol{k}}(\boldsymbol{r})e^{i\boldsymbol{k}\cdot\boldsymbol{r}} = \Phi_{\boldsymbol{k}}(\boldsymbol{r})$, where $U_{\boldsymbol{k}}(\boldsymbol{r})$ has the periodicity of the lattice. The conduction electrons with wave vector $\boldsymbol{k}$ are scattered by a magnetic 4f ion at position $\boldsymbol{R}_i$. The wave vector after scattering is $\boldsymbol{k}'$. Due to s–f exchange this scattering is spin dependent, resulting in a spin polarization around the scattering centre. The s–f exchange matrix element can be shown to be

$$-2(g-1)G(\boldsymbol{k},\boldsymbol{k}')\boldsymbol{s}\cdot\boldsymbol{J}_i\,e^{i(\boldsymbol{k}-\boldsymbol{k}')\boldsymbol{R}}$$

where the conduction electron spin density is $\boldsymbol{s}$ and $\boldsymbol{J}_i$ the angular momentum quantum number of the 4f scattering centre, $G(\boldsymbol{k},\boldsymbol{k}')$ is the exchange integral of the s–f interaction. In the usual RKKY model the simplifying approximation is made that $G(\boldsymbol{k},\boldsymbol{k}')=G(\boldsymbol{k}-\boldsymbol{k}')=G$, and that the Fermi surface is spherical (free electrons). The spin polarization around the scattering centre is then given by

$$\boldsymbol{s}(\boldsymbol{r})=-\frac{9\pi n^2}{2E_F}G\boldsymbol{S}F(2k_Fr)$$

where n is the electron density,

$$E_F=\hbar^2k_F^2/2m^*,\qquad F(x)=(\sin x-x\cos x)/x^4.$$

We see that this spin polarization is a spherical oscillating function of distance. If the free electron approximation is good the k_F can be expressed as $(3\pi^2n)^{1/3}$ and the effective electronic mass $m^*=m_0$. The spin polarization interacts by exchange with a localized neighbour ion at distance R_{ij} from the scattering centre. The corresponding energy is

$$E=-2G\boldsymbol{s}(\boldsymbol{R})\boldsymbol{S}_j=\frac{9\pi n^2}{E_F}G^2\boldsymbol{S}_i\cdot\boldsymbol{S}_jF(2k_FR_{ij}).$$

Since the ion j also influences the ion i the total exchange energy of the indirect interaction between i and j is

$$E=\frac{18\pi n^2}{E_F}G^2\boldsymbol{S}_i\cdot\boldsymbol{S}_jF(2k_FR_{ij}).$$

Substituting this interaction energy into the molecular field expression (Bleaney and Bleaney, 1965) for T_C or θ_p, it can be shown that

$$T_C=\theta_p=\frac{3\pi n^2}{kE_F}G^2(g-1)^2J(J+1)\sum_{i\neq0}F(2k_FR_{0i}). \tag{14.3}$$

θ_p is proportional to the molecular field at a central ion 0 resulting from an interaction with all neighbours i at distance R_{0i}. This type of summation is of course only valid when all magnetic ions are crystallographically identical. Otherwise a summation for all R_{ij} is necessary.

For antiferromagnetic materials there exists some other spin arrangement ($q\neq0$). Here $\boldsymbol{q}$ is the wave vector of some spin spiral structure (see fig. 14.2) whose wavelength λ is equal to $2\pi/q$. Conical spin arrangements need not be considered here since they are only stabilized by the presence of anisotropy.

The stable structure (described by $\boldsymbol{q}_0$) is that for which the energy of the system is a minimum. This gives (see Mattis, 1965)

$$T_N=\frac{3\pi n^2G^2(g-1)^2J(J+1)}{kE_F}\sum_{i\neq0}F(2k_FR_{0i})\cos(\boldsymbol{q}_0\cdot\boldsymbol{R}_{0i}). \tag{14.4}$$

The expression for the Fermi energy above contains the effective mass m^* of the conduction electrons. This should of course be equal to m_0 if the application

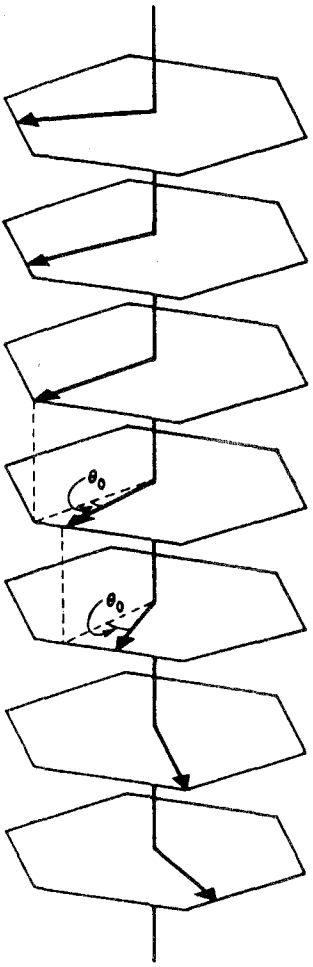

Fig. 14.2. A schematic representation of a helical spin structure for the example of a hexagonal lattice. The spins in a plane are parallel, but the direction rotates from plane to plane (Martin, 1967).

of the RKKY model is valid. We can thus use the deviation of m^*/m_0 from unity as a check of the possible validity of the model. The exchange integral G is another unknown quantity. The summation over $F(2k_F R_{0i})$ can, however, be calculated theoretically. Since we have two unknowns m^* and G, we require another equation in addition to the expression for θ_p. This is supplied e.g. by resistivity measurements, from which the spin disorder resistivity can be measured in many cases (see fig. 14.36 in subsection 2.5). The expression for the spin disorder resistivity ρ_{spd} is

$$\rho_{spd} = \frac{3\pi N m^*}{2\hbar e^2 E_F} G^2 (g-1)^2 J(J+1). \tag{14.5}$$

Equations (14.3) and (14.5) can be solved for the two quantities m^* and G, which

can be expressed as a function of (ρ_{spd}/θ_p) according to the method of Dekker (1965).

It should be pointed out that the application of this procedure should be restricted to materials which are ferromagnetic at absolute zero temperature. This is because of the possible existence of superzone boundaries (Elliott and Wedgwood, 1963) arising from the periodicity of the spin structure which has a different periodicity to that of the lattice. These superzone boundaries cut the Fermi surface, distorting it and changing the conduction electron properties. Thus the effective mass m^* in the ordered antiferromagnetic state differs from that in the paramagnetic state where these effects are absent. The extrapolation (shown schematically in fig. 14.36 of subsection 2.5) then gives an experimental value ρ_m, whose magnitude is not only determined by the relaxation time τ of the electron scattering due to spin disorder, but also by the conduction electron characteristic m^*. Since m^* is not uniquely determined the application of eq. (14.5) where m^* is implicitly constant, is invalid.

2.1.5. *Applications and modifications of the* RKKY *model*

None of the modifications of the RKKY model which eliminate the two main simplifying assumptions (free electrons and no dependence of the scattering upon $k - k'$) can be said to have superceded the simple model in practicability and ease of application. It must be stressed, however, that the RKKY model is rarely a realistic basis upon which to describe magnetic ordering in real metals. The usual method of application of the simple model is as follows. The theoretical quantity proportional to θ_p (it may be the RKKY sum or the sum multiplied by some power of k_F) is plotted as a function of k_F, and compared with the experimental θ_p as a function of k_F assuming that the density n of conduction electrons is known and that they are free, i.e. $k_F = (3\pi^2 n)^{1/3}$. (The n value is usually varied within a pseudobinary series by replacing one non-magnetic component by another.) The theoretical RKKY sum is, however, an oscillating function of k_F. Thus, in 50% of all cases theory will predict the correct sign of θ_p. Of all experiments whose signs agree with theory, 50% of these will agree with theory as far as the sign of the slope $d\theta_p/dk_F$ is concerned. Thus the comparison of theory with experiment appears reasonable in a quarter of all cases just by probability considerations alone. Needless to say, many attempts at comparing theory with experiments are not successful. The usual procedure in this case is to shift the theoretical k_F values until agreement is achieved. One then considers the parameter k_F/k_F^0 as a measure of the deviation of the conduction electrons from the free character (k_F^0 is for free electrons and k_F is the shifted value.) Since the wavelength of the oscillations is usually a fraction of k_F^0 (of the order of $\frac{1}{3}$) it is clear that in the worst cases a shift of less than 30% from k_F^0 can rectify the situation, even if the RKKY model were totally wrong. A survey of the literature shows that k_F/k_F^0 ratios of about 0.8 are often obtained and attributed to deviations from the free electron character. However, such conclusions should be made with caution since as we have seen, such values can be expected to be obtained just by laws of chance alone. The situation is slightly

more convincing when one does not limit oneself to the paramagnetic temperature range, but rather extends applications to calculations of the possible stable spin structures and the occurrence of ferromagnetic–antiferromagnetic transitions (Mattis, 1965; Gartmayer, 1969). Theoretical magnetic structures cannot be compared easily with experiment, however, since Gd (the only magnetic lanthanide with $L = 0$, and hence the only lanthanide to which the RKKY model is well-suited) is a strong neutron absorber in the natural isotopic mixture. Therefore it is difficult to obtain the magnetic structure of Gd compounds experimentally by neutron diffraction.

A number of modifications of the simple model have been developed. However, in many cases the improvements achieved are minimal and in some cases even the simple model achieves better agreement with experiment. One modification which does not affect the two main simplifying assumptions takes into account the finite mean free path λ of the conduction electrons. The long-range polarization given by $F(2k_F R)$ is multiplied by an empirical factor $\exp(-R/\lambda)$ which shortens the range of the spin polarization. A generalization of the RKKY model to non-spherical Fermi surfaces was developed by Roth et al. (1966). Whereas the simple theory gives a r^{-3} decay they obtain in some directions r^{-2} and even r^{-1} decays. It was suggested that the model may find applications in describing the dilute systems of lanthanides in Pd. Some modifications of the RKKY model in which realistic energy band structures are taken into account find no application to real systems due to the lack of accurate data from band structure calculations. Bambakidis (1970) for example calculated the indirect exchange between neighbouring spins for Gd using non-relativistic APW for the electronic bands. This calculation yielded a sign for the exchange between nearest neighbours which disagrees with the ferromagnetism of Gd, whereas the RKKY model based on free electrons predicts ferromagnetism, although the Fermi surface is known to be by no means spherical. Taking into account the real band structure leads to the introduction of anisotropy into the interaction. Another extension of the RKKY model was developed by Debray and Sakurai (1974) in which account is taken of inter-electron interactions and the s–f exchange integral is approximated by the form factor of the local-moment density. This model was applied to $GdZn_2$ in an attempt to account for the positive value of the paramagnetic Curie temperature. The details will be presented later (subsect. 2.5).

2.1.6. *The Néel two sublattice model of antiferromagnetism*

In this model, due to Néel (1957), an antiferromagnet is divided into two sublattices of opposing spin direction. The spontaneous magnetization of each sublattice is M_a and M_b. An ion in sublattice a experiences an exchange field $n'M_a - nM_b$ and the exchange field acting on an ion in sublattice b is $n'M_b - nM_a$, where n' and n are the intra- and intersublattice molecular field coefficients respectively. At high temperatures the Curie–Weiss law is obeyed giving $\theta_p = \frac{1}{2}C(n' - n)$ where C is the Curie constant. Below the temperature T_N antiferromagnetic ordering develops if n' and n are positive and each sublattice has a

magnetization $\frac{1}{2}M$ which will depend on temperature. The spontaneous magnetization of each sublattice drops to zero at T_N given by $T_N = \frac{1}{2}C(n' + n)$. At temperature T_N the susceptibility χ is given by $\chi = 1/n$. The simplifying assumptions made are that $n' \gg n$ so that each sublattice is a magnetically rigid entity, and that the crystal is uniaxial so that the exchange energy can be expressed as

$$E_w = \mu_0 n \boldsymbol{M}_a \cdot \boldsymbol{M}_b = \mu_0 n \tfrac{1}{4} M^2 \cos(\theta - \theta')$$

where $M_a = M_b = \frac{1}{2}M$ and θ and θ' are the angles between the crystal axis and $\boldsymbol{M}_a$ and $\boldsymbol{M}_b$ respectively.

In the absence of anisotropy the model cannot account for metamagnetic transitions with critical fields. The uniaxial magnetocrystalline anisotropy energy (arising from crystal fields) is equal to $-\frac{1}{2}K_0(\cos^2\theta + \cos^2\theta')$. In addition another anisotropy term arising from the anisotropic part of the magnetic dipole interactions is introduced and can be expressed as $-K_1 \cos\theta \cos\theta'$. The isotropic part of the dipole interactions is incorporated into the exchange term thus modifying the value of n. At low temperatures the stable antiferromagnetic structures are (A_p) where the moments are parallel to the axis this being for $K_0 - K_1 > 0$ and (A_n), normal to the axis, for $K_0 - K_1 < 0$. Upon applying a field normal to the antiferromagnetism direction the moments are generally folded up into the direction of the field with a constant susceptibility. For a field parallel to the moment directions two types of behaviour can occur: spin flip and spin flop for anisotropy strong and weak compared with inter-sublattice exchange, respectively. These types of behaviour are illustrated in fig. 14.3. In calculating the energetics of the problem only the initial and final energies before and after the transitions are compared, nothing being said about how the potential barrier due to anisotropy is to be overcome. For fields applied parallel to the moment directions in the A_p spin structure a spin-flip transition is characterized by a critical field

$$H_c = \tfrac{1}{2}nM - 2K_1/\mu_0 M \tag{14.6}$$

whereas for the A_n spin structure (spins in the basal plane) we have

$$H_c = \tfrac{1}{2}nM. \tag{14.7}$$

It should be pointed out that for a uniaxial crystal with spin structure A_n no

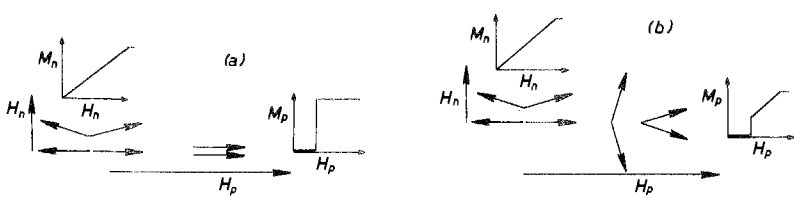

Fig. 14.3. Schematic representation of (a) the spin-flip and (b) the spin-flop transitions and their associated magnetization curves (Poldy and Taylor, 1973a). The subscripts n and p denote normal and parallel, respectively.

mechanism is available for the occurrence of critical field transitions since the spins have a freedom in the basal plane. Thus, when the field is applied parallel to the antiferromagnetism direction the spins are in no way constrained to remain parallel to the field since anisotropy within the basal plane is absent. Thus eq. (14.7) is unrealistic for a uniaxial crystal. The expressions for the critical fields in spin-flop transitions contain terms involving K_0. For details the reader is referred to the original article by Néel (1957). The susceptibility χ_n perpendicular to the moment direction is given by

$$(A_p\text{-type}): \qquad \chi_n = n\left[1+\frac{2(K_0-K_1)}{\mu_0 n M^2}\right]^{-1}; \tag{14.8}$$

$$(A_n\text{-type}): \qquad \chi_n = n\left[1-\frac{2(K_0-K_1)}{\mu_0 n M^2}\right]^{-1}. \tag{14.9}$$

The n' and n parameters are related by

$$\frac{n'}{n} = \frac{T_N+\theta_p}{T_N-\theta_p}. \tag{14.10}$$

In subsection 2.6 an example will be given of a system to which this theory was applied. In the following sections a description of the magnetic properties of the various intermetallics with no 3d moments will be given.

2.2. RAl_2 *compounds*

The most extensively investigated B-element with a zero magnetic moment in rare earth intermetallic compounds is aluminium. Obviously different reasons can be given for this fact, but our opinion is that the two most important reasons are firstly the easy accessibility of these compounds even in the form of single crystals, because many of these compounds are congruently melting, and secondly, their relatively simple crystal structure, $MgCu_2$ type with space group Fd3m. The RAl_2 compounds are therefore a prototype of R-intermetallics in general.

Due to the availability of single crystals a large number of physical methods can be applied to the study of RAl_2 compounds. These include magnetic measurements in various crystallographic directions, NMR on the ^{27}Al nucleus, EPR measurements, neutron diffraction, resistivity, specific heat, Mössbauer-measurements and so on. These experiments are valuable for comparison with theoretical models of magnetic ordering. A rough proportionality of θ_p with de Gennes factor is obtained only for the heavy lanthanides (fig. 14.4). For the light lanthanides the experimental values deviate considerably. Kanematsu (1968) was able, by taking account of 4f orbitals, to rectify this discrepancy. Calculations show that the influence of the crystal field can be large. The rare earth atoms in this structure belong to a diamond lattice. The Al atoms form tetrahedra. If the magnetic interactions are described by a molecular field model then it is possible to analyze the experimental results by means of the following hamiltonian

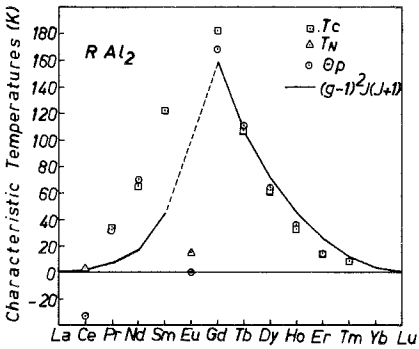

Fig. 14.4. Characteristic temperatures for RAl_2 compounds and the theoretical de Gennes factor.

(Purwins et al., 1976):

$$\mathcal{H} = B_4^0(\hat{O}_4^0 + 5\hat{O}_4^4) + B_6^0(\hat{O}_6^0 - 21\hat{O}_6^4) - g\mu_B \boldsymbol{J}(\boldsymbol{H} + \boldsymbol{H}_M). \tag{14.11}$$

This hamiltonian is applicable for crystal structures where only the cubic terms, without any terms of higher order, are sufficient. By means of the parameter H_M, which corresponds to the molecular field, and the two crystal field parameters designated B_4^0 and B_6^0 practically all properties of these materials can be described coherently. In table 14.2 are shown the Curie temperatures, the crystal field parameters and the moments of some RAl_2 compounds. These data are based on single crystal measurements and can therefore be regarded as being of special importance. The magnetization curves for $PrAl_2$, $NdAl_2$, $DyAl_2$ and $ErAl_2$ can be explained quantitatively. Furthermore with the same set of parameters H_M, B_4^0 and B_6^0 the different behaviours of the magnetization in the three principle axes of this cubic crystal can be explained and quantitatively described. Especially the anisotropy in $PrAl_2$, $NdAl_2$ (Purwins et al., 1974) and

TABLE 14.2.
Magnetic and crystal field parameters of RAl_2 compounds. χ_s is the high field susceptibility.

	T_C (K)	θ_p (K)	gJ	M_s (μ_B)	$\chi_s 10^6$ (μ_B/G)	$B_4^0 10^{-4}$ (meV)	$B_6^0 10^{-6}$ (meV)	Easy axis	References
$CeAl_2$	4	−28+	2.14	0.70	2.0	250	–	[111]++	Barbara et al. (1974b) Purwins et al. (1976) Purwins et al. (1974)
$PrAl_2$	33	33	3.2	2.88	0.25	−44	−88	[100]	Barbara et al. (1974b) Purwins et al. (1976)
$NdAl_2$	65	79	3.27	2.45	1.4	−10.6	55	[100]	Barbara et al. (1974a) Purwins et al. (1976)
$TbAl_2$	100	112	9.0	8.90	1.1	3.0	0.26	[111]	Barbara et al. (1974d) Purwins et al. (1976)
$ErAl_2$	15	16	9.0	7.80	3.2	0.8	−1.21	[111]	Barbara et al. (1974b) Purwins et al. (1976)
$HoAl_2$	33	36	10	9.18	–	−0.69	0.65	[110]+++	Barbara et al. (1975b)

+Extrapolated from high temperatures; ++In field larger than 50 kOe; +++Below 20 K.

also the discontinuous change of the magnetization in $DyAl_2$ in an external magnetic field can be explained (Purwins et al., 1975).

Neutron diffraction measurements, which had been performed on polycrystalline $ErAl_2$ (Nereson et al., 1968; Will, 1968) and $DyAl_2$ (Nereson et al., 1966) are not completely consistent with these calculations and findings on single crystals. A weak antiferromagnetic component in the magnetic coupling of these compounds was found in contrast to the single crystal measurements which explain the behaviour of these materials solely on the basis of a ferromagnetic coupling.

Measurements of the magnon dispersion relationship on $NdAl_2$ and $TbAl_2$ and also crystal field and molecular field calculations agree well with the values calculated using the above-mentioned hamiltonian (Houmann et al., 1974).

Based on measurements of the specific heat on $NdAl_2$ it has been shown that the crystal field energy is of the same order of magnitude as the exchange energy (Bak, 1974). Therefore a realistic calculation of the properties of a RAl_2 compound must take into account calculations of the crystal field energy and of the exchange energy, in order to be able to explain the experimental facts. In the last term of eq. (14.11) the molecular field H_M is representative for the specific exchange energy of the intermetallic compound considered. From this it can be seen that, naturally, the minimum value of the energy which is characteristic for the stable magnetic configuration depends simultaneously on all terms, i.e. on the crystal field energy and on the exchange energy. The hamiltonian, however, should not be overstressed. The calculation of the crystal field energy is based on a point charge model, and such a model is naturally a very crude approximation of a far more complicated situation within a real crystal with real atoms. On the other hand the exchange energy is described by a crude model, as for instance the RKKY model. Therefore it is not useful to calculate one of several terms with an extremely high accuracy, when at the same time other terms are known only to a fraction of an order of magnitude.

In RAl_2 compounds where the R-atom bears a magnetic moment, the measured R-moment depends on the direction in which it is measured. In the so-called hard direction the change and influence on the R-moment is far larger than in the easy axis. The measured R-moments in the hard direction, expressed as percentages of the free ion values, are: for Ce 33%, Pr 90%, Nd 75%, Tb 99%, Er 87%, (Barbara et al., 1974b). One sees, therefore, that the R-moments by no means show the simple behaviour of free R^{3+} ions. Furthermore, upon cooling below the magnetic ordering temperature, a tetragonal distortion of the lattice is sometimes observed. Although the distortion factor is only 10^{-3} the magnetic moment of Nd in the hard direction is, as discussed above, only 75% of the magnetic moment of a Nd^{3+} ion in the easy direction (Barbara et al., 1974a).

A large amount of information has been gained, especially in the case of RAl_2 compounds, by means of neutron diffraction and neutron scattering experiments. Investigations were performed by Nereson et al. (1966) on $DyAl_2$ and $NdAl_2$, by Olsen et al. (1967) on $PrAl_2$, by Nereson et al. (1968) on $PrAl_2$ and $ErAl_2$, by Will

(1968) on $ErAl_2$ and by Millhouse et al. (1972) on $HoAl_2$ and $TbAl_2$. While Nd, Pr and Dy in RAl_2 are distinctly influenced by the crystal field, in $ErAl_2$ this influence is very small. For Er in $ErAl_2$ $9.2 \pm 0.2\ \mu_B$ was observed which is in agreement with the 3+ ion value $9\ \mu_B$. Also by measurements on (Er, Y)Al_2 it has been found that the Curie temperature decreases linearly with increasing Y-concentration (Will and Bargouth, 1972). Since one can assume, to a first approximation, that the exchange remains constant and since the lattice spacing varies linearly in this series, the calculated RKKY sum would also predict a linearly decreasing Curie temperature. Therefore this additional assumption (constant exchange) seems to be valuable in explaining the temperature behaviour of this pseudobinary series. For an Y-concentration of as high as 50% the Er-moment is however decreased to $8.8\ \mu_B$ and this means that with an increasing Y-concentration the crystal field influence is also increasing. This is in agreement with Mössbauer measurements on ^{166}Er in (Er, Gd)Al_2 performed by Purwins (1970) and (Er, Y)Al_2 performed by Zinn (1971). The Curie temperature T_C increases in the (Er, Gd)Al_2 series beginning with $ErAl_2$ linearly from 5 K to 161 K. Similarly the hyperfine field also increases linearly, at small Gd-concentrations; however, a large change in the quadrupole splitting is observed. This is explained by mixing of the $\frac{3}{2}$, $\frac{9}{2}$ and other excited states into the $\frac{15}{2}$ ground state of Er. For large Gd concentrations this effect becomes smaller because of the increase in influence of the Gd exchange field.

For the mixed crystal series (Tm, Y)Al_2 EPR measurements have been compared with neutron diffraction and susceptibility measurements (Devine et al., 1973). Agreement between these different measurement techniques with respect to the crystal field splitting of Tm would only be obtained if a considerable change of the crystalline electric field parameters with respect to various host lattices can be assumed. On the other hand Heer et al. (1974) show for (Er, Y)Al_2 that the crystal field parameters are not significantly changed by increasing Y-content, although no statement with respect to the set of crystal field parameters could be made. This shows that a complete description of the magnetic properties only by crystal field parameters does not seem to be possible.

Specific heat measurements performed on RAl_2 where R = La, Ce, Pr, Nd, Gd, Tb, Ho have been used in order to obtain information about the magnetic contribution in the specific heat (Deenadas et al., 1971; Hungsberg and Gschneidner, 1972; Hill et al., 1973; Inoue et al., 1977). This was performed by subtracting the nonmagnetic contribution by means of parallel measurements on $LaAl_2$, $LuAl_2$ and YAl_2. The results show that the magnetic entropy can be equated with $R \ln (2J + 1)$. Curiously $GdAl_2$ and $TbAl_2$ show no λ anomalies, but rather, the smeared out effect of magnetic ordering suggests that the ordering is very gradually lost upon heating the samples through the Curie temperature. It must be added that this effect is by no means well understood. However it was established that, with increasing atomic number in the lanthanide series, the position of the 4f levels lies progressively more well-defined below the Fermi energy.

Nuclear magnetic resonance measurements (NMR) have been performed on many RAl_2 compounds. Since Al has no magnetic moment of its own the contribution from the R-atoms can be deduced directly. A negative exchange between the conduction electrons and the localized 4f-electrons of the order of -0.1 eV was observed by Jaccarino et al. (1960).

From the measurements on (Gd, Y)Al_2 the hyperfine field at the Gd site has been determined and is found to be directly proportional to the Gd concentration. The moment of the Gd atom is not changed by dilution. However the calculation only takes into account contributions from the nearest neighbours. The sign of the hyperfine field is in agreement with RKKY calculations (Dintelmann and Buschow, 1971). The results of the determination of the easy axes of magnetization by NMR measurements are at this time only partly in agreement with the determinations by means of magnetic measurements on single crystals (Kaplan et al., 1973).

From the small magnetic moment of Ce in $CeAl_2$ it can be seen that this compound is a special case. Since Ce is the first lanthanide which has a magnetic moment, it is of special interest. On $CeAl_2$ single crystals high magnetic field measurements have been performed in the temperature range from 1.5 K to 30 K in fields up to 15 T (Barbara et al., 1975a). The explanation of most measurements is based on the two following considerations: In one case it is assumed that Ce has a fluctuating valency between 3+ and 4+. The other explanation is based on the assumption that a mixture of Ce^{3+} and Ce^{4+} ions is present in the alloys. In $CeAl_2$ at 3.4 K and at approximately 4.5 K phase transitions are observed (Walker et al., 1973; Barbara et al., 1975a). The shape of the (M, H) curve shows a distinct difference, if measured above and below the phase transition at approximately 4.5 K. At high magnetic fields an explanation of the magnetic properties of $CeAl_2$ by means of a simple crystal field model is not possible. Nevertheless in high magnetic fields and at temperatures above 6 K $CeAl_2$ yields, after extrapolating to $T = 0$ K, 0.71 μ_B which is consistent with a Ce^{3+} ion and therefore with $J = \frac{5}{2}$. The results of Barbara et al. (1975a) reveal metamagnetism at 1.7 K. Barbara et al. (1977) conclude on the grounds of neutron diffraction studies that $CeAl_2$ has an antiferromagnetic sinusoidally modulated spin structure below 3.8 K. Measurements of the dilatation show a peak at 3.36 K which is in agreement with measurements of the specific heat. These measurements, however, exclude a Ce^{3+} to Ce^{4+} transition although in (Y, Ce)Al_2 with small Ce-concentrations Ce is incorporated as Ce^{4+}. A possible explanation for the transition in the range of 4.5 K to 5 K could be that short-range ordering effects are present which become dominant only above 5 to 6 K. The crystalline electric field splits the $J = \frac{5}{2}$ ground state of the Ce^{3+} ion at temperatures lower than 3.4 K into a doublet and a quartet ($\Delta E = 100$ K, Barbara et al., 1975a). At high temperatures the resistivity of $CeAl_2$ can be explained by means of the Kondo effect (van Daal and Buschow, 1970). The influence of the crystalline electric field on the spin disorder resistivity is only essential for temperatures smaller than the above-mentioned crystal field splitting of Ce^{3+}.

When discussing the magnetic properties of rare earth Al-compounds, the properties of the corresponding Y, La and Lu-compounds are usually taken as a basis, because in these compounds a magnetic moment is not present. While, however, the YAl_2 and the $LuAl_2$ compounds show a similar behaviour, the $LaAl_2$ compound drops out because superconductivity (with $T_c = 3.29$ K) has been observed in this compound (Hungsberg and Gschneidner, 1972). Also EPR measurements on the compounds (Lu, Ce)Al_2 and (Y, Ce)Al_2 show that no agreement even in the sign of the crystal field parameters is observed, although band-structure calculations (Switendick, 1973) are very similar for these isostructural compounds (Rettori et al., 1975). The influence of additions of magnetic rare earth elements on the superconductivity has been extensively studied. (La, Ce)Al_2 shows, as a function of the Ce-content, a very complex behaviour, also see ch. 11, subsection 3.2. Either superconductivity or the Kondo effect was found by Steglich and Winzer (1973). Riblet and Winzer (1971) show that at low temperatures firstly superconductivity and at even lower temperatures normal electrical resistivity appear. These temperatures naturally depend on the Ce-content. Small amounts of Gd in the ppm-range in $LaAl_2$ yield no Kondo effect. The magnetic moment of Gd is however larger by 1 μ_B than has been observed by ESR measurements. This fact can be connected with a polarization of the conduction electrons. The low temperature mobility of the electrons is obviously determined by the Al-atoms in $LaAl_2$. This can be deduced from measurements of the Debye temperature. The electronic specific heat in $LaAl_2$ is far larger than the corresponding values at low temperatures of YAl_2 and $LuAl_2$. This fact is probably intimately connected with the appearance of superconductivity in $LaAl_2$ (Maple, 1973). For $SmAl_2$ a large influence of the crystal field on the Sm^{3+} ground state is observed. The properties of $SmAl_2$ can be explained by assuming a mixture of $J = \frac{5}{2}$ with excited states corresponding to $J = \frac{7}{2}$ and $J = \frac{9}{2}$. Connected with this, Sm shows a behaviour which could be characterized, with respect to L–S coupling, as similar to the behaviour of a "heavy rare earth". Therefore the magnetic moment changes its sign relative to the spin and a magnetic moment of about 0.2 μ_B is observed, compared to the expected moment 0.71 μ_B which is characteristic of $J = \frac{5}{2}$, (Buschow et al., 1973a; van Diepen, 1968). The influence on the magnetic moment, of the conduction electrons resulting from the presence of Al-atoms, can be neglected.

$YbAl_2$ the last of the RAl_2 compounds with unfilled 4f-shells is complicated with respect to its electronic structure, especially compared to $LaAl_2$. Similarly to $LuAl_2$ and YAl_2, $YbAl_2$ does not become superconducting down to 0.05 K. It is not possible to explain the behaviour of $YbAl_2$ by a simple ionic model. At low temperatures a high density of states and therefore an enhanced magnetic susceptibility is observed. This can be explained by means of a virtual bound 4f-state. The number of the holes in the 4f-level is calculated to be 0.5/Yb-atom. The high temperature susceptibility of this compound can be explained with the help of a 2-level model where the higher level is a localized Yb^{3+} state which is approximately 1800 K above the ground state (Havinga et al., 1973). This

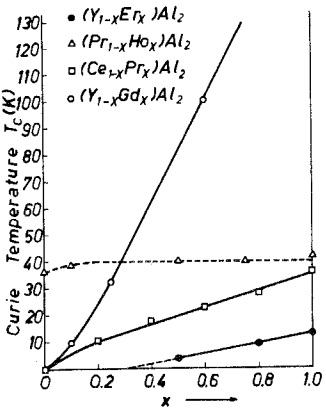

Fig. 14.5. Curie temperatures of pseudobinary systems: (Y, Er)Al_2 (Will and Bargouth, 1972); (Pr, Ho)Al_2, (Ce, Pr)Al_2 (Swift and Wallace, 1968); (Y, Gd)Al_2 (Buschow et al., 1967).

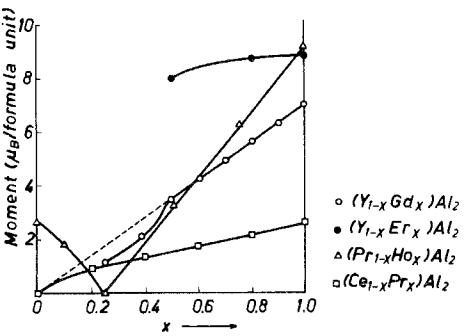

Fig. 14.6. Moments of pseudobinary systems: (Y, Gd)Al_2 (Dintelmann and Buschow, 1971); for other systems literature as in fig. 14.5.

statement is however in disagreement with NMR-measurements which seem to indicate, from the nuclear electric quadrupole interaction constant, that Yb in $YbAl_2$ is divalent (Jaccarino et al., 1960).

Upon substituting a magnetic lanthanide R into YAl_2 or $LaAl_2$ a linear increase of the Curie temperature has been observed (Buschow et al., 1967). On the other hand it was found by Will and Bargouth (1972) that an appreciable substitution (of the order of 10%) is required before any finite ordering temperatures appear. The latter is probably the more realistic situation.

Whereas the valency of the heavy lanthanides in RAl_2 (Yb excepted) appears clearly to be 3+ in all cases, the light lanthanides show a more complex behaviour. For example, in (Ce, Eu)Al_2 antiferromagnetism at 4 K was found (for more than 80% Eu). For Eu contents between 20% and 60% paramagnetism prevails (Swift and Wallace, 1968). Paramagnetic measurements on RAl_2 with the light lanthanides indicate a trivalent R ion in all cases except Eu which appears to be divalent. Figures 14.5 and 14.6 show the results of the Curie temperatures and the magnetic moments for various pseudobinary systems.

2.3. *Compounds with* CsCl *structure*

Much information is available concerning the magnetic properties of the equiatomic RB compounds with the CsCl structure. The causes of the popularity of these compounds are perhaps the wide range of possible non-magnetic

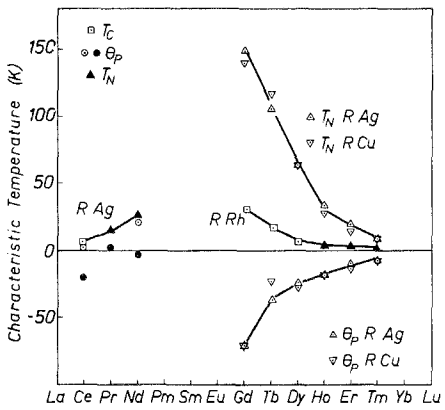

Fig. 14.7. Characteristic temperatures for RCu, RAg and RRh compounds. ● and ○ correspond to θ_p values extrapolated from high and low temperatures respectively.

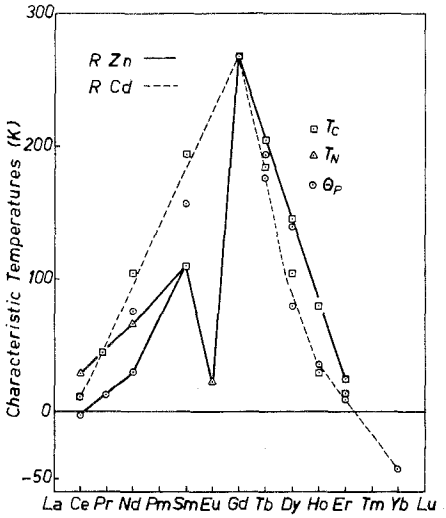

Fig. 14.8. Characteristic temperatures for RZn and RCd compounds (Eckrich et al., 1973; Alfieri et al., 1967; PrCd: Buschow, 1974).

B-elements available as a partner for the R-components, as well as the high symmetry of the structure. This is a cubic structure where the R and B atoms belong to two separate interpenetrating simple cubic lattices.

The possible B-elements include Mg, Cu, Zn, Pd, Rh, Ag, Cd, In, Au, Hg. The CsCl structure is not always stable for all the lanthanides, being unstable for example in the RCu and RAu series, for the light lanthanides, also see ch. 13, subsection 6.2. Most compounds involving Eu and Yb (YbAu excepted) do not form the CsCl structure and this is associated with the tendency of these lanthanides to adopt a divalent state. The instability of RRh with the light lanthanides and all RPd compounds except ErPd, TmPd and LuPd, is associated with the Fermi level lying above the peaks in the density of states function $N(E_F)$ due to 4d-electrons arising from Pd and Rh (Belakhovsky et al., 1975). It appears that the d-electrons play a large part in contributing to the cohesive energy of the lattice. As shown by Ihrig et al. (1973) band Jahn–Teller effects can also be effective in causing instability of this structure.

Most of the RB compounds with the CsCl structure show magnetic ordering below room temperature either of the antiferromagnetic or ferromagnetic type, although in some cases, as we shall see later there exist mixtures of these two possibilities. The ordering temperatures and paramagnetic Curie temperatures θ_p are displayed in figs. 14.7, 14.8 and 14.9. A general conclusion which can be drawn at this stage is that the monovalent B-elements (e.g. Cu, Ag) tend to give rise to antiferromagnetic order, and the divalent B-elements (Mg, Zn, Cd) tend to give ferromagnetic order (Cable et al., 1964; Morin et al., 1973; Walline and Wallace, 1964a,b, 1965). θ_p is generally roughly proportional to the de Gennes

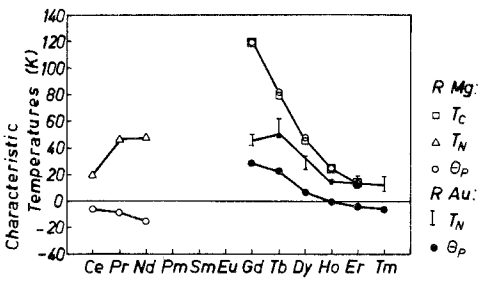

Fig. 14.9. Characteristic temperatures for RMg and RAu compounds.

factor in all cases except RAu. Paramagnetic measurements by Kissel and Wallace (1966) indicate however a good Curie–Weiss behaviour and agreement of p_{eff} with that expected for trivalent ions in YbAu, where there appears to be a mixture of divalent and trivalent ions, the latter increasing in abundance at high temperatures (see also $YbAl_3$, subsection 2.7). It should also be noted that YbAu is exceptional in forming the CsCl structure. Valence changes also appear to occur in CeAg and NdAg as the temperature is varied, resulting in variable θ_p values (fig. 14.7). The values extrapolated from high temperature results correspond to trivalent ions, whereas a higher valence sets in at low temperatures.

Whereas the RCu and RAg compounds are all antiferromagnetic, the RZn and RMg (Buschow, 1973b) compounds are not exclusively ferromagnetic. The difference between RZn compounds containing light and heavy lanthanides is due to a difference in the characters of the conduction electron wave functions and the shape of the Fermi surface (Buschow et al., 1974b). The magnetic properties have been measured by Eckrich et al. (1973), whose results differ a little from the original measurements of Kanematsu et al. (1969). The magnetic properties of RCd were investigated by Alfieri et al. (1967). All RCd compounds are ferromagnetic but SmCd showed diamagnetism which was not in agreement with later measurements by Buschow (1974). It should be pointed out that all samples of Alfieri et al. (1967) were melted with excess lanthanide element of the order of 20%. Generally good agreement was found between p_{eff} and the theoretical paramagnetic moment of the tripositive lanthanide ions except for YbCd and SmCd. SmCd shows no simple Curie–Weiss behaviour. Stewart et al. (1974) analyzed the susceptibility successfully as follows

$$\chi(T) = \chi_0 + D/(T - \theta_p'). \tag{14.12}$$

The θ_p' value from this equation was incorporated into fig. 14.8 as θ_p. From the measurements of Buschow (1974) PrCd appears to be ferromagnetic, and not antiferromagnetic as previously reported. The (M, H) curve of PrCd at 4.2 K shows an apparent metamagnetism accompanied by a large hysteresis. It is believed that domain wall pinning may be influencing the magnetic properties, being responsible for ambiguous behaviour.

The departure of the proportionality of the θ_p values to the de Gennes factor can be used as a measure of the variation of the s–f exchange energy G within a

series. This procedure was performed by Buschow (1974) who derived the expression

$$\frac{G_R^2}{G_{Gd}^2} = \frac{\theta_p(RB)}{\theta_p(GdB)} \frac{\frac{7}{2} \times \frac{9}{2}}{(g-1)^2 J(J+1)}. \tag{14.13}$$

This has been plotted for the various lanthanides and for the RCd, RZn and RMg series in fig. 14.10. RZn is seen to be reasonably well behaved whereas RCd and RMg show an appreciable deviation of the expression from unity, even becoming negative for RMg. The negative θ_p values for the light lanthanides, as opposed to the positive values for the heavies, may be due (Buschow and Oppelt, 1974) to variable effects of indirect couplings via d-electrons as the lattice parameter changes across the RMg series. Perhaps a similar explanation may be valid for RZn, where the light lanthanides give antiferromagnetism (fig. 14.8). It was concluded that in the RCd and RMg series there is an additional exchange between the R-moments which in the light lanthanides prevails over the RKKY interactions, and that the sign in the RCd series is different from that in the RMg series. These deviations were associated with possible influences of high densities of states at E_F due to d-electrons or to variable degrees of interband mixing. However these d-electrons, as mentioned later, are also expected to be present in the RZn series.

The ordering temperatures of RRh are extremely small compared with those of RZn, RCu, RAg. It was suggested by Morin et al. (1973) that in RRh dipole energies may be significant compared with the RKKY type of interactions. The compounds RRh with R = Gd, Tb, Dy show ferromagnetism, whereas for R = Ho, Er, Tm we have antiferromagnetism with a (π 0 0) magnetic structure. This means that the moments within a (1 0 0) plane are ferromagnetically coupled with each other and antiferromagnetically coupled with those in neigh-

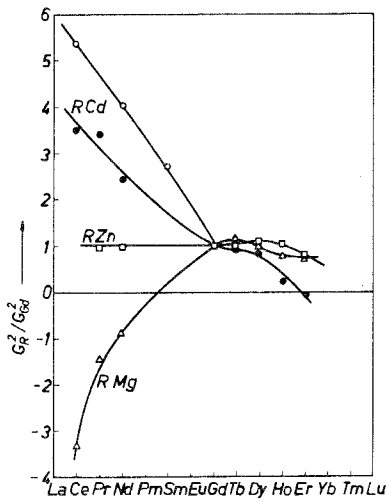

Fig. 14.10. Dependence upon atomic number, of the ratio $(G_R/G_{Gd})^2$. For RCd the open circles refer to data obtained from T_C values; all other data points refer to θ_p values (Buschow, 1974).

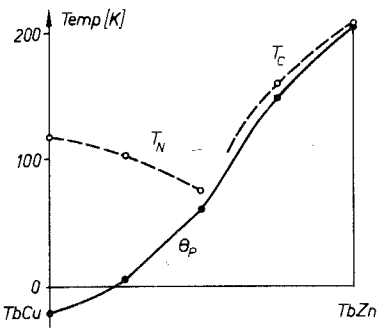

Fig. 14.11. Characteristic temperatures of the Tb(Cu, Zn) system (Pierre, 1969).

bouring planes. Strangely the T_C value for GdRh is smaller than that for $GdRh_2$ even though the latter has a lower concentration of magnetic ions.

Generally the application of the RKKY model to the compounds with the CsCl structure is not too successful. It always needs a shift of k_F from the free electron value k_F^0 before agreement is achieved. The cause of any discrepancies is usually ascribed to the presence of d-electrons (Morin et al., 1973), which can be present in the bands to a considerable extent. Many attempts at applying the RKKY model have involved pseudobinary series, such as Tb(Cu, Zn) in which case k_F/k_F^0 was found to be 0.85 (Pierre, 1969). The characteristic temperatures are shown in fig. 14.11 for this series. Buschow et al. (1975c) have concluded that the RKKY model fails for divalent B-elements, whereas better agreement is found for monovalent metals such as Ag and Cu.

The effect of conduction electron concentration upon magnetic interactions was studied systematically by Alfieri et al. (1966). These results, together with an RKKY fit by Buschow et al. (1972) are shown in fig. 14.12. The series involved are Gd(In, Ag), Gd(Zn, Ag) and it was assumed that Gd contributes three electrons, Ag one, Zn two, and In three electrons to the sea of conduction electrons. Also included are results of Sekizawa and Yasukochi (1966b). In this

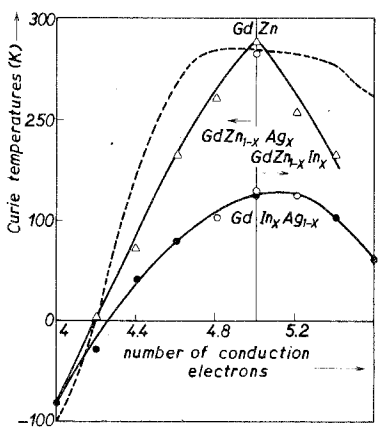

Fig. 14.12. Paramagnetic Curie temperatures as a function of electron concentration of some pseudobinary systems with the CsCl structure (Buschow et al., 1972). The dashed line is the theoretical RKKY fit. △ Alfieri et al. (1966), ● Sekizawa and Yasukochi (1966b), ○ Buschow et al. (1972).

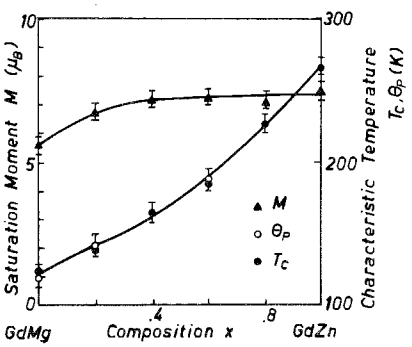

Fig. 14.13. Characteristic temperatures of Gd(Mg, Zn) together with saturation moments per formula unit (Buschow and Oppelt, 1974).

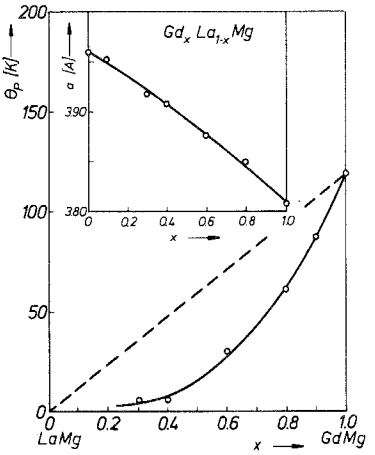

Fig. 14.14. Variation of θ_p for (Gd, La)Mg. The inset shows the variation of the lattice constant (Buschow and Schinkel, 1976).

figure it can be seen that the sample $Gd(Ag_{0.5}In_{0.5})$, although it has the same electron concentration as GdZn, has a considerably smaller value of the Curie temperature θ_p. This was explained by Buschow et al. (1972) as being due to the effect of the finite mean free path of the conduction electrons influencing the strength of the indirect exchange.

A similar phenomenon, which however requires another explanation is the fact that GdMg has a T_C value (118 K), which is much lower than that of GdZn and GdCd (268 and 270 K respectively), even though all three have the same electron concentration. Apart from this the saturation moment of GdMg was found to be 5.6 μ_B which is much lower than the free ion value 7 μ_B. In fig. 14.13 these two parameters are displayed with θ_p for the Gd(Mg, Zn) pseudobinary series. These phenomena were accounted for by Buschow and Oppelt (1974) by assuming a partial exchange of Gd sites with Mg sites in the otherwise ordered lattice. They then showed that a small degree of an antiferromagnetic coupling would thus be introduced which would account for the low value of θ_p in GdMg. Evidence for the partial lattice disorder was obtained from NMR measurements. However, neutron diffraction work by Buschow et al. (1974b) failed to reveal any evidence of this disorder in the isomorphous compound NdMg and the above explanation is put in doubt. Although the mechanism by which these antiferromagnetic coupling components arise is questionable, their presence was confirmed by studies on (Gd, La)Mg (Buschow and Schinkel, 1976). In this pseudobinary series the Gd–Gd distances were increased by dilution with La, whereupon the already low θ_p value decreased nonlinearly (fig. 14.14). The La substitution was found to introduce critical fields into the (M, H) curves (fig. 14.15) suggesting an increasingly strong antiferromagnetic component, which

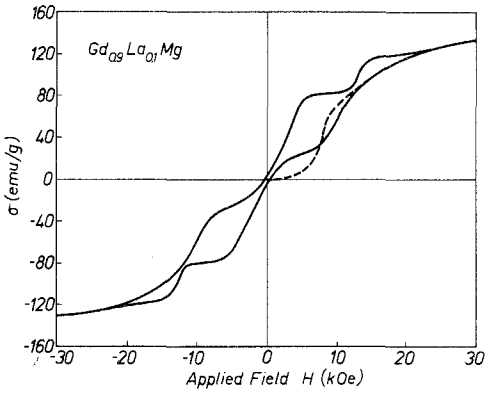

Fig. 14.15. Magnetic isotherms of $Gd_{0.9}La_{0.1}Mg$ at 4.2 K (Buschow and Schinkel, 1976).

becomes visible by La substitution. This suggests that GdMg is a borderline case where the antiferromagnetic interactions are extremely small. Since the relatively strong ferromagnetic interactions in GdZn are due mainly to the coupling via 5d electrons it is argued that the sensitivity of the indirect interactions via 5d electrons to interatomic distances could account for the variation in the exchange within the series Gd(Mg, Zn) and (Gd, La)Mg where antiferromagnetic interactions, presumably due to non-5d electrons, play a role. Recent work by Schäfer et al. (1976) confirms this type of behaviour in the heavy lanthanide RMg compounds, where the coexistence of antiferromagnetic and ferromagnetic components in TbMg was established by neutron diffraction. The magnetic structure has one cube direction twice as long as the crystallographic cell $(a, a, 2a)$. Magnetization measurements revealed large thermomagnetic history effects which may be associated with the pinning of narrow domain walls, section 5.

Determinations of spin structure have been performed by neutron diffraction experiments on the antiferromagnetic compounds where in many cases the results are inconclusive. In some cases conclusions have had to await confirmation by means of crystal field calculations and other methods such as thermal expansion measurements. In the case of DyCu neutron diffraction data (Winterberger et al., 1971) leave an ambiguity between a collinear antiferromagnetic structure with moments pointing along a four-fold axis and a non-collinear structure with moments directed along the four three-fold axes. These two possible structures are shown in fig. 14.16. After considering crystal field and dipolar energy calculations as well as Mössbauer data the non-collinear possibility was favoured, as is consistent with later measurements of thermal expansion (Morin and Pierre, 1974). Figure 14.17 shows the thermal variations (Morin et al., 1977) of the changes in the length along the c and a directions of a magnetized single crystal of DyZn. The volume strain ϵ_v is also included. In fig. 14.18 the thermal variation of the lattice parameters of DyCu and TbCu (Morin and Pierre, 1974) is depicted. Here we see that TbCu shows a large tetragonal distortion upon ordering, whereas DyCu does not. This is consistent with the

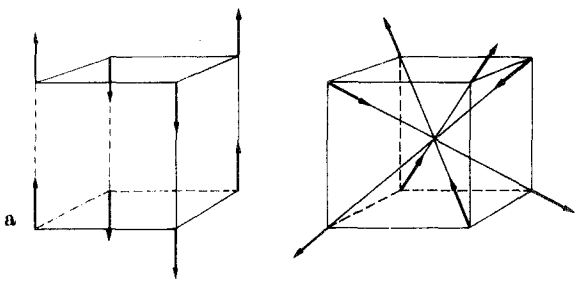

Fig. 14.16. Magnetic structures a) TbCu and TbAg, b) DyCu and DyAg (Morin and Pierre, 1974).

non-collinear structure for DyCu and the collinear structure for TbCu being adopted. Very similar thermal expansion results were obtained for TbAg and DyAg. The ferromagnetic compounds TbZn and DyZn show distortion as may be expected, except that in the case of TbZn the distortion becomes extremely small below 63 K and of another type, believed to be a small orthorhombic distortion. This low temperature first order transition corresponds to a moment rotation at 63 K from the [101] direction at low temperatures to [001] at higher temperatures below the Curie point. The change in moment direction in TbZn at 63 K is also evidenced by an anomaly in the specific heat measurements (Morin et al., 1974a). A similar transition at 23 K in HoZn is observed (Schmitt et al., 1977). The moment direction in HoZn rotates from [111] above 23 K to [110] below 23 K. The magnetization isotherms above and below this transition temperature are shown in fig. 14.19, together with those calculated theoretically. The crystalline electric field hamiltonian is expressed as

$$\mathcal{H} = WxO_4/F_4 + W(1-|x|)O_6/F_6 = A_4\beta\langle r^4\rangle O_4 + A_6\gamma\langle r^6\rangle O_6. \tag{14.14}$$

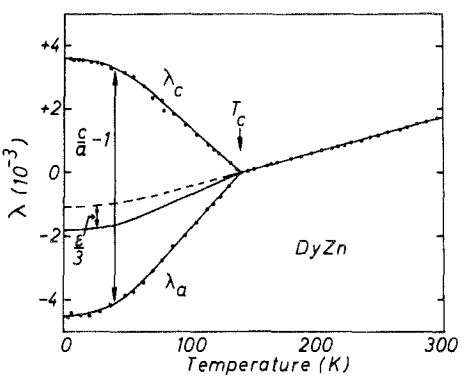

Fig. 14.17. Thermal variations for DyZn of the changes of length, measured along the c-axis (parallel to the magnetization) and the a-axis (a fourfold axis perpendicular to the magnetization). The paramagnetic curve is extrapolated down to 0 K (dashed line) according to the Grüneisen law (Morin et al., 1977).

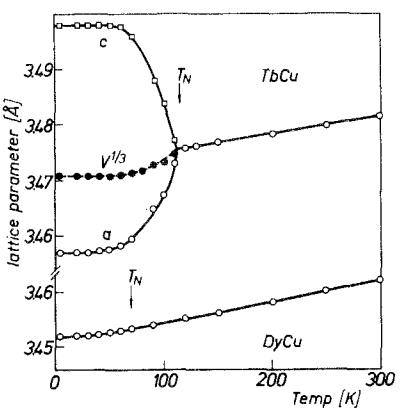

Fig. 14.18. The thermal variation of the lattice parameters of TbCu and DyCu (Morin and Pierre, 1974).

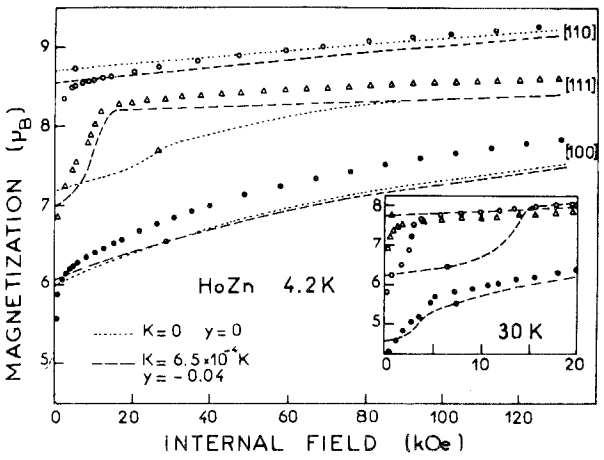

Fig. 14.19. Magnetization curves for a monocrystalline HoZn sample at 4.2 K (and 30 K for inset). Dotted curves are calculated with $W = 0.36$ K, $x = 0.08$ (eq. (14.14)); dashed curves are obtained by adding biquadratic exchange and magnetoelastic terms. To avoid confusion the axes symbols are repeated once on the theoretical curves (Schmitt et al., 1977).

For DyZn and ErZn no rotations occur and the easy direction remains [100] (Morin and Pierre, 1973a; Morin et al., 1977). The single crystal magnetization results for ErZn at 4.2 K are shown in fig. 14.20. The description of the anisotropy in terms of two parameters K_4 and K_6 is however not valid (Pierre, private communication). Magnetostriction leads to second order anisotropy terms and it is necessary to diagonalize the whole hamiltonian containing exchange, crystal field, as well as magnetoelastic terms, as discussed in the work of Schmitt, Morin and Pierre (Schmitt et al., 1977).

In addition to the above order–order transition as observed in ferromagnetic TbZn and HoZn, there exists a similar phenomenon in some antiferromagnetic compounds, where two transitions are also observed, at T_N and another lower transition temperature. This was observed by Walline and Wallace (1965) from magnetization measurements on TbCu and HoCu. Details of such behaviour were later observed for example in ErAg by neutron diffraction (Nereson, 1973). It was found that there were two antiferromagnetic phases both having tetragonal symmetry, the low temperature phase being commensurate with the lattice, and the higher temperature phase non-commensurate. Investigations by Buschow et al. (1975c) for the light lanthanides show that PrZn, NdZn and NdMg have a $(0\,0\,\pi)$ magnetically ordered structure. The RHg compounds, for

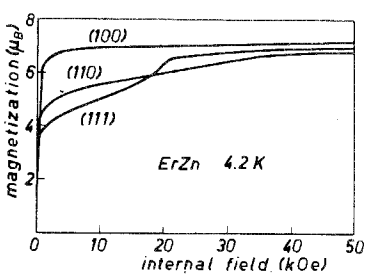

Fig. 14.20. Magnetization curve of ErZn at 4.2 K (Morin and Pierre, 1973a).

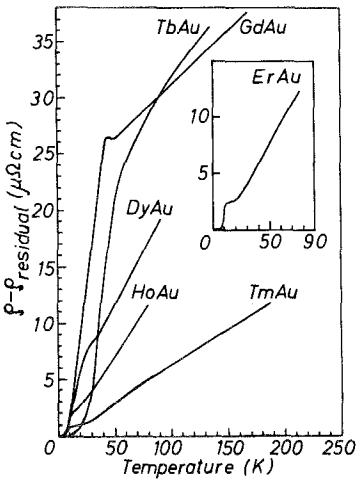

Fig. 14.21. Resistivity as a function of temperature for some RAu compounds (Chao, 1966). The compounds HoAu, ErAu (inset) and TmAu have low ordering temperatures in the range where the phonon contribution is non-linear.

example TbHg, appear to be ferromagnetic in keeping with the divalency of Hg. This series has been less extensively investigated than the others. The variety of magnetic structures generally available is influenced to a large extent by crystal fields. In PrAg, for example, the magnetic structure is ($\pi\,\pi\,0$) and the ground state of the crystal field levels, as determined by neutron diffraction (Brun et al., 1974) is the Γ_5 level.

Resistivity measurements were performed by Chao (1966) between 4 K and 250 K, for YAg and NdAg, as well as the heavy lanthanide RCu, RAg, and RAu compounds (fig. 14.21). The spin disorder resistivities were obtained by the conventional extrapolation procedure (see fig. 14.36) which yielded some negative values for the compounds with low ordering temperatures where the phonon contribution is small. The curves were subsequently re-examined by Pierre (1969) using a more realistic method of analysis. The resulting values of spin disorder resistivity were all positive, but not proportional to the de Gennes factor, which suggests that the effective mass or exchange constant may vary across the lanthanide series. The conduction electron effective masses obtained by combining the results with θ_p results are much in excess of m_0.

Band structure calculations are needed in order to determine the shape of the Fermi surface in intermetallics. The RKKY model would then have a more respectable foundation if applied to a compound whose Fermi surface is known to be approximately spherical and if the model could be explicitly avoided for the cases where the Fermi surface is distinctly nonspherical. As already mentioned in subsection 2.1 modifications of the RKKY model for general Fermi surface shapes are extremely difficult to apply. Band structure calculations up till now have been confined to the more symmetrical lattices. As a consequence, a very large fraction of such calculations involves the CsCl structure. As a first approximation the objects of the investigations contain no magnetic components, in order to find the undisturbed state of the Fermi surface. When

this is known then magnetic components can be introduced to approximate the situation in intermetallics with magnetic lanthanides. Thus most investigations involve such compounds as YCu, YZn.

Belakhovsky et al. (1972) performed APW calculations of the electronic structure of YCu and YZn for which they obtained +0.42 and 0.47 Ry for the Fermi energies of YCu and YZn respectively, with corresponding densities of states $N(E_F)$ equal to 1.9 and 2.35 electrons/eV unit cell. This is in agreement with specific heat measurements for YCu. De Haas–van Alphen effect measurements by Jan (1973) performed upon YZn single crystals have revealed two topological features of the Fermi surface one of which cannot be accounted for without a drastic modification of the APW calculation. It was suggested that a self-consistent calculation may improve the results. The features revealed by de Haas–van Alphen measurements are a small spherical pocket of carriers, as well as an open sheet, the latter giving the more serious discrepancy with the APW results. Additional experimental support for the de Haas–van Alphen results was obtained by magnetoresistance measurements (Sellmeyr et al., 1975). Hasegawa and Kübler (1974) performed APW calculations which were in agreement with the de Haas–van Alphen results, though the calculations were not self-consistent. The Fermi surface in the third band obtained from this calculation is shown in fig. 14.22. Some extremal cross sections of the third band Fermi surface are shown in fig. 14.23. Yashiro et al. (1976) were able to interpret their results of the Tb(Cu, Zn) system with the help of these band calculations for YZn. The Tb(Cu, Zn) system was studied by neutron diffraction which revealed a range of compositions where canted spin structures were present. The corresponding phase diagram is shown in fig. 14.24 (compare with fig. 14.11).

Apart from the above calculations, LCAO calculations by Breeze and Perkins (1975) also provided a reasonable description of the electronic structure in YZn.

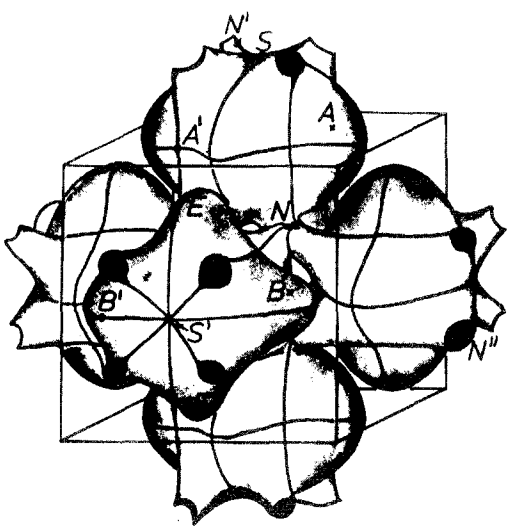

Fig. 14.22. Third band Fermi surface of YZn shown in extended zone scheme (Hasegawa and Kübler, 1974).

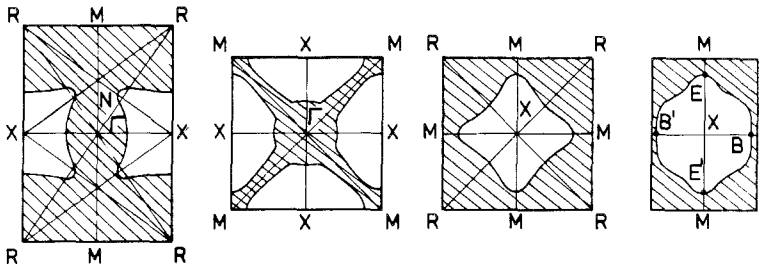

Fig. 14.23. Selected extremal cross sections of the third band Fermi surface of YZn (Hasegawa and Kübler, 1974).

Large effective masses are expected, in agreement with the results of Jan (1973) and the resistivity measurements of Chao (1966). The results of Breeze and Perkins (1975) reveal two distinct regions in the band structure, the lower involving Zn-4s and Y-5p orbitals, the higher band near the Fermi level being a mixture of Zn-4p and Y-4d orbitals. Energy band calculations have also been performed for LaAg and LaCd by Hasegawa et al. (1975). Peaks in the density of states were obtained for LaAg just above the Fermi energy which provide the conditions needed for the band–Jahn–Teller effect to influence the stability of the CsCl structure, discussed at the beginning of this section. Belakovsky et al. (1975) have obtained evidence, from theoretical studies of the electronic structure of DyZn, DyCu and DyRh, of the importance of d-electrons in these systems. In DyRh there appears to be a large transfer of electrons from Rh to Dy which suggests the necessity of performing self-consistent calculations. From isomer shift measurements Belakhovsky and Pierre (1971) deduce that the s-character decreases on going from DyCu to DyZn. This is in line with the belief that the d-character in RZn compounds is particularly strong compared with that in RB compounds with monovalent B-elements. APW calculations of

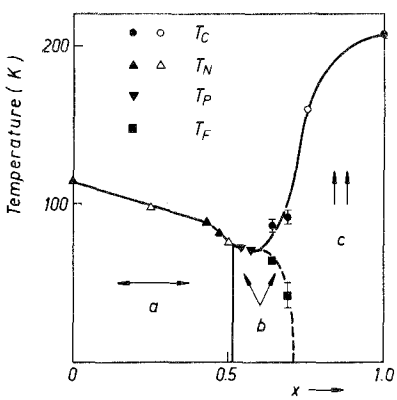

Fig. 14.24. The magnetic phase diagram for the Tb(Cu, Zn) system. The open symbols show the results of Pierre (1969). T_P and T_F are the transition temperatures from the canted to a paramagnetic state and to a ferromagnetic state, respectively (Yashiro et al., 1976).

Ray (1974) also provide evidence that d-electrons play a large role in both isotropic and anisotropic exchange in DyZn. The importance of d-electrons as a medium for 4f–4f exchange has often been hinted at on the grounds of experimental results, e.g. NMR on GdZn (Dormann and Buschow, 1976), and theoretical calculations have been shown to be in line with this. This accounts for the difficulties in reconciling simple models of exchange interactions, such as the RKKY model, with experimental results. When one considers that we are here dealing with one of the simplest possible crystal structures then this does not leave much room for optimism when considering the attempts to apply simple models to interpret the magnetic properties of the other crystallographically more complicated compounds to be discussed in this work. On the other hand, it must be noted that a highly symmetrical lattice does not necessarily result in a good approximation to a spherical Fermi surface.

The above-mentioned increase in d-character on replacing a monovalent by a divalent B-element, as deduced from experimental as well as theoretical work, also appears to occur in the RB_2 compounds with the orthorhombic $CeCu_2$ structure, to be discussed in subsection 2.5. For this relatively complex structure, however, no theoretical band structure calculations are available. Before considering the more complex crystal structures we shall discuss, in the following subsection, the magnetic properties of the cubic RB_2 compounds.

2.4. *Laves phase* RB_2 *compounds*

The RB_2 intermetallics with Laves phase structures comprise a large group of compounds which have been intensively investigated. The RAl_2 compounds, which also belong to this group, have been particularly well documented and were discussed previously in subsection 2.2. Apart from Al the following elements form Laves phases with the lanthanides: Mg, the 3d series Mn, Fe, Co, Ni, the 4d series Tc, Ru, Rh, and the 5d series Re, Os, Ir, Pt. In each case the second half of the d-transition series is involved. Fe and Co will not be discussed here since the magnetic properties are strongly influenced by the presence of 3d-moments. Although no moment has been detected on Mn in RMn_2 it will be discussed together with Fe and Co in subsection 3.4. The compounds with the 4d and 5d transition series, perhaps for economic reasons, have not been intensively investigated, compared with RNi_2 (cubic C 15 structure) for which much information exists. The C 15 structure occurs in RRu_2 (light lanthanides), RRh_2, RIr_2, whereas the C 14 structure occurs for RRu_2 (heavy R), ROs_2, also see ch. 13 subsection 6.3.

The Curie temperatures of the various RB_2 series are plotted in fig. 14.25 (compare with fig. 14.4 for RAl_2). The T_C values of RNi_2 are no larger than the average values for the other series. This supports the belief that Ni indeed possesses no 3d-moment in these compounds. In addition the effective paramagnetic moments of most RNi_2 compounds agree with the theoretical values for free tripositive ions, and in $GdNi_2$, where no crystal field quenching is expected, the saturation moment 7.1 μ_B is very close to gJ. The other RNi_2

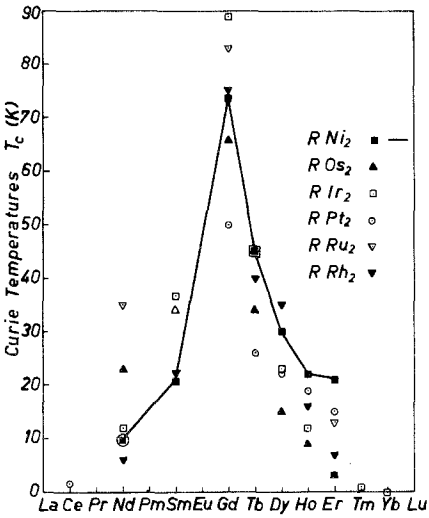

Fig. 14.25. The Curie temperatures of the various RB_2 Laves phase compounds with no B-moment.

compounds show some degree of quenching by crystal fields. A rough proportionality to the de Gennes factor is noted.

The valency of Ce, and Yb is usually expected to be anomalous, not tripositive. However, Eu in $EuRh_2$ is trivalent, whereas Eu in $EuPd_2$ (C 15 structure) is divalent (Wickmann et al., 1968). Eu is trivalent in compounds with relatively small unit cells (e.g. Eu in $SmFe_2$) and divalent for large unit cells (e.g. $EuAl_2$ or $EuPt_2$). In compounds with intermediate cell sizes, such as (Eu, La)Rh_2 and (Eu, Pr)Rh_2, non-unique charge states have been inferred from recoilless absorption spectra (Bauminger et al., 1974). Evidence was found for charge fluctuations of the order of 10^{-3} sec as well as influence of local environment upon the energy of the 4f states in (Eu, La)Rh_2. The valency of Ce appears to be almost 4 in $CeNi_2$ (Wallace et al., 1970a). This accounts for the anomalous magnetic properties of $CeNi_2$ which show no agreement with the Curie–Weiss law. The susceptibility is extremely low, the ratio of susceptibility expected (Ce^{3+}) to that measured being 100 at 4.2 K, decreasing to 3.5 at room temperature. Substitution of Cu into $CeNi_2$ is not possible whereas 17% Cu can be substituted into $GdNi_2$ (Wallace et al., 1970a; Poldy and Kirchmayr, 1974).

$PrNi_2$ shows Van Vleck paramagnetism. Although Pr shows normal Curie–Weiss behaviour at high temperatures with a paramagnetic moment, this moment disappears at low temperatures before $PrNi_2$ has a chance to order. Specific heat measurements (Wallace et al., 1970b) indicated no λ anomaly in $PrNi_2$, which is consistent with the notion that no ordering takes place. For further information about specific heat measurements for various RNi_2 compounds, see Wallace (1973). The ground state due to crystal field interactions is the nonmagnetic Γ_1 state (Mader and Wallace, 1968). However a moment on the Pr ion can be induced by substitution of a heavy magnetic lanthanide (Leon and Wallace, 1970). All RNi_2 compounds order ferromagnetically if they order at all. $PrNi_2$ however has

a negative paramagnetic Curie point. It appears that, if $PrNi_2$ were to order before occupation of the ground state sets in, then the ordering would be antiferromagnetic. Additional evidence was obtained to show that RNi_2 compounds are not all simple ferromagnets. Neutron diffraction results of Felcher et al. (1965) showed superstructure lines in $TbNi_2$ which increase at low temperatures. However, magnetic scattering was sensitive to sample preparation. Arif et al. (1977) investigated the RNi_2 compounds by means of the Mössbauer effect for ^{57}Fe added as an impurity. The easy axes derived at 5 K are $GdNi_2$ [110], $HoNi_2$ and $DyNi_2$ [100], $TbNi_2$ and $ErNi_2$ [111]. They conclude that the Curie temperatures and internal fields are determined mainly by the 4f–4f interactions.

Table 14.3 shows the saturation magnetic moments of Sm and Gd compounds. It is seen that the moments are reduced from the respective values expected of free tripositive ions. The moment reduction in SmB_2 compounds was accounted for by Stewart (1972a,b, 1973a) in terms of effects from conduction electron polarization. Buschow et al. (1973a), however, offered an alternative interpretation pointing out that crystal field effects must be taken into account. The magnetic moment can be expressed as $\langle L_z + 2S_z \rangle$ which is the expectation value in Bohr magnetons for the ground state of the J multiplet. In the absence of crystal fields this reduces to gJ. Due to s–f exchange one obtains a conduction electron polarization which should reduce the moment value for the light lanthanides, and enhance it for the heavy ones, assuming the s–f exchange integral to be positive. If it is negative the situation is the reverse. Thus if the conduction electron polarization is negative for the heavy lanthanides, as appears to be the case (table 14.3), then one would expect the Sm^{3+} moment to be enhanced instead of reduced, assuming no crystal field effects. Buschow et al. (1973a), taking account of crystal field effects showed that the Sm moment can

TABLE 14.3.
Curie temperatures, low-temperature saturation moments, and lattice parameters of some Sm and Gd cubic Laves-phase compounds (Buschow et al., 1973a).

Compound	T_C (K)	$\lvert\mu\rvert$ (μ_B)	a (Å)
$SmAl_2$	120	0.2	7.945
$SmIr_2$	37	0.2	–
$SmRh_2$	22	0.53	7.537
$SmNi_2$	21	0.25	7.218
$SmPt_2$	6	0.19	7.662
$GdAl_2$	171	7.0	7.900
$GdIr_2$	90	6.83	7.550
$GdRh_2$	75	6.80	7.517
$GdNi_2$	85	7.1	7.193
$GdPt_2$	37	6.77	7.636

be reduced and even change sign if mixing of higher J multiplet levels into the ground state is included. One then has the moment $\langle L_z + 2S_z \rangle$ parallel to S_z which makes Sm appear to behave as a heavy lanthanide. It was pointed out that this might have important consequences when Sm is alloyed with a 3d-element, for example in $SmFe_2$, $SmCo_5$, Sm_2Co_{17}, or Sm_2Fe_{17} (see e.g. subsect. 3.4).

From measurements of the hyperfine field (Dormann and Buschow, 1973) in various cubic GdB_2 (B = Al, Ir, Pt, Rh) compounds it was concluded, when considering these in conjunction with magnetic measurements, that the RKKY theory is not applicable. $GdAl_2$ was considered to be a possible exception. $GdAl_2$ has [111] whereas $GdIr_2$ has [100] as the easy axis. Attempts to apply the RKKY model to $GdNi_2$ were made by considering the effect of substituting Cu into the lattice (Poldy and Kirchmayr, 1974). 17% Cu can be substituted into $GdNi_2$ resulting in a T_C increase from 74 K up to 100 K. The calculations also revealed a T_C increase but k_F had to be shifted by at least a few percent from the free electron value. NMR investigations (Dormann et al., 1976) have revealed the importance of d-electrons in influencing exchange in (Gd, Y)Ir_2 and (Gd, La)Ir_2. This appears often to be the case, as in $GdAl_2$ and GdZn where high Curie temperatures are obtained, and reduces the chances of successful application of the RKKY model.

Superconductivity has been observed in RRu_2 compounds for R = Ce, Sc, Y, La, Lu (Wilhelm and Hillenbrand, 1971). $CeRu_2$ which has a relatively high superconducting transition temperature T_c has particularly received much attention, where attempts have been made to raise the magnitude of T_c by various substitutions. Ce has been substituted by Sc, Y, La, Pr, Nd, Gd, Tb, Dy, Ho, Er, and Lu; and Ru has been substituted by Cr, Fe, Rh, Pd, Os, Ir, Pt, (Wilhelm and Hillenbrand, 1971; Hillenbrand et al., 1971b). The substitution of R for Ce usually results in a decrease of T_c with a small maximum at low concentration, but when magnetic 3d metals, e.g. Fe and Mn, are substituted for Ru a rapid decrease in T_c is noted, even nonmagnetic metals substituting for Ru have a stronger effect on lowering T_c than the magnetic rare earths when substituting for Ce, indicating that the superconductivity is carried on the Ru chains. The exchange interaction between the conduction electrons and localized spins in (R, Ce)Ru_2 is extremely small, which is presumed to be the cause of the weak decrease of T_c found upon substituting magnetic lanthanides for Ce (Hillenbrand et al., 1971b).

According to paramagnetic measurements on $CeRu_2$ the Ce-moment is very small and Ce appears to have a valency of almost 4. $LaRu_2$ appears to be a d-band superconductor (Rettori et al., 1973). This was inferred from magnetic resonance investigations of dilute $LaRu_2$: Gd, both in the superconducting and normal states. From the concentration independence of thermal broadening and g value there appears to be no bottleneck in the normal state. Coexistence of short range order with superconductivity was found in (Ce, Tb)Ru_2 by Roth et al. (1974) using neutron small-angle scattering. For 20% Tb ferromagnetic short range order was detected below 10 K and superconductivity below 2.6 K. The transition to superconductivity is completely unaffected by the short range

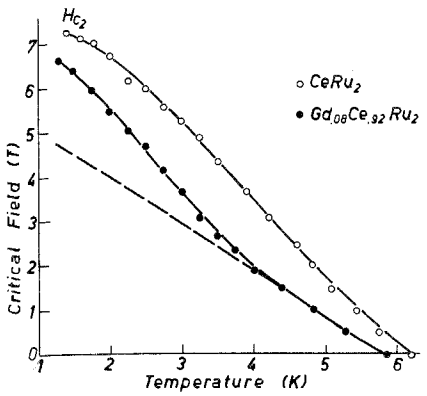

Fig. 14.26. The upper critical field versus temperature for pure $CeRu_2$ (which has no magnetic moment) and with 8% Gd substitution. In the latter the internal and external fields have different signs (Hillenbrand et al., 1971a).

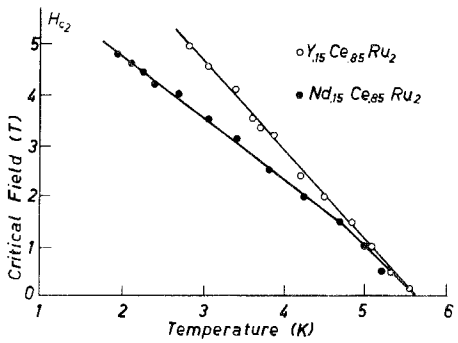

Fig. 14.27. The upper critical field versus temperature for $CeRu_2$ containing 15% Y and 15% Nd. In the latter case the internal and external fields have the same sign (Hillenbrand et al., 1971a).

ordering. The ordering is very weak, Tb appearing to be associated with 0.1 μ_B per atom, instead of 9 μ_B for the free ion. However it is not clear whether the Tb-moments are depressed in magnitude of whether they are only weakly correlated.

An attempt was made by Hillenbrand et al. (1971a) to compensate the effects of an external field applied to $CeRu_2$ by an exchange field arising from substituted magnetic lanthanides. The situation is favourable for substitutions of heavy lanthanides, but unfavourable for light ones. However, in each case the critical field decreases upon substitution. For Gd substitutions the exchange field appears to supply a negative contribution as desired and for Nd the contribution appears to be positive, when compared with the tendency of the critical field (H_{c2}) curves as a function of temperature just below the superconducting transition temperature, figs. 14.26 and 14.27.

2.5. RB_2 *compounds without Laves phase structures*

We have seen in subsections 2.2 and 2.4 that the cubic Lave phase RB_2 compounds are all ferromagnetic if they order magnetically. This cannot be said of the RB_2 compounds with other structures. The RB_2 compounds to be dealt with here involve Cu, Zn, Ag, Au, and Ga, as well as some other elements forming the Fe_2P structure. Except for $LaCu_2$ the RCu_2 and RZn_2 compounds occur with the body centred orthorhombic $CeCu_2$ structure (otherwise called the KHg_2 structure). This is also true for the RNiGa compounds with 1:1 Ni:Ga ratio, and for the RAg_2 and RAu_2 compounds with the light lanthanides, as well as $YbAg_2$ and $YbAu_2$. With the heavy lanthanides RAg_2 and RAu_2 possess the

body centred tetragonal structure categorized as either the $MoSi_2$ or CaC_2 type. RGa_2 and RCd_2 have the AlB_2 and CdI_2 structures respectively; see ch. 13 subsection 6.3.

The $CeCu_2$ structure was first described by Duwell and Baenziger (1955). The crystal chemistry of this structure has been the subject of considerable discussion (e.g. Debray, 1973a,b; Michel, 1973; Bruzzone et al., 1973). Debray (1973b) pointed out that this structure occurs only for zero B-moment, the occurrence of this structure for RNiGa involving an electron transfer from Ga to Ni filling the 3d band of the latter. No strict requirements are found for relative size of components and conduction electron concentration. An absence of directed chemical bonding is reported. Both Debray (1973a) and Michel (1973) have established that this structure forms primarily on the basis of space-filling. Debray et al. (1967) have pointed out the similarity of the radius of the atom on the R site with CN 12 metallic radius, and conclude that there exists very little electronic interaction between the ions in the $CeCu_2$ structure. This is a layer structure with layers in the (100) plane.

The magnetic properties of the RCu_2 compounds were first investigated by Sherwood et al. (1964) who reported metamagnetism (fig. 14.28) which they attributed to a relatively weak antiferromagnetic coupling of ferromagnetic (100) planes. The antiferromagnetism is however strong enough to prevent saturation of the $GdCu_2$ moment even in a field of 70 kOe. The RZn_2 compounds, unlike RCu_2, show a tendency to exhibit ferromagnetic ordering, $NdZn_2$ and $GdZn_2$ appearing to be ferromagnetic whereas the other RZn_2 compounds show antiferromagnetism. See fig. 14.29 which summarizes the characteristic temperatures of RCu_2 and RZn_2 for all the lanthanides. Debray et al. (1967) reported Curie–Weiss behaviour for Ho, Tb, Nd and even Sm but not for $YbZn_2$ which showed diamagnetism at room temperature and a zero paramagnetic moment, indicating Yb

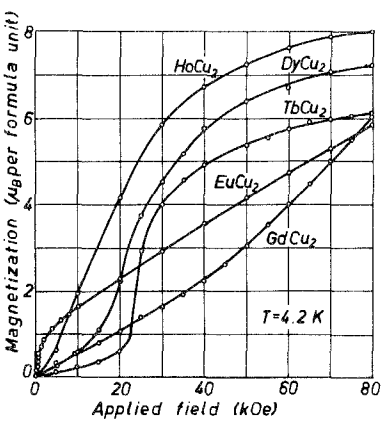

Fig. 14.28. Magnetization isotherms of RCu_2 at 4.2 K (Sherwood et al., 1964).

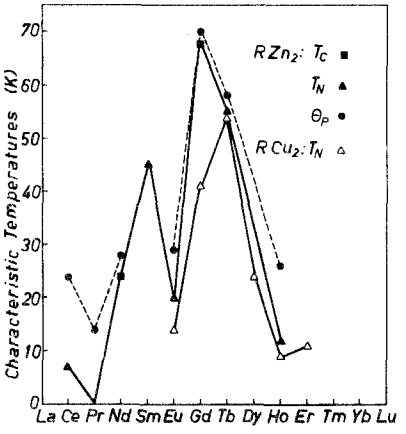

Fig. 14.29. Characteristic temperatures of RCu_2 and RZn_2 compounds.

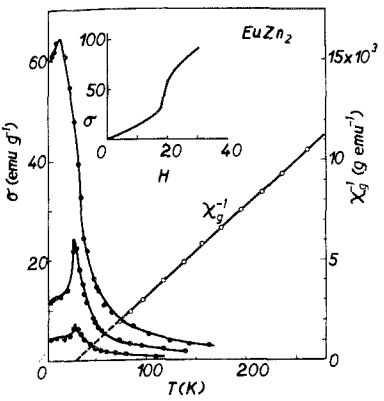

Fig. 14.30. Temperature dependence of magnetization σ and reciprocal susceptibility of $EuZn_2$. For the (σ, T) curves the applied fields are 3 kOe, 9 kOe and 18 kOe, in the order from low to high values of σ. The insert shows the metamagnetic behaviour at 4.2 K (Buschow et al., 1975a).

to be divalent. The paramagnetic moments were in good agreement with those of the free tripositive R ions except for $GdZn_2$ which had a θ_p value of 36 K and a large moment $p_{eff} = 8.97\ \mu_B$ which is to be compared with 7.94 μ_B expected for the free Gd^{3+} ion. Large moments occur often when Gd is associated with a non-magnetic partner, for example GdCu, GdAg, and the binary solid solutions (Gd, Y) and (Gd, La). This cannot therefore be explained on the basis of structural arguments (Debray et al., 1970). The later work of Debray et al. (1970) reveals a θ_p value of $GdZn_2$ of 70 K which is close to the T_C value 68 K. $SmZn_2$ showed a departure from Curie–Weiss behaviour attributed to a close multiplet spacing. $EuZn_2$ and $YbZn_2$ showed also no Curie–Weiss behaviour whereas Buschow et al. (1975a) observed a Curie–Weiss behaviour in $EuZn_2$ (fig. 14.30) revealing a θ_p value of 29 K and indicating Eu to be divalent in this metamagnetic compound. If Eu is divalent then it is an S-state ion like Gd^{3+}. Thus the difference in magnetic ordering type between $GdZn_2$ and $EuZn_2$ can probably be attributed largely to the difference in conduction electron concentration although lattice parameter changes are also present. Debray et al. (1970) observed paramagnetic moments of RZn_2 in agreement with the tripositive ions for R = La, Ce, Pr, Gd, Tb, and Ho. $PrZn_2$ however shows Van Vleck paramagnetism and $NdZn_2$ is partially quenched by crystal fields.

Van Vleck paramagnetism was observed in $PrCu_2$ (Andres et al., 1972) the ground state being a non-magnetic singlet. There is a specific heat anomaly at approximately 7 K which corresponds to the appearance of temperature independent paramagnetism (fig. 14.31). This anomaly is associated with the depopulation of the first excited singlet state. At higher temperatures Curie–Weiss behaviour occurs which gives a θ_p value of -4 K. In addition to this at still lower temperatures (fig. 14.32) cooperative nuclear antiferromagnetic order sets in below 54 mK. This rather high nuclear ordering temperature is due to exchange interactions between Pr ions whose strength is close to the critical value necessary for spontaneous electronic magnetic order.

The RKKY model has been applied to $GdZn_2$ and $GdCu_2$ by Debray et al. (1970), Debray and Ryba (1971), Poldy and Kirchmayr (1974), and Buschow et

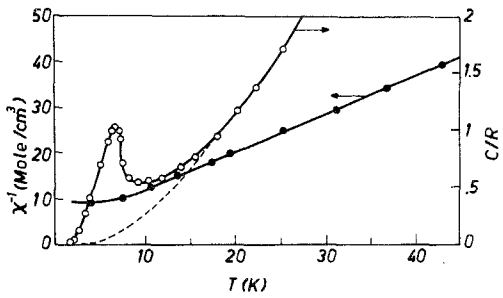

Fig. 14.31. Molar susceptibility (closed circles) and specific heat (open circles) of $PrCu_2$ above 2 K (Andres et al., 1972).

al. (1975a). There arises some contradictory information due not only to the restricted validity of the RKKY model in these systems when considered on a broad basis, but also to the use of unpublished values of θ_p for $GdCu_2$ whose sign was for a long time uncertain. The correct k_F^0 value of $GdCu_2$ was also not well established. Debray and Ryba (1971) adopted a k_F/k_F^0 ratio of 0.8 and deduced, in conjunction with paramagnetic resonance and susceptibility measurements, that the effective s–f exchange parameter in $GdZn_2$ is 0.018 eV, taking correlation effects into account. Poldy and Kirchmayr (1974) applied the RKKY model to $Gd(Ni, Cu)_2$. The ordering temperatures in this system are shown in fig. 14.33 together with some values included for the $Gd(Co, Ni)_2$ systems. The substitution of magnetic Co into $GdNi_2$ raises the T_C values. If Ni were magnetic in $GdNi_2$ then one would expect the substitution of Cu for Ni to lower T_C. The reverse is the case, which was shown to be consistent with RKKY calculations at the Ni-rich end. This supports the belief that Ni does not possess any 3d-moment in this system. The substitution of Ni into $GdCu_2$ results in a weakening of the antiferromagnetism (fig. 14.34), the T_N values giving way to T_C values between 10 and 15% Ni, followed by a rapid rise of T_C and a maximum which occurred before the $CeCu_2$ structure became unstable between 40 and 50%. The two-phase region showed two Curie points which could hardly be resolved from one another. The expected variation of the ordering temperatures and θ_p was calculated using the RKKY model (fig. 14.35) which predicted the

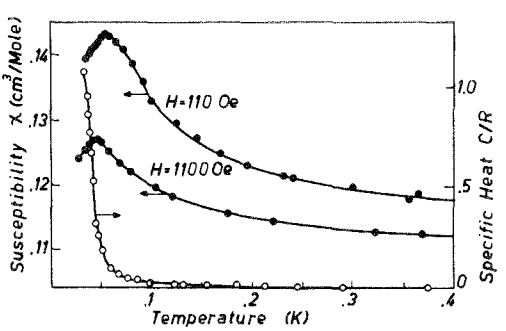

Fig. 14.32. Molar susceptibility (closed circles) and specific heat (open circles) of $PrCu_2$ below 0.5 K (Andres et al., 1972).

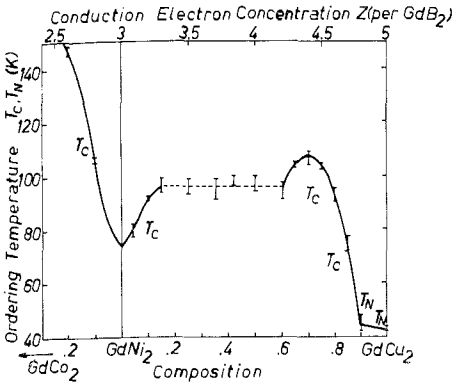

Fig. 14.33. Ordering temperatures of $Gd(Ni, Cu)_2$ and Ni-rich $Gd(Co, Ni)_2$ pseudobinaries plotted against electron concentration (Poldy and Kirchmayr, 1974).

transition at 13% Ni and also the maximum at 30% Ni. This was performed taking into account the finite mean free path λ of the conduction electrons. No shift of k_F from the free electron value was required for a λ value of 10 Å. When the finite λ is not taken into account a k_F shift of only 3% is necessary. If the success is not just a coincidence then the real situation lies somewhere between these limits. The calculated stable spin structure of $GdCu_2$ involved ferromagnetic (100) planes coupled with a turn angle of 35° between neighbouring planes in the layer structure. This type of antiferromagnetic spin structure is exactly in agreement with the intuitive prediction of Sherwood et al. (1964) mentioned above. Within this picture $GdZn_2$ should have a k_F^0 value near the node at 1.52 $Å^{-1}$, which is not in agreement with its relatively high ferromagnetic Curie temperature. On the other hand if we were to take a k_F/k_F^0 value of the order of 80 or 90%, following Debray and Ryba (1971) and Buschow et al. (1975a), then this disadvantage could in principle be rectified since the k_F

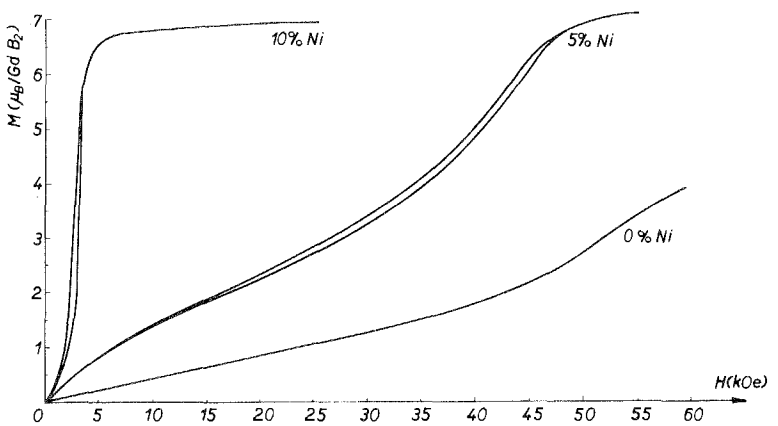

Fig. 14.34. Magnetization isotherms of antiferromagnetic samples of $Gd(Ni, Cu)_2$ at 4.2 K (Poldy and Kirchmayr, 1974).

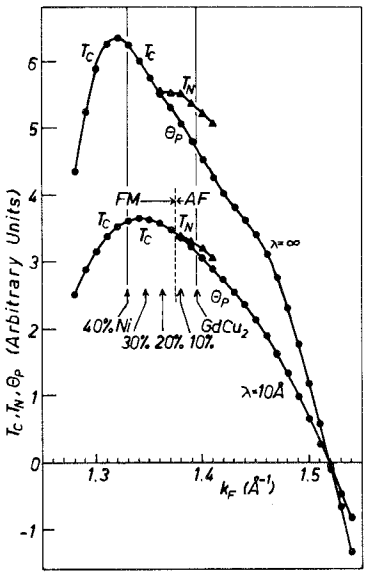

Fig. 14.35. The theoretical characteristic temperatures of $Gd(Ni, Cu)_2$ plotted against k_F (Poldy and Kirchmayr, 1974).

value for $GdZn_2$ would then lie in the maximum (fig. 14.35) and $GdCu_2$ to the left of the maximum.

Although the application of the RKKY model to various neighbouring systems presents difficulties, it appears to succeed exceptionally well within the isolated system $Gd(Ni, Cu)_2$. Spin disorder resistivity measurements have been performed and combined with the magnetic data (according to the method of Dekker, 1965) in order to determine the strength of exchange G and magnitude of the effective mass m^* (Gratz and Poldy, 1977). The results indicate a ratio m^*/m^0 greater than unity but approaching unity for high Ni contents. As explained in subsection 2.1 the departure of m^*/m^0 from unity may be taken as a measure of the nonsphericity of the Fermi surface. Thus the RKKY model may be applicable for the Ni-rich ferromagnetic samples, but inapplicable for higher electron concentrations (that is, for the Cu-rich samples in $Gd(Ni, Cu)_2$ and even less applicable when Zn is substituted). It is also believed that the ρ_{spd} values obtained from the antiferromagnetic samples cannot be used for calculating m^* and G for two possible reasons: The first (see fig. 14.36) is due to superzone boundaries changing the electron characteristics when ordering, as explained in subsection 2.1. The second applies to the Ni-substituted compositions, where inhomogeneities (on a sub-microscopic or atomic scale) in the Ni/Cu concentration (such as cluster formation), result in a spin structure whose wavelength varies from position to position in the sample. Thus the spin system is not perfectly ordered even at zero temperature and there will exist a so-called frozen-in spin disorder resistivity which results in a low apparent value of spin disorder resistivity obtained by the usual extrapolation procedure illustrated in fig. 14.36a.

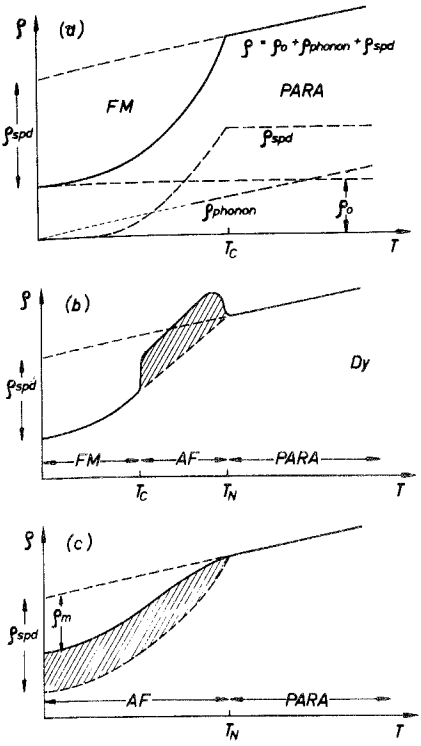

Fig. 14.36. Schematic representation of the evaluation of the spin disorder resistivity ρ_{spd}. (a) Usual extrapolation scheme valid from temperatures above the Debye temperature. (b) The case of dysprosium which has an antiferromagnetic temperature range where superzone boundaries raise the resistivity. (c) The case of an antiferromagnet which does not become ferromagnetic at low temperatures: Superzone boundaries may distort results in the whole ordered range (Gratz and Poldy, 1977).

It is not easy to establish which of these effects plays the larger role in $Gd(Ni, Cu)_2$.

An attempt to account for the sign of θ_p in $GdZn_2$ without shifting k_F was made by Debray and Sakurai (1974). They developed an extended form of the RKKY model as mentioned in subsection 2.1. The simple model predicts a very small value of θ_p since the k_F^0 value 1.504 $Å^{-1}$ for $GdZn_2$ lies near a node. In this calculation the simple model as applied by Debray and Sakurai predicts a negative θ_p whereas the extended model shifts the node just enough to predict a positive θ_p in agreement with experiment. Needless to say the probability is 50% that any shift produces the desired effect even if this RKKY extension were inapplicable to the $GdZn_2$ system. More serious, however, is that the resulting positive θ_p has a value still very near the node. Thus, the model most probably does not account for the ferromagnetism, since the switch from an antiferromagnetic stable state to a ferromagnetic stable state hardly ever occurs together with the switch from negative to positive θ_p. In addition the experimental T_C value 68 K for $GdZn_2$ is rather high compared with 41 K for $GdCu_2$.

Summarizing, it seems that the RKKY model, though surprisingly successful within one system, cannot account on a broad basis for the magnetic properties of the compounds with the $CeCu_2$ structure. In these compounds the failure of this model may be due to an increasing d-character of the conduction electrons

on going from left to right in the periodic table, the d-character increasing with increasing Cu content in the $Gd(Ni, Cu)_2$ series, and $GdZn_2$ having much more d-character than $GdCu_2$. A parallel behaviour was found in the RCu and RZn compounds with CsCl structure (see subsection 2.3). This d-character may then be responsible for the relatively high ordering temperatures in RZn_2 compared with RCu_2. In this connection it would be instructive to examine in detail the pseudobinary system $Gd(Cu, Zn)_2$.

The spin structures of the RCu_2 compounds where an orbital moment exists do not appear to conform with the predictions of Sherwood et al. (1964) concerning the supposed antiferromagnetic coupling between (100) planes. A relatively complex but collinear antiferromagnetic spin structure was detected by Brun et al. (1971) for $TbCu_2$ by means of neutron diffraction (see fig. 14.37). This structure has a magnetic unit cell tripled in the a direction but not all moments in the (100) plane are parallel to one another. There are two collinear sublattices, with Tb moments parallel to the a-axis, one part of a given sublattice losing its magnetization with increasing temperature at a different rate from the other part, although they both have magnetizations at 5 K corresponding to parallel Tb moments possessing the full gJ value. The stable magnetic structure and the temperature dependence of sublattice magnetizations can be explained by the molecular field model but only if anisotropy energies are introduced which are comparable to the exchange energies. The anisotropy suppresses the spiral structures which would otherwise be stable if only exchange interactions were present. In 56 kOe the full gJ moment per Tb atom at 4.2 K can be detected as long as the field is applied during cooling. This is much larger than the 5.5 μ_B moment achieved by Sherwood et al. (1964). It appears that magnetic after-effect

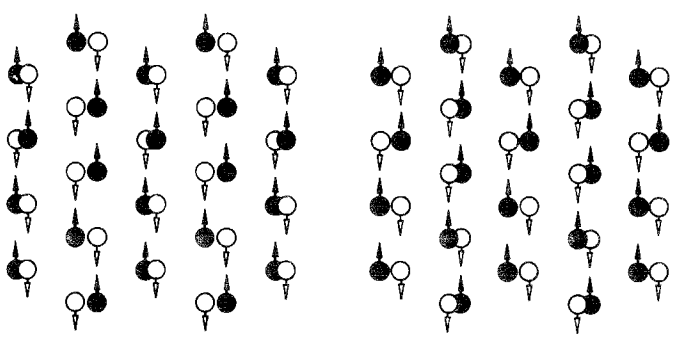

Fig. 14.37. The spin structure of $TbCu_2$ at 4.2 K from neutron diffraction results of Brun et al. (1971). This is a stereoscopic representation in which the left and right images are to be viewed by the right and left eyes respectively. This can be achieved either by direct observation with the lines of vision crossed, or by means of a pair of viewers in which case diapositives of the two separate images are required. Only the Tb atoms are drawn. The plane of the figure is the a–c plane, with spins in the a-direction. The spin structure can be regarded as ferrimagnetic within an a–c plane, $\frac{2}{3}$ of the spins up, and $\frac{1}{3}$ down. The spin directions are reversed from plane to plane, giving a net antiferromagnetism.

may be present here as a consequence of the large anisotropy which appears to set in below 30 K. The existence of an antiferromagnetism direction in the a-axis, as found by Brun et al. (1971), is in agreement with the magnetization measurements of Hashimoto et al. (1975) performed on single crystals. The latter authors observed metamagnetism for fields applied parallel to the a-axis, not only for $TbCu_2$ but also for $DyCu_2$. The b and c directions were magnetically hard, especially in $TbCu_2$. Anisotropy was also revealed by paramagnetic measurements, from which the crystal field parameters were deduced. These were found to be in fair agreement with point charge calculations.

The spin structures have been reported for $CeZn_2$ and $TbZn_2$ (Debray et al., 1972), $HoZn_2$ (Debray and Sougi, 1972) and $NdZn_2$ (Debray and Sougi, 1973). Debray (1973b) points out that a common feature of these spin structures is that the antiferromagnetic alignment occurs parallel to the b-axis. $HoZn_2$ and $TbZn_2$ have collinear antiferromagnetic structures at low temperatures which transform to sinusoidally modulated structures at higher temperatures. The modulation occurs in the c-direction and involves an oscillation of the magnetic moment magnitude. The measurements for $TbZn_2$ appear however to have been made above the ordering temperature 55 K reported by Debray et al. (1970). The neutron diffraction results of Debray (1973b) reveal a hysteresis of satellite line intensities as a function of field. This is considered to indicate that the moment directions are trapped in deep potential wells, due to anisotropy. In this respect these compounds are not unlike $TbCu_2$. By considering the effects of applied fields on spin structures of $TbZn_2$ and $HoZn_2$ values have been obtained for the anisotropy constants in these compounds with the $CeCu_2$ structure which are an order of magnitude smaller than in the corresponding pure lanthanides.

The $CeCu_2$ structure also forms with RAg_2 and RAu_2 for the light lanthanides. However these compounds have been neglected to a large extent compared with the RAg_2 and RAu_2 compounds with the heavy lanthanides.

The RAg_2 and RAu_2 compounds with the heavy lanthanides form the tetragonal $MoSi_2$ structure (Conner, 1967). These compounds have received much attention due to the interesting magnetic structures and transitions occurring within the magnetically ordered state. The ordering temperatures and θ_p values, as seen in fig. 14.38, are characteristic of antiferromagnets since θ_p is negative and of approximately the same magnitude as the T_N values. It is seen also that the RAg_2 and the RAu_2 series do not differ markedly from one another. Susceptibility measurements (Miura et al., 1971; Miura et al., 1974) have revealed effective moments in agreement with the tripositive free lanthanide ions and susceptibility peaks which indicate antiferromagnetic ordering. The magnetization process upon applying a field is however not a simple one, as exemplified by the case of $DyAu_2$ (fig. 14.39) measured by Miura et al. (1971). They interpreted this behaviour in terms of two types of antiferromagnetic structure, the transition from one to the other depending upon applied field and temperature.

The RKKY model was applied to the RAg_2 compounds by Miura et al. (1974) in connection with magnetic measurements and by Ohashi et al. (1975) in

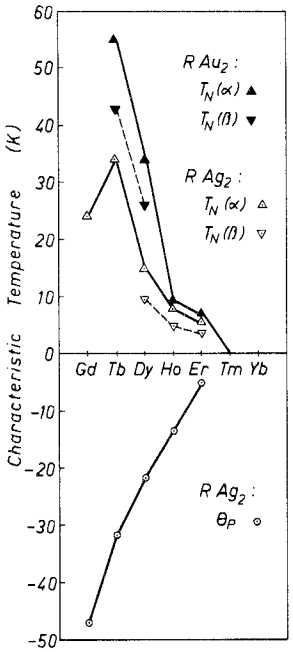

Fig. 14.38. Characteristic temperatures of RAg_2 and RAu_2 compounds.

connection with spin disorder resistivity measurements. The s–f exchange interaction was calculated independently by means of each set of results presumably taking m^*/m_0 to be unity. The interaction energies deduced from the magnetic data θ_p were approximately twice as large as those from spin disorder resistivity measurements. These values for $GdAg_2$ were 0.14 eV and 0.09 eV respectively.

A phenomenon characteristic of the RAg_2 and RAu_2 compounds is the existence of two transition temperatures $T_N(\alpha)$ and $T_N(\beta)$. The former is the normal Néel temperature otherwise denoted by T_N, and the latter is a first order-like transition temperature within the magnetically ordered range. Thus $T_N(\alpha) > T_N(\beta)$. The presence of $T_N(\beta)$ was detected by many types of measurements,

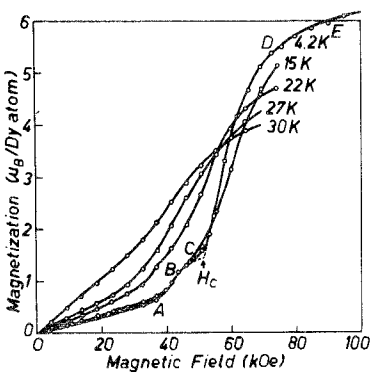

Fig. 14.39. Magnetization isotherms of $DyAu_2$ (Miura et al., 1971).

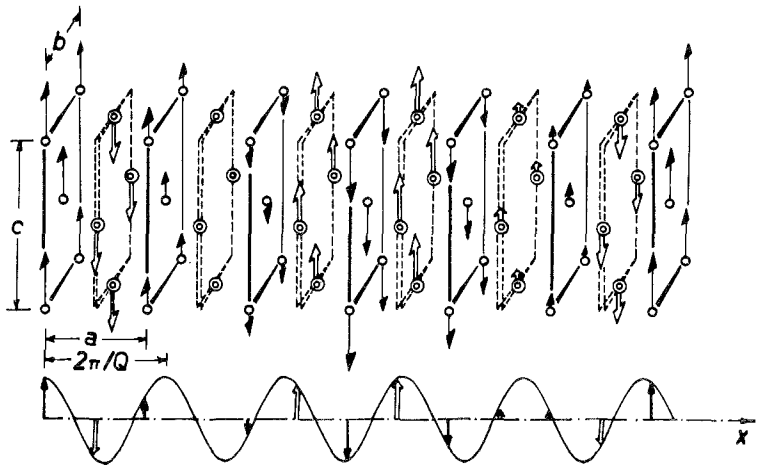

Fig. 14.40. A schematic representation of the high temperature incommensurate magnetic structure of $TbAu_2$. The gold atoms are not shown. (Atoji, 1968a).

such as susceptibility where a discontinuity is observed, thermal expansion, resistivity, and neutron diffraction.

Neutron diffraction investigations have revealed the nature of this apparent first order-like transition. $T_N(\beta)$ is a transition temperature between two types of antiferromagnetic spin structure. The usual trend is that a low temperature spin structure which is commensurate with the lattice in the [100] direction transforms at $T_N(\beta)$ to an incommensurate spin structure. This is the case in $TbAu_2$, $DyAu_2$, $DyAg_2$ and $HoAg_2$. As an example the spin structures of $TbAu_2$ (Atoji, 1968a) are illustrated in fig. 14.40 and fig. 14.41 where it is seen that the

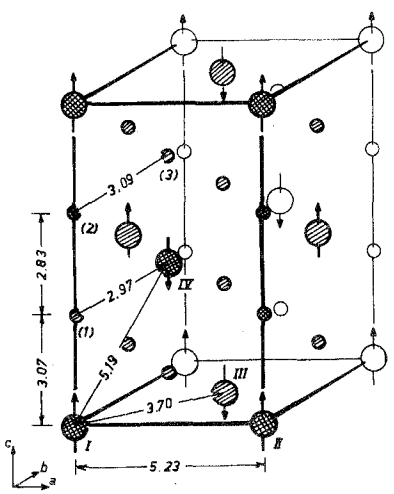

Fig. 14.41. The low temperature commensurate magnetic structure of $TbAu_2$ below 42.5 K. The larger and smaller circles represent Tb and Au, respectively. The pertinent interatomic distances are given in Ångstroms (Atoji, 1968a).

incommensurate spin structure involves an oscillation of the magnitude of the Tb-moments. In both spin structure types the Tb-moments point in the c-axis direction. On the other hand a different behaviour is observed in $TbAg_2$ (Atoji, 1968b) which only shows a commensurate structure in the whole ordered range and no order–order transition. This structure is exactly like that found in $TbAu_2$ below $T_N(\beta)$. Another exception is illustrated by $HoAg_2$ which presents two incommensurate structures on either side of the transition $T_N(\beta)$ (Atoji, 1969). In $HoAg_2$ longitudinal as well as transverse waves are involved, whereas for the usual behaviour as described above only transverse modulations occur. Fedro and Shaffer (1971) have succeeded in accounting for the transitions from commensurate to incommensurate spin structures as found in RAu_2. They showed that, by taking into account the non-zero width of the 4f wave functions as done by Robinson et al. (1971), the existence of an incommensurate spin structure at high temperatures could be explained. The introduction of anisotropy energies was shown to cause the transition to the commensurate structure at low temperatures. This is not unlike the situation in the pure lanthanides.

Another series of compounds showing metamagnetic behaviour is RGa_2 (Barbara et al., 1971a). The structure of these compounds is the AlB_2 hexagonal structure which also forms for $LaCu_2$. The neutron diffraction results of Barbara (1971a) reveal the spin structures where the moments of Ho and Dy are in the basal plane (fig. 14.42). The directions of the moments are determined by the crystal fields whose main terms arise from Ga nearest neighbours. Strangely, no magnetic order could be detected by Buschow and v.d. Hoogenhof (1976) for $GdGa_2$. The θ_p values change sign in the lanthanide series, being positive for the light and negative for the heavy lanthanides. The RKKY approach appears to fail here completely. It may be that anisotropic interactions play an exceptionally important role in these compounds.

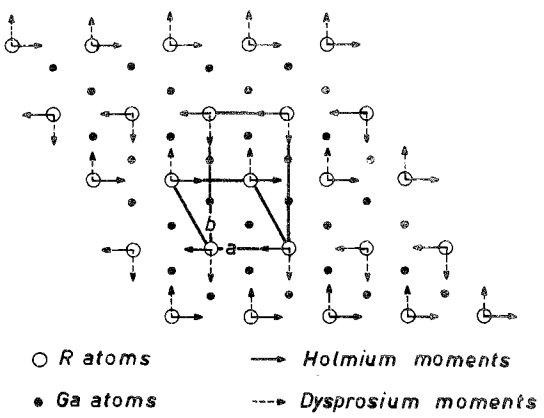

Fig. 14.42. Projection of the crystallographic and magnetic structures of $DyGa_2$ and $HoGa_2$ (Barbara et al., 1971a).

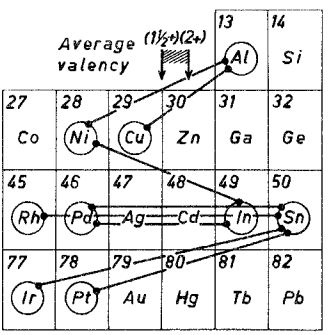

Fig. 14.43. The occurrence of the Fe_2P structure for pairs of B-elements in the compounds with formula RB^1B^2.

The hexagonal Fe_2P structure forms for the rare earths with the pairs of B-elements as shown in fig. 14.43 each pair of B-elements being present in the ratio 1:1. Evidence has been found by Dwight et al. (1971) for HoPtSn indicating that ordering of the two B-elements takes place, Sn being confined to the 3(f) crystallographic site and Pt being distributed among the 1(b) and 2(c) sites. It cannot however be assumed that the ordering for all possible pairs of B-atoms follows this scheme. None of the pairs of B-atoms are neighbours in the periodic table. Thus the ordering of the two B-elements can be expected to occur with no wide homogeneity range around the 1:1 B-elements ratio. Size effects play an important role, the larger B-element tending to occupy the 3(f) sites. The assignment of B-elements to the different sites in the Fe_2P structure has been investigated by Jeitschko (1970). Apart from size effects it appears that the average electron concentration may be important in stabilizing the Fe_2P structure. This can be seen in fig. 14.43 where it is apparent that the average B-atom valency for all possible combinations lies within the relatively narrow range ($1\frac{1}{2}+$, 2+). From magnetic considerations Buschow (1975) concluded that the 3d and 4d shells of Ni and Pd are full in all these compounds. From the lattice parameters of RRhSn Dwight et al. (1971) deduced that Yb occurs here in the trivalent state.

In general the magnetic properties of the intermetallics with the Fe_2P structure tend to exhibit ferromagnetic behaviour as far as exchange interactions are concerned. For example GdCuAl ($\theta_p = T_C = 90$ K), GdPdIn ($\theta_p = T_C = 103$ K) and GdNiAl ($\theta_p = T_C = 70$ K) all appear to be well-behaved ferromagnets. In addition, the change of average B-valency from $1\frac{1}{2}+$ to 2+ appears to have no significant effect upon the T_C and θ_p values when comparing the RNiAl and RCuAl results of Österreicher (1973a). However, the (M, H) curves indicate that the compounds where R is not Gd do not show such well-behaved ferromagnetism (Öesterreicher, 1972, 1973a). Critical fields are observed in many cases, such as in ErNiAl and TmNiAl for example. It is not clear whether this indicates a type of magnetization process involving domain wall pinning or metamagnetism involving a delicate balance between ferromagnetic and antiferromagnetic interactions as suggested by Österreicher (1972) or a mixture of these two.

Measurements have been performed of the Knight shift in GdCuAl by Buschow et al. (1971). From the gradient of the Knight shift versus susceptibility a value of -0.31 eV was obtained for the s–f coupling constant. This was performed in conjunction with measurements assuming the RKKY model. The RKKY model, however, appears not to be valid for GdCuAl as far as paramagnetic measurements of the $Gd_xTh_{1-x}CuAl$ series are concerned. Substitution of Gd by Th increases the electron concentration, and this should have definite effects upon θ_p. Whereas dilution of Gd by Y (constant electron concentration) seems to result in a linear θ_p decrease as expected from long range exchange interactions, the Th substitution results in a θ_p variation which cannot be accounted for within the RKKY model without assuming an overall k_F shift corresponding to $k_F/k_F^0 = 0.72$. Figure 14.44 displays θ_p/x as a function of Gd concentration in the RCuAl and RPdIn compounds. The RPdIn compounds

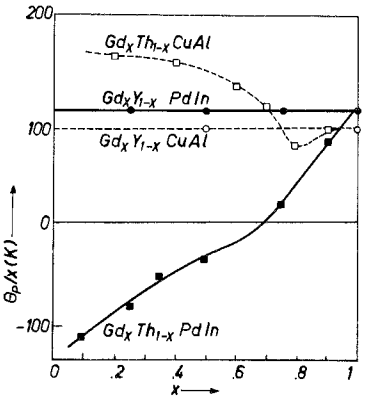

Fig. 14.44. Effective paramagnetic Curie temperatures θ_p/x versus Gd content x in the various pseudobinaries with the Fe_2P structure (Buschow, 1975).

however show excellent agreement with the RKKY model, firstly since the constancy of θ_p/x indicates long range interactions to be present, and secondly since the change in sign of θ_p (or θ_p/x) can be accounted for by the RKKY model without shifting the k_F value from k_F^0. See Buschow (1975).

2.6. *Compounds with low structural symmetry*

The main compounds to be discussed in this section are R_3Co, R_3Ni, RNi, RAl, R_3Al_2 and R_2Al. The basic building block which all these structures have in common is a trigonal prism consisting of R-atoms at the corners and a B-atom in the centre. This unit is arranged in various ways to give the various structures most of which are orthorhombic. The surroundings of a rare earth site are of low symmetry. This gives rise, for lanthanides other than Gd, to magnetic properties which tend to be characterized by a strong magnetocrystalline anisotropy due to the low symmetry of the crystal field acting on the magnetic ions.

The RNi compounds form the CrB structure for the light lanthanides as well as Gd. For the heavy lanthanides to the right of Tb the FeB structure is stable. Both these structures are orthorhombic. TbNi is dimorphic, showing two rather complex derivations of these two structures depending upon heat treatment. The FeB structure of TbNi can be stabilized by replacing 10% of the Ni atoms by larger Cu atoms (Gignoux, 1974). It appears that the choice of FeB or CrB is then determined largely by size effects. Magnetic measurements of the RNi compounds performed by Abrahams et al. (1964) have revealed effective paramagnetic moments in excellent agreement with those expected from free tripositive ions. However the saturation moments were lower than gJ in all cases except GdNi. This suggests considerable effects from crystal fields. The moment of Sm in SmNi at 4.2 K is strongly reduced. Measurements on a single crystal of SmNi reveal a large square hysteresis loop in the easy [010] direction characteristic of ferromagnetism. However anomalous behaviour due to high anisotropy effects below 5 K appears. Walline and Wallace (1964b) detected a large magnetic moment on Gd in GdNi in excess of the gJ value, which they attribute

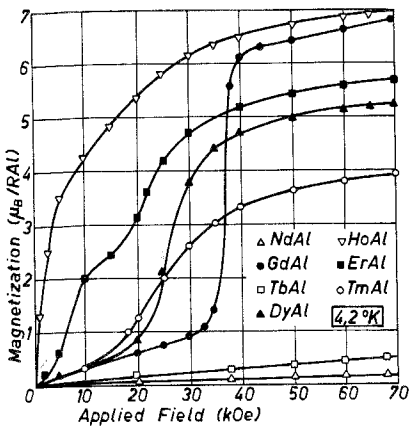

Fig. 14.45. Magnetization isotherms of RAl compounds at 4.2 K (Bécle et al., 1970).

to conduction electron polarization. Large moments on Gd often appear when Gd is combined with a nonmagnetic partner. Ce appears to be quadrivalent in CeNi. The RA1 compounds form the so-called DyAl structure. This is orthorhombic with the Pbcm space group. The (M, H) curves at 4.2 K (fig. 14.45) show an exotic variety of behaviours including metamagnetism suggesting an antiferromagnetic spin structure except for HoAl which is easily magnetized in small fields. Figure 14.46 shows the characteristic temperatures of the RNi and RAl series. The data for RNi, taken from Walline and Wallace (1964b), indicate ferromagnetic behaviour with $T_C \approx \theta_p$ on average. The proportionality with the de Gennes factor is however not well fulfilled. The variation of θ_p and the ordering temperatures in RAl is even more irregular. This suggests that anisotropic interactions may be as important as isotropic exchange or even more important. Any proportionality to the de Gennes factor is then not to be expected (Bécle et al., 1970). The spin structures of RNi and RAl are to be discussed later together with R_3Co and R_3Ni.

The magnetic properties of R_3Co and R_3Ni (orthorhombic Fe_3C structure) have been investigated by Féron et al. (1968, 1969) and Strydom and Alberts

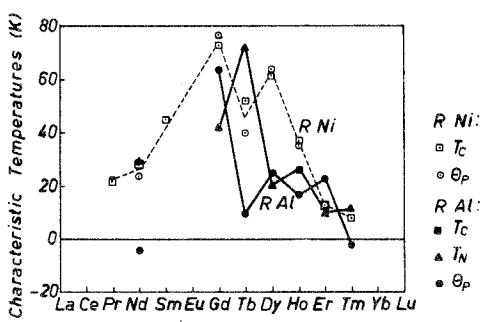

Fig. 14.46. Characteristic temperatures of the RAl and RNi compounds (RAl, Bécle et al., 1970; RNi, Walline and Wallace, 1964b).

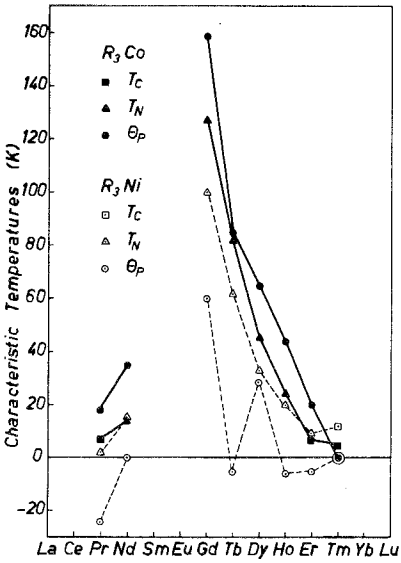

Fig. 14.47. Characteristic temperatures of the R_3Co and R_3Ni compounds (Féron et al., 1969, the θ_p value for Tb_3Ni is taken from Féron et al., 1968).

(1970). In fig. 14.47 are shown the characteristic temperatures. It is apparent, from the fact that the θ_p values of R_3Ni are lower than T_N and sometimes negative that these compounds may be strongly antiferromagnetic, though this cannot be said of the R_3Co compounds. The (M, H) curves suggest magnetization processes of a complex nature which are characteristic of nonlinear spin-structures. Figure 14.48 shows the pulsed field results of Taylor and Primavesi (1971) for various R_3Co and R_3Ni compounds at 4.2 K. The (M, H) curve of Gd_3Ni at 4.2 K shows a complex magnetization process involving two critical fields with saturation being only achieved in high fields, whereas Gd_3Co shows a critical field transition H_c at about 8 kOe followed by saturation in less than 20 kOe. The T_N value of Gd_3Co is larger than that of Gd_3Ni suggesting that Gd_3Co may be an example of a material with weak antiferromagnetic coupling between magnetically rigid sublattices. Féron et al. (1969) applied the appropriate Néel model of antiferromagnetism, which is described in subsection 2.1, to Gd_3Co. They deduced the inter-sublattice molecular field coefficient ($n = 40$) from the critical field at 4.2 K and also using the initial susceptibility obtained a value of 5.1×10^6 erg/cm^3 for the anisotropy constant which is of the same order of magnitude as that of pure Gd (1×10^6 erg/cm^3) at 4.2 K. Poldy and Taylor (1973a) investigated the variation of the metamagnetic properties by changing the conduction electron concentration. This was performed in the series $Gd_3(Co, Ni)$ and in the series $Gd_3(Fe, Co)$ where it was found that the structure became unstable for more than 10% Fe substitution. The critical field H_c was found to increase continuously with conduction electron concentration (fig. 14.49). Substitution of Fe into Gd_3Co appeared to suppress the antiferromagnetism, the H_c value becoming zero at the concentration where the

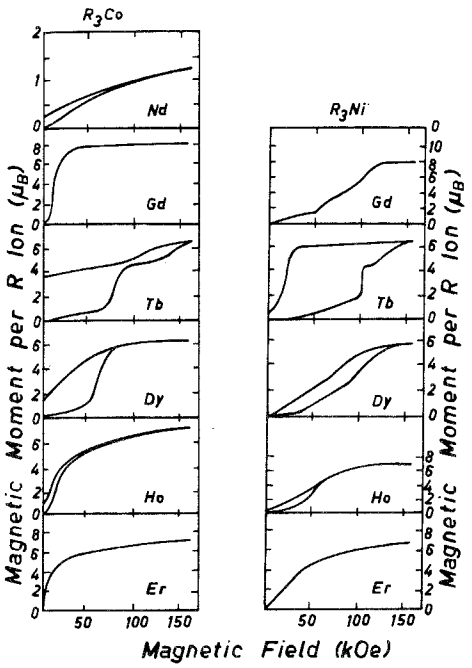

Fig. 14.48. Magnetization isotherms of R_3Co and R_3Ni in pulsed fields at 4.2 K (Taylor and Primavesi, 1971).

structure became unstable. There appears to be a correlation between the existence of antiferromagnetism and structural stability. It was suggested that for 10% Fe the Fermi level is near the top of the 3d band where the density of states begins to increase. Further removal of electrons from the conduction band system is no longer accompanied by a rapid lowering of the Fermi level and this may cause the structural instability (Poldy and Taylor, 1972a, 1973b). At the same time, the depopulation of the 3d-band results in 3d-moments which have a strong influence upon the magnetic ordering. It is known that R–3d intermetallics

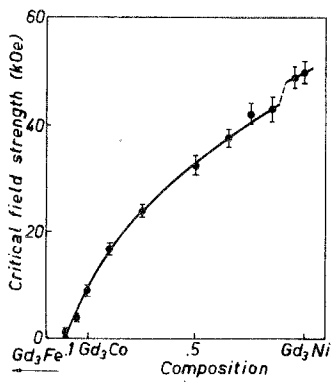

Fig. 14.49. The variation of the critical field strength with electron concentration for Gd_3(Co, Ni) and Gd_3(Fe, Co) at 4.2 K (Poldy and Taylor, 1973a).

are almost invariably ferrimagnetic (see subsection 3.3) all 3d-moments being coupled parallel to each other, and antiparallel to the R-moments. Thus even though the indirect exchange between the R-moments may tend to favour antiferromagnetism, the presence of 3d-moments and ferrimagnetic R–3d exchange will force a parallel arrangement of R-moments, thus suppressing the antiferromagnetism. The above-mentioned correlation between structural stability and the existence of antiferromagnetism can then be understood on the basis of this model. The Néel two-sublattice model of antiferromagnetism was applied to the measured magnetic parameters, T_N, H_c and initial susceptibility at 4.2 K. The values of n', n and anisotropy constants were calculated. It was deduced that the samples with low critical field show spin-flip transitions, which transform to spin-flop transitions for more than 25% Ni. The condition of applicability of the two-sublattice model ($n' \gg n$) was not valid for the Ni-rich samples. The complex nature of the (M, H) curve of Gd_3Ni may indicate the presence of more than two sublattices. Gd_3Co however is a weak antiferromagnet and appears to fulfill the requirements of the Néel model, although no direct evidence is available for assuming that Gd_3Co only possesses two magnetic sublattices.

The spin structures of various compounds with low symmetry structures have been obtained by neutron diffraction measurements. The spin structures of Er_3Co and Er_3Ni have been reported by Gignoux et al. (1970). Lemaire and Paccard (1969) and Gignoux (1974) have investigated the spin structures of RNi compounds. Bécle et al. (1970) have reported on the spin structures of RAl and RNi. The spin structure of DyNi was investigated by Gignoux and Shah (1972). A rather complex behaviour in Tb_3Co was found by Gignoux et al. (1973). NdNi was shown by Lemaire and Paccard (1969) to be a pure ferromagnet (fig. 14.50). All the other investigated compounds showed non-collinear spin structures. These can be divided into two groups: those showing pure antiferromagnetism with no resultant moment, and those showing a mixture of antiferromagnetic and ferromagnetic structures. The latter have a resultant moment and can perhaps be regarded as basically ferromagnetic structures which have been disturbed by some other mechanism arising from magnetocrystalline anisotropy. Thus the moments are deflected to some extent out of the resultant moment direction,

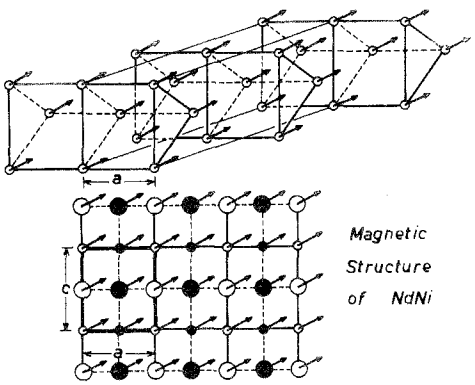

Fig. 14.50. Magnetic structure of NdNi (Lemaire and Paccard, 1969).

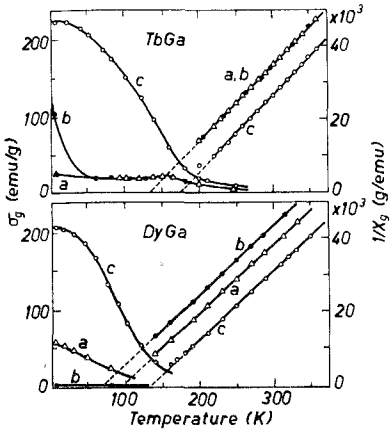

Fig. 14.51. Single crystal magnetic results for TbGa and DyGa (Shohata et al., 1974).

giving an antiferromagnetic component to the spin structure. It is apparent here that difficulties may arise as to whether the ordering temperatures of such compounds are to be classified as Néel points or Curie points. Indeed a single crystal sample may display characteristically ferromagnetic as well as characteristically antiferromagnetic (M, T) curves with Néel peaks, depending upon the direction of the applied field. TbGa and DyGa which have the CrB structure are examples showing such a behavior as seen in fig. 14.51 (Shohata et al., 1974). The

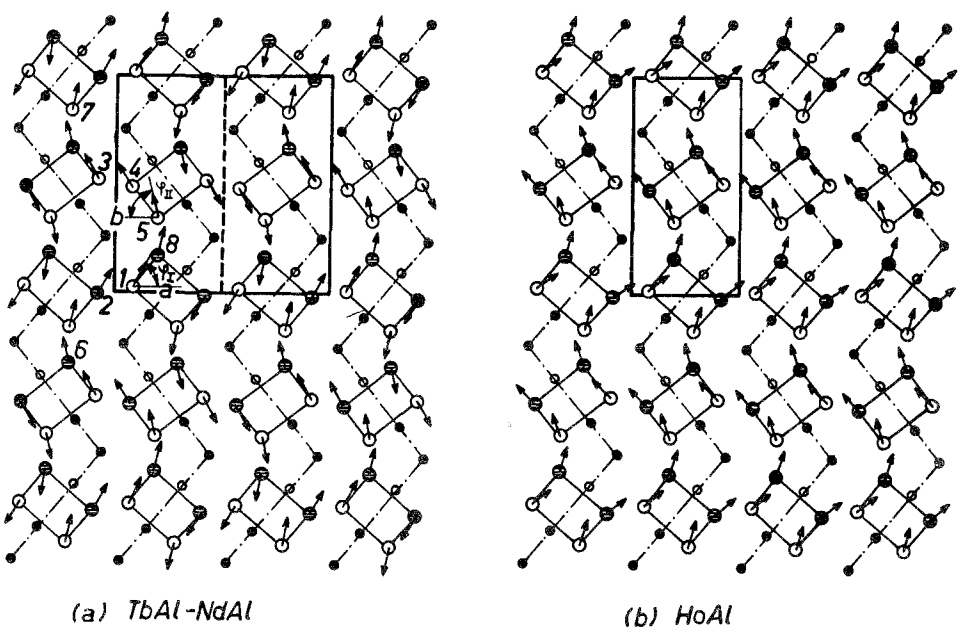

Fig. 14.52. Examples of the two basic types of non-collinear magnetic structures: (a) antiferromagnetic, (b) mixed ferro- and antiferromagnetic (Bécle et al., 1970).

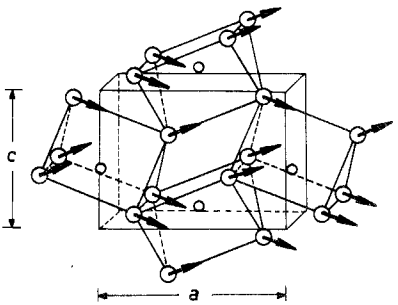

Fig. 14.53. The magnetic structure of HoNi (Bécle et al., 1970).

above categorization of spin structures into two groups is exemplified in fig. 14.52 where fig. 14.52a shows an antiferromagnetic structure, as in TbAl and NdAl, and fig. 14.52b shows a mixed spin structure with both ferro- and antiferromagnetic components, as in HoAl. HoNi is also an example of a mixed structure, (fig. 14.53). The various spin structures are tabulated qualitatively (table 14.4) with a view to decide whether the exchange interactions have a tendency to result in ferro- or antiferromagnetic coupling. The case of R_3Ni is

TABLE 14.4.
Categorization of the magnetic structures of the RAl, RNi, R_3Co and R_3Ni compounds (AF = Antiferromagnetic, FM = Ferromagnetic).

	RAl	RNi	R_3Co	R_3Ni
Nd	AF	FM		
Sm		M vs H (FM)		
Gd	Metamagnetic	M vs H (FM)	Metamagnetic	Metamagnetic
Tb	AF	Mixed AF + FM (in $Tb_{0.5}Y_{0.5}Ni$)	Mixed AF + FM	
Dy	Metamagnetic	Mixed AF + FM	Metamagnetic	Metamagnetic
Ho	Mixed AF + FM	Mixed AF + FM		
Er	AF	Mixed AF + FM	Mixed AF + FM	AF
Tm	AF	Mixed AF + FM		
		$\theta_p \approx T_{ord}$	θ_p positive $\theta_p > T_N$	θ_p sometimes negative $\theta_p < T_N$
	Basically Antiferro.	Basically Ferromag.		Definitely Antiferro.

unambiguous since Gd_3Ni is hard to saturate in high magnetic fields, and the reluctance to saturate cannot be due to anisotropy. In addition Er_3Ni was shown to be antiferromagnetic, and θ_p is always less than T_N for all R_3Ni. The R_3Ni compounds are definitely antiferromagnetic. The situation for R_3Co is not so clear since the antiferromagnetism is weak. In addition Er_3Co and Tb_3Co have mixed spin structures which could be due to distortion of a basically ferromagnetic spin structure. It appears that small changes arising on passing from Gd to the other lanthanides may be sufficient to turn a basically antiferro- into a basically ferromagnetic spin structure. Small electron concentration changes as discussed above for the $Gd_3(Fe, Co)$ series were seen to be able to suppress the antiferromagnetism of Gd_3Co. Thus R_3Co appears to be on the border between the two categories. RNi shows mixed structures as well as ferromagnetism in NdNi and no metamagnetism in GdNi. Thus RNi is basically ferromagnetic. Except for HoAl, all the RAl compounds can be classified as antiferromagnetic. Non-collinear antiferromagnetic spin structures need not necessarily indicate the presence of high anisotropy since exchange interactions can in principle be responsible for such structures. However, non-collinearity within a basically ferromagnetic material usually does point to the presence of large anisotropy.

Crystal field levels were calculated for the tripositive ions Tb, Dy, Ho, Er, Tm in order to account for the spin structures of RNi, (Gignoux, 1974). For Tb the case of $Tb_{0.5}Y_{0.5}Ni$ was considered. The theoretical calculations agreed with experiment without needing to introduce anisotropic exchange. The crystal field acting on low symmetry sites as in these systems can either split the multiplet ground state J for non-Kramers lanthanide ions or give rise to doublets. The splittings can be of the order of a few hundred Kelvin. This is of the same order of magnitude as the exchange interactions. The competition between these effects can lead to complex spin structures (Barbara et al., 1973).

Order–order transitions have been observed in Tb_3Co and Er(Ni, Cu). Gignoux et al. (1973) report for Tb_3Co a transition in the ordered temperature range from a commensurate structure at low temperatures to a non-commensurate structure 10 K below T_N. The low temperature spin structure is neither collinear nor coplanar. Evidence was found for narrow domain walls frozen in by strong anisotropy which is consistent with magnetic after-effect found in Tb_3Co (section 5). In $ErNi_{0.6}Cu_{0.4}$ a transition was detected by Gignoux and Gomez-Sal (1974) between a non-commensurate spin structure below T_N (7 K) to an antiphase structure at 1.3 K. This transition is due to the fact that Er^{3+} is a Kramers ion.

A celebrated example of a material with a large anisotropy to exchange ratio at low temperatures is Dy_3Al_2. See Barbara et al. (1971b, c). The spin structure is a mixed one, consisting of two magnetic sublattices with different easy axes. The (M, H) curve shows an open square hysteresis loop (fig. 14.54), with a large coercivity of 20 kOe at 4.2 K. Gd_3Al_2 shows typical ferromagnetic behaviour with θ_p almost equal to T_C. Buschow (1975) investigated effects of substituting Gd by Y and Th. Strangely, the θ_p values showed a pure linear decrease

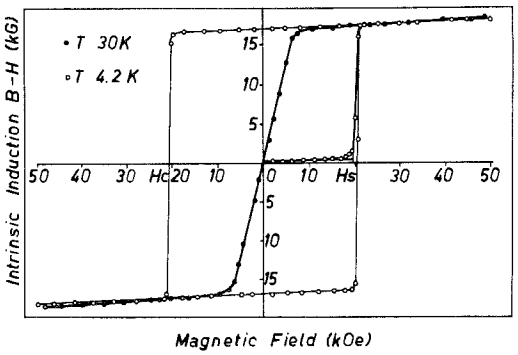

Fig. 14.54. Initial magnetization curve and hysteresis loop of Dy_3Al_2 measured along the c-axis (Barbara et al., 1971b).

characteristic of dilution for both pseudobinary series. This is to be expected for Y where the electron concentration remains constant, but not for Th which is quadrivalent. Applying the RKKY model, assuming $k_F/k_F^0 = 0.85$, and taking account of the lattice parameter variations in $(Gd, Th)_3Al_2$ this effect could be explained. Buschow and Fast (1966a) investigated the RGe compounds (CrB and FeB structures) which display both ferro- and antiferromagnetic ordering. HoGe shows a field induced transition from an antiferrimagnetic state at 4.2 K and SmGe shows contributions to the susceptibility from higher multiplets. The RGa compounds (CrB structure) have been investigated by Barbara et al. (1972) who report ferromagnetic behaviour. GdGa is ferromagnetic (Buschow and van den

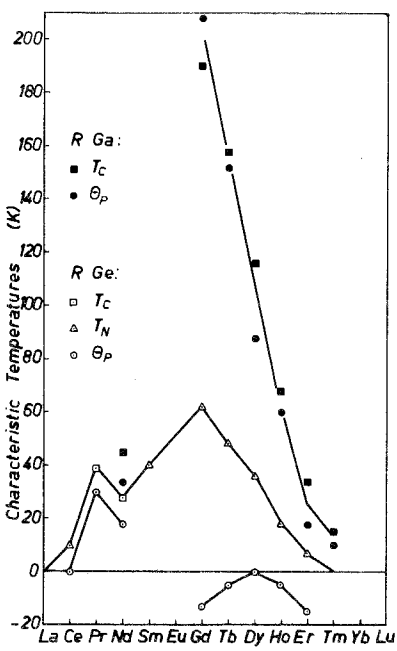

Fig. 14.55. Characteristic temperatures of RGa (Barbara et al., 1972) and RGe (Buschow and Fast, 1966a).

Hoogenhof, 1976). However Shohata et al. (1974) performed magnetic measurements on single crystals of DyGa and TbGa from which it appears that antiferromagnetic components may be present, especially in TbGa (fig. 14.51). However confirmation must await neutron diffraction investigations. The characteristic temperatures of RGa and RGe are shown in fig. 14.55. The R_2Al compounds, possessing the Ni_2Si structure appear to be antiferromagnetic. Gd_2Al, Tb_2Al and Dy_2Al show metamagnetism, whereas Ho_2Al, Er_2Al and Tm_2Al possess anomalously low ordering temperatures. This irregular behaviour as well as the irregular behaviour of θ_p point to large anisotropy effects. Gd_2Al appears to have a non-collinear spin structure. Longworth and Harris (1973) have investigated the magnetic properties of EuPd and have concluded that Eu is divalent in this compound. From Mössbauer measurements they deduce that EuPd is either an antiferromagnet or a strongly anisotropic ferromagnet, since very little turning of 4f-moments takes place at 60 kOe. Since the divalent Eu ion is an S-state ion the conclusion that EuPd is antiferromagnetic is to be preferred.

The inclusion of these asymmetrical structures in one category as in this section, irrespective of which non-magnetic B-elements are involved, appears to be meaningful from a physical point of view since the effect of strong anisotropy upon the spin structures appears to be a common feature in all of these systems.

2.7. *The* RB_3 *compounds*

The RB_3 compounds form the cubic $AuCu_3$ structure with In, Sn, Pb, and Pd. The RSn_3 series is only stable for the light lanthanides, Gd and Yb. The $AuCu_3$ structure is found in RAl_3 for the smaller lanthanides R = Yb and Tm and in β-$ErAl_3$. There also exists a rhombohedral form α-$ErAl_3$, which is usually described in hexagonal coordinates. However β-$ErAl_3$ is the stable form, the rhombohedral structure being stabilized only by the presence of impurities (Meyer, 1970). The lanthanides with intermediate size, Ho, Dy, Tb, give rise to structures with mixed hexagonal and cubic stacking, the cubic character decreasing with increasing lanthanide size (Buschow and Fast, 1966b). The large lanthanides including Gd and the light lanthanides form the cubic Ni_3Sn structure in RAl_3. $EuAl_3$ does not exist (for more on this subject see ch. 13 subsection 6.4).

Figures 14.56 and 14.57 summarize the Néel temperatures T_N and paramagnetic Curie temperatures in the various RB_3 series. Except for RPd_3 most of these series are strongly antiferromagnetic as exemplified by the large negative θ_p values. Buschow et al. (1969a) investigated the magnetic susceptibilities of RIn_3. The paramagnetic properties conform with the behaviour expected of the free tripositive ions, except for $CeIn_3$, $SmIn_3$ and $YbIn_3$. Although Ce appears to be trivalent as far as p_{eff} is concerned the large θ_p and T_N values of $CeIn_3$ are believed to be partly due to crystal field effects and partly due to the tendency of Ce^{3+} to lose its 4f electron thus changing the coupling mechanism between the localized moments. The lattice parameter of $CeIn_3$ is anomalous, as is also the

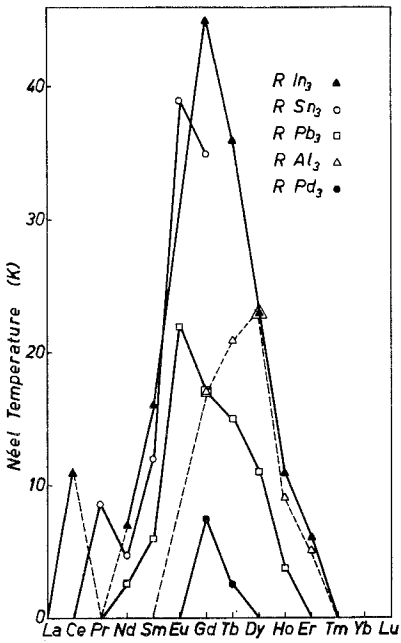

Fig. 14.56. Néel temperatures of the various RB_3 compounds.

case in $YbIn_3$ suggesting that Yb tends to possess a full 4f shell. The susceptibility of $YbIn_3$ increases rapidly on cooling, suggesting a change to the trivalent state at low temperatures, the susceptibility at 4.2 K agreeing with that expected of Yb^{3+}. The anomalous behaviour of $SmIn_3$ is attributed to effects of the excited J multiplet states. $PrIn_3$ becomes a Van Vleck paramagnet at low temperatures before ordering sets in. Lethuillier et al. (1973a, b) have investigated the magnetic properties of the RPb_3, RIn_3, and RSn_3 systems. The magnetization isotherms of some compounds in these systems at 4.2 K and 1.7 K are shown in figs. 14.58 and 14.59. The RPb_3 and RIn_3 compounds show very similar metamagnetic behaviour for R = Tb, Dy, and Ho. The metamagnet $PrSn_3$ is a

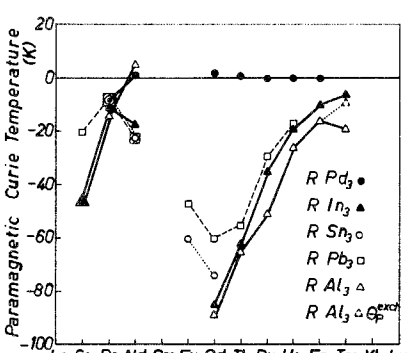

Fig. 14.57. Paramagnetic Curie temperatures of the various RB_3 compounds.

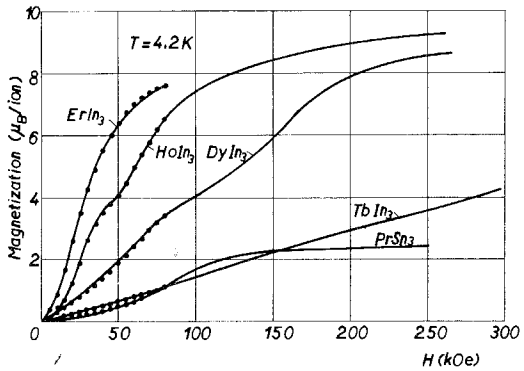

Fig. 14.58. Magnetization isotherms of $PrSn_3$ and some RIn_3 compounds (Lethuillier et al., 1973b). The points and continuous curves correspond to static and pulsed field results, respectively.

Kondo system. Lethuillier (1973) has discussed the magnetic properties and spin structures of the RIn_3, RSn_3 and RPb_3 systems. Arnold and Nereson (1969) and Nereson and Arnold (1970) have performed neutron diffraction measurements on some RIn_3 compounds. Neutron diffraction investigations of the RSn_3 and RIn_3 systems, where the B-partner valencies are different, have been performed by Lethuillier et al. (1973b). They report a difference in the magnetic structures: RIn_3 being of the $(\pi\pi 0)$ type and RSn_3 of the (00π) type, see fig. 14.60. The pseudobinary series $Tb(In, Sn)_3$ was investigated and the transition from one spin structure to the other was observed to occur at about 35% Sn concentration. This was accompanied by a minimum in the T_N value as shown in fig. 14.61. It is believed that the transition may be due to changes in the conduction electron concentration influencing RKKY-type interactions. The propagation vector of the spin structure does not change from one lanthanide to the other in any one of the series RSn_3 or RIn_3. However the moment directions do vary, this being due to the varying crystal field effects. However, attempts to account for the observed moment directions by means of point charge calculations were not successful (Lethuillier et al., 1973b) without changing the sign of the fourth order crystal field term. The spin structure of $TbIn_3$ was investigated by Crangle

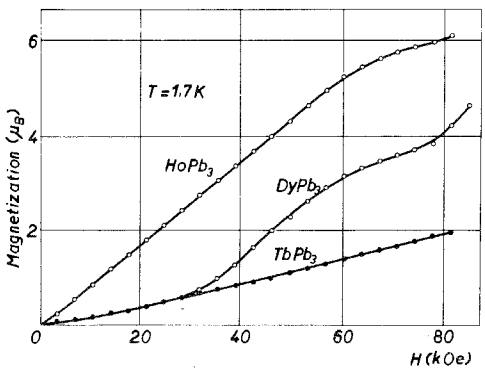

Fig. 14.59. Magnetization isotherms of some RPb_3 compounds (Lethuillier et al., 1973a).

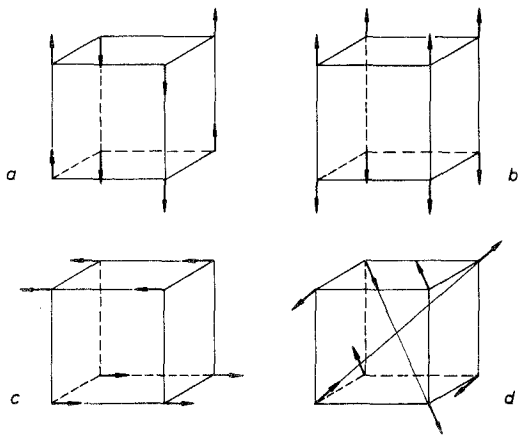

Fig. 14.60. Magnetic structures (a) $ErIn_3$, $NdIn_3$; (b) $PrSn_3$; (c) $NdSn_3$; (d) possible structure of $DyIn_3$ (Lethuillier et al., 1973b).

(1974). In agreement with the above trends the observed spin structure was found to be $(\pi\pi 0)$, with a magnetic moment of $7.2\,\mu_B$ almost parallel to the c-axis. This value is well below $9\,\mu_B$ expected of Tb^{3+} and is attributed to a partial quenching by the crystal field. This was also found by Arnold and Nereson (1969) in $DyPt_3$ where the Dy moment was $9\,\mu_B$ instead of $10\,\mu_B$ as expected from Dy^{3+}. In this investigation a $(\pi\pi\pi)$ magnetic structure type was found for $DyPt_3$. $TbPt_3$ was also shown to possess a $(\pi\pi\pi)$ spin structure (Nereson and Arnold, 1970).

Electrical resistivity measurements on single crystals in the [001] direction by Stalinski et al. (1973) showed that the spin disorder resistivity of RSn_3 compounds was not proportional to the de Gennes factor. Since these materials are antiferromagnetic superzone boundary effects might render impossible the estimation of the spin disorder resistivity as described in subsection 2.1. On the other hand, since the shape of the $d\rho/dT$ curve of $NdSn_3$ around the Néel temperature was qualitatively similar to that expected by the theory of

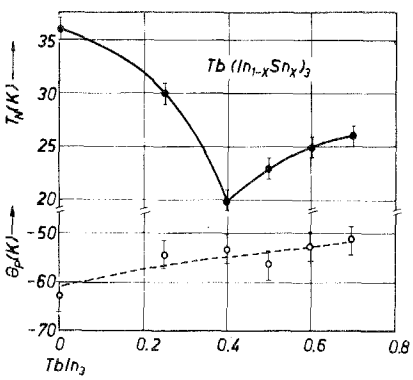

Fig. 14.61. Néel and paramagnetic Curie temperatures of the $Tb(In, Sn)_3$ system (Lethuillier et al., 1973b).

Fisher and Langer (1968) for ferromagnets, Stalinski et al. (1973) deduced that magnetic Brillouin zones do not play a role here.

The RAl_3 compounds possess a variety of crystal structures as already described at the beginning of this section. The Néel temperatures, as shown in fig. 14.56 exhibit an exceptional variation across the lanthanide series, being non-existent for the light lanthanides and showing a maximum at $DyAl_3$. This unusual decrease from $DyAl_3$ to $GdAl_3$ is probably a result of the gradual structure change. This is however not seen in the paramagnetic Curie temperature values which show a maximum at $GdAl_3$ as expected from a proportionality to the de Gennes factor. However the θ_p variation is anomalous at the beginning and end of the lanthanide series. The large value of θ_p for $CeAl_3$ may have a similar cause to that in $CeIn_3$. The anomalous θ_p value of $TmAl_3$ will be discussed later. We cannot resort to an explanation of $TmAl_3$ in terms of structure changes since the characteristic temperatures of $ErAl_3$ appear to be insensitive to structure.

The magnetic properties of the RAl_3 compounds were reported by Buschow and Fast (1966b). The paramagnetic measurements at high temperatures indicated Curie–Weiss behaviour for all except $SmAl_3$. Good agreement was achieved between the paramagnetic moments and those expected of the tripositive ions, even for $CeAl_3$ and $YbAl_3$, where one might expect departures from trivalency. Antiferromagnetic susceptibility peaks were obtained for all samples which ordered, except $ErAl_3$. However later neutron diffraction measurements have shown $ErAl_3$ also to be antiferromagnetic. The low temperature susceptibility shows deviations from the Curie–Weiss law in $YbAl_3$, $CeAl_3$ and of course in $SmAl_3$ which shows a deviation at all temperatures. The reasons for the deviation in $YbAl_3$ and $CeAl_3$ are not clear. Similar effects had been found in $CePb_3$ and CeAg, Pierre and Pauthenet (1965), where the anomalous behaviour was explained in terms of valence changes. It is however possible that crystal field effects may be a preferred explanation, especially for $YbAl_3$ where a valence change from Yb^{3+} to the larger Yb^{2+} ion would not be expected to be consistent with a lattice contraction upon cooling. Van Vleck temperature independent paramagnetism was observed in $PrAl_3$ and $TmAl_3$. This was explained in terms of crystal field splitting of the $(2J + 1)$ multiplet giving rise to a non-magnetic ground state which becomes populated upon cooling before magnetic ordering occurs. The case of $TmAl_3$ was discussed in detail by Buschow (1968) in terms of a cubic crystal field potential. The results can be explained by a crystal field splitting of the order of 290 cm^{-1}. The experimental θ_p value of -19 K consists of a crystal field contribution of -11 K and an exchange contribution of -8 K. The latter value is also shown in fig. 14.57 which is in line with the trend of θ_p values due to the other lanthanides. In this work clear Néel susceptibility peaks at T_N were obtained for α-$ErAl_3$ and β-$ErAl_3$. The difference in structure does not appear to influence the magnetic properties to any large extent. Neutron diffraction investigations of α-$ErAl_3$ and β-$ErAl_3$ have been reported by Bargouth and Will (1971) and Will and Cox (1974) respectively. The spin structures deduced are shown in figs. 14.62 and 14.63. The

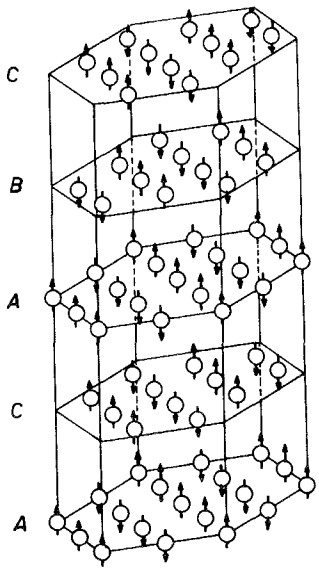

Fig. 14.62. Magnetic structure of α-$ErAl_3$ (Bargouth and Will, 1971).

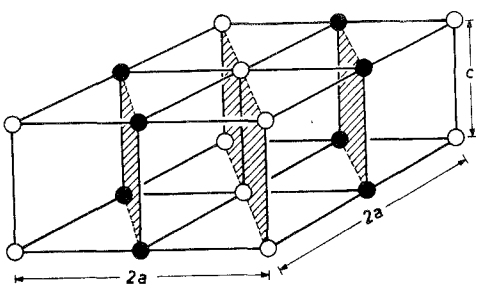

Fig. 14.63. Magnetic structure of β-$ErAl_3$, showing the doubled tetragonal cell. The circles denote Er ions. The moments are perpendicular to the c-axis (Will and Cox, 1974). The filled circles denote one spin direction and the open circles the opposing spin direction.

moments at 4.2 K were considerably less than the gJ values. This is considered to be due to quenching. Mössbauer measurements on a single crystal of α-$ErAl_3$ by Weber (1973) have provided evidence of the existence of four sublattices. The Er ion could be divided into two groups with moments 7.2 μ_B and 4.8 μ_B whereas Bargouth and Will (1971) reported only one value 6.15 μ_B at 2.15 K. Consistent with the latter authors, Weber (1973) finds that α-$ErAl_3$ is a uniaxial antiferromagnet. However magnetization isotherms indicate a complex process with two critical fields not characteristic of simple spin-flopping (fig. 14.64). See also Weber (1976).

The RPd_3 compounds, as seen in fig. 14.56 are different from the other RB_3 compounds in that the ordering temperatures are either extremely low or non-existent (Gardner et al., 1972). This can be understood partly if one considers that Pd has a tendency to fill its 4d-shell. This is the case even in dilute alloys of rare earths dissolved in Pd, which are not discussed here. A Pd ion with a full 4d-shell then contributes no electrons to the conduction band and indirect exchange via the

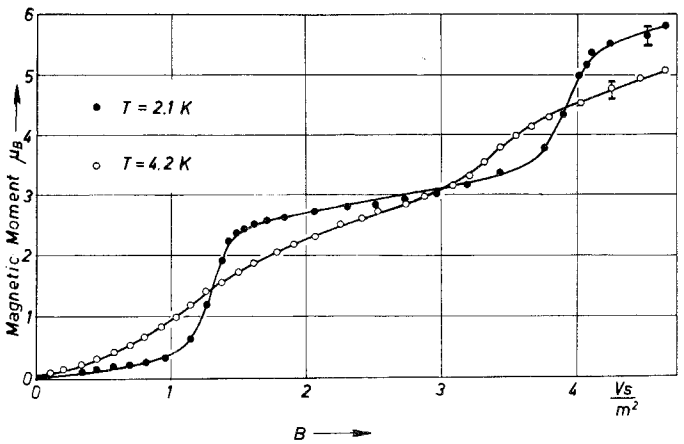

Fig. 14.64. Magnetization isotherms along the c-axis of a single crystal of α-$ErAl_3$ (Weber, 1973).

conduction electrons must then be correspondingly weaker, proceeding only via the electrons contributed from the rare earth ions. Since Pd has an affinity for absorbing electrons one may expect that the rare earth ions will not tend to form any divalent ions. Thus Eu in $EuPd_3$ and Yb in $YbPd_3$ should be trivalent as found in the other lanthanides. Correspondingly Ce may be expected to show a valency in excess of three. The unusual findings of Hutchens et al. (1971), that Eu and Yb are trivalent in RPd_3 are consistent with these considerations and also consistent with the conclusions of Harris and Raynor (1965) drawn from crystallographic results. In the latter work the lattice constants showed no anomalous values for $EuPd_3$ and $YbPd_3$. This is to be contrasted with $EuSn_3$, $YbSn_3$ and $YbIn_3$ for example where the R-ion is divalent. From lattice size considerations Gardner et al. (1972) deduce a valency of 3.45 for Ce in $CePd_3$. The electrical resistivity of $CePd_3$ was investigated by Hutchens et al. (1971). They find a maximum at low temperatures followed by a negative slope up to the highest investigated temperatures. This is ascribed to the existence of a Kondo anomaly and the occurrence of Kondo sidebands (Maranzana, 1970). The rise of the spin disorder resistivity in $GdPd_3$ up to $T_N = 7$ K shows a maximum which can perhaps be attributed to the effects of magnetic Brillouin zones. Apart from antiferromagnetic ordering found in $GdPd_3$ only $TbPd_3$ appears to order, $T_N = 2.5$ K (Gardner et al., 1972). However no definite peak was observed in the susceptibility of $TbPd_3$. In the paramagnetic state all trivalent RPd_3 compounds except $SmPd_3$ and $EuPd_3$ show a Curie–Weiss behaviour with the expected moment of the tripositive ion (Hutchens et al., 1971; Gardner et al., 1972). The paramagnetic Curie temperatures are all extremely low, being centred around absolute zero. The relatively large value -7 K for $PrPd_3$ (Hutchens et al., 1971) is not consistent with the value $\theta_p = 0$ K obtained by Gardner et al. (1972). It may well be that all θ_p values are effectively zero.

Since exchange is extremely weak in the RPd_3 system we could regard this to a good approximation, as a crystal field-only system (Furrer and Purwins, 1976). The crystal field effects in the light lanthanide RPd_3 compounds have been investigated by Furrer and Purwins (1976) using neutron inelastic scattering. They detect no crystal field transitions in $CePd_3$ and attribute this absence to the large width of the 4f electronic state compared with the crystal field splitting since the intermediate valency of Ce between 3+ and 4+ requires a description in terms of a virtual bound state near the Fermi level. Apart from this, it was found that the energies and widths of the crystal field transition in $PrPd_3$ and $NdPd_3$ are effectively temperature independent. This was interpreted assuming the exchange to be the dominant contribution to relaxation effects since inter-ionic exchange, as pointed out above, is small in these RPd_3 compounds.

Another series of RB_3 compounds exists for Mg, this having the cubic Fe_3Al structure. Investigations by Buschow (1976) of the RMg_3 series reveal a change in sign of θ_p from the light to the heavy lanthanides. This is very similar to the behaviour found in RMg compounds (subsection 2.3) with the CsCl structure. The interpretations are similar, involving interactions via 5d-electrons which are sensitive to lattice parameters and not of the RKKY form.

2.8. *Other compounds*

In the foregoing we have discussed the most extensively investigated intermetallics with no B-moments. Naturally the treatment has not been exhaustive and there remains a number of systems yet to be mentioned. Due to lack of space however only a brief description of the known magnetic properties of a selection of remaining compounds will be given. These can be conveniently divided into the following groups: relatively dilute R compounds with stoichiometries RB_{13}, RB_{12} and R_2B_{17}; the RB_6, RB_5 and RB_4 systems; the intermediate R_7B_3 and R_3B stoichiometries.

The characteristic temperatures of the dilute intermetallic compounds are shown in fig. 14.65. The RBe_{13} compounds have not been thoroughly investigated because of the difficulty in preparing specimens and the hazard involved in

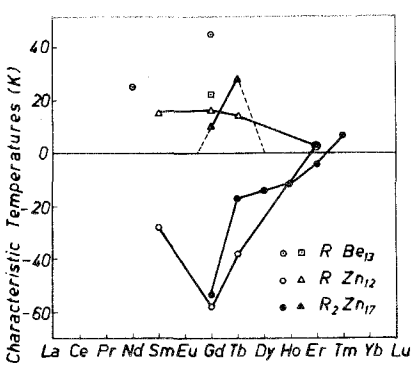

Fig. 14.65. Characteristic temperatures of some dilute compounds RBe_{13} (Borsa and Olcese, 1973), RZn_{12} and R_2Zn_{17} (Stewart and Coles, 1974). Squares denote T_C; triangles, T_N; circles θ_p.

handling metallic beryllium (Borsa and Olcese, 1973). The RBe_{13} compounds with Gd, Nd, Ce and La have been investigated by Borsa and Olcese (1973). These have the cubic $NaZn_{13}$ structure in which the R atoms are arranged in a simple cubic sublattice. $GdBe_{13}$ and $NdBe_{13}$ both show Curie–Weiss behaviour at high temperatures. The former orders ferromagnetically, with θ_p not equal to T_C, which is not understood. The latter shows a susceptibility maximum at 2 K. However no magnetic ordering occurs and crystal field effects play an important role at low temperatures. In both compounds exchange dominates the spin dynamics, at least at high temperatures. $LaBe_{13}$ is non-magnetic and $CeBe_{13}$ shows no Curie–Weiss behaviour. Ce in this compound is present as a mixture of trivalent and non-magnetic tetravalent ions whose ratio changes with temperature.

Investigations of magnetism and resistivity of the RZn_{12} and R_2Zn_{17} compounds have been reported by Stewart and Coles (1974) for example. The low ordering temperatures mean that resistivity measurements in the ordered range and a little above the ordering temperatures reveal spin disorder resistivity effects without the presence of a strong phonon contribution. This is especially true of $ErZn_{12}$. These two sets of compounds show antiferromagnetic ordering, but in the R_2Zn_{17} system the only compounds for which ordering could be detected are Gd_2Zn_{17} and Tb_2Zn_{17}. It appears that the exchange interactions in R_2Zn_{17} compounds are weaker than those in RZn_{12} even though the latter is more dilute. It is suggested that the dominant interaction is of the RKKY type. Short range order effects have however been observed well above the Néel temperatures. $SmZn_{12}$ shows large conduction electron polarization effects (Stewart, 1973b). The susceptibility as a function of temperature is fitted according to the expression of eq. (14.12) where χ_0 is a temperature independent term. It was pointed out that this term only makes its presence known in Sm compounds because the Sm moment is weak, and that this term is also present for compounds with other lanthanides.

The RCu_6 compounds form with the orthorhombic $CeCu_6$ structure for the lanthanides Ce, Pr, Nd, Sm and Gd. The magnetic properties have been investigated by Coldea and Pop (1973). The susceptibilities are analysed as arising from a temperature independent term and a Curie–Weiss term. An enhanced Pauli susceptibility was detected and attributed to a non-sphericity of the Fermi surface. Anomalous behaviour was found in $SmCu_6$ resulting mainly from a Van Vleck-type paramagnetism with free tripositive Sm ions. The RCu_5 compounds occur with two structure types, the hexagonal $CaCu_5$ and cubic $AuBe_5$ structures for the light (larger) and heavy (smaller) lanthanides respectively, the compounds with Gd, Tb, Dy and Y showing both structure types (Buschow et al., 1969b). The RZn_5 compounds with Ho, Er, Tm, Lu and Y occur with the $EuMg_5$ structure whereas RZn_5 compounds with La, Ce and Eu form the $CaCu_5$ structure. The RNi_5 compounds form with the $CaCu_5$ structure. They all order ferromagnetically with low Curie temperatures (fig. 14.71). These values are however higher than in the RCu_5 compounds which also show a change in the type of ordering (Buschow et al., 1970) from ferromagnetic (R = Tm, Er, Ho)

to antiferromagnetic for $TbCu_5$. $DyCu_5$ shows metamagnetic behaviour and a susceptibility peak at 8 K. $TbCu_5$ has a T_N value of 15 K. The magnetic results are discussed using the RKKY model. Takeshita et al. (1976) were able to stabilize the $AuBe_5$ structure for the whole range (R = Nd to Tm) by replacing 20% of the Cu by Ag. The RCu_4Ag compounds were found to be antiferromagnetic with negative θ_p values from Nd to Yb and ferromagnetic for Dy and Ho. The RAu_4 compounds with the $MoNi_4$ structure have been investigated by Sill et al. (1971). No magnetic order for R = Er, Tm and Yb was detected down to 6.1 K.

Nuclear order effects in $PrCu_6$ and $PrCu_5$ have been investigated by Andres and Bucher (1972) and Andres et al. (1975). The Van Vleck paramagnet $PrCu_6$ is an example of a singlet system with sufficiently low exchange such that Van Vleck paramagnetism persists down to the mK temperature range and subsequently undergoes nuclear magnetic ordering at very low temperatures. $PrCu_6$ can be used for nuclear magnetic cooling down to 2.6 mK. As we have seen in subsection 2.5 $PrCu_2$ has sufficiently strong exchange interactions for these to be near the critical value for spontaneous electronic magnetic order.

The R_7B_3 compounds form with Ni, Pd, Pt, and Ir for the light lanthanides and with Rh for all the lanthanides (Olcese, 1973). This stoichiometry has been the object of some controversy. Some compounds which were believed to have a stoichiometry 5 : 2 have been shown to have in fact a stoichiometry of 7 : 3 with the Th_7Fe_3 structure (Moreau and Parthé, 1973). On the other hand Dy_5Pd_2 has been shown to be in reality $Dy_{68}Pd_{28}$ with a cubic symmetry (Fornasini and Palenzona, 1974). Olcese (1973) has reported susceptibility measurements for the various 7 : 3 systems without detecting any magnetic ordering except in Gd_7Rh_3 which orders ferromagnetically below 170 K. All lanthanides occur in these

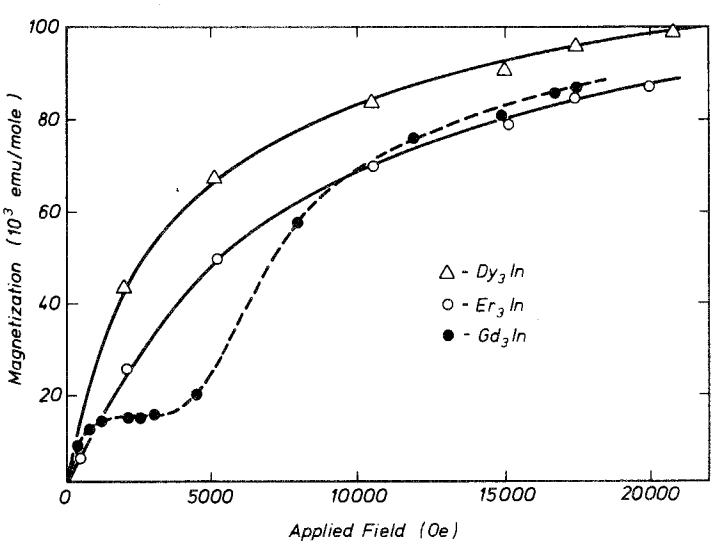

Fig. 14.66. Magnetization isotherms of some R_3In compounds at 4.2 K (Hutchens et al., 1974).

compounds in the trivalent state except for Ce whose valency is in excess of three. This is to be compared with behaviour in RPd_3 (subsection 2.7).

Apart from the RB_3 compounds many of which have the $AuCu_3$ structure (see subsection 2.7) there exist also rare earth-rich compounds with the Cu_3Au structure having the R_3B stoichiometry. Hutchens et al. (1974) have investigated the magnetic properties of R_3In compounds which reveal a rather varied magnetic behaviour. Gd_3In shows metamagnetic behaviour indicative of a complex magnetization process. See fig. 14.66 which shows this together with the relatively normal behaviour of Dy_3In and Er_3In. The positive θ_p values for the R_3In compounds indicate the predominance of ferromagnetic exchange. Gd_3In has a θ_p of 196 K and a value of 213 K for T_C where ferromagnetism is assumed. Nd_3In displays an extremely low moment of about 10% of the gJ value. Neutron diffraction investigations showed that this low value is indeed real and not a result of a non-collinear magnetic structure. This low moment indicates a very strong effect from the crystal field which would preclude any continuity of magnetic properties across the lanthanide series in this system.

3. Intermetallics with non-zero B-moment

3.1. *Introduction and theoretical concepts*

The interactions in intermetallics R–3d where the 3d-element is magnetic are even now basically not well understood†. The difficulties in describing these compounds even qualitatively with theoretical models arise from the inherently different nature of the various types of moments and the interactions between them. In the R–3d intermetallics we can distinguish three main types of interaction: R–R, R–3d, and 3d–3d.

Due to the small spatial extent of the 4f wave functions of the lanthanides, the magnetic moments are well-localized and to a large extent screened from crystal fields, this screening being due to the outer shell electrons. The magnetic exchange interactions R–R arise by means of indirect interactions via the conduction electrons. These interactions are described by the RKKY model which includes a number of simplifying assumptions (subsection 2.1). These assumptions are not usually valid in real systems, but the model is however repeatedly applied qualitatively especially in systems with zero 3d moment. For systems with R–3d and 3d–3d interactions, the R–R interactions certainly still exist, but their description in terms of the simple model is made even more complicated by the presence of interactions involving 3d moments, and the arguments used become rather qualitative.

The more spatially extensive 3d wave functions (compared with 4f wave functions) give rise to overlap which in most cases forces one to discuss the 3d electrons in terms of electron bands rather than 3d states with sharp energy

†It has recently been shown (Szpunar and Lindgard, 1977) that a combination of RKKY and CPA theory is quite successful for calculating the temperature dependence of magnetization and Curie temperatures for various Gd–3d (3d = Fe, Co, Ni) compounds.

levels. Theoretical discussions of R–3d interactions have a tendency to be rather phenomenological.

Although 3d electrons are usually treated as itinerant, especially in Ni and Co compounds, intermetallics involving Mn and Fe tend to require a more localized picture. In the R–3d intermetallics there exists a large number of isotypic compounds in which replacement of one component by another can lead to mixed crystal series. Such substitutions usually take place statistically and often without change of crystal structure type. In these disordered systems the magnetic properties are determined not only by local effects upon the magnetic 3d ions but can also be described in many cases by an average electronic parameter such as the density of states $N(E_F)$ at the Fermi level. According to which system is considered the disordered distribution of ions in homogeneous mixed crystals can, especially at low temperatures, give way to heterogeneous systems in which clusters are present. Partial ordering of components can also occur. Models for describing mixed crystal series are also here to a large extent phenomenological. Homogeneous models, beginning with the simplest, are for example the rigid band model, Stoner–Wohlfarth model, and Mathon model. In these models the crystal structures and local surroundings of magnetic ions are not explicitly taken into account. On the other hand the Jaccarino–Walker and cluster models do consider local effects. As long as band structure calculations for the compounds of a mixed crystal series are available (only for simple crystal structures) the electronic structures of the end compounds (such as densities of states) can be combined to calculate the electronic properties within a mixed crystal series using CPA (Coherent Potential Approximation) and related methods. For example, in binary transition metal alloys (Ni–Cu, Ni–Fe) good agreement with experiment has been obtained (Zuckermann, 1974). However this is not realizeable for the R–3d intermetallics, since the simplest available structure ($MgCu_2$, 24 atoms per unit cell) already presents many difficulties in calculation.

In the light of these considerations it is apparent that the description of magnetic properties with the help of simple models, such as the Néel molecular field model or a band model, can only in isolated cases be expected to be successful. In the following an outline will be given of a number of relevant simple theoretical models.

3.1.1. *Néel molecular field model*

Generally it can be said that the R-moments couple ferromagnetically with 3d moments for the light lanthanides, whereas ferrimagnetism is observed for the heavy lanthanides. Exceptions are found for some Sm compounds, but otherwise this general rule appears to be valid to a remarkably high degree.

In order to estimate the strengths of the three basically different types of interactions the Néel model has been successfully applied in a large number of cases. The model involves a localized picture of magnetic moments on one or a number of sublattices. The total magnetization for two sublattices is given by $M = M_A - M_B$ where $M_i = M_i(0)B_{Ji}(x)$. Here we use the notation i = A or B. The molecular fields on each sublattice are $H_A = M_A n_{AA} + M_B n_{AB}$, $H_B =$

$M_B n_{BB} + M_A n_{AB}$. The three terms n_{AA}, n_{AB}, n_{BB} are the molecular field coefficients between and within the two sublattices A and B, B_{Ji} is the Brillouin function.

From the temperature variation of the magnetization or susceptibility one can calculate the molecular field coefficients, nothing being said however, about the physical nature of the various interactions. Especially the determination of n_{ij} from the susceptibility can be rather problematic. Although this model is particularly successful for insulators, such as garnets for example, it is surprising how powerful it is in describing intermetallics. In most cases the application of the model reveals that the R–R interaction is weak compared with 3d–3d interactions, the R–3d interactions lying between these extremes (Burzo, 1973a; Hilscher et al., 1973; Fischer and Meyer, 1975). Various authors have concluded that the molecular field acting on the 3d moments is mainly determined by 3d–3d interactions, and that these are the largest contributions determining the ordering temperatures.

On the other hand compensation temperatures T_k tend to be mainly determined by R–3d interactions (Buschow, 1971). This fact is made use of in a modified molecular field model due to Clark and Callen (1968), in which the strong dependence of the magnetization upon field in the vicinity of the compensation temperature is described. In this treatment the sublattice magnetizations are not collinear. This results in two critical fields: a lower field H_ℓ at which the antiparallel coupling becomes distorted, and a higher one H_u where a parallel coupling sets in. For intermediate fields H_0 the magnetization is given by $M = M_R \cos\theta_R + M_{3d} \cos\theta_{3d} = H_0/n_{R3d}$, which only depends on the applied field and the coefficient n_{R3d}. This model has been applied, for example, to Er_6Fe_{23}, described in subsection 3.8.

Although amorphous magnetic materials are not discussed in this chapter (see ch. 16), it is of interest to compare the molecular field treatments of intermetallic compounds in the crystalline and amorphous states. See Tao et al. (1973) and Burzo (1975a). Table 14.5 displays these data for $GdCo_2$ and $GdFe_2$. T_C of amorphous $GdCo_2$ is 30% larger than for crystalline $GdCo_2$. The exchange field on Co rises also by 23%. On the other hand T_C of $GdFe_2$ falls by 37% while

TABLE 14.5.
Comparison of the molecular field parameters for amorphous and crystalline $GdFe_2$ and $GdCo_2$ (Burzo, 1975a).

		n_{GdGd}	n_{GdCo}	n_{CoCo}	H_{exch}(Co)	H_{exch}(Gd)	T_C(K)
$GdCo_2$	cryst.	17.6	−88.4	270	6.5 MG	1.7 MG	400
	amorph.	4.6	−81	309	8 MG	1.5 MG	520
		n_{GdGd}	n_{GdFe}	n_{FeFe}	H_{exch}(Fe)	H_{exch}(Gd)	T_C(K)
$GdFe_2$	cryst.	15.7	−138	315	11.1 MG	3.1 MG	795
	amorph.	19.4	−59.5	281.4	7.2 MG	1.8 MG	500

going from the crystalline to the amorphous state. The fall in exchange field on Fe is 35%. This model is capable of estimating the strength of exchange, although the local surroundings of the ions are not taken into account. On the other hand one cannot expect the model to predict the direction of the T_C change on going from one state to another (e.g. crystalline-amorphous). An explanation of the T_C changes is given by Tao et al. (1973) in terms of charge transfer from the R to the 3d elements.

The application of the molecular field model to pseudobinary systems such as $R(Fe, Co)_2$ is complicated by the fact that three magnetic sublattices are present and therefore one has to deal with six molecular field coefficients. The problem is to define the magnetic sublattices in a solid solution. In order to make some progress the problem is simplified to the consideration of two sublattices. This means that the coefficient n_{3d3d} involves coefficients $n_{3d(1)3d(2)}$, $n_{3d(1)3d(1)}$ and $n_{3d(2)3d(2)}$.

Within pseudobinary systems it has been attempted to explain the variation of 3d magnetic moments, if a localized model is assumed, in terms of the model of Jaccarino and Walker (1965). This model attempts to explain discontinuous occurrences of localized moments in binary or pseudobinary alloys. It is suggested that the local environment is responsible for magnetizing the impurity. A disordered binary alloy system A_xB_{1-x} (where A atoms are the only atoms without a moment), with nearest neighbour coordination number Z is considered. The number of nearest neighbours B is given by a binomial distribution function. The critical value of the number of nearest B neighbours for the onset of magnetic ordering is obtained by fitting the experimental data. Considerations using such a model are of particular value for the cases where a 3d-moment arises within a pseudobinary system (section 4).

3.1.2. *Crystal fields*

Apart from the isotropic exchange which has been discussed up till now, the R–3d compounds are also characterized by anisotropic interactions. Considering the magnetocrystalline anisotropy to arise mainly from the interactions of the 4f shells with the crystal field, we can express the hamiltonian of a 4f ion by

$$\mathcal{H} = \mathcal{H}_{\text{free}} + g\mu_B J_z H_{\text{Reff}} + W_{\text{CF}}, \tag{14.15}$$

where $H_{\text{Reff}} = H_a + \Sigma_j n_{ij} M_j$, H_a = applied field, n_{ij} = molecular field coefficients. M_j = magnetization of j-sublattice. The crystal field energy is expressed by

$$W_{\text{CF}} = \sum_i q_i V_i = \sum_{i \neq j} q_i q_j / (R_j - r_i), \tag{14.16}$$

where q_i = charge of the R ion under consideration in position r_i, upon which the potential V_i is acting, and q_j = charge of ions in position R_j which are responsible for the potential V_i at r_i.

Due to the relatively good screening and small spatial extension of the 4f shells, the crystal field and interionic exchange energies are usually much smaller than the L–S coupling energy. Although the crystal fields acting upon the 4f ions

are not large in RFe_2 or RAl_2 for example, these fields produce the largest contributions to the magnetocrystalline anisotropy of these compounds and are instrumental in determining the easy axis. This affects the contribution of the magnetic moments to the hyperfine field at 3d sites and the easy axis can be determined experimentally by means of the Mössbauer effect and NMR on polycrystalline samples.

The crystal field potential W_{CF} is developed in Legendre polynomials, and with the help of the Wigner–Eckhart theorem (Edmonds, 1957), can be expressed in terms of operator equivalents $\hat{O}_n^m$ which are functions of angular momentum operators $\hat{J}_z$, $\hat{J}_+$, $\hat{J}_-$. This method of Stevens (1952) is described in detail by Hutchings (1966), whose nomenclature is adopted here. The hamiltonian as a function of angular momentum operators is

$$\mathcal{H}_{exch} + \mathcal{H}_{CF} = g\mu_B J_z H_{R\,eff} + \sum_{n,m} B_n^m \hat{O}_n^m. \tag{14.17}$$

Using this notation the calculation of matrix elements (Hutchings, 1966) is especially simplified.

From symmetry considerations it can be shown that only terms with $n \leqslant 6$ contribute to the crystal field potential. In the above equation $B_n^m = A_n^m \langle r^n \rangle\ \theta_n$ where $\langle r^n \rangle$ = expectation value of r^n for 4f electrons (Freeman and Watson, 1962). θ_n depends upon the reduced matrix elements in the Wigner–Eckhart theorem and upon the electron configuration. For 4f electrons all terms $\theta_2 = \alpha_J$, $\theta_4 = S_J$ and $\theta_6 = \gamma_J$ (tabulated by Hutchings) disappear. The terms A_n^m depend only on the crystallographic surroundings and can be calculated according to a point charge model. Since screening effects and moment induction in the ligands are neglected not much more than the order of magnitude of the crystal field splitting can be deduced. For high symmetry (e.g. cubic Laves phase) and considering both nearest and next nearest neighbours the A_n^m can be analytically represented (Hutchings, 1966; Bleaney, 1963).

$$A_4^0 = \frac{7e^2}{36R_R^5}(q_R - 1.2\,q_B) \qquad A_6^0 = -\frac{e^2}{18R_R^7}(q_R + 0.3\,q_B). \tag{14.18, 14.19}$$

The crystal field coefficients also depend upon the charges q_B on the 3d sites, whose valency is usually not exactly known in intermetallics. In R–3d compounds the errors due to this are larger than those due to ignoring effects of screening. Despite this, success was achieved by a number of authors, e.g. Atzmony et al. (1973), Déportes et al. (1974), Purwins et al. (1974, 1976), Buschow et al. (1973b), Dublon et al. (1975), in determining the easy axis of some R–3d compounds. Apart from the energy eigenvalues ϵ_i obtained by crystal field calculations, the molecular field H_R at the R site is needed to calculate the isotropic free energy $F_{J,iso}$ given by

$$F_{J,iso} = -kT \ln Z_{J,iso} \qquad Z_{J,iso} = \sinh\left(\frac{2J+1}{2J}x\right) \Big/ \sinh\left(\frac{1}{2J}x\right)$$

where $x = g\mu_B J H_R / kT$. If the $\epsilon_i^{(j)}$ from the crystal field calculations are obtained

for the various quantization axes (j) then the direction for which $\Delta F = F^{(j)} - F_{J,\mathrm{iso}}$ is a minimum should correspond to the easy axis. The free energy corresponding to the jth quantization axis (cf. for the cubic Laves phase $j = 1, 2, 3$ correspond to [100], [110], and [111]) is given by $F^{(j)} = -kT \ln Z^{(j)}$,

$$Z^{(j)} = \sum_{i=-J}^{J} \exp(-\epsilon_i^{(j)}/kT). \tag{14.20}$$

Crystal field and exchange field induced mixing of the excited levels ($J = \frac{7}{2}, \frac{9}{2}$) into the ground state ($J = \frac{5}{2}$) accounts successfully for the more complex magnetic properties of Sm^{3+} in some intermetallics (Buschow et al., 1973b; Dublon et al., 1975).

Segal and Wallace (1970, 1973, 1974, 1975) have treated crystal fields of rare earth ions in hexagonal fields, which is relevant to RCo_5 and R_2Co_{17} compounds. It was shown by Buschow et al. (1974a) and Sankar et al. (1975) that $A_2^0\langle r^2\rangle$ is the significant term since the axial ratio (c/a) in these compounds does not have the ideal value of $(\frac{8}{3})^{1/2} = 1.63$ for hexagonal close packed structures.

3.1.3. *Rigid band model applied to pseudobinary systems*

In order to study the stability and occurrence of magnetic moments a powerful method is to investigate the magnetic properties of pseudobinary systems. In R–3d systems one has two possibilities: either replacing one rare earth by another, or replacing one 3d element by another. These latter substitutions often occur without any structural changes in contrast to the binary 3d alloys. In some investigations the above two types of substitution are employed at the same time, giving four-component systems.

The Néel model was shown to be successful for obtaining insight into the order of magnitude of the various interactions in the R–3d compounds. The localization of the lanthanide moments is well established. However the 3d moments tend to show both localized and itinerant behaviour and therefore a pure localized picture as used in the original Néel model cannot be expected to describe the magnetic properties in detail.

The simplest band model for 3d transition metals is the rigid band model. This model assumes a fixed density of states curve which can often be obtained from experimental data such as magnetic moments and specific heat. The main assumption is that E_F shifts to higher or lower energies, without $N(E_F)$ changing shape, depending upon whether electrons are added or removed. By assuming a special form for the density of states curve and by assuming a special splitting of the two spin sub-bands of ferromagnetic alloys, the moment variation of a variety of alloys in the Slater–Pauling curve could be explained successfully but phenomenologically, fig. 14.67. This is also true for $R_2(Fe, Co)_{17}$, $R_2(Co, Ni)_{17}$, and $R(Fe, Co)_2$. The model as applied to (Fe, Co) and (Co, Ni) involves the assumption that, starting from Fe both spin-up and spin-down 3d sub-bands are unfilled. In addition a minimum in the density of states is required at which the Fermi level of the less full sub-band is trapped. Due to this feature, on adding electrons to the band system, the electrons enter the majority sub-band thus raising the

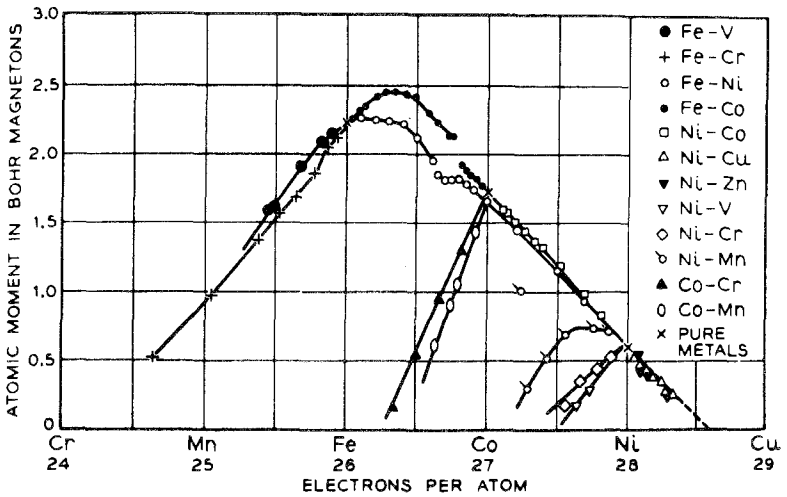

Fig. 14.67. The Slater–Pauling curve (Bozorth, 1951).

moment at the rate of 1 μ_B per electron. When full, the minority spin sub-band starts to fill, lowering the moment at the rate of 1 μ_B per electron added.

Thus the Fe–Co, Co–Ni and Ni–Cu systems can be explained roughly, the moment at last disappearing in the Ni–Cu system for 60% Cu. The well-known deviations from the Slater–Pauling curve are e.g. Ni–V, Ni–Cr. These can be explained with the concept of localized moments formed by itinerant electrons, which will be briefly discussed later (Friedel, 1958; Friedel et al., 1961). In the Ni–Cu system the disappearance of ferromagnetism is accompanied by a decrease in specific heat. Detailed magnetic measurements show that the onset of ferromagnetic order is caused by clustering. By means of XPS spectra of Ni–Cu, Hüfner et al. (1972, 1973) demonstrate the inapplicability of the rigid band model, reporting that the shape of the density of states curve changes.

In conclusion the concept of the rigid band model is often useful as a first approximation, but the applicability and conclusions drawn from the model should be treated with caution.

3.1.4. *Stoner–Wohlfarth model*

Ferromagnetism in a band can occur when exchange has a tendency to split the two sub-bands of opposing spin but only when this splitting is energetically favourable. This means that the inevitable rise in kinetic energy due to splitting is at least balanced by the corresponding drop of the exchange energy. This spontaneous splitting is energetically favourable only if the exchange energy and the magnitude of the density of states at the Fermi level are large enough. The critical value of one depends upon the value of the other, and this can be expressed by the Stoner criterion for spontaneous ferromagnetism:

$$IN(E_F) \geq 1. \tag{14.21}$$

I is the effective Coulomb exchange interaction energy and $N(E_F)$ is the density of states at the Fermi level. By changing the alloy concentration in a binary or pseudobinary solid solution of transition metals the value of this product can be varied. The critical concentration x_F at which ferromagnetism appears is found for $IN(E_F) = 1$. The magnetic order arising can be strong or weak. The latter is characterized by a small relative magnetization $\xi = M(H, T)/N_g n' \mu_B$. $M(H, T)$ is the magnetization per g, n' is the number of conduction electrons per atom, and N_g is the number of atoms per g. In the case of weak ferromagnetism the Stoner–Wohlfarth model (Stoner, 1938; Wohlfarth, 1949) can be applied if the magnetization is assumed to be spatially homogeneous. The Landau theory of second order phase transitions has been applied to weak ferromagnetism by Edwards and Wohlfarth (1968). The difference of the free energy between the ferromagnetic and the paramagnetic state is

$$\Delta F = \tfrac{1}{2}A(T) \cdot M^2(H, T) + \tfrac{1}{4}B(T) \cdot M^4(H, T) - H \cdot M(H, T). \tag{14.22}$$

Minimizing ΔF with respect to $M(H, T)$ gives $H/M(H, T) = A + B \cdot M(H, T)^2$. As a result of the Stoner–Wohlfarth model, following the method of Edwards and Wohlfarth (and for higher terms de Chatel and de Boer, 1970) one obtains

$$\frac{H}{M(H, T)} = \frac{1 - IN(E_F)}{N_g N(E_F) \mu_B^2} \left(1 + \frac{T^2 \alpha}{1 - IN(E_F)} + \cdots\right) + \frac{3\nu_1^2 - \nu_2}{6N(E_F)^3 N_g^3 \mu_B^4} \left(1 + \frac{\beta T^2}{3\nu_1^2 - \nu_2}\right) M(H, T)^2 \tag{14.23}$$

with

$$\nu_m = \frac{1}{N(E)} \left(\frac{d^m N(E)}{dE^m}\right)_{E=E_F}, \qquad \alpha = \tfrac{1}{6}\pi^2 k_B^2 (\nu_1^2 - \nu_2)$$

$$\beta = \tfrac{1}{6}\pi^2 k_B^2 (15\nu_1^4 - 25\nu_1^2\nu_2 + 4\nu_2^2 + 7\nu_1\nu_3 - \nu_4).$$

The phenomenological expansion coefficients A and B can be related to the band parameters and the effective exchange parameter I, or to the spontaneous magnetization $M_0 = M(0, 0)$ and the initial susceptibility χ_0:

$$A(T) = -\frac{1}{2\chi_0}\left(1 - \frac{T^2}{T_C^2}\right) = \frac{1 - IN(E_F)}{N_g N(E_F) \mu_B^2} \left(1 + \frac{\alpha T^2}{1 - IN(E_F)} + \cdots\right), \tag{14.24}$$

$$B(T) = \frac{3\nu_1^2 - \nu_2}{6N(E_F)^3 N_g^3 \mu_B^4} \left(1 + \frac{\beta T^2}{3\nu_1^2 - \nu_2} + \cdots\right) \simeq \frac{1}{2M_0^2 \chi_0}. \tag{14.25}$$

From eq. (14.23) one obtains a quadratic temperature dependence of the reciprocal susceptibility and a linear dependence of M^2 versus H/M over a large temperature region (so-called Arrott plots). Mathon discussed the concentration dependence of $M(0, 0)$, T_C and χ_0 by using the Landau theory for weak ferromagnets in the critical region. There exists a close analogy between what happens for a fixed concentration when the temperature is varied and what happens for a fixed temperature when the concentration is varied: $A(T, x) =$

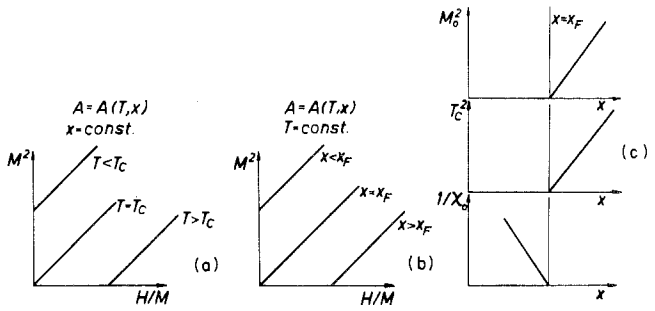

Fig. 14.68. Predictions of weak ferromagnetism theory for normal pressures (a) and (b): the square of the magnetization $M(H, T)$ is a linear function of $H/M(H, T)$ for different temperatures and constant concentration (a), or constant temperature and different concentrations (b). (Arrott plots, a and b). (c): Variation of the square of the spontaneous magnetization $[M(0, 0) = M_0]$, T_c^2 and the reciprocal susceptibility as a function of concentration (Mathon plots).

$a(T) - (x_F(T) - x)$ where x_F is the critical concentration. The results at constant pressure are summarized in fig. 14.68.

3.1.5. *Pressure effects*

A powerful tool for discussing magnetic properties is to investigate pressure and magnetovolume effects. Pressure and magnetovolume effects are taken into account by adding $\frac{1}{2}\kappa\omega^2 - C'\omega M(H, T)$ to the ΔF expansion (eq. (14.22)) with ω = relative volume change, κ = compressibility and C' = magneto-elastic coupling constant. Minimizing ΔF with respect to ω leads to the pressure dependence of T_C. For a more detailed discussion see some recent reviews on this topic: Wohlfarth (1973), Alberts et al. (1974), Wohlfarth (1974), Franse (1977). In the itinerant electron model, following Wohlfarth (1969) and Edwards and Bartel (1972) the pressure dependence of T_C can be written: $\partial T_C/\partial p = \frac{5}{3}\kappa T_C - \alpha/T_C$. α is related to band parameters and the bare and effective exchange-parameters (see Kanamori, 1963). Whereas for strong ferromagnets one finds small and positive pressure dependences of the Curie temperature, the pressure dependence in the limit of weak itinerant ferromagnets is large and negative. This means for the latter the second term is dominant, $\partial T_C/\partial p = -\alpha/T_C$. On this basis the pressure dependences of several R–Co, R–Fe and R–Ni compounds are discussed and successfully explained by Brouha and Buschow (1973, 1975b) and Brouha et al. (1974).

The negative pressure derivative $(\partial T_C/\partial p)$ of RCo_2 compounds (Voiron and Bloch, 1971) is related dominantly to the pressure dependence of the enhanced susceptibility. Here the pressure dependence of the enhanced susceptibility is used to calculate, within the exchange enhanced model (Bloch and Lemaire, 1970), the pressure dependence of T_C, which agrees well with the experimental data (Voiron et al., 1973). Jaakkola et al. (1975) discussed qualitatively the

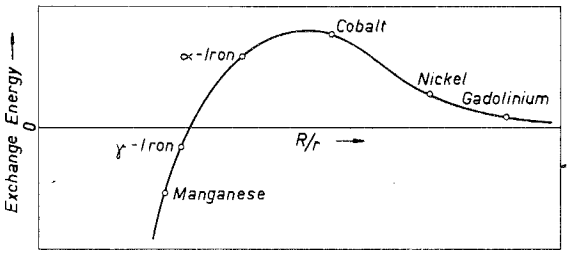

Fig. 14.69. The Bethe–Slater curve relating exchange energy to the distance R between atomic centres. r is the radius of the 3d shell (Goodenough, 1963).

pressure dependence of R_2Fe_{17} compounds not only on the basis of the itinerant electron model but also in terms of the Bethe-Slater curve for localized moments (see fig. 14.69).

3.1.6. *Localized and itinerant models*

The application of a pure itinerant model (such as the Stoner–Wohlfarth or the Fermi-liquid model) is limited in R–3d compounds. Such models, if they are valid, are confined to systems where R possesses no moment, e.g. Y, Lu, Zr.

Various attempts (Stearns, 1973; Schurer et al., 1973) were made to combine an itinerant and a localized model (see Sakoh and Edwards, 1975). The model hamiltonian which describes itinerant electrons and localized moments, following Sakoh and Edwards, is

$$\mathcal{H} = \sum_{k\sigma} \epsilon_k n_{k\sigma} + I_{\text{eff}} \sum_i n_{i\uparrow} n_{i\downarrow} - 2\mathcal{J}_{\text{eff}} \sum \boldsymbol{\sigma}(i)\boldsymbol{S}_i - 2\mathcal{J} \sum_{i<j} \sum \boldsymbol{S}_i \cdot \boldsymbol{S}_j. \tag{14.26}$$

The first two terms are of the Hubbard type (Hubbard, 1963, 1964), where the bare interaction (I) between itinerant electrons is reduced by correlation effects to I_{eff} (Kanamori, 1963). The interaction between a localized spin $\boldsymbol{S}_i$ and the itinerant spin density $\boldsymbol{\sigma}(i)$ is described by an effective Hund's rule interaction $\mathcal{J}_{\text{eff}}$. The last term includes also a superexchange interaction between the localized moments. Applying molecular field theory to this hamiltonian gives

$$E = -n_{\text{ii}}M_{\text{i}}^2 - n_{\text{il}}M_{\text{i}}M_{\text{l}} - n_{\text{ll}}M_{\text{l}}^2$$

where M_{l} is the localized magnetization described in terms of Brillouin functions. The itinerant magnetization M_{i} is related to the results of the Stoner–Wohlfarth theory involving band parameters. A similar model combining itinerant and localized moments was used by Bloch et al. (1975) to discuss the first order and second order transitions in RCo_2 compounds.

Recently spin fluctuations (Moriya and Kawabata, 1973a,b) which are characterized by electron correlations turned out to be important for describing the susceptibility, electrical-, thermal- and magneto-resistivities of itinerant ferromagnets. Moriya (1976) pointed out that the thermodynamic properties of itinerant ferro- and antiferromagnets are mainly governed by the exchange enhanced spin fluctuation modes. At present the results of the spin fluctuation theory can account for the Curie–Weiss susceptibility without localized mo-

ments. The results for the electrical resistivity (Ueda and Moriya, 1975) can be summarized as follows: $\rho \propto T^2$ dependence at low temperatures with a large coefficient of T^2; $\rho \propto T^{5/3}$ dependence near and above T_C, the change of slope at T_C is small; $\rho \propto T^1$ or T^0 dependence at high temperatures.

Sakoh and Shimizu (1976) discussed the electronic structure and magnetic properties of a half-filled Hubbard band in the paramagnetic state with and without localized moments by the functional integral method. The result is that the character of the well localized spins caused by strong correlation at $T = 0$ K fades out and is gradually replaced by the character of itinerant electrons at T_C. In the molecular field approximation discussed above (Sakoh and Edwards, 1975) the localized spins are never destroyed at any temperature. Therefore the treatment of localized spins which are rigid at all temperatures may be improved by the recent results of Sakoh and Shimizu.

The formation of localized moments within an itinerant electron model was suggested by Friedel (1958, 1962). Various related models, such as the Anderson and Wolff models (Anderson, 1961; Schrieffer and Wolff, 1966) derived from the impurity problem were recently reviewed theoretically and experimentally in Magnetism V (Rado and Suhl, 1973). The deviations from the Slater–Pauling curve, which have already been mentioned, could be explained by means of the Friedel model with the concept of virtual bound states. This may be one way to understand the complex variation of the transition metal moments within the pseudobinary R–($3d_1$, $3d_2$) systems. The assumption is that the repulsive potential, as a result of a charge perturbation, is strong enough to push virtual bound d-states through the Fermi level. Consequently the magnetic moment is lowered, which is a general feature of the deviations from the Slater–Pauling curve. A more detailed extension of this idea was made by Gomes (1966) and Gomes and Campbell (1967).

The treatment of localized moments in the theory of band magnetism by Lederer and Blandin (1966) was discussed by Buschow (1971) with respect to R–3d compounds. This model is an extension of the model of Friedel et al. (1961) and considers the energetics of creating a localized moment around an individual atom using a Stoner type of criterion $N(E_F)\ I \geqslant 1$ and also considers the interaction between such moments. This interaction is oscillatory and can give rise to both antiferromagnetic and ferromagnetic couplings. Such a model may be applicable to account for the helical spin structures observed in R_2Fe_{17} compounds (R = Lu, Ce) for example and the lowering of the ordering temperatures with increasing Fe concentration in R–Fe systems (subsect. 3.3).

3.1.7. *Model of Bloch and Lemaire*

Bloch and Lemaire (1970) developed a model for describing two-component alloys in which one component A has a permanent localized moment and the other B an exchange enhanced paramagnetic susceptibility. This B component can possess an exchange induced moment of itinerant nature induced by interaction with the localized A moment. In the paramagnetic temperature range the respective components are assumed to have magnetizations M_A and M_B in

the presence of an applied field H

$$M_A = (C_A/T)(H + n_{AA}M_A + n_{AB}M_B), \qquad M_B = \chi_{B,0}(H + n_{BB}M_B + n_{AB}M_A),$$

where $\chi_{B,0}$ is the paramagnetic susceptibility of the B component without enhancement. n_{AA}, n_{BB} and n_{AB} are the molecular field coefficients for sublattices A and B. The exchange enhanced susceptibility of B is given by $\chi_y = \chi_{B,0}/(1 - n_{BB}\chi_{B,0})$. Expressions are derived for the total susceptibility in the paramagnetic temperature range, the Curie temperature and the magnetization M_B in the ordered range just below T_C, where M_B is proportional to M_A. The reciprocal susceptibility in the paramagnetic temperature range shows no linear Curie–Weiss behaviour. However by fitting theoretical curves to experimental data the interaction parameters can be deduced. Bloch and Lemaire performed this for the RCo_2 compounds where such a model is thought to be particularly applicable, and obtained χ_y values in agreement with the room temperature susceptibilities of YCo_2 and others where R is nonmagnetic. Values of J_{AB} and J_{AA} were deduced from n_{AB} and n_{AA} where $J_{AB} = g_J n_{AB}/(g_J - 1)$ and $J_{AA} = (g_J)^2 n_{AA}/2(g_J - 1)^2$. J_{AA} and J_{AB} were positive (+60) and negative (−150) respectively, as expected for ferrimagnets and were approximately constant for all lanthanides.

The Néel model for ferrimagnets also gives a non-linear $(1/\chi, T)$ behaviour above T_C for localized A and B moments. This behaviour becomes linear at high temperatures. Burzo (1972b) presented an interpretation, different from the Bloch–Lemaire model, in which he analysed the paramagnetic data according to this Néel model where the paramagnetic susceptibility is expressed by

$$\frac{1}{\chi} = \frac{1}{\chi_0'} + \frac{T}{C'} - \frac{\sigma'}{T - \theta'}.$$

From the high temperature asymptote he deduced C' and from this evaluated the p_{eff} value for the B-moments.

Both models have been applied to RCo_2. The B-moments owe their existence in the ordered temperature range to being induced by the magnetized A-sublattice. It is then improbable that these B-moments can still exist in the paramagnetic range where the A-sublattice shows no magnetic order. As will be seen in subsection 3.3 the Néel model was applied to all the intermetallic R–Fe, R–Co, and R–Ni stoichiometries and 3d moments were reported in the paramagnetic range whenever 3d moments were found in the ordered range. Definite acceptance of these localized paramagnetic 3d moments in the absence of a field, especially for the exchange induced systems, must await further evidence from neutron diffraction experiments. A polarized neutron study by Gignoux et al. (1976) of $TmCo_2$ has revealed the absence of spontaneous localized Co moments in the paramagnetic range. A similar result was obtained for $HoCo_2$ (Gignoux et al., 1977a). The Bloch–Lemaire model has the advantage that it gives a consistent picture not only for the ordered but also for the paramagnetic temperature ranges.

3.2. *Structures of binary rare earth-3d transition metal compounds*

The crystal structures of almost all of the compounds with a B-moment can be derived from the hexagonal $CaCu_5$ structure. This situation is rather similar to that for some of the compounds with no B-moment for which the trigonal prism was regarded as a building block for the crystal structures of low symmetry. The following is an attempt, based upon the work of Schubert (1964), to collect most of the intermetallic compounds together and relate them to each other as far as possible.

The crystal structures of the binary rare earth-3d transition metal compounds are typical for all rare earth-transition metal compounds. We concentrate on the 3d transition metals Mn, Fe, Co and Ni because, of all 3d metals these four metals are the only ones which form intermetallic compounds with the rare earth metals. The 3d transition metals Ti, V, Cr do not form a single intermetallic compound with any of the rare earth metals. The crystal chemistry of the rare earth-intermetallic compounds is discussed in the foregoing chapter (13) by Iandelli and Palenzona. Here we shall discuss the specifics of the rare earth-transition intermetallic compounds, as far as their crystal structure is important for the understanding of the magnetic properties.

As can be seen from fig. 14.70, starting from the cubic close packed or hexagonal close packed structures, the systematics of the rare earth–5d transition metal compounds, as far as their crystal structure is concerned, can be understood. If in the cubic close packed structure of a 3d metal B two specific B atoms are replaced by an R-atom, a cubic RB_2 structure is formed ($MgCu_2$-type, so-called double replacement). A different stacking sequence results in the hexagonal $MgZn_2$ structure which is formed with some RB_2 compounds (RMn_2 where R = Sc, Pr, Nd, Sm, Er, Tm and Lu). Practically all other RB_2 compounds (B = Fe, Co, Ni) crystallize in the cubic $MgCu_2$ type.

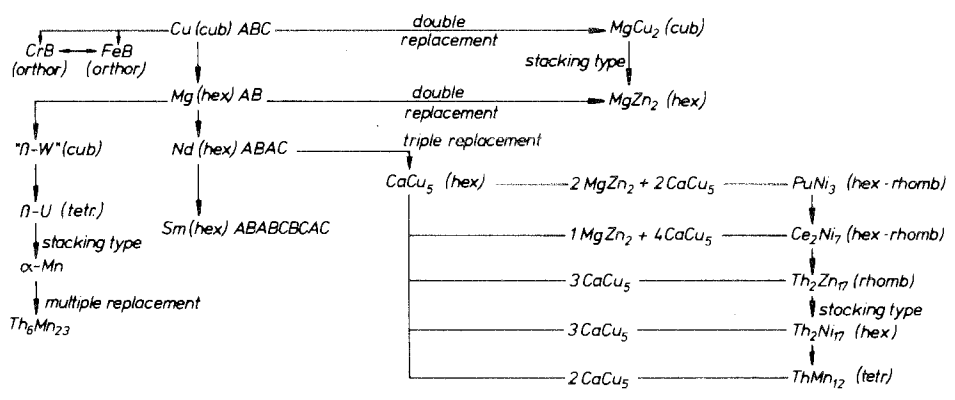

Fig. 14.70. The relation between the structures of the various R–3d metal compounds (Kirchmayr, 1969b).

The ratio of the radii of the atoms in Laves compounds is nearly $r_R/r_B = \sqrt{\frac{3}{2}} = 1.225$. The ratios of atomic radii (Teatum et al., 1960) can be determined from the elemental lattice spacing. In reality this value ranges from 1.32 ($LuMn_2$) to 1.15 ($LaNi_2$).

The RB_2 compounds are, in the R–Mn and R–Fe systems, the compounds with the highest R-content. This is probably due to the fact that without a total rearrangement of the 3d basis lattice two 3d atoms can be replaced by an R-atom. However, if R-richer compounds were to be formed, either the majority of the 3d atoms of an element must be replaced by R-atoms or in an R basis lattice few 3d atoms must be fitted in. This however would result in a deviation from the principal of close packed structures. The result would obviously be a large increase of the Gibbs free energy G. Therefore these structures and compounds are not stable compared to the neighbouring structures or neighbouring compounds.

If in a hexagonal close packed 3d-metal basis lattice (with doubled lattice spacing in the basal plane) instead of three 3d atoms one R-atom is fitted in, then the structure of the RB_5 compounds is formed ($CaCu_5$-type, D^1_{6h}–P6/mmm). This structure is observed in all R–(Ni, Co) systems. It can be regarded as a series of layers which consist only of 3d atoms and other layers in which a replacement of 3d atoms by R atoms has taken place.

Starting from the very important $CaCu_5$ structure now the majority of the B-rich R–3d metal structures can be deduced. When two $CaCu_5$ layers and two $MgZn_2$ layers (one however a little buckled) are put above each other, the $PuNi_3$ structure is formed. This structure is observed in R compounds with Fe, Ni, Co. The R_2Co_7 compounds can be built up from nine $CaCu_5$ cells stacked one above the other (Bertaut et al., 1965). In a similar manner by the combination of $CaCu_5$ cells also the two very important structures of Th_2Zn_{17} and Th_2Ni_{17} can be built up. Th_2Ni_{17} is formed by a layering of three $CaCu_5$ basal planes, but with a doubled c-axis. Therefore a equals $\sqrt{3}a_{CaCu_5}$ and c equals $2c_{CaCu_5}$. Th_2Zn_{17} has the same basic structure, however in this case c equals $3c_{CaCu_5}$ (Schubert, 1964; Ostertag and Strnat, 1966). These latter structures are observed in many systems of R metals with Fe, Ni and Co. Usually these compounds are the richest compounds with respect to the 3d metals in all R(Fe, Co, Ni) systems. The structures of the compounds with the composition R_2B_7 can be formed in an analogous manner. See Ray (1966).

Only one single stoichiometry in all R–3d metal compounds has a higher 3d atom content. This forms for the RMn_{12} compounds which crystallize in a so-called $ThMn_{12}$ type (Florio et al., 1952). Also this structure type can be deduced from the $CaCu_5$ type by a combination of two basis nets of the $CaCu_5$ structure. The compounds with the $ThMn_{12}$ structure are the representatives of all R–Mn compounds which are richest in Mn and are also observed in many ternary compounds of the R-metals (e.g. Al) (Zarechnuyuk, 1966; Zarechnuyuk and Kripyakevich, 1962; Zarechnuyuk et al., 1967). In the Lu–Mn system $LuMn_5$ is the phase richest in Mn. This phase can be deduced from the $CaCu_5$ type.

All of these structures of the rare earth–3d metal compounds can therefore be

deduced from close packed structures and are therefore very intimately connected with each other.

Two other R–3d metal stoichiometries (if one does not consider some Sc compounds, which because of the smallness of the Sc atom have other structures), namely the structure type Th_6Mn_{23} as well as FeB and CrB, have not been treated up till now in this subsection.

Compounds of the type Th_6Mn_{23} have been observed in the systems R–Mn and R–Fe as well as in many ternary compounds (Kripyakevich and Frankevich, 1965; Kirchmayr, 1967). These compounds are isotypic with the frequently observed phase of the type $Mg_6Si_7Cu_{16}$ (Bergman and Waugh, 1953, 1956). This structure consists of a cubic giant cell which contains 116 atoms (Wang et al., 1964). This structure can also be formed by a multiple replacement of 3d atoms, in this case starting from an α-Mn cell. The structures of α-Mn and Th_6Mn_{23} both contain a so-called "tetrahedral star", i.e. a tetrahedral group of Mn atoms. The α-Mn structure can be deduced from the β-U structure and these from the so-called β-W structure, which in turn can be deduced from the Mg type. It is clear, therefore, that also the Th_6Mn_{23} structure must be considered as a close packed structure. In this structure the R-atoms possess one crystallographically equivalent atom position, while four groups of 3d metals possess four different crystallographic atomic positions.

Finally, in the R–Ni system the compounds of the type CrB and FeB are observed. These structures can be transformed into each other by changing the stacking sequence (Hohnke and Parthé, 1966). These structures can also be deduced from the cubic close packed structure. Only in the R–Co system are the hexagonally ($P6_3/m$) crystallizing R_4Co_3 compounds of the so-called Ho_4Co_3 type observed (Berthet-Colominas et al., 1968; Lemaire and Schweizer, 1967). In some specific R–Co and many R–Ni systems the orthorhombic structure of the type Al_3Ni is observed.

A comparison of the just mentioned compounds shows that all these compounds are related to each other and in a systematic combination of crystal structures (Schubert, 1964) are positioned nearly in the same category. Therefore all these structures are close packed in a typical metallic structure. Since in a simple minded view the magnetic properties depend on the atomic distances, it is important to know the typical distances between the R and 3d atoms. The smallest distances are always between two 3d metals. This is an indication that the magnetic properties of these compounds are dominated by the 3d-metals and not by the R-metals. This is in good agreement for instance with the high Curie temperatures of the R-transition metal compounds, which are comparable to the Curie points of the 3d metals themselves.

Naturally the crystal structures, the intermetallic distances, and also the angles and symmetry properties of the position of a single atom are essential for the explanation of the magnetic properties including the explanation of the Mössbauer data. The correlations between the crystal structures and the magnetic properties will however be discussed in detail in connection with the magnetic properties.

3.3. *General magnetic considerations*

Before dwelling on the details of the magnetic properties of the intermetallics with non-zero B-moment we shall first survey the general magnetic properties. The ordering temperatures of all the systems of relevance are shown in figs. 14.71–14.73. These ordering temperatures correspond almost exclusively to the onset of magnetic order in which all 3d-moments are ferromagnetically coupled to one another. In addition the R-moments are also coupled parallel to one another. The coupling between the R- and B-moments is such that the spins in all cases are antiparallel. This results in ferromagnetic coupling for the light and ferrimagnetic coupling for the heavy lanthanides. Here we can note a very striking difference between the compounds with zero B-moment and those with non-zero B-moment. In the former, as we have seen in section 2, the R-moments can show not only parallel but also antiparallel and non-collinear coupling. In the latter only parallel coupling between R-moments is observed, apart from a couple of exceptions which need not disturb us at this stage. The difference must be due to the influence of the B-moment. The fact that the B-moments always couple parallel to each other points very suggestively to their itinerant character relative to the R-moments. In addition it is our opinion that the R-moments, if left to themselves, would prefer in a large percentage of the cases to adopt an antiferromagnetic ordering since R–R couplings are of the indirect type. It appears therefore that the presence of 3d-moments, even in small quantities, suppresses these antiferromagnetic cases. We get here the impression that the 3d–3d couplings and R–3d couplings rule the lattice and that the R-moments

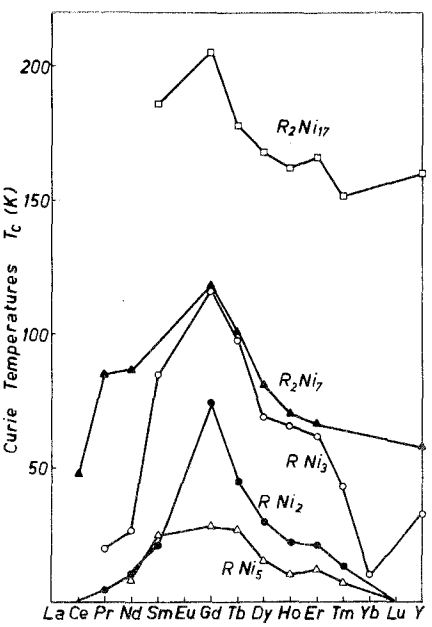

Fig. 14.71. The Curie temperatures of R–Ni compounds.

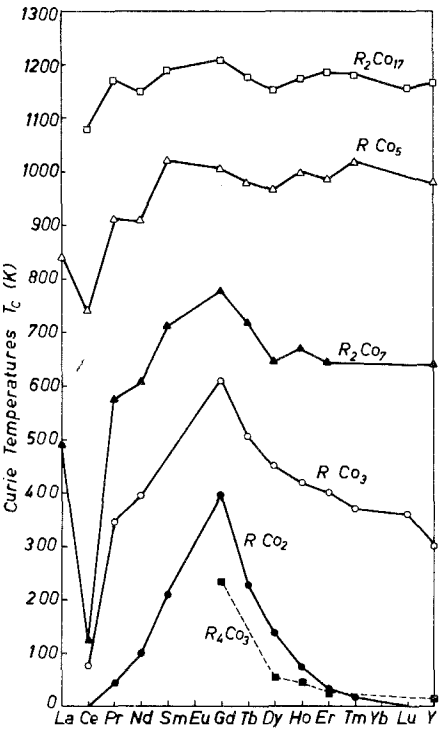

Fig. 14.72. The Curie temperatures of R–Co compounds.

must orient themselves with one another according to these even if the R–R couplings alone tend to give rise to another type of coupling.

The fact that the 3d–3d couplings are extremely strong compared to R–R couplings also suggests that a considerable degree of itineracy must be present in the 3d-electrons. This follows from the fact that exchange requires overlap of wave functions which then implies some degree of itineracy. Since this concept

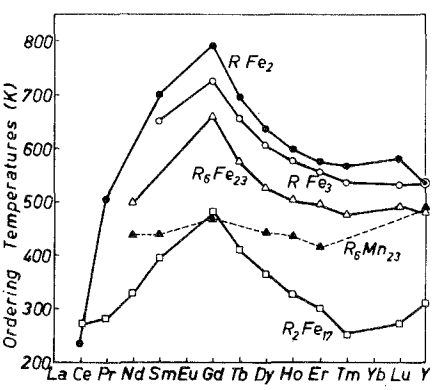

Fig. 14.73. The ordering temperatures of R–Fe compounds.

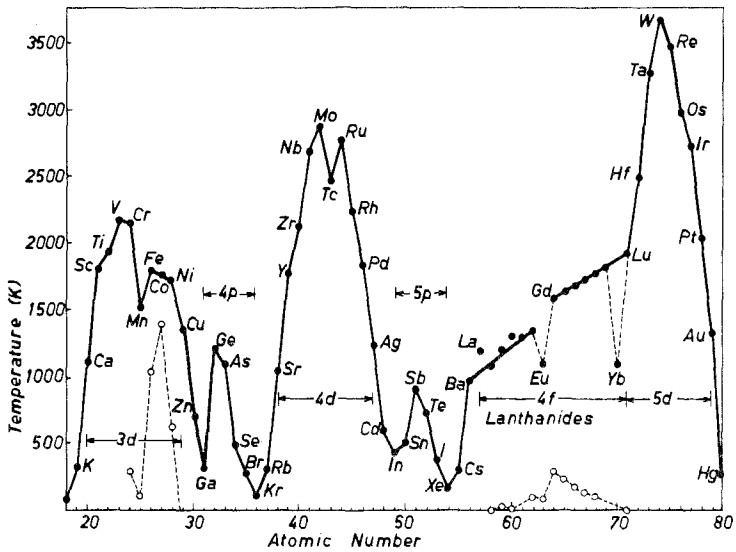

Fig. 14.74. The melting points of the elements as a function of atomic number. Shown also are the magnetic ordering temperatures of the 3d and 4f elements (open circles).

of itineracy is rather important in the R–3d intermetallics we mention another consideration supporting the opinion that the 3d-electrons are itinerant. Figure 14.74 shows the melting points of the elements as a function of atomic number. We see that the 3d, 4d and 5d series show high melting points which peak in the middle of each transition series. It is clear therefore that the d-electrons play a role in the cohesion which in turn implies a certain degree of itineracy. This is also seen to be the case in the 4p and 5p series. The lanthanide series however does not show this effect and this implies that the 4f-electrons do not normally play any significant role in the cohesion of the lanthanides (see however, ch. 2 section 7), and that they are well-localized. The ratio of the ordering temperatures to magnetic moment T_C/μ can be taken as a rough measure of the itineracy of the magnetic electrons. In the case of Co for example we have a Curie temperature as high as 1390 K with a small moment of 1.7 μ_B, whereas the relatively large moment of 7 μ_B for Gd corresponds to a Curie temperature of only 300 K. This consideration, applied to Ni, Co and Fe supports the general opinion that Fe is the least itinerant of the three.

Compared with the compounds with no B-moment the R–3d compounds are simpler with respect to spin structures, only ferrimagnetic coupling being present in the vast majority of cases, whereas the compounds with no B-moment exhibit an elaborate variety of spin structures as seen in section 2. On the other hand, however, the R–3d intermetallics possess three types of magnetic coupling (R–R, R–3d, 3d–3d) which are more difficult to describe theoretically than the R–R interactions in compounds where 3d-moments are absent. In addition magneto-crystalline anisotropy of the 3d-moments is extremely difficult to treat

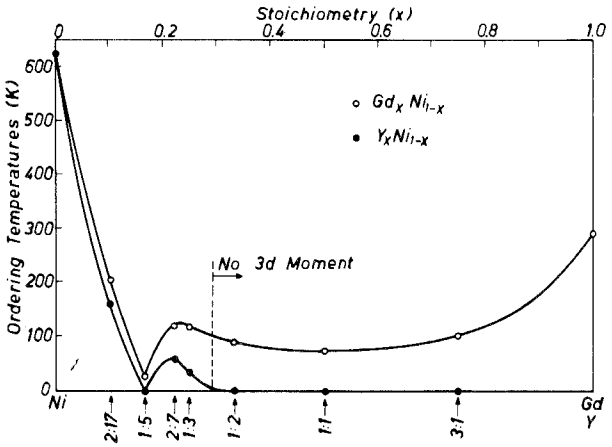

Fig. 14.75. The ordering temperatures of the Y–Ni and Gd–Ni systems.

theoretically where strong quenching is present. Referring to figs. 14.71, 14.72 and 14.73 we note an interesting difference between the Fe compounds and the Co and Ni compounds. The Co and Ni compounds show a general increase in ordering temperature for increasing 3d-element concentration. This is the case in Y–Ni and Y–Co compounds as may be expected, and also in the Gd–3d and other R–3d compounds. However the R–Fe compounds show, even for Y–Fe, a decrease in ordering temperature as the Fe concentration increases. This can be considered as a symptom of the more localized nature of Fe-moments compared with Co and Ni-moments, as explained later in this section.

The comparison of the R–B systems with Fe, Co and Ni can be made most meaningfully by considering the ordering temperatures and 3d moments as a function of stoichiometry for Y on the one hand and Gd on the other. The ordering temperatures are shown in figs. 14.75–77. From these curves the above

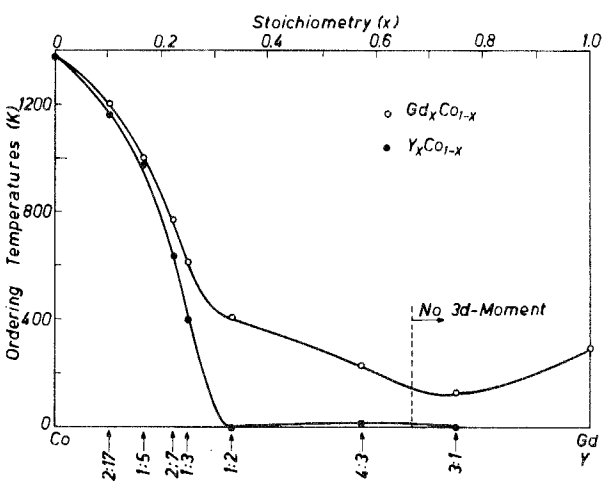

Fig. 14.76. The ordering temperatures of the Y–Co and Gd–Co systems.

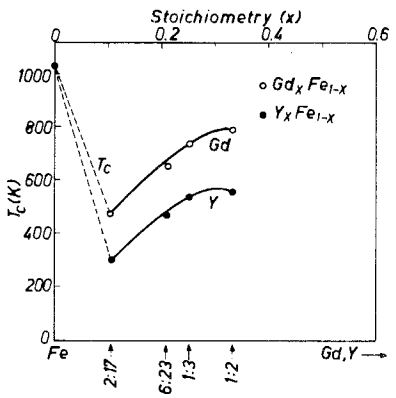

Fig. 14.77. The Curie temperatures of the Y–Fe and Gd–Fe systems.

mentioned different behaviour of Fe is evident. The Co and Ni systems show a general decrease in the ordering temperatures on introducing both Gd and Y. The Y–Ni system shows a decrease on introducing Y up to the concentration for YNi_5 which does not order. The reappearance of ordering for higher Y contents may be due to the details of the relatively complex crystal structures or may be explainable in terms of the rigid band model assuming a minimum in the density of states. The possible causes of this reappearance of ordering are discussed in subsection 4.2. YNi_2 is a Pauli paramagnet and higher Y contents yield no further ordering. The Gd–Ni system reflects the same type of variation, except that the ordering temperatures are higher due to interactions with the Gd moments. For the Gd-rich compounds the ordering temperatures rise again, even though no 3d moment is present, due to the closer proximity of the Gd ions to one another. Other factors, due to changes of structure for example, of course also influence the ordering temperatures which may be responsible for $GdNi_2$ not having a lower T_C value than GdNi although the former is magnetically more dilute. Ni is non-magnetic in both compounds (subsections 2.4 and 2.6). Ni is also non-magnetic in $GdNi_5$, the low T_C value being due to Gd–Gd interactions. To the right of the vertical dashed line in fig. 14.75 no 3d moments are present in any R–Ni compounds.

The Y–Co system shows a decrease of T_C on introducing Y up to the composition YCo_2 which is a Pauli paramagnet. The ordering however reappears for Y_4Co_3 which is perhaps analogous to the reappearance in the Y–Ni system. This may be due to structural peculiarities. The R_4Co_3 compounds (Berthet-Colominas et al., 1968) possess an atomic site (2b site in hexagonal Ho_4Co_3 structure) which is only partially and randomly occupied by Co. The distance between the 2b sites is so short that the mean Co–Co distance would be too small if they were all occupied. This is the only system showing a non-zero B-moment whose structure can be derived from trigonal prisms (as described in subsection 2.6). However the anomalously short distances between the 2b sites may be responsible for the spontaneous appearance of a Co moment in Y_4Co_3, which is augmented in other R_4Co_3 with magnetic R. It may therefore be that

only some of the Co sites in R_4Co_3 compounds have a moment. YCo_2 as seen in fig. 14.76 does not order. However $GdCo_2$ has an exceptionally high T_C value which is due to an induced 3d moment. The vertical dashed line in fig. 14.76 separates the regions where a 3d moment exists from that where no 3d moments are found. It is to be noted that this line is situated more to the R-rich end of the R–Co system than the corresponding line in the R–Ni system. The filling of the 3d band by electrons from R^{3+} must occur for higher R concentrations in the R–Co system since Co has, of itself, less 3d electrons than Ni.

The R–Fe system (fig. 14.77) shows the anomalous T_C increase as the Fe concentration decreases even for the Y–Fe system. As we shall see in the following sections Fe tends to show more localized character than Ni and Co. The application of the Friedel model (subsection 3.1.6), with couplings between semi-localized 3d-moments within a band, could in principle account for the increased strength of exchange on diluting Fe with Y since the 3d polarization around an impurity centre oscillates in space.

The ordered 3d-moment can be obtained by assuming ferro- or ferrimagnetic coupling between the R and 3d sublattices and in the case of Gd–B compounds it can be calculated from the saturation moment by assuming that a Gd ion contributes 7 μ_B. These 3d moments are displayed in figs. 14.78 and 14.79 for the Y–B and Gd–B systems. Figure 14.79 shows also the 3d moments in the paramagnetic range deduced by Burzo (1973b) assuming the Néel model for localized moments. All these 3d moments are the average values of the 3d moments on the various inequivalent crystallographic sites. The individual moments on the different sites can differ considerably from one another especially in the sensitive 1 : 3 and 2 : 7 stoichiometries of the R–Co systems as shown in fig. 14.101 of subsection 3.7. In connection with the average ordered and paramagnetic moments Burzo (1970, 1973b) has summed up the results and pointed out the constant ratio M_p/M_s found between the effective moment M_p in the paramagnetic range estimated from the Curie constant assuming localized 3d moments and the 3d moment M_s obtained from saturation measurements in the ordered range. In the Gd–Fe, Y–Fe and Gd–Co systems this ratio is fixed at the

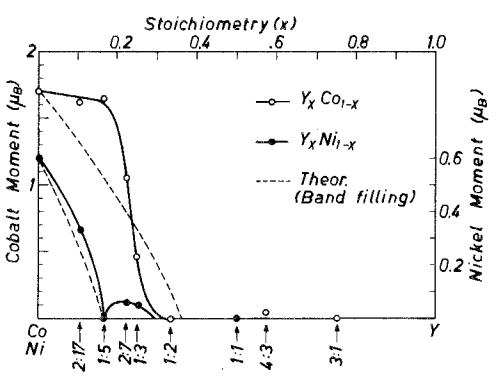

Fig. 14.78. The mean 3d-moment in the Y–Ni and Y–Co systems. The theoretical dashed lines were calculated assuming that all valence electrons from Y^{3+} populate the 3d-band and that one spin sub-band is full.

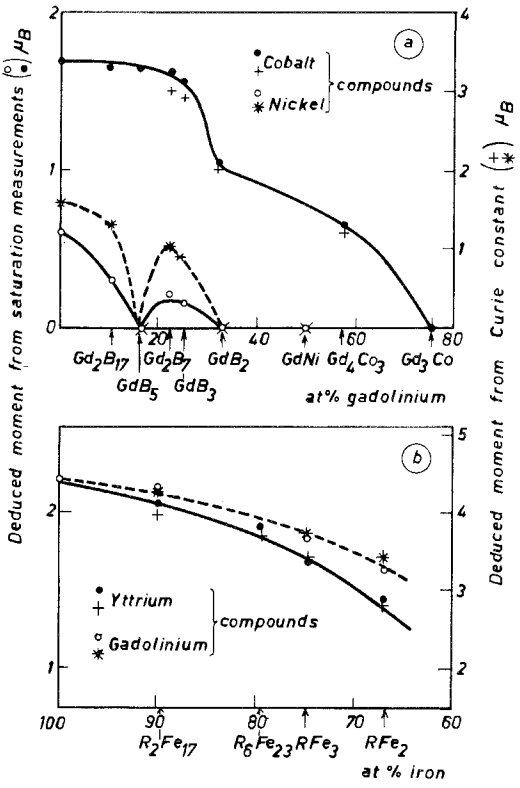

Fig. 14.79. The dependence of the mean 3d-moment of Fe, Co and Ni upon Gd or Y content (Burzo, 1973b).

value 2. For the Gd–Ni system the ratio is somewhat variable and can be as large as 5 but the two types of measurement reveal the same form of variation as a function of stoichiometry. It should be pointed out that a departure of the ratio from unity is anyway to be expected since we are comparing (in the notation for localized moments) gJ with $g\sqrt{J(J+1)}$, where g is expected to be of the order of 2 for quenched 3d ions, in which case $J \simeq S$. The weaker the 3d moment the larger will be the discrepancy between M_p and M_s, which may explain the large M_p/M_s ratios for the R–Ni compounds. We notice here that, consistent with the remarks made above in connection with the ordering temperatures, the 3d moments disappear between Gd_4Co_3 and Gd_3Co in the Gd–Co system and between $GdNi_3$ and $GdNi_2$ in the Gd–Ni system. $GdNi_5$ shows no 3d moment. If it is assumed that all three valence electrons from Y^{3+} in the Y–Ni and Y–Co systems enter the 3d band and that pure Ni and pure Co have holes only in one spin sub-band then the filling of the 3d band is predicted to occur in YNi_5 and just to the Y-rich side of YCo_2 respectively (fig. 14.78). The reappearance of a 3d moment is however not normally expected. The compounds $GdCo_2$, Gd_4Co_3, Gd_2Ni_7 and $GdNi_3$ appear to have a large part of their 3d moments induced by Gd, when compared with the corresponding systems with Y. These are in all

cases ferrimagnetically coupled to the Gd moments. These induced moments in the ordered range appear to persist even into the paramagnetic temperature range (Burzo and Laforest, 1972). This is hard to understand and it is likely that the Néel model is not applicable here. Burzo (1974) concludes that in the Gd–Co and Gd–Fe systems the 3d moments present both band and localized behaviour which may be described within the Friedel model. The Fe moments in R–Fe systems do not show any anomalous behaviour corresponding to the T_C variations, the Fe moment decreasing slowly and monotonically with increasing R concentration.

The magnetic properties of the various rare earth transition metal compounds were discussed by Gomes and Guimarães (1974) who proposed a model for the electrónic structure of these compounds. In this model the s-electrons are spread throughout the crystal, the d-states being mostly localized on the transition metal sites. However the degree of localization varies from 3d to 4d and 5d. Two cases are discussed: (a) Magnetization is driven by the localized 4f moments (e.g. $GdCo_2$). The density of d electrons on the R sites is negligible. It is assumed that the fields H_s and H_d act on the s and d band respectively. H_s corresponds to the exchange field induced by the 4f spin and $H_d = 0$ here. The paramagnetic susceptibility is derived (see also Bloch and Lemaire, 1970, who use a single band model). An expression is found which describes g shifts measured in R–Co systems. A negative sign is obtained, in agreement with Burzo (1972b). (b) Magnetism is sustained by the d band. This is found in the R–Fe system and R–Co system for more than 67% Co where the Stoner criterion is satisfied by the d band. The magnetization of the d states is transferred via H_{sd} to the s band and then coupled through J_{sf} to the 4f spin. Since no band calculations are available calculations are performed assuming a model density of states consisting of two overlapping parabolae.

It will have been noticed, when comparing fig. 14.75 with fig. 14.76, that the 4 : 3 stoichiometry present in the R–Co systems is absent in the R–Ni systems where in its place a 1 : 1 stoichiometry exists which is absent in the R–Co systems. It was pointed out by Poldy and Taylor (1973b) that this may be symptomatic of a correlation between the presence of 3d moments and the stability of a given structure. The magnetic moments were considered to reflect whether or not the 3d band is full since an unfilled band would split, especially in the presence of Gd, and give rise to a 3d moment opposing the Gd moment. Since pure Gd has a moment of 7.55 μ_B (in excess of the gJ value, due to conduction electron polarization) the absence of a 3d moment is not necessarily proved when the saturation moment in a compound is 7 μ_B per Gd. Rather, the appearance of a 3d moment could well be marked by a departure of the saturation moment from some value in excess of gJ. As seen in fig. 14.80 it appears that, in the Gd–Ni system a 3d moment is absent for GdNi and present in Gd_4Co_3 as has already been discussed. The Gd_3B stoichiometry, however, forms for both Gd–Co and Gd–Ni systems for which we have a full 3d band. However on lowering the Fermi level in Gd_3Co as described in subsection 2.6 the top of the 3d band is very soon reached which is heralded by a structural

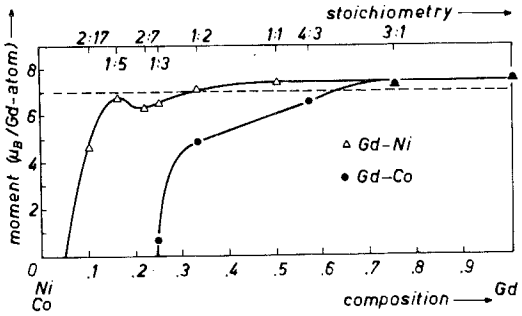

Fig. 14.80. Moment per $GdB_{m/n}$ unit for the Gd_nNi_m and Gd_nCo_m systems (Poldy and Taylor, 1973b).

break-down. It appears that the structure of the R_4Co_3 compounds is stabilized by the Fermi level lying below the top of the 3d band and the structures of GdNi, Gd_3Ni and Gd_3Co are stabilized by the Fermi level lying above the top of the 3d band. A structural stability rule was deduced for the influence of 3d states upon structural stability. This rule states that, if a stable phase A exists with E_F below the top of the 3d band then raising E_F will probably result in some other phase B (or mixture of phases) being more stable when E_F encounters the top of the 3d band. This is reasonable since the further introduction of electrons will result in a more rapid rise of E_F (per electron added) above the 3d band where the density of states is lower. Such a large E_F rise will not help to stabilize phase A and the probability becomes larger, that some other phase (or mixture of phases) may have a lower energy. An exactly complementary rule and energy argument must of course exist for any stable phase B which is stable with E_F above the 3d band. Such a phase will probably become unstable upon lowering the Fermi energy. This rule has the advantage that it cannot be disproved by the cases where it appears not to be valid! It predicts only when a phase has the highest probability of becoming unstable. Of course the choice of which structures are stable is a problem for which no general solution exists. The main energy term is associated with s and p conduction electrons and the difference in energy between any two phases can be small. In such cases small factors such as the one described above can play a decisive role in determining which of various phases is to be stable.

At the beginning of this section we pointed out the remarkable simplicity of the R–B compounds (with magnetic B partner) compared with the R–B (B-moment zero), as far as the spin structures are concerned, the former showing always a parallel alignment within each of the two sublattices. This observation was considered to be a sign of the relatively itinerant nature of the 3d moments. At that stage no mention was made of the exceptions to this rule. In the following sections however it will be apparent that a number of systems do not show this trend: Lu_2Fe_{17}, Ce_2Fe_{17}, $(Y, Th)Fe_3$, $Th(Fe, Co)_5$ for high Fe content, where various exotic noncollinear spin structures occur. This is consistent with the general view that Fe tends to show a more localized behaviour than Co and Ni. However, even the system $Th(Co, Ni)_5$ (see subsection 4.3) shows an

antiparallel moment arrangement giving ferrimagnetism. Although Th is not strictly a rare earth this exception is not consistent with the general conclusions we have drawn (about the relative itineracy of Co and Ni moments in rare earth compounds). The concept of an itinerant moment can be regarded as one in which localized 3d moments with oscillatory Friedel fringes (Friedel, 1962) are collected together with such short nearest neighbour distances that the first broad maximum of polarization for each moment overlaps with the neighbours thus producing a smeared out spin density without oscillations (only ripples) which is best treated as itinerant. In the case of Fe compounds the oscillations tend to have shorter wavelengths thus allowing nearest neighbours to experience antiferromagnetic coupling forces. In Co and Ni intermetallics the wavelengths λ tend to be longer with respect to the interatomic distance d. In fact the ratio λ/d is the important parameter and Buschow (1971) deduced that this parameter decreases progressively from Ni to Co to Fe, thus accounting for the appearance of antiferromagnetic components in the Fe–Fe interactions. Within this picture it appears that at least one exception occurs where Co and Ni moments can be regarded as having effective λ/d values which are smaller than usual. This may be a result of exceptional conditions, such as quadrivalent Th^{4+} (instead of R^{3+} ions) in combination with preferential site occupancy as is the case in $Th(Co, Ni)_5$. One other exception to the expected collinearity where a 3d moment exists is found in some RNi_3 compounds (see subsection 3.7). Here however it should be noted that these neutron diffraction results referred only to the R-moments and the presence of a moment on Ni in all RNi_3 compounds has not been unambiguously established. If Ni is magnetic for magnetic lanthanides then the strength of its influence on the R moments must be very low. Thus anisotropic interactions could just be strong enough to pull the basically ferromagnetic R-moments away from strict alignment, as found for some equiatomic RNi compounds (see subsection 2.6).

The various stoichiometries $R(Fe, Co)_2$, $R(Fe, Co)_3$, $R_2(Fe, Co)_{17}$, show the common feature of a maximum in the average 3d moment at approximately 20–40% Co which is parallel to the behaviour of the binary (Fe, Co) alloys which form a part of the Slater–Pauling curve. Maxima are found for the Fe hyperfine field in $Y(Fe, Co)_3$ (see subsection 3.7). Similar maxima are also found in some $R(Fe, Co)_2$ systems and Arif et al. (1975c) point out the similarity in magnetic behaviour between these Laves phases and the pseudobinaries $R(Fe, Co)_3$, $R_2(Fe, Co)_{17}$ as well as (Fe, Co). A similar conclusion was reached by Taylor and Poldy (1975) as regards the density of states curves of the various Y–(Fe, Co) and Y–(Co, Ni) systems after analysing magnetic results using the rigid band model. Considering the changes in crystal structure any such similarity is at first surprising. However the close structural relationship (subsection 3.2) of all these systems may be responsible for this apparently uniform shape of the density of states if one assumes the rigid band model. Since there appears to be a real correlation of the maximum 3d-moment for all these systems containing Fe and Co the problem of explaining the maximum for the pseudobinaries reduces to that of explaining the Slater–Pauling curve. The rather artificial assumption of a

minimum in the density of states which is necessary for the explanation (as described in subsection 3.1.3) in terms of the rigid band model is unsatisfactory for two reasons. The binary (Fe_xCo_{1-x}) alloys are not structurally related to the Y–(Fe_xCo_{1-x}) systems. The density of states curve should be entirely different. Therefore this same strategically placed minimum is unlikely to be present in all systems. The second point is that the position of the maximum should wander, towards higher x values, progressively from stoichiometry to stoichiometry due to electrons contributed by Y^{3+} partly filling the 3d-band. However the maximum does not show any such tendency to shift and one is therefore tempted to regard it as being a characteristic of the Fe ions. Thus Fe shows, also in this respect, a relatively localized behaviour. As will be seen in subsection 3.5 it is believed that the maximum in the c-lattice parameter of $R_2(Fe, Co)_{17}$ is also a characteristic of Fe rather than Co. The various Y–(Co, Ni) stoichiometries generally show magnetic moment behaviour corresponding to the right flank of the Slater–Pauling curve where the rigid band model is more applicable. When interpreting the experimental results of a pseudobinary series it is often tempting to assume implicitly the rigid band model which does not always give a realistic description. This is because the motivation in preparing pseudobinary systems and the ideas behind this are often founded upon a simple rigid band picture, for example to test the effect of electron concentration by replacing one element by another. The concept of an average electron concentration loses much of its physical significance in the case where the rigid band model is inapplicable.

From the foregoing and also in the following sections we see some cases of experimental results which are difficult to interpret unambiguously with a single realistic model. Two widely different models with opposing assumptions are often capable of explaining a single set of experimental data. This demonstrates the need to combine as many different experimental techniques as possible in investigations of a single intermetallic system. Only then can one narrow down the number of possible models to be applied and obtain a coherent picture of all related intermetallic systems.

3.4. *The* RB_2 *compounds*

The compounds to be discussed here with the RB_2 stoichiometry are RMn_2, RFe_2 and RCo_2. RMn_2 perhaps belongs to subsection 2.4 since no moment has yet been detected on Mn in these compounds but, since the 3d shell is most probably not filled, it is included here. The RMn_2 compounds with R = Y, Gd, Tb, Dy and Ho have the cubic C15 structure, those with Sc, Pr, Nd, Er, Tm and Lu exhibit the hexagonal C14 structure, while $SmMn_2$ is polymorphic and crystallizes in both structures and La, Ce, Eu and Yb do not form a compound at the RMn_2 stoichiometry. The RMn_2 compounds have been neglected compared with the Fe and Co compounds, and the information available about the magnetic properties is incomplete. Investigations have been performed by Nesbitt et al. (1963), Corliss and Hastings (1963), Felcher et al. (1965), Kirchmayr (1968), Merches et al. (1976). The neutron diffraction measurements by Felcher

et al. (1965) indicated that Mn possesses no moment in $ErMn_2$ and $TmMn_2$. This appears also to be the case for the other rare earths. Antiferromagnetic behaviour has been reported and many measurements reveal negative values for θ_p. Felcher et al. (1965) reported that $ErMn_2$ is ferromagnetic, with a moment of 7.72 μ_B aligned in the c-axis direction, whereas $TmMn_2$ appears to have a small antiferromagnetic component and the Tm moment is 4.95 μ_B. These moments are considerably smaller than the free ion values, which appears to indicate quenching effects from crystal fields. Nesbitt et al. (1963) have observed anomalous effects in $TbMn_2$ which seems to exhibit antiferromagnetism measured in a field after cooling in zero field and ferromagnetism when cooled in an applied field. More systematic investigations are required before these compounds are to be understood. Measurements by Corliss and Hastings (1964) have revealed a helical spin structure in $TbMn_2$. $GdMn_2$ has a T_C (86 K) no larger than those of the other GdB_2 compounds with no B-moment (B = Ir, Ru, Rh, Os, Ni), see fig. 14.25.

The RFe_2 compounds (with some exceptions, e.g. $ScFe_2$, which form the hexagonal Laves phase) exhibit the cubic C15 structure, but do not form for most lanthanides to the left of Sm, and also for Eu and Yb. However $CeFe_2$ does exist, its stability being associated with the fact that Ce is quadrivalent here. The Fe moment in RFe_2 is to some extent variable. The moment is approximately 1.4 μ_B in YFe_2, $LuFe_2$ and $TmFe_2$, rising to about 1.6 μ_B for the other lanthanides. Thus a small component of the Fe moment appears to be induced by the R–Fe interactions. The Curie temperature of YFe_2 is 545 K and that of $GdFe_2$ is 785 K, the difference being partly due to relatively weak R–R and R–Fe interactions compared with Fe–Fe interactions.

The Curie temperature of $CeFe_2$ (refer to fig. 14.73) is seen to be exceptionally low, this being also associated with the valency of Ce being 4 instead of 3 as found in the other lanthanides. Consistent with this valency of Ce in $CeFe_2$ the Fe moment is 1.2 μ_B, lower than in the other RFe_2 compounds. This was accounted for (see Atzmony and Dariel, 1974) by the transfer of electrons from Ce into the 3d-band, rendering Ce non-magnetic and reducing the moment of Fe. The anisotropy is also affected by the filling of the Fe 3d-states, since $CeFe_2$ has an easy [100] axis up to 150 K whereas YFe_2 has an easy [111] type. $GdFe_2$ however has the [100] type of anisotropy. It is deduced that the anisotropy of the Gd–Fe interactions must be considerable enough to overcome the effects of the Fe–Fe interactions.

Crystal field calculations based on the one-ion model were performed by Atzmony et al. (1973) and Dariel and Atzmony (1973) for various RFe_2 and pseudobinary (R_1, R_2) Fe_2 compounds. The calculated temperature dependence of K_1 and K_2 in $ErFe_2$ is shown in fig. 14.81. This demonstrates the large values of $|K_2/K_1|$ characteristic of this family of compounds.

The RFe_2 compounds display giant magnetostrictions which have been the object of intensive investigations by Clark and his co-workers. A number of exceptional effects can therefore be expected which are associated with magnetostriction. A self-induced rhombohedral distortion has been observed to

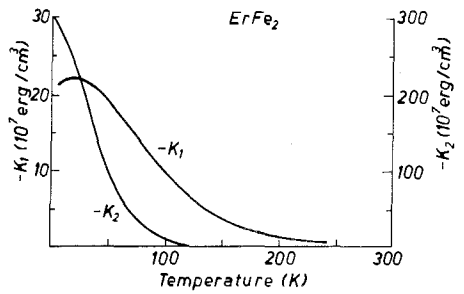

Fig. 14.81. Theoretical temperature dependence of the anisotropy constants of $ErFe_2$ (Dariel and Atzmony, 1973).

occur, which in the case of $TbFe_2$ extends up to room temperature. Magnetostriction in RFe_2 will not be discussed here since it is treated in detail in ch. 15.

As in the other series of R–3d compounds where R is a heavy lanthanide the RFe_2 compounds show ferrimagnetic coupling between the R and Fe moments. The magnetization versus temperature curves can be well described by molecular field calculations (Hilscher et al., 1973; Burzo, 1974). Compensation points are found only for R = Tm and Er. The absence of compensation points for the other lanthanides is a result of the considerable negative R–Fe interaction (Buschow and van Stapele, 1971). The Fe–Fe interaction is however still the strongest (Burzo, 1974).

In $SmFe_2$, apart from temperature dependent spin reorientations, there is another interesting feature which deserves mention. This is the ferrimagnetic coupling, as observed by Dublon et al. (1975) between the Fe and Sm sublattices, which one usually expects only for the heavy lanthanides. The possibility of this anomalous behaviour was predicted by Buschow et al. (1973a) on grounds of calculations of crystal field effects upon SmB_2 compounds (where B is non-magnetic) taking into account admixture of excited J multiplet levels into the ground state, see subsection 2.4. A sign reversal of $\langle S_z \rangle$ relative to $\langle L_z + 2S_z \rangle$ was found to be possible, making Sm appear to behave as a heavy lanthanide. The magnetic moment as a function of temperature and applied field is shown in fig.

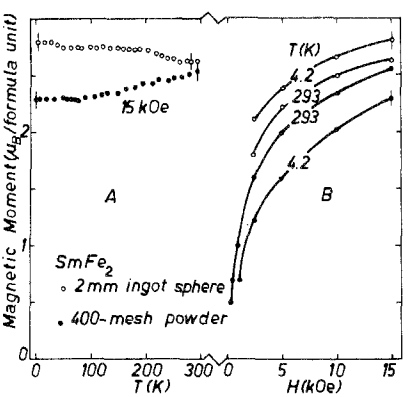

Fig. 14.82. The magnetic moment of polycrystalline $SmFe_2$ as a function of (A) temperature and (B) field (Dublon et al., 1975).

14.82. Dublon et al. (1975) came to the conclusion, after a general survey, that a reasonable value for the Fe moment could only lie well within the range 1.5–2.0 μ_B. If this is assumed then the coupling must indeed be ferrimagnetic in $SmFe_2$. If an Fe moment of 1.45 μ_B were assumed then a Sm moment with 0.1 μ_B magnitude coupled ferromagnetically with Fe would be just conceivable. However this result is only obtained with a rather liberal use of error bars.

The RCo_2 compounds, in contrast to the RFe_2 compounds, have extremely variable moments on the Co atoms. These 3d-moments appear to exist only in the presence of a magnetic lanthanide and range from 1.05 μ_B in $GdCo_2$ down to 0 μ_B in $LuCo_2$ or YCo_2. The growth of a 3d-moment from zero due to appropriate substitutions in YCo_2 will be discussed in section 4. Due to the variability of the Co-moments in combination with relatively stable permanent moments on the R atoms Bloch and Lemaire (1970) used the concept of an exchange enhanced paramagnetic susceptibility for the Co sublattice and developed a phenomenological model to describe the exchange induced moment on Co. This model is outlined in subsection 3.1.7. From this model it was deduced that the R–Co interactions are dominant and are about twice as strong as the Co–Co interactions, which is in agreement with the conclusion of Lee and Pourarian (1976) who investigated the magnetoelastic properties. The ordering temperatures arise from $n_{RR}C_R$ and $n_{RB}^2 C_R \chi_y$ (A = R = rare earth, B = B, see subsection 3.1.7) which are of approximately the same magnitude. However the R–R interactions in RCo_2 are about twice as strong as in RNi_2. Since the lattice parameters are similar this indicates that the 3d electrons take part in the R–R exchange. On grounds of paramagnetic investigations Burzo (1972a) proposed a different interpretation. These measurements showed a paramagnetic Co-moment about twice as large as the ordered moment which is similar to the situation in elemental Co. Thus in RCo_2 even though the Co-moment appears to be exchange-induced a large moment seems to persist into the paramagnetic temperature range if it is assumed that a certain degree of localization is present in the 3d-moments. It should be noted however that an excess susceptibility in the paramagnetic range (of $GdCo_2$ for example) above that expected for paramagnetic Gd ions is in any case expected. This is because a non-magnetic itinerant 3d band without any exchange splitting will be partly polarized by the applied field at a given temperature. One can of course analyse this excess polarization assuming localized moments on Co and obtain a value for p_{eff} of Co. This however does not necessarily mean that Co has a moment in the absence of an applied field. Since any Co moment (whether exchange or field induced) would tend to interact ferrimagnetically with Gd one may expect that the 3d moments tend to be oppositely oriented to any R-magnetization. Gignoux et al. (1976, 1977b) have reported 3d moments in the paramagnetic range detected by neutron diffraction for $HoCo_2$ and $TmCo_2$. These moments however only exist in the presence of an applied field and are indeed negatively oriented to the field and to the R-moments which induce them.

A high anisotropy is observed in RCo_2 compounds. This is confirmed by measurements of magnetostriction (del Moral and Melville, 1975) which indicate

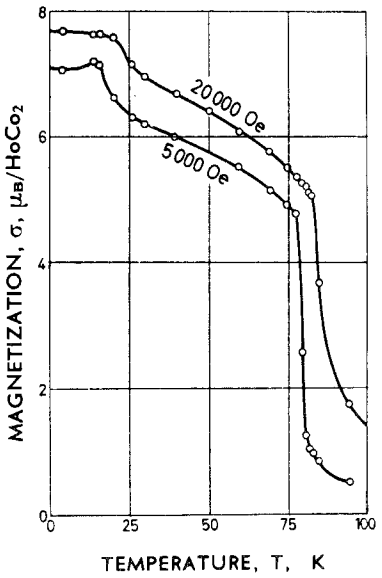

Fig. 14.83. Temperature dependence of the magnetization of $HoCo_2$ (Lemaire, 1966b).

that the lanthanide ions are the main source of magnetostriction. In connection with anisotropy variations at low temperatures anomalies have been observed in the (M, T) curves well below the ordering temperatures (which are denoted by T_C even though many of these materials are ferrimagnetic). Lemaire (1966b) reported such anomalies in $NdCo_2$ and $HoCo_2$ (fig. 14.83) and suggested that these may have a similar origin to that found in $NdCo_5$ (see subsection 3.6), where the easy axis showed a rotation at a critical temperature. These anomalies were observed in low fields and became less sharp for high fields. They also have been detected by specific heat measurements (Voiron et al., 1974). The interpretation of Lemaire that the easy axis changes is supported by the thermal expansion measurements of Lee and Pourarian (1976), see fig. 14.84. Not to be confused with this type of anomaly, are the so-called two step magnetization-

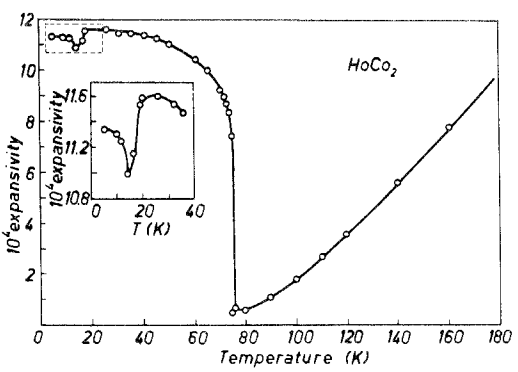

Fig. 14.84. Expansivity of $HoCo_2$ as a function of temperature (Lee and Pourarian, 1976).

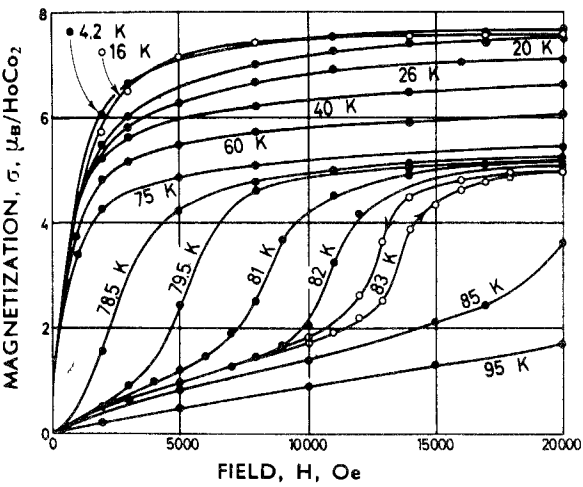

Fig. 14.85. Magnetization isotherms of $HoCo_2$ (Lemaire, 1966b).

temperature curves. These have been reported by various workers including Burzo et al. (1969) for $GdCo_2$ and Taylor et al. (1966). The low temperature step in $GdCo_2$ occurs at 220 K which is rather near the Curie temperature 230 K of Gd_4Co_3. Tsuchida et al. (1975) observed no such anomalies in their investigations of $GdCo_2$ and $(Gd, Y)Co_2$.

Another type of anomaly, well established in the vicinity of the Curie points in some RCo_2 compounds, are the first order transitions observed for R = Er, Ho and Dy. In fig. 14.83 this effect can be seen in $HoCo_2$ (Lemaire, 1966b) where the magnetization drops sharply at the Curie point. This transition is accompanied by a hysteresis in temperature. Lemaire (1966b) observed metamagnetic behaviour above the first order transition temperature (fig. 14.85). Givord and Shah (1972) also observed such metamagnetic behaviour in $ErCo_2$. Magnetic ordering in $HoCo_2$ is accompanied by a sharp increase in the lattice parameter on lowering the temperature. The occurrence of first and second order transitions in RCo_2 compounds for heavy lanthanides was interpreted by Bloch et al. (1975) to be due to the Landau parameter $B(T)$ of the 3d-band (see subsection 3.1.4) changing sign at about 200 K since the compounds with second order transitions (R = Gd, Tb) have $T_C > 200$ K. Givord and Shah (1972) have suggested that a modification of the electronic structure of Co may be responsible for the first order transitions. This appears plausible since the Co moments in the RCo_2 compounds are in a very sensitive state, moment changes being strongly amplified by small external influences. Thus a small change in the electronic state of Co may be sufficient to cause a large drop in its moment which in turn would drive the system prematurely into the paramagnetic state. This would be accompanied by a sharp collapse in the magnetization as observed.

The pseudobinary systems $R(Fe, Co)_2$ and $R(Co, Ni)_2$ where R = Nd, Gd, Dy, Ho and Er, have been investigated by Slanicka et al. (1971). Changes of R and 3d

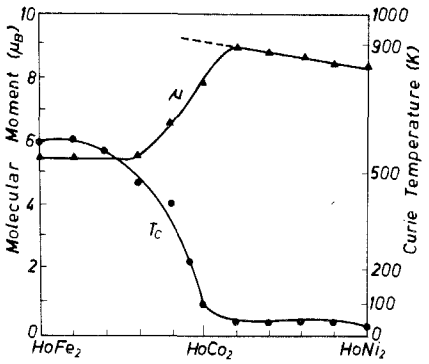

Fig. 14.86. The composition dependence of the molecular moment $\mu_{Ho}-2\mu_{3d}$ and Curie temperature of the HoB_2 pseudobinaries. The extrapolation of the moment to $HoCo_2$ is done on the basis of a linear variation across the series (Slanicka et al., 1971).

moments were observed, especially at compositions to the Ni side of the RCo_2 compound (fig. 14.86). It was suggested that these changes were interdependent and were interpreted in terms of a bootstrap mechanism. Considerable and variable quenching of the R-component was allowed for. This is consistent with a large anisotropy present in these compounds. In such materials very large fields are required before meaningful values can be obtained for the saturation magnetization. The Dy(Co, Ni)$_2$ series which shows strong time dependence was left out of the discussion (see section 5). The importance of crystal fields in RCo_2 compounds is exemplified by the work of Primavesi et al. (1971) on (Gd, Nd)Co_2. For 57% Nd the resultant moment of the ferrimagnet is zero at 4.2 K. The remanence variation with temperature is shown in fig. 14.87, together with the

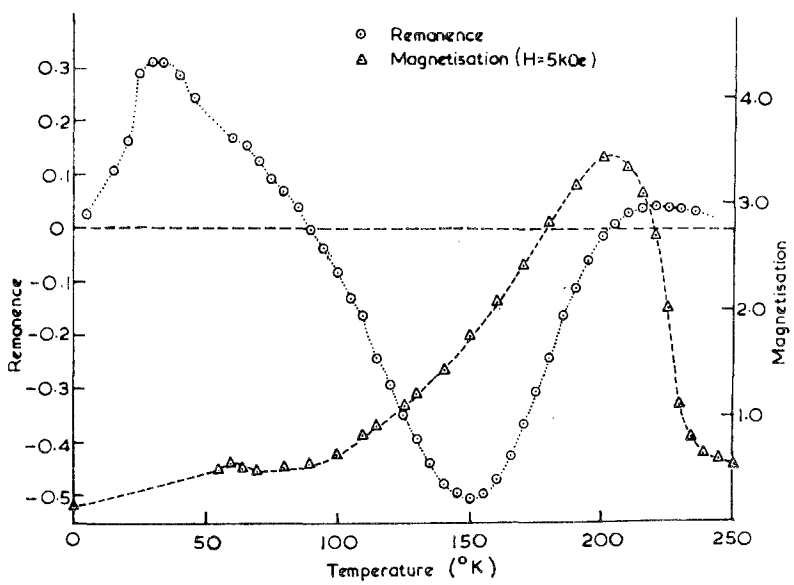

Fig. 14.87. Temperature dependence of the remanence and the magnetization at 5 kOe applied field for $Nd_{0.57}Gd_{0.43}Co_2$ (Primavesi et al., 1971).

magnetization variation. The abnormal oscillatory behaviour was interpreted in terms of crystal field splitting of the Nd^{3+} ground state. The change in remanence with temperature depends on the detailed balance of the sublattices. The remanence is not normally expected to cross the T-axis twice. However the change in Nd moment upsets the magnetization balance in the system causing the observed behaviour.

The $R(Fe, Co)_2$ systems usually show a maximum in T_C and a minimum in the 3d-moment at high Fe content. (e.g. fig. 14.86). This can be interpreted in the same way as the maximum in the Slater–Pauling curve within the rigid band model. However NMR measurements on $Gd(Fe, Co)_2$ by Belov et al. (1974) show a discontinuity in the hyperfine field at the Co sites due to a change in the degree of localization of the 3d-electrons. They interpret the results in terms of the Friedel model (Friedel et al., 1961). Changes in the contribution to the hyperfine field due to 3d-neighbours are attributed to changes in the local spin densities. The increase in exchange on replacing 10% Fe in $GdFe_2$ by Co is discussed in terms of shifting of the nodes of the Friedel oscillations.

In the above we have discussed RFe_2 and RCo_2. The latter is further discussed with other borderline cases in subsection 4.1. After Fe and Co the next element expected in the periodic table is Ni. The RNi_2 compounds are however treated in subsection 2.4 together with other cubic RB_2 compounds with no B-moment. The only stoichiometry existing for Fe, Co and Ni where the B-moment never disappears is R_2B_{17} and this is dealt with in the following section.

3.5. *The* R_2B_{17} *compounds*

This stoichiometry occurs principally in two possible crystal structures, the rhombohedral Th_2Zn_{17} and the hexagonal Th_2Ni_{17} structure. Most R_2Fe_{17} and R_2Co_{17} compounds show both structure types, the rhombohedral predominantly for the light and the hexagonal for the heavy lanthanides, whereas the R_2Ni_{17} compounds exhibit only the hexagonal form. These structures can be derived from the $CaCu_5$ structure by a partial replacement of R atom sites with pairs of B atoms arranged as dumb-bells in the c-axis direction. The structural properties are rather complicated, in many cases excess R content being necessary to achieve single phase samples. The existence of the Th_2Ni_{17} structure in R_2Ni_{17} has even been doubted (D. Givord et al., 1972). This structure was claimed to be an ideal case, whereas reality involves a more random distribution of dumb-bells than that implied by the Th_2Ni_{17} structure.

The Ni moment is strongly dependent upon the presence of R atoms, being decreased from 0.6 μ_B in pure Ni to about 0.3 μ_B in R_2Ni_{17}, whereas in the R_2Co_{17} and R_2Fe_{17} compounds the B moments are similar to those in the pure transition metals, about 1.6 μ_B and 2.1 μ_B respectively. However, once the 2 : 17 stoichiometry is achieved, the Ni moments are not strongly dependent upon which lanthanide is present. The ordering temperatures are also not very sensitive to the type of R atoms (see fig. 14.71).

Magnetic measurements have been performed by Laforest et al. (1967), Carfagna and Wallace (1968), Steiner and Hrubec (1975), Burzo and Laforest

(1972), Burzo and Lazar (1973), as well as by many other investigators. Compensation points occur for all heavy lanthanide R_2Ni_{17} compounds. With increasing atomic number these compensation points shift to lower temperatures. The Curie temperatures range from 160 K for Y_2Ni_{17} to 205 K for Gd_2Ni_{17}. An apparent Curie temperature of the order of 620 K is sometimes observed in R_2Ni_{17} compounds but this can be traced to the presence of small quantities of free Ni in the samples. This conclusion is supported by the investigations of Steiner et al. (1976) who find that the inclusion of excess lanthanide causes the disappearance of this higher Curie temperature. Apart from this, molecular field calculations for Gd_2Ni_{17} (Burzo and Laforest, 1972; Burzo and Lazar, 1973) are in agreement with the choice of the lower values for the Curie point. Effects of pressure have been investigated by Parviainen and Jaakkola (1975) and Jaakkola et al. (1975). Negative values are obtained for dT_C/dp. It is believed that $N(E_F)$ for all R_2Ni_{17} compounds is approximately the same.

The most intensively studied compounds with the 2 : 17 stoichiometry are those involving Co. This is connected with the search for improved permanent magnet materials. However, although T_C and saturation moments are larger than in RCo_5 the easy axes are often in the basal plane. Crystal field calculations by Greedan and Rao (1973) reveal two different influences upon the lanthanide ion. These arise from neighbours in the c-direction and from those in the equatorial plane. The former give a negative and the latter a positive contribution to the parameter A_2^0. Thus the easy axis direction is sensitive to the relative magnitudes of these two contributions. Although the calculations are only approximate it can be shown, for example, that the c-axis is easy in R_2Co_{17} for R = Sm, Er and Tm.

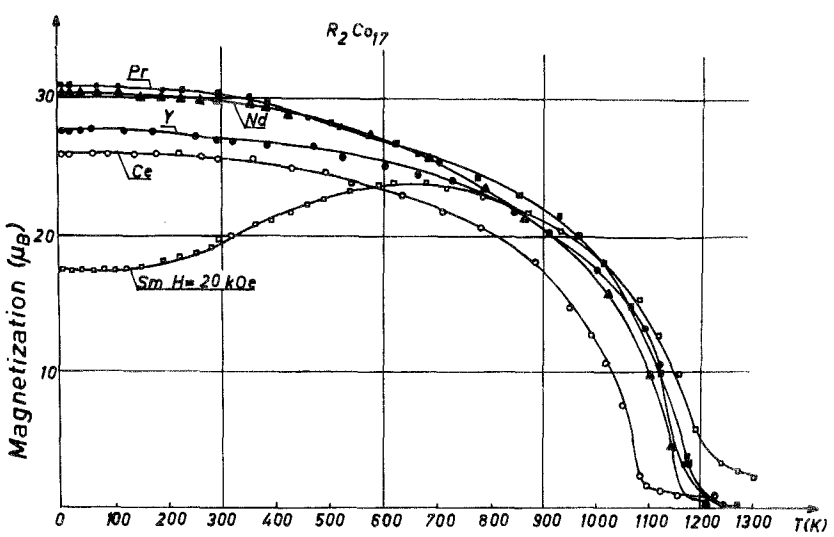

Fig. 14.88. Temperature variation of magnetization for R_2Co_{17} with the light lanthanides and Y, in a field of 20 kOe, showing the ferrimagnetic character for R = Sm. The other compounds appear to show ferromagnetism (Laforest et al., 1966).

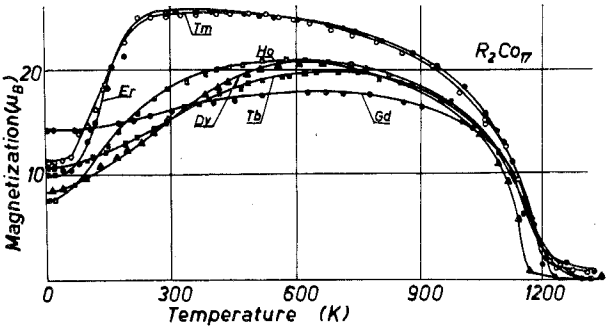

Fig. 14.89. Temperature variation of magnetization in a field of 20 kOe for R_2Co_{17} with the heavy lanthanides, showing the ferrimagnetic character (Laforest et al., 1966).

Magnetic investigations of saturation moments and Curie temperatures have shown that the light lanthanides order ferromagnetically and that the heavy ones ferrimagnetically with respect to Co (Lemaire, 1966a,b; Laforest et al., 1966). Sm in Sm_2Co_{17}, however, appears to behave like a heavy lanthanide, showing ferrimagnetic properties (figs. 14.88 and 14.89). The valencies of the lanthanides in Ce_2Co_{17} and Pr_2Co_{17} appear to be in excess of 3 (Strnat et al., 1966). For Pr a valency of 3.3 is most probable from crystallographic considerations, whereas 3.5 is more probable from magnetic considerations. Ce may have a valency of 4.

Single crystal measurements (see for example Deryagin and Kudrevatykh, 1975) confirm an easy c-axis in Er_2Co_{17} and Tm_2Co_{17}. For R = Gd, Y and La saturation is reached in low fields, whereas all other lanthanides do not show saturation in the hard direction for fields less than the anisotropy field which is of the order of 100 kOe. Anisotropy appears to come from R, rather than from Co. Thus, upon cooling, the anisotropy increases rapidly from a low value when the R sublattice begins to order (fig. 14.90) which is signalled by a drop in σ_s on cooling this ferrimagnet. Neutron diffraction measurements (Schweizer and Tasset, 1973) show

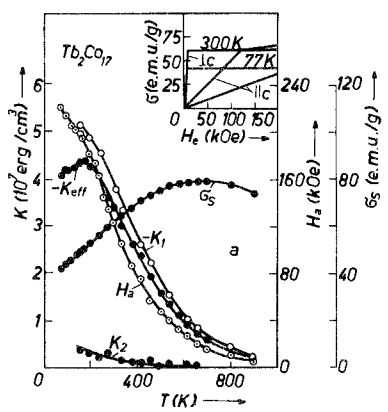

Fig. 14.90. Temperature dependence for Tb_2Co_{17} of the spontaneous magnetization σ_s, anisotropy field H_a and anisotropy constants. The field dependence of magnetization in the two crystallographic directions is shown in the inset (Deryagin and Kudrevatykh, 1975).

a collinear spin structure in Y_2Co_{17}. Co moments from the various sites are in excess of the saturation moment. The same situation is found by Elemans and Buschow (1973). The discrepancy is accounted for by postulating a diffuse negative polarization equal to 0.02 $\mu_B/Å^3$.

The ordering temperatures in R_2Fe_{17} compounds, of the order of 400 K, are extremely low compared with pure Fe and R_2Co_{17} compounds, and this is believed to be connected with a high degree of localization of the Fe moments. There appears to be very little conduction electron transfer from R^{3+} into the 3d band. The R_2Fe_{17} compounds have a number of peculiar features in contrast to the more band-like or itinerant behaviour of R_2Co_{17} and R_2Ni_{17}.

A special feature of R_2Fe_{17} compounds is revealed by thermal expansion measurements (Givord and Lemaire, 1974). As opposed to Y_2Co_{17} and Y_2Ni_{17}, we see in Y_2Fe_{17} a negative thermal expansion coefficient below the Curie temperature (fig. 14.91). In R_2Fe_{17} the Fe–Fe distances and number of nearest neighbours appear to influence strongly the exchange interactions (Givord et al., 1971b). In the dumb-bell pairs of Fe atoms the Fe–Fe distance is less than in pure Fe. This increases the possibility of direct exchange which may be antiferromagnetic for small distances, according to the Bethe–Slater curve (fig. 14.69). In these Fe atom pairs much exchange energy is stored and thus, in order to minimise the energy the distances can be strongly influenced by magnetic ordering. This explains the deviation of the lattice parameters from normal behaviour below the Curie temperature.

Lu_2Fe_{17} shows a transition, upon raising the temperature, from ferromagnetism to helimagnetism (Givord and Lemaire, 1972, 1974; Givord et al., 1971a). This transition is not due to changes in electron configuration, but rather, to the sensitivity of the exchange interactions to Fe–Fe distances (Givord and Lemaire, 1974). For Y_2Fe_{17} a collinear spin structure is observed (Givord and Lemaire, 1974). According to neutron diffraction measurements on Th_2Fe_{17} at 4.2 K (Elemans and Buschow, 1973) the f-sites in the $z = 0$ and $z = \frac{1}{2}$ planes have moments 2.9 μ_B and 2.3 μ_B respectively at low temperatures. At 300 K all Fe atoms have the same moment 1.1 μ_B. It is shown, by comparison with $ThFe_5$,

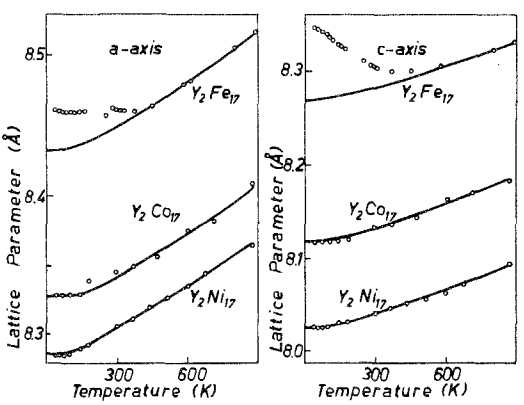

Fig. 14.91. Thermal variation of the lattice parameters of Y_2Ni_{17}, Y_2Co_{17} and Y_2Fe_{17}. The full lines represent the lattice contribution to the thermal expansion (Givord and Lemaire, 1974).

that not only the Fe–Fe distances but also indirect interactions have an influence upon magnetic ordering. Ce_2Fe_{17} is a helimagnet below the ordering temperature but, in contrast to Lu_2Fe_{17}, it does not become ferromagnetic at low temperatures. Rather, it shows, in a field of 6.5 kOe a transition at 55 K to a fan structure in the basal plane (Plumier and Sougi, 1973). Ferrimagnetic Tm_2Fe_{17} shows at high temperatures an easy basal plane. The spins however turn into the c-direction upon cooling. This can be accounted for, within terms of the Bethe–Slater curve, by postulating a change from positive to negative exchange interactions between localized Fe atoms as the lattice parameters vary. Mössbauer studies (Gubbens et al., 1976) have revealed large hyperfine fields at the dumb-bell sites of Fe in R_2Fe_{17} systems. Easy axis directions are reported, as well as a preference of Fe to occupy the dumb-bell sites for R = Tm.

The pseudobinary $R_2(Fe, Co)_{17}$ series has the rhombohedral structure for the light lanthanides and partly, depending on the R-radius, the hexagonal structure for the heavy lanthanides. In $R_2(Fe, Co)_{17}$ there always occurs a maximum in the room temperature lattice parameter c at a Co concentration ranging from 30 to 40%. To explain this phenomenon we refer to the thermal expansion data for the R_2Fe_{17} compounds, see fig. 14.91. The maximum arises out of the opposing effects of the c expansion, on going from the Co end to the Fe end, and the anomalous magnetoelastic properties which arise below the ordering temperatures at the Fe-rich end of the series, where T_C is not far above room temperature. Thus the appearance of the maximum appears to be a characteristic of Fe rather than Co. In this connection see Deryagin et al. (1974), Ray et al. (1971b) and Ray and Strnat (1972a). This effect, absent in $R_2(Co, Ni)_{17}$ is however also absent in $R_2(Fe, Ni)_{17}$.

Figures 14.92 and 14.93 show the 3d moment and T_C variations. The behaviour

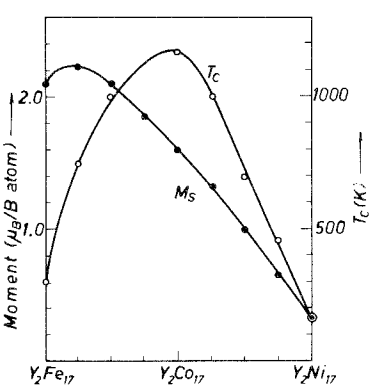

Fig. 14.92. The Curie temperatures and spontaneous moments of $Y_2(Fe, Co)_{17}$ and $Y_2(Co, Ni)_{17}$ as a function of electron concentration. Note the resemblance to the Slater–Pauling curve (fig. 14.67). (Taylor and Poldy, 1975).

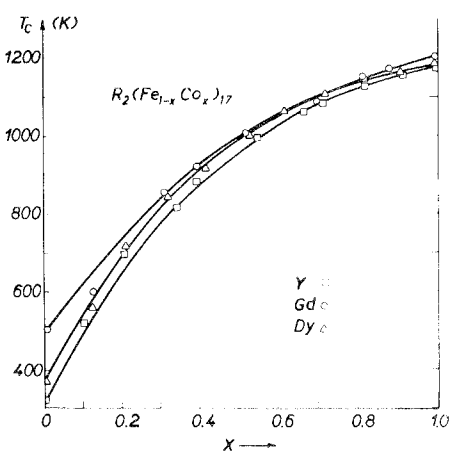

Fig. 14.93. The Curie temperatures of $R_2(Fe, Co)_{17}$ showing minimal effect of replacing Y by Dy or Gd (Steiner et al., 1973).

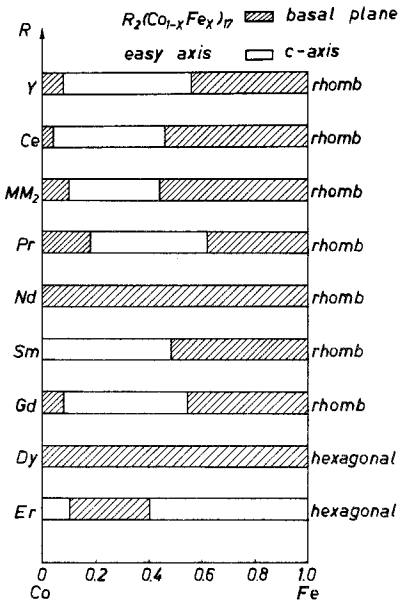

Fig. 14.94. The easy axis directions in the $R_2(Fe, Co)_{17}$ pseudobinaries.

of the lattice parameters and T_C values for the various series is not strongly affected upon replacing one lanthanide with another (Steiner et al., 1973). The influence of the 4f-electrons seems therefore to be weak, T_C being mainly determined by 3d–3d exchange. The 3d-moment variation for each R = Y series is similar to that in the corresponding binary series where R is absent. This can, as for the Slater–Pauling curve, be explained in terms of the rigid band model in which holes are present in both 3d sub-bands in the Fe-rich samples, see fig. 14.67.

Data for the easy axis directions are summarized in fig. 14.94 and fig. 14.95. Single crystal measurements of anisotropy constants and anisotropy fields (Perkins and Nagel, 1975) have been performed on $Y_2(Fe, Co)_{17}$ which establish a change in anisotropy type with composition and temperature. Concentration

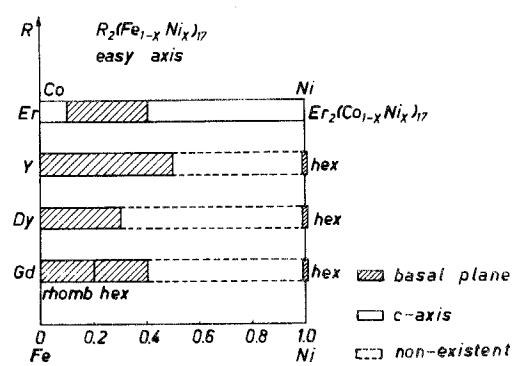

Fig. 14.95. The easy axis directions in the $R_2(Fe, Ni)_{17}$ and $R_2(Co, Ni)_{17}$ pseudobinaries.

dependence of the easy axes is not well understood. Investigations upon single crystals of $(Y, Dy)_2Co_{17}$ (Miller et al., 1974b) show that anisotropy within the basal plane appears in the substitution range. Miller et al. (1974a) have detected for $(Lu, Tm)_2Co_{17}$ a change of the easy axis from the basal plane in Lu_2Co_{17} to the c-axis in Tm_2Co_{17}. Measurements of magnetization, anisotropy and magnetostriction performed on single crystals (Miller et al., 1976) have revealed a uniformly easy basal plane for Tb_2Co_{17} and Ho_2Co_{17} and an easy c-axis in Er_2Co_{17}.

3.6. *The* RB_5 *compounds*

The main group of compounds with the $CaCu_5$ structure and non-zero B-moment is the RCo_5. RFe_5 compounds generally do not exist. This may be due, to some extent, to the effect of conduction electron concentration which is lower in any hypothetical RFe_5 compared with RCo_5. The exception is $ThFe_5$ which does exist due to the fact that Th is quadrivalent. This compensates partly the lowering of the electron concentration on going from RCo_5 to RFe_5. The existence of the stoichiometry 1 : 5 is not sharp. An extended homogeneity region has been observed in RCo_5 compounds (Dworschak and Khan, 1974). In the R–Co systems for the smaller R ions, the stability appears to be shifted from RCo_5 to RCo_6 (Buschow and van der Goot, 1968) associated with a partial replacement of R atoms by dumb-bell pairs of B atoms in the c-direction. It was suggested (Taylor and Poldy, 1972) that this may be occurring when Fe is substituted into YCo_5 where a drastic increase of the c/a ratio occurs before structural instability sets in. The RNi_5 compounds possess no 3d moment and have as a consequence rather low ordering temperatures compared with RCo_5 compounds.

As generally observed in R–3d intermetallics the RB_5 compounds exhibit ferromagnetism with the light lanthanides and ferrimagnetism for the heavy lanthanides. In the latter compensation points are found as for example in Tb, Dy, Ho and Er (Cherry and Wallace, 1962; Lemaire, 1966a,b). Figure 14.96 shows the compensation point for $TbCo_5$. However for this compound as well as $NdCo_5$ in this figure we see another effect at higher temperatures, namely the relatively sharp peak in the magnetization at low fields (Lemaire, 1966a,b). This anomaly was investigated by means of neutron diffraction and it was found (fig. 14.97) that a turning of the easy axis of magnetization was responsible for the increase in susceptibility at the temperature of the anomaly. This is due to anisotropy changes as a function of temperature.

Hyperfine fields in YCo_5, $LaCo_5$ and $ThCo_5$ have been investigated by Heidemann et al. (1975) by means of inelastic spin flip scattering of neutrons. They find rather low hyperfine fields on the Co sites which they interpret as being due to a partial cancellation of the contributions from core polarization, orbital moments and conduction electron polarization. It is concluded from this work that the orbital contribution is positive in RCo_5 and larger than in elemental cobalt. This may be responsible for the large anisotropy of RCo_5 even where R has no moment (Schweizer and Tasset, 1973).

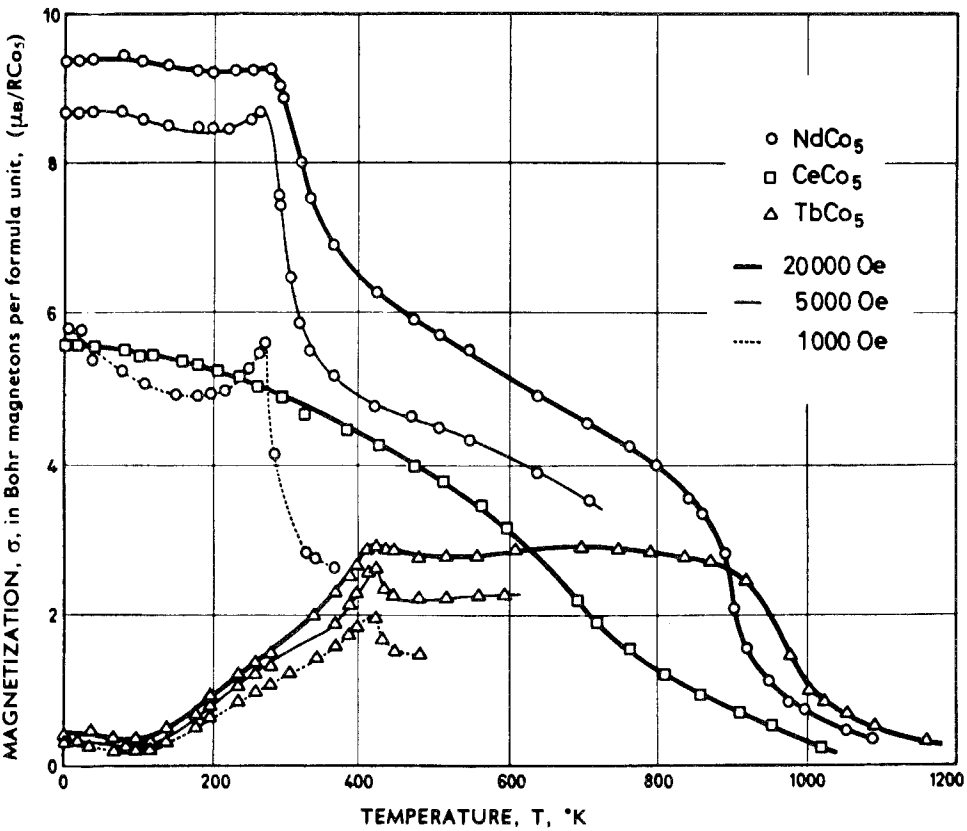

Fig. 14.96. Temperature dependence of the magnetization of the RCo_5 compounds, with R = Ce, Nd and Tb, in various fields (Lemaire, 1966a).

Although the Co contribution to the anisotropy of RCo_5 compounds is comparable to that of the lanthanides, the latter have received more attention in crystal field calculations. The treatment of the lanthanide contribution has been performed by Greedan and Rao (1973), Buschow et al. (1974a), Malik et al. (1976), Ermolenko (1976). Greedan and Rao (1973) used a hamiltonian of the form $\mathcal{H} = B_2^0\hat{O}_2^0 + g\mu_B JH_{R,exch}$. The first term arises from the crystal field acting on the R ion and the second term mainly from the Co sublattice. A point charge model is assumed considering only nearest R neighbours. In general the crystal field interaction in RCo_5 can be described by

$$\mathcal{H}_{CF} = B_2^0\hat{O}_2^0 + B_4^0\hat{O}_4^0 + B_6^0\hat{O}_6^0 + B_6^6\hat{O}_6^6. \tag{14.27}$$

The dominant term is the first one where $\hat{O}_2^0 = 3J_z^2 - J(J+1)$ and B_2^0 is a product of several factors involving a shielding factor of approximately 0.5 for 4f wave functions. The exchange field consists of two contributions, R–R and R–Co where the latter is much larger. The R–Co interaction in $DyCo_5$ has been

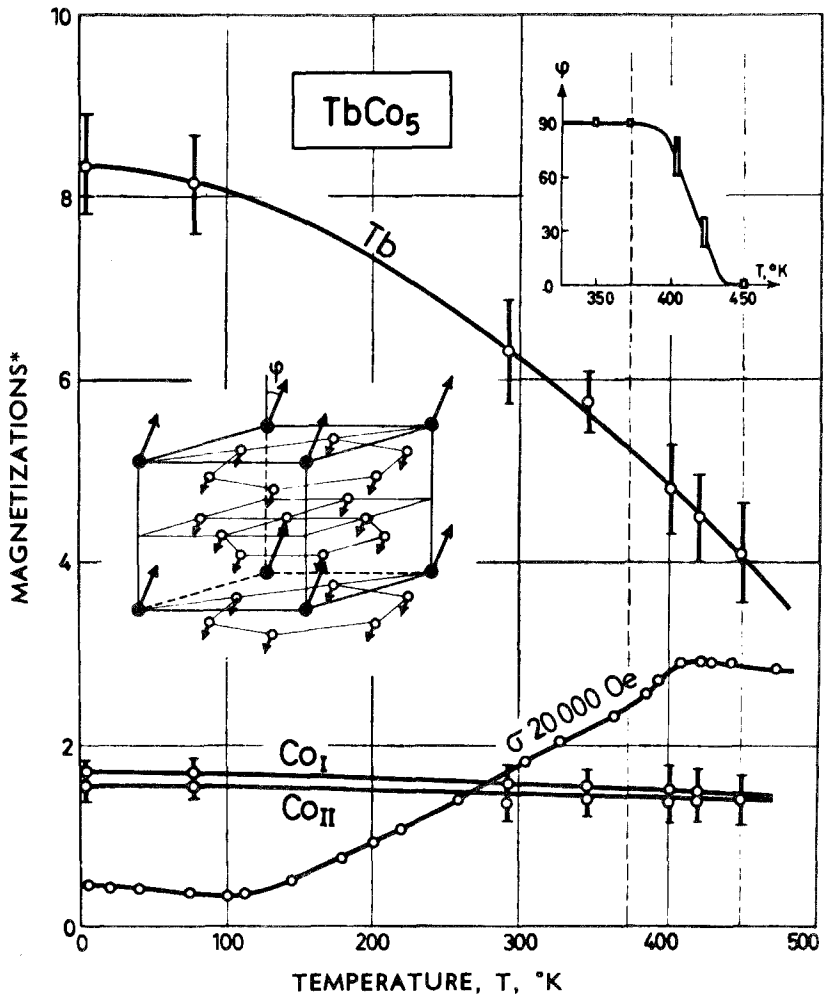

Fig. 14.97. Magnetic structure of $TbCo_5$ and magnetization σ per $TbCo_5$ unit, magnetization of the Tb and Co sublattices per Tb and Co atom, respectively (Lemaire, 1966a). The insert shows the angle between spin and c-axis directions as a function of temperature.

estimated by Nowik and Wernick (1965) from Mössbauer data in connection with molecular field calculations to be $gJ\mu_B H_{exch}(0)/k_B = 142\,K$ which yields $H_{exch} = 1570\,kOe$. The R-sublattice orientation is determined by the sign of B_2^0. As seen from table 14.6 theoretical and experimental results agree well with the exception of $PrCo_5$. The stabilization energy corresponds to the relative stability of the R-sublattice in its preferred direction. The effective charge associated with the Co atoms is estimated to be very small and the R ions are tripositive.

Buschow et al. (1974a) investigated the anisotropy of Sm^{3+} in $SmCo_5$ in detail. For a hexagonal crystal structure the angular dependence of the free energy has

TABLE 14.6.
Crystal field parameters of RCo_5 compounds (Greedan and Rao, 1973). CFOAS is the "crystal field overall splitting".

R	$g\mu_B H_{ex}$(K)	$\alpha_J(\times 10^3)$	$A_2^0\langle r^2\rangle$(K)	B_2^0(K)	CFOAS(K)	Rare earth sublattice preferred direction		Stabilization energy (K)
						Theory	Expt	
Pr	84	−21.0	−1110	+4.5	215	Plane	Cone	180
Nd	115	−6.4	−1030	+1.3	82	Plane	Plane	80
Sm	–	+41.2	−970	−7.9	144	Axis	Axis	–
Tb	210	−10.1	−775	+1.4	160	Plane	Plane	150
Dy	140	−6.3	−745	+0.9	160	Plane		150
Ho	104	−2.1	−720	+0.3	55	Plane	Plane	45
Er	84	+2.69	−680	−0.4	70	Axis		65

the general form

$$F = K_1 \sin^2\theta + K_2 \sin^4\theta + K_3 \sin^6\theta + K_4 \sin^6\theta \cos^6\varphi. \tag{14.28}$$

Experiments show that the anisotropy can be well described by K_1 alone. In the case of non-magnetic R ions the anisotropy is roughly equal. K_1 then represents the Co contribution to the anisotropy, see fig. 14.98. In the presence of 4f electrons additional contributions to the anisotropy arise: (a) dipole contributions due to the magnetic moments of R ions, (b) due to the crystalline electric field for R ions with orbital moments. The contribution (a) can be estimated from $GdCo_5$ which has no orbital moment. Since Sm^{3+}, whose moment is less than 0.7 μ_B, has a much smaller moment than that of Gd^{3+} the dipole contribution in $SmCo_5$ can be neglected, and the huge anisotropy can be attributed to the influence of the crystal field on the Sm^{3+} ion.

The case of $SmCo_5$ is to be treated as an exception as will be seen below. $LaCo_5$, YCo_5 and $CeCo_5$ possess approximately equal anisotropies which are

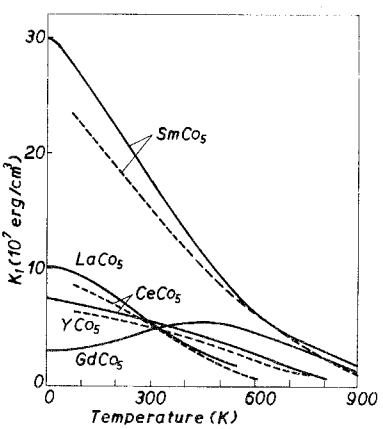

Fig. 14.98. Experimental values of the uniaxial anisotropy constant K_1 as a function of temperature for various RCo_5 compounds (Buschow et al., 1974a). The full curves represent the data obtained with applied fields up to 83 kOe (Ermolenko, 1973), while the dashed curves are data obtained with applied fields up to 16 kOe (Klein et al., 1975).

TABLE 14.7.
Crystal field data for $SmCo_5$.

$A_2^0\langle r^2\rangle k_B^{-1}$ (K)	$A_4^0\langle r^4\rangle k_B^{-1}$ (K)	$A_6^0\langle r^6\rangle k_B^{-1}$ (K)	$A_6^6\langle r^6\rangle k_B^{-1}$ (K)	$H_{exch}\mu_B k_B^{-1}$ (K)	Reference
−420	−25	1	6	240	Sankar et al. (1975)
−180	-	-	-	200	Buschow et al. (1974a)

about one third of that in $SmCo_5$. As mentioned above, K_1 in these compounds without 4f electrons represents the Co contribution alone (Buschow et al., 1974a). The contribution of the R sublattice can therefore be obtained by subtraction of the values for YCo_5 from those for $SmCo_5$. For Sm^{3+} however where the energy separation between the ground multiplet ($J = \frac{5}{2}$) and the first excited state is small the usual crystal field calculation using operator equivalents cannot be employed. The more general approach using the tensor operator technique developed by Racah (1943) has to be applied. As a result of the crystal field calculations the importance of the second order crystal field parameter can be seen from table 14.7 where the two sets of results from Sankar et al. (1975) and Buschow et al. (1974a) are compared. The direction of the easy axis (c-axis or basal plane) is mainly determined by the sign (negative or positive) of the second order term of the reduced matrix element (see Sankar et al., 1975). In conclusion it can be said that the high uniaxial anisotropy of $SmCo_5$ and its temperature dependence can be explained in terms of the single ion anisotropy of Sm^{3+} which arises through the combined action of the crystal fields and exchange fields and involves a mixing of the excited multiplet levels into the ground level ($J = \frac{5}{2}$) (Buschow et al., 1974a).

As in many intermetallics with Sm it is found that in $SmCo_5$ the moments of Sm and Co couple parallel as if Sm were a heavy lanthanide. Malik et al. (1976) find that, as a consequence of the low lying first excited multiplets, crystal fields admix these levels which leads to the appearance of such behaviour. The coupling is however temperature dependent again becoming ferrimagnetic for $T > 300$ K as found for a normal light lanthanide if only an exchange field is considered. This crossover temperature varies sensitively with changes in the crystal field parameters. Streever (1975) performed NMR investigations to obtain the Sm hyperfine field in $SmCo_5$. The observed value of 3.42×10^6 G (342 T) agrees exactly with the expected "free ion" value that one calculates only for the ground state $J = \frac{5}{2}$. Taking into account the mixing of the excited J-levels into the ground multiplet an increase of 8% of the hyperfine field is expected. This increase is offset by the reduction of the Sm hyperfine field due to conduction-electron polarization effects. Barbara and Uehara (1976) have shown that the anisotropy in $SmCo_5$ also depends on Sm–Co exchange.

Investigations on the pseudobinary systems of RB_5 compounds with Th have revealed a number of extraordinary effects such as preferential site occupation

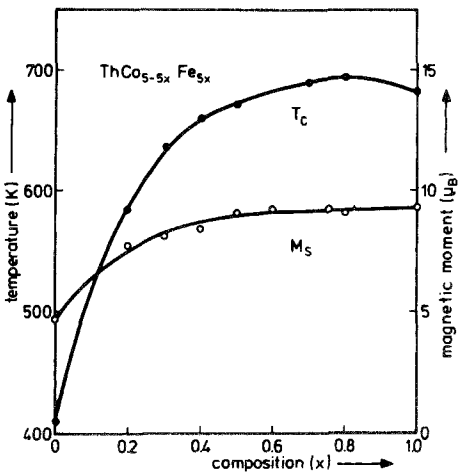

Fig. 14.99. Saturation moments per formula unit at 4.2 K and Curie temperatures as a function of composition for the $Th(Fe, Co)_5$ pseudobinaries (van Diepen et al., 1971).

and even complex spin arrangements of B-moments. Magnetic and X-ray diffraction measurements have been performed on magnetically aligned powders (Rothwarf et al., 1973; Elemans and Buschow, 1976). Laforest and Shah (1973), Elemans and Buschow (1974), Elemans et al. (1975), Buschow et al. (1975b) and Elemans and Buschow (1976) have performed neutron diffraction investigations. Mössbauer investigations on ^{57}Fe have been performed by van Diepen et al. (1971). The study of systems with Th presents the only possibility of performing Mössbauer investigations of Fe-rich RB_5 compounds since the other R elements do not form RFe_5.

In the system $Th(Fe_xCo_{1-x})_5Fe$ has a preference for the (g) site $(\frac{1}{2}, 0, \frac{1}{2})$ and Co dominates the (c) site $(\frac{1}{3}, \frac{2}{3}, 0)$ (Rothwarf et al., 1973; Elemans and Buschow, 1974). The saturation moments and ordering temperatures are shown in fig. 14.99. Ferromagnetism is found for $x \leqslant 0.6$ with an easy c-axis. However in compounds with $x = 1$ and $x = 0.8$ antiferromagnetic components are also present (Elemans and Buschow, 1974), see fig. 14.100. The anisotropy field decreases sharply with increasing x (Rothwarf et al., 1973). In $Th(Co_xNi_{1-x})_5$ ferromagnetism prevails for $x \geqslant 0.8$ and ferrimagnetism was reported for $0.5 \leqslant$

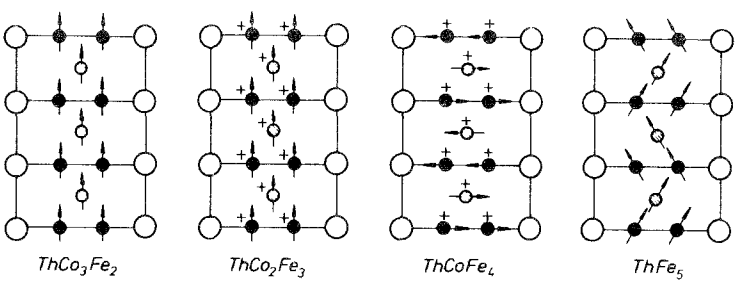

Fig. 14.100. Magnetic structures in the system $Th(Fe, Co)_5$. The ferromagnetic and antiferromagnetic components perpendicular to the c-axis are arbitrarily drawn normal to and in the plane of the paper, respectively. The normal component is indicated by a + sign (Elemans and Buschow, 1974).

$x \leq 0.8$ with an easy direction parallel to the c-axis (Buschow et al., 1975b). In both systems $Th(Fe, Co)_5$ and $Th(Co, Ni)_5$ there are similar deviations from a strictly random distribution of B atoms on the 2(c) sites (Elemans and Buschow, 1976).

Neutron diffraction on the system $Y_xLa_{1-x}(Co_yFe_{1-y})_5$ has revealed an easy c-axis (Barrick et al., 1974). The intrinsic coercivity and the saturation induction decrease on substituting Fe for Co. Other pseudobinary systems such as $Th(Co, Ni)_5$, $Th(Fe, Ni)_5$, $La(Co, Cu)_5$ and $Y(Co, Ni)_5$ will be described in section 4.

3.7. *The* RB_3 *and* R_2B_7 *compounds*

These two stoichiometries with 3 and 3.5 B-atoms per R atom can be derived from the $CaCu_5$ structure (see subsection 3.2) by suitable replacements resulting in unit cells with approximately the same a lattice parameter values as the $CaCu_5$ structure but giant c-values of 24.35 and 36.21 Å for YCo_3 and Y_2Co_7 for example as compared with 4.95 Å for YCo_5. Although these derived structures are mostly rhombohedral they are usually described in hexagonal coordinates. The R_2Ni_7 compounds with Pr, Nd, Gd, Tb and Dy present both rhombohedral and hexagonal forms. $CeNi_3$ and Ce_2Ni_7 occur only in hexagonal forms. The RB_3 stoichiometry occurs for rare earths in combination with Ni, Co as well as Fe, whereas the R_2B_7 occurs only for Ni and Co. For this reason the RB_3 compounds have been more thoroughly investigated since more compounds are available and Mössbauer studies can readily be performed on the RFe_3 compositions.

The RNi_3 and R_2Ni_7 compounds have relatively low ordering temperatures compared with the other RB_3 and R_2B_7 compounds. See figs. 14.71, 14.72 and 14.73. The Ni moment is very small, many experiments not being sufficiently sensitive to reveal it. The RNi_3 and R_2Ni_7 compounds have been investigated by Paccard and Pauthenet (1967) and Lemaire et al. (1967a) respectively. Though this Ni moment seems to be larger when R is magnetic its presence is not due to the R moment. YNi_3 and Y_2Ni_7 possess a moment of 0.05 and 0.06 μ_B per Ni atom respectively. In combination with the heavy lanthanides the R and Ni moments appear to be ferrimagnetically coupled. On the other hand the situation is not so clear since non-collinear moment arrangements have been detected in RNi_3 compounds by means of neutron diffraction (Rossat–Mignod and Yakinthos, 1971; Paccard et al., 1971; Yakinthos and Paccard, 1972). Though YNi_3 definitely possesses a moment and shows ferromagnetic ordering it is not unambiguously established that all other RNi_3 compounds possess a moment on Ni. A non-collinear arrangement of R moments would lead to a measured saturation moment smaller than the expected gJ value. This could all too readily be attributed to a ferrimagnetically coupled Ni moment if the possibility of non-collinearity is not taken into account. The neutron diffraction measurements of Rossat–Mignod and Yakinthos (1971) revealed no Ni moment and they concluded that the 3d band is full. The collinearity or non-collinearity depends on the ratio of crystal field to exchange energy. RNi_3 with Pr, Ho and Tm are collinear and Nd, Tb, Er in RNi_3 form non-collinear magnetic structures. Ce_2Ni_7

has a lower Curie temperature than Y_2Ni_7 (fig. 14.71) and the moment is also lower (Lemaire et al., 1967a). Thus the Ce appears to be quadrivalent but the extra electron does not appear to fill completely the Ni 3d band since ordering does not disappear.

The RCo_3 compounds have been reported by Lemaire (1966b) who detected compensation points for some of the heavy lanthanides which is in line with the expected ferrimagnetism. YCo_3 has a Curie point at 301 K whereas $CeCo_3$ has a lower value of 78 K. For R–Co systems this 1 : 3 stoichiometry is a particularly sensitive one in which the 3d moment is only just stable and does not yet possess the largest observed value of 1.7 μ_B. In YCo_3 the 3d moment is 1.4 μ_B but introduction of electrons into the 3d band rapidly lowers the moment and splitting of the band is decreased. This can be done by replacing the Co by Ni (see subsection 4.2) or Y by Ce. This appears to be the case here where Ce is non-magnetic, therefore quadrivalent, and able to supply the electron to contribute to the filling of the 3d band. The Co moment in $CeCo_3$ is 0.07 μ_B. Another striking example (Elemans et al., 1975) of such behaviour is given by comparing La_2Co_7 with the isostructural Th_2Co_7. The former has a moment of about 1 μ_B per Co whereas Th_2Co_7 is a Pauli paramagnet. The extra electron from Th which is quadrivalent appears to enter the 3d band of Co and render it non-magnetic.

A simple band model for the 3d band of RCo_3 and R_2Co_7 is however not sufficient since the Co moments have different magnitudes depending upon which sites they occupy. This was established for various RCo_3 compounds by neutron diffraction (Schweizer and Yakinthos, 1969). Krén et al. (1969) have presented corresponding results for YCo_3 and Y_2Co_7 (fig. 14.101) which emphasize how sensitive the magnetic properties are in these stoichiometries: the Co moment varying from site to site and also the average moment doubling its value on taking the small step from 1 : 3 to the 1 : 3.5 stoichiometry. In addition it was inferred from the results of Schweizer and Yakinthos (1969) that those sites which have a large number of nearest R neighbours possess correspondingly larger moments, a part of which being induced by the R moments. The anisotropy of the RCo_3 and R_2Co_7 series is extremely high. The studies of Buschow (1973a) on magnetically aligned powders of R_2Co_7 compounds revealed

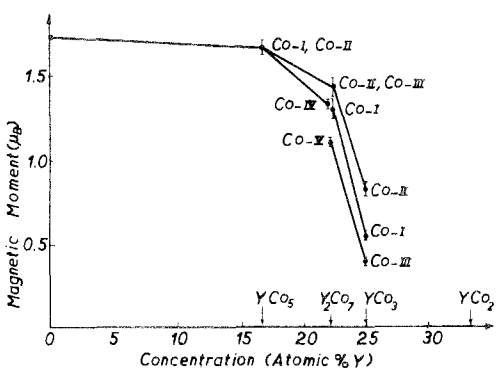

Fig. 14.101. Magnetic moments associated with the different Co sites in Co, YCo_5, Y_2Co_7, and YCo_3 (Krén et al., 1969).

easy axes and anisotropy fields as large as 200 kOe for Sm_2Co_7 for example. This shows that these compounds have anisotropy values comparable to those of the RCo_5 compounds.

The RFe_3 compounds have received very much attention, especially in recent years as regards Mössbauer investigations. The Curie temperatures have been determined by Salmans et al. (1968) by means of initial susceptibility measurements, see fig. 14.73. The Fe moments are less sensitive to the rare earth partner than the Co moments in RCo_3 or Ni moments in RNi_3. Compensation points have been detected for some heavy lanthanides such as in $HoFe_3$ (Simmons et al., 1973) for which ferrimagnetism was inferred as may be expected. The magnetic structure was also determined by neutron diffraction where it was found that the moments lie in the basal plane. Molecular field calculations yield for the exchange coefficients $n_{FeFe} = 115$, $n_{HoHo} = 2$ and $n_{HoFe} = 21$ which shows that the 3d–3d interactions are by far the strongest. In connection with compensation points Nikitin et al. (1975) detect an anomaly in the thermal expansion at the compensation temperature (239 K) of $ErFe_3$ in the presence of a magnetic field. The anomaly is attributed to the change in magnetostriction due to spin reorientations at the compensation temperature with non-collinear spin structures in the presence of a field.

Numerous investigations have been performed by using Mössbauer techniques which can reveal moment orientations in the RFe_3 compounds. In $HoFe_3$ a spin reorientation occurring at 85 K from the a-axis to the b-axis both within the basal plane is attributed to a competition between the two inequivalent R sites in fixing the easy direction of magnetization (Arif et al., 1974). Mössbauer measurements (Arif et al., 1975a) reveal an easy b-axis in YFe_3 and $YbFe_3$ whereas $ErFe_3$ has an easy c-axis for all temperatures despite a marked change in character of the spectrum between 4.2 K and 77 K. Local dipole field calculations in conjunction with hyperfine parameters were used by Arif et al. (1975b) to infer the easy directions in various RFe_3 compounds. It was shown that at 77 K $GdFe_3$ and $HoFe_3$ have an easy a-axis and $ErFe_3$ has an easy axis either along or close to the c-axis. The case of $DyFe_3$ is however more complicated, it being suggested that the easy axis may lie in the a–c plane at an angle of 26° to the basal plane. In $ErFe_3$ (van der Kraan et al., 1975) a magnetic phase transition is observed at 50 K. The magnetization is reported to turn from the b-axis above 50 K into the c-axis for temperatures below 50 K. This appears to be in contradiction to the results of Arif et al. (1975b) for $ErFe_3$. In general very complex Mössbauer spectra can be observed due to the three inequivalent Fe sites.

The substitution of Th into RFe_3 has been performed to investigate the effects of increasing the electron concentration since Th is quadrivalent. The effect in the system $(Y, Th)Fe_3$ (Kunesh et al., 1975) is to introduce some complex spin structures with associated magnetic anomalies and to decrease the moment per formula unit. This decrease suggests that YFe_3 has, say, an almost full spin-up 3d sub-band and that the excess electron from Th populates the spin-down 3d sub-band (Narasimhan et al., 1975). On the other hand

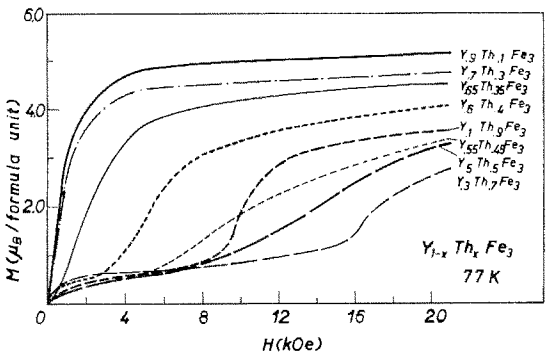

Fig. 14.102. Magnetization isotherms of $(Y, Th)Fe_3$ at 77 K (Kunesh et al., 1973a).

Mössbauer investigations of $Dy(Fe, Ni)_3$ (Tsai et al., 1974) have shown that the spin-up sub-band is not full in $DyFe_3$. Narasimhan et al. (1975) also concluded that the anomalous transitions (see fig. 14.102) between 35 and 90% Th are not due to a change in anisotropy. The magnetic structure is such that Fe moments on some sites are ferromagnetically coupled in the whole ordered temperature range whereas Fe moments on other sites couple antiferromagnetically below the transition temperature. Kunesh et al. (1973a) had explained the anomalous magnetic behaviour in $(Y, Th)Fe_3$ as well as in $(Lu, Th)Fe_3$ in terms of changes with temperature and composition of the detailed couplings via Friedel oscillations whose wavelength decreases with increasing Th content. $ThFe_3$ however is a typical ferromagnet (Greedan, 1971a). Anomalous behaviour is also observed in other $(R, Th)Fe_3$ systems (Kunesh et al., 1973b) which was also accounted for in terms of Friedel oscillations of d-band polarizations. The anomalous spin structures in $(Gd, Th)Fe_3$ occur for more than 50% Gd (Greedan, 1971a).

In the $R(Fe, Co)_3$ systems with Dy and Ho a shallow maximum in the 3d moment was found for about 30% and 50% Co content respectively (Narasimhan et al., 1973) which was interpreted in terms of the filling of a rigid 3d band in the same way as has been done for the binary (Fe, Co) (subsection 3.1) and pseudobinary $Y(Fe, Co)_2$ (Taylor, 1969) systems. However in the case of the (Fe, Co) system neutron diffraction results (Collins and Forsyth, 1963) have shown that the Co moment remains constant and that the Fe moment goes through a maximum of 3 μ_B. It may be that in the $R(Fe, Co)_3$ system a similar behaviour is to be found. The shallowness of the maximum is due to the fact that the Co-rich samples have a part of their moment induced by the R moments. Thus in the $Y(Fe, Co)_3$ system (Taylor and Poldy, 1975) the moment drop from the maximum value to that of YCo_3 is much larger (fig. 14.114). Arif et al. (1975c) studied the $Dy(Fe, Co)_3$ and $Y(Fe, Co)_3$ systems by means of Mössbauer measurements and detected a maximum in T_C for both series at about 40% Co content (fig. 14.103) and also found a change in the magnetization direction as a function of the composition. The results were interpreted with the rigid band model. The differences in the ordering temperatures of the Y and Dy systems indicate that the R–3d and R–R interactions are considerably smaller than the 3d–3d interactions. It also appears that the Fe–Co interactions are stronger than those between Fe–Fe and Co–Co in the intermediate composition range. They

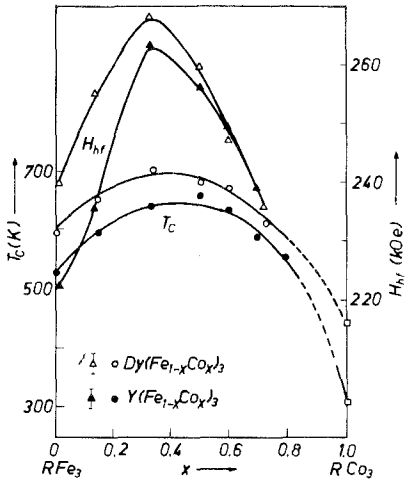

Fig. 14.103. The ordering temperatures and average ^{57}Fe hyperfine fields of the Y(Fe, Co)$_3$ and Dy(Fe, Co)$_3$ pseudobinaries (Arif et al., 1975c). The values for YCo_3 and $DyCo_3$ were taken from Lemaire et al. (1967b).

detect also a maximum in the average hyperfine field at 33% Co content suggesting that the hyperfine field changes are due mainly to the core polarization terms arising directly from the d-moment changes in the Fe atoms as a result of the rigid band model.

The Gd(Co, Ni)$_3$ and Gd(Fe, Ni)$_3$ systems have been studied by Greedan (1971b). The measured 3d moment drops linearly in the former system from 1.4 μ_B at the Co end to zero for $GdNi_3$. The results could not be rationalized within the rigid band model. As pointed out at the beginning of this section the existence of a Ni moment in RNi_3 is not clear. The choice of extrapolation methods for obtaining a measure of the saturation moment seriously affects the deduced Ni moment value. Burzo (1972c) for example could detect a Ni moment in $GdNi_3$ of 0.16 μ_B in the ordered state and 0.97 μ_B in the paramagnetic state. Greedan (1971b) detects a linearity of the Curie temperature as a function of 3d moment for high Fe and Co contents. It is deduced from the results that a rigid band model may be appropriate for the Gd(Co, Ni)$_3$ system but not for the Gd(Fe, Ni)$_3$ system. Arif and Bunbury (1976) conclude from measurements of Dy(Fe, Ni)$_3$ and Y(Fe, Ni)$_3$ in conjunction with considerations of the (Fe, Co) and (Fe, Ni) systems that Fe tends to be less localized when partially replaced by a magnetic ion than by a non-magnetic ion. It is also concluded that the immediate environment of the Fe atoms is especially important in determining the magnetic behaviour of these systems and that the 3d sublattice moment is to a large extent independent of the crystalline structure and the presence or absence of a rare earth. Some further results of pseudobinary systems with R_2B_7 and RB_3 stoichiometries are presented in section 4 where the Y(Co, Ni)$_3$ and Y_2(Co, Ni)$_7$ systems will be discussed.

3.8. R_6(Fe, Mn)$_{23}$

The Th_6Mn_{23} structure is a cubic crystal structure with 116 atoms per unit cell and 5 crystallographic sublattices. Six R atoms form an octahedron which is

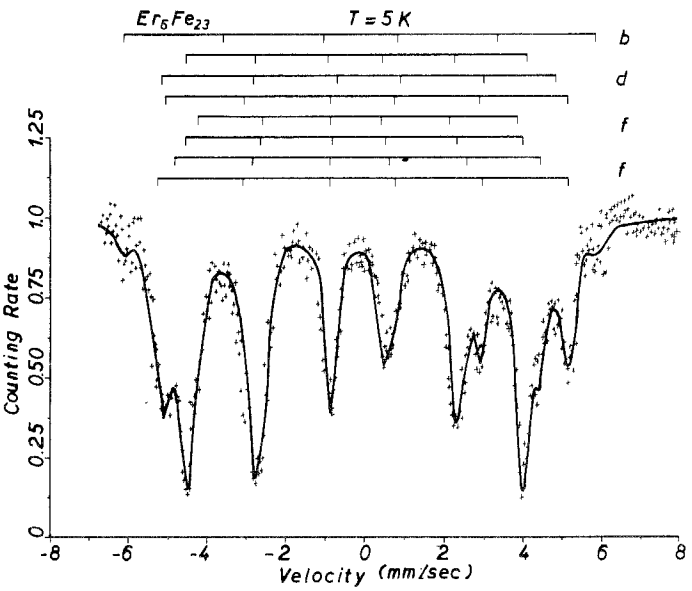

Fig. 14.104. The Mössbauer spectrum of Er_6Fe_{23} (Wiesinger, 1974).

surrounded by 50 3d atoms. A collection of these units forms a face centred cubic unit cell (Florio et al., 1952). This structure forms for R–3d intermetallic compounds with Fe and Mn only. Generally the R and B moments in R_6B_{23} compounds couple antiparallel for the heavy lanthanides, as found in other stoichiometries. An exception however is Gd_6Mn_{23}, which appears to be ferromagnetic (de Savage et al., 1965). From Mössbauer experiments it is known that in Y_6Fe_{23} the four non-equivalent lattice positions of Fe possess several different fields (Kirchmayr, 1969a; Wiesinger, 1974; Morariu et al., 1974). This result is consistent with neutron diffraction on Ho_6Fe_{23} where two different Fe-moments 2.4 and 1.9 μ_B were found (O'Keefe et al., 1970). Dipole field calculations have been performed to determine the local field at the iron sites (Wiesinger, 1974). Because an easy axis is present the atoms in a crystallographic sublattice are no longer magnetically equivalent. In the case of a [101] easy axis this gives rise to eight superposed 6-line spectra (fig. 14.104). For Y_6Fe_{23} (Gubbens et al., 1974) and Dy_6Fe_{23} (Wiesinger, 1974) [001] is the easy axis of magnetization. This does not conform with the experimental data reported for Y_6Fe_{23} (Morariu et al., 1974).

The existing pseudobinary systems $R_6(Fe_{1-x}Mn_x)_{23}$ have been investigated recently (Kirchmayr and Steiner, 1971; Hilscher et al., 1971; Hilscher, 1974; Bechman et al., 1976), since it was known that a disappearance of magnetic order occurs in $Y_6(Fe, Mn)_{23}$ (Kirchmayr, 1968). This Y system is discussed in section 4. For x values $0.4 \leq x \leq 0.7$ no magnetic order in the Y system could be detected at 4 K and for $x = 0.5$ and $x = 0.55$ the disappearance of long range magnetic order could be established down to 30 mK (Goblirsch, 1976).

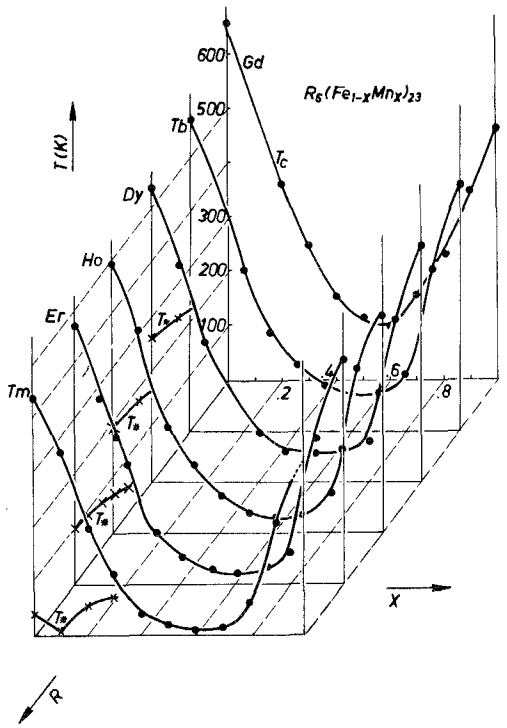

Fig. 14.105. The Curie temperatures T_C and compensation points T_* of the various $R_6(Fe, Mn)_{23}$ systems (Hilscher, 1974; Kirchmayr and Steiner, 1971).

In the case where R is a magnetic atom magnetic order exists for the whole concentration range. The variation (fig. 14.105) of T_C with x is similar for systems $R_6(Fe, Mn)_{23}$ (R = Gd, Tb, Dy, Ho, Er, Tm), and does not deviate much from that for the Y system. On the other hand the variation of the magnetic moment (fig. 14.106) becomes rather complex and has not been understood until now.

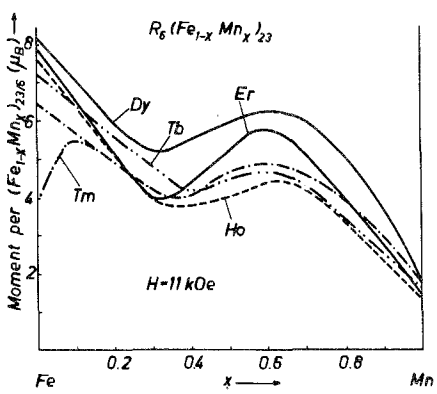

Fig. 14.106. The variation of the average 3d moment in the various $R_6(Fe, Mn)_{23}$ systems (Hilscher et al., 1971; Hilscher, 1974).

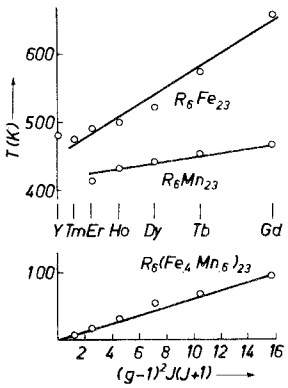

Fig. 14.107. The variation of the ordering temperatures of R_6Fe_{23}, $R_6(Fe_{0.4}Mn_{0.6})_{23}$ and R_6Mn_{23} as a function of the de Gennes factor (Hilscher, 1974).

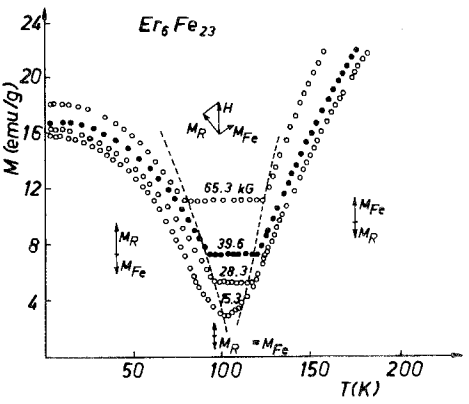

Fig. 14.108. The thermal variation of magnetization of Er_6Fe_{23} in the region of the compensation point (Hilscher, 1974).

In fig. 14.107 the Curie temperatures of R_6Fe_{23}, R_6Mn_{23} and $R_6(Fe_{0.4}Mn_{0.6})_{23}$ (which has the lowest T_C within the pseudobinary system) are plotted as a function of the de Gennes factor. This figure demonstrates the dominance of the 3d-exchange for R_6Mn_{23} and R_6Fe_{23}. For compounds in the pseudobinary system with $x = 0.6$ magnetic order is predominantly due to 4f-exchange.

The magnetization versus temperature curves (M, T) of the Fe and Mn-rich ternaries can be analysed in terms of the Néel molecular field model, whereas for compounds with $0.3 \leq x \leq 0.7$ the simple two-sublattice model is not sufficient. According to the model of Clark and Callen (1968) already discussed in subsection 3.1 the magnetization is predicted to be temperature independent in the region of the compensation point if the applied field is strong enough to produce a non-collinear spin structure. Here the magnetization in the vicinity of compensation point is field dependent only. From the field dependent magnetization (fig. 14.108) of Er_6Fe_{23} the molecular field coefficient $n_{R\text{-}3d}$ can be determined from experimental values of M as a function of applied field. The derived $n_{R\text{-}3d}$ values are approximately 86 kG/μ_B. From molecular field calculations in terms of the Néel model the values $n_{3d\text{-}3d} = 572$, $n_{R\text{-}3d} = 86.2$ and $n_{R\text{-}R} = 28.6$ kG/μ_B were derived, which demonstrates the successful application in the boundary compounds (Hilscher, 1974). On the other hand with such a simple localized model it is not possible to explain the moment variation in these ternaries. Therefore more detailed investigations such as pressure experiments (Hilscher et al., 1977), specific heat (Bechman et al., 1976) and resistivity measurements (Gratz and Kirchmayr, 1976) on the simpler $Y_6(Fe, Mn)_{23}$ system should clarify the magnetic break-down which is the key for understanding these systems.

4. Borderline cases

The substitution of magnetic ions into non-magnetic intermetallics can have various effects. One possibility is that the magnetic ions are simply present in a dilute form in the non-magnetic matrix. Another more interesting variety is the type of behaviour found in substitution systems where a magnetic impurity activates the non-magnetic matrix into adopting a moment and taking part in magnetic ordering, for impurity concentrations above some critical value. Such behaviour is found in systems like (Pd, Fe) where the Fe atoms induce a moment on the Pd neighbours (Martin, 1967). Pure Pd shows basically no magnetic ordering but is susceptible to influences from magnetic impurities. Magnetic measurements on (Pd, Fe) reveal giant moments arising from Fe impurity moments coupled with the induced Pd moments around the impurity. It may be that palladium and YCo_2 are to some extent analogous since both appear to have the Fermi level just at the top of the 4d and 3d bands respectively. However this analogy cannot be taken too rigorously since the situation in YCo_2 is even today not yet satisfactorily resolved. The next section will deal with the YCo_2 problem and the various magnetic substitutions which can induce a moment on the Co atoms. This is to be followed by descriptions of some other cases such as $Y(Co, Ni)_5$ and $Y(Co, Ni)_3$ etc. where the 3d moments drop to small values or even disappear within a pseudobinary system. Finally in this section the fascinating phenomenon of the absence of magnetic ordering in the middle of the $Y_6(Fe, Mn)_{23}$ system is discussed.

4.1. *The* YCo_2 *problem*

YCo_2 is one of the most enigmatic of the rare earth intermetallic compounds. The problem of why Co apparently possesses no magnetic moment in this compound has fascinated research workers for a long time. The lack of a moment or magnetic ordering in YCo_2 has relatively recently been accepted. This however has been with reluctance since elemental cobalt is one of the most powerful ferromagnets. Antiferromagnetic arrangements of Co moments in YCo_2 have often been invoked to explain the apparent lack of moment. The problem has been made complicated by the fact that YCo_2 is difficult to prepare in the pure state free of other phases. The neighbouring phases such as YCo_3 are ferromagnetic and small quantities of such impurities can give rise to samples showing ordering temperatures which have often been all too readily accepted as being characteristic of YCo_2. In addition more frequent reports have arisen in the last few years of the impossibility of preparing the 1 : 2 stoichiometry and of excess Y being required before single phase samples can be achieved. Such samples have a composition closer to $YCo_{1.8}$. It has been suggested in the past that YCo_2 is ferromagnetic (Wallace and Skrabek, 1963; Farrell and Wallace, 1966; Abel and Craig, 1968; Piercy and Taylor, 1968) and even antiferromagnetic (Taylor et al., 1966). At present it has been established with reasonable certainty that YCo_2 is basically a Pauli paramagnet (Lemaire and Schweizer, 1966;

Lemaire, 1966a,b; Burzo, 1972d; Taylor, 1971a; Steiner and Ortbauer, 1974). $LuCo_2$ having no 4f moment shows behaviour very similar to that of YCo_2 and has also been established to be a Pauli paramagnet (Burzo and Lazar, 1976; Beille et al., 1975). The susceptibility of YCo_2 and $LuCo_2$ is however not quite temperature independent as expected from a typical Pauli paramagnet, but shows a broad maximum in the temperature range between 100 and 300 K. Supporting the view that no magnetic ordering occurs is the fact that no anomalies exist in the lattice parameter (F. Givord et al., 1972) or in the specific heat (Bloch et al., 1972). A much used approach in tackling the YCo_2 problem has been to replace either Y or Co (or both) with magnetic elements in order to investigate how a moment can be induced on Co since RCo_2 compounds with magnetic lanthanides are known to contain magnetic moments on Co (subsection 3.4).

It appears (subsection 3.4) that a moment can be induced on Co as a result of magnetic substitutions. This fact has lead to the concept of an exchange enhanced paramagnetism (Bloch and Lemaire, 1970). The exchange enhancement factor obtained for RCo_2 from magnetic measurements is about 10 and from specific heat measurements (Bloch et al., 1972) the factor obtained is approximately 9. The maximum in the susceptibility has been analysed within two models. One of them is that of Burzo and Lazar (1976) using the Fermi liquid model of Landau. Good agreement was obtained between the experimental and theoretical curves. The other approach (Bloch et al., 1975) makes use of the Stoner–Wohlfarth model. It is assumed here that the density of states of YCo_2 is not quite high enough to give rise to ferromagnetic ordering (Voiron et al., 1974). The induced moment in RCo_2 is approximately $1\,\mu_B$ and this may mean that one hole per Co atom is available in the 3d band and this band is polarized by the magnetic lanthanide. The high field magnetization data (Bloch et al., 1975) of YCo_2 are plotted in fig. 14.109. From these curves it follows that the parameter $B(T)$ in the Stoner–Wohlfarth theory (eq. (14.25)) is negative for $T < 200$ K and positive for higher temperatures. The maximum in the susceptibility of YCo_2 is thus explained. From the temperatures of the first order phase transitions in RCo_2 and with the assumption that the Co-moment is saturated below the ordering temperatures in the RCo_2 compounds, a critical field for the

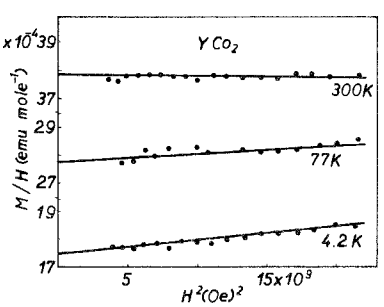

Fig. 14.109. High field magnetization results of YCo_2 at various temperatures (Bloch et al., 1975).

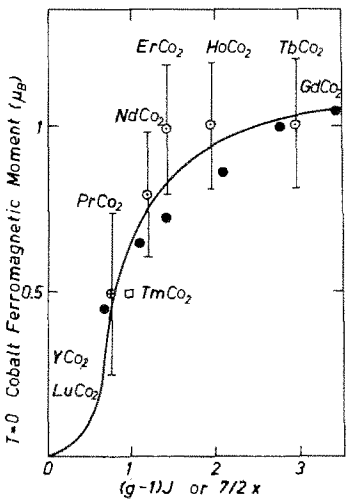

Fig. 14.110. The mean ferromagnetic moment of cobalt in RCo_2 (⊙ Moon et al., 1965; ⊕ Schweizer, 1967; □ Déportes et al., 1974) and $Gd_xY_{1-x}Co_2$ (● Lemaire and Schweizer, 1966) plotted against the mean spin. The full line is a guide for the eyes. Beille et al. (1975).

establishment of ferromagnetism is estimated to be 1.42 MOe. This critical field can be supplied by the molecular field from R ions. From the estimation within the molecular field model the field necessary for the appearance of a Co-moment in (Gd, Y)Co_2 is 1.57 MOe where it is assumed that a Co atom with less than two Gd nearest neighbours has no moment. The specific heat measurements on $HoCo_2$ and $TbCo_2$ by Voiron et al. (1974) show that the contribution of Co to the magnetic entropy is considerably less than that expected from a spin $\frac{1}{2}$ state. A band model is thus more suitable for YCo_2 in which it is on the verge of becoming ferromagnetic.

Beille et al. (1975) have found a correlation for the Co-moment as a function of the factor $(g-1)J$ and $\frac{7}{2}x$ in the systems RCo_2 for various lanthanides, and $(Gd_xY_{1-x})Co_2$ for increasing Gd concentrations respectively, see fig. 14.110. This shows the equivalent effects of the exchange fields in the two systems for inducing a moment on Co. Saturation appears to be approached for Co moments a little in excess of 1 μ_B. A curve which cuts the abscissa at 0.35 is perhaps more realistic than one going through the origin at least for the (Gd, Y)Co_2 system if it is assumed, as above, that the substitution of Gd into YCo_2 does not give rise to a moment on Co until at least two Gd nearest neighbours are present. The critical concentration for this is about 10% Gd.

It is established that the rigid band model is insufficient in these systems. The disappearance of a Co moment must be connected with the crystalline state since amorphous YCo_2 shows a moment of 1.6 μ_B. On the other hand $GdCo_2$ shows in the amorphous state 1.4 μ_B/Co. In addition grinding can cause a rise in the susceptibility of YCo_2 by a factor of 3. This is due to the introduction of lattice imperfections (Steiner and Ortbauer, 1974). The Jaccarino–Walker model which takes into account the various surroundings of a Co atom in the region of

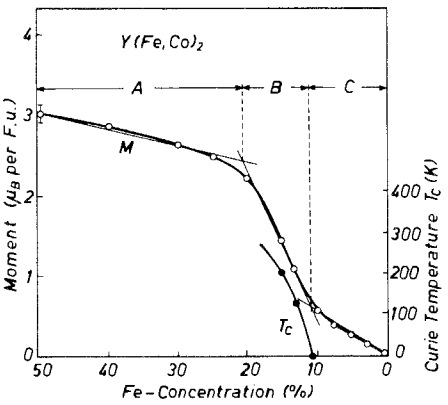

Fig. 14.111. The variation of the magnetic moment and Curie temperature in the $Y(Fe, Co)_2$ system (Steiner and Ortbauer, 1974).

the critical concentration shows that, after saturating the ferromagnetic regions or paramagnetic clusters, a high susceptibility occurs. In YCo_2 the susceptibility is field independent. Pressure experiments on $(Gd, Y)Co_2$ support the assumption of an exchange enhanced paramagnetic susceptibility (Voiron et al., 1973). Burzo and Lazar (1976) report a moment on Co in the paramagnetic state which is consistent with the results of Tsuchida et al. (1975) on $(Gd, Y)Co_2$ at high Gd concentration. In the ordered state of this system Burzo (1975b) finds ferrimagnetic order up to 60% Y. The magnetization curves can be well explained with the Néel model. A conclusion is that Co shows both localized as well as itinerant properties. NMR measurements on Y^{89} in $Y(Fe, Co)_2$ by Oppelt and Buschow (1976) show various hyperfine fields on Y depending on the Fe–Co environment around Y. Analogous to the $(Gd, Y)Co_2$ system (Lemaire and Schweizer, 1966; Lemaire, 1966b) where for less than 10% Gd no magnetic ordering is detected down to 2 K, i.e. the Gd–Gd or Gd–Co interactions are too weak to give rise to long range order, the $Y(Fe, Co)_2$ system likewise shows no ordering down to 4 K for Fe concentrations less than or equal to 10% (Steiner and Ortbauer, 1974), see fig. 14.111 and fig. 14.112. The magnetization character changes at 10% Fe, the samples with lower Fe-concentration showing no tendency to saturate. The concentration dependence of magnetic moment can be divided into three regions. In region A each Fe atom has at least one Fe nearest neighbour. In region C, i.e. up to 10% Fe, the probability of finding two Fe atoms as nearest neighbours is low. Here there is a linear increase of the magnetization in 65 kOe as a function of concentration. From this is calculated a moment of 2.74 μ_B per Fe atom. This agrees well with measurements of Burzo (1971), who determined 2.8 μ_B for the Fe moment in paramagnetic YFe_2. Although the picture is strongly localized and therefore only a first approximation to reality it seems that the interaction of Fe atoms is only possible when they are nearest neighbours. Associated with this is the presence of Fe–Co and Co–Co interactions which cause a rapid rise in the average moment in region B.

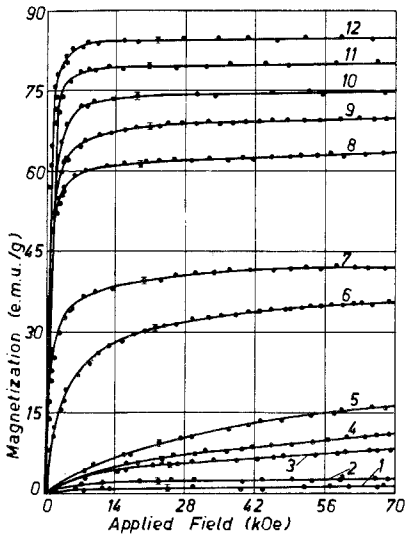

Fig. 14.112. Magnetization curves at 4.2 K for $Y(Fe, Co_{1-x})_2$ (1) $x = 0.00$, (2) $x = 0.025$, (3) $x = 0.05$, (4) $x = 0.075$, (5) $x = 0.10$, (6) $x = 0.13$, (7) $x = 0.15$, (8) $x = 0.20$, (9) $x = 0.25$, (10) $x = 0.30$, (11) $x = 0.40$, (12) $x = 0.50$. (Steiner and Ortbauer, 1974).

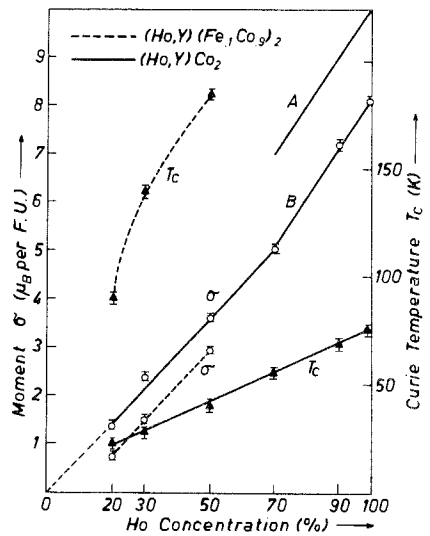

Fig. 14.113. Concentration dependence of the saturation moment and Curie temperature of (Ho, Y)Co_2 and (Ho, Y)$(Fe_{0.1}Co_{0.9})_2$ (Steiner and Ortbauer, 1975). Line A shows the expected contribution to σ from Ho alone. The parallel displacement of A from B indicates that the Co moment is initially constant upon dilution of Ho by Y.

Complementary to these experiments are the investigations by Steiner and Ortbauer (1975) of the systems (Ho, Y)Co_2 and (Ho, Y)$(Fe._1Co._9)_2$, see fig. 14.113. With increasing Ho content the Curie temperatures and moments rise linearly. Ignoring the crystal field effects of Ho this system is analogous to (Gd, Y)Co_2. Increasing Ho concentration causes a polarization of the Co matrix. Down to 1.8 K for Ho contents less than or equal to 10% no spontaneous order is detected and also no Curie–Weiss behaviour for $T < 300$ K. Introduction of Ho has only a small influence upon the 3d moment. The moment rises linearly for Ho substitutions from 20% to 50% in (Ho, Y)Co_2. This is also the case in (Ho, Y)$(Fe_{0.1}Co_{0.9})_2$ but the two curves are displaced from one another by 0.73 μ_B. Attributing this to localized Fe atoms leads to a moment per Fe atom which is too large to be accepted. The displacement is therefore due in part to Co moments. The large displacement of T_C values is also attributed in part to the appearance of Co moments.

In conclusion it can be said that Fe in these systems is relatively strongly localized whereas Co shows more band-like behaviour. Upon substituting magnetic components into YCo_2 long range ordering does not occur immediately, but only after a critical concentration is reached. This is connected with the importance of the local environment of an atomic site. The substitution of Y by a magnetic lanthanide gives rise to a concentration dependent polarization of the

3d band of Co. It is however not unambiguously established whether the 3d band is just full in YCo_2 with polarization introducing holes, or whether the Fermi level is situated within the 3d band at a position where the density of states is small enough not to split the 3d band. This position of the Fermi level however is probably not at a sharp minimum in the density of states, since the substitution of Ni into YCo_2 would then give rise to the appearance of magnetic ordering which is not the case.

4.2. *The* $Y(Co, Ni)_3$ *and* $Y_2(Co, Ni)_7$ *systems*

The RB_3 and R_2B_7 stoichiometries show an interesting type of behaviour of the 3d moment on substituting Co for Ni. It is known (subsection 3.7) that YNi_3 and Y_2Ni_7 possess a small but nonzero moment even though YNi_5, which has a higher Ni concentration, shows no moment and no ordering. This may be associated with the relative complexity of the crystal structure compared with the $CaCu_5$ structure, where many non-equivalent sites are available to Ni. On the other hand another interpretation for the reappearance of a moment upon increasing the Y content in the order YNi_5, Y_2Ni_7, YNi_3 may be made by assuming a minimum in the density of states as mentioned in subsection 3.3. The valence electrons of Y^{3+} gradually fill the 3d band. When the Fermi level is situated at a minimum the Stoner criterion is not fulfilled and splitting of the 3d spin sub-bands disappears. Further filling of the 3d band then results in a reappearance of the splitting. This is under the implicit assumption that the 3d band has a similar shape for the various stoichiometries. Since they are all derived from the $CaCu_5$ structure this possibility is not to be ruled out. A test of this interpretation is provided by examining the effect of lowering the Fermi level in YNi_3 or Y_2Ni_7 when replacing Ni by Co for example. Such substitutions should result in the disappearance of a 3d moment at a critical Co concentration. The results of Poldy and Taylor (1972b) for the $Y(Co, Ni)_3$ and $Y_2(Co, Ni)_7$ systems at 4.2 K are shown in figs. 14.114 and 14.115.

For completeness the Fe substitution series is also included to show the smoothness of the moment variations as a function of electron concentration even around the 100% Co concentration. The lack of any slope discontinuity is consistent with an interpretation using the rigid band model. YFe_3, though it has been reported with the $PuNi_3$ structure, could not be prepared in this investigation†. 40% Fe could be substituted into Y_2Co_7. Returning to the low moment compositions the magnetic moment behaviour appears to be exactly that expected from the above considerations assuming a minimum in the density of states. However, for a critical discussion of the results, it is necessary to mention how the moments were estimated. The end compounds YNi_3 and Y_2Ni_7 presented no problem since saturation was achieved in low fields. For the other samples (M, H) curves were obtained from pulsed field measurements on powder samples in which the crystallites were free to orient themselves in the applied field. Prepulsing a couple of times was sufficient to obtain reproducible

†The instability of the YFe_3 compound was confirmed by Kunesh et al. (1973a) who reported that a small Th substitution for Y greatly stabilizes this crystal structure.

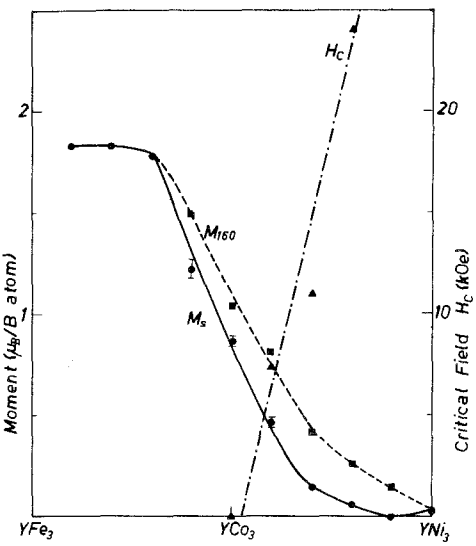

Fig. 14.114. Variation as a function of electron concentration of the spontaneous moment M_s, moment M_{160} at 160 kOe, and critical field H_c of the $Y(Fe, Co)_3$ and $Y(Co, Ni)_3$ systems (Poldy, 1972).

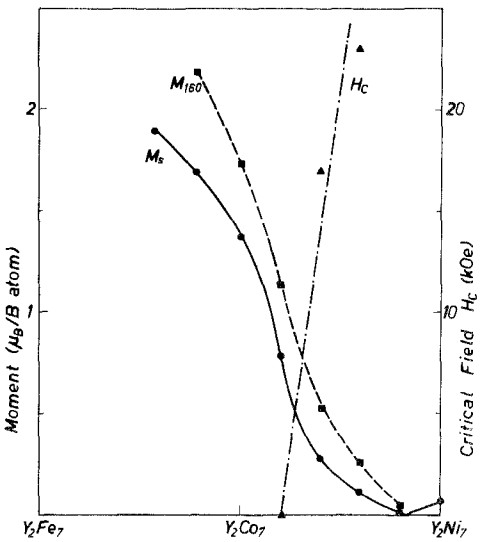

Fig. 14.115. The magnetic characteristics of the $Y_2(Fe, Co)_7$ and $Y_2(Co, Ni)_7$ systems. For explanation of symbols see fig. 14.114 (Poldy, 1972).

results. Fields up to 160 kOe were available. The spontaneous moment was deduced by extrapolating the high field (M, H) curves back to $H = 0$ since it was believed that not only anisotropy but also an additional splitting of the bands due to the applied field was responsible for lack of saturation. Thus an extrapolation procedure up to infinite fields would have given saturation moments in excess of the spontaneous value. The spontaneous moment obtained in this fashion as well as the magnetization at 160 kOe are shown in figs. 14.114 and 14.115. The 20% Co samples showed effectively linear (M, H) curves up to 160 kOe and the spontaneous moment therefore appears to be zero. In addition initial susceptibility measurements down to 4.2 K revealed no ordering temperatures in the 20% Co samples. As shown in the figures the samples with higher Co concentration showed critical field transitions characteristic of after-effect due to a high anisotropy to exchange ratio (see section 5). It could be that extremely high potential barriers hinder the motion of the narrow domain walls to such an extent that the samples with 20% Co are not magnetizable even though they order. Thus it is not yet unambiguously clear that the 20% Co samples really do not order. It is possible that just in these samples the anisotropy is so large that the initial susceptibility shows no visible peak at the Curie temperature. Initial susceptibility measurements on materials with high anisotropy often do not reveal sharp transitions at the ordering temperatures. The samples with 20% Co might have such a large anisotropy compared with exchange that the moment directions are effectively locked in the lattice and not susceptible to external

fields even when ordering is present. In this case these systems would not belong to this section on borderline cases. It is clear that these fascinating systems deserve more attention before a definite interpretation of the apparent 3d-moment disappearance can be made.

4.3. *The* RB_5 *systems with disappearing* 3d *moments*

We discuss here some RB_5 systems with the $CaCu_5$ structure where R is a non-magnetic rare earth metal. The $Y(Co, Ni)_5$ and $La(Co, Ni)_5$ systems (Brouha and Buschow, 1975a) are significantly different from the $Th(Co, Ni)_5$ system in that magnetic ordering and a 3d moment appear relatively early on replacing Ni by Co in the former, whereas ordering appears only for more than 50% Co in $Th(Co, Ni)_5$ (Buschow et al., 1975b). This can be seen from figs. 14.116 and 14.117. This difference between the two systems is due to the fact that Th is quadrivalent and therefore contributes more electrons to the 3d band. In $Y(Co, Ni)_5$ the dotted line (fig. 14.116) shows the expected moment decrease according to the rigid band model. The $La(Co, Ni)_5$ system for high Co content can be described in terms of the rigid band model but a certain degree of localization is also present. This is in agreement with the results of pressure effects on this system. The results are discussed in terms of the Stoner–Wohlfarth theory. It is concluded that $N(E_F)$ and the 3d–3d interactions are affected by Co–Ni replacement. The $Th(Co_xNi_{1-x})_5$ series shows a discontinuity in the ordering temperatures (fig. 14.117) associated with a change in the magnetic order type. For more than 80% Co ferromagnetism prevails whereas for lower Co contents ($0.5 \leqslant x \leqslant 0.8$) we have ferrimagnetism between the 3(g) and 2(c) sites with spins parallel to the c-axis. A negative pressure dependence of the ordering temperature is observed in $Th(Co, Ni)_5$ as well as a pronounced magnetic history effect in the (M, T) curves. This is believed to be due to narrow domain walls which may form since the exchange energy is relatively low in the

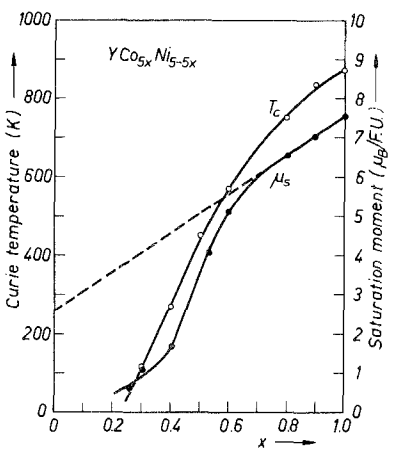

Fig. 14.116. Composition dependence of the Curie temperature and saturation moment for the $Y(Co, Ni)_5$ system (Buschow and Brouha, 1976).

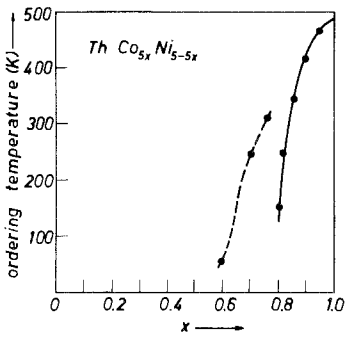

Fig. 14.117. Composition dependence of the Curie temperature of $Th(Co, Ni)_5$ (Buschow et al., 1975b).

Ni-rich samples. Critical fields characteristic of after-effect have also been observed in Ni-rich samples of $Y(Co, Ni)_5$ (Poldy, 1972; Taylor and Poldy, 1975; Buschow and Brouha, 1976). The $La(Co, Cu)_5$ series (Brouha and Buschow, 1975b) displays the $CaCu_5$ structure over the whole composition range. The Curie temperatures are shown in fig. 14.118 where it is seen that magnetic ordering disappears for 80% Cu content. The magnetic properties are explained in terms of the collective electron model with a 3d band whose shape depends upon the composition. A certain degree of localization of the 3d electrons is taken into account. The dotted line in the figure shows how T_C values should change if Co were well localized.

The system $Th(Fe_{1-x}Ni_x)_5$ shows the coexistence of ferromagnetism in the c-axis with an antiferromagnetic component perpendicular to the c-axis for $x \leq 0.2$. For $0.2 < x < 0.6$ a ferrimagnetic component in addition to the ferro-

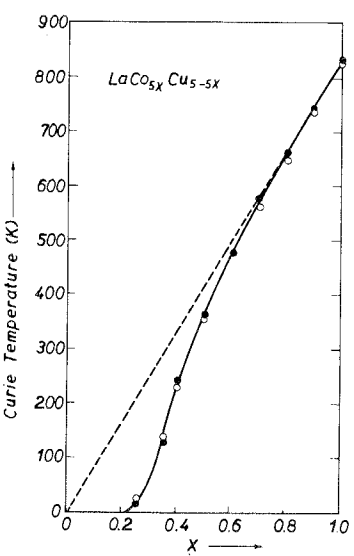

Fig. 14.118. Composition dependence of the Curie temperature of $La(Co, Cu)_5$. The open circles refer to permeability measurements, while the black dots refer to magnetization measurements (Arrott plots). (Brouha and Buschow, 1975b).

magnetic component is predicted (Elemans et al., 1975). It was deduced that the 3d electrons do not share a common band in this system, the magnetic properties being better described in terms of a localized model (Jaccarino–Walker) assuming an Fe moment of 1.88 μ_B and a Ni moment 0.4 μ_B for Ni atoms which have at least one nearest Fe neighbour. This is not unlike the effect of Fe upon Co in the system $Y(Fe, Co)_2$ as has already been discussed. However in the $Th(Fe, Ni)_5$ system no critical concentration was reported at which magnetic ordering sets in. In all the three ThB_5 systems where B = (Fe, Co), (Fe, Ni) and (Co, Ni) a preferential occupancy of the 2c sites was detected (Elemans and Buschow, 1976) which could be described by Ni > Co > Fe.

4.4. $Y_6(Mn, Fe)_{23}$

The magnetic properties of this system are shown in fig. 14.119. Up till now two different assumptions were made for explaining the magnetic properties of $Y_6(Fe_{1-x}Mn_x)_{23}$. The first, starting from a localized picture applied to the boundary phases, assumes an antiferromagnetic coupling of Fe and Mn moments which leads to a decrease of the magnetic moment and as a consequence also to a decreasing T_C (Kirchmayr and Steiner, 1971). The second, a band model where Fe and Mn forms a common band is assumed. The transition from ferromagnetism to paramagnetism and again to ferromagnetism with increasing x-values was discussed in terms of the Stoner–Wohlfarth model. This suggestion (Hilscher, 1974) is based on the following arguments, valid especially for $0.2 < x < 0.9$:

1) The reciprocal susceptibility shows a quadratic temperature dependence;
2) Arrott plots (M^2, H/M) are more or less straight lines;

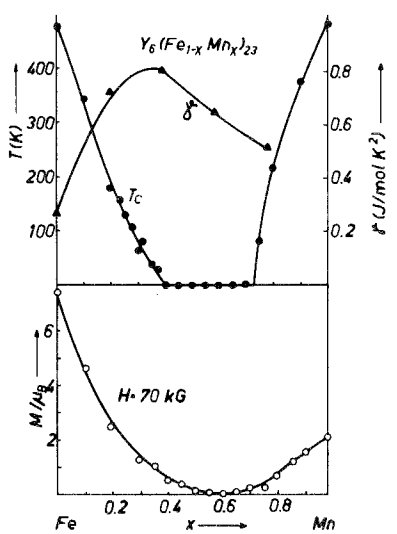

Fig. 14.119. Curie temperatures and magnetic moments of $Y_6(Fe, Mn)_{23}$ as a function of composition. (Kirchmayr and Steiner, 1971; Hilscher, 1974). The specific heat results are taken from Bechman et al. (1976).

3) Plots of χ^{-1}, T_C^2 and M_0^2 versus concentration x (Mathon plots) show a linear relationship for $x > 0.7$. Resistivity measurements (Gratz and Kirchmayr, 1976) also support this picture.

Bechman et al. (1976) deduced from specific heat measurements on $Y_6(Fe_{1-x}Mn_x)_{23}$ which has a maximum at $x = 0.4$, that Fe and Mn couple antiparallel and an itinerant model is not applicable. The magnetic breakdown in the region $0.4 < x < 0.7$ cannot be explained as a result of a decreasing density of states. However a maximum in specific heat γ is not in contradiction to an itinerant model. For several other itinerant systems such a maximum in γ is found near the critical concentration, which can be understood in terms of band splitting (Alben and Wohlfarth, 1974; Wohlfarth, 1974).

On the other hand Hilscher et al. (1977) found by recent pressure experiments that $\partial T_C/\partial p$ is zero around the critical concentration $0.3 < x < 0.4$. In the same region spin glass behaviour is found. From this one can conclude that the Stoner–Wohlfarth theory does not apply simply, and the magnetic breakdown cannot be correlated with a minimum of the density of states curve.

Until now we have concentrated on the problem of why the middle of the $Y_6(Fe, Mn)_{23}$ series shows no magnetic ordering. The problem is by no means solved and it may therefore be instructive to approach it from another angle. Such an approach might be to ask why Y_6Mn_{23} is at all ferromagnetic. If one considers how weak the magnetic ordering in α-Mn is (see fig. 14.74) then it is not obvious that dilution of Mn by Y should increase the ordering temperature. On the other hand ferromagnetism in Y_6Fe_{23} is more to be expected since elemental Fe is already ferromagnetic with a reasonably large Curie temperature. From this point of view it is conceivable that the dilution of Y_6Fe_{23} by weakly magnetic Mn should lead to a disappearance of ordering. The reappearance of ferromagnetism for the Mn-rich compositions is then difficult to understand and may perhaps be connected with the close proximity of Mn atoms to each other in this crystal structure.

5. Time dependence

In the previous sections magnetic properties of intermetallics have been discussed in such a way as if it were not important how rapidly the relevant experiments were performed. In most cases this implicit assumption is indeed valid since most experiments are performed quasi-statically and the system under investigation usually has a sufficiently short relaxation time for it to be in equilibrium at all stages of an experiment. One then finds that doubling the speed of an experiment, for example in measuring an (M, H) curve, has no effect upon the results. This is usually the case in metamagnetic materials where a critical field transition has the same value independent of whether the field is increasing or decreasing. Critical field transitions can however also be observed in ferromagnetic materials where the critical field value depends upon how fast the field is increasing or decreasing. Time dependence, otherwise known as after-effect,

has been described, quite generally by Kneller (1962) as being the retarded return of a thermodynamic equilibrium which had been disturbed by some external influence, for example an applied field. The re-establishment of equilibrium takes place by means of some sort of diffusional process, i.e. transport of thermal energy, atoms, ions, crystallographic lattice defects or electrons. The after-effect is characterised by a relaxation time τ within which the equilibrium state is re-established. In this section we shall deal with intermetallics which show time-dependent behaviour and shall discuss the conditions necessary for the occurrence of such behaviour. We shall firstly consider some of the experimental techniques for revealing time dependent behaviour. This will be followed by a survey of theoretical models and a discussion of experiments showing up time dependence in rare earth intermetallics.

5.1. *Experimental methods*

Experiments revealing after-effect usually involve changing an applied field, for example by switching it on or off, and observing how the magnetization subsequently changes. Other methods involve applying an oscillating field and observing how the magnetization follows the field. Kronmüller (1968) differentiates between three types of experiment: 1) Retardation experiments, in which the magnetization as a function of time is measured at constant applied field, 2) Relaxation experiments, where the applied field necessary to maintain a constant magnetization is measured, and 3) Disaccommodation experiments, involving the measurements of the reversible susceptibility as a function of time for a given magnetic field. Experiments in after-effect can be used for obtaining information about the various interactions present in a magnetic material. Conclusions can be drawn, for example about the strength of magnetocrystalline anisotropy energy and the diffusion of atoms and defects. Materials with high anisotropy tend to show after-effect at low temperatures.

5.2. *Models of after-effect*

These have been thoroughly treated by Kronmüller (1968). A brief outline of the theoretical background is given here. One of the models, known as the Jordan-type of after-effect arose after investigations by Jordan (1924, 1930) of pressed permalloy powder revealed a behaviour which could only be interpreted as an after-effect. A possible interpretation in terms of eddy current effects was therefore excluded. Theoretical interpretations of the Jordan after-effect involved the concept of thermally activated fluctuations of Bloch domain walls. Figure 14.120 shows schematically the isothermal magnetization variation with time for Jordan after-effect. A logarithmic law can be used in order to describe this variation $M(t) = M_0 + S \ln(1 + t/t_0)$ where M_0, S and t_0 are temperature dependent parameters. Below the Curie temperature S can be described according to Barbier (1950) by $S \propto T^{3/4}$ or according to Street and Wooley (1950) by $S \propto T$. The validity of these two expressions depends upon the material and temperature range investigated.

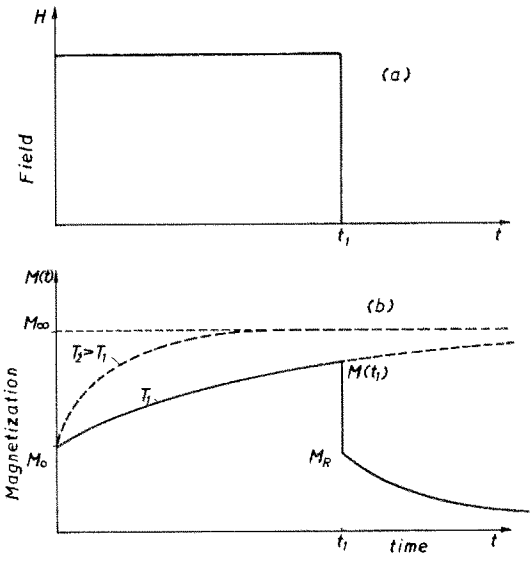

Fig. 14.120. Schematic representation of the time variation of (a) field and (b) magnetization for the Jordan after-effect (Kronmüller, 1968). M_R = Remanence, T = temperature.

Another form of after-effect is the Richter after-effect. This is the type observed in Fe containing impurities such as carbon or silicon. It is also found in RCo_5 compounds with absorbed hydrogen. This type of after-effect can be described by the expressions

$$M(t) = M_0 - M_s[1 - \exp(-t/\tau_H)], \qquad \chi(t) = \chi_0 - \chi_s[1 - \exp(-t/\tau_H)], \tag{14.29, 14.30}$$

where $M_s = M_0 - M_\infty$, $\chi_s = \chi_0 - \chi_\infty$ and τ_H is the relaxation time given by

$$\tau_H = \tau_0 \exp(Q/kT), \tag{14.31}$$

with $\tau_0 \sim 10^{-13}$ sec and Q the activation energy. The temperature dependence of Richter after-effect is stronger than that of Jordan after-effect. The microscopic origins of the Jordan and Richter types of after-effect are due to lattice defects such as substitutional defects and to interstitials such as C, H, N, etc. respectively.

A type of after-effect to be associated with intrinsic pinning of narrow domain walls, of particular relevance in rare earth intermetallics, was treated theoretically by Zijlstra (1970), van den Broek and Zijlstra (1971) and Egami (1973a). This type requires a large ratio K/W, i.e. a large anisotropy to exchange energy ratio. This condition is met with particularly in the lanthanides and their intermetallics because of the relatively low exchange energies and high anisotropies. Since, according to Kittel (1949), the thickness of a Bloch wall can be expressed as

$$N = (\pi^2 JS^2/Ka^3)^{1/2} \tag{14.32}$$

it is evident that a large ratio K/W leads to narrow domains. In this expression N is the number of atomic planes in the wall, J is the exchange integral, S is the

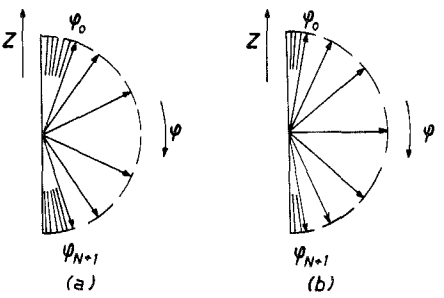

Fig. 14.121. View along row of spins perpendicular to domain wall. (a) Centre of wall just between two spins (equilibrium). (b) Centre of wall at spin site (transition). Shaded sections indicate continuous zones (van den Broek and Zijlstra, 1971).

spin angular momentum, K is the anisotropy energy and a is the lattice constant. The thickness of a very narrow domain wall can be of the order of the inter-atomic spacing, in which case the above formula is no longer valid. It can be shown, that the coercive force in a reduced form can be expressed as $h_c = H_c/H_a = \pi\Delta E/4aK$ (van den Broek and Zijlstra, 1971), where ΔE is the energy difference between the two types of narrow domain configuration (fig. 14.121). Craik and Hill (1974) showed that in the extreme case this pinning field is equal to the anisotropy field. In practice it can be problematic to decide whether after-effect in a given case is due to a large K/W ratio or due to other causes such as lattice defects since lattice defects are also present in cases where intrinsic pinning is playing a role. The realistic situation in most cases is probably a mixture of the two types of mechanisms. The shifting of narrow domain walls requires the passing of a large potential energy barrier due to anisotropy. This can be encouraged by thermal activation or by tunnelling. The tunnel effect in this connection was treated theoretically by Egami (1973b). This effect can only be observed at low temperatures where thermal activation is absent, and is believed to play a role in dysprosium since the wall diffusion mobility is observed to become temperature independent at low temperatures (Egami, 1973b).

The redistribution of electronic charges can give rise to after-effect. This has been suggested for dilute Yb in Mg by Burr (1975) where thermally activated valence fluctuations cause time-dependent behaviour. A redistribution of electronic densities as a result of high magnetostriction is also a possible cause of after-effect associated with magneto-elastic coupling. This was believed to occur in Tb, Dy and Tb–Y (Belov et al., 1969) which is in contrast to the interpretation by Egami for Dy. Magnetic after-effect in spin glasses has been treated by Tholence and Tournier (1974), and Guy (1975) for the case of dilute alloys of Fe in Au, in which time constants of the order of 70 minutes have been found.

5.3. *Experiments revealing time dependence*

Theoretically we can divide after-effect into two groups: so-called extrinsic and intrinsic effects. The former is caused by introduction of atoms which are foreign to the lattice. After-effect due to defects can also be regarded as

belonging to this group. In the latter group the after-effect arises as a result of properties characteristic of the pure material. To this group belongs the intrinsic pinning of domain walls due to a high K/W ratio.

A representative of the extrinsic case is Fe with interstitial foreign atoms such as Si. Magnetization in a given crystallographic direction involves magnetostriction and a corresponding extension or contraction in this direction. There follows then a gradual diffusion of the interstitials to energetically more favourable sites. A change in the field direction then corresponds to a retarded magnetization change due to the slow redistribution of the interstitials via diffusion. Such effects are also observed in RCo_5 compounds with absorbed hydrogen (Maartense, 1973). The after-effect is here associated with the formation of dumb-bell pairs of hydrogen atoms oriented in particular directions.

The effect of a large K/W ratio in being responsible for after-effect is more commonly observed in the lanthanides and their intermetallics. In Gd and its compounds however these effects are absent which is a confirmation that anisotropy plays an important part for the other lanthanides. For the lanthanides, as we have already seen, Belov et al. (1969) presented a different explanation from that of Egami (1973b). It is however not clear to what extent lattice defects play a role. $SmCo_5$ is an example of a material with large anisotropy. However calculations by van den Broek and Zijlstra (1971) predict an intrinsic coercivity of only about 10 Oe, which does not correspond to the large value which makes $SmCo_5$ a permanent magnet material. Lattice defects are extremely important in this case. The role of defects in RB_5 compounds has been revealed by substitutions of Al (Österreicher, 1974) and Cu (Ray et al., 1971a). The basis for the theoretical estimation was the high anisotropy of $SmCo_5$. Hilzinger and Kronmüller (1972) have shown that lattice defects are largely responsible for the coercive force in RCo_5 compounds.

A different type of time dependence (intrinsic) is found in such compounds as Dy_3Al_2 and Tb_3Co (Barbara et al., 1971c; Barbara, 1973). According to van den Broek and Zijlstra (1971) the high anisotropy in such materials leads to narrow domain walls. In his investigations of Dy_3Al_2 Buschow (1969) detected a drop in the magnetization perpendicular to the easy axis of a pseudo-single crystal below 20 K indicative of a large change in the anisotropy. Neutron diffraction on a single crystal of Dy_3Al_2 showed no change in spin structure below 20 K. The Curie point of Dy_3Al_2 is 76 K and it appears that below 20 K the anisotropy has risen sufficiently to give a different domain structure. Specific heat measurements reveal an anomaly at 24 K (Sankar et al., 1974) which is most probably associated with the anisotropy change. A number of investigations of after-effect have involved some substitutions in pseudobinary series, aimed at raising the anisotropy or lowering the exchange. TbNi develops a critical field at 1.8 K upon replacing 20% of the Ni by Cu. The substitution raises the K/W ratio (Barbara et al., 1971b).

In many cases there seem to exist two sublattices whose magnetizations are not quite parallel. The important exchange parameter is that between the sublattices each of which behaves as a unit. This inter-sublattice exchange

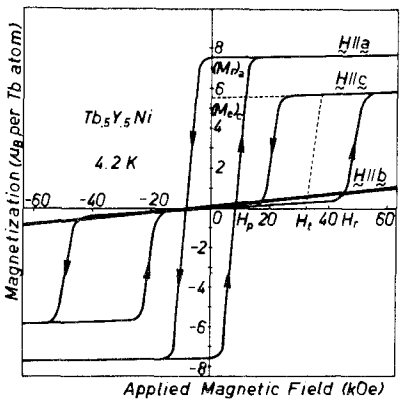

Fig. 14.122. Variations of the magnetization of $Tb_{0.5}Y_{0.5}Ni$ along various crystallographic directions (Gignoux and Lemaire, 1974).

parameter determines the time dependence. Characteristic is a high remanence. If the sample is cooled in a high field then the behaviour is different from that after cooling in a low field. The ferromagnetic state can be frozen in by the high anisotropy at low temperatures even if the equilibrium state is non-collinear.

The temperature dependence of remanence, and critical field reflects the temperature dependence of the anisotropy. The temperature T_K' below which the anisotropy rises is often considerably smaller than T_C, being about 0.3 T_C. The difficulty of differentiating between critical fields due to metamagnetism and critical fields due to narrow domain walls was evident for a long time, as exemplified by the investigations upon the R_3Al_2 compounds (Barbara et al., 1968), where some compounds were considered to be metamagnetic.

An excellent example of a material with large K/W ratio is $Tb_{0.5}Y_{0.5}Ni$. A single crystal of this alloy was investigated by Gignoux and Lemaire (1974). The (M, H) curves in the various directions are shown in fig. 14.122. Because of the large K/W ratio the domain wall thickness is an interatomic distance. The magnetic structure is a non-collinear one very similar to that of HoNi (fig. 14.53). The domain wall structures in zero field and under the influence of large fields in the a and c directions are shown in fig. 14.123. This is a mixed ferro- and antiferromagnetic structure in zero field. In the c-direction metamagnetic

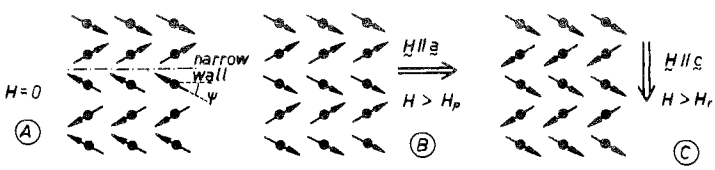

Fig. 14.123. (A): Schematic representation of the magnetic structure and domain configuration in $Tb_{0.5}Y_{0.5}Ni$. (B): Effect of a field applied parallel to the ferromagnetic direction a. (C): Effect of a field applied parallel to the antiferromagnetic direction c: magnetization reversal of one sublattice (Gignoux and Lemaire, 1974).

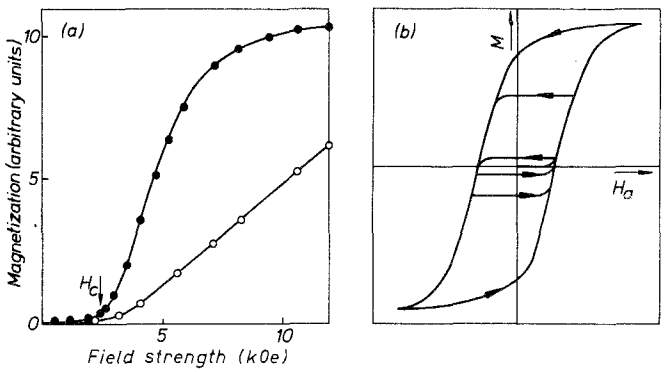

Fig. 14.124. (a) The magnetization curve of DyCoNi obtained with fast and slow "quasistatic" field increases. The measurements shown by open circles were taken with a speed of 1 kOe s^{-1}, those shown by filled circles were obtained with a 60 s stay at each point. (b) The hysteresis loop and minor loops for DyCoNi in "quasistatic" fields (Taylor et al., 1972).

behaviour is observed with hysteresis due to the magnetic viscosity characteristic of these materials. The average transition field H_t is a measure of the energy gap between the arrangements before and after the metamagnetic transition (Gignoux and Lemaire, 1974). The metamagnetic curve can even have such a large hysteresis that the lower critical field is negative. One then obtains a wasp-waist hysteresis loop. In the *a* direction the hysteresis loop is of a ferromagnetic type, a critical field for the first magnetization occurring at H_p which is the transition from the no-field state to the domainless non-collinear state. A general conclusion of these measurements is that for large enough anisotropy the narrow domain wall propagation as well as metamagnetic process depend only on exchange (Gignoux and Lemaire, 1974). We can thus see that mixed metamagnetic and ferromagnetic behaviour can be observed even in a single sample, and magnetic viscosity is present for all processes. Therefore attempts to categorize materials into these two groups can in many cases be artificial. Single crystal measurements are necessary for revealing the true nature of the transition, and neutron diffraction measurements are necessary for determining the magnetic structures.

After-effect has been observed in DyCoNi by Taylor (1971b) by means of pulsed field measurements where the field was an oscillating decaying function of time with a period of 1 ms. Measurements were also performed in a vibrating sample magnetometer. Slowly increasing the field up to 3 kOe gave a low susceptibility characteristic of a metamagnet, see fig. 14.124. Above this field the magnetization in fixed fields increased spontaneously slowly approaching an equilibrium value. In pulsed fields the hysteresis loops obtained are shown in fig. 14.125, a critical field being observed much greater than that in static fields. The magnetization process at a fixed field was described by $M(t) = M_0[1 - \exp(-t/\tau)]$ where τ is the time constant of the after-effect. Barbara and Gignoux (1972) also investigated these effects in DyCoNi. The Dy and transition metal moments are

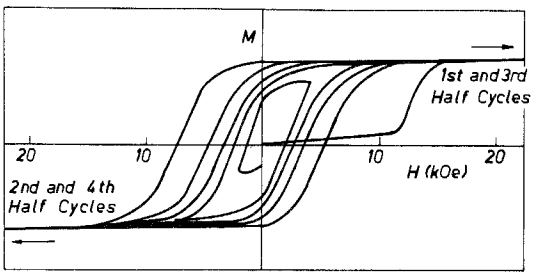

Fig. 14.125. The hysteresis loop for DyCoNi obtained with pulsed fields. The field axis has been truncated at about 20 kOe, and does not contain the maximum fields for the first to fourth half cycles (Taylor, 1971b).

ferrimagnetically coupled. The anisotropy rises below 45 K whereas the Curie temperature is about 70 K. The same behaviour is observed for other samples in the pseudobinary $Dy(Co, Ni)_2$ series (Taylor et al., 1972). The critical fields in pulsed fields are shown in fig. 14.126. Two pulsed field magnetometers were used, with pulse lengths of 0.2 and 2.5 ms. Since the Curie temperature decreases with increasing Ni content the increase of the critical field can be understood as being due to the increase of the K/W ratio assuming K undergoes no large changes. Taylor et al. (1972) interpreted the subsequent decrease as being due to a decrease of K resulting from the decrease in Co concentration, Co ions being inherently more anisotropic compared with Ni. If this is the case then the Co ions must possess a 3d moment even at low concentrations and may behave as magnetic impurities raising the T_C on substituting Co into Ni. If Co has a 3d moment in $Dy(Co, Ni)_2$ for the Ni-rich samples then this will certainly be the case in $Gd(Co, Ni)_2$. Thus the interpretation of the T_C variation in the Ni-rich $Gd(Co, Ni)_2$ as being due to magnetic Co as mentioned in subsection 2.5 is consistent with these findings. On the other hand the critical field decrease on approaching Ni could also have another origin. It is known that the high anisotropy develops at temperatures well below T_C and that large critical fields are only observed for T much lower than T_C. The T_C value of the Ni-rich end of the series is perhaps not sufficiently large compared with the temperature of measurement, 4.2 K, see fig. 14.126 where the T_C values are seen to decrease

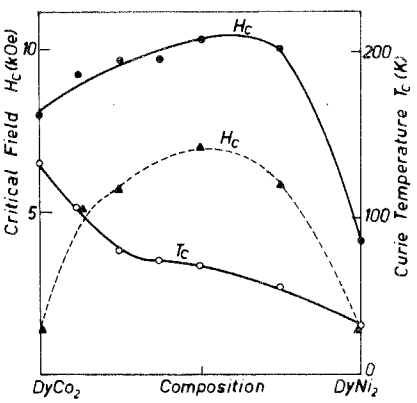

Fig. 14.126. The Curie temperatures and critical fields in the $Dy(Co, Ni)_2$ system at 4.2 K. The critical field values were obtained with two pulsed field magnetometers with pulse lengths of 0.2 ms (circles) and 2.5 ms (triangles), (Taylor et al., 1972).

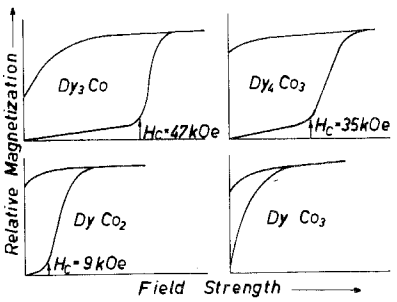

Fig. 14.127. The magnetization curves of four Dy–Co compounds. The critical field values are marked (Taylor and Primavesi, 1972a).

towards the $DyNi_2$ end of the series. Noting that the inequality $T_C \gg 4.2$ K is invalid the observed decrease of H_c towards the Ni-rich end of the series can also be understood by this consideration.

The various Dy-rich compounds between Dy and Co were investigated by Taylor and Primavesi (1972a) who found critical fields whose values changed monotonically as a function of Co content. The various (M, H) curves obtained by pulsed field measurements are shown in fig. 14.127. Figure 14.128 shows the critical field, Curie point and magnetic moment variations. All compounds are considered to be basically ferromagnetic with critical fields due to narrow domain walls. The width of the walls increases with decreasing Dy content due to the increase of the exchange. Thus K/W decreases and the critical field disappears at $DyCo_3$. Interestingly ferromagnetic Dy at 4.2 K appears to fit into the behavior of the compounds, as shown in fig. 14.128 where the ordering temperature of Dy appears to be just on the verge of being large enough to cause the critical field to disappear. The behaviour of the compounds was described in the formalism of van den Broek and Zijlstra (1971) where the critical field is expressed as

$$H_c = \text{const.}(1/aM_s)(\Delta E/K)K. \tag{14.33}$$

ΔE is a measure of the energy barrier inhibiting domain wall motion, a is the

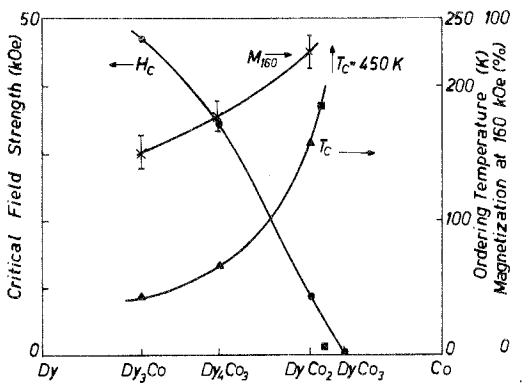

Fig. 14.128. The variation of the ordering temperature and critical field with composition of Dy–Co compounds. The magnetization at 160 kOe is given as a rough indication of anisotropy effects. Elemental dysprosium is shown in the form of filled squares with the ordering temperature normalized to the T_C curve (Taylor and Primavesi, 1972a).

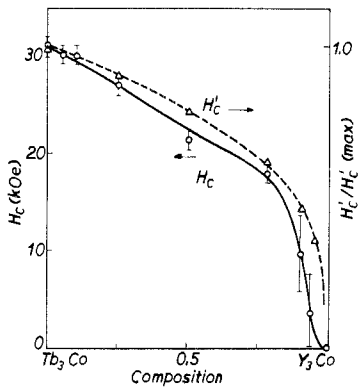

Fig. 14.129. Comparison of the observed critical field values H_c of (Tb, Y)$_3$Co with a theoretical curve H_c' derived for the magnetization process in a specimen containing narrow domain walls (Taylor and Primavesi, 1972b).

average interatomic distance, M_s is the saturation magnetization, and K is the anisotropy energy. It can be shown that, as K/W decreases, the $\Delta E/K$ value also decreases. Changes of aM_s are not considered to be significant in the Dy–Co series.

The R_3Co and R_3Ni compounds investigated by Primavesi and Taylor (1971) show critical fields but not all can be interpreted as narrow domain effects. Especially in R_3Ni compounds an interpretation along these lines cannot simply be made since they are antiferromagnetic. Tb_3Ni which is believed to be antiferromagnetic, however, is an interesting example of an antiferromagnet showing large hysteresis with critical fields and a remanence, but only at low temperatures $T < \frac{1}{2}T_N$ (see Féron et al., 1968). For $T > \frac{1}{2}T_N$ normal reversible metamagnetic behaviour is observed as expected for an antiferromagnet. It appears that hysteresis due to intrinsic pinning is also possible in antiferromagnets when K/W is very high, as is the case in Tb_3Ni at low temperatures. However the R_3Co compounds, except Gd_3Co may well be ferromagnetic as discussed in subsection 2.6. The $(Tb_xY_{1-x})_3Co$ system was investigated in detail by Taylor and Primavesi (1972b). The variation of the critical field was accounted for theoretically within the model of van den Broek and Zijlstra (1971) from which the relation $H_c = \text{const.}\ x^{1/3}$ was derived for large K/W. The experimental and theoretical variations are shown in fig. 14.129 where the agreement is seen to be good. The case of (Gd, Ho)$_3$Co was investigated by Primavesi and Taylor (1971). The critical field and ordering temperature variations are shown in fig. 14.130. Here the case of Gd_3Co cannot be treated as an example of after-effect since it is known to be antiferromagnetic (subsection 2.6). If the Ho-containing samples are treated as ferromagnetic then it can be expected that K/W increases as T_C decreases since Ho is no S-state ion. This explains the H_c increase with Ho concentration. The subsequent decrease for more than 50% Ho could be perhaps understood with the same argument as used above for the Dy(Co, Ni)$_2$ system, namely that the Curie temperature approaches the measuring temperature too closely.

Although after-effect of the type requiring a large K/W ratio is most com-

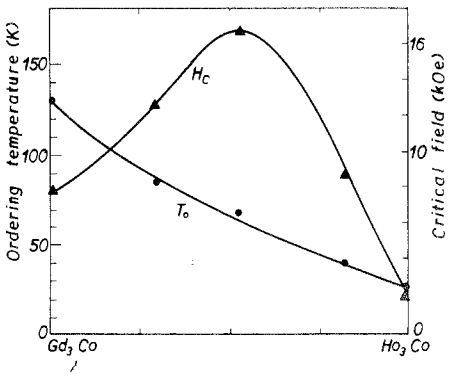

Fig. 14.130. The variation of the critical field and ordering temperature in the (Gd, Ho)$_3$Co system (Primavesi and Taylor, 1971).

monly observed in compounds with 4f moments, after-effect is by no means confined to this group. Intermetallics with finite B-moments and no R-moments can show after-effect when exchange is weak but anisotropy still large. This occurs in such systems as Y(Co, Ni)$_5$, Y(Co, Ni)$_3$ which are discussed in section 4. Buschow and Brouha (1976) have investigated these effects in detail for the Y(Co, Ni)$_5$ system and argue that the large intrinsic coercive forces observed are due to narrow Bloch walls.

A study of time dependence in Dy_3Al_2, DyCoNi and Dy over a wide range of rates of change of fields was performed by Barbara (1973). Quasi-static and pulsed fields were applied, thus achieving a span of 0.1 to 10 Oe/sec as well 10^7 to 10^9 Oe/sec, respectively. Magnetization rates as a function of internal field were measured. The results could be plotted, as in fig. 14.131, for the magnetiza-

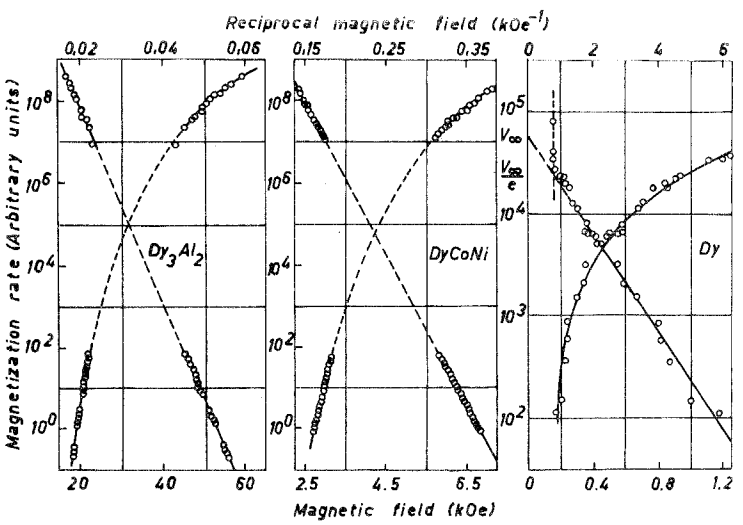

Fig. 14.131. Logarithmic variation of magnetization rate as a function of internal field and its reciprocal for Dy_3Al_2, DyCoNi and Dy at 4.2 K (Barbara, 1973).

tion rate as a function of field and reciprocal field. A similarity of the dynamic behaviour of the various samples was observed and the processes could be expressed as $\ln(dM/dT) = f(1/H)$ where the function is linear.

A system studied by Grössinger et al. (1976a) which shows magnetic after-effect but cannot be described within the model above is $Dy(Fe, Al)_2$. Other lanthanides show similar behaviour, but we shall consider the Dy system as being representative. The interesting feature here is that $DyFe_2$ and the other RFe_2 series show no time-dependent behaviour, as observed in quasi-static magnetometer measurements. However minimal quantities of a few percent Al give rise to the appearance of critical fields (fig. 14.132). From Clark and his co-workers, see for example Clark and Belson (1972), we know that the anisotropy in many RFe_2 compounds is large. In addition the introduction of Al decreases the Curie temperatures. We cannot however argue that the K/W ratio here increases up to the value necessary for narrow domains, since it would be too great a coincidence that the ratio in $DyFe_2$ is just below the necessary critical value needed for small quantities of Al to cause the crossing of the critical K/W ratio. In addition minimal quantities of Al are sufficient also in the $Ho(Fe, Al)_2$ system, which has other values of T_C and K. It is preferable therefore to regard this after-effect as being an extrinsic one which arises as a result of Al impurities in the lattice. The introduction of impurities can impair the mobility of the domain walls, as can the introduction of lattice defects. Support for this interpretation can be taken from the work of Clark (1973) who observed similar effects in sputtered $DyFe_2$ samples. In the $Dy(Fe, Al)_2$ samples the variation of the critical field is difficult to account for in detail since structure changes occur. It appears that the anisotropy is important in these systems for

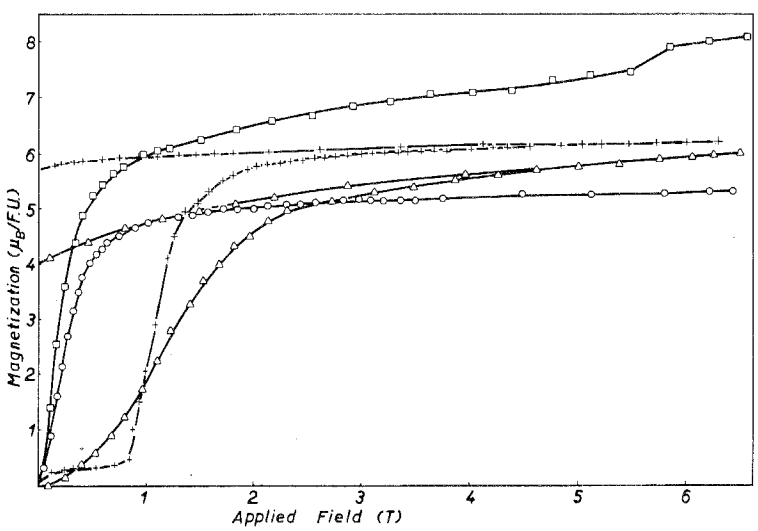

Fig. 14.132. Magnetization curves of samples in the $Dy(Fe_{1-x}Al_x)_2$ system at 4.2 K: (○) $x = 0$, (+) $x = 0.1$, (△) $x = 0.5$, (□) $x = 1$ (Grössinger et al., 1976a).

causing magnetic viscosity since $Gd(Fe, Al)_2$ and $Y(Fe, Al)_2$ do not show these effects (Grössinger et al., 1976a). However the mechanism is not the same as for the intrinsic pinning since the crossing of a critical value of K/W alone is clearly not a sufficient condition for the appearance of critical fields. We can therefore conclude that both a large anisotropy as well as lattice imperfections are necessary for after-effect in $R(Fe, Al)_2$ compounds. The effect of the high anisotropy in causing after-effect is not felt until impurities or defects are introduced. An attempt to obtain information about K/W from the ratio T_R/T_C (Grössinger, 1975), where T_R is the temperature at which remanence disappears, showed that this ratio alone could not account for the observations of time dependence. The value of this ratio is about an order of magnitude lower than in materials with intrinsic after-effect such as Dy_3Al_2 or DyCoNi. The extrinsic after-effect in $R(Fe, Al)_2$ can be considered to correspond to the Jordan type. Thermal fluctuations are needed for overcoming the potential barriers of the domain walls due to Al impurities. Similar effects were found by Österreicher (1973b) in $R(Co, Al)_2$ systems. Generally in ferromagnetic strongly anisotropic lanthanide compounds such as Tb or Dy compounds rather narrow domain walls can be expected to be present. The introduction of non-magnetic impurities can give rise to pinning centres which in many cases may be effective in causing magnetic viscosity and time dependent behaviour.

6. Hard magnetic materials

6.1. *Introduction*

In the spring of 1966, K. Strnat reported at the INTERMAG meeting in Stuttgart on measurements by Hoffer and himself (Hoffer and Strnat, 1966) of the anisotropy of YCo_5 and Y_2Co_{17}. For YCo_5 an anisotropy constant $K_1 = 5.7 \times 10^7$ erg/cm^3 was reported (fig. 14.133). This finding was identical with the statement that YCo_5 represents a material with extremely high uniaxial magnetocrystalline anisotropy. Starting from this purely scientific result in the following years numerous other hard magnetic materials based on R–Co alloys have been prepared. Nowadays,

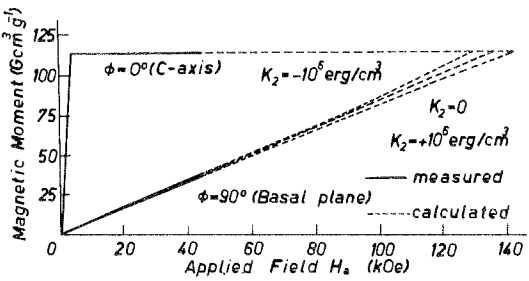

Fig. 14.133. Measured and calculated values of $\sigma_\parallel$ versus H_a for YCo_5. $\sigma_\parallel$ is the component of the magnetization parallel to the applied field H_a (Hoffer and Strnat, 1966).

only a decade later, rare earth permanent magnets possess their distinct place in industry, while continuously new applications are emerging.

The initial finding of the high anisotropy of YCo_5 was not an accident. For some years several laboratories had been investigating R–3d metal compounds with the aim to explore new magnetic materials for applications as soft or hard magnetic materials. One of the essentials in such a process is to combine materials with a large magnetic moment. Therefore Wallace and his group at the University of Pittsburgh (see e.g. Nassau et al., 1960), Hubbard, Adams and coworkers at the Naval Research Laboratory (Hubbard et al., 1960), Nesbitt, Wernick and coworkers (Nesbitt et al., 1962) at the Bell Laboratories and others had been systematically investigating, since the late 50's, R–3d metal alloys and compounds in order to increase the number of useful magnetic materials. One of the basic ideas in this connection was to combine the high magnetic moments of iron or cobalt with the high moment of one of the heavy rare earths, while retaining the high magnetic ordering temperature of the 3d metals. This approach had only limited success because the spins of the 3d and the R-metal couple antiparallel (see subsection 3.3). This means that, in the case of the heavy lanthanides where $J = L + S$, the moments of the R and 3d metal combined in an intermetallic compound have to be subtracted instead of added. The result is not the extremely high magnetic moment, possible only theoretically for a Dy–Co alloy, for example $DyCo_5$ ($\mu_{Dy} + 5\mu_{Co} = 10\,\mu_B + 5 \times 1.68\,\mu_B = 18.4\,\mu_B$). In practice $DyCo_5$ possesses only a moment of $1.6\,\mu_B$, corresponding to $\mu_{Dy} - 5\,\mu_{Co}$. Therefore, when Hubbard and coworkers (Hubbard et al., 1960) observed for $GdCo_5$ a small magnetic moment corresponding to $\mu_{Gd} - 5\,\mu_{Co}$ where the Gd and Co moments almost cancel each other out this was of no practical interest. The really exciting finding, however, that a $GdCo_5$ powder showed a coercivity ${}_MH_c$ of 8000 Oe (the highest coercive field achieved at that time) was neglected because of the small moment of $GdCo_5$, which made $GdCo_5$ uninteresting as a permanent magnet material. The nowadays seemingly trivial conclusion, that if $GdCo_5$ had a high coercive force, perhaps other compounds of the same $CaCu_5$ structure, but with a higher saturation magnetization, would also have a comparable high coercive force and would therefore be interesting for practical applications, was not drawn at that time.

Therefore Strnat and coworkers in 1965 independently made the observation of the high anisotropy of YCo_5, which opened the field of rare earth permanent magnets. These measurements have also been possible because at that time a single crystal of YCo_5 was available for the first time.

We have mentioned in the above paragraphs the raw lines of development because these seem to be typical for the successes and errors of science.

While in principle the content of fig. 14.133 gives the answer how to produce an YCo_5-permanent magnet, in practice no YCo_5 permanent magnet exists today, but other compounds, especially $SmCo_5$ have brought the technical success. In fact, more than 10 years have been necessary to develop technical and economic processes to make R-permanent magnets not only feasible, but a reality. Some more years of hard work may be necessary to establish these magnets more firmly in the

everyday life of any permanent magnet consumer. It seems therefore appropriate to discuss a little the complex question of hard magnetic materials in general. The term "hard magnetic material" is to some extent arbitrary. The same material may be called "hard magnetic" or "soft magnetic", depending on the application purpose. The so-called "hysteresis loop" contains most of the essential magnetic data of a hard magnetic material. This hysteresis loop depends, on the one hand on macroscopic parameters e.g. the size of the grains, the real structure of the lattice, impurities, the dimensions of the samples, etc., and on the other hand on the intrinsic properties of the materials, such as e.g. the crystal structure, the magnetic anisotropy and so on.

Usually, especially if a material is to be used as a hard magnetic material in the form of a permanent magnet, the remanence B_r as well as the coercive field H_c shall reach the highest possible values. In a graph where B (magnetic induction) is plotted versus H (magnetic field strength) an ideal hard magnetic material is represented by a line connecting numerically equal B- and H-values if the units Gauss and Oersted are used. The energy which is stored in a hard magnetic material in the unit of volume can be represented as $(BH)_{max}$ ($1\ \mathrm{VA\ sec/m^3} = 1\ \mathrm{Joule/m^3} = 126$ Gauss-Oersted, $1\ \mathrm{MGOe} = 7.958\ \mathrm{kJ/m^3}$). This so-called "energy product $(BH)_{max}$" is a very important, however not sufficient measure of the quality of a permanent magnet material.

The quantities which are connected by a hysteresis loop are, as has been said, simultaneously functions of microscopic and macroscopic parameters. Essential data, which can be deduced from the hysteresis loop are especially the saturation induction M_s, the remanence B_r and the coercive fields ${}_BH_c$ and ${}_MH_c$.

The saturation magnetization M_s is by definition that magnetization which can be measured in the field $H = \infty$. Naturally the induction can be measured only in a finite field. From this value the value of M_s is to be extrapolated. In this case there is the implicit underlying assumption, that even extremely high magnetic fields do not change the spin structure and therefore the coupling of the moments. This assumption is, however, not always valid, as can be seen from the fact that metamagnetic alloys are known, which change their spin structure if a magnetic field of sufficient strength is applied. Furthermore especially in the case of hard magnetic materials wrong measurements of the saturation induction can be performed if samples are used which are not completely magnetically aligned and if fields are applied which are not sufficient for saturation. This is one of the reasons that for many years for $SmCo_5$ the value which was believed to be correct was $4\pi M_s = 9.6$ kG, while in reality the correct value is near 11 kG.

If one neglects these just mentioned difficulties, the saturation induction, however, is a real material constant which is independent of macroscopic influences. It corresponds to the complete parallel alignment of all magnetic moments present if the spin structure is not changed. In ferrimagnetic materials therefore only the difference of the moments of the magnetic sub-lattices yields the corresponding saturation magnetization. M_s is furthermore a temperature-dependent value. Therefore measurements of M_s as a function of temperature are scientifically as well as technologically of great value.

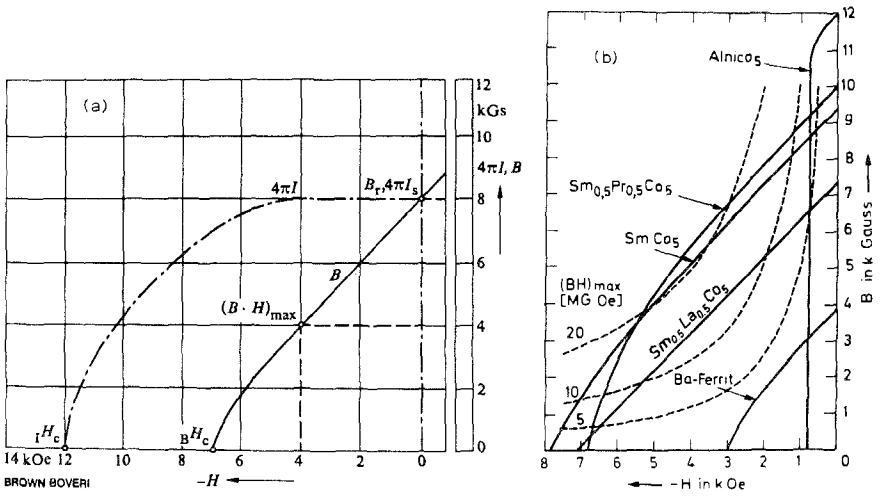

Fig. 14.134. Demagnetization curves of permanent magnets. (a) Schematic curves in two representations to demonstrate the fundamental parameters for permanent magnets. $4\pi I$ vs H: magnetization curve; B vs H: induction curve. The relation between the two representations is given by $B = 4\pi I + H$, where I has the same meaning as M used in the text. $4\pi I_s$ = saturation magnetization, B_r = remanence, ${}_IH_c$, ${}_BH_c$ = coercivity for magnetization and induction respectively, $(BH)_{max}$ is the maximal energy product (Bachmann, 1972). (b) Experimental curves of conventional permanent magnets as well as some RCo_5 magnets of 1971. Also drawn are lines (dashed) of constant (BH) (Bachmann, 1971).

Intimately linked with $4\pi M_s$ is the remanence B_r (this value is also called remanent induction). B_r however, in contrast to M_s, depends strongly on the real structure of the sample. $4\pi M_s$ is therefore only an upper limit for B_r, but gives however no direct measure for B_r.

In the case of hard magnetic materials it is usually tried to increase B_r to the same value as $4\pi M_s$. This is however only possible if a strongly anisotropic material is either present in single crystal form or if at least all magnetic easy axes of all crystallites are magnetically aligned parallel. This latter condition is fulfilled in many R–Co compounds.

Of a very complex character is the so-called coercive field ${}_BH_c$. The coercive field ${}_MH_C$ is connected with the former by the equation $B = H + 4\pi M$. ${}_BH_c$ or ${}_MH_c$ are the data taken from the respective hysteresis loops in the (B, H) or (M, H) diagrams if $B = 0$ or $M = 0$ respectively. These various concepts are illustrated schematically in fig. 14.134a (Bachmann, 1972). The symbol I for magnetization which appears in some figures of this section has the same meaning as M used throughout the text.

From fig. 14.134b can be seen that a good, however conventional, hard magnetic material such as ALNICO-5 has a B_r of 12 kG, connected however with ${}_BH_c$ of less than 1 kOe. This means that for ALNICO-5, not because of its saturation magnetization but because of its low coercive field, the maximum of

the energy product is limited to 7 MGOe. Alnico could primarily be improved by increasing the coercive field, but not primarily increasing the saturation magnetization. Ba-ferrite, however, makes full use of its potential, since ${}_BH_c$ is nearly equal to B_r. B_r however could only be improved by changing the composition i.e. by the replacement of atoms with small magnetic moment by atoms with a higher magnetic moment or a change of the spin structure.

As can also be seen in fig. 14.134b $SmCo_5$ or $Sm_{0.5}Pr_{0.5}Co_5$ show good B_r and ${}_BH_c$ values. Therefore already in 1971 such magnets yielded energy products above 20 MGOe. Also in this case the primary interest is ${}_BH_c$, since M_s and therefore also B_r are more or less given by the composition.

A high coercive field of a magnetic material is based essentially on two primary sources: a) A primarily soft magnetic material as e.g. iron can become a hard magnetic material if it is sub-divided into very small particles with large shape-anisotropy. Then any change of the magnetization requires a large magnetic field, this means a ${}_BH_c$ because of the stray fields. This is realized in the case of the so-called ESD (elongated single domain) magnets. b) Another possibility for a permanent magnet exists if the material has a high magneto-crystalline anisotropy. In this case even the directional change of magnetization of spherical particles needs a high magnetic field. This case is realized in Ba-ferrite or in Alnico, but especially in RCo_5 magnets. The assumption that in these cases ${}_MH_c$ will equal the anisotropy field H_A is however erroneous. In this case a coherent rotation of the magnetization would be necessary. Usually, however, the coherent rotation of the magnetization is not found, but the coercive field is determined either by the so-called nucleation field, i.e. the field to create a new domain, or the so-called domain wall pinning field, i.e. the field which is necessary to overcome some barriers in the motion of a domain wall. In both cases the coercive field ${}_MH_c$ is far smaller than H_A. Both processes which have been mentioned just above and their relative importance for the coercive field strength of RCo_5 alloys are not completely clear at the moment. The coercive field depends in any case, however, in a very complex manner on the real structure of the final processed permanent magnet. By real structure we mean not only the crystal structure, but also the shape, surface properties of the samples, contaminations, dislocation structure, size and orientation of the crystallites, the grain boundaries and precipitations. In general the coercive field may be interpreted by a pinning or a nucleation mechanism. Pinning mechanisms may be due to the interaction between domain walls and point defects, antiphase and grain boundaries or boundaries between different phases (Kronmüller and Hilzinger, 1976). Calculations by Kronmüller and Hilzinger (1973) showed that dislocations are less important in high coercivity materials because their contribution to the coercive field decreases for thin domain walls according to a $d^{1/2}$-law (d = domain wall width), whereas point defects lead to a $d^{-1/2} - d^{-5/2}$ dependence (Kronmüller and Hilzinger, 1973) of the coercive field. Nevertheless by transmission electron microscopy studies it could be shown that in $SmCo_5$, which has a narrow domain wall with thickness of about 50 Å, an interaction between a dislocation and a domain wall existed, as illustrated in fig. 14.135

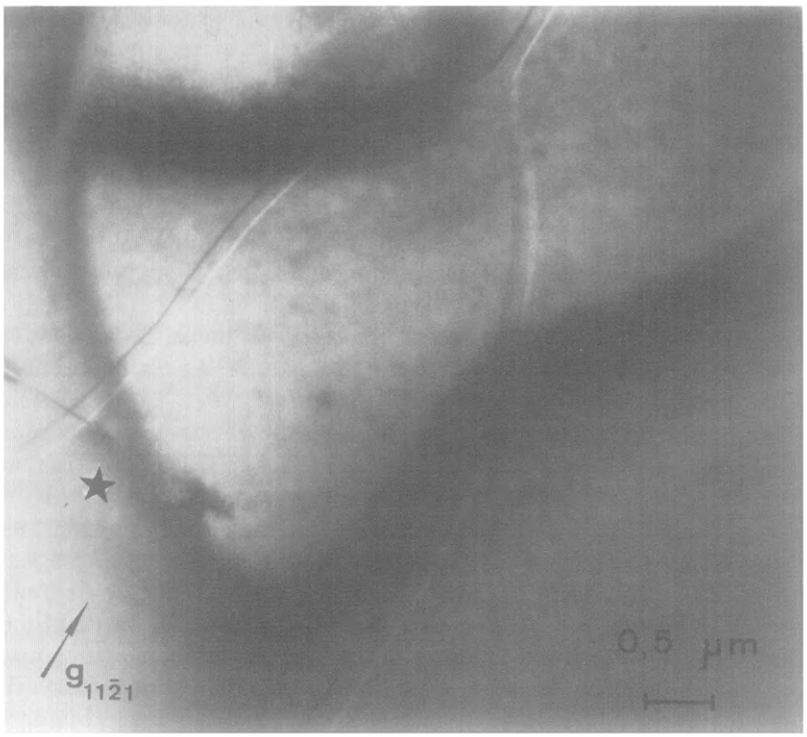

Fig. 14.135. Untypical curved domain shape in $SmCo_5$ caused by a dislocation (next to star on photograph). The fork shaped structure represents a domain with magnetization direction opposite to that on the rest of the picture. Transmission electron microscope, 200 kV, specimen thickness = 2000 Å (Fidler, 1976).

(Fidler, 1976). The coercive field due to antiphase boundaries shows even a d^{-1}-dependence (Hilzinger and Kronmüller, 1975; Craik and Hill, 1974), thus giving rise to large pinning effects for narrow domain walls. In addition in ferromagnetic materials with narrow domain walls the wall energy depends periodically on the position of the wall centre with respect to the crystal lattice. This gives rise to an additional intrinsic coercive field (Hilzinger and Kronmüller, 1972, 1973). In any case, however, a high crystal anisotropy and therefore a high anisotropy field H_A are an essential prerequisite for high coercive fields. The other properties which determine the practicability of a permanent magnet, as e.g. the long time stability, the thermal stability, the dynamic magnetic behaviour, the mechanical properties, etc. are also of great importance.

A good hard magnetic material which shall be used in technology must therefore fulfil a number of boundary conditions:

a) good temperature stability (ordering temperature, stability against deterioration),

b) high energy product,

c) appropriate coercive field and remanence,
d) mechanical and chemical stability,
e) possibility to obtain specific shapes by machining or sintering etc.,
f) other properties such as availability and price of the starting materials etc. and other physical properties.

Considering the above mentioned points a) to f), one finds that a potential new permanent magnet material must be judged approximately in the same sequence. In practice no material with a magnetic ordering temperature below 200°C is useful. There exist a large number of excellent hard magnetic materials containing lanthanides, such as e.g. Dy_3Al_2, but with a Curie temperature in the 100 K range. These materials are at present of no practical interest and probably will never have any significance even for exotic applications.

A useful permanent magnetic material must have an ordering temperature well above the operating temperature of many electrical and electronic devices which approaches sometimes 170°C (~450 K). Typical examples are Alnico, Ba-ferrite and PtCo. Simultaneously at the operating temperatures no deterioration should take place which irreversibly diminishes the magnetic properties.

The most important single parameter to be assigned to a permanent magnet is the so-called energy product $(BH)_{max}$. From fig. 14.134 the definition of the energy product and also the corresponding values for selected permanent magnet materials can be seen. The corresponding values for RCo_5 magnets reflect the state of the art in 1971. The dimensions of the product BH are erg/cm^3, i.e. the magnetic energy stored in the unit volume of the permanent magnet material. $(BH)_{max}$ is reached only under a specific working condition of the magnet material, i.e. a specific demagnetizing field $-H$. In order to make use of the full potential of the material, the machinery or device in which the magnet is used must be designed in such a way, that in operation this value of H is approximately reached. For Alnico the result of this operation is a lengthy magnetic path and furthermore usually the necessity to magnetize the magnets in situ i.e. while the magnets are already in place in the device.

The ferrites (and similarly the R–Co permanent magnets) are best used in short magnetic paths, e.g. as discs, thin layers etc. Also these magnets can be handled in the magnetized state, without danger of destroying the full power of the magnets because of the demagnetization factor. In the S.I. Units B is measured in Tesla and H in A/m. T A/m is naturally again an energy per volume, in these units Joule m^{-3}. (1 MGOe = 10^6 GOe = 7.958 Joule m^{-3}). Up to now usually the energy product is given in MGOe and 1–30 MGOe are customary values. Intimately linked with the problems to achieve an energy product as high as possible are the remanence and the coercive force, as has been stressed above and will be discussed in detail later.

6.2. *Preparation and analysis of alloys*

Since the rare earth metals are highly reactive, see ch. 2, section 3, special precautions have to be taken in order to melt the alloys with each other and with transition metals like Fe, Co and Ni. In the case of the flint-stone production, the

purity of the material is not an essential point, and for many years a technical production of iron-containing misch-metal alloys has been performed. The same production methods, however, cannot usually be used for the preparation of the highly sophisticated rare earth-Co permanent magnet alloys. In this case even small oxygen contents, which are tolerable in flint-stone, deteriorate the magnetic properties.

In the last 15 years in connection with scientific investigations the preparation of rare earth-transition metal alloys has either been done in cold crucibles by means of a high frequency induction furnace or in crucibles such as boron nitride or alumina. The latter however is slowly attacked by the melt. However for the production of large quantities of alloys newer technologies had to be invented. A survey of the present day technology of preparing rare earth-cobalt alloys is given by Herget and Domazer (1975). If one starts from the mixture of the rare earth metals and Co, then either small ready made ceramic crucibles or crucibles which are rammed and fired in situ using an inner graphite core can be used. Also the melting in an arc furnace is possible if small quantities are to be prepared. A clean method to prepare these alloys is based on the vacuum induction melting. It is, therefore, mainly a question of economy which of these methods, namely arc melting, levitation melting, induction melting or resistance melting, is used.

Since the R–Co alloys have become technically significant, many efforts have been made to lower the cost of the R–Co alloys which are the starting materials for the magnet production. In the last three years new methods have been developed, which avoid the preparation of pure R metals which are later melted with Co and other transition metals, but start with rare earth oxides (R_2O_3) and Co oxide. These processes are known under the names "reduction-diffusion process" and "co-reduction process".

The reduction-diffusion (R–D) process is based on developments by General Electric guided by Cech (1974). The main reaction can be written as follows

$$R_2O_3 + 10\,Co + 3\,CaH_2 \xrightarrow[3\text{ hours}]{1150°C,\,H_2} 2\,RCo_5 + 3\,CaO + 3\,H_2. \tag{14.34}$$

The present production scheme has been described by McFarland (1973) and by Jones et al. (1976). Also the alternative processes, e.g. the use of Co_3O_4, are described there. In the R–D process a rare earth oxide, Co-powder and Ca-granules are blended and fed in a steel container. This steel container is placed in a furnace which is flushed with hydrogen gas. The charge is heated for approximately 3 hours at 1150°C. After cooling the charge the resulting sintered cake is reacted with moist nitrogen for several hours to destroy the excess Ca. The Ca-oxide is hydrated and by this reaction the cake is disintegrated. Then the mass is mixed with an excess of water and the lime is removed. The alloy powder is filtered off and dried in vacuum at no more than 50°C. This process is now used in the USA in several plants. The grain size of the resulting R–Co alloy depends on the grain size of the Co powder which is used for the feed. With a very fine Co powder an average alloy fineness of 5 μm can be achieved.

However such a fine Co powder cannot usually be used in large scale production. The main advantage of the R–D process is that the installations are simple and therefore are of low cost. The process can be applied to a very wide range of RB_5 compounds.

The co-reduction process has been developed by H.G. Domazer and co-workers at Goldschmidt in Essen, Germany. Similar to the reduction-diffusion process they started with a rare earth oxide and not with a rare earth metal. In contrast to the modified (technological) reduction-diffusion process (see McFarland, 1973) Co_3O_4 is used deliberately in order to achieve a strongly exothermic reaction. Therefore the rare earth oxide and the Co oxide are reduced simultaneously. The summary equation of the process is given below:

$$R_2O_3 + nCo_3O_4 + (10 - 3n)Co + (4n + 3)Ca \xrightarrow[3\text{ hours}]{1000°,\text{ vacuum}} 2\,RCo_5 + (4n + 3)CaO, \qquad n = 0 \ldots \tfrac{10}{3}. \tag{14.35}$$

The process starts with thoroughly dried oxides, Co powder of various grades with particle sizes up to 60 μm and Ca granules. These materials are homogenized in a mechanical mixer. The mixture is pressed into tablets and fed into a container made of heat resistant steel which is lined inside with sintered calcia. The container is then welded vacuum tight, except for a pipe that is left on top for evacuation. The reactor is then transferred into an electrical resistance furnace and is evacuated. The heating cycle starts. Above 850°C the reaction starts, perceptible by a large temperature rise within the reaction mixture. Finally the charge is heated for 2 hours at 1000°C. At this temperature the reaction is accomplished mainly by means of Ca vapour. After cooling the reacted mass is crushed and milled. The mass is fed into water and after several hours of stirring the Ca oxide is hydrated. Then similar to the reduction-diffusion process the Ca hydroxide is dissolved with diluted acid and the alloy powder is filtered off. The wet alloy powder is fed into a vacuum dryer and dried at 80 to 100°C.

The scheme of the co-reduction process is given in fig. 14.136. An essential part in the preparation of the alloys is the analysis. This analysis is done with respect to the chemical composition, the phase composition and also with respect to the shape and size of the grains etc.

The main components, namely the rare earth elements and also the Co or iron components can be analysed by standard gravimetric or titrimetric methods. Also the X-ray fluorescence is a very valuable tool in these investigations. A very important constituent, which is undesirable, is oxygen. The oxygen is usually determined by means of vacuum fusion.

The grain size distribution can be judged by sieves, by means of microscopic and especially also by means of scanning electron microscopic methods.

The phase analysis is for the major constituents performed by X-ray diffraction, for the minor constituents in the case of magnetic phases this can also be done by so-called thermomagnetic phase analysis.

A review of the analytical chemistry of rare earth-cobalt alloys has been recently given by Brusdeylins (1975).

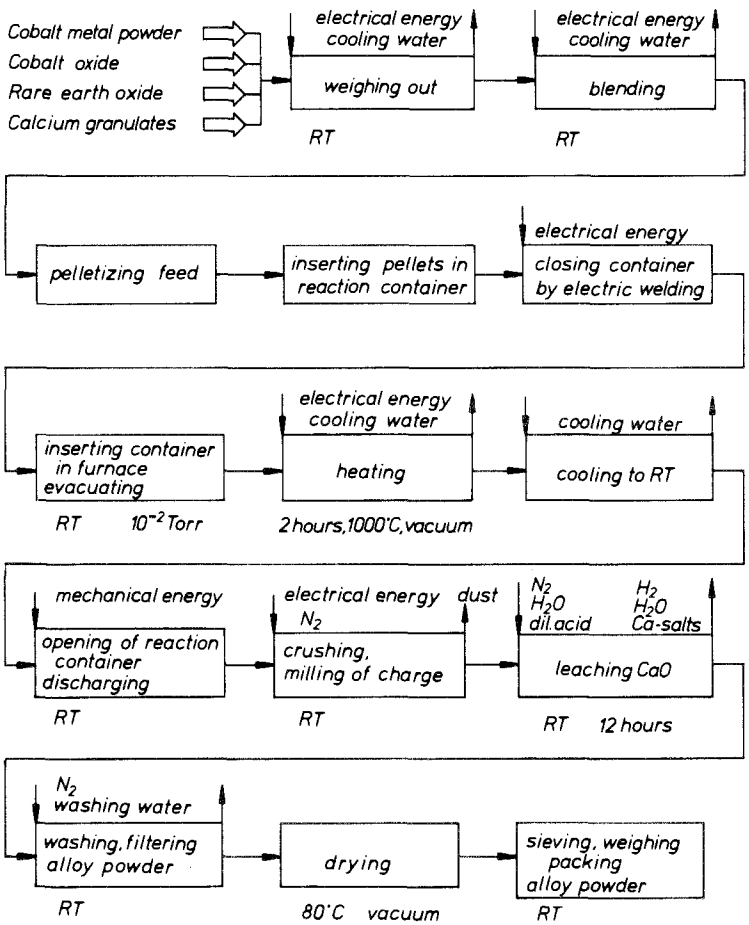

Fig. 14.136. Flow chart of the co-reduction process (Herget and Domazer, 1975).

6.3. *Production schemes for rare earth-cobalt permanent magnets*

In the following paragraphs the present day production schemes for rare earth-cobalt permanent magnets are discussed. These production schemes have been developed in the last 10 years and are naturally the result of many independent efforts. Also in the near future these production methods will be improved and changed. Nevertheless it can be expected that the basic features of these processes will be valid for some time to come.

The primary aim for all these production schemes is the preparation of permanent magnets with a very high energy product, which are stable at room temperature and at elevated temperatures for an extended period of time.

The main problem is to achieve a high enough coercive force based on the magnetocrystalline anisotropy of the starting materials. While the magnetocrystalline anisotropy is a basic property of a given composition and crystal structure, the coercive force cannot be deduced directly from the magnetocrystalline anisotropy. Much effort has therefore been made to try to understand the connection between magnetocrystalline anisotropy and coercive force.

The anisotropy field of different RCo_5 compounds is given in table 14.8. The anisotropy field can be measured either on single crystals or on aligned uniaxially directed alloy powders. In the last years there has been achieved an understanding of the differences in the anisotropy field for different RCo_5 compounds. However the basic problem of why YCo_5, which possesses a rare earth atom without a magnetic moment, has the high anisotropy field by itself has not been solved. The main line of thinking for the understanding of the influence of the different rare earth atoms in RCo_5 and related compounds on the anisotropy field has been discussed in subsection 3.1 (see also Buschow et al., 1974a; Barbara and Uehara, 1976; Perkins et al., 1975, 1976).

6.3.1. *Production scheme of* "$SmCo_5$" *magnets*

These so-called "$SmCo_5$" magnets are the oldest and still the most important R–Co magnets. In the following paragraphs the production scheme which is at present the most general and successful production scheme will be discussed. This scheme is a result of ten years of very hard scientific work. In the preceeding paragraphs we have discussed the production of rare earth-cobalt alloys. Starting from a specific alloy and following in general the lines which are given in the schematic diagram of fig. 14.137, the following steps are involved: grinding, magnetic alignment, die or isopressing, sintering, heat treatment, machining of magnets and magnetizing. The hot pressing process is however not extensively used. These steps have the following purposes and will now be discussed in some detail.

The production of $SmCo_5$ magnets can either begin with an alloy powder of uniform composition or with a mixture of two alloys with different Co amount or even with a chemically different rare earth composition in the two alloy components. If one starts with a single powder, the preparation and especially the melting of the starting materials is simpler, however this method cannot easily be adapted to magnets with different properties. The starting materials in any case are ordinary melted alloys, reduction-diffusion produced alloys or alloy powders produced by the co-reduction process. A micrograph of a typical $SmCo_5$ bulk sample, photographed in polarized light is shown in fig. 14.138 (Fidler et al., 1977). The different grains as well as the spontaneous magnetization, yielding different domain patterns can be seen. In any case one of the first steps is a diminution process by grinding, jet or ball milling. It is very important to achieve a correct particle size distribution (Paladino et al., 1975). Since under-sized particles pick up more oxygen than particles of the correct size, the metallic composition must be corrected for the formation of Sm_2O_3. Furthermore the oxygen content should be as low as possible, in any case lower than

TABLE 14.8.
Main data of RCo_5 compounds (Kirchmayr, 1973).

RCo_5	Lattice parameter a [Å]	Lattice parameter c [Å]	Density [g cm^{-3}]	$T_{Eutectoid}$ [°C]	T_C [°C]	$4\pi M_s$ [kG]	Anisotropy constant K_1 [10^7 erg cm^{-3}]	Anisotropy field H_A [kOe]	$(BH)_{max}$ theor [MG Oe]
YCo_5	4.937	3.978	7.60	–	650	10.6	5.5	130	28.1
$LaCo_5$	5.105	3.966	8.03	600	570	9.1	6.3	175	20.6
$CeCo_5$	4.926	4.020	8.56	600	375	7.7	5.2	170	14.8
$PrCo_5$	5.024	3.988	8.33	600	610	12.0	6.9	145	36.0
$NdCo_5$	5.012	3.978	8.39	600	630	12.3	–	30	–
$SmCo_5$	4.989	3.981	8.60	740	725	10.7	11.2	290	28.6
$GdCo_5$	4.976	3.973	8.86	760	735	3.6	–	270	3.2
$CeMMCo_5$	–	–	8.35	–	495	8.9	6.4	195	19.8

CeMM = Cerium-mischmetal: 50–55% Ce, 20–25% La, 4.5–5.5% Pr, 15–17% Nd.

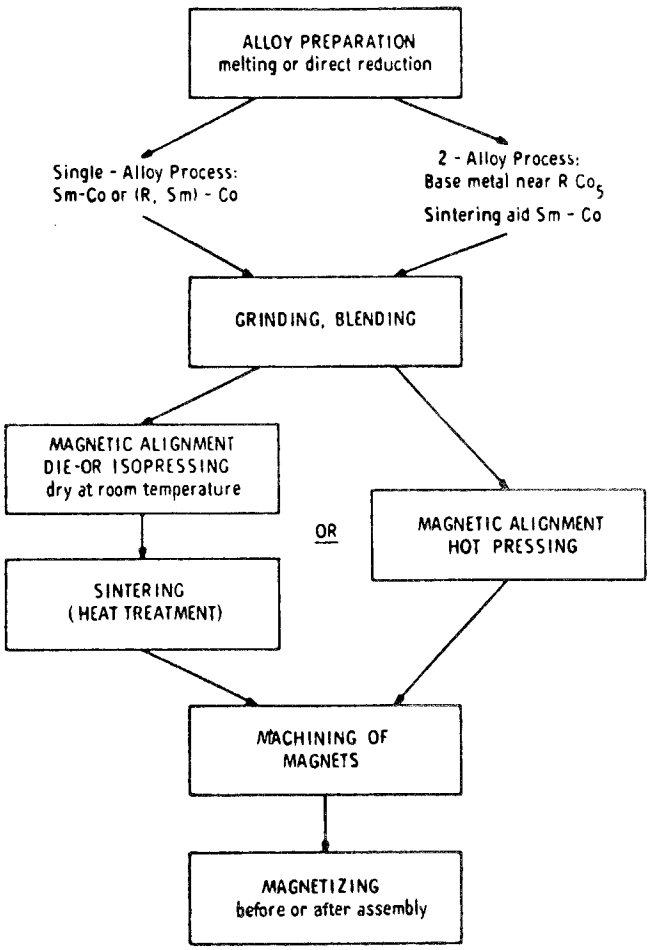

Fig. 14.137. Basic production steps for sintered R–Co magnets (Strnat, 1976b).

3000 ppm. If a mixture of two alloys is used, the total composition is usually chosen in such a way, that the samarium content is higher than the stoichiometric amount corresponding to $SmCo_5$. Thus the formation of Sm_2Co_{17} is avoided. Instead of samarium recently a samarium-rich alloy has been developed which is superior or at least equivalent in its properties to pure samarium while the price is appreciably lower (Domazer and Strnat, 1976). The basic composition of the alloys is $Sm_xR_{1-x}Co_5$, $x = 0.70 \pm 0.02$. The R-component consists primarily of Nd, La, Pr, Gd and Y with small quantities of other heavy rare earth metals. Chemical analysis shows the following impurities: Fe = 0.11–0.15, Al < 0.08, Mg < 0.03 and Ca = 0.10–0.14 wt %. Especially noteworthy is the low

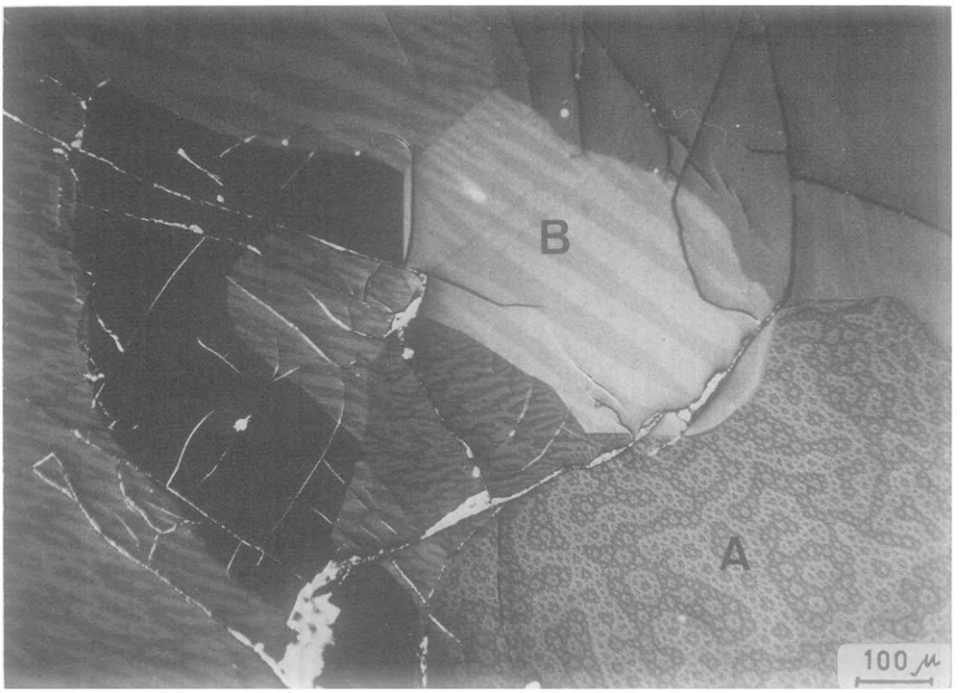

Fig. 14.138. $SmCo_5$ sample seen in polarized light. The orientation of the c-axis of part A is perpendicular to the surface, of part B practically in the surface (Fidler et al., 1977).

oxygen content of the co-reduced, leached and dried powder of 1500 ± 300 ppm. If one tries to prepare rare earth-cobalt magnets with a very small temperature coefficient of magnetization, one can also start from a mixture of Gd_2O_3 and Sm_2O_3 and use the co-reduction process in the presence of Co powder (Jones and Tokunaga, 1976). If for the preparation of the $(Gd_xSm_{1-x})Co_5$ alloy x is chosen to be 0.42 the reversible temperature coefficient of saturation magnetization is near zero. However the energy product is also lowered because of the lower saturation magnetization due to Gd and a best value of 9.9 MGOe is achieved for $x = 0.40$. In the case of Ho with $x = 0.20$ also a temperature coefficient $\alpha = 0$ is obtained while $(BH)_{max}$ is increased to 12.4 MGOe.

Frequently a mixture of a rare earth-rich R–Co alloy (where R is not necessarily Sm) and a samarium-rich Sm–Co alloy is used. These alloys will be discussed later in connection with the so-called $CeMMCo_5$ magnets, which normally need a Sm-rich alloy as a sintering aid.

The next step is usually the magnetic alignment combined with die or isopressing. The applied field, which is a d.c. and/or a pulsed field, exceeds 10 kOe. Usually a compromise with respect to the aligning field is to be made, because the die materials are optimized with respect to the mechanical properties, but not with respect to the magnetic properties of the die. An alternative to

the die pressing is the isostatic pressing. However this method is not suited for mass production, even if very good properties are achieved. The aligning fields are usually only in the 1 T range, although higher fields above 2 T are preferable, because in a 2 T field B_r is 95% of the value obtained in a 10 T field (Weihrauch et al., 1972).

The magnetic alignment is followed by the sintering procedure which may include an annealing procedure or which is followed separately by an annealing procedure. The development of a correct sintering method was one of the main break-throughs for the R–Co magnets. In 1969 the first $SmCo_5$ magnet with an energy product of 20 MGOe was successfully sintered. Even today the sintering is one of the most difficult steps in the production. The physical difficulty consists in a sintering procedure which shall result in a magnet with more than 95% theoretical density, while the magnetic particles shall nevertheless act magnetically as single particles. The sintering temperature which must be optimized with respect to the magnetic properties is to be closely controlled. The optimum temperature is usually near 1120°C (Paladino et al., 1975). By the use of hydrogen, i.e. a reacting atmosphere instead of argon during the sintering process the quality of the magnets can be improved (Doser and Jones, 1976). By changing the typical sinter-anneal cycle the coercive field and therefore the second quadrant characteristics can be changed. The optimum sintering temperature has to be determined independently for every new composition and R-metal.

Independent of the sintering process or combined with the sintering process an annealing cycle is to be performed. This annealing cycle is essential for a good permanent magnet. Usually the annealing temperature is chosen near 850–900°C. It is of very great importance that the cooling from the annealing temperature to room temperature is performed quickly, because in the temperature range from 700–850°C the magnetic properties of the magnet are strongly reduced. It is believed that this phenomenon is related to a eutectoid decomposition (Broeder et al., 1974) resulting in Sm_2Co_{17} precipitates that are sites for nucleation of reverse domains. This annealing procedure is practically the last possibility to change and improve the magnetic quality of the magnets. The steps after this can only slightly improve the properties.

After the sintering step the final shape of the magnets has to be obtained. The machining process can consist of a large variety of steps. The primary concern must be to consider the brittleness of the magnets. Therefore only special machining methods are used. Either the magnets are cut with a diamond blade etc. or they are machined by grinding or drilling. Shaping and turning is usually not applicable. Because of the large variety of the applications of magnets, usually a compromise between the ease of production of a magnet and the optimum shape with respect to the application is to be found. In any case a complete re-design of the magnetic circuit needs to be done if a low coercivity material, as. e.g. Alnico is to be replaced by a high coercivity material like $SmCo_5$. Usually a short magnetic path within the permanent magnet is sufficient in the case of $SmCo_5$ magnets and therefore discs or flat pieces magnetized

perpendicular to the disc area are used. The production scheme just described gives magnets which are automatically anisotropic not only with respect to the magnetic properties but also with respect to the mechanical properties. Therefore during the alignment step the magnetization direction which is parallel to the alignment direction is already defined. For some special applications especially if highly sophisticated magnetization schemes are to be applied to the final magnet (e.g. codes of magnetic keys etc.) isotropic magnets are necessary. In this case no magnetic field must be applied during the pressing procedure.

The final step which is part of the magnet production is naturally the magnetizing step. Since the RCo_5 magnets are high coercivity materials, in contrast e.g. to Alnico, the magnets can be magnetized before the assembling. Nevertheless it depends completely on the specific problem if the magnetizing step is done before or after the final assembling. The magnetizing is performed in a magnetic field as high as possible. In many cases conventional d.c. driven magnets are used. The main draw-back however is the low field near 2 T achieved in the magnetizing coil. Better suited to many needs are pulsed fields. By specific circuits either from the main electric lines or by means of a discharge of a condensor high electric currents in the 10 kA range are produced within a typical time of 10 milliseconds (Allain et al., 1965). In this case by proper design the magnet can be magnetized in a specific way. One possibility for example is the magnetization of radial rings, of arc segments etc. (Paladino et al., 1975). If the discharge of a condensor yields however a damped oscillating current, then instead of magnetizing the magnet the contrary is achieved. This can be used to demagnetize samples.

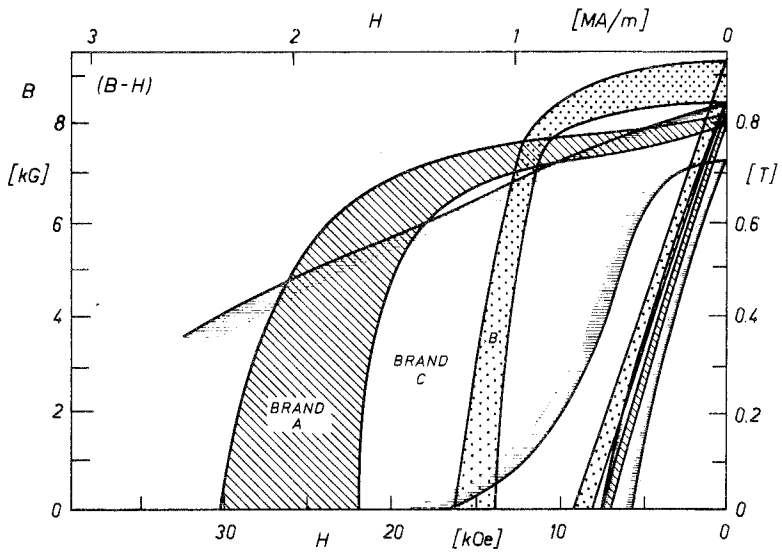

Fig. 14.139. Demagnetization curve (B-H vs. H) ranges for $SmCo_5$ magnets from three major manufacturers, Brand A, B and C (Strnat, 1976b). The unlabeled group of steep curves represents the corresponding B vs. H curves.

The best method to achieve high magnetic fields in the 10 T range is by using superconducting magnets. However field configurations different from a parallel, nearly homogeneous field are difficult to obtain. Typical demagnetization curves of commercially available sintered magnets are given in fig. 14.139.

6.3.2. *Production of "$MMCo_5$" magnets*

The production of $MMCo_5$ magnets follows in general the same lines as the production of $SmCo_5$ magnets. The main idea is the replacement of Sm at least partially by the cheaper MM. Therefore mainly economic reasons have prompted this development. In view of the newly developed R–D and co-reduction processes, which have brought down the price of the $SmCo_5$ alloy within the last years by a factor of 5, the price of a Sm–Co alloy is now only two to three times larger than the price of a MM–Co alloy. Therefore the incentive to use MM instead of Sm is not as great now as it was earlier. Nevertheless the use of MM which contains a considerable amount of cerium, increases the raw material basis by a great factor.

Nagel and Menth (1975) report the state of art of the development of $MMCo_5$ permanent magnets. Usually by adding Sm–Co alloys as a sintering base, the magnetic properties can be improved, especially by increasing of the coercive field. In the $MM_{1-x}Sm_xCo_5$ series for $x = 0.4$ a coercive field of 23 kOe can be achieved. In fig. 14.140 for different R additions the change of the anisotropy field H_A and of the coercivity ${}_MH_c$ of a MM-based alloy is shown. A further improvement of the magnetic properties can be achieved for a fixed Sm content by addition of lanthanum or neodymium, while the further addition of cerium is not desirable. In fig. 14.141 demagnetization curves of similar magnets with a fixed Sm content corresponding to $(MM_{1-x}R_x)_{0.85}Sm_{0.15}Co_5$ are shown. From the investigations by Nagel and Menth it can be concluded that at present, by a proper choice of alloy composition and heat treatment, magnets with $MMCo_5$ as the main component with a coercivity of 1.28 kA/m (16 kOe) and an energy product of 144 kJ/m^3 (18 MGOe) can be prepared.

The reduction of coercivity of MM magnets compared to $SmCo_5$ magnets is in

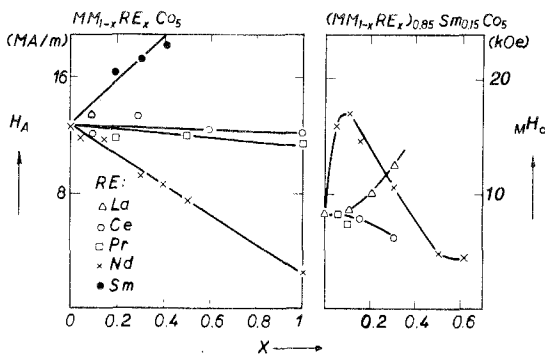

Fig. 14.140. Influence of the MM composition on the crystal anisotropy field H_A and the coercivity ${}_MH_c$ of MM-based alloys (Nagel and Menth, 1975)

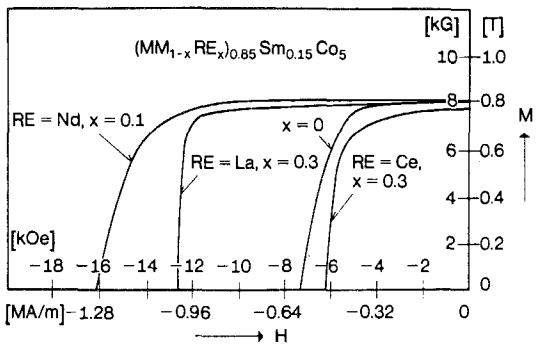

Fig. 14.141. Demagnetization curves of $(MM_{1-x}R_x)_{0.85}Sm_{0.15}Co_5$ magnets (Nagel and Menth, 1975).

some applications no hindrance for the use of MM instead of Sm metal. Therefore Sm-free $MMCo_5$ magnets can compete with the $SmCo_5$ based magnets which show the highest possible energy product.

6.3.3. *Production of cast magnets*

For some time after the observation of the high crystal anisotropy of YCo_5 it was believed that only by subdividing the alloys into fine, single-domain particles could full use of the potentials of these materials be made. Nesbitt, Wernick and coworkers (see for example Nesbitt and Wernick, 1973; Tawara and Senno, 1968) following the old idea of dispersion hardened magnets, developed alloy compositions suited to be cast and yielding after proper heat treatment magnets with medium to good magnetic properties.

After much development work, for example a composition $Co_{3.3}Cu_{1.2}Fe_{0.5}Ce_{0.25}Sm_{0.75}$ was developed which showed a $B_r = 7070$ G, ${}_BH_c = 5000$ Oe and an energy product of 12.3 MGOe (Nesbitt et al., 1971). Later especially in Japan the copper-containing magnets have been investigated. The copper content is responsible for the possibility to harden these samples magnetically, while a proper annealing procedure is essential. Usually a spinoidal decomposition is responsible for this hardening process. Some years ago these cast alloys were produced commercially. Although the magnetic properties were more or less satisfactory, especially the problem to obtain magnets which had a definite shape could not be solved properly. Therefore at present only one company (Japanese Shinetsu Company) is offering these copper-containing magnets commercially, which have however been processed by sintering and not by casting. The corresponding production scheme is given in fig. 14.142. Following the alloy preparation a multi-component alloy is ground, magnetically aligned and pressed, sintered, followed by a heat treatment which brings about the magnetic hardening, machined and finally magnetized. By shifting the rare earth-transition metal ratio from 1 : 5 to 1 : 7 an energy product of over 26 MGOe has been achieved, while commercially magnets with 18 to 25 MGOe are offered. The precipitation hardened magnets are sintered between 1000 to 1200°C for one

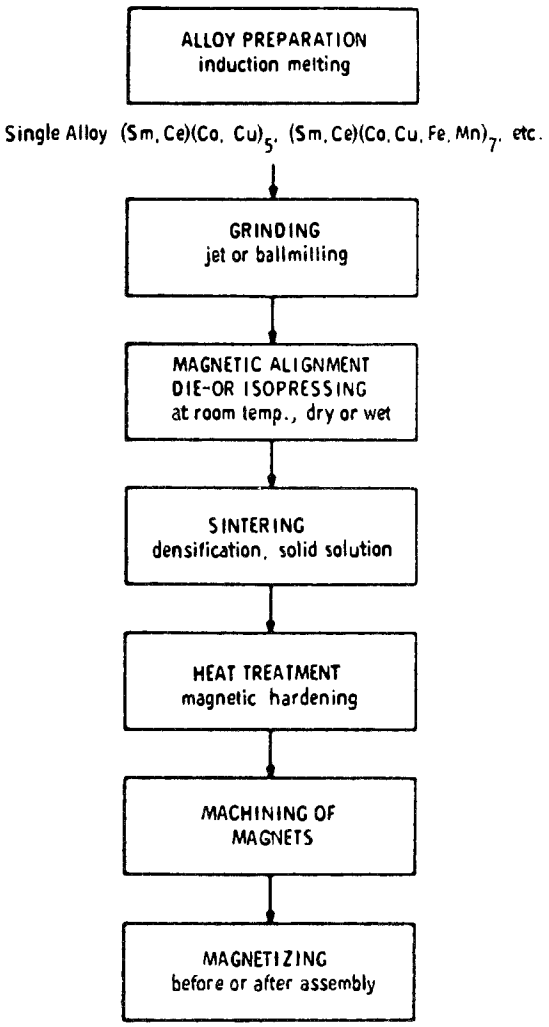

Fig. 14.142. Basic production steps for sintered Cu-containing magnets (Strnat, 1976b).

hour, while the ageing process is performed between 300 to 400°C for approximately four hours. As a model for these magnets cast $YFe_xCo_{3.4-x}Cu_{1.6}$ samples can be taken which show very different intrinsic coercive fields as a function of the iron content, see fig. 14.143. Usually the iron content is also used in order to increase the saturation magnetization. From fig. 14.143 it can be seen, however, that no simple relationship between the iron content and the saturation magnetization is observed. For a given annealing procedure however and for a specific iron content a maximum of $_MH_c$ is observed. Similar to the conventional

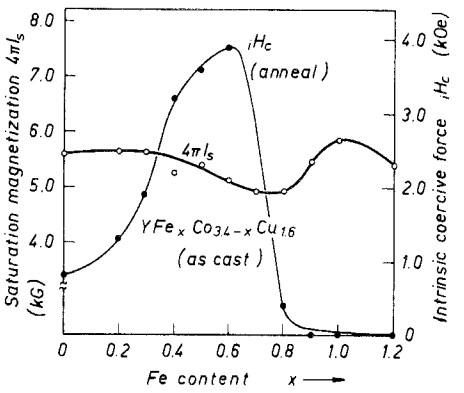

Fig. 14.143. Variations of the saturation magnetization and coercive force $_iH_c$ vs. iron content for $YFe_xCo_{3.4-x}Cu_{1.6}$ systems (Narita, 1976).

$SmCo_5$ magnets the annealing temperature and time as well as the cooling technique are of fundamental importance for the properties which are finally achieved.

6.3.4. *Polymer-bonded or metal bonded magnets*

Similar to flexible or bonded ferrites, also bonded magnets on the basis of R–Co have been developed and produced. The advantages of polymer bonded and flexible magnets are especially seen if magnets with a distinct and sometimes complicated shape are necessary. In this and many similar applications the advantages overcome the disadvantage of poor magnetic properties. Also special production processes for fastening the magnets to the device are possible. The starting material can either be any sintered material or copper-containing magnets. Furthermore the so-called 2 : 17 magnets discussed below, and also chips of any magnetic material which frequently are the scrap of sintered or cast magnets may be used. The bonded magnets are obviously promising in the near future, especially if the cost of material can further be decreased (Kamino and Yamane, 1976). In fig. 14.144 the main features of the production of polymer bonded magnets are summarized. Another possibility to produce isotropic magnets is the soldering of magnetic particles to form a bulk magnet. These soft metal bonded rare earth-cobalt magnets have some advantages, especially since they can be machined with steel tools (Strnat, 1976a).

6.3.5. 2 : 17 *magnets*

Hoffer and Strnat in their 1966 paper also gave the anisotropy constant for Y_2Co_{17}. This material however did not hold much promise as a magnetic material because the easy axis of magnetization lies in the basal plane. Later, however, Ray and Strnat (1972b), immediately followed by similar investigations by Schaller et al. (1972) observed that by the addition of iron the easy axis of magnetization in R_2Co_{17} compounds can be turned into the c-axis (fig. 14.145). The 2 : 17 compounds are especially attractive because in principle energy products in excess of 60 MGOe could be possible (Strnat, 1976b). Recently

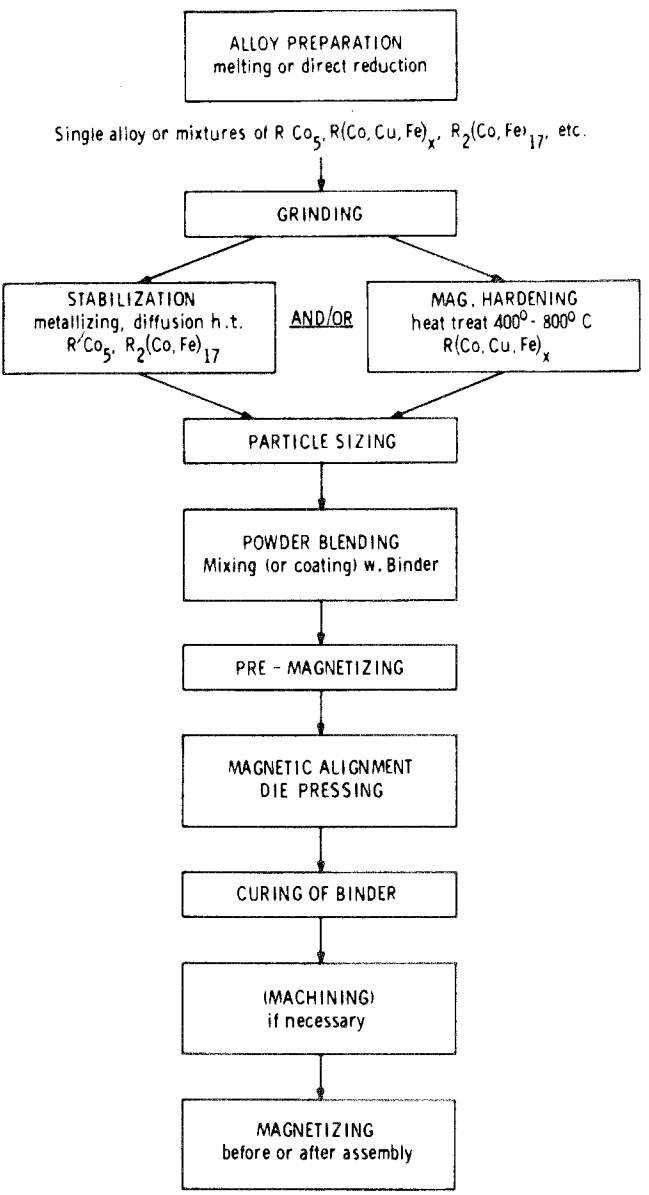

Fig. 14.144. Basic production steps for polymer-bonded magnets (Strnat, 1976b).

especially due to the efforts of Menth, Nagel and coworkers at BBC Switzerland (Menth, 1975; Nagel, 1975; Menth and Nagel, 1976; Nagel et al., 1976) 2 : 17 magnets have become reality and are now commercially produced. The basic composition is $Sm(Co, Cu, Fe, Mn)_z$ with $z \leq 7$. While the primary phase is of the Sm_2B_{17}-type, the matrix is of the SmB_5 type. Useful magnetic properties can be

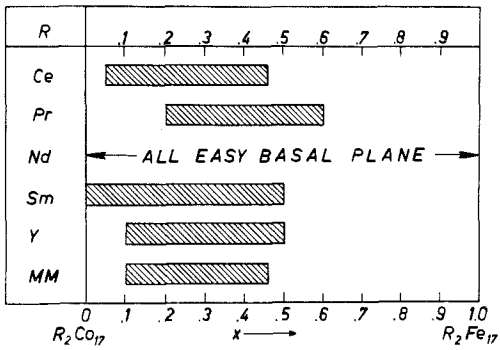

Fig. 14.145. Magnetic symmetry of $R_2(Co_{1-x}Fe_x)_{17}$ phases. Shaded areas indicate values of x where the easy axis of magnetization is in the c-axis (Ray and Strnat, 1972b).

achieved again by a precipitation hardening process, which is very sensitive to the annealing temperature. From fig. 14.146 it can be seen that the useful area lies between the 1 : 5 and 2 : 17 region in the Sm–Co–Cu phase diagram. From the magnetization curves it can be deduced that the pinning of domain walls is the dominant mechanism (Menth and Nagel, 1976). The nature of the pinning centres is presently not known. Although no precipitation within the 2 : 17 phase has been observed, this possibility cannot be ruled out. Also stacking faults, anti-phase boundaries and twin bands may act as pinning centres.

Instead of using bulk hardening, the 2 : 17 magnets can also be prepared by sintering techniques. It has, however, not been established which process is to be preferred (with or without Cu). Figure 14.147 shows the influence of the iron-chromium and iron-manganese ratios on the demagnetization. From fig.

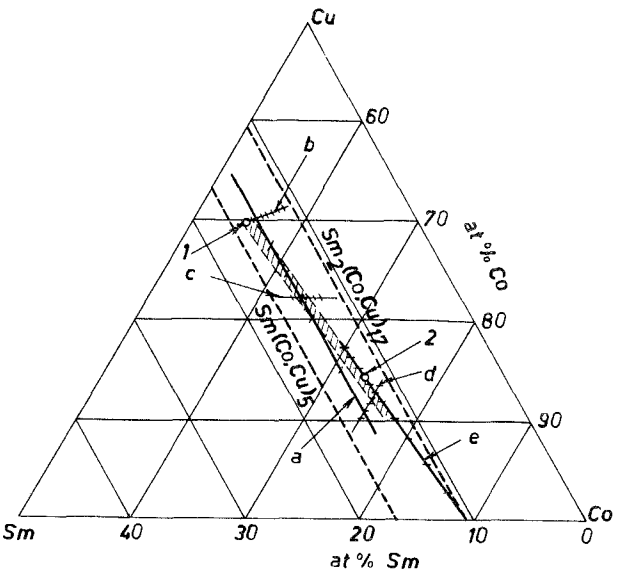

Fig. 14.146. Phase diagram of the Sm–Co–Cu systems reproducing the investigated alloys. The shaded area marks the region of useful magnetic properties (Menth, 1975).

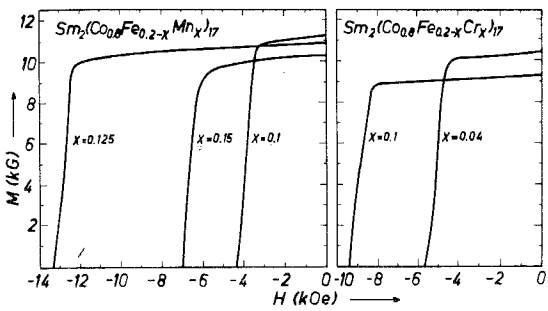

Fig. 14.147. Demagnetization curves of sintered Sm_2B_{17} magnets (Nagel, 1975).

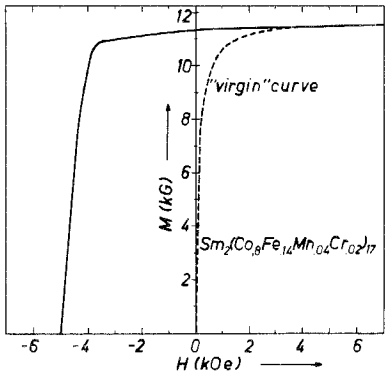

Fig. 14.148. "Virgin" magnetization curve and demagnetization curve of a $Sm_2(Co_{0.8}Fe_{0.14}Mn_{0.04}Cr_{0.02})_{17}$ magnet (Nagel, 1975).

14.148 the magnetization curve of a specific 2 : 17 magnet can be seen. The addition of manganese or chromium increased the magnetic anisotropy. This increase in anisotropy field H_A is however accompanied by a decrease of the saturation magnetization M_s. Therefore an optimum value exists for the manganese and chromium content. At present the single phase alloys are melted, the powdered magnetic alloys aligned, then isostatically pressed, sintered and heat treated.

The potential of the 2 : 17 compounds is sufficiently high to justify more effort in the near future in order to develop permanent magnets with unique properties and new record values in excess of 30 MGOe. This value is three times the record value of Alnico magnets which were the best magnets ten years ago. For some applications, however, rare earth-transition metal permanent magnets are superior compared to older magnets by a factor of ten or even more.

6.4. *Short survey of the applications of rare earth-transition metal magnets*

In principle rare earth permanent magnets can be applied in all cases where other magnets have been used in the past. Because of the generally far better quality and higher energy product of the R–Co permanent magnets, however, a simple replacement of the other magnets is not meaningful. In order to take full advantage of a R–Co magnet, especially of the high coercivity, a redesign of the magnetic field path is necessary.

The main advantage of a R–Co permanent magnet lies in the following: for the same magnetic field and the same stored magnetic energy a far smaller and lighter magnet is sufficient. This means that many devices can be scaled down by a factor of 3 or 10, and nevertheless have an increased performance. Another point is that new applications become feasible by means of the rare earth permanent magnet. In the next paragraphs we can only give some examples of the

many applications which have been found for rare earth permanent magnets in the last few years. Many new applications will come up in the near future.

From the proceedings of the "Second international workshop on rare earth-Co permanent magnets" held in June 1976 in Dayton/Ohio (Strnat, 1976a) and from the program of the forthcoming 3rd workshop (San Diego 1978) it can be seen that rare earth permanent magnets are now finding application in many different fields. We refer the reader therefore to these proceedings for details. Rare earth-Co permanent magnets are finding for instance applications in small d.c. motors. In this case the price of the permanent magnet material does not play a dominant role, because the size of the magnets is usually small. At present in more than 20 million wrist-watches rare earth permanent magnets are an essential part in stepping motors. In slightly larger d.c. motors rare earth permanent magnets find an increasing application. In these cases new design principles are necessary in order to make full use of the advantages of these new materials. The applications include small industrial motors, torquers, servo-motors etc. (see for example Noodleman, 1976). High speed permanent magnet generators up to 200 kVA have been designed by the General Electric Company (Bailey and Richter, 1976). Because of the high force exerted by a rare earth-Co permanent magnet compared to its own weight a complete new set of devices as for example those with magnetic bearings and suspensions have become possible. At the just cited workshop six papers were concerned only with these just mentioned applications.

Besides these applications in many other different devices rare earth permanent magnets are now used. These include for instance line printers, aerospace inertial systems, klystrons, magnetrons, precision accelerometers, multifunctional speed sensors, over-speed switches, jet engine sensors, tunable magnetic circuits for micro-wave filters etc. (see Strnat, 1976a). Another application is for magnetic couplings (e.g. autoclaves). From this list it can be seen that the rare earth permanent magnets are increasingly finding applications in very specialized fields where the quality and not the price of the permanent magnetic material is essential.

Because of the unique properties of rare earth permanent magnets they are also finding applications in seemingly strange applications, e.g. in biomedicine (Hennig et al., 1975). The field of applications of permanent magnets will undoubtedly broaden in the near future because of new design principles, which become feasible and because of the increasing knowledge of the users of permanent magnets in general.

An essential prerequisite of the successful application of new materials as e.g. the newest R–Co permanent magnets are stringent tests and quality controls which are adapted to the different applications. Just recently Mildrum and Iden (1975) have made a comparison of nearly all commercially available R–Co permanent magnets with respect to their magnetic and physical properties. They have tried to measure or to compile physical properties of R–Co magnets which are interesting especially if these magnets are used in micro-wave tubes as e.g. travelling wave tubes, klystrons, in rotating machinery, in magnetic bearings or in precision aerospace instruments. Many physical properties of these magnets

as e.g. the density, the strength, the hardness, the specific heat, coefficients of thermal expansion, electrical resistivity and so on have been measured and determined. At present however there is much scattering not only between magnets from different producers, but also between magnets of the same producer but from different charges. Since many of these magnets are used at elevated temperatures and in varying magnetic fields, the changes of the properties with time and with different environmental conditions are to be tested and have to be known. At present the knowledge which is available is not completely satisfactory. In due time, when new applications have emerged also new testing methods will become necessary.

6.5. *Conclusion and summary*

The development of the rare earth-Co permanent magnets has opened a completely new field. Because of the unique properties of these materials a large number of companies and research institutions are now engaged in further increasing the knowledge about these materials and will enhance the quality of these permanent magnets. Especially interesting in the near future seems to be the development of even better permanent magnets, measured by the energy product on the basis of the compounds R_2B_{17}. Undoubtedly the research and development in the near future in this field will not only be directed towards new record values with respect to the energy product, but also to a better and more stable quality and new applications. Furthermore the economics is naturally an essential part. At present in our opinion the "point of no return" has already been reached. This means that the R–Co permanent magnets have their place in modern technology and will not lose this place in the next decades. This is in contrast to other permanent magnets which have been developed in the past and which after some initial success have not found the reception which it was originally thought that they would receive.

We do not wish to conclude this chapter without at least mentioning that the rare earth-Co permanent magnets are not the only magnetic materials based on rare earth-transition metals, which have found practical application. Similar compositions between rare earths and iron or cobalt have recently, in the form of amorphous or sputtered thin films (see ch. 16), found applications in the field of computer technology. These materials have been developed as a medium for bubble domain storage devices (see e.g. Chaudhari and Herd, 1976). Especially at IBM much of the research work in this field has been done in the last years. It is not unlikely that these rare earth-transition metal based memories will play an essential role in the next computer generation and in similar devices. At recent magnetism conferences these materials and devices have found great interest.

We believe therefore that the possible applications of rare earth-transition metal intermetallic compounds either as hard or soft magnetic materials or in other connections are at present not yet exhausted. By the intensive research performed in this field, new applications in science and technology will emerge in the not too distant future.

References

Abel, A.W. and R.S. Craig, 1968, J. Less-Common Metals **16**, 77.

Abrahams, S.C., J.L. Bernstein, R.C. Sherwood, J.H. Wernick and H.J. Williams, 1964, J. Phys. Chem. Solids **25**, 1069.

Alben, R. and E.P. Wohlfarth, 1974, Phys. Lett. **49A**, 271.

Alberts, H.L., J. Beille, D. Bloch and E.P. Wohlfarth, 1974, Phys. Rev. **B9**, 2233.

Alfieri, G.T., E. Banks and K. Kanematsu, 1966, J. Appl. Phys. **37**, 1254.

Alfieri, G.T., E. Banks, K. Kanematsu and T. Ohoyama, 1967, J. Phys. Soc. Jap. **23**, 507.

Allain, Y., F. Varret and A. Miedan-Gros, 1965, C.R. Acad. Sci., Paris 260, 4677.

Anderson, P.W., 1961, Phys. Rev. **124**, 41.

Andres, K., E. Bucher, J.P. Maita and A.S. Cooper, 1972, Phys. Rev. Lett. **28**, 1652.

Andres, K. and E. Bucher, 1972, J. Low. Temp. Phys. **9**, 267.

Andres, K., E. Bucher, P.H. Schmidt, J.P. Maita and S. Darack, 1975, Phys. Rev. **B11**, 4364.

Arif, S.K., G.J. Bowden and D.St.P. Bunbury, 1974, 18th. Ampère Conf., Nottingham, p. 85.

Arif, S.K., D.St.P. Bunbury and G.J. Bowden, 1975a, J. Phys. **F5**, 1785.

Arif, S.K., D.St.P. Bunbury, G.J. Bowden and R.K. Day, 1975b, J. Phys. **F5**, 1048.

Arif, S.K., D.St.P. Bunbury and G.J. Bowden, 1975c, J. Phys. **F5**, 1792.

Arif, S.K. and D.St.P. Bunbury, 1976, Phys. Status Solidi **33a**, 91.

Arif, S.K., I. Sigalas and D.St.P. Bunbury, 1977, Phys. Status Solidi **41a**, 585.

Arnold, G. and N. Nereson, 1969, J. Chem. Phys. **51**, 1495.

Arnold, G., N. Nereson and C. Olsen, 1967, J. Chem. Phys. **46**, 4041.

Atoji, M., 1968a, J. Chem. Phys. **48**, 560.

Atoji, M., 1968b, J. Chem. Phys. **48**, 3380.

Atoji, M., 1969, J. Chem. Phys. **51**, 3882.

Atzmony, U., M.P. Dariel, E.R. Bauminger, D. Lebenbaum, I. Novik and S. Ofer, 1973, Phys. Rev. **B7**, 4220.

Atzmony, U. and M.P. Dariel, 1974, Phys. Rev. **B10**, 2060.

Bachmann, K., 1971, Cobalt-Rare Earth, a new class of permanent magnets, Brown-Boveri Research Reports, KLR-71-04.

Bachmann, K., 1972, Brown Boveri Mitteilungen **59**, 464.

Bailey, L.J. and E. Richter, 1976, in: Strnat, K.J., 1976a, ed., Proceedings of the 2nd internat. workshop on Rare Earth-Cobalt permanent magnets and their applications, University of Dayton, Ohio, June 8–11, 1976, p. 235.

Bak, P., 1974, J. Phys. **C7**, 1497.

Bambakidis, G., 1970, J. Phys. Chem. Solids **31**, 503.

Barbara, B., C. Bécle, R. Lemaire and R. Pauthenet, 1968, C.R. Acad. Sci., Paris, Ser. **B267**, 309.

Barbara, B., C. Bécle and E. Siaud, 1971a, J. Phys. (Paris) **32**, C1-1126.

Barbara, B., C. Bècle, R. Lemaire and D. Paccard, 1971b, J. Phys. (Paris) **32**, C1-299.

Barbara, B., C. Bécle, R. Lemaire and D. Paccard, 1971c, IEEE Trans. Magn., MAG 7, 654.

Barbara, B. and D. Gignoux, 1972, C.R. Acad. Sci., Paris, Ser. **B274**, 319.

Barbara, B., N.V. Nguyen and E. Siaud, 1972, C.R. Acad. Sci., Paris, Ser. **B274**, 1053.

Barbara, B., 1973, J. Phys. (Paris) **34**, 1039.

Barbara, B., D. Gignoux, D. Givord, F. Givord and R. Lemaire, 1973, Int. J. Magnetism **4**, 77.

Barbara, B., J.X. Boucherle and M.F. Rossignol, 1974a, Phys. Status Solidi **25a**, 165.

Barbara, B., M.F. Rossignol, H.G. Purwins and E. Walker, 1974b, Proc. Conf. Champs Intenses, Grenoble.

Barbara, B., M.F. Rossignol and E. Siaud, 1974c, C.R. Acad. Sci., Paris, Ser. **B278**, 513.

Barbara, B., M.F. Rossignol, H.G. Purwins and E. Walker, 1974d, Phys. Status Solidi **22a**, 553.

Barbara, B., M.F. Rossignol, H.G. Purwins and E. Walker, 1975a, Solid State Comm. **17**, 1525.

Barbara, B., M.F. Rossignol and J.X. Boucherle, 1975b, Phys. Lett. **55A**, 321.

Barbara, B. and M. Uehara, 1976, Proc. of the Joint MMM-Intermag. Conf., Pittsburgh.

Barbara, B., J.X. Boucherle, J.L. Buevoz, M.F. Rossignol and J. Schweizer, 1977, Solid State Comm. **24**, 481.

Barbier, J.C., 1950, C.R. Acad. Sci., Paris **230**, 1040.

Bargouth, M.O. and G. Will, 1971, Phys. Lett. **36A**, 50.

Barrick, J.C., M. Simmons, W.J. James, J. Laforest and J.S. Shah, 1974, J. Less-Common Metals **37**, 379.

Bauminger, E.R., I. Felner, D. Levron, I. Novik and S. Ofer, 1974, Phys. Rev. Lett. **33**, 890.

Bechman, C.A., K.S.V.L. Narasimhan, W.E. Wallace, R.S. Craig and R.A. Butera, 1976, J. Phys. Chem. Solids **37**, 245.

Bécle, C., R. Lemaire and D. Paccard, 1970, J. Appl. Phys. **41**, 855.

Beille, J., D. Bloch and J. Voiron, 1975, Ann. Conf. Magn. and Magn. Mat., Philadelphia.

Belakhovsky, M. and J. Pierre, 1971, Solid State Comm. **9**, 1409.

Belakhovsky, M., J. Pierre and D.K. Ray, 1972, Phys. Rev. **B6**, 939.

Belakhovsky, M., J. Pierre and D.K. Ray, 1975, J. Phys. **F5**, 2274.

Belov, K.P., S.A. Nikitin and K.G. Gurtovoi, 1969, Sov. Physics JETP **28**, 84.

Belov, K.P., V.A. Vasilkovskii, N.M. Kovtun, A.K. Kupriyanov and S.A. Nikitin, 1974, JETP Lett. **20**, 304.

Bergman, G. and J.L.T. Waugh, 1953, Acta Crystallogr. **6**, 93.
Bergman, G. and J.L.T. Waugh, 1956, Acta Crystallogr. **9**, 214.
Bertaut, E.F., R. Lemaire and J. Schweizer, 1965, Bull. Soc. Fr. Minéral. Cristallogr. **88**, 580.
Berthet-Colominas, C., J. Laforest, R. Lemaire, R. Pauthenet and J. Schweizer, 1968, Cobalt **39**, 97.
Bleaney, B., 1963, Proc. Roy. Soc., Ser. **A276**, 28.
Bleaney, B.I. and B. Bleaney, 1965, Electricity and Magnetism, Clarendon Press, Oxford, p. 621.
Bloch, D. and R. Lemaire, 1970, Phys. Rev. **B2**, 2648.
Bloch, D., D.L. Camphausen, J. Voiron, J.B. Ayasse, A. Berlon and J. Chaussy, 1972, C.R. Acad. Sci., Paris, Ser. **B275**, 601.
Bloch, D., D.M. Edwards, M. Shimizu and J. Voiron, 1975, J. Phys. **F5**, 1217.
Borsa, F. and G. Olcese, 1973, Phys. Status Solidi **17A**, 631.
Bozorth, R.M., 1951, Ferromagnetism, D. van Nostrand, Princetown.
Breeze, A. and P.G. Perkins, 1975, J. Phys. **F5**, 255.
Broeder, F.J.A., G.D. Westerhout and K.H.J. Buschow, 1974, Z. Metallk. **65**, 501.
Brouha, M. and K.H.J. Buschow, 1973, J. Appl. Phys. **44**, 1813.
Brouha, M., K.H.J. Buschow and A.R. Miedema, 1974, I.E.E.E. MAG-10, 182.
Brouha, M. and K.H.J. Buschow, 1975a, J. Phys. **F5**, 543.
Brouha, M. and K.H.J. Buschow, 1975b, J. Appl. Phys. **46**, 1355.
Brun, T.O., G.P. Felcher and J.S. Kouvel, 1971, Proc. AIP Conf., No. 5, Part 2, 1376.
Brun, T.O., G.H. Lander, D.L. Price, G.P. Felcher and J.F. Reddy, 1973, ICM, 590.
Brun, T.O., G.H. Lander, D.L. Price, G.P. Felcher and J.F. Reddy, 1974, Phys. Rev. **B9**, 248.
Brusdeylins, A., 1975, Goldschmidt Informiert **4**, 34.
Bruzzone, G., M.L. Fornasini and F. Merlo, 1970, J. Less-Common Metals **22**, 253.
Bruzzone, G., M.L. Fornasini and F. Merlo, 1973, J. Less-Common Metals **32**, 317.
Bührer, W., M. Godet, H.G. Purwins and E. Walker, 1973, Solid State Comm. **13**, 881.
Burr, C.R., 1975, Solid State Comm. **16**, 965.
Burzo, E., I. Pop and V.I. Tchetchernikov, 1969, Les Elements des Terres Rares, Tome II, 87.
Burzo, E., 1970, C.R. Acad. Sci., Paris, Ser. **B271**, 1159.
Burzo, E., 1971, Z. Angew. Phys. **32**, 127.
Burzo, E., 1972a, Phys. Rev. **B6**, 2882.
Burzo, E., 1972b, Int. J. Magn. **3**, 161.
Burzo, E., 1972c, C.R. Acad. Sci., Paris, Ser. **B274**, 114.
Burzo, E., 1972d, Proc. Conf. Deutsche Phys. Gesellschaft, Freudenstadt.
Burzo, E. and J. Laforest, 1972, C.R. Acad. Sci., Paris, Ser. **B274**, 114.
Burzo, E., 1973a, Proc. 10th R.E. Conf., Carefree, Ariz., p. 96.
Burzo, E., 1973b, Stud. Cercet. Fiz. **25**, 425.
Burzo, E. and R. Baican, 1973, XVII. Congress Ampere, North Holland Publishing Co.
Burzo, E. and D.P. Lazar, 1973, C.R. Acad. Sci., Paris, Ser. **B276**, 239.
Burzo, E., 1974, Solid State Comm. **14**, 1295.
Burzo, E., 1975a, Invited Lecture at Symposium on Metal Physics, Zloty-Potok, Poland.
Burzo, E., 1975b, Solid State Comm. **16**, 759.
Burzo, E. and D.P. Lazar, 1976, Solid State Comm. **18**, 381.
Buschow, K.H.J. and J.F. Fast, 1966a, Phys. Status Solidi **16**, 467.
Buschow, K.H.J. and J.F. Fast, 1966b, Z. Phys. Chem. **50**, 1.
Buschow, K.H.J., J.F. Fast, A.M. van Diepen and H.W. de Wijn, 1967, Phys. Status Solidi **24**, 715.
Buschow, K.H.J., 1968, Z. Phys. Chem. **59**, 21.
Buschow, K.H.J. and A.S. van der Goot, 1968, J. Less-Common Metals **14**, 323.
Buschow, K.H.J., 1969, Phys. Lett. **29A**, 12.
Buschow, K.H.J., H.W. de Wijn and A.M. van Diepen, 1969a, J. Chem. Phys. **50**, 137.
Buschow, K.H.J., A.S. van der Goot and J. Birkhan, 1969b, J. Less-Common Metals **19**, 433.
Buschow, K.H.J., A.M. van Diepen and H.W. de Wijn, 1970, J. Appl. Phys. **41**, 4609.
Buschow, K.H.J., 1971, Phys. Status Solidi **7a**, 199.
Buschow, K.H.J. and R.P. van Stapele, 1971, J. Phys. **C1**, 672.
Buschow, K.H.J., A.M. van Diepen and H.W. de Wijn, 1971, J. Appl. Phys. **42**, 4315.
Buschow, K.H.J., A. Oppelt and E. Dormann, 1972, Phys. Status Solidi **50b**, 647.
Buschow, K.H.J., 1973a, J. Less-Common Metals **33**, 311.
Buschow, K.H.J., 1973b, J. Less-Common Metals **33**, 239.
Buschow, K.H.J. and A.M. van Diepen, 1973, Proc. ICM Moscow.
Buschow, K.H.J., A.M. van Diepen and H.W. de Wijn, 1973a, Phys. Rev. **B8**, 5134.
Buschow, K.H.J., A.M. van Diepen and H.W. de Wijn, 1973b, Phys. Rev. **B8**, 1125.
Buschow, K.H.J., 1974, J. Chem. Phys. **61**, 4666.
Buschow, K.H.J. and A. Oppelt, 1974, J. Phys. **F4**, 1246.
Buschow, K.H.J., A.M. van Diepen and H.W. de Wijn, 1974a, Solid State Comm. **15**, 903.
Buschow, K.H.J., B. van Laar and J.B.A.A. Elemans, 1974b, J. Phys. **F4**, 1517.
Buschow, K.H.J., 1975, J. Less-Common Metals **39**, 185.
Buschow, K.H.J., W.J. Huiskamp, H.Th. Le Fever, F.J. v. Steenwijk and R.C. Thiel, 1975a, J. Phys. **F5**, 1625.
Buschow, K.H.J., M. Brouha and J.B.A.A. Elemans, 1975b, Phys. Status Solidi **30a**, 177.

Buschow, K.H.J., J.P. de Jong, H.W. Zandbergen and B. van Laar, 1975c, J. Appl. Phys. **46**, 1352.
Buschow, K.H.J., 1976, J. Less-Common Metals **44**, 301.
Buschow, K.H.J. and C.J. Schinkel, 1976, Solid State Comm. **18**, 609.
Buschow, K.H.J. and W.W. van den Hoogenhof, 1976, J. Less-Common Metals **45**, 309.
Buschow, K.H.J. and M. Brouha, 1976, J. Appl. Phys. **47**, 1653.
Cable, J.W., W.C. Koehler and E.O. Wollan, 1964, Phys. Rev. **136A**, 240.
Cable, J.W., W.C. Koehler and H.R. Child, 1965, J. Appl. Phys. **36**, 1096.
Carfagna, P.D. and W.E. Wallace, 1968, J. Appl. Phys. **39**, 5259.
Cech, R.E., 1974, J. Metals **26**, 32.
Chao, C.C., 1966, J. Appl. Phys. **37**, 2081.
Chaudhari, P. and S.R. Herd, 1976, IBM Journal of Research and Development **20**, 101.
Cherry, L.V. and W.E. Wallace, 1962, J. Appl. Phys. **33**, 1515.
Clark, A.E. and H.S. Belson, 1972, 8th Conf. Magn., Denver.
Clark, A.E., 1973, Appl. Phys. Lett. **23**, 642.
Clark, A. and E. Callen, 1968, J. Appl. Phys. **39**, 5972.
Cock, G.J., L.W. Roeland, H.G. Purwins, E. Walker and A. Furrer, 1974, Solid State Comm. **15**, 845.
Coldea, M. and I. Pop, 1973, Phil. Mag. **28**, 881.
Collins, M.F. and J.B. Forsyth, 1963, Phil. Mag. **8**, 401.
Conner, R.A., 1967, Acta Crystallogr. **22**, 745.
Corliss, L.M. and J.M. Hastings, 1963, La Diffraction et la Diffusion des Neutrons, Coll. Int. C.N.R.S., Grenoble, **126**, 133.
Corliss, L.M. and J.M. Hastings, 1964, J. Appl. Phys. **35**, 1051.
Craik, D.J. and E. Hill, 1974, Phys. Lett. **48A**, 157.
Crangle, J., 1974, Phys. Letters **48A**, 370.
Dariel, M.P. and U. Atzmony, 1973, Int. J. Magnetism **4**, 213.
Debray, D.K., E. Ryba and L.N. Mulay, 1967, J. Appl. Phys. **38**, 3459.
Debray, D.K., W.E. Wallace and E. Ryba, 1970, J. Less-Common Metals **22**, 19.
Debray, D.K. and E. Ryba, 1971, J. Phys. (Paris) **32**, C1-1130.
Debray, D.K., M. Sougi and P. Meriel, 1972, J. Chem. Phys. **56**, 4325.
Debray, D.K. and M. Sougi, 1972, J. Chem. Phys. **57**, 2156.
Debray, D.K. and M. Sougi, 1973, J. Chem. Phys. **58**, 1783.
Debray, D.K., 1973a, J. Less-Common Metals **30**, 237.
Debray, D.K., 1973b, Phys. Status Solidi **18a**, 227.
Debray, D.K. and J. Sakurai, 1974, Phys. Rev. **B9**, 2129.
de Chatel, P.F. and F.R. de Boer, 1970, Physica **48**, 331.
Deenadas, C., A.W. Thompson, R.S. Craig and W.E. Wallace, 1971, J. Phys. Chem. Solids **32**, 1853.
de Gennes, P.G., 1962, J. Phys. Radium **23**, 510.
Dekker, A.J., 1965, J. Appl. Phys. **36**, 906.
de Moral, A. and D. Melville, 1975, J. Phys. **F5**, 1767.
Déportes, J., D. Gignoux and F. Givord, 1974, Phys. Status Solidi **64b**, 29.
Deryagin, A.V., A. Ulyanov, N. Kudrevatykh, E. Barabanova, Y. Bashkov, A. Andreev and E. Tarasov, 1974, Phys. Status Solidi **23a**, K15.
Deryagin, A.V. and N.V. Kudrevatykh, 1975, Phys. Status Solidi **30a**, K129.
de Savage, B.F., R.M. Bozorth, F.E. Wang and E.R. Callen, 1965, J. Appl. Phys. **36**, 992.
Devine, R.A.B., W. Zingg, J.M. Morel and D. Shaltiel, 1973, Solid State Comm. **12**, 515.
de Wijn, H.W., K.H.J. Buschow and A.M. van Diepen, 1968, Phys. Status Solidi, **30**, 759.
Dintelmann, F. and K.H.J. Buschow, 1971, Z. Angew. Phys. **31**, 181.
Domazer, H.G. and K.J. Strnat, 1976, in: Strnat, 1976a, Proc. of the 2nd Int. Workshop on Rare Earth-Cobalt Permanent Magnets and their Applications, University of Dayton, Ohio, June 8–11, 1976, p. 348.
Dormann, E. and K.H.J. Buschow, 1973, Phys. Status Solidi **59b**, 411.
Dormann, E. and K.H.J. Buschow, 1976, J. Appl. Phys. **47**, 1662.
Dormann, E., L. Schaafhausen and K.H.J. Buschow, 1976, J. Magn. Magn. Mat. **2**, 177.
Doser, M. and F.G. Jones, 1976, Proc. of the 12th Rare Earth Research Conf., Vail, Colorado.
Dublon, G., M.P. Dariel and U. Atzmony, 1975, Phys. Lett. **51A**, 262.
Duwell, E.J. and E.J. Baenziger, 1955, Acta Crystallogr. **8**, 705.
Dwight, A.E., W.C. Harper and C.W. Kimball, 1971, Proc. of the 9th Rare Earth Res. Conf., p. 189.
Dworschak, G. and Y. Khan, 1974, J. Phys. Chem. Solids **35**, 1021.
Eckrich, K., E. Dormann, A. Oppelt and K.H.J. Buschow, 1973, Int. J. Magnetism **5**, 75.
Eckrich, K., E. Dormann, A. Oppelt and K.H.J. Buschow, 1976, Z. Phys. **B23**, 157.
Edmonds, A.R., 1957, Angular Momentum in Quantum Mechanics, Princeton Univ. Press.
Edwards, D.M. and E.P. Wohlfarth, 1968, Proc. Roy. Soc., Ser. **A303**, 127.
Edwards, R.L. and L.C. Bartel, 1972, Phys. Rev. **B5**, 1064.
Egami, T., 1973a, Phys. Status Solidi **19a**, 747.
Egami, T., 1973b, Phys. Status Solidi **57b**, 211.
Elemans, J.B.A.A. and K.H.J. Buschow, 1973, Phys. Status Solidi **57b**, K153.
Elemans, J.B.A.A. and K.H.J. Buschow, 1974, Phys. Status Solidi **24a**, 393.
Elemans, J.B.A.A., K.H.J. Buschow, H.W. Zandbergen and J.P. de Jong, 1975, Phys. Status Solidi **29a**, 595.

Elemans, J.B.A.A. and K.H.J. Buschow, 1976, Phys. Status Solidi **34a**, 355.
Elliott, R.J., 1961, Phys. Rev. **124**, 346.
Elliott, R.J. and F.A. Wedgwood, 1963, Proc. Phys. Soc. **81**, 846.
Elliott, R.J., 1971, Proc. of the 9th Rare Earth Res. Conf., p. 200.
Ermolenko, A.S., 1973, Proc. Int. Conf. Mag., Moscow.
Ermolenko, A.S., 1976, I.E.E.E. Trans. Mag. MAG-12, 992.
Farrell, J. and W.E. Wallace, 1966, Inorg. Chem. **5**, 105.
Fedro, A.J. and J.C. Shaffer, 1971, Proc. of the AIP Conf. Nr. 5, part 2, 1390.
Felcher, G.P., L.M. Corliss and J.M. Hastings, 1965, J. Appl. Phys. **36**, 1001.
Féron, J.L., R. Lemaire, D. Paccard and R. Pauthenet, 1968, C.R. Acad. Sci., Paris, Ser. **B269**, 371.
Féron, J.L., D. Gignoux, R. Lemaire and D. Paccard, 1969, Les Elements des Terres Rares, CNRS, Tome II, p. 75.
Fidler, J., 1976, Dissertation, TU Wien.
Fidler, J., H. Kirchmayr and P. Skalicky, 1977, Phil. Mag. **35**, 1125.
Fischer, G. and A. Meyer, 1975, Solid State Comm. **16**, 355.
Fisher, M.E. and J.S. Langer, 1968, Phys. Rev. Lett. **20**, 665.
Florio, J.V., R.E. Rundle and A.I. Snow, 1952, Acta Crystallogr. **5**, 449.
Fornasini, M.L. and A. Palenzona, 1974, J. Less-Common Metals **38**, 77.
Franse, J.J.M., 1977, Physica **86–88B**, 283.
Freeman, A.J. and R.E. Watson, 1962, Phys. Rev. **127**, 2058.
Friedel, J., 1958, Nuovo Cimento, Suppl. 7, 287.
Friedel, J., G. Leman and S. Olszewski, 1961, J. Appl. Phys., Suppl. **32**, 325.
Friedel, J., 1962, J. de Phys. et le Radium **23**, 501.
Furrer, A., 1975, J. Phys. **C8**, 824.
Furrer, A. and H.G. Purwins, 1976, J. Phys. **C9**, 1491.
Gardner, W.E., J. Penfold, T.F. Smith and I.R. Harris, 1972, J. Phys. **F2**, 133.
Gartmayer, F., 1969, Diplomarbeit, Techn. Univ. Wien.
Gignoux, D., R. Lemaire and D. Paccard, 1970, Solid State Comm. **8**, 391.
Gignoux, D. and J.S. Shah, 1972, Solid State Comm. **11**, 1709.
Gignoux, D., R. Lemaire and J. Chaussy, 1973, ICM, p. 361.
Gignoux, D., 1974, J. Phys. **35**, 455.
Gignoux, D. and J.C. Gomez-Sal, 1974, Phys. Lett. **50A**, 63.
Gignoux, D. and R. Lemaire, 1974, Solid State Comm. **14**, 877.
Gignoux, D., D. Givord, F. Givord, W.C. Koehler and R.M. Moon, 1976, Phys. Rev. **B14**, 162.
Gignoux, D., F. Givord and J. Schweizer, 1977a, J. Phys. **F7**, 1.
Gignoux, D., F. Givord and W.C. Koehler, 1977b, Physica **86–88B**, 165.
Givord, D., F. Givord and R. Lemaire, 1971a, J. Phys. Paris **32**, C1-668.
Givord, D., R. Lemaire, W.J. James, J.M. Moreau and J.S. Shah, 1971b, IEEE Trans. Magn., MAG 7, 657.
Givord, D. and R. Lemaire, 1972, C.R. Acad. Sci., Paris, Ser. **B274**, 1166.
Givord, D., F. Givord, R. Lemaire, W.J. James and J.S. Shah, 1972, J. Less-Common Metals **29**, 389.
Givord, D. and R. Lemaire, 1974, IEEE Trans. Magn., MAG 10, 109.
Givord, F. and J.S. Shah, 1972, C.R. Acad. Sci., Paris, Ser. **B274**, 923.
Givord, F., R. Lemaire and J.S. Shah, 1972, C.R. Acad. Sci., Paris, Ser. **B274**, 161.
Goblirsch, R., 1976, Dissertation, Univ. Wien.
Goebel, U., E. Dormann and K.H.J. Buschow, 1975, J. Phys. **F5**, 2198.
Gomes, A.A., 1966, J. Phys. Chem. Solids **27**, 451.
Gomes, A.A. and I.A. Campbell, 1967, Proc. Phys. Soc. **89**, 319.
Gomes, A.A. and A.P. Guimarães, 1974, J. Phys. **F4**, 1454.
Goodenough, J.B., 1963, Magnetism and the Chemical Bond, Interscience Publ., New York.
Gratz, E. and H.R. Kirchmayr, 1976, J. Magn. Magn. Mat. **2**, 187.
Gratz, E. and C.A. Poldy, 1977, Phys. Status Solidi **82b**, 159.
Greedan, J.E., 1971a, Proc. AIP Conf. No. 5, 1425.
Greedan, J.E., 1971b, Proc. of the 9th Rare Earth Res. Conf., 208.
Greedan, J.E. and V.U.S. Rao, 1973, J. Solid State Chem. **6**, 387.
Grössinger, R., 1975, Dissertation, Techn. Univ. Wien.
Grössinger, R., W. Steiner and K. Krec, 1976a, J. Magn. Magn. Mat. **2**, 196.
Grössinger, R., W. Steiner, F. Culetto and H.R. Kirchmayr, 1976b, Proc. ICM, Amsterdam 1976. (See also Physica (1977) **86–88B**, 210).
Gubbens, P.C.M., J.H.F. van Appeldoorn, A.M. van der Kraan and K.H.J. Buschow, 1974, J. Phys. **F4**, 921.
Gubbens, P.C.M., A.M. van der Kraan, J.J. van Loef and K.H.J. Buschow, 1976, I.E.E.E. Trans. Mag. MAG-12, 991.
Guy, C.N., 1975, J. Phys. **F5**, L242.
Harris, I.R. and G.V. Raynor, 1965, J. Less-Common Metals **9**, 263.
Hasegawa, A. and J. Kübler, 1974, Z. Phys. **269**, 31.
Hasegawa, A., B. Bremicker and J. Kübler, 1975, Z. Phys. **B22**, 231.
Hashimoto, Y., H. Fujii and T. Okamoto, 1975, J. Phys. Soc. Jap. Lett. **40**, 1519.
Havinga, E.E., K.H.J. Buschow and H.J. van Daal, 1973, Solid State Comm. **13**, 621.
Heer, H., A. Furrer, E. Walker, A. Treyvaud, H.G. Purwins and D. Kjems, 1974, J. Phys. **C7**, 1207.
Heidemann, A., D. Richter and K.H.J. Buschow, 1975, Z. Phys. **B22**, 367.

Hennig, G., H. Fenstel and K. Hennig, 1975, Goldschmidt Informiert **4**, 85.
Herget, C. and H.G. Domazer, 1975, Goldschmidt Informiert, **4**, 3.
Hill, T.W., W.E. Wallace, R.S. Craig and T. Inoue, 1973, J. Solid State Chem. **8**, 964.
Hillenbrand, B., K. Schuster and M. Wilhelm, 1971a, Phys. Lett. **36A**, 383.
Hillenbrand, B., K. Schuster and M. Wilhelm, 1971b, Z. Naturforsch. **A26**, 1684.
Hilscher, G., H.R. Kirchmayr and W. Steiner, 1971, Z. Angew. Phys. **32**, 203.
Hilscher, G., H. Rais and H.R. Kirchmayr, 1973, Phys. Status Solidi **59b**, K5.
Hilscher, G., 1974, Dissertation, Techn. Univ. Wien.
Hilscher, G., N. Buis and J.J.M. Franse, 1977, Physica **91B**, 170.
Hilzinger, H.R. and H. Kronmüller, 1972, Phys. Status Solidi **54b**, 593.
Hilzinger, H.R. and H. Kronmüller, 1973, Phys. Status Solidi **59b**, 71.
Hilzinger, H.R. and H. Kronmüller, 1975, Phys. Lett. **51A**, 59.
Hiraoka, T., 1974, J. Phys. Soc. Jap. **37**, 1238.
Hiraoka, T. and X. Fuchikami, 1974, J. Phys. Soc. Jap. **36**, 1488.
Hoffer, G. and K.J. Strnat, 1966, IEEE Trans. Magn., MAG 2, 487.
Hohnke, D. and E. Parthé, 1966, Acta Crystallogr. **20**, 572.
Houmann, J.G., P. Bak, H.G. Purwins and E. Walker, 1974, J. Phys. **C7**, 2691.
Hubbard, W.M., E. Adams and J.V. Gilfrich, 1960, J. Appl. Phys., Suppl. **31**, 368.
Hubbard, J., 1963, Proc. Roy. Soc., Ser. **A276**, 238.
Hubbard, J., 1964, Proc. Roy. Soc., Ser. **A277**, 237.
Hüfner, S., G.K. Wertheim, R.L. Cohen and J.H. Wernick, 1972, Phys. Rev. Lett. **28**, 488.
Hüfner, S., G.K. Wertheim and J.H. Wernick, 1973, Phys. Rev. **B8**, 4511.
Hungsberg, R.E. and K.A. Gschneidner, Jr., 1972, J. Phys. Chem. Solids **33**, 401.
Hutchens, R.D., V.U.S. Rao, J.E. Greedan, W.E. Wallace and R.S. Craig, 1971, J. Appl. Phys. **42**, 1293.
Hutchens, R.D., W.E. Wallace and N. Nereson, 1974, J. Solid State Chem. **9**, 152.
Hutchings, M.T., 1966, Solid State Phys. **16**, 227.
Ihrig, H., D.T. Vigren, J. Kübler and S. Methfessel, 1973, Phys. Rev. **B8**, 4525.
Inoue, T., S.G. Sankar, R.S. Craig, W.E. Wallace and K.A. Gschneidner, Jr., 1977, J. Phys. Chem. Solids, **38**, 487.
Jaakkola, S. and S. Parviainen, 1974, Phys. Status Solidi **21a**, K53.
Jaakkola, S., S. Parviainen and H. Stenholm, 1975, Z. Phys. **B20**, 109.
Jaccarino, V., B.T. Matthias, M. Peter, H. Suhl and J.H. Wernick, 1960, Phys. Rev. Lett. **5**, 251.
Jaccarino, V. and L.R. Walker, 1965, Phys. Rev. Lett. **15**, 258.
Jan, J.P., 1973, Phys. Rev. **B8**, 3590.
Jan, J.P., N.L. Martin and A. Wenger, 1974, Phys. Rev. **B9**, 1377.
Jeitschko, W., 1970, Acta Crystallogr. **B26**, 815.
Jones, F.G. and M. Tokunaga, 1976, Proc. of the Joint MMM-Intermag. Conf., Pittsburgh.
Jones, F.G., J.H. Thoe, H.E. Lehmann and R.B. Downs, 1976, Proc. of the 12th Rare Earth Conf., Vail, Colorado.
Johnson, Qu., D.H. Wood, G.S. Smith and A.E. Ray, 1968, Acta Crystallogr. **B24**, 274.
Jordan, H., 1924, El. Nachr. Techn. **1**, 7.
Jordan, H., 1930, Z. Techn. Phys. **11**, 2.
Kamino, K. and T. Yamane, 1976, in: Strnat, 1976a, Proc. of the 2nd Workshop on Rare Earth-Cobalt Perm. Magnets and their Applications, Univ. of Dayton, June 8–11, 1976, p. 377.
Kanamori, J., 1963, Progr. Theor. Phys. (Kyoto) **30**, 275.
Kanematsu, K., 1968, J. Phys. Soc. Jap. **25**, 628.
Kanematsu, K., G.T. Alfieri and E. Banks, 1969, J. Phys. Soc. Jap. **26**, 244.
Kaplan, N., E. Dormann, K.H.J. Buschow and D. Lebenbaum, 1973, Phys. Rev. **B7**, 40.
Kasuya, T., 1956, Progr. Theor. Phys. (Kyoto) **16**, 45.
Kirchmayr, H.R., 1966, IEEE Trans. Magn., MAG 2, 493.
Kirchmayr, H.R., 1967, Z. Kristallogr. **124**, 152.
Kirchmayr, H.R., 1968, J. Appl. Phys. **39**, 1088.
Kirchmayr, H.R., 1969a, Z. Angew. Phys. **27**, 18.
Kirchmayr, H.R., 1969b, Z. Metallk. **60**, 778.
Kirchmayr, H.R. and W. Steiner, 1971, J. Phys. (Paris) **32**, C1-665.
Kirchmayr, H.R., 1973, Appl. Phys. **1**, 187.
Kissel, F. and W.E. Wallace, 1966, J. Less-Common Metals **11**, 417.
Kittel, C., 1949, Rev. Mod. Phys. **21**, 541.
Klein, H.P., A. Menth and R.S. Perkins, 1975, Physica **20B**, 153.
Kneller, E., 1962, Ferromagnetismus, Springer, Berlin, 616.
Krén, E., J. Schweizer and F. Tasset, 1969, Phys. Rev. **186**, 479.
Kripyakevich, P.I. and D.P. Frankevich, 1965, Kristallografiya **10**, 560.
Kronmüller, H., 1968, Nachwirkung in Ferromagnetika, Springer, Berlin.
Kronmüller, H. and H.R. Hilzinger, 1973, Int. J. Magnetism Vol. 5, 27.
Kronmüller, H. and H.R. Hilzinger, 1976, J. Magn. Magn. Mat. **2**, 3.
Kunesh, C.J., K.S.V.L. Narasimhan and R.A. Butera, 1973a, J. Phys. Chem. Solids **34**, 2003.
Kunesh, C.J., K.S.V.L. Narasimhan and R.A. Butera, 1973b, J. Phys. Chem. Solids **34**, 817.
Kunesh, C.J., K.S.V.L. Narasimhan and R.A. Butera, 1975, J. Appl. Phys. **46**, 1349.
Laforest, J., R. Lemaire, R. Pauthenet and J. Schweizer, 1966, C.R. Acad. Sci., Paris, Ser. **B262**, 1260.
Laforest, J., R. Lemaire, D. Paccard and R. Pauthenet, 1967, C.R. Acad. Sci., Paris, Ser. **B264**, 676.

Laforest, J. and J.S. Shah, 1973, IEEE Trans. Magn., MAG 9, 217.
Lederer, P. and A. Blandin, 1966, Phil. Mag. **14**, 363.
Lee, E.W. and F. Pourarian, 1976, Phys. Status Solidi **33a**, 483.
Lemaire, R., 1966a, Cobalt **32**, 132.
Lemaire, R., 1966b, Cobalt **33**, 201.
Lemaire, R. and J. Schweizer, 1966, Phys. Lett. **21**, 366.
Lemaire, R. and J. Schweizer, 1967, C.R. Acad. Sci., Paris **264**, 642.
Lemaire, R., D. Paccard and R. Pauthenet, 1967a, C.R. Acad. Sci., Paris, Ser. **B265**, 1280.
Lemaire, R., R. Pauthenet, J. Schweizer and I.S. Silvera, 1967b, J. Phys. Chem. Solids **28**, 2471.
Lemaire, R. and D. Paccard, 1969, Les Elements des Terres Rares, CNRS, Tome II, p. 231.
Leon, B. and W.E. Wallace, 1970, J. Less-Common Metals **22**, 1.
Lethuillier, P., 1973, ICM, 50.
Lethuillier, P., G. Quezel-Ambrunaz and A. Percheron, 1973a, Solid State Comm. **12**, 105.
Lethuillier, P., J. Pierre, G. Fillion and B. Barbara, 1973b, Phys. Status Solidi **15a**, 613.
Longworth, G. and I.R. Harris, 1973, J. Less-Common Metals **33**, 83.
Maartense, I., 1973, Can. J. Phys. **51**, 2407.
Mader, K.H. and W.E. Wallace, 1968, Inorg. Chem. **7**, 1027.
Malik, S.K., S.G. Sankar, V.U.S. Rao and W.E. Wallace, 1976, 22nd Conf. Magnetism, Pittsburgh.
Maple, M.B., 1973, Solid State Comm. **12**, 653.
Mattis, D.C., 1965, The Theory of Magnetism, Harper and Row, New York.
Maranzana, F.E., 1970, Phys. Rev. Lett. **25**, 239.
Martin, D.H., 1967, Magnetism in Solids, M.I.T. Press.
McFarland, C.M., 1973, Proc. 10th R.E. Res. Conf., 692, Carefree, Arizona.
McMasters, O.D. and K.A. Gschneidner, 1973, J. Less-Common Metals **30**, 325.
Menth, A., 1975, Proc. of the 21st Conf. Magn. Magn. Mat., Philadelphia.
Menth, A. and H. Nagel, 1976, Appl. Phys. Lett., in press.
Merches, M., K.S.V.L. Narasimhan, W.E. Wallace and A. Ilyushin, 1976, Proc. 22nd Mag. Conf., Pittsburgh, 233.
Meyer, A., 1970, J. Less-Common Metals **20**, 353.
Michel, D.J., 1973, J. Less-Common Metals **33**, 177.
Mildrum, H.F. and D.J. Iden, 1975, Goldschmidt Informiert **4**, 54.
Miller, A.E., T. D'Silva and K. Miura, 1974a, Proc. 11th. R.E. Research Conf. 461.
Miller, A.E., J.F. Shanley and T. D'Silva, 1974b, Proc. 11th R.E. Research Conf. 469.
Miller, A.E., T. D'Silva and H. Rodrigues, 1976, I.E.E.E. Trans. Mag. MAG-12, 1006.
Millhouse, A.H., H.G. Purwins and E. Walker, 1972, Solid State Comm. **11**, 707.
Miura, S., T. Kaneko, M. Ohashi and K. Kamigaki, 1971, J. Phys. (Paris) **32**, C1-1124.
Miura, S., T. Kaneko, M. Ohashi and H. Yamauchi, 1974, J. Phys. Soc. Jap. **37**, 1464.
Moon, R.M., W.C. Koehler and J. Farrel, 1965, J. Appl. Phys. **36**, 978.
Morariu, M., E. Burzo and D. Barbara, 1974, Phys. Status Solidi **62b**, K55.
Moreau, J.M. and E. Parthé, 1973, J. Less-Common Metals **32**, 91.
Morin, P. and J. Pierre, 1973a, Phys. Status Solidi **17a**, 479.
Morin, P. and J. Pierre, 1973b, Solid State Comm. **13**, 537.
Morin, P., J. Pierre, M. Belakhovsky, R. Chamard-Bois and D.K. Ray, 1973, Proc. ICM, 48.
Morin, P. and J. Pierre, 1974, Phys. Status Solidi **21a**, 161.
Morin, P., J. Pierre and J. Chaussy, 1974a, Phys. Status Solidi **24a**, 425.
Morin, P., J. Pierre, J. Rossat-Mignod, K. Knorr and W. Drexel, 1974b, Phys. Rev. **B9**, 4932.
Morin, P., J. Rouchy and E. du Tremolet de Lacheisserie, 1977, Phys. Rev. B (Oct. 1st.)
Moriya, T. and A. Kawabata, 1973a, J. Phys. Soc. Jap. **34**, 639.
Moriya, T. and A. Kawabata, 1973b, J. Phys. Soc. Jap. **35**, 669.
Moriya, T., 1976, Proc. ICM, Amsterdam. (See also Physica (1977) **86–88B**, 356).
Nagel, H. and A. Menth, 1975, Goldschmidt Informiert **4**, 42.
Nagel, H., 1975, Proc. of the 21st Conf. Magn. Magn. Mat., Philadelphia.
Nagel, H. and A. Menth, 1976, Proc. MMM-Intermag. Meeting, June 1976, Pittsburgh.
Nagel, H., A.J. Perry and A. Menth, 1976, J. Appl. Phys. **47**, 2662.
Narasimhan, K.S.V.L., R.A. Butera and R.S. Craig, 1973, J. Phys. Chem. Solids **34**, 1075.
Narasimhan, K.S.V.L., R.A. Butera and C.J. Kunesh, 1975, Proc. 21st Ann. Conf. Magn. Magn. Mat., AIP Conf.
Narita, K., 1976, in Strnat, K.J., 1976a, ed., Proc. of the 2nd Workshop on Rare Earth Cobalt Perm. Magnets and their Applications, Univ. of Dayton, June 8–11, 1976, p. 55.
Nassau, K., L.V. Cherry and W.E. Wallace, 1960, J. Phys. Chem. Solids **16**, 123.
Néel, L., 1957, Nuovo Cimento, Suppl. **6**, 942.
Nereson, N., C. Olsen and G. Arnold, 1966, J. Appl. Phys. **37**, 4575.
Nereson, N., C. Olsen and G. Arnold, 1968, J. Appl. Phys. **39**, 4605.
Nereson, N. and G. Arnold, 1970, J. Chem. Phys. **53**, 2818.
Nereson, N., 1973, J. Appl. Phys. **44**, 4727.
Nesbitt, E.A., H.J. Williams, J.H. Wernick and R.C. Sherwood, 1962, J. Appl. Phys. **33**, 1674.
Nesbitt, E.A., H.J. Williams, J.H. Wernick and R.C. Sherwood, 1963, J. Appl. Phys. **34**, 1347.

Nesbitt, E.A., G.Y. Chin, P.K. Gallagher, R.C. Sherwood and J.H. Wernick, 1971, J. Appl. Phys. **42**, 1530.
Nesbitt, E.A. and J.H. Wernick, 1973, Rare Earth Permanent Magnets, Academic Press.
Nikitin, S.A., D. Kim, A.K. Zvezdin and A.F. Popkov, 1975, J. Exp. Theor. Phys. Lett. **22**, 137.
Noodleman, S., 1976, in: Strnat, 1976a, Proc. of the 2nd Workshop on Rare Earth-Cobalt Perm. Magnets and their Applications, Univ. of Dayton, June 8–11, 1976, p. 214.
Nowik, I. and J.H. Wernick, 1965, Phys. Rev. **140**, 131.
Österreicher, H., 1972, Phys. Status Solidi **12a**, K109.
Österreicher, H., 1973a, J. Less-Common Metals **30**, 225.
Österreicher, H., 1973b, J. Phys. Chem. Solids **34**, 1267.
Österreicher, H., 1974, Solid State Comm. **14**, 571.
Ohashi, M., T. Kaneko, S. Miura and K. Kamigaki, 1972, J. Phys. Soc. Jap. **34**, 553.
Ohashi, M., T. Kaneko and S. Miura, 1975, J. Phys. Soc. Jap. **38**, 588.
O'Keefe, T.J., G.J. Roe and W.J. James, 1970, Coll. Int., Les Elements des Terres Rares, Tome II, 251.
Olcese, G.L., 1973, J. Less-Common Metals **33**, 71.
Olsen, C.E., G. Arnold and N. Nereson, 1967, J. Appl. Phys. **38**, 1395.
Oppelt, A., E. Dormann and K.H.J. Buschow, 1972, Phys. Status Solidi **51b**, 275.
Oppelt, A. and K.H.J. Buschow, 1976, Phys. Rev. **B13**, 4698.
Ostertag, W. and K.J. Strnat, 1966, Acta Crystallogr. **21**, 560.
Paccard, D. and R. Pauthenet, 1967, C.R. Acad. Sci., Paris, Ser. **B264**, 1056.
Paccard, D., J. Schweizer and J. Yakinthos, 1971, J. Phys. (Paris) **32**, C1-663.
Paladino, A.E., N.J. Dionne, P.F. Weihrauch and E.C. Wettstein, 1975, Goldschmidt Informiert **4**, 63.
Parviainen, S. and S. Jaakkola, 1975, Europhys. Conf. Abstr. **1A**, 33.
Perkins, R.S. and H. Nagel, 1975, Physica **80B**, 143.
Perkins, R.S., S. Strässler and A. Menth, 1975, AIP Conf. Proc. **29**, 610.
Perkins, R.S., S. Strässler and A. Menth, 1976, Proc. MMM-Intermag Conf., Pittsburgh.
Piercy, A.R. and K.N.R. Taylor, 1968, J. Phys. **C1**, 1112.
Pierre, J. and R. Pauthenet, 1965, C.R. Acad. Sci., Paris **260**, 2739.
Pierre, J., 1967, C.R. Acad. Sci., Paris, **265**, 1169.
Pierre, J., 1969, Les Elements des Terres Rares, CNRS, Tome II, 55.
Plumier, R. and M. Sougi, 1973, Proc. ICM Moscow, Tome III, 487.
Poldy, C.A., 1972, Ph.D. Thesis, Durham.
Poldy, C.A. and K.N.R. Taylor, 1972a, J. Less-Common Metals **27**, 95.
Poldy, C.A. and K.N.R. Taylor, 1972b, J. Phys. **F2**, L105.
Poldy, C.A. and K.N.R. Taylor, 1973a, J. Phys. **F3**, 145.
Poldy, C.A. and K.N.R. Taylor, 1973b, Phys. Status Solidi **18a**, 123.
Poldy, C.A. and H.R. Kirchmayr, 1974, Phys. Status Solidi **65b**, 553.
Primavesi, G.J. and K.N.R. Taylor, 1971, Proc. 9th Rare Earth Conf.
Primavesi, G.J., K.N.R. Taylor and I.R. Harris, 1971, J. Phys. (Paris) **32**, C1-661.
Purwins, H.G., 1970, Phys. Lett. **31A**, 523.
Purwins, H.G., 1972, Ann. Phys. **7**, 329.
Purwins, H.G., E. Walker, B. Barbara, M.F. Rossignol and P. Bak, 1974, J. Phys. **C7**, 3573.
Purwins, H.G., E. Walker, B. Barbara, M.F. Rossignol and A. Furrer, 1975, Conf. Deutsche Physikalische Geselschaft VI.
Purwins, H.G., E. Walker, B. Barbara, M.F. Rossignol and A. Furrer, 1976, J. Phys. **C9**, 1025.
Racah, G., 1943, Phys. Rev. **63**, 367.
Rado, G.T. and H. Suhl, 1973, Magnetism V.
Ray, A.E., 1966, Acta Crystallogr. **21**, 426.
Ray, A.E., H. Mildrum, K.J. Strnat and R. Harmer, 1971a, J. Phys. (Paris) **32**, Suppl. 2–3, C1-554.
Ray, A.E., K.J. Strnat and A.T. Biermann, 1971b, IEEE Trans. Magn., MAG 7, 656.
Ray, A.E. and K.J. Strnat, 1972a, IEEE Trans. Magn., MAG, **8**, 516.
Ray, A.E. and K.J. Strnat, 1972b, AFML-Report 22-99, Dayton, Ohio.
Ray, D.K., 1974, Solid State Comm. **15**, 1471.
Rettori, C., D. Davidov, P. Chaikin and R. Orbach, 1973, Phys. Rev. Lett. **10**, 437.
Rettori, C., D. Davidov, G. Ng, E.P. Chock, 1975, Phys. Rev. **B12**, 1298.
Riblet, G. and K. Winzer, 1971, Solid State Comm. **9**, 1663.
Robinson, L.B., L.M. Ferguson and F. Milstein, 1971, Phys. Rev. **B3**, 1025.
Rossat-Mignod, J. and J. Yakinthos, 1971, Phys. Status Solidi **47b**, 234.
Roth, L.M., H.J. Zeiger and T.A. Kaplan, 1966, Phys. Rev. **149**, 519.
Roth, S., K. Ibel and W. Just, 1974, J. Appl. Cryst. **7**, 230.
Rothwarf, F., H.A. Leupold, J. Greedan, W.E. Wallace and D.K. Das, 1973, Int. J. Magn. **4**, 267.
Ruderman , M.A. and C. Kittel, 1954, Phys. Rev. **96**, 99.
Sakoh, M. and D.M. Edwards, 1975, Phys. Status Solidi **70b**, 611.
Sakoh, M. and M. Shimizu, 1976, J. Phys. Soc. Jap. **40**, 974.
Sakurai, J., Y. Kubo, T. Kondo, J. Pierre and E.F. Bertaut, 1973, J. Phys. Chem. Solids **34**, 1305.
Salmans, L.R., K. Strnat and G.I. Hoffer, 1968, Techn. Report AFML-TR-68-159, 1.
Sankar, S.G., D.A. Keller, T. Inoue, R.S. Craig

San Diego, 1978, "Proceedings of the Third International Workshop on Rare Earth - Cobalt Permanent Magnets and their Applications", Ed. K.J. Strnat, June 27-30, 1978, University of California - San Diego, San Diego, CA.

and N.G. Nereson, 1974, Proc. of the 11th Rare Earth Conf., 327.
Sankar, S.G., V.U.S. Rao, E. Segal, W.E. Wallace, W.G.D. Frederick and H.J. Garrett, 1975, Phys. Rev. **B11**, 435.
Schäfer, W., G. Will and K.H.J. Buschow, 1976, J. Magn. Magnetic Materials (in press); Proc. 12th R.E. Research Conf., Vail, Colorado 1976.
Schaller, H.J., R.S. Craig and W.E. Wallace, 1972, J. Appl. Phys. **43**, 3161.
Schmitt, D., P. Morin and J. Pierre, 1977, Phys. Rev. **B15**, 1698.
Schrieffer, J.R. and P.A. Wolff, 1966, Phys. Rev. **149**, 491.
Schubert, K., 1964, Kristallstrukturen zweikomponentiger Phasen, Springer, Berlin.
Schurer, P.J., F. van der Worde and G.A. Sawatzky, 1973, Proc. Int. Conf. Magn., Moscow, **4**, 495.
Schweizer, J., 1967, Phys. Lett. **24A**, 739.
Schweizer, J. and J. Yakinthos, 1969, Les Elements des Terres Rares, CNRS, Tome II, 239.
Schweizer, J. and F. Tasset, 1973, Proc. ICM Moscow, 257.
Segal, E. and W.E. Wallace, 1970, J. Solid State Chem. **2**, 347.
Segal, E. and W.E. Wallace, 1973, J. Solid State Chem. **6**, 99.
Segal, E. and W.E. Wallace, 1974, J. Solid State Chem. **11**, 203.
Segal, E. and W.E. Wallace, 1975, J. Solid State Chem. **13**, 201.
Sekizawa, K. and K. Yasukochi, 1964, Phys. Lett. **11**, 216.
Sekizawa, K. and K. Yasukochi, 1966a, J. Phys. Soc. Jap. **37**, 1254.
Sekizawa, K. and K. Yasukochi, 1966b, J. Phys. Soc. Jap. **21**, 684.
Sellmeyr, D.J., F.R. Szofran and J.W. Weymouth, 1975, J. Low Temp. Phys. **18**, 85.
Sherwood, R.C., H.J. Williams and J.H. Wernick, 1964, J. Appl. Phys. **35**, 1049.
Shohata, N., H. Fujii and T. Okamoto, 1974, J. Phys. Soc. Jap. **37**, 567.
Sill, L.R., W.J. Mass, A.J. Fedro, J.C. Schaffer and C.W. Kimball, 1971, J. Appl. Phys. **42**, 1297.
Simmons, M., J.M. Moreau, W.J. James, F. Givord and R. Lemaire, 1973, J. Less-Common Metals **30**, 75.
Slanicka, M.I., K.N.R. Taylor and G.J. Primavesi, 1971, J. Phys. **F1**, 679.
Stalinski, B., Z. Kletowski and Z. Henkie, 1973, Phys. Status Solidi **19a**, K165.
Stearns, M.B., 1973, Phys. Rev. **B8**, 4383.
Steglich, F. and K. Winzer, 1973, Proc. ICM Moscow, V, 97.
Steiner, W., B.K. Choi, G. Hilscher, G. Wiesinger and H. Kirchmayr, 1973, Proc. ICM **4**, 63.
Steiner, W. and H. Ortbauer, 1974, Phys. Status Solidi **26a**, 451.
Steiner, W. and J. Hrubec, 1975, J. Less-Common Metals **41**, 165.
Steiner, W. and H. Ortbauer, 1975, Phys. Status Solidi **31a**, K119.
Steiner, W., A. Planck and G. Weihs, 1976, J. Less-Common Metals **45**, 143.
Stevens, K.W.H., 1952, Proc. Roy. Soc., Ser. **A65**, 502.
Stewart, A.M., 1972a, Phys. Status Solidi **52b**, K1.
Stewart, A.M., 1972b, Phys. Rev. **B6**, 1985.
Stewart, A.M., 1973a, Phys. Rev. **B8**, 2214.
Stewart, A.M., 1973b, J. Phys. **F3**, 1024.
Stewart, A.M. and B.R. Coles, 1974, J. Phys. **F4**, 458.
Stewart, A.M., G. Costa and G. Olcese, 1974, Aust. J. Phys. **27**, 383.
Stoner, E.C., 1938, Proc. Roy. Soc., Ser. **A165**, 372.
Street, R. and J.C. Wooley, 1950, Proc. Phys. Soc. (London) **63B**, 509.
Streever, R.L., 1975, Phys. Rev. **B12**, 4653.
Strnat, K.J., G. Hoffer, W. Ostertag and J.C. Olson, 1966, J. Appl. Phys. **37**, 1252.
Strnat, K.J., 1976a, (Editor) Proc. of the 2nd Int. Workshop on Rare Earth Perm. Magnets and their Applications, Univ. of Dayton, Ohio, June 8–11.
Strnat, K.J., 1976b, in Strnat 1976a, p. 5.
Strydom, O.A. and L. Alberts, 1970, J. Less-Common Metals **22**, 503.
Swift, W.M. and W.E. Wallace, 1968, J. Phys. Chem. Solids **29**, 2053.
Switendick, A.C., 1973, Proc. 10th Rare Earth Conf.
Szpunar, B. and P.A. Lindgard, 1977, Phys. Status Solidi **82b**, 449.
Takeshita, T., S.K. Malik, A.A. El-Attar and W.E. Wallace, 1976, Proc. 22nd Magnetism Conf., Pittsburgh, 230.
Tao, L.J., S. Kirkpatrick, J.R. Gambino and J.J. Cuomo, 1973, Solid State Comm. **13**, 1491.
Tawara, Y. and H. Senno, 1968, D-AS 1809535.
Taylor, K.N.R. and M.I. Darby, 1972, Physics of Rare Earth Solids, Chapman and Hall Ltd.
Taylor, K.N.R., H.D. Ellis and M.I. Darby, 1966, Phys. Lett. **20**, 327.
Taylor, K.N.R., 1969, Phys. Lett. **29A**, 372.
Taylor, K.N.R., 1971a, Advan. Phys. **20**, 551.
Taylor, K.N.R., 1971b, Phys. Lett. **35A**, 153.
Taylor, K.N.R. and G.J. Primavesi, 1971, J. Phys. **F1**, L7.
Taylor, K.N.R. and C.A. Poldy, 1972, J. Less Common Metals **27**, 255.
Taylor, K.N.R. and G.J. Primavesi, 1972a, J. Less-Common Metals **29**, 97.
Taylor, K.N.R. and G.J. Primavesi, 1972b, J. Phys. **F2**, L32.
Taylor, K.N.R., D. Melville and G.J. Primavesi, 1972, J. Phys. **F2**, 584.
Taylor, K.N.R., J. Hunter and C.A. Poldy, 1973, Proc. 7th Rare Earth Conf., Moscow.
Taylor, K.N.R. and C.A. Poldy, 1975, J. Phys. **F5**, 1593.
Teatum, E., K. Gschneidner Jr. and J. Waber, 1960, Los Alamos Scientific Lab. Report LA 2345.

Tellenbach, U., A. Furrer and A.H. Millhouse, 1975, J. Phys. **C8**, 3833.
Tholence, J.C. and R. Tournier, 1974, J. Phys. (Paris) **35**, Coll. C4-229.
Tsai, S.C., K.S.V.L. Narasimhan, C.J. Kunesh and R.A. Butera, 1974, J. Appl. Phys. **45**, 3582.
Tsuchida, T., S. Sugaki and Y. Nakamura, 1975, J. Phys. Soc. Jap. **39**, 340.
Ueda, K. and T. Moriya, 1975, J. Phys. Soc. Jap. **39**, 605.
Van Daal, H.J. and K.H.J. Buschow, 1970, Phys. Status Solidi **3a**, 853.
Van den Broek, J.J. and H. Zijlstra, 1971, IEEE Trans. Magn., MAG 7, 226.
Van der Kraan, A.M., P.C.M. Gubbens and K.H.J. Buschow, 1975, Phys. Status Solidi **31a**, 495.
Van Diepen, A.M., 1968, Thesis, Amsterdam.
Van Diepen, A.M., K.H.J. Buschow, J.S. van Wieringen, 1971, J. Appl. Phys. **43**, 645.
Van Diepen, A.M., H.W. de Wijn and K.H.J. Buschow, 1973, Phys. Rev. **B8**, 1125.
Van Vleck, J.H., 1941, J. Chem. Phys. **9**, 85.
Voiron, J. and D. Bloch, 1971, J. Phys. (Paris) **32**, 949.
Voiron, J., J. Beille, D. Bloch and C. Vettier, 1973, Solid State Comm. **13**, 201.
Voiron, J., A. Berton and J. Chaussy, 1974, Phys. Lett. **50A**, 17.
Walker, E., H.G. Purwins, M. Landolt and F. Hulliger, 1973, J. Less-Common Metals **33**, 203.
Wallace, W.E. and E.A. Skrabek, 1963, Proc. 3rd Rare Earth Conf., Clearwater.
Wallace, W.E., T.V. Volkmann and R.S. Craig, 1970a, J. Phys. Chem. Solids **31**, 2185.
Wallace, W.E., R.S. Craig, A. Thompson, C. Deenadas, M. Dixon, M. Aoyagi and N. Marzouk, 1970b, Les Elements des Terres Rares, Coll. Int. CNRS, No. 180, 427.
Wallace, W.E., 1973, Rare Earth Intermetallics, Acad. Press Inc., New York, London.
Walline, R.E. and W.E. Wallace, 1964a, J. Chem. Phys. **41**, 3285.
Walline, R.E. and W.E. Wallace, 1964b, J. Chem. Phys. **41** 1587.
Walline, R.E. and W.E. Wallace, 1965, J. Chem. Phys. **42**, 604.
Wang, F.E., J.V. Gilfrich and D.W. Ernst, 1964, Acta Crystallogr. **7**, 931.
Weber, K., 1973, Proc. 5th Int. Conf. Mössbauer Spectrometry, Bratislava.
Weber, K., 1976, Proc. I.C.M.
Weihrauch, P.F., A.F. Paladino, D.K. Das, W.R. Reid, L. Lesensky, E.C. Wettstein and A.A. Gale, 1972, Proc. 18th Ann. Conf. Magn. Magn. Mat.
Westbrook, J.H., 1967, Intermetallic Compounds, Wiley, N.Y.
Wickman, H.H., J.H. Wernick, R.C. Sherwood and C.F. Wagner, 1968, J. Phys. Chem. Solids **29**, 181.
Wiesinger, G., 1974, Dissertation, Techn. Univ. Wien.
Wilhelm, M. and B. Hillenbrand, 1971, Z. Naturforsch. **23A**, 142.
Will, G., 1968, Z. Naturforsch. **27A**, 1581.
Will, G. and M.O. Bargouth, 1972, Z. Naturforsch. **27A**, 1581.
Will, G. and D.E. Cox, 1974, J. Phys. Chem. Solids **35**, 861.
Winterberger, M., R. Chamard-Bois, M. Belakhovsky and J. Pierre, 1971, Phys. Status Solidi **48b**, 705.
Wohlfarth, E.P., 1949, Proc. Roy. Soc., Ser. **A195**, 434.
Wohlfarth, E.P., 1969, J. Phys. **C2**, 68.
Wohlfarth, E.P., 1973, Proc. Int. Conf. Magn., Moscow **2**, 28. (See also Physica **91B** (1977) 305.
Wohlfarth, E.P., 1974, Phys. Lett. **47A**, 125.
Yakinthos, J. and D. Paccard, 1972, Solid State Comm. **10**, 989.
Yashiro, T., Y. Hamaguchi and H. Watanabe, 1976, J. Phys. Soc. Jap. **40**, 63.
Yosida, K., 1957, Phys. Rev. **106**, 893.
Zarechnuyuk, O.S. and P.I. Kripyakevich, 1962, Kristallografiya **7**, 543.
Zarechnuyuk, O.S., 1966, Dopov. Akad. Nauk. Ukr. RSR, 767.
Zarechnuyuk, O.S., P.I. Kripyakevich, E.E. Tserkaschin and I.F. Kolonev, 1967, Neorg. Mater. **3**, 182.
Zijlstra, H., 1970, IEEE Trans. Magn., MAG 6, 179.
Zinn, W., 1971, J. Phys. (Paris) **32**, C1-724.
Zuckermann, M.J., 1974, Can. J. Phys. **52**, 2177.

Handbook on the Physics and Chemistry of Rare Earths, edited by K.A. Gschneidner, Jr. and L. Eyring

Chapter 15

MAGNETOSTRICTIVE RFe_2 INTERMETALLIC COMPOUNDS

A.E. CLARK
White Oak Laboratory, Naval Surface Weapons Center, Silver Spring, MD 20910, USA

Contents

Symbols

B = magnetoelastic coupling
E = Young's modulus
H = magnetic field
$\hat{I}_{l+1/2}$ = hyperbolic Bessel function
J = quantum number
K = magnetic anisotropy
M = magnetization
Q = quality factor
T = temperature
U = energy
V = volume
c_{11}, c_{12}, c_{44} = elastic moduli
f = frequency
k = magnetomechanical coupling
m = sublattice magnetization
n_B = Bohr magneton number
r_f = radius of 4f electron
v = sound velocity
$\mathscr{L}$ = Langevin function
α = Stevens' factor
α_j = magnetization direction cosines
λ = magnetostriction
μ = permeability
μ_B = Bohr magneton
ρ = density
σ = magnetic moment

1. Introduction

Extensive research on the magnetostrictive properties of the rare earth elements was carried out in the early 1960's. At that time it was widely recognized that the rare earths possessed many extraordinary magnetic properties. Of particular interest were the heavy lanthanide metals, which crystallize into the h.c.p. structure and possess complex magnetic ordering configurations. Huge atomic moments were found, as high as $10\,\mu_B$, which dwarfed the con

ventional values of 0.6 μ_B and 2.2 μ_B of Ni and Fe. Enormous magnetic anisotropies were also measured for these elements. In 1963 a breakthrough in magnetostrictive materials occurred with the measurement of the basal plane magnetostrictions of Dy and Tb at low temperatures (Legvold et al., 1963; Clark et al., 1963, 1965; Rhyne and Legvold, 1965). These basal plane strains are 100 to 10 000 times typical magnetostrictions and still remain today the largest known ($\sim$1%). Large uniaxial magnetic anisotropies inhibited the measurement of the remaining magnetostriction constants and those of other rare earth elements. At about the same time efforts were made to understand both the temperature dependences of the magnetostrictions as well as their atomic origin (Tsuya et al., 1964; Callen and Callen, 1963). The application of these materials to magnetostrictive devices operating at room temperature, however, was severely restricted because of the low ordering temperatures of the lanthanide elements. Only Gd, which is essentially non-magnetostrictive, possesses a Curie point as high as room temperature.

A search for magnetostrictive materials with high magnetostriction at room temperature was started in 1971. Highly magnetostrictive lanthanides Tb and Dy were combined with the magnetic transition metals: Ni, Co, and Fe. The largest room temperature magnetostriction by far (2600×10^{-6}) was found in the cubic Laves phase compound $TbFe_2$. Of all rare earth–iron compounds, the RFe_2 compounds possess the strongest exchange interactions and the highest ordering temperatures (Buschow et al., 1970, 1971; Burzo, 1971). It is this strong exchange, coupled with the high concentration of lanthanide ions in these compounds which lift the magnetostrictive and anisotropic properties of the lanthanide elements (heretofore available only at cryogenic temperatures) to room temperature. Large magnetocrystalline anisotropies ($>10^7$ ergs/cm^3) as well as magnetostriction constants (>2000 ppm) derive from the lanthanide in these compounds in spite of the high ($\bar{4}3m$) point symmetry at the lanthanide site. This high symmetry, however, effectively shorts out one of the two cubic magnetostriction constants, yielding a huge $\lambda_{111} \gg \lambda_{100}$ anisotropy (Clark et al., 1976).

This chapter presents an overview of the magnetostriction studies of the highly magnetostrictive RFe_2 alloys, dealing with binary compounds, magnetic anisotropy, the importance of ternary and quaternary compounds, magnetomechanical effects, and elastic properties. The magnetostriction of binary rare earth iron alloys is presented first (section 2). Here the magnetostriction of RF_2 alloys (R = Sm, Tb, Dy, Ho, Er, Tm) are compared to other magnetic materials at room temperature. The source of the magnetostriction and its unusual anisotropy is discussed. Single crystal and polycrystal data are presented. In sections 3 and 4, the basic magnetic data: magnetization, sublattice magnetic moment, and magnetic anisotropy are presented. Some heavy lanthanide RFe_2 compounds possess magnetic anisotropies far in excess of those characteristic of cubic materials. In section 5, the magnetostrictive properties of multicomponent RFe_2 alloys are reported. Elastic energies, magnetomechanical coupling, and dynamic magnetoelastic effects are discussed in sections 6 and 7. Values of the magnetomechanical coupling factor, which are important for dynamic transducer applications are

presented. Associated with the highly magnetostrictive Tb and Sm alloys is a huge "ΔE effect," or change in elastic modulus upon magnetization. Unprecedented changes in Young's modulus of over 150% were found in Tb–Dy alloys. Finally in section 8, recent measurements of linear and volume magnetostriction on the amorphous form of the RFe_2 alloys are reported.

The objective of this chapter is to focus on the magnetostrictive RFe_2 alloys. For a broad review of the magnetic properties of rare earth-transition metal alloys, the reader is referred to ch. 14 of this handbook. Chapter 16 deals specifically with rare earth alloys in the amorphous form. Earlier comprehensive reviews of the structural and magnetic properties of the rare earth-transition metal compounds are also available, e.g. Taylor (1971), Rhyne and McGuire (1972), Wallace (1973).

2. Binary lanthanide iron alloys

The first compound observed to exhibit a huge magnetostriction ($>10^{-3}$) at room temperature is $TbFe_2$ (Clark and Belson, 1972a,b). This compound still possesses the largest known room temperature magnetostriction. Unusually high magnetostrictions are also found over a wide range of Tb_xFe_{1-x} alloys ($0.1 < x < 0.7$) (Clark, 1974). In fig. 15.1 the room temperature magnetostriction, $\lambda_\parallel - \lambda_\perp$, is plotted vs applied field for five Tb_xFe_{1-x} alloys. ($\lambda_\parallel - \lambda_\perp$) denotes the fractional

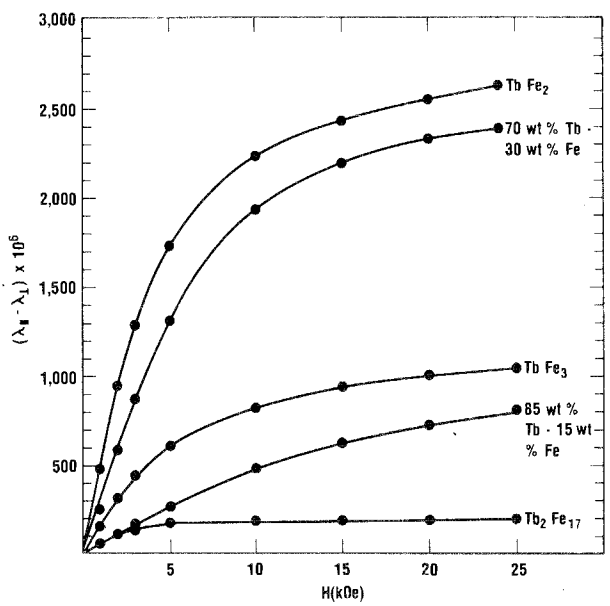

Fig. 15.1. Magnetostriction of terbium-iron alloys.

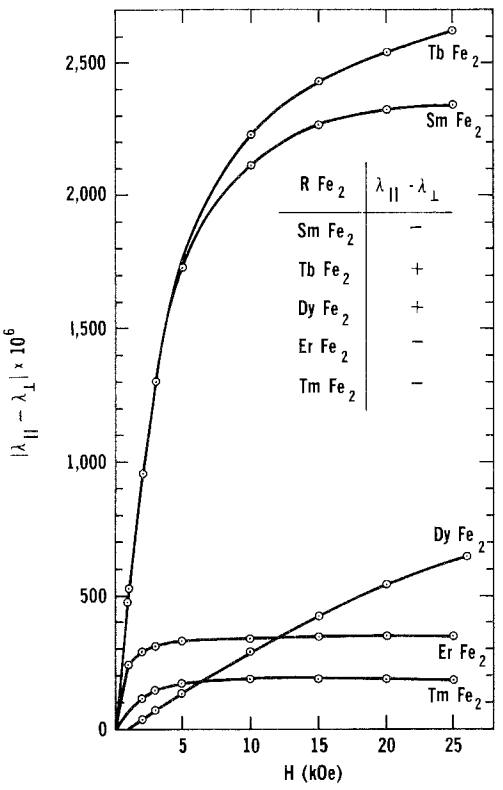

Fig. 15.2. Magnetostriction of rare earth-Fe_2 alloys (taken from Clark, 1974).

change in length as an applied field is rotated from perpendicular to parallel to the measurement direction. In isotropic materials, $\lambda_{\parallel} - \lambda_{\perp} = \frac{3}{2}\lambda_s$, where λ_s is the conventional polycrystalline magnetostriction constant (Bozorth, 1951). All three intermetallic compounds shown exhibit large magnetostrictions at room temperature: 1040 ppm for $TbFe_3$, 194 ppm for Tb_2Fe_{17} and 2630 ppm for $TbFe_2$ at 25 kOe. For a 3 a/o Tb in Fe sample (not shown) the magnetostriction is far from saturation with $(\lambda_{\parallel} - \lambda_{\perp})/H = 6.5 \times 10^{-10}$/Oe. Both $Tb_{0.03}Fe_{0.97}$ and Tb_2Fe_{17} display large volume magnetostrictions. In $Tb_{0.03}Fe_{0.97}$, $\Delta V/VH = 88 \times 10^{-10}$/Oe, in Tb_2Fe_{17}, $\Delta V/VH = 37 \times 10^{-10}$/Oe. The Tb rich alloys ($x > \frac{1}{3}$) contain a Tb–Fe eutectic and are substantially more rugged in the as-cast state than the pure intermetallic compounds.

Figure 15.2 illustrates the field dependence of the room temperature magnetostriction for the RFe_2 compounds (R = Sm, Tb, Dy, Er, Tm). $TbFe_2$ and $SmFe_2$ stand out as unique binary compounds with giant magnetostrictions. For $SmFe_2$, $\lambda < -2000 \times 10^{-6}$; for $TbFe_2$, $\lambda > 2000 \times 10^{-6}$. These compounds possess huge magnetostrictions because: (1) the rare earth ion is highly anisotropic (Sm – most prolate in form; Tb – most oblate in form), and (2) large iron–iron and rare

earth–iron exchange constants maintain the rare earth sublattice magnetization relatively intact at room temperature so that the magnetostriction does not fall appreciably from its low temperature value.

The slow increase in magnetostriction with field observed for $DyFe_2$ is indicative of a very large magnetocrystalline anisotropy. A similar nonsaturating behavior was observed for $HoFe_2$ by Koon et al. (1971). As shown in section 4, the anisotropy is indeed large, with values of $K \sim 10^7$ ergs/cm^3 at room temperature. While the magnetostrictions of $DyFe_2$ and $HoFe_2$ are far from saturation, the magnetostrictions of the remaining compounds display rather well defined knees. In these compounds: $SmFe_2$, $TbFe_2$, $ErFe_2$ and $TmFe_2$, the magnetization lies along the [111] axis, whereas for $DyFe_2$ it lies parallel to [100] (see section 4). Because of this, the absence of a large magnetostriction at low fields for $DyFe_2$ leads to the speculation that $\lambda_{111} \gg \lambda_{100}$. The increasing magnetostriction with increasing field in the case of polycrystal $DyFe_2$ is attributed solely to the rotation of the magnetization away from the easy [100] axis, thereby sensing λ_{111}; while the magnetostriction of the Sm, Tb, Er and Tm compounds comes directly from λ_{111}. Here λ_{100} and λ_{111} are the conventional magnetostriction constants for cubic crystals. See for example, Bozorth (1951).

TABLE 15.1
Magnetostrictions of some polycrystalline materials at room temperature

Material	$10^6 \lambda_s$	Material	$10^6 \lambda_s$
Fe	−9[b]	YFe_2	1.7[a]
Ni	−35[b]	$SmFe_2$	−1560[a]
Co	−62[b]	$TbFe_2$	1753[a]
Sm, Tb, Dy, Ho	~0[c]	$TbFe_2$ (sputtered)	308[a]
Fe_3O_4	40[d]	$Tb_{0.3}Dy_{0.7}Fe_2$	1068[a]
$CoFe_2O_4$	−110[d]	$DyFe_2$	433[a]
$NiFe_2O_4$	−26[d]	$HoFe_2$	85[f]
$Y_3Fe_5O_{12}$	−2[e]	$ErFe_2$	−299[a]
Tb_2Co_{17}	47[a]	$TmFe_2$	−123[a]
YCo_3	0.4[a]	$TbFe_{1.6}Co_{0.4}$	1487
$TbCo_3$	65[a]	$TbFe_{1.6}Ni_{0.4}$	1151
		85% Tb–15% Fe	539[a]
		70% Tb–30% Fe	1590[a]
		$TbFe_3$	693[a]
		Tb_2Fe_{17}	131[a]

[a]Clark, A.E., 1974, AIP Conference Proc. No. 18, 1015. λ_s denotes $\frac{2}{3}(\lambda_\parallel - \lambda_\perp)$ at 25 kOe. [b]Taken from R.M. Bozorth, Ferromagnetism (Van Nostrand, New York, 1951). [c]Non-magnetic at room temperature. [d]Taken from J. Smit and H.P. Wijn, Ferrites (Wiley, New York, 1959). [e]Clark, A.E., B.F. DeSavage, W. Coleman, E. Callen and H. Callen, 1963, J. Appl. Phys. **34**, 1296. [f]Koon, N., A. Schindler, C. Williams and F. Carter, 1974, J. Appl. Phys. **45**, 5389.

In table 15.1, the magnetostriction constants of some highly magnetostrictive polycrystalline compounds are compared to those of transition metals, oxides and other rare earth-transition metal compounds.

Single crystals of $TbFe_2$, $DyFe_2$, $HoFe_2$, $ErFe_2$ and $TmFe_2$ were prepared by Czochralski (Milstein, 1975) and by induction zoning methods (McMasters, unpublished). In fig. 15.3, values of $|\lambda_{111}|$ are shown for $TbFe_2$ and $ErFe_2$, at room temperature. In both crystals, [111] is the easy magnetization direction. Efforts to measure λ_{100} with fields up to 25 kOe proved fruitless in both cases. Although some rotation of the magnetization away from the easy [111] direction occurs at these fields, no λ_{100} was detected (Clark, 1974). The compounds $DyFe_2$ and $HoFe_2$, on the other hand, possess [100] easy. Hence in these materials, λ_{100}, rather than λ_{111}, is sensed at remanence. In remarkable contrast to the huge values of λ_{111} for $TbFe_2$ and $ErFe_2$, for $DyFe_2$, $\lambda_{100} = 0 \pm 4 \times 10^{-6}$ and for $HoFe_2$, $\lambda_{100} = -59 \times 10^{-6}$ (Clark et al., 1976; Koon, unpublished). Such a highly anisotropic magnetostriction ratio, $\lambda_{111} \gg \lambda_{100}$, is unusual. It reveals the important role of grain orientation in achieving high magnetostriction in polycrystal RFe_2 materials. A fully oriented polycrystal yields $\lambda_s \cong \lambda_{111}$; while for an isotropic polycrystal, $\lambda_s = 0.6\,\lambda_{111}$, and a poorly oriented polycrystal, $\lambda_s \cong 0$. The effect of crystallite orientation is two-fold beneficial. In addition to the increase in magnetostriction constant, λ_s, a preferentially oriented polycrystal possesses far lower internal losses at grain boundaries. This is particularly important in applications where a high magnetostriction at low applied fields is required.

An atomic model for the anisotropic magnetostriction based upon the structure of the cubic Laves phase C15 compounds has been proposed by Clark et al. (1976) and Cullen and Clark (1977). In this model, potentially huge values of λ_{100},

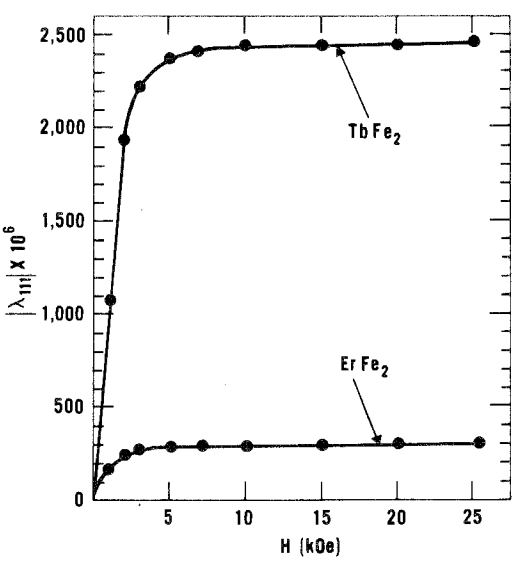

Fig. 15.3. λ_{111} of $TbFe_2$ and $ErFe_2$ at room temperature.

arising from the asymmetry of the rare earth 4f electron shell, are effectively shorted out because of the high tetrahedral ($\bar{4}3m$) symmetry at the lanthanide sites. On the other hand, huge λ_{111}'s are allowed because two inequivalent tetrahedral sites exist in the C15 structure which permit internal distortions along [111] directions. *This internal distortion lowers the symmetry and drives an external rhombohedral distortion* (λ_{111}). In fig. 15.4a, the distortion is illustrated for $TbFe_2$ and other RFe_2 compounds containing lanthanides with oblate 4f charge densities. The two inequivalent sites, situated at 0, 0, 0 and $\frac{1}{4}, \frac{1}{4}, \frac{1}{4}$, are denoted by A (or A′) and B (or B′) respectively. The iron atoms are not shown. λ_{111} signifies the fractional change in length along the [111] direction when the material is magnetized along this direction. In fig. 15.4a, the magnetization is directed along [111]. The oblate 4f electron cloud ($-e$) lies perpendicular to the magnetization axis. Considering only the electrostatic Coulomb interaction, the closer proximity of the 4f electron cloud on A to atoms B′ than B, causes an extension of the A–B bond, the magnitude of which depends upon the internal A–B modulus. The resultant increase in linear dimension *a* exceeds a small decrease in length *b*, yielding a net positive external magnetostriction along [111]. See fig. 15.4a. Similarly, for compounds with lanthanides possessing prolate 4f charge densities, e.g. for $SmFe_2$, $ErFe_2$ and $TmFe_2$, a contraction of *a* occurs producing the observed negative magnetostrictions (λ_{111}). A large rhombohedral distortion thus exists whenever the magnetization points along [111], i.e. for $TbFe_2$, $SmFe_2$, $ErFe_2$ and $TmFe_2$. The remaining case of [100] easy, i.e. for $DyFe_2$ and $HoFe_2$, is depicted in fig. 15.4b. With the easy direction of magnetization parallel to the [100] direction, the 4f electron cloud becomes equidistant to all rare earth nearest neighbors, allowing no magnetostric-

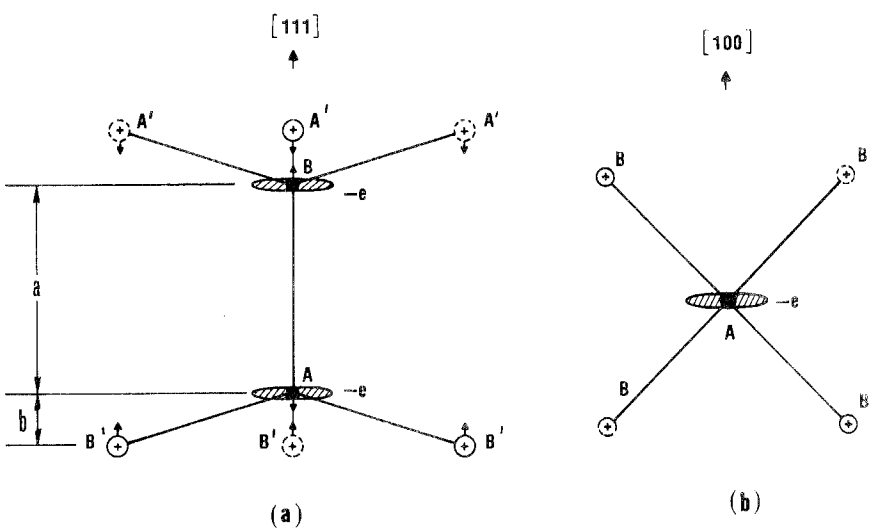

Fig. 15.4. Model of magnetostriction in Laves phase RFe_2 compounds: (a) $M \| [111]$, (b) $M \| [100]$. Open circles, ○, denote atoms above plane of figure; broken circles, ◌, denote atoms below (taken from Clark et al., 1976).

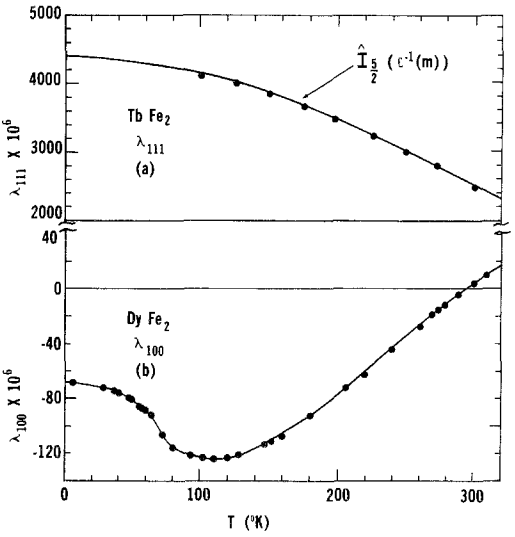

Fig. 15.5. Magnetostriction of single crystal $TbFe_2$ and $DyFe_2$ (taken from Clark et al., 1977).

tively driven internal distortion via point charge electrostatic interactions. All A–B bonds are equivalent, the symmetry remains high, and the potentially huge magnetostriction constant, λ_{100}, does not appear.

In fig. 15.5, $\lambda_{111}(T)$ of $TbFe_2$ and $\lambda_{100}(T)$ of $DyFe_2$ are contrasted. In $TbFe_2$, $\lambda_{111}(T)$ is well behaved. The magnetostriction monotonically decreases with increasing temperature according to $\hat{I}_{5/2}$ (Clark et al., 1977). At absolute zero, $\lambda_{111}(0) = 4400 \times 10^{-6}$, the largest known value for a cubic material. On the other hand, $\lambda_{100}(T)$ for $DyFe_2$ is small and cannot be fit by any simple single-ion function. For $TbFe_2$, using the elastic constants of Rinaldi et al. (1977), the magnetoelastic coupling coefficient $B_2 = -3c_{44}\lambda_{111} = -6.4 \times 10^9$ erg/cm^3 at $T = 0$.

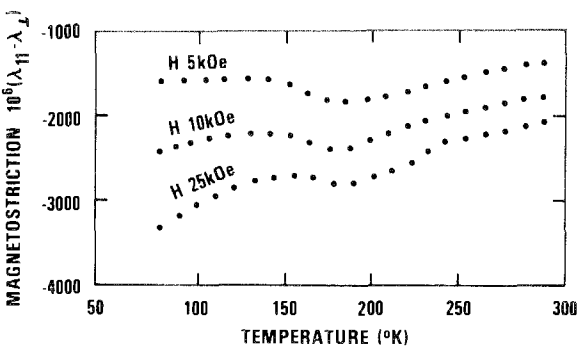

Fig. 15.6. Magnetostriction of $SmFe_2$ (taken from Rosen et al., 1974).

This is comparable to the coefficient $B^{\gamma} \cong -2.3 \times 10^9$ erg/cm^3 calculated for the elemental rare earths Tb and Dy.

A large magnetoelastic coupling is also inferred for λ_{111} of $SmFe_2$. In fig. 15.6 is plotted the magnetostriction of polycrystal $SmFe_2$ as a function of temperature taken from Rosen et al. (1974). The magnetoelastic coupling indeed is high. An analysis of the temperature dependence is difficult, however, because of a low lying $J = \frac{7}{2}$ multiplet.

There is a total of fifteen lanthanide rare earths. Only certain ones are suitable for magnetostrictive transduction. In table 15.2 are listed the lanthanide elements in order of increasing number of 4f electrons. La with no 4f electrons and Lu with a full shell of fourteen 4f electrons are omitted. It is possible to calculate the intrinsic ($T = 0$ K) magnetostriction of each 3^+ lanthanide ion for a particular compound (assuming its existence) given the magnetostriction of at least one compound (e.g. $TbFe_2$). The theory utilizes the Stevens' Equivalent Operator Method. According to Stevens (1952), the ratio of the intrinsic magnetostriction of one lanthanide ion to another is given by the ratio of $\alpha J(J - \frac{1}{2})\langle r_f^2 \rangle$ where α is the lowest order Stevens' factor, J is the ground state angular momentum for the 3^+ ion and $\langle r_f^2 \rangle$ is the average radius squared of the 4f electron shell. In table 15.2, the values of J, α, and $\langle r_f^2 \rangle$ are given along with the calculated values of λ_{111} for RFe_2 compounds normalized to 4400 for $TbFe_2$. The estimated uncertainty in the absolute magnitude of $\lambda_{111}(0)$ is $\pm 15\%$. Note that the largest positive intrinsic magnetostrictions are calculated for $CeFe_2$,

TABLE 15.2
Magnetostriction of $R^{3+}Fe_2$ compounds

R	$\alpha \times 10^{2a}$	J	$\langle r_f^2 \rangle^b$	$\lambda_{111} \times 10^6$ (calc) 0 K	$\lambda_{111} \times 10^6$ (exp) room temperature
Ce	−5.72	$\frac{5}{2}$	1.20	6000	—
Pr	−2.10	4	1.086	5600	—
Nd	−0.643	$\frac{9}{2}$	1.001	2000	—
Pm	0.772	4	0.942	−1800	—
Sm	4.13	$\frac{5}{2}$	0.883	−3200	−2100[e]
Eu	0	0	0.834	0	—
Gd	0	$\frac{7}{2}$	0.785	0	—
Tb	−1.01	6	0.756	4400	2460[d]
Dy	−0.635	$\frac{15}{2}$	0.726	4200	1260[e]
Ho	−0.222	8	0.696	1600	185[e]
Er	0.254	$\frac{15}{2}$	0.666	−1500	−300[d]
Tm	1.01	6	0.639	−3700	—
Yb	3.18	$\frac{7}{2}$	0.613	−3600	—

[a]Stevens, K.W.H., 1952, Proc. Phys. Soc. **65**, 209. [b]Freeman, A.J. and Watson, R.E., 1962, Phys. Rev. **127**, 2058. [c]Koon, N., private communication. [d]Clark, A., J. Cullen and K. Sato, 1975, AIP Conf. Proc. 24, 670. [e]Clark, A., J. Cullen, O. McMasters and E. Callen, 1976, AIP Conf. Proc. No. 29.

$PrFe_2$, $TbFe_2$ and $DyFe_2$; the largest negative magnetostrictions are predicted for $SmFe_2$, $TmFe_2$ and $YbFe_2$. However, not all of these compounds have been synthesized. Ce and Yb are not found in their trivalent states. The quadrivalent state of Ce and the divalent state of Yb yield zero magnetostriction. $PrFe_2$ and $NdFe_2$ do not form the cubic Laves phase compounds. While both $DyFe_2$ and $TmFe_2$ have high incipient magnetostrictions, the large magnetostriction is not realized in $DyFe_2$ since [111] is magnetically hard, and the large magnetostriction of $TmFe_2$ is realized only at low temperatures because of a weak lanthanide–iron exchange interaction. Thus only $TbFe_2$ and $SmFe_2$ emerge with large room temperature magnetostrictions.

Experimental values of λ_{111} measured at room temperature are given in table 15.2 for the binary compounds: $SmFe_2$, $TbFe_2$, $DyFe_2$ (see section 5), $HoFe_2$ and $ErFe_2$.

3. Magnetization and sublattice magnetization

Extensive magnetization measurements on a large number of RFe_2 binary and pseudobinary polycrystals have been made by Buschow and Van Stapele (1970, 1971) and Burzo (1971). It is clear from this work and the earlier work of Wallace and Skrabek (1964) that the lanthanides couple antiferromagnetically to the iron moments in these compounds. These data, which appear in ch. 14, section 3.4, will not be reported in detail here. In table 15.3, however, are collected Curie temperatures, atomic magnetic moments, and theoretical densities from these sources and from recent single crystal magnetization measurements.

The temperature dependences of the magnetic moments of $TbFe_2$, $DyFe_2$, and $ErFe_2$ have been measured on single crystal specimens prepared by horizontal

TABLE 15.3
Magnetic moments and Curie temperatures of RFe_2

RFe_2	σ(emu/gm) 0 K	300 K	ρ_t gm/cm^3	M(emu/cm^3) 0 K	300 K	n_B 0 K	300 K	n^d_{BFe}	T^c_c K
$TbFe_2$[a]	120	88	9.06	1090	800	5.81	4.26	1.60	697,711
$DyFe_2$[a]	140	87	9.28	1300	810	6.87	4.27	1.57	635
$ErFe_2$[a]	116	29	9.62	1120	280	5.79	1.45	1.61	590,597
$SmFe_2$[b]	48	47	8.53	410	400	2.25	2.2	—	676
$HoFe_2$[c]	120(137)	59	9.44	1130(1290)	560	5.94(6.8)	2.92	—	597,612
$TmFe_2$[c]	50(75.7)	11	9.79	490(740)	110	2.5(3.8)	0.55	—	566,610

[a]From single crystal data. See A.E. Clark et al. (1972, 1975, unpublished). [b]From polycrystal data of K.H.J. Buschow (unpublished). [c]From polycrystal data of K.H.J. Buschow and R.P. Van Stapele, 1971, and E. Burzo, 1971. Values in ( ) are calculated values assuming $n_B = gJ - 3.2$. [d]Calculated assuming $n_{B_R} = gJ$.

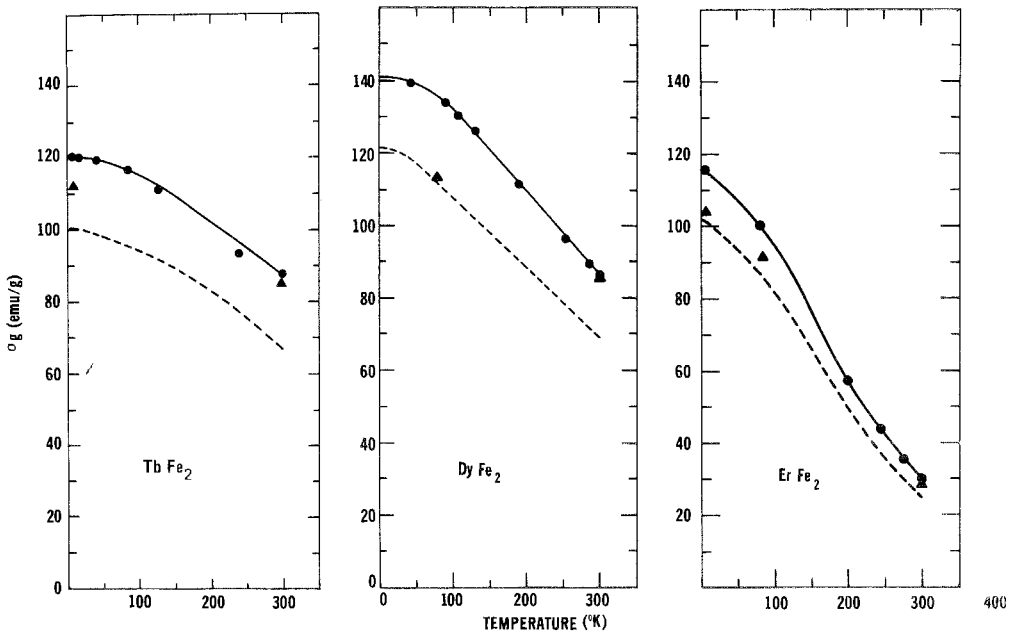

Fig. 15.7. Fig. 15.8. Fig. 15.9.

Fig. 15.7–15.9. Magnetic moments of (15.7) $TbFe_2$, (15.8) $DyFe_2$ and (15.9) $ErFe_2$ (Clark , 1974, unpublished). —●— single crystal (along easy direction); ▲ polycrystal (at 120 kOe); - - - - polycrystal (taken from Burzo, 1971).

induction zoning and Czochralski methods. In figs. 15.7, 15.8 and 15.9, the magnetic moment along the easy magnetization directions are compared to data on polycrystalline samples at moderate and high magnetic fields. Although the compounds are cubic and only moderate anisotropies are expected, it is clear that the full saturation magnetization is not achieved in polycrystal specimens at low temperatures. Instead huge cubic anisotropies were measured in all compounds (R = Tb, Dy, Er). See section 4. The easy directions of magnetization are consistent with those predicted by the earlier Mössbauer measurements: Wertheim et al. (1964), Bowden et al. (1968) and Atzmony et al. (1973). In fig. 15.7, the magnetic moment vs temperature for $TbFe_2$ is shown. The upper curve depicts the moment parallel to the [111] easy direction. Data for polycrystals in high fields (120 kOe) as well as moderate fields are shown. In a polycrystal in which crystallites are distributed uniformly over all directions, if the [111] axis is easy and the magnetization lies along the [111] axis in each crystallite closest to the external field direction, the polycrystal remanent moment is 0.866 of the aligned saturation moment. See Chikazumi and Charap (1964). This is close to the observed polycrystal/single crystal moment ratio at 4 K. The moment of $DyFe_2$ is shown in fig. 15.8. In $DyFe_2$ the [100] axis is easy and the magnetization is saturated in the single crystal data of the upper curve. The lower curve shows polycrystal data. As in $TbFe_2$, it is not possible to saturate polycrystal samples at

4 K even with 120 kOe. In $DyFe_2$ the moment of the polycrystal is about 14% below the single crystal value. When [100] is easy, an isotropic polycrystal with the magnetization in each crystallite aligned along the [100] nearest the field direction is calculated to have a moment of 0.832 times the fully aligned moment. In fig. 15.9, the magnetic moment of $ErFe_2$ parallel to its easy [111] direction is shown. As in $TbFe_2$, [111] is easy. However, the magnetic moment decreases much more rapidly with increasing temperature. No single crystal moments have been reported for $SmFe_2$, $HoFe_2$, or $TmFe_2$. Calculated values assuming an atomic moment for Fe of 1.6 μ_B are found in table 15.3.

The decrease of the magnetic moment with temperature over this temperature range is almost entirely due to the temperature change of the magnetic moment of the lanthanide sublattice. The Fe moment is nearly temperature independent. Since the magnetostriction and magnetic anisotropy derive essentially from the lanthanide, their temperature dependences are related to the temperature dependences of the lanthanide sublattice moments rather than to the temperature dependences of the total moments. Whenever the magnetostriction and anisotropy are single ion in nature, Callen and Callen (1963) have shown that their temperature dependences can be calculated from the temperature dependence of the sublattice moment $m_R(T)$ by:

$$\lambda(T) = \lambda(0)\hat{I}_{5/2}[\mathscr{L}^{-1}(m_R(T))], \qquad K_1(T) = K_1(0)\hat{I}_{9/2}[\mathscr{L}^{-1}(m_R(T))].$$

K_1 denotes the lowest order anisotropy constant for cubic crystals defined in section 4; λ denotes any of the lowest order magnetostriction constants: λ_s, λ_{100} or λ_{111}. $\hat{I}_{l+1/2}$ is a reduced hyperbolic Bessel function of order l, and $\mathscr{L}^{-1}[m_R]$

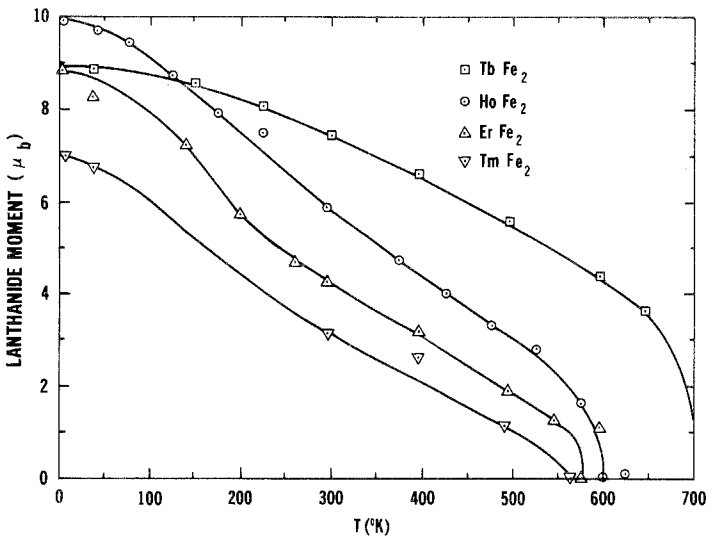

Fig. 15.10. Lanthanide sublattice magnetic moment in RFe_2 compounds (Taken from Rhyne, unpublished).

denotes the inverse Langevin function of the lanthanide sublattice moment normalized to one at $T = 0$. $\hat{I}_{5/2}$ and $\hat{I}_{9/2}$ are graphically displayed by Callen and Callen (1963). The temperature dependence of the lanthanide sublattice moments as determined from neutron scattering by Rhyne (unpublished) is plotted in fig. 15.10. Note that the 0 K moments for $TbFe_2$, $HoFe_2$, $ErFe_2$ and $TmFe_2$ are in good agreement with the values calculated from gJ, where g is the Landé g factor and J is the ground state quantum number of the 3^+ rare earth ion.

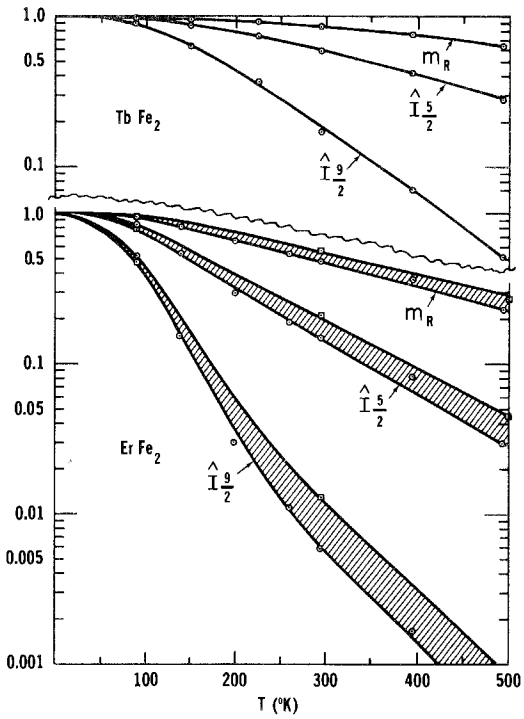

Fig. 15.11. Normalized sublattice magnetizations and single ion functions $\hat{I}_{5/2}$ and $\hat{I}_{9/2}$ for $TbFe_2$ and $ErFe_2$ (taken from Rhyne, unpublished; and Bargouth and Will, 1971).

The magnitude of the room temperature sublattice moment varies considerably with lanthanide, R. In fig. 15.11, the sublattice moment, normalized to one at $T = 0$, and the hyperbolic Bessel functions, $\hat{I}_{5/2}$ and $\hat{I}_{9/2}$, are plotted from 0 K to 500 K for $TbFe_2$ and $ErFe_2$. Because of the higher sublattice moment, the room temperature anisotropy and magnetostriction calculated on the basis of these functions are clearly much larger for $TbFe_2$. The sublattice moment of Tb decreases by only 17% from 0 K to room temperature, while the Er moment drops by about 50%. This results in substantially smaller room temperature values of K_1 and λ for $ErFe_2$. Even lower values are predicted for $TmFe_2$.

4. Magnetic anisotropy

Magnetic anisotropy refers to the difference in energy required to rotate the magnetization from one crystalline direction to another. This energy is often expressed in direction cosines (α_i's) of the magnetization with respect to the crystalline axes. For cubic crystals the lowest order expression is:

$$E_a = K_1(\alpha_1^2\alpha_2^2 + \alpha_2^2\alpha_3^2 + \alpha_3^2\alpha_1^2).$$

If $K_1 < 0$, the energy is lowest when the magnetization points along the [111] direction; if $K_1 > 0$, [100] is the preferred direction of magnetization. When [111] is easy, λ_{111} is sensed at remanence; when [100] is easy, λ_{100} is sensed at remanence. The total expression for the anisotropy, in general, contains higher order terms. When a direction other than [100] or [111] is easy, these terms must be included and the magnetostriction referred to that particular easy direction is sensed at remanence. In some cases, e.g. some ternary alloys, the easy direction varies as a function of temperature. See Atzmony et al. (1973).

Magnetic anisotropy values were experimentally determined by both magnetization measurements and magnetic torque measurements (Clark et al., 1973; Williams and Koon, 1975). Both methods employ single crystals. Using the former method, the anisotropy is calculated from magnetization measurements, taken along principal crystallographic directions. This method is useful when the anisotropy is very large. Torque methods are more accurate and are particularly applicable for moderate and low magnetic anisotropies. The largest recorded anisotropy of a cubic crystal at room temperature is that of $TbFe_2$. It is negative. The largest known positive anisotropy is that of $DyFe_2$. See table 15.4. In fig.

TABLE 15.4
Anisotropy constants of some cubic metals and ferrites at room temperature

Metal	$10^{-4}K_1$(ergs/cm^3)	Ferrite	$10^{-4}K_1$(ergs/cm^3)
Fe	45[a]		
Ni	−5[a]		
70% Fe-Co	−43[b]	$Ga_{0.44}Fe_{2.54}O_4$	−81[f]
65% Co-Ni	−26[c]	$CoFe_2O_4$	260[g]
$ErFe_2$	−330[d]	$Co_{0.8}Fe_{2.2}O_4$	290[h]
$DyFe_2$	2100[d]	$Co_{0.3}Zn_{0.2}Fe_{2.2}O_4$	150[h]
$TbFe_2$	−7600[d]		
$HoFe_2$	580[e]		

[a]Hoffman, U., 1967, Z. angew. Phys. **22**, 106. [b]McKeehan, L.W., 1937, Phys. Rev. **51**, 136. [c]Shih, J.W., 1936, Phys. Rev. **50**, 376. [d]Clark, A.E., H.S. Belson and N. Tamagawa, 1972, AIP Conf. Proc. **10**, 749; Clark, A.E., J.R. Cullen and K. Sato, 1975, AIP Conf. Proc. **24**, 670. [e]Williams, C., N. Koon and J. Milstein, 1975, Proc. 21st Conf. on Mag. & Mag. Mat'ls, Philadelphia, Pa. Dec. [f]Pearson, R.F., 1960, J. Appl. Phys. **31**, 160S. [g]Perthel, R., G. Elbinger and W. Keileg, 1966, Phys. Status Solidi **17**, 151. [h]Bozorth, R.M., E.R. Tilden and A.J. Williams, 1955, Phys. Rev. **99**, 1788.

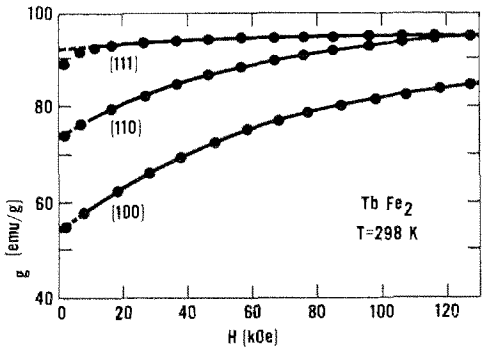

Fig. 15.12. Magnetic moment of single crystal $TbFe_2$ at room temperature (taken from Clark et al., 1975).

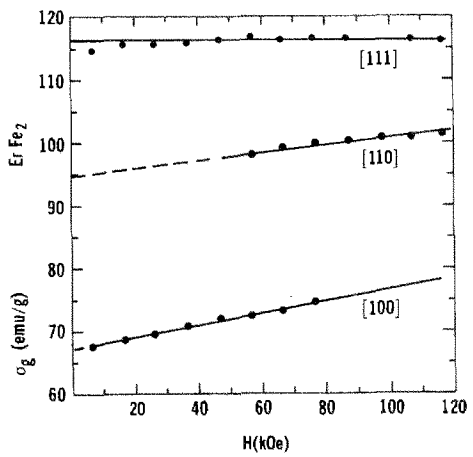

Fig. 15.13. Magnetic moment of single crystal $ErFe_2$ at 4.2 K (taken from Clark, 1974).

15.12 are illustrated the magnetization curves for $TbFe_2$ at room temperature. Even in an applied field of 120 kOe, the moment cannot be aligned along its hard [100] direction. Similar curves exist for $DyFe_2$. For $ErFe_2$, the anisotropy at room temperature is much smaller because of its lower room temperature sublattice magnetization. However, it becomes enormous at low temperatures. Figure 15.13 shows the magnetization curves vs field for $ErFe_2$ at 4 K. From these measurements an anisotropy energy, $K_1 \cong -5 \times 10^8$ erg/cm^3, is calculated by Clark et al. (1973). This corresponds to an anisotropy field, $2K_1/M$, of 10^6 Oe. On the other hand, certain pseudobinary RFe_2 compounds possess very small magnetic anisotropies. See section 5. Using torque magnetometry, Williams and Koon (1975, 1977) have determined the two lowest order anisotropy constants, K_1 and K_2, for $Tb_{1-x}Ho_xFe_2$ ($x = 0.85$) and for $Tb_{1-x-y}Ho_xDy_yFe_2$ ($x = 0.58$, $y = 0.22$).

TABLE 15.5
Anisotropy constants from Mössbauer effect measurements (10^7 ergs/cm^3)[a]

	K_1(4.2 K)	K_2(4.2 K)	K_1(300 K)
$TbFe_2$	−63.9	7.3	−3.85
$DyFe_2$	83.5	−252.6	2.69
$HoFe_2$	4.9	334.0	0.66
$ErFe_2$	−21.3	−294.4	−0.33
$TmFe_2$	−43.7	35.0	−0.12

[a]Taken from Dariel and Atzmony (1973).

In section 5, the values of K_1 at room temperature for $Tb_{1-x}Ho_xFe_2$ ($0.82 < x < 0.91$) are illustrated.

In table 15.4 are listed the anisotropy constants of some cubic metals and ferrites at room temperature. The anisotropy of the binary RFe_2 compounds is one to two orders of magnitude larger than the cubic transition metal alloys. Dariel and Atzmony (1973), from Mössbauer effect measurements, have calculated the anisotropy constants, K_1 and K_2. Their values of K_1 and K_2 at 4 K and their values of K_1 at room temperature are given in table 15.5. At low temperatures $K_2/K_1 \gg 1$ for $DyFe_2$, $HoFe_2$ and $ErFe_2$.

5. Magnetostriction of pseudobinary Laves phase compounds

For many magnetostrictive materials applications, high strains at low applied fields are important. This generally requires a large magnetostriction to anisotropy ratio. While the magnetostriction, λ, and anisotropy, K, are both intrinsically large in the lanthanide elements and compounds; unlike the lanthanide elements, a large λ/K ratio can be achieved in pseudobinary RFe_2 compounds. In table 15.6 are the signs of λ, K_1 and K_2 for the binary RFe_2 compounds, taken from the signs of the Stevens' Equivalent Operator Coefficients (Stevens, 1952).

Using this table pseudobinary compounds can be constructed in such a way as to minimize the magnetic anisotropy while still maintaining a large positive (or

TABLE 15.6
Polarity of λ, K_1 and K_2

	$PrFe_2$[a]	$SmFe_2$	$TbFe_2$	$DyFe_2$	$HoFe_2$	$ErFe_2$	$TmFe_2$	$YbFe_2$[a]
λ	+	−	+	+	+	−	−	−
K_1	+	−	−	+	+	−	−	+
K_2	−	0	+	−	+	−	+	−

[a]The binary $PrFe_2$ and $YbFe_2$ compounds are not readily synthesized.

negative) magnetostriction. The procedure is to select compounds with the same magnetostriction sign but with opposite signs of anisotropy. Ternary compounds yielding a positive magnetostriction must contain Tb. Hence they are $Tb_{1-x}Dy_xFe_2$, $Tb_{1-x}Ho_xFe_2$, and $Tb_{1-x}Pr_xFe_2$. Spin orientation diagrams for $Tb_{1-x}Dy_xFe_2$ and $Tb_{1-x}Ho_xFe_2$ are shown in fig. 15.14. Ternary compounds possessing a negative magnetostriction must possess Sm. However, Yb, the only suitable element with the correct signs is not found in a trivalent state. Fortunately, the ratio of λ/K is much larger for Sm than for the heavy lanthanides. Hence certain ternary alloys, such as $Sm_{1-x}Dy_xFe_2$ and $Sm_{1-x}Ho_xFe_2$ are attractive.

The largest saturation magnetostrictions have been found in the compensated $Tb_{1-x}Dy_xFe_2$ and $Tb_{1-x}Pr_xFe_2$ systems. The $Tb_{1-x}Dy_xFe_2$ system has been investigated in detail. In fig. 15.15 the magnetostriction at room temperature of polycrystalline samples of $Tb_{1-x}Dy_xFe_2$ for $H = 10$ kOe and $H = 25$ kOe is

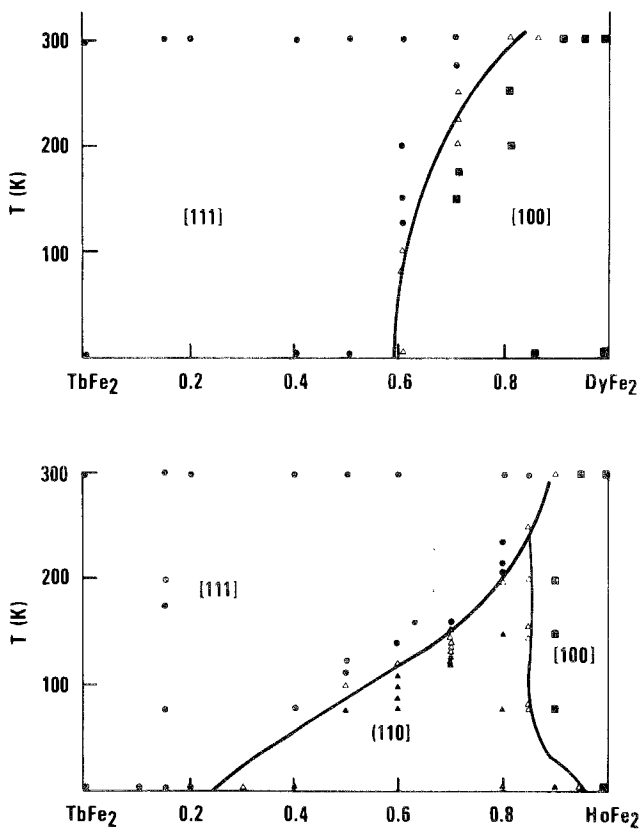

Fig. 15.14. Spin orientation of $Tb_{1-x}Dy_xFe_2$ and $Tb_{1-x}Ho_xFe_2$ systems (taken from Atzmony et al., 1973). Filled circles, triangles and squares correspond to [111], [110] and [100] axes of magnetization, respectively. Open triangles correspond to intermediate directions.

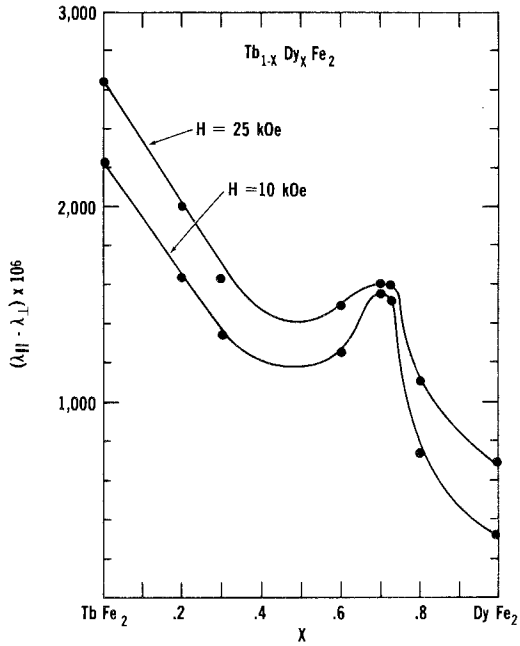

Fig. 15.15. Magnetostriction of $Tb_{1-x}Dy_xFe_2$ system at room temperature (taken from Clark, 1974).

plotted. Near $x = 0.7$, the magnetostriction at these fields exhibits a peak, reflecting the near-zero magnetic anisotropy at this concentration. Figure 15.16 illustrates how the single crystal magnetostriction constant λ_{111} varies with Dy concentration. λ_{111} was determined by X-ray techniques, utilizing a method developed to accurately pinpoint the value of x for anisotropy sign reversal (Dwight

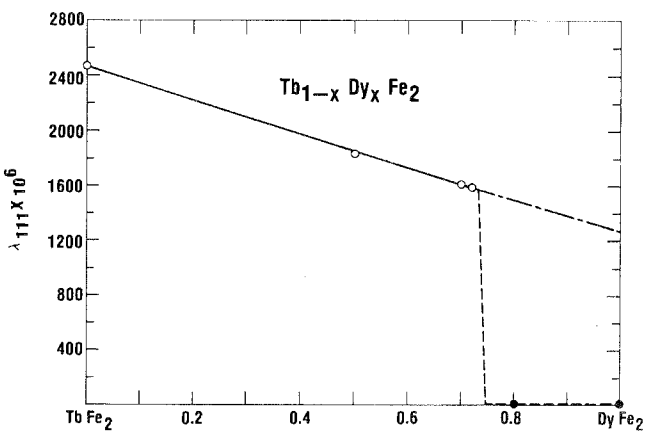

Fig. 15.16. λ_{111} of $Tb_{1-x}Dy_xFe_2$ at room temperature. Open circles are λ_{111}; solid circles denote region where no spontaneous λ_{111} exists (taken from Clark et al., 1976).

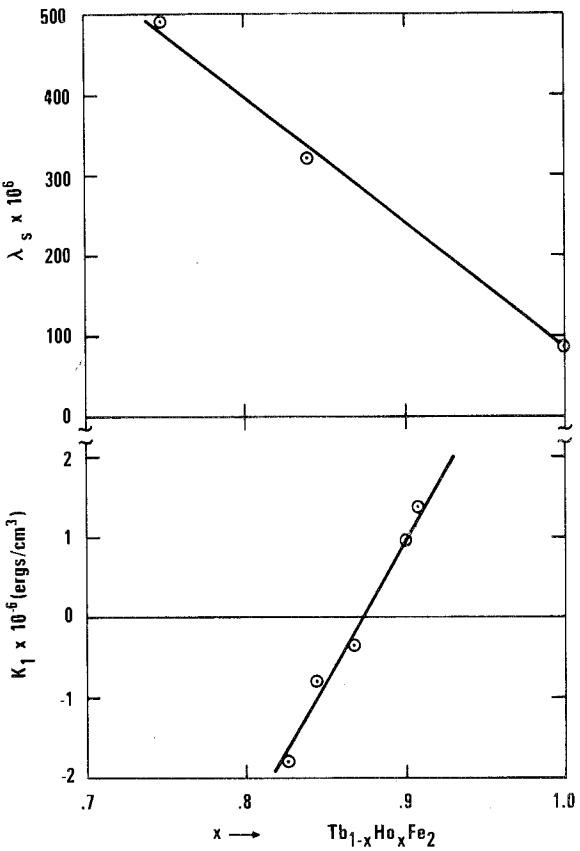

Fig. 15.17. Magnetostriction, λ_s, and magnetic anisotropy, K_1, of $Tb_{1-x}Ho_xFe_2$ (taken from Koon et al., 1974; and Williams, unpublished).

and Kimball, 1974; Clark et al., 1976). When [111] is easy ($K_1 < 0$), a large rhombohedral distortion occurs, contributing to a large X-ray splitting of the (440) and (620) lines. When [100] is easy ($K_1 > 0$) only a tiny distortion is realized ($\lambda_{100} \cong 0$) and X-ray splittings effectively disappear. The concentration at which the magnetostriction disappears clearly identifies the point of anisotropy sign reversal. At the compensating concentration, $\lambda_{111} = 1600 \times 10^{-6}$. The extrapolated value of λ_{111} for $DyFe_2$ is 1260×10^{-6}. In fig. 15.17, the room temperature saturation magnetostriction measurements of Koon et al. (1974) for $Tb_{1-x}Ho_xFe_2$ are shown as a function of composition x. Here compensation occurs near $x = 0.86$.

From table 15.6 multicomponent systems such as $Tb_xPr_yDy_zFe_2$, $Tb_xDy_yHo_wFe_2$, and $Tb_xPr_yDy_zHo_wFe_2$ can be selected to achieve maximum magnetostrictions with simultaneous minimization of more than one anisotropy constant. In the quaternary $Tb_xDy_wHo_yFe_2$ system, $\lambda_s = 530 \times 10^{-6}$ at anisotropy compensation (Williams and Koon, 1977).

In fig. 15.18, the absolute value of λ_{111} is plotted vs. x ($0 < x < 0.4$) for some ternary Sm alloys ($\lambda_{111} < 0$) and for some Tb ternary alloys ($\lambda_{111} > 0$). The

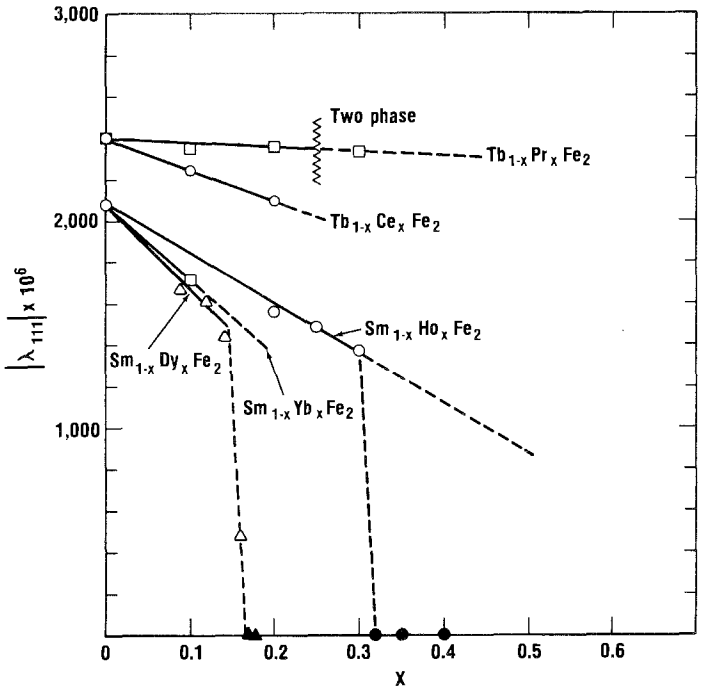

Fig. 15.18. λ_{111} of some $Tb_{1-x}R_xFe_2$ and $Sm_{1-x}R_xFe_2$ alloys. Open symbols are $|\lambda_{111}|$; solid symbols denote region where no spontaneous λ_{111} exists (taken from Clark et al., 1977).

replacement of Tb by ~20% Pr does not appreciably alter the magnetostriction. On the other hand, Ce is not trivalent and its substitution for Tb results in a linear decrease in magnetostriction. Since Yb is divalent, a similar decrease is found when Sm is replaced by Yb. No anisotropy is expected in these cases. However as predicted, anisotropy sign reversal has been observed with relatively small additions of $DyFe_2$ and $HoFe_2$ to $SmFe_2$. For $Sm_{1-x}Dy_xFe_2$, sign reversal occurs near $x = 0.15$; for $Sm_{1-x}Ho_xFe_2$, it occurs near $x = 0.3$. In both alloys, $|\lambda_{111}| > 1000 \times 10^{-6}$ at these compensating concentrations.

6. Elastic properties

Room temperature sound velocities, densities, and moduli are listed in table 15.7 for polycrystalline $TbFe_2$, $ErFe_2$, YFe_2 and $TbFe_3$. The moduli are midway between those of the soft rare earth elements and the stiffer magnetic transition metals, such as Fe and Ni. The moderate magnitudes of the moduli and the huge magnitudes of the magnetostrictions combine to yield huge magnetoelastic forces and energies for these compounds. Values of λ_s, $E\lambda_s$, and the energy

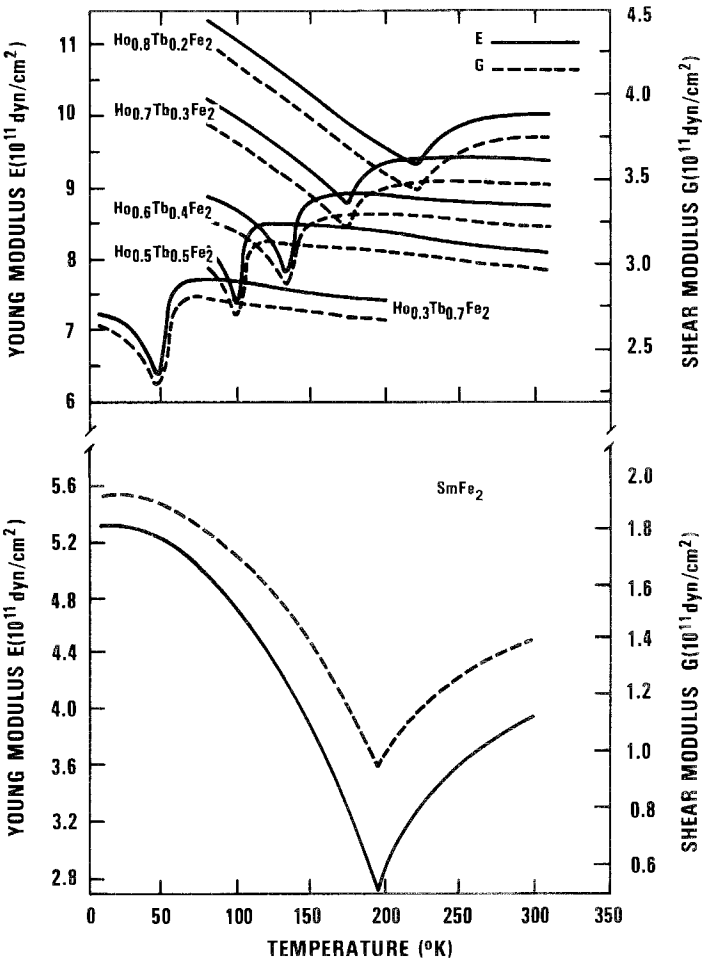

Fig. 15.19. Temperature dependence of Young's modulus, E, and shear modulus, G for $Tb_{1-x}Ho_xFe_2$ and $SmFe_2$ (taken from Rosen et al., 1973, 1974).

density, $\frac{1}{2}E\lambda_s^2$, are shown in table 15.7. They are compared to those of elemental Ni, a typical magnetostrictive material. The quantity $E\lambda_s$ is a measure of the pressure exerted by a constrained bar of the material which is magnetized to saturation. The energy density, $\frac{1}{2}E\lambda_s^2$, represents the amount of magnetic energy which can be transformed to elastic energy per unit volume of the material. For $TbFe_2$, this energy is about 1000 times that of earlier magnetostrictive materials, such as Ni.

The elastic constants of single crystal $Tb_{0.27}Dy_{0.73}Fe_2$ have been measured ultrasonically by Rinaldi et al. (1977). The shear modulus $\frac{1}{2}(C_{11} - C_{12}) = 3.83 \times 10^{11}$ dynes/cm^2 and is essentially field independent. In contrast, C_{44}, which reflects the large magnetoelastic coupling, depends strongly on magnetic field and

TABLE 15.7
Elastic and magnetoelastic properties[a]

	$TbFe_2$	$ErFe_2$	YFe_2	$TbFe_3$	Ni
v_l(m/sec)	3940	4120	4340	4230	—
v_s(m/sec)	1980	2180	2720	2320	—
ρ(gm/cm^3)	9.1	9.7	6.7	9.4	—
$E \times 10^{-10}$ (newton/m^2)	9.4	12.1	12.7	13.1	21[b]
$\lambda_s \times 10^6$	1750	−229	—	693	−31[c]
$E\lambda_s \times 10^{-7}$ (newton/m^2)	17	2.8	—	9	0.7
$\frac{1}{2}E\lambda_s^2 \times 10^{-3}$ (joule/m^3)	145	3.2	—	32	0.1

[a]Clark, A.E., H.S. Belson and R.E. Strakna, J. Appl. Phys. **44**, 2913 (1973). [b]"Nickel", The International Nickel Co. Inc., (1951). [c]J.J. Went, Physica **17**, 98 (1951).

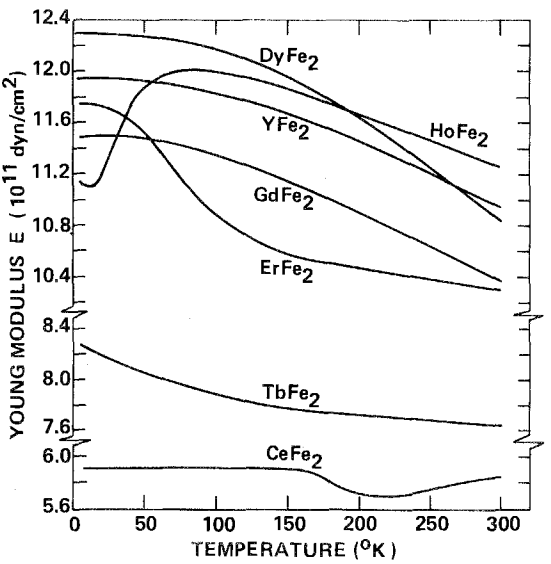

Fig. 15.20. Temperature dependence of the Young's moduli of the RFe_2 compounds.

ranges from a low field (coupled) value $< 2.1 \times 10^{11}$ dynes/cm^2 to a high field (intrinsic) value of 4.87×10^{11} dynes/cm^2. C_{11} is calculated to be 14.1×10^{11} dynes/cm^2.

Rosen et al. (1973, 1974) have determined Young's modulus and the shear modulus for the ternary $Tb_{1-x}Ho_xFe_2$ system and for $SmFe_2$ as a function of temperature. Their values are illustrated in fig. 15.19. The temperature dependence of Young's moduli for the RFe_2 compounds (R = Y, Ce, Gd, Tb, Dy, Ho and Er) taken from Klimker et al. (1974) are given in fig. 15.20.

7. Magnetomechanical coupling and resistivity

An important low signal transducer parameter is the magnetomechanical coupling factor, k. The square of this factor is a measure of the elastic energy generated by small signal alternating magnetic excitation, i.e. $U_{elas} = k^2 U_{mag}/(1-k^2)$. U_{elas} and U_{mag} denote the energy stored in the elastic and magnetic systems respectively. The coupling factor is conventionally obtained by measuring the complex impedance of a coil containing the magnetostrictive material. When the mechanical motion is parallel to the exciting field, k is specified as k_{33}. A successful method was developed by Savage et al. (1975) to determine the complex impedance for the low permeability RFe_2 alloys as a function of frequency. The magnetomechanical coupling k_{33}, quality factor Q, and permeability μ, for the highly magnetostrictive $Tb_{0.3}Dy_{0.7}Fe_2$ alloy calculated in this way are shown in fig. 15.21 as a function of magnetic bias. The range of the high coupling factor lies between 100 and 500 Oe. The permeability is low, a necessary consequence of a highly magnetostrictive polycrystal.

In fig. 15.22 are plotted the resonant frequencies vs. bias field for a 10 cm thin rod of $Tb_{0.3}Dy_{0.7}Fe_2$. In a magnetostrictive material the resonant frequency at constant field H and at constant induction B are different. This difference is related to the coupling factor k by: $k^2 = 1-(f_H/f_B)^2$. Also, in a highly magnetostrictive material both these resonant frequencies depend strongly upon applied magnetic field. The difference in resonant frequency between the low (nearly zero) bias state and the saturated state is due to a reduction in Young's modulus at low fields primarily because of domain wall motion. This fractional

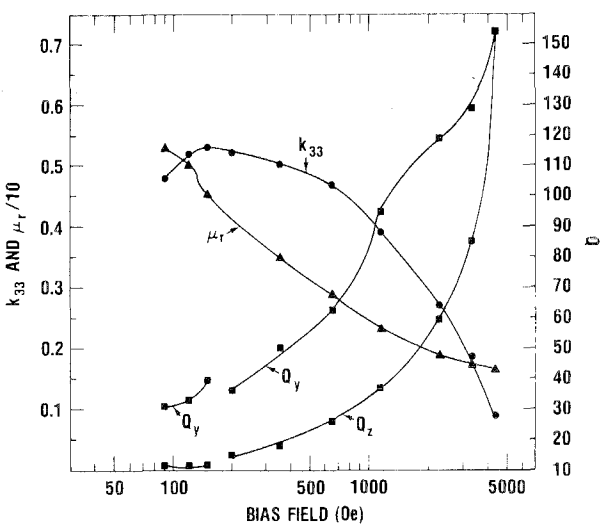

Fig. 15.21. Coupling factor, k_{33}, Q factor and relative permeability μ_r of $Tb_{0.3}Dy_{0.7}Fe_2$ as a function of bias field (taken from Savage et al., 1975). Q_z, the quality factor at constant current drive, includes both mechanical and electrical losses, whereas Q_y, the quality factor at constant voltage drive, includes only mechanical losses.

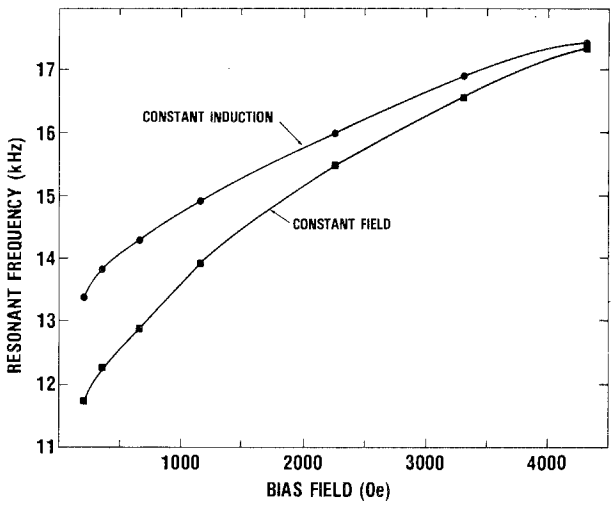

Fig. 15.22. Resonant frequency (at constant induction and constant field) vs. bias field of a 10 cm bar of $Tb_{0.3}Dy_{0.7}Fe_2$ (taken from Savage et al., 1975).

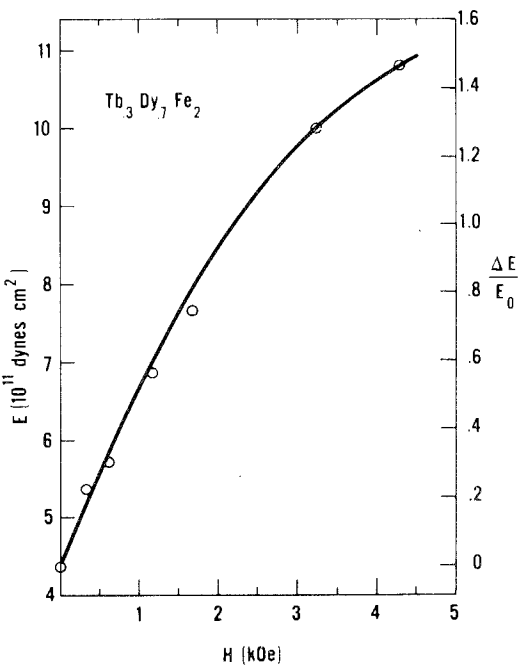

Fig. 15.23. Young's modulus and "ΔE Effect" at room temperature for $Tb_{0.3}Dy_{0.7}Fe_2$.

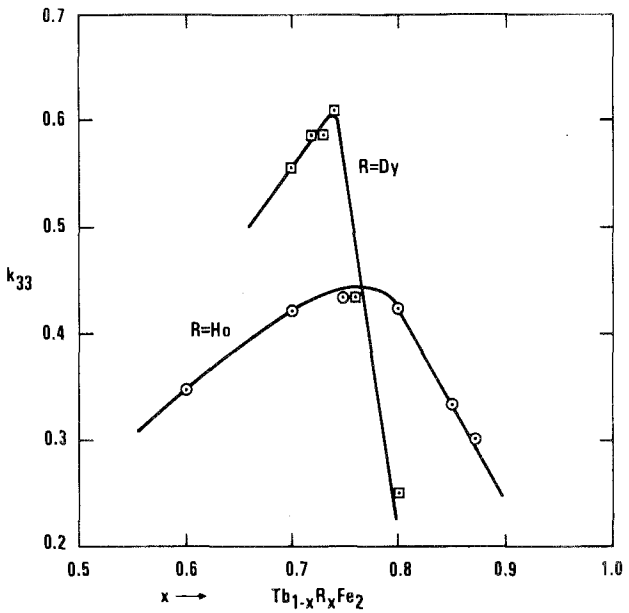

Fig. 15.24. Magnetomechanical coupling, k_{33}, for $Tb_{1-x}Dy_xFe_2$ and $Tb_{1-x}Ho_xFe_2$. (Data taken from Timme, 1976; and Savage et al., 1975.)

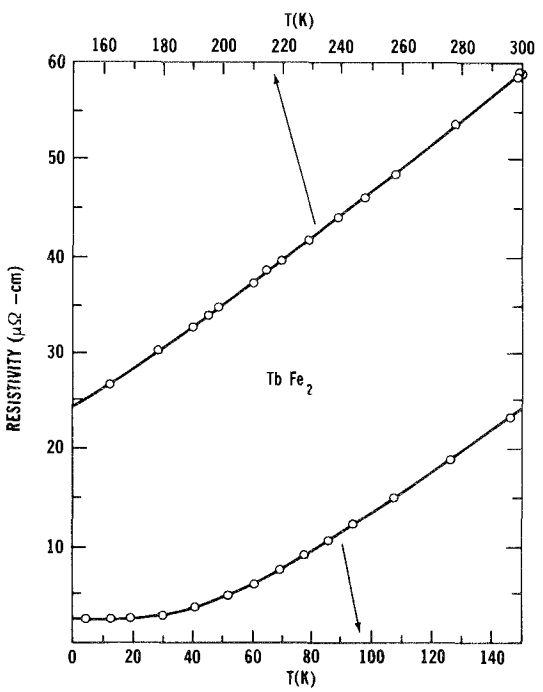

Fig. 15.25. Resistivity of $TbFe_2$ vs. temperature (Data taken from Savage. See Clark, 1974).

change in modulus with field, $\Delta E/E$, is known as the "ΔE effect". The modulus and "ΔE effect" at constant field, calculated from f_H for $Tb_{0.3}Dy_{0.7}Fe_2$, are plotted in fig. 15.23. The increase in modulus is about 150%. This is by far the largest known.

In fig. 15.24, k_{33} is plotted vs. x for $Tb_{1-x}Dy_xFe_2$ and $Tb_{1-x}Ho_xFe_2$. With the addition of $DyFe_2$ and $HoFe_2$ to $TbFe_2$, the value of k_{33} increases to a peak $k_{33} \cong 0.6$ for $Tb_{0.26}Dy_{0.74}Fe_2$, and $k_{33} \cong 0.44$ for $Tb_{0.25}Ho_{0.75}Fe_2$.

Eddy current losses, which exist in metallic transducers, become important for high frequency applications. In fig. 15.25, the electrical resistivity measurements of Savage for $TbFe_2$ are plotted as a function of temperature. At room temperature, its value, which is comparable to that of the rare earths, is much larger than that of Ni and Fe. The resistivity of the amorphous $TbFe_2$ alloy is much higher still. See Clark (1974).

8. Amorphous RFe_2 alloys

Sputtered alloys of composition RFe_2 are both structurally and magnetically amorphous, see Rhyne et al. (1972), and their Curie temperatures range from below room temperature to 230°C. See ch. 16, sections 3 and 4. A striking feature of these alloys is the large coercivity at low temperatures (Clark, 1973; Rhyne et al., 1974). This is attributed to the combination of high anisotropy and the absence of crystal structure. The maximum energy product calculated for amorphous $TbFe_2$ at 4 K is 29.5×10^6 GOe, which is comparable to the largest measured values for Sm–Co alloys. While the intrinsically high magnetic anisotropy of the rare earth persists to

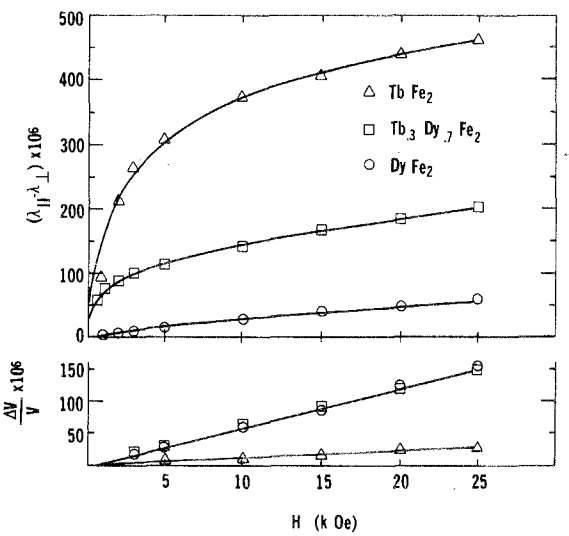

Fig. 15.26. Magnetostriction of amorphous $TbFe_2$, $Tb_{0.3}Dy_{0.7}Fe_2$ and $DyFe_2$ at room temperature (taken from Clark, unpublished).

room temperature, the thermal energy is too high to inhibit magnetization reversal. Consequently coercivities of only ~100 Oe are observed at room temperature.

Like the anisotropy, large room temperature magnetostrictions are also found, even in the amorphous state. The room temperature magnetostrictions of amorphous $TbFe_2$, $Tb_{0.3}Dy_{0.7}Fe_2$, and $DyFe_2$ are shown in fig. 15.26. $TbFe_2$ has a large unsaturated magnetostriction and amorphous $DyFe_2$ has a spontaneous magnetostriction near zero. This difference is accounted for by the difference in Curie temperature. For amorphous $TbFe_2$, $T_c >$ room temperature; for amorphous $DyFe_2$, $T_c <$ room temperature. Unlike crystalline $DyFe_2$, where $d\lambda/dT < 0$, the magnetostriction of amorphous $DyFe_2$ increases rapidly with decreasing temperature.

Similar to the RFe_2 compounds, the amorphous alloys exhibit a large linear forced magnetostriction. This magnetostriction is large near the Curie temperature. For these alloys $\Delta V/VH$ is of the order of 10^{-9}/Oe at room temperature, a value comparable to that of Gd metal at room temperature.

9. Summary

The RFe_2 alloys derive their magnetostriction from the large anisotropic 4f electron charge density. It is preserved at room temperature because of the strong Fe–Fe exchange interaction present in the Laves phase Fe compounds. The high symmetry of the close-packed Laves phase structure allows only a large λ_{111}, yielding a large magnetostriction anisotropy ($\lambda_{111} \gg \lambda_{100}$). Because of this, crystallite orientation is important. Single crystals were prepared by horizontal induction zoning and Czochralski techniques. The high anisotropy of the 4f electron cloud and high Curie temperatures lead to a huge cubic magnetic anisotropy at room temperature as well as large magnetostriction. In $TbFe_2$ and $DyFe_2$ the anisotropy is over an order of magnitude larger than typical cubic materials. Because of the high symmetry of the Laves phase RFe_2 compounds (unlike the hexagonal heavy rare earth elements), the lowest order anisotropy and magnetostriction possess a different sign sequence as R is changed from one element to another. Thus RFe_2 alloys, where R is composed of various rare earths, yield compounds with a wide assortment of magnetic properties.

References

Atzmony, U., M. Dariel, E. Bauminger, D. Lebenbaum, I. Nowik and S. Offer, 1973, Phys. Rev. B **7**, 4220.

Bargouth, M. and G. Will, 1971, J. de Physique **32**, C1-675.

Bowden, G.J., D. Bunbury and A.P. Guimares, 1968, J. Appl. Phys. **39**, 1323.

Bozorth, R., 1951, Ferromagnetism (Van Nostrand, New York).

Burzo, E., 1971, Z. Angew. Physik **32**, 127.

Buschow, K.J. and R.P. Van Stapele, 1970, J. Appl. Phys. **41**, 4066.
Buschow, K.H.J. and R.P. Van Stapele, 1971, J. de Physique **32**, C1-672.
Callen, E. and H. Callen, 1963, Phys. Rev. **129**, 578.
Chikazumi, S. and S. Charap, 1964, Physics of Magnetism (Wiley, New York).
Clark, A., R. Bozorth and B.F. DeSavage, 1963, Phys. Letters **5**, 100.
Clark, A., B.F. DeSavage and R. Bozorth, 1965, Phys. Rev. **138**, A216.
Clark, A. and H. Belson, 1972a, AIP Conf. Proc. No. 5 (American Institute of Physics, New York) p. 1498.
Clark, A. and H. Belson, 1972b, Phys. Rev. B **5**, 3642. Also IEEE Trans. Mag. **MAG-8**, 477.
Clark, A., H. Belson and N. Tamagawa, 1973, AIP Conf. Proc. No. 10 (American Institute of Physics, New York) p. 749. Also Phys. Letters **42A**, 160.
Clark, A., 1973, Appl. Phys. Letters **11**, 642.
Clark, A., 1974, AIP Conf. Proc. No. 18 (American Institute of Physics, New York) p. 1015. Also Proc. 11th Rare Earth Research Conf. (U.S.A.E.C. Tech. Inf. Center, Oak Ridge) p. 972.
Clark, A., J. Cullen and K. Sato, 1975, AIP Conf. Proc. No. 24 (American Institute of Physics, New York) p. 670.
Clark, A., J. Cullen, O.D. McMasters and E. Callen, 1976, AIP Conf. Proc. No. 29 (American Institute of Physics, New York) p. 192.
Clark, A., R. Abbundi, O.D. McMasters and H. Savage, 1977, Physica **86–88B**, 73.
Cullen, J. and A. Clark, 1977, Phys. Rev. **15B**, 4510.
Dariel, M. and U. Atzmony, 1973, Int. J. Magnetism **4**, 213.
Dwight, A.E. and C.W. Kimball, 1974, Acta Crys. **B30**, 2791.
Klimker, H., M. Rosen, M.P. Dariel and U. Atzmony, 1974, Phys. Rev. B **10**, 2968.
Koon, N., A. Schindler and F. Carter, 1971, Phys. Letters **37A**, 413.
Koon, N., A. Schindler, C. Williams and F. Carter, 1974, J. Appl. Phys. **45**, 5389.
Legvold, S., J. Alstad and J.J. Rhyne, 1963, Phys. Rev. Letters **10**, 509.
Milstein, J., 1975, AIP Conf. Proc. No. 29 (American Institute of Physics, New York) p. 592.
Rhyne, J.J. and S. Legvold, 1965, Phys. Rev. **138**, A507.
Rhyne, J.J. and T.P. McGuire, 1972, IEEE Trans. Mag. **MAG-8**, 105.
Rhyne, J.J., S.J. Pickart and H.A. Alperin, 1972, Phys. Rev. Letters **29**, 1562.
Rhyne, J.J., J.H. Schelleng and N.C. Koon, 1974, Phys. Rev. B **10**, 4672.
Rinaldi, S., J. Cullen and G. Blessing, 1977, Phys. Letters **61A**, 465.
Rosen, M., H. Klimker, U. Atzmony and M. Dariel, 1973, Phys. Rev. B **8**, 2366.
Rosen, M., H. Klimker, U. Atzmony and M. Dariel, 1974, Phys. Rev. B **9**, 254. 1975,
Savage, H., A. Clark and J. Powers, IEEE Trans. Mag. **MAG-11**, 1355.
Stevens, K., 1952, Phys. Soc. **65**, 209.
Taylor, K., 1971, Advances in Physics **20**, 551.
Timme, R., 1976, J. Acoust. Soc. Am. **59**, 459, also NRL Report 8064.
Tsuya, N., A. Clark and R. Bozorth, 1964, Proc. Int. Conf. on Magnetism, Nottingham (Inst. of Phys. and Physical Society, London) p. 250.
Wallace, W. and E. Skrabek, 1964, Rare Earth Research II (Gordon and Breach, New York) p. 431.
Wallace, W., 1973, Rare Earth Intermetallics (Academic Press, New York).
Wertheim, G.K., V. Jaccarino and J.H. Wernick, 1968, Phys. Rev. A **135**, 151.
Williams, C. and N. Koon, 1975, Phys. Rev. B **11**, 4360.
Williams, C. and N. Koon, 1977, Physica **86–88B**, 147.
Freeman, A.J. and R.E. Watson, 1962, Phys. Rev. 127, 2058.
Smit, J. and H.P. Wijn, 1959, Ferrites (Wiley, New York).

Handbook on the Physics and Chemistry of Rare Earths, edited by K.A. Gschneidner, Jr. and L. Eyring

Chapter 16

AMORPHOUS MAGNETIC RARE EARTH ALLOYS

JAMES J. RHYNE
Institute for Materials Research, National Bureau of Standards, Washington, DC 20234, USA*

Contents

Symbols

$\boldsymbol{k}$ = wave vector of X-ray or neutron beam
λ = wavelength of neutron or X-ray
$\boldsymbol{Q}$ = wave vector transfer in X-ray or neutron scattering
$\boldsymbol{q}$ = wave vector transfer for an excitation: $\boldsymbol{Q} = 2\pi\boldsymbol{\tau} + \boldsymbol{q}$ where $\boldsymbol{\tau}$ is a reciprocal lattice vector [Note: $Q = q$ for amorphous materials where measurements are taken about the (0, 0, 0) reflection ($\tau = 0$).]
ΔE = neutron energy transfer
$I(Q)$ or $I(\theta)$ = intensity of scattered neutrons as a function of wave-vector transfer (Q) or scattering half-angle (θ) respectively
σ = neutron cross-section and magnetic moment per gram
$\mathrm{d}^2\sigma/\mathrm{d}\Omega\mathrm{d}E$ = neutron differential cross-section per unit solid angle and unit energy transfer
$G(r, t)$ = space- and time-dependent pair correlation function
e^{-2W} = Debye–Waller temperature factor
$G_e(r)$ = equilibrium spatial pair correlation function for atoms
$G_0(r)$ = instantaneous spatial pair correlation function
b = neutron nuclear scattering amplitude (units of 10^{-12} cm)
RDF(r) = radial distribution function
ρ_0 = bulk density of material
$Y_l^m(\theta, \phi)$ = spherical harmonics of spherical coordinates (r, θ, ϕ)
$\langle r_{4f} \rangle$ = average radii of 4f magnetic electrons
A_{lm} = crystal field potential
H, H_a = applied magnetic field

*Contribution of the National Bureau of Standards, not subject to copyright.

H_i = internal magnetic field corrected for demagnetization
M = bulk magnetization
M_s = saturation bulk magnetization
H_{HF} = magnetic hyperfine field
σ_0 = bulk spontaneous moment per gram
T_c = transition temperatures from paramagnetic to ordered magnetic state (Curie temperature for a ferromagnet)
T_{comp} = spin compensation temperature
K_u = axial anisotropy constant for film
$(g-1)^2 J(J+1)$ = deGennes factor with g = Landé g factor, and J = total angular momentum
$\mathcal{J}_{ij}$ = exchange constant for spins i, j
μ_B = Bohr magneton
μ = atomic moment (in units of Bohr magnetons)
ρ_H = Hall resistivity
R_0 = normal Hall coefficient
R_H = anomalous Hall coefficient

1. Introduction

Materials in the solid phase are generally perceived to be crystalline with atoms arranged periodically on a lattice at positions defined by a symmetry group. This is because in thermodynamic equilibrium the state of lowest free energy is usually an ordered state. However, solid materials can be prepared which are disordered and do not exhibit atomic translational invariance, and as such are called amorphous. Such solids are generally meta-stable with respect to crystallization into one or more ordered phases. Spontaneous recrystallization is inhibited by nucleation barriers which limit the formation of crystalline cells and/or by kinetic effects which inhibit the rate of recrystallization. Both processes tend to be very temperature sensitive, which generally limits the range over which an amorphous solid can be maintained.

Historically, most examples of amorphous solids (glasses) have been that of super-cooled liquids (e.g. SiO_2) and nearly all of these are insulating or semiconducting (e.g. Si, Ge). Recently, however, a new class of amorphous solid, the *metallic* amorphous glass has been produced [initially by Brenner (1950)] and has received rather intensive study and interest in the last five years. The materials generally consist of a transition metal host (e.g. Ni, Fe, or Co) combined with a group IV or V (e.g. Si, P, C) metalloid element in the role of a "glass-former". This latter component must usually be in the range of 15 to 30 atomic percent for the amorphous phase to form. Examples of such systems which have been studied are Co_4P, Fe–Pd–P, Fe–P–C, etc. An excellent comprehensive review of these systems and their physical properties is contained in a review by Cargill (1975), which also contains many other general references on amorphous systems and properties. These "metal-metalloid" amorphous alloys are produced typically by either rapid quenching from the liquid state ("splat cooling"), electro-deposition from solution, electro-less deposition, or evaporation onto cooled substrates. In general a basic requirement for producing amorphous metallic materials from the melt is very rapid cooling of the alloy at rates of 10^6 degrees per second or higher, otherwise micro-crystalline or macro-crystalline material will be found. The presence of the

"glass-former" atoms is also of critical importance as in most cases attempts to form elemental amorphous metals, for example by evaporation onto a cold substrate, result in meta-stable materials which crystallize when heated to room temperature.

The experimental verification of the amorphous state for a given material is not an easy task, nor are the criteria well defined. In general a material is said to be amorphous if the physical result of a measurement (e.g. X-ray or neutron diffraction pattern) can not be constructed from any ensemble of possible micro-crystalline states of the material. This will be discussed in more detail in section 2.2 of this chapter.

In late 1972 a new class of amorphous materials was produced: the rare earth-transition metal amorphous alloys (e.g. $Tb_{0.33}Fe_{0.66}$ or simply $TbFe_2$) which contained no metalloid or "glass-former" atoms. Results on their structural and magnetic properties were reported almost simultaneously by groups at IBM (Chaudhari et al., 1973; Gambino, 1974) and the Naval Ordnance Laboratory (NOL) (Rhyne et al., 1972, 1974) using materials prepared by sputtering. The IBM alloys were produced as thin films ($\simeq 1\,\mu$m thick) using conventional RF sputtering techniques while the NOL materials were in the form of bulk plates 1 to 3 mm in thickness produced by rapid dc sputtering at Battelle Northwest Laboratories (Stewart, 1973). Later similar materials were also produced as thin films by co-evaporation (e.g. Lee et al., 1975). The rare earth alloys can be produced in amorphous form over a wide range of composition, for example samples from the Tb_xFe_{1-x} system have been studied and found to be amorphous from 2% to 75% Tb (Pickart et al., 1974a; Alperin et al., 1976).

The rare earth amorphous alloys were found to possess a number of unique features, most related to their magnetic state, including magnetic bubble domain propagation (Chaudhari, 1973), a giant coercive field behavior at low temperatures (Clark, 1973, Rhyne et al., 1974b), evidence of angstrom-sized magnetic micro-domains (Pickart et al., 1974b) and a unique dependence of bulk magnetic ordering temperatures (Curie points) on magnitude of the rare earth effective spin (Heiman et al., 1976, 1976b, Rhyne, 1976). The remainder of the chapter is devoted to these and other aspects of the rare earth transition metal amorphous materials.

2. Structure of amorphous alloys

In a study of amorphous materials, it is important to develop an understanding of the atomic correlations present in the substance and of the range of these correlations. Such information is vital to characterizing the degree to which the atomic arrangement can be described as truly amorphous (lacking all order of a range greater than a relatively short (~ 10 Å) but quite arbitrary distance) as opposed to micro-crystalline or poly-crystalline materials which exhibit complete cells or complexes of crystalline order and much longer range atomic correlations. Further tests of the amorphous state include evidence for or against

local atomic environments characteristic of specific crystalline compounds of the same composition and the degree to which the average "coordination number" of the atoms in the amorphous alloy departs from that of analogous crystalline material. Finally information derived from structure studies can be compared against calculated (e.g. computer-generated) models of the random atomic stacking sequences of hard spheres (so called dense-random packed atomic models) such as developed by Polk (1973), Bennett (1972), and others and described in detail in Cargill (1975).

The important structural information for amorphous materials is usually derived (as in crystalline counterparts) from X-ray diffraction, neutron diffraction, or electron diffraction or a combination of these methods.

2.1. *Diffraction techniques for structure analysis*

Neutron (Rhyne et al., 1974a, Pickart et al., 1974a) and X-ray (Cargill, 1974) scattering techniques have been used to examine the structure of several RFe_2 amorphous alloys, and X-ray methods have been applied to a number of compositions in the Gd_xCo_{1-x} system (Wagner, 1976). A brief description of the neutron method follows. Complete details of the application of X-ray diffraction to amorphous solids can be found in the books by Warren (1969) and Guinier (1963) and for neutron scattering in Ledbetter (1971), Marshall and Lovesey (1971) and elsewhere.

In neutron scattering, incident neutrons of wave vector $\boldsymbol{k}_0$ are scattered from the sample into a final wave vector state $\boldsymbol{k}_f$ and may have gained or lost energy $\pm \Delta E$ by creating or annihilating a basic excitation of the solid (e.g. phonon or magnon). The wave vector dependence of the scattering can be described by a quantity $\boldsymbol{Q} = \boldsymbol{k}_f - \boldsymbol{k}_0$ which for purely elastic processes ($\Delta E = 0$) is $Q = 4\pi \sin \Theta/\lambda$, where Θ is half the scattering angle and λ is the wavelength. The measured intensity $I(Q)$ is proportional to a double differential cross-section $d^2\sigma/d\Omega dE$ which describes the number of neutrons scattered into solid angle $d\Omega$ and final energy interval dE. The cross section in turn is proportional to the Fourier transform of a space and time-dependent pair correlation function $G(r, t)$. For structural determinations it is convenient to evaluate the cross-section in two limits: (1) the total (or energy integrated) limit in which all elastic and inelastic processes satisfying conservation of initial state momentum and energy are added together and (2) the elastic ($\Delta E = 0$) limit. The elastic limit, which is unique to the neutron technique and not available in X-ray scattering results in a normalized cross-section per unit solid angle for N atoms is of the form

$$\left(\frac{d\sigma}{d\Omega}\right)_{elas} = N\bar{b}^2\left(1 + \int_0^\infty G_e(r) \sin Qr \, dr\right)e^{-2W}, \tag{16.1}$$

where $G_e(r)$ is the reduced equilibrium pair correlation function (corresponding to $t = \infty$), e^{-2W} is the Debye–Waller temperature factor and $\bar{b}$ is the bare atomic scattering length. In the second limit, that of total scattering, the energy integration is usually performed in the static approximation which effectively

ignores the contribution to the integral of the experimental dependence of Q on energy. Experimentally this approximation becomes increasingly more valid with higher incident beam energies and in particular is quite rigorous for X-ray scattering. In the static approximation then the total cross-section is

$$\left(\frac{d\sigma}{d\Omega}\right)_{\text{total}} = N\bar{b}^2\left(1 + \int_0^\infty G_0(r) \sin Qr \, dr\right) \tag{16.2}$$

where now $G_0(r)$ is the instantaneous ($t = 0$) reduced pair correlation function. In an amorphous solid, $G_0(r)$ and $G_e(r)$ are not expected to be appreciably different, and thus the principal difference in cross-section is in the inclusion of the Debye–Waller temperature factor when only the elastic scattering component is selected out of the total scattering.

The function $G(r)$ is related to the radial distribution function (RDF), which specifies the number of atoms in a shell dr at a distance r from an arbitrary reference atom, by the relation

$$\text{RDF}(r) = 4\pi r^2 \rho_0 + rG(r) \tag{16.3}$$

where ρ_0 is the average or macroscopic atom density.

The above treatment assumes a single atomic component system whereas the rare earth transition metal amorphous materials (R–T) are two component and thus three pair correlation functions, $G(r)$, exist, one each for the possible R–R, R–T, and T–T combinations. These are lumped together to produce the observed scattered intensity function, but may be separated by experiments on isotopically substituted alloys which have different neutron scattering amplitudes, or as in the case of Co–P by separating the magnetic components using polarized neutrons (Bletry and Sadoc, 1975).

2.2. *Scattering functions for $R\text{Fe}_2$ alloys*

One of the unique features of the rare earth amorphous alloys is the existence of many crystalline counterpart compounds (e.g. the Laves phase $R\text{Fe}_2$ compounds) which allow direct comparison of structural and magnetic properties in both amorphous and crystalline phases.

The observed scattered intensity distributions (proportional to the scattering cross-section) for the amorphous alloy of composition TbFe_2 obtained from neutrons by Rhyne et al. (1974a) and that for GdFe_2 from X-rays by Cargill (1974) are shown in fig. 16.1. The TbFe_2 results were taken above the magnetic ordering temperature using elastic scattering to remove the inelastic paramagnetic contribution. Both curves show broad distributions much like that of a liquid with no evidence of coherent Bragg peaks. The positions of the lowest Bragg reflections from crystalline Laves phase TbFe_2 are indicated in the figure and the absence of appreciable scattering at (111) and (331) positions (particularly at low temperatures, where these peaks would become quite intense due to the magnetic scattering contribution) is a strong confirmation of the basic amorphous, as opposed to micro-crystalline, nature of the alloys. A second

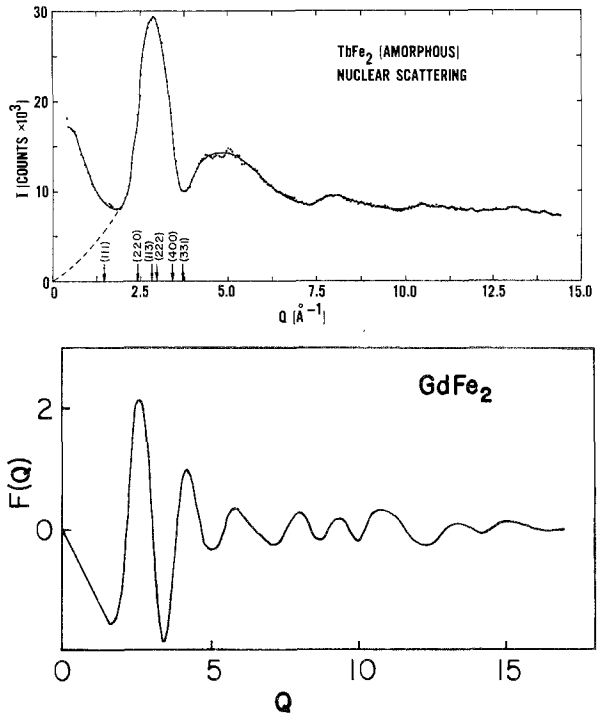

Fig. 16.1. Atomic scattering pattern (interference function) for amorphous $TbFe_2$ (top) at 300 K as obtained from neutron scattering and for amorphous $GdFe_2$ (bottom) obtained from X-ray scattering. The arrows indicate the positions of the first six Bragg lines in the crystalline Laves phase compound. The structure near $Q = 5$ Å^{-1} in the $TbFe_2$ is residual Al Bragg line contamination from the sample holder. The dotted line in the $TbFe_2$ pattern and the straight segment in the $GdFe_2$ pattern near $Q = 0$ are extrapolations used for the transform procedure. (Gd – Cargill, 1974; Tb – Rhyne et al., 1974a.)

indication is the overall breadth of the diffuse peak, which is ascribed to particle size broadening, and would indicate a coherent region of order 10 Å. However, this criterion alone is misleading since it does not eliminate a possible microcrystalline distribution for which *a series* of severely broadened Bragg peaks can, when added together, form an unresolved broad maximum.

2.3. *Atomic structure of* $R\mathrm{Fe}_2$ *alloys*

The real-space atomic pair correlation function $G(r)$ (also called the reduced radial distribution function) is obtained by Fourier inversion of the data of fig. 16.1:

$$G_0(r) = \frac{2}{\pi}\int_0^{Q_{max}} Q[I(Q) - C]\sin Qr \, dQ, \tag{16.4}$$

where (for neutrons), C is the large-Q asymptote of the scattering (equal to

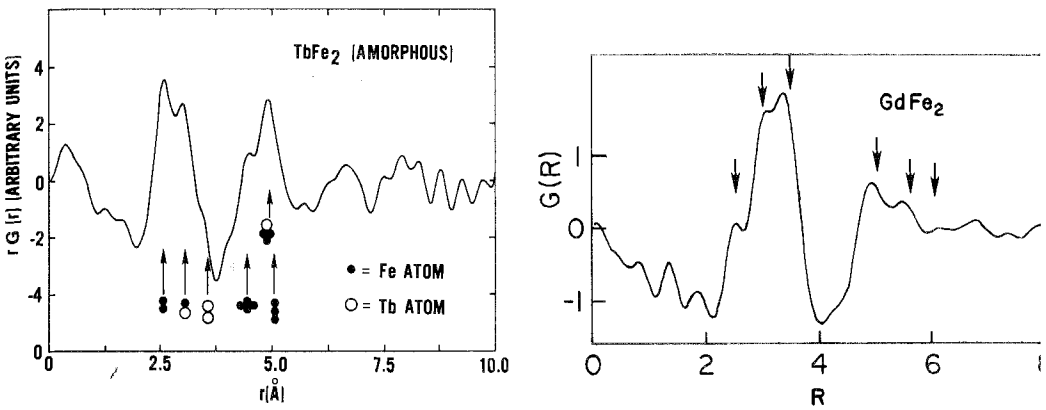

Fig. 16.2. Reduced radial distribution functions for $TbFe_2$ (left) and $GdFe_2$ (right) derived from the transform of the neutron and X-ray scattering data of fig. 16.1. The atomic spacings corresponding to several combinations of hard sphere atoms in contact with radii equal to the Goldschmidt radii are indicated by the arrows. (Gd – Cargill, 1974; Tb – Rhyne et al., 1974a).

$\bar{b}^2$/atom if there is no incoherent scattering) and $I(Q)$ is the normalized scattered intensity. The exact transform requires $Q_{max} = \infty$, and the effect of the finite experimentally attainable Q_{max} is to broaden the resulting $G(r)$ distribution and to cause oscillations at small r.

Figure 16.2 shows the derived (multiple) pair correlation function for $TbFe_2$ and $GdFe_2$ which in effect gives the relative probability of finding an atom at position r relative to one at the origin. The principal differences in the curves arise from the vastly different atomic scattering amplitudes for neutrons and for X-rays, the latter weighting the rare earth contribution much more strongly. Examination of the figures shows that the first major peak representing the shortest range atomic correlation is partially resolved into three sub-peaks, corresponding to nearest neighbor pairs of R–R, R–Fe and Fe–Fe atoms. Furthermore, as shown by the arrows, these sub-peaks fall at distances strikingly close to the sum of the Goldschmidt or 12-fold coordination diameters for the respective atoms in contact. Such a hard sphere contact model is in fact quite appropriate for many amorphous metallic glasses as discussed later (also see Cargill, 1975). In comparison with the RFe_2 crystalline Laves phase (C 15) compounds, one notes that the observed 3.6 Å spacing for the R–R atoms in the amorphous phase is significantly relaxed from the 3.2 Å distance observed for the crystalline compounds. Higher r peaks in fig. 16.2 correspond to more complex stacking arrangements of the atoms. It is significant to note that the overall probability of finding longer range correlations dies off rapidly at higher r while the number of possible atomic arrangements which can give rise to these correlations is increasing as a power of r. This is further confirmation of the basic amorphous character of the alloys. By placing the observed intensities on an absolute electron basis, Cargill (1975) has determined approximate coor-

TABLE 16.1
Atomic separation distances and coordination numbers for amorphous and crystalline $GdFe_2$ (Cargill, 1974)

	Nearest neighbor distances			Coord. Numbers	
At. Pair	Amorph.	Cryst.	From Goldschmidt diameters	Amorph.	Cryst.
Fe–Fe	2.54 ± 0.05 Å	2.60 Å	2.54 Å	6.3 ± 0.5	6
Fe–Gd	3.04	3.05	3.07	3.3 ± 0.3	6
Gd–Fe				6.7 ± 0.6	12
Gd–Gd	3.47	3.18	3.60	6 ± 1	4

dination numbers of the Gd and Fe atoms by fitting three Gaussian functions within the first triply split peak of the $GdFe_2$ RDF. These coordination numbers and the respective crystalline values are given in table 16.1.

Computer generated statistical atomic stacking models for the rare earth alloys based on the dense random packed hard sphere (DRPHS) models of Bennett (1972) and Polk (1973) have been produced by Cochrane et al. (1974) and Cargill and Kirkpatrick (1976). The latter study contained an important refinement of the Bennett stacking criteria and produced calculated $G(r)$ functions in much closer agreement with the experimental results. An example is shown in fig. 16.3 for the experimental and calculated X-ray total atomic correlation function $G(r)$ for amorphous $Gd_{32}Co_{68}$ alloy. The agreement in detail is quite significant. The Cargill–Kirkpatrick model also permits calculation of the three separate atomic

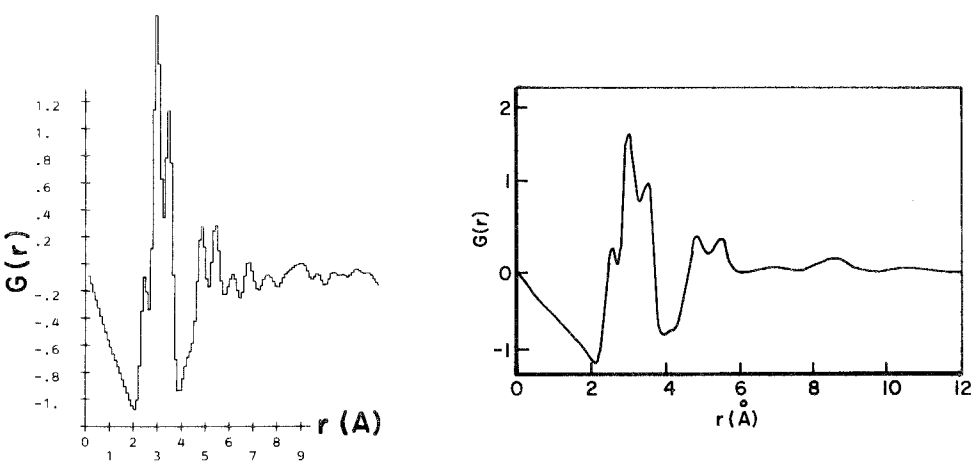

Fig. 16.3. (left) Reduced radial distribution function calculated from binary dense random packing hard sphere model (DRPHS) for $Gd_{32}Co_{68}$ compared (right) to the X-ray experimental $G(r)$. (Cargill and Kirkpatrick, 1976; Wagner et al., 1976).

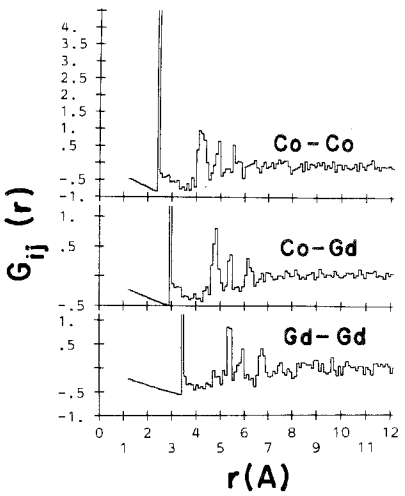

Fig. 16.4. Separate atomic pair correlation functions from the DRPHS model calculated for $Gd_{32}Co_{68}$. (Cargill and Kirkpatrick, 1976).

pair distribution functions mentioned above, many of the individual details of which can be masked by interference in the total correlation functions of figs. 16.2, 16.3. Figure 16.4 shows the results for the Gd–Gd, Gd–Co and Co–Co individual correlation functions in $Gd_{32}Co_{68}$. This DRPHS model has also been used to calculate $G(r)$ and the intensity function for a number of other compositions in the Gd–Co system and the results compare very favorably with the X-ray results of Wagner et al. (1976).

2.4. *Magnetic RDF for* $R\text{Fe}_2$ *alloys*

In addition to their utility as an atomic structure probe through their interaction with the nucleus, neutrons acting as a magnetization wave also sense magnetic spin distributions. As such one can derive a magnetic intensity function similar to that of fig. 16.2 by subtraction of neutron scattering data taken above and below the Curie temperature. This procedure results in a scattered distribution coming purely from the ordered magnetic spins which can then be transformed to coordinate space by a procedure analogous to that used to obtain the results of fig. 16.3. The result for the magnetic $S(r)$ is shown in fig. 16.5 (Rhyne et al., 1974a) which shows similar features to the atomic function except for the absence of the split first peak. In contrast to the atomic case in which all three partial pair correlation functions have approximately equal weights, the magnetic scattering is dominated by the Tb–Tb spin pair correlation due to its much larger moment (compared to Fe–Fe) and by the Tb–Fe spin pairs due to their large number. This explains the maximum in fig. 16.5 occurring at the exact r position of the Tb–Tb pairs in fig. 16.3; however, as pointed

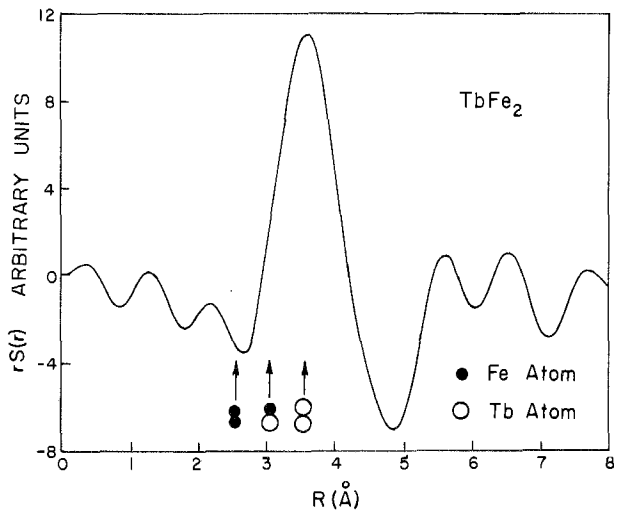

Fig. 16.5. Magnetic reduced radial distribution function for amorphous $TbFe_2$ from the transform of the difference of high (above T_c) and low (4 K) temperature scattering patterns. (Rhyne et al., 1974a).

out by Cargill (1975) the large *negative* contribution expected from the antiparallel alignment of the Tb–Fe spins is not observed in $S(r)$. This may arise from a breakdown of the collinear spin structure in the presence of strong local crystal field anisotropy (see ch. 16, section 3). The increased breadth of the peak in fig. 16.5 is a consequence of the truncation of the magnetic scattering function at a relatively small Q due to the magnetic form factor.

3. Macroscopic magnetization

The response of a magnetic material to an applied field generally provides direct evidence of the intrinsic correlations among the magnetic electron spins, in particular whether they are disordered (paramagnetic), or exhibit long range magnetic order such as a ferromagnetic (parallel) antiferromagnetic (anti-parallel) or ferrimagnetic (antiparallel alignment of two dissimilar species) spin arrangement. The temperature dependence of the magnetic response also provides clues to the nature of the ordering and often to the strength of the interaction (proportional to the paramagnetic-ordered moment transition temperature) if long-range ordering occurs.

In materials which do not have long-range magnetic order but which are not fully paramagnetic, information about the degree of short range (local) spin correlation may be obtained also from the field and temperature dependence of the bulk measured magnetic moment and from the initial susceptibility dM/dH_i, where M is the magnetization and H_i the internal field.

Crystalline heavy lanthanide elements and many compounds have been particularly instructive and appropriate for magnetization studies due to their well defined 4f local moment where the net moment is generally that of the ground state spin–orbit or Russell–Saunders coupled magnetic ion. A thorough discussion of these magnetic properties is found in other chapters of this book, ch. 6 sections 1–4 and ch. 14 sections 1–5.

In comparison to many of the crystalline rare earth elements and compounds, the magnetic properties of the amorphous rare earth-based alloys are exceedingly complex and, as will be discussed, are far from fully understood. Consider, for example $TbFe_2$ or $GdCo_2$ in which magnetic exchange coupling can be viewed as consisting of three basic mechanisms in analogy with the crystalline Laves phase compounds: a ferromagnetic exchange between the transition metal ions, $\mathcal{J}_{T\text{-}T}$; a competing antiferromagnetic exchange between the lanthanide and the transition metal $\mathcal{J}_{T\text{-}R}$, and a much weaker ferromagnetic coupling between lanthanides $\mathcal{J}_{R\text{-}R}$. In the molecular field sense these exchange fields can be considered to have a distribution in magnitude arising from the variable atomic separations found in amorphous materials, and from the randomized numbers of like and unlike magnetic ions surrounding any given site. These effects strongly influence the magnetic ordering temperatures as illustrated by the calculations of Kobe and Handrick (1972) and others. Montgomery et al. (1973) have shown that the general form of the Curie temperature change is given by

$$T_c^a = T_c^c[1 - 2/Zj^2/\mathcal{J}_0^2], \tag{16.5}$$

where j^2 is the fluctuation in the exchange, T_c^a and T_c^c are respectively the amorphous and crystalline Curie temperatures, Z is the average number of near neighbors, and $\mathcal{J}_0$ is the effective crystalline exchange constant.

In the non S-state ion lanthanide alloys (e.g. other than $GdFe_2$) there is present an additional strong perturbation from a local anisotropy interaction. Being structurally amorphous these materials would not be expected to exhibit any net magnetic anisotropy or preferred magnetic direction, and they do not, at least in bulk forms. However, at an individual lanthanide site a strong anisotropy is present arising from the Coulomb interaction of the 4f charge cloud of the lanthanide with the *local* crystalline electric field of the neighboring ions. This field is of spatially varying strength and symmetry, but due to its existence and the strong spin–orbit coupling on the lanthanide, a net local magnetic anisotropy energy of large magnitude is generated. The effect of this anisotropy energy on the magnetic properties is significant as will be discussed later. Calculations of the non-uniform anisotropy have been made by Harris et al. (1973) and also by Chi and Alben (1976), the latter including the effect also of the exchange field distribution. For the amorphous case the anisotropy is written

$$H_{\text{anis}} = \sum_l \sum_{m=-l}^{l} A_{lm} \langle r_{4f}^l Y_l^m(\theta, \phi) \rangle \qquad \text{for} \quad l \leq 6 \text{ and even}, \tag{16.6}$$

where the crystal field potentials A_{lm} are not constants in space as in the crystalline case, but must be calculated by appropriate averaging over the

random atomic site model. Harris et al. (1973) have shown that the A_{lm} are surprisingly uniform in magnitude (exhibiting a 2% RMS distribution) in spite of the completely uncorrelated spatial distribution of minimum energy directions. An important distinction in the amorphous case is the inclusion of second order ($l = 2$) crystal field coefficients which are forbidden in cubic symmetry. In the amorphous state the local symmetry is effectively lowered, allowing the $l = 2$ terms to become the dominant anisotropy energy terms. The total magnetic free energy E_F is then the sum of the applied field energy, the random anisotropy energy and the average exchange energy, the latter containing three contributions as discussed above:

$$E_F = E_{app} + E_{anis} + E_{exch}. \tag{16.7}$$

The direction of a given spin or group of local spins is determined by the minimum of this free energy expression at a given site including the spatially-varying exchange and anisotropy energies. Overall, the result is a material in which macroscopically all directions are "hard" magnetic directions and energy is required to align the lanthanide spins along any single magnetization direction.

This spin structure may be visualized as a type of conical anti-parallel arrangement as depicted in fig. 16.6. Assuming a predominant Fe–Fe exchange interaction (only partly justified from the high Curie temperature as discussed later) and only a nominal Fe anisotropy field, the Fe spins in a given region will align parallel. The lanthanide spins which are antiferromagnetically coupled to the Fe will order in a cone whose half angle Ψ is determined by the relative directions and magnitudes of the lanthanide local anisotropy and exchange fields. If these latter fields are then approximately equal to laboratory applied fields, the angle Ψ will be field-dependent giving rise to a susceptibility as is in fact observed in $TbFe_2$ and other compositions as discussed in section 3.2. This

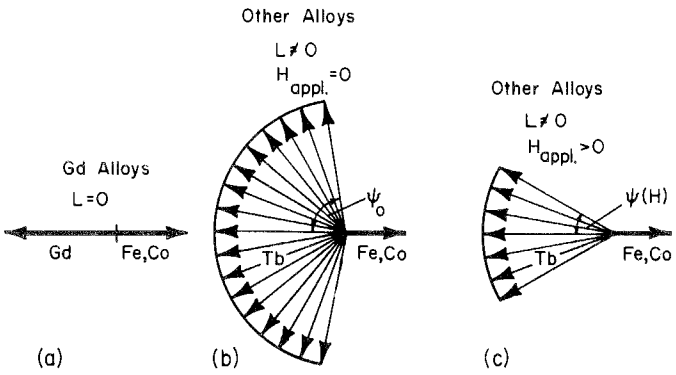

Fig. 16.6. Two dimensional projection of probable spin alignments of amorphous lanthanide alloys: (A) ferrimagnetic for Gd materials (e.g. $GdFe_2$) and (B), (C) canted ferrimagnetic for materials with lanthanide ions possessing a strong local anisotropy (e.g. $TbFe_2$) at 0 applied field (B) and finite field (C).

spin-canting model is also consistent with the Mössbauer data of Coey et al. (1976) on $DyCo_{3.4}$ which indicated a uniform distribution of Dy moments in a cone of half angle 70°.

3.1. *Magnetization of* Gd–Fe

The amorphous alloys of Gd offer the least complex magnetic behavior of the rare earth transition-metal materials due to the absence of the local magnetic anisotropy interaction in this S-state (orbital quantum number $L = 0$) ion.

Figure 16.7 illustrates the dependence of magnetic moment per gram ($1\ \text{emu/g} = 10^{-3}\ \text{JT}^{-1}\text{g}^{-1}$; $1\ \text{Oe} = 79.58\ \text{A/m}$) on applied magnetic field for $GdFe_2$ (Rhyne et al., 1974b). The curves are characteristic of a ferro- or ferrimagnet with a well-defined saturation behavior and quite small high field susceptibility. The spontaneous magnetic moment derived from the intercept of the high-field moment extrapolated to the demagnetizing field is shown in fig. 16.8 and compared to the analogous $GdFe_2$ crystalline Laves phase compound data of Burzo (1971). The Curie temperatures of the amorphous and crystalline materials are quite different, the former being suppressed significantly by the effect of exchange field disorder. It is noted that the 0 K saturation value of the magnetization in the crystalline material is characteristic of an antiparallel alignment of the 7 μ_B Gd spins and 1.55 μ_B iron spins. Due to band structure effects the iron spin is significantly lower than the normal 2.2 μ_B of Fe metal.

However, in spite of the similarity of the zero temperature bulk magnetization in the amorphous and crystalline systems, there is evidence the Fe moments are

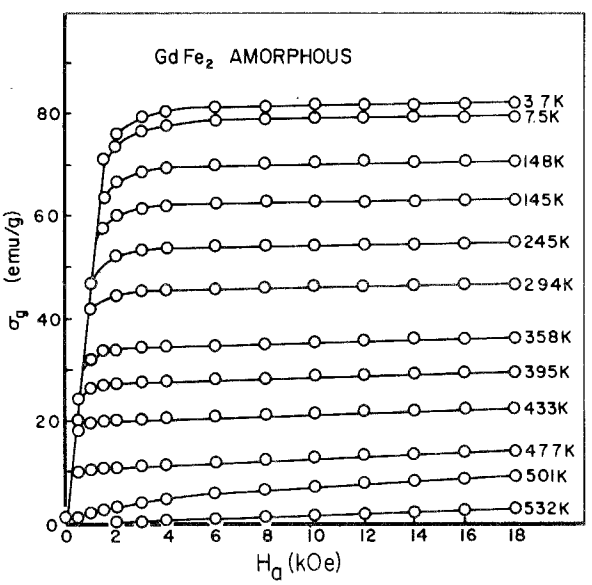

Fig. 16.7. Magnetization isotherms of $GdFe_2$ from above $T_c = 500$ K to 3.7 K. (Rhyne et al., 1974b).

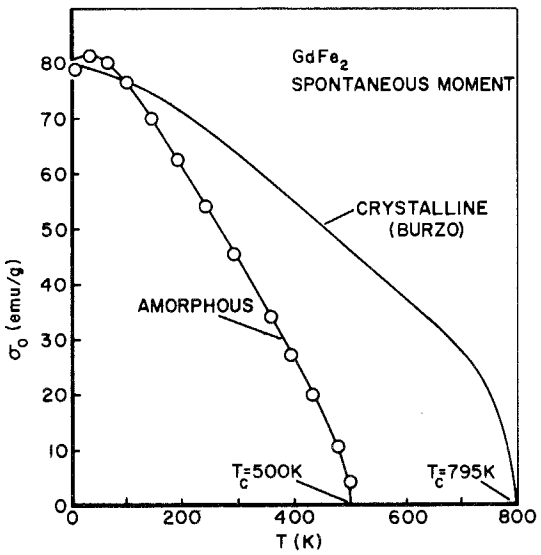

Fig. 16.8. Spontaneous moments for amorphous and crystalline $GdFe_2$ as a function of temperature (Burzo, 1971; and Rhyne et al., 1974b).

not exactly the same. Sublattice moment determinations in ferrimagnets are very sensitive to exact composition due to partial cancellation of the sublattice moments in the bulk moment measurement. In the case of the $GdFe_2$ specimen, electron microprobe results show the composition to be $Gd_{36}Fe_{64}$ with an uncertainty of about $\pm 2\%$. If one assumes these values and the free ion moment of Gd ($7\,\mu_B$), then the zero Kelvin Fe moment is found to be $1.9\,\mu_B$, somewhat larger than the crystalline value. This would indicate a significant shift in the d band states between amorphous and crystalline materials. Such a shift in the context of a charge transfer model is consistent with the X-ray photoemission studies on Gd–Fe alloys by Guntherodt and Shevchik (1976) which have shown that the charge transfer from Gd to Fe d bands is smaller in the amorphous phase than that which would be inferred from other measurements in the crystalline compounds. The measured shift of the Gd 4d core level also indicates an increasing charge transfer with reduced Fe concentration although never more than 1 eV.

The values of the Fe magnetic moment which can be inferred from the Mössbauer studies (an absolute determination of $\langle S_Z \rangle$ is not possible by this technique) on amorphous $GdFe_2$ are somewhat contradictory (see section 5).

Magnetization data on several Gd_xFe_{1-x} alloys by Taylor (1976) in the range $0.19 < x < 0.25$ indicate Fe moment values at 0 K of $2.2 \pm 0.07\,\mu_B$, a value somewhat larger than that observed for crystalline $GdFe_3$ again suggesting somewhat less charge transfer in the amorphous alloys.

The magnetization of $GdFe_2$ is dominated at all temperatures by the Gd "sublattice" moment, thus the material does not exhibit a spin compensation

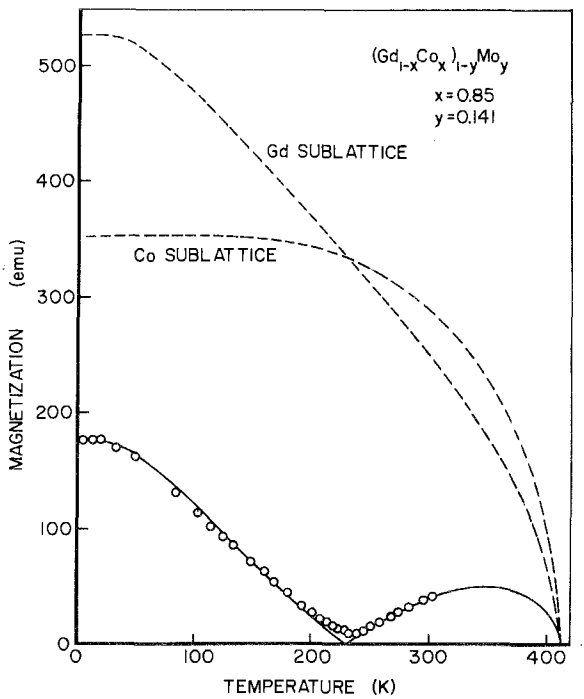

Fig. 16.9. Calculated total and sublattice moments for a Gd–Co–Mo alloy compared to experimental values. Note compensation temperature near 230 K. (Hasegawa et al., 1975).

temperature at which the atomic moments cancel and the overall moment is zero. In contrast, RCo_3 through RCo_4 alloys do exhibit a compensation temperature which can be varied widely by additions of Mo which, as shown by Hasegawa et al. (1975), effects a filling of the Co d-band states and a resulting lowering of the Co moment from 1.2 μ_B for 10% Mo in $(Gd_{1-x}Co_x)_{1-y}Mo_y$ ($x = 0.8$) to 0.75 μ_B for 16% Mo. This reduction in Co moment leads to the behavior shown in fig. 16.9 for a 14.1% Mo alloy which shows a compensation temperature at 230 K. The dotted lines for the atomic moments are the result of a two-sublattice molecular field model from which they also derived the exchange constants as a function of composition.

3.2. *Magnetization of RFe_2 alloys with $L \neq 0$*

The inclusion of spin-orbit coupling on the lanthanide site and its accompanying magnetic anisotropy severely perturbs the magnetization behavior as described above. Data on $TbFe_2$ will be used as an example, although similar results are found in the magnetization of other R–Fe and R–Co alloys mentioned in section 3.3.

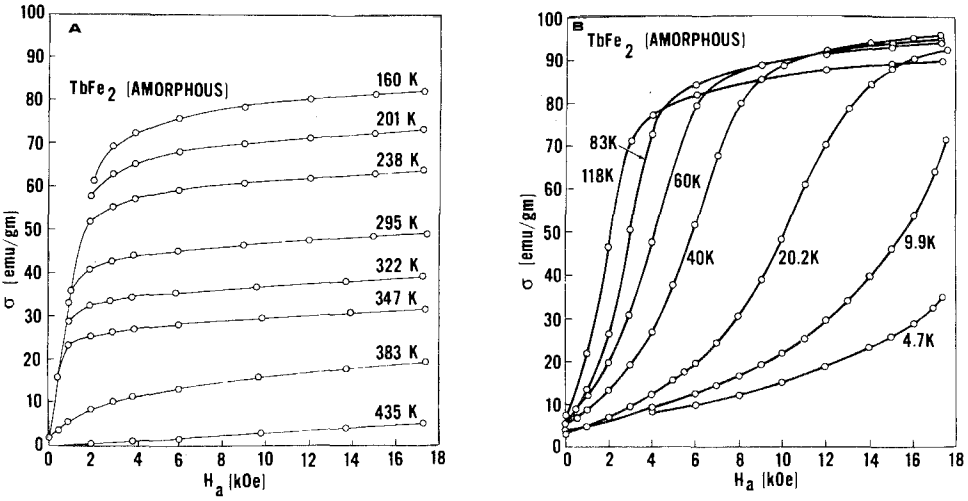

Fig. 16.10. (A) Magnetization isotherms for amorphous $TbFe_2$ above 120 K. H_a is the applied field. (B) Isotherms below 120 K showing the development of the anomalous "coercive" field dependence. (Rhyne et al., 1974b).

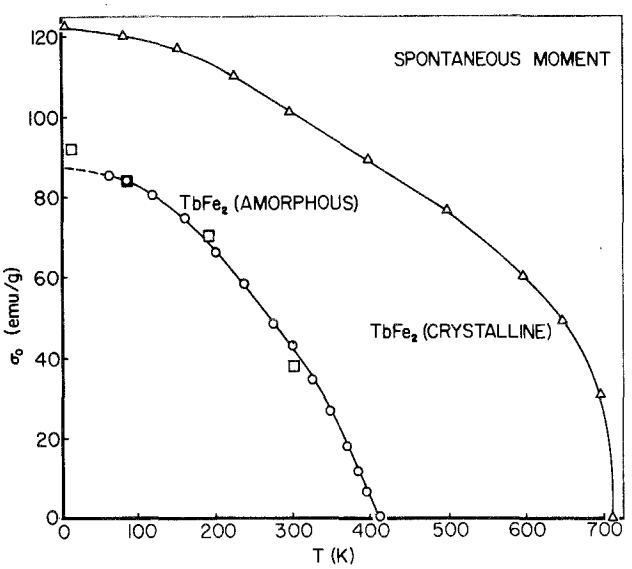

Fig. 16.11. Spontaneous magnetic moment for amorphous and crystalline $TbFe_2$ as a function of temperature. The square symbols are data from neutron small-angle scattering (see section 4). (Rhyne et al., 1974b).

Magnetization data as a function of applied field are shown in fig. 16.10A from 435 K (above the bulk Curie temperature) down to 160 K. Below about 150 K an anomalous "coercive field" behavior develops as discussed in section 3.3.

The isotherms of fig. 16.10A indicate a conventional ferrimagnetic response for $TbFe_2$ above 160 K except for the rather large high field susceptibility above technical saturation. This suggests the somewhat loosely coupled spin system discussed in the last section; one in which the spin alignment is far from collinear in zero field and does not in fact achieve complete antiparallel alignment of lanthanide and iron spins in the highest fields used. Using the 1.5 K magnetization data of fig. 16.12 and assuming the Fe moment value of 1.9 μ_B from amorphous $GdFe_2$ and the 9 μ_B free ion value for Tb, the half angle Ψ of the "fan" moment structure of fig. 16.5 is found to be 47 degrees for the $H = 0$ state and 36 degrees in an applied field of 60 kOe. A second effect of this spin-canting model on the bulk magnetization is to lower the apparent "spontaneous" moment significantly below that of crystalline $TbFe_2$ as shown in fig. 16.11. The crystalline data shown are neutron diffraction determined values. It is noted that both the moment reduction and the high field susceptibility are absent in $GdFe_2$ which, due to the S-state character of Gd^{3+}, is expected to be a simple aligned ferrimagnet.

3.3. *Low temperature "coercive" fields*

At low temperatures (for $TbFe_2$ below 150 K or 0.4 T_c) the magnetization isotherms of many amorphous R-based alloys (Clark, 1973; Rhyne et al., 1974b, 1976; Alperin et al., 1976) depart anomalously from the conventional ferrimagnet behavior, and as shown in fig. 16.10B and fig. 16.12 develop large coercive fields and hysteresis loops as the temperature is lowered. As discussed by Rhyne et al. (1974b) the occurrence of such phenomena at temperatures at and below 0.1 T_c suggests a thermal activation process for the flipping of discrete spin groups, much as is present in a superparamagnet. For such a model to be plausible for

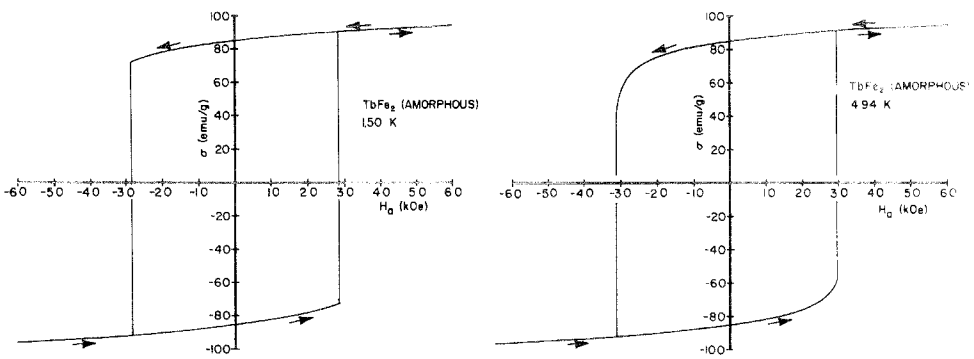

Fig. 16.12. Hysteresis loops at low temperature showing the giant "coercive" fields in $TbFe_2$. The "squaring-off" of the 150 K curve is ascribed to magnetothermal heating. (Rhyne et al., 1974b).

materials containing only magnetic atoms such as $TbFe_2$, it certainly must consist of tightly coupled spin regions separated by regions when the spin coupling and alignment is altered or less strong, rather than discrete ordered spin clusters distributed in a non-magnetic matrix as in a conventional superparamagnet. Such a "micro-domain" model is given strong support by the low-angle neutron scattering measurements discussed in section 3.4 and by the theoretical model of Chi and Alben (1976) discussed below. Ignoring the intercluster coupling as a first approximation, and using conventional superparamagnetic theory with a cluster size of 520 $Å^3$ (5.2×10^{-28} m^3) and a rare earth ion anisotropy $K = 1.5 \times 10^7$ ergs/cm^3 (1.5×10^{-6} J/m^3), the dashed curve in fig. 16.13 was calculated and is compared to the experimental coercive fields.

Alperin et al. (1976) have also noted the occurrence of large coercivities in Tb_xFe_{1-x} alloys and find H_c in excess of 10 kOe even for the dilute alloy $Tb_{0.02}Fe_{0.98}$.

Recently, Chi and Alben (1976) have calculated the expected 0 K coercivity and remanence for an amorphous ferromagnet and have obtained remarkable agreement with the giant hysterisis loop data on $TbFe_2$ and similar alloys. Their model hamiltonian includes the random local site anisotropy as calculated by Harris et al. (1973), the applied field and nearest neighbor exchange (atoms closer than 1.25 atomic diameters). The exchange energy was randomized by the variation in number of neighboring atoms occurring in a monatomic dense-

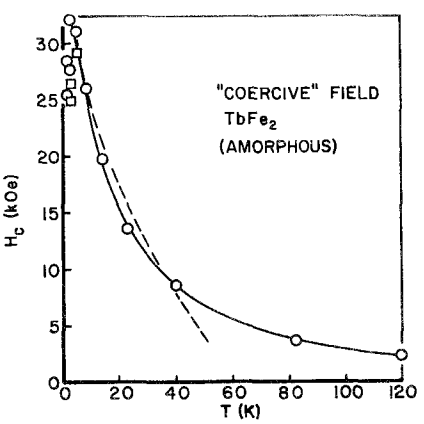

Fig. 16.13. Temperature dependence of the "coercive" field obtained from the hysteresis loop measurements. The dashed line is the result of an approximate calculated temperature dependence. H_c values at the lowest temperatures are affected by magnetothermal heating. (Rhyne et al., 1974b).

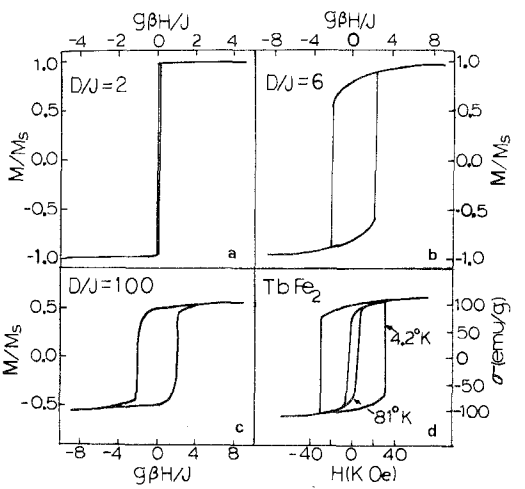

Fig. 16.14. (a, b and c) Calculated hysteresis loops for three values of the ratio of anisotropy to exchange (see text). M/M_s is the predicted fraction of complete magnetic saturation. The applied field on the abscissa is given in units of the average exchange field. The observed hysteresis loops for amorphous $TbFe_2$ are shown in (d) at 81 K and 4.2 K for comparison. Complete saturation spin alignment at 4.2 K would produce a moment of 140 emu/g. (Chi and Alben, 1976; and Clark, 1973.)

random-packed structure. Their results show a strong dependence of the coercivity on the ratio of the uniaxial anisotropy constant, D, to the average exchange parameter J. Only a small coercivity is observed up to a value $D/J = 5$ followed by an abrupt rise to a large coercivity of approximately 20% of H_{exch}. For larger values of D/J, the coercivity is relatively insensitive to this ratio. The remanence on the other hand is a smooth function of D/J, dropping from $M_{rem}/M_{sat} = 1$ for $D/J = 5$ to about 0.5 for large D/J. The overall calculated hysteresis loops for $D/J = 2$, 6, and 100 are shown in fig. 16.14 along with the experimental results for $TbFe_2$ at two temperatures. Note that the model also predicts an incomplete saturation of the magnetization for large D/J as is observed (see fig. 16.12) in $TbFe_2$.

3.4. *Anisotropy in thin film amorphous R–T alloys*

As previously mentioned, bulk (mm thick) specimens of the amorphous R–Fe alloys do not exhibit detectable macroscopic magnetic or crystallographic anisotropy. However, this is not true of thin film ($\simeq 1\ \mu$m) specimens prepared by co-evaporation and particularly by rf bias sputtering. It is in fact the occurrence of perpendicular macroscopic magnetic anisotropy that makes the Gd materials attractive for bubble memory applications (Chaudhari et al., 1973; Minkiewiez et al., 1976). Cronemeyer (1974) using a combination of ferromagnetic resonance and magnetization, studied the anisotropy in thin rf sputtered films of Gd_xCo_{1-x} on glass substrates. He found a perpendicular uniaxial anisotropy constant K_u which had a maximum value of 4×10^5 ergs/cm^3, a value considerably below the values for similar crystalline compounds. Furthermore, there appeared to be a minimum in K_u when zero voltage bias was applied to the sputtering substrate which results in a film of the same composition as the target as shown in fig. 16.15(a). Heimen et al. (1975) and Taylor (1976) also found that evaporated thin film Ho–Co, Ho–Fe, Tb–Co, Tb–Fe, Ho–Ni and Gd–Fe possessed uniaxial anisotropy $K_u > 2\pi M_s^2$. In contrast to the bias sputtered material, evaporated

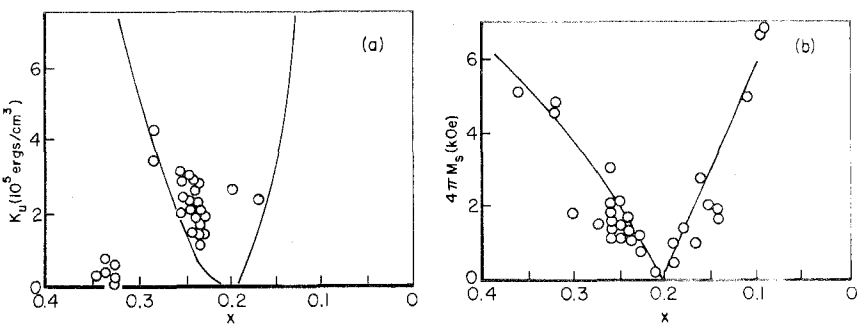

Fig. 16.15. (a) Bulk uniaxial anisotropy constant K_u at 300 K versus composition for bias sputtered Gd_xCo_{1-x} films (order of 1 μm thickness). The target was $GdCo_2$. Note the minimum in K_u for the zero bias ($x = 0.33$) composition. The solid line is the boundary where $K_u = 2\pi M_s^2$ using the room temperature M_s given in (b). The solid line is a theoretical dependence. (Cronemeyer, 1974).

GdCo showed an in plane easy direction. The correlation of K_u with bias in the sputtering led Wagner et al. (1976) to examine the X-ray scattering, both parallel and perpendicular to the film surface. The X-ray interference functions $I(Q)$ in the two orientations were identical within experimental error, eliminating any large scale preferred atomic orientation in the biased film as the origin of the anisotropy. However, comparisons between biased and unbiased films did show some shifting of the first and second peaks in $I(Q)$, and the peaks in the transformed $G(r)$ function for r greater than 6 Å did have larger amplitude in the bias sputtered film than in the unbiased. This apparent increase in intermediate range atomic order would then correlate with the larger perpendicular anisotropy. Gambino et al. (1974), Cronemeyer (1974), and Chaudhari and Cronemeyer (1975) have made studies to examine the origin of the macroscopic anisotropy and have concluded that a selective pair ordering process linking Gd–Co pairs and a probable tendency for Co atoms to coordinate with other Co in layers is responsible. Chaudhari and Cronemeyer (1975) also found that the measured anisotropy of Gd–Co–Mo films fits a pseudo-dipolar expression for the "sublattice" magnetization. Addition of Mo was found to substantially alter the weight of the three sublattice dipole coupling parameters.

4. Nature of the phase transition

All of the heavy lanthanide-transition metal amorphous alloys which are magnetic show antiferromagnetic coupling between the lanthanide and transition metal spins. The Curie temperatures as previously noted, are perturbed significantly from the crystalline values and may be either depressed (R–Fe alloys) or increased (R–Co alloys) due to fluctuations in exchange and anisotropy interactions or band structure effects. The latter has been ascribed by Tao et al. (1974) to explain the anomalous increase in the T_c of R–Co alloys. They suggested a reduced electron transfer from the rare earth conduction bands to the Co d-band in the amorphous state compared to the crystalline. In the case of the RFe_2 alloys the situation is more complex due to the population of both minority and majority spin bands of the Fe.

The phase transition between the disordered state and the magnetically ordered state (Curie temperature for a ferromagnet) has been studied for many amorphous alloys by conventional bulk measurements (magnetization, Kerr rotation etc.), and in many cases investigators have observed that the transition is not as clearly defined as in crystalline systems, implying an unusually high degree of short-range magnetic correlations persisting above T_c. This leads, for example, to curvature of magnetization isotherms plotted as σ^2 vs. H/σ (Belov–Goryaga plot) where σ is the magnetic moment per gram and H is the internal field, or to an imprecise determination of the spontaneous moment derived from moment measurements versus applied field or from Kerr rotation studies.

Neutron critical scattering provides a direct means for probing the characteristics of the magnetic phase transition and has been carried out on several of

the RFe_2 alloys (Pickart et al., 1974b, 1975). In conventional ferromagnets, as the temperature is decreased toward T_c from above, fluctuating regions of magnetic order build up and increase in size and finally become static and infinite in range at the phase transition temperature. A second order phase transition gives rise to a neutron scattering cross-section for total scattering which is Lorentzian in q (for small q) above T_c (see Marshall and Lovesey, 1971) of the form:

$$\frac{d\sigma}{d\Omega} \propto \frac{S(S+1)}{r_1^2} \frac{1}{\kappa_1^2 + q^2}, \tag{16.8}$$

where S is the spin, κ_1 is the inverse magnetic correlation length and r_1 is an interaction range parameter. As T_c is approached κ_1^{-1} increases rapidly [$\kappa_1 \propto (T - T_c)^\nu$ where ν is a critical exponent whose value depends on the universality class of the transition] and finally diverges at T_c in the limit of long-range order. Thus, at small q the scattered neutron intensity should sharply increase on approach to T_c and then drop abruptly below T_c as long range order sets in.

In contrast to the conventional behavior described above, almost no evidence of a critical anomaly at the magnetization-determined T_c is observed in amorphous $TbFe_2$ (or $HoFe_2$) as shown in fig. 16.16a. Only a weak inflection in the scattering is observed at T_c which is not sharp, but of a rounded character as

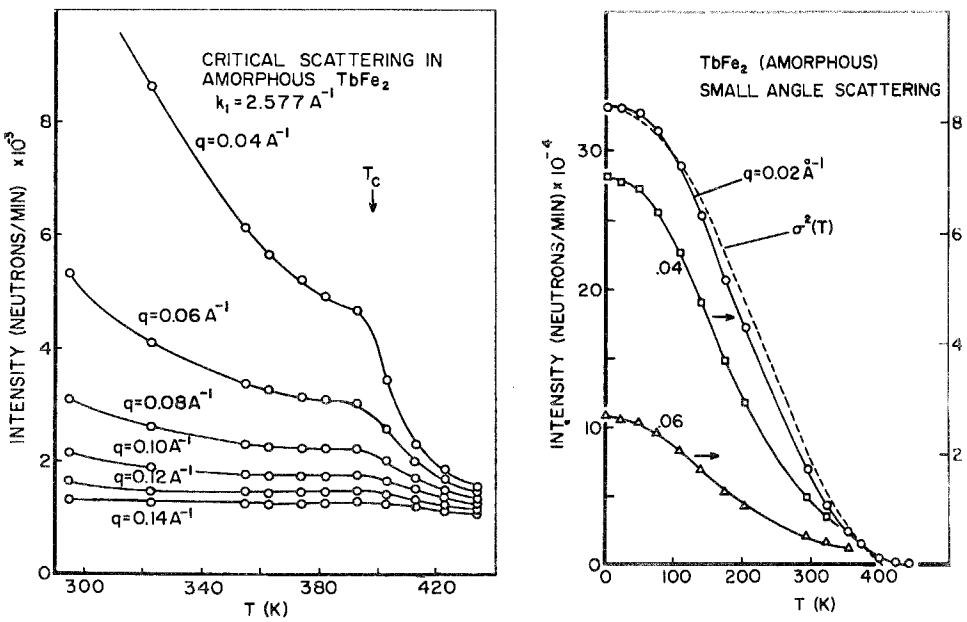

Fig. 16.16. (a) Small angle neutron scattering from amorphous $TbFe_2$ in the critical region near the magnetization-determined T_c. (b) The small angle scattering component over the full temperature range. The $q = 0.02$ Å^{-1} data are compared to the bulk magnetization as shown. (Pickart et al., 1974b).

more detailed temperature data show. The scattering above T_c does have the expected Lorentzian shape in q [eq. (16.8)] and derived values of correlation length κ_1^{-1} increase from 15 Å at 435 K to only 70 Å at *and somewhat below* T_c. This lack of divergence strongly suggests that the phase transition in the amorphous alloys is not of conventional second-order form but is smeared out in temperature, possibly resulting from a spatially varying T_c in the material and/or a lack of true long range magnetic order which is replaced rather by "frozen-in" regions of local magnetic order. This cluster viewpoint is further strengthened by the occurrence of an anomalous and intense small angle component of magnetic scattering below T_c (fig. 16.16a,b). Since neutron experiments on amorphous materials are done close to the (000) (forward beam) position in reciprocal space (the only point at which the scattering is in-phase), the occurrence of such a low angle component represents a magnetic analog of chemical particle size broadening in conventional systems. The absence of appreciable low angle scattering above T_c, however, eliminates chemical clustering as a source of the observed effect. The scattering does reflect inhomogeneities in the magnetic order or "micro-domains" on a scale large compared to the inter-atomic spacing but two orders of magnitude smaller than conventional magnetic domains. The average magnetization of the clusters as measured by the neutrons has the same temperature dependence as the overall bulk magnetization measured with a magnetometer as shown in fig. 16.16b. The scattering below T_c has a $q^{2.4}$ dependence over a wide temperature range and corresponds to scattering from magnetic inhomogeneities or domains of order 100 Å in linear dimension. In principle the shape and size distributions can be obtained from a detailed analysis of the scattering as described by Guinier and Fourner (1955) for the case of chemical particles.

A similar absence of a critical anomaly and a finite κ_1^{-1} at T_c was found also in $HoFe_2$ ($\kappa_1^{-1} = 40$ Å at T_c), and in $Tb_{0.02}Fe_{0.98}$. The intense magnetic low angle scattering below T_c was also observed in both materials. This latter effect is, however, absent in $GdFe_2$ suggesting that the origin of the inhomogeneous "micro-domain" ordering may lie in the strong local magnetic anisotropy. In such a picture the Fe spins would be largely aligned by the exchange field (negligible Fe anisotropy) and a micro-domain would be prescribed as a region within which the lanthanide spins have essentially parallel directions as dictated by the competing effects of the exchange and local anisotropy interactions, and outside of which the lanthanide spins would be largely uncorrelated in direction.

4.1. *Curie temperatures of the alloys*

As mentioned in the last section the ordering temperatures of the amorphous alloys differ significantly from crystalline compounds of the same composition. Tables 16.2–16.4 list the Curie temperatures (T_c) and moment compensation temperatures (T_{comp}) of many of the amorphous rare earth alloys studied along with the equivalent crystalline compounds. In the tables an element name under the compensation temperature indicates that its sublattice moment is dominant

TABLE 16.2
Curie and compensation temperatures of R–Co amorphous and crystalline alloys

Composition	T_c^{amorph}	T_c^{crys}	T_{comp}^{amorph}	T_{comp}^{crys}	Reference
$Gd_{65}Co_{35}$	167	—	—	—	Biesterbos et al. (1976)
$Gd_{55}Co_{45}$	220	—	—	—	Biesterbos et al. (1976)
$Gd_{40}Co_{60}$	330	—	—	—	Biesterbos et al. (1976)
$GdCo_2$	550	409	510	Gd	Tao et al. (1974)
$GdCo_3$	750	612	400	Gd	Tao et al. (1974)
Gd_2Co_{17}	>500*	775	300	410	Tao et al. (1974)
$GdCo_5$	>500*	1008	80	—	Tao et al. (1974)
$TbCo_2$	>600*	256	500	Tb	Lee and Heiman (1975)
$TbCo_3$	>600*	506	250	Tb	Lee and Heiman (1975)
$TbCo_5$	>600*	980	Co	100	Lee and Heiman (1975)
$DyCo_3$	>900*	450	230	—	Arrese-Boggiano et al. (1977)
$Ho_{45}Co_{55}$	375	—	Ho	—	Lee and Heiman (1975)
$Ho_{40}Co_{60}$	600	—	325	—	Lee and Heiman (1975)
$HoCo_2$	>600*	85	270	Ho	Lee and Heiman (1975)
$HoCo_3$	>600*	418	150	350	Lee and Heiman (1975)
$HoCo_5$	>600*	1000	Co	80	Lee and Heiman (1975)
YCo	550	—	—	—	Lee and Heiman (1975)
YCo_2	>600*	294	—	—	Lee and Heiman (1975)
YCo_3	>600*	301	—	—	Lee and Heiman (1975)
YCo_5	>600*	977	—	—	Lee and Heiman (1975)
$(Gd_{1-x}Co_x)_{1-y}Mo_y$:					
$x = 0.80$, $y = 0.144$	335	—	—	—	Hasegawa et al. (1975)
$x = 0.86$, $y = 0.16$	383	—	238	—	Hasegawa et al. (1975)
$x = 0.85$, $y = 0.15$	390	—	266	—	Hasegawa et al. (1975)
$x = 0.83$, $y = 0.11$	—	—	238	—	Hasegawa et al. (1975)

*Indicates recrystallization temperature interferes with determining T_c.

at all temperatures below T_c. Crystalline data are from Taylor (1971) and references cited therein. Differences in Curie temperatures between investigators may be due to the "fuzzy" nature of the phase transition discussed previously.

From the data of tables 16.2–16.4 several conclusions can be drawn:

1. Curie temperatures of R–Co amorphous alloys are generally increased over their crystalline counterparts.
2. Curie temperatures of R–Fe_2 alloys are strongly suppressed below the crystalline values which are the highest of the R_xFe_{1-x} series.
3. Amorphous Mn compounds are not magnetically ordered.
4. Amorphous Ni alloys reported have anomalous dependence of T_c with concentration especially for high Ni concentration.

Biesterbos et al. (1976) have investigated the pressure dependence of T_c in a series of amorphous R–Fe and R–Co alloys, and find quite large values of dT_c/dP (-1 to -5 K/kbar) similar in magnitude to the analogous crystalline compounds. In general the R–Co alloys showed a less severe depression of T_c with pressure than the R–Fe series. They also measured the decrease in

TABLE 16.3
Curie and compensation temperatures of R–Fe amorphous and crystalline alloys

Composition	T_c^{amorph}	T_c^{crys}	T_{comp}^{amorph}	T_{comp}^{crys}	Reference
$Gd_{57}Fe_{43}$	350	—	Gd	—	Lee and Heiman (1975)
$Gd_{40}Fe_{60}$	>500*	—	Gd	—	Lee and Heiman (1975)
$GdFe_2$	490	785	450	Gd	Lee and Heiman (1975)
$GdFe_2$	500	785	Gd	Gd	Rhyne et al. (1974b)
$GdFe_3$	460	728	150	—	Lee and Heiman (1975)
$GdFe_{23}$	420	659	≃100	—	Lee and Heiman (1975)
$Tb_{75}Fe_{25}$	190	—	Tb	—	Alperin et al. (1976b)
$Tb_{45}Fe_{55}$	298	—	Tb	—	Alperin et al. (1976b)
$Tb_{40}Fe_{60}$	399	—	Tb	—	Heiman et al. (1976)
$TbFe_2$	390	711	Tb	Tb	Lee and Heiman (1975)
$TbFe_2$	383	711	Tb	Tb	Rhyne et al. (1974b)
$TbFe_3$	393	648	—	—	Heiman et al. (1976)
$TbFe_3$	405	648	Tb	Tb	Alperin et al. (1976a)
Tb_6Fe_{23}	387	574	Tb	Tb	Heiman et al. (1976)
$TbFe_5$	380	—	—	—	Alperin et al. (1976a)
Tb_2Fe_{17}	365	409	—	—	Alperin et al. (1976a)
$Tb_{0.02}Fe_{0.98}$	245	—	Fe	—	Alperin et al. (1976a)
$Dy_{40}Fe_{60}$	283	—	—	—	Heiman et al. (1976)
$DyFe_2$	315	638	Dy	Dy	Heiman et al. (1976)
$DyFe_2$	287	638	Dy	Dy	Rhyne (1976)
$DyFe_3$	333	600	Dy	Dy	Heiman et al. (1976)
$DyFe_3$	350	600	Dy	Dy	Arrese-Boggiano (1977)
Dy_6Fe_{23}	351	524	—	—	Heiman et al. (1976)
$Ho_{49}Fe_{51}$	255	—	—	—	Biesterbos et al. (1976)
$Ho_{42}Fe_{58}$	272	—	—	—	Biesterbos et al. (1976)
$HoFe_2$	195	612	Ho	Ho	Rhyne (1976)
$HoFe_2$	260	612	120	Ho	Lee and Heiman (1975)
$HoFe_3$	290	567	50	400	Lee and Heiman (1975)
$HoFe_3$	270	567	—	400	Biesterbos et al. (1976)
Ho_6Fe_{23}	300	501	Fe	40	Lee and Heiman (1975)
$ErFe_2$	105	575	Er	Er	Rhyne (1976)
$TmFe_2$	<50	565	Tm	Tm	Rhyne (1976)
$Y_{45}Fe_{55}$	280	—	Fe	—	Biesterbos et al. (1976)
YFe_2	see text	550	—	Fe	Heiman et al. (1976)
YFe_2	non-mag	550	—	Fe	Rhyne et al. (1974b)
YFe_4	250	—	Fe	—	Biesterbos et al. (1976)
$Y_{13}Fe_{87}$	218	—	Fe	—	Biesterbos et al. (1976)
$LaFe_2$	275	—	—	—	Heiman et al. (1976)
$NdFe_2$	360	—	—	—	Heiman et al. (1976)
$LuFe_2$	119	—	—	—	Heiman et al. (1976)
$LuFe_3$	211	—	—	—	Heiman et al. (1976)
Lu_6Fe_{23}	229	—	—	—	Heiman et al. (1976)

*Indicates recrystallization temperature interferes with determining T_c.

magnetic moment in several Y_xFe_{1-x} alloys and found extremely large values (e.g. for $Y_{12}Fe_{84}$ $(1/M_0)dM/dp = 4\times 10^{-2}$/kbar) almost one order of magnitude larger than for the crystalline compounds. This suggests that the magnetic state of Y–Fe compounds near YFe_2 cannot be described as conventional long-range-ordered magnetism as discussed in section 6.

It is instructive to examine the variation of the Curie temperatures of the RFe_2 alloys with the deGennes factor of the rare earth (equivalent to the square of the R effective spin). This is shown in fig. 16.17 for both crystalline and amorphous RFe_2 materials. In the crystalline case the strong Fe–Fe exchange provides a base Curie temperature of 535 K which increases monotonically to 793 K for $GdFe_2$ as the rare earth spin is increased.

TABLE 16.4
Curie temperatures of other alloys

Composition	T_c^{amorph}	T_c^{crys}	Reference
$GdNi_2$	38	85	Lee and Heiman (1975)
$HoNi_2$	15	22	Lee and Heiman (1975)
$HoNi_5$	400	10	Lee and Heiman (1975)
Ho_2Ni_{17}	>400	162	Lee and Heiman (1975)
$DyNi_3$	47	69	Arrese-Boggiano (1977)
$GdMn_2$	non-mag	AFM (86)	Lee and Heiman (1975)
Gd_6Mn_{23}	non-mag	473	Lee and Heiman (1975)
$HoMn_2$	non-mag	—	Lee and Heiman (1975)
Ho_6Mn_{23}	non-mag	434	Lee and Heiman (1975)
$Gd_{24}Cu_{76}$	53	—	Heiman et al. (1976)
$Gd_{18}Cu_{82}$	40	—	Heiman et al. (1976)
$Gd_{14}Cu_{86}$	35	—	Heiman et al. (1976)

In contrast the amorphous data is quite anomalous. The Curie temperature of $GdFe_2$ is 500 K, however as the lanthanide spin is reduced, the Curie temperature drops abruptly and in the limit $(g-1)^2J(J+1) = 0$ (YFe_2) one finds either the absence of long range magnetism (Rhyne, 1974b) or an ordering temperature slightly above 100 K (Heiman, 1976b), depending on the interpretation of the magnetization data (see discussion of YFe_2). In either case the data strongly suggest that the ferromagnetic Fe–Fe exchange coupling present in the crystalline compounds is severely weakened in the disordered state and the rapid rise in

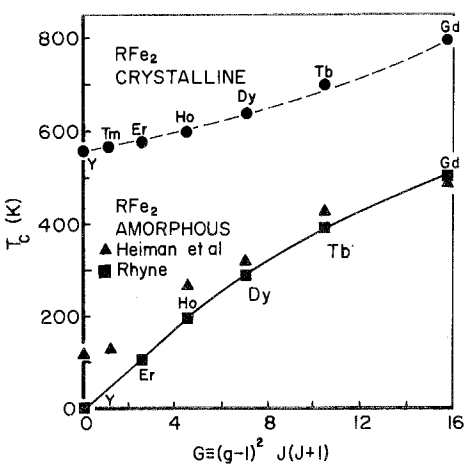

Fig. 16.17. Plot of observed Curie temperatures for heavy RFe_2 crystalline compounds and amorphous alloys versus the deGennes factor. The dashed line is the result of a molecular field fit. (Burzo, 1971; Heimen et al., 1974b; Rhyne, 1976).

T_c with increased rare earth spin suggests an enhancement effect on the $\mathcal{J}_{Fe\text{-}Fe}$ as one adds the lanthanides. The weakening of the overall exchange for small values of the deGennes factor also leads to ambiguities in determining T_c for these alloys. The implied predominance of the lanthanide spins in affecting T_c may be a consequence of the fact that the exchange interactions involving the lanthanide spins are of indirect nature (e.g. RKKY) and produce a polarization wave in the conduction bands. Such an exchange coupling may be less affected by the topological atomic disorder than the direct overlap Fe–Fe exchange of potentially much shorter range, perhaps only between nearest neighbors.

The anomalous decrease in T_c as the lanthanide spin is decreased, or replaced by non-magnetic Y, is in marked contrast to the change in T_c with R concentration for a specific R_xFe_{1-x} alloy system. Heiman et al. (1976a) have made a molecular field model fit to their Curie temperature and moment data on R_xFe_{1-x} alloys and also to the hyperfine field as measured by the Mössbauer effect. They took as adjustable parameters the three exchange constants $\mathcal{J}_{Fe\text{-}Fe}$, $\mathcal{J}_{Fe\text{-}R}$, $\mathcal{J}_{R\text{-}R}$ and the iron spin S_{Fe}, and allowed these to vary with composition. The variation in S_{Fe} was derived from Heiman et al.'s data for the hyperfine splitting on the Fe site in the heavy R_xFe_{1-x} alloys which showed that the effective hyperfine field decreases linearly with lanthanide concentration. If this is assumed proportional to the Fe spin, then as a function of lanthanide concentration x: $S_{Fe} = 1.1 - x[2.3\text{–}0.47(g-1)J]$. Likewise the exchange parameters were assumed to be a function of x, and the calculation produced the following values:

$$\mathcal{J}_{R\text{-}Fe} = 2.25 - 53.0x, \qquad \mathcal{J}_{Fe\text{-}Fe} = 20.5 + 120.0x \tag{16.9}$$

(all in units of 10^{-16} ergs). $\mathcal{J}_{R\text{-}R}$ was fixed at 1.6×10^{-16} ergs from the value appropriate for RNi_2. Using these expressions and the two sublattice molecular field models of Hasegawa et al. (1975) they were able to fit the composition dependence of the Curie temperature and magnetization of a variety of R_xFe_{1-x} alloys as shown in fig. 16.18. It is noted that the extrapolation to pure "amorphous Fe" indicates a T_c of 270 K. Data of Alperin et al. (1976) on $Tb_{0.02}Fe_{0.98}$ give a somewhat lower measured value of 245 K.

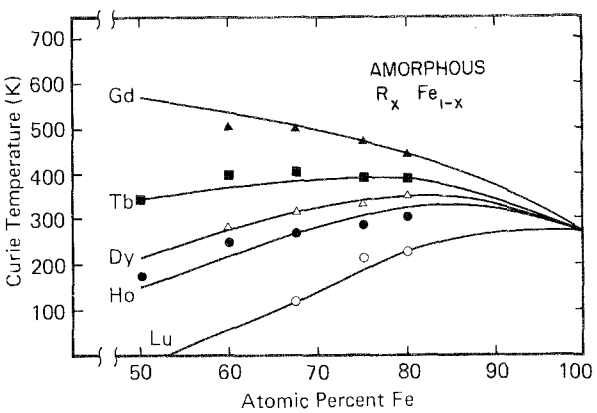

Fig. 16.18. Curie temperatures of a variety of R_xFe_{1-x} alloys versus iron concentration. The solid lines are the results of a molecular field calculation (see text). (Heiman et al., 1976).

5. Mössbauer and ferromagnetic resonance studies

The recoilless absorption of gamma rays (Mössbauer effect) provides a method for examining the local magnetic field at the nuclear sites (magnetic hyperfine field) in amorphous as well as crystalline materials. The technique is limited by the number of appropriate Mössbauer nuclei, however, both ^{57}Fe and ^{161}Dy are easily studied. Forester et al. (1975) have studied amorphous $DyFe_2$ and spectra for both the Dy site and Fe site are shown in figs. 16.19 and 16.20. Both sites show broadened but fully resolved hyperfine spectra. The Fe site exhibits a hyperfine field H_{HF} at 4.2 K of 225 kOe, almost identical to that in crystalline $DyFe_2$, although severely broadened by a Gaussian distribution of exchange fields of width approximately 90 kOe (40% of H_{HF}). Such extreme width distributions are characteristic of amorphous materials with random site symmetry. On the Dy site a field of 6.3 MOe is observed, approximately midway between that of Dy metal and $DyFe_2$, with a broadening of about 100 kOe. The solid line in fig. 16.20 represents a model calculation of the hyperfine field assuming a randomly distributed axial electric field gradient and a pseudo–dipolar magnetic field averaged over a powder distribution. The result is a broadened and skewed spectrum which agrees favorably with the observed 14 K ^{57}Fe pattern. Studies on amorphous $GdFe_2$ (Forester, 1976) again showed a severe broadening ($\simeq$90 kOe) of the iron field; however, unlike $DyFe_2$ the pattern was not skewed, leading to the conclusion that this feature is associated with the strong local random uniaxial anisotropy.

The integrated absorbed intensity from the data of fig. 16.20 shows an anomalous reduction of about 40% as the temperature is lowered below the Curie temperature. This phenomena is believed associated with a softening of the phonons via the large magneto-elastic interaction. As a result the acoustic impedance should be strongly temperature dependent.

It is noted that Mössbauer spectra taken by Heiman and Lee (1975) on evaporated (as opposed to sputtered) samples showed a significantly higher value of H_{HF} with less broadening, suggesting a higher degree of short range chemical order in these samples.

Arrese-Boggianq et al. (1977) have studied $DyFe_3$ and again find a Dy hyperfine field close to the crystalline values and broadened by only about 1%, while in contrast the Fe field is broadened by 20% and is higher than that in the crystalline counterpart compound; a result found also in $DyNi_3$, $DyCo_3$, and YFe_3 with small amounts of ^{57}Fe introduced as a Mössbauer probe. For example in amorphous $DyFe_3$, $H_{HF} = 280$ kOe and in crystalline $DyFe_3$, $H_{HF} = 240$ kOe leading to the conclusion that the net iron moment is increased from 1.6 μ_B to 1.9 μ_B in going from the crystalline to the amorphous state.

Ferrimagnetic resonance studies (FMR) have been made on evaporated amorphous thin films of Ho-, Gd-, Tb- and $DyFe_2$ by Lubitz et al. (1976) and on bulk sputtered Tb-, Gd-, and YFe_2 by Bhagat and Paul (1976). The former study indicated broadened linewidths which were consistent with a Landau–Lifshitz relaxation parameter of order 10^8/sec for the Gd and Ho alloys, comparable with that observed in crystalline transition metal systems. The Dy and Ho systems

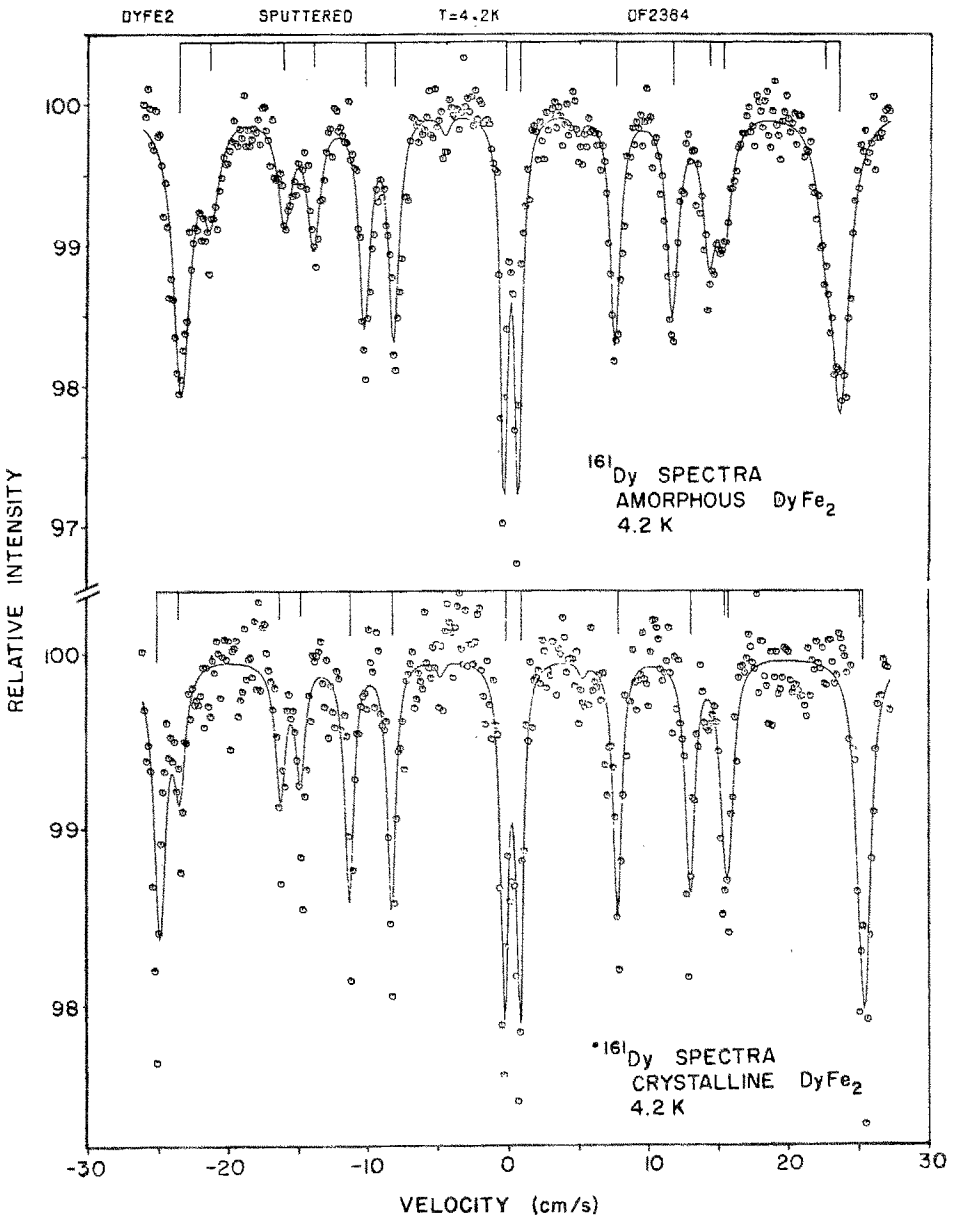

Fig. 16.19. ^{161}Dy Mössbauer spectra of polycrystalline and amorphous $DyFe_2$ at 4 K. (Forester et al., 1975).

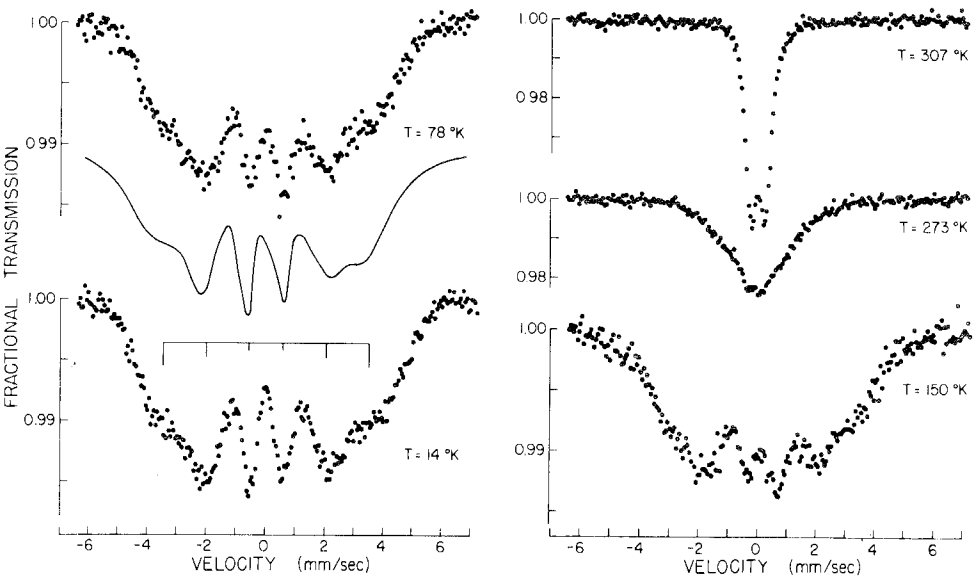

Fig. 16.20. ^{57}Fe Mössbauer spectra of amorphous $DyFe_2$ as a function of temperature ($T_c = 287$ K). The bar graph and solid line represent a theoretical calculation of line positions and spectrum intensity. (Forester, 1976).

showed significant differences between $4\pi M_s$ determined by FMR and that determined by a magnetometer indicating the possible presence of local microscopic regions of inhomogeneous composition in the evaporated materials.

FMR data for the magnetization on the bulk sputtered samples by Bhagat and Paul (1976) showed good agreement with magnetometer data in $TbFe_2$ and $GdFe_2$. However in YFe_2, $4\pi M_s$ at room temperature was found to be even larger than for $GdFe_2$, while the bulk data show YFe_2 to be paramagnetic. This and other anomalies of YFe_2 will be reviewed in section 6. Bhagat and Paul also found the room temperature spectra of all three systems to contain three weak additional lines below 10 kOe, which represent much weaker magnetizations in addition to the fundamental resonance. At lower temperatures in $TbFe_2$ the fundamental resonance broadened and then disappeared while the highest field satellite remained essentially unaffected down to 77 K. At temperatures above room temperature in $TbFe_2$ the highest field resonance is mysteriously maintained unaltered to 500 K even though the bulk Curie temperature is 388 K. The fundamental also has a T-dependence which requires the g-value to vary strongly with temperature. In $GdFe_2$ the principal line moves to lower field in a conventional manner as T decreases.

It is clear that a complete interpretation of the information contained in FMR experiments on the amorphous rare earth alloys is a formidable task. Richards (1976) has presented a model for the interpretation of Gd–Co resonance data based on the random anisotropy model. He shows that the measured effective

anisotropy constant K_u depends strongly on the ratio of local anisotropy to exchange fields and on the distribution of anisotropy field directions. However, the effect of the random directions of the local field cancels out of the expression for the resonance frequency which is then the same as for a uniform system with an anisotropy equal to the average bulk anisotropy.

6. The anomalies of YFe_2

As has been alluded to in several previous sections, amorphous YFe_2 is the most puzzling and contradictory of the amorphous rare earth-transition metal alloys. By comparison to the crystalline counterpart, amorphous YFe_2 would be expected to be a prototype amorphous ferromagnet, one with only one exchange interaction and with a relatively high ordering temperature. Magnetization data for this alloy, however, are quite anomalous. Data of Rhyne et al. (1974b) show no evidence of magnetic saturation at 4 K even in fields as high as 60 kOe. In fact the moment per iron atom developed at 60 kOe and $T = 1.5$ K is only 1.1 μ_B, even less than that expected from a system of free paramagnetic Fe spins. Recent data of Heiman and Lee (1976b) are also consistent with this observation. At temperatures below 50 K a small hysterisis and remanence develops with the coercive field attaining 2.2 kOe at 3.5 K, but again with no evidence of moment saturation. Plots of the square of the magnetic moment σ versus H/σ shown in fig. 16.21 indicate paramagnetic intercepts for all temperatures above

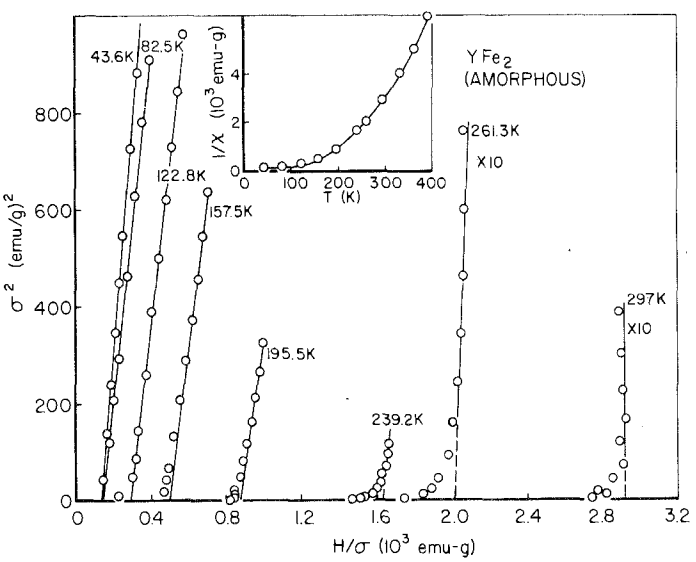

Fig. 16.21. Belov–Goryaga plot of the temperature dependence of the magnetization of YFe_2. The inset shows the high field susceptibility derived from the H/σ intercept.

40 K (below this temperature hysterisis effects make the analysis invalid) with some evidence of curvature toward the origin suggestive of a cluster-ordered system. The susceptibility obtained from the H/σ intercept is not Curie–Weiss-like nor does it vary as T^2 as appropriate for an itinerant system. Very low field susceptibility ($H < 5$ Oe) data (Forester et al., 1976) do show evidence for a "spin-glass" like cusp at 55 K. The magnetic coherence length determined from small-angle neutron scattering remains less than 10 Å to the lowest temperature measured with no evidence of a critical anomaly characterizing the onset of long-range magnetic order. The scattered intensity at the smallest q measured ($q = 0.04$ A^{-1}) shows a pronounced broad maximum at 50 K with a decrease at lower temperatures. Such behavior is consistent with that expected for a "spin-glass" for which the largest clusters exhibit the highest freezing temperature.

The above information strongly suggests a frozen spin cluster system at low temperatures in which there are strong spin correlations (possibly both ferromagnetic and antiferromagnetic) within small regions or clusters, but of insufficient strength to produce long range order in spite of the fact that two-thirds of the atoms are iron.

In this light it is of interest to examine the results of the microscopic probes, the Mössbauer effect and ferromagnetic resonance, which potentially look inside clusters of sufficient size. FMR, as already mentioned (Bhagat and Paul, 1976), gives a large value of $4\pi M_s = 5.4$ kOe even at room temperature. Mössbauer studies of Pala et al. (1976) show a hyperfine field developing at 55 K which increases with decreasing temperature, reaching a magnitude of 233 kOe at 4 K comparable to fields observed in other RFe$_2$ alloys. The T dependence is well represented by a mean-field model. The spectra do show evidence of significant line broadening as in other amorphous RFe$_2$ alloys. Very recent Mössbauer data (Forester et al., 1976) taken in a magnetic field show a strong $\Delta M = 0$ transition which is not removed by the application of fields as high as 70 kOe. This clearly indicates a frozen-in canted structure for the Fe spin or *local* antiferromagnetic order of the Fe spins in small regions. As such YFe$_2$ and its counterpart GdAl$_2$, which Mizoguchi et al. (1977) have shown to have similar low field susceptibility properties, may be prototype truly amorphous spin glasses.

The magnetism of YFe$_2$ definitely offers a challenge to both experimentalists and to theorists to illuminate its understanding.

7. Other properties of amorphous alloys

The RFe$_2$ materials in crystalline form possess very large magnetic-elastic interactions even at room temperature (Clark, 1974) (see also ch. 15, sections 1 and 2). Clark (1974) has shown that the 0 K lanthanide magnetoelastic coupling coefficients are of the same order of magnitude in the RFe$_2$ compounds as in the lanthanide elements despite the overall cubic symmetry of the compounds. In the amorphous state, as expected, bulk magnetostrictions are smaller than in the

crystalline form by nearly one order of magnitude. In $TbFe_2$ at room temperature (Clark and Abbundi, 1976), the anisotropic magnetostriction observed on rotating the magnetization through 90° in the plane of the sample reached $\Delta l/l = 450 \times 10^{-6}$ at a field of 25 kOe, and like the magnetization, exhibited a large high field dependence indicating incomplete magnetic saturation. The anisotropic magnetostriction of $GdFe_2$ on the other hand was 16.5×10^{-6} and almost field independent. $GdFe_2$ did exhibit a forced volume magnetostriction almost twice as large as $TbFe_2$. This term usually comes from the strain dependence of the exchange energy as opposed to the anisotropic magnetostriction which has its origin in the single-ion anisotropy strain dependence.

The existence and character of the spin wave spectrum in the amorphous lanthanide alloys is intriguing in light of the apparent anomalies in the long-range-magnetic-order. Spin wave measurements using inelastic neutron scattering at low Q where discrete excitations would be most likely observed are complicated by the large elastic low angle scattering coming from the "micro-domain" order. Due to finite energy resolution this effect overwhelms the inelastic scattering for small energy transfers and makes the spin waves unobservable. Using the Oak Ridge polarized beam correlation time of flight spectrometer, Rhyne et al. (1975) were able to observe an acoustic spin wave mode which was barely statistically resolvable up to about $Q = 0.5\ A^{-1}$ in $TbFe_2$. This mode had quadratic dispersion $\hbar\omega = DQ^2$ with $D = 15$ meV-A^2. Two additional branches of magnetic excitations were observed at higher Q and higher energy all of which resemble the modes seen in crystalline Laves phase RFe_2 compounds (see ch. 7, section 5.3).

The anomalous or magnetization-dependent Hall effect in metals arises from a "skew-scattering" of the conduction electrons by the magnetic spins via a spin–orbit coupling. This effect is described in terms of a Hall resistivity of the form

$$\rho_H = R_0 H + R_s 4\pi M \tag{16.10}$$

where R_0 is the normal Hall coefficient and R_s the anomalous coefficient. Ogawa et al. (1975), Okamato et al. (1974) and McGuire et al. (1977) have shown that the anomalous effect is very large in amorphous rare earth alloys and that the normal term is negligibly small by comparison. In Gd–Co amorphous films, Ogawa et al. (1975) found that the Gd contribution was negative and dominated the Hall resistivity, and that R_s reversed sign at the compensation temperature as the direction of the Gd spins reversed relative to the applied field.

McGuire et al. (1977) studied Gd–Fe–Ni and Gd–Co–Mo alloys and reported that the Hall resistivity contributions from Ni and Gd were both negative and that from Fe and Co were positive. They treat the individual ionic "sublattice" contributions to the total Hall resistivity contributions additively, taking into account the sign of the intrinsic effect from each element and the direction of its magnetization. As a fraction of the conventional resistivity, which is relatively

independent of temperature and composition due to its large disorder component, they have found that Fe (in YFe_2) produces a +6.0% anomalous Hall effect, Gd (in Gd–Au samples) a −4.1% effect, and Co (in YCo_2) a +2.7% Hall effect. These values are all quite large for a metallic compound and are comparable to those found for the normal Hall effect in semiconducting materials.

8. Conclusion

It is clear that the field of amorphous alloys and, in particular rare earth-transition metal-alloys, is one of intense and rapidly expanding interest in magnetism. It has been commented that it is a mistake to delve into amorphous magnetism while one is still far from understanding crystalline magnetic systems, yet the profusion of unique and anomalous phenomena accompanying magnetism in the amorphous state is sure to whet the appetite of many more curious experimentalists and theorists in the future.

It is also apparent that there are significant areas of deficiency in present research which point to the need for future work. Most apparent is that of a more complete knowledge and characterization of the materials, particularly on a microscopic scale, regarding the tendency to local clustering or microcrystallinity and compositional inhomogeniety, and the role of gaseous and solid impurities. Criteria and methods for determining the degree to which a material is really amorphous also need to be refined. These questions must be resolved also on a relative basis between similar samples produced by different techniques, particularly differences between sputtered materials with and without substrate bias and for co-evaporated specimens.

In the magnetism of these systems, the fundamental effect of topological disorder on the exchange, both Heisenberg-type and indirect, and on the anisotropy is far from understood. Additionally the effects of randomized local anisotropy of magnitude too large compared to the exchange to be treated by perturbation methods need to be further examined. Inherent in this investigation is the true nature of the magnetism, even to the question of the existence of conventional long range magnetic order and the character of the expected phase transitions.

The aim of this chapter has been to cover some of the fundamental properties of the rare earth amorphous alloys known at present. Inevitably much work has been omitted and apologies are due those investigators whose work has been neglected in this rapidly expanding field. By intent some areas were omitted, in particular little attention has been given to large domain properties and the promising application of specific materials to computer bubble memories and registers. In addition the potential of such alloys for acoustic or microwave delay lines and work on partially recrystallized compounds for high energy product permanent magnets was not discussed.

9. Recent developments

A review article has been written by Cochrane et al. (1978) emphasizing theoretical work on exchange and crystal field interactions in amorphous metals. Also a review by Coey (1978) has been published which provides detailed information on the various types of magnetic ordering found in amorphous systems.

The individual atom pair correlation functions have been obtained by O'Leary (1975) from an analysis of combined X-ray and magnetic and nuclear neutron scattering data on $GdFe_2$ and $TbFe_2$. Feldman et al. (1978) have also made a detailed analysis of the RDF for $SmFe_2$ and $TbFe_2$ and have indicated the presence of an atomic correlation at 4.0 Å corresponding to a tetrahedral network of iron atoms. This peak is not found in conventional DRP models.

In clarifying the role of the lanthanide exchange in the magnetic ordering, alloys of the S-state Gd ion with Ag (Boucher, 1977; Hauser, 1975), and Au (Poon and Durand, 1977) have been studied. For high Gd concentration these systems exhibit ferromagnetism and show spin-glass ordering for more dilute Gd concentrations. The remanent magnetization in a TbAg alloy was examined by Boucher (1977) who found that the exponential temperature dependence (see section 3.3) only occurs for long measurement times ($t \gg 10^{-5}$ sec).

Amorphous alloys of composition $R_{66}Co_{33}$ have been prepared by Gerber et al. (1978) and by Gruzalski et al. (1978) using a "splat-cooling" method. They have also prepared $R_xZr_{40}Cu_{60-x}$ ($0 < x < 10$) by the same procedure. These latter alloys show magnetic behaviour characteristic of the spin-glass state while the Co alloys show ferrimagnetic order, strongly perturbed by the local anisotropy.

The heat capacity of the spin glass systems $GdAl_2$ and DyCu has been studied by Coey et al. (1978) who found an anomalously large linear term at temperatures well below the spin freezing in the Cu system which is interpreted on the basis of single ion excitations of the Kramers ion in the random direction crystal field and weak exchange.

Further theoretical refinements to the local anisotropy model were made by Harris and Zobin (1977), Callen et al. (1977), Bhattacharjee et al. (1977), and Patterson et al. (1978) among others. Patterson et al. also calculated the heat capacity and found a peak as about $0.44D$ (D = second order anisotropy energy). The zero temperature results of Callen et al. (1977) showed that the coercive field B_c in the limit of large D was of order D in contrast to the results of Chi and Alben (1976), who found B_c of order the exchange.

Much of the recent work (e.g. Harris and Zobin, 1977; Chen and Lubensky, 1977; Patterson et al., 1978; Harris et al., 1978) on the magnetic phase transition in amorphous alloys has centered on the conditions under which a low-T spin-glass state is formed of the Edwards–Anderson (1975) type in place of a true ferromagnetic (or ferrimagnetic) state below T_c.

Aharony (1975) and Pelcovits et al. (1978) have investigated the nature of the phase transition for an anisotropic amorphous magnet with an *isotropic* distribution of easy axis directions using renormalization group techniques. The latter

authors have shown that no ferromagnetic state is possible for such a system having fewer than four spatial dimensions.

Acknowledgements

The author is indebted to many collaborators whose efforts and discussions have been most helpful in gaining insight into the rare earth transition metal systems. In particular S. Pickart, H. Alperin, A. Clark, J. Cullen, J. Schelleng, and N. Koon have been closely involved with many aspects of these studies. It is a pleasure to acknowledge many helpful discussions of amorphous structure and magnetism with S. Cargill who also made valuable comments on the chapter. The work of Mrs. C. O'Connor and of F. Shorten in preparing the manuscript and figures is greatly appreciated.

References

Alperin, H.A., J.R. Cullen and A.E. Clark, 1976, A.I.P. Conf. Proc. Series **29**, 186.
Arrese-Boggiano, R., J. Chappert, J.M.D. Coey, A. Liénard and J.P. Rebouillat, 1976, Proc. Conf. on Applications of the Mössbauer Effect, Corfu, J. Physique, **C6**, 771.
Belov, K.P. and A.N. Goryaga (1956) Fiz. Met. Metallov. **2**, 3.
Bennett, C.H., 1972, J. Appl. Phys. **43**, 2727.
Bhagat, S.M. and D.K. Paul, 1976, A.I.P. Conf. Proc. Series **29**, 176.
Biesterbos, J.W.M., M. Brouha and A.G. Dirks, 1976, A.I.P. Conf. Proc. Series **29**, 184.
Bletry, J. and J.F. Sadoc, 1975, J. Phys. F. **5**, L 110.
Brenner, A., D.E. Couch and E.K. Williams, 1950, J. Res. National Bureau of Standards **44**, 109.
Burzo, E., 1971, Zeit. für Angew. Phys. **32**, 127.
Buschow, K.H.J. and R.P. Von Stapele, 1970, J. Appl. Phys. **41**, 4066.
Cargill, G.S., 1974, A.I.P. Conf. Proc. Series **18**, 631.
Cargill, G.S., 1975, "Structure of Metallic Alloy Glasses," Solid State Physics, Vol. 30, edited by Seitz, Turnbull, and Ehrenreich, (Academic Press, New York), pp. 227–289.
Cargill, G.S. and S. Kirkpatrick, 1976, A.I.P. Conf. Proc. Series **31**, 339.
Chaudhari, P., J.J. Cuomo and R.J. Gambino, 1973, I.B.M. J. Res. and Dev. **17**, 66.
Chaudhari, P. and D.C. Cronemeyer, 1975, A.I.P. Conf. Proc. Series **24**, 573.
Chi, M.C., R. Alben, 1976, A.I.P. Conf. Proc. Series **34**, 316.
Clark, A.E., 1973, Appl. Phys. Letters **23**, 642.
Clark, A.E. and R. Abbundi, 1976, (private communication).
Cochrane, R.W., R. Harris and M. Plischke, 1974, J. Non-Crystalline Solids **15**, 239.
Coey, J.M.D., J. Chappert, J.P. Rebouillat and T.S. Wang, 1976, Phys. Rev. Letters **36**, 1061.
Cronemeyer, D.C., 1974, A.I.P. Conf. Proc. Series **18**, 85.
Dirks, A.G., J.W.M. Biesterbos and K.H.J. Buschow, 1977, Physica **B86–88**, 761.
Forester, D.W., R. Abbundi, R. Segnan and D. Sweger, 1975, A.I.P. Conf. Proc. Series **24**, 115.
Forester, D.W., 1976, A.I.P. Conf. Proc. Series **31**, 384.
Forester, D.W., W.P. Pala and R. Segnan, 1977, Amorphous Magnetism II (Plenum, New York) p. 135; Forester, D.W., W.P. Pala, R. Segnan, N.C. Koon and J.J. Rhyne, 1978, to be published.
Gambino, R.J., J. Ziegler and J.J. Cuomo, 1974, Appl. Phys. Letters **24**, 99.
Gambino, R.J., 1974, A.I.P. Conf. Proc. Series **18**, 578.
Guinier, A. and G. Fourner, 1955, Small Angle Scattering of X-Rays, Wiley, New York.
Guinier, A., 1963, X-Ray Diffraction (W.H. Freeman and Co., San Francisco).
Güntherodt, G. and N.J. Svevchik, 1976, A.I.P. Conf. Proc. Series **29**, 174.
Harris, R., M. Plischke and M.J. Zuckermann, 1973, Phys. Rev. Letters **31**, 160.
Hasegawa, R., B.E. Argyle and L.J. Tao, 1975, A.I.P. Conf. Proc. Series **24**, 110.
Heiman, N. and K. Lee, 1974, Phys. Rev. Letters **33**, 778.
Heiman, N., A. Onton, D.F. Kyser, K. Lee and C.R. Guarnieri, 1975, A.I.P. Conf. Proc. Series **24**, 573.
Heiman, N., K. Lee and R.I. Potter, 1976, J. Appl. Phys. **47**, 2634; and A.I.P. Conf. Proc. Series **29**, 130.

Heiman, N. and K. Lee, 1976., A.I.P. Conf. Proc. Series **34**, 319.
Kobe, S. and K. Handrich, 1972, Phys. Status Solidi **54**, 663.
Leadbetter, A.J., A.C. Wright and A.J. Apling, 1971, Phys. of Non-Crystalline Solids, (Wiley Press, New York) 423.
Lee, K. and Neil Heiman, 1975, A.I.P. Conf. Proc. Series **24**, 108.
Lubitz, P., J. Schelleng, C. Vittoria and K. Lee, 1976, A.I.P. Conf. Proc. Series **29**, 178.
Marshall, W. and S.W. Lovesey, 1971, Theory of Thermal Neutron Scattering, (Oxford Press, Oxford, England), Chapt. 11.
McGuire, T.R., R.J. Gambino and R.C. Taylor, 1977, J. Appl. Phys. **48**, 2965.
Minkiewicz, V.J., P.A. Albert, R.I. Potter and C.R. Guarnieri, 1976, A.I.P. Conf. Proc. Series **29**, 107.
Mizoguchi, T., T.R. McGuire, R.J. Gambino and S. Kirkpatrick, 1977, Physica **B86–88**, 783.
Montgomery, C.G., J.I. Krugler and R.M. Stubbs, 1970, Phy. Rev. Letters **25**, 669.
Ogawa, A., T. Katayama, M. Hirano and T. Tsushima, 1975, AIP Conf. Proc. Series **24**, 575.
Okamoto, K., T. Shirakawa, S. Matsushita and Y. Sakurai, 1974, IEEE Trans. **MAG-10**, 799.
Pala, W.P., D.W. Forester and R. Segnan, 1976, A.I.P. Conf. Proc. Series **34**, 322.
Pickart, S.J., J.J. Rhyne, H.A. Alperin and H. Savage, 1974a, Phys. Letters **47A**, 73.
Pickart, S.J., J.J. Rhyne and H.A. Alperin, 1974b, Phys. Rev. Letters **33**, 424.
Pickart, S.J., J.J. Rhyne and H.A. Alperin, 1975, A.I.P. Conf. Proc. Series **24**, 117.
Polk, D.E., 1973, J. Non-Crystalline Solids **2**, 381, based on the monatomic model of J.D. Bernal, Proc. Roy. Society (London) **A280**, 299 (1964).
Rebouillat, J.P., A. Lienard, J.M.D. Coey, R. Arrese-Boggiano and J. Chappert, 1977, Physica **B86–88**, 773.
Rhyne, J.J., S.J. Pickart and H.A. Alperin, 1972, Phys. Rev. Letters **29**, 1562.
Rhyne, J.J., S.J. Pickart and H.A. Alperin, 1974a, A.I.P. Conf. Proc. Series **18**, 563.
Rhyne, J.J., J.H. Schelleng and N.C. Koon, 1974b, Phys. Rev. B **10**, 4672.
Rhyne, J.J., D.L. Price and H.A. Mook, 1975, A.I.P. Conf. Proc. Series **24**, 121.
Rhyne, J.J., 1976, A.I.P. Conf. Proc. Series **29**, 182.
Richards, P.M., 1975, Phys. Letters **55A**, 121 and A.I.P. Conf. Proc. Series (1976), **29**, 180.
Stewart, R.W., 1973, Battelle Northwest Laboratories Research Report (unpublished).
Tao, L.J., R.J. Gambino, S. Kirkpatrick, J.J. Cuomo and H. Lilienthal, 1974, A.I.P. Conf. Proc. Series **18**, 641.
Taylor, K.N.R., 1971, Advances in Phys. **20**, 551.
Taylor, R.C., 1976, J. Appl. Phys. **47**, 1164.
Wagner, C.N.J., N. Heiman, T.C. Huang, A. Onton and W. Parrish, 1976, A.I.P. Conf. Proc. Series **29**, 188.
Warren, B.E., 1969, X-Ray Diffraction (Addison Wesley, Reading, Mass.).

References to section 9

Ahrony, A., 1975, Phys. Rev. **B12**, 1038.
Bhattacharjee, A.K., B. Coqblin, R. Julien and M.J. Zuckermann, 1977, Physica **91B**, 179.
Boucher, B.Y., 1977, IEEE Trans. **Mag-13**, 1601.
Callen, E., Y.J. Liu and J.R. Cullen, 1977, Phys. Rev. **B16**, 263.
Chen, J.H. and T.C. Lubensky, 1977, Phys. Rev. **B16**, 2106.
Chi, M.C. and R. Alben, 1976, AIP Conf. Proc. **34**, 316.
Cockrane, R.W., R. Harris and M.J. Zuckermann, 1978, Physics Reports **48**, 1.
Coey, J.M.D., 1978, J. Appl. Phys. **49**, 1646.
Coey, J.M.D., S. Von Molnar and R.J. Gambino, 1978a, Solid State Comm. **24**, 167, and to be published.
Edwards, S.F. and P.W. Anderson, 1975, J. Phys. **F5**, 965.
Feldman, J.L., F. Carter, E.F. Skelton and D. Forester, 1978, The Rare Earths in Modern Science and Technology, eds. G. McCarthy and J. Rhyne (Plenum Publishing, New York) p. 375.
Gerber, J.A., D.J. Miller and D.J. Sellmyer, 1978, J. Appl. Phys. **49**, 1699.
Gruzalski, G.R., J.D. Patterson and D.J. Sellmyer, 1978, J. Appl. Phys. **49**, 1696.
Harris, R., S.H. Sung and M.F. Zuckerman, 1978, IEEE Trans. Mag., to be published.
Harris, R. and D. Zobin, 1977, J. Phys. F **7**, 337.
Hauser, J.J., 1975, Phys. Rev. **B12**, 5160.
O'Leary, W.P., 1975, J. Phys. **F5**, L175.
Patterson, J.D., G.R. Gruzalski and D.J. Sellmyer, 1978, Phys. Rev., to be published.
Pelcovits, R.A., E. Pytte and J. Rudnick, 1978, Phys. Rev. Letters **40**, 476.
Poon, S.J. and J. Durand, 1977, Phys. Rev. **B16**, 316.

Handbook on the Physics and Chemistry of Rare Earths, edited by K.A. Gschneidner, Jr. and L. Eyring

Chapter 17

CRYSTAL FIELDS

Peter FULDE
Max-Planck-Institut für Festkörperforschung, (7) Stuttgart, Fed. Rep. Germany

Contents

Symbols

$a_i(l)\}$, $a_i^+(l)\}$ = Fermi destruction and creation operators of CEF eigenstate i at site l

$a_{q\mu}\}$, $a_{q\mu}^+\}$ = destruction and creation operators of phonons of wave number q and polarization μ

B_ℓ^m = crystal-field parameters

$B_{\mu\nu}^{\Lambda\Sigma}$ = dimensionless unit tensor operators acting on 4f–electron

$c_{11} - c_{12}$ = elastic constant

c_{66} = elastic constant

$c_{k\sigma}\}$, $c_{k\sigma}^+\}$ = destruction and creation operators of conduction electrons

c_0, c = sound velocity

c_α = symmetry elastic constants

C = specific heat

$C_{\mu\nu}^{\Lambda\Sigma klk'l'}$ = electronic double tensor operators which are used in describing the generalized k–f interactions

$C_{\alpha\beta\gamma}^{lmn}$ = cubic Clebsch–Gordan coefficients

$d^2\sigma/d\Omega\, d\omega$ = differential neutron-cross section

D = conduction electron band width

D = diffusion constant

$D(l, i, \omega_n)$ = frequency dependent temperature Green's function at site l of CEF-state i

$D_{op}(q, \omega)$ = propagator of optical phonons

$D_\mu(q, \omega)$ = phonon propagator

e = electron charge

$e_\alpha(q\mu)$ = α-component of unit-polarization vector

E_i = eigenvalues of the molecular-field hamiltonian

E_{ij} = energy difference of CEF-states

E_F = Fermi energy

f = second order magneto-elastic coupling constant

$f(Q)$ = single ion form factor

$f(\omega)$ = Fermi distribution function

F_{s-n} = free energy difference between superconducting and normal state

$F_{\alpha\beta\gamma\delta}(J^m)$ = magneto-elastic coupling tensors
g = Landé factor
$g, \bar{g}$ = magneto-elastic coupling constant
g_0 = Landé factor of an impurity
$g_{op}, \bar{g}_{op}$ = coupling constants of the optical phonon interaction with RE-ions
$\boldsymbol{G}$ = reciprocal lattice vector
$G_{\alpha\beta}$, $G_{\alpha\beta\gamma\delta}$ = magneto-elastic coupling constants
$G_{\alpha\beta}(\boldsymbol{J}^m)$, $G_{\alpha\beta\gamma\delta}(\boldsymbol{J}^m)$ = magneto-elastic coupling tensors
$\boldsymbol{h}$ = molecular field
$\boldsymbol{H}_a$ = applied magnetic field
H_{c2} = upper critical field
$H_c(T)$ = thermodynamic critical field
H_{ex} = exchange hamiltonian
H_{ion} = single ion hamiltonian
H_{int} = interaction hamiltonian
$H_{k\text{-}f}$ = conduction electron–4f-electron scattering hamiltonian
$H_{me}^{(1)}$ = linear magneto-elastic interaction
$H_{me}^{(2)}$ = second order magneto-elastic interaction
H_{Ze} = Zeeman hamiltonian
H_{AC} = hamiltonian describing aspherical Coulomb charge scattering
H_{CEF}, H_{CEF}^0, H_{CEF}^m = CEF-hamiltonian (at site m)
$H_{lattice}$ = lattice hamiltonian
H^{MF} = molecular field hamiltonian
H_{Rot} = hamiltonian describing the rotational interaction
H_{Strain} = hamiltonian describing the strain interaction
$H_{\mu\nu klk'l'}^{\Delta\Sigma}$ = hamiltonian describing the generalized k–f interaction
I_2 = Coulomb integral
$J_{crit}(0)$ = critical coupling constant
$J_{eff}(\boldsymbol{q}, \omega)$ = effective RE-ion coupling
J_{ex} = exchange integral
J_{ij}^{ex} = magnetic coupling constant between sites i and j
$\boldsymbol{J}, \boldsymbol{J}_i$ = total-angular momentum(at site i)
J_0 = coupling constant of an impurity to its nearest neighbours
$J(\boldsymbol{q})$ = Fourier transform of J_{ij}^{ex}
$J_{eff}^Q(\boldsymbol{q}, \omega)$ = effective quadrupolar coupling
k_B = Boltzmann factor
$K(\boldsymbol{q})$ = quadrupolar coupling function
L = total orbital momentum
m = electron mass
M = ionic mass
M_e = elastic scattering matrix element
M_i = inelastic scattering matrix element
M_{ij} = matrix elements describing CEF-transitions
M_0 = matrix element at an impurity site
n_e = thermal population of an excited state
n_g = thermal population of the ground state
$\bar{n}_i$ = CEF-level occupational numbers in the presence of a molecular field (or applied field)
n_i = thermal occupation number of CEF-state i
n_I = impurity concentration
N = number of RE-ions
$N(0)$ = electron density of states
O_e^m = Stevens operators
$O_{\alpha d}^n(m)$ = irreducible representations of O_n in terms of J^m
$\boldsymbol{p}^m$ = momentum of ion m
P = time ordering operator
$\boldsymbol{q}$ = momentum vector
q_j = effective charges
$\boldsymbol{Q}$ = scattering vector
Q_1 = anomalous contribution to the thermoelectric power
Q_2 = quadrupole moment of RE-ion
$Q(T)$ = thermoelectric power
$Q_\alpha^n(m)$ = irreducible combinations of $\varepsilon_{\alpha\beta}^m$, $\omega_{\alpha\beta}^m$
$Q_{\alpha\beta}^+$, $Q_{\alpha\beta}^-$ = see defining eq. (17.37)
R = lattice parameter
$\boldsymbol{R}_l^{(0)}$ = equilibrium lattice positions
$\boldsymbol{R}_i$ = lattice positions
R_0 = gas constant
$\boldsymbol{s}$ = conduction electron spin
$\boldsymbol{S}$ = total spin
$\boldsymbol{S}_{4f}$ = RE-ion spin
T = temperature
T_c, T_{co} = transition temperature (in the absence of impurities)
T_D = transition temperature of a structural phase transition
$\boldsymbol{u}^m$ = displacements from rest positions
$u_Q(V_1, \omega)$ = single-ion quadrupolar susceptibility
$u(\omega, T)$ = one-ion susceptibility
$v(\boldsymbol{q}, T)$ = paramagnon velocity
v_F = Fermi velocity
V = volume
$V_2(J_i\boldsymbol{q}\mu, \boldsymbol{q}\mu)$ = second order magneto-elastic interaction

V_1^m, V_2^m = first and second order contributions in the phonon operators of the magneto-elastic interactions
$V(\boldsymbol{r})$ = electrostatic potential
$v_{\alpha\beta}^m$ = components of the deformation tensor
$V_{\alpha\beta}(J^m)\}$ / $V_{\alpha\beta\gamma\delta}(J^m)\}$ = magneto-elastic coupling tensors
w = parameter of a cubic CEF
$w_{and}^{\sigma}(\omega)$ = "mixed" susceptibility
W = Debye–Waller factor
x = parameter of a cubic CEF
$Y_c^m(\theta, \phi)$ = spherical harmonics
Z = nuclear charge
Z = partition function
$Z_{c\alpha}(\theta, \phi)$ = tessarial harmonics
α = pair-breaking parameter
γ = line broadening of CEF-eigenstate
Γ_n = irreducible representations of the cubic group
$\bar{\delta}_i$ = CEF eigenvalues in the presence of a molecular field (or applied field)
δ_i = energy of crystal-field state i
δ_{ij} = energy difference of CEF-eigenstates i and j
δ_0 = level splitting of an impurity
$\delta_{\omega,0}$ = Kronecker symbol
Δ = energy level separation
Δ_g = gap in the electronic excitation spectrum
Δ, Δ_0 = superconducting order parameter (in the absence of magnetic impurities)
$\varepsilon_{\alpha\beta}^m$ = symmetric part of deformation tensor
η^m = finite strain tensor
κ = compressibility
$\kappa(T)$ = thermal conductivity
$\lambda(l)$ = chemical potential at site l
μ_B = Bohr magneton
ρ = electron resistivity
$\rho(\boldsymbol{R})$ = charge distribution
σ = Pauli spin matrices
$\sigma(T)$ = electrical conductivity
$\Sigma_R(\omega)$ = self-energy of conduction electrons
τ_i = normalized inverse pair-breaking scattering length
τ_{ij} = inverse relaxation rates between states i and j
τ_s = conduction-electron life time due to exchange scattering
τ_Q = electronic quadrupolar relaxation time
$\tau(\omega)$ = frequency dependent conduction electron life time
ϕ_k = conduction-electron wave function
$\chi_{+-}(\boldsymbol{q}, \omega)$ = transverse susceptibility
$\chi_e^Q(\boldsymbol{q}, \omega)$ = electronic quadrupolar susceptibility
$\chi_{ij}(\omega)$ = magnetic susceptibility
$\chi(\boldsymbol{q}, \omega)$ = electronic susceptibility
$\chi_{zz}(\boldsymbol{q}, \omega)$ = longitudinal susceptibility
$\psi^{(1)}(z)$ = trigamma function
$\psi(z)$ = digamma function
ω_n = Matsubara frequencies
$\omega_{op}(\boldsymbol{q})$ = dispersion of optical phonons
$\omega(\boldsymbol{q})$ = dispersion of magnetic excitons
$\omega_{q\mu}^0$ = phonon mode frequencies
$\omega_{\alpha\beta}$ = antisymmetric part of deformation tensor

1. General introduction

The theory of crystal fields originates from the work of Bethe (1929). He showed that the eigenvalues of a Hamiltonian describing an open atomic shell of electrons in a crystal can be classified according to the irreducible representations of the point group of the site. Since that time the theory has made substantial progress in becoming elegant, and simple to apply especially as far as the unfilled 4f-shell is concerned. Hereby the work of Stevens (1952, 1967), Elliott and Stevens (1952, 1953a, 1953b) and Judd (1955, 1957, 1962, 1963) deserves special mentioning. Early experimental work is due to Hellwege,

Bleaney, Dieke and their coworkers. A number of excellent review articles have appeared which deal with the description of the crystal fields in rare-earth (RE) systems and provide substantial help for practical applications. We mention here only the ones by Hutchings (1964) and Newman (1971) which provide also an extensive list of references to related work. Although the description of crystal fields is rather well known and standard by now, their computation from microscopic theory is far from being understood. Only in some cases do simple models such as the point charge model give good results. However, this shortcoming has had no retarding effects on a large field of research which has developed, and which deals with the various physical effects caused by the crystal field splitting of the RE-ions. It is the aim of this chapter to discuss these effects in some detail and to indicate possible directions of futural research. In order to achieve this one needs to know as a prerequisite the different interactions which RE-ions experience especially with conduction electrons and phonons. They couple the crystal-field split ions to the rest of the solid and lead to many observable macroscopic effects.

2. Description of crystal fields

2.1. *Crystal-field hamiltonian*

We consider the electrostatic potential $V(\boldsymbol{r})$ which a 4f-electron experiences due to a charge distribution $\rho(\boldsymbol{R})$ of its surrounding. If there is no overlap between this charge distribution and the 4f-electron the potential has to fulfill Laplace's equation $\Delta V(\boldsymbol{r}) = 0$. This implies that $V(\boldsymbol{r})$ may be expanded in terms of the multipoles of the 4f-electrons as

$$V(r) = \sum_{l,m} \gamma_{lm} r^l Y_l^m(\theta, \phi). \tag{17.1}$$

The spherical harmonics $Y_l^m(\theta, \phi)$ are assumed to be normalized to $\int \mathrm{d}\cos\theta \, \mathrm{d}\phi \, |Y_l^m(\theta, \phi)|^2 = 1$. The summation is restricted to $l \leqslant 6$ since a 4f-electron with $l_{4f} = 3$ does not have multipoles larger than $2l_{4f} = 6$. Alternatively one may expand $V(\boldsymbol{r})$ in tessarial harmonics. This has the advantage that the expansion is with respect to real functions. It is

$$V(\boldsymbol{r}) = \sum_{l\alpha} \gamma_{l\alpha} r^l Z_{l\alpha}(\theta, \phi), \tag{17.2}$$

where the tessarial harmonics $Z_{l\alpha}(\theta, \phi)$ are defined by (Hutchings 1964)

$$Z_{l0} = Y_l^0,$$

$$Z_{lm}^c = (2)^{-1/2}[Y_l^{-m} + (-1)^m Y_l^m], \qquad Z_{lm}^s = \mathrm{i}(2)^{-1/2}[Y_l^{-m} - (-1)^m Y_l^m]. \tag{17.3}$$

The index α in eq. (17.2) is understood such that for given value of l, $Z_{l\alpha}$ runs over Z_{l0}, Z_{lm}^c, Z_{lm}^s. A list of the $Z_{l\alpha}$ (as well as the Y_l^m) can be found in Hutchings (1964). The expansion coefficients $\gamma_{l\alpha}$ are calculated from the charge distribution

$\rho(\boldsymbol{r})$ as

$$\gamma_{l\alpha} = \frac{4\pi}{2l+1}\int \mathrm{d}^3\boldsymbol{r}\, \frac{\rho(\boldsymbol{r})}{r^{l+1}}\, Z_{l\alpha}(\theta, \phi) \tag{17.4}$$

The point charge model is characterized by ascribing effective charges q_j to the neighboring sites of the RE-ion under consideration. In that case $\rho(\boldsymbol{r})$ is given by

$$\rho(\boldsymbol{r}) = \sum_j q_j \delta(\boldsymbol{R}_j - \boldsymbol{r}), \tag{17.5}$$

where the $\boldsymbol{R}_j$ denote the positions of the neighboring ions. Until now we have considered only one 4f-electron. In the presence of an unfilled 4f-shell the potential energy of the ion in the crystalline electric field is given by

$$H_{\mathrm{CEF}} = e\sum_i V(\boldsymbol{r}_i), \tag{17.6}$$

where i runs over all 4f-electrons. For the RE-ions the spin–orbit interaction energy is usually much larger than the crystal field energy. For that reason one may restrict oneself to the lowest J multiplet in calculating matrix elements of H_{CEF}. Exceptions, i.e. situations in which the admixture of other J multiplets is of importance are discussed for example by Furrer (1974) and de Wijn et al. (1974). This restriction to the lowest J multiplet simplifies the calculations considerably as demonstrated by Stevens (1967). He showed that the sum of polynomials in x_i, y_i, z_i occurring in eq. (17.6) can be replaced by a sum of polynomials of J_x, J_y, J_z operators, which have the same transformation properties as the original expression. They act on the unfilled 4f-shell as a whole and therefore are much more convenient than the x_i (y_i, z_i) polynomials which act on a particular 4f-electron. The rules for transforming an expression of the form $\Sigma_i f(x_i, y_i, z_i)$ into an equivalent operator expression can be stated as follows. Replace any product of x, y, z by the corresponding product of J_x, J_y, J_z but written in a symmetrized form. Hereby we understand the sum of all different sequences of the J_μ [e.g. $xy \to \frac{1}{2}(J_xJ_y + J_yJ_x)$]. The constants of proportionality depend on the degree of the polynomial and on L, S and J. Furthermore the r_i^l operators have to be replaced by the averages $\langle r^l\rangle$ over the 4f-wave functions. Examples are

$$\begin{aligned}
&\sum_i (x_i^2 - y_i^2) \equiv \alpha_J \langle r^2\rangle [J_x^2 - J_y^2] = \alpha_J \langle r^2\rangle O_2^2,\\
&\sum_i \tfrac{1}{2}\{(x_i + iy_i)^4 + (x_i - iy_i)^4\} \equiv \beta_J \langle r^4\rangle \tfrac{1}{2}[J_+^4 + J_-^4]\\
&\qquad\qquad = \beta_J \langle r^4\rangle O_4^4,\\
&\sum_i (x_i^6 - 15x_i^4y_i^2 + 15x_i^2y_i^4 - y_i^6) \equiv \gamma_J \langle r^6\rangle \tfrac{1}{2}[J_+^6 + J_-^6]\\
&\qquad\qquad = \gamma_J \langle r^6\rangle O_6^6.
\end{aligned} \tag{17.7}$$

Here we have adopted the convention (Elliott and Stevens 1953a, 1953b) to

label the proportionality constants by α_J, β_J, γ_J for polynomials of second, fourth and sixth degree. A complete list of the O_n^m can be found in Hutchings (1964). Furthermore we give in table 17.1 a list of the α, β, γ for the different trivalent RE-ions. A list of the $\langle r^l \rangle$ for some of the trivalent RE-ions is given in table 17.2 where the 4f-wave functions as determined by Freeman and Watson (1962) were used. Very often one is describing the crystal field with respect to axes chosen such that $\gamma_{l\alpha} = 0$ for α corresponding to Z_{lm}^s [see eqs. (17.3) and (17.4)]. In that case one can write H_{CEF} in the form

$$H_{\mathrm{CEF}} = \sum_{l,m} A_l^m \langle r^l \rangle \theta_l O_l^m, \tag{17.8}$$

where θ_l equals α_J, β_J, γ_J for $l = 2, 4, 6$. The A_l^m are up to a numerical factor equal to Z_{lm}^c. The appropriate numerical factors can be found in Hutchings (1964). Often eq. (17.8) is also written as

$$H_{\mathrm{CEF}} = \sum_{l,m} B_l^m O_l^m. \tag{17.9}$$

We list now the crystal-field hamiltonian for some of the most common situations.

(a) *Cubic point symmetry*

Often one can choose the four-fold axes as the ones in which the J-operators are expressed in. In that case one finds

$$H_{\mathrm{CEF}} = B_4^0[O_4^0 + 5\,O_4^4] + B_6^0[O_6^0 - 21\,O_6^4]. \tag{17.10}$$

For the special case of a point charge model one can derive expressions for B_4^0, B_6^0. If the neighboring ions carrying an effective charge q are placed at distance

TABLE 17.1
List of Steven's factors α_J, β_J, γ_J for the trivalent RE-ions (from Elliott, 1972).

Ions	$\alpha_J \times 10^2$	$\beta_J \times 10^4$	$\gamma_J \times 10^6$
Ce	−5.71	63.5	0
Pr	−2.10	−7.35	61.0
Nd	−0.643	−2.91	−38.0
Pm	0.771	4.08	60.8
Sm	4.13	25.0	0
Tb	−1.01	1.22	−1.12
Dy	−0.635	−0.592	1.03
Ho	−0.222	−0.333	−1.30
Er	0.254	0.444	2.07
Tm	1.01	1.63	−5.60
Yb	3.17	−17.3	148.0

TABLE 17.2
$\langle r^l \rangle$ for the different trivalent RE-ions (from Freeman, 1972)

Ions	$\langle r^2 \rangle$	$\langle r^4 \rangle$	$\langle r^6 \rangle$
Ce	1.200	3.455	21.226
Pr	1.086	2.822	15.726
Nd	1.001	2.401	12.396
Sm	0.883	1.897	8.775
Eu	0.938	2.273	11.670
Gd	0.785	1.515	6.281
Dy	0.726	1.322	5.102
Er	0.666	1.126	3.978
Yb	0.613	0.960	3.104

d from the RE-ion one finds

eightfold coordination (cube)

$$B_4^0 = \frac{7}{18}\frac{|e|q}{d^5}\beta_J \langle r^4\rangle \qquad B_6^0 = -\frac{1}{9}\frac{|e|q}{d^7}\gamma_J \langle r^6\rangle$$

sixfold coordination (octahedron)

$$B_4^0 = -\frac{7}{16}\frac{|e|q}{d^5}\beta_J \langle r^4\rangle \qquad B_6^0 = -\frac{3}{64}\frac{|e|q}{d^7}\gamma_J \langle r^6\rangle$$

The eigenvalues and eigenfunctions of H_{CEF} as given by eq. (17.10) have been tabulated by Lea et al. (1962) for $J = 5/2, 3, \ldots, 8$. They did this by rewriting eq. (17.10) in the form

$$H_{CEF} = W\left(\frac{x}{F(4)}(O_4^0 + 5\,O_4^4) + \frac{1-|x|}{F(6)}(O_6^0 - 21\,O_6^4)\right), \tag{17.11}$$

where $B_4^0 F(4) = Wx$ and $B_6^0 F(6) = W(1-|x|)$ with $-1<x<1$ and listing the eigenvalues and eigenfunctions as function of x. The factors $F(4)$, $F(6)$ depend only on J and are also listed there. Sometimes it is necessary to express the crystal field with respect to axes other than the fourfold axes used above. Then eq. (17.10) is changed correspondingly. In particular when z is chosen along a threefold axis one finds (Hutchings 1964).

$$H_{CEF} = \bar{B}_4^0[O_4^0 - 2^{1/2}20\,O_4^3] + \bar{B}_6^0[O_6^0 + \tfrac{35}{4}2^{1/2}O_6^3 + \tfrac{77}{8}O_6^6]. \tag{17.12}$$

This hamiltonian applies for example to Tb^{3+} in TbSb.

(b) *Hexagonal point symmetry*

Here the crystal field hamiltonian has the form

$$H_{CEF} = B_2^0 O_2^0 + B_4^0 O_4^0 + B_6^0 O_6^0 + B_6^6 O_6^6. \tag{17.13}$$

Due to the large number of parameters there is no convenient way to list the eigenvalues and eigenvectors as in the cubic case.

The computation of the crystal field parameters B_l^m from a microscopic theory is a very difficult task which until now has had limited success. For the RE-salts there is a considerable amount of work available dealing with this problem and a semi-empirical understanding of the crystal-field parameters has been reached. Even here there are no successful *ab initio* calculations available. For the metallic RE-systems the situation is much worse. The more surprising is the experiment observation that for certain classes of RE-compounds the point charge model seems to be valid.

In order to understand better the difficulties one is encountering let us consider first the RE-salts. One of the basic assumptions of the crystal field

description given above has been a vanishing overlap between the charges, which are responsible for the crystal field and the 4f-wave functions. However the observation has been made (Freeman and Watson 1962) that the parameters B_l^m, when measured for a series of RE-ions and divided by $\langle r^l \rangle$ are not constant. Furthermore the B_6^m fall off less rapidly with increasing nuclear charge than one expects from the corresponding variation of $\langle r^6 \rangle$. This suggests strongly that the other electrons belonging to the RE-ion are important in setting up the crystal field. First there is their shielding effect on the 4f-electrons. The filled 5s and 5d-shells are distorted to shield from the 4f-electrons the electric field of the neighbouring ions. This effect can be taken into account by multiplying $A_n^m \langle r^m \rangle$ as calculated from a point charge model by a shielding factor $(1 - \sigma_n)$ so that (Hutchings 1964)

$$A_l^m \langle r^l \rangle \text{effective} = (1 - \sigma_l) A_l^m \langle r^l \rangle \text{point charge}. \tag{17.14}$$

Furthermore there are the overlap and covalency contributions (Jorgensen et al. 1963, Watson and Freeman 1967, Ellis and Newman 1967, Freeman 1972).

In metallic RE-systems there is the additional effect of the conduction electrons. There have been APW calculations to determine their effect (Das and Ray 1969). They show that the contribution to $A_2^0 \langle r^2 \rangle$ is particularly large and may even lead to a change of sign of that term. There have been also phenomenological approaches to the problem (Dixon and Dupree 1971a,b, 1973). They consist in finding appropriate conduction-electron wave functions ϕ_k with which the 4f-electrons Coulomb interact. The net result is a new expression replacing $A_l^m \langle r^l \rangle$ which can be calculated and compared with experiments.

2.1.1. *The case of* Gd *and* Eu

Gd and Eu are S-state ions and therefore have a spherical 4f-charge cloud with vanishing multipole moments. However given the lowest J multiplet ($J = 7/2$ for Gd) there can be admixtures (via spin–orbit interaction) of $L \neq 0$ wave functions into that J state. This may lead to a CEF splitting. But since the excitation energy is comparatively large the CEF splitting is very small (of the order of 10^{-3} K).

2.2. *Methods for determining crystal-field levels*

Obviously a measurement of the crystal-field energy levels has to employ different experimental methods in a salt and in a metal. For example the important techniques of optical absorption and fluorescence which are used for the RE-salts cannot be used for the metals. Mainly for that reason crystal-field level schemes in metals have been investigated only recently in considerable detail. We will list in the following some experimental methods which can be applied to metals and we will leave out the optical methods since they have been extensively covered for example by Wybourne (1965) and Dieke (1968).

2.2.1. *Specific heat: Schottky anomaly*

An indirect way to determine the crystal-field levels is via a measurement of the specific heat. The different levels show up in Schottky type of contributions. Per mole of RE-ions the specific heat is given by

$$C = R_0 Z^{-2} \left\{ Z \sum_i (\beta\delta_i)^2 \exp(-\beta\delta_i) - \left(\sum_i \beta\delta_i \exp(-\beta\delta_i) \right)^2 \right\} \tag{17.15}$$

Here i is over all $(2J + 1)$ crystal-field states which may be degenerate. Their energy is denoted by δ_i and $\beta = (k_B T)^{-1}$ where k_B and T denote the Boltzmann factor and temperature. Z is the partition function i.e. $Z = \Sigma_i \exp(-\beta\delta_i)$, and R_0 is the gas constant.

From the measured Schottky anomaly one can often deduce successfully the crystal-field parameters. The former is determined from the difference between a RX_n compound and LaX_n or LuX_n. A typical example is shown in fig. 17.1. The method has been applied to concentrated systems as well as to dilute alloys (see for example Hoenig et al., 1974; Heiniger et al., 1974). The accuracy of the measurements is limited by spin-phonon interactions and exchange effects among the RE-ions which distort the Schottky contribution. Often one finds several crystal-field parameters W, x which fit equally well the specific heat.

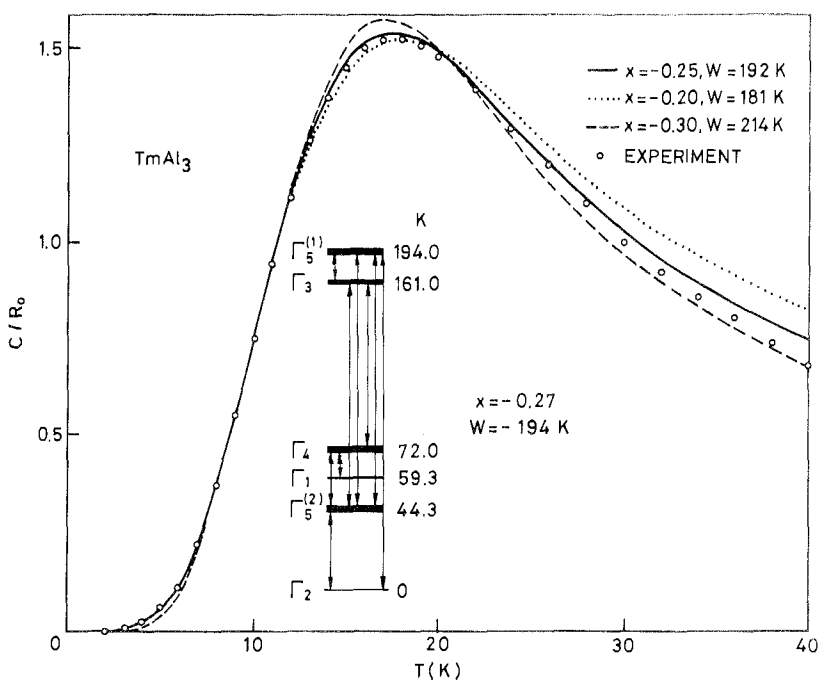

Fig. 17.1. Schottky anomaly and CEF-level sequence for $TmAl_3$ (from Bucher et al., 1974).

2.2.2. *Susceptibility measurements*

Limited information about the CEF-levels can also be obtained from a measurement of the temperature dependent Van Vleck susceptibility (Hirst et al. 1968, Williams and Hirst 1970), which is given by

$$\chi(T) = N\mu_B^2 g^2 Z^{-1} \left\{ \sum_i \frac{|M_{ii}|^2}{T} \exp(-\beta\delta_i) + 2 \sum_{\delta_i \neq \delta_j} \frac{|M_{ij}|^2}{\delta_j - \delta_i} \exp(-\beta\delta_i) \right\}. \tag{17.16}$$

Here g is the Landé factor and μ_B denotes the Bohr magneton. The matrix elements M_{ij} are defined as $M_{ij} = \langle i|J|j\rangle$ where $|n\rangle$ denote the different CEF-eigenstates. One notices the Curie terms resulting from the diagonal matrix elements (first term) and the Van Vleck terms resulting from the off-diagonal contributions. For an impurity which is in a nonmagnetic ground state there is no Curie term at low temperatures. This is seen clearly in fig. 17.2. Again this method is limited by exchange interactions among the RE-ions.

2.2.3. *Magnetization in high magnetic fields*

A high applied magnetic field H_a can mix to a considerable amount the different CEF-eigenstates. This leads to (anisotropic) nonlinear effects in the magnetization which can be measured (Vogt and Cooper 1968, Cooper and Vogt 1970, Roeland 1974). An analysis of the data can be used to infer from it the CEF-energy level scheme. Thereby one determines first the eigenstates of $H_{CEF} + g\mu_B \boldsymbol{J}\boldsymbol{H}_a$ and from them computes the magnetization for a given direction of H_a and temperature. The CEF-parameters are varied until agreement is obtained with the experiments.

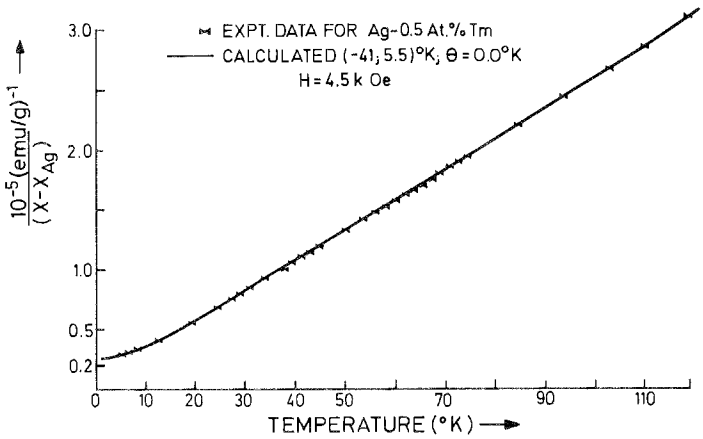

Fig. 17.2. Inverse susceptibility of Ag with 0.5 at.% Tm (from Williams and Hirst, 1969).

2.2.4. *Paramagnetic resonance*

In a paramagnetic resonance experiment one is measuring the Zeeman splitting of a given CEF-level (ground state) i.e. one determines the g-tensor of the level. This method has had very extensive applications in RE-salts and we refer to the book of Abragam and Bleaney (1970) for details. Resonance measurements on non S-state ions in metals are comparatively recent. (Griffiths and Coles 1966, Hirst et al. 1968, Burr and Orbach 1967). For more details we refer to ch. 18.

2.2.4. *Mössbauer effect*

Sometimes it is possible to use the Mössbauer effect to observe a zero-field magnetic hyperfine splitting of a RE-impurity at low temperatures (Hirst and Seidel 1969). This yields again the g-tensor of the CEF-ground state in addition to some information about the hyperfine-interaction strengths. In a Mössbauer experiment one can measure the interaction of a nuclear state having a quadrupole moment with the quadrupolar part of the crystalline electric field. Thus one can learn something about the parameter $A_2^0\langle r^2\rangle$ where the quadrupole shielding factor $(1-\sigma_2)$ is already included (compare eq. (17.14)). The method has been applied for example to Tm metal (Ulrich and Barnes 1967) and is described in greater detail in ch. 18.

2.2.5. *Inelastic neutron scattering*

The method of inelastic neutron scattering has become the dominant method for studying crystal fields in metals. Early work on RE-salts is due to Cribier and Jacrot (1960) while the first experments on metallic RE-systems were done by Rainford et al. (1968). The method has been recently extended to a large number of compounds (see for example: Birgeneau et al. 1970, Turberfield et al. 1970, Birgeneau et al. 1973, Furrer et al. 1972, Heiniger et al. 1974, Morin et al. 1974, Chamard-Bois et al. 1973, Heer et al. 1974, Brun et al. 1974, Bucher et al. 1972). In such an experiment monochromatic neutrons are scattered from the sample and are analysed afterwards according to their energy and momentum. This determines energy- and momentum transfer ω and $|\boldsymbol{Q}|$. The differential cross section for a system of N noninteracting RE-ions is given for small momentum transfer by

$$\frac{\mathrm{d}^2\sigma}{\mathrm{d}\Omega\,\mathrm{d}\omega} = N\left(\frac{1.91e^2g}{2mc^2}\right)^2 \frac{k_\mathrm{f}}{k_\mathrm{i}} f^2(Q)\,\mathrm{e}^{-2W}$$

$$\times \sum_{i,j} n_i |\langle j|J_\perp|i\rangle|^2 \delta(\delta_j - \delta_i - \omega). \tag{17.17}$$

Here $k_\mathrm{i}, k_\mathrm{f}$ are the momenta of the incoming and outgoing neutrons. $f(Q)$ is the form factor of a single ion and e^{-2W} is the Debye–Waller factor. n_i is the occupational probability of the CEF-eigenstate $|i\rangle$. $J_\perp$ is the component of $\boldsymbol{J}$ perpendicular to

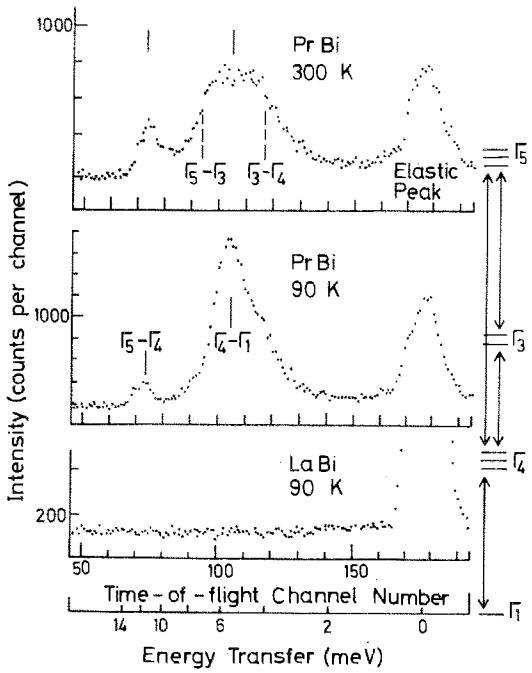

Fig. 17.3. Inelastic neutron scattering results on PrBi. The different inelastic peaks correspond to different transitions between the CEF-levels. For comparison LaBi does not show the inelastic scattering (from Birgeneau et al., 1970).

the scattering vector $\boldsymbol{Q}$. The cross section for the crystal field transitions competes with the one for phonon scattering. The latter is proportional to $Q^2 e^{-2W}$ instead of $f^2(Q) e^{-2W}$. In fig. 17.3 we show the experimental results for PrBi and for comparison also for LaBi. It is seen that there are no phonon effects interfering with the scattering from the CEF-energy levels.

Inelastic neutron scattering is also extremely useful for studying the excitations of a system of interacting RE-ions. This will be discussed in sections 5.1.2 and 5.1.4.

2.2.6. *Other methods*

There are some other experimental methods available from which indirect information can be obtained concerning the CEF-energy levels. Among them we mention the transport coefficients such as electrical and thermal conductivity, the thermoelectric power and the influence of CEF-split impurities on superconductivity. Those phenomena will be described in section 4. Finally it is worth pointing out that there may be also other spectroscopic methods developing in the future. One is superconducting tunneling spectroscopy and the other is absorption measurements of high-frequency phonons as they may be generated in superconduction tunneling junctions (Eisenmenger 1969).

2.3. *Experimental results*

Systematic studies have been made of the crystal-field parameters for several different structures.

2.3.1. *NaCl structure*

The RE-pnictides (Birgeneau et al. 1973, Furrer et al. 1972, Mook and Davis 1972) and RE-chalcogenides (Turberfield et al. 1971) have been investigated in detail. It was found that the results for the pnictides could be well explained by using a simple nearest-neighbour effective-point-charge model with $Ze = -1.2$. This astonishing result is shown in fig. 17.4 where the fourth-order term $A_4^0\langle r^4\rangle$ is plotted as function of the number of 4f-electrons. Only for the heavy RE one finds deviations from the point-charge model. While $A_4^0\langle r^4\rangle$ can be read off from that figure for any RX, where X may vary from P to Bi one may take $A_6^0\langle r^6\rangle = 0.4 \pm 0.2$ meV for all compounds. The RE-chalcogenides, too seem to obey a point-charge model.

2.3.2. *CsCl structure*

Here the systems ErX with X = Ag, Cu, Zn, Rh have been investigated by inelastic neutron scattering (Chamard-Bois et al. 1973, Knorr et al. 1974). The parameters $A_4^0\langle r^4\rangle$ and $A_6^0\langle r^6\rangle$ are found to be negative and of comparable size. These findings cannot be explained with a point-charge model. Similar results were found for HoRh and TmRh (Knorr et al. 1974). RZn compounds were also investigated by magnetization measurements and agreement with neutron data was found where a comparison was possible.

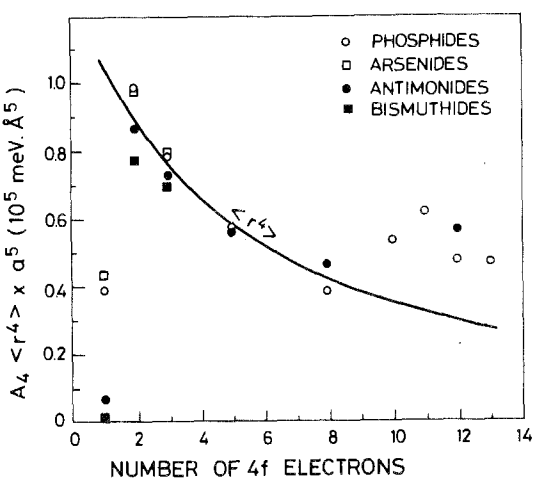

Fig. 17.4. Plot of $A_4\langle r^4\rangle$ for the different RE-pnictides. The solid line shows $\langle r^4\rangle$ (from Birgeneau et al., 1973).

2.3.3. *$MgCu_2$ structure*

The compounds RAl_2 were studied by inelastic neutron scattering (Furrer et al. 1973) as well as systems like $Er_xY_{1-x}Al_2$ (Heer et al. 1974). Here Y reduces the magnetic interactions between the Er ions (see also Devine et al. 1973 and Wallace 1974). For $Tm_xY_{1-x}Al_2$ see Purwins et al. (1973).

2.3.4. *Cu_3Au structure*

We mention merely that PrX_3 compounds have been studied where X = Pd, Sn, Pb, Tl, In (Bucher and Maita 1973, Wallace 1974).

2.4. *Diagrammatic description*

For many purposes it is very useful to describe the different CEF-eigenstates $|i>$ of a RE-ion at site l by Fermi-operators $a_i^+(l)$, $a_i(l)$. Those operators were introduced by Abrikosov (1965) in a different context and were adopted to the present problem by Fulde and Peschel (1972). The method, however, introduces non-physical states since, incorrectly, several CEF-levels can be occupied at the same time. In order to remedy this one introduces a chemical potential $\lambda(l)$ which serves to "freeze out" the non-physical states. This is done by taking the limit

$$\prod_l \lim_{\lambda(l)\to\infty} \left\{ \frac{\exp(\lambda(l)/T)}{Z} [\ldots..] \right\} \tag{17.18}$$

at the end of every calculation of thermal expection values. This way all configurations except those with one occupied state per site are eliminated. Here and in the following we set $k_B = \hbar = 1$ for simplicity. The hamiltonian of a system of noninteracting CEF-split ions is then given by

$$H = \sum_{li} [\delta_i + \lambda(l)]\, a_i^+(l)\, a_i(l). \tag{17.19}$$

The frequency dependent temperature Green's function $D(l, i, \omega_n)$ is given by (see Fulde and Peschel 1972)

$$D(l, i, \omega_n) = [i\omega_n - \lambda(l) - \delta_i]^{-1}, \tag{17.20}$$

where the Matsubara frequencies $\omega_n = 2\pi T(n + 1/2)$ with n being an integer. The Green's function is introduced since one can calculate with it in a very simple way the frequency dependent single-ion susceptibility. For that purpose the interaction of an ion at site 0 with an applied magnetic field H_a is written as

$$H = -g\mu_B H_a \sum_{ij} M_{ij} a_i^+(0)\, a_j(0), \tag{17.21}$$

where $M_{ij} = \langle i|J|j\rangle$. The single-ion susceptibility $g^2\mu_B^2 u(\omega, T)$ is then given by

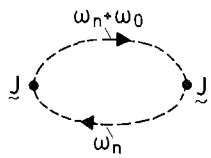

Fig. 17.5. Diagram for the computation of the frequency dependent single ion susceptibility. The dashed lines denote the different CEF energy levels as described by $D(l, i, \omega_n)$. The susceptibility is obtained after continuing analytically ω_0 to the imaginary axis.

the diagram in fig. 17.5. One finds

$$u(\omega, T) = \sum_{ij=1}^{2J+1} |M_{ij}|^2 \frac{\delta_{ij}}{\delta_{ij}^2 - (\omega + i0^+)^2} (n_j - n_i), \tag{17.22}$$

where $\delta_{ij} = \delta_i - \delta_j$. The n_i are given by $n_i = Z^{-1} \exp(-\delta_i/T)$. This expression for $u(\omega, T)$ will be used very often in the following. For the special case of two singlets separated by an energy δ and neglecting all other states eq. (17.22) simplifies to

$$u(\omega, T) = \frac{2\delta|M|^2}{\delta^2 - \omega^2} \tanh(\delta/2T). \tag{17.23}$$

It should be mentioned that there is a difficulty connected with the freezing out procedure described above. Namely it turns out that the linked cluster theorem is violated (Keiter 1968). This has no implications for the evaluation of diagrams for the coupled RE-ion and phonon or conduction-electron system as long as one uses the mean field or random-phase approximation (RPA). However the method can not be easily applied to more sophisticated approximation schemes. For more details we refer to Fulde and Peschel (1972). Since most of the following considerations are restricted to the above approximations the method can be applied and has considerable advantages because of its simplicity.

3. Interactions of crystal-field split ions

Rare earth ions with crystal-field split energy levels experience interactions of different kinds. First there is the interaction which results from the vibrations of the ions which are setting up the crystal field at a particular lattice site. The resulting fluctuations in the crystal field cause virtual transitions between the $(2J + 1)$–states of the ions. In addition to changing the crystal field the lattice vibrations may cause other types of magneto-elastic coupling. Assume that the RE-ions are interacting with each other via direct overlaps of the 4f-wave functions or superexchange. In first approximation we can write this interaction in the form $K(\boldsymbol{R}_i - \boldsymbol{R}_j)\boldsymbol{J}_i\boldsymbol{J}_j$. Deviations of the vectors $\boldsymbol{R}_{i,j}$ from equilibrium positions $\boldsymbol{R}_{i,j}^{(0)}$ due to lattice vibrations result in a magneto-elastic coupling. This is seen by expanding $K(\boldsymbol{R}_i - \boldsymbol{R}_j)$ in terms of the displacements $(\boldsymbol{R}_{i,j} - \boldsymbol{R}_{i,j}^{(0)})$. Since the crystal field does not play a dominant part hereby we will consider this

interaction only aside. Furthermore if we are dealing with a metal there is the interaction of the RE-ions with the conduction electrons. The latter will scatter elastically and inelastically from the ions and there will be Coulomb and exchange scattering. It is apparent that the crystal-field splitting of the ionic levels will be of great importance for those interactions.

3.1. *Interactions with phonons*

In the following we outline the derivation of the magneto-elastic interactions. Further details can be found in Dohm and Fulde (1975). The starting hamiltonian is of the form (for simplicity we restrict ourselves to Bravais lattices):

$$H = H_{\text{Lattice}} + \sum_{m=1}^{N} H^m_{\text{CEF}},$$

$$H_{\text{Lattice}} = \frac{1}{2M} \sum_{m=1}^{N} (\boldsymbol{p}^m)^2 + \phi(\boldsymbol{R}_1, \ldots . \boldsymbol{R}_N),$$

$$H^m_{\text{CEF}} = V\{\boldsymbol{J}^m;\ \boldsymbol{R}_m - \boldsymbol{R}_1, \ldots . , \boldsymbol{R}_m - \boldsymbol{R}_N\}. \tag{17.24}$$

H_{Lattice} includes the kinetic and potential energy of the N ions of mass M, momenta $\boldsymbol{p}^m$ and positions $\boldsymbol{R}_m$. H^m_{CEF} describes the CEF at site m and its dependence on the positions of the other ions. In order to demonstrate the influence of the lattice deformations on the crystal field we introduce the displacements from the rest positions $\boldsymbol{u}^m = \boldsymbol{R}_m - \boldsymbol{R}^{(0)}_m$. The latter are defined by the minima of the lattice potential. The components of the deformation tensor $\boldsymbol{v}^m$ are then defined by

$$v^m_{\alpha\beta} = \frac{\partial u_\alpha(\boldsymbol{R}^{(0)}_m)}{\partial \boldsymbol{R}^{(0)}_{m,\beta}}, \tag{17.25}$$

where the continuous displacement field $\boldsymbol{u}(\boldsymbol{R}^{(0)})$ fulfills the condition $\boldsymbol{u}(\boldsymbol{R}_n{}^{(0)}) \equiv u^n$. The magneto-elastic interactions are then obtained by expanding H^m_{CEF} in terms of the deformations $v^m_{\alpha\beta}$. Thereby it is important to include all second order terms in the deformations. The reason for this will become clear in section 5.2.1 when we discuss the temperature and magnetic field dependence of the elastic constants and phonons. A lattice deformation around $\boldsymbol{R}_m{}^{(0)}$ can be viewed as a strain followed by a rotation of the lattice. Consequently the expansion of H^m_{CEF} in terms of the displacements can be written as

$$H^m_{\text{CEF}} = H^{(0)}_{\text{CEF}}(\boldsymbol{J}^m) + H_{\text{Strain}}(\boldsymbol{J}^m) + H_{\text{Rot}}(\boldsymbol{J}^m). \tag{17.26}$$

The zeroth-order term $H^{(0)}_{\text{CEF}}(\boldsymbol{J}^m)$ is the conventional CEF hamiltonian while H_{Strain} and H_{Rot} represent the strain and rotational magneto-elastic interactions. Up to second order in $v^m_{\alpha\beta}$ the pure-strain interaction can be written as

$$H_{\text{Strain}}(\boldsymbol{J}^m) = G_{\alpha\beta}(\boldsymbol{J}^m)\eta^m_{\alpha\beta} + \tfrac{1}{2}F_{\alpha\beta\gamma\delta}(\boldsymbol{J}^m)\epsilon^m_{\alpha\beta}\epsilon^m_{\gamma\delta}. \tag{17.27}$$

Here we have introduced the finite strain tensor η^m which is defined in terms of

the $v^m_{\alpha\beta}$ by

$$\eta^m_{\alpha\beta} = \tfrac{1}{2}(v^m_{\alpha\beta} + v^m_{\beta\alpha} + v^m_{\gamma\alpha} v^m_{\gamma\beta})$$
$$= \varepsilon_{\alpha\beta} + \tfrac{1}{2}(\varepsilon^m_{\gamma\alpha} + \omega^m_{\gamma\alpha})(\varepsilon^m_{\gamma\beta} + \omega^m_{\gamma\beta}). \tag{17.28}$$

Here $\varepsilon^m_{\alpha\beta}$ and $\omega^m_{\alpha\beta}$ are the symmetric and antisymmetric part of the deformation tensor, respectively. It is $\varepsilon^m_{\alpha\beta} = \frac{1}{2}(v^m_{\alpha\beta} + v^m_{\beta\alpha})$ and $\omega^m_{\alpha\beta} = \frac{1}{2}(v^m_{\alpha\beta} - v^m_{\beta\alpha})$. Equation (17.28) shows how the antisymmetric part $\omega^m_{\alpha\beta}$ enters into the finite strain tensor $\eta^m_{\alpha\beta}$. The tensors $G_{\alpha\beta}$ and $F_{\alpha\beta\gamma\delta}$ can be calculated directly from the CEF-potential (see Dohm and Fulde 1975). Similarly $H_{\mathrm{Rot}}(\boldsymbol{J}^m)$ is written up to second order in the deformation tensor $v^m_{\alpha\beta}$ as

$$H_{\mathrm{Rot}}(\boldsymbol{J}^m) = -V_{\alpha\beta}(\boldsymbol{J}^m)[\omega^m_{\alpha\beta} - \tfrac{1}{2}(\omega^m_{\alpha\gamma}\omega^m_{\gamma\beta} + \varepsilon^m_{\alpha\gamma}\omega^m_{\gamma\beta} - \varepsilon^m_{\beta\gamma}\omega^m_{\gamma\alpha})]$$
$$- G_{\alpha\beta\gamma\delta}(\boldsymbol{J}^m)\varepsilon^m_{\alpha\beta}\omega^m_{\gamma\delta} + \tfrac{1}{2}V_{\alpha\beta\gamma\delta}(\boldsymbol{J}^m)\omega^m_{\alpha\beta}\omega^m_{\gamma\delta} \tag{17.29}$$

Again the $V_{\alpha\beta}$, $V_{\alpha\beta\gamma\delta}$ and $G_{\alpha\beta\gamma\delta}$ can be calculated from the CEF-potential. It turns out and is important that the $V_{\alpha\beta}$ and $V_{\alpha\beta\gamma\delta}$ contain the same CEF-parameters and thus are related to each other. The same holds true for $G_{\alpha\beta}$ and $G_{\alpha\beta\gamma\delta}$. These relations are necessary to ensure rotational invariance. Until now we have shown how the different (strain and rotational) interactions can be derived. It has been left open what combinations of $\boldsymbol{J}$-operators go with the different combinations of $\varepsilon_{\alpha\beta}$ and $\omega_{\alpha\beta}$. This information is of course contained in the different tensors $G_{\alpha\beta}$, $F_{\alpha\beta\gamma\delta}$ etc. which can be calculated from the CEF-potential. However one would prefer a simple prescription how to construct the proper combinations of $\boldsymbol{J}$-operators for a given symmetry. Such a prescription can indeed be given but for the price that the connection is lost between the different coupling constants which was pointed out above (see Thalmeier and Fulde 1975, the conventional linear strain interaction was derived this way in the pioneering work of Callen and Callen 1965). To demonstrate this we consider cubic symmetry and form the irreducible combinations of $\varepsilon_{\alpha\beta}$ and $\omega_{\alpha\beta}$ which we denote by $Q^n_\alpha(m)$. It is

$$\begin{aligned}
&\Gamma_1: && Q_1(m) = \varepsilon^m_{xx} + \varepsilon^m_{yy} + \varepsilon^m_{zz} \\
&\Gamma_3: && Q^1_3(m) = \tfrac{1}{2}\sqrt{3}(2\varepsilon^m_{zz} - \varepsilon^m_{xx} - \varepsilon^m_{yy}); \quad Q^2_3(m) = \tfrac{1}{2}\sqrt{3}(\varepsilon^m_{xx} - \varepsilon^m_{yy}) \\
&\Gamma_4: && Q^1_4(m) = \omega^m_{yz}; \quad Q^2_4(m) = \omega^m_{zx}; \quad Q^3_4(m) = \omega^m_{xy} \\
&\Gamma_5: && Q^1_5(m) = \varepsilon^m_{yz}; \quad Q^2_5(m) = \varepsilon^m_{zx}; \quad Q^3_5(m) = \varepsilon^m_{xy}
\end{aligned} \tag{17.30}$$

Γ_2 has been omitted since it contains terms of third order in $\varepsilon^m_{\alpha\beta}$ only. In the same way we can write down the irreducible representations of O_h in terms of the $\boldsymbol{J}^m$ operators. We denote them by $O^n_{\alpha d}(m)$. Hereby is α the representation index (in Bethe's notation $\alpha = 1, \ldots 5$) d is the degree of representation (or maximum degree of $\boldsymbol{J}$), n is the index of degeneracy (we omit n for singlets) and m is the site of the RE-ion. For demonstration we list the operators for $d = 2$ (second degree in $\boldsymbol{J}$) except for $\alpha = 4$ (rotational part, see eq. 17.30) where the lowest degree in $\boldsymbol{J}$ is $d = 4$.

and $\alpha = 1$

Γ_3: $Q^1_3(m) = \frac{1}{2}\sqrt{3}(2\varepsilon^m_{zz} - \varepsilon^m_{xx} - \varepsilon^m_{yy})$; $Q^2_3(m) = \frac{1}{2}$

$$
\begin{aligned}
&O_{14} = 35J_z^4 - [30J(J+1) - 25]J_z^2 - 6J(J+1) + 3J^2(J+1)^2 + \tfrac{5}{2}(J_+^4 + J_-^4)\\
&O_{32}^1 = 6^{-1/2}(3J_z^2 - J(J+1)); \qquad O_{32}^2 = 2^{-1/2}(J_x^2 - J_y^2)\\
&O_{44}^1 = 2^{-3/2}[(J_zJ_y + J_yJ_z)(J_y^2 - J_z^2) + (J_y^2 - J_z^2)(J_zJ_y + J_yJ_z)]\\
&O_{44}^2 = 2^{-3/2}[(J_zJ_x + J_xJ_z)(J_z^2 - J_x^2) + (J_z^2 - J_x^2)(J_zJ_x + J_xJ_z)]\\
&O_{44}^3 = 2^{-3/2}[(J_xJ_y + J_yJ_x)(J_x^2 - J_y^2) + (J_x^2 - J_y^2)(J_xJ_y + J_yJ_x)]\\
&O_{52}^1 = 2^{-1/2}(J_yJ_z + J_zJ_y); \qquad O_{52}^2 = 2^{-1/2}(J_zJ_x + J_xJ_z);\\
&O_{52}^3 = 2^{-1/2}(J_xJ_y + J_yJ_x)
\end{aligned}
\tag{17.31}
$$

The normalization is the same as in Callen and Callen (1965) except for his n_l which have been replaced by one. The hamiltonian $H_{\text{me}}(\boldsymbol{J}^m) = H_{\text{Strain}}(\boldsymbol{J}^m) + H_{\text{Rot}}(\boldsymbol{J}^m)$ is then written as

$$
H_{\text{me}}(\boldsymbol{J}^m) = -\sum_{\alpha dn} g_1(\alpha, d) Q_\alpha^n(m) O_{\alpha d}^n(m) - \sum_{\substack{\alpha\beta\gamma \\ lsn}} g_2(\alpha\beta\gamma, d) C_{\alpha\beta\gamma}^{lsn} Q_\alpha^l(m) Q_\beta^s(m) O_{\gamma d}^n(m)
\tag{17.32}
$$

where $C_{\alpha\beta\upsilon}^{lmn}$ denote the cubic Clebsch–Gordan coefficients. This equation contains in a transparent way the correct combinations of $\varepsilon_{\alpha\beta}^m$, $\omega_{\alpha\beta}^m$ and $O_{\alpha\beta}^n(m)$. However the relations between the different g_1, g_2 which are necessary to ensure rotational invariance are not apparent here (see Thalmeier and Fulde (1975).

In order to describe the interaction of the RE-ions with homogeneous and inhomogeneous deformations in a condensed form it is advantageous to introduce phonons. We shall derive this interaction for acoustic phonons (Dohm and Fulde 1975). An extension to optical phonons is straightforward but is not considered here explicitly. In the harmonic approximation the lattice hamiltonian is given by

$$
H_{\text{phonon}} = \sum_{q,\mu} \omega_{q\mu}^0 (a_{q\mu}^+ a_{q\mu} + \tfrac{1}{2})
\tag{17.33}
$$

where $a_{q\mu}^+$, $a_{q\mu}$ are the creation and destruction operators for phonons of wave vector $\boldsymbol{q}$, polarization index $\mu = 1, 2, 3$ and mode frequency $\omega_{q\mu}^0$. The deformation tensor is written in terms of phonons as

$$
v_{\alpha\beta}^m = \mathrm{i} \sum_{q\mu} \frac{e_\alpha(q\mu) q_\beta}{(2MN\omega_{q\mu}^0)^{1/2}} \exp(\mathrm{i}\boldsymbol{q}\boldsymbol{R}_m^{(0)}) (a_{q\mu} + a_{q\mu}^+)
\tag{17.34}
$$

Here $e_\alpha(q\mu)$ is the α-component of the unit-polarization vector of the mode $(q\mu)$ and M is the mass of the ions in the assumed Bravais lattice. Furthermore we write

$$
H_{\text{Rot}}(\boldsymbol{J}^m) + H_{\text{Strain}}(\boldsymbol{J}^m) = V_1^m + V_2^m
\tag{17.35}
$$

where V_1^m and V_2^m denote the contributions which are first and second order in

the phonon operators. It is

$$V_1^m = \sum_{q\mu} V_1(\boldsymbol{J}^m;\ q\mu)\exp(\mathrm{i}\boldsymbol{q}\boldsymbol{R}_m^{(0)})\,(a_{q\mu} + a^+_{-q\mu})$$

$$V_2^m = \sum_{\substack{q\mu \\ q\mu}} V_2(\boldsymbol{J}^m;\ q\mu,\ q'\mu')\exp[\mathrm{i}(\boldsymbol{q}+\boldsymbol{q}')\boldsymbol{R}_m^{(0)}](a_{q\mu} + a^+_{-q\mu})(a_{q'\mu'} + a^+_{-q'\mu'}) \qquad (17.36)$$

The functions V_1 and V_2 are obtained from eqs. (17.27, 17.29). With the notation

$$Q^+_{\alpha\beta} = \tfrac{1}{2}[e_\alpha(q\mu)q_\beta + e_\beta(q\mu)q_\alpha], \qquad Q^-_{\alpha\beta} = \tfrac{1}{2}[e_\alpha(q\mu)q_\beta - e_\beta(q\mu)q_\alpha] \qquad (17.37)$$

one finds

$$V_1(\boldsymbol{J}^m;\ q\mu) = \mathrm{i}(2MN\omega^0_{q\mu})^{-1/2}\{G_{\alpha\beta}(\boldsymbol{J}^m)Q^+_{\alpha\beta} - V_{\alpha\beta}(\boldsymbol{J}^m)Q^-_{\alpha\beta}\} \qquad (17.38)$$

and a similar expression for $V_2(\boldsymbol{J}^m;\ q\mu,\ q'\mu')$. Since the latter is very lengthy we do not write it down explicitly but refer instead to Dohm and Fulde (1975).

The rotations $\omega_{\alpha\beta}$ correspond to $Q^-_{\alpha\beta}$ and can be easily identified. Similarly $\varepsilon_{\alpha\beta}$ and $Q^+_{\alpha\beta}$ correspond to each other. In the conventional linear strain theory only the first term in the expression for $V_1(\boldsymbol{J}^m;\ q\mu)$ is kept. Even there only the terms of second degree in $\boldsymbol{J}$ are kept although there are also fourth- and sixth-degree contributions. This may lead to several shortcomings. The following statements hold true:

a) Only in the absence of a magnetic field and in the limit $q \to 0$ (homogeneous deformations) may the rotational terms be neglected. But even in that case one must keep the second order strain terms since generally they will give as large contributions to the elastic constants and the phonon dispersion as the linear strain contributions. However their temperature dependence is much weaker than that of the first order strain contribution.

b) In the presence of a magnetic field the rotational contributions are as big as the magnetic field dependent changes of the strain contributions. Their neglectance leads then to unreliable results. In taking into account the rotational terms it is crucial to keep the second order contributions since the coupling constants $G_{\alpha\beta}$ and $G_{\alpha\beta\gamma\delta}$ and furthermore $V_{\alpha\beta}$ and $V_{\alpha\beta\gamma\delta}$ are related to each other. An omittance of the second-order rotational terms destroys rotational invariance.

c) Even in zero external field the rotational terms contribute to the phonon dispersion curves for finite q-values. However for the examples which have been studied explicitly so far they gave corrections of only a few percent. There is no reason, however, that this must be always so.

d) The fourth- and sixth-degree contributions in $\boldsymbol{J}$ to the magneto-elastic interaction can give appreciable contributions and therefore should not be neglected. They can be calculated from eq. (17.24) for any given crystal-field potential.

The formal description of the phonon-RE ion interaction developed here will be used in section 5,2 extensively.

3.2. *Interactions with conduction electrons*

The conventional interaction which is usually assumed to take place between RE-ions and conduction electrons is the isotropic exchange interaction of the form $-2J_{ex}sS_{4f}$. Here s, S_{4f} denote the conduction electron and RE-ion spin. In terms of electron creation and annihilation operators $c^+_{k\sigma}$, $c_{k\sigma}$ the interaction hamiltonian is written as

$$H_{ex} = -\sum_{kk'} J_{ex}(g-1)\{J_z(c^+_{k'\uparrow}c_{k\uparrow} - c^+_{k'\downarrow}c_{k\downarrow}) + J_+c^+_{k'\downarrow}c_{k\uparrow} + J_-c^+_{k'\uparrow}c_{k\downarrow}\} \tag{17.39}$$

where J_{ex} is the exchange integral. In terms of the operators $a^+_i(l)$, $a_i(l)$ which describe the CEF-energy levels we can write H_{ex} for a system of ions at positions $\boldsymbol{R}_l$ as

$$H_{ex} = \sum_{lq} \exp(i\boldsymbol{q}\boldsymbol{R}_l) \sum_{\substack{ij \\ k\sigma\sigma'}} M_{ij\sigma\sigma'} a^+_i(l) a_j(l) c^+_{k+q\sigma'} c_{k\sigma} \tag{17.40}$$

where $M_{ij\sigma\sigma'}$ is the transition matrix element.

The finite extension of the 4f-wave functions is responsible that anisotropic parts of the exchange and Coulomb scattering interaction may become important (see for example Liu, 1951, Kaplan and Lyons, 1963). They are discussed in ch. 3 section 2. Since they will be used in the present chapter at several places we give a brief summary by using a very systematic and elegant formulation due to Hirst (1978). According to his theory the general conduction electron-4f (k–f) interaction can be written as

$$H_{k\text{-}f} = \sum_i \sum_{\substack{\Lambda\Sigma \\ \mu\nu}} \sum_{\substack{kl \\ k'l'}} \exp(i(\boldsymbol{k}-\boldsymbol{k}')\boldsymbol{R}_i) H^{\Lambda\Sigma}_{\mu\nu,klk'l'} \tag{17.41}$$

where as before $\boldsymbol{R}_i$ denotes the positions of the ions. It is

$$H^{\Lambda\Sigma}_{\mu\nu,klk'l'} = J^{ll'\Lambda\Sigma}(B^{\Lambda\Sigma}_{\mu\nu})^+ C^{\Lambda\Sigma klk'l'}_{\mu\nu} \tag{17.42}$$

Here $B^{\Lambda\Sigma}_{\mu\nu}$ is a dimensionless unit tensor operator acting in the 4f-electrons. It transforms under rotations like an angular momentum state with total angular momentum Λ and z-component μ and under spin rotations like an angular momentum Σ with z-component ν.

The $C^{\Lambda\Sigma klk'l'}_{\mu\nu}$ consist of a sum of products $c^+_{k'l'm'\sigma'}c_{klm\sigma}$ where l,l' combine to Λ, furthermore $-m'$ and m to μ and similarly the spins to Σ,ν. They describe the scattering of the conduction electrons from states $|klm\sigma\rangle$ into states $|k'l'm'\sigma'\rangle$.

The orbital rank, Λ, of the spherical double-tensors can be 0 to 6 and Σ can be 0 or 1. $H_{k\text{-}f}$ describes the scattering of conduction electrons by the $4f$-shell and Λ, μ and Σ, ν specify the exchange of orbital and spin momentum between both systems. The $J^{ll'\Lambda\Sigma}$ denote the coupling strengths of the different interactions. Before we give some specific examples let us mention that in case that we are considering only the lowest J-multiplet it is advantageous to project the spherical double tensors $B^{\Lambda\Sigma}_{\mu\nu}$ onto new spherical single tensors B^Q_M. Hereby

$$B_{\mu\nu}^{\Lambda\Sigma} = \sum_{Q=|\Lambda-\Sigma|}^{|\Lambda+\Sigma|} \sum_{M=-Q}^{Q} \alpha_{\Lambda\Sigma}^{QM} B_M^Q \tag{17.43}$$

The B_M^Q can be directly expressed in terms of J-operator products. Within the formalism just outlined the spherical Coulomb interaction is specified by $(\Lambda, \Sigma) = (0, 0)$ with $l' = l$. The isotropic exchange interaction with a q-independent J_{ex} is characterized by $(\Lambda, \Sigma) = (0, 1)$ and $l = l' = 0$. $\Lambda = 0$ implies that it is not depending on the orbital moment and $\Sigma = 1$ states that the spin part transforms like a vector (tensor of rank equal to one).

Another type of interaction which has obtained some attention is the quadrupolar Coulomb scattering (see for example Fulde et al. 1970). It is specified by $(\Lambda, \Sigma) = (2, 0)$. One can write it as

$$H_{AC} = \sum_{\sigma} \sum_{m=-2}^{+2} I_2(k's;kd) \left(\frac{5}{4\pi}\right)^{1/2} Q_2 \left\{ y_2^m(\boldsymbol{J}) c_{k's\sigma}^{+} c_{kdm\sigma} + h.c. \right\} \tag{17.44}$$

Here I_2 is a Coulomb integral as defined in Fulde et al. (1970). Q_2 is the quadrupole moment of the RE-ion as listed in the same reference. The $y_2^m(\boldsymbol{J})$ are operators bilinear in J. It is

$$y_2^{\pm 2} = (J^{\pm})^2/N, \qquad y_2^{\pm 1} = \mp (J_z J^{\pm} + J^{\pm} J_z)/N,$$
$$y_2^0 = (\tfrac{2}{3})^{1/2}(3J_z^2 - J(J+1))/N$$

with $N = (\frac{2}{3})^{1/2}(2J^2 - J)$. The conduction electrons are characterized by the quantum numbers k, l, m, σ and for simplicity we have assumed in eq. (17.44) only s-wave scattering into d-wave scattering and vice versa. More correctly one should also include p–p, d–d scattering etc. While the isotropic exchange interaction leads to a spin polarization around the RE-ion the quadrupolar Coulomb scattering leads to a quadrupole polarization of the conduction electron system around the RE-ions. Similarly one can consider interactions of the type $(\Lambda, \Sigma) = (1, 0)$, $(2, 1)$ etc.

The isotropic exchange interaction and the aspherical Coulomb scattering have different selection rules for CEF-energy level transitions. This is demonstrated in table 17.3 for cubic point symmetry. The corresponding table for hexagonal symmetry D_6 can be found in Fulde et al. (1970). The k–f interaction modifies the one-ion susceptibility. It leads to a shift of the CEF-eigenstates and to a line broadening. For the special case of two singlets it was shown by Fulde and Peschel (1972) and Schotte (1975) that eq. (17.23) is changed into

$$u(\omega, T) = -\frac{2\delta |M|^2 \tanh(\delta/2T)}{\omega^2 - \delta^2 - \Delta^2 + i\gamma\omega} \tag{17.45}$$

where Δ^2 and γ are given by

$$\Delta^2 = -16\delta^2 M^2 [N(0) J_{ex}]^2 (g-1)^2 \{\log(D/2\pi T) - \mathrm{Re}\, \Psi(i\delta/2\pi T)\}$$
$$\gamma = 4\pi M^2 [N(0) J_{ex}]^2 (g-1)^2 \delta \coth(\delta/2T) \tag{17.46}$$

Here $H_{k\text{-}f}$ has been restricted to H_{ex}. D is the conduction-electron band width and $N(0)$ is the electron density of states. Furthermore $\Psi(z)$ denotes the

TABLE 17.3
Selection rules for k–f interactions of type $(\Lambda, \Sigma) = (0, 1)$ and $(2, 0)$ in cubic symmetry

Irreducible representation	Connected by exchange scatt. (0, 1) to	Connected by aspheric. Coulomb scatt. (2, 0) to
Γ_1	Γ_4	Γ_3, Γ_5
Γ_2	Γ_5	Γ_3, Γ_4
Γ_3	Γ_4, Γ_5	$\Gamma_1, \Gamma_2, \Gamma_3, \Gamma_4, \Gamma_5$
Γ_4	$\Gamma_1, \Gamma_3, \Gamma_4, \Gamma_5$	$\Gamma_2, \Gamma_3, \Gamma_4, \Gamma_5$
Γ_5	$\Gamma_2, \Gamma_3, \Gamma_4, \Gamma_5$	$\Gamma_1, \Gamma_3, \Gamma_4, \Gamma_5$

digamma function. The special feature one should notice is that γ reduces to the Korringa broadening ($\gamma \sim T$) for $T \gg \delta$ while it approaches a constant for $T \ll \delta$. This is very different to the usual Korringa relaxation (see also Rainford 1969).

3.3. *Effective-interaction models*

The interactions of the RE-ions with phonons and conduction electrons cause indirect interactions between different RE-ions. Phonons and conduction electrons serve as medium for these interactions. In the effective-interaction model they are eliminated and replaced by an ion – ion interaction. Since the latter is an instantaneous interaction all retardation effects are lost which are connected with the dynamical properties of the medium. This shows the limitations of the effective interaction model. The isotropic exchange interaction as described by eq. (17.40) leads to an effective ion – ion interaction of the form

$$H_{\text{int}} = -\tfrac{1}{2}\sum_{ij} J_{ij}^{\text{ex}} \boldsymbol{J}^i \cdot \boldsymbol{J}^j \tag{17.47}$$

which is of the Heisenberg type. This interaction is responsible for magnetic phase transitions in RE-ion systems. The quadrupolar Coulomb interaction as given by eq. (17.44) and the interactions with phonons lead to an ion–ion interaction which for a cubic lattice is of the form

$$H_{\text{int}} = -\tfrac{1}{2}\sum_{ij} K_{ij}(\alpha d) O_{\alpha d}^n(i) O_{\alpha d}^n(j) \tag{17.48}$$

Here the $O_{\alpha d}^n(i)$ denote tensor cubic operators defined before. The interaction given by eq. (17.48) is responsible for quadrupolar phase transitions in RE-systems.

The other k–f interactions (Λ, Σ) lead in a similar way to effective ion–ion interactions. These interactions consist of products of $B_M^Q(i) \cdot B_M^Q(j)$ operators which were defined before. They may lead to higher multipole phase transitions which however have not yet been found experimentally. Therefore we will discard these interactions in the following. Their formal treatment is very similar to those described by eqs. (17.47) and (17.48).

4. Effects on conduction electrons

This section deals with the influence of crystal-field split RE-ions on the properties of conduction electrons. Where it is necessary we shall distinguish between RE-ions put as impurities into a metallic matrix and ions forming a regular lattice. In the former case the matrix may be normal or superconducting. Particular attention will be paid to effects which result from the internal degree of freedom of the impurities. The Kondo effect is the best known example of this kind and it may occur if the ground state is degenerate. Here we will concentrate our attention on impurities with two low lying singlet crystal field states and will study the many-body effects which will result in that particular situation. It will be shown that they are qualitatively different to the Kondo problem. The thermoelectric power is a characteristic example for demonstrating this. If the matrix is a superconductor then it is well known that magnetic impurities destroy superconductivity. Again one would like to know how the crystal-field splitting of the lowest J multiplet changes the nature of the pair-breaking effect of the RE-ions. It will be shown that the pair-breaking effect of a single ion is now a temperature dependent quantity while it is a constant in the absence of crystal-field splitting. This leads to many interesting differences for the two situations and there is a considerable number of experiments which demonstrate these.

4.1. *Normal metals*

4.1.1. *Electrical conductivity*

The electrical conductivity is related to a current–current correlation function. In order to evaluate it we write the interaction hamiltonian in the form

$$H_{\text{int}} = \sum_{l,q} e^{iqR_l} \sum_{\substack{ijk \\ \sigma\sigma'}} M_{ij,\sigma\sigma'}(q) a_i^\dagger(l) a_j(l) c^\dagger_{k+q,\sigma} c_{k,\sigma'} \tag{17.49}$$

where $M_{ij,\sigma\sigma'}(q)$ is the matrix element for the transition between states $|j\rangle$, $|i\rangle$ of the RE-ions situated at positions R_l. For the particular case of q-independent matrix elements $M_{ij,\sigma\sigma'}$ (this implies a δ-function type of interaction and excludes therefore interactions involving orbital degrees of freedom) the evaluation of the conductivity leads to particularly simple results. One finds

$$\sigma(T) = \frac{Ne^2}{m} \int_{-\infty}^{+\infty} d\omega \left(-\frac{\partial f}{\partial \omega}\right) \tau(\omega) \tag{17.50}$$

where N is the conduction electron density and $\tau(\omega)$ is the frequency (and temperature) dependent lifetime of the electrons. It is related to the self-energy $\Sigma_R(\omega)$ of the conduction electron via

$$\text{Im}\, \Sigma_R(\omega) = -1/2\tau(\omega) \tag{17.51}$$

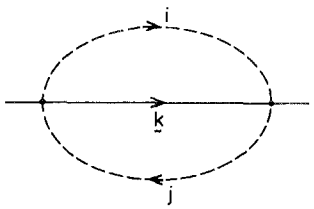

Fig. 17.6. Second order diagram for the conduction electron self-energy due to the interaction with CEF split ions. i, j denote different CEF levels. The solid line is the propagating electron.

and can be calculated by computing the former to the required order in M_{ij}. Hereby one has to distinguish between the dilute impurity case and the case of a regular lattice.

Dilute alloy. Early calculations are due to Hirst (1967). To second order in M_{ij} (see fig. 17.6) one finds for the contribution linear in the impurity concentration n_1

$$\operatorname{Im} \Sigma_{\mathrm{R}}^{(2)}(\omega) = -\tfrac{1}{2}\pi n_1 N(0) \sum_{ij} |M_{ij}|^2 \left((n_i + n_j) + (n_j - n_i) \tanh \frac{\omega - \delta_{ij}}{2T} \right) \tag{17.52}$$

The reciprocal lifetime consists of two parts. One part takes into account the elastic scattering processes within the levels while the other part describes the inelastic processes. It is seen that as ω increases above δ_{ij} new scattering channels are opened. This is demonstrated nicely in fig. 17.7 (see Hessel Andersen et al., 1974) where the experimental results for the alloy $\mathrm{Tb}_x\mathrm{Y}_{1-x}\mathrm{Sb}$

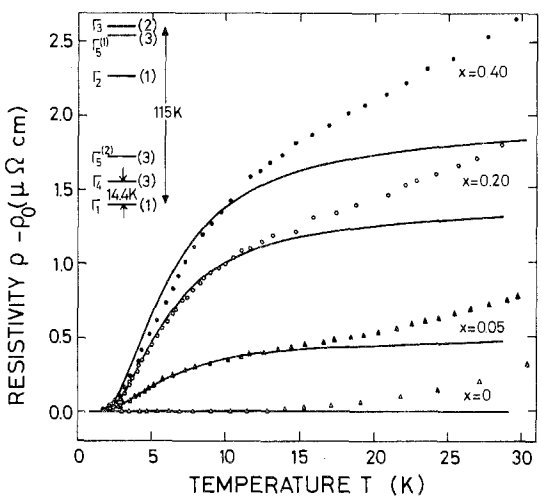

Fig. 17.7. Resistivity as function of temperature for $\mathrm{Tb}_x\mathrm{Y}_{1-x}\mathrm{Sb}$. The residual resistivity has been subtracted. The solid lines correspond to a theoretical plot using the indicated level scheme (from Hessel Andersen et al., 1974).

($x \ll 1$) are shown. For a given CEF-level scheme and isotropic Coulomb and exchange interaction one can evaluate $\sigma(T)$ by inserting eq. (17.52) into (17.50) and performing the ω-integration numerically. It is interesting to realize that for an appropriate CEF-level scheme one can obtain a resistivity minimum in first order Born approximation. This is seen immediately for a ground state Γ_5 and a first excited state Γ_1. At low temperatures only Γ_5 is occupied which strongly scatters the conduction electrons. At higher temperature also Γ_1 is populated which scatters much weaker. Therefore the total scattering rate can be smaller at finite temperatures than at $T = 0$. Sometimes in eq. (17.50) $(-\partial f/\partial\omega)$ has been replaced by a δ-function (Rao and Wallace, 1970). Although this has computational advantages it causes quantitative inaccuracies in the results.

In the presence of additional non-magnetic scattering centers Matthiessen's rule holds only approximately. For details we refer to Fulde and Peschel (1972).

If interactions are included which involve orbital degrees of freedom eq. (17.50) has to be slightly modified to include angular integrations. If one computes $\mathrm{Im}\,\Sigma_R(\omega)$ to third order in the electron–ion interaction one enters into the Kondo problem and how it is influenced by crystal-field splitting. This problem was investigated in detail by Cornut and Coqblin (1972) and earlier by Maranzana (1970). A prerequisite thereby is that one is dealing either with Kramers ions or with a ground state which is degenerate by symmetry. Theoretical and experimental attention has been focused mainly on Ce impurities. We shall not discuss those results but refer to ch. 11, section 3.2 instead.

Concentrated system. If the RE-ions form a regular lattice then the conduction electron Bloch states are eigenstates to the periodic part of the scattering potential. The scattering is then caused by the internal degree of freedom of the RE-ions (spin-disorder scattering). $\sigma(T)$ is again calculated from eq. (17.50). In case that the interactions between the RE-ions may be neglected $\mathrm{Im}\,\Sigma_R(\omega)$ is given by an expression similar to eq. (17.52) where n_I has been replaced by one and the matrix elements M_{ij} are formed with $\boldsymbol{J} - \langle \boldsymbol{J} \rangle$ instead of only $\boldsymbol{J}$. The brackets indicate a thermal average. In case that the ions are strongly interacting so that the CEF excitations form excitation bands it is simpler to work with the resistivity instead of the conductivity. The former can be expressed (Fulde and Peschel, 1972) as

$$\rho = a \int \mathrm{d}q\, q^3 \int \mathrm{d}\omega\, \mathrm{Im}\,\chi(\boldsymbol{q}, \omega)\, \frac{\omega}{T}\, n(\omega)(n(\omega) + 1)$$

Here a is a constant proportional to the square of the electron–ion exchange constant and $n(\omega)$ is a Bose factor. The function $\chi(\boldsymbol{q}, \omega)$ is the wave number and frequency dependent susceptibility of the interacting RE-ions. It is discussed at length in section 5.1.1 (see for example eq. 17.82). The above expression has been used successfully by Hessel Andersen et al. (1976) to analyse their data for $Tb_xY_{1-x}Sb$.

Calculations of the conductivity due to the interaction $(\Lambda, \Sigma) = (2, 0)$ are due to Elliott (1954) and Sablik et al. (1972).

4.1.2. *Thermal conductivity*

The thermal conductivity is related to a heat current – heat current correlation function. It is therefore given by an expression very similar to eq. (17.50) namely

$$\kappa(T) = \frac{N}{mT}\int_{-\infty}^{+\infty} d\omega\, \omega^2 \left(-\frac{\partial f}{\partial \omega}\right) \tau(\omega) \tag{17.53}$$

The integral can be evaluated numerically by using the expression (17.51–17.52) for $\tau(\omega)$. For the concentrated system the same modifications have to be made as before. The only experimental results available are by Wong and Lüthi (1976). Their results for TmSb are shown in fig. 17.8 together with a theoretical plot due to Thalmeier (1977). By comparison with the measurements on LaSb one can subtract off contributions from phonons etc.

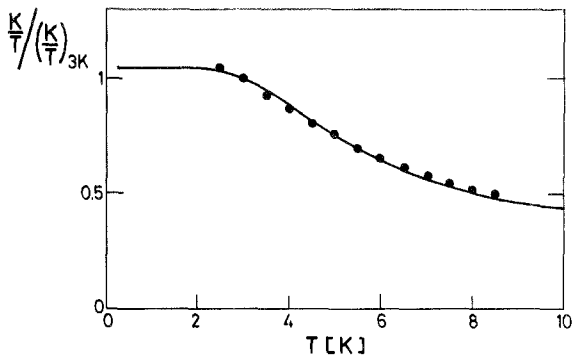

Fig. 17.8. Thermal conductivity for TmSb due to Wang and Lüthi (1976). The solid line is a theoretical plot due to Thalmeier (1977). Thereby the CEF-level scheme was used as given by Birgeneau et al. (1971). The only fit parameter is the ratio of the electron scattering rates due to RE-ions and other impurities.

4.1.3. *Thermoelectric power*

It is well known that the thermoelectric power can be a very sensitive tool for studying scattering processes. To demonstrate this we write it in the form

$$Q = -\frac{Ne}{m\sigma T}\int_{-\infty}^{+\infty} d\omega \left(-\frac{\partial f}{\partial \omega}\right) \omega \left(1 + \frac{a\omega}{E_F}\right) \tau(\omega) \tag{17.54}$$

The term $(1 + a\omega/E_F)$ results from changing a momentum summation Σ_k into an energy integration $\int d\omega$ thereby replacing k^2 by $k_F^2[1 + a\omega/E_F]$, where a is a measure of the variation of the electron density of states near E_F. The ω-factor in the integrand is a consequence of Q being related to a current – heat current correlation function. As a consequence the thermopower would vanish for an energy independent electronic lifetime $\tau(\omega) = \tau_0$ were it not for the fact that the small energy variation of the electronic density of states near E_F leads to a finite contribution proportional to T/E_F. This is the reason why the thermoelectric

power of a metal

$$Q_0 = \frac{a^2 \pi T}{3eE_F} \tag{17.55}$$

is usually so small.

However if there is an electronic scattering mechanism present which leads in $\tau(\omega)$ to a term proportional to ω then one does not need the small term $a\omega/E_F$ in order to obtain a nonvanishing thermoelectric power. For example the giant thermopowers of Kondo systems are due to that effect. As will be demonstrated below there are also anomalies in the thermopower due to CEF-splitting.

Dilute alloys. We consider for simplicity again a RE-ion with two singlets as lowest lying crystal-field states. Their energy separation is δ. Furthermore we assume that the elastic charge scattering is the same for both levels. From eq. (17.52) it is seen that $\mathrm{Im}\,\Sigma_R^{(2)}(\omega)$ does not contain odd powers in ω and hence there will be no anomaly in $Q(T)$ to that order. However this is different if we calculate the self energy to third order in the interaction as shown in fig. 17.9. By keeping only the leading terms one finds (Peschel and Fulde, 1970)

$$\mathrm{Im}\,\Sigma_R(\omega) = -\pi n_I N(0) M_e^2 + \pi n_I N^2(0) M_e M_i^2 \tanh\frac{\delta}{2T}[h(\omega-\delta) - h(\omega+\delta)] \tag{17.56}$$

Here M_e, M_i denote the matrix elements for elastic and inelastic scattering and $M_e \gg M_i$. Furthermore the function $h(x)$ is defined by

$$h(x) = P\int_{-D}^{+D} \frac{d\epsilon}{\epsilon - x} \tanh\frac{\epsilon}{2T} \tag{17.57}$$

where P denotes the principal value of the integral and $2D$ is the line width of the conduction band. The factor $\tanh \epsilon/2T$ in the integrand has its origin in the Fermi-distribution function. It represents a many body effect since it is due to the fact that the Pauli principle enters in the scattering rate of a conduction electron. From eq. (17.56) it is seen that the effect vanishes as δ approaches zero. It is proportional to the difference in population of the two singlet crystal-field states. This demonstrates its difference to the many-body effect which one encounters in the Kondo problem. For small values of ω one finds

$$h(\omega-\delta) - h(\omega+\delta) = 4\omega/\delta \qquad (\omega, T \ll \delta) \tag{17.58}$$

Fig. 17.9. Third order contributions to the electron self-energy. Solid and dashed lines correspond to electron and impurity propagators, respectively.

which gives the required odd power in ω. Usually $(M_i/M_e)^2 \ll 1$ (the isotropic Coulomb scattering is considerably larger than the isotropic exchange scattering). Then the result for Q can be written as

$$Q = Q_0 + Q_1 \tag{17.59}$$

where

$$Q_1 = -\frac{4N(0)M_i^2}{eM_e}\frac{\delta}{2T}\tanh\frac{\delta}{2T}\left[1+\frac{\delta}{2\pi T}\,\mathrm{Im}\,\psi^{(1)}\left(\frac{i\delta}{2\pi T}\right)\right] \tag{17.60}$$

Here $\psi^{(1)}(x)$ denotes the trigamma function. The function

$$H(T/\delta) = \frac{\delta}{2T}\tanh\frac{\delta}{2T}\left[1+\frac{\delta}{2\pi T}\,\mathrm{Im}\,\psi^{(1)}\left(\frac{i\delta}{2\pi T}\right)\right] \tag{17.61}$$

has a maximum at $T \simeq 0.3\delta$ and is shown in fig. 17.10. At the maximum the ratio

$$Q_1/Q_0 \simeq 4N(0)(M_i^2/M_e)(E_F)\delta).$$

Thus one expects a low temperature anomaly in the thermopower due to the crystal-field splitting. Such an anomaly has indeed been observed by Umlauf et al. (1973) on $La_{1-x}Tb_xAl_2$. Their experimental findings are shown in fig. 17.11. The ground state of Tb is a nonmagnetic doublet Γ_3 with a first excited state (Γ_4) at 5 K. This requires a generalization of eq. (17.60). Under the assumption that the elastic Coulomb scattering is the same for each level one finds for a multi-level system

$$Q_1 = -\frac{1}{2e}\sum_{ij}\alpha_{ij}\frac{\delta_{ij}}{2T}(n_j - n_i)\left[1+\frac{\delta_{ij}}{2\pi T}\,\mathrm{Im}\,\psi^{(1)}\left(\frac{i\delta_{ij}}{2\pi T}\right)\right] \tag{17.62}$$

where $\alpha_{ij} = 4N(0)\ M_{ij}^2/M_e$. If the ground state is degenerate and magnetic the effect described above may be masked by the anomalous contribution calculated by Kondo (1967), Fischer (1967), Maki (1969) and Chow and Everts (1969).

Concentrated systems. The extension of the theory from the dilute alloy case to concentrated systems leads to interesting new results. We have seen that for

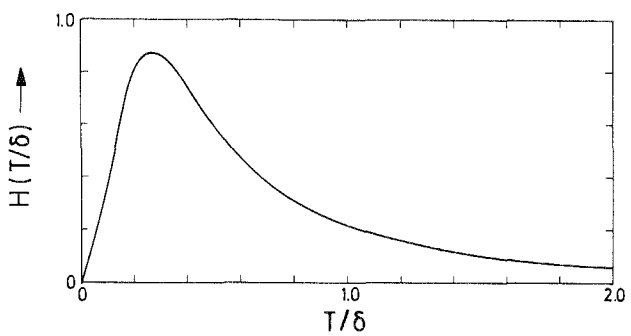

Fig. 17.10. $H(T/\delta)$ as function of T/δ (from Peschel and Fulde, 1970).

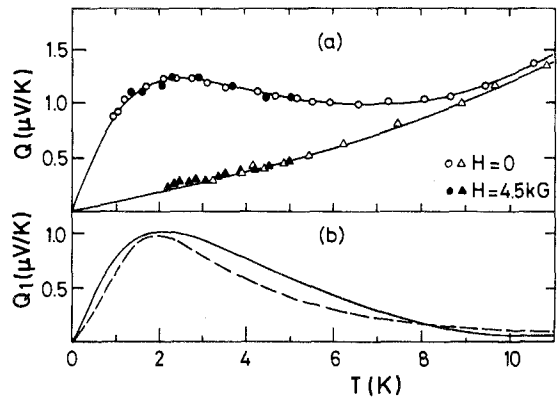

Fig. 17.11. (a) Thermoelectric power of $La_{1-x}Tb_xAl_2$ for $x = 0.02$ (circles) and $x = 0$ (triangles). (b) The anomalous contribution Q_1: experiment (solid line) and theoretical curve (dashed line) (from Umlauf et al., 1973).

dilute alloys the anomalous contribution to the thermopower Q_1 is proportional to $J_{ex}^2 V(M_e \sim V, M_i \sim J_{ex})$. However for the regular lattice case the Bloch electrons are eigenstates to the periodic potential and therefore there is no elastic scattering resulting from the isotropic Coulomb interaction.

The situation is different if the generalized k–f interactions are considered. In that case the elastic scattering may be different for the ground state and the excited state. The periodic part $\langle V \rangle$ of the elastic scattering processes is taken into account by the introduction of the Bloch electrons. It is

$$\langle V \rangle = n_g V_g + n_e V_e$$

where n_g, n_e are the occupational probabilities for the ground state and the excited state. $V_{g,e}$ are the corresponding elastic scattering potentials. The electron relaxation rate $\tau(\omega)$ is again calculated up to third order in the electron-RE ion interaction. One obtains for the scattering rate (Takayama and Fulde, 1975)

$$\tau^{-1}(\omega) = 2\pi N(0)\Big\{M_i^2 I\left(\frac{\omega}{T}, \frac{\delta}{T}\right) + M_e^2 L(\delta/T) + N(0)M_e M_i^2\Big[2L(\delta/T) - \tfrac{1}{2}I\left(\frac{\omega}{T}, \frac{\delta}{T}\right)\Big][h(\omega+\delta) - h(\omega-\delta)]\Big\} \tag{17.63}$$

where

$$L(x) = e^x(1+e^x)^{-2} \tag{17.64}$$

$$I(x, x_0) = 1 - \tfrac{1}{2}\tanh\frac{x_0}{2}\left(\tanh\frac{x+x_0}{2} - \tanh\frac{x-x_0}{2}\right)$$

Furthermore $M_e = V_e - V_g$. The first two terms in eq. (17.63) are due to the ordinary Born approximation and correspond to the calculations given in section

4.1.1. The last term is due to the second-order Born approximation and is again odd in ω. It vanishes for $V_e = V_g$. By setting eq. (17.63) into (17.54) one obtains again an anomalous contribution Q_1. Numerical results can be found in Takayama and Fulde (1975). They look very similar to $H(T/\delta)$ except that the maximum appears now at $T \simeq 0.5\delta$. Experimental results are shown in fig. 17.12 for $PrPb_3$ and TmCd (Sierro et al., 1975). The crystal-field level scheme for these systems is known from a specific heat measurement and in the case of TmCd from a weak resistance anomaly (see Lüthi et al., 1973). One notices that the anomaly in the thermopower is positive for TmCd and negative for $PrPb_3$. This is in agreement with the theoretical result that the effect occurs in third order perturbation theory. Thus it can have either sign depending on the sign of $V_g - \langle V \rangle$. The point which has been left open until now is which of the generalized k–f interactions $H^{(\Lambda,\Sigma)}$ discussed in section 3.2 will lead to the required eq. (17.63). Although we must refer to Takayama and Fulde (1975) for a detailed analysis we state here some of the results. Let us start from the generalized interactions after the projection of the spherical double tensors $B^{\Lambda\Sigma}$ onto new spherical single tensors B^Q has been performed.

The following two rules are found:

a) A third order process characterized by $\Pi_{i=1}^{3}(B^{Q_i}C^{\Lambda_i\Sigma_i})$ contributes to the electron-relaxation time only if the corresponding operator product contains an invariant i.e. a tensor of type 0 or (0, 0) for single or double tensors, respectively. The operator products are found by the usual rules for combining angular momenta.

b) Only those processes contribute to the anomalous thermopower Q_1 for which the parity of the product of the three electron operators is even. The parity of an operator $C^{\Lambda\Sigma}$ is even or odd depending on whether $\Lambda + \Sigma$ is even or odd.

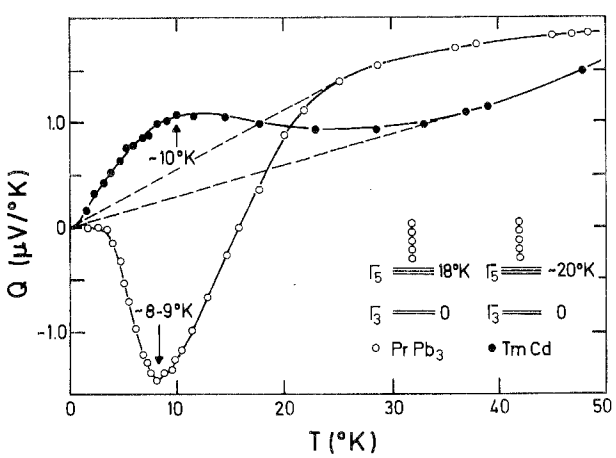

Fig. 17.12. Thermoelectric power as function of temperature for $PrPb_3$ and TmCd. Only the two lowest CEF levels are indicated (from Sierro et al., 1975). The five open circles indicate the higher CEF levels which are not explicitly shown.

Processes with odd parity contribute to the resistivity anomaly instead. No rigorous justification of this rule has been given, instead it has been derived by considering several explicit examples. It coincides with a conjecture of Hirst (private comm.). From the two conditions it follows immediately that the isotropic exchange interaction is excluded from being the origin of an anomalous Q_1. We consider now some specific examples for the ground state and first excited state:

Γ_1 singlet – Γ_4 triplet. Non-Kramers ions in a CEF of cubic symmetry have often a ground state Γ_1 and a first excited state Γ_4. Restricting ourselves to the lowest possible rank we obtain the elastic and inelastic processes from B^2 and B^1. This implies as the simplest example $H^{(2,0)} \cdot (H^{(1,0)})^2$.

Γ_1 singlet – Γ_5 triplet. Here an anomalous Q_1 may result from B^2 or $(H^{(2,0)})^3$. A similar situation holds for Γ_1 singlet – Γ_3 doublet.

Γ_3 doublet – Γ_5 triplet. In this case $H^{(2,0)}(H^{(1,1)})^2$ may give the anomalous thermopower.

The thermopower has been measured for a considerable number of compounds such as $PrCu_5$, $PrNi_2$, Pr_3Tl, $PrSn_3$, $PrPd_3$, TmSb and TmS. For a more detailed discussion we refer to Bucher et al. (1974).

4.2. *Superconducting alloys*

4.2.1. *General considerations*

It is well known that magnetic impurities have strong effects on superconductors. For example the superconductive transition temperature is decreased with increasing impurity concentration and eventually vanishes as the concentration exceeds a critical value. This is very different when compared to nonmagnetic impurities which have only a very weak effect on the transition temperature (see for example Markowitz and Kadanoff, 1963). The strong effect of magnetic impurities on the superconducting transition temperature is attributed to their tendency to break the Cooper pairs, which are responsible for the superconducting ground state. This is described by a pair-breaking parameter α which is a measure of the pair-breaking strength. The latter results from the fact that a magnetic impurity acts differently on the partners of a Cooper pair $(\boldsymbol{p}, \sigma_z = 1)$ and $(-\boldsymbol{p}, \sigma_z = -1)$. It is seen by inspection that for example the isotropic exchange interaction as given by eq. (17.39) has different signs for the two electrons forming a Cooper pair. As a result it will have a tendency of breaking them. More generally, since Cooper pairs are formed from electrons in time-reversed states, any interaction will break the pairs which is not invariant under time reversal symmetry as applied to the conduction electrons (i.e. $\boldsymbol{p} \rightarrow -\boldsymbol{p}$, $\boldsymbol{\sigma} \rightarrow -\boldsymbol{\sigma}$ etc.).

If the impurity is a RE-ion then with the exception of Ce and perhaps Eu and Yb one needs not to worry about complications which are connected with the Kondo effect (see ch. 11.3). Thus the first-order Born approximation is sufficient in calculating the conduction-electron scattering rates from the RE-ions.

For the case of randomly distributed magnetic impurities with a freely rotating

spin (i.e. no crystal-field splitting) the theory of Abrikosov and Gorkov (1960) describes very well their influence on superconductivity. Our aim here will be to demonstrate how the results of that theory are changed if the crystal-field splitting of the RE-ion is taken properly into account. Special attention will be paid thereby to non-Kramers ions in a singlet ground state. Here one expects particularly large effects since for level splittings much larger than the superconducting transition temperature all pair-breaking effects can result only from the virtual excitation of higher crystal-field energy levels. In a way this resembles the problem of electrons interacting with additional Einstein oscillators put into the matrix. The role of the phonon propagator is taken here by the frequency dependent single-ion Van Vleck susceptibility. But, while the interaction of the electrons with Einstein phonons leads to pair formation, the Van Vleck susceptibility leads to pair breaking. As mentioned above the reason is the non-time reversal invariance of the exchange interaction.

We shall also discuss possible new effects resulting from interactions other than the isotropic exchange interaction. For example all interactions (Λ, Σ) with $\Lambda + \Sigma =$ even are invariant under time-reversal symmetry and therefore do not break Cooper pairs. A representative is the aspherical Coulomb charge scattering $(\Lambda, \Sigma) = (2, 0)$. Via inelastic scattering processes those interactions can *enhance* superconductivity. This time the situation truly resembles the one of an additional number of Einstein oscillators put into a superconducting matrix. This also would lead to an enhancement of superconductivity. However there is no clear-cut experimental indication yet for the importance of those interactions. Such evidence would have to come from experiments which are sensitive to the different selection rules of the different interactions. Superconducting tunneling would be such an experiment.

4.2.2. *Dependence of T_c on impurity concentration*

We start from the Abrikosov–Gorkov theory and its predictions for T_c. In that theory the effect of the randomly distributed magnetic scattering centers of concentration n_I is characterized by a pair-breaking parameter α which is given by

$$\alpha = (\tau_s \Delta_0)^{-1} \tag{17.65}$$

with

$$\tau_s^{-1} = 2\pi n_I N(0)(g-1)^2 J(J+1) J_{ex}^2 \tag{17.66}$$

Hereby Δ_0 is the superconducting order parameter at $T = 0$ in the absence of any impurities. Furthermore an isotropic exchange interaction has been assumed. The dependence of T_c as function of n_I or α is shown in fig. 17.13. α_{crit} denotes the critical value of the pair-breaking parameter α beyond which superconductivity can no longer exist. It is $\alpha_{crit} = \frac{1}{2}$. The functional dependence of T_c (n_I) is described by

$$\ln(T_c/T_{c0}) + \psi(\tfrac{1}{2} + (2\pi T_c \tau_s)^{-1}) - \psi(\tfrac{1}{2}) = 0 \tag{17.67}$$

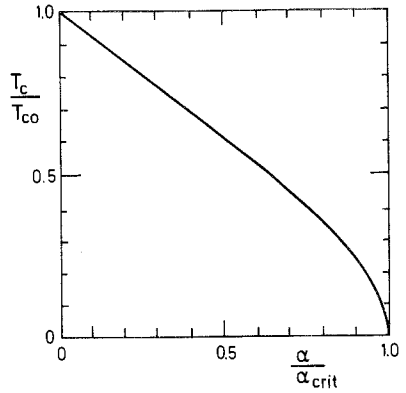

Fig. 17.13. T_c/T_{c0} as function of the pair-breaking parameter α/α_{crit} as predicted by the theory of Abrikosov and Gorkov (1960).

where $\psi(x)$ denotes the digamma function. Systems such as $La_{1-x}Gd_xAl_2$ are well described by that equation.

Next we consider systems with RE-impurities in a singlet ground state. Examples are $La_{1-x}Pr_xPb_3$, $(La_{1-x}Pr_x)_3$ In, $La_{1-x}Pr_xSn_3$ and many others. The first measurements on such systems were done by Bucher et al. (1968). It is instructive to consider first the dilute impurity concentration limit (Fulde et al., 1970). From it we can learn how the initial slope dT_c/dn_I at $T_c = T_{c0}$ depends on the splitting energy for example between the ground state Γ_1 and the excited state Γ_4.

The simplest case is that of RE-ions with two singlets separated by an energy δ. Of interest is then to know, how the pair-breaking parameter α depends on the ratio δ/T_c. One expects to recover the Abrikosov–Gorkov result for $\delta/T_c \to 0$. For $\delta/T_c \to \infty$ the pair-breaking parameter should go to zero since in that case one is left with the problem of non-magnetic impurities (the other crystal-field levels are no longer virtually excited). The calculations can be done with the help of the Green's function method. The results for the dilute concentration limit are shown in fig. 17.14. Here $y = -(8/\pi)T_c\tau_s \ln T_c/T_{c0}$ is plotted as function of

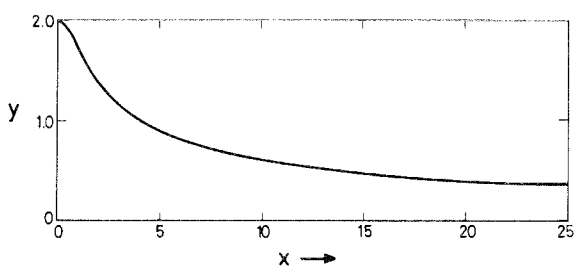

Fig. 17.14. Pair-breaking parameter y versus $x = \delta/2T_c$ for inelastic exchange scattering (from Fulde et al., 1970).

$x = \delta/2T_c$ and characterizes the strength of the pair-breaking effect. The Abrikosov–Gorkov theory corresponds to $y = 2$. One notices that as x increases the pair-breaking strength y decreases. However this decrease is rather slow. Even for $x = 25$ the pair-breaking effect due to virtual excitations of the upper singlet level is appreciable. For example if we assume that T_{c0} is of the order of a few degrees then crystal-field levels as high as 100 K are still important and may not be discarded as far as their influence on T_c is concerned. The physical reason for this is the fact that the virtual Cooper-pair scattering involves states far away from the Fermi surface. This requires the introduction of a cut-off at the Debye-energy ω_D in the BCS gap equation. Here it has the consequence that high lying crystal-field states have to be taken into account although they are certainly not thermally populated. The present dynamical mutual interaction of conduction electrons, which is mediated by the two-level RE-ions does not require a cut-off but leads to convergent results.

If instead of the isotropic exchange interaction $(\Lambda, \Sigma) = (0, 1)$ we consider the aspherical Coulomb interaction $(\Lambda, \Sigma) = (2, 0)$ we obtain fig. 17.15 instead. The negative sign for y indicates pair-enhancement instead of pair-breaking. Since this is a dynamical effect it vanishes for $\delta = 0$. The maximum effect occurs for $\delta \simeq 10T_c$. It resembles the one of additional Einstein oscillators put into the matrix. The quantity τ_s in the definition of y has to be replaced by τ_0 which is defined in a similar way as τ_s (see eq. (17.66)) but now with H_{AC} instead of H_{ex}.

We proceed in discussing the extension of the above results to finite impurity concentrations and the full crystal-field energy level scheme (Keller and Fulde, 1971). The dependence of T_c on n_I is obtained as the self-consistent solution of the following set of three equations.

$$\begin{aligned}
\tilde{\omega}_n &= \omega_n + T_c \sum_{\substack{\omega_m \\ ij}} \frac{\delta_{ij}}{2\tau_{ij}} \frac{(n_j - n_i)\ \mathrm{sgn}\ \omega_m}{(\omega_n - \omega_m)^2 + \delta_{ij}^2} \\
\tilde{\Delta}_n &= \Delta + T_c \sum_{\substack{\omega_m \\ ij}} \frac{\delta_{ij}\eta_{ij}}{2\tau_{ij}} \frac{(n_j - n_i)\ \mathrm{sgn}\ \omega_m}{(\omega_n - \omega_m)^2 + \delta_{ij}^2} \frac{\tilde{\Delta}_m}{\tilde{\omega}_m} \qquad (17.68) \\
\ln \frac{T_c}{T_{c0}} &= 2\pi T_c \sum_{\omega_n > 0} \left\{ \frac{1}{\Delta} \frac{\tilde{\Delta}_n}{\tilde{\omega}_n} - \frac{1}{\omega_n} \right\}
\end{aligned}$$

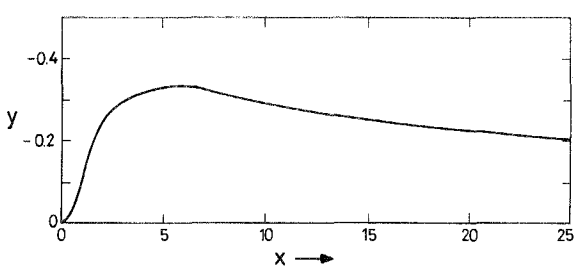

Fig. 17.15. Pair-enhancement parameter y versus $x = \delta/2T_c$ for aspherical Coulomb scattering $(\Lambda, \Sigma) = (2, 0)$ (from Fulde et al., 1970).

Hereby the ω_n are the Matsubara frequencies $\omega_n = 2\pi T_c(n + \frac{1}{2})$ where n is an integer. Furthermore

$$\eta_{ij} = \begin{cases} +1 \text{ for interactions } (\Lambda, \Sigma) \text{ with } \Lambda + \Sigma = \text{even} \\ -1 \text{ for interactions } (\Lambda, \Sigma) \text{ with } \Lambda + \Sigma = \text{odd} \end{cases}$$

The relaxation rates τ_{ij}^{-1} are defined by

$$\tau_{ij}^{-1} = 2\pi n_I N(0)|M_{ij}|^2 \tag{17.69}$$

where M_{ij} are the matrix elements for transitions between the crystal field states $|i\rangle$, $|j\rangle$ for the interaction in question. For $(\Lambda, \Sigma) = (0, 1)$ one obtains

$$\tau_{ij}^{-1} = 2\pi n_I N(0) J_{ex}^2 (g-1)^2 |\langle i|\boldsymbol{J}|j\rangle|^2 \tag{17.70}$$

In the following we will refer to this particular interaction. The eqs. (17.68) can be solved numerically for a given crystal-field level scheme and a given electron-RE-ion interaction. In fig. 17.16 we show the results for a two singlet system for various different ratios δ/T_{c0}.

For the purpose of comparison it is advantageous to normalize the curves for $T_c(n_I)$ such that they start with the same slope at $n_I = 0$ independent of the ratio δ/T_{c0}. This is achieved by plotting T_c/T_{c0} as a function of the dimensionless quantity $(\tau_N T_{c0})^{-1}$ where τ_N is defined such that the slope at T_c equals minus one.

From fig. 17.16 one notices characteristic differences between the Abrikosov–Gorkov theory and the case of RE-ions in a singlet ground state. These differences can be easily understood by going back to fig. 17.14. There we have seen that the pair-breaking effect of a single impurity depends on the ratio δ/T_c. Therefore it will be different depending whether there is only a small amount of impurities present so that $T_c \simeq T_{c0}$ or whether there are many impurities present so that T_c is only a fraction of T_{c0}. This implies that the pair-breaking effect of a single RE-ion decreases as more and more impurities are added to the super-

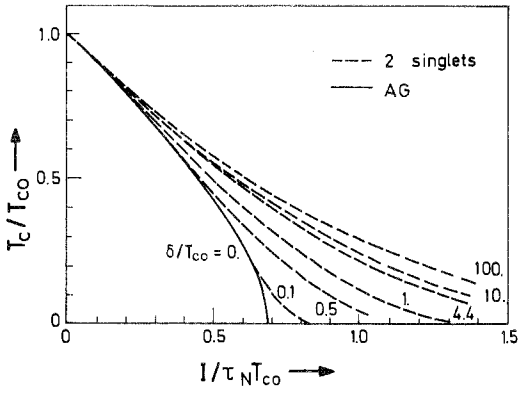

Fig. 17.16. T_c versus impurity concentration for RE-impurities with two singlet CEF levels separated by an energy δ. The scattering rate τ_N^{-1} is normalized such that the slope at $T_c = T_{c0}$ equals unity. AG refers to the Abrikosov–Gorkov theory (from Keller and Fulde, 1971).

conduction probe. In contrast to this there is no temperature dependence of the pair-breaking effect of a single ion in the Abrikosov–Gorkov theory. This explains why in the present case the $T_c(n_I)$ curves have a different curvature than in the Abrikosov–Gorkov theory. The impurities become less and less effective as T_c decreases towards zero. Furthermore one notices that for $\delta/T_{c0} > 4$ the function is rather insensitive to the value of δ/T_{c0}. It approaches a limiting form for δ/T_{c0} becoming very large. Within the present theory one can explain very well the $T_c(n_I)$ behavior of many alloys with impurities in a singlet ground state. As an example we show in fig. 17.17 some results for $La_{1-x}Pr_xPb_3$. After one has adjusted the initial slope at T_{c0} there is no adjustable parameter in the theory since the crystal-field level scheme is usually determined independently from susceptibility and specific heat measurements. It should be pointed out that if one is interested in approximate results only then instead of solving eqs. (17.68) numerically one can use the Abrikosov–Gorkov theory and just replace the temperature independent pair-breaking scattering rate by the temperature dependent quantity $y(x)$ shown in fig. 17.14. This way one obtains instead of eq. (17.67) the following relation

$$\ln \frac{T_c}{T_{c0}} + \psi\left(\tfrac{1}{2} + \frac{2}{\pi^2 T_c \tau_N} \frac{y(\delta/2T_c)}{y(\delta/2T_{c0})}\right) - \psi(\tfrac{1}{2}) = 0 \tag{17.71}$$

For T_c/T_{c0} values which are not too small the results of this equation agrees quite well with the accurate numerical results.

The difference to the Abrikosov–Gorkov theory are much less pronounced if the ground state is a Kramers doublet or more generally a degenerate state which is magnetic. For details we refer to Keller and Fulde (1971).

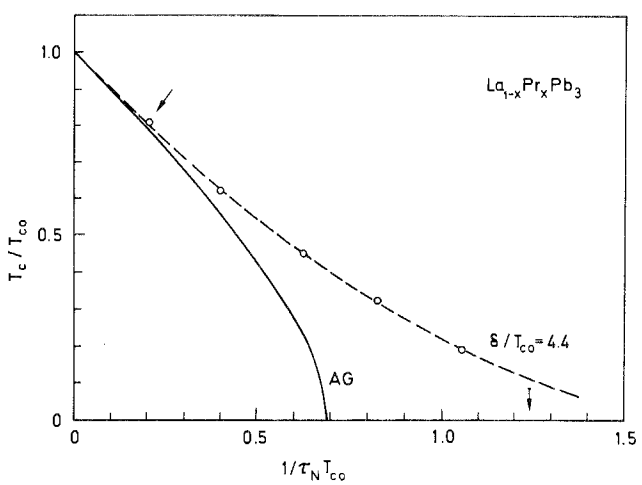

Fig. 17.17. T_c as function of impurity concentration for $La_{1-x}Pr_xPb_3$ (from Bucher et al., 1968). The dashed line is the theoretical curve for $\delta/T_{c0} = 4.4$. The point denoted by an arrow has been fitted to give the initial slope.

Finally we mention some anomalous situations which may arise due to a particular sequence of energy levels. For example if the ground state is a triplet Γ_5 and the first excited state is Γ_1 and if furthermore the other states are not too close to Γ_1 then it may happen that the pair-breaking effect *increases* with decreasing temperature. Namely at very low temperatures only Γ_5 will be populated which can strongly scatter elastically and therefore break the Cooper pairs. At higher temperatures Γ_1 may be thermally populated and in that state there is no elastic scattering hence less pair-breaking (compare the analog situation for the resistivity as described in section 4.1.1). As a result the curve $T_c(n_I)$ may be double-valued in a concentration interval $n_{I,1} > n_I > n_{I,crit}$. For n_I in that interval the probe is normal conducting at high enough and low enough temperatures while it is superconducting in a temperature interval in between. Re-entrance behavior of that type has been found in a very different context, namely for Kondo-type impurities in superconductors (Müller–Hartmann and Zittartz, 1971; Ludwig and Zuckermann, 1971; Riblet and Winzer, 1971; Maple, 1973). There one also obtains a temperature dependent pair-breaking effect which increases with decreasing temperature due to the Kondo effect.

4.2.3. *Pressure dependence of* T_c

It was demonstrated that the superconducting transition temperature depends on the CEF-splitting of the RE-impurities dissolved in the matrix. One expects therefore that there should exist also a pronounced pressure dependence since pressure changes the CEF-energy levels. Such a pressure dependence was found experimentally by Guertin et al. (1973) and Umlauf et al. (1974) on $La_{1-x}Tb_xAl_2$. This system can be compared with $La_{1-x}Gd_xAl_2$ where no crystal-field effects are present. Experimental results are shown in fig. 17.18. One notices a different pressure dependence in both cases. The small pressure dependence of T_c for $La_{1-x}Gd_xAl_2$ results from the small pressure dependence of the exchange integral J_{ex}. The pressure dependence for $La_{1-x}Tb_xAl_2$ is much bigger. Here one has to take into account the pressure dependence of the CEF-parameters. Let us consider a crystal field of cubic symmetry. We use the scheme of Lea et al. (1962) in which the CEF is described by eq. (17.11) with the parameters W, x related to B_4^0 and B_6^0 as described there. The energy difference δ_{ij} between two CEF levels is given by $\delta_{ij} = (E_i(x) - E_j(x))W$ and the $E_i(x)$ are tabulated in the paper of Lea et al. (1962). Both, B_4^0 and B_6^0 depend on the lattice parameter R as

$$B_4^0 \sim R^{-5}; \qquad B_6^0 \sim R^{-7} \tag{17.72}$$

If hydrostatic pressure p is applied the change ΔR of R is given by

$$\Delta R/R = -\tfrac{1}{3}\kappa p \tag{17.73}$$

where κ is the compressibility of the material. With the compressibility given one can calculate $\Delta R/R$ and with it

$$\frac{\Delta W}{W} = -(7 - 2|x|)\Delta R/R \qquad \frac{\Delta x}{x} = 2(1 - |x|)\Delta R/R \tag{17.74}$$

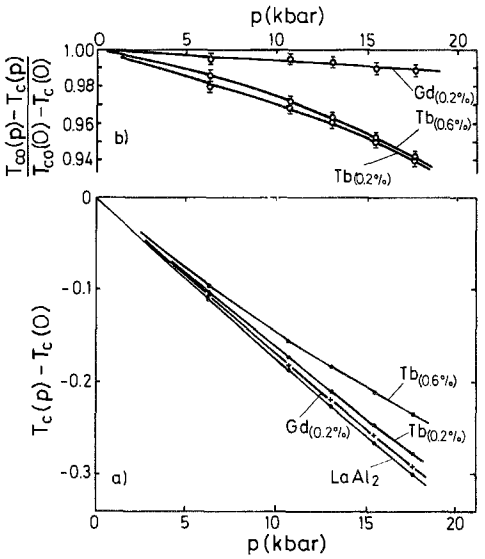

Fig. 17.18. (a) Pressure dependence of T_c for $LaAl_2$ and the alloys $La_{1-x}Gd_xAl_2$ and $La_{1-x}Tb_xAl_2$. (b) Relative change of the pair-breaking effect of the impurities $[T_{c0}(p)-T_c(p)]/[T_{c0}(0)-T_c(0)]$ as function of pressure (from Umlauf et al., 1974).

The relative change of the energy separation of the two lowest crystal-field levels with an allowed transition matrix element between them i.e. $\Delta\delta/\delta$ is given by

$$\frac{\Delta\delta}{\delta}=\frac{\Delta W}{W}+\frac{\Delta E}{E} \tag{17.75}$$

The first term is always positive and reflects the increase of the strength of the crystal field due to pressure. The second term reflects the change in the relative magnitude of B_4^0 and B_6^0 and is proportional to ΔX. It is important near the crossing points of energy levels. With the scheme outlined here and using the data for $La_{1-x}Gd_xAl_2$ to determine the change of $J_{ex}^2N(0)$ with pressure the experimental results have been successfully analysed (Umlauf et al., 1974). For more details we refer to the original work.

4.2.4. *Upper critical field* $H_{c2}(T)$

The temperature dependence of the upper critical field in the presence of RE-impurities is determined by the following pair-breaking mechanisms:

α) the effect of the magnetic field acting on the electron orbits. This leads to Abrikosov flux lines in type II superconductors. This effect is mean free path dependent;

β) the effect of the randomly distributed magnetic scattering centers which was discussed above;

γ) an interference effect, which occurs if the external field is strong enough to polarize the magnetic scattering centers. This implies a temperature dependent exchange field set up by the polarized ions which also breaks the Cooper pairs.

What changes do we expect if we are dealing with impurities with a singlet ground state; The effect (α) is present independent of the RE-ions. The effect of the level splitting on (β) was discussed in detail in the preceding paragraph. The effect (γ) will strongly depend on whether or not we have a singlet ground state with appreciable crystal-field splitting. If the splitting is of the order of a few tens of degrees then a magnetic field of several tens of Kilogauss will not lead to any appreciable impurity polarization. On the other hand for a degenerate ground state such as it is present for Gd or Kamers ions a noticeable polarization will result.

This changes the character of the temperature dependence of H_{c2}. To demonstrate this let us first exclude (γ) and neglect crystal field splitting. In that case $H_{c2}(T)$ is given by the solution of the following equation (Fulde and Maki, 1966).

$$\ln \frac{T_c}{T_{c0}} + \psi\left(\frac{1}{2} + \frac{1}{2\pi T_c \tau_s} + \frac{DeH_{c2}(T_c)}{2\pi T_c}\right) - \psi(\tfrac{1}{2}) = 0 \tag{17.76}$$

Here D is the electronic diffusion constant. Numerical results are shown in fig. 17.19. Corresponding measurements were done by Guertin and Parks (1968). Now we include (γ). Then characteristic maxima in $H_{c2}(T_c)$ will result. This is due to the temperature dependence of the exchange field which becomes larger as the temperature decreases, since the impurity polarization becomes larger. Thus a smaller external field is needed at low temperatures to suppress superconductivity than at higher temperatures where the impurity polarization and hence the pair-breaking effect (γ) is smaller. This effect can clearly be seen from fig. 17.20 where data on $(La_{1-x}Gd_x)_3In$ are shown (Crow et al., 1967). If Gd is replaced by Pr this effect is absent (Heiniger et al., 1975) (see fig. 17.21). Pr is in a singlet ground state Γ_1 with the first excited state Γ_4 at 119 K. Thus fields of up to 70 kG will lead

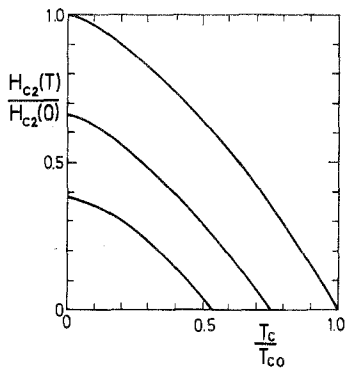

Fig. 17.19. Upper critical field for different impurity concentrations as given by eq. (17.76).

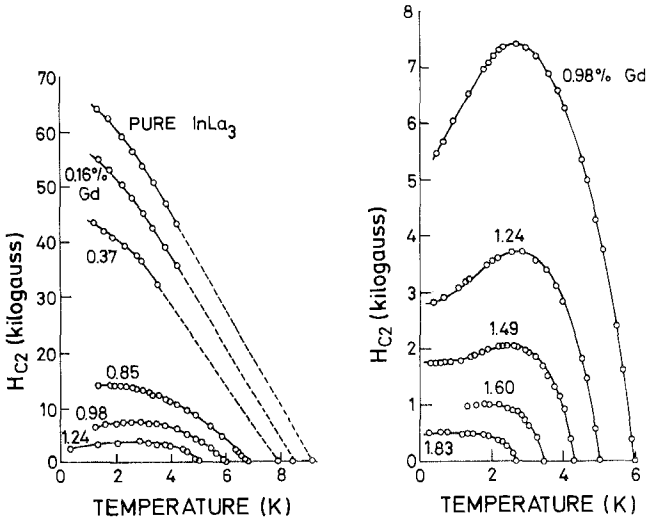

Fig. 17.20. $H_{c2}(T)$ for $(La_{1-x}Gd_x)_3In$. The maxima are due to the pair-breaking effect (γ) (from Crow et al., 1967).

only to a small Pr polarization due to the large energy denominators (Heiniger et al., 1973). In order to see how $H_{c2}(T)$ as shown in fig. 17.19 is changed for singlet ground state RE-ions one has to solve a set of three equations (Keller and Fulde, 1973). They are the same as eqs. (17.68) except that the left hand side of those equations is changed from $\tilde{\omega}_n$ to $(\tilde{\omega}_n - \frac{1}{2}DeH_{c2} \operatorname{sgn} \omega_n)$ and $\tilde{\Delta}_n$ to $(\tilde{\Delta}_n + \frac{1}{2}DeH_{c2} \operatorname{sgn} \omega_n(\tilde{\Delta}_n/\tilde{\omega}_n))$, respectively.

Numerical results are shown in fig. 17.22 for the case of two singlets separated

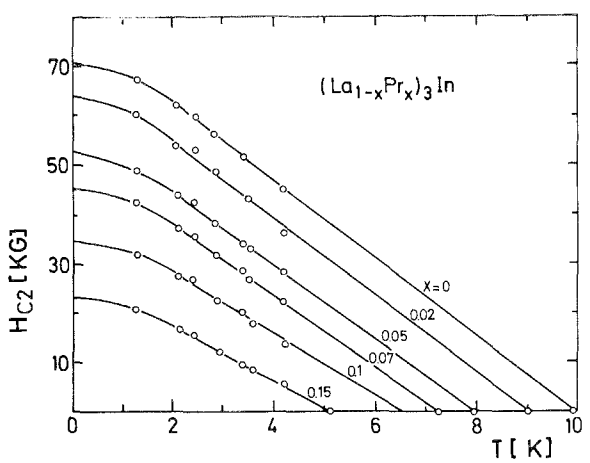

Fig. 17.21. $H_{c2}(T)$ for $(La_{1-x}Pr_x)_3In$. Since Pr is in a singlet ground state the maxima found for $(La_{1-x}Gd_x)_3In$ are absent (from Heiniger et al., 1975).

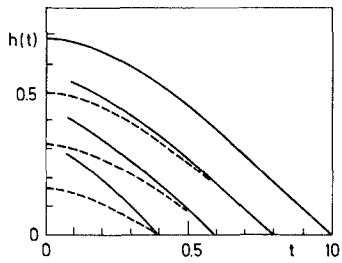

Fig. 17.22. Upper critical field versus $t = T_c/T_{c0}$ for different amounts of impurities which are in a singlet ground state with an excited singlet at energy $\delta = T_{c0}$. Also shown for comparison are the corresponding curves for $\delta = 0$ (dashed lines). The normalization is such that $h(t) = H_{c2}(T)[-(\partial H_{c2}(T)/\partial T)_{T=T_{c0}}]^{-1}$ (from Keller and Fulde, 1973).

by an energy $\delta = T_{c0}$. Also shown for comparison are the curves corresponding to fig. 17.19. The deviations can be understood again by realizing that the pair-breaking effect of a single impurity decreases with decreasing temperature. Thus a larger external field is required to suppress superconductivity than in the case of no crystal-field splitting. The deviations just described are not seen in the system $(La_{1-x}Pr_x)_3In$. There are two possible reasons for this. Firstly one has to take into account that pure La_3In is a strong-coupling superconductor (Heiniger et al., 1973). This implies that $H_{c2}(T)$ for the pure system does not agree with the weak-coupling theory presented above and requires a different treatment (Rainer and Bergmann, 1974). Secondly, although the polarization of the Pr-ions is much less than for Gd for example, it is not zero and should be also taken into account for a quantitative comparison (Heiniger et al., 1973). There is also data available for $H_{c2}(T)$ of the alloys $(La_{1-x}Tm_x)Sn_3$ and $(La_{1-x}Tb_x)Al_2$ (see Guertin et al., 1973; Pepperl et al., 1974).

In both cases the RE-ions are in a non-magnetic ground state. A comparison with the corresponding data where Gd is replacing Tm and Tb shows effects of the type seen in fig. 17.22. For a detailed quantitative comparison one needs to know how the mean free path changes with impurity concentration since the pair-breaking effect (α) depends on it.

4.2.5. *Jump in the specific heat at T_c*

In order to understand how the crystal-field splitting of RE-impurities influences the jump in the specific heat at T_c i.e. $\Delta C(T_c)$, one needs a more detailed theory than for the determination of $T_c(n_I)$ or $H_{c2}(T)$. This can be seen by expanding the free energy difference between the superconducting and normal state F_{s-n} near T_c in terms of the order parameter Δ (Ginzburg–Landau expansion).

Symbolically one may write

$$F_{s-n} = A(T - T_c, n_I)|\Delta|^2 + B(T_c, n_I)|\Delta|^4 \tag{17.77}$$

where the functions A, B have to be determined from the theory. The deter-

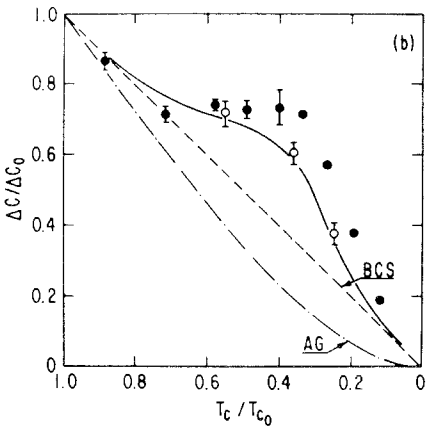

Fig. 17.23. Jump in the specific heat ΔC as function of T_c/T_{c0} for the system $La_{1-x}Pr_xSn_3$. The solid line represents the theoretical curve which does not contain any fit parameter. Also shown for comparison is the result of the Abrikosov–Gorkov theory (AG) (from McCallum et al., 1975).

mination of $T_c(n_I)$ and $H_{c2}(T)$ requires only a knowledge of the function $A(T - T_c, n_I)$ but not of $B(T_c, n_I)$. In contrast to this one needs also to know $B(T_c, n_I)$ in order to determine the jump in the specific heat at T_c. The question then arises how $B(T_c, n_I)$ is changed due to the crystal-field splitting of the RE-impurities. In particular one is interested in impurities with a singlet ground state. The theory for this problem has been worked out in detail (Keller and Fulde, 1973) including the complete level scheme of the ions. For details we refer to that reference. Instead we present here only the experimental results for $(La_{1-x}Pr_x)Sn_3$ (McCallum et al., 1975). For that system the level scheme has been determined from specific heat and magnetic susceptibility measurements. It is found to be Γ_1 (0 K), Γ_5 (8.6 K), Γ_4 (14.6 K), Γ_3 (25 K). The characteristic feature is the triplet Γ_5 between Γ_1 and Γ_4. Note that Γ_5 does not couple magnetically to the ground state Γ_1. The theoretical and experimental results for $\Delta C(T_c)$ are shown in fig. 17.23. In that figure the theoretical curve does not contain any fit parameter.

Also shown for comparison are the results for the BCS theory and the Abrikosov–Gorkov theory. Other systems which have been investigated are $La_{1-x}Tb_xAl_2$ by Happel and Hoenig (1973) where crystal-field effects were found and $(La_{1-x}Pr_x)_3Tl$ and $(La_{1-x}Pr_x)_3In$ (see Bucher et al., 1972; and Heiniger et al., 1975). In the last two systems strong coupling effects are larger than crystal-field effects. However nowhere are the crystal-field effects so dramatic as in $(La_{1-x}Pr_x)Sn_3$ where they are caused by the particular position of the Γ_5 level.

4.2.6. *Thermodynamic critical field*

The thermodynamic critical field $H_c(T)$ is directly related to the free energy difference F_{s-n} between superconducting and normal state via

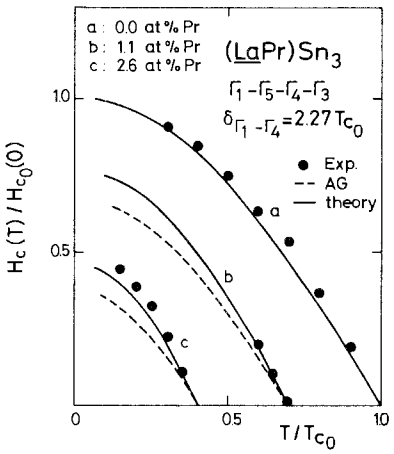

Fig. 17.24. Thermodynamic critical field $H_c(T)$ for $La_{1-x}Pr_xSn_3$. The theoretical results are due to Keller et al. (1977) while the experimental data are from McCallum et al. (1975).

$$H_c^2(T)/8\pi = -F_{s-n} \tag{17.78}$$

It has been calculated by Keller et al. (1976) with the help of diagrams in a way similar to that employed by Rainer and Bergmann (1974) for strong coupling superconductors. These calculations provide the first test of the theory well within the superconducting region where Δ is finite. The above authors obtained analytical expressions for $H_c(T)$ which were numerically evaluated for the system $La_{1-x}Pr_xSn_3$. Results are shown in fig. 17.24 together with the experimental data as obtained by McCallum et al. (1975). The same CEF level scheme has been used as in section 4.2.5. There is an agreement between the theory and the experimental data although the data is rather scarce.

4.2.7. *Tunneling density of states*

Superconducting tunneling measurements are known to be a powerful spectroscopic tool for investigating excitations in metals. For example they allow the determination of the phonon density of states multiplied by the square of the electron–phonon coupling constant for such elements as Sn, Pb, Tl etc. (for a review see McMillan and Rowell, 1969). They even allow the detection of localized phonon modes which appear if In impurities are added to Pb for example.

This suggests to exploit tunneling as an experimental tool to detect crystal field levels of RE-impurities (Fulde et al., 1970). The physical process which should enable this is the energy dependent life time of the conduction electrons. This leads to a frequency dependent superconducting order parameter. The latter causes a structure in the tunneling density of states which can be measured. In order to demonstrate the crystal-field effects we have plotted in fig. 17.25a the tunneling density of states of a superconductor containing RE-

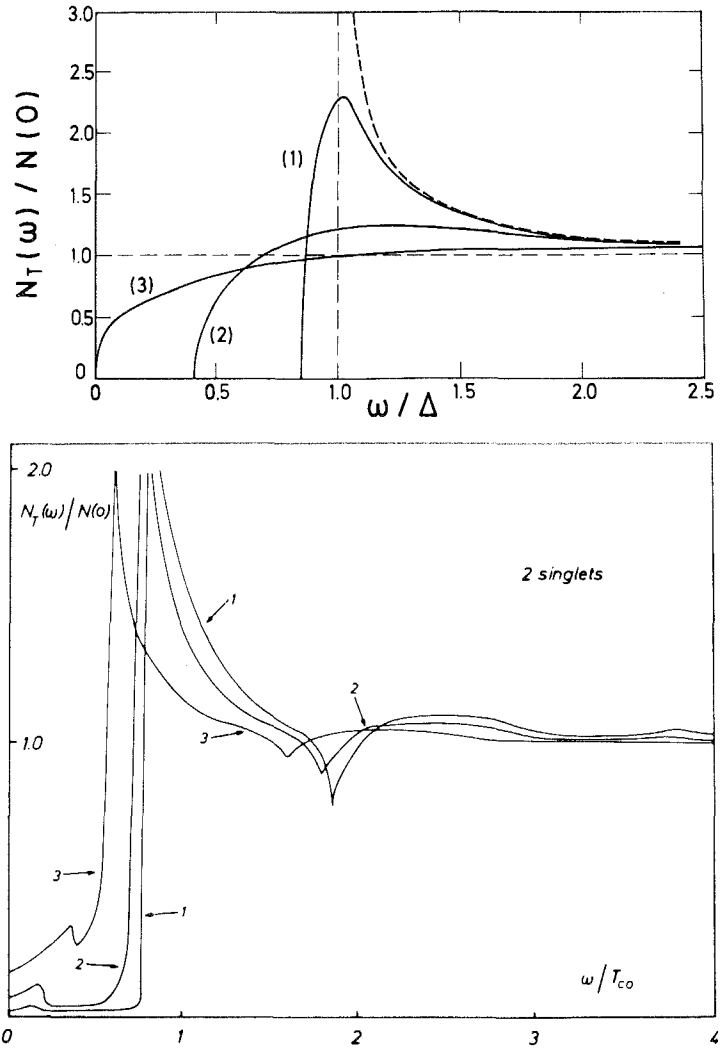

Fig. 17.25. (a) Tunneling density of states of a superconductor containing magnetic impurities without crystal-field splitting. The transition temperatures corresponding to curves (1)–(3) are $T_c/T_{c0} = 0.95$, 0.7, 0.25, respectively. (b) Tunneling density of states for the case of impurities in a singlet ground state and a singlet excited state at $\delta = T_{c0}$. Furthermore, T_c/T_{c0} was chosen to be 0.5. The temperatures corresponding to curves 1–3 are $T/T_c = 0.4$, 0.6 and 0.8, respectively (from Holzer et al., 1974).

impurities without crystal field splitting (Skalski et al., 1964). This has to be compared with the density of states in the presence of RE-impurities in a singlet ground state (Holzer et al., 1974) as shown in fig. 17.25b. For simplicity the case of two singlets has been assumed with a level splitting of $\delta = T_{c0}$. Several differences between figs. 17.25a,b are noticed. The main effect of the singlet ground state is a density of states which is BCS-like and does not show the

broadening as it is found for impurities with a degenerate ground state. Furthermore one notices structure in the density of states at $\omega \simeq \Delta_g + \delta$ where Δ_g is the gap in the excitation spectrum. There are higher harmonics at $\Delta_g + n\delta$ with $n = 2, 3$ etc.

5. Cooperative phenomena in lattices of crystal-field split ions

There are a large number of theoretical and experimental investigations available which deal with cooperative phenomena in lattices of CEF-split ions. These cooperative phenomena result from the mutual interactions between the RE-ions which were discussed in section 3. In the following we will focus our attention on two particular types of effective ion–ion interactions, namely the isotropic exchange and the quadrupolar Coulomb interaction. As mentioned in section 3 there may be also other types of interactions present but it is easy to understand their theoretical treatment after one has understood the examples which will be discussed here. The two types of interactions which we shall consider have the property that they lead to different types of phase transitions if they are strong enough. The isotropic exchange interaction can lead to magnetic phase transitions which include the so called "induced moment systems" or "exchange induced Van Vleck magnets", while the quadrupolar interactions may lead to structural phase transitions which are commonly known as collective Jahn–Teller transitions.

Furthermore in order to understand the dynamics of the coupled RE-ion system it is often not sufficient to work with the effective ion–ion interaction model. Instead it is important not to eliminate the particles (or excitations) from the dynamical treatment which are mediating the interaction from ion to ion. For example if the conduction electrons are mediating the RE-ion interactions via (generalized) Ruderman–Kittel interaction then the dynamics of the electronic excitations will enter into the dynamics of the coupled RE-ion system. But if the conduction electrons are eliminated from the considerations by replacing their effect by an effective RE ion–ion interaction this dynamical influence is lost and the resulting excitation spectrum may be over-simplified in certain regions in q-space. The same holds true if the phonons are mediating the ion–ion interaction. We will pay special attention to this problem as we proceed.

5.1. *Magnetic interactions, excitations and instabilities*

The large interest in the problem of magnetic excitations in RE-systems has been stimulated to a great deal by the inelastic neutron scattering experiments which were done on systems such as Pr_3Tl, dhcp Pr and TbSb. Although these are all metallic systems a theoretical analysis of the experimental results has been attempted only within a simplified model in which the conduction electrons are eliminated and replaced by an effective RE-ion interaction. Since this model can explain the available data rather well we will first discuss it before studying

the influence of the conduction electrons in more detail. This has the advantage that we are able to demonstrate most of the physically important points with a relatively simple model.

5.1.1. *The effective-interaction model*

As it was discussed in section 3.3 the conduction electrons lead to an effective ion–ion interaction which for the case of isotropic exchange we shall write as

$$H_{\text{int}} = -\tfrac{1}{2}\sum_{mn} J^{\text{ex}}_{mn} \boldsymbol{J}^m \boldsymbol{J}^n \tag{17.79}$$

Thus the total hamiltonian reads $H = H_{\text{CEF}} + H_{\text{int}}$. In order to discuss the excitations corresponding to this hamiltonian we have to calculate the appropriate frequency and wave number dependent response function. Its poles yield directly the various excitations. In the present case the relevant response function is the magnetic susceptibility. Since the magnetic field couples directly with $\boldsymbol{J}^m$ it causes a response of the system which is sensitive to H_{int}. The simplest way to calculate the magnetic susceptibility $g^2\mu_{\text{B}}^2\chi_{ij}(\omega)$ is via the diagrams shown in fig. 17.26. The corresponding algebraic equation is

$$\chi_{ij}(\omega) = u(\omega)\delta_{ij} + u(\omega)\sum_l J^{\text{ex}}_{il}\chi_{lj}(\omega) \tag{17.80}$$

Hereby $g^2\mu_{\text{B}}^2 u(\omega)$ denotes the frequency dependent single-ion susceptibility as given by eq. (17.22).

By confining ourselves to a simple Bravais lattice we can solve the integral equation by a Fourier transformation

$$\chi_{ij}(\omega) = \frac{1}{N}\sum_{\boldsymbol{q}} \exp[\mathrm{i}\boldsymbol{q}(\boldsymbol{R}_i^{(0)} - \boldsymbol{R}_j^{(0)})]\chi(\boldsymbol{q}, \omega) \tag{17.81}$$

where N is the number of ions.

One obtains

$$\chi(\boldsymbol{q}, \omega) = \frac{u(\omega)}{1 - J(\boldsymbol{q})u(\omega)} \tag{17.82}$$

where $J(\boldsymbol{q})$ is the Fourier transform of J^{ex}_{ij}. For a simple cubic lattice with nearest neighbor interactions it is given by

$$J(\boldsymbol{q}) = \tfrac{1}{3}J(0)[\cos(q_x a) + \cos(q_y a) + \cos(q_z a)] \tag{17.83}$$

where a is the lattice constant.

Equation (17.82) represents the magnetic susceptibility (up to a factor $\mu_{\text{B}}^2 g^2$)

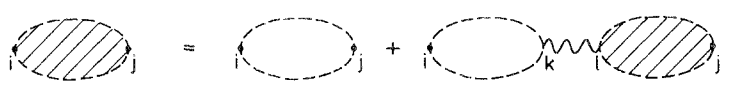

Fig. 17.26. Diagrams for the susceptibility (shaded bubble) as expressed by the one-ion susceptibility (dashed bubble) and the interaction between ions J^{ex}_{kl} (wavy line).

for an arbitrary crystal-field level scheme. The poles of $\chi(\boldsymbol{q}, \omega)$ determine the possible excitations of the systems. At this stage it is useful to recapitulate the approximations involved in deriving eq. (17.82). The geometrical series shown in fig. 17.26 is a typical random phase approximation (RPA) (see for example Schrieffer, 1964). However since the occupational numbers n_i in eq. (17.22) are usually assumed to be the mean-field (MF) values the approximation is sometimes called RPA–MF approximation. An alternative way of deriving eq. (17.82) is with the help of the equation of motion method (Holden and Buyers, 1974) for which the RPA was originally devised (see Pines, 1963). The Green's function method and the equation of motion method correspond to each other and therefore have the same power and weakness.

It should be mentioned that in special cases one has been able to go beyond the approximation outlined here. However these extensions were mainly done for the case of two singlets only and will be discussed in the following subsection. We proceed now by discussing the excitation spectrum for several special cases. Thereby we consider first the paramagnetic phase.

5.1.1.1. *Two singlets model*

The simplest case which one can consider is that of two singlets. For example Pr^{3+} in a crystal field of hexagonal symmetry can have a ground state $|g\rangle = 2^{-1/2}(|+3\rangle - |-3\rangle)$ and a first excited state $|e\rangle = 2^{-1/2}(|+3\rangle + |-3\rangle)$. Neglecting all the other levels leads to a two singlets problem.

It is not difficult to show that the special case of two singlets maps to the problem of an Ising model in a transversal field. The hamiltonian is then written as

$$H = -\frac{\delta}{2}\sum_i \sigma_i^x - \tfrac{1}{2}\sum_{ij} \tilde{J}_{ij}\sigma_i^z\sigma_j^z \tag{17.84}$$

where δ is the energy separation between $|g\rangle$ and $|e\rangle$ and the σ's are the Pauli matrices. They act in a two-dimensional space which is spanned by $|g\rangle$ and $|e\rangle$. The model hamiltonian given by eq. (17.84) appears at different places in solid state physics and has been also used to describe hydrogen bonded ferroelectrics such as KH_2PO_4 (de Gennes, 1963; Vaks and Larkin, 1965; Villain and Stamenkovic, 1966; Brout et al., 1966; Cochran, 1969) for example, or quasi-one dimensional conductors (Dieterich, 1974). It is exactly solvable only in one dimension. Then the problem is closely related to the X–Y model of Lieb et al. (1961) and the hamiltonian can be transformed into one of non-interacting fermions.

The study of the above hamiltonian for a lattice of RE-ions has had a large influence on the understanding of "induced moment systems". Especially to mention is the work of Trammell (1963), Bleaney (1963), Cooper (1967, 1969), Wang and Cooper (1968, 1969, 1970) and Pink (1968), but there are also many other important contributions. A more complete list can be found for example in Fulde and Peschel (1972), Birgeneau (1973) and Cooper (1974).

For the discussion of the excitation spectrum we start out from eq. (17.82) and

specialize $u(\omega)$ to a two singlets system. In that case eq. (17.23) applies where $M = \langle e|J|g\rangle$. The poles of $\chi(q, \omega)$ are then determined from

$$1 = J(q)\frac{2\delta|M|^2}{\delta^2 - \omega^2}\tanh \delta/2T \tag{17.85}$$

which yields

$$\omega(q) = \delta\left\{1 - \frac{2}{\delta}|M|^2 J(q)\tanh \delta/2T\right\}^{1/2} \tag{17.86}$$

The corresponding dispersion curve is shown in fig. 17.27 for $J(q)$ given by eq. (17.83). One notices that the excitation energy δ is broadened into a band as a consequence of the ion–ion interaction. This broadening is seen to be temperature dependent due to the temperature dependent occupation of the excited state $|e\rangle$. If $|M|^2 J(q)$ is sufficiently large than $\omega(q)$ may approach zero (soft mode). This implies a magnetic instability since it becomes extremely easy to excite the excitonic modes. Depending on whether $J(q)$ has its largest value for $q = 0$ or $q = \pi/a$ we will obtain an exchange induced Van Vleck ferromagnet or antiferromagnet. The transition temperature T_c is determined from

$$J(q)u(0, T_c) = 1 \tag{17.87}$$

For ferromagnetic coupling this requires a minimum value for $J(0)$ given by

$$J(0)_{crit} = \delta/2M^2 \tag{17.88}$$

Only if $J(0) > J(0)_{crit}$ a phase transition will occur. Near T_c the phase transition $\omega(0, T)$ depends on T as $(T - T_c)^{1/2}$. An excitation spectrum of the form of eq. (17.86) was also obtained using a Bogoljubov transformation approach (Grover, 1965) which works in the vicinity of $T = 0$.

There has been a considerable effort to go beyond the mean field approximation just discussed. However in doing so one has always to keep in mind that a serious approximation has been made by eliminating the conduction electrons from the problem. For metals this approximation is so drastic that it hardly pays to go beyond the simplest approximation within the effective-ion interaction model. Nevertheless it is an interesting mathematical question how the hamiltonian defined by eq. (17.84) can be solved more accurately. There exist several refinements as compared with the mean field results. Using a Green's function decoupling method it was shown (Pytte and Thomas, 1968) that the

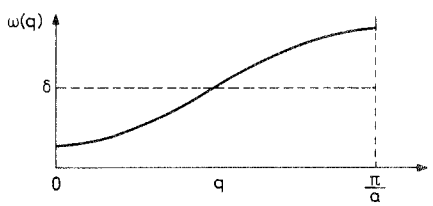

Fig. 17.27. Dispersion for a two singlet level system.

RPA expression for $\chi(q,\omega)$ differs from eq. (17.82) only by replacing in $u(\omega, T)\tanh \delta/2T$ by $\langle\sigma_i^x\rangle$. The latter is determined selfconsistently by employing an exact relation (Zubarev, 1960) namely

$$\langle\sigma_i^z\sigma_i^z\rangle = -\frac{1}{N}\sum_q \int \frac{d\omega}{2\pi} \coth\frac{\omega}{2T}\frac{1}{M^2}\operatorname{Im}\chi(q,\omega) \tag{17.89}$$
$$= 1$$

Since $\langle\sigma_i^x\rangle$ appears in $\operatorname{Im}\chi(q,\omega)$ one can determine it from that equation. The equation for T_c is modified somewhat and reads now

$$2J(0)M^2\delta^{-1} = N^{-1}\sum_q [1 - J(q)/J(0)]^{1/2}\coth\{(\delta/2T_c)[1 - J(q)/J(0)]^{1/2}\} \tag{17.90}$$

which shows that not only $J(0)$ but all values of $J(q)$ enter into the determination of T_c.

A similar result was obtained by other authors (Wang and Cooper, 1968, 1969, 1970; Pink, 1968) using a slightly different procedure except that the prefactor $(1 - J(q)/J(0))^{1/2}$ on the right hand side of eq. (17.90) is replaced by

$$\tfrac{1}{2}[(1 - J(q)/J(0))^{-1/2} + (1 - J(q)/J(0))^{1/2}].$$

Generally the critical temperature is lower in the more refined approximations than it is in the mean field approximation. It is not very different from the one obtained using high temperatures series expansions (Elliott et al., 1971). A numerical comparison of different approximations is shown in fig. 17.28. Somewhat subtle is the question of the order of the phase transition. The decoupling approximations going beyond the RPA–MF approximation lead to first order phase transitions for some or even all values of the relevant parameters.

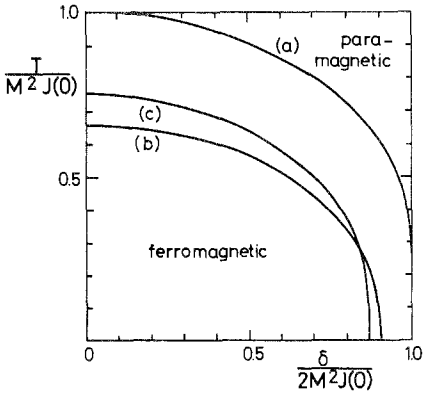

Fig. 17.28. Phase diagram for a two singlet system applying different approximations (a) RPA–MF approximation; (b) Green's function method, see eq. (17.90); (c) series expansion (Elliott et al., 1971) (from Fulde and Peschel, 1972).

This is in opposition to the MFA but also to the results of series expansion (Elliott et al., 1971) which yield a second order phase transition to the magnetic state.

All approximations discussed until now give an infinitely sharp line width which of course is not physical. There are a number of treatments with the aim to incorporate life-time effects of the magnetic exciton and which are based on the effective ion interaction hamiltonian. Here of course the elimination of the conduction electrons implies that the broadening due to electron-hole excitations can not be taken into account. From that point of view caution has to be exercised to apply the findings of the more refined treatments to metallic systems. One way to incorporate life-time effects is by applying Mori's continued fraction method to the computation of the susceptibility. This was done by Cheung (1973) who found that the longitudinal susceptibility has in addition to the magnetic exciton poles a third pole on the imaginary axis which leads to a quasi-elastic contribution (central peak) in the spectral density. The residuum of this pole was calculated in a certain approximation and it was shown that at the phase transition the quasi-elastic peak diverges while the frequency of the $q = 0$ magnetic exciton stays finite. This implies that there is no true soft mode but that instead the mode becomes overdamped. Similar in spirit and in the results is an analysis of the moments of the line shape function given by Huber and Tommet (1973). Other studies of the dynamics of the singlet-singlet model were made by Chock and Dagonnier (1971), Moore and Williams (1972), and Stinchcombe (1973). It has also been argued (Hohenberg and Swift, 1975) that the critical dynamics of the Ising model in a transversal field is the same as the one of the kinetic Ising model which was investigated by Halperin et al. (1972). Again this would imply a diverging central peak near the phase transition whose width goes to zero.

5.1.1.2. *Complete crystal field level scheme*

It is easy to extend the RPA–MF calculations to the case where the full crystal field level scheme of the RE-ions is taken into account (Peschel et al., 1972; Holden and Buyers, 1974). There have been a number of treatments of the singlet–triplet system as a generalization of the singlet–singlet system (Smith, 1972; Hsieh and Blume, 1972; Kitano and Trammell, 1966). But since in the RPA–MF approximation it is as easy to include the full level scheme we shall not treat the singlet–triplet system separately. Possible extensions of the RPA–MF approximation are of course much simpler for the singlet–triplet system (Hohenberg and Swift, 1975; Blume and Birgeneau, 1974; Lines, 1974) than for the full level scheme (Yang and Wang, 1974). In order to calculate the excitation spectrum one uses again eq. (17.82) but now with $u(\omega)$ as given by eq. (17.22). It is instructive to rewrite the latter equation in such a way that the elastic scattering processes are separated from the inelastic ones i.e.

$$u(\omega) = \sum_{\delta_i \neq \delta_j} |M_{ij}|^2 \frac{\delta_{ij}(n_j - n_i)}{\delta_{ij}^2 - (\omega + \mathrm{i}O^+)^2} + \frac{\delta_{\omega,0}}{T} \sum_{\delta_i = \delta_j} |M_{ij}|^2 n_i \tag{17.91}$$

It should be mentioned that we are dealing here with the isothermal susceptibility. This one can see by first calculating the temperature dependent susceptibility in terms of the Matsubara frequencies $\omega_n = i2\pi Tn$ (n is an integer) and then properly continuing it to the real axis. Since a second order phase transition will occur for $J(\boldsymbol{q})u(0, T_c) = 1$ it is seen right away that due to the $\delta_{\omega,0}$ term in eq. (17.91) there will be no longer a soft mode connected with it (Fulde and Peschel, 1972). The elastic processes prevent that the dynamical excitations approach $\omega = 0$ as T_c is approached from above. Thus already a Γ_1 groundstate, Γ_4 excited state system will show no true soft mode (Smith, 1972) due to the elastic scattering processes within the excited state triplet Γ_4. However for that particular case the effect of the elastic scattering processes is usually quantitatively small. More dramatic effects do occur if Γ_5 is included.

For the extreme case of a Γ_1 groundstate Γ_5 excited state system there are no inelastic processes ($\langle\Gamma_1|\boldsymbol{J}|\Gamma_5\rangle = 0$) and hence there is no dynamics at all and the problem of the soft mode becomes irrelevant.

The molecular field theory of this particular system has been worked out by Blume (1966) in order to explain the magnetism of UO_2. Only for relatively small level separation Γ_1–Γ_5 is the phase transition of second order. Larger level separation leads either to a first order phase transition or no transition depending on the coupling strength.

In fig. 17.29 we show for a specific example a numerical evaluation of the excitation spectrum as given by the poles of eq. (17.82) with $u(\omega)$ given by eq. (17.91). The calculations were done for $Pr^{3+}(J = 4)$ in a cubic crystal field with a nearest neighbour coupling $J(0)$ such to give magnetic order at a $T_c = 0.256\delta_{41}$.

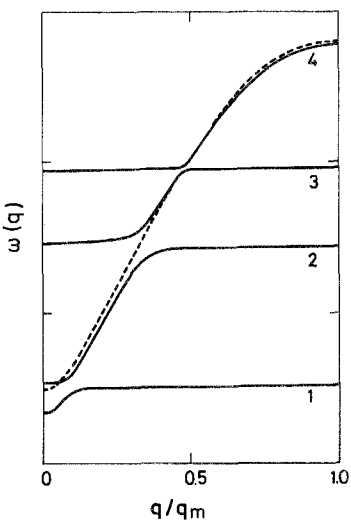

Fig. 17.29. Excitation spectrum of Pr^{3+} in a cubic crystalline field with nearest neighbour interactions. The CEF level scheme is shown in fig. 17.30, $\boldsymbol{q}$ is in (111) direction and $T = 1.21T_c$ (from Peschel et al., 1972).

The temperature for which the excitation spectrum was calculated was chosen to be $T = 1.2T_c$ and the level scheme used can be read off from fig. 17.30. The point to notice from fig. 17.29 is that transitions between high-lying levels show up in the excitation spectrum irrespective of whether or not these levels are thermally populated. The exchange interaction is responsible for the formation of different bands from the four transition energies Γ_1–Γ_4, Γ_4–Γ_5, Γ_3–Γ_4, Γ_3–Γ_5. Also shown for comparison is in fig. 17.29 the single band which would result from the Γ_1–Γ_4 model alone. One can see from that figure that for certain q-values the excitations should repel each other resulting in a splitting of the various magnetic exciton lines. This can be observed in inelastic neutron scattering experiments. In order to demonstrate this more clearly we use the following relation for the scattering cross section

$$d^2\sigma/d\Omega\, d\omega \sim [1 - \exp(-\beta\omega)]^{-1} \operatorname{Im} \chi(q, \omega) \tag{17.92}$$

We calculate the residues of the poles of $\chi(q, \omega)$, weight them with the temperature factor and normalize them such that their sum is unity for any given q value. The results are shown in fig. 17.30 from which one can read off immediately the relative strengths of the different satellite peaks.

5.1.2. *Experimental results (paramagnetic phase)*

In order to observe the collective magnetic properties experimentally one has to study proper substances with the help of inelastic neutron scattering. There are several model substances available which have been extensively investigated. TmSb is a model Van Vleck paramagnet with $J(0)/J_{crit}(0) \ll 1$ so that the collective excitations are unimportant. Pr_3Tl is a model system for an exchange induced Van Vleck ferromagnet ($T_c = 11.6$ K) with $J(0)$ barely exceeding $J_{crit}(0)$, $(J(0))/J_{crit}(0) = 1.014$).

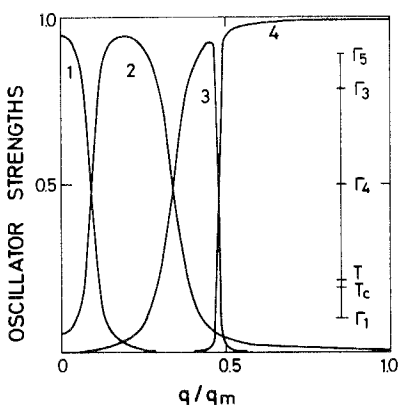

Fig. 17.30. Relative oscillator strengths of the four excitation branches numbered in accordance to fig. 17.29 (from Peschel et al., 1972).

Finally TbSb is a strongly overcritical antiferromagnet with $J(q_0)/J_{crit}(q_0) = 3.5$ and $T_N = 14.9$ K.

In the following we shall concentrate our attention on Pr_3Tl because of its interesting features (Birgeneau et al., 1971, 1972; Birgeneau, 1973; Holden and Buyers, 1974; Buyers et al., 1975).

Pr_3Tl has the Cu_3Au structure. This implies that the Pr^{3+} point symmetry is strictly tetragonal. However if the charge of Tl is taken to be equal to that of Pr^{3+} then within the point charge model the symmetry becomes effectively cubic. The crystal field parameters B_4^0 and B_6^0 are found to be -49.7×10^{-3} eV and 0.333×10^{-3} eV respectively. The ground state is Γ_1 with the first excited state Γ_4 at 77 K. The interesting feature found by inelastic neutron scattering is a temperature *independence* of the magnetic excitons. This can be seen in fig. 17.31 where typical exciton scans are shown at different temperatures for a fixed value of $|q|$. This feature can certainly not be explained within a simplified singlet–singlet or singlet–triplet model. Both models predict a temperature dependent excitonic band. However the inclusion of the full level scheme leads indeed to the result that the excitonic modes are nearly temperature independent (Holden and Buyers, 1974). Numerical results are shown in fig. 17.32. The two

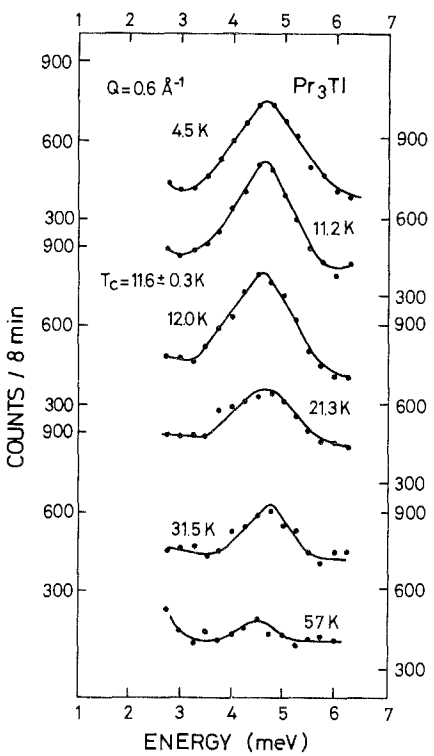

Fig. 17.31. Typical neutron scans at $k = 0.6$ A^{-1} for Pr_3Tl as function of temperature. The instrumental width is 1.25 meV (from Birgeneau et al., 1971).

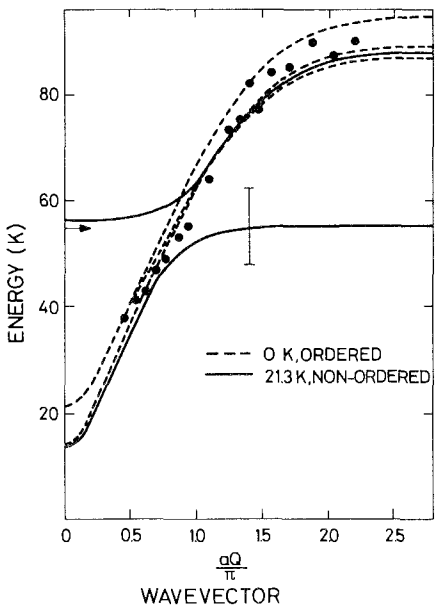

Fig. 17.32. Magnetic excitons in Pr_3Tl. The solid circles represent the neutron measurements by Birgeneau et al. (1971). The broken and solid lines are the theoretical results of Holden and Buyers (1974).

branches correspond to the Γ_1–Γ_4 and Γ_4–Γ_3 transitions. Their splitting was not observed in the experiment due to the insufficient resolution as indicated by the error bar. Also shown for comparison are the excitation modes in the ferromagnetic phase at $T = 0$. It is seen that they coincide almost with the branch in the paramagnetic phase. For a more detailed explanation we refer to the following paragraphs.

The measurements have been also extended to $(Pr_{1-x}La_x)_3Tl$ alloys (Bucher et al., 1972; Birgeneau, 1973; Buyers et al., 1975) and to dhcp Pr (Johansson et al., 1970; Birgeneau et al., 1971; Lebech and Rainford, 1971; Lebech et al., 1975), both of which have an exchange coupling close to the critical value. The results are similar to those found for Pr_3Tl. The problem of the line width of the excitons can not be solved within the theory outlined here since it has to include the damping via electron-hole excitations. For an outline how this has to be done we refer to section 5.1.5.

Finally we mention that in the paramagnetic phase of TbSb no magnetic excitons were found (Holden et al., 1974). The scattering is dominated by a strong quasi-elastic peak at $\omega = 0$. This implies a strong damping which is understandable in view of the strong exchange coupling.

5.1.3. *Magnetically ordered phase*

The ordered phase is characterized by a molecular field proportional to $\langle \boldsymbol{J} \rangle$ acting on the RE-ions. The total hamiltonian is then written as

$$H = H^{\mathrm{MF}} + H_{\mathrm{int}} \tag{17.93}$$

where the mean field hamiltonian H^{MF} is the sum of a crystal field part and a molecular field part

$$H^{\mathrm{MF}} = H_{\mathrm{CEF}} - \boldsymbol{h} \sum_i \boldsymbol{J}_i \tag{17.94}$$

Here $\boldsymbol{h} = J(0)\langle J\rangle$ is the molecular field. H_{int} is again given by eq. (17.79) but with the $\boldsymbol{J}^r$ replaced by the deviations $\hat{\boldsymbol{J}}^r$ from the mean field values. The difference to the paramagnetic case is that one has to diagonalize the single ion hamiltonian H^{MF} instead of only H_{CEF} as before. h is then determined self-consistently by requiring that

$$\langle \boldsymbol{J}\rangle = \sum_i \langle i|\boldsymbol{J}|i\rangle \mathrm{e}^{-\beta E_i} \Big/ \sum_n \mathrm{e}^{-\beta E_n} \tag{17.95}$$

where $H^{\mathrm{MF}}|i\rangle = E_i|i\rangle$. The excitations can again be calculated from the poles of the susceptibility (Klenin and Peschel, 1973; Holden and Buyers, 1974) but since there is now a preferred direction along $\boldsymbol{h}$ one has to distinguish between the longitudinal susceptibility $\chi_{zz}(\boldsymbol{q}, \omega)$ and the transverse ones $\chi_{+-}(\boldsymbol{q}, \omega)$, $\chi_{-+}(\boldsymbol{q}, \omega)$. In the RPA–MF approximation they are given by

$$\begin{aligned} \chi_{zz}(\boldsymbol{q}, \omega) &= \frac{\chi^{(0)}_{zz}(\omega)}{1 - J(\boldsymbol{q})\chi^{(0)}_{zz}(\omega)} \\ \chi_{+-}(\boldsymbol{q}, \omega) &= \frac{\chi^{(0)}_{+-}(\omega)}{1 - \frac{1}{2}J(\boldsymbol{q})\chi^{(0)}_{+-}(\omega)} \end{aligned} \tag{17.96}$$

The $\chi^{(0)}_{\mu\nu}(\omega)$ are defined in analogy to $u(\omega)$ (see eq. (17.22)) but now by using the eigenvectors and eigenvalues of H^{MF} instead of H_{CEF} only. It is

$$\begin{aligned} \chi^{(0)}_{zz}(\omega) &= \sum_{i,j=1}^{2J+1} \frac{|\langle i|J_z|j\rangle|^2 E_{ij}}{E_{ij}^2 - (\omega + \mathrm{i}O^+)^2}(n_j - n_i) \\ \chi^{(0)}_{+-}(\omega) &= \sum_{i,j=1}^{2J+1} \frac{\langle i|J_-|j\rangle\langle j|J_+|i\rangle}{E_{ij}^2 - (\omega + \mathrm{i}O^+)^2} E_{ij}(n_j - n_i) \end{aligned} \tag{17.97}$$

where $E_{ij} = E_i - E_j$.

For the purpose of demonstration we quote some results for the simplified case of two singlets.

In that case only $\chi^{(0)}_{zz}(\omega) \neq 0$. It is

$$\chi^{(0)}_{zz}(\omega) = \frac{2\Delta M^2}{\Delta^2 - \omega^2}(n_0 - n_1) \tag{17.98}$$

Here $M(T) = \langle 0|J_z|1\rangle$ and $\Delta(T)$ is the energy difference of the eigenstates $|1\rangle$, $|0\rangle$ of H^{MF} ($\Delta = E_1 - E_0$). They have to be calculated selfconsistently for any given temperature. From eq. (17.96) one obtains for the excitation spectrum

$$\omega(\boldsymbol{q}) = \Delta[1 - (n_0 - n_1)2J(\boldsymbol{q})M^2\Delta^{-1}]^{1/2} \tag{17.99}$$

It contains a gap which vanishes for $T \to T_c$ and is largest for $T = 0$. The

magnetization $\langle J \rangle$ has been evaluated by Cooper (1967, 1969) and we refer to his work for more details. With the help of eqs. (17.96–17.97) it is easy to calculate the excitation spectrum for an arbitrary crystal-field level scheme as discussed in the following paragraph. Here we want to mention only that for a complex CEF level scheme the temperature dependent magnetization can show very anomalous behaviour. For example it is possible that the system is ordered in a limited temperature interval and is disordered again as T approaches zero (Klenin and Peschel, 1973).

5.1.4. *Experimental results (ordered phase)*

With the help of eqs. (17.96) and (17.97) Holden and Buyers (1974) and Buyers et al. (1975) were able to explain in detail the excitation spectrum of Pr_3Tl and of $(Pr_{1-x}La_x)_3Tl$ compounds. The branches which correspond to the three Γ_1–Γ_4 transitions in Pr_3Tl at $T = 0$ are shown in fig. 17.32. One notices that the dispersion is almost the same as in the paramagnetic phase at $T = 21.3$ K. It should be mentioned that near $T = 0$ one can also apply a method based on the

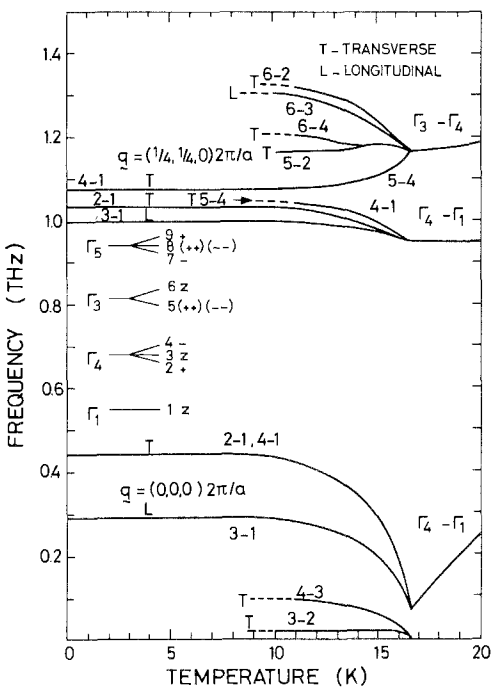

Fig. 17.33. Magnetic excitations in the ordered phase of Pr_3Tl($T_c = 11.6$ K). The zone center modes (see lower part of the figure) are compared with those at wave vector $(\frac{1}{4}, \frac{1}{4}, 0)2\pi/a$. It is seen that in the latter case the temperature dependence is very weak in accordance with the neutron measurements (from Buyers et al., 1975).

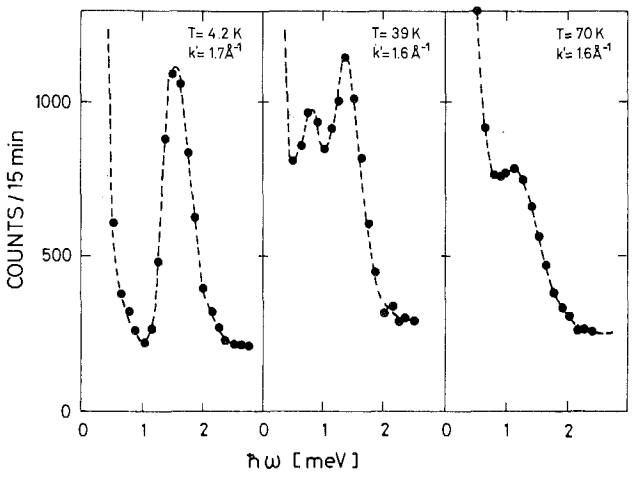

Fig. 17.34. Level repulsion of different excitation modes in the ferromagnetic phase of $TbAl_2$ as seen by inelastic neutron scattering. The intensity was measured at the (111) reciprocal lattice point corresponding to $q = 0$. $\hbar\omega$ is the energy transfer and k' is the wave vector of the scattered neutrons (from Purwins et al., 1973).

Bogoljubov transformation to calculate the excitation spectrum including all energy levels (Cooper, 1972).

In fig. 17.33 it is demonstrated how the zone-center modes behave as function of temperature especially as one goes through the ferromagnetic phase transition. Approaching T_c from above one notices that the Γ_1–Γ_4 transition does not become soft due to the elastic processes within the triplets.

Below T_c low lying spin-wave modes appear since now the triplets Γ_4, Γ_5 are split by the molecular field. The level repulsion of different excitation modes was first observed by Purwins et al. (1973) on $TbAl_2$ (see fig. 17.34). By keeping the momentum transfer fixed but varying the temperature these authors were able to observe the level repulsion in the ordered phase. Due to the temperature dependence of the excitation spectrum the region of mode anticrossing (compare with figs. 17.29, 17.32, 17.33) is sweeping through the fixed momentum transfer regime.

Furthermore there is a detailed inelastic neutron scattering study available of the magnetic excitations in TbSb (Holden et al., 1971, 1974). As mentioned above TbSb is a model substance for a system of strongly interacting singlet ground state ions. It orders antiferromagnetically at $T_N = 14.9$ K. Below T_N there are [111] ferromagnetic planes of spins with antiparallel successive sheets along the (111) axis. As mentioned before one can not resolve the magnetic excitons in the paramagnetic state due to strong damping. However below T_N at 4.5 K one observes two well defined excitation branches. The interesting result hereby is the temperature dependence of the scattering. As T_N is approached from below the exciton peaks decrease while a quasi-elastic peak at $\omega = 0$ becomes very intense.

The data can be well explained within the multi-level theory described above (Holden et al., 1974).

5.1.5. *Coupled electron–ion system*

It has been shown above how the magnetic excitations look like within the effective-interaction model. In that model the conduction electrons have been eliminated and their influence has been replaced by an effective interaction between the RE-ions. This way all the information has been lost concerning the dynamics of the conduction electrons. Therefore the excitation spectrum calculated within that model will be only approximately correct and erroneous in those parts in q-space in which the dynamics of the conduction electrons is of importance (Fulde and Peschel, 1972). The purpose of this paragraph is to demonstrate explicitly the influence of the conduction electrons on the magnetic excitation spectrum.

In order to do this we calculate the dynamical susceptibility of the RE-ions directly for the interacting conduction electrons – RE-ions system. For the mutual interaction we shall assume the isotropic exchange interaction in the form $H = -J_{ex}(\boldsymbol{r} - \boldsymbol{R})(g-1)\sigma(\boldsymbol{r})\boldsymbol{J}(\boldsymbol{R})$. The susceptibility divided by $\mu_B^2 g^2$ is then given by the diagrammatic equation shown in fig. 17.35. It is seen that the electron-hole response function enters directly into $\chi(i, j)$. The corresponding algebraic expression for the Fourier transform $\chi(\boldsymbol{q}, \omega)$ is given by (we restrict ourselves to a simple Bravais lattice)

$$\chi(\boldsymbol{q}, \omega) = \frac{u(\omega)}{1 - J_{\text{eff}}(\boldsymbol{q}, \omega)u(\omega)} \tag{17.100}$$

One notices the resemblance of eq. (17.100) with eq. (17.82). The only difference is the frequency dependence of $J_{\text{eff}}(\boldsymbol{q}, \omega)$. The latter contains the dynamics of the conduction electrons and is given by

$$J_{\text{eff}}(\boldsymbol{q}, \omega) = 2(1/N)^2(g-1)^2 \times \left(\sum_{\boldsymbol{G}} \chi_e(\boldsymbol{q} + \boldsymbol{G}, \omega)J_{ex}^2(\boldsymbol{q} + \boldsymbol{G}) - \frac{1}{N}\sum_{\boldsymbol{k}} \chi_e(\boldsymbol{k}, \omega)J_{ex}^2(\boldsymbol{k})\right) \tag{17.101}$$

Hereby $\chi_e(\boldsymbol{q}, \omega)$ is the Lindhard function (see for example Schrieffer, 1964). $\boldsymbol{G}$ are the reciprocal lattice vectors and $J_{ex}(\boldsymbol{k})$ is the Fourier transform of $J_{ex}(\boldsymbol{r} - \boldsymbol{R})$.

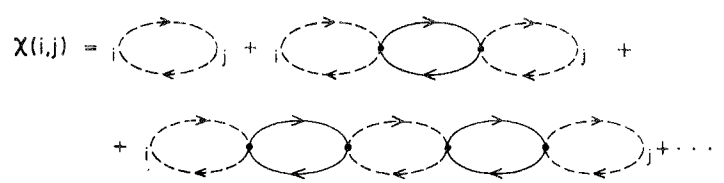

Fig. 17.35. Diagrammatic equation for the susceptibility of the coupled RE ion-conduction electron system. The solid lines correspond to electron-hole propagators while the dashed lines denote as before the CEF states at different lattice sites.

The second term in eq. (17.101) arises since we have excluded the interaction of a RE-ion with itself. This implies that the crystal-field energy levels as they appear in $u(\omega)$ are those of a single RE-ion imbedded in the conduction electron see i.e. lineshifts resulting from the interaction with the conduction electrons are supposed to be already included there (see for example eq. 17.45). The excitation spectrum is again calculated from the poles of the susceptibility. Of special interest is the range of small ω, $\boldsymbol{q}$ values. In that regime the important part of $J_{\text{eff}}(\boldsymbol{q}, \omega)$ is the term with $\chi_e(\boldsymbol{q}, \omega)$ i.e. for $G = 0$. The Lindhard function has different behavior depending in which sequence the limit $\boldsymbol{q} \to 0$, $\omega \to 0$ is taken. Let us assume that we are close to a phase transition which is defined by

$$J_{\text{eff}}(\boldsymbol{q}, 0, T_c)u(0, T_c) = 1 \tag{17.102}$$

Furthermore let us assume for simplicity that we are dealing with a two singlets system. In that case we find the following two types of poles

a) A paramagnon pole

$$\omega = -iv(\boldsymbol{q}, T)|\boldsymbol{q}| \qquad \text{for } T \to T_c \tag{17.103}$$

with the paramagnon velocity

$$v(\boldsymbol{q}, T) = v_F(\epsilon + aq^2); \qquad \epsilon \simeq (T - T_c)/T_c$$

b) A pair of poles on the real axis with

$$\omega = \pm\delta(1 - u(0, T)C)^{1/2}$$

where δ is the level separation and C is a constant.

This "optical branch" stays at finite frequency at the phase transition. This demonstrates that the inclusion of the dynamics of the conduction electrons changes completely the excitation spectrum in the small $\boldsymbol{q}$, ω regime. There are two coupled modes of the system instead of only one as in the effective interaction model. It is the paramagnon mode which goes soft at the phase transition while the 4f-electronic mode remains at a frequency of order δ as the phase transition is approached. The complete excitation spectrum is indicated in fig. 17.36. The two modes are restricted to a small part in momentum space since one of them vanishes in the particle-hole continuum as $|\boldsymbol{q}| \gtrsim \delta/v_F$. The other mode is always in the electron-hole continuum but is overdamped only for small q-values. For large q-values it is broadened but otherwise qualitatively similar to the mode of the effective interaction model. One can also investigate how a finite mean free path of the conduction electrons changes the above results (Fulde and Peschel, 1972). It remains an interesting problem to find experimentally the "optical branch" for small q-values.

5.2. *Quadrupolar interactions, excitations and instabilities*

In the preceding subsection it was demonstrated in detail how crystal-field effects show up in the magnetic properties of RE-systems. Here it will be shown that equivalent crystal-field effects do exist with respect to the elastic and

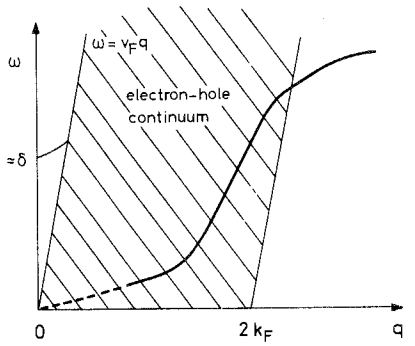

Fig. 17.36. Excitation spectrum of the coupled electron-ion system. The dashed line indicates the paramagnon pole.

vibrational properties of RE-systems. The following (incomplete) list of corresponding features will illustrate this:

a) Except for direct overlap (or superexchange) the magnetic interaction of RE-ions is mediated by conduction electrons. The quadrupolar interaction is mediated by conduction electrons *and* phonons.
b) Magnetic excitations manifest themselves as poles in the magnetic susceptibility. The analogue holds for quadrupolar excitations and the quadrupole susceptibility.
c) The test field for the magnetic susceptibility is an external (homogeneous or inhomogeneous) magnetic field. The test field for the quadrupole susceptibility is an external (homogeneous or inhomogeneous) strain field.
d) Interacting ions with a Kramers degenerate ground state will always become magnetic at low enough temperatures. Ions with a non-magnetic doublet ground state (such as Γ_3 in cubic symmetry) will always show a cooperative Jahn–Teller effect at low enough temperatures.
e) A singlet ground state system will become an exchange induced Van Vleck Magnet if the exchange interaction is sufficiently strong. Similarly it will become an induced Jahn–Teller system if the quadrupole interaction is sufficiently strong.

We shall proceed by discussing the various physical effects resulting from the quadrupolar type of interactions in close analogy to the magnetic interactions. We start by discussing the elastic properties including the effect of an external magnetic field and the occurrence of collective Jahn–Teller phase transitions. This is followed by a computation of the excitation spectrum in the non-ordered phase, which includes the dynamics of conduction electrons. Next a discussion of the ordered phase is given. The mutual influence of magnetic and structural phase transitions is left for a new subsection.

5.2.1. *Elastic properties*

We start out from the hamiltonian

$$H = H_{\text{Lattice}} + \sum_{m=1}^{N} H_{\text{CEF}}^{m} + H_{\text{Ze}} \tag{17.104}$$

with H_{Lattice} and H^m_{CEF} given by eqs. (17.24) and

$$H_{\text{Ze}} = \sum_{m=1}^{N} \mu_{\text{B}} g \boldsymbol{J}^m \boldsymbol{H} \tag{17.105}$$

Furthermore we will add later a term $H_{\text{k-f}}$ as given by eq. (17.41) which describes the coupling of conduction electrons to the RE-ions. The aim will be to discuss the temperature dependence of the elastic constants following from the above hamiltonian. In order to do this we compute the phonon propagator in the presence of the above interactions. This has the advantage that we can later extract the complete excitation spectrum from the same calculation. The phonon propagator is defined as

$$D_\mu(\boldsymbol{q}, \omega) = -\mathrm{i}\int_0^{-\mathrm{i}\beta} \mathrm{d}\tau\, \mathrm{e}^{-\mathrm{i}\omega\tau} \langle P\{(a_{q\mu}(\tau) + a^+_{-q\mu}(\tau))(a^+_{q\mu}(0) + a_{-q\mu}(0))\}\rangle_{\text{H}} \tag{17.106}$$

with P denoting the time ordering operator and $\langle \ldots\ldots\ldots \rangle_H$ the thermal average with respect to the above hamiltonian. In the absence of the magneto-elastic interactions $D_\mu(\boldsymbol{q}, \omega)$ is given by $D^0_\mu(\boldsymbol{q}, \omega) = 2\omega^0_{q\mu}/[\omega^2 - (\omega^0_{q\mu})^2]$. In the absence of conduction electrons the full phonon propagator is given in RPA by the diagrammatic equation shown in fig. 17.37 (Dohm and Fulde, 1975).

The corresponding algebraic equation is written as

$$D_\mu(\boldsymbol{q}, \omega) = D^0_\mu(\boldsymbol{q}, \omega) - D^0_\mu(\boldsymbol{q}, \omega) N [u_{\text{Q}}\{V_1(J; \boldsymbol{q}\mu), \omega\} + 2\langle V_2(J; \boldsymbol{q}\mu, \boldsymbol{q}\mu)\rangle_{H_{\text{ion}}}] D_\mu(\boldsymbol{q}, \omega) \tag{17.107}$$

A weak, field dependent coupling of modes of different polarization μ, μ' has been neglected at this stage. It is apparent that the linear magneto-elastic interaction V_1 enters through the single-ion (quadrupolar) susceptibility

$$u_{\text{Q}}\{O, \omega\} = \sum_{\delta_i \neq \delta_j} \frac{|O_{ij}|^2 \delta_{ij}}{\delta^2_{ij} - (\omega + \mathrm{i}O^+)^2} (n_j - n_i) + \frac{1}{T}\delta_{\omega,0} \sum_{\delta_i = \delta_j} |O_{ij}|^2 n_i - \frac{1}{T}\langle O\rangle^2_{H_{\text{ion}}} \delta_{\omega,0} \tag{17.108}$$

which is written in close analogy to eq. (17.91). The only difference is that the matrix elements $O_{ij} = \langle i|O|j\rangle$ are formed with the quadrupolar type of operators appearing in V_1 (see eq. 17.36) and that the mean-field term has been subtracted out. This implies that the phonons are defined by the displacements from the equilibrium positions which are generally magnetic field dependent and will be

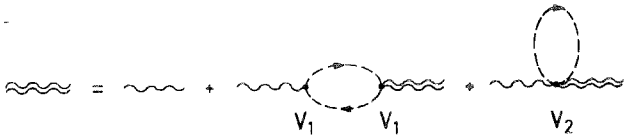

Fig. 17.37. Diagrams for the computation of $D_\mu(\boldsymbol{q}, \omega)$ (double wavy line). The bare phonon propagator $D^0_\mu(\boldsymbol{q}, \omega)$ is shown as a single wavy line.

used in the following. They have to be contrasted with the rest positions used before which are defined by the minima of the lattice potential. The second order interaction V_2 appears as a thermal average with respect to the single-ion hamiltonian $H_{\text{ion}} = H^0_{\text{CEF}}(\boldsymbol{J}) + \mu_B g \boldsymbol{J}\boldsymbol{H}$. Equation (17.107) is readily solved and one obtains

$$D_\mu(\boldsymbol{q}, \omega) = \frac{2\omega^0_{q\mu}}{\omega^2 - (\omega^0_{q\mu})^2 + 2\omega^0_{q\mu} N(u_Q\{V_1, \omega\} + 2\langle V_2\rangle)} \tag{17.109}$$

From the diagrams shown in fig. 17.37 and from eq. (17.108) it is very transparent why the effect of the second order magneto-elastic interaction is not small as compared with the first order interaction. Namely the second-order interaction enters linearly into the phonon propagator while the first-order interaction enters quadratically.

The poles of $D_\mu(\boldsymbol{q}, \omega)$ describe the excitations of the system. They are given by

$$\omega^2(\boldsymbol{q}\mu) = (\omega^0_{q\mu})^2 - 2\omega^0_{q\mu} N[u_Q\{V_1, \omega\} + 2\langle V_2\rangle] \tag{17.110a}$$

In the limit $|\boldsymbol{q}| \to 0$ one has $\omega^0_{q\mu} = c_0|\boldsymbol{q}|$ and $\omega_{q\mu} = c|\boldsymbol{q}|$. Then eq. (17.110a) allows us to determine the sound velocity c or the elastic constant ($\sim c^2$) in the presence of the magneto-elastic interactions and a magnetic field by dividing it by q^2 and taking the limit $|\boldsymbol{q}| \to 0$. In the absence of a magnetic field the rotational terms do not contribute and by using the expression for V_1, V_2 one finds

$$c^2 = c_0^2 - \frac{1}{M} u_Q\{G_{\alpha\beta} Q^+_{\alpha\beta}/q, 0\} + \frac{1}{M}\langle G_{\alpha\beta}\rangle \frac{q_\alpha q_\beta}{q^2}$$

$$+ \frac{1}{M}\langle F_{\alpha\beta\gamma\delta}\rangle Q^+_{\alpha\beta} Q^+_{\gamma\delta}/q^2 \tag{17.110b}$$

In replacing in $u_Q\{V, \omega\}$ the frequency ω by $\omega = 0$ we are also counting the elastic processes in eq. (17.108) which occur for $\delta_i = \delta_j$. This remedies the shortcomings of the RPA which does not contain lifetime effects (Dohm and Fulde, 1975). In the next paragraph we will give some explicit examples for the functional dependence of u_Q, $\langle G\rangle$ and $\langle F\rangle$ on temperature. Here we want to draw attention only to the following fact. If the crystal-field ground state is degenerate and contributes to the elastic part of the susceptibility $u_Q\{G_{\alpha\beta}(\boldsymbol{J}) Q^+_{\alpha\beta}/q, 0\}$ then this implies a contribution to the sound velocity of the form $-A^2/T$ where A is a constant. Thus the sound velocity will always go to zero at sufficiently low temperatures. This causes an instability of the system which will undergo a collective Jahn–Teller phase transition. The situation is very similar to the magnetic case where a degenerate magnetic ground state always causes a magnetic phase transition.

At this stage a comment is in order concerning possible self-energy corrections to eqs. (17.109) and hence (17.110) (see for example Gehring and Gehring, 1975). For that purpose let us consider a system of RE-ions which have an orbitally degenerate ground state and furthermore the other CEF levels so

high up in energy that they may be neglected. In that case the phonons will scatter elastically and will be influenced by the magneto-elastic interactions only in the limit $|\boldsymbol{q}| \to 0$ (see the remark following eq. 17.110b).

For that particular case one can show that processes in which phonons scatter repeatedly at the same ion at site i for example do not contribute and have to be excluded. They lead only to a constant in the hamiltonian. This exclusion has the effect of renormalizing the magneto-elastic coupling constants or alternatively the functions $u_Q\{V_1, 0\}$ and $\langle V_2 \rangle$.

In our formalism the exclusion can be achieved simply by replacing $u_Q\{G_{\alpha\beta}Q^+_{\alpha\beta}/q, 0\}$ by

$$\frac{u_Q\{G_{\alpha\beta}Q_{\alpha\beta}/q, 0\}}{1 + (1/3Mc_0^2)u_Q\{G_{\alpha\beta}Q^+_{\alpha\beta}/q, 0\}} \tag{17.111}$$

Equivalent replacements hold for $\langle G_{\alpha\beta} \rangle\, q_\alpha q_\beta/q^2$ and $\langle F_{\alpha\beta\gamma\delta} \rangle Q^+_{\alpha\beta} Q^+_{\gamma\delta}/q^2$. Hereby the assumption has been made that the Debye-approximation holds for the phonons and that we are dealing with one RE-ion per unit cell. It is seen that for $u_Q(T) \sim 1/T$ the modifications due to the denominators may become important. If set into eq. (17.110b) they lead to a lowering of the temperature at which c^2 and hence the corresponding elastic constant becomes soft.

The situation is somewhat different if instead of a degenerate ground state we consider the case of two singlets. Here the previous arguments concerning the exclusion of repeated scattering do not hold. Therefore to lowest order in the magnetoelastic coupling eq. (17.109) is correct as it stands and the denominator in eq. (17.111) is an incomplete higher order correction in the interaction. Other corrections would involve changes in the CEF energy level separation as well as life-time effects. As a consequence $u_Q\{V_1, \omega\}$ would be changed for example. However, in order to treat different CEF splittings on equal footing it may seem advantageous to exclude repeated scattering on the same site in *all* situations and to assume that the δ_{ij} occurring in eq. (17.108) are renormalized quantities which may be temperature dependent and also have an imaginary part. In the following we will not pay particular attention to the self-energy subtractions. Corrections as described by eq. (17.111) can be made wherever required.

If a magnetic field is applied, then the first and second order rotational terms have to be added. Their contribution is as big as the magnetic field dependent contributions from the pure strains. Not only is the sound velocity magnetic field dependent but it is also directional dependent with the preferred axis given by the direction of the magnetic field. In order to demonstrate this more explicitly we consider a crystal of cubic symmetry with a magnetic field pointing along one of the three principal axes in z-direction. Consider now two transverse sound waves propagating along the x-axis and the z-axis of the crystal with the polarization in the z-direction and x-direction, respectively. Without an applied magnetic field the corresponding sound velocities are of course equal. In a magnetic field this is no longer the case. As seen in fig. 17.38a both sound waves have the same first order strain deformation but their rotational deformations have opposite signs relative to the strain deformation. This implies that the

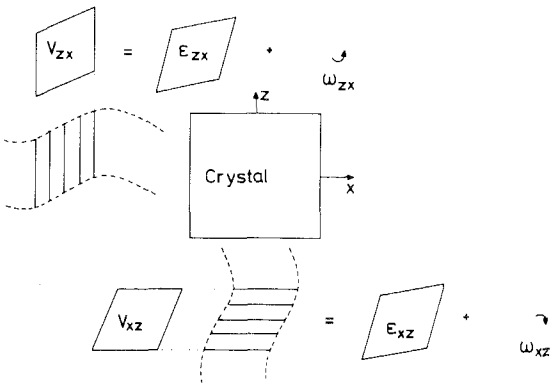

Fig. 17.38a. Transverse sound waves propagating along the x-axis and z-axis of a cubic crystal with polarization in the z and x-direction, respectively. Both waves contain identical linear-strain deformation but opposite rotational deformations.

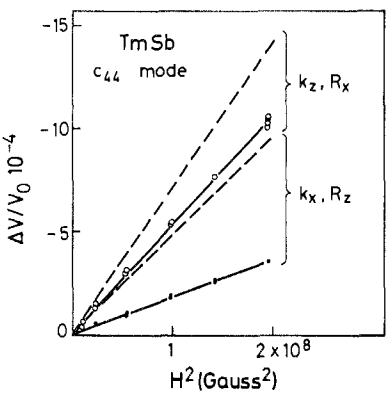

Fig. 17.38b. Measured difference in the velocity of the c_{44} mode in TmSb parallel and perpendicular to an applied field in z-direction. The polarizations are as indicated. The dashed lines correspond to a calculation using the point charge model. There is then no adjustable parameter in the theory since the magneto-elastic coupling constants are fixed this way. Second order strain effects are included as well as first and second order rotational effects (from Wang and Lüthi, 1977).

product $Q^+_{xz}Q^-_{xz}/q^2 = \pm\frac{1}{4}$ for the two waves. From eq. (17.38) and the corresponding one for V_2 it follows then, that their sound velocities are different. A similar difference results from the second-order strain term (Dohm, 1975). The differences in the sound velocities are small but large enough to be measurable with fields of the order of 50 kG.

Experimental results are shown in fig. 17.38b for the c_{44}-mode of TmSb (Wang and Lüthi, 1977). One notices the H^2-dependence of the difference of the mode velocities in agreement with the theory.

Recently strong CEF effects have been found also for the temperature dependence of the thermal expansion of TmSb (Ott and Lüthi, 1976).

As the next step we want to include the aspherical Coulomb charge scattering of the conduction electrons as described by H_{AC} (see eq. 17.44). For simplicity let us assume that there is no external magnetic field.

5.2.2. *Inclusion of conduction electrons*

The presence of conduction electrons can lead to an additional quadrupolar coupling of the RE-ion. In addition they will lead to damping of the collective excitations due to possible electron-hole excitations. It will be demonstrated that the damping of sound waves due to that mechanism is particularly large in the vicinity of a Jahn–Teller phase transition.

In order to study the influence of conduction electrons we restrict ourselves to the aspherical Coulomb charge scattering $(\Lambda, \Sigma) = (2, 0)$ which is described by the hamiltonian H_{AC} as given by eq. (17.44). Furthermore we consider again the simple case of cubic symmetry and specialize our considerations to a shear wave polarized in x-direction and propagating in z-direction. The interaction of the RE-ions via the conduction electrons is taken into account by extending the diagrammatic equations for the mode under consideration so that they are of the form shown in fig. 17.39.

It is seen how the interaction with the conduction electrons leads to a renormalization of the quadrupole susceptibility u_Q and hence of the phonon propagator. At this stage it is worth pointing out that there is a certain similarity between the effect of conduction electrons and of optical phonons. As will be shown later (see fig. 17.42) the diagrams for the renormalization of the acoustical phonons look the same except for the replacement of the electron-hole propagator $\chi_e^Q(\boldsymbol{q}, \omega)$ by the optical phonon propagator $D_{op}(\boldsymbol{q}, \omega)$.

The response function $\chi_e^Q(\boldsymbol{q}, \omega)$ is closely related to the Lindhard function $\chi_e(\boldsymbol{q}, \omega)$ except that it has quadrupolar character.

The diagrammatic equations are trivially solved. One finds that $u_Q\{V_1, \omega\}$ and $\langle V_2 \rangle$ are enhanced. u_Q is replaced by

$$u_Q \rightarrow u_Q/[1 - J_{eff}^Q(\boldsymbol{q}, \omega) u_Q] \tag{17.112}$$

where due to a selfenergy subtraction as discussed following eq. (17.101) the

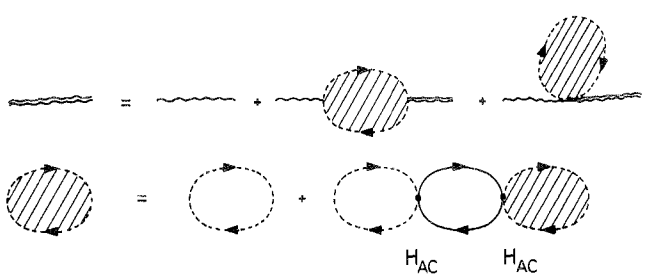

Fig. 17.39. Renormalization of the phonon propagator due to the interaction H_{AC} which leads to an indirect quadrupolar coupling of the RE-ions. Wavy lines are phonons, solid lines are conduction electrons and dashed lines denote the CEF-states.

effective interaction is given by

$$J_{\text{eff}}^{Q}(\boldsymbol{q}, \omega) = a\frac{5}{4\pi} I_2^2 Q_2^2 N^{-2} \left(\sum_{\boldsymbol{G}} \chi_e^Q(\boldsymbol{q} + \boldsymbol{G}, \omega) - \frac{1}{N} \sum_{\boldsymbol{k}} \chi_e^Q(\boldsymbol{k}, \omega) \right)$$

where a is a reduced matrix element depending on J. Again $\boldsymbol{G}$ is a reciprocal lattice vector. A similar result holds for $\langle V_2 \rangle$. For typical ultrasonic frequencies one may replace $\chi_e^Q(\boldsymbol{q}, \omega)$ by $\chi_e^Q(0, 0)$ and then the selfenergy correction leads just to a renormalization of I_2. Therefore it has sometimes been neglected. Equation (17.112) shows that conduction electrons can considerably enhance the coupling of the RE-ions to the acoustic phonons. Therefore the effective coupling constants should be much larger in metals than in insulators. There is an additional renormalization of the RE-ion-acoustic phonon interaction which results from the direct coupling of the phonons to the conduction electrons which in turn couple to the RE-ions. For details we refer to Fulde (1975). The attenuation of the elastic waves due to electron-hole excitations can be calculated from the imaginary part of $\chi_e^Q(\boldsymbol{q}, \omega)$.

In the vicinity of a Jahn–Teller phase transition one finds

$$\omega^2 = c_0^2 q^2 \left[A \frac{T - T_c}{T_c} - i\omega\tau_Q B \left(\frac{T_c}{T - T_c} \right)^2 \right] \tag{17.113}$$

where A and B are dimensionless constants and τ_Q is an electronic quadrupolar relaxation time. This demonstrates that the ultrasonic attenuation may become appreciable near the phase transition point.

From the point of view of experiments TmCd appears to be an example in which the conduction electron effects are important. TmCd has the CsCl structure. The ground state of the Tm^{3+} ions is Γ_3 with the first excited state Γ_5 at 20 K. The system undergoes a distortion to a tetragonal structure at $T_D = 3.16$ K (Lüthi et al., 1975). The mode c_{11}–c_{12} shows strong softening which can be fitted to an equation of the form (17.110b) i.e.

$$\frac{c_{11}-c_{12}}{(c_{11}-c_{12})_0} = 1 - \frac{g_0^2 u_Q \{3J_z^2 - J(J+1)\}}{1 - g_1^2 u_Q \{3J_z^2 - J(J+1)\}} \tag{17.114}$$

Here $(c_{11}-c_{12})_0$ is the elastic constant in the absence of magneto-elastic interactions. The second order strain effects have been left out for simplicity. They may be responsible for some of the deviations between the experiments and the simplified expression (17.114). g_1 is found to be such that the denominator vanishes for $T = 1.7$ K. One knows that $\boldsymbol{k} = 0$ optical phonons can not contribute for a CsCl structure as source of the enhancement factor (Levy, 1973). Further evidence for the importance of the conduction electrons comes from the thermopower discussed in section 4.1.3 and a measurement of the electrical resistivity as function of temperature. The latter shows a kink at the structural phase transition temperature indicating that the conduction electrons feel the tetragonal distortion (Sablik et al., 1972). This strongly suggests the presence of an interaction $(\Lambda, \Sigma) = (2, 0)$ as given by H_{AC}. Furthermore there is a strong damping of the sound waves as the transition temperature is approached in qualitative agreement with the picture just presented.

A similar situation seems to prevail in DySb where also an enhancement factor of the type as it occurs in eq. (17.114) is necessary to explain the softening of the elastic constants (Levy, 1973). However this has also been attributed to exchange (Levy, 1973).

5.2.3. *Experimental results*

There are experiments available on various RE-systems which show a strong temperature dependence of the elastic constants due to crystal-field effects. In some cases one of the elastic constants goes soft at a particular temperature and then the system undergoes collectively a Jahn–Teller phase transition in analogy to a magnetic phase transition. The order parameter is then a spontaneous quadrupole moment instead of the spontaneous magnetic moment in the magnetic case. Collective Jahn–Teller phase transitions have been found in metallic and non-metallic systems. They have been discussed in detail in a very complete review article by Gehring and Gehring (1975), in which also an extensive list of references can be found. We shall limit ourselves here in discussing some of the outstanding features of these systems in as close analogy to the magnetic case as possible.

(*a*) *RE-antimonides*

We start out with the RE-antimonides which show the rocksalt structure and for which the crystal-field levels are generally well known from inelastic neutron scattering (see section 2.3). The various materials may be divided into two classes (Mullen et al., 1974). To the first class there belong those substances for which the CEF-ground state has vanishing quadrupole matrix elements. It is Γ_1 (PrSb, TmSb), Γ_7 (SmSb) or Γ_6 (DySb). Substances in the second class have a ground state with nonvanishing quadrupole matrix elements such as Γ_3 (HoSb) and Γ_8 (ErSb). Substances in the first class have elastic constants which show characteristic structure in their temperature behaviour but usually remain finite at all temperatures. An exception is DySb which has an unusually large quadrupole susceptibility at low temperatures. Substances in the second class show always a softening of an elastic constant at low temperatures since their quadrupole susceptibility diverges as $1/T$ at low temperatures. Since these substances are all metallic one might think that the effect of conduction electrons is very important in order to understand the temperature dependence of the elastic constants. Nevertheless it turns out that the data for some compounds (PrSb, TmSb, SmSb) can be analysed successfully without a denominator as it occurs in eq. (17.114). For these substances the conduction-electrons just lead to a renormalization (enhancement) of the magneto-elastic coupling constants. For DySb (Moran et al., 1973; Levy, 1973) see also the remarks in section 5.2.2. Neglecting the effect of the conduction electrons the temperature dependence of the elastic constants with or without applied magnetic field can then be analysed with the help of eq. (17.110).

We shall demonstrate this explicitly for one particular example (SmSb). This will

show the usefulness and simplicity of the theoretical analysis given above. It also makes transparent the approximations which are commonly made in analysing the experimental data and which may be responsible for some of the unexplained discrepancies between the experiments and the theory.

Let us consider pure shear waves within the x–z plane of a cubic crystal, i.e. $Q^{\pm}_{\alpha\beta} = 0$ except $Q^{\pm}_{xz}$ and $Q^{\pm}_{zx}$. In order to calculate $G_{\alpha\beta}(\boldsymbol{J})$ (see Dohm and Fulde, 1975) one has to know H_{CEF}. We use the simplified form

$$H^{0}_{\mathrm{CEF}}(\boldsymbol{J}) = -20\, B_4 \sum_{\alpha\neq\beta} J^2_{\alpha} J^2_{\beta} \tag{17.115}$$

i.e. we neglect sixth-degree terms for simplicity and omit pure c-number contributions. This leads to $G_{xz} = G_{zx} = (g/2)(J_xJ_z + J_zJ_x)$. The first order magneto-elastic interaction reads then

$$V_1(\boldsymbol{J}; \boldsymbol{q}\mu) = \mathrm{i}(2MN\omega^{0}_{\boldsymbol{q}\mu})^{-1/2}[g(J_xJ_z + J_zJ_x)Q^{+}_{xz} - 20\, B_4 \Lambda_{xz} Q^{-}_{xz}] \tag{17.116}$$

The coefficient of the rotational term is found to be of the form

$$\Lambda_{xz} = (J_xJ_z + J_zJ_x)(J^2_x - J^2_z) + (J^2_x - J^2_z)(J_xJ_z + J_zJ_x) \tag{17.117}$$

Usually all experimental data (even in the case of an applied field) has been analysed in terms of $V_1(\boldsymbol{J}, \boldsymbol{q}\mu)$ only, that is neglecting $V_2(\boldsymbol{J}; \boldsymbol{q}\mu, \boldsymbol{q}\mu)$ and furthermore neglecting the linear rotational interaction. In that case the transverse sound velocity (c_{44} mode) is simply

$$c^2 = c^2_0 - \frac{g^2}{4M}\, u_{\mathrm{Q}}\{J_xJ_z + J_zJ_x, 0\} \tag{17.118}$$

Let us consider SmSb which has a ground state doublet Γ_7 and the excited state quartet Γ_8 at $\Delta = 65$ K. In that case $M = M_{\mathrm{Sm}} + M_{\mathrm{Sb}}$ and

$$u_{\mathrm{Q}}\{J_xJ_z + J_zJ_x, 0\} = \frac{160}{3\Delta}\,\frac{1-\exp(-\beta\Delta)}{1+2\exp(-\beta\Delta)} \tag{17.119}$$

A comparison of this result with the experimental data is shown in fig. 17.40. The fit to the data is remarkably good. It allows the determination of $g = 75$ K. The same calculation can be done also for the shear waves of the c_{11}–c_{12} mode. The measurements of the temperature dependence of the elastic constants and their theoretical analysis have been used to determine the magneto-elastic coupling constants across the LnSb series (see Mullen et al., 1974). These values were then compared with the corresponding ones calculated from a point charge model. The same trends were found in both cases and even the absolute values agreed better than expected (Lüthi et al., 1973 and 1974; Mullen et al., 1974). The deviations seen in fig. 17.40 may result from the approximations involved. In addition to neglecting the effect of the conduction electrons they can be listed as follows: first of all $G_{\alpha\beta}(J)$ has been calculated only to second degree in J. There are also fourth- and sixth-degree contributions which should be taken into account. They can be calculated directly from the crystal-field potential. Furthermore there are the second-order magneto-elastic interactions. We write

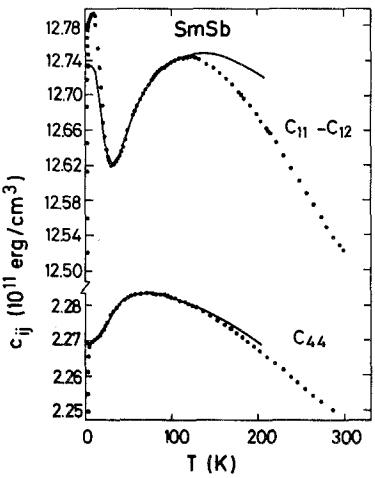

Fig. 17.40. Temperature dependence of the elastic constants of SmSb. The full line represents the theoretical fit to the experimental data (from Mullen et al., 1974).

them down for completeness including the rotational terms. One finds for the second-order strain terms (see Dohm, 1976)

$$V_2^{\text{strain}}(\boldsymbol{J};\boldsymbol{q}\mu,\boldsymbol{q}\mu) = -(2MN\omega_{q\mu}^0)^{-1}[\tfrac{1}{2}G_{\alpha\beta}(\boldsymbol{J})q_\alpha q_\beta + \tfrac{1}{2}F_{\alpha\beta\gamma\delta}(\boldsymbol{J})Q_{\alpha\beta}^+ Q_{\gamma\delta}^+] \tag{17.120}$$

where

$$\tfrac{1}{2}G_{\alpha\beta}(\boldsymbol{J})q_\alpha q_\beta = \bar{g}(J_z^2 - J_x^2)Q_{xz}^+ Q_{xz}^+ + \tfrac{1}{2}\bar{g}(J_x^2 + J_z^2)[(Q_{xz}^+)^2 + (Q_{xz}^-)^2] \tag{17.121}$$

$$\tfrac{1}{2}F_{\alpha\beta\gamma\delta}(\boldsymbol{J})Q_{\alpha\beta}^+ Q_{\gamma\delta}^+ = f[J_x^2 + J_z^2 - \tfrac{3}{5}J(J+1)](Q_{xz}^+)^2$$

Here $\bar{g}$ is the coupling constant of the $(c_{11}-c_{12})$-mode. Values of $|\bar{g}|$ for different RE-antimonides can be found in Dohm (1976). For SmSb it is $|\bar{g}| = 356$ K. The coupling constant f can be estimated only from a point charge model. This leads to $f = -(\frac{175}{2})\beta_J \cdot \langle r^4\rangle Ze^2/a^5$. For SmSb one finds $f \simeq 30$ K. For the second order rotational terms one finds

$$V_2^{\text{rot}}(\boldsymbol{J};\boldsymbol{q}\mu,\boldsymbol{q}\mu) = -(2MN\omega_{q\mu}^0)^{-1}[2g(J_x^2 - J_z^2)Q_{xz}^+ Q_{xz}^- + 40\, B_4\lambda_{xz}(Q_{xz}^-)^2]$$

where

$$\lambda_{xz} = (J_xJ_z + J_zJ_x)^2 - (J_x^2 - J_z^2)^2$$

In zero magnetic field their effect just cancels the contribution of the first-order rotational interaction but as pointed out before they may become important for $\boldsymbol{H} \neq 0$. In zero field the velocity of a shear wave propagating in z-direction and polarized in x-direction is simply

$$c^2 = c_0^2 - \frac{g^2}{4M}u_Q\{J_xJ_z + J_zJ_x\} + \frac{\bar{g}}{M}\langle J_z^2\rangle + \frac{f}{2M}\langle J_x^2 + J_z^2 - \tfrac{3}{5}J(J+1)\rangle \tag{17.122}$$

Although the first- and second-order strain effects are generally of comparable

size the second-order effects are less interesting because of their weak temperature dependence. This may explain why the first-order terms alone can often fit the experimental results so well.

(*b*) *RE-zircons*

Another class of materials which has been investigated in great detail are the RE-zircons which have the general composition RXO_4 where X stands for V, As or P.

Especially interesting are some of the vanadates which show collective Jahn–Teller phase transitions. Three widely investigated representatives are $TmVO_4$, $DyVO_4$ and $TbVO_4$ with transition temperatures $T_D = 2.1$ K; 14.0 K and 33 K, respectively. The energy scheme of the lowest crystal-field levels is shown in fig. 17.41. $TmVO_4$ has an orbital doublet as ground state with the first-excited state sufficiently high up in energy ($\simeq 50\,cm^{-1}$) (Becker et al., 1972) that it has only a weak influence (Melcher et al., 1973). With respect to the ground state it corresponds to HoSb. The quadrupole susceptibility diverges as T^{-1} at low temperatures. $DyVO_4$ has two Kramers doublets as lowest states with a low energy separation ($9\,cm^{-1}$). Finally $TbVO_4$ has a singlet, a doublet and a singlet as lowest crystal-field states with an energy separation of $9\,cm^{-1}$ each. The elastic constants can be calculated in the same way as outlined for the RE-antimonides with the only difference that the symmetry of the crystal field is tetragonal instead of cubic. The Jahn–Teller transition temperature is defined by the condition that the sound velocity of a certain mode as given by eq. (17.110b) is zero at that temperature. For example for $TmVO_4$ the soft acoustic mode transforms like B_{2g} and the corresponding elastic constant is c_{66}. The experimental data have been analysed in detail for $TmVO_4$ (Melcher et al., 1973; Pytte, 1974) $DyVO_4$ (Melcher and Scott, 1972; Gorodetsky et al., 1971) and $TbVO_4$ (Elliott et al., 1972; Pytte and Stevens, 1971).

For more details we refer to the review article of Gehring and Gehring (1975). Here we mention only that the analysis involves the inclusion of the optical phonons, which lead to an additional interaction between the RE-ions. Since the

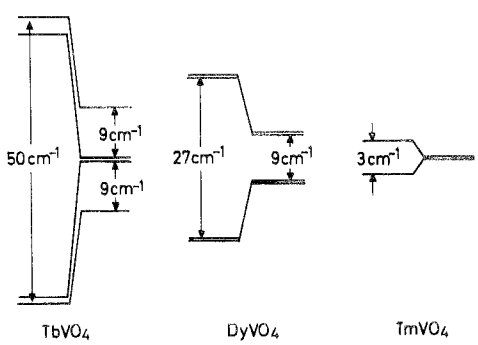

Fig. 17.41. Lowest CEF-energy levels for three vanadates below (left) and above (right) the Jahn–Teller transition temperature (from Gehring and Gehring, 1975).

inclusion of optical phonons is very instructive and very easy to achieve with the help of the diagrammatic approach we demonstrate it and apply the result to the c_{66} elastic constant of $TmVO_4$. In order to avoid the complexity of the most general case let us consider the simple case of cubic symmetry and as before a shear wave polarized in x-direction and propagating in z-direction. The sound velocity is then given by eq. (17.122). In order to include the interaction of the RE-ions via optical phonons we extend the diagrammatic equations shown in fig. 17.37 so that they look as shown in fig. 17.42. This implies that in eq. (17.122) $u_Q\{J_xJ_z + J_zJ_x\}$, $\langle J_z^2\rangle$ and $\langle J_x^2 + J_z^2 - \frac{3}{5}J(J+1)\rangle$ are now replaced by new functions $\bar{u}_Q$, $\overline{\langle J_z^2\rangle}$, $\overline{\langle J_x^2 + J_z^2 - \frac{3}{5}J(J+1)\rangle}$ which fulfill equations of the form ($V_1 = J_xJ_z + J_zJ_x$):

$$\bar{u}_Q\{V_1\} = u_Q\{V_1\} - Ng_{op}^2 u_Q\{V_1\} D_{op}(\boldsymbol{q}, \omega)\bar{u}_Q\{V_1\} \tag{17.123}$$

$$\overline{\langle J_z^2\rangle} = \langle J_z^2\rangle - N\bar{g}_{op}^2 u_Q\{J_z^2\} D_{op}(\boldsymbol{q}, \omega)\overline{\langle J_z^2\rangle}$$

and similarly for $\overline{\langle J_x^2 + J_z^2 - \frac{3}{5}J(J+1)\rangle}$. Hereby g_{op} and $\bar{g}_{op}$ denote coupling constants of the RE-ions to optical phonons in a similar way as g and $\bar{g}$ denote coupling constants to acoustic phonons. $D_{op}(\boldsymbol{q}, \omega)$ is the propagator for optical phonons which we write as $D_{op}(\boldsymbol{q}, \omega) = 2\omega_{op}(\boldsymbol{q})/[\omega^2 - \omega_{op}^2(\boldsymbol{q})]$.

The above equations are trivially solved. For example

$$\bar{u}_Q = u_Q/[1 + Ng_{op}^2 D_{op}(\boldsymbol{q}, \omega)u_Q] \tag{17.124}$$

In the limit $\boldsymbol{q}, \omega \to 0$, $D_{op}(\boldsymbol{q}, \omega)$ reduces to $D_{op}(0, 0) = -2/\omega_{op}(0)$. By setting $\bar{u}_Q$, $\overline{\langle J_z^2\rangle}$ and $\overline{\langle J_x^2 + J_z^2 - \frac{3}{5}J(J+1)\rangle}$ into eq. (17.122) one finds thus

$$c^2 = c_0^2 - \frac{g^2}{4M}\frac{u_Q(J_xJ_z + J_zJ_x)}{1 - 2g_{op}^2\omega_{op}^{-1}(0)Nu_Q\{J_xJ_z + J_zJ_x\}} + \frac{\bar{g}}{M}\frac{\langle J_z^2\rangle}{1 - 2\bar{g}_{op}^2\omega_{op}^{-1}Nu_Q\{J_z^2\}} + \frac{f}{2M}\frac{\langle J_x^2 + J_z^2 - \frac{3}{5}J(J+1)\rangle}{1 - 2f_{op}^2\omega_{op}^{-1}Nu_Q\{J_x^2 + J_z^2 - \frac{3}{5}J(J+1)\}} \tag{17.125}$$

The inclusion of optical phonons thus leads to an enhancement of the different contributions of the acoustic phonons. This is intuitively obvious since the

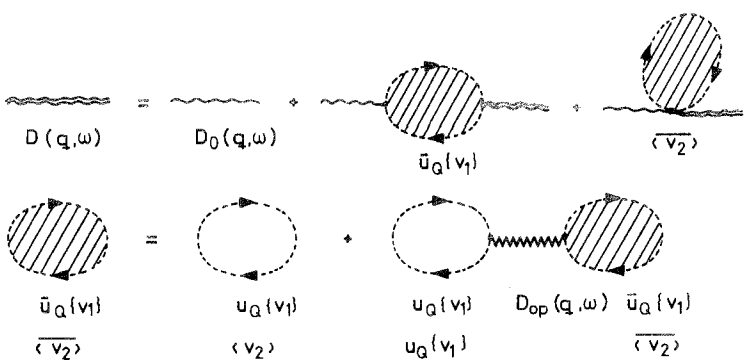

Fig. 17.42. Diagrams for the computation of the propagator $D(\boldsymbol{q}, \omega)$ for shear waves in the presence of interactions between the RE-ions and optical phonons. Compare with fig. 17.39 where the interaction is via electron-hole excitations instead of optical phonons.

interaction of the RE-ions due to the optical phonons favours a Jahn–Teller phase transition to occur.

Equation (17.125) is very simple in spite of the lengthy appearance. In order to demonstrate how easily one can extract information out of it we apply our findings to the softening of the elastic constant c_{66} in $TmVO_4$. As pointed out before the susceptibility corresponding to $u_Q\{J_xJ_z + J_zJ_x\}$ behaves as $1/T$ at low temperature while the second order strain contributions show only a weak temperature dependence. The equation for c^2 has thus the structure

$$c^2 = c_0^2 - \frac{A}{T}\frac{1}{1-\lambda/T} + B(T) = c_0^2\left(1 - \frac{A}{c_0^2}\frac{1}{T-\lambda} + \frac{B(T)}{c_0^2}\right) \tag{17.126}$$

Here A and λ are constants which are proportional to the square of the coupling constants. $B(T)$ represents the weakly temperature dependent second-order strain effects. Latter are usually neglected for no obvious reason. A comparison of the experimental data with eq. (17.126) is shown in fig. 17.43.

5.2.4. *The excitation spectrum*

The excitation spectrum is determined from the poles of $D_\mu(\boldsymbol{q}, \omega)$ (see eq. 17.110a). It contains the dynamics of the elastic medium (phonons) as well as the one of the RE-system (CEF energy states excitations). The latter enter via the frequency dependent susceptibility $u_Q\{V_1, \omega\}$ (see eq. 17.108). The mutual interaction between both types of modes leads to a hybridization (Elliott et al., 1972). Due to the elastic scattering processes within a CEF-energy level there are $\delta_{\omega=0}$-contributions to the quadrupole susceptibility (see eq. 17.108). It was shown that these processes have to be included in the expressions for the elastic constants and therefore contribute to a Jahn–Teller phase transition. However they do not show up in the acoustic phonon dispersion which one would measure

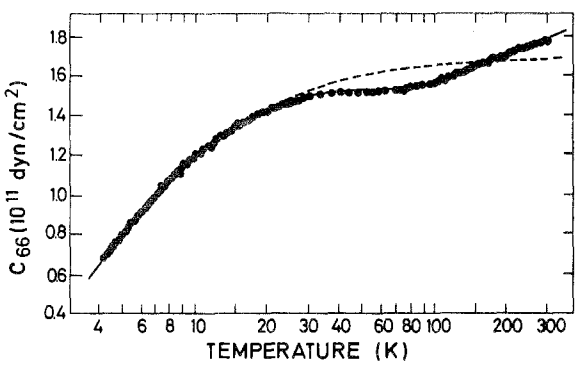

Fig. 17.43. Temperature dependence of the elastic constant c_{66} for $TmVO_4$. The dashed line corresponds to eq. (17.126) while the solid line is an extension of the theory to include the excited levels (from Melcher et al., 1973).

in a neutron scattering experiment. In such an experiment ω is always sufficiently large so that these processes do not contribute. The explicit computation of the excitation spectrum is in close analogy to section 5.1.1. If optical phonons (Halperin, 1973) and/or conduction electrons are included, the situation is conceptually not more difficult. There is additional dynamics entering the problem via the denominator of the susceptibility u_Q (compare with eq. 17.112). The conduction electrons do not only lead to a line broadening but they also change the excitation spectrum totally for sufficiently small q-values. The situation is similar to the magnetic case where for small values of q a paramagnon branch was found in the excitation spectrum near the phase transitions. Here the same holds true except that we are dealing with the quadrupole analogue of paramagnons, namely critically damped electronic quadrupole modes. For a Γ_1 ground-state system with an excited state Γ_3 at energy δ this mode appears for $q < (\delta/v_F)T/(T - T_c)$ and is of the form as given by eq. (17.103). Further details are found in Fulde (1975).

Extensions of the theory as to include several Jahn–Teller ions per unit cell (Halperin and Englmann, 1970) distant dependent exchange interactions (Pytte, 1974; Gehring, 1974) applied magnetic fields (Jacobsen and Stephens, 1963) proceed in a way which is similar to the one described above.

The measurement of the coupled modes has been extensively described in the review article by Gehring and Gehring (1975). Therefore we summarize here only the results. The experimental methods in studying these modes consist in optical spectroscopy, Raman scattering and inelastic neutron scattering. Optical spectroscopy has been mainly applied to measure some features of the spectrum in the ordered phase i.e. below the Jahn–Teller transition temperature. These measurements will be briefly discussed in section 5.2.5. The method of Raman scattering was used to study the phonon and electronic modes in $DyVO_4$, $DyAsO_4$ and $TbVO_4$ above and below T_D (Elliott et al., 1972) and in $TmVO_4$ and $TmAsO_4$ (Harley et al., 1972). For example the level schemes shown in fig. 17.41 are deduced from Raman data. Furthermore one can compare the zone centre energy of an electronic excitation which is obtained if the creation of such an excitation is measured and the zone average energy which is obtained if one vibronic excitation is destroyed and another one is created. Such a comparison gives information concerning the dispersion due to anticrossing with the phonons.

Inelastic neutron scattering is a very powerful method to investigate the excitation spectrum. However while it is relatively easy to see phonons it is very difficult to induce with neutrons electronic quadrupole transitions between different CEF-levels. Thus the electronic branch can be observed only in the hybridization regime, in which it has also phonon character. The system $PrAlO_3$ has been investigated in great detail (Kjems et al., 1973; Birgeneau et al., 1974) and an anticrossing of the phonons and electronic states was observed this way. Since $PrAlO_3$ undergoes several structural phase transitions it is not a simple model system.

Inelastic neutron scattering has also been used to demonstrate the influence of an applied magnetic field on the phonon dispersion. The orbitally degenerate

ground state of $TmVO_4$ was Zeeman split by an applied field and the hybridization of this split level with the phonons was observed (Kjems et al., 1975). The mixed modes can be immediately found by computing $u_Q\{V_1, \omega, H_a\}$ and $\langle V_2 \rangle$ in the presence of a field and setting this into eq. (17.110a).

5.2.5. *Ordered phase*

The ordered phase of systems undergoing a structural phase transition (cooperative Jahn–Teller effect) can be treated in complete analogy to the magnetically ordered phase. In order to demonstrate this we start out from the magneto-elastic interactions as given by eq. (17.32) and add to it an interaction which is described by the hamiltonian

$$H_{\text{int}} = -\tfrac{1}{2} \sum_{ij} K_{ij}(n, \alpha, d) O^n_{\alpha d}(i) O^n_{\alpha d}(j) \tag{17.127}$$

This hamiltonian is supposed to represent the mutual interaction of RE-ions via optical phonons and/or conduction electrons. We assume that below the transition temperature there is a static distortion of representation α. In that case the order parameters are given by $\langle Q^n_{\alpha d} \rangle$. Separating out the mean field parts we write for the operators

$$Q^n_\alpha(i) = \hat{Q}^n_\alpha(i) + \langle Q^n_\alpha \rangle \qquad O^n_{\alpha d}(i) = \hat{O}^n_{\alpha d}(i) + \langle O^n_{\alpha d} \rangle \tag{17.128}$$

The $\hat{Q}^n_\alpha(i)$ are then the strains with respect to the new equilibrium positions of the RE-ions in the ordered phase. Since the orientation of the crystal is supposed to be fixed we have to require the boundary condition $\langle Q^n_4 \rangle = 0$ $(n = 1, 2, 3)$. The homogeneous strains $\langle Q^n_\alpha \rangle$ are calculated from the requirement that the sum of the elastic energy and the magnetoelastic interaction energy is minimized.

The former is given by

$$H_{\text{el}} = \frac{V}{2} \sum_{\alpha n} c_\alpha \langle Q^n_\alpha \rangle^2 \tag{17.129}$$

where c_α are the symmetry elastic constants i.e. $c_1 = \frac{1}{3}(c_{11} + 2c_{12})$, $c_3 = \frac{2}{15}(c_{11} - c_{12})$, $c_5 = c_{44}$. V is the volume of the sample. By using for simplicity only first order terms in the magneto-elastic interaction one finds

$$\langle Q^n_\alpha \rangle = \frac{N}{V c_\alpha} \sum_d g_2(\alpha, d) \langle O^n_{\alpha d} \rangle \tag{17.130}$$

The total hamiltonian consists then of a mean-field part H_{MF} and an interaction part which can be expressed in terms of $\hat{Q}^n_\alpha(i)$, $\hat{O}^n_{\alpha d}$.

The former is written as

$$H_{\text{MF}} = \sum_i \left[H^{(0)}_{\text{CEF}}(i) - \sum_\alpha \left(\frac{g_1^2(\alpha) N}{c_\alpha V} + K_{q=0}(\alpha) \right) \sum_n \langle O^n_\alpha \rangle O^n_\alpha(i) \right] \tag{17.131}$$

Here we have suppressed the degree of representation label d for simplicity. Furthermore $K_q(\alpha)$ is the Fourier transform of $K_{ij}(\alpha, d)$. The interaction part is

then of the form

$$H_{\mathrm{me}}^{(1)} = -\sum_i \sum_{\alpha d} g_1(\alpha, d) \sum_n \hat{Q}_\alpha^n(i) \hat{O}_{\alpha d}^n(i) \tag{17.132}$$

The expression for H_{MF} is very similar to the corresponding one for the magnetic case (compare with eq. 17.94). The $\langle O_\alpha^n \rangle$ have to be determined in a self-consistent manner as it was done for $\langle \boldsymbol{J} \rangle$ in the magnetic case.

The case of a one-dimensional distortion (α is non-degenerate) is completely analogous to the magnetic case. Since the latter was discussed in section 5.1.3 we do not discuss it here again. If the distortion is two-dimensional this requires special attention. For example if the crystal-field ground state is Γ_3 one needs to include anharmonic interaction terms as they may occur for example via $H_{\mathrm{me}}^{(2)}$ in order to avoid that the elastic constants are soft at all temperatures below T_{D} (Kanamori, 1960; Pytte, 1971). Furthermore a two-dimensional distortion will lead very often to first order phase transitions as it has been discussed by Kino and Miyahara (1966).

The excitations of the system are again calculated from the poles of the phonon propagator. As mentioned above the phonons refer now to the deviations of the ions from the equilibrium positions $\boldsymbol{R}_i$ in the distorted phase.

This implies

$$\hat{Q}_\alpha^n(i) = \sum_{k\mu} \hat{Q}_\alpha^n(k\mu)(a_{k\mu}^+ + a_{-k\mu}) \, \mathrm{e}^{\mathrm{i}k\boldsymbol{R}_i} \tag{17.133}$$

The diagrammatic and algebraic equations for the phonons are the same as before (see fig. 17.37 and eq. 17.107) with the only difference that the eigenfunctions and eigenvalues of the RE-ion states are calculated from H_{MF} instead of from the crystal-field hamiltonian $H_{\mathrm{CEF}}^{(0)}$ alone.

There is a considerable amount of experimental data available concerning the ordered phase of cooperative Jahn–Teller systems. It has been reviewed excellently by Gehring and Gehring (1975) (see in particular p. 82–85) and we can therefore limit ourselves in choosing some representative examples.

First of all there are the macroscopic structural changes which can be detected by X-ray or elastic neutron scattering. Shown in fig. 17.44 is the static strain for $TmVO_4$ by X-ray diffraction. Furthermore there are the spectroscopic methods which were already discussed briefly in section 5.2.4 when we were dealing with the paramagnetic phase.

For example from optical absorption measurements the temperature dependence of the ground-state splitting of $TmVO_4$ was measured (see fig. 17.45). Thereby optical transitions are taking place between the (split) ground-state doublet and an excited singlet state. The results can be compared with the molecular field equation

$$\Delta(t) = \Delta_0 \tanh[\Delta(t)/kT] \tag{17.134}$$

and one notices excellent agreement. Raman spectroscopy enables one to determine the changes in the electronic Raman lines. While their temperature

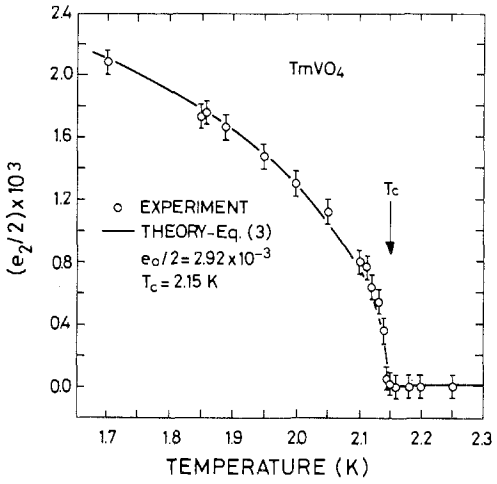

Fig. 17.44. Static strain $\epsilon_{xy} = \frac{1}{2}e_2$ as function of temperature for $TmVO_4$. The solid line corresponds to eq. (17.134) (from Segmüller et al., 1974).

dependence is very weak above the transition temperature T_D there are pronounced changes below T_D (Elliott et al., 1972). This is understood from fig. 17.41 in which the changes in the electronic energies are indicated as one goes below T_D.

Other experimental methods include the Mössbauer effect, which can measure the quadrupole moment at the site of the Mössbauer nucleus, and birefringence. The latter method makes use of the fact that tetragonal and orthorhombic crystals are optically uniaxial and biaxial, respectively. The change from uniaxial to biaxial behavior at T_D can be seen experimentally in a rather dramatic way (Becker et al., 1972; Harley et al., 1972).

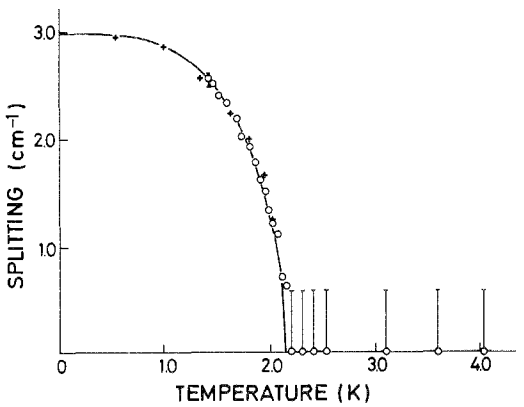

Fig. 17.45. Temperature dependence of the ground-state splitting in $TmVO_4$ as obtained from optical absorption (circles) and magnetic measurements (crosses) (from Becker et al., 1972).

5.3. *Coupling of magnetic and structural properties*

It was demonstrated in section 5.2.1 that an applied magnetic field will influence the elastic properties of RE-systems. For example it was shown that in a cubic crystal with the field parallel to a principal axis the sound velocities of transverse acoustic modes are different in field direction and perpendicular to it. This was shown to be a consequence of the rotational interactions as well as the second-order strain effects. The aim of this paragraph is to show how the magnetic and the elastic properties of RE-systems can couple to each other. We start out by demonstrating that an applied magnetic field or more generally a molecular field will induce a coupling of magnetic excitons to phonons (Thalmeier and Fulde, 1975). The hamiltonian under consideration is written as

$$H = \sum_m [H^{(0)}_{\mathrm{CEF}}(\boldsymbol{J}^m) + \mu_B g \boldsymbol{H} \cdot \boldsymbol{J}^m + V_1^m + V_2^m] - \tfrac{1}{2} \sum_{m \neq n} J^{\mathrm{ex}}_{mn} \boldsymbol{J}^m \boldsymbol{J}^n \tag{17.135}$$

Here V_1^m, V_2^m describe the magneto-elastic interaction and contain terms of even power in $\boldsymbol{J}^m$. The last term describes the magnetic interaction between different RE-ions. The coupling of the magneto-elastic interaction and the magnetic interactions can be discussed in terms of the "mixed" susceptibility

$$w^{\sigma}_{\alpha n d}(\omega) = \sum_{\bar{\delta}_i \neq \bar{\delta}_j} \frac{\bar{n}_i - \bar{n}_j}{\omega - \bar{\delta}_{ij}} \langle \bar{i} | O^n_{\alpha d} | \bar{j} \rangle \langle \bar{j} | J_\sigma | \bar{i} \rangle$$

$$+ \frac{1}{T} \delta_{\omega,0} \sum_{\bar{\delta}_i = \bar{\delta}_j} \bar{n}_i \langle \bar{i} | \hat{O}^n_{\alpha d} | \bar{i} \rangle \langle \bar{i} | \hat{J}_\sigma | \bar{i} \rangle \tag{17.136}$$

The bar is a reminder that the eigenstates $|\bar{i}\rangle$ and eigenvalues $\bar{\delta}_i$ include an applied magnetic field and/or molecular field, respectively. The diagrammatic equation for $D(\boldsymbol{q}, \omega)$ is shown in fig. 17.46 demonstrating the role of $w(\omega)$ as a coupling susceptibility. In the absence of an external field the real part vanishes. This is due to the different behavior under time reversal transformation of $V^m_{1,2}$ and $\boldsymbol{J}^m$. The imaginary part Im $w^{\alpha}_{\alpha n d}(\omega)$ is generally nonzero even for $\boldsymbol{H} = 0$. However it is then proportional to ω and therefore has no influence on the elastic constants.

The situation is different if an external field or molecular field is present. In that case Re $w^{\sigma}_{\alpha n d}(\omega) \neq 0$ and there can be considerable hybridization between the phonon like and magnetic exciton-like branches. The excitation spectrum is found from the poles of $D(\boldsymbol{q}, \omega)$ as before. (Thalmeier and Fulde, 1975). An example is shown in fig. 17.47 where the hybridization is seen for a given external field. This behavior seems to be the explanation for the inelastic neutron scattering results found in Pr when a magnetic field was applied (Houmann et al., 1975; Jensen, 1976).

The next step consists in including the quadrupole interactions among RE-ions as described by eq. (17.127). Again there is no difficulty in extending the diagrams shown in fig. (17.46) and finding the excitation spectrum. Depending on the relative size of the interaction parameters J^{ex}_{ij}, K_{ij} the system will undergo

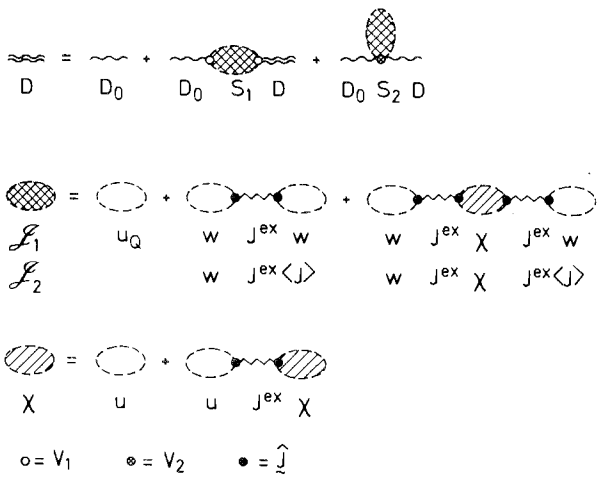

Fig. 17.46. Diagrammatic equation for the phonon propagator $D(\boldsymbol{q}, \omega)$ in the presence of a magnetic and/or molecular field which leads to a coupling to the magnetic excitations. The susceptibilities u, u_Q, w are calculated from the eigenstates of the hamiltonian $H^{(0)}_{\mathrm{CEF}}(\boldsymbol{J}^m) - (\mu_B g \boldsymbol{H} + J^{ex}(0)\langle \boldsymbol{J}\rangle)\boldsymbol{J}^m$ indicated by dashed lines. Furthermore $\hat{\boldsymbol{J}}^m = \boldsymbol{J}^m - \langle \boldsymbol{J}^m\rangle$. χ is the magnetic susceptibility (compare with eq. (17.82)). $\mathscr{I}_1$ and $\mathscr{I}_2$ are the same as S_1, S_2 except for the missing factors V_1, V_2.

different types of phase transitions (Sivardiere and Blume, 1972; Sivardiere, 1973). This is shown schematically in fig. 17.48 for Kramers ions which always show a magnetic phase transition at low enough temperatures due to the Kramers degeneracy of the CEF-ground state. In the magnetically ordered phase the ground state will always have a quadrupole moment since the symmetry of the magnetic state is lower.

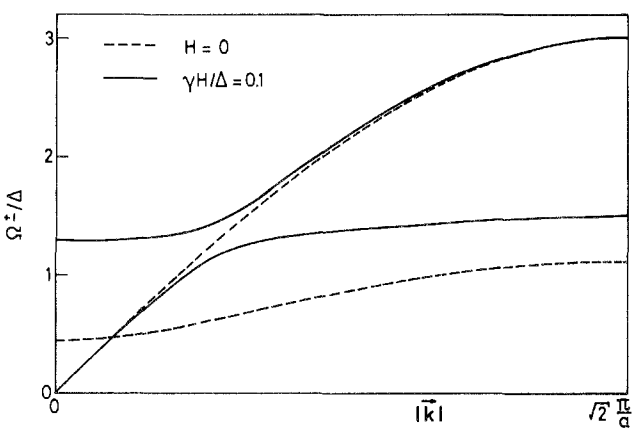

Fig. 17.47. Mixing of Γ_1–Γ_4 magnetic excitons and [101] transverse phonons in an external magnetic field. Δ is the energy difference between Γ_4 and Γ_1 and it has been assumed that $\omega(2^{1/2}\pi/a) = 3\Delta$. The rotational interaction has been neglected (from Thalmeier and Fulde, 1975).

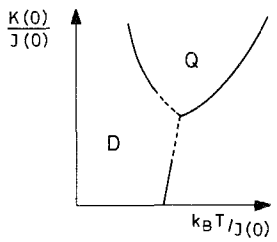

Fig. 17.48. Schematic representation of the different types of phase transition which may result depending on the relative strengths of the magnetic exchange [$J(0)$] and quadrupole [$K(0)$] interaction of the RE-ions. D indicates the regime in which there is dipole and quadrupole order while Q indicates the one in which there is quadrupole order. The broken line indicates first-order phase transitions while the solid line stands for second order transitions (from Sivardiere and Blume, 1972).

This implies that the inverse is not true i.e. a quadrupole order does not imply a ground state with a magnetic moment. Depending on the relative strength of $K(\boldsymbol{q}=0)/J^{ex}(\boldsymbol{q}=0)$ the quadrupole order or the magnetic order will set in first. In the first case there will be a second (lower) transition temperature at which the magnetic order will set in. At the second order quadrupole transition the corresponding elastic constant is soft. If magnetic order sets in first then the onset of it is also reflected in the elastic properties. However there is no elastic soft mode. Instead the elastic constants show a (relatively small) change in the temperature dependence at T_c which results from the fact that $\langle O\rangle \sim \langle J\rangle^2$. Characteristic examples are $TmVO_4$ for the first case and ErSb for the second case. Also shown in fig. 17.48 is the regime of first order phase transition which may occur.

The hamiltonian as given by eqs. (17.135) and (17.127) is a simplifying approximation for metallic systems in so far as the conduction electron which causes the interactions have been eliminated. The question arises therefore whether an additional coupling of magnetic and structural phase transitions may result by keeping the conduction electrons in the problem. This is indeed possible. The simplest possibility is indicated in fig. 17.49. It resembles the one considered by Paulson and Schrieffer (1968) for the coupling of spin fluctuations to density fluctuations. The coupling is achieved by a third order process which

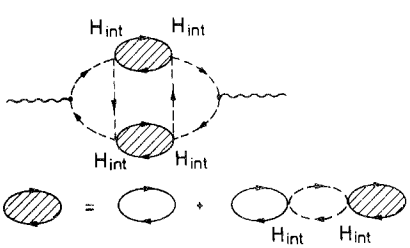

Fig. 17.49. Coupling of structural and magnetic phase transitions via a factorization of the four spin correlation function. $H_{int} = (g-1)J_{ex}\boldsymbol{\sigma}\cdot J$. The solid bubble is the electronic Lindhard function.

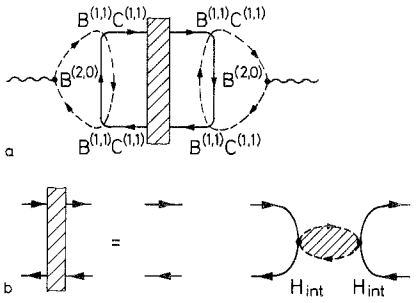

Fig. 17.50. Magneto-elastic coupling by invoking an interaction of the type $(\Lambda, \Sigma) = (1, 1)$.

ensures that $V_1^m H_{ex}^2(J^m)$ has diagonal matrix elements for some of the CEF eigenstates. A divergence in the magnetic susceptibility leads then to a divergence (in molecular field approximation) in the quadrupole susceptibility of the form $[T_c/(T - T_c)]^{1/2}$. However this may be all rather misleading since Lüthi and Pollina (1968) have shown that the factorization of the 4-spin correlation function to which the diagram in fig. 17.49 corresponds does grossly overestimate the mutual coupling. A different and more promising possibility to couple elastic and magnetic properties is shown in fig. 17.50. This coupling requires the presence of the general k–f interactions which were discussed in section 3.2.

It turns out that a third order process is possible which combines V_1 and the k–f interaction characterized by $(\Lambda, \Sigma) = (1, 1)$. Details can be found in Fulde (1975). The net result is that this time the quadrupole susceptibility diverges as $T_c/(T - T_c)$ in molecular field approximation as the magnetic phase transition is approached from above. This would imply that an elastic constant becomes soft at a second order magnetic phase transition. In practice this requires the presence of the interaction $(\Lambda, \Sigma) = (1, 1)$ with reasonable strength.

6. Impurities in lattices of crystal-field split ions

We consider a lattice of crystal-field split ions in which some of the ions are replaced by impurities. These impurities can be either other RE-ions with different crystal-field splitting and/or different coupling parameter to the neighbouring ions or they can be ions such as La which act like "holes" in the lattice due to the absence of 4f electrons. In the following we want to discuss the influence of such impurities on the properties of the otherwise perfect lattice system. We shall divide the problem into two parts. First we shall consider the one impurity problem. Here the changes of the excitation spectrum are of interest (local modes, resonant modes) as well as the possible occurrence of such phenomena as giant moments or giant Jahn–Teller distortions. After this we consider finite impurity concentrations and their effect on the transition temperature.

Although all considerations do apply for magnetic systems as well as to Jahn–Teller systems we shall restrict ourselves to the magnetic case. It is very easy to transform the results to Jahn–Teller systems.

6.1. *One impurity problem*

Suppose we are dealing with a lattice of CEF-split ions. For simplicity we consider a system of non-Kramers ions with two singlets as lowest CEF-eigenstates separated by an energy δ. This enables us to use Pauli matrices for a description of the system. In the presence of magnetic coupling the hamiltonian is given by eq. (17.84). For the present purpose it is advantageous to write $J_{ij}^{ex} = J_{ij}^{ex} M_i M_j$ where $M_i = \langle 1|\boldsymbol{J}(i)|0\rangle$ is the matrix element for transitions between the two crystal-field states. Suppose one of the ions is replaced by an impurity. This impurity may be different to the original ion in several respects.

α) The level splitting δ_0 of the two lowest crystal-field states is different from δ. Of special interest is the case of a Kramers ion impurity with $\delta_0 = 0$.

β) The matrix element $M_0 = \langle 1|\boldsymbol{J}|0\rangle$ is different from the one of the other ions. $M_0 = 0$ implies a non-magnetic impurity or vacancy.

γ) The coupling constant J_0 to the nearest neighbours is different from the one of the other ions. The case $J_0 = 0$ implies a magnetic "hole".

δ) The impurity may have a different Lande-factor g_0 then the other ions.

The excitation spectrum can be calculated as before from the poles of the susceptibility $\chi(i, j)$ which now depends on $\boldsymbol{R}_i$, $\boldsymbol{R}_j$ separately. In molecular field approximation $\chi(i, j)$ is easily calculated from a diagrammatic equation (Fulde and Peschel, 1971). Thereby one has to take into account that the one-ion susceptibility $u(i)$ is given by

$$u(i) = \begin{cases} \dfrac{2M^2\delta}{\delta^2 - \omega^2} \tanh \delta/2T; & i \neq 0 \\ \dfrac{2M_0^2\delta_0}{\delta_0^2 - \omega^2} \tanh \delta_0/2T; & i = 0 \end{cases} \tag{17.137}$$

Furthermore for nearest neighbors i, j

$$J_{ij}^{ex} = \begin{cases} J_0 & i = 0 \text{ or } j = 0 \\ J & \text{otherwise} \end{cases} \tag{17.138}$$

The equation for $\chi(i, j)$ can be solved and the resulting excitation spectrum is shown in fig. 17.51. One notices there the excitation band of the pure lattice and the possible occurrence of a local mode which depends on δ_0, J_0 and T. The local mode is in the vicinity of $\omega \simeq \delta_0$ and may merge into the excitation band close to the ordering temperature. In molecular field approximation one obtains the erroneous result that the local mode may become soft and hence unstable at a temperature $T > T_c$. This is a shortcoming of the approximation which has been corrected by Wang (1973), Villain and Pataud (unpublished) and Mais (1975). One can show that the shortcoming of the theory mentioned above results from the replacement of $\langle \sigma^x \rangle$, $\langle \sigma_0^x \rangle$ by their free ion values $\tanh \delta/2T$ and

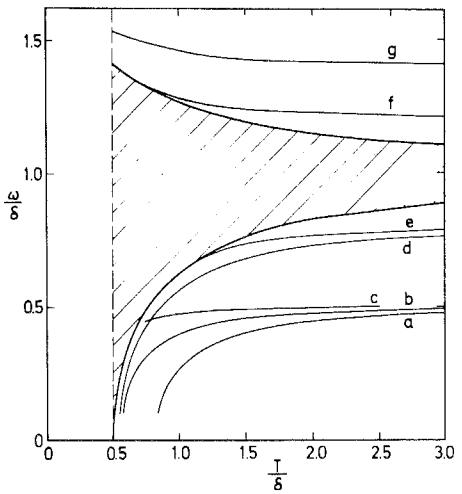

Fig. 17.51. Excitation spectrum in the presence of impurities as function of temperature. The shaded area indicates the excitation band of the pure lattice (see fig. 17.27). The different lines (a)–(g) correspond to different values of $(\delta_0/\delta; J_0/J)$: (0.5; 3.0), (0.5; 2.0), (0.5; 1.0), (0.8; 2.0), (0.8; 1.3), (1.2; 1.0), (1.4; 1.3) (from Fulde and Peschel, 1971).

$\tanh \delta_0/2T$ in the expression for $u(i)$ (see eq. 17.137). Correct results are obtained if $\langle\sigma^x\rangle$, $\langle\sigma_0^x\rangle$ are determined self-consistently (Mais, 1975). The determining conditions are very similar to eq. (17.89). In particular $\langle\sigma_0^x\rangle$ is determined from the requirement

$$1 = M_0^{-2} g_0^{-2} \lim_{it \to 0^+} \chi(i = 0, j = 0, it)$$

$$= g_0^{-2} M_0^{-2} \int_{-\infty}^{+\infty} \frac{d\omega}{2\pi} \coth \frac{\omega}{2T} \operatorname{Im} \chi(i, i, \omega) \tag{17.139}$$

while $\langle\sigma^x\rangle$ is determined from

$$1 = M^{-2} g^{-2} \int_{-\infty}^{+\infty} \frac{d\omega}{2\pi} \coth \frac{\omega}{2T} \operatorname{Im} \chi^{(0)}(i, i, \omega) \tag{17.140}$$

where $\chi^{(0)}(i, j, \omega)$ is the susceptibility in the absence of impurities. With these values of $\langle\sigma^x\rangle$, $\langle\sigma_0^x\rangle$ one obtains results which can be used to calculate the polarization around a Kramers ion with a two-fold degenerate ground state (Mais, 1975). Results are shown in fig. 17.52. One notices a large increase in the polarization as the system approaches the critical value for the exchange interaction. This implies the occurrence of giant moments in RE-systems in analogy to the ones found in transition metals such as Pd. Physically this is what one might expect: as the matrix is close to a magnetic instability, a magnetic impurity placed into it will find it easy to polarize the surrounding. The polarization falls off for large distances R as $R^{-1} \exp[-R/a(6(1-x)/x)^{1/2}]$ where $x = 1.2JM^2\langle\sigma^x\rangle/\delta$ and a is the lattice spacing. The "enhancement factor" of the

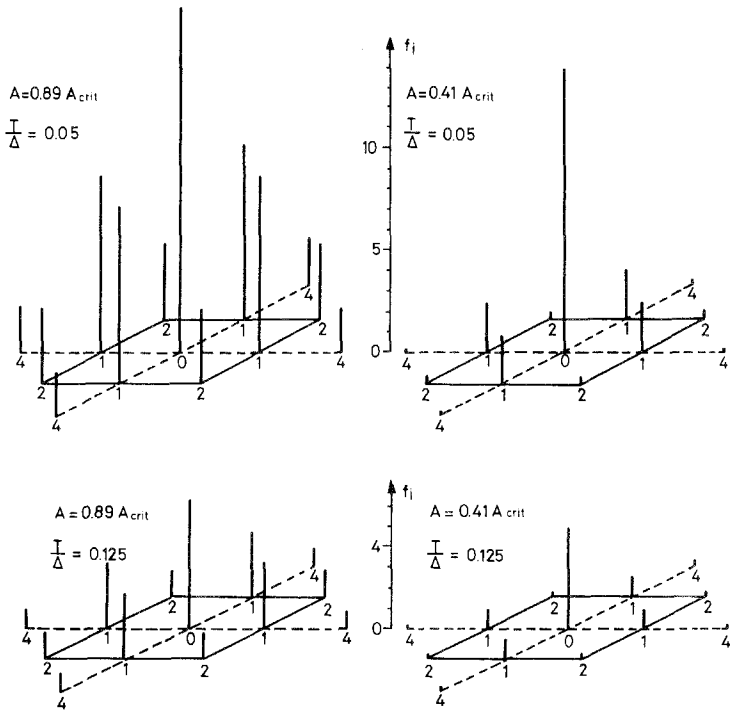

Fig. 17.52. Magnetization in the neighbourhood of a Kramers ion impurity in a Van Vleck paramagnet (two singlet system). f_i is the change in the susceptibility divided by the susceptibility of the pure system. A/A_{crit} is a measure of how close to the critical value the exchange interaction is in the host. Δ is the energy separation of the ground state and excited state singlet (from Mais, 1975).

Curie-susceptibility is of the form $(1-x)^{-1}$ and becomes very large as x approaches the critical value $x = 1$ at which the matrix becomes magnetic. This corresponds to an anomalous large Bohr magneton of the Kramers ion. It should be very interesting to check these findings experimentally perhaps with the help of neutron scattering. In Jahn–Teller systems the analogue of giant moments are giant quadrupolar distortions. For example consider Tm impurities in $DyVO_4$. The orbitally degenerate ground state of Tm corresponds to a Kramers doublet in the magnetic case while Dy is analogue to a two singlet system in the magnetic case (the Kramers doublets of Dy have no diagonal matrix elements with respect to the quadrupole interaction). The role of the applied magnetic field is taken by an applied external stress which splits the degeneracy of the ground state of Tm. Of course it is more difficult to measure the giant quadrupole deformation in such a case than it is to measure the giant magnetic moment.

6.2. *Finite impurity concentrations*

There are experiments available on induced Van Vleck ferromagnets (Pr_3Tl, Pr_3Se_4) (Andres et al., 1972; Bucher et al., 1974) and antiferromagnets (TbSb)

(Cooper and Vogt, 1970) which show that a finite number of magnetic holes such as La or Y decreases T_c quite effectively. This has its reason in a decrease of the effective ion interaction with increasing La and/or Y concentration. If the effective interaction drops below the critical value the system is no longer magnetic even at $T = 0$. The effective coupling constant is $J_{\text{eff}} = J(1 - c)$ where c is the concentration of "holes" (i.e. La or Y). With J_{eff} put into eq. (17.82) the behaviour of the transition temperature as function of hole concentration can be calculated. The agreement with experiments (Cooper and Vogt, 1970) is reasonably good. The calculations can be refined by taking the lattice structure into account (Fulde and Peschel, 1971). Also series expansions have been applied (Elliott and Saville, 1974) as well as the coherent potential approximation (Schmidt, 1974). The critical hole concentration which destroys magnetism can be very small provided the exchange coupling in the matrix is just above the critical value as in Pr_3Tl. The interaction is more complex if the impurities are also crystal-field split or Kramers ions. In that case T_c may increase or decrease depending on details. A mean field theory can be worked out also for that situation and we refer to the literature for more details (Fulde and Peschel, 1971; Shiles, 1973). Again, all the findings for the magnetic systems can be transferred to Jahn–Teller systems although some caution has to be exercised due to long range character of the interaction in the latter case.

7. Surface effects

The local environment of a surface atom has a lower symmetry than inside the bulk. As a consequence the CEF which a surface atom experiences is very different to the one inside the bulk. This results in a different level splitting of the RE-ions at the surface. Hence strong surface effects are expected in those quantities which depend on the CEF splitting. We shall demonstrate this for a Van Vleck exchange induced moment system (Peschel and Fulde, 1973; Hsieh and Pink, 1974). Very similar considerations hold true for collective Jahn–Teller systems.

Let us consider a system of RE-ions in a cubic environment. Inside the bulk the crystal field hamiltonian is given by eq. (17.10). At the surface some of the ligands of the surface atoms are cut off. If we choose the surface perpendicular to one of the principal axes of the crystal then the crystal field hamiltonian $H_{\text{CEF,s}}$ at the surface is of the form

$$H_{\text{CEF,s}} = B_2 O_2^0 + B_4' O_4^0 + B_4'' 5 O_4^4 + B_6' O_6^0 - B_6'' 21 O_6^4$$

One notices the appearance of a term proportional to O_2^0 due to the lower symmetry at the surface which is expected to dominate the other terms. For the particular case of a 8-fold coordination $B_2 = 0$ and $B_4' = B_4'' = \frac{1}{2}B_4^0$ and $B_6' = B_6'' = \frac{1}{2}B_6^0$. This implies that the CEF-level scheme at the surface is the same as inside the bulk but with only half the splitting energies. For the 6- and 12-fold coordination the point group is C_{4v}. In case that a point charge model is describing

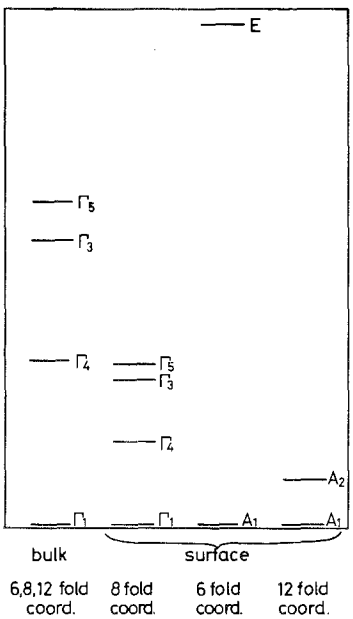

Fig. 17.53. CEF level scheme for $J = 4$ inside the bulk and at a 100 surface for a cubic lattice with 6, 8 and 12-fold coordination. The computations were done within the point charge model (from Peschel and Fulde, 1973).

the crystalline field one can calculate explicitly the different B's. The results for $J = 4$ are shown in fig. 17.53. The $B_2O_2^0$ dominates for the 6- and 12-fold coordination and the level scheme is completely changed as compared with the one inside the bulk. Since the point charge model is not expected to hold except in special cases there will be in general not a simple relationship between the level scheme at the surface and inside the bulk. It is apparent that such drastic changes in the level scheme at the surface will have strong influence on the magnetic properties of the surface. For example if we are dealing with a singlet ground state system then it is the competition between the interactions with the (nearest) neighbours and the crystalline field which determines whether or not the system will become ferromagnetic at low temperatures. At the surface the number of nearest neighbours is reduced compared with the situation inside the bulk. This would disfavour the occurrence of magnetic ordering at the surface. However we have seen that the level splitting at the surface may be much smaller than inside the bulk and this favours surface magnetism. It is therefore very likely that systems will be found which will order at the surface at a higher temperature than inside the bulk. Even bulk paramagnets may show surface ferromagnetism if the CEF-level scheme at the surface is favourable. There is no conceptual difficulty in having a two dimensional Van Vleck ferromagnetic surface layer. General theorems concerning the non-existence of long range order in two dimensions (Mermin and Wagner, 1966) do not apply

here. There is no continuous symmetry of the hamiltonian which is broken by the ground state. Ferromagnetic surface magnetism of a metal should be detectable by observing spin polarized photo-electrons coming out of a paramagnetic bulk sample for example.

The possible existence of localized surface excitations is another intriguing consequence of the energy splitting caused by the crystalline field (Hsieh and Pink, 1974).

Acknowledgement

I would like to thank Prof. B. Bucher and Prof. B. Lüthi for many very fruitful discussions concerning the experimental aspects of crystal fields. Furthermore I want to acknowledge a large number of discussions with Dr. V. Dohm, Prof. L. Hirst, Prof. J. Keller, Dr. H. Mais, Dr. I. Peschel and Dipl. Phys. P. Thalmeier on the theoretical aspects of the problem which have helped me very much. Last but not least I want to thank Miss T. Getzinger for patiently preparing the manuscript.

Recent developments

In the following we want to list some of the developments which have taken place since the completion of the article.

Thereby we shall leave out (as in the article) all phenomena which result from the interaction of CEF-split RE-ions with nuclei.

We shall proceed in parallel with the classification scheme which was used in the article.

To 2.2

The method of EPR has been applied to studies of excited CEF-states (Huang et al. 1977). With the help of inelastic neutron scattering CEF-levels of less than 1 meV energy separation could be detected (Loewenhaupt and Hoenig 1978).

To 2.3

The experimental results on various NaCl, CsCl, $MgCu_2$ and Cu_3Au structures described in the article have been extended and improved. Measurements were extended also to the RE-hydrides. Further informations can be found in the Proceedings of the 2nd International Conference on Crystal Field Effects in Metals and Alloys, ed. by A. Furrer, Plenum Press (1977).

To 3.1

The magnetic field dependence of the elastic constants in paramagnetic hcp structures was studied by Goddings (1977). Furthermore a theory was developed

for the coupling of optical phonons to CEF-split ions, in particular in an applied magnetic field (Thalmeier and Fulde, 1977).

To 4.1 and 4.2

There is increasing evidence developing for the importance of other than the isotropic exchange interaction $(\Lambda, \Sigma) = (0, 1)$ between conduction electrons and RE-ions. Earlier work by Fert and Friederich (1974, 1975) on the Hall effect and the anisotropy in the magnetoresistance of Ag, Au and Al containing RE-impurities required aspherical Coulomb scattering for explanation. As was shown in section 4.1.3 the same holds true for the thermopower anomaly in concentrated systems. Recent evidence for the importance of aspherical Coulomb scattering are the behaviour of the electrical resistivity in PrB_6 (Fisk and Johnston 1977) and the superconducting behaviour of the system $La_{1-x}Pr_xSn_3$ (Keller and Holzer 1977).

There has been some evidence for the existence of a Kondo effect in singlet ground state systems where it can arise only from excited CEF-levels. Examples are $La_{1-x}Pr_xSn_3$ (Abou-Aly et al. 1975, Lethuillier and Haen 1975, Borchi et al. 1977) and $Tb_xY_{1-x}As$ (Huang et al. 1977). However one should keep in mind that the generalized k–f interactions can also produce resistivity minima in the presence of CEF-levels.

Magnetoresistance measurements were extended to concentrated systems (Temple and McEwen 1977).

It is likely that the CEF-splitting is important for the understanding of the distinct temperature behaviour of the critical-field in superconductors of the type RMo_6S_8 (Fischer et al. 1975, Ishikawa and Fischer 1977). It also plays a role in $ErRh_4B_4$ (Ott et al. 1978) which is as $HoMo_6S_8$ a reentrant superconductor.

To 5.1

Lindgard (1977) has made important progress in bridging the gap between conventional spin-wave description and the pseudofermion (or alternatively the pseudo-boson) description used in the article (see section 5.1.3).

The divergence of the central-peak in Pr_3Tl at T_c was investigated in detail by quasi-elastic neutron scattering (Als-Nielsen et al. 1977). The interesting result is that the data can not be explained within the frame work of the Effective Interaction Models. However, the inclusion of the dynamics of the conduction electrons (see section 5.1.5) leads to the required results (Becker et al. 1977). This gives support to the model described in section 5.1.5.

Similar considerations may hold for the quasi-elastic scattering found in Pr metal (Houmann et al. 1977). Furthermore the dynamical electron–RE-ion coupling can be used to develope a theory of linewidth for the CEF-levels. The broadening results then from conduction electron-hole excitations. This is in contrast to a theory of line broadening resulting from magnetic exciton–exciton interactions (Bak 1975). Inelastic neutron scattering experiments under pressure have revealed a strong pressure induced softening of the magnetic excitons in PrSb (Vettier et al. 1977).

To 5.2

CEF-effects were found to be strikingly absent in valence fluctuating systems such as TmSe (Ott et al. 1977).

Magnetostriction experiments were performed in the paramagnetic phase of different RSb compounds (Lüthi et al. 1977). Such measurement enables one to determine size and sign of some of the magneto-elastic coupling constants. The effects result from the magnetic field dependence of the lattice equilibrium positions (see section 5.2.1).

A strong elastic softening in a magnetic field was found in Pr_3Te_4 by Bucher et al. (1976). The effect results from magnetic field induced quadrupolar matrix elements between the singlet ground state and an excited CEF-state.

An induced Jahn–Teller effect was found in the singlet ground state system $PrCu_2$ by Ott et al. (1977). This experiment constitutes the complete analogue to the exchange induced moment systems. The effect results from the aspherical Coulomb scattering of the conduction electrons in close correspondence to the magnetic case where it results from the exchange interaction.

A divergent central peak was found by quasi-elastic neutron scattering at the Jahn–Teller transition temperature of $TbVO_4$ (Hutchings et al. 1975).

A magnetic field dependent splitting of some of the doubly degenerate zone center optical phonons was found in RCl_3 (Schaack 1975, 1977). The effects result from the CEF-splitting of the RE-ions. It can be shown that they are the analogues of the Cotton–Mouton effect and the Faraday rotation of acoustic phonons. For a microscopic theory see Thalmeier and Fulde (1977).

References

Abragam, A. and B. Bleaney, 1970, "Electron Paramagnetic Resonance of Transition Ions", (Clarendon Press, Oxford).

Abrikosov, A.A., 1965, Physics **2**, 5.

Abrikosov, A.A. and L.P. Gorkov, 1960, Zh. eksp. theor. Fiz. **39**, 1781, English translation: Soviet Phys. JETP **12**, 1243 (1961).

Andres, K., E. Bucher, S. Darack and J.P. Maita, 1972, Phys. Rev. **B6**, 2716.

Bakanowski, S., J.E. Crow, N.F. Berk and T. Mihalisin, 1975, Sol. State Commun. **17**, 1111.

Becker, P.J., M.J.M. Leask and R.N. Tyte, 1972, J. Phys. C: Solid State Phys. **5**, 2027.

Bethe, H.A., 1929, Ann. Phys. **3**, 133.

Birgeneau, R.J., 1973, AIP Conf. Proc. **10**, 1664.

Birgeneau, R.J., J. Als-Nielsen and E. Bucher, 1971, Phys. Rev. Letters **27**, 1530, and 1972, Phys. Rev. **B6**, 2724.

Birgeneau, R.J., E. Bucher, J.P. Maita, L. Passell and K.C. Turberfield, 1973, Phys. Rev. **B8**, 5345.

Birgeneau, R.J., E. Bucher, L. Passell, D.L. Price and K.C. Turberfield, 1970, J. Appl. Phys. **41**, 900.

Birgeneau, R.J., E. Bucher, L. Passell and K.C. Turberfield, 1971, Phys. Rev. **B4**, 718.

Birgeneau, R.J., J.K. Kjems, G. Shirane and L.G. Van Uitert, 1974, Phys. Rev. **B10**, 2512.

Bleaney, B., 1963, Proc. Royal Soc. **A276**, 19.

Blume, M., 1966, Phys. Rev. **141**, 512.

Blume, M. and R.J. Birgeneau, 1974, J. Phys. C: Solid State Phys. **7**, 282.

Brout, R., K.A. Müller and H. Thomas, 1966, Solid State Comm. **4**, 507.

Brun, T.O., G.H. Lander, D.L. Price, G.P. Felcher and J.F. Reddy, 1974, Phys. Rev. **B9**, 248.

Bucher, E., K. Andres, F.J. de Salvo, J.P. Maita, A.C. Gossard, A.S. Cooper and G.W., Hull, Jr., 1975, Phys. Rev. **B11**, 500.

Bucher, E., K. Andres, A.C. Gossard and J.P. Maita, 1972, Proc. LT13, Boulder, Colorado.

Bucher, E., K. Andres, J.P. Maita and G.W. Hull, 1968, Helv. Phys. Acta **41**, 723.

Bucher, E. and J.P. Maita, 1973, Sol. State Commun. **13**, 215.

Bucher, E., J.P. Maita and A.S. Cooper, 1972, Phys. Rev. **B6**, 2709.

Bucher, E., J.P. Maita, G.W. Hull, Jr., J.

Sierro, C.W. Chu and B. Lüthi, 1974, Proc. 1. Conf. on Cryst. Elect. Field Effects in Metals and Alloys, ed. by R.A.B. Devine, Montreal.
Burr, C. and R. Orbach, 1967, Phys. Rev. Lett. **19**, 1133.
Buyers, W.J.L., T.M. Holden and A. Perreault, 1975, Phys. Rev. **B11**, 266.
Callen, E. and H.B. Callen, 1965, Phys. Rev. **139**, 455.
Chamard-Bois, R., J. Rossat-Mignod, K. Knorr and W. Drexel, 1973, Sol. State Commun. **13**, 1549.
Cheung, T.H., 1973, Phys. State Solidi (b) **58**, 567.
Chock, D.P. and R. Dagonnier, 1971, Physica **53**, 393.
Chow, R.K.M. and H.U. Everts, 1969, Phys. Rev. **188**, 947.
Cochran, W., 1969, Adv. Phys. **18**, 157.
Cooper, B.R., 1967, Phys. Rev. **163**, 444, and 1969, J. Appl. Phys. **40**, 1334, and 1971, Sol. State Comm. **9**, 1429, and 1972, Phys. Rev. **B6**, 2730 and 1974, Lectures given at the XIth Annual Winter School for Theoretical Physics, Karpacz, Poland.
Cooper, B.R. and O. Vogt, 1970, Phys. Rev. **B1**, 1211 and 1218.
Cornut, B. and B. Coqblin, 1972, Phys. Rev. **B5**, 4541.
Cribier, D. and B. Jacrot, 1960, hebd. Séance. Acad. Sci., Paris **250**, 2851.
Crow, J.E., R.P. Guertin and R.D. Parks, 1967, Phys. Rev. Lett. **19**, 77.
Das, K.C. and D.K. Ray, 1969, Phys. Rev. **187**, 777.
de Gennes, P.G., 1963, Solid State Commun. **1**, 132.
Devine, R.A.B., W. Zingg, J-M. Moret and D. Shaltiel, 1973, Sol. State Commun. **12**, 515.
de Wijn, H.W., A.M. van Diepen and K.H.J. Buschow, 1974, Proc. first Conf. on Crystal. Elect. Field Effects in Metals and Alloys, ed. by R. Devine, Universite de Montreal.
Dieke, G.M., 1968, "Spectra and Energy Levels of Rare Earth Ions in Crystals" (Interscience Publishers Inc., New York).
Dieterich, W., 1974, Z. Phys. **270**, 239.
Dixon, J.M. and R. Dupree, 1971a, J. Phys. F: Metal Phys., **1**, 539, 1971b, ibid. **1**, 549, 1973, ibid. **3**, 118.
Dohm, V., 1976, Z. Physik **B23**, 153.
Dohm, V. and P. Fulde, 1975, Z. Physik **B21**, 369.
Eisenmenger, W., 1969, in "Tunneling Phenomena in Solids" ed. by E. Burstein and Lundqvist, S., Plenum Press, N.Y.
Elliott, R., 1954, Phys. Rev. **94**, 564, and 1972, in "Magnetic Properties of Rare Earth Metals" ed. by R.J. Elliott, Plenum Press, London and N.Y.
Elliott, R.J., R.T. Harley, W. Hayes and S.R.P. Smith, 1972, Proc. R. Soc. **A328**, 217.
Elliott, R.J., P. Pfeuty and C. Wood, 1971, J. Phys. C: **4**, 2359.
Elliott, R.J. and I.D. Saville, 1974, J. Phys. C: Solid State Phys. **7**, 4293.
Elliott, R.J. and K.W.H. Stevens, 1952, Proc. R. Soc. **A215**, 437; 1953a ibid., **218**, 553; 1953b, ibid., **219**, 387.
Ellis, M.M. and D.J.J. Newman, 1967, J. Chem. Phys. **47**, 1989.
Fischer, K., 1967, Phys. Rev. **158**, 613.
Freeman, A.J., 1972, in "Magnetic Properties of Rare Earth Metals" ed. by R.J. Elliott, Plenum Press, London, and N.Y.
Freeman, A.J. and R.E. Watson, 1962, Phys. Rev. **127**, 2058.
Fulde, P., 1975, Z. Physik **B20**, 89.
Fulde, P., L.L. Hirst and A. Luther, 1970, Z. Phys. **230**, 155.
Fulde, P. and K. Maki, 1966, Phys. Rev. **141**, 215.
Fulde, P. and I. Peschel, 1971, Z. Phys. **241**, 82, and 1972, Adv. Phys. **21**, 1.
Furrer, A., 1974, Proc. first Conf. on Crystal. Elect. Field Effects in Metals and Alloys, ed. by R. Devine, Universite de Montreal.
Furrer, A., W. Bührer, H. Heer, H.-G. Purwins and E. Walker, 1973, Int. J. Magnetism **4**, 63.
Furrer, A., J. Kjems and O. Vogt, 1972, J. Phys. C: Solid State Phys. **5**, 2246.
Gehring, G.A., 1974, J. Phys. C: Solid State Phys. **1**, L379.
Gehring, G.A. and K.A. Gehring, 1975, Rep. Prog. Phys. **38**, 1.
Gorodetsky, G., B. Lüthi and B. Wanklyn, 1971, Solid State Commun. **8**, 1555.
Griffiths, D. and B.R. Coles, 1966, Phys. Rev. Lett. **16**, 1093.
Grover, B., 1965, Phys. Rev. **A140**, 1944.
Guertin, R.P., J.E. Crow, A.R. Sweedler and S. Foner, 1973, Solid State Commun. **13**, 25.
Guertin, R.P. and R.D. Parks, 1968, Solid State Commun. **7**, 59.
Guertin, R.P., W. Voivin, J.E. Crow, A.R. Sweedler and M.B. Maple, 1973, Solid State Commun. **11**, 1889.
Halperin, B.I., 1973, Phys. Rev. **B7**, 894.
Halperin, B.I., P.C. Hohenberg and S. Ma, 1972, Phys. Rev. Lett. **29**, 1548, and 1974, Phys. Rev. **B10**, 139.
Halperin, B. and R. Englman, 1970, Solid State Commun. **8**, 1555.
Harley, R.T., W. Mayes and S.R.P. Smith, 1972, J. Phys. C: Solid State Phys. **5**, 1501.
Happel, H. and H.E. Hoenig, 1973, Solid State Commun. **13**, 1641.
Heer, H., A. Furrer, E. Walker, Treyvaud, H.G. Purwins and J. Kjems, 1974, J. Phys. C: Solid State Phys. **7**, 1207.
Heiniger, F., E. Bucher, J.P. Maita and P. Descouts, 1973, Phys. Rev. **B8**, 3194.
Heiniger, F., E. Bucher, J.P. Maita and L.D. Longinotti, 1975, Phys. Rev. **B12**, 1778.
Heiniger, F., H.G. Purwins and E. Walker, 1974, Phys. Lett. **47A**, 53.
Hessel Andersen, N., P.E. Gregers-Hansen, E. Holm, H. Smith and O. Vogt, 1974, Phys. Rev. Lett. **32**, 1321.
Hessel Andersen, N., P.E. Lindelof, H. Smith and O. Splittorff, 1976, Phys. Rev. Lett. **37**, 46.
Hirst, L.L., 1967, Solid State Commun. **5**, 751, and 1978 Adv. Phys.

Hirst, L.L. and E.R. Seidel, 1969, J. Phys. Chem. Solids **31**, 857.
Hirst, L.L., G. Williams, D. Griffiths and B.R. Coles, 1968, J. Appl. Phys. **39**, 844.
Hoenig, H.E., H. Mappel, H.K. Njoo and H. Seim, 1974, Proc. I. Conf. on Cryst. Elect. Field Effects in Metals and Alloys, ed. by R.A.B. Devine, Universite de Montreal.
Hohenberg, P.C. and J.B. Swift, 1974, J. Phys. C: Solid State Phys. **7**, 4009.
Holden, T.M. and W.J.L. Buyers, 1974, Phys. Rev. **B9**, 3797.
Holden, T.M., W.J.L. Buyers, E. Swenson and O. Vogt, 1971, Bull. Amer. Phys. Soc. **16**, 325.
Holden, T.M., E. Swenson, W.J.L. Buyers and O. Vogt, 1974, Phys. Rev. **B10**, 3864.
Holzer, P., J. Keller and P. Fulde, 1974, J. Low Temp. Phys. **14**, 247.
Houmann, J.G., M. Chapellier, A.R. Mackintosh, P. Bak, O.D. McMasters and K.A. Gschneidner, Jr., 1975, Phys. Rev. Lett. **34**, 587.
Hsieh, Y.Y. and M. Blume, 1972, Phys. Rev. **B6**, 2684.
Hsieh, Y.Y. and D.A. Pink, 1974, J. Phys. Chem. Solids **35**, 1481.
Huber, D.L. and T. Tommet, 1973, Solid State Commun. **12**, 803.
Hutchings, M.T., 1964, Solid State Phys. **16**, 227 (Ed. Seitz and Turnbull, Academ. Press).
Jacobsen, E.H. and K.W.H. Stephens, 1963, Phys. Rev. **129**, 2036.
Jensen, J., 1976, J. Phys. C: Solid State Phys. **9**, 111.
Johansson, T., B. Lebech, M. Nielsen, H. Bjerrum Møller and A.B. Mackintosh, 1970, Phys. Rev. Lett. **25**, 524.
Jorgensen, C.K., R. Pappalado and H.H. Schmidtke, 1963, J. Chem. Phys. **39**, 1422.
Judd, B.R., 1955, Proc. R. Soc. A, **232**, 458; 1957, Ibid., **241**, 414; 1962, Phys. Rev. 127, 750; 1963, "Operator Techniques in Atomic Spectroscopy" (McGraw-Hill Book Co., Inc.).
Kanamori, J., 1960, J. Appl. Phys. **31**, 145.
Kaplan, T.A. and D.H. Lyons, 1963, Phys. Rev. **129**, 2012.
Keiter, H., 1968, Z. Phys. **213**, 466.
Keller, J. and P. Fulde, 1971, J. Low Temp. Phys. **4**, 289, and 1973, Ibid., **12**, 63.
Keller, J., P. Holzer, R.W. McCallum, C.A. Luengo, M.B. Maple and A.R. Sweedler, 1977, J. Low Temp. Phys. **26**, 357.
Kino, Y. and S. Miyahara, 1966, J. Phys. Soc. Japan **21**, 2732.
Kitano, Y. and G.T. Trammell, 1966, Phys. Rev. Lett. **16**, 572.
Kjems, J.K., W. Hayes and S.H. Smith, 1975, Phys. Rev. Letters **35**, 1089.
Kjems, J.K., G. Shirane, R.J. Birgeneau and L.G. Van Uitert, 1973, Phys. Rev. Letters **31**, 1300.
Klenin, M. and I. Peschel, 1973, Phys. kondens. Materie **16**, 219.
Knorr, K., W. Drechsel, R. Chamard-Bois, J. Rossat-Mignod, P. Morin and J. Pierre, 1974, Proc. I. Conf. on Cryst. Elect. Field Effects in Metals and Alloys, ed. by R.A.B. Devine, Universite de Montreal.
Kondo, J., 1967, Solid State Phys. **23**, 183.
Lea, K.R., M.J.M. Leask and W.P. Wolf, 1962, J. Phys. Chem. Solids **23**, 1381.
Lebech, B. and B.D. Rainford, 1971, Journ. Physique **32**, 370.
Lebech, B., K.A. McEwen and P.A. Lindgard, 1975, J. Phys. C.: Solid State Phys. **8**, 1684.
Levy, P.M., 1973, J. Phys. C: Solid State Phys. **6**, 3545.
Lieb, E., T. Schultz and D. Mattis, 1961, Ann. Phys. **16**, 407.
Lines, M.E., 1974, J. Phys. C: Solid State Phys. **7**, L287.
Liu, S.H., 1961, Phys. Rev. **121**, 451.
Ludwig, A. and M.J. Zuckermann, 1971, J. Phys. F: Metal Phys. **1**, 516.
Lüthi, B., M.E. Mullen and E. Bucher, 1973, Phys. Rev. Lett. **31**, 95.
Lüthi, B., M.E. Mullen, K. Andres, E. Bucher and J.P. Maita, 1973, Phys. Rev. **B8**, 2639.
Lüthi, B., P.S. Wang and E. Bucher, 1974, Proc. I. Conf. on Crystal Elect. Field Effects in Metals and Alloys, ed. by R.A.B. Devine, Montreal.
Lüthi, B. and R.J. Pollina, 1968, Phys. Rev. **167**, 488.
Mais, H., 1975, doctoral thesis, Saarbrücken.
Maki, K., 1969, Prog. theor. Phys., Osaka **41**, 586.
Maple, M.B., 1973, in "Magnetism" Vol. V, edit. by H. Suhl, Academic Press, N.Y.
Maranzana, F.E., 1970, Phys. Rev. Lett. **25**, 239.
Markowitz, D. and L.P. Kadanoff, 1963, Phys. Rev. **131**, 563.
McCallum, R.W., W.A. Fertig, C.A. Luengo, M.B. Maple, E. Bucher, J.P. Maita, A.R. Sweedler, L. Mattix, P. Fulde and J. Keller, 1975, Phys. Rev. Lett. **34**, 1620.
McCallum, R.W., C.A. Luengo and M.B. Maple, 1975, Proceed. 14th Int. Conf. on Low Temp. Phys. edit. by M. Krusius and M. Vuorio, Vol. **2**, 541.
McMillan, W.L. and J.M. Rowell, 1969, in "Superconductivity" Vol. 2 edited by R. Parks (New York: M. Dekker Inc.).
Melcher, R.L., E. Pytte and B.A. Scott, 1973, Phys. Rev. Letters **31**, 307.
Mermin, N.D. and H. Wagner, 1966, Phys. Rev. Lett. **17**, 1133.
Mook, H.A. and H.L. Davis, 1972, AIP Conf. Proc. **5**, 1451.
Moore, M.A. and H.C.W. Williams, 1972, J. Phys. C: Solid State Phys. **5**, 3185.
Moran, T.J., R.L. Thomas, P.M. Levy and H.A. Chen, 1973, Phys. Rev. **B7**, 3238.
Morin, P., J. Pierre, J. Rossat-Mignod, K. Knorr and W. Drechsel, 1974, Phys. Rev. **B9**, 4932.
Mullen, M.E., B. Lüthi, P.S. Wang, E. Bucher, L.D. Longinotti, J.P. Maita and H.R. Ott, 1974, Phys. Rev. **B10**, 186.
Müller-Hartmann, E. and J. Zittartz, 1971, Phys. Rev. Lett. **26**, 428.

Newman, D.J., 1971, Adv. in Phys. **20**, 197.
Ott, H.R. and B. Lüthi, 1976, Phys. Rev. Lett. **36**, 600.
Paulson, R.H. and J.R. Schrieffer, 1968, Phys. Lett. **27A**, 289.
Pepperl, G., E. Umlauf, A. Meyer and J. Keller, 1974, Solid State Commun. **14**, 161.
Peschel, I. and P. Fulde, 1970, Z. Phys. **238**, 99, and 1973, ibid. **259**, 145.
Peschel, I., M. Klenin and P. Fulde, 1972, J. Phys. C: Solid State Phys. **5**, L194.
Pines, D., 1963, Elementary Excitations in Solids (W.A. Benjamin Inc., New York).
Pink, D.A., 1968, J. Phys. C: Solid State Phys. **1**, 1246.
Purwins, H.-G., J.G. Houmann, P. Bak and E. Walker, 1973, Phys. Rev. Lett. **31**, 1585.
Pytte, E., 1971, Phys. Rev. **B3**, 3503, and 1974, ibid. **B9**, 932.
Pytte, E. and K.W.H. Stevens, 1971, Phys. Rev. Lett. **27**, 862.
Pytte, E. and H. Thomas, 1968, Phys. Rev. **175**, 610.
Rainer, D. and G. Bergmann, 1974, J. Low Temp. Phys. **14**, 501.
Rainford, B., 1969, Thesis Oxford University.
Rainford, B. , K.C. Turberfield, G. Busch and O. Vogt, 1968, J. Phys. C: Solid State Phys. **1**, 679.
Rao, V.U.S. and W.E. Wallace, 1970, Phys. Rev. **B2**, 4613.
Riblet, G. and K. Winzer, 1971, Sol. State Commun. **9**, 1663.
Roeland, L.W., 1974, Proc. I. Conf. on Cryst. Elect. Field Effects in Metals and Alloys, ed. by R.A.B. Devine, Universite de Montreal.
Sablik, M.J., H.H. Teitelbaum and P.M. Levy, 1972, AIP Conf. Proc. **10**, 548.
Sandercock, J.R., S.B. Palmer, R.J. Elliott, W. Hayes, S.R.P. Smith and A.P. Young, 1972, J. Phys. C: Solid State Phys. **5**, 3126.
Schmidt, U., 1974, Z. Phys. **267**, 277.
Schotte, K.-D., 1975, Phys. stat. sol. (b) **71**, 221.
Schrieffer, J.R., 1964, "Theory of Superconductivity" (W.A. Benjamin, Inc. New York).
Segmüller, A., R.L. Melcher and H. Kinder, 1974, Solid State Commun. **15**, 101.
Shiles, E., 1973, Phys. Rev. **B7**, 4931.
Sierro, J., E. Bucher, L.D. Longinotti, H. Takayama and P. Fulde, 1975, Solid State Commun. **17**, 79.
Sivardiere, J., 1973, J. Phys. Chem. Solids **34**, 267.
Sivardiere, J. and M. Blume, 1972, Phys. Rev. **B5**, 1126.
Skalski, S., O. Betbeder-Matibet and P.R. Weiss, 1964, Phys. Rev. **136**, A 1500.
Smith, H. and O. Vogt, 1974, Phys. Rev. Lett. **32**, 1321.
Smith, S.R., 1972, J. Phys. C: Solid State Phys. **5**, L157.
Sternheimer, R.M., M. Blume and R.F. Peierls, 1968, Phys. Rev. **173**, 376.
Stevens, K.W.H., 1952, Proc. Phys. Soc. **A65**, 209; 1967, Rep. Progr. Phys. **30**, 189.
Stinchcombe, R.B., 1973, J. Phys. C: Solid State Phys. **6**, 2484.
Takayama, H. and P. Fulde, 1975, Z. Phys. **B20**, 81.
Thalmeier, P., 1977, doctoral thesis. Darmstadt.
Thalmeier, P. and P. Fulde, 1975, Z. Phys. **B22**, 359.
Trammell, G.T., 1963, Phys. Rev. **131**, 932.
Turberfield, K.C., L. Passell, R.J. Birgeneau and E. Bucher, 1970, Phys. Rev. Lett. 25, 752, and 1971, J. Appl. Phys. **42**, 1746.
Uhrich, D.L. and R.G. Barnes, 1967, Phys. Rev. 164, 428.
Umlauf, E., P. Holzer, J. Keller, M. Dietrich, W. Gey and R. Meier, 1974, Z. Phys. **271**, 305.
Umlauf, E., G. Pepperl and A. Meyer, 1973, Phys. Rev. Lett. **30**, 1173.
Vaks, V.G. and A.J. Larkin, 1965, Zh. eksp. theor. Fiz. **49**, 975, Engl. translation: Soviet Phys. JETP **22**, 678.
Villain, J. and S. Stamenkovic, 1966, Phys. Status Sol. **15**, 585.
Vogt, O. and B.R. Cooper, 1968, J. Appl Phys. **39**, 1202.
Wallace, W.E., 1974, Proc. I. Conf. on Cryst. Elect. Field Effects in Metals and Alloys, ed. by R.A.B. Devine, Universite de Montreal.
Wang, P.S. and B. Lüthi, 1977, Phys. Rev. **B15**, 2718.
Wang, Y., 1973, Phys. Rev. **B8**, 2365.
Wang, Y.L. and B.R. Cooper, 1968, Phys. Rev. **172**, 539, and 1969, ibid., **185**, 696, and 1970, ibid. **B2**, 2607.
Watson, R.E. and A.J. Freeman, 1967, Phys. Rev. **156**, 251.
Williams, G. and L.L. Hirst, 1969, Phys. Rev. **185**, 407.
Wong, Y.M. and B. Lüthi, 1976, AIP Conf. Proc. **29**, 534.
Wybourne, B.G., 1965, "Spectroscopic Properties of Rare Earths" (Interscience Publishers Inc., New York).
Yang, D.H.-Y. and Y.L. Wang, 1974, Phys. Rev. **B10**, 4714.
Zubarev, D.N., 1960, Usp. fis. Nauk **71**, 71, English translation: Soviet Phys. Usp. **3**, 320.

References (Recent developments)

Als-Nielsen, J., J.K. Kjems, W.J.L. Buyers and R.J. Birgeneau, 1977, Physica **86–88B**, 1162; 1977 J. Phys. C: Solid State Phys. **10**, 2673.
Bak, P., 1975, Phys. Rev. Lett. **34**, 1230.
Becker, K.W., P. Fulde and J. Keller, 1977, Z. Physik **B28**, 9.
Borchi, E., S. De Gennaro, G. Pelosi and A. Rettori, 1977, Phys. Rev. **B16**, 1146.
Bucher, E., J.P. Maita, G.W. Hull, Jr., L.D. Longinotti, B. Lüthi and P.S. Wang, 1976, Z. Physik **B25**. 41.
Fert, A. and A. Friederich, 1974, Phys. Rev. Lett. **33**, 1214; 1975, AIP Conf. Proc. **24**, 466.

Fischer, Ø, M. Decroux, S. Roth, R. Chevrel and M. Sergent, 1975, J. Phys. C: Solid State Physics **8**, L474.
Fisk, Z. and D.C. Johnston, 1977, Solid State Comm. **22**, 359.
Goodings, D.A., 1977, Z. Physik **B26**, 37.
Houmann, J.G., B. Lebech, A.R. Mackintosh, W.J.L. Buyers, O.D. McMasters and K.A. Gschneidner Jr., 1977, Physica **86–88b**, 1156.
Huang, C.Y., K. Sugawara and B.R. Cooper, 1977, Proc. 2nd Conf. on CEF-Effects in Metals and Alloys, ed. by A. Furrer, Plenum Press, N.Y. and 1977, Phys. Rev. **B15**, 3003.
Hutchings, M.T., R. Scherm, S.H. Smith and S.R.P. Smith, 1975, J. Phys. C: Solid State Phys. **8**, L393.
Ishikawa, M. and Ø. Fischer, 1977, Solid State Comm. **23**, 37 and to be published.
Keller, J. and P. Holzer, 1977, Proc. 2nd Conf. on CEF-Effects in Metals and Alloys, ed. by A. Furrer, Plenum Press, N.Y.
Lindgard, P.A., 1977, Proc. 2nd Conf. on CEF-Effects in Metals and Alloys, ed. by A. Furrer, Plenum Press, N.Y.
Lüthi, B., P.S. Wang, Y.H. Wong, H.R. Ott and E. Bucher, 1977, Proc. 2nd Conf. on CEF-Effects in Metals and Alloys, ed. by A. Furrer, Plenum Press, N.Y.
Loewenhaupt, M. and H.E. Hoenig, 1978, Solid State Commun. (in print).
Ott, H.R., K. Andres, P.S. Wang, Y.H. Wong and B. Lüthi, 1977, Proc. 2nd Conf. on CEF-Effects in Metals and Alloys, ed. by A. Furrer, Plenum Press, N.Y.
Ott, H.R., B. Lüthi and P.S. Wang, 1977, in: Valence Instabilities and Related Narrow-Band Phenomena, ed. by R.D. Parks, Plenum Press, N.Y.
Ott, H.R., D.C. Johnston and B.T. Matthias, 1978, to be published.
Schaack, G., 1975, Solid State Comm. **17**, 505 and 1977, Z. Physik **B26**, 49.
Temple, J.A.G. and K.A. McEwen, 1977, Proc. 2nd Conf. on CEF-Effects in Metals and Alloys, ed. by A. Furrer, Plenum Press, N.Y.
Thalmeier, P. and P. Fulde, 1977, Z. Physik **B26**, 323.
Vettier, C., D.B. McWhan, E.I. Blount and G. Shirane, 1977, Phys. Rev. Lett. **39**, 1028.

Handbook on the Physics and Chemistry of Rare Earths, edited by K.A. Gschneidner, Jr. and L. Eyring

Chapter 18

NMR, EPR AND MÖSSBAUER EFFECT: METALS, ALLOYS AND COMPOUNDS*

R.G. BARNES
Ames Laboratory – DOE and Department of Physics, Iowa State University, Ames, Iowa 50011, USA

Contents

* This work was supported by the US Department of Energy, Office of Basic Energy Sciences, Materials Sciences Division.

Symbols

$A, \tilde{A}$ = magnetic hyperfine constant, magnetic hyperfine tensor
A_x, A_y, A_z = various components of magnetic hyperfine tensor
$A_\parallel, A_\perp$ = various components of magnetic hyperfine tensor
A_n^m = crystalline electric field lattice sums
a = magnetic hyperfine energy parameter; lattice constant
B_n^m = energy coefficients in crystalline electric field hamiltonian
b_n^m = scaled energy coefficients
b = lattice constant etc.
C_{mn} = crystalline electric field energy parameters
c = lattice constant
D = diffusion
E, E_1, etc. = energies
ΔE = energy change or increment
E_{act} = activation energy
E_{exc} = excitation energy
$E_I^{(2)}$ = isomer shift energy
δE = isomer shift energy difference
$E_Q^{(2)}$ = nuclear quadrupole interaction energy
E_F = Fermi energy
E_γ = gamma-ray energy
F = proportionality factor
$F(\omega)$ = Fourier transform of correlation function
f_n^m = crystalline field parameter scaling factors
f = recoil-free fraction
$g, \tilde{g}$ = g-factor, g-tensor
g_x, g_y, g_z = various components of g-tensor
$g_\parallel, g_\perp$ = various components of g-tensor
g_J = Landé g-factor
g_N = nuclear g-factor
Δg = g-shift
$g(\nu)$ = resonance lineshape function
H_0 = applied magnetic field
H_1 = radiofrequency (rotating) magnetic field
ΔH = resonance linewidth
H_c = Fermi contact hyperfine field
H_{eff} = effective hyperfine field
$H_{eff}^{(4f)}$ = 4f electron contribution to effective hyperfine field
$H_{eff}^{(cp)}$ = core-polarization contribution to effective hyperfine field
h = Planck's constant. ($\hbar = h/2\pi$)
$H_{hf}^{(s)}, H_{hf}^{(d)}$ etc = s, d, etc., contributions to hyperfine field
$\mathcal{H}_M, \mathcal{H}_{para}$ = magnetic dipole hamiltonian operator
$\mathcal{H}_{SO}$ = electronic spin–orbit hamiltonian operator
$\mathcal{H}_{CEF}$ = electronic crystalline electric field hamiltonian operator
$\mathcal{H}_{hf}$ = magnetic hyperfine interaction hamiltonian operator
I = nuclear spin angular momentum
J = electronic total angular momentum
$J(\nu)$ = spectral density function
J_{ij} = exchange interaction coupling parameter
$\mathcal{J}_{sf}$ = s–f exchange interaction coupling parameter
$K, \tilde{K}$ = Knight shift, Knight shift tensor
K_x, K_y, K_z = various components of Knight shift tensor
$K_\parallel, K_\perp$ = various components of Knight shift tensor
k = Boltzmann's constant
k_F = Fermi wavevector
L = electronic total orbital angular momentum
l = atomic jump length
l_i = orbital angular momentum of ith electron
M = magnetization
$M(T)$ = magnetization at temperature T
m_I, m_J = z-component of nuclear (electronic) angular momentum
$N(E_F)$ = electronic density of states at Fermi level
$\langle J \| N \| J \rangle$ = reduced matrix element
O_n^m = angular momentum operator equivalents
P = nuclear quadrupole energy parameter

p = conduction electron d-band partition factor

Q, $Q_{\alpha\alpha}$ = nuclear electric quadrupole moment

q = conduction electron d-band partition factor

q_{ij} = elements of spatially dependent part of electric field gradient tensor

$\langle q \rangle_T$ = average value of q at temperature T

q_F = axial anisotropy of conduction electron distribution at Fermi level

R = gas constant; nuclear radius; distance

ΔR = change in nuclear radius

R_Q, R_{ce} = Sternheimer shielding factors

R_{mn} = distance from mth to nth ion

r_i = radial coordinate of ith electron

r_{ij} = distance from ith to jth nucleus

$\langle r^n \rangle$ = average or expectation value of r^n

S = electronic total spin angular momentum

$S'(Z)$ = relativistic correction factors

s_i = spin angular momentum of ith electron

T = absolute temperature

T_C, T_N = Curie temperature, Néel temperature

T_1 = spin–lattice relaxation time

T_2 = spin–spin relaxation time

T_{ij} = shift tensor components

$V(r)$ = electrostatic potential at r

$V_{\alpha\beta}$ = second derivatives of $V(r)$, components of electric field gradient tensor

V_{zz} = maximum principal component of electric field gradient tensor

δ_v = Doppler-shifted velocity increment

W = cubic crystalline electric field parameter

x = cubic crystalline electric field parameter

x = concentration in nonstoichiometric compounds

$\langle x^2 \rangle$ = mean-square displacement

Z = atomic number; number of conduction electrons per atom

z = number of nearest-neighbor atoms

α_J, β_J, γ_J = reduced matrix elements

β = Bohr magneton

β_N = nuclear magneton

Γ = energy width of nuclear level; zero wavevector component of exchange hamiltonian

Γ_6, etc. = crystalline electric field state symbols

γ_e, γ_N = electronic (nuclear) gyromagnetic ratio

γ_∞ = Sternheimer antishielding factor

Δ = excitation energy; energy gap

δ_{iL}, δ_{ie}, etc. = spin relaxation rates

η = asymmetry parameter of electric field gradient tensor

θ = polar coordinate co-latitude angle

θ_2, θ_4, θ_6 = reduced matrix elements

θ_p = paramagnetic Curie temperature

λ = wavelength of radiation; spin-orbit interaction parameter

μ = magnetic dipole moment

ν = frequency of radiation; resonance frequency

ν_{ex} = exchange interaction characteristic frequency

$\Delta\nu$ = frequency shift or splitting

ρ = fractional s-character of conduction electrons at Fermi level

$\rho(r)$ = charge density at r

σ_n = electronic shielding factors

$\left.\begin{matrix}\sigma_x, \sigma_y, \sigma_z \\ \sigma_\parallel, \sigma_\perp\end{matrix}\right\}$ = chemical shift tensor components

τ = lifetime of nuclear level; nuclear precession time

τ_c = correlation time

ϕ = polar coordinate azimuthal angle.

χ_0 = nuclear Curie susceptibility

χ_s, χ_d, etc. = s, d, etc., contributions to susceptibility

χ_P = Pauli spin susceptibility

χ', χ'' = dispersion (absorption) components of radiofrequency nuclear spin susceptibility

ψ_s = s electron wavefunction

$|\psi(0)|^2$ = electron density at nucleus

$\langle |\psi(0)|^2 \rangle_F$ = electron density at nucleus averaged over conduction electrons at Fermi level

Ω = atomic volume

ω = angular frequency of radiation

1. Nuclear resonance methods and hyperfine interactions

The methods of nuclear magnetic resonance (NMR) and of Mössbauer effect or nuclear gamma resonance (NGR) spectroscopy furnish a broad basis for the study of the structural, electronic, and magnetic properties of rare-earth metals, alloys, and compounds. Taken together, there is hardly a rare-earth or non rare-earth nucleus whose hyperfine interactions cannot be measured. In many cases, results can be cross-checked with measurements on several isotopes of the same element.

Nuclear hyperfine interactions are those interactions of the electro-magnetic moment properties of the nucleus – especially the magnetic dipole and electric quadrupole moments – with the corresponding electromagnetic field quantities at the nuclear site which arise from the host atom (ion) itself as well as from all other atoms (ions) and nuclei in the molecule or crystal. From the standpoint of the physics or chemistry of solids, the nuclear moment properties may be regarded as known quantities, although this is not always entirely true.

Nuclear hyperfine interactions are sensitive to structural details molecular, crystallographic, and magnetic. The effective electromagnetic field quantities at the nuclear site arise from the electronic configuration of the host atom or ion, in the case of metals from conduction electrons both at the Fermi level and below, from neighboring ions via a variety of coupling mechanisms, and from the magnetic dipole moments of neighboring nuclei. Hyperfine interactions probe the magnetic interactions leading to ferro- and antiferromagnetism, the electronic interactions leading to superconductivity, and the translational and rotational diffusion of atoms and molecular groups in solids. These interactions may be studied under variation of the usual variables – temperature, pressure, and composition.

The advantages of Mössbauer effect spectroscopy have been summarized by Nowik (1966). These and others may be cited in respect to nuclear resonance methods in general. Thus: (1) by means of hyperfine interaction measurements it is possible to measure the magnetization of a single site or sublattice rather than only the total sum of the moments of all crystalline sites. In particular, when inequivalent sites (magnetic or nonmagnetic) occur in the crystal, their properties can be separately studied. (2) In consequence of (1), the magnetic moments of ions in antiferromagnetic materials are directly measurable. (3) By virtue of their microscopic nature, hyperfine measurements of magnetic moments are not reduced by anisotropy effects as are bulk measurements. (4) The magnetic structure may be studied in zero applied field as well as under the application of such fields. (5) Different phases present in a sample are usually easily distinguishable via their differing hyperfine interactions so that corrections for the lack of single-phase character of the sample are not needed. (The sensitivity often exceeds that of X-ray measurements used to determine the single-phase character.) (6) Similarly, impurity ions present in the crystal, which may significantly affect bulk property measurements, often have little or no effect on hyperfine parameters.

In addition to NMR and NGR methods, which form the experimental basis of discussion of nuclear hyperfine interactions in this review, a variety of other nuclear techniques based on nuclear orientation (NO) and perturbed angular correlation (PAC) of gamma radiation are gaining increasing significance in solid state investigations [Cohen (1967), Matthias (1967), Stone (1967 and Ch. 5, §1.6)]. Low temperature heat capacity measurements have also furnished valuable results pertaining to hyperfine interactions, particularly in the rare-earth metals themselves [Lounasmaa (1967), Bleaney (1972)], but these also lie outside the bounds of this review.

1.1. *Experimental methods*

1.1.1. *Nuclear magnetic resonance (NMR)*

Nuclear magnetic resonance, first demonstrated by Purcell et al. (1946) and Bloch et al. (1946), is now a standard experimental method of the physical and biological sciences. In the simplest form of NMR experiment, transitions are induced between the quantized energy levels of the nuclear magnetic dipole moment in a constant magnetic field (the so-called Zeeman levels). These transitions are induced by means of a weak radio frequency magnetic field applied perpendicular to the strong, constant field, and of frequency ν matching the Bohr condition, $h\nu = \Delta E = E_2 - E_1$, where ΔE is the energy difference between the levels E_2 and E_1. In the case of non-magnetically ordered materials, the strong magnetic field is usually provided by a laboratory magnet. Resonance frequencies range from roughly 1 MHz to 40 MHz in a field strength of 1 T (= 10 kOe), depending upon nuclear moment strength, which is the essential nuclear property involved. Nuclear species (isotopes) which possess non-zero intrinsic angular momentum (spin) also possess magnetic dipole moments, and the two quantities are parallel, though possibly opposed. Roughly half of all stable nuclear isotopes meet this requirement, being primarily those with an odd proton or odd neutron in their structure. Such nuclei have half-integral spin, ranging from 1/2 to 9/2 and reflecting the fact that both the proton and neutron have 1/2 unit of spin. Isotopes possessing even numbers of protons and neutrons (even–even nuclei) have zero spin and zero magnetic moment (including ^{4}He, ^{12}C, ^{16}O, and ^{32}S). Isotopes with an odd number of both protons and neutrons (odd–odd nuclei) have non-zero spin and magnetic moment. There are only five examples of these among the stable isotopes, but these include the important cases of ^{2}H and ^{14}N, both with one unit of spin.

In general, the energy levels are determined not only by the applied field, but also by contributions arising from the host ion or atom, from neighboring ions and nuclei, and from the conduction electrons in the case of metallic solids. In addition, if the nucleus possesses an electric quadrupole moment this interacts with the gradient of the total electrostatic field at the nuclear site. This contribution to the hyperfine energy may be a perturbation of the magnetic dipole energy or may dominate it so that the dipole energy becomes a perturbation of the

electric quadrupole energy. In the former case, a spectrum of transitions will arise whose dependence on applied magnetic field strength can be analyzed to yield the various interaction parameters. This is not so readily accomplished in the latter case which yields itself better to NGR study.

Direct detection of the NMR in a ferromagnetic metal in zero applied field was first achieved by Gossard and Portis (1959). Subsequently, the method has been extended to ferro- and antiferromagnetic solids in general, and sophisticated techniques have been developed. The subject has been thoroughly reviewed from the standpoint of both theory and experiment by Turov and Petrov (1972). In brief, the essential features are that the energy levels and spectra are determined by the magnetic hyperfine interaction between the nuclear and ionic magnetic moments plus the electric quadrupole interaction projected onto the hyperfine field direction. The observed transitions satisfy the magnetic dipole radiation selection rule, just as in NMR in an applied field. In addition, the applied radio frequency field (H_1) is strongly enhanced by the induced motion of the domain walls which in turn oscillate the ionic moment and thus the hyperfine field. This effect becomes less significant at the high radio frequencies typically encountered in the rare earths. Present experiments rely primarily on spin-echo methods [Budnick (1967), Turov and Petrov (1972)] for increased sensitivity and ease of searching over wide frequency ranges.

In the case that the energy levels are determined solely by the nuclear quadrupole interaction magnetic dipole transitions may still be observed in the radio frequency region. This specialization of NMR is referred to as nuclear quadrupole resonance (NQR), and furnishes a means of measuring the quadrupole interaction parameters with great precision. The theoretical background, experimental methods, and reviews of results obtained in many areas of solid state physics and chemistry are contained in a number of standard books on the subject [Lucken (1969), Smith (1974)].

Some examples of the many books concerned with the theory and practice of NMR in general are: Abragam (1960), Slichter (1963), Ingram (1967), Carrington and McLachlan (1967). Articles of a more specialized review nature will be cited when appropriate.

To serve as a basis for the discussion of experimental results, the natural abundances, spins, effective gyromagnetic ratios, and electric quadrupole moments of the ground states of those nuclei, rare-earth and non-rare earth, significant for the study of rare-earth metals, alloys, and compounds, are listed in tables 18.1 and 18.2, respectively.

1.1.2. *Nuclear gamma resonance (NGR)*

In nuclear gamma resonance (Mössbauer effect) experiments, the nuclear hyperfine interactions are measured via their influence on the energy of the gamma ray emitted (or absorbed) when the nucleus undergoes a transition between an excited state and its ground state (or between two excited states). Since the nuclear hyperfine energies are small ($\approx 10^{-6}$–10^{-5} eV) compared with

TABLE 18.1
Ground state nuclear moment properties of rare-earth nuclei, including Sc and Y, for NMR purposes, adapted from Fuller (1976).

Nucleus	Natural abundance (%)	Spin (I)	Effective gyromagnetic ratio (MHz/10^4 Oe)	Electric quadrupole moment (b)
^{139}La	99.9	$\frac{7}{2}$	6.014	+0.22
^{141}Pr	100	$\frac{5}{2}$	12.958	−0.058
^{143}Nd	12.2	$\frac{7}{2}$	2.315	−0.48
^{149}Sm	13.8	$\frac{7}{2}$	1.45	+0.052
^{151}Eu	47.8	$\frac{5}{2}$	10.559	+1.16
^{153}Eu	52.2	$\frac{5}{2}$	4.638	+2.8
^{157}Gd	15.6	$\frac{3}{2}$	1.710	+1.7
^{159}Tb	100	$\frac{3}{2}$	10.133	+1.3
^{163}Dy	25.0	$\frac{5}{2}$	2.05	+2.5
^{165}Ho	100	$\frac{7}{2}$	8.777	+2.4
^{167}Er	22.8	$\frac{7}{2}$	1.04	+2.8
^{169}Tm	100	$\frac{1}{2}$	3.522	0
^{171}Yb	14.3	$\frac{1}{2}$	7.499	0
^{173}Yb	16.1	$\frac{5}{2}$	2.066	+3.0
^{175}Lu	97.4	$\frac{7}{2}$	4.86	+5.6
^{89}Y	100	$\frac{1}{2}$	2.086	0
^{45}Sc	100	$\frac{7}{2}$	10.343	−0.22

typical nuclear gamma ray energies (10^3–10^5 eV), measurement of the hyperfine energy is achieved without actually measuring the gamma ray energy to the implied precision on the order of 10^{-11}. That this can be achieved rests on Mössbauer's discovery [Mössbauer (1958)] that a fraction f of the gamma rays are emitted (or absorbed) by nuclei bound in a solid without their energy being shifted by the nuclear recoil which necessarily accompanies the emission or absorption process in consequence of the conservation of momentum. The fraction f is called the recoil-free fraction and is given by

$$f = \exp(-k_\gamma^2 \langle x^2 \rangle), \tag{18.1}$$

where $k_\gamma = 2\pi/\lambda$ is the wave vector of the gamma ray and $\langle x^2 \rangle$ is the mean-square deviation of the nucleus from its equilibrium position in the lattice (in the direction of k_γ) due to thermal motion of the parent atom [see for example, Gonser (1975)]. In quantum mechanical terms, the recoil-free process is seen as the emission (absorption) of the gamma ray without accompanying creation (annihilation) of lattice vibration energy quanta (phonons). For this reason, the Mössbauer effect is more correctly termed a zero-phonon process.

The recoil-free fraction depends on temperature through the thermal vibration amplitude. Hence, f increases with decreasing temperature. In addition, f increases with decreasing k_γ, and therefore with decreasing gamma ray energy, E_γ. In practice, Mössbauer gamma ray energies range up to ≈ 150 keV. For

TABLE 18.2
Ground state nuclear moment properties of selected non-rare earth nuclei, for NMR purposes, adapted from Fuller (1976).

Nucleus	Natural abundance (%)	Spin (I)	Effective gyromagnetic ratio (MHz/10^4 Oe)	Electric quadrupole moment (b)
^{1}H	99.9	$\frac{1}{2}$	42.576	0
^{2}H	0.1	1	6.535	+0.0028
^{9}Be	100	$\frac{3}{2}$	5.983	+0.05
^{11}B	81.2	$\frac{3}{2}$	13.660	+0.041
^{14}N	99.6	1	4.315	+0.01
^{19}F	100	$\frac{1}{2}$	40.055	0
^{27}Al	100	$\frac{5}{2}$	11.094	+0.15
^{31}P	100	$\frac{1}{2}$	17.236	0
^{35}Cl	75.5	$\frac{3}{2}$	4.172	−0.10
^{55}Mn	100	$\frac{5}{2}$	10.553	+0.4
^{57}Fe	2.2	$\frac{1}{2}$		0
^{59}Co	100	$\frac{7}{2}$	10.103	+0.38
^{63}Cu	69.1	$\frac{3}{2}$	11.285	−0.211
^{69}Ga	60.2	$\frac{3}{2}$	10.219	+0.19
^{75}As	100	$\frac{3}{2}$	7.292	+0.29
^{77}Se	7.5	$\frac{1}{2}$	8.131	0
^{79}Br	50.6	$\frac{3}{2}$	10.667	+0.37
^{103}Rh	100	$\frac{1}{2}$	1.3401	0
^{105}Pd	100	$\frac{5}{2}$	1.948	+0.8
^{107}Ag	51.4	$\frac{1}{2}$	1.723	0
^{111}Cd	12.9	$\frac{1}{2}$	9.028	0
^{115}In	95.8	$\frac{9}{2}$	9.329	+0.82
^{119}Sn	15.9	$\frac{1}{2}$	15.869	0
^{121}Sb	57.3	$\frac{5}{2}$	10.189	−0.28
^{127}I	100	$\frac{5}{2}$	8.519	−0.79
^{195}Pt	33.8	$\frac{1}{2}$	9.153	0
^{207}Pb	22.6	$\frac{1}{2}$	8.9077	0

higher gamma ray energies, f is too small for practical purposes even at liquid helium temperature.

Whereas the energy width of the gamma ray emitted by a nucleus in a liquid is on the order of 10^{-3} eV due to the Doppler broadening resulting from the random thermal motion of the atoms (molecules) in the liquid, the width of the recoil-free gamma ray fraction is determined by the lifetime of the excited nuclear state through the uncertainty principle. Thus, since $\Gamma\tau \approx \hbar$, where Γ and τ are the uncertainty (width) in energy and lifetime, respectively, of the excited state, a lifetime of 10^{-7} sec leads to an energy width of only 10^{-8} eV. The longer the lifetime τ of the excited state, the greater will be the capability of the gamma ray to resolve the differences arising from the hyperfine interaction energies. Practicable excited state lifetimes range from $\sim (0.1\text{–}10^4) \times 10^{-9}$ sec.

Excited nuclear states suitable for Mössbauer spectroscopy are normally populated following the radioactive β-decay (including positron emission and

K-capture) of the parent isotopic species. The most frequently utilized Mössbauer isotope, ^{57}Fe, is obtained in its first excited state following the decay by K-capture of the parent ^{57}Co, which is itself obtained by a cyclotron bombardment procedure. Additional practical considerations are (usually) that the half-life of the radio-active parent be long enough that experiments can reasonably be performed without frequent changes of the source, and that the natural abundance of the Mössbauer isotope be sufficiently great that the use of isotopically enriched absorber materials is not required. Characteristics of many typical Mössbauer effect sources have been summarized by Ofer et al. (1968).

The hyperfine interaction spectrum of a Mössbauer nucleus is normally detected by a direct transmission measurement. The gamma ray energy from nuclei in a source is Doppler-shifted by a translational velocity of the source, and in this manner scanned across the hyperfine spectrum. Since the energy range of the latter is small, the Doppler-shifting velocity need only be on the order of 0.1 – 100 cm/sec in most cases to accomplish this scan. For simplicity of interpretation of the resultant spectrum, and to avoid needless complexity, the source material and its temperature are usually chosen so that the hyperfine structure vanishes in the source (e.g., a cubic site has zero quadrupole interaction, etc.). In this way the observed spectrum results entirely from the hyperfine properties of the absorber. The gamma rays are suitably detected and the resulting "counts" stored in a scaling or memory device. At resonance, the Doppler-shifted energy exactly matches one of the possible transitions in the hyperfine spectrum of the absorber, and an increase in absorption occurs, hence a decrease in the detected counting rate. Spectra are collected and displayed as a function of the Doppler-shifting velocity. Complete, detailed accounts of experimental procedures and techniques are contained in a variety of books dealing with the Mössbauer effect, for example Goldanskii and Herber (1968), Greenwood and Gibb (1971), and Gonser (1975).

To serve as a basis for the discussion of experimental results, the spins and nuclear moment properties of the ground and excited states of the (thus-far) most significant Mössbauer nuclei, rare-earth and non rare-earth, are listed in tables 18.3 and 18.4, respectively. Other experimentally relevant information pertaining to gamma ray energies, excited state lifetimes, parent half-life, etc., may be found in the books and data compilations for the Mössbauer effect previously cited.

1.2. *The magnetic dipole interaction*

A nucleus with spin angular momentum $\boldsymbol{I}\hbar$ possesses a magnetic dipole moment, $\boldsymbol{\mu} = g_N\beta_N\boldsymbol{I}$ the energies of which in a magnetic field $\boldsymbol{H}_0$ are given by the eigenvalues of the hamiltonian,

$$\mathcal{H}_M = -\boldsymbol{\mu}\cdot\boldsymbol{H}_0 = -g_N\beta_N\boldsymbol{I}\cdot\boldsymbol{H}_0 = -\gamma_N\hbar\boldsymbol{I}\cdot\boldsymbol{H}_0, \tag{18.2}$$

a total of $2I + 1$ equally-spaced levels, the so-called Zeeman levels, corresponding to the $2I + 1$ values of the z component quantum number m_I ($m_I = -I, -I +$

TABLE 18.3

Nuclear moment properties of the ground and excited states of selected rare-earth nuclei frequently utilized in nuclear gamma resonance (Mössbauer effect) measurements, adapted from Stevens and Dunlap (1976). Nuclear moment values are given in units of the nuclear magneton (nm).

Nucleus	Natural abundance (%)	Gamma ray energy (keV)	Excited state lifetime (nsec)	Ground state			Excited state		
				Spin	μ_g (nm)	Q_g (barns)	Spin	μ_e (nm)	Q_e (barns)
^{141}Pr	100	145.2	1.85	$\frac{5}{2}$	+4.162	−0.059	$\frac{7}{2}$	+2.80	0.3
^{145}Nd	8.3	67.25	29.4	$\frac{7}{2}$	−0.654		$\frac{5}{2}$	−0.320	
^{147}Pm		91.03	2.57	$\frac{7}{2}$	+2.62	+0.71	$\frac{5}{2}$	3.60	0.6
^{149}Sm	13.8	22.5	7.6	$\frac{7}{2}$	−0.670	0.06	$\frac{5}{2}$	−0.623	0.50
^{151}Eu	47.8	21.64	9.7	$\frac{5}{2}$	+3.465	+1.14	$\frac{7}{2}$	2.587	+1.50
^{157}Gd	15.7	64.0	460	$\frac{3}{2}$	−0.339	2.0	$\frac{5}{2}$	−0.513	3.6
^{159}Tb	100	58.0	13	$\frac{3}{2}$	+2.008		$\frac{5}{2}$	+2	
^{161}Dy	18.8	43.84	920	$\frac{5}{2}$	−0.479	+2.35	$\frac{7}{2}$	−0.140	0.49
^{166}Er	33.4	80.6	1.82	0	0	0	2	0.63	−1.6
^{169}Tm	100	8.42	3.9	$\frac{1}{2}$	−0.231	0	$\frac{3}{2}$	+0.534	−1.2
^{171}Yb	14.3	66.7	0.86	$\frac{1}{2}$	+0.4919	0	$\frac{3}{2}$	0.349	−1.6

TABLE 18.4

Nuclear moment properties of the ground and excited states of selected non rare-earth nuclei frequently utilized in nuclear gamma resonance (Mössbauer effect) measurements, adapted from Stevens and Dunlap (1976). Nuclear moment values are given in units of the nuclear magneton (nm).

Nucleus	Natural abundance (%)	Gamma ray energy (keV)	Excited state lifetime (nsec)	Ground state			Excited		
				Spin	μ_g (nm)	Q_g (barns)	Spin	μ_e (nm)	Q_e (barns)
^{57}Fe	2.2	14.4	99.3	$\frac{1}{2}$	+0.0906	0	$\frac{3}{2}$	−0.1553	+0.209
^{61}Ni	1.1	67.4	5.2	$\frac{3}{2}$	−0.7498	+0.16	$\frac{5}{2}$	−0.478	−0.20
^{119}Sn	8.5	23.8	18.3	$\frac{1}{2}$	−1.0461	0	$\frac{3}{2}$	+0.633	−0.065
^{121}Sb	57.3	37.2	3.5	$\frac{5}{2}$	+3.3591	−0.28	$\frac{7}{2}$	+2.47	−0.38
^{193}Ir	61.5	73.1	6.2	$\frac{3}{2}$	+0.1583	+0.70	$\frac{1}{2}$	0.486	0

$1, \ldots, I-1, I$). The field $\boldsymbol{H}_0$ may be externally applied as in conventional NMR of paramagnetic or diamagnetic substances; it may arise entirely from interactions with unpaired electron spins within ferro- or antiferromagnetic solids (the hyperfine field) as in most NGR experiments; or it may be the sum of fields of both these origins.

Since the Zeeman levels are equally spaced, the transitions between the levels, governed in NMR by the magnetic dipole radiation selection rule, $|\Delta m_I| = 1$, are all identical and have the value

$$\Delta E = h\nu = g_N \beta_N H_0 = \gamma_N \hbar H_0. \tag{18.3}$$

The observed transition (resonance) frequency is therefore

$$\nu = g_N \beta_N H_0 / h = \gamma_N H_0 / 2\pi. \tag{18.4}$$

The situation is more complex in NGR spectra since in general both ground and excited nuclear levels have magnetic moments so that (18.2) and (18.3) apply to both. In addition, the selection rule for the transitions is governed by the multipolarity of the gamma radiation (magnetic dipole, electric quadrupole, etc., or some mixture thereof).

1.2.1. *The magnetic hyperfine field*

The magnetic interaction of a nucleus with its electronic environment can usually be written in the form of (18.2) with the non-nuclear part of $\mathcal{H}_M$ represented by an effective magnetic field, $\boldsymbol{H}_{eff}$, which acts on the nuclear dipole moment. (Some exceptions to this are considered in section 1.4.1.) The term "hyperfine field" refers generally to this effective magnetic field at the nucleus arising from electronic moments within the solid. For the nuclei of the rare-earths, the principal contribution to $\boldsymbol{H}_{eff}$ is due to the unpaired 4f electron spins. Other contributions arise from the conduction electrons in the case of metals and from the core polarization effect caused by the exchange interaction between the 4f electrons and the spins of inner shell electrons [Watson and Freeman (1967)]. The nuclei of non rare-earth elements bonded to rare-earths in alloys and compounds experience a "transferred hyperfine field" arising from the transference via bonding or conduction electrons of a portion of the magnetic character of the rare-earth. The hyperfine field varies in strength between roughly 0.01 T and 10^3 T, the latter being the field at a rare-earth nucleus and the former being the dipolar field at, for example, the protons in water of hydration in a rare-earth salt. Intermediate field strengths occur at the nuclei of atoms bonded to the rare-earth ion (e.g., at ^{19}F in RF_3 compounds).

The direct 4f electron contribution to $\boldsymbol{H}_{eff}$ can be written as

$$\boldsymbol{H}_{eff}^{(4f)} = -2\beta \sum_i \{r_i^{-3}[\boldsymbol{l}_i - \boldsymbol{s}_i + 3\boldsymbol{r}_i(\boldsymbol{r}_i \cdot \boldsymbol{s}_i)/r_i^2]\} \tag{18.5}$$

where the sum is over the 4f electrons, β is the Bohr magneton, and $\boldsymbol{r}_i$, $\boldsymbol{s}_i$, and $\boldsymbol{l}_i$ are the position, spin, and orbital angular momentum operators of the i^{th}

electron, respectively. Since for most of the rare-earths (except Sm^{3+} and Eu^{3+}) the total angular momentum, $J = L \pm S$, is a good quantum number, reflecting the strong LS coupling, the complicated expression (18.5) may be replaced by the operator equivalent form,

$$H_{\text{eff}}^{(4f)} = -2\beta\langle r^{-3}\rangle \langle J\|N\|J\rangle \boldsymbol{J}, \tag{18.6}$$

as described, for example, by Abragam and Bleaney (1970) and by Bleaney (1972). Here, $\langle r^{-3}\rangle$ is the average value of r^{-3} for the 4f electrons in a given J state of a rare-earth, and it is assumed that the distinction between the average for the orbital and spin parts of (18.5) can be neglected. Similarly, the g-factor for the electron spin is taken to be exactly 2. Finally, $\langle J\|N\|J\rangle$ is a reduced matrix elemént defined by the operator equivalence

$$[(\boldsymbol{N}\cdot\boldsymbol{J})/J(J+1)]\boldsymbol{J} = \langle J\|N\|J\rangle \boldsymbol{J}. \tag{18.7}$$

Values of $\langle r^{-3}\rangle$ are based primarily on theoretical calculations of the 4f wave functions, for example, those of Freeman and Watson (1962) and of Judd (1963). In table 18.5 are listed the values of $\langle J\|N\|J\rangle$, $\langle r^{-3}\rangle$, and $H_{\text{eff}}^{(4f)}$ for the tripositive rare-earth ions. Strictly speaking, correction factors differing from unity by a few percent should be applied to these $\langle J\|N\|J\rangle$ values [Bleaney (1972)] to take account of intermediate coupling effects which arise from the admixture into the ground state (L, S, J) wave function of states of different L, S, but the same J, by the spin–orbit interaction. A table of these values is included in Bleaney (1972).

The hyperfine field may also be expressed in terms of the hyperfine constant A

TABLE 18.5

Magnetic hyperfine field parameters for the lanthanide ions based on the results of Freeman and Watson (1962). The experimental "free ion" values of the total hyperfine field are derived from electron spin resonance data on dilute lanthanide impurities in insulators [Bleaney (1972)]. A positive sign for H_{eff} means that the field has the same direction as the electronic moment.

Tripositive lanthanide ion	Landé factor g_J	$\langle J\|N\|J\rangle$	$\langle r^{-3}\rangle$ ($\times 10^{23}$ cm^3)	$H_{\text{eff}}^{(4f)}$ (MOe)	Experimental free ion H_{eff} (MOe)
Ce	$\frac{6}{7}$	1.38	3.19	+2.04	+1.83(5)
Pr	$\frac{4}{5}$	1.32	3.63	+3.55	+3.37(4)
Nd	$\frac{8}{11}$	1.31	4.07	+4.45	+4.30(2)
Pm	$\frac{3}{5}$	1.36	–	–	+4.26(12)
Sm	$\frac{2}{7}$	1.55	4.97	+3.57	+3.42(1)
Eu	0	0	5.46	–	0
Gd	2	0	5.97	–	−0.32
Tb	$\frac{3}{2}$	0.56	6.47	+4.03	+3.14(3)
Dy	$\frac{4}{3}$	0.71	6.98	+6.89	+5.70(10)
Ho	$\frac{5}{4}$	0.77	7.54	+8.61	+7.40(9)
Er	$\frac{6}{5}$	0.78	8.11	+8.80	+7.64(3)
Tm	$\frac{7}{6}$	0.78	8.69	+7.54	+6.62
Yb	$\frac{8}{7}$	0.76	9.34	+4.61	+4.13(1)

by comparing the hyperfine interaction hamiltonian

$$\mathscr{H}_{\rm hf} = A\boldsymbol{I}\cdot\boldsymbol{J}, \tag{18.8}$$

with the magnetic dipole interaction hamiltonian of (18.2). Thus,

$$\boldsymbol{H}_{\rm eff}^{(4f)} = -A\boldsymbol{J}/\gamma_{\rm N}h. \tag{18.9}$$

The core polarization contribution to the hyperfine field arises from the alteration in the radial wave function of the two s electrons in a closed shell brought about by the fact that their exchange couplings with the net spin $\boldsymbol{S}$ in the 4f shell are different since one s electron has its spin parallel to s and the other antiparallel. Hence, the net magnetic field at the nucleus due to closed s shells no longer cancels exactly. Because s electrons have finite density at the nucleus ($\psi_s(0) \neq 0$), a small difference is effectively magnified. In a general way [Bleaney (1972)] the core polarization field may be written analogously to the Fermi contact hyperfine field [Fermi (1930)],

$$\boldsymbol{H}_{\rm c} = -\tfrac{16}{3}\pi\beta|\psi_{\rm A}(0)|^2 s, \tag{18.10}$$

as

$$\boldsymbol{H}_{\rm eff}^{(cp)} = -\tfrac{16}{3}\pi\beta\{|\psi_\uparrow|^2 - |\psi_\downarrow|^2\}s \tag{18.11}$$

where $|\psi_{\rm A}(0)|^2 s$ is the spin density at the nucleus due to an unbalanced (valence) s electron in a free atom, and $\{|\psi_\uparrow|^2 - |\psi_\downarrow|^2\}s$ is the unbalanced spin density at the nucleus of a rare-earth ion due to closed s shells.

For the rare-earths (except Gd^{3+} and Eu^{2+}) the core polarization field is relatively small compared to the direct 4f contribution and is estimated to be represented by [Watson and Freeman (1967)],

$$\boldsymbol{H}_{\rm eff}^{(cp)} \cong -90(g_J - 1)\boldsymbol{J}\ (\text{kOe}), \tag{18.12}$$

where g_J is the Lande g-factor. For the 3d series of ions, on the other hand, $\boldsymbol{H}_{\rm eff}^{(cp)}$ makes the dominant contribution to the hyperfine field, and this is also true of the rare-earth ions Gd^{3+} and Eu^{2+} where the direct 4f contribution is very small.

In metals the conduction electrons also contribute to the hyperfine field via their nonvanishing spin density at the nucleus when they are polarized either by an external magnetic field or by their exchange interaction with the rare-earth ion spins. In the former case, in the paramagnetic state, the resultant contribution to the total field results in the Knight shift, discussed further in section 1.2.2.3. In the latter case, in the magnetically ordered state at low temperatures, it can be shown [Bleaney (1972)] that the conduction electron hyperfine field, $\boldsymbol{H}_{\rm eff}^{(ce)}$, is proportional to the s–f exchange interaction parameter $\mathscr{J}_{\rm sf}$ which is responsible for the coupling of the rare-earth ions in the metal. Thus,

$$\boldsymbol{H}_{\rm eff}^{(ce)} \sim -(g_J - 1)\mathscr{J}_{\rm sf}\tfrac{1}{2}\boldsymbol{J}. \tag{18.13}$$

The temperature dependence of the net hyperfine field is controlled mainly by the temperature dependence of $\boldsymbol{H}_{\rm eff}^{(4f)}$ and $\boldsymbol{H}_{\rm eff}^{(cp)}$ since in most cases $\boldsymbol{H}_{\rm eff}^{(ce)}$ is small. Since both of these terms are proportional to $\boldsymbol{J}$, and since the ionic magnetiza-

tion is also proportional to J, it follows that the temperature dependence of H_{eff} will parallel that of the spontaneous magnetization M. So long as crystalline field effects are negligible, and the molecular field approximation is valid, the hyperfine field may be expected to follow a Brillouin function dependence on the molecular field and hence on the temperature. An immediate consequence of this is that in many cases the magnetic ordering temperature and Brillouin function dependence may be determined solely on the basis of hyperfine field measurements, either by NMR or NGR. Exceptions to the parallelism (tracking) of H_{eff} and M arise from non-negligible conduction electron contributions, particularly in the case of intermetallic compounds with iron.

1.2.2, *Chemical and Knight shifts*

In NMR experiments on dia- and paramagnetic materials, the magnetic field at the nuclear site differs in general from the applied field [Abragam (1960), Slichter (1963)]. This difference is usually not very great, amounting to at most a few percent apart from some exceptional cases, and is proportional to the applied field strength, reflecting the dia- or paramagnetic nature of the material. Phenomenologically, for the purpose of parametrizing experimental measurements, these *shift* effects are treated by introducing a shift tensor T_{ij} so that the magnetic field components at the nuclear site, $\boldsymbol{H}^{(i)}_{\text{nucl}}$, are given in terms of the applied field components, $\boldsymbol{H}^{(i)}_{\text{appl}}$, by

$$\boldsymbol{H}^{(i)}_{\text{nucl}} = \sum_{j=1}^{3} (1 + T_{ij}) H^{(j)}_{\text{appl}}, \tag{18.14}$$

where $i, j = 1, 2, 3$ refer to coordinate directions in the crystal. Since T_{ij} can always be referred to its own principal axes system, and since the effects are usually quite small, it normally suffices to employ only the diagonal elements of $T (T_{ii} = T_i)$.

As a consequence of the different behavior anticipated for diamagnetic solids (e.g., salts, etc.) as compared with paramagnetic ones (e.g., metals), the shift tensors for these two cases have opposing definitions. The chemical shift tensor σ_i is defined by

$$H^{(i)}_{\text{nucl}} = (1 - \sigma_i) \boldsymbol{H}^{(i)}_{\text{appl}}. \tag{18.15}$$

For metallic solids, the Knight shift tensor [Knight (1949)] K_i is defined by

$$\boldsymbol{H}^{(i)}_{\text{nucl}} = (1 + K_i) H^{(i)}_{\text{appl}}. \tag{18.16}$$

A paramagnetic Knight shift has $K > 0$, and a paramagnetic chemical shift has $\sigma < 0$.

Often the shift tensor has axial symmetry, and it is then convenient to employ components $K_{\parallel} = K_z$ and $K_{\perp} = K_x = K_y$ (and analogously, $\sigma_{\parallel}$ and $\sigma_{\perp}$), taking the z direction along the symmetry axis. In addition, reflecting the fact that in many cases the shift originates from isotropic and anisotropic contributions, an alter-

native form is

$$K_{iso} = \tfrac{1}{3}(K_x + K_y + K_z) = \tfrac{1}{3}(K_\parallel + 2K_\perp) \tag{18.17}$$

and

$$K_{ax} = \tfrac{1}{3}(K_\parallel - K_\perp). \tag{18.18}$$

Since the applied field is fixed in the laboratory, the components in the crystal coordinate system will be $H_z = H_0 \cos\theta$, $H_x = H_0 \sin\theta \cos\phi$, and $H_y = H_0 \sin\theta \sin\phi$, where θ and ϕ are the usual spherical coordinate angles. Thus, for NMR in a single crystal of a metallic solid for which the Knight shift tensor has axial symmetry, the dependence of the resonance frequency ν on crystal orientation with respect to the laboratory field H_0 will be given by [Abragam (1960)]:

$$\nu = (\gamma_N/2\pi)[1 + K_{iso} + K_{ax}(3\cos^2\theta - 1)]H_0. \tag{18.19}$$

1.2.2.1. *The chemical shift*

In a uniform magnetic field, the precession motion of the entire electron cloud of a free atom constitutes an induced electron current which gives rise to a weak secondary magnetic field at the nucleus proportional to the applied field. In a molecule the electrons are in general not completely free to precess about the direction of H_0, and in consequence the secondary field may contain a second term of opposite sign to the first. In addition, in molecules and solids, the total secondary field may not be parallel to H_0 so the chemical shift must be represented by a tensor quantity rather than a simple scalar.

The first, or diamagnetic, contribution to the chemical shift is proportional to the expectation value, $\langle(x^2 + y^2)r^{-3}\rangle$, for the electronic ground state of the atom or molecule, and is generally small [Ramsey (1950)]. The second, or paramagnetic, contribution is related to the second-order (Van Vleck) contribution to the molecular susceptibility [Ramsey (1950)]. This contribution involves a sum of terms like $\langle 0|L_z|n\rangle\langle n|2L_z r^{-3}|0\rangle/(E_n - E_0)$, each summed over all electrons, where L_z is the operator for the z component of the orbital angular momentum, and E_n and E_0 refer to the electronic excited state and ground state energies. Since the paramagnetic terms depends on matrix elements of r^{-3} between ground and excited states, its magnitude increases with increasing atomic number, and it becomes the dominant contribution to the chemical shift for heavy nuclei. Nonetheless, in the NMR of most rare-earth containing materials the chemical shift plays a relatively minor role and will not be treated in further detail.

1.2.2.2. *Hyperfine interaction shifts*

In paramagnetic solids, an important consideration arises from the fact that the correlation time τ_c of the ionic spin fluctuations is shorter than the characteristic nuclear precession time τ in the effective hyperfine field of (18.9). Thus, $\tau_c < \tau$, or $\tau_c^{-1} > |AS/h|$. Under this condition, the nuclear moment senses only the average hyperfine field which is proportional to the average value of the spin,

$\langle \boldsymbol{S} \rangle$. An effective nuclear hamiltonian can therefore be written as

$$\mathcal{H}_{\text{para}} = -\gamma_N \hbar \boldsymbol{H}_0 \cdot \boldsymbol{I} + \boldsymbol{I} \cdot \boldsymbol{A} \cdot \langle \boldsymbol{S} \rangle. \tag{18.20}$$

At temperatures appreciably higher than the magnetic ordering temperature of the material, the average value $\langle \boldsymbol{S} \rangle$ is much less than $\boldsymbol{S}$ itself. For S-state ions (e.g., Gd^{3+}), in a first-order approximation, $\langle S_z \rangle$ is proportional to χH_0, and if A is isotropic, the resonance will be shifted to the frequency

$$\nu = (\gamma_N/2\pi)\,[1 - (A\chi/\gamma_e\gamma_N\hbar^2)]H_0. \tag{18.21}$$

A consequence of the smallness of $\langle \boldsymbol{S} \rangle$ in the paramagnetic state is that the spin fluctuations, represented by $\boldsymbol{S} - \langle \boldsymbol{S} \rangle$, are very large. Observation of the NMR signal requires however that the field sensed by the nuclear moments have a sufficiently well-defined value. This requirement can be shown to be met [Narath (1967)] if the correlation time τ_c of the ionic spins is much shorter than the nuclear precession time, or if $\tau_c^{-1} \gg \nu_0$. This condition is difficult to satisfy in dilute paramagnetic solids. On the other hand, in magnetically dense solids, exchange interactions between the ions involving a coupling of the form $-J_{ij}\boldsymbol{S}_i \cdot \boldsymbol{S}_j$, lead in the case of nearest-neighbor interactions to an exchange frequency given by

$$\nu_{ex} = (2\pi)^{-1}[8J^2zS(S+1)/3\hbar^2]^{1/2}, \tag{18.22}$$

where z is the number of nearest-neighbor coupled ions. The corresponding correlation time, τ_c, can be as short as 10^{-13} sec. Under these conditions the resonance linewidth becomes proportional to $(A/h)^2S(S+1)/3\nu_{ex}$, indicating that the narrowest resonances will be found when the hyperfine interaction is weak, but the exchange frequency is large. This combination is most frequently met in the NMR of non rare-earth nuclei in rare-earth compounds, where the relevant hyperfine interaction is of the "transferred" variety.

In analyzing shift measurements for such non rare-earth nuclei, account usually must also be taken of the classical dipolar field due to the rare-earth ionic moments. This field can be calculated on the basis of lattice sums, since the mean magnetization per ion is proportional to the susceptibility, and its effect subtracted from the measured total shift obtained experimentally in order to obtain the hyperfine shift. This procedure has been described in detail by Shulman and Knox (1960).

1.2.2.3. *Knight shift in metallic solids*

In simple metals in the paramagnetic state, the frequency at which NMR occurs is slightly shifted to higher values (at constant magnetic field) with respect to the frequency for the same nucleus in diamagnetic non-metallic solids. This effect, first noted by Knight (1949) and hence referred to as the Knight shift, has the properties: (1) the magnitude of the shift in resonance frequency, $\Delta\nu_0$, is proportional to the applied field strength and is positive, (2) the shift is independent of temperature, (3) the shift increases with increasing atomic number of the element, and (4) the shift is the same for different isotopes of the

same element. The shift is much too great to result simply from the bulk magnetization of the sample. Rather, as shown by Townes et al. (1950), it is a consequence of the Fermi contact hyperfine interaction (Fermi, 1930), the hyperfine field for which is given by eq. (18.10) and which leads to the relation

$$K = \Delta\nu_0/\nu_0 = \tfrac{8}{3}\pi\chi_P\Omega\langle|\psi(0)|^2\rangle_F, \tag{18.23}$$

for the Knight shift K. Here, χ_P is the Pauli spin susceptibility per unit volume, Ω is the atomic volume, and $\langle|\psi(0)|^2\rangle_F$ is the average value of the electronic probability density at the nucleus taken over electrons having energies at the Fermi level. The external magnetic field polarizes the conduction electrons slightly, giving rise to the Pauli paramagnetic susceptibility, and this is enhanced at the nucleus by the contact interaction.

Strictly speaking, the shift given by (18.23) is the isotropic component of the total shift tensor. It applies directly to nuclei at crystalline sites of cubic symmetry. Otherwise, in general, the shift tensor possesses additional components, as discussed in section 1.2.2. For axially symmetric conduction electron distributions, the axial component of the Knight shift in simple metals is given by:

$$3K_{ax} = \tfrac{8}{3}\pi\Omega\Delta\chi_P\langle|\psi(0)|^2\rangle_F + 3\Omega q_F\bar{\chi}_P, \tag{18.24}$$

where $\Delta\chi_P = \chi_P^{\parallel} - \chi_P^{\perp}$, $\bar{\chi}_P = \frac{1}{3}(\chi_P^{\parallel} + 2\chi_P^{\perp})$, and the quantity q_F is a measure of the axial anisotropy of the conduction electron distribution at the Fermi surface [Bloembergen and Rowland (1953)], given by:

$$q_F = \langle\int\psi^*(3z^2 - r^2)r^{-5}\psi\,d\theta\rangle_F. \tag{18.25}$$

$\chi_P^{\parallel}$ and $\chi_P^{\perp}$ are the parallel and perpendicular components of the Pauli susceptibility tensor with respect to the symmetry axis.

In a transition metal the Knight shift is considered to be partitioned into contributions which parallel the partitioning of the magnetic susceptibility. As discussed for example by Narath (1967) and by Clogston et al. (1964) the simplest model of transition metals assumes that the s and d bands are distinguishable at the Fermi level. If this is not the case, and s–d mixing is significant, then the states at the Fermi level may be characterized by their average fractional s and d character with accompanying appropriate fractional s and d band densities of states, the relative importance of these depending on the symmetry of the metal structure and the details of the band structure of the metal. If spin–orbit interactions are not too important, the magnetic susceptibility may be represented by a sum of spin and orbital contributions and diamagnetic terms,

$$\chi = \chi_s + \chi_d + \chi_{VV} + \chi_L + \chi_D. \tag{18.26}$$

Here, χ_s and χ_d are the s and d spin susceptibilities, which can be related to the fractional densities of states mentioned above, χ_{VV} is the field-induced orbital paramagnetic susceptibility (Van Vleck susceptibility) arising from the orbital

degeneracy of the atomic d states, and χ_L and χ_D are the Landau diamagnetic susceptibility of the conduction electrons and the diamagnetic susceptibility of the ion cores, respectively.

In the tight-binding approximation [Clogston et al. (1964)], the Knight shift is written as

$$K = K_s + K_d + K_{orb} \tag{18.27}$$

and is related to the magnetic susceptibility contributions by

$$K = -(2/\gamma_e\hbar)\,[H_{hf}^{(s)}\chi_s + H_{hf}^{(d)}\chi_d + H_{hf}^{(orb)}\chi_{vv}], \tag{18.28}$$

where $H_{hf}^{(s)}$ and $H_{hf}^{(d)}$ are the effective hyperfine fields per electron due to the Fermi direct contact interaction [eq. (18.10)] and to the d spins via the core-polarization of the inner (closed shell) s electrons [eq. (18.11)]. $H_{hf}^{(orb)}$ is the orbital hyperfine field per unit orbital angular momentum. The orbital hyperfine field is related to the expectation value of r^{-3} over all excited states that contribute to χ_{vv}. Thus,

$$H_{hf}^{(orb)} = \gamma_e\hbar\langle r^{-3}\rangle. \tag{18.29}$$

Inasmuch as $H_{hf}^{(d)}$ is negative, whereas the other two hyperfine fields are positive, the total shift may be of either sign in transition metals. The temperature dependence of the shift is usually presumed to reside in the d spin contribution via the temperature dependence of χ_d.

In the case of a non-magnetic, non rare-earth nucleus in a rare–earth intermetallic compound, the temperature-dependent Knight shift of such a nucleus can be expressed in the form

$$K(T) = K_0 + K_f(T), \tag{18.30}$$

where K_0 is the Knight shift resulting from the band paramagnetism only and $K_f(T)$ is due to the presence of the 4f electrons via a transferred hyperfine interaction of the general form $A\,\boldsymbol{I}\cdot\langle\boldsymbol{S}\rangle$. Here, A is a hyperfine interaction constant, and $\langle\boldsymbol{S}\rangle$ is the time-averaged value of the 4f spin component of the total angular momentum $\langle\boldsymbol{J}\rangle$. The distinction between $\langle\boldsymbol{S}\rangle$ and $\langle\boldsymbol{J}\rangle$ is important only for Sm^{3+} and Eu^{3+} compounds, since in these cases $\langle\boldsymbol{S}\rangle$ is not proportional to $\langle\boldsymbol{J}\rangle$ in the vicinity of room temperature. Particular forms for the shift $K_f(T)$ in terms of conduction electron spin–polarization models have been developed, and experimental results for the Knight shift in rare-earth intermetallics are interpreted in the light of these formulations [Jaccarino et al. (1960), de Wijn et al. (1968)].

1.2.3. *Nuclear dipolar second moment*

The full hamiltonian describing the energy of a system of nuclear spins, such as is found in a solid, must include terms due to the dipole–dipole interaction of each spin with all other spins, including those of differing nuclear species, and of paramagnetic ions present in the material. Adding the dipolar hamiltonian to the

simple Zeeman hamiltonian given by eq. (18.2), and summing over all spins in order to describe properly the spin system in a solid, yields:

$$\mathcal{H} = \gamma\hbar H_0 \sum_i I_{zi} + \sum_{i<j} \frac{\gamma^2\hbar^2}{r_{ij}^3}\{\boldsymbol{I}_j \cdot \boldsymbol{I}_j - 3[(\boldsymbol{I}_i \cdot \boldsymbol{r}_{ij})(\boldsymbol{I}_j \cdot \boldsymbol{r}_{ij})]r_{jk}^{-2}\}. \tag{18.31}$$

The sums on i and j are over all nuclei in the system, and the first term of eq. (18.31) is just the sum of all the Zeeman energies of eq. (18.2) for the individual spins interacting with the applied field H_0. The second term represents the dipole–dipole interaction energy, the sum on j being the effective dipole field at the ith nucleus due to all other nuclei (and/or paramagnetic ions), and r_{ij} being the radius vector between the ith and jth nuclei.

The effect of the dipole–dipole interaction is to give the nuclear magnetic resonance a finite width and shape. If it were not for this interaction, the resonance would approximate a "spike" (delta-function) at the resonance frequency. However, the width and shape frequently depend on the temperature via the diffusive motion of the host atoms or ions in the lattice. At temperatures low enough that the effects of diffusion can be neglected, information about the crystal structure of the solid can be obtained through the second moment of the experimental lineshape by comparing it with the theoretical value based on the formula due to Van Vleck (1948). The second moment of the resonance is defined as

$$M_2 = \int_{-\infty}^{+\infty} (\nu - \nu_0)^2 \, g(\nu - \nu_0) \, \mathrm{d}\nu, \tag{18.32}$$

where $g(\nu - \nu_0)$ is the lineshape function (normalized to unity) with ν_0 being the center frequency of the resonance. In many cases $g(\nu - \nu_0)$ can be reasonably approximated by a gaussian function. The formula given by Van Vleck (1948) is based on the hamiltonian of (18.31) and gives the second moment exactly as

$$M_2 = \tfrac{3}{5}\gamma_I^4\hbar^2 I(I+1)\sum_i r_i^{-6} + \tfrac{4}{15}\gamma_I^2\gamma_S^2\hbar^2 S(S+1)\sum_j r_j^{-6} \tag{18.33}$$

for a powder (polycrystalline) sample, taking a resonant nucleus at the origin, with $r_i(r_j)$ being the distance from the origin to the ith (jth) nucleus. The sum on i in (18.33) extends over all "like" nuclei with spin I (those of the same species as the resonant nucleus) and the sum on j extends over all "unlike" nuclei with spin S (those of other non-resonant nuclear species). Crystallographic information enters through the sums on r^{-6}. Expressions for the theoretical second moment in single crystals, in which case M_2 depends on the crystal orientation in the applied field H_0, are given in the NMR literature [e.g., Abragam (1960)].

In solids, in addition to the classical dipolar interaction described above, interactions between the nuclear spins are also mediated by the bonding and/or conduction electrons. These "exchange" and "pseudo-dipolar" interactions were already included by Van Vleck (1948) in his general treatment, and specific application to NMR in solids was given by Bloembergen and Rowland (1953). These interactions are generally most consequential for relatively heavy nuclei.

1.3. *Electrostatic hyperfine interactions*

The nuclear electric quadrupole splitting and the isomer shift effect have their origins in the interaction of the nucleus with its electrostatic environment. Assuming that the electric potential $V(r)$ due to all charges other than the nuclear charges varies slowly over the nuclear volume, it may be expanded about the origin (at the center of charge of the nucleus) as:

$$V(r) = V(0) + \sum_{\alpha=1}^{3} (\partial V/\partial x_\alpha)_0 x_\alpha + \tfrac{1}{2} \sum_{\alpha,\beta=1} (\partial^2 V/\partial x_\alpha \partial x_\beta)_0 x_\alpha x_\beta + \ldots \tag{18.34}$$

in an obvious notation. The classical electrostatic energy of the nucleus, having charge density $\rho(r)$, in this potential is

$$E = \int \rho(r) V(r)\, d\tau, \tag{18.35}$$

Where the integral is over the nuclear volume. Substituting from (18.34) for $V(r)$ yields the usual form for the energy E in terms of the electric multipole moments of the nuclear charge distribution:

$$E = ZeV(0) + \sum_{\alpha=1}^{3} (\partial V/\partial x_\alpha)_0 \int \rho(r) z_\alpha \, d\tau$$

$$+ \tfrac{1}{2} \sum_{\alpha,\beta=1}^{3} (\partial^2 V/\partial x_\alpha \partial x_\beta)_0 \int \rho(r) x_\alpha x_\beta \, d\tau + \ldots, \tag{18.36}$$

where $Ze = \int \rho(r)\, d\tau$ is the total nuclear charge. The first term represents the Coulomb interaction of a point nucleus with the electric potential at the origin and contributes to the total potential energy of the crystal lattice or molecule, but it is independent of the nuclear orientation or spin state and does not contribute to the hyperfine interaction.

The second (linear) term in (18.36) vanishes because nuclear states, having definite parity, cannot (and do not) possess electric dipole moments. The third (second order) term gives rise to both the electric quadrupole and isomer shift interactions.

The second derivatives of the potential, $\partial^2 V/\partial x_\alpha \partial x_\beta$, constitute a symmetrical second-rank tensor which is usually abbreviated $V_{\alpha\beta}$. In its principal axes system, this tensor is diagonal, and the energy becomes

$$E^{(2)} = \tfrac{1}{2} \sum_{\alpha=1}^{3} V_{\alpha\alpha} \int \rho(r) x_\alpha^2 \, d\tau. \tag{18.37}$$

Adding and subtracting the quantity $r^2 = \Sigma_{\alpha=1}^{3} x_\alpha^2$ under the integral allows this equation to be written as the sum of two terms:

$$E^{(2)} = \tfrac{1}{6} \sum_{\alpha=1}^{3} V_{\alpha\alpha} \int \rho(r)(3x_\alpha^2 - r^2)\, d\tau + \tfrac{1}{6} \sum_{\alpha=1}^{3} V_{\alpha\alpha} \int \rho(r) r^2 \, d\tau; \tag{18.38}$$

the first of these terms being identified with the electric quadrupole interaction

and the second with the isomer shift. This may be seen as follows:

For all charges external to the nucleus, the potential $V(\boldsymbol{r})$ satisfies Laplace's equation, $\Sigma_{\alpha=1}^{3} V_{\alpha\alpha} = 0$. For this source of $V(\boldsymbol{r})$, the second term in (18.38) vanishes. The first term, which does not vanish, is the electric quadrupole interaction energy, $E_{\mathrm{Q}}^{(2)}$, with the (classical) quadrupole moment tensor of the nucleus given by $Q_{\alpha\alpha} = \int \rho(\boldsymbol{r})(3x_\alpha^2 - r^2)\,\mathrm{d}\tau$. Electrons having s character penetrate the nucleus, however, since for such electrons the wave function does not vanish at the origin [as with the Fermi contact interaction, eq. (18.10)]. For these electrons, $\Sigma_{\alpha=1}^{3} V_{\alpha\alpha} = 4\pi e|\psi(0)|^2$, so that the second term in (18.38) becomes the isomer shift energy,

$$E_{\mathrm{I}}^{(2)} = \tfrac{2}{3}\pi e|\psi(0)|^2 \int \rho(\boldsymbol{r}) r^2\,\mathrm{d}\tau. \tag{18.39}$$

This shift may be regarded as the energy difference resulting from the finite nuclear volume as compared to a point nucleus.

Thus, in summary,

$$E^{(2)} = E_{\mathrm{I}}^{(2)} + E_{\mathrm{Q}}^{(2)} \tag{18.40}$$

with $E_{\mathrm{I}}^{(2)}$ given by (18.39) and

$$E_{\mathrm{Q}}^{(2)} = \tfrac{1}{6}\sum_{\alpha=1}^{3} V_{\alpha\alpha} Q_{\alpha\alpha}. \tag{18.41}$$

It may also be noted that those electrons for which $|\psi(0)|^2 \neq 0$ are also spherically symmetric so that for them, $V_{xx} = V_{yy} = V_{zz}$, and hence their contribution to $E_{\mathrm{Q}}^{(2)}$ vanishes identically.

1.3.1. *The isomer shift in NGR*

For a given nuclear state (e.g., the ground state), the isomer shift interaction contributes only an additive constant to the sum of all hyperfine interactions – a shift of the center-of-gravity of the nuclear level. Consequently, the isomer shift interaction has no effect on measurements made on a single nuclear state, as in the case of nuclear magnetic resonance. In Mössbauer effect measurements, on the other hand, the observed gamma-radiation quantum results from a transition of the nucleus from an excited state to the ground state (in emission, and vice-versa in absorption). Writing

$$\int \rho(\boldsymbol{r}) r^2\,\mathrm{d}\tau = Ze\langle r^2\rangle, \tag{18.42}$$

where $\langle r^2\rangle$ represents the average of r^2 over the nucleus in (18.39) and recognizing that this quantity will not be same for the excited and ground states, leads to

$$E_{\mathrm{I}}^{(2)}(\mathrm{exc}) - E_{\mathrm{I}}^{(2)}(\mathrm{gr}) = \tfrac{2}{3}\pi Ze^2|\psi(0)|^2(\langle r^2\rangle_{\mathrm{exc}} - \langle r^2\rangle_{\mathrm{gr}}) \tag{18.43}$$

for the energy difference between the excited and ground states due to this interaction.

To a very good approximation, the nucleus may be regarded as spherical,

having radius R and constant charge density, $\rho(r) = 3Ze/4\pi R^3$. Substitution in (18.42) yields the average of r^2 over the nuclear volume as $\langle r^2 \rangle = \frac{3}{5}R^2$. Since the change in R between ground and excited states is quite small, one may write $R_{exc} - R_{gr} = \Delta R$ and let R denote the average of R_{exc} and R_{gr}. Then,

$$\langle r^2 \rangle_{exc} - \langle r^2 \rangle_{gr} = \tfrac{3}{5} 2R^2(\Delta R/R), \tag{18.44}$$

and the expression for the isomer shift energy difference becomes

$$E_I^{(2)}(\text{exc}) - E_I^{(2)}(\text{gr}) = \tfrac{4}{5} \pi Ze^2R^2|\psi(0)|^2(\Delta R/R). \tag{18.45}$$

In a Mössbauer experiment the measured quantity is the change in this energy difference due to the fact that the source and absorber, being different materials, have different $|\psi(0)|^2$ values. Denoting these by $|\psi_S(0)|^2$ and $|\psi_A(0)|^2$, the measured energy shift, δE, for an absorber referred to a source, becomes

$$\delta E = \tfrac{4}{5} \pi Ze^2R^2(|\psi_A(0)|^2 - |\psi_S(0)|^2)(\Delta R/R). \tag{18.46}$$

A similar equation applies in the case that two absorbers are referred to the same source, the shift between absorbers being the measured quantity.

Because of relativistic effects which arise from the high kinetic energy of the electrons very close to the nucleus (especially in heavy elements), the non-relativistic wave functions ψ_A and ψ_S should be multiplied by a factor $S'(Z)$ [Shirley (1964)].

Finally, expressing the energy shift δE in terms of the Doppler-shifted velocity required for Mössbauer resonance, yields

$$\delta v = \frac{4\pi Ze^2R^2cS'(Z)}{5E_\gamma} \Delta|\psi(0)|^2 \left(\frac{\Delta R}{R}\right), \tag{18.47}$$

where δv is in cm/sec, c is the velocity of light, E_γ is the gamma ray energy, and $\Delta|\psi(0)|^2$ represents the change in $|\psi(0)|^2$ between source and absorber or between two absorbers. When the nuclear quantities are known, this last expression shows that the isomer shift provides a direct measurement of changes in electronic density at the nucleus.

1.3.2. *The electric quadrupole interaction*

The electric quadrupole interaction arises from the orientation dependent energy of the non-spherical nucleus in the gradient of the electrostatic field at the nuclear site. In quantum-mechanical terms, the quadrupole interaction energy, $E_Q^{(2)}$, of (18.41) becomes the quadrupolar hamiltonian operator $\mathcal{H}_Q$:

$$\mathcal{H}_Q = \tfrac{1}{6} \sum_{\alpha,\beta}^{3} V_{\alpha\beta} Q_{\alpha\beta}^{(\text{op})}, \tag{18.48}$$

where $V_{\alpha\beta} = \partial^2 V/\partial x_\alpha \partial x_\beta$ as in (18.41), and the quadrupole moment operator is

$$Q_{\alpha\beta}^{(\text{op})} = \int (3x_\alpha x_\beta - \delta_{\alpha\beta} r^2) \rho^{(\text{op})}(\boldsymbol{r})\, d\tau, \tag{18.49}$$

where the integral is over the nuclear volume. Application of the Wigner–Eckart

theorem [Slichter (1963)] converts this form of $Q^{(op)}$ to a function of the nuclear spin operators I^2, I_x, I_y, and I_z, so that $\mathcal{H}_Q$ becomes (in the principal axes system of $V_{\alpha\beta}$):

$$\mathcal{H}_Q = \frac{eQ}{4I(2I-1)}[V_{zz}(3I_z^2 - I^2) + (V_{xx} - V_{yy})(I_x^2 - I_y^2)]. \tag{18.50}$$

It is clear from (18.50) that only two parameters are needed to describe the field gradient tensor $V_{\alpha\beta}$. These are customarily taken to be the *field gradient*, V_{zz}, and the *asymmetry parameter*, $\eta = (V_{xx} - V_{yy})/V_{zz}$, with the additional requirement that the axes are chosen so that $|V_{zz}| \geq |V_{yy}| \geq |V_{xx}|$ in order that $0 \leq \eta \leq 1$.

In terms of these quantities the final expression for the quadrupole hamiltonian is

$$H_Q = \frac{eQV_{zz}}{4I(2I-1)}[(3I_z^2 - I^2) + \eta(I_x^2 - I_y^2)]. \tag{18.51}$$

This transcription to spin operators has also involved the actual definition of the nuclear quadrupole moment Q as an average over the nuclear volume of the quantity $e(3z^2 - r^2)$ summed over the nuclear protons in the state in which the z component of the nuclear spin has its maximum value, I, [Slichter (1963)]. A consequence of this is that the nuclear spin I must satisfy the condition $I \geq 1$ in order for the nucleus to possess an electric quadrupole moment. Finally, it should be emphasized that the spin operators in (18.51) refer to the principal axes coordinate system of the field gradient tensor, $V_{\alpha\beta}$. This coordinate system may or may not coincide with that of the magnetic hyperfine or Zeeman interaction. Depending on the relative strength of the electric and magnetic interactions, one of these interactions must be projected onto the other when perturbation theory calculations are made. In the following subsections the results are briefly outlined for the energy levels and transitions in the three important cases: (a) quadrupole interaction only, (b) quadrupole interaction with weak magnetic (Zeeman) perturbation, and (c) weak quadrupole interaction perturbing a strong magnetic interaction.

1.3.2.1. *Pure quadrupole levels and transitions*

In the pure quadrupole regime the energy levels are the eigenvalues of (18.51). For an axially symmetric field gradient tensor ($\eta = 0$), these are just

$$E_Q(m_I) = \frac{eQV_{zz}}{4I(2I-1)}[3m_I^2 - I(I+1)], \tag{18.52}$$

where m_I is the z component quantum number. For half-integral spins these levels are all doubly-degenerate, and for integer spins all levels except that for $m_I = 0$ are. When $\eta \neq 0$, the levels continue to be doubly-degenerate, but the energies become functions of η. For small η values (roughly, $0 \leq \eta \leq 0.2$), expansion in powers of η by perturbation theory suffices, but for larger η values numerical solutions of (18.51) are required. Such solutions have been published in tabular form for the spin values $\frac{5}{2}$, $\frac{7}{2}$, and $\frac{9}{2}$ [Semin et al. (1975)].

In so-called pure nuclear quadrupole resonance (NQR) spectroscopy, the magnetic dipole transitions between the levels of (18.51) satisfy the selection rule $|\Delta m| = 1$. For spin $\frac{5}{2}$ there are two transitions, $\nu_1 = 3eQv_{zz}/20h$ and $\nu_2 = 2\nu_1$ when $\eta = 0$. For spin $\frac{7}{2}$, $\nu_1 = eQV_{zz}/14h$ and $\nu_2 = 2\nu_1$, $\nu_3 = 3\nu_1$ when $\eta = 0$. In these cases both the coupling constant, eQV_{zz}, and asymmetry parameter may be determined from frequency measurements alone.

In the important case that $I = \frac{3}{2}$, the eigenvalues of (18.51) may be obtained in closed form:

$$E_Q(m_I) = \frac{eQV_{zz}}{4I(2I-1)}[3m_I^2 - I(I+1)](1+\tfrac{1}{3}\eta^2)^{1/2}. \tag{18.53}$$

Now the NQR spectrum consists of just the single transition between the $\pm\frac{1}{2}$ and $\pm\frac{3}{2}$ levels, and is given by

$$\nu = \frac{eQV_{zz}}{2h}(1+\tfrac{1}{3}\eta^2)^{1/2}. \tag{18.54}$$

Hence, eQV_{zz} and η are not separately determined from the NQR spectrum.

In Mössbauer spectroscopy the pure quadrupole case occurs whenever the effective hyperfine field vanishes, as is typical of the non-magnetically ordered regime of rare-earth materials. Since the Mössbauer transitions occur between excited and ground nuclear levels, the complexity of the spectrum will depend on the spins of the two levels and also on the selection rule for the gamma radiation (magnetic dipole, electric quadrupole, etc.). In the important case that $I_e = \frac{3}{2}$ for the excited level and $I_g = \frac{1}{2}$ for the ground level (e.g., ^{57}Fe, ^{119}Sn, ^{169}Tm), the ground state has no quadrupole interaction. With magnetic dipole radiation the result is a two-line Mössbauer spectrum, the splitting of which is again

$$\Delta E = (eQV_{zz}/2)(1+\tfrac{1}{3}\eta^2)^{1/2}. \tag{18.55}$$

1.3.2.2. *Magnetic field perturbation of quadrupole levels*

When the quadrupole energy is much greater than the magnetic dipole energy the latter acts as a perturbation of the former. This case typically arises in magnetically ordered materials at temperatures near (but below) the critical temperature, when $M(T)$ and hence $H_{\text{eff}}(T)$ approach zero. It also arises in the paramagnetic state when an external magnetic field is applied. In first order perturbation theory only the diagonal elements of the magnetic dipole energy hamiltonian (18.2) in the pure quadrupole representation of (18.51) are required. For half-integer spins, however, the degenerate $\pm\frac{1}{2}$ states of (18.52) are mixed by the off-diagonal elements of the magnetic interaction, leading to two new states, often denoted by $(\pm)$. The transitions, $+\frac{3}{2} \leftrightarrow -\frac{1}{2}$ and $-\frac{3}{2} \leftrightarrow +\frac{1}{2}$, which were forbidden in the pure quadrupole case, are now permitted in the form $+\frac{3}{2} \leftrightarrow (-)$ and $-\frac{3}{2} \leftrightarrow (+)$.

To first order in H_0, and when $\eta = 0$, the energy levels are

$$E(m_I) = \frac{eQV_{zz}}{4I(2I-1)}[3m_I^2 - I(I+1)] - m_I\gamma_N\hbar H_0\cos\theta, \tag{18.56}$$

where θ specifies the spherical co-latitude of the field H_0 with respect to the z axis of the field gradient tensor. When $\eta \neq 0$, more complicated expressions arise which are functions of η as well as of θ and ψ, the latter being the azimuthal angle for the orientation of the magnetic field in the field gradient tensor axes system [Lucken (1969), Goldanskii and Herber (1968)]. In general, with single crystals, the application of a magnetic field enables the determination of the asymmetry parameter as well as the orientation of the field gradient tensor coordinate system in the crystal. The latter information in particular cannot be determined from measurements made on powder (polycrystalline) samples, nor by NQR measurements alone.

1.3.2.3. *Weak quadrupole perturbation of magnetic levels*

In this case the quadrupole interaction operator (18.51) must be projected onto the coordinate system associated with the magnetic (Zeeman) hamiltonian (18.1). Since the former is actually a tensor operator, the projection introduces a more complicated angular dependence than in the converse case considered in section 1.3.2.2. The energy levels become, on the basis of first-order perturbation theory:

$$E(m_I) = -m_I \gamma_N h H_0 + \frac{eQV_{zz}}{8I(2I-1)}[3m_I^2 - I(I-1)][3\cos^2\theta - 1 + \eta \cos 2\psi(\cos^2\theta - 1)]. \tag{18.57}$$

The angles θ and ψ have the same significance as in (18.56). For somewhat stronger quadrupole interaction strengths, second and higher order corrections have been worked out [e.g., Abragam (1960)].

In NMR, the field H_0 is either an applied (external) field or the hyperfine field. In the former case the NMR spectrum consists of a number of transitions whose frequencies are functions of ψ and θ when a single crystal is studied. With polycrystalline (powder) samples, a spectral distribution is obtained, the principal features of which are determined by the conditions:

$$\partial\nu(\theta, \psi)/\partial(\cos\theta) = 0, \qquad \partial\nu(\theta, \psi)/\partial\phi = 0. \tag{18.58}$$

More complex situations arise in connection with the analysis of the NMR spectra of rare-earth compounds, when the magnetic interaction is affected by a shift tensor, as described in section 1.2.2. The appropriate energy levels and transition frequencies for such cases have also been given in the literature [e.g., Jones et al. (1963)]. For a detailed treatment of the analysis of Mössbauer spectra resulting from mixed magnetic and quadrupole interactions of arbitrary strength, see for example, Goldanskii and Herber (1968) or Grant (1975).

1.4. *Spin relaxation processes*

The various hyperfine interactions described in the preceding sections have been considered in relation to the parameters characterizing the steady-state or Mössbauer effect spectra. On the other hand, when the dynamical properties of

the nuclear spin system are studied, the behavior may be characterized in terms of *relaxation* times. In NMR, two such times are usually considered. These are the spin–lattice relaxation time, T_1, which characterizes the return of the z-component of the nuclear magnetization (i.e., the component parallel to the applied or hyperfine field) to its equilibrium value following a disturbance, and the spin–spin relaxation time, T_2, which characterizes the return of the transverse component of the nuclear magnetization (i.e., perpendicular to the applied or hyperfine field) to its equilibrium value of zero, also following a disturbance. Alternatively, the spin–lattice time T_1 is indicative of the rate at which the nuclear spin system exchanges energy with its external surroundings (the "lattice"), whereas the spin–spin time T_2 is indicative of the rate at which energy is exchanged within the spin system itself. Apart from some exceptional cases, the time T_2 is much shorter (faster) than T_1 in solids.

Although relaxation times can sometimes be determined by steady-state spectroscopic methods, so-called pulse or transient methods are generally preferred. In such experiments, appropriately spaced (in time) short, intense pulses of radio frequency radiation at the resonance frequency are applied to the nuclear spin system, and the subsequent behavior of the nuclear magnetization is monitored in various ways. A wide variety of specific pulse sequences and methods may be utilized [Abragam (1961), Farrar and Becker (1971)].

Relaxation effects in Mössbauer spectroscopy are of a different nature from those in NMR. The term "relaxation effects" or "relaxation spectra" in nuclear gamma resonance spectroscopy refers to averaging effects that occur in the hyperfine spectrum when the hyperfine interactions fluctuate at a rate more rapid than the nuclear frequency characteristic of the hyperfine interaction itself. This situation is a consequence of the rapid relaxation of the host ion among its energy levels, and the relaxation time for such effects is characteristic of the ion and not of the nuclear spins. The relaxation processes involved also affect electron spin resonance spectra, and their discussion is best considered in that context (see sections 3.3. and 3.4.). In the following subsections the principal interactions which contribute to the nuclear spin relaxation times in NMR experiments are briefly considered, and the connections between these and the parameters characterizing the steady-state spectrum are outlined.

1.4.1. *The spin–spin relaxation time*

In an NMR experiment the resonance signal contains components in-phase and out-of-phase with the incident radio frequency radiation so that a complex susceptibility χ can usefully be defined, such that $\chi = \chi' - i\chi''$. The dispersion component χ' is in-phase, and the absorption component χ'' is out-of-phase. By introducing phenomenologically the exponential decay constants T_1 and T_2 for the nuclear magnetization parallel and perpendicular to the applied field H_0, Bloch et al. (1946) derived expressions for the magnetization as a function of frequency. These may be related to expressions for χ' and χ'', the results being:

$$\chi' = \tfrac{1}{2}\chi_0\nu_0 \frac{4\pi^2 T_2^2(\nu_0 - \nu)}{1 + T_2^2 4\pi^2(\nu_0 - \nu)^2 + \gamma^2 H_1^2 T_1 T_2}, \tag{18.59}$$

$$\chi'' = \tfrac{1}{2}\chi_0\nu_0 \frac{2\pi T_2}{1 + T_2^2 4\pi^2(\nu_0 - \nu)^2 + \gamma^2 H_1^2 T_1 T_2}, \tag{18.60}$$

where χ_0 is the static Curie (nuclear) susceptibility, H_1 is the amplitude of the radio frequency magnetic field, and γ is the nuclear gyromagnetic ratio. Usually the term in H_1^2 in the denominator is taken to be small compared to the other terms.

The absorption component in particular is seen to have a Lorentz shape-function dependence on the frequency variable ν. If H_1 is small (i.e., if $\gamma^2 H_1^2 T_1 T_2$ is small) the resonance shape is independent of the longitudinal time T_1, but does depend on the transverse time T_2. In this case, if the expression for the absorption component χ'', eq. (18.60) is written as

$$\chi'' = \tfrac{1}{2}\pi\chi_0\nu_0 g(\nu), \tag{18.61}$$

then the *shape function* $g(\nu)$ is given by

$$g(\nu) = \frac{2(T_2)^{-1}}{(T_2)^{-2} + 4^2(\nu_0 - \nu)^2}. \tag{18.62}$$

Since this is a Lorentz function, the half-width at half-height $\delta\nu$ is related to T by

$$T_2 = (2\pi\delta\nu)^{-1}. \tag{18.63}$$

Alternatively, T_2 may be related to the peak height, $g(\nu)_{\max}$ at $\nu = \nu_0$ of the absorption shape by

$$T_2 = \tfrac{1}{2}g(\nu)_{\max}. \tag{18.64}$$

These determinations of T_2 based on resonance shape are often also employed when the lineshape is not Lorentzian, but gaussian as is frequently the case for NMR in solids.

In most cases, the line shape and width are a consequence of the dipolar interaction between the nuclear moments which leads to the second moment of the resonance. This has been discussed in sections 1.2.3. For a given resonance lineshape, the second moment M_2 and linewidth are related [Abragam (1961)].

1.4.2. *The spin–lattice relaxation time*

In general terms, any interaction which gives rise to a fluctuating magnetic field at the nucleus contributes to the spin–lattice relaxation process. Such a random fluctuating field has a spectrum of values depending on the particular interaction and the motional process to which it owes its existence. Lattice vibrations, diffusion, molecular rotation, etc., each give rise to a characteristic spectral density function, $J(\nu)$, and the component of this spectral density at the resonance frequency ν_0 acts in the same manner as the applied radio frequency field H_1 to induce transitions between the energy levels of the spin system and to

maintain a thermal equilibrium population distribution among the levels. $J(\nu)$ is also a function of the correlation time, τ_c, which characterizes the exponential decay of correlation between successive random configurations which are responsible for the fluctuating field. In simplest terms, the spin–lattice relaxation rate can be expressed as a product,

$$(T_1)^{-1} = Cf(\nu, \tau_c),$$

where C is a strength parameter appropriate to the particular interaction involved, and $f(\nu, \tau_c)$ is a function of $J(\nu)$ and $J(2\nu)$ [Abragam (1961)].

As an example, the dipole–dipole interaction between nuclei (18.31) may be modulated by the random jumping motion due to diffusion of the host atoms (ions). The relaxation rate is then given by

$$(T_1)^{-1} = C\left[\frac{\tau_c}{1+(2\pi\nu\tau_c)^2} + \frac{4\tau_c}{1+4(2\pi\nu\tau_c)^2}\right]. \tag{18.66}$$

Assuming that the diffusive motion is a thermally activated process, τ_c will obey an Arrhenius relation in its dependence on temperature. Measurement of the temperature dependence of $(T_1)^{-1}$ of a diffusing species then yields a value for the activation energy for diffusion. The application of such measurements to the study of hydrogen diffusion in rare-earth hydrides is discussed in section 2.2.3.4.

From the standpoint of the rare-earth metals and their compounds, the important interactions contributing to nuclear spin–lattice relaxation are the magnetic dipole interaction outlined above and the Fermi contact interaction with conduction electrons which also gives rise to the Knight shift in metals (section 1.2.2.3). In addition, the electric quadrupole interaction can act as a strong relaxing mechanism for nuclei with substantial quadrupole moments. In the latter case, it is the fluctuating electric field gradient which provides the coupling with the nuclear spins. The form of the expression for the relaxation rate is again given by (18.66), the interaction strength parameter C depending, however, on the square of the quadrupole coupling.

In metallic materials the most important mechanism contributing to the spin–lattice relaxation is normally the contact hyperfine interaction with the unpaired conduction electron spins [eq. (18.10)]. The basic relationship between the Knight shift [eq. (18.23)] and T_1 was stated by Korringa (1950) who derived the expression

$$(T_1)^{-1} = \pi hkT[\tfrac{8}{3}\pi\beta\gamma_N\Omega\langle|\psi(0)|^2\rangle_F N(E_F)]^2 \tag{18.67}$$

for the relaxation rate. In view of (18.23) this leads at once to the relation

$$K_0^2 T_1 T = (\pi hk)^{-1}(\beta/\gamma_N)^2, \tag{18.68}$$

between T_1 and the isotropic component of the Knight shift, K_0. Here, $N(E_F)$ is the s-band density of states at the Fermi level, and the other quantities have the same meanings as in (18.23).

The "Korringa product", defined as $(\pi hk)(\beta/\gamma_N)^{-2}K_0^2 T_1 T$, should equal unity

according to this basic theory. This is hardly ever the case, however, even for the simplest metals. Many-body effects in the electronic interactions enhance both the Knight shift and relaxation rate, but not in the same way [Narath (1967)]. Usually the shift is enhanced more than the relaxation rate so that the Korringa product exceeds unity. Another reason is that mechanisms other than the basic s-electron contact interaction contribute to both K_0 and $(T_1)^{-1}$. Nevertheless, the fundamental dependence on temperature, expressed as $T_1T =$ constant, remains unchanged by these considerations.

In transition metals the spin–lattice relaxation rate is partitioned into contributions that parallel the contributions to the total magnetic susceptibility in the same manner as the Knight shift is partitioned [Eq. (18.27)]. Analogously to (18.28), the relaxation rate may be written, in the case of cubic symmetry, as [Narath (1967)]:

$$(T_1)^{-1} = 4\pi\gamma_N^2\hbar kT[N(E_F)^2]\{[\rho H_{hf}^{(s)}]^2 + [(1-\rho)H_{hf}^{(d)}]^2 q + [(1-\rho)H_{hf}^{(orb)}]^2 p\}, \tag{18.69}$$

where $\rho = N_s(E_F)/N(E_F)$ is the fractional s character of the conduction electron states at the Fermi level, $N(E_F)$ being the total density of states, and p and q are complicated factors that depend on the mixing of the d orbitals at the Fermi level [Narath (1967)]. The hyperfine fields, $H_{hf}^{(s)}$, etc., are the same as in (18.28).

2. Survey of applications of NMR and NGR methods

The following brief survey attempts to present an overview of the extent of NMR and NGR hyperfine interaction studies of the rare earths themselves, their alloys and compounds. The material presented is intended to be representative – an exhaustive survey would overflow the space limitations of this review. In many cases, particular features of these investigations are discussed in relation to the significance of the work for the physics and/or chemistry of the rare earths.

For metallic materials, and some non-metallic, the comprehensive *Permuted Materials Index*, Carter et al. (1971) containing references to NMR, NGR, and ESR work through 1969 (with some 1970), provides the most thorough single source for all the earlier investigations involving the rare earths. Reviews of NGR (Mössbauer effect) results appear biannually in *Analytical Chemistry Annual Reviews*: DeVoe and Spijkerman (1966, 1968, 1970), Stevens et al. (1972), Stevens and Travis (1974, 1976). In addition, the *Mössbauer Effect Data Index*, Stevens and Stevens (1975, and prior years) provides an even more comprehensive annual listing of all experimental and theoretical literature dealing specifically with NGR studies. Other reviews that concern NGR work with the rare earths, such as Ofer et al. (1968) and Nowick (1966), have contained listings of materials investigated. A review of hyperfine interactions in the rare-earth metals by Bleaney (1972) emphasized NMR measurements as the source of experimental data.

2.1. *Rare earth metals and alloys*

2.1.1. *NMR and NGR in magnetically ordered systems*

Direct observations of the NMR of lanthanide nuclei in the ferromagnetic state of the metals themselves or of intra-lanthanide alloys are summarized in table 18.6. Since in their ground state, all rare earth nuclei have half-integral

TABLE 18.6

Nuclear magnetic resonance in the ferromagnetic state of lanthanide metals and alloys. The magnetic hyperfine parameter a and quadrupole coupling parameter P are obtained by fitting eq. (18.70) to the experimental data. Unless noted, the temperature is in the range 1.4–4.2 K.

Metal or alloy system	Nucleus	Concentration in alloy (%)	a (MHz)	P (MHz)	References
Nd–Gd	^{143}Nd	10	834(3)	2.3(5)	Kobayashi (1967)
Sm–Gd	^{147}Sm	10	624(3)	4.8(5)	Kobayashi (1967)
Gd	^{155}Gd		46.6(10)	24.8(10)	Durand and Robert (1973)
Gd	^{155}Gd		49.1	18.6	Seiwa et al. (1973)
Tb	^{159}Tb		3120	327	Sano et al. (1972a)
Tb–Gd	^{159}Tb	10–90			Sano et al. (1975a)
Tb–Dy	^{159}Tb	10–90			Sano et al. (1975a)
Tb–Er	^{159}Tb	10–90	3180–3125	360–337	Sano et al. (1975a)
Dy	^{163}Dy		1162(3)	204(2)	Sano et al. (1970)
Dy–Gd	^{163}Dy				Sano et al. (1975a)
Dy–Tb	^{163}Dy	10–90			Sano et al. (1975a)
Dy–Er	^{163}Dy	10–90	1169–1162	215–205	Sano et al. (1975a)
Ho	^{165}Ho		6440(5)	55.0(2)	Wagg et al. (1975)
Ho–Gd	^{165}Ho	1–75	6352–6436	57.3–54.2	Mackenzie et al. (1974)
Ho–Tb	^{165}Ho	1–30	6395–6414	53.1–52.8	Mackenzie et al. (1974)
Ho–Dy	^{165}Ho	1–20	6431–6438	52.4–52.7	Mackenzie et al. (1974)
Er	^{167}Er		913(3)	53(2)	Sano et al. (1972)
Er–Gd	^{167}Er	10–80	900–912	58–55	Sano et al. (1975a)
Er–Tb	^{167}Er	10–90	912–915	76–58	Sano et al. (1975a)
Er–Dy	^{167}Er	10–90	913–911	75–56	Sano et al. (1975a)
Lu–Tb	^{175}Lu	2	146.3	13.5	Shimizu et al. (1975)
Lu–Dy	^{175}Lu	2	116.3	13.8	Shimizu et al. (1975)
Dy	^{163}Dy	(T_2 measurements at 1.4–20 K)			Berthier and Barak (1975)
Tm–Gd	^{169}Tm	10	2223(3)		Kobayashi et al. (1967)
Tb–Er	^{159}Tb	10–90	(determination of semi-cone angle)		Sano et al. (1975b)
Tb–Er	^{167}Er	10–90	(determination of semi-cone angle)		Sano et al. (1975b)
Dy–Er	^{163}Dy	10–90	(determination of semi-cone angle)		Sano et al. (1975b)
Dy–Er	^{167}Er	10–90	(determination of semi-cone angle)		Sano et al. (1975b)
Gd	^{155,157}Gd	$H_{\text{eff}} = 364.4 \pm 6$kOe	(also measured T_1 and T_2)		Dintelmann et al. (1970b)
Dy	^{161,163}Dy	(T_1 and T_2 measurement)			Gill and Kaplan (1968)

spin, their NMR spectra consist of a central line plus equally spaced (in frequency units) satellites arising from the quadrupole interaction (except ^{169}Tm). The spectra may be parametrized in terms of an effective hyperfine field and a quadrupole coupling in the simple first-order energy level scheme based on eq. (18.57)

$$E(m_I) = am_I + P[m_I^2 - \tfrac{1}{3}I(I+1)], \tag{18.70}$$

where $P = 3eQV_{zz}/4I(2I+1)h$ characterizes the quadrupole interaction strength. The case of Gd nuclei is somewhat more complicated due to the nearly equal significance of the magnetic and quadrupole interactions which cause the simple perturbation theory treatment to be inappropriate.

Mössbauer effect measurements of hyperfine fields at rare earth nuclei in either the ferro or antiferromagnetic state may also be analyzed in terms of the energy level scheme of eq. (18.70) with in some cases the addition of an isomer shift parameter δE as in eq. (18.47). Unlike the NMR measurements, which for reasons of signal intensity, have been almost entirely made in the liquid helium temperature range, NGR measurements have frequently been made over much wider temperature ranges, including up to and through the ordering temperature. As is evident from the data summary in table 18.7, this has frequently included measurements in the antiferromagnetic as well as in the ferromagnetic state. An additional important point is that in many cases the signs of the hyperfine fields (couplings) may be determined, even with polycrystalline samples.

As with the NMR measurements, the a and P values at low temperatures agree within a few percent with the free ion values. The NMR and NGR results are considered together in sections 2.1.1.1 and 2.1.1.2 where the separate contributions to the magnetic hyperfine field and quadrupole coupling are discussed.

2.1.1.1. *Magnetic hyperfine interaction*

The origins of the magnetic hyperfine fields in the rare-earth metals have been the subject of recent reviews by Bleaney (1972), Pelzl (1972) and Eagles (1973). As outlined in section 1.2.1., in the ferromagnetic state at low temperatures, the hyperfine field is considered to arise from three sources. These are, (1) the field $H_{\text{eff}}^{(4f)}$ of the 4f electrons [eq. (18.6)] which are fully polarized by the exchange field, (2) the core-polarization field $H_{\text{eff}}^{(cp)}$ of the inner s-shells of the RE ion brought about by their exchange interaction with the 4f shell [eq. (18.12)], and (3) the field $H_{\text{eff}}^{(ce)}$ due to polarization of the conduction electrons [eq. (18.13)]. Analyses of measured hyperfine field values are customarily compared with the "free ion" values deduced from electron spin resonance (ESR) data for dilute concentrations of RE ions in insulating host crystals, as compiled for example, by Bleaney (1962). The free ion values include the core-polarization contribution to H_{eff}, so that an estimate of the conduction electron contribution can be inferred from the comparison. Table 18.5 includes values of the free-ion H_{eff} together with calculated estimates of $H_{\text{eff}}^{(4f)}$. Departures from the free-ion values are typically on the order of a few percent, rarely exceeding 5% in the RE metals

TABLE 18.7

Resumé of nuclear gamma resonance studies and results in the magnetically ordered state of lanthanide metals and alloys. The magnetic hyperfine parameter a (or effective field, H_{eff}) and quadrupole coupling parameter P are obtained by fitting eq. (18.70) to the experimental data.

Metal or alloy	Nucleus	Concentration in alloy (%)	Temperature range (K)	a (MHz)	P (MHz)	Reference
Sm	^{149}Sm		4, 80, 300			Ofer et al. (1965a)
Sm	^{149}Sm		4.2	-500 ± 15		Ofer and Novick (1967)
Eu	^{151}Eu		15–90	$H_{eff} = -0.264(2)$		Kienle (1964)
Eu	^{151}Eu		4.2–196	identified "16 K anomaly" as probably EuH_2		Lounasmaa and Kalvius (1967)
Eu–Yb	^{151}Eu	8–100	1.7–4.2	$H_{eff} = -0.265(5)$ in Eu metal (-0.160 in $Eu_{0.08}Yb_{0.92}$)		Hüfner (1967), Hüfner and Wernick (1968)
Eu–Ba	^{151}Eu	50–100	1.7–4.2	$H_{eff} = -0.206(6)$ in $Eu_{0.5}Ba_{0.5}$		Hüfner and Wernick (1968)
Eu	^{151}Eu		4.2–90	first-order magnetic transition at 88.5 K		Cohen et al. (1969)
Eu	^{151}Eu		4.2	pressure dependence to 16 K bars		Klein et al. (1976a)
Gd	^{157}Gd		4.2	$H_{eff} = -0.324(11)$	4.9(2)	Göring (1972)
Gd	^{155}Gd	(single crystal)	4.2	$H_{eff} = -0.382(10)$		Bowden et al. (1975)
Gd	^{155}Gd	(single crystal)	4.1	$H_{eff} = -0.373(5)$	26.4(7)	Bauminger et al. (1975)
Gd–(Sc, Y, Lu, Tm, Tb)	^{155}Gd	various	4.2	42.2–48.8	26.4–30.0	Bauminger et al. (1975)
Tb	^{159}Tb			unresolved spectrum		Woolum and Bearden (1966)
Dy	^{161}Dy		85–175			Boyle and Hall (1962)
Dy	^{161}Dy		20	-825 ± 30	165 ± 15	Ofer et al. (1965b)
Dy	^{161}Dy		4.2–300			Bowden et al. (1967)
Gd–Dy	^{161}Dy	25–100	4.2–250			Sweger et al. (1974)
Er	^{166}Er		4.2–40	-900 ± 50	115 ± 25	Hüfner et al. (1965)
Er	^{166}Er	(single crystal)	4.2–80	-900 ± 50	114	Reese and Barnes (1967)
Ho–Er	^{166}Er	10 ppm Er in Ho single crystal	4.2–50	-900 ± 50		Reese and Barnes (1969)
Tm	^{169}Tm		5, 25	-2300 ± 120		Kalvius et al. (1963)
Tm	^{169}Tm		5–55	-2230 ± 100	497	Cohen (1968)

or their alloys. Much greater departures are found in the case of intermetallic compounds with iron (section 2.2.2.).

In the cases of Eu^{2+} and Gd^{3+}, the direct 4f contribution to H_{eff} vanishes (table 18.5), and the core-polarization and conduction electron contributions account for H_{eff}. Hüfner (1967) and Hüfner and Wernick (1968) studied the NGR of ^{151}Eu in alloys of Eu with Yb and Ba which are non-magnetic but have the same electronic structure as Eu except for the 4f shell. Using the value $H_{eff}^{(cp)} = -340$ kOe based on Eu^{2+} in a diamagnetic environment, the remaining contributions to the observed $H_{eff} = -265 \pm 5$ kOe were concluded to be $+190 \pm 20$ kOe from conduction electrons polarized by the parent ion and -115 ± 20 kOe from polarization of the conduction electrons by neighboring ions as well as overlap and covalency effects. A similar decomposition can be applied to account for H_{eff} in Gd metal which has been determined with greater precision by the NMR measurements of Seiwa et al. (1973) and of Durand and Robert (1973) (table 18.6).

In intra lanthanide alloys, the change in H_{eff} (i.e., the shift of the NMR frequency) is a linear function of concentration for a particular lanthanide species. This point is exemplified in the work of Sano, et al. (1975a, 1975b) and of MacKenzie et al. (1974). In the latter case, detailed investigation of the NMR of ^{165}Ho in alloys with Gd, Tb, and Dy showed that the conduction electron field $H_{eff}^{(Ce)} = H_{eff} - H_{eff}^{(free\ ion)}$ could be analyzed in terms of contributions from electrons polarized by the parent ion and from electrons polarized by neighboring ions. The former quantity was found to be proportional to the spin of the parent ion as expected whereas the latter was found to be proportional to the mean spin $\bar{S}$ of the alloy.

The role of the 5d electrons in respect to the origins of the magnetic hyperfine field has been investigated by Eagles (1973). Instead of considering these electrons to be entirely incorporated in a conduction band of mixed 5d–6s character, a model was proposed in which the atomic 5d states are broadened into bands about 1 eV wide. It is argued that in the metal the 5d level is shifted down about 2 eV, putting the $4f^n5d6s^2$ configuration below the $4f^{n+1}6s^2$ (unlike the atomic case). Finally, although analysis of melting points, heats of sublimation, and bond energies by Gschneidner (1971) had indicated a small f-electron character, as well as significant p character in the conduction band, these two components were not included in the calculations in the interest of simplification. With about one d electron per atom, there results a negative contribution to H_{eff}, but a positive or essentially zero contribution to the magnetic moment.

As remarked in the introduction, section 1, the temperature dependence of the hyperfine field provides a measurement of the temperature dependence of the magnetization on the microscopic level. This point is illustrated by the data of Sweger et al. (1974) for H_{eff} in Dy metal. In this case, $H_{eff}(T)$ is not well represented by a Brillouin function. Paralleling the bulk magnetization data, the behavior of H_{eff} for $T \lesssim 100$ K can be interpreted in terms of a spin-wave model of the form [Niira (1960)],

$$M(T) = M(0)[1 - A(T/T_C)^{3/2}e^{-\Delta/kT}] \tag{18.71}$$

where Δ is an energy gap arising from the magnetic anisotropy. For Dy metal, $\Delta/k = 22$ K and $A = 0.379$ are obtained from this parametrization of the Mössbauer data, in very good agreement with the theoretical prediction of $\Delta/k = 24$ K [Cooper (1968)] and of $\Delta/k = 20$ K obtained by Niira (1960) from magnetic moment data.

2.1.1.2. *Nuclear quadrupole interaction*

As outlined in section 1.3.2., the nuclear quadrupole interaction is characterized by two parameters, the coupling constant eQV_{zz} expressed in suitable energy units, and an asymmetry parameter η indicating the degree of departure of the electric field gradient (efg) tensor V_{ij} from axial symmetry. Information relevant to the lanthanide-containing metal, alloys, or compound is contained in these two parameters, since from the standpoint of the physics or chemistry of solids the quadrupole moment Q is taken to be a known property of the nuclear state.

The components of the efg tensor are interpreted as the sum of contributions arising from sources within the atomic sphere of the ion containing the nucleus under observation (the "parent sphere" or PS), and from sources external to this sphere. Writing $eq_{ij} = V_{ij}$ to separate the electric charge from the spatially dependent part q_{ij} of V_j, then

$$q_{ij} = q_{ij}^{(\mathrm{lat})}(1 + F)(1 - \gamma_\infty) + q_{ij}^{(4\mathrm{f})}(1 - R_Q) + q_{ij}^{(\mathrm{ce})}(1 - R_{ce}). \tag{18.72}$$

Here, the first term contains the contributions to the efg from sources external to the PS. These are the efg due to the lattice of ion charges and that due to the conduction electrons outside the PS. This latter contribution is taken to be proportional to the former, the proportionality factor being F [Das and Ray (1969)], thereby recognizing that the conduction electron distribution reflects the symmetry of the ion lattice. Both contributions are screened by the closed shells of the parent ion, giving rise to the Sternheimer (1966) antishielding factor $(1 - \gamma_\infty)$. The raw ion–lattice contribution $q_{ij}^{(\mathrm{lat})}$ can be calculated from knowledge of the crystal structure and assumed values of the ionic charges.

Of the local contributions to q_{ij}, the term $q_{ij}^{(4\mathrm{f})}$ dominates in the magnetically ordered regime of a lanthanide solid, and has essentially the free-ion value at low temperatures. This is also true of the paramagnetic state at low temperatures (i.e., temperatures approaching the ordering temperature). The principal (zz) component of $q_{ij}^{(4\mathrm{f})}$ is given by

$$q_{zz}^{(4\mathrm{f})} = \alpha_J \langle r^{-3} \rangle \langle 3J_z^2 - J(J+1) \rangle, \tag{18.73}$$

with similar, more complex expressions for $q_{xx}^{(4\mathrm{f})}$ and $q_{yy}^{(4\mathrm{f})}$ [Bleaney (1972)]. Here, α_J (also often written $\langle J \| \alpha \| J \rangle$) is a reduced matrix element which enters in converting the field gradient operator from coordinate to angular momentum components (see also section 3.2.2.).

In general, $q_{ij}^{(4\mathrm{f})}$ is a thermal average of the efg contributions arising from each of the populated angular momentum sublevels within a given J manifold that is split

either by the effective field (Weiss or molecular field) or by the crystal field. The factor $(1 - R_Q)$ is a shielding factor which takes account of the distortion of the inner closed shells of the parent ion by the open 4f shell.

The last term in (18.72) represents that part of the conduction electron contribution arising from non-spherically symmetric electron states within the PS. Watson et al. (1965) have formulated this contribution and its temperature dependence in terms of three contributions: (1) from the conduction electrons in non s-states of a crystalline potential spherical within the PS, (2) from a change in level occupation near the Fermi surface resulting from first order shifts of the Bloch energies due to the existence of the crystal field with the PS, and (3) from the spatial distortion of the bands due to the existence of the crystal field. Calculations of the conduction electron contribution to the efg in the heavy lanthanides, based on a modified orthogonalized-plane-wave (OPW) method, have been reported by Devine and Dixon (1973) and by Devine (1973). Taking account of non-spherical effects due to the magnetic ordering in these metals, D'Onofrio and Iraldi (1977) also calculated the conduction electron contribution due to the redistribution of the conduction electron at the Fermi level, assuming that the density-of-states at the Fermi level has predominantly d character.

A detailed review and summary of the experimental data as well as the results of calculations of the efg in the heavy lanthanide metals at low temperatures has been given by Pelzl (1972). It was found that in the metal the radial averages $\langle r^{-3} \rangle$ of the 4f electrons appropriate to the quadrupole interaction are 10% smaller than in ionic compounds. In comparison with the magnetic hyperfine interaction (section 2.1.1.1) the additional reduction arises from increased closed shell shielding $(1 - R_Q)$ in the metallic case. In addition, the conduction electrons increase the antishielding of the lattice efg due to their greater density outside the atomic sphere via the factor $(1 + F)$ and to an increased Sternheimer factor $(1 - \gamma_\infty)$ in the metal.

Each of the terms in (18.72) has a characteristic temperature dependence so that measurement of the temperature dependence of the quadrupole interaction parameters yields insight into the relative importance of the different terms, and in favorable circumstances, with the aid of those contributions that can be calculated with confidence, considerable resolution of the total efg can be achieved. Similarly, the fact that the ion lattice contribution depends on the lattice parameters also enables a study of the efg at a particular nucleus in a series of alloys with changing lattice parameters to resolve the several contributions to the total efg.

The NMR measurements of Mackenzie et al. (1974) on ^{165}Ho and of Sano et al. (1975) on ^{159}Tb, ^{163}Dy, and ^{167}Er in the ferromagnetic state of these metals and their alloys illustrate the dependence of the quadrupole coupling on lattice parameter changes. The measured coupling constants are analyzed in terms of $q_{zz}^{(4f)}$, $q_{zz}^{(lat)}$, and $(q_{zz}^{(ce)})_{PS}$. For the hexagonal close-packed lattice, the formula of Das and Pomerantz (1961), assuming trivalent ions, is

$$q_{zz}^{(lat)} = 3[0.0065 - 4.3584(c/a - 1.633)]a^{-3}, \tag{18.74}$$

where c and a are the lattice parameters. Since the z axis of the lattice efg lies along the crystalline c axis, this contribution must be projected onto $q_{zz}^{(4f)}$ which is the dominant component of the total efg, and to the extent that part of the conduction electron contribution from outside the PS reflects the symmetry of the ion lattice, the term $Fq^{(lat)}$ will also be projected onto the z axis of $q^{(4f)}$. Thus,

$$q_{zz}^{(ext)} = \tfrac{1}{2}q_{zz}^{(lat)}(1+F)(1-\gamma_\infty)(3\cos^2\theta - 1) \tag{18.75}$$

represents the total efg from sources outside the parent sphere (PS), θ being the angle between the c axis and $\langle J\rangle$ since $q_{zz}^{(4f)}$ lies along $\langle J\rangle$.

For generality, Mackenzie et al. (1974) write the last term in (18.72) as

$$q_{PS}^{(ce)} = B(3\cos^2\theta - 1) + C \tag{18.76}$$

to allow for disturbance of the conduction electron distribution within the parent sphere by the aspherical charge distribution of the parent ion. Thus, the total non-4f electron contribution to the efg may be written

$$q_{zz}^{(non\text{-}4f)} = q_{zz}^{(ext)} + (q_{zz}^{(ce)})_{PS} = [\lambda q_{zz}^{(lat)} + B](3\cos^2\theta - 1) + C, \tag{18.77}$$

where $\lambda = \frac{1}{2}(1+F)(1-\gamma_\infty)$.

Mackenzie et al. (1974) analyzed their measured coupling constant values (at 4.2 K) and those of Itoh et al. (1968) and of Sano et al. (1970, 1972) for ^{159}Tb and ^{163}Dy for alloys in which θ is known to be 90°. For $\theta = 90°$, (18.77) becomes

$$q_{zz}^{(non\text{-}4f)} = -\lambda\bar{q}_{zz}^{(lat)} - B + C, \tag{18.78}$$

where $\bar{q}_{zz}^{(lat)}$ is an average value of $q_{zz}^{(lat)}$ appropriate to the interpolated lattice parameters of the particular alloy.

Letting q_{zz} represent the measured efg values obtained from the measured coupling constants (after a small correction for the pseudoquadrupole contribution), then

$$q_{zz} = -\lambda\bar{q}_{zz}^{(lat)} + q_{zz}^{(4f)} - B + C \tag{18.79}$$

should be a linear function of $\bar{q}_{zz}^{(lat)}$ with slope λ and intercept at $\bar{q}_{zz}^{(lat)} = 0$ given by $q_{zz}^{(4f)} - B + C$. The data for alloys of Dy, Tb, and Ho showed that the dependence of the measured q_{zz} on $\bar{q}_{zz}^{(lat)}$ was indeed linear, the dependence being the same for all three nuclei studied. Assuming that the Sternheimer factor $(1-\gamma_\infty) = 76$, a value of $(1+F) = (8.5 \pm 1.5)$ is obtained, showing that the conduction electron contribution from electrons outside the parent sphere substantially outweighs the direct lattice contribution.

2.1.1.3. *Magnetic structure determinations*

In certain cases details of the magnetic structure can be elucidated from hyperfine interaction measurements. For example, in Mössbauer effect experiments employing single crystal absorbers, the relative intensities of the component lines of the spectrum depend on the angle between the gamma ray quantum and the hyperfine field at the nucleus. The latter is in turn parallel to the ionic moment. By such an experiment, Reese and

Barnes (1967) measured the cone angle in the conical (ferromagnetic) phase of erbium metal, obtaining $(26 \pm 3)°$ in good agreement with neutron diffraction measurements. Similarly, making use of the fact that the radioactive parent for Mössbauer experiments with ^{166}Er is ^{166}Ho, produced by neutron irradiation of ^{165}Ho (a 100% abundant isotope), Reese and Barnes (1969) employed irradiated single crystals of holmium metal as sources and analyzed the intensities of the source lines with a single line paramagnetic absorber. For an Er concentration of roughly 20 parts per million produced in the holmium, the measurements showed that the Er ionic moments were aligned with the Ho moments.

Sano et al. (1975) were able to determine the cone angle of both lanthanide constituents in alloys of Dy–Er and Tb–Er on the basis of their NMR measurements of the quadrupole couplings in these alloys. From eq. (18.75) the lattice efg contribution which lies along the c axis is projected onto the direction of the 4f contribution by the factor $\frac{1}{2}(3\cos^2\theta - 1)$, where θ is the angle between the c axis and the ionic moment. Since both the lattice and ionic (4f) contributions to the efg remain unaffected by changes in their relative orientations, the observed changes in the quadrupole coupling arise from changes in θ.

2.1.2. *NMR in the paramagnetic state*

In general the NMR of the nuclei of the magnetic rare earths is not observable in the paramagnetic state because of the extreme resonance line broadening that results from the rapidly fluctuating effective hyperfine field at the nucleus which is a consequence of the short relaxation time of the ionic magnetic moment. There has, however, been considerable work on the non-magnetic metals (La, Y, Sc, in particular) and to a certain extent on alloys of these with the magnetic rare earths. The various studies are summarized briefly in table 18.8.

Regarding the sequence Sc, Y, and fcc La, the Knight shifts of ^{45}Sc and ^{139}La were first reported by Blumberg et al. (1960), and of ^{89}Y by Jones et al. (1960). The Knight shift anisotropy in Sc and Y and the quadrupole interaction in Sc were further investigated by Barnes et al. (1965). The spin–lattice relaxation time T_1 in Sc, Y, and dhcp La were measured in the temperature range 1–4 K by Narath and Fromhold (1967) and compared with predictions based on the modified Korringa formula and the Knight shift data. In the case of Sc, Fradin (1968) reported T_1 measurements on a single crystal at 77 K. Hexagonal La metal was investigated in detail by Narath (1969) who identified signals from the so-called "cubic" and "hexagonal" sites and measured the Knight shifts, T_1, and quadrupole couplings at these sites. Poteet et al. (1970) observed, by means of NQR, resonances from both sites in dhcp La in both the normal and superconducting states in the temperature range 4.2–12 K. The fcc form of La was studied by Zamir and Schrieber (1964) who measured T_1, T_2, and the Knight shift over the temperature range 295–825 K. The relaxation times exhibited a temperature dependence which was explained by vacancy diffusion and annealing effects that perturb the nuclear spin system via the quadrupole interaction. Narath (1969) summarized the low temperature Knight shift and T_1 results for

TABLE 18.8
Resumé of NMR studies of rare-earth nuclei (Sc, Y, La, Yb) in the paramagnetic state of rare-earth metals and alloys.

Metal or alloy	Nucleus	Knight shift (%)	Spin–lattice relaxation (sec · deg)	Quadrupole coupling (MHz)	Temperature range (K)	Reference
Sc	^{45}Sc	$K_0 = +0.28 \pm 0.01$ $K_{ax} = -0.024$		2.02 ± 0.03	295	Barnes et al. (1965)
Sc	^{45}Sc		1.3 ± 0.2		1–4	Narath and Fromhold (1965)
Sc	^{45}Sc		$1.25–0.58 \sin^2 \theta$		77	Fradin (1968)
Sc	^{45}Sc	+0.28(4.2 K)	0.6		4.2–300	Blumberg et al. (1960)
Sc–Gd	^{45}Sc				1.6–4.2, 77, 295	Fradin (1972)
Y	^{89}Y	$K_0 = +0.37 \pm 0.01$				
		$K_{ax} = 0.026$			295	Barnes et al. (1965)
Y	^{89}Y		15 ± 2		1–4	Narath and Fromhold (1967)
Y–Ce alloys	^{89}Y	+0.35			1.8–77	Silhouette (1970)
La(hex)	^{139}La			7.700(2) 6.798(4)	4.2–12	Poteet et al. (1970)
La(hex)	^{139}La	+0.82	0.56 ± 0.05	7.8 ± 0.3	1–210	Narath (1969)
La(fcc)	^{139}La	0.64 (295 K)			295–825	Zamir and Schreiber (1964)
La(fcc)	^{139}La	0.71(77 K)	0.2		4.2–300	Blumberg et al. (1960)
La(hex)	^{139}La		0.58 ± 0.03		1–4	Narath and Fromhold (1967)
Yb	^{171}Yb	0.0 ± 0.1			1.8–20.4	Gossard et al. (1964)

the three metals, Sc, Y, and La, and analyzed the T_1 data in terms of calculated d-spin core-polarization and d-orbital contributions to the relaxation rates. This analysis strongly suggests that the dominant magnetic hyperfine coupling in all three metals is the direct s-contact interaction [i.e., the Fermi contact interaction of eq. (18.23) and (18.67)]. It could also be concluded on the basis of the available band-structure calculations that the electron–phonon enhancement of the electronic specific heat is quite large. A comparison of the quadrupole interaction strengths in scandium and lanthanum with calculated values based on the lattice contribution indicates that the relative importance of the conduction electron contribution to the total interaction is about the same in both metals.

Scandium-base alloys with Ce, Gd, and Dy were studied by Fradin (1972) who measured T_1 and the ^{45}Sc linewidth in the temperature range 1.6–4.2 K as well as at 77 K and 295 K. The Knight shift of ^{89}Y in alloys of Y with Ce was studied by Silhouette (1970) in the temperature range 1.8–77 K. Measurements of the Knight shift and T_1 of ^{171}Yb metal were reported by Gossard et al. (1964).

2.1.3. *NGR in the paramagnetic state*

In the paramagnetic state of a lanthanide metal, in the absence of an external field, one would expect an NGR experiment to be sensitive only to the nuclear quadrupole interaction, and to provide a means of studying its temperature dependence. Unfortunately, due to the fact that for most of the lanthanide metals the onset of antiferromagnetism occurs at a relatively high temperature ($T_N \sim 100$ K or higher), the quadrupole splitting has in most cases already been reduced essentially to zero at the Néel temperature, and measurements in the paramagnetic state are not particularly informative. Additionally, in several cases, (e.g., ^{166}Er), the high energy of the Mössbauer gamma ray causes the observable effect (Mössbauer fraction) to be extremely small for $T > T_N$. In such cases useful measurements in the paramagnetic state are not possible. A resumé of experimental studies is given in table 18.9.

The one lanthanide metal in which it has been possible to study the quadrupole splitting over an extended temperature range in the paramagnetic state is thulium [Uhrich and Barnes (1967)]. The strong quadrupole interaction and

TABLE 18.9
Resumé of nuclear gamma resonance measurements on lanthanide nuclei in the paramagnetic state of lanthanide metals and alloys.

Metal	Nucleus	Temperature range (K)	Remarks	Reference
Sm	^{149}Sm	80, 300	isomer shift measured	Ofer et al. (1965a)
Eu	^{151}Eu	100	isomer shift measured	Steichele (1967)
Dy	^{161}Dy	300	isomer shift measured	Ofer et al. (1965b)
Tm	^{169}Tm	59–156	temperature dependence of quadrupole coupling measured	Uhrich and Barnes (1967)

simple level scheme for the ^{169}Tm nucleus (see table 18.3), together with the low gamma ray energy, are particularly favorable for this. The measurements provide a determination of the crystalline electric field (CEF) in the metal since the temperature dependence of the major contribution to the total efg, $q_{zz}^{(4f)}$, is given by a Boltzmann average over the contributions from the Tm^{3+} ionic levels whose splitting depends on the strength of the CEF parameters. The recent development of inelastic neutron scattering techniques for the direct measurement of the CEF level spacings has subsequently eclipsed the application of Mössbauer spectroscopy to this aspect of rare-earth studies.

Following Uhrich and Barnes (1967) and Mössbauer (1965), the temperature dependence of the efg is ascribed to $q^{(4f)}$ (since the efg in Tm metal has axial symmetry we drop the zz subscript for brevity):

$$\langle q\rangle_T = (1-\gamma_\infty)q^{(\mathrm{lat})} + (1-R_Q)\langle q^{(4f)}\rangle_T + q^{(\mathrm{ce})}, \tag{18.81}$$

with

$$\langle q^{(4f)}\rangle_T = \sum_{\nu=1}^{2J+1} \langle \nu|q^{(4f)}|\nu\rangle \exp(-E_\nu/kT) \sum_{\nu=1}^{2J+1} \exp(-E_\nu/kT), \tag{18.82}$$

where the energies E_ν and wave functions $|\nu\rangle$ of the separate CEF levels are determined by diagonalization of the CEF hamiltonian [eq. (18.108)] for the $4f^{12}$ configuration, using as basis functions the $2J+1$ degenerate functions belonging to the electronic ground state ($J=6$). Parametrization of the CEF Hamiltonian is in terms of the products C_n^m given by

$$C_n^m = A_n^m\langle r^n\rangle(1-\sigma_n). \tag{18.83}$$

Here the lattice sums A_n^m and radial averages $\langle r^n\rangle$ are the same as discussed in section 3.2.2. The shielding factors $(1-\sigma_n)$ are introduced to take account of the shielding of the 4f electrons from the CEF by the outer $5s^25p^6$ shells of the rare-earth ion. This shielding has been shown to be of greatest importance for the C_2^0 parameter, hence only σ_2 was included. In addition to appearing implicitly in $\langle q^{(4f)}\rangle_T$, the C_2^0 parameter appears explicitly in the lattice efg as

$$e^2q^{(\mathrm{lat})} = -4A_2^0. \tag{18.84}$$

Since the ground state spin of ^{169}Tm is $\frac{1}{2}$ and the excited state spin is $\frac{3}{2}$, the quadrupole splitting of the NGR transition results entirely from the excited state and is given by (18.55) with $\eta = 0$. Thus,

$$\langle \Delta E\rangle_T = (\tfrac{1}{2})e^2Q\langle q\rangle_T, \tag{18.85}$$

The temperature dependence was measured over the temperature range 59–160 K in which measurements were attainable (the Néel temperature of Tm is 56 K, and the NGR line could no longer be resolved into two components above 160 K). The CEF parameters were adjusted to yield the best fit of (18.81) to the data points.

These measurements showed that the effects of the CEF parameters C_4^0, C_6^0, and C_6^6 were negligible in comparison to C_2^0 insofar as the quadrupole interaction

is concerned. These latter parameters were all found to be effectively zero, with $C_2^0 = -70\ \text{cm}^{-1}$. This result is in keeping with calculated estimates of the CEF parameters based on the model used by Elliott (1961), assuming complete screening of all ions beyond the first nearest neighbors. Roughly speaking, the parameters C_4^0, C_6^0, and C_6^6 must be about an order of magnitude smaller than C_2^0 in the metal.

At high temperatures, $\langle q^{(4f)} \rangle_T = 0$, reflecting the average spherical symmetry of the ion when all substates of the $J = 6$ manifold are equally populated. In this limit the efg is due only to the lattice and conduction electron contributions.

Recently, a number of investigations have been made of Dy, Er, and Yb present as very dilute impurities in the noble metals and in hexagonal transition metals [e.g., Stöhr et al. (1975b)] and references cited therein]. In these experiments with for example, Er, the ^{166}Er hyperfine interactions are studied by incorporating a very small amount (500–1000 ppm) of holmium in the host, then neutron-irradiating to produce the ^{166}Ho parent isotope, and finally analyzing the hyperfine pattern with a single-line absorber ($ErAl_3$). That resolved hyperfine spectra may be obtained in the paramagnetic state is possible because the relaxation of the electronic moment at low temperatures becomes sufficiently slow. Similar NGR spectra have also been obtained in insulators (see section 2.3.2.). In metallic hosts, the relaxation rate is determined essentially by the exchange coupling $\mathcal{J}_{sf}$ between the lanthanide local moment and the conduction electrons, and this quantity is typically only about 0.1 eV for the lanthanides in these hosts [Hirst et al. (1969)]. These NGR measurements complement electron spin resonance (ESR) studies of the same lanthanide ions (see section 4.2.).

2.2. *Rare earth intermetallic compounds*

Intermetallic compounds, or ordered alloys, are characterized by well-defined crystal structures in contrast to the random arrangement of true alloys or solid solutions. The electromagnetic environment of a nucleus in an intermetallic compound is usually much more homogeneous (i.e., less "smeared out") than in an alloy, and hyperfine interaction parameters can often be determined with much greater precision. In addition, the typical sharpness of the hyperfine transitions in intermetallic compounds often enables the experimenter to observe fine-structure details which are obscured in alloys. The rare earths form a vast array of intermetallic compounds with both transition and non-transition metals [Wallace (1973), Taylor (1971)], and extensive investigations utilizing both NMR and NGR methods have dealt with many of these. An important feature of such work with intermetallics is the fact that in many instances the hyperfine interactions of both rare earth and non-rare earth nuclei may be measured. Hence, the effective hyperfine fields, both magnetic and electrostatic, are known at all lattice sites in the compound. Frequently, the goal has been to determine the s–f exchange parameter, $\mathcal{J}_{sf}$, characterizing the interaction between the localized 4f electronic moment and the s conduction electrons.

2.2.1. *NMR in magnetically ordered compounds*

In the following sections an overview and brief cataloging of many such investigations is given. Some of the cases are taken up in greater detail to illustrate their relevance to the study of specific properties.

2.2.1.1. *Cubic Laves phase compounds*

The NMR investigations of cubic Laves phase compounds in the magnetically ordered state (zero-field NMR) are summarized in table 18.10. As in the case of the metals themselves, the NMR spectra may be parametrized in terms of the a and P parameters of eq. (18.70). Budnick and Skalski (1967) investigated the NMR of Gd and $GdAl_2$, $GdPt_2$, $GdRh_2$, and $GdFe_2$ and compared their results with Mössbauer effect determinations of H_{eff} in similar Dy compounds by Nowick (1966). The NMR of ^{27}Al in $GdAl_2$ was studied by Shamir et al. (1971), and Dormann et al. (1973) have investigated both ^{27}Al and the Gd isotopes in the systems $Gd_{1-x}Y_xAl_2$ and $Gd_{1-x}La_xAl_2$. Herbst et al. (1973) studied the temperature dependence of the Gd NMR in $GdAl_2$ up to $0.5T_C$ and of the ^{27}Al NMR up to $0.7T_C$. The measurements of the Gd NMR in the system $Ce_{1-x}Gd_xRu_2$ by

TABLE 18.10
Nuclear magnetic resonance in the magnetically ordered state of rare-earth Laves phase compounds. Unless noted, the temperature is 4.2 K.

Compound or system	Nuclei observed	Remarks	Reference
GdX_2	^{155}Gd	X = Fe, Rh, Pt, Mn, Al	Budnick and Skalski (1967)
$Gd_xY_{1-x}Al_2$	^{27}Al, ^{155}Gd	$0.4 \leq x \leq 1.0$	Dintelmann et al. (1970a)
$GdAl_2$	^{27}Al		Shamir et al. (1971)
$GdAl_2$	^{27}Al	$4.2\,K \leq T \leq 0.64T_c$ observed transferred magnetically induced ^{27}Al quadrupole interaction	Degani and Kaplan (1973)
RAl_2	^{27}Al	R = Pr, Nd, Sm, Gd, Tb, Dy, Ho	Kaplan et al. (1973)
$Gd_{1-x}Y_xAl_2$ to $Gd_{1-x}La_xAl_2$	^{27}Al, ^{155}Gd	general confirmation of RKKY-like oscillatory polarization of conduction electrons	Dormann et al. (1973)
$GdAl_2$	^{27}Al, ^{155}Gd	Gd NMR to $0.5T_c$ Al NMR to $0.7T_c$ (T_c = 172 K)	Herbst et al. (1974)
$Ho_{0.03}Gd_xY_{0.97-x}Co_2$	^{165}Ho	$0.27 \leq x \leq 0.97$ shows well-resolved contribution from Gd nearest neighbors	Arif and McCausland (1975)
$Ce_{1-x}Gd_xRu_2$	^{155}Gd	$0.5 \leq T \leq 1.2$ K	Kumagai and Asayama (1975)
$GdAl_2$	^{27}Al	single crystal; angular dependence of spectra with respect to applied field	Fekete et al. (1975)

TABLE 18.11
Nuclear magnetic resonance in the magnetically ordered state of rare earth intermetallic compounds excluding Laves phase compounds. Unless noted, the temperature is 4.2 K.

Compound or system	Structure type	Nuclei observed	Remarks	Reference
GdZn	CsCl	^{155}Gd, ^{67}Zn	H_{eff}(Zn) = 175 kOe H_{eff}(Gd) = 393 kOe	Oppelt et al. (1972)
$GdAg_{1-x}Zn_x$	CsCl	^{155}Gd, ^{67}Zn, ^{107}Ag		Oppelt et al. (1972)
$GdZn_{1-x}In_x$	CsCl	^{155}Gd, ^{67}Zn		Oppelt et al. (1972)
$GdCd_{1-x}Zn_x$	CsCl	^{155}Gd, ^{67}Zn	variation of H_{eff}	Oppelt et al. (1972)
$GdAg_{1-x}In_x$	CsCl	^{155}Gd, ^{107}Ag	with cond. electron	Oppelt et al. (1972)
GdMg	CsCl	^{155}Gd	concentration	Buschow and Oppelt (1974)
$GdMg_{1-x}Zn_x$	CsCl	^{155}Gd, ^{67}Zn		Buschow and Oppelt (1974)
GdZn	CsCl	^{155}Gd, ^{67}Zn	temperature dependence of H_{eff} to $0.7T_c$	Herbst et al. (1974)
$Gd_{1-x}La_xRh$	CsCl	^{155}Gd, ^{139}La, ^{103}Rh	decomposition of H_{eff} into host and transferred contributions	Dormann and Buschow (1976)
$Gd_{1-x}La_xZn$	CsCl	^{155}Gd, ^{67}Zn, ^{139}La		
YCo_3	$PuNi_3$	^{89}Y	determined H_{eff} at different crystal sites	Figiel et al. (1976)
Y_2Co_7	Gd_2Co_7	^{89}Y		
YCo_5	$CaCu_5$	^{89}Y	determined H_{eff} at different crystal sites	Figiel et al. (1976)
Y_2Co_{17}	Th_2Zn_{17} Th_2Ni_{17}	^{89}Y		
R_2Co_{17}	Th_2Zn_{17} Th_2Ni_{17}	^{59}Co	R = Ce, Pr, Gd, Tb, Dy, Ho. T = 77 K.	Inomata (1976)
$(Y_{1-x}Gd_x)_2Co_{17}$		^{59}Co	T = 77 K and also temperature dependence of H_{eff} in some cases	Nagai et al. (1976)
$(Y_{1-x}Gd_x)Co_5$	$CaCu_5$	^{59}Co		Yoshie et al. (1976)

Kumagai et al. (1975) bear on the question of the coexistence of superconductivity and ferromagnetism and are referred to again in section 4.2.2. in connection with ESR studies of these compounds. The observation of the ^{27}Al NMR in a wall-free single crystal sphere of $GdAl_2$ has been achieved by Fekete et al. (1975). In this case, the quadrupole splitting of the ^{27}Al resonance was observed as well as the dependence of the resonance frequencies on the orientation of the crystal with respect to an applied field. We refer to this work again in connection with the analysis of transferred hyperfine interactions in section 2.2.3.3.

2.2.1.2. *Other intermetallic compounds*

NMR work on the magnetically ordered state of other intermetallic compounds is summarized in table 18.11. Many of these compounds have the CsCl structure, and in general a major objective has been to understand the dependence of the s–f exchange interaction on conduction electron concentration.

2.2.2. *NGR in magnetically ordered compounds*

Mössbauer effect methods have received wide application to the study of intermetallic compounds. This subject was first reviewed by Nowik (1966) and more recently by Taylor (1971) and also Wallace (1973) as part of general reviews of the properties of lanthanide intermetallics. Many examples are also included in the NGR review by Ofer et al. (1968) as well as in the text by Greenwood and Gibb (1971).

Among the lanthanides, nuclei of Nd, Sm, Eu, Gd, Dy, Er, Tm, and Yb have been utilized for hyperfine interaction measurements. The nuclei of non-rare earth metals involved in intermetallic compounds have also been extensively utilized, in particular those of Fe, Sn, Ir, and Au. Study of the transferred hyperfine interactions at non-magnetic nuclei are valuable for establishing the exchange interaction between the localized lanthanide moment and the conduction electrons.

As remarked in section 2.1.2, NGR measurements may frequently be made over wide temperature ranges, including up to and through the ordering temperature. In addition, unlike bulk property measurements (magnetic moment, susceptibility, etc.), Mössbauer spectra are sensitive to magnetically inequivalent sites, and the magnetization on individual sublattices can be directly measured. Moreover, the algebraic sign of the interactions in eq. (18.70) can usually be measured. Finally, the isomer shift [eq. (18.47)] provides an additional unique piece of information related to the electronic structure of the compound.

2.2.2.1. *NGR of rare earth nuclei*

Intermetallic compounds in which NGR measurements have been made at the lanthanide nucleus are summarized in table 18.12. The most utilized nuclear species have been ^{151}Eu and ^{161}Dy, reflecting primarily practical considerations in regard to ease of source preparation, parent half-life, and convenience of the gamma ray energy (see section 1.1.2). Similarly, the cubic Laves phase and CsCl type compounds have received the most attention.

Nowik et al. (1966) measured the hyperfine fields in a variety of such dysprosium intermetallics at 4.2 K, finding only small differences from the free-ion values in compounds with non-magnetic metals. However, in compounds with Fe and Co substantial departures from the free-ion values arise.

Measurements with ^{151}Eu are interesting because Eu may occur as the dipositive or tripositive ion, and the isomer shift is very sensitive to this difference. The intermetallic compounds investigated by Wickman et al. (1966, 1968) showed primarily the presence of Eu^{2+}. More recently, charge fluctuation effects in the Eu valence have been observed via the isomer shift changes in the Eu NGR spectrum in $EuCu_2Si$ and in $Eu_x\ La_{1-x}Rh_2$ by Bauminger et al. (1974). The spectra may be interpreted in terms of fast fluctuations of electrons between a localized 4f level and the conduction band, causing a fluctuating charge density to be seen by the Eu nucleus. The pressure dependence of such inter-configuration fluctuations in $Eu_{0.25}La_{0.75}Rh_2$ has been investigated by Wortmann et al. (1976).

TABLE 18.12
Resumé of nuclear gamma resonance measurements on lanthanide nuclei in the magnetically ordered state of lanthanide intermetallic compounds.

Compound	Nucleus	Temperature range (K)	Remarks	Reference
$SmAl_2$, $SmFe_2$, $SmNi_2$	^{149}Sm	20		Ofer and Nowik (1967)
$EuAl_2$, $EuAl_4$	^{151}Eu	1.8–77	measured H_{eff} and isomer shift	Wickman et al. (1966)
EuX_2	^{151}Eu	4.2	X = Cu, Zn, Pt, Pd, Rh measured H_{eff} and isomer shift	Wickman and Wernick (1968)
EuSn, $EuSn_3$	^{151}Eu	4.2–300	measured H_{eff} and isomer shift	Loewenhaupt and Hüfner (1969)
$EuZn_2$, $EuZn_5$, $EuZn_{13}$	^{151}Eu	4.2–300	measured temperature dependence of H_{eff} and isomer shift	Buschow et al. (1975)
GdX	^{151}Gd	4.2	X = Ag, In, Cu, Ga measured isomer shifts in these and in pseudobinaries	Ross and Sigalas (1975)
$DyAl_2$, $DyFe_2$	^{161}Dy	4.2–300	temperature dependence of H_{eff}, quadrupole coupling and isomer shift	Ofer et al. (1965b)
$DyNi_5$, $DyCo_5$	^{161}Dy	4.2–300	temperature dependence of H_{eff}, quadrupole coupling and isomer shift	Nowik and Wernick (1965)
$DyNi_2$, $DyCo_2$	^{161}Dy	4.2–300	temperature dependence of H_{eff}, quadrupole coupling and isomer shift	Ofer and Segal (1966)
DyX_2	^{161}Dy	4.2	X = Al, Mn, Fe, Co, Ni, Cu, Ga, Ru, Rh, Ir, Pt measured H_{eff}, quadrupole coupling and isomer shift	Nowik et al. (1966)
DyX_2	^{161}Dy	4.2–147	spin relaxation effects	Khurgin et al. (1970)
$DyCo_3$	^{161}Dy	4.2	measured H_{eff} and quadrupole coupling	Yakinthos and Chappert (1975)
Dy_2Fe_{17}, Dy_2Co_{17}	^{161}Dy	4.2	measured H_{eff} and quadrupole coupling	Bowden et al. (1973)
Dy_2Ni_{17}	^{161}Dy	4.2	measured H_{eff} and quadrupole coupling	Chappert and Yakinthos (1977)
DyH_2	^{161}Dy	0.23–4.2	spectrum arises from two very closely spaced crystal field levels	Hess et al. (1971)
$ErFe_2$	^{166}Er	20	measured H_{eff} and quadrupole coupling	Cohen and Wernick (1964)

TABLE 18.12 (*cont.*)

Compound	Nucleus	Temperature range (K)	Remarks	Reference
$ErCo_2$	^{166}Er	4.2–40	temperature dependence of H_{eff} and quadrupole coupling	Petrich and Mössbauer (1968)
$ErAl_2$ } $ErAl_3$ }	^{166}Er	1.5–80	spin relaxation effects in the temperature dependence of H_{eff} and quadrupole coupling	Zinn and Wiedemann (1968)
ErX_2	^{166}Er	0	X = Al, Ni, Co spin relaxation effects	Petrich (1969)
ErH_2	^{166}Er	2.4	measured H_{eff} and identified crystal field ground state	Shenoy et al. (1976)
$TmFe_2$	^{169}Tm	4–400	measured temperature dependence of H_{eff} and quadrupole coupling	Cohen (1964)
$YbPd_3$	^{170}Yb	1.4–4.2	spin relaxation effects and determination of crystal field levels	Nowik et al. (1972)

2.2.2.2. *NGR of non-rare earth nuclei*

Magnetically ordered intermetallic compounds of the rare earths with iron and tin have been the subject of numerous investigations, reflecting the relative ease of carrying out Mössbauer effect measurements with these two convenient nuclei (^{57}Fe and ^{119}Sn). A variety of pseudo-binary systems may also be formed (e.g., $R(Fe_xCo_{1-x})_2$) in which the iron or tin may be diluted without altering the crystal structure.

The cubic Laves phase compounds RFe_2 were first studied by Wertheim and Wernick (1962) who found a low temperature hyperfine field of roughly 230 kOe at the iron nucleus, essentially independent of the rare earth element in the compound. Although this value is considerably smaller than in 3d metal alloys ($\approx$320 kOe), the isomer shifts are similar in the two cases, indicating that the electronic configuration of the iron is the same. The conclusion is that conduction electron polarization is responsible for the decreased hyperfine field in the rare earth compounds. Examples of NGR work on the pseudo-binary Laves phases with iron include $R(FeCo)_2$ [Guimaraes and Bunbury (1973)] and $Dy(Fe_xNi_{1-x})_2$ [Burzo et al. (1975)]. These results are summarized in table 18.13.

An interesting feature of the cubic Laves phases with iron is the fact that the direction of the magnetic axis is determined by the rare earth [Bowden et al. (1968), Bowden (1973)]. In $DyFe_2$ and $HoFe_2$ the ^{57}Fe spectra show that the axis of magnetization lies along a [001] direction whereas in $TbFe_2$, $ErFe_2$, and others, the appearance of two NGR patterns shows that the magnetic axis lies along [111].

TABLE 18.13

Resumé of representative nuclear gamma resonance studies of non-rare earth nuclei in the magnetically ordered state of intermetallic compounds. Unless otherwise noted, the interaction parameters measured were the effective hyperfine field, quadrupole coupling, and isomer shift.

Compound	Nucleus	Temperature range (K)	Remarks	Reference
RFe_2	^{57}Fe	77, 300	R = Y, Ce, Sm, Gd, Dy, Ho, Er, Tm, Lu	Wertheim and Wernick (1962)
RFe_2	^{57}Fe	4.2–300	R = Y, Ce, Sm, Gd, Tb, Dy, Ho, Er	Bowden et al. (1968)
RFe_2	^{57}Fe	80–300	R = Ce, Gd, Lu	Atzmony and Dariel (1974)
$R_xY_{1-x}Fe_2$	^{57}Fe	4.2, 80, 300	R = Tb,Er ($0 \leq x \leq 1$)	Dariel et al. (1973)
$Ho_xTb_{1-x}Fe_2$ $Ho_xEr_{1-x}Fe_2$ $Dy_xTb_{1-x}Fe_2$ $Dy_xEr_{1-x}Fe_2$ $Ho_xTm_{1-x}Fe_2$	^{57}Fe	4.2–300	determined (x, T) orientation diagrams for magnetization	Atzmony et al. (1973)
$R(Fe_{1-x}Co_x)_2$	^{57}Fe	78	R = Y, Ho ($0.2 \leq x \leq 0.8$)	Guimaraes and Bunbury (1973)
$R(Co_{1-x}Fe_x)_2$	^{57}Fe	4.2, 20, and others	R = Pr, Nd, Tb, Dy, Ho, Er ($0.01 \leq x \leq 0.05$)	Atzmony and Dublon (1977)
$R(Co_{1-x}Fe_x)_2$	^{57}Fe	4.2–300	R = Nd, Ho ($x \leq 0.05$)	Atzmony et al. (1976)
RNi_2	^{57}Fe	5, 300	R = Gd, Tb, Dy, Ho, Er samples doped with 2% enriched ^{57}Fe	Arif et al. (1977)
$Dy(Fe_{1-x}Ni_x)_2$	^{57}Fe	4.2–500	$0.2 \leq x \leq 0.8$ measured H_{eff} and isomer shift	Burzo et al. (1975)
$HoFe_3$	^{57}Fe	4.2–300	determined temperature dependence of magnetization and its orientation	Arif et al. (1975d)
$ErFe_3$ YFe_3	^{57}Fe	4.2–550	determined temperature dependence of magnetization and its orientation	van der Kraan et al. (1975)
RFe_3	^{57}Fe	4.2–700	R = Y, Tb, Er determined temperature dependence of magnetization and its orientation	Arif et al. (1975b)
$R(Fe_{1-x}CO_x)_2$	^{57}Fe	77, 300, 715	R = Y, Dy ($0 \leq x \leq 0.8$) determined temperature dependence of magnetization and its orientation	Arif et al. (1975c)

TABLE 18.13 (*cont.*)

Compound	Nucleus	Temperature range (K)	Remarks	Reference
R_2Fe_{17}	^{57}Fe	77–500	R = Ce, Pr, Nd, Gd, Tm, Lu	Levinson et al. (1970)
$CeSn_3$	^{119}Sn	4.2		Kanekar et al. (1968)
RSn_3	^{119}Sn	1.6–293	R = Ce, Pr, Nd	Shenoy et al. (1970)
RIr_2	^{193}Ir	4.2	R = Pr, Nd, Sm, Gd, Tb, Dy, Ho	Atzmony et al. (1967)
RIr_2	^{193}Ir	4.2	R = La, Ce, Pr, Nd, Gd, Tb, Dy, Ho, Yb	Tanner et al. (1975)
RAu	^{197}Au	4.2–77	R = Sc, Ho, Er, Tm, Yb, Lu	Kimball et al. (1975)
$TbAu_2$	^{197}Au	4.2		Sill et al. (1971)

The RFe_3 compounds present greater complexity from the NGR standpoint since there are three sets of crystallographically inequivalent sites for the iron. Nonetheless, several detailed studies of these compounds have been made, including the temperature dependence of the hyperfine fields at the different sites [Arif et al. (1975a), 1975b, van der Kraan et al. (1975)]. The pseudo-binary systems of $DyFe_3$ and YFe_3 with nickel and cobalt have also been investigated [Tsai et al. (1972), Arif et al. (1975c)], as shown in table 18.13.

The NGR of ^{119}Sn in the $AuCu_3$ structure RSn_3 compounds of the light lanthanides has been investigated in the antiferromagnetic state by Shenoy et al. (1970). Since these compounds have rather low Neel temperatures, (<10 K), the Mössbauer spectra were followed down to 1.6 K. Since tin is a non-magnetic ingredient in these compounds, the magnetic hyperfine field is entirely transferred from the lanthanide ion. In the case of $PrSn_3$ and $NdSn_3$ the measurements show that the antiferromagnetic ordering must be of the first kind (ferromagnetic sheets in the [100] plane, coupled antiferromagnetically) so that $\frac{1}{3}$ of the Sn nuclei experience a nonzero hyperfine field whereas the others experience zero field. In the case of $CeSn_3$ Shenoy et al. (1970) were unable to detect magnetic ordering down to 1.6 K, whereas Kanekar et al. (1968) had reported the occurrence of ferromagnetic ordering in the vicinity of 4.2 K.

Transferred hyperfine fields at ^{193}Ir in the ferromagnetic state of RIr_2 compounds (cubic Laves phase) were measured by Atzmony et al. (1967) and by Heuberger et al. (1967). At 4.2 K the spectra show a quadrupole coupling which decreases by about 10% from $PrIr_2$ to $HoIr_2$, and magnetic hyperfine fields which have a maximum value at $GdIr_2$. Orientation of the lanthanide moment in these compounds has been established by Tanner et al. (1974) from detailed study of the ^{193}Ir spectra as in the case of the corresponding iron compounds mentioned above. The results of these measurements are summarized in table 18.13.

The hyperfine field, quadrupole interaction, and isomer shift of ^{197}Au in $TbAu_2$ (tetragonal, $MnAu_2$ type) have been measured by Sill et al. (1971). At 4.2 K, a

hyperfine field of approximately 50 kOe was estimated, insufficient to cause splitting of the spectrum, and indicating clearly that no local moment forms on the gold.

2.2.3. *NMR in the paramagnetic state*

2.2.3.1. *NMR of rare earth nuclei*

As remarked in section 2.1.2, the NMR of the nuclei of the magnetic lanthanides is not normally observable in the paramagnetic state. A notable class of exceptions to this rule is furnished by cases in which the paramagnetic ion has a singlet level as its crystalline field ground state, the reason being that the hyperfine interaction then vanishes in first order. This possibility had been considered theoretically for some time [Elliott (1957), Altshuler et al. (1965)] before the first successful observation of the ^{141}Pr NMR was made by Altshuler et al. (1967) in single crystal $Pr_2(SO_4)_3 8H_2O$.

In intermetallic compounds the crystal field splitting of the lanthanide ion ground term is typically an order of magnitude smaller than in non-metallic compounds, and consequently the Van Vleck magnetic-field induced susceptibility in the singlet ground state is about an order of magnitude larger than found in insulators. A large frequency shift of the resonance is therefore to be expected (on the order of 100%), so that the resonance occurs in very weak applied fields at normal resonance frequencies.

Detection of such resonances in lanthanide intermetallics was first reported by Jones (1967) on ^{141}Pr in PrP and PrAs, and on ^{169}Tm in TmP, TmAs, and TmSb, all of which have the cubic NaCl structure. Of all the lanthanide nuclei, only ^{169}Tm has spin $\frac{1}{2}$, hence quadrupolar complications are completely absent, and its NMR spectrum is determined entirely by the magnetic hyperfine interaction. In the case of ^{141}Pr, which has a small quadrupole moment (table 18.1), the cubic environment is helpful in reducing the quadrupolar complications in the spectrum. Resonances have also been reported for ^{141}Pr in PrSe and for ^{169}Tm in TmSe and $TmAl_3$ [Jones (1968)]. All of these studies are briefly summarized in table 18.14.

In addition to these examples, the non-magnetic rare-earths Sc, Y, La, Yb, and Lu, furnish opportunity for NMR investigation. Of these, only ^{45}Sc affords readily detectable NMR in both cubic and non-cubic sites. The strong quadrupole interactions usually encountered with ^{139}La and ^{175}Lu limit the study of these to lattice sites of cubic symmetry. Although it has spin $\frac{1}{2}$ and is a 100% abundant isotope, ^{89}Y has a very small magnetic moment (table 18.1) so that strong magnetic fields are needed for useful study of its NMR.

Despite these drawbacks, a variety of intermetallics have been studied, utilizing the NMR of these nuclei. These have included examples from both the cubic and hexagonal Laves phases and the NaCl and CsCl structures. NMR of the metal has also been studied in the dihydrides of Sc, Y, and La, including measurements of the spin–lattice relaxation time T_1. These investigations have generally been directed toward obtaining a partitioning of the Knight shift, T_1,

and susceptibility in the manner outlined in sections 1.2.2.3. and 1.4.2. that may be compared with band structure calculations. A representative sample of these cases is included in table 18.14.

2.2.3.2. *NMR of non-rare earth nuclei*

Of the many intermetallic compounds formed by the rare-earths, three classes have received the greatest attention insofar as NMR studies of the non-rare earth nuclei in the paramagnetic state are concerned. These are the intermetallic compounds with aluminum, the face-centered ($AuCu_3$) compounds RX_3 (X = Sn, In, etc.), and the NaCl monopnictides, RX (X = N, P, As, etc.). The reasons for this generally have to do with the nuclear quadrupole interaction. Thus, in the monopnictides, the pnictide element occupies a cubic site and hence even though all of the nuclei, ^{14}N, ^{75}As, etc., except for ^{31}P, have substantial quadrupole moments, resonances are readily observed. Similarly, in the R–Al compounds, although in most instances the Al position in the structure does not have cubic point symmetry, the quadrupole interactions of ^{27}Al are usually small enough that good NMR spectra can be obtained from polycrystalline samples. Since ^{119}Sn has no quadrupole moment, its NMR has been extensively studied in the $AuCu_3$ type compounds even though the Sn site is a non-cubic site.

In the following survey, these three categories of intermetallics are considered separately. Work on all other types of intermetallic compounds is summarized collectively.

Rare Earth–Al Compounds. The NMR of ^{27}Al in the various RAl compounds has received the most attention by far, beginning with the pioneering study of Jaccarino et al. (1960) on the RAl_2 cubic Laves phase compounds. Interpretation of the temperature-dependent Knight shifts observed in these compounds in terms of the s–f exchange interaction is discussed in section 2.2.3.3. These and other NMR measurements on RAl compounds are summarized in table 18.15. Further work on the RAl_2 series has included the study of the spin-lattice relaxation time T_1 in $La_{1-x}Gd_xAl_2$ by McHenry et al. (1972) which also yields an estimate of the exchange parameter $\mathcal{J}_{sf}$. Similarly, Abe (1975) has studied T_1 in the system $Y_{1-x}Dy_xAl_2$. The RAl series (R = La, Gd, Tb, Dy, Ho, Er) was studied by van Diepen et al. (1968) who measured the Knight shift of ^{27}Al in the temperature range 150–350 K, obtaining an average value of $\mathcal{J}_{sf} = -0.15$ eV for the series. Similarly, in the case of the RAl_3 series, van Diepen et al. (1967) obtained somewhat higher values of $\mathcal{J}_{sf}$, ranging from −0.22 eV for the Nd, Gd, and Tb compounds to −0.41 eV for $CeAl_3$. The compounds R_3Al_{11} (R = La, Pr, Nd) were also investigated by van Diepen et al. (1969). In these, resonances from two inequivalent sites are observed, and for the Pr and Nd compounds the $\mathcal{J}_{sf}$ values are again greater than in the RAl_2 series, being in the range −0.31 to 0.51 eV. The compound $EuAl_4$ was found by van Diepen et al. (1969) to yield $\mathcal{J}_{sf} = -0.14$ eV.

The rare earth monopnictides. Because of their metallic nature, their interesting magnetic properties and the simplicity of their crystal structure, the rare-earth monopnictides form a particularly interesting series of intermetallic

TABLE 18.14
Nuclear magnetic resonance results for rare earth nuclei in the paramagnetic state of rare earth intermetallic compounds.

Compound	Nucleus	Temperature range (K)	Knight shift (%)	Remarks	Reference
ScH_2	^{45}Sc	77, 300	+0.07	$T_1T = 25.0$ sec · K	Schreiber (1965)
$ScMn_2$	^{45}Sc	77–295	−0.09	$e^2Qq/h = 0.78$ MHz	Barnes and Lunde (1970)
$ScCo_2$	^{45}Sc	295	−0.43		Barnes et al. (1966)
$ScNi_2$	^{45}Sc	295	+0.39		Barnes et al. (1966)
$Sc(Ni_xCo_{1-x})_2$	^{45}Sc	295		average shift varies smoothly with x	Barnes et al. (1966)
ScB_6	^{45}Sc		−0.04		Gossard and Jaccarino (1962)
ScB_2	^{45}Sc	4–300	+0.06		Carter and Swartz (1971)
ScB_2	^{45}Sc	295	+0.07		Barnes et al. (1970)
ScP	^{45}Sc	4–600	+0.04	temperature independent shift	Jones (1968)
ScAs	^{45}Sc	4–600	+0.04		Jones (1968)
ScSb	^{45}Sc	4–600	+0.05		Jones (1968)
$ScAl_2$	^{45}Sc	10–80	+0.18	$T_1T = 3.7$ sec · K	Chock et al. (1977)
YH_2	^{89}Y	77, 300	+0.11		Schreiber (1965)
YH_2	^{89}Y			$T_1T = 550$ sec · K	Narath and Fromhold (1967)
YB_2	^{89}Y	295	+0.16		Barnes et al. (1970)
YB_2	^{89}Y	4–300	+0.20		Carter and Swartz (1971)
YP, YAs	^{89}Y	4–600	+0.11	temperature independent shifts	Jones (1969)
YSb, YBi					
YAg	^{89}Y	77	+0.37		Schmidt (1973)
YCu	^{89}Y	1.5–300	+0.30		von Meerwall et al. (1975)
LaH_2	^{139}La		+0.23	$T_1T = 11.2$ sec · K	Schreiber and Cotts (1963)
LaB_6	^{139}La		−0.04		Gossard and Jaccarino (1962)
LaP, LaAs	^{139}La	4–600	+0.16	temperature independent shifts	Jones (1969)
LaSb	^{139}La	4–600	+0.17	temperature independent shifts	Jones (1969)
$LaAl_2$	^{139}La	4.2–295	+0.65		Jaccarino et al. (1960)

$LaPt_2$	^{139}La		+0.77		Schulman et al. (1961)
LaZn	^{139}La	4.2–300	+0.244		Goebel et al. (1975)
LaAg	^{139}La	4.2–300	+0.669		Goebel et al. (1975)
LaAg	^{139}La	1.5–300	+0.70	$T_1T = 0.537$ sec · K	von Meerwall et al. (1975)
$La_{1-x}Th_xRu_2$	^{139}La	1.4–300	−0.05	$0 \leq x \leq 1.0$	Shaltiel et al. (1965)
$LaIn_3$	^{139}La	1.6–300	+0.40(1.6 K) +0.37(300 K)	$T_1T = 1.1$ sec · K at 1.6 K	Welsh et al. (1971a)
$LaSn_3$	^{139}La	1.6–300	+0.207(1.6 K) +0.228(300 K)	$T_1T = 1.25$ sec · K(1.6 K) $T_1T = 1.75$ sec · K(300 K)	Welsh et al. (1971a)
$LaPb_3$	^{139}La	1.5–300	+0.01(1.6 K) +0.16(300 K)	$T_1T = 0.59$ sec · K(4.2 K)	Welsh et al. (1972)
$LaSn_{3x}In_{3(1-x)}$	^{139}La	1.6–300		K and T_1T vary with composition	Toxen et al. (1973)
$LaIn_3$ $La(Gd)Sn_3$ $La(Gd)Pb_3$ $La(Ce)Pb_3$ $La(Ce)Sn_3$	^{139}La	1.6–4.2		Gd and Ce substituted for La in small concentrations find $\mathcal{J}_{sf} \approx$ 0.008 eV in $LaPb_3$, 0.018 eV in $LaSn_3$, 0.032 eV in $LaIn_3$	Welsh et al. (1975)
PrP	^{141}Pr	1.4–300	638(@ 4 K)	temperature dependence of shift measured	Jones (1967)
PrAs	^{141}Pr	4–77	650(@4 K)	temperature dependence of shift measured	Jones (1967)
PrS	^{141}Pr	4.2	484		Bucher et al. (1975)
PrSe	^{141}Pr	4.2	452		Bucher et al. (1975)
PrTe	^{141}Pr	4.2	678		Bucher et al. (1975)
TmP	^{169}Tm	4–27	7670(@4 K)	temperature dependence of shift measured	Jones (1967)
TmAs	^{169}Tm	4–27	7090(@4 K)	temperature dependence of shift measured	Jones (1967)
TmSb	^{169}Tm	4–27	8870(@4 K)	temperature dependence of shift measured	Jones (1967)
TmBi	^{169}Tm	4.2	8000		Smith (1971)
TmSe	^{169}Tm	4	6600		Jones (1970)
$TmAl_3$	^{169}Tm	4	3940		Jones (1970)

TABLE 18.15

Nuclear magnetic resonance of ^{27}Al in the paramagnetic state of R–Al intermetallic compounds. Values of the s–f exchange interaction parameter $\mathcal{J}_{sf}$ are based on the uniform polarization model [Jaccarino et al. (1960)].

Compound	Temperature range (K)	$\mathcal{J}_{sf}$ (eV)	e^2Qq/h (MHz)	Remarks	Reference
$ScAl_2$				Knight shift is temperature dependent	Chechernikov et al. (1969)
YAl_2				$K_{iso} = +0.026\%$	Barnes and Jones (1967)
$LaAl_2$	4.2–300		4.63	$K_{iso} = +0.13\%$	Jaccarino et al. (1960)
$LaAl_2$	295			$K_{iso} = +0.055\%$	Barnes and Jones (1967)
$LaAl_2$	20		4.95	T_1 also measured	MacLaughlin and Dougherty (1972)
$LaAl_2$	1.2–300			T_1 measurements ($T_1T = 14.3 \pm 1.0$) sec · K at 4.2 K	McHenry et al. (1972)
$LaAl_2$	90–300		4.86	temperature dependence of Knight shift	Silbernagel and Wernick (1973)
$CeAl_2$	4.2–300	−0.24	4.54		Jaccarino et al. (1960)
$PrAl_2$	4.2–300	−0.18	4.54		Jaccarino et al. (1960)
$PrAl_2$	77–300		4.66(77 K)	determined ordering temperature from temperature dependence of Knight shift	Jones et al. (1963)
$NdAl_2$	4.2–300	−0.14			Jaccarino et al. (1960)
$SmAl_2$	4.2–300				Jaccarino et al. (1960)
$SmAl_2$	150–400	0.23	4.79		De Wijn et al. (1973)
$EuAl_2$	4.2–300	−0.10			Jaccarino et al. (1960)
$GdAl_2$	4.2–300	−0.05			Jaccarino et al. (1960)
$GdAl_2$	350–575	−0.13	4.27		Jones and Budnick (1966)
$La_{1-x}Gd_xAl_2$	20			quadrupole resonance and T_1 measurements	MacLaughlan and Daugherty (1972)
$La_{1-x}Gd_xAl_2$	1.2–300	0.09		T_1 measurements, $0.0013 \leq x \leq 0.10$	McHenry et al. (1972)
$TbAl_2$	4.2–300	−0.10			Jaccarino et al. (1960)
$DyAl_2$	4.2–300	−0.09			Jaccarino et al. (1960)

$Y_{1-x}Dy_xAl_2$	1.6–20.4			T_1 measurements $x = 0.003, 0.005, 0.007$	Abe (1975)
$HoAl_2$	4.2–300	−0.13			Jaccarino et al. (1960)
$ErAl_2$	4.2–300	−0.10			Jaccarino et al. (1960)
$TmAl_2$	4.2–300	−0.12			Jaccarino et al. (1960)
$TmAl_2$	295		3.05		Barnes et al. (1961)
$YbAl_2$	4.2–300		2.30		Jaccarino et al. (1960)
$YbAl_2$	295		2.58	$K_{iso} = +0.026\%$	Barnes et al. (1961)
$LuAl_2$	295			$K_{iso} = +0.028\%$	Barnes and Jones (1967)
LaAl	150–350			$K_{iso} = +0.11\%$	van Diepen et al. (1968b)
GdAl	150–350	−0.16			van Diepen et al. (1968b)
TbAl	150–350	−0.15			van Diepen et al. (1968b)
DyAl	150–350	−0.15			van Diepen et al. (1968b)
HoAl	150–350	−0.16			van Diepen et al. (1968b)
ErAl	150–350	−0.14			van Diepen et al. (1968b)
$LaAl_3$	78–450		0.7	$K_{iso} = +0.056\%$	van Diepen et al. (1967)
$CeAl_3$	78–450	−0.41	0.7		van Diepen et al. (1967)
$PrAl_3$	78–450	−0.35	0.8		van Diepen et al. (1967)
$NdAl_3$	78–450	−0.22	0.9		van Diepen et al. (1967)
$GdAl_3$	78–450	−0.23	0.7		van Diepen et al. (1967)
$TbAl_3$	78–450	−0.22			van Diepen et al. (1967)
$DyAl_3$	100–420	−0.24			van Diepen et al. (1968a)
$HoAl_3$	100–420	−0.20			van Diepen et al. (1968a)
$ErAl_3$	100–420	−0.18			van Diepen et al. (1968a)
$ScAl_3$	295			$K_{iso} = +0.16\%$	Chechernikov et al. (1969)
La_3Al_{11}	86–300			$k_{iso} = +0.05\%$	van Diepen et al. (1969)
Pr_3Al_{11}	86–300	−0.51		two inequivalent Al sites	van Diepen et al. (1969)
		−0.32			
Nd_3Al_{11}	86–300	−0.38		two inequivalent Al sites	van Diepen et al. (1969)
		−0.31			
$EuAl_4$	86–300	−0.14			van Diepen et al. (1969)

TABLE 18.16

Nuclear magnetic resonance results for non-rare earth nuclei in the paramagnetic state of the cubic rare earth monopnictides. The s–f exchange parameter $\mathcal{J}_{sf}$ is evaluated on the basis of the uniform polarization model.

Compound	Nucleus	Temperature range (K)	Knight shift (%)	$\mathcal{J}_{sf}$ (eV)	θ_p (K)	Remarks	Reference
ScP	^{31}P	4–600	+0.07			temperature independent shift	Jones (1969)
YP	^{31}P	4–600	+0.05			temperature independent shift	Jones (1969)
LaP	^{31}P	4–600	+0.06			temperature independent shift	Jones (1969)
CeP	^{31}P	76–600	1.8–0.5	−1.1	3.6		Jones (1969)
CeP	^{31}P	76–600				T_1 measured	Myers and Narath (1974)
PrP	^{31}P	1–600	5.5–0.5	−0.68	21.5		Jones (1969)
PrP	^{31}P	76–300				T_1 measured	Myers and Narath (1974)
NdP	^{31}P	76–600	18–1	−0.56	8.9		Jones (1969)
NdP	^{31}P	76–300				T_1 measured	Myers and Narath (1974)
SmP	^{31}P	4–600	+1.2–−0.1	−0.35			Jones (1969)
SmP	^{31}P	76–300				T_1 measured	Myers and Narath (1974)
EuP	^{31}P	100–600	−118–−0.5	−0.41			Jones (1969)
EuP	^{31}P	76–300				T_1 measured	Myers and Narath (1974)
GdP	^{31}P	150–600	−9–−2	−0.37	−22.4		Jones (1969)
GdP	^{31}P	300				T_1, T_2 results	Myers and Narath (1973)
TbP	^{31}P	150–600	−7–−2	−0.31	−15.6		Jones (1969)
TbP	^{31}P	76–300				T_1 results	Myers and Narath (1974)
DyP	^{31}P	150–600	−7–−1.5	−0.27	−10.5		Jones (1969)
DyP	^{31}P	76–300				T_1 results	Myers and Narath (1974)
HoP	^{31}P	150–600	−4.5–−1	−0.24	−22.3		Jones (1969)
HoP	^{31}P	300				T_1 results	Myers and Narath (1974)
ErP	^{31}P	100–600	−3.7–−0.7	−0.23	−14.9		Jones (1969)
ErP	^{31}P	76–300				T_1 results	Myers and Narath (1974)
TmP	^{31}P	1–550	−12–−0.3	−0.19			Jones (1969)
TmP	^{31}P	76–300				T_1 results	Myers and Narath (1974)

YbP	^{31}P	80–600	−0.73–−0.05	−0.27	−30.0		Jones (1969)
YbP	^{31}P	76–300				T_1 results	Myers and Narath (1974)
LuP	^{31}P	4–600	+0.05				Jones (1969)
ScAs	^{75}As	4–600	+0.14			temperature independent shift	Jones (1969)
YAs	^{75}As	4–600	+0.16			temperature independent shift	Jones (1969)
LaAs	^{75}As	4–600	+0.16			temperature independent shift	Jones (1969)
PrAs	^{75}As	1–600	11.5–1.3	−0.50	19.5		Jones (1969)
NdAs	^{75}As	27–500	30–2	−0.50	5.9		Jones (1969)
CeAs	^{75}As	100–550	2.8–0.8	−0.74	9.9		Jones (1969)
SmAs	^{75}As	27–550	2.7–−0.2	−0.28			Jones (1969)
GdAs	^{75}As	150–550	−15–−4	−0.28	−32.6		Jones (1969)
TmAs	^{75}As	1–550	−23–−0.8	−0.16			Jones (1969)
ScSb	^{121}Sb	4–600	+0.28			temperature independent shift	Jones (1969)
YsB	^{121}Sb	4–600	+0.20			temperature independent shift	Jones (1969)
LaSb	^{121}Sb	4–600	+0.29			temperature independent shift	Jones (1969)
SmSb	^{121}Sb	27–550	3.8–−0.4	−0.22			Jones (1969)
TmSb	^{121}Sb	76–550	−9–−1	−0.15			Jones (1969)
YBi	^{209}Bi	4–600	+0.27			temperature independent shift	Jones (1969)
SmBi	^{209}Bi	100–550	+2–−0.5	−0.36			Jones (1969)

compounds for NMR investigation. Jones (1969) determined the temperature dependence, signs and magnitudes of the Knight shifts of ^{31}P, ^{75}As, ^{121}Sb, and ^{209}Bi in the temperature range 1.5–680 K, and the results are summarized in table 18.16. Together with susceptibility data, these measurements yielded determinations of the s–f exchange parameter $\mathcal{J}_{sf}$. On the basis of the uniform conduction-electron spin–polarization model for the Knight shift [Jaccarino et al. (1960)], $\mathcal{J}_{sf}$ was found to be negative and relatively constant, $\mathcal{J}_{sf} \cong -0.3$ eV. A brief review of this work is given in section 2.2.3.3 in conjunction with other determinations of $\mathcal{J}_{sf}$ in rare-earth intermetallics.

Spin–lattice relaxation time measurements on ^{31}P, which is unaffected by quadrupole interactions in contrast to all other pnictide nuclei, in these monopnictides were reported by Myers and Narath (1974). These data reflect the paramagnetic fluctuation spectra of the lanthanide electronic angular momenta, the spectra depending on the strength of the lanthanide–lanthanide exchange interaction, as well as on the magnetic level structure in the cubic crystalline field. Detailed analysis showed that the exchange depends in a complex way on the f-shell occupation and is not representable by an essentially invariant constant for all of the lanthanides. In an earlier investigation, Myers and Narath (1973) had studied the magnetic field dependence of both T_1 and T_2 in GdP and in the magnetically dilute systems LaP: Gd and LuP: Gd.

$AuCu_3$ type compounds. The RSn_3 compounds have received much attention. In these, the RE site has cubic symmetry, and in addition, ^{119}Sn has spin $\frac{1}{2}$ so that quadrupolar complications are completely avoided. Moreover, the ^{119}Sn quadrupole interactions can be investigated independently of the NMR by means of the Mössbauer effect since the first excited nuclear level of ^{119}Sn has spin $\frac{3}{2}$ and a quadrupole moment (table 18.4). The first NMR studies by Barnes et al. (1965) on RSn_3 measured the temperature dependence of both the isotropic and anisotropic Knight shift components of ^{119}Sn. This work was extended by Borsa et al. (1967) to include NGR measurements of the isomer shift and quadrupole interaction.

Welsh and co-workers (Welsh et al. 1971; Toxen et al. 1973) have studied the ^{119}Sn NMR in detail in $LaSn_3$ and in the pseudobinary system $LaSn_3$–$LaIn_3$, making both Knight shift and T_1 measurements over the entire temperature range from approximately 1.5 K to 300 K. In conjunction with the measurements of the paramagnetic susceptibility of these compounds, a variety of parameters characterizing the McMillan strong-coupling model of superconductivity were derived. These investigations are referred to again in section 4.2.2. in connection with ESR studies of super-conducting compounds.

Malik et al. (1975) studied the ^{119}Sn Knight shift and the susceptibility of $CeSn_3$ over the temperature range 1.5–300 K. The Knight shift is not proportional to the bulk susceptibility over this range. A sizeable 4f occupation near the Fermi level in $CeSn_3$ is suggested by the results.

The NMR of ^{207}Pb in $LaPb_3$ has been studied by Welsh et al. (1972). Knight shift and T_1 measurements were made, the latter being about 4 times faster than in Pb metal, thus indicating a larger s contact interaction contribution than in the

TABLE 18.17

Nuclear magnetic resonance results for non-rare earth nuclei in the paramagnetic state of $AuCu_3$ type intermetallic compounds.

Compound	Nucleus	Temperature range (K)	Knight shift (%)	Remarks	Reference
$LaSn_3$	^{119}Sn	77–300	$K_{iso} = +0.64$ (300 K)	K_{ax} strongly temperature dependent	Borsa et al. (1967)
$LaSn_3$	^{119}Sn	1.6–300	$K_{iso} = +0.64$ $K_{ax} = +0.11$ (1.6 K)	$T_1T = 0.033$ sec · K at 1.6 K K_{ax} temperature dependent	Welsh et al. (1971b)
$LaSn_{3x}In_{3(1-x)}$	^{119}Sn	1.6, 4.2	+0.5 to 10 (4.2 K)	K is composition dependent	Toxen et al. (1973)
$CeSn_3$	^{119}Sn	77–300		K strongly temperature dependent	Borsa et al. (1967)
$CeSn_3$	^{119}Sn	1.2–300		K strongly temperature dependent $T_1T = 50 \times 10^{-3}$ sec · K ($T = 1.2$)	Malik et al. (1975)
$PrSn_3$	^{119}Sn	77–400		K_{iso} and K_{ax} proportional to susceptibility $\Gamma \approx 0.2$ eV	Borsa et al. (1967)
$NdSn_3$	^{119}Sn	77–400			
$SmSn_3$	^{119}Sn	77–300	$K_{iso} = +0.17$ (300 K)	K_{iso} decreases with decreasing temperature	Borsa et al. (1967)
$SmSn_3$	^{119}Sn	300		interpretation of measurements	de Wijn et al. (1973)
$SmSn_3$	^{119}Sn	15–300		extended temperature range and interpretation	Malik et al. (1977)
$YbSn_3$	^{119}Sn	77–400	$K_{iso} = 0.31$ $K_{ax} = 0.09$	K temperature independent Yb is divalent	Borsa et al. (1967)
$LaPb_3$	^{207}Pb	1.5–77	$K_{iso} = +0.70$ $K_{ax} = +0.14$ (4.2 K)	$T_1T = 63 \times 10^{-4}$ sec · K	Welsh et al. (1972)
La_3In	^{115}In	14–300	+0.058(300 K) −0.155(14 K)	shift strongly temperature dependent, proportional to susceptibility	Heiniger et al. (1973)
La_3Tl	^{203}Tl	6.5–300	+0.32(300 K) −0.265(14 K)	as above	Heiniger et al. (1973)

TABLE 18.18
Nuclear magnetic resonance results for non-rare earth nuclei (except ^{27}Al) in the paramagnetic state of intermetallic compounds

Compound	Nucleus	Temperature range (K)	Knight shift (%)	Remarks	Reference
LaH_x	^1H	76–670	≈ 0	$0.4 \leq x \leq 2.85$, hydrogen diffusion studied	Schreiber and Cotts (1963)
YH_x	^1H	77–515	≈ 0	$2.61 \leq x \leq 2.94$, T_1 measurements, hydrogen diffusion studied	Weaver (1972a)
ScH_x	^1H	500–1000	≈ 0	$1.7 \leq x \leq 1.98$, T_1 measurements, hydrogen diffusion studied	Weaver (1972c)
$ScH_{0.37}$	^1H	300–600	≈ 0	T_1 measurements, hydrogen diffusion studied	Weaver (1972b)
CeH_x	^1H	6–12		$2 \leq x \leq 3$ temperature dependent Knight shift	Kopp and Schreiber (1967)
CeH_x, PrH_x, NdH_x, SmH_x	^1H	77–300		$T_1T \sim (T-\theta)^2$ $2 \leq x \leq 3$	Shen et al. (1969)
$LuH_{0.17}$	^1H	173–425		hydrogen diffusion studied	Barrere and Tran (1971)
$LaNi_5H_x$	^1H, ^2H	4.2–400		hydrogen diffusion studied	Barnes et al. (1976)
$LaNi_{5.3}H_6$	^1H	118–300	≈ 0	hydrogen diffusion studied	Halstead (1974)
$LaNi_{5+x}H_6$	^1H	150–300		T_1, $T_{1\rho}$, and T_2 measurements to study hydrogen diffusion	Halstead et al. (1976)
RB_6	^{11}B	300	small	R = La, Eu, Y, Ce, Nd, Gd, Yb quadrupole interaction not measured	McNiff and Shapiro (1963)
RB_6	^{11}B	4.2, 20, 77, 300	0	R = Sc, Y, La	Gossard and Jaccarino (1962)
RB_6	^{11}B	4.2, 20, 77, 399		R = Ce, Pr, Nd, Sm, Gd, Dy, Ho temperature-dependent Knight shifts, $1.05 < e^2Qq/h < 1.27$ MHz	Gossard and Jaccarino (1962)
ScB_2	^{11}B	4.2, 77, 300	0	$e^2Qq/h = 0.52$ MHz	Carter and Swartz (1971)

YB_2	^{11}B	4.2, 77, 300	0	$e^2Qq/h = 0.34$ MHz	Carter and Swartz (1971)
LaB_4	^{11}B	77, 296	0	3 sites, quadrupole parameters measured	Creyghton et al. (1973)
NdB_4	^{11}B	77, 296	+0.33, +0.26, +0.23	3 sites, quadrupole parameters measured	Creyghton et al. (1973)
$ScMn_2$	^{55}Mn	77, 300	+0.9, +0.69	2 sites, shifts are temperature independent, quadrupole parameters measured	Barnes and Lunde (1970)
$ErMn_2$ $TmMn_2$	^{55}Mn	77, 300	+0.9, +0.56 +0.58, +0.34	2 sites, shifts are temperature independent, quadrupole parameters measured	Barnes and Lunde (1975)
RCo_2	^{59}Co	300		R = Sc, Y, Ce, Pr, Nd, Er, Tm, Lu quadrupole couplings measured	Barnes and Lecander (1967)
RCu_5	^{63}Cu	2.1–300	temperature dependent	find $\mathcal{J}_{sf} \approx -0.11$ eV R = Tb–Tm, inclusive	Buschow et al. (1970)
RPt_5	^{195}Pt	80–300	temperature dependent	R = Ce, Pr, Nd, 2 sites find $\mathcal{J}_{sf} \approx +0.3$ eV	Vijayaraghavan et al. (1968)
$LaPt_2$	^{95}Pt	80–300	+0.7		Vijayaraghavan et al. (1968)
$LaPt_5$	^{195}Pt	80–300	+1.0, +0.1	2 sites	Vijayaraghavan et al. (1968)
$LaNi_{5-x}Pt_x$	^{195}Pt	4.2, 77, 300		$0 \leqslant x \leqslant 5$ detailed study of shifts and T_1	Weisman et al. (1975)
$LaRh_2$	^{103}Rh	4.2	+0.78		Seitchik et al. (1965)

metal. In conjunction with the Knight shift data, this also suggests the presence of a large negative (d-spin) component in the shift.

A summary of these various investigations is given in table 18.17.

NMR of other nuclei. NMR studies of rare earth intermetallic compounds utilizing non-rare earth nuclei not included in previous subsections are summarized in table 18.18 and in the following remarks about each element.

Hydrogen. There have been numerous hydrogen NMR studies of the metallic hydrides of the lanthanides, as well as Sc and Y, beginning with the work of Schreiber and Cotts (1963) on La–H. Subsequent work has included the Sc–H system [Weaver (1972b; 1972c)], the Y–H system [Weaver (1972a)], and Lu–H [Barrere and Tran (1971)]. In these cases the resonance linewidth and/or spin–lattice relaxation time were measured over wide temperature ranges in order to obtain information pertaining to hydrogen diffusion in these compounds (see section 1.4.2.). Studies of hydrogen NMR in respect to the magnetic properties of the hydrides include work on the Ce–H, Pr–H, and Nd–H systems by Kopp and Schreiber (1967) in which Knight shifts were correlated with susceptibility data and further work by Shen et al. (1969) involving T_1 measurements. T_1 measurements were also made on Y–Ce–H compounds by Khodosov et al. (1974). The NMR of deuterium (^{2}H) in La–H has been studied by Barrere (1967; 1969), also from the standpoint of diffusion.

Hydrogen-storing intermetallic compounds, in particular, $LaNi_5$, have also been investigated. Halstead (1974) measured the activation energy for hydrogen diffusion in the hydride phase, $LaNi_5H_6$, from the motional narrowing of the proton resonance line as a function of temperature. Measurements of the spin–spin and spin–lattice relaxation times were made by Halstead et al. (1976) on samples in which the nickel content was varied around the stoichiometric composition 5, and these are discussed in greater detail in section 2.2.3.4. Both proton and deuteron NMR were utilized by Barnes et al. (1976) in deriving the most probable location of the hydrogen in the hydride structure.

Beryllium. The spin–lattice relaxation time of ^{9}Be has been measured in the series RBe_{13} (R = La, Ce, Nd, Gd) by Borsa et al. (1973). The Knight shifts were found to be very small.

Boron. The temperature dependence of the Knight shift of ^{11}B in a series of RB_6 compounds was measured by Gossard and Jaccarino (1962). Comparison with susceptibility data furnished an estimate of the effective s–f exchange interaction. The results were compared with similar findings for the RAl_2 series [Jaccarino et al. (1960)]. Creyghton et al. (1973) investigated the tetraborides LaB_4 and NdB_4 in which three different crystallographic sites for boron occur and analyzed the NMR spectra to yield the shifts and quadrupole interactions at the three sites. Interpretation of the isotropic component of the shift in terms of the s–f exchange was attempted. Barnes et al. (1970) and Carter and Swartz (1971) measured the quadrupole couplings of ^{11}B in ScB_2 and YB_2 which have the AlB_2 structure and also found that the Knight shifts in these non-magnetic compounds were extremely small.

Manganese. The NMR of ^{55}Mn has been studied in the hexagonal Laves phase

compounds $ScMn_2$, $ErMn_2$, and $TmMn_2$ by Barnes and Lundé (1970; 1975). In this structure, unlike the cubic Laves phase, the B element occurs in two crystallographically inequivalent sites, one having axial symmetry and the other not. The Knight shifts in the three compounds do not differ significantly and show essentially no temperature dependence in the range 77–300 K, indicating that the shifts are determined primarily by the orbital susceptibility of the Mn, with negligible contribution from s–f exchange between lanthanide and conduction electron spins.

Cobalt. The quadrupole couplings of ^{59}Co were measured in a series of cubic Laves phase compounds RCo_2 by Barnes and Lecander (1967) at 300 K.

Copper. The Knight shift of ^{63}Cu was measured for the cubic symmetry site in RCu_5 compounds in the temperature range 100–300 K by Buschow et al. (1970). The results are compatible with an average s–f exchange parameter, $\mathcal{J}_{sf} = -0.11$ eV. Both the Knight shift and T_1 were measured in the CsCl type compound YCu by von Meerwall et al. (1975) in the temperature range 1.5–200 K. De Wijn et al. (1968) had previously measured the Knight shifts in a series of RCu compounds in the range 140–300 K, finding the shifts compatible with an average value of $\mathcal{J}_{sf} = -0.21$ eV.

Rhodium. The 100% abundant isotope ^{103}Rh has spin $\frac{1}{2}$, so that its NMR is not complicated by quadrupolar effects. However, its magnetic moment is small (table 18.2), and rather high magnetic field strengths are required for effective measurements. Its NMR has been studied in the cubic Laves phase, $LaRh_2$, by Seitchik et al. (1965).

Silver. Both silver isotopes also have spin $\frac{1}{2}$ and small magnetic moments. The Knight shift of ^{109}Ag was measured by von Meerwall et al. (1975) in LaAg (CsCl structure) between 1.5 and 300 K. The shift is approximately one-half that in silver metal itself.

Platinum. Vijayaraghavan et al. (1968a; 1968b) measured the Knight shift of the ^{195}Pt resonances in a series of RPt_2 and RPt_5 compounds. In the latter case, the shift was measured at the two inequivalent sites in these $CaCu_5$ type compounds. More extensive studies were made of the pseudo-binary alloys, $LaNi_{5-x}Pt_x$, by Weisman et al. (1975), measuring both Knight shift and T_1 of the ^{195}Pt. Exchange enhancement was shown to be especially important at the Ni-rich end of the system.

2.2.3.3. *NMR determinations of the s–f exchange parameter*

The first measurements by Jaccarino et al. (1960) of the ^{27}Al Knight shift in the cubic Laves phase compounds RAl_2 showed that the shift increased with decreasing temperature in the same manner as the susceptibility, and that in fact when the shift was plotted against the susceptibility, with temperature as an implicit parameter, the dependence of the shift on the susceptibility is linear. The sign of the shift was found to be positive for the light lanthanides ($J = L - S$) and negative for the heavy ones ($J = L + S$). These findings were interpreted by Jaccarino et al. (1960) in terms of a uniform polarization of the conduction electron spins arising from the exchange interaction between these and the

localized lanthanide spins (the s–f exchange interaction), leading to an expression for the (isotropic) Knight shift K as a function of the magnetic susceptibility per lanthanide ion χ_f:

$$K = K_0\{1 + [\mathcal{J}_{sf}(g_J - 1)\chi_f/2g_J\beta^2]\}. \tag{18.86}$$

Here, g_J is the Landé g factor of the rare-earth ion, β the Bohr magneton, and K_0 the Knight shift due to band paramagnetism only (see section 1.2.1.). The parameter $\mathcal{J}_{sf}$ is a phenomenological exchange constant, which enters from the assumed Hamiltonian for the sf exchange interaction,

$$\mathcal{H}_{exch} = -\mathcal{J}_{sf}\boldsymbol{S} \cdot s. \tag{18.87}$$

Since $(g_j - 1) < 0$ for the light rare earths and >0 for the heavies, the observed Knight shift behavior is consistent with a negative value of $\mathcal{J}_{sf}$.

Values of the phenomenological exchange constant $\mathcal{J}_{sf}$ derived from measurements on rare earth–aluminum compounds are listed in table 18.15, those for the RX compounds (X = N, P, As, Sb, Bi) are listed in table 18.16, and those for other nuclei (B, Sn, Pt, Cu, etc.) are in tables 18.17 and 18.18. In cases where two or more inequivalent sites occur in the structure of the compound, the Knight shifts at the different sites are observed to be different, leading to different values of the constant $\mathcal{J}_{sf}$. Examples of this type are furnished by the R_3Al_{11} compounds, the RB_4 compounds, and the RPt_5 compounds.

Values of the uniform polarization model parameter $\mathcal{J}_{sf}$ derived from the temperature dependence of the Knight shift of a non-magnetic nucleus are seen to be consistently negative, falling within the range -0.4 eV to -0.05 eV, approximately. As is evident from 18.86, the value of $\mathcal{J}_{sf}$ depends rather sensitively on that of K_0, the isotropic Knight shift parameter in the absence of polarization effects. As noted by Barnes and Jones (1967), this latter quantity is not readily measured in cases where the resonant nucleus is located in a non-cubic site and experiences both quadrupole and anisotropic shift effects. This situation applies to all of the rare earth–aluminum compounds, for example. On the other hand, in the RX (NaCl-type) compounds, the non-rare earth nucleus is located at a site of cubic symmetry, and these uncertainties are greatly reduced.

In the theory of the conduction electron–local moment exchange interaction developed by Rudermann and Kittel (1954), Kasuya (1956), and Yosida (1957), referred to as the RKKY interaction, it is shown that the conduction electron polarization is localized on the lanthanide ion and falls off as r^{-3} with periodic oscillations. The spin polarization is proportional to

$$F(2k_FR) = (2k_FR\cos 2k_FR - \sin 2k_FR)/(2k_FR)^4, \tag{18.88}$$

where k_F is the Fermi wave vector. The phenomenological exchange constant $\mathcal{J}_{sf}$ of the uniform polarization model is related to the zero wave vector constant $\Gamma = 2J(0)$ of the RKKY exchange hamiltonian corresponding to (18.87) (i.e., $\mathcal{H}_{exch} = -\Gamma\boldsymbol{S} \cdot s$) by

$$\mathcal{J}_{sf} = -6\pi Z\Gamma \sum_n F(2k_FR_{mn}), \tag{18.89}$$

where Z is the number of conduction electrons per atom. The summation runs over all lanthanide ion sites with respect to a generic non-rare-earth site.

Within the RKKY theory, the polarization of the conduction electrons is also responsible for the long-range indirect coupling between the spins of the lanthanide ions. As shown by De Gennes (1962), in terms of molecular field theory, the paramagnetic Curie temperature is proportional to the average interaction of one lanthanide ion with all the other lanthanide ions,

$$\theta_P = -\left(\frac{3\pi Z^2 \Gamma^2}{4kE_F}\right)(g_J - 1)^2 J(J+1) \sum_{n \neq m} F(2k_F R_{mn}). \tag{18.90}$$

Here k is the Boltzmann constant, E_F the Fermi energy, and in this case the sum extends over all lanthanide sites with respect to a given lanthanide site. Hence, the sums appearing in eqs. (18.89) and (18.90) are different.

Treating the Fermi wave vector k_F as an adjustable parameter, Buschow et al. (1967) and De Wijn et al. (1968), for example, have utilized the measured values of $\mathcal{J}_{sf}$ and θ_P to determine the RKKY parameter Γ within the spirit of the free electron model. De Wijn et al. (1968) find that the k_F values which satisfy 18.89 and 18.90 are generally somewhat less than the free-electron values for a wide range of aluminum, tin, copper, and platinum intermetallic compounds. The Γ values for the aluminum and tin compounds determined in this manner are negative (as are the $\mathcal{J}_{sf}$ values), however in the case of the copper and platinum compounds, Γ is positive. These results showed that a correlation exists between k_F and Γ, with Γ becoming negative for larger k_F values (roughly for $k_F > 1.4(\text{Å})^{-1}$). As emphasized by de Wijn et al. (1968), negative Γ values are incompatible with the traditional RKKY theory in which Γ, or $J(0)$, is an electrostatic exchange integral which must be positive.

This apparent incompatibility is resolved by considering a mechanism, "interband mixing", whose contribution to the net effective exchange coupling has its sign opposite to that of the direct electrostatic exchange integral. Interband mixing occurs between conduction electron states near the Fermi surface and localized, empty 4f states in its vicinity, with the result that the energies of conduction electrons having spins parallel to the localized 4f spin are raised and those with spins opposite to the localized 4f spin are lowered. A negative conduction electron polarization results, giving rise to an $\boldsymbol{S} \cdot \boldsymbol{s}$ contribution opposite in sign to that of the direct exchange integral. Watson et al. (1965) showed on the basis of numerical calculations that for large values of k_F contributions to Γ are greater than the direct exchange integral, resulting in a net negative effective exchange parameter Γ. As remarked by de Wijn et al. (1968), despite the simplifications introduced by the free electron model, the RKKY theory together with the idea of interband mixing furnishes a consistent interpretation of Knight shift and susceptibility data (e.g., Curie temperatures) in the rare-earth intermetallic compounds. Further discussion of Γ and $\mathcal{J}_{sf}$ is given in section 4.2. in connection with their determination from ESR results for rare-earth ions in metallic hosts.

2.2.3.4. *Hydrogen diffusion in rare earth hydrides*

The parameters characterizing the nuclear magnetic resonance in a solid, in particular the linewidth, second moment, and the spin–spin and spin–lattice relaxation times, are strongly affected by molecular reorientations and atomic diffusive motions. Application of NMR methods to the study of hydrogen (and deuterium) diffusion in the non-magnetic rare-earth hydrides has been extensive.

The qualitative effects of diffusion on the second moment and relaxation times can be easily seen. When the motion of atoms becomes significant the diffusing spins will begin to sample several different local (dipolar) fields in a time which is on the order of the inverse linewidth frequency, $(\Delta\nu)^{-1}$. The effect of these small random changes leads to an average dipolar field which approaches zero as the motion becomes more rapid. The strict criterion for this "motional narrowing" of the resonance is that the atomic jump frequency exceed the value $(M_2)^{1/2}$ where M_2 is the second moment of the resonance, given by (18.33). Also associated with the random motion of the nuclear dipoles there will be at each lattice site a frequency spectrum of locally oscillating magnetic fields. The portion of this spectrum near the Larmor frequency ($\nu_0 = \gamma H_0/2\pi$) is effective in causing transitions between energy levels of the spin system. The energy lost or gained by the spins is thus transferred to or from the thermal motion of the atoms, and the characteristic time for this process is the spin–lattice relaxation time T_1. For extremely slow or rapid diffusive motion, the spectrum of fluctuating fields will be strongest at frequencies either well below or well above the Larmor frequency, and only the tail of this spectrum will be effective in causing transitions. Somewhere between the two extremes the spectrum peaks at the Larmor frequency, and the spin–lattice coupling will be strongest. This occurs when the time a nucleus spends at any one lattice site equals approximately the Larmor frequency. Consequently, the spin–lattice relaxation time T_1 first decreases with the onset of diffusion, reaches a minimum when the coupling is strongest, and increases again with more rapid diffusion motion.

Specifically, the dependence of T_1 on the dipolar correlation time τ_c is given by

$$(T_1)^{-1} = \tfrac{2}{5}C_I\{F(\omega_I) + 4F(2\omega_I)\}\sum_i^{\text{protons}} r_i^{-6} + \tfrac{2}{5}C_S\{\tfrac{1}{3}F(\omega_I - \omega_S) + F(\omega_I) + 2F(\omega_I + \omega_S)\}\sum_j^{\text{metal ions}} (r_j^{-6}), \tag{18.91}$$

where the subscripts I and S refer to the hydrogen and metal nuclei, respectively, $C_I = \gamma_I^4\hbar^2 I(I+1)$, $C_S = \gamma_I^2\gamma_S^2\hbar^2 S(S+1)$, [as in eq. (18.33)], and ω_I and ω_S are the resonant (Larmor) frequencies of the proton and metal nuclei in the applied field H_0. $F(\omega)$ is proportional to the Fourier transform of the correlation function for the randomly fluctuating dipole–dipole interaction between the nuclear spins (18.31) which is assumed to decay exponentially with characteristic time τ_c,

$$F(\omega) = \frac{\tau_c}{1 + \omega^2\tau_c^2}. \tag{18.92}$$

The minimum value of T_1, $T_{1\min}$, occurs for $\omega\tau_c \approx 1$. For $\omega\tau_c \ll 1$, $\ln T_1$ decreases linearly with increasing $\omega\tau_c$, and for $\omega\tau_c \gg 1$, $\ln T_1$ increases linearly with increasing $\omega\tau_c$. This theory applies in the "motionally-narrowed" regime in which the dipolar correlation frequency, $\nu_c = \tau_c^{-1}$, is much faster than the characteristic frequency of the rigid lattice second moment, $(M_2)^{1/2}$, [see eq. (18.33)].

Bloembergen et al. (1948) first applied the concept of motional narrowing to the NMR linewidth and second moment in liquids. For application to solids, the formulation of Kube and Tomita (1954) is usually employed,

$$\tau_c^{-1} = (2(2\ln 2)^{1/2})\Delta\nu/\tfrac{1}{2}\tan[\pi(\Delta\nu/\Delta\nu_0)^2]. \tag{18.93}$$

Here τ_c is the dipolar correlation time, $\Delta\nu$ is the observed linewidth, and $\Delta\nu_0$ is the "rigid lattice" linewidth measured at a temperature low enough that diffusion effects are no longer detectable. For $\Delta\nu \ll \Delta\nu_0$ (18.93) reduces to $\tau_c \sim \Delta\nu$ so that the temperature dependence of $\Delta\nu$ and τ_c is normally set equal to the atomic jump time on the grounds that an atomic jump from one site to another alters the dipolar interaction between neighboring spins substantially. Since the atomic jump frequency is expected to obey an Arrhenius relation [Zener (1952)], τ_c should also show such a dependence on temperature. The τ_c values obtained from line-narrowing measurements have usually been fit to the relation

$$\tau_c = \tau_0 \exp(E_{act}/RT), \tag{18.94}$$

where E_{act} is the activation energy for diffusion.

With some additional assumptions as to the possible jump steps within the lattice, the self-diffusion constant D can also be obtained from the measured values of τ_c. This follows from the fact that if the mean-squared jump distance of the diffusing atom is $\langle l^2\rangle$ then D is given by

$$D = \langle l^2\rangle/6\tau_c. \tag{18.95}$$

Extensive linewidth measurements of the proton resonance in the lanthanum-hydrogen system, LaH_x $(0.4 \leqslant x \leqslant 2.85)$ were made by Schreiber and Cotts (1963). These results are consistent with a single hydride phase LaH_2 mixed with La metal for averaged values of $x < 2$. For $x > 2$, the activation energy decreases rapidly with increasing concentration, from 1.0 eV/atom at $x \cong 1.95$ to 0.13 eV/atom at $x = 2.85$. The high activation energies and frequency factors $(\tau_0)^{-1}$ imply that the tetrahedral sites in the dihydride region are in a relatively deep, steep-sided potential well. The fact that all the adjacent octahedral sites can hold a hydrogen implies the existence of a potential maximum between octahedral and tetrahedral sites. The constancy of the proton resonance rigid lattice linewidth and second moment for $x \leqslant 1.95$ is expected if the hydrogens occupy tetrahedral sites only in this concentration range. Beyond $x = 1.95$ the octahedral sites begin to fill randomly, causing an increase in the rigid lattice second moment. In addition, it is expected that the addition of one occupied site lowers the activation energies of each of its eight nearest proton neighbors by Coulomb repulsion.

In the La–H system, the proton diffusive motion also has significant effects on the linewidth, relaxation time T_1, and Knight shift of the ^{139}La resonance via the nuclear quadrupole interaction of the ^{139}La with the fluctuating electrostatic environment resulting from the proton motion. All of these parameters of the ^{139}La spectrum are strongly temperature and concentration dependent. Schreiber and Cotts (1963) show in detail that the ^{139}La data confirm and support the model of proton diffusion based on the proton NMR results alone.

Measurements of the proton resonance lineshape and T_1 in yttrium trihydride were made by Weaver (1972a) in the temperature range 77–715 K. The objective was to investigate the hydrogen diffusion parameters of the hexagonal hydrogen-deficient trihydride phase which is unique among the transition metal hydrides. From the line-narrowing behavior, and using eqs. (18.93) and (18.94), values of $E_{act} = (1.1 \pm 0.1)$ eV for $YH_{2.61}$ and $E_{act} = (0.86 \pm 0.05)$ eV for $YH_{2.83}$ were obtained. Analysis of the T_1 data was complicated by the occurrence of non-exponential magnetization decays following 90° pulses, indicative of the occurrence of two non-equivalent hydrogen systems with differing diffusion coefficients.

Both proton and ^{45}Sc NMR measurements were made by Weaver (1972b) on $ScH_{0.37}$. On the basis of 18.91 and normalization of the T_1 data to the T_1 minimum, an activation energy of 0.44 eV/atom was obtained from the proton T_1 measurements. At this concentration, hydrogen is in solid solution in the hcp scandium metal, and the observed rigid lattice second moment falls midway between the calculated values based on exclusively tetrahedral and octahedral site occupation, respectively, indicating that the hydrogen is distributed among both types of sites. At higher hydrogen concentrations in the non-stoichiometric hydride phase, ScH_x, $(1.7 \leq x \leq 1.98)$, Weaver (1972c) found that the second moment measurements in the rigid lattice (i.e., at low temperatures) did not unambiguously distinguish between various models based on tetrahedral and/or octahedral site occupation. However, the data appear to exclude the possibility of having a constant number of tetrahedral atoms with the number in octahedral sites varying with x.

T_1 measurements in the temperature range 500–1000 K were interpreted in terms of activation energies of 0.55 eV/atom and 0.73 eV/atom for $x = 1.7$ and 1.8, respectively. For $x = 1.9$ and 1.98, however, a clear break in the linear dependence of $\ln \tau_c$ on $1/T$ occurred near the minimum in T_1. Thus, for $x = 1.9$, $E_{act} = 0.42$ eV/atom at higher temperatures, with similar behavior observed for $x = 1.98$. The higher activation energy process is explained by Weaver (1972c) in terms of the diffusion of a vacancy–interstitial pair relative to the lattice of tetrahedral sites. Such a configuration results when a tetrahedral atom moves into an octahedral site, the formation of these defects being presumably favored at higher hydrogen concentrations.

Hydrogen motion has also been studied in the lutetium–hydrogen system by Barrere and Tran (1971). At the composition $LuH_{0.17}$ the hydrogen is in solid solution in the close-packed-hexagonal phase of the lutetium metal. The observed rigid lattice second moment was compatible with random occupation of

octahedral sites only. The activation energy for hydrogen diffusion, based on the temperature dependence of the linewidth and eqs. (18.93) and (18.94), was found to be $E_{act} = 0.28$ eV/atom.

In metallic systems the total effective spin–lattice relaxation rate is the sum of the separate rates resulting from the interaction with the conduction electrons, $(T_{1e})^{-1}$, and from the effect of diffusion, $(T_{1d})^{-1}$. If $(T_{1e})^{-1}$ is very fast, then the effects due to diffusion are completely masked, and this was found to be the case in the Y–Ce–H system by Khodosov et al. (1974).

As remarked in section 2.2.3.2, hydrogen motion has been studied in the hydrogen-storing compound, $LaNi_5H_x (2 \leq x \leq 6.8)$ by Halstead (1974) using proton resonance line-narrowing measurements, and more recently by Halstead et al. (1976) using pulsed NMR methods. Barnes et al. (1976) observed averaging of the deuteron quadrupole interaction resulting from deuterium diffusion in $LaNi_5$-deuterides.

2.2.4. *NGR in the paramagnetic state*

In the paramagnetic state of intermetallic compounds the NGR spectra are primarily characterized by the electric quadrupole and isomer shift interactions. In some instances magnetic splittings can be achieved with the application of an external magnetic field, and in addition, in some cases long spin–lattice relaxation times lead to the observation of magnetic hyperfine structure at low temperatures in the paramagnetic state. A representative listing of intermetallic compounds investigated by NGR methods in the paramagnetic state is given in table 18.19.

Utilization of the temperature dependence of the electric quadrupole interaction in the paramagnetic state for the determination of crystal field (CEF) level spacings and parameters was described in section 2.1.3. for the case of thulium metal. This technique was employed by Uhrich et al. (1968) to determine the CEF level schemes and parameters in the hexagonal Laves phase compounds $TmRu_2$, $TmRe_2$, and $TmMn_2$, as indicated in table 18.19. The determination of the CEF parameters on the basis of the magnetic splitting of the NGR spectrum is exemplified by the work of Nowik et al. (1972) on $YbPd_3$ and of Shenoy et al. (1976) on ErH_2, among others. In these compounds, the lanthanide ion occupies a site of cubic symmetry, so that only two parameters are required to completely characterize the CEF. As shown by Lea et al. (1962), the cubic CEF may be conveniently specified by the parameters W and x defined by

$$W_x = A_4\langle r^4\rangle\theta_4 F(4), \quad \text{and} \quad W(1-|x|) = A_6\langle r^6\rangle\theta_6 F(6), \tag{18.96}$$

where A_4 and A_6 are the fourth and sixth order lattice sums (as in sections 2.1.3 and 3.2.2), $\langle r^4\rangle$ and $\langle r^6\rangle$ are the electronic radial averages, and θ_4 and θ_6 are reduced matrix elements tabulated for each lanthanide ion (as in section 3.2.2). The $F(4)$ and $F(6)$ are numerical factors. For the Yb^{3+} ion, the $^2F_{7/2}$ ground state splits into two doublets and one quartet under the influence of the cubic field, the wave functions of the levels being independent of the above parametrization [Lea et al. (1962)]. In the case of Er^{3+}, since the ground state $J = \frac{15}{2}$, two doublets

TABLE 18.19
Resumé of representative nuclear gamma resonance studies of rare earth nuclei in the paramagnetic state of intermetallic compounds

Compound	Structure type	Nucleus	Temperature range (K)	Remarks	Reference
EuX_2Si_2	$ThCr_2Si_2$	^{151}Eu	4–700	measured temperature dependence of isomer shifts; observed inter-configuration fluctuation (ICF) effects	Bauminger et al. (1974a)
$EuRh_2$	$MgCu_2$	^{151}Eu	4–500	as above	Bauminger et al. (1974a)
$Eu_xLa_{1-x}Rh_2$	$MgCu_2$	^{151}Eu	4–400	as above ($0.075 \leq x \leq 0.5$)	Bauminger et al. (1974a)
$EuRh_{2-x}Pt_x$	$MgCu_2$	^{151}Eu	4–500	as above ($0.125 \leq x \leq 1.0$)	Bauminger et al. (1974a)
$Eu_{0.25}La_{0.75}Rh_2$	$MgCu_2$	^{151}Eu	4.2–295	measured pressure and temperature dependence of isomer shift	Wortmann et al. (1976)
$Gd_{0.1}La_{0.9}Ni_5H_x$ ($0 \leq x \leq 6.7$) $Gd_{0.1}La_{0.9}Co_5H_x$ ($0 \leq x \leq 4.2$)	$CaCu_5$	^{151}Gd	4.2	measured H_{eff}, quadrupole coupling and isomer shift as function of hydrogen content	Bauminger et al. (1977)
$Dy_xY_{1-x}H_2$	CaF_2	^{160}Dy	1.4–4.2	relaxation effects, paramagnetic hyperfine structure; determined probable CEF ground state ($0.06 \leq x$)	Stöhr and Cashion (1975)
Er_xY_{1-x}	CaF_2	^{166}Er	1.4–4.2	relaxation effects, paramagnetic hyperfine structure; determined probable CEF ground state ($0.06 \leq x$)	Stöhr and Cashion (1975)
ErH_2	CaF_2	^{166}Er	1.7–77	determined cubic CEF parameters from temperature and applied field dependence of H_{eff} magnetic ordering temperature = 2.4 K	Shenoy et al. (1976)
TmX_2	$MgZn_2$	^{169}Tm	4.2–150	X = Mn, Ru, Re determined hexagonal CEF parameter C_2O from temperature dependence of quadrupole splitting	Uhrich et al. (1968)
$YbPd_3$	Cu_3Au	^{170}Yb	1.4–4.2	determined cubic CEF parameters from temperature and applied field dependence of H_{eff} relaxation effects	Nowik et al. (1972)

and three quartets occur in a cubic field. The conventional notation for the doublet levels is Γ_6 and Γ_7 and for the quartet levels, $\Gamma_8^{(i)}$.

Nowik et al. (1972) showed that if the ground state is a doublet well separated from the first excited state, the hyperfine field, H_{eff}, will depend on the external field, H_{ext} according to

$$H_{\text{eff}} = H_{\text{sat}} \tanh(g\mu_B S' H_{\text{ext}}/kt), \tag{18.97}$$

where S' is the effective spin, $(\frac{1}{2})$ for the doublets and $(\frac{3}{2})$ for the quartets, and g is the electronic g-factor appropriate to the particular multiplet. Thus, in the case of Er^{3+}, $g = -6$ for the Γ_6 state and $g = \frac{34}{5}$ for the Γ_7 state. This field dependence is isotropic for the doublet states but is anisotropic for the quartet states. For ^{166}Er in ErH_2, the measurements made at various low temperatures and in magnetic field strengths up to 35 kOe show clearly that the ground state is a well-isolated Γ_6 doublet with H_{eff} described by (18.97). The first excited CEF level lies about 150 K above the ground state [Shenoy et al. (1976)].

Stöhr and Cashion (1976) studied the paramagnetic hyperfine structure of ^{160}Dy and of ^{166}Er at low temperatures arising from very dilute (2000 ppm) concentrations of Dy and Er in YH_2. In these experiments the hydrides were used as the Mössbauer sources, and the source spectrum was analyzed by means of a single-line absorber, in contrast to the usual experimental arrangement. The measurements showed that in both cases (i.e., dilute Dy^{3+} and Er^{3+} in YH_2) the ground state is a Γ_7 doublet. Assuming that the CEF is determined solely by the eight nearest-neighbor hydrogens, the calculated A_4 will be negative and A_6 positive if the hydrogen carries a negative formal charge (H^-). The fast ionic relaxation times observed with more concentrated alloys (e.g., 8%) indicates that the CEF parameter A_4 is negative and A_6 positive in these cases, in agreement with the expectation based on the hydridic (H^-) model [Stöhr and Cashion (1975c)].

Some hydrides of intermetallic compounds have also been studied via the NGR of a lanthanide nucleus. Bauminger et al. (1977) observed the NGR of ^{155}Gd incorporated as a dilute impurity in the interesting hydrogen-storing compound, $LaNi_5H_x$ $(0.95 \leq x \leq 6.7)$ at 4.1 K. Consistent with phase diagram studies of this system, the NGR spectra at intermediate hydrogen concentrations result from the superposition of two quadrupole-split spectra characteristic of $Gd_{0.1}La_{0.9}Ni_5$ and $Gd_{0.1}La_{0.9}Ni_5H_{6.7}$. The isomer shift data show that the s electron density at the Gd nucleus is reduced in the hydride phase compared to the hydrogen-free compound. An unusual feature is that in the corresponding cobalt compound, $Gd_{0.1}La_{0.9}Co_5H_{3.2}$, which is ferromagnetic at 4.2 K, the hyperfine field at the ^{155}Gd is one of the strongest measured in any Gd compound, having the value 366 ± 4 kOe.

In the case of ^{170}Yb in $YbPd_3$, Nowik et al. (1972) found that the field dependence predicted by 18.97 was not observed, at either 1.4 K or 4.2 K and in field strengths up to 44 kOe. This indicates that the Zeeman (magnetic dipole) energy of the ion is comparable with the CEF splitting and that in $YbPd_3$ the ground state of Yb^{3+} is not an isolated level as is the case for Er^{3+} in ErH_2.

Nowik et al. (1972) solved the full hamiltonian for an ion in a cubic crystal field with an applied (external) magnetic field. This is done in the manner outlined in section 3.2 for the ESR of lanthanide ions, and the temperature dependence of the magnetic hyperfine field is then calculated from a Boltzmann average over all states as was done for the quadrupole hyperfine splitting in section 2.1.3. For $YbPd_3$, the cubic crystal field parameters are found to be: $A_4\langle r^4\rangle = -12\,\mathrm{cm}^{-1}$ and $A_6\langle r^6\rangle = 0.6\,\mathrm{cm}^{-1}$. These values imply that the ground state is a Γ_7 doublet with the Γ_8 quartet and Γ_6 doublet at $29\,\mathrm{cm}^{-1}$ and $39\,\mathrm{cm}^{-1}$ above the ground state, respectively.

The large and well-defined range of isomer shifts observed for the NGR of ^{151}Eu in the di- and trivalent states of the europium ion make this isotope particularly valuable for the study of intermediate valency states in lanthanide intermetallics. Such intermediate valency states have their origin in inter-configuration fluctuations (ICF's). In the case of europium intermetallics, the unusual isomer shifts observed are interpreted in terms of fast fluctuations, on the order of 10^{-11} sec, of an electron between a localized 4f level and the conduction band, resulting in a fluctuating charge density at the ^{151}Eu nuclei.

Much of the experimental and theoretical work has been recently reviewed by Bauminger et al. (1974a). The compounds investigated are listed in table 18.19 together with other recent work by Bauminger et al. (1974b) and Wortmann et al. (1976).

Basically what is observed is that whereas isomer shifts for divalent Eu compounds fall in the range -8.7 to -14.5 mm/sec (relative to Eu_2O_3) and those for trivalent Eu in the range -1.0 to $+3.6$ mm/sec, intermetallic compounds of Eu are found in which the isomer shift falls in the intermediate range -1.0 to -9.0 mm/sec [Bauminger et al. (1974a)]. In addition, the shift is strongly temperature dependent in the paramagnetic state. As shown by Bauminger et al. (1974), the probability that the fluctuating electron will be in the conduction band and produce an Eu^{3+} ($4f^6$) configuration is given by

$$P_3(T, E_{\mathrm{exc}}) = \frac{1 + 8\exp(-E_{\mathrm{exc}}/kT)}{1 + 3\exp(-480/kT) + 5\exp(-1330/kT)}. \tag{18.98}$$

This formulation takes account of the ground state multiplicity 8 of the Eu^{2+} ion, of the singlet ground state of Eu^{3+}, and of the multiplicities (3 and 5, respectively) of the first and second excited states of Eu^{3+} which occur approximately 480 K and 1330 K above the ground state. E_{exc} is the excitation energy required to transfer an electron from the conduction band at the Fermi energy E_F to the localized $4f$ level. For a specific compound in which these fluctuations occur, if S_2 and S_3 designate the isomer shifts corresponding to the pure Eu^{2+} and Eu^{3+} states, then the measured intermediate shift S will be given by

$$S = [1 - P_3(T, E_{\mathrm{exc}})]S_2 + P_3(T, E_{\mathrm{exc}})S_3, \tag{18.99}$$

from which the value of P_3 may be determined. The excitation energy may then be evaluated from (18.98).

As an example, Bauminger et al. (1974a) studied the ^{151}Eu isomer shift in the

intermetallic $EuCu_2Si_2$ over the temperature range 20–670 K, the shift changing smoothly from approximately −2.0 mm/sec at low temperatures to −7.0 mm/sec at high temperature. Using the formulation described, a value of $E_{exc} = 0.07$ eV (800 K) was obtained. This value is slightly dependent on the choice of S_2. Similar results were obtained for other Eu intermetallics. For $EuRh_2$, $E_{exc} = 0.086$ eV at 90 K and $E_{exc} = 0.12$ eV at 500 K. Mixed intermetallics (pseudo-binary systems) of the form $Eu_xLa_{1-x}Rh_2$ were also investigated [Bauminger et al. (1974a; 1974b)]. In these, the temperature dependent isomer shifts were also interpreted in terms of the fast fluctuation model, with the additional assumption that the excitation energy E_{exc} as well as the width of the localized level are functions of the number of nearest neighbor La ions. A study of the pressure dependence of the isomer shift in this system has been reported by Wortmann et al. (1976), who found that the strong pressure induced shift could be ascribed to an increased energy separation between the Eu^{2+} and Eu^{3+} states.

2.3. *Insulating compounds of the rare earths*

The category of insulating compounds of the rare-earths is large and ranges from those compounds in which the crystal field levels of the lanthanide ions were first investigated by optical spectroscopic and ESR methods, such as the ethylsulfates, to the anhydrous trifluorides and other trihalides to the garnets and mixed oxides such as the vanadates and phosphates. Many of these materials have great technological significance.

Aside from the rare-earth iron garnets, the insulating compounds generally have very low magnetic ordering temperatures, or do not order at all (i.e., are Van Vleck paramagnets). Accordingly, measurements in the ordered state, either NMR or NGR, are restricted to the low temperature region. NMR measurements on non-RE nuclei in the paramagnetic state can cover a wide temperature range, however the transferred hyperfine interaction in insulators is generally substantially weaker than in metallic materials, and consequently such measurements need to be made fairly near the ordering temperature to be most effective.

In the following overview the subject matter is divided according to compounds without regard to the type of hyperfine measurement technique employed. The compilations in the tables are intended to be representative and indicative of the breadth of the investigations which have been made. Comprehensive listings may be found in the books and reviews referred to at the beginning of section 2.

2.3.1. *Ethylsulfates*

In the rare-earth ethylsulfates, $R(C_2H_5SO_4)_3 \cdot 9H_2O$, the RE ions are well-separated and for this reason these compounds were among the first to be extensively investigated by optical and ESR spectroscopy, utilizing primarily non-magnetic yttrium and lanthanum to further dilute the lanthanide ions. In this way, essentially "free ion" spectra are attainable. The point symmetry at the lanthanide site is hexagonal, C_{3h}, so that four parameters suffice to characterize

the electrostatic crystalline field. For the analysis and interpretation of ESR measurements in the ethylsulfates, see section 4.1.1.

Since the magnetic ordering temperatures of these salts are either very low or non-existent, the Mössbauer effect spectrum of the lanthanide nucleus reflects the temperature dependence of the quadrupole interaction, except that in cases where the ionic relaxation rate is sufficiently slow, magnetic hyperfine structure may also appear at low temperatures.

A summary of ethylsulfates which have been investigated by NMR or NGR is given in table 18.20. (For ESR work on the lanthanide ions in the ethylsulfates, see section 4.1.1 and table 18.27.) Beginning with non-magnetic lanthanum ethylsulfate (LaES), Edmonds (1963) measured the quadrupole coupling of ^{139}La by means of the NMR spectrum of a single crystal. Mössbauer effect measurements of the quadrupole coupling in the case of magnetic lanthanide ions include ^{161}Dy at 4.2 K [Wickman and Nowik (1968)] and ^{169}Tm in the range 10–300 K [Barnes et al. (1964)]. Magnetic hyperfine structure has been measured in the cases of DyES [Wickman and Nowik (1966) and Hüfner et al. (1968)] and ErES [Seidel et al. (1967)]. In the latter case, the quadrupole coupling of ^{166}Er was too small to be measured.

The temperature dependence of the quadrupole splitting of ^{169}Tm in TmES yielded an estimate of the values of the CEF parameters for the Tm^{3+} ion in the ethylsulfate structure. Since optical absorption spectroscopy had previously furnished estimates of the four parameters needed to characterize the CEF in this structure [Wong and Richman (1961)], their determination in this case provided a valuable cross-check on the validity of the method which has been outlined in section 2.1.3. The experiments also revealed a substantial shielding of the 4f electrons from the crystal field, as has been described for the case of thulium metal in section 2.1.3.

The NMR of ^{169}Tm has also been studied in single crystal TmES. Since in this case the lowest ionic level in the CEF potential is a singlet, the magnetic hyperfine interaction vanishes in first order (section 2.2.3.1) enabling conventional NMR to be observed. In addition, ^{169}Tm has spin $\frac{1}{2}$ so that quadrupole effects are not involved. Teplov (1969) investigated the ^{169}Tm NMR in single crystal TmES at low temperatures, and Al'tshuler (1969) measured the spin–lattice relaxation time T_1, also at low temperatures.

The ethylsulfates also furnish an opportunity to investigate the interaction between the electronic moment on the lanthanide ion and the nuclear spins of neighboring non-magnetic ions or atoms. In particular, in the ethylsulfates nine waters of hydration directly surround the lanthanide ion, and although the oxygen positions of these water molecules have been determined by X-ray analysis, the hydrogen positions have generally only been estimated on the basis of chemical arguments. King et al. (1972) first reported the direct observation of the NMR of the near-neighbor hydrogens to Nd^{3+} in single crystal yttrium ethylsulfate (YES). More recently, Wolfe (1977) completed a detailed study of the hydrogen NMR in Yb-doped YES. As emphasized by Wolfe (1977), the basic criterion for the appearance of well-resolved near-nuclei magnetic resonances is

TABLE 18.20
Representative hyperfine interaction studies (NMR and NGR) of rare earth ethylsulfates (ES)

Compound	Nucleus	Method	Temperature (K)	Quantities measured	References
LaES	^{139}La	NMR	300	quadrupole coupling	Edmonds (1963)
TmES	^{169}Tm	NGR	10–300	quadrupole coupling temperature dependence	Barnes et al. (1964)
DyES	^{161}Dy	NGR	4.2	single crystal quadrupole coupling H_{eff}	Wickman and Nowik (1966)
ErES	^{166}Er	NGR	4.2	H_{eff}	Seidel et al. (1967)
DyES	^{161}Dy	NGR	4.2–14	single crystal quadrupole coupling H_{eff}	Hüfner et al. (1968)
TmES	^{169}Tm	NMR	1.5–4.2	single crystal hyperfine enhancement factor	Teplov (1969)
TmES	^{169}Tm	NMR	2–4.2	single crystal T_1	Al'tshuler (1969)
Nd:YES	^{1}H	NMR	1.5–4.2	single crystal transferred and dipolar H_{eff}	King et al. (1972)
Yb:YES	^{1}H	NMR	1.5–4.2	single crystal transferred and dipolar H_{eff}	Wolfe (1977)
Yb:YES	^{1}H	NMR	1.2	proton spin refrigerator	Potter and Stapleton (1972)

that the impurity moment reorientation rate be slower than the NMR dipolar linewidth. The latter is about $10^5\,\mathrm{sec}^{-1}$ for abundant hydrogen spins, and the criterion is satisfied for lightly doped lanthanide ions in host crystals at temperatures below 4.2 K. Substantial shifts of the near-neighbor nuclei resonances are observed, which may be approximately accounted for in terms of the point-dipolar field of the lanthanide impurity ion. Deviations from this simple interpretation are however revealed by the field and angular dependences of the resonances and most likely arise from the finite extent of the ionic wave function [Wolfe (1977)].

2.3.2. *Halides*

In principle, hyperfine fields can be determined at both the RE and halogen sites in the lanthanide halides. However, the nuclei of chlorine, bromine, and iodine all possess substantial quadrupole moments (table 18.2), and in these non-cubic solids the resultant quadrupole coupling is large, preventing conventional NMR studies with these nuclei except with single-crystal specimens. For this reason, the NMR of ^{19}F (spin $\frac{1}{2}$) has been most extensively studied, mainly in the paramagnetic state of the trifluorides. Mössbauer effect measurements have been made on a number of the lanthanide nuclei in the trihalides and also in the hydrated trihalides. A representative selection of both NMR and NGR investigations is given in table 18.21.

Beginning with NMR in the trifluorides, measurements made with polycrystalline samples have not been too successful due to overlapping spectra which reflect the occurrence of inequivalent fluorine ion sites in the structure. The trifluorides of the heavy lanthanides have an orthorhombic structure with two types of fluorine sites, and those of the light lanthanides crystallize in a hexagonal (or trigonal) structure. Andersson and Proctor (1968) carried out a detailed study of the ^{139}La NMR in a single crystal of LaF_3 in addition to measuring the ^{19}F NMR in the crystal at several temperatures. Lee and Sher (1965) had previously observed that the ^{19}F resonance showed motional narrowing characteristic of rapid diffusive motion of the fluorine ions at temperatures above 300 K (see section 1.4.2), a surprising result in view of the high melting temperature of LaF_3 (1770 K). The measurements of Lee and Sher, however, were made at too weak an applied magnetic field strength to distinguish the inequivalence of the fluorine sites, the chemical shifts being obscured by the dipolar line broadening. Andersson and Proctor (1968) were able to show that at least two, and possibly four, inequivalent sites occur in the LaF_3 structure. Their measurements of the dependence of the ^{139}La quadrupole splitting on crystal orientation showed that the Laue symmetry of LaF_3 must be 6/mm, and they chose the structure $P6_3cm$–C_{6v}^3 as being consistent with both the NMR and X-ray data.

The diffusive motion of the fluorine ions in LaF_3 was studied in greater detail by means of pulsed NMR methods by Goldman and Shen (1966) and in powdered samples containing Pr^{3+} and Nd^{3+} ions by Shen (1968). The measurements of Goldman and Shen (1966) utilized single crystals and covered the

temperature range 370–830 K. They showed that at temperatures up to approximately 570 K, the motion of the fluorine ions on one sublattice is much faster than that on the other sublattice. There is an exchange of atoms between the two sublattices, the rate of which is slow up to about 570 K, and then becomes faster. Approximate values were derived for the activation energies associated with these two types of motion. This picture was confirmed in further detail by Shen (1968).

Of the other light lanthanide trifluorides, PrF_3 has been studied in single crystal form by Aukhadeev and Kosov (1974). As discussed in section 2.2.3 the magnetic resonance of the nucleus of a magnetic rare earth ion can be observed in cases where the crystalline field ground state level of the ion is a singlet. This is the case of Pr^{3+} in PrF_3, and the ^{141}Pr NMR was observed as well as the ^{19}F NMR in this investigation. Measurements of the spin–lattice relaxation time T_1 were also made. The remaining light lanthanide trifluorides have only been studied in polycrystalline form.

With respect to the heavy lanthanide trifluorides, a detailed study of the ^{19}F NMR in a single crystal of ErF_3 by Mustafa *et. al.* (1977) furnishes unambiguous resolution of the spectra from the two types of fluorine sites. The temperature dependence of the ^{19}F shift tensors has been analyzed in detail in terms of direct dipolar, polarization, and spin-transfer mechanisms for the transferred hyperfine interaction in insulators [Mustafa *et. al.* (1977)].

The work of Hessler (1973) furnishes an example of ^{35}Cl NMR in a single crystal. $GdCl_3$ is a ferromagnetic insulator with a Curie temperature of 2.214 K, and the ^{35}Cl NMR was studied in the temperature range 0.032–4.2 K. The crystal structure of $GdCl_3$ is hexagonal ($P6_3/m$) so that in the paramagnetic state there is just one quadrupole transition [eq. (18.54)], but in the ferromagnetic state the transferred hyperfine field splits this resonance into three transitions whose temperature dependence was studied. The transferred hyperfine field at the ^{35}Cl nucleus was found to be antiparallel to the magnetization of the sample.

Nuclear quadrupole resonance (NQR) has been employed by Carlson and co-workers [Carlson and Adams (1969)] to measure the nuclear quadrupole interaction of ^{35}Cl in the trichlorides of La, Ce, Pr, Nd, Sm, Eu, and Gd in the paramagnetic state at 4.2 K. The point-charge model for the electric field gradient was found not to predict satisfactorily the trend of the observed resonance frequencies.

Nuclear gamma resonance studies at the lanthanide site in the halides are also listed in table 18.21. As in the ethylsulfates, magnetic hyperfine structure can be observed at low temperatures in those cases in which the ionic relaxation rate is sufficiently slow, even though the system is still in the paramagnetic state. Such has been the case with ^{161}Dy in the trichloride hexahydrate [Wickman and Nowik (1967)] and with ^{171}Yb in the similar compound [Henning et al. (1966), Dunlap et al. (1974)]. The nuclear quadrupole coupling may also be measured, and particularly in the case of europium compounds, a substantial isomer shift. Since Eu forms both di- and trivalent halides, the isomer shifts have been measured in both valence states in the NGR spectrum of ^{151}Eu [Gerth et al. (1968)]. The NGR of ^{169}Tm in $TmCl_3 \cdot 6H_2O$ furnishes an example of the

TABLE 18.21
Representative hyperfine interaction studies (NMR and NGR) of lanthanide halides

Composition	Nucleus	Method	Temperature range (K)	Quantities measured	References
LaF_3	^{19}F	NMR	100–520	chemical shift, E_{act}	Saraswati and Vijayaraghavan (1967)
LaF_3	^{19}F	NMR	173–273	shift, E_{act}	Lundin and Gabuda (1966)
LaF_3	^{19}F	NMR	173–573	single crystal, E_{act}	Lee and Sher (1965)
LaF_3	^{19}F	NMR	100–560	single crystal relaxation times, T_2, T_1	Goldman and Shen (1966)
LaF_3	^{19}F	NMR	150–800	also doped with Pr^{3+} and Nd^{3+} T_1, T_2	Shen (1968)
LaF_3	^{19}F	NMR	300–400	shift	Andersson and Proctor (1968)
LaF_3	^{139}La	NMR	300	quadrupole interaction	Andersson and Proctor (1968)
CeF_3, PrF_3	^{19}F	NMR	100–520	shift E_{act}	Saraswati and Vijayaraghavan (1967)
PrF_3	^{19}F	NMR	4.2–77	single crystal shift T_1	Aukhadeev and Kosov (1974)
PrF_3	^{141}Pr	NMR	4.2–77	single crystal shift T_1	Aukhadeev and Kosov (1974)
NdF_3	^{19}F	NMR	100–520	shift	Saraswati and Vijayaraghavan (1967)
SmF_3	^{19}F	NMR	100–520	shift E_{act}	Saraswati and Vijayaraghavan (1967)
PrF_3	^{141}Pr	NGR	5	isomer shift	Groves et al. (1970)
EuF_3	^{151}Eu	NGR	300	isomer shift	Large et al. (1969)
EuF_2	^{151}Eu	NGR	20–600	isomer shift	Nitsche et al. (1972)
GdF_3, TbF_3, DyF_3, HoF_3	^{19}F	NMR	100–520	shift	Saraswati and Vijayaraghavan (1967)
HoF_3	^{19}F	NMR	220–300	shift	Carr and Moulton (1971)
ErF_3	^{19}F	NMR	100–520	shift	Saraswati and Vijayaraghavan (1967)
ErF_3	^{19}F	NMR	220–300	shift	Carr and Moulton (1971)
ErF_3	^{19}F	NMR	200–400	single crystal shift	Mustafa et. al. (1977)
YbF_3	^{19}F	NMR	100–520	shift	Saraswati and Vijayaraghavan (1967)

YbF_3	^{19}F	NMR	12–300	shift	Carr and Moulton (1971)
$GdCl_3$	^{35}Cl	NMR and NQR	0.032–4.2	quadrupole interaction H_{eff}, single crystal	Hessler (1973)
$YbCl_3 \cdot 6H_2O$	^{171}Yb	NGR	1.6–45	H_{eff}, quadrupole coupling, relaxation effects	Dunlap et al. (1974)
$LaCl_3$, $CeCl_3$	^{35}Cl	NQR	4.2	quadrupole coupling	Carlson and Adams (1969)
$PrCl_3$, $PrCl_3$	^{35}Cl	NQR	0.3	H_{eff}, quadrupole coupling	Hessler and Carlson (1968)
$NdCl_3$, $SmCl_3$, $GdCl_3$	^{35}Cl	NQR	4.2	H_{eff}, quadrupole coupling	Carlson and Adams (1969)
$SmCl_3 \cdot 6H_2O$	^{149}Sm	NGR	4.2	H_{eff}, quadrupole splitting,	Ofer and Nowik (1967)
EuF_2–EuF_3	^{151}Eu	NGR	77	isomer shift	Catalano et al. (1969)
EuI_2, $EuBr_2$, $EuCl_2$, EuF_2	^{151}Eu	NGR	300	isomer shift	Gerth et al. (1968)
EuF_3, $EuCl_3$, $EuBr_3$, EuI_3	^{151}Eu	NGR	300	isomer shift	Gerth et al. (1968)
$DyCl_3 \cdot 6H_2O$	^{161}Dy	NGR	4.2	quadrupole coupling, H_{eff},	Wickman and Nowik (1967)
$TmCl_3 \cdot 6H_2O$	^{169}Tm	NGR	1.2–4.2	quadrupole coupling	Clauser et al. (1966)
TmF_2	^{169}Tm	NGR	18–365	CEF effects	Triplett et al. (1974)
TmF_3	^{169}Tm	NGR	18–365	quadrupole coupling	Triplett et al. (1974)
$YbCl_3 \cdot 6H_2O$	^{171}Yb	NGR		single crystal	Henning et al. (1966)
$LaCl_3$	^{139}La	NMR	300	single crystal quadrupole coupling	Edmonds (1963)

"pseudoquadrupole" interaction which occurs when the first-excited electronic state in the crystalline field lies only very slightly above the ground state (e.g., ~1 K) [Clauser et al. (1966)].

2.3.3. *Oxides*

A number of the lanthanide oxides have been studied in detail via the Mössbauer effect of the lanthanide nucleus. Oxygen is not particularly amenable to NMR study since ^{17}O, the only naturally occurring isotope with non-zero spin, has a very low abundance (0.04%) as well as a substantial quadrupole moment. The NMR of ^{151}Eu and ^{153}Eu have also been extensively studied, in particular in EuO which is ferromagnetic. A representative selection of hyperfine interaction work on the RE oxides is given in table 18.22.

Since the magnetic ordering temperatures of the oxides are generally low (on the order of liquid helium temperature), except for EuO, NGR experiments at higher temperatures can be expected to furnish only measurements of the quadrupole interaction and isomer shift. In the case of Tm_2O_3, the ^{169}Tm quadrupole interaction is strong and the spectra are so well-resolved that the interaction could be studied over a wide temperature range (up to almost 2000 K) [Barnes et al. (1964)]. The spacing of the Tm^{3+} crystal field levels responsible for the quadrupole interaction and its temperature dependence were derived from the measurements in the manner described for thulium metal in section 2.1.3.

NMR measurements on ferromagnetic EuO include a single crystal study by Fekete et al. (1974) which showed that in the magnetically saturated state both the electric field gradient and the magnetic hyperfine tensor are anisotropic even though EuO is a cubic solid. The authors showed that these results could be accounted for in terms of the ionic displacements due to the magnetoelastic crystal stresses in the magnetized state. Other NMR measurements with ^{153}Eu have dealt with both spin-lattice relaxation processes [Barak et al. (1974)] and spin–spin relaxation [Bohn et al. (1975), Lütgemeier et al. (1975)].

2.3.4. *Garnets*

Rare-earth garnets which have the general formula $R_3M_5O_{12}$ (or better $5M_2O_3 \cdot 3R_2O_3$) have been the subject of much research with respect to their magnetic and optical properties and also their magnetic and electric crystalline fields. The iron garnets (M = Fe) are ferromagnetic to about 600 K, whereas the aluminum and gallium garnets (M = Al, Ga) are paramagnetic to liquid helium temperature. The garnet structure is cubic, with the rare earth ions occurring at dodecahedral (c) sites which possess orthorhombic symmetry. The local orthorhombic axes of these sites take on six orientations with respect to the cubic axes so that in general there are six magnetically inequivalent rare earth sites. The Fe, Al, or Ga ions occupy tetrahedral (d) or octahedral (a) sites.

Hyperfine interaction studies, both NMR and NGR, are especially useful in complicated materials such as these because these methods enable the occupation and magnetization at all three types of sites to be studied directly. In

TABLE 18.22
Representative hyperfine interaction studies (NMR and NGR) of lanthanide oxides

Composition	Nucleus	Method	Temperature range (K)	Quantities measured	References
Eu_3O_4	^{151}Eu	NGR	1.2–77	isomer shifts, H_{eff}	Wickman and Catalano (1968)
EuO	^{151}Eu	NGR	1.2–77	isomer shifts, H_{eff}	Wickman and Catalano (1968)
EuO	^{153}Eu	NMR	4.2	single crystal quadrupole coupling tensor, H_{eff} anisotropy	Fekete et al. (1974)
EuO	^{153}Eu	NMR	1.7–20	spin–lattice relaxation time T_1	Barak et al. (1974)
EuO	^{153}Eu	NMR	4.2	spin–spin relaxation in zero field and saturated state	Bohn et al. (1975)
EuO	^{153}Eu	NMR	4.2	field dependence of spin–spin relaxation	Lütgemeier et al. (1975)
Tm_2O_3	^{169}Tm	NGR	9.6–1970	temperature dependence of quadrupole splitting	Barnes et al. (1964)
Dy_2O_3	^{161}Dy	NGR	4.2	quadrupole coupling and H_{eff}	Wickman and Nowik (1967)
Gd_2O_3	^{161}Dy	NGR	300	quadrupole interaction and relaxation time	Mørup and Trumpy (1970)
PrO_2	^{141}Pr	NGR	20	isomer shift	Groves et al. (1970)
Pr_2O_3	^{141}Pr	NGR	5	isomer shift	Groves et al. (1970)
Pr_6O_{11}	^{141}Pr	NGR	5	isomer shift	Groves et al. (1970)
Yb_2O_3	^{171}Yb	NGR	4.2–50	quadrupole coupling	Kalvius (1965)
Nd_2O_3	^{145}Nd	NGR	4.2	unresolved quadrupole splitting	Kaindl and Mössbauer (1968)
Gd_2O_3	^{155}Gd	NGR	4.2	isomer shift	Rehm et al. (1969)
Dy_2O_3	^{161}Dy	NGR	2.5–7.0	quadrupole splitting	Forester and Ferrando (1976)

addition, the exchange interactions between the different sub-lattices can be investigated.

A variety of Mössbauer effect investigations of the garnets have been carried out, utilizing primarily the NGR of ^{57}Fe, but also that of several of the rare earths. Measurements with lanthanide nuclei were reviewed by Ofer et al. (1968) and those with ^{57}Fe by Danon (1968). More recent summaries have been given by Greenwood and Gibb (1971) and by Gibb (1976). A representative listing of hyperfine interaction measurements on the garnets is given in table 18.23.

In general terms, the hyperfine fields on the two iron sublattices can be determined in garnets containing a non-magnetic rare earth (e.g., yttrium). The principal magnetic exchange interaction is between the two types of iron sites, resulting in the ferromagnetic anti-parallel coupling of the two sublattices. The lanthanide moment is then found to be coupled anti-parallel to the resultant (net) moment of the iron sublattices. The ordering temperatures are not strongly affected by the magnetic or non-magnetic character of the rare earth, but details such as the direction of the magnetization are. In addition, by studying the NGR of ^{119}Sn substituted for Fe, for example, the transferred hyperfine interaction at this non-magnetic ion incorporated in the magnetic sub-lattice can be determined, providing further information on the details of the exchange mechanisms.

NMR work in the magnetically ordered state of the iron garnets has relied primarily on the spin-echo technique mentioned in section 1.1.1 to detect the resonance transition in the hyperfine field alone (i.e., in zero applied field). Myers et al. (1968) studied the temperature dependence of the ^{57}Fe NMR in the garnets of Gd, Tm, and Lu. These measurements give directly the temperature dependence of the (a) and (d) iron sublattice magnetization, and although these latter quantities are only slightly affected by the particular rare earth ion on the (c) sublattice, the measurements are precise enough to detect the changes that occur. When the iron sublattice data are combined with total magnetization data, the temperature dependence of the (c) sublattice is obtained. Myers et al. (1968) found that in the case of gadolinium iron garnet, a spin-wave treatment was possible at low temperatures and that a molecular field approximation adequately described the (c) sublattice magnetization over a wide temperature range.

With regard to the NMR of the RE nuclei, Streever (1969) studied the NMR of ^{151}Eu and ^{153}Eu in europium iron garnet at 4.2 K, utilizing powder specimens. The magnetic hyperfine field and quadrupole couplings were measured. Streever and Caplan (1971) detected the ^{161}Dy and ^{163}Dy NMR in polycrystalline dysprosium iron garnet at 4.2 K. The NMR of ^{167}Er has been investigated in single crystal erbium iron garnet at 4.2 K by Streever and Caplan (1973). This study showed the occurrence of two types of RE sites consistent with the total magnetization being directed along a ⟨100⟩ direction. Relaxation time measurements were also made and compared with theoretical expectations.

The NMR of ^{27}Al in the aluminum garnets has received considerable attention. Brog et al. (1966), Edmonds and Lindop (1968), Schmidt and Jones (1970), and Tsang and Ghose (1971) all studied the ^{27}Al NMR at the (a) and (d) sites in

various aluminum garnets, determining magnetic shift tensor components and quadrupole coupling constants at the two sites. The (d) sites have ^{27}Al coupling constants of about 6 MHz, which are roughly an order of magnitude larger than at the (a) sites, indicating that at the (a) sites the symmetry approaches closely that of a perfect octahedron. For the thulium garnet, Schmidt and Jones (1970) used the measured temperature dependence of the ^{27}Al magnetic shift (section 1.2.2.2) to determine the temperature dependence of the Tm^{3+} ion susceptibility. The ^{27}Al shifts could be accounted for quite well in terms of the dipolar field from the Tm^{3+} ions, although the possibility of a transferred hyperfine field, as in section 1.2.2.2, was not ruled out.

Finally, Jones (1968) and Schmidt and Jones (1970) detected the NMR of ^{169}Tm in single crystals of the gallium and aluminum thulium garnets at low temperatures. This shows clearly that the Tm^{3+} ion ground state is an orbital singlet, and the angular dependence of the NMR spectra demonstrated the importance of the orthorhombic crystalline field interaction at the rare earth ion site.

2.3.5. *Miscellaneous insulating compounds*

The extensive NMR work on the rare-earth pnictides (RN, RP, etc.) was reviewed in section 2.2.3 and 2.2.3.2. Various of the rare-earth chalcogenides (oxides, sulfides, etc.) also form in the cubic rock-salt structure, in particular those of Eu and Sm. The europium monochalcogenides are semiconducting magnetic materials whose properties have been reviewed by Wachter (1972); also see ch. 19. Both NGR and NMR methods afford opportunity to study these compounds, and the work on oxides has been reviewed in the fore-going section (section 2.3.3). Table 18.24 provides a brief summary listing of experimental work.

Measurements of the NGR of ^{151}Eu were first reported by Wickman et al. (1966) for EuS and EuSe. The isomer shifts showed clearly that the Eu is divalent in these compounds, and at low temperatures, in the magnetically ordered state, the hyperfine field was found to be $H_{eff} = -331 \pm 10$ kOe. More recently, Sauer et al. (1974) made detailed measurements of the ^{151}Eu NGR in applied (external) magnetic field strengths of up to 130 kOe at 4.2 K. In the saturated ferromagnetic phase of these compounds, the H_{eff} values were -305, -330, -328, and -306 kOe, in EuO, EuS, EuSe, and EuTe, respectively. By comparison, the value expected from a pure $4f^{7-8}S_{7/2}$ configuration of Eu^{2+} is -342 kOe, and Sauer et al. (1974) interpret the differences as arising from orbital admixtures which vary between EuO and EuTe in relation to the location of the 4f level within the energy bands. For EuTe in the antiferromagnetic phase ($2.8 \leq T \leq 4.6$ K), $H_{eff} = -256$ kOe, the difference of -50 kOe between this value and that in the ferromagnetic phase being interpreted in terms of the transferred hyperfine field contributions from the neighboring Eu ions.

The pressure dependence of the hyperfine fields and isomer shifts in the europium chalcogenides has also been studied [Klein et al. (1973), Kalvius et al. (1974), Klein et al. (1976)]. In EuO and EuS there occurs a pronounced increase in H_{eff} with high pressure (up to 60 kbars), whereas in EuTe there is a very small

TABLE 18.23
Representative hyperfine interaction studies (NMR and NGR) of rare earth garnets

Compound	Nucleus	Method	Temperature range (K)	Quantities measured	Reference
EuIG*	^{151}Eu	NMR	4.2	resonance spectrum in zero field in powder sample	Streever (1969)
EuGaIG	^{151}Eu	NGR	4.2	determined contributions of Fe neighbor ions to the exchange field at the Eu sites	Nowik and Ofer (1967)
RIG	^{153}Eu	NGR	4.2	R = Gd–Lu, inclusive, and Y determined variation of exchange field at Eu sites	Atzmony et al. (1968)
EuIG	^{153}Eu	NGR	4.2	quadrupole interaction at two inequivalent Eu sites find second order CEF components	Bauminger et al. (1969)
EuIG	^{151}Eu	NGR	1.5–450	temperature dependence of H_{eff} and quadrupole coupling	Stachel et al. (1969)
SmIG	^{149}Sm	NGR	16–300	temperature dependence of H_{eff}	Ofer et al. (1965a)
SmIG	^{149}Sm	NGR	16–300	H_{eff} at low temperatures is determined mainly by CEF ground state splitting due to the exchange field	Nowik and Ofer (1968)
DyIG	^{161}Dy	NMR	4.2	resonance spectrum in zero field in powder sample	Streever and Kaplan (1971)
DyIG	^{161}Dy	NGR	4.2, 20, 100	determined H_{eff} and quadrupole coupling at two inequivalent Dy sites	Crecelius et al. (1969)
ErIG	^{167}Er	NMR	4.2	single crystal and powder samples measured H_{eff} and T_1 the two Er sites	Streever and Kaplan (1973)
TmIG	^{169}Tm	NGR	90, 300	measured H_{eff} and quadrupole coupling	Nowik and Ofer (1963)
TmAlG	^{169}Tm	NMR	1.5–230	single crystal measurements show orthorhombic CEF at Tm site	Schmidt and Jones (1970)

LuIG	^{175}Lu	NMR	4.2, 77, 300	essentially pure quadrupole resonance spectra in zero field	Khoi and Rotter (1971)
RIG	^{57}Fe	NMR	4.2–380	determined sublattice magnetizations at different sites R = Gd, Tm, Lu	Myers et al. (1968)
SmIG YIG	^{57}Fe	NGR	85–600	determined sublattice magnetizations and orientations	Van Loef (1968)
YIG	^{119}Sn	NGR	4.2	H_{eff} at Sn sites results primarily from nearest neighbor Fe ions	Nowik et al. (1971)
YIGaG	^{57}Fe				
RIG	^{119}Sn	NGR	4.2	R = Eu–Lu inclusive and Y determined RE ion contribution to H_{eff} at Sn sites	Bauminger et al. (1972)
ErAlG GdAlG	^{27}Al	NMR	300	single crystal work determined quadrupole couplings at two inequivalent Al sites	Tsang and Ghose (1971)

*IG = iron garnet (see text).

TABLE 18.24
Representative hyperfine interaction studies (NMR and NGR) in miscellaneous rare earth compounds

Compound	Nucleus	Method	Temperature range (K)	Quantities measured	Reference
EuS EuSe	^{151}Eu	NGR		H_{eff} and isomer shift	Wickman et al. (1966)
EuX	^{151}Eu	NGR	4.2	X = S, Se, Te effect of applied field on H_{eff}	Sauer et al. (1974)
EuTe	^{151}Eu	NGR	2–4.2	pressure dependence of H_{eff}	Klein et al. (1976)
EuS	^{151}Eu	NGR	2–4.2	pressure dependence of H_{eff}	Kalvius et al. (1974)
EuX	^{119}Sn	NGR	4.2	X = S, Se, Te samples contained 1% Sn measured H_{eff} at Sn sites	Bykovetz (1976)
TmSe	^{169}Tm	NGR	0.05–365	estimate Tm^{2+} character of the ground state electronic configuration from measured H_{eff}	Triplett et al. (1974)
SmSe SmS_xSe_{1-x}	^{77}Se	NMR		transferred hyperfine field in paramagnetic state	Brog and Kenan (1973)
RVO_4	^{51}V	NMR	300	R = Pr, Nd, Sm, Eu, Lu measured paramagnetic shift	Pletnev et al. (1975)
$RFeO_3$	^{57}Fe	NGR	85–560	temperature dependence of sublattice magnetization and quadrupole couplings R = La–Lu, inclusive except Pm	Eibschütz et al. (1967)

decrease. However, the isomer shifts and therefore the charge density at the nucleus decrease with increasing pressure in all three compounds. Sauer et al. (1974) discuss in detail the interpretation of these results in terms of increased admixture of 5d orbital contributions into the $4f^7$ configuration resulting from the reduction of the energy gap between the 4f and 5d bands.

Bykovetz (1976) has utilized the NGR of ^{119}Sn to study transferred hyperfine fields at the Sn site in solid solutions of EuS, EuSe, and EuTe with the corresponding tin monochalcogenides. The transferred hyperfine fields, on the order of 50 kOe at 4.2 K, in dilute solid solutions were shown to be "supertransferred" from the second Eu neighbors.

In the case of TmSe which also has the cubic rock-salt structure, Triplett et al. (1974) obtained fully resolved magnetic hyperfine structure in the NGR of ^{169}Tm at temperatures, $T < 1.8$ K, without quadrupolar complications, consistent with the cubic environment. At temperatures above the Néel temperature of 2.8 K a narrow single line spectrum was observed, with relaxation effects being important in the spectra in the intermediate temperature range, $1.8 \leqslant T \leqslant 2.8$ K. This compound furnishes another example in which interconfiguration fluctuations are believed to occur on a very fast time scale (see section 2.2.4), in this case between Tm^{2+} and Tm^{3+}. Assuming that $H_{\text{eff}} = 0$ for the Tm^{3+} configuration, and using the free ion value of $H_{\text{eff}} = 3.83$ MOe for Tm^{2+}, estimates of the Tm^{2+} character of the ground state configuration were derived from the measured value, $H_{\text{eff}} = 1.93$ MOe, at low temperatures [Triplett et al. (1974)].

Large negative shifts of the ^{77}Se NMR were observed by Brog et al. (1973) in SmSe and SmS_xSe_{1-x} and were found to be correlated with the expectation value of the rare-earth spin. For SmSe the transferred hyperfine field at the Se site was found to be -29 ± 4 kOe per unit 4f spin.

Many salts of the rare-earths, such as nitrates, sulfates, etc., not covered in the previous sections, have been examined via the NGR of the lanthanide nucleus, in particular ^{151}Eu, ^{161}Dy, ^{169}Tm, and ^{170}Yb. In some cases, slow electronic relaxation permits the observation of magnetic hyperfine structure at low temperatures. Otherwise, in general, quadrupole couplings and isomer shifts have been measured. The texts and reviews already cited in sections 1.1.2 and 2 should be consulted for detailed listings of these materials.

The NMR of a number of non-RE nuclei, primarily ^{19}F, ^{27}Al, ^{31}P, and ^{51}V, has been utilized to gain information on transferred hyperfine fields and the extent of covalent bonding contributions in a variety of insulating compounds, such as the aluminates, orthophosphates, orthovanadates, the mixed fluorides (e.g., $LiRf_4$), and others. Representative examples are included in the listing in table 18.24.

3. Electron resonance methods

Electron paramagnetic resonance (EPR, often also termed electron spin resonance, or ESR) was first experimentally demonstrated by Zavoiskiy (1945). As in NMR, section 1.1.1, energy levels result basically from the interaction of

an electronic moment with a magnetic field, and transitions between these levels are detected by absorption of suitable quanta of radio frequency radiation in the frequency range 10^3–10^5 MHz, approximately. The higher frequencies in comparison to NMR are a consequence of the roughly 2000 times stronger magnetic moment of the electron as compared with nuclei. Development of this new spectroscopy proceeded very rapidly after 1945 with the availability of microwave (radar) equipment and techniques.

The basic requirement for EPR is that the sample to be studied contain unpaired electron spins. Lanthanide ions, having incompletely filled 4f shells, certainly meet this requirement, and when present in sufficiently low concentrations (typically less than 0.1%) they may be regarded as not interacting with each other. Under these circumstances the single ion approximation normally applies.

The lanthanide ion serves as a probe of its environment in the host crystal, providing information on the site symmetry, and on the crystalline electric field (CEF) components and the CEF levels of the ion. In addition, the hyperfine interaction with the lanthanide nucleus or with the nuclei of other atoms (transferred hyperfine interaction) provides information on the electronic wave functions of both lanthanide and non-lanthanide ions. Unlike NMR and the Mössbauer effect which utilize the invariant electric and magnetic moment properties of nuclei as probes, these properties of magnetic ions are in general not invariant, but are themselves conditioned by the ionic environment. In the case of the lanthanides however, since these properties reside in the incomplete 4f shell, which is relatively well screened from the ionic environment by the filled 5s and 5p shells, they are not so strongly affected as in the case of the magnetic 3d ions, for example.

The magnetic lanthanide ion is typically introduced as an impurity into a host crystal which may be non-metallic or metallic. In many cases the lanthanide ion replaces an inert yttrium or lanthanum ion in a compound or alloy, or alternatively the yttrium or lanthanum may be regarded as diluting the magnetic lanthanide species in a compound of the latter. In other cases, the lanthanide ion is substituted into an altogether different crystal lattice, as for example into NaCl, CaF_2, or into a metal such as silver.

General introductions to the subject of EPR spectroscopy may be found in a wide range of books and reviews. Among those emphasizing the study of transition metal ions, including lanthanides, are Low (1960), Abragam and Bleaney (1970), and Al'tshuler and Kozyrev (1974).

As with NMR, the EPR experiment can be performed by varying the frequency of the radiation while holding the magnetic field constant or by holding the frequency constant and sweeping the field through the resonance condition. The latter method is in fact almost always employed, due primarily to the fact that microwave frequency circuitry (waveguide components, etc.) is not particularly broadband in nature. Experimental methods and spectrometers are discussed in detail in books by, among others, Ingram (1967), Wilmshurst (1968), and Alger (1968).

3.1. *Introduction*

Analogously to the nuclear case (section 1.2) an ion with total angular momentum $J\hbar$ possesses a magnetic dipole moment, $\boldsymbol{\mu} = -g\beta_0\boldsymbol{J}$, the energies of which in a magnetic field $\boldsymbol{H}_0$ are given by the eigenvalues of the hamiltonian

$$\mathcal{H}_M = -\boldsymbol{\mu} \cdot \boldsymbol{H}_0 = g\beta_0 \boldsymbol{J} \cdot \boldsymbol{H}_0 = g\beta_0 m_J H_0, \tag{18.100}$$

where g and β_0 are the g-factor and Bohr magneton, respectively. The negative sign in the relation between $\boldsymbol{\mu}$ and $\boldsymbol{J}$ is introduced explicitly to recognize the fact that the negative charge of the electron causes its magnetic moment to be directed oppositely to its angular momentum. Accordingly, g is a positive number. For a free electron, having no orbital angular momentum, the g-factor is that for spin angular momentum only, $g_S = 2.00232$.

The energy levels of 18.100 are equally spaced, and the transitions between them, satisfying the magnetic dipole radiation selection rule, $\Delta m_J = \pm 1$, are all identical, with energy

$$h\nu = g\beta_0 H_0. \tag{18.101}$$

For free ions, subject to Russell–Saunders (LS) coupling between spin and orbital moments, the g-factor is

$$g_J = \frac{J(J+1)(g_L + g_S) + \{L(L+1) - S(S+1)\}(g_L - g_S)}{2J(J+1)}.$$

Taking the orbital and spin g-factors to be $g_L = 1$ and $g_S = 2$ results in the conventional Landé formula

$$g_J = \tfrac{3}{2} - \frac{L(L+1) - S(S+1)}{2J(J+1)}. \tag{18.102}$$

In the general case of an ion incorporated in a solid the g-factor will no longer be given by the Landé formula. However, it is customary to retain the form of (18.101) and write

$$h\nu = g_{\text{eff}}\beta_0 H_0, \tag{18.103}$$

where the effective g-factor, g_{eff}, now has a complex origin in light of the interactions between the ion and its environment. Moreover, g_{eff} will depend on the orientation of the applied field H_0 with respect to coordinate axes fixed in the crystal lattice, and characterizes the interaction between an effective spin, S', and the applied field. The resonance condition specified by (18.103) will be further modified by interaction of the ionic moment with the nuclear moment properties of the ion itself and/or ligand ions, that is, by hyperfine interactions.

The effective spin approximation amounts to replacing the hamiltonian of the ion in the lattice, with all its states and energies, by another hamiltonian which accurately describes only the low-lying states [Stevens (1963)]. This concept was introduced by Van Vleck (1940). It furnishes a convenient means of expressing the results of many different measurements in a compact way, and it furnishes a

point of reference for theoretical discussion of the interaction of the ion with its surroundings in the solid. The following subsections furnish a brief outline of the method by which the effective spin and g-factor are derived from and related to the parameters in the actual spin hamiltonian of the ion in the lattice.

3.2. *The spin hamiltonian*

The energy of a paramagnetic ion in a solid is a complicated function of the coordinates and spins of the unpaired electrons in the ion and of the coordinates and charges of the surrounding ions which produce the crystalline electric field (CEF). The development of the spin hamiltonian idea for paramagnetic ions is due mainly to Abragam and Pryce (1951), and its application to the RE ions may be considered to start with the work of Elliott and Stevens (1953).

Neglecting initially the hyperfine interactions, the hamiltonian for a lanthanide ion in a solid may be represented by

$$\mathcal{H}_{RE} = \mathcal{H}_{SO} + \mathcal{H}_{CEF} + \mathcal{H}_{M} \tag{18.104}$$

where it is assumed that the unpaired electron configuration may be described by total orbital and spin quantum numbers L and S, respectively. The hamiltonian of (18.104) therefore represents a perturbation of the free ion states, the several terms representing, respectively, the spin–orbit interaction, the interaction of the ion with the crystalline electric field, and the magnetic (Zeeman) interaction with the applied field. In the lanthanide case, the magnitudes of the energies associated with these terms follow in the same sequence as in (18.104).

$$\mathcal{H}_{SO} \gg \mathcal{H}_{CEF} \gg \mathcal{H}_{M}$$

The procedure followed in establishing the spin hamiltonian is to first utilize $\mathcal{H}_{SO}$ to determine the ground state term within the ground multiplet, the latter following from the free ion configuration $4f^n$ by application of Hund's rules. The ground state term is itself split by the CEF hamiltonian, $\mathcal{H}_{CEF}$, yielding a lowest level (possibly degenerate) whose wavefunction(s) depend on the point symmetry of the CEF. In conclusion, the g-factor appropriate to the lowest levels is determined from the magnetic hamiltonian, $\mathcal{H}_{M}$, using the equivalence

$$\beta_0 \boldsymbol{H}_0 \cdot (\boldsymbol{L} + 2\boldsymbol{S}) = g_{\text{eff}} \beta_0 \boldsymbol{H}_0 \cdot \boldsymbol{J}. \tag{18.105}$$

In the effective spin formulation, $\mathcal{H}_{M}$ becomes

$$\mathcal{H}_{M} = \beta_0 \boldsymbol{H}_0 \cdot \tilde{g} \cdot \boldsymbol{S}'$$

where $\tilde{g}$ represents the g-tensor whose components depend on the orientation of $\boldsymbol{H}_0$ with respect to the principal axes of the CEF, and S' is the effective spin of the lowest levels. The hyperfine interaction contributions are then added as a final perturbation.

3.2.1. *The spin–orbit interaction*

The spin–orbit interaction term of (18.104) is given by

$$\mathcal{H}_{SO} = \lambda \boldsymbol{L} \cdot \boldsymbol{S}. \tag{18.106}$$

Although the coupling between the 4f electrons is very close to pure *LS*, corrections do arise due to the fact that the spin–orbit energy is not entirely negligible in comparison to the electrostatic (Coulomb) energy. As pointed out by Abragam and Bleaney (1970), the splittings within the ground multiplet do not obey the Landé interval rule. Corrections which must be applied in deriving the spin–orbit parameter λ have been summarized by Judd and Lindgren (1961) and by Conway and Wybourne (1963). A comparison of the energy levels of the $4f^6\,{}^7F$ multiplet in the Sm I spectrum, with and without various corrections, is given by Abragam and Bleaney (1970).

In table 18.25, adapted from Blume et al. (1964), are summarized various relevant properties appropriate to the tripositive lanthanide ions. Included are the $4f^n$ configuration of the ion, the ground state term, first excited term, and the energy separation between these (in cm^{-1}), as well as experimental and calculated values of the spin–orbit parameter λ, the calculated values being those of Blume et al. (1964).

3.2.2. *The crystalline electric field interaction*

Basically, the operator for the interaction of the magnetic ion with the CEF potential is the classical electrostatic potential energy

$$\mathcal{H}_{\mathrm{CEF}} = -|e| \sum_i V(x_i, y_i, z_i), \tag{18.107}$$

where the sum is over the magnetic electrons. For the lanthanide ions the wavefunctions on which $\mathcal{H}_{\mathrm{CEF}}$ operates will be characterized by the quantum numbers L, S, J, J_z following the application of the spin–orbit hamiltonian to the free-ion states, as described in section 3.2.1. To calculate the matrix elements of $\mathcal{H}_{\mathrm{CEF}}$, either of two methods may be used, i.e., that of direct integration [Bleaney and Stevens (1953), Hutchings (1964)] or of operator equivalents [Stevens (1953), Hutchings (1964)]. The latter method is more convenient and has been almost exclusively employed in the construction of spin hamiltonians for analysis of ESR spectra.

Briefly, the interaction of (18.107) is expressed in a multipole expansion in the same manner as described in section 1.3 for the electrostatic portion of the hyperfine interaction. Qualitatively, this expansion contains terms corresponding to the electric quadrupole, hexadecapole, etc., interactions of the ion with the CEF. These separate interactions will be characterized by products of parameters $\langle r^2\rangle$, $\langle r^4\rangle$, and $\langle r^6\rangle$, averaged over the $4f^n$ electron configuration of the ion, with lattice sums A_n^m representing the contributions of the surrounding ions to the various successive gradients of the CEF.

In the method of operator equivalents, the hamiltonian operator of (18.107) is replaced by "equivalent" angular momentum operators which operate on the L, S, J, J_z states of the ion resulting from the spin–orbit interaction. Thus,

$$\mathcal{H}_{\mathrm{CEF}} = \sum_{n,m} [A_n^m \langle r^n\rangle \theta_n] O_n^m, \tag{18.108}$$

TABLE 18.25

Summary of calculated and experimental spin–orbit interaction parameters λ for the tripositive lanthanide ions, adapted from Blume, et al. (1964), together with the electronic configurations and spectroscopic terms of the ground state and first excited state and their separation

Tripositive lanthanide ion	Ionic configuration	Ground-state term	Excited state term	Energy separation (cm^{-1})	Spin–orbit experimental (cm^{-1})	Parameter λ calculated (cm^{-1})
Ce	$4f^1$	$^2F_{5/2}$	$^2F_{7/2}$	2200	+640	+740
Pr	$4f^2$	$^3H_4$	$^3H_5$	2100	+375	+440
Nd	$4f^3$	$^4I_{9/2}$	$^4I_{11/2}$	1900	+300	+340
Pm	$4f^4$	$^5I_4$	$^5I_5$	1600		
Sm	$4f^5$	$^6H_{5/2}$	$^6H_{7/2}$	1000	+235	+270
Eu	$4f^6$	$^7F_0$	$^7F_1$	400		
Gd	$4f^7$	$^8S_{7/2}$	^6P	30 000		+245
Tb	$4f^8$	$^7F_6$	$^7F_5$	2000	−270	−320
Dy	$4f^9$	$^6H_{15/2}$	$^6H_{13/2}$		−365	−435
Ho	$4f^{10}$	$^5I_8$	$^5I_7$		−520	−590
Er	$4f^{11}$	$^4I_{15/2}$	$^4I_{13/2}$	6500	−820	−870
Tm	$4f^{12}$	$^3H_6$	$^3H_5$		−1375	−1430
Yb	$4f^{13}$	$^2F_{7/2}$	$^2F_{5/2}$	10 000	−2950	−3160

where for RE ions in general, $n = 2, 4, 6$ only, and $m = -n, -n+1, \ldots, 0, n-1, n$. The number of terms that enter is however greatly restricted by the point symmetry of the lanthanide site. The factors θ_n are numerical factors, the so-called reduced matrix elements (independent of m), frequently denoted in the literature by the alternative notations, $\theta_2 = \alpha_J = \langle J\|\alpha\|J\rangle$, $\theta_4 = \beta_J = \langle J\|\beta\|J\rangle$, $\theta_6 = \gamma_J = \langle J\|\gamma\|J\rangle$. Finally, the O_n^m represent the actual angular momentum operators corresponding to the cartesian coordinate forms that appear in the classical hamiltonian of (18.107).

A listing of the most commonly occurring terms appearing in (18.108) is given in table 18.26. Extensive tabulations of the reduced matrix elements θ_n are given in various sources in the literature [Hutchings (1964)] as well as in Abragam and Bleaney (1970) and in Alt'shuler and Kozyrev (1974). Similarly, these sources (and others) contain tabulations of the matrix elements of these operators between the various J, J_z states, so that the practical utilization of the operator equivalents method amounts for the most part to looking up various tabulated results.

In practice, the notation of the CEF hamiltonian (18.108) is compressed still further to the form [Hutchings (1964)]:

$$\mathcal{H}_{\text{CEF}} = \sum_{n,m} B_n^m O_n^m, \tag{18.109}$$

where the coefficients B_n^m replace the quantities in square brackets in (18.108). The principal axes system of the CEF is chosen so that the site symmetry reduces the number of terms in the sum on m to the smallest possible number in (18.108) or (18.109). For computational convenience, scaling factors f_n^m of the form, $b_n^m = f_n^m B_n^m$, are also usually introduced, chosen so as to be independent of m. Thus,

$$f_2^m = 3, \qquad f_4^m = 60, \qquad f_6^m = 1260.$$

Other scaling factor values are possible, however [Newman and Urban (1975)].

As remarked above, the operators O_n^m appearing in the CEF hamiltonian are determined by the site symmetry. For some of the most common symmetries occurring for lanthanide ions, the required operator complements are as follows [Hutchings (1964)]:

D_2 (garnets, lanthanide site)	$O_2^0, O_2^2, O_4^0, O_4^2, O_4^4, O_6^0, O_6^2, O_6^4, O_6^6$
C_{3v} (double nitrates)	$O_2^0, O_4^0, O_4^3, O_6^0, O_6^3, O_6^6$
C_{3h} (ethylsulfates, and some trichlorides)	$O_2^0, O_4^0, O_6^0, O_6^6$
Cubic (4-fold axes; CaF_2, ThO_2, etc.)	$O_4^0, O_4^4, O_6^0, O_6^4$
Cubic (trigonal axes; fluosilicates, etc.)	$O_4^0, O_4^3, O_6^0, O_6^3, O_6^6$.

Finally, in the important case of cubic symmetry, the B_n^m parameters referred

TABLE 18.26
Most commonly occurring operator equivalents required in crystalline electric field splitting calculations ($J_\pm = J_x \pm iJ_y$)

Operator	Angular momentum equivalent
O_2^0	$3J_z^2 - J(J+1)$
O_2^2	$\frac{1}{2}(J_+^2 + J_-^2)$
O_4^0	$[35J_z^4 - [30J(J+1) - 25]J_z^2 - 6J(J+1) + 3J^2(J+1)^2]$
O_4^2	$\frac{1}{4}\{[7J_z^2 - J(J+1) - 5](J_+^2 + J_-^2) + (J_+^2 + J_-^2)[7J_z^2 - J(J+1) - 5]\}$
O_4^3	$\frac{1}{4}[J_z(J_+^3 + J_-^3) + (J_+^3 + J_-^3)J_z]$
O_4^4	$\frac{1}{2}[J_+^4 + J_-^4]$
O_6^0	$231J_z^6 - 105[3J(J+1) - 7]J_z^4 + [105J^2(J+1)^2 - 525J(J+1) + 294]J_z^2 - 5J^3(J+1)^3 + 40J^2(J+1)^2 - 60J(J+1)$
O_6^2	$\frac{1}{4}\{[33J_z^4 - \{18J(J+1) + 123\}J_z^2 + J^2(J+1)^2 + 10J(J+1) + 102](J_+^2 + J_-^2) + (J_+^2 + J_-^2)[33J_z^4 - \{18J(J+1) + 123\}J_z^2(J+1)^2 + 10J(J+1) + 102]\}$
O_6^4	$\frac{1}{4}\{[11J_z^2 - J(J+1) - 38](J_+^4 + J_-^4) + (J_+^4 + J_-^4)[11J_z^2 - J(J+1) - 38]\}$
O_6^6	$\frac{1}{2}(J_+^6 + J_-^6)$

to axes coincident with the 4-fold symmetry directions satisfy the relations

$$B_4^4 = 5B_4^0 \qquad \text{and} \qquad B_6^4 = -21B_6^0,$$

with b_n^m behaving similarly. When the trigonal axes are used,

$$b_4^3 = \sqrt{2}b_4^0, \qquad b_6^3 = b_6^0\sqrt{8}, \qquad b_6^6 = 8b_6^0$$

[Buckmaster and Shing (1972)].

Operators such as O_n^m having $m = 0$ depend only on J_z and J^2 (see table 18.26), and in the J, J_z representation have diagonal matrix elements only. Further, the dependence on J_z is limited to even powers of J_z, so the matrix elements are the same for $+J_z$ and $-J_z$. States labelled by different values of $|J_z|$ will have different energies. The net effect of the CEF operators of type O_n^0 will be to yield a series of doubly-degenerate levels (exactly analogous to the pure nuclear quadrupole levels of section 1.3.2.1). In the case that J is an integer there will also be a singlet level corresponding to $J_z = 0$.

Those operators in the CEF hamiltonian for which $m \neq 0$ connect states of different J_z values only (off-diagonal elements). The difference in the J_z values of the states connected equals the value of m. The values of the coefficients B_n^m determine the degree of admixture of states of such different J_z values into the wave function of the basic doublet levels described above.

3.2.3. *Effective spins and g-tensors of lowest-lying CEF levels*

The g-tensor is obtained by evaluating the matrix elements of the magnetic hamiltonian $\mathcal{H}_M$ (18.105) using the wave functions of the lowest levels that result from solution of the eigenvalue problem for $\mathcal{H}_{CEF}$ (18.109). Illustrative calculations of the g-factors for lanthanide ions in various cases are given, for example, by Al'tshuler and Kozyrev (1974) and by Abragam and Bleaney (1970), among many others.

Considering first RE ions other than Eu^{2+}, Gd^{3+}, and Tb^{4+} (for which see section 3.2.5), four different cases account for the basic behavior encountered [Al'tschuler and Kozyrev (1974)]. The four cases correspond to ions with even and odd numbers of f-electrons (non-Kramers and Kramers ions, respectively) in CEF's of low and high symmetry (less-than-cubic and cubic, respectively). The properties associated with the four cases may be summarized as follows:

(a) Kramers ion in a CEF of low symmetry. The lowest spin–orbit term is split into doublets. Each Kramers doublet may be characterized by an effective spin $S' = \frac{1}{2}$ with an appropriate g-tensor. ESR is normally observed only for the lowest-lying doublet. If the first-excited doublet lies close to the ground doublet, second-order corrections to the g-tensor elements may be required.

(b) Non-Kramers ion is a CEF of low symmetry. Three different situations arise according to whether the lowest level is a doublet, two closely-spaced singlets, or a singlet. The first two cases may be described by effective spin $S' = \frac{1}{2}$. If the low-lying singlet level is sufficiently far below the first-excited level, no ESR absorption can occur in typical magnetic field strengths.

(c) Kramers ion in a CEF of cubic symmetry. The CEF levels are doublets

and quartets. If the lower level is a doublet, a single ESR transition occurs, independent of orientation of the magnetic field relative to the CEF axes. If the quartet level is lowest, the ESR transition is a complicated function of field orientation [Bleaney (1959)], corresponding to an effective spin $S' = \frac{3}{2}$.

(d) Non-Kramers ion is a CEF of cubic symmetry. The CEF levels are singlets, doublets, and triplets. ESR cannot occur for these doublets [Griffith (1963)], nor of course for the singlets, but can occur in principle for the triplets with effective spin $S' = 1$.

In many instances, observation of an ESR signal and measurement of the principal values of the g-tensor suffices to determine the symmetry of the lanthanide ion site in the crystal lattice. In addition, in many cases estimates of the B_n^m parameters which characterize the CEF (or at least the ratios of these parameters) may be inferred from the measured g-tensor values.

3.2.4. *Hyperfine interactions*

The energy levels of the lanthanide ionic moment are perturbed somewhat by interaction with the magnetic dipole and electric quadrupole moments of its nucleus and to a lesser extent the nuclei of ligand ions. The magnetic hyperfine interaction has been described from the nuclear standpoint in section 1.2.1 where the hyperfine constant A was introduced in the hamiltonian $\mathcal{H}_{\rm hf} = \boldsymbol{A}\boldsymbol{I} \cdot \boldsymbol{J}$ of (18.8). In any subset of levels resulting from the CEF interaction (18.109) which are characterized by an effective spin S', the magnetic hyperfine interaction can be written in the form

$$\mathcal{H}_{\rm hf} = \boldsymbol{S}' \cdot \tilde{A} \cdot \boldsymbol{I} \tag{18.110}$$

where $\tilde{A}$ is a tensor having the same principal axes as the g-tensor, and which satisfies the relations

$$\frac{A_x}{g_x} = \frac{A_y}{g_y} = \frac{A_z}{g_z} = \frac{A}{g_J} \tag{18.111}$$

[Elliott and Stevens (1953)], where

$$A = 2\beta_0\gamma_N\hbar\langle r^{-3}\rangle\langle J\|N\|J\rangle \tag{18.112}$$

results from combining (18.6) and (18.9) and g_J is the Landé g-factor given by (18.102). In consequence of these relations, the value of A can be obtained from the measured values of $\tilde{g}$ and $\tilde{A}$ along the principal axes without knowledge of the CEF parameters.

The nuclear electric quadrupole moment may also interact with the electric field gradient arising from the non-spherical distribution of the 4f electrons when the lanthanide ion is situated in a solid. The general form of the quadrupole interaction has been given in section 1.3.2. The principal value of the field gradient tensor, V_{zz}, due to the 4f electrons is given by (18.73) in section 2.1.1.2, and as indicated there in (18.72) should be multiplied by the Sternheimer shielding factor $(1 - R_Q)$ to take account of the distortion of the inner closed shells of the lanthanide ion by the open 4f shell. Other contributions to the total

field gradient at the nucleus, in particular the contributions from ionic charges in the lattice and from the conduction electrons, have been discussed in section 2.1.1.2.

3.2.5. *S-state ions*

The S-state ions are those with the 4f shell half-filled, yielding a $^8S_{7/2}$ ground state, and include Eu^{2+}, Gd^{3+}, and Tb^{4+}. For these ions $\langle \boldsymbol{L} \rangle = 0$ to a good approximation so that it is usually sufficient to take the magnetic (Zeeman) hamiltonian of (18.100) to be

$$\mathcal{H}_M = g\beta \boldsymbol{S} \cdot \boldsymbol{H}_0. \tag{18.113}$$

Departures of g from the isotropic free-electron value of 2.0023 are usually difficult to establish experimentally. Both Abragam and Bleaney (1970) and Newman and Urban (1975) discuss attempts to measure and to account for higher order Zeeman terms in the ESR of S-state ions, particularly Gd^{3+}.

Admixture of the spherically symmetric ground state with the anisotropic ($L \neq 0$) states leads to coupling of the crystalline site anisotropy with the spins. These interactions are similar to the usual crystal-field parametrization outlined in section 3.2.2 and may be expressed in the general form

$$\mathcal{H}_{CEF} = \sum_{\substack{\text{even} \\ n<2S}} \sum_m B_n^m O_n^m(S), \tag{18.114}$$

the operators O_n^m being the same as those in (18.80), only now expressed in terms of the components of $\boldsymbol{S}$ rather than of $\boldsymbol{J}$. As remarked by Newman and Urban (1975), the principal axes are chosen in practice so that the site symmetry reduces the number of terms in the sum on m to a small number. For the S-state ions, the interpretation of the parameters B_n^m is more complex than in the case of the non S-state ions outlined in section 3.2.2.

The so-called generalized spin hamiltonian for the S-state ions is the sum of $\mathcal{H}_M$ and $\mathcal{H}_{CEF}$. Since the strength of $\mathcal{H}_{CEF}$ is usually weak in comparison to the magnetic interaction, the resulting energy levels are entirely analogous to the corresponding nuclear case involving a weak quadrupole perturbation of magnetic levels, described in section 1.3.2.3. For $S = \frac{7}{2}$, there occur in zero applied field three levels, each doubly degenerate, reflecting the CEF interaction. Each of these levels is split by the applied field, resulting in a "fine structure" spectrum of transitions which become equally spaced in sufficiently strong fields. As in the nuclear case, the behavior of the energy levels and transitions depends on the orientation of $\boldsymbol{H}_0$ with respect to the axes of the CEF. In practice most investigations are carried out with single crystal specimens so that $\boldsymbol{H}_0$ may be oriented along specific crystalline directions.

Hyperfine interaction splittings are normally included in the form

$$\mathcal{H}_{hf} = \boldsymbol{S} \cdot \tilde{A} \cdot \boldsymbol{I}, \tag{18.115}$$

where $\tilde{A}$ is the hyperfine interaction tensor described in section 3.2.4. To a very

good first approximation one expects the magnetic hyperfine constant to be zero in the case of a half-filled electron shell. The small values observed in practice arise principally from the core-polarization contribution already mentioned in section 1.2.1. The nuclear quadrupole coupling due to the 4f electron shell is zero, but the coupling resulting from the electric field gradient due to the ionic charges in the lattice is not if the site symmetry is less than cubic.

3.3. *Electron spin relaxation processes*

Nuclear spin relaxation processes were discussed in section 1.4. As in the nuclear case, the dynamical properties of the electron spin system may be characterized principally by the two relaxation times, T_1 and T_2, the spin–lattice and spin–spin times, respectively. Of these, the spin–lattice time T_1 has by far the greater significance insofar as the study of ESR of RE ions is concerned, and this section will concern only the origins of T_1.

The understanding of spin–lattice relaxation processes for electron spins began with the papers of Van Vleck (1939, 1940) in which two types of interaction between the spin system and the lattice vibrations were described. These are still called the *direct process*, in which the spins exchange energy quanta with lattice vibrational modes which have the same frequency as the spin resonance itself, and the *Raman process* in which the difference frequency of two lattice modes is the spin resonance frequency. The frequencies of the lattice modes follow a Debye spectrum. In the direct process, the relaxation of an excited spin is accompanied by the emission of a phonon (an acoustic energy quantum) within a narrow range of energies into one of these modes. The Raman process is a second-order process and has a lower probability of occurrence than the direct process, but the number of different combinations of frequencies which satisfy the resonance condition is large. Whereas the relaxation rate in the direct process increases linearly with temperature, the rate in the Raman process increases much more rapidly, following a T^7 or T^9 law. Thus, the direct process tends to dominate at low temperatures (i.e., liquid helium temperature), and the Raman process dominates at higher temperatures. In addition to these two processes, a third, composite process, usually referred to as the Orbach process [Orbach (1961)], is important for RE ions. This is also a two-phonon process, but in this case a third energy level exists at an energy Δ' above the upper level of the lowest pair of levels. Relaxation proceeds via excitation to this level, followed by essentially instantaneous decay to the ground level.

In addition to the original papers in the literature, detailed derivations of the theoretical expressions for the relaxation rates according to these different processes may be found, for example, in Abragam and Bleaney (1970), in Al'tshuler and Kozyrev (1974), and in texts concerned exclusively with spin relaxation, such as Standley and Vaughan (1969) and Poole and Farrach (1971). Here we list only the dependence of the relaxation rate on temperature and the separation Δ of the lowest pair of levels. The direct process gives for non-Kramers ions, under the condition that $\Delta < kT$,

$$(T_1)^{-1} \sim \Delta^2 T \tag{18.116}$$

and for Kramers ions,

$$(T_1)^{-1} \sim \Delta^4 T. \tag{18.117}$$

The Raman process gives for non-Kramers ions

$$(T_1)^{-1} \sim T^7 \tag{18.118}$$

and for Kramers ions,

$$(T_1)^{-1} \sim T^9. \tag{18.119}$$

The Orbach process predicts that for both Kramers and non-Kramers ions

$$(T_1)^{-1} \sim \exp(-\Delta'/kT), \tag{18.120}$$

where Δ' is the energy of excitation to the third level, as defined above.

This brief outline of electron spin–lattice relaxation processes has assumed that all vibrational modes of the lattice are in thermal equilibrium with the large thermal reservoir provided by the surrounding cryogenic fluid or other thermal bath. However, these vibrational modes may not be in equilibrium with the spin system, as such equilibrium requires a certain time to become established. The situation can arise in which some vibrational modes absorb energy from the spin system faster than they can transfer it to other modes or to the thermal reservoir. This situation is referred to as the *phonon bottleneck*, and the spin lattice relaxation is said to be *bottlenecked.* In this case, the initial relaxation rate can be shown to be faster than the unbottlenecked rate, followed by a transition to a slower than normal rate. The overall behavior therefore cannot be described by a single exponential process. Detailed treatments of all aspects of phonon bottlenecking and its dependence on the nature of the particular ionic species involved may be found in the general references cited above.

3.4. *Relaxation effect in nuclear gamma resonance spectra*

Electron spin relaxation is also important in nuclear gamma resonance spectroscopy. When the spin relaxation rate $(T_1)^{-1}$ is slow in comparison to the natural (or lifetime) broadening of the excited nuclear level, the gamma resonance spectrum is that due to the hyperfine interaction arising from the host ion in the paramagnetic state. In this case, a fully resolved magnetic hyperfine spectrum is obtained in the paramagnetic state without application of an external magnetic field. For the typical case of electronic doublet levels described by an effective spin $S' = \frac{1}{2}$, between which an ESR transition would be observed, the magnitude of the hyperfine field is the same for both levels, but the signs are opposite. In the slow relaxing limit, the ion remains in one of these levels long enough to contribute this hyperfine splitting to the gamma resonance of its nucleus. In the absence of an applied field, the sign of the hyperfine field is undetected, hence the observed spectrum is just the magnetic hyperfine spectrum. A quadrupole contribution may also be observed, however.

At an intermediate relaxation rate, when $(T_1)^{-1}$ becomes comparable to the overall hyperfine splitting, expressed as a frequency, ω_{hf}, the resolved spectrum is replaced by a single broad resonance of approximately the same extent as the resolved hyperfine spectrum. Finally, when $(T_1)^{-1}$ becomes significantly faster than the hyperfine splitting, ω_{hf}, the spectrum collapses completely to a single narrow line. In this case, the two values of the hyperfine field (i.e., of opposite sign) have been effectively averaged to zero. In principle, a small shift analogous to the paramagnetic shift in NMR (or to the Knight shift in metals) can be detected in an external field, but this is only rarely the case. If there is an electric field gradient contribution from the electronic doublet levels, then there will still remain a quadrupole splitting of the gamma resonance transition.

Particularly at low temperatures, where the relaxation rate is very slow, it is possible to identify the crystal field ground state of a rare-earth ion present as a dilute impurity in a non-magnetic host crystal or metal. A general and detailed review of spin relaxation effects in nuclear gamma resonance has been given by Wickman and Wertheim (1968). Application to the case of rare-earth impurities in metals has been reviewed by Hirst (1974). Of particular significance is the fact that the NGR technique can be rather readily adapted to extreme low temperature systems (e.g., dilution refrigerators), making it important for the study of low-lying closely-spaced crystal field levels [Scherg et al. (1974)].

3.5. *Electron spin resonance in metals*

Under suitable conditions the ESR of several of the lanthanide ions may also be detected and studied when these are present as dilute impurities in metallic host crystals. In particular, during roughly the past ten years increases in spectrometer sensitivity have enabled the impurity concentrations required for such studies to be reduced to the parts-per-million level and in addition have made it possible to utilize single crystals of host metals, alloys, and intermetallic compounds. Consequently, there has occurred a strong surge of interest and activity in this aspect of the ESR of the lanthanide ions. Comprehensive reviews of the subject, including work on both lanthanide and non-lanthanide ions, have been given by Orbach et al. (1974) and by Taylor (1975). Baberschke (1976) has reviewed the applications of the ESR of Gd^{3+} and Eu^{2+} to the study of superconductors.

3.5.1. *g-shift and linewidth of the ESR in metals*

In brief, in a metallic host crystal, the presence of the conduction electrons contributes to a shift of the g-value of the impurity ion ESR from that observed for the same ion isolated in an insulating crystal. The conduction electron (CE) and impurity ion spin systems are coupled by an exchange interaction, the isotropic part of which is conventionally expressed by the Hamiltonian of eq. (18.87),

$$\mathcal{H}_{exch} = -\mathcal{J}_{sf}\boldsymbol{S}\cdot\boldsymbol{s},$$

where $\boldsymbol{S}$ and s are the spins of the impurity ion and the CE, respectively, and $\mathcal{J}_{sf}$ is the sf exchange interaction parameter. Neglecting relaxation effects, the g-shift Δg_0 from the g-value in an insulator host crystal is given to a first approximation by

$$\Delta g_0 = \mathcal{J}_{sf} N(E_F), \tag{18.121}$$

where $N(E_F)$ is the density-of-states of the conduction electrons at the Fermi level.

At sufficiently low impurity concentrations the relaxation rate of the conduction electrons to the lattice, δ_{eL}, is much faster than the relaxation rate to the impurity spins, δ_{ei}, ($\delta_{eL} \gg \delta_{ei}$), and consequently the conduction electron system is in thermal equilibrium with the lattice. This causes the ESR linewidth ΔH, which is proportional to the relaxation rate, δ_{ie}, of the impurity spins to the conduction electrons, to have a temperature dependence given by

$$\Delta H = a + bT \tag{18.122}$$

with

$$b = \frac{\mathrm{d}(\Delta H)}{\mathrm{d}T} = \frac{k\pi}{g\beta_0}(\Delta g_0)^2, \tag{18.123}$$

and where a is the residual, temperature-independent linewidth. Implicit in this formulation is the fact that at low impurity concentrations the rate of direct impurity spin relaxation to the lattice, δ_{iL}, is negligible in comparison to δ_{ie}. The relation expressed by (18.123) is entirely analogous to the Korringa relation between the nuclear spin relaxation time and the Knight shift in a metal [eq. (18.67)], and for this reason the impurity concentration and temperature regime within which this behavior is observed is frequently referred to as the Korringa limit.

In terms of the relaxation rate δ_{ie}, the temperature dependence of the linewidth is given by

$$b = \mathrm{d}(\Delta H)/\mathrm{d}T = \hbar\delta_{ie}/g\beta_0 T, \tag{18.124}$$

with the rate δ_{ie} given in terms of $\mathcal{J}_{sf}$ and $N(E_F)$ by

$$\delta_{ie} = \pi N^2(E_F)\mathcal{J}_{sf}^2 kT. \tag{18.125}$$

Measurement of the g-shift and thermal broadening of the impurity spin resonance therefore provide two separate means of estimating $\mathcal{J}_{sf}$. These basic equations must be modified, in particular, to take account of exchange enhancement of the conduction electron susceptibility [Rettori, et al. (1974)], and this point is considered further briefly in section 4.2.2. in connection with the analysis of ESR results on the RAl_2 compounds.

More generally, at arbitrary temperature and concentration of the lanthanide impurity ion, the dynamical consequences of the coupling of the two spin systems must be taken into account. The principal complication arises from the so-called bottleneck in the relaxation rate δ_{ie}. This occurs when the rate of

conduction electron spin relaxation to the impurity ions, δ_{ei}, becomes comparable to the direct CE relaxation rate to the lattice, δ_{eL}. Hasegawa (1959) first derived generalizations of (18.121) and (18.123) appropriate to these conditions. More recently, Cottet et al. (1968) obtained coupled equations of greater generality for the two spin systems. In a somewhat simplified form [Baberschke (1976)], the linewidth and g-shift expressions become:

$$\Delta H = \frac{\delta_{eL}}{\delta_{ei} + \delta_{eL}} \Delta H_K \tag{18.126}$$

and

$$\Delta g = \left(\frac{\delta_{eL}}{\delta_{ei} + \delta_{eL}}\right)^2 \Delta g. \tag{18.127}$$

where the subscript K has been added to ΔH on the right-hand side of (18.126) to indicate that this is the linewidth in the Korringa limit, as given by eqs. (18.122), (18.123) and (18.125). As emphasized by Baberschke (1976), the experiments become complicated in the bottlenecked regime because the ESR parameters must be determined as functions of temperature *and* impurity concentration. By decreasing the impurity ion concentration the spin-flip scattering rate of the CE spins to the impurity spins is reduced, breaking the bottleneck and bringing the system into the isothermal or Korringa limit. However, increasing the CE spin-flip scattering rate to the lattice, δ_{eL}, by for example introducing additional impurities (e.g., Th) whose strong spin–orbit scattering increases δ_{eL}, can also open the bottlenecked condition. Fitting the concentration dependence of ΔH and Δg enables the relaxation rates δ_{ei} and δ_{eL} to be determined.

4. Survey of applications of ESR methods

As in section 2, the present section presents a brief overview of the extent of ESR studies of lanthanide ions in the rare earth metals, their alloys, and compounds. The material presented is intended to be representative and most attention is paid to the main classes of rare earth compounds which have been most thoroughly investigated. These include the ethylsulfates and halides. Relatively recent studies of metals, alloys, and intermetallic compounds are also briefly reviewed.

Investigations of the ESR spectra of lanthanide ions present as dilute impurities in host crystals of non rare earth compounds (halides, oxides, tungstates, molydates, semiconductors, etc.) have provided much information on site symmetries and crystalline electric field parameters in such materials. A review of these applications of lanthanide ion ESR lies beyond the scope of this chapter, however various tabulations of such data for lanthanide ions appear in the books by Abragam and Bleaney (1970), Al'tshuler and Kozyrev (1974), and Wertheim et al. (1971), as well as in reviews concerned with particular classes of host crystals, as for example, in the survey of ESR spectra of Gd^{3+} in single

crystals [Buckmaster and Shing (1972)], and in the review of ESR of ions in complex oxides [Low and Offenbacher (1965)].

4.1. *ESR in non-metals*

4.1.1. *The rare earth ethylsulfates*

The experimental results for the various lanthanide ions diluted in host crystals of lanthanum and/or yttrium ethylsulfate are summarized in table 18.27. Historically, the ethylsulfates were the first class of compounds on which ESR measurements of the lanthanide ions were made. As noted in section 3.2.2, the point symmetry at the lanthanide site is C_{3h}, and just four parameters are required to characterize the crystalline electric field (CEF). These are, in notation of eq. (18.109), B_2^0, B_4^0, B_6^0, and B_6^6. In consequence of the axial symmetry of the site, the g-factor and magnetic hyperfine coupling constant A are characterized by parallel and perpendicular components, $g_\parallel$ and $g_\perp$, and $A_\parallel$ and $A_\perp$, respectively. Nuclear quadrupole coupling constants are generally small and have not been included in the table.

The ESR spectra do not themselves yield estimates of the CEF parameters. However, when taken in conjunction with other data the wave-functions of the lowest levels can be accurately checked by the g-factor values which they yield. In the case of Pr^{3+} in lanthanum ethyl sulfate, for example, Baker and Bleaney (1958) originally estimated the CEF parameters on the basis of the magnetic susceptibility data then available. Subsequently, these parameters have been determined from high resolution optical data for all of the lanthanide ions in the ethylsulfates. A complete listing of these is given, for example, in Abragam and Bleaney (1970).

In addition to the ESR studies involving the non S-state ions, there have also been many experiments and measurements concerning the S-state ions Gd^{3+} and Eu^{2+} in the ethylsulfates. As outlined briefly in section 3.2.5, the theoretical understanding of the origin of the CEF hamiltonian is much more complex. In addition, the CEF and Zeeman hamiltonians are of about equal significance, so that the experimental parametrization of the observed spectra becomes considerably more involved. Even though the g-tensor is isotropic or very close to isotropic, four crystal field parameters are required in C_{3h} symmetry.

Among the mechanisms which have been considered in detail, the first results from the simultaneous action of the CEF and the spin–orbit coupling [Van Vleck and Penney (1934)]. Further mechanisms have been considered by Pryce (1950) and have been reviewed by, for example, Hutchison et al. (1957). Wybroune (1966) made detailed calculations of the CEF splitting of Gd^{3+} in the ethylsulfate (actually $3B_2^0$), obtaining a value twice the experimental, but of opposite sign. These difficulties have been considered in detail most recently by Newman and Urban (1975) who have reviewed much of the experimental data as well as the theoretical approaches. An extensive tabulation of experimental data for Gd^{3+} has been given by Buckmaster and Shing (1972).

TABLE 18.27

Resumé of results and studies of the ESR of lanthanide ions (except Gd^{3+} and Eu^{2+}) in ethylsulfate (ES) host crystals. g-tensor and hyperfine tensor components are given in the order $g_\parallel$, $g_\perp$ and $A_\parallel$, $A_\perp$, respectively.

Ion	Host crystal	Temperature (K)	g-tensor	Isotope	Hyperfine constants (MHz)	Remarks	Reference
Ce^{3+}	LaES	4.2	0.955, 2.185				Bogle et al. (1951)
Ce^{3+}	LaES	1.4–1.8				T_1 measurements	Scott and Jeffries (1962)
Ce^{3+}	YES	1.2–2.5				T_1 measurements	Larson and Jeffries (1966)
Pr^{3+}	LaES	20	1.69, <0.03	141	2490		Baker and Bleaney (1958)
Pr^{3+}	LaES	1.2–3				T_1 measurements	Larson and Jeffries (1966)
Pr^{3+}	YES	1.2–3				T_1 measurements	Larson and Jeffries (1966)
Nd^{3+}	LaES	4.2	3.6274, 2.2163	143	-1125, -595		Erikson (1966)
Nd^{3+}	LaES	1.4–5				T_1 measurements	Scott and Jeffries (1962)
Nd^{3+}	YES	1.2–5				T_1 measurements	Larson and Jeffries (1966)
Pm^{3+}	LaES	4.2	0.432	147	495		Stapleton et al. (1961)
Sm^{3+}	LaES	4.2	0.596, 0.604	147	-180, 750		Bogle and Scovil (1952)
Sm^{3+}	LaES YES	1.4–5				T_1 measurement	Larson and Jeffries (1966)
Tb^{3+}	YES	20	17.72, <0.3	159	6265		Baker and Bleaney (1958)
Tb^{3+}	YES	1.5–5				T_1 measurement	Larson and Jeffries (1966)
Ho^{3+}	YES	13	15.41	165	10 060		Baker and Bleaney (1958)
Er^{3+}	LaES	4.2	1.47, 8.85	167	-156, 941		Bogle et al. (1952)
Er^{3+}	LaES YES	1.2–4.6				T_1 measurement	Larson and Jeffries (1966)

The ethylsulfates have been the basis for detailed investigations of the spin–lattice relaxation processes discussed in section 3.3. Scott and Jeffries (1962) and Larson and Jeffries (1966) studied the relaxation of most of the lanthanide ions in both lanthanum and yttrium ethylsulfate host crystals. The Raman and Orbach process are usually observed, and in some cases the direct process is observed as well at low temperature (e.g., Nd^{3+} in the La salt). The latter possibility arises when the first excited CEF level lies too far above the ground doublet to yield significant Orbach contribution. In two cases the phonon bottleneck effect was observed, in that at low temperatures a T^2 dependence of $(T_1)^{-1}$ was obtained rather than the T dependence expected on the basis of the direct process (section 3.3). In addition, in several cases (Ce in the Y salt and Sm in both the Y and La salts) the measured Orbach relaxation rate yielded a determination of a crystal field level which had not been previously determined. The value of the splitting Δ' determined for these magnetically dilute crystals was also found to differ significantly from the corresponding value in magnetically concentrated cases. Complete tabulations of the measured relaxation rates have been given by Standley and Vaughan (1969) and by Al'tshuler and Kozyrev (1974).

4.1.2. *The rare earth halides*

ESR studies of the rare earth halides have been concerned primarily with the trichlorides and trifluorides. As mentioned in section 2.2.3 in connection with NMR work on these compounds, the trichlorides have the rare earth ion in a hexagonal site (C_{3h}). As an example, we consider the measurements of Hutchison and Wong (1958) in which the ESR of essentially all the lanthanide ions incorporated in single crystal $LaCl_3$ was studied. The direct experimental results, g-factors and hyperfine constants are listed in table 18.28. Using optical data then available [Freed and Sayre (1955)] for Pr^{3+} in $LaCl_3$, together with the calculated ratio B_6^0/B_6^6 based on the crystal structure, the four CEF parameters required for the C_{3h} symmetry were estimated. These values were then scaled to the other RE ions according to the estimated dependence, $\langle r^n \rangle \sim (Z-55)^{-n/4}$. The wavefunctions and energies of the CEF levels were then determined and the g-values of the lowest pair of levels calculated. These are generally in good agreement with the experimental values, showing the correctness of the basic theory. However, many differences in detail appear, due to the method of estimating the CEF parameters as well as to the neglect of higher order effects (e.g., contributions for admixtures of higher lying levels). Detailed discussion of many of these points has been given by Abragam and Bleaney (1970).

The ESR of Ce^{3+}, Nd^{3+}, Dy^{3+}, Er^{3+}, and Yb^{3+} in the hydrated trichloride, $YCl_3 \cdot 6H_2O$, has been investigated by Schulz and Jeffries (1967). In these materials the lanthanide site symmetry is only C_2, however the ESR results indicate an effective CEF of nearly C_6 or C_{3h} symmetry. Spin–lattice relaxation time measurements were also made on these systems (except for Yb^{3+}) as indicated by the data tabulation in table 18.28. Usually a Raman process term was found, of order $(T_1)^{-1} \sim 10^{+4}\, T^9\, \mathrm{sec}^{-1}$. An exponential Orbach process was

TABLE 18.28

Representative ESR results and studies of lanthanide ions in the rare earth halides. g-tensor components are given in the order g_x, g_y, g_z or $g_\parallel$, $g_\perp$.

Ion	Host crystal	Temperature (K)	g-tensor	Remarks	Reference
Ce^{3+}	LaF_3	20	0.32, 0.90, 2.61		Baker and Rubins (1960)
Ce^{3+}	LaF_3	1.3–5		T_1 measurements	Schulz and Jeffries (1966)
Nd^{3+}	LaF_3	4.2	1.356, 1.092, 3.11		Baker and Rubins (1960)
Nd^{3+}	LaF_3	0.2–5		T_1 measurements	Schulz and Jeffries (1966)
Sm^{3+}	LaF_3	1.4–5		T_1 measurements	Schulz and Jeffries (1966)
Gd^{3+}	LaF_3	90	1.990	CEF parameters determined	Jones et al. (1959)
Gd^{3+}	LaF_3	1.3–5		T_1 measurements	Schulz and Jeffries (1966)
Dy^{3+}	LaF_3	4.2	7.0, 1.5, 13.8		Baker and Rubins (1960)
Dy^{3+}	LaF_3	1.3–5		T_1 measurements	Schulz and Jeffries (1966)
Er^{3+}	LaF_3	14	2.98, 4.91, 11.09		Baker and Rubins (1960)
Er^{3+}	LaF_3	0.2–5		T_1 measurements	Schulz and Jeffries (1966)
Yb^{3+}	LaF_3	20	3.76, 5.20, 1.21		Baker and Rubins (1960)
Yb^{3+}	LaF_3	0.2–5		T_1 measurements	Schulz and Jeffries (1966)
Pr^{3+}	$LaCl_3$	4.2	1.035, 0.10	$A_\parallel = 1500$ MHz for ^{141}Pr	Hutchison and Wong (1958)
Pr^{3+}	$LaCl_3$	1.7–4.2		T_1 measurements	Mikkelson and Stapleton (1965)
Nd^{3+}	$LaCl_3$	4.2	3.996, 1.763	$A_\parallel = -1275$ MHz $A_\perp = 500$ MHz for ^{143}Nd	Hutchison and Wong (1958)
Nd^{3+}	$LaCl_3$	1.1–10		T_1 measurements	Mangum and Hudson (1966)
Sm^{3+}	$LaCl_3$	4.2	0.584, 0.613	$A_\parallel = -1820$ MHz $A_\perp = 735$ MHz for ^{147}Sm	Hutchison and Wong (1958)
Sm^{3+}	$LaCl_3$	1.0–4.2		T_1 measurements	Mangum and Hudson (1966)
Gd^{3+}	$LaCl_3$	4.2	1.9927	CEF parameters determined temperature dependence of g and CEF in range 2–293 K	Boatner and Abraham (1967)
Tb^{3+}	$LaCl_3$	4.2	17.78, 0.01	$A_\parallel = 6365$ MHz for ^{159}Tb	Hutchison and Wong (1958)
Tb^{3+}	$LaCl_3$	1.7–4.2		T_1 measurements	Mikkelson and Stapleton (1965)
Ho^{3+}	$LaCl_3$	4.2	16.01, 0	$A_\parallel = 10\,520$ MHz for ^{165}Ho	Hutchison and Wong (1958)
Ho^{3+}	$LaCl_3$	1.14		T_1 measurement	Mangum and Hudson (1966)
Er^{3+}	$LaCl_3$	4.2	1.989, 8.757	$A_\parallel = -200$ MHz $A_\perp = -910$ MHz for ^{167}Er	Hutchison and Wong (1958)
Er^{3+}	$LaCl_3$	1.1–10		T_1 measurements	Mangum and Hudson (1966)
R^{3+}	$YCl_3 6H_2O$	0.2–5.5		T_1 measurements R = Ce, Nd, Dy, Er, Yb	Schulz and Jeffries (1967)

also observed in all four cases and the separation Δ' of the excited level above the ground state (see section 3.3) so determined was found to be in excellent agreement with results of optical measurements in the corresponding concentrated salts.

The ESR measurements on lanthanide ions in LaF_3 indicate six magnetically inequivalent sites having C_{2h} symmetry or lower [Baker and Rubins (1961)]. This result is not in agreement with the NMR measurements of Andersson and Proctor (1968) which indicate only three inequivalent sites (see section 2.3.2). In any event, each of the six ESR sites is described by identical spin Hamiltonian parameters, the only difference being in the orientation of the principal axes of the g-tensor with respect to the crystalline c axis. Because of the low symmetry of the CEF, one expects that all degeneracy in the ground state multiplet will be completely lifted in the case of non-Kramers ions so that in these cases ESR will not be detectable [Schulz and Jeffries (1966)]. The measured g-tensor components are listed in table 18.28.

Schulz and Jeffries (1966) made a detailed study of spin–lattice relaxation in the trifluorides. The general features of these measurements are that a Raman process is usually found with $(T_1)^{-1} \sim 10^{-3}\, T^9\, \mathrm{sec}^{-1}$. For Nd^{3+} and Er^{3+} an Orbach term was found with the splitting Δ' in close agreement with optical measurements. No evidence was found for an Orbach term in the case of Yb^{3+}, indicating that the first excited level must lie at least 75 K above the ground state. In other cases (Ce^{3+} and Dy^{3+}) it appeared that cross-relaxation to other impurities or by way of strongly coupled pairs of ions prevented the observation of the Orbach term. Similarly, the true direct process was not detected at low temperatures, except possibly for Er^{3+} and Nd^{3+} in very low concentrations, because of pair coupling. More detailed summaries of the results of spin–lattice relaxation time measurements have been given by Standley and Vaughan (1969) and by Al'tshuler and Kozyrev (1974).

With respect to Gd^{3+} ESR spectra in the halides, Sharma (1971) has studied the systematics of the CEF parameters of Gd^{3+} in a series of RE trifluorides, and Misra and Sharp (1977) have investigated Gd^{3+} in the trichloride hexahydrates of Y, Nd, Sm, Eu, as well as the remaining heavy rare-earths. In all cases, it is found that the axial zero-field (CEF) splitting parameter, $b_2^0 = 3\, B_2^0$ is a linear function of the ionic radius of the host crystal rare earth ion.

4.2. *ESR in metallic systems*

Similarly to the ESR of the lanthanide ions in insulators, in metallic systems ESR contributes to understanding of the spectroscopic state of the ion in the host lattice and the symmetry and magnitude of the crystalline electric field at the lanthanide site. The g-shift of the resonance may be related to the sf exchange interaction and the spin polarization of the conduction electrons, and the temperature and concentration dependence of the g-shift and resonance linewidth relate to the bottleneck effect in the spin relaxation process. These relationships have been outlined in section 3.5.

TABLE 18.29
Resumé of representative electron spin resonance studies of lanthanide ions in the rare-earth metals.

Host metal	Impurity ion	g-shift	Remarks	Reference
Sc	Gd^{3+}	+0.14	single crystal strongly bottlenecked system $3B_2^0 = -330$ Oe	Nagel and Baberschke (1977)
Sc	Er^{3+}		single crystal find Γ_7 ground state with $g_\parallel = 10.40$ and $g_\perp = 5.02$	Keller et al. (1974)
Y	Gd^{3+}	+0.15	single crystal: bottlenecked estimate $\mathcal{J}_{sf}(0) = 0.08$ eV $3B_2^0 = -150$ Oe	Weimann and Elschner (1973)
La	Gd^{3+}	+0.117	fcc phase; bottlenecked	Koopmann et al. (1975)
La	Eu^{2+}		fcc phase; similar to Gd:La	Koopmann et al. (1975)
La	Er^{3+}		hexagonal phase; powder sample find $g = 6.80$ consistent with Γ_7 ground state	Kochalayev et al. (1975)
Eu	Eu^{2+}	+0.038		Guimaraes et al. (1977)
Yb	Eu^{2+}	−0.023		Schäfer et al. (1969)
Lu	Gd^{3+}	+0.108	single crystal; not bottlenecked $3B_2^0 = -63$ Oe	Baberschke and Nagel (1976)

This section presents a brief survey of metallic systems in which ESR of lanthanide ions have been studied. Only those host materials are included which may be classed as metals, alloys, or intermetallic compounds of the rare earths, in parallel with the survey of applications of ESR in insulators in section 4.1. The following subsections treat, respectively, rare-earth metals and alloys (especially those based on La, Y, Sc, and Lu), Laves phase intermetallic compounds, and the so-called Van Vleck para-magnetic compounds, of which many fall in the category of the rare earth mono-pnictides. The ESR of lanthanide ions in non-lanthanide host materials such as the noble metals is not included. Such systems are discussed in the extensive reviews by Orbach et al. (1974) and by Taylor (1975).

4.2.1. *ESR in the rare earth metals*

The electron spin resonance of the S-state ion Gd^{3+} present as a dilute impurity has been studied in the non-magnetic host metals scandium, yttrium, lanthanum and lutetium. Nagel and Baberschke (1977) found the ESR of Gd^{3+} in single-crystal Sc to be strongly bottlenecked, leading to an anomalously large variation of the resonance field and linewidth with crystal orientation in the applied field. At the other extreme of the rare earth series, the ESR of Gd^{3+} in lutetium is unbottlenecked (Baberschke and Nagel, 1976). However, the g-shift (section 3.5) is in both cases positive. The g-shift is also positive for Gd^{3+} in

lanthanum and yttrium. Since the positive g-shift implies a positive value of the exchange interaction and therefore ferromagnetic coupling, these results show that in all these metals the s band contribution to the exchange interaction dominates over any d band contribution. On the other hand, the g-shift of Eu^{2+} in ytterbium was found to be negative, implying the reverse situation [Schäffer, et al. (1969)]. These measurements are summarized briefly in table 18.29.

Detailed discussion of the various relaxation rates, in particular that from the localized moment to the conduction electrons, δ_{ie}, and the reverse thereof, δ_{ei}, (section 3.5) and their origins has been given by Orbach et al. (1974), Taylor (1975), and Baberschke (1976). The significance of these for understanding the properties of superconducting metals is emphasized by Baberschke (1976).

ESR has also been observed in the paramagnetic state of the metals Eu and Gd themselves. Difficulties arise in this case because of the high concentration of magnetic moments which leads to a very substantial magnetization of the sample in the presence of an applied magnetic field. As discussed by Guimaraes et al. (1977) two instrumental effects occur which make measurement of the g-shift and linewidth difficult. These are the displacement of the apparent g-value by the local field and the additional line broadening which results from the spread in local field values in a powder sample. The recent measurements of Guimaraes et al. (1977) find Δg to be negative in Gd, in agreement with several earlier measurements [Peter et al. (1962), Burzo and Domsa (1972)]. However, in the case of Eu metal the g-shift is found to be positive ($\Delta g = +0.038 \pm 0.004$). In light of calculated densities of states for metallic Gd and Eu [Keeton and Loucks (1968), Freeman (1972)] which show that the Fermi level falls at a peak in Gd and at a minimum in Eu, the positive shift in europium is interpreted as arising from the resultant strong reduction of the d band susceptibility. The s band contribution, even though largely bottlenecked, may then dominate that of the d band, causing a resultant positive shift.

4.2.2. *ESR in intermetallic compounds*

Two classes of rare earth intermetallic compounds have been extensively investigated by means of the ESR of lanthanide ions, particularly Gd^{3+}. These are the cubic Laves phase compounds, RM_2, where R is typically La or Y and M is a transition metal or aluminum, and the rare earth monopnictides, RX, where X = N, P, As, Sb, and Bi, and R is La, Pr, or Tm. These two classes of compounds have received the greatest attention because in these structures the rare earth ion occupies a site with cubic symmetry and because many of these do not order magnetically. In the case of the monopnictides, even for the nominally magnetic ions Pr^{3+} and Tm^{3+}, the lowest CEF level is a singlet so that for example, TmAs, TmSb, etc. do not order but possess a temperature independent Van Vleck susceptibility at low temperatures. This point has been discussed in connection with the so-called hyperfine-enhanced NMR of ^{169}Tm and ^{141}Pr in section 2.2.3.1. Some of the Laves phase compounds are superconducting, and the introduction of paramagnetic impurities provides an opportunity to study their effects on the superconducting parameters as well as the

TABLE 18.30
Resumé of representative electron spin resonance studies of lanthanide ions in the cubic Laves phase compounds. Except where noted, the ion studied was Gd^{3+}.

Compound	Limiting g-shift	Remarks	Reference
$LaAl_2$	+0.065	concentration dependence of Δg indicates bottlenecking except at lowest Gd concentrations (< 2500 ppm)	Taylor (1973)
$LaAl_2$	+0.11	introduced Th impurities to open bottleneck	Davidov et al. (1973)
$LuAl_2$	+0.085	concentration dependence of Δg indicates bottlenecking added Th to open bottleneck	Rettori et al. (1974)
YAl_2	+0.076		Schäfer et al. (1972)
$ScAl_2$	+0.072	introduced Th impurities to open bottleneck	Chock et al. (1977)
$LaAl_2$	+0.11	opened bottleneck by adding Ce impurities	Beuermann and Fischer (1976)
$LuAl_2$	+0.085	studied spin–flip scattering	Rettori et al. (1975)
YAl_2	+0.07	of Ce by opening bottleneck with Ce impurities	
$LuAl_2$		observed ESR of Er^{3+} $g = 6.80$ appropriate to Γ_7 CEF ground state	Rettori et al. (1975)
$LaRu_2$	−0.15	lowest Gd concentration 500 ppm	Davidov et al. (1969)
$LaRu_2$	−0.172	Δg reduced to −0.155 in superconducting state spin–flip scattering rates determined	Rettori et al. (1973c)
$ThRu_2$	−0.035	Δg increased to −0.038 in superconducting state	Davidov et al. (1974c)
$CeRu_2$	−0.05	Δg increases to −0.065 in superconducting state	Davidov et al. (1974)
$LaOs_2$	−0.062	minimum concentration of Gd was 100 ppm	Schrittenlacher et al. (1975)

co-existence of ferromagnetism and superconductivity. Tables 18.30 and 18.31 provide a brief summary of the experimental work.

The results obtained from the ESR of Gd^{3+} in the cubic Laves phase compounds RAl_2, with R = Sc, Y, La, and Lu, have been summarized and interpreted by Chock et al. (1977). The ESR of Gd^{3+} in these compounds shows bottlenecked behavior (section 3.5), indicating that the relaxation rate of the conduction electron spins to the lattice is not fast enough to accomodate relaxation of the local moments. This bottleneck can be broken by going to sufficiently dilute concentrations of the paramagnetic impurity, as observed by Taylor (1973) in the case of $LaAl_2$, or by adding a non-magnetic impurity (e.g., thorium) as observed in the case of $ScAl_2$ by Chock et al. (1977). Assuming

TABLE 18.31
Resumé of representative recent studies of the ESR of lanthanide ions in the cubic rare-earth monopnictides.

Host compound	Ion	Temperature range (K)	Remarks	Reference
LaSb	Gd^{3+}	1.3, 4.2	single crystal resolved fine structure CEF parameter $b_4 = 30$ Oe	Davidov et al. (1974a)
YSb	R^{3+}	1.8–4.2	R = Gd, Dy, Er, Yb, Ce some single crystals CEF ground states determined and CEF parameter b_4 measured (for Gd)	Davidov et al. (1974b)
TmSb	Gd^{3+}	4–80	giant g-shift at low temperature temperature dependence follows host susceptibility	Davidov and Baberschke (1975)
LaSb	Gd^{3+}	1.7–300	single crystals temperature dependence of line shape studied	Urban et al. (1975)
LaSb	Dy^{3+}	1.4	single crystal angular variation of linewidth interpreted in terms of random stress model with tetragonal distortions	Davidov et al. (1975a)
YX	Gd^{3+}	4.2–300	X = P, As, Sb very small g-shifts estimate $\mathcal{F}_{sf} \cong 0.015$ eV in YSb	Sugawara and Huang (1975)
RX	Gd^{3+}	1.3–4.2	R = Pr, Tm; X = Sb, Bi giant g-shifts observed some single crystals	Rettori et al. (1975a)
PrSb	Gd^{3+}	4.2–70	some single crystals studied temperature dependence of linewidth	Davidov et al. (1975b)
RsB	Er^{3+}	1.3–4.2	R = Y, La, Pr, Tm single crystals fine structure observed	Rettori et al. (1975b)
PrX TmZ	Dy^{3+}	5–250	X = P, As, Sb, Bi; Z = P, As temperature dependence of g-shifts follows susceptibilities determined exchange coupling between host and impurity ions	Sugawara and Huang (1976)
PrX TmZ	Ce^{3+}	5–250	X = S, P; Z = S, As same comments as above	Sugawara and Huang (1976)
PrSb TmBi	Dy^{3+}	1.8	determined exchange coupling between host and impurity ions	Levin et al. (1977)
RBi	Er^{3+}	1.4, 1.8	single crystals fine structure resolved determined exchange coupling between host and impurity ions	Levin et al. (1977)
PrSb	Yb^{3+}	1.8	negligible g-shift	Levin et al. (1977)

wavevector independent model for the conduction electron – local moment exchange interaction, Chock et al. (1977) concluded that the s bands of this series of compounds are very similar and that the exchange parameters and scattering rates due to both Gd and Th impurities are essentially constant throughout the series. Why $LaAl_2$ should be a superconductor, whereas the others are not, may be a consequence of the presence of band electrons other than s in this case.

As listed in table 18.30, a large number of studies have been made of the ESR of Gd^{3+} in both the normal and superconducting phases of the compounds $LaRu_2$, $CeRu_2$, and $LaOs_2$. As outlined by Baberschke (1976), the conduction electron – impurity spin relaxation rate, δ_{ei}, is related to the initial depression of the superconducting transition temperature T_c caused by the magnetic impurity moment. In a bottlenecked system, the measurement of the ESR linewidth may therefore be directly compared with the experimental depression of T_c without recourse to estimates of the density of states for the conduction electrons. Almost perfect agreement is obtained between these two measured quantities in the cases of $LaAl_2$ and fcc La metal. Only qualitative agreement is obtained in the cases of $LaOs_2$, $LaRu_2$, and $CeRu_2$ because of the difficulty of estimating δ_{ei} in these systems in which full bottlenecking of the relaxation process does not occur.

References

Abe, T., 1975, J. Phys. Soc. Japan **38**, 1782.

Abragam, A. and M.H.L. Pryce, 1951, Proc. Roy. Soc. **A206**, 173.

Abragam, A., 1961, "The Principles of Nuclear Magnetism" (Oxford University Press, London).

Abragam, A. and B. Bleaney, 1970, "Electron Paramagnetic Resonance of Transition Ions" (Oxford University Press, London).

Alger, R.S., 1968, "EPR: Techniques and Applications (Interscience).

Al'tshuler, S.A. and R.M. Mineeva, 1965, Fiz. Tverd. Tela **7**, 310. (Translation: Societ Physics–Solid State **7**, 247).

Al'tshuler, S.A. and M.A. Teplov, 1967, Zh. Eksperim i Teor. Fiz.–Pis'ma Redakt. **5**, 209 (translation: JETP Lett. **5**, 167).

Al'tshuler, S.A., 1969, JETP Lett. **9**, 26.

Al'tshuler, S.A. and B.M. Kozyrev, 1974, "Electron Paramagnetic Resonance in Compounds of Transition Elements", 2nd revised edition (John Wiley, New York).

Andersson, L.O. and W.G. Proctor, 1968, Z. Kristal. **127**, 366.

Arif, S.K. and M.A.H. McCausland, 1975a, J. Phys. F **5**, L247.

Arif, S.K., D.St.P. Bunbury and G.J. Bowden, 1975b, J. Phys. F **5**, 1785.

Arif, S.K., D.St.P. Bunbury and G.J. Bowden, 1975c, J. Phys. F **5**, 1792.

Arif, S.K., G.J. Bowden and D.St.P. Bunbury, 1975d, in: P.S. Allen, E.R. Andrew and C.A. Bates, eds., "Magnetic Resonance and Related Phenomena" (North-Holland, Amsterdam), p. 85.

Arif, S.K., I. Sigalas and D.St.P. Bunbury, 1977, Phys. Stat. Solidi (a) **41**, 585.

Atzmony, U., E.R. Bauminger, D. Lebenbaum, A. Mustachi, S. Ofer, and J.H. Wernick, 1967, Phys. Rev. **163**, 314.

Atzmony, U., E.R. Bauminger, R. Einhorn, J. Hess, A. Mustachi and S. Ofer, 1968, J. Appl. Phys. **39**, 1250.

Atzmony, U., M.P. Dariel, E.R. Bauminger, D. Lebenbaum, I. Nowik and S. Ofer, 1973, Phys. Rev. **B7**, 4220.

Atzmony, U. and M.P. Dariel, 1974, Phys. Rev. **B10**, 2060.

Atzmony, U., M.P. Dariel and G. Dublon, 1976, Phys. Rev. **B14**, 3713.

Atzmony, U. and G. Dublon, 1977, Physica **B86**, 167.

Aukhadeev, F.L. and I.S. Kosov, 1974, Sov. Phys.–Solid State **15**, 1929.

Baberschke, K., 1976, Z. Physik B **24**, 53.

Baberschke, K. and J. Nagel, 1976, Phys. Rev. **B13**, 2793.

Baker, J.M. and B. Bleaney, 1958, Proc. Roy. Soc. **A245**, 156.

Baker, J.M. and R.S. Rubins, 1961, Proc. Phys. Soc. **78**, 1353.

Barak, J., A. Gabai and N. Kaplan, 1974, Phys. Rev. **B9**, 4914.

Barnes, R.G., W.H. Jones, Jr. and T.P. Graham, 1961, Phys. Rev. Lett. **6**, 221.

Barnes, R.G., R.L. Mössbauer, E. Kankeleit

and J.M. Poindexter, 1964, Phys. Rev. **136**, A175.
Barnes, R.G., F. Borsa and D.T. Peterson, 1965, J. Appl. Phys. **36**, 940.
Barnes, R.G., F. Borsa, S.L. Segel and D.R. Torgeson, 1965, Phys. Rev. **137**, A1828.
Barnes, R.G., B. Beaudry and R.G. Lecander, 1966, J. Appl. Phys. **37**, 1248.
Barnes, R.G. and E.D. Jones, 1967, Solid State Commun. **5**, 285.
Barnes, R.G. and R.G. Lecander, 1967, J. Phys. Soc. Japan **22**, 930.
Barnes, R.G. and B.K. Lunde, 1970, J. Phys. Soc. Japan **28**, 408.
Barnes, R.G., R.B. Creel and D.R. Torgeson, 1970, J. Chem. Phys. **53**, 3762.
Barnes, R.G. and B.K. Lunde, 1975, AIP Conf. Proc. **24**, 217.
Barnes, R.G., W.C. Harper, S.O. Nelson, D.K. Thome and D.R. Torgeson, 1976, J. Less-Common Metals **49**, 483.
Barrere, H. and K.M. Tran, 1971, Comptes Rendus **273**, 823.
Bauminger, E.R., I. Nowik and S. Ofer, 1969, Phys. Lett. **29A**, 199.
Bauminger, E.R., J. Hess, I. Nowik and S. Ofer, 1972, Solid State Commun. **10**, 365.
Bauminger, E.R., I. Felner, D. Froindlich, D. Levron, I. Nowik, S. Ofer and R. Yanovsky, 1974, J. de Phys. **35**, C6–61.
Bauminger, E.R., A. Diamant, I. Felner, I. Nowik and S. Ofer, 1975, Phys. Rev. Lett. **34**, 962.
Bauminger, E.R., D. Davidov, I. Felner, I. Nowik, S. Ofer and D. Shaltiel, 1977, Physica B **86**, 201.
Berthier, Y. and J. Barak, 1975, J. Phys. F **5**, 2388.
Beuermann, G. and B. Fischer, 1976, Z. Physik B **24**, 251.
Bleaney, B. and K.W.H. Stevens, 1953, Rept. Progr. in Phys. **16**, 108.
Bleaney, B., 1959, Proc. Phys. Soc. **73**, 939.
Bleaney, B., 1962, Proc. Phys. Soc. Japan Suppl. **17** B **1**, 435.
Bleaney, B., 1972, "Hyperfine Interactions", in: Elliott, R.J., ed., Magnetic Properties of Rare Earth Metals (Plenum Press, New York).
Bloch, F., W.W. Hansen and M. Packard, 1946, Phys. Rev. **69**, 127.
Bloembergen, N., R.V. Pound and E.M. Purcell, 1948, Phys. Rev. **73**, 679.
Bloembergen, N. and T.J. Rowland, 1953, Acta Met. **1**, 731.
Bloembergen, N. and T.J. Rowland, 1955, Phys. Rev. **97**, 1679.
Blumberg, W.E., J. Eisinger, V. Jaccarino and B.T. Matthias, 1960, Phys. Rev. Lett. **5**, 52.
Blume, M., A.J. Freeman and R.E. Watson, 1964, Phys. Rev. **134**, A320.
Boatner, L.A. and M.M. Abraham, 1967, Phys. Rev. **163**, 213.
Bogle, G.S., A.H. Cooke and S. Whitley, 1951, Proc. Phys. Soc. **A64**, 931.
Bogle, G.S. and H.E.D. Scovil, 1952, Proc. Phys. Soc. **A65**, 368.
Bogle, G.S., H.J. Duffus and H.E.D. Scovil, 1952, Proc. Phys. Soc. **A65**, 760.
Bohn, H.G., R.R. Arons and H. Lutgemeier, 1975, in: P.S. Allen, E.R. Andrew and C.A. Bates, eds., "Magnetic Resonance and Related Phenomena" (North-Holland, Amsterdam) p. 75.
Borsa, F., R.G. Barnes and R.A. Reese, 1967, Phys. Stat. Solidi **19**, 359.
Borsa, F., G. Olcese and G.B. Silbernagel, 1973, in: V. Hovi, ed., Proc. XVII Congr. Ampere (North-Holland, Amsterdam) p. 326.
Bowden, G.J., D.St. P. Bunbury and J.M. Williams, 1967, Proc. Phys. Soc. (London) **91**, 612.
Bowden, G.J., D.St.P. Bunbury, A.P. Guimaraes and R.E. Snyder, 1968, J. Phys. C: **1**, 1376.
Bowden, G.J., 1973, J. Phys. F: **3**, 2206.
Bowden, G.J., R.K. Day and M. Sarwar, 1973, Intern. Conf. Magnetism, Moscow.
Bowden, G.J., J.W. Ross and K.A. McEwen, 1975, in: P.S. Allen, E.R. Andrews and C.A. Bates, eds., "Magnetic Resonance and Related Phenomena (North-Holland, Amsterdam) p. 77.
Boyle, A.J.F. and H.E. Hall, 1962, Rept. Progr. Phys. **25**, 441.
Brog, K.C., W.H. Jones, Jr. and C.M. Verber, 1966, Physics Lett. **20**, 258.
Brog, K.C. and R.P. Kenan, 1973, Phys. Rev. **B8**, 1492.
Bucher, E., K. Andres, F.J. di Salvo, J.P. Maita, A.C. Gossard, A.S. Cooper and G.W. Hull, Jr., 1975, Phys. Rev. **B11**, 500.
Buckmaster, H.A. and Y.H. Shing, 1972, Phys. Stat. Sol. (a) **12**, 235.
Budnick, J.I. and S. Skalski, 1967, NMR in Some Magnetically Ordered Systems, in: A.J. Freeman and R. Frankel, eds., Hyperfine Interactions (Academic Press, New York).
Burzo, E. and F. Domsa, 1972, Rev. Roum. Phys. **17**, 893.
Burzo, E., M. Bodea and D. Barb, 1975, in: P.S. Allen, E.R. Andrew and C.A. Bates, eds., "Magnetic Resonance and Related Phenomena (North-Holland, Amsterdam) p. 71.
Buschow, K.H.J., J.F. Fast, A.M. van Diepen and H.W. de Wijn, 1967, Phys. Stat. Sol. **24**, 715.
Buschow, K.H.J., A.M. van Diepen and H.W. de Wijn, 1970, J. Appl. Phys. **41**, 4609.
Buschow, K.H.J. and A. Oppelt, J. Phys. F: **4**, 1246.
Buschow, K.H.J., W.J. Huiskamp, H.Th. Lefever, F.J. Steenwijk and R.C. Thiel, 1975, J. Phys. F: **5**, 1625.
Bykovetz, N., 1976, Solid State Commun. **18**, 143.
Carlson, E.H. and H.S. Adams, 1969, J. Chem. Phys. **51**, 388.
Carr, S.L. and W.G. Moulton, 1971, J. Magn. Res. **4**, 400.
Carrington, A. and A.D. McLachlan, 1967, "Introduction to Magnetic Resonance, with Applications to Chemistry and Chemical Physics", (Harper and Row, New York).

Barrere, H., 1967, Compt. Rend. Series C 264, 1731-3.
Barrere, H., 1969, Compt. Rend. Series C 268, 895-7.
Bauminger, E.R., I. Felner, D. Levron, I. Nowik and S. Ofer, 1974b, Phys. Rev. Lett. 33, 890.

Carter, G.C. and J.C. Swartz, 1971, J. Phys. Chem. Solids **32**, 2415.
Carter, G.C., D.J. Kahan, L.H. Bennett, J.R. Cuthill and R.C. Dobbyn, 1971, Permuted Materials Index, NBS Special Publication no. 324.
Catalano, E., R.G. Bedford, V.G. Silveira and H.H. Wickman, 1969, J. Phys. Chem. Solids **30**, 1613.
Chappert, J. and J.K. Yakinthos, 1977, in: Furrer, A., ed., "Crystal Field Effects in Metals and Alloys" (Plenum Press, New York).
Chechernikov, V.I., V.I. Nedel'ko and A.V. Vedyaev, 1969, Sov. Phys. JETP **28**, 255.
Chock, E.P., R.A.B. Devine, S.A. Dodds, R. Orbach and L. Tippie, 1977, J. Phys. F: **7**, 1097.
Clauser, M.J., E. Kankeleit and R.L. Mössbauer, 1966, Phys. Rev. Lett. **17**, 5.
Cohen, R.L., 1964, Phys. Rev. **134**, A94.
Cohen, R.L. and J.H. Wernick, 1964, Phys. Rev. **134**, B503.
Cohen, R.L., 1968, Phys. Rev. **134**, A94.
Cohen, R.L., S. Hüfner and K.W. West, 1969, Phys. Lett. **28A**, 582.
Cohen, S.G., 1967, Hyperfine interactions and angular distribution and correlations of nuclear gamma rays, in: A.J. Freeman and R. Frankel, eds., Hyperfine Interactions (Academic Press, New York).
Conway, J.G. and B.G. Wybourne, 1963, Phys. Rev. **130**, 2325.
Cooper, B.R., 1968, in: F. Seitz, D. Turnbull and H. Ehrenreich, eds., Solid State Physics, vol. 21 (Academic Press, New York).
Cottet, H., P. Donze, J. Dupraz, B. Giovannini and M. Peter, 1968, Z. angew. Phys. **24**, 249.
Crecelius, G., S. Hüfner and D. Quitmann, 1969, Proceed. ICM 507.
Crecelius, G. and S. Hüfner, 1970, J. Appl. Phys. **41**, 1329.
Creyghton, J.H.N., P.R. Locher and K.H.J. Buschow, 1973, Phys. Rev. **B7**, 4829.
Dariel, M.P., U. Atzmony and D. Lebenbaum, 1973, Phys. Stat. Sol. (b) **59**, 615.
Das, K.C. and D.K. Ray, 1969, Phys. Rev. **187**, 777.
Das, T.P. and M. Pomerantz, 1961, Phys. Rev. **119**, 70.
Davidov, D., H. Lotem and D. Shaltiel, 1969, Phys. Lett. **28A**, 672.
Davidov, D., A. Chelkowski, C. Rettori, R. Orbach and M.B. Maple, 1973, Phys. Rev. **B7**, 1029.
Davidov, D., C. Rettori, G. Ng and E.P. Chock, 1974a, Phys. Lett. **49A**, 320.
Davidov, D., C. Rettori and D. Shaltiel, 1974b, Phys. Lett. **50A**, 392.
Davidov, D., C. Rettori and H.M. Kim, 1974c, Phys. Rev. **B9**, 147.
Davidov, D. and K. Baberschke, 1975, Phys. Lett. **51A**, 144.
Davidov, D., V. Zevin, J.M. Bloch and C. Rettori, 1975a, Solid State Commun. **17**, 1279.
Davidov, D., C. Rettori and V. Zevin, 1975b, Solid State Commun. **16**, 247.
Degani, J., and N. Kaplan, 1973, Phys. Rev. **B7**, 2132.
DeGennes, P.G., 1962, J. Phys. Rad. **23**, 630.
Devine, R.A.B. and J.M. Dixon, 1973, Phys. Rev. **B7**, 4902.
Devine, R.A.B., 1973, Solid State Commun. **13**, 1495.
DeVoe, J.R. and J.J. Spijkerman, 1966, Anal. Chem. Annual Reviews **38**, 382R.
DeVoe, J.R. and J.J. Spijkerman, 1968, Anal. Chem. Annual Reviews **40**, 472R.
DeVoe, J.R. and J.J. Spijkerman, 1970, Anal. Chem. Annual Reviews **42**, 366R.
deWijn, H.W., K.H.J. Buschow and A.M. van Diepen, 1968, Phys. Stat. Solidi **30**, 759.
deWijn, H.W., A.M. van Diepen and K.H.J. Buschow, 1973, Phys. Rev. **B7**, 524.
Dintelmann, F., E. Dormann and K.H.J. Buschow, 1970a, Solid State Comm. **8**, 1911.
Dintelmann, F., E. Dormann and A. Oppelt, 1970b, Solid State Commun. **8**, 1257.
D'Onofrio, L. and B. Iraldi, 1977, Solid State Commun. **21**, 963.
Dormann, E., K.H.J. Buschow, K.N.R. Taylor, G. Brown and M.A.A. Issa, 1973, J. Phys. F: **3**, 220.
Dormann, E. and K.H.J. Buschow, 1976, J. Appl. Phys. **47**, 1662.
Dunlap, B.D., 1974, Phys. Rev. **B10**, 26.
Durand, J. and C. Robert, 1973, J. Phys. F: **3**, L90.
Eagles, D.M., 1973, Phys. Kondens. Materie **16**, 181.
Edmonds, D.T., 1963, Phys. Rev. Letters **10**, 129.
Edmonds, D.T. and A.J. Lindop, 1968, **39**, 1008. J. Appl. Phys.
Eibschütz, M., S. Shtrikman and D. Treves, 1967, Phys. Rev. **156**, 562.
Elliott, R.J. and K.W.H. Stevens, 1953, Proc. Roy. Soc. **A218**, 553.
Elliott, R.J., 1957, Proc. Phys. Soc. **70**, 119.
Erikson, L.E., 1966, Phys. Rev. **143**, 295.
Farrer, T.C. and E.D. Becker, 1971, "Pulse and Fourier Transform NMR, Introduction to Theory and Methods" (Academic Press, New York).
Fekete, D., N. Kaplan and T.B. Reed, 1974, Solid State Commun. **15**, 1827.
Fekete, D., A. Grayevskey, N. Kaplan and E. Walker, 1975, Solid State Commun. **17**, 573.
Fermi, E., 1930, Z. Physik **60**, 320.
Figiel, H., A. Oppelt, E. Dormann and K.H.J. Buschow, 1976, Phys. Stat. Solidi (a) **36**, 275.
Forester, D.W. and W.A. Ferrando, 1976, Phys. Rev. **B14**, 4769.
Fradin, F.Y., 1968, Phys. Lett. **28A**, 441.
Fradin, F.Y., 1972, Phys. Rev. **B5**, 1119.
Freed, S. and E.V. Sayre, 1955, J. Chem. Phys. **23**, 2066.
Freeman, A.J. and R.E. Watson, 1962, Phys. Rev. **127**, 2058.
Freeman, A.J. and R.E. Watson, 1965, "Hyperfine Interactions in Magnetic Materi-

Clogston, A.M., V. Jaccarlus and Y. Yafet, 1964, Phys. Rev. 134, A8.
Danon, J., 1968, Chemical Applications of Mössbauer Spectroscopy, V.I. Goldanskii and R. H. Herber, eds. (Academic Press, New York, 1968).
Elliott, R.J., 1961, Phys. Rev. 124, 346-53.

als, in: G.T. Rado and H. Suhl, eds., Magnetism, vol. IIA (Academic Press, New York).
Freeman, A.J., 1972, in: R.J. Elliott, ed., "Magnetic Properties of Rare Earth Metals", (Plenum Press, New York).
Fuller, G.H., 1976, J. Phys. Chem. Ref. Data **5**, 835.
Gerth, G., P. Kienle and K. Luchner, 1968, Phys. Lett. **27A**, 557.
Gibb, T.C., 1976, "Principles of Mössbauer Spectroscopy", (Chapman and Hall).
Gill, D. and N. Kaplan, 1968, Phys. Lett. **26A**, 505.
Goebel, U., E. Dormann and K.H.J. Buschow, 1975, J. Phys. F: **5**, 2198.
Goldanskii, V.I. and R.H. Herber, 1968, "Chemical Applications of Mössbauer Spectroscopy", (Academic Press, London).
Goldman, M. and L. Shen, 1966, Phys. Rev. **144**, 321. 1975,
Gonser, U.,vin: Gonser, U., ed., Mössbauer Spectroscopy, (Springer-Verlag, Berlin), p. 1.
Göring, J., 1972, Z. Physik **251**, 185.
Gossard, A.C. and A.M. Portis, 1959, Phys. Rev. Letters **3**, 164.
Gossard, A.C. and V. Jaccarino, 1962, Proc. Phys. Soc. **80**, 877.
Gossard, A.C., V. Jaccarino and J.H. Wernick, 1964, Phys. Rev. **133**, A881.
Grant, R.W., 1975, "Mössbauer Spectroscopy in Magnetism: Characterization of Magnetically-Ordered Compounds", in: Gonser, U., ed., Mössbauer Spectroscopy, (Springer-Verlag, Berlin).
Greenwood, N.N. and T.C. Gibb, 1971, Mössbauer Spectroscopy, (Chapman and Hall).
Griffith, J.S., 1963, Phys. Rev. **132**, 316.
Groves, J.L., P. DeBrunner and G. de Pasquali, 1970, Phys. Lett. **33A**, 51.
Gschneidner, Jr., K.A., 1971, J. Less-Common Metals **25**, 405.
Guimaraes, A.P. and D.St.P. Bunbury, 1973, J. Phys. F: **3**, 885.
Guimaraes, A.P., C. Larica and W. Vanoni, 1977, J. Magnetic Resonance **25**, 507.
Halstead, T.K., 1974, J. Solid State Chem. **11**, 114.
Halstead, T.K., N.A. Abood and K.H.J. Buschow, 1976, Solid State Commun. **19**, 425.
Hasegawa, H., 1959, Prog. Theor. Phys. **27**, 483.
Heiniger, F., E. Bucher, J.P. Maita, and P. Descouts, 1973, Phys. Rev. **B8**, 3194.
Henning, W., P. Kienle, E. Steichele, and F. Wagner, 1966, Phys. Lett. **22**, 446.
Herbst, U., J. Schraub, E. Dormann and K.H.J. Buschow, 1974, Phys. Stat. Sol. (b) **61**, K101.
Hess, J., E.R. Bauminger, A. Mustachi, I. Nowik and S. Ofer, 1971, Physics Lett. **37A**, 185.
Hessler, J.P. and E.H. Carlson, 1968, J. Appl. Phys. **39**, 1014.
Hessler, J.P., 1973, Phys. Rev. **B8**, 3151.
Heuberger, A., F. Pobell and P. Kienle, 1967, Z. Physik **205**, 503.
Hirst, L.L., E.R. Seidel and R.L. Mössbauer, 1969, Physics Lett. **29A**, 673.
Hirst, L.L., 1974, J. Phys. Collq. **35**, C6-21.
Hüfner, S., P. Kienle, W. Wiedemann and H. Eicher, 1965, Z. Physik **182**, 499.
Hüfner, S., 1967, Phys. Rev. Lett. **19**, 1034.
Hüfner, S. and J.H. Wernick, 1968, Phys. Rev. **173**, 448.
Hüfner, S., H.H. Wickman and C.F. Wagner, 1968, Phys. Rev. **169**, 247.
Hutchings, M.T., 1964, Solid State Physics **16**, 227.
Hutchison, C.A., Jr., B.R. Judd and D.F.D. Pope, 1957, Proc. Phys. Soc. **B70**, 514.
Hutchison, C.A., Jr. and E. Wong, 1958, J. Chem. Phys. **29**, 754.
Inomata, K., 1976, J. Phys. Soc. Japan **41**, 1890.
Itoh, J., S. Kobayashi and N. Sano, 1968, J. Appl. Phys. **39**, 1325.
Ingram, D.J.E., 1967, "Spectroscopy at Radio and Microwave Frequencies", (Plenum Press, New York).
Jaccarino, V., B.T. Matthias, M. Peter, H. Suhl and J.H. Wernick, 1960, Phys. Rev. Lett. **5**, 251.
Jones, D.A., J.M. Baker and D.F.D. Pope, 1959, Proc. Phys. Soc. **74**, 249.
Jones, E.D. and J.I. Budnick, 1966, J. Appl. Phys. **37**, 1250.
Jones, E.D., 1967, Phys. Rev. Lett. **19**, 432.
Jones, E.D., 1968, J. Appl. Phys. **39**, 1090.
Jones, E.D., 1969, Phys. Rev. **180**, 455.
Jones, E.D., 1970, Colloq. Intl. Cent. Natl. Rech. Sci. **2**, 495.
Jones, W.H., Jr., T.P. Graham and R.G. Barnes, 1963, Phys. Rev. **132**, 1898.
Judd, B.R., 1963, Proc. Phys. Soc. **82**, 874.
Judd, B.R. and I. Lindgren, 1961, Phys. Rev. **122**, 1802.
Kaindl, G. and R.L. Mössbauer, 1969, Physics Lett. **26B**, 386.
Kalvius, G.M., P. Kienle, H. Eicher, W. Wiedemann and C. Schuler, 1963, Z. Physik **172**, 231.
Kalvius, G.M., 1965, Phys. Rev. **137**, B1441.
Kalvius, G.M., U.F. Klein and G. Wortmann, 1974, J. Phys. Collq. **35**, C6-139.
Kanekar, C.R., K.R.P.M. Rao and V.U.S. Rao, 1969, Phys. Lett. **27A**, 85.
Kaplan, N., E. Dormann, K.H.J. Buschow and D. Lebenbaum, 1973, Phys. Rev. **B7**, 40.
Kasuya, T., 1956, Prog. Theor. Phys. **16**, 58.
Keeton, S.C. and T.L. Loucks, 1969, Phys. Rev. **168**, 672.
Keller, G., H. Luft and B. Elschner, 1974, Phys. Lett. **49A**, 273.
Khodosov, E.F., 1974, Sov. Phys.–Solid State **16**, 157. V.K. Prokopenko and A.I. Linnik,
Klein, U.F., G. Wortmann and G.M. Kalvius, 1976, Solid State Commun. **18**, 291.
Khoi, L.D. and M. Rotter, 1971, Phys. Lett. **34A**, 382.
Khurgin, B., I. Nowik, S. Ofer and M. Rakavy, 1970, J. Phys. Chem. Solids **31**, 49.

move to p. 509

Jones, W.H., Jr., T.P. Graham and R.G. Barnes, 1960, Acta Met. 8, 663.

Kienle, P., 1964, Rev. Mod. Phys. **36**, 372.
Kimball, C.W., A.E. Dwight, G.M. Kalvius, B. Dunlap and M.V. Nevitt, 1975, Phys. Rev. **B12**, 819.
King, A.R., J.P. Wolfe and R.L. Ballard, 1972, Phys. Rev. Lett. **28**, 1099.
Klein, U.F., G. Wortmann and G.M. Kalvius, 1973, Proceed. ICM 73, vol. III, 149.
Knight, W.D., 1949, Phys. Rev. **76**, 1259.
Kobayashi, S., N. Sano and J. Itoh, 1967, J. Phys. Soc. Japan **22**, 676.
Kochalayev, B.I., E.G. Kharakhashyan, I.A. Garifullin and N.E. Alekseevsky, 1975, in: P.S. Allen, E.R. Andrew and C.A. Bates, eds., "Magnetic Resonance and Related Phenomena" (North-Holland, Amsterdam) p. 23.
Koopmann, G., K. Baberschke and S. Hüfner, 1975, Phys. Lett. **50A**, 407.
Kopp, J.P. and D.S. Schreiber, 1967, J. Appl. Phys. **38**, 1373.
Korringa, J., 1950, Physica **16**, 601.
Kubo, R. and K. Tomita, 1954, J. Phys. Soc. Japan **9**, 888.
Kumagai, K. and K. Asayama, 1975, J. Phys. Soc. Japan **39**, 543.
Large, N.R., R.J. Bullock, P. Glentworth and D.A. Newton, 1969, Phys. Lett. **29A**, 352.
Larson, G.H. and C.D. Jeffries, 1966, Phys. Rev. **141**, 461.
Lea, K.R., M.J.M. Leask and W.P. Wolf, 1962, Phys. Chem. Solids **23**, 1381.
Lee, K. and A. Sher, 1965, Phys. Rev. Lett. **14**, 1027.
Levin, R., D. Davidov, C. Rettori, J. Suassuna and D. Shaltiel, 1977, J. Phys. F: **7**, 703.
Levinson, L.M., E. Rosenberg, A. Shaulov, S. Shtrikman and K. Strnat, 1970, J. Appl. Phys. **41**, 910.
Loewenhaupt, M. and S. Hüfner, 1969, Phys. Lett. **30A**, 309.
Lounasmaa, O.V., 1967, "Nuclear Specific Heats in Metals and Alloys", in: A.J. Freeman and R. Frankel, eds., Hyperfine Interactions, (Academic Press, New York).
Lounasmaa, O.V. and G.M. Kalvius, 1967, Phys. Lett. **26A**, 21.
Low, W., 1960, "Paramagnetic Resonance in Solids", (Academic Press, New York).
Low, W. and E.L. Offenbacher, 1965, Solid State Phys. **17**, 135.
Lucken, E.A.C., 1969, "Nuclear Quadrupole Coupling Constants", (Academic Press, New York).
Lütgemeier, H., R.R. Arons and H.G. Bohn, 1975, in: P.S. Allen, E.R. Andrew and C.A. Bates, eds., "Magnetic Resonance and Related Phenomena", (North-Holland, Amsterdam) p. 81.
Mackenzie, I.S., M.A.H. McCausland and A.R. Wagg, 1974, J. Phys. F: **4**, 315.
MacLaughlin, D.E. and M. Daugherty, 1972, Phys. Rev. **B6**, 2502.
Malik, S.K., R. Vijayaraghavan, S.K. Garg and R.J. Ripmeester, 1975, Phys. Stat. Solidi (b) **68**, 399.
Malik, S.K., R. Vijayaraghavan, S.K. Garg and R.J. Ripmeester, 1977, Solid State Commun. **21**, 245.
Mangum, B.W. and R.P. Hudson, 1966, J. Chem. Phys. **44**, 704.
Matthias, E., 1967, Recent applications of PAC, in: A.J. Freeman and R. Frankel, eds., "Hyperfine Interactions", (Academic Press, New York).
McHenry, M.R., B.G. Silbernagel and J.H. Wernick, 1972, Phys. Rev. **B5**, 2958.
McNiff, E.J. and S. Shapiro, 1963, J. Phys. Chem. Solids **24**, 939.
Mikkelson, R.C. and H.J. Stapleton, 1965, Phys. Rev. **140**, A1968.
Mössbauer, R.L., 1958, Z. Physik **151**, 124; Naturwissenschaften **45**, 538.
Mustafa, M.R., 1977, J. Magn. Res. **25**, 341.
Myers, S.M., R. Gonano and H. Meyer, 1968, Phys. Rev. **170**, 513.
Myers, S.M. and A. Narath, 1973, Phys. Rev. **B7**, 4776.
Myers, S.M. and A. Narath, 1974, Phys. Rev. **B9**, 227.
Nagai, H., H. Yoshie, T. Unate, A. Tsujimura and J. Deportes, 1976, J. Phys. Soc. Japan **41**, 1907.
Nagel, J. and E. Baberschke, 1977, in: Crystal Field Effects in Metals and Alloys, ed. by A. Furrer (Plenum Press, New York).
Narath, A. and A.T. Fromhold, 1964, Phys. Rev. **139**, A794.
Narath, A., 1967, in: A.J. Freeman and R. Frankel, eds., Hyperfine Interactions (Academic Press, New York).
Narath, A. and A.T. Fromhold, Jr., 1967, Phys. Lett. **25A**, 49.
Narath, A., 1969, Phys. Rev. **179**, 359.
Newman, D.J. and W. Urban, 1975, Advances in Physics **24**, 793.
Niira, K., 1960, Phys. Rev. **117**, 129.
Nitsche, N., J. Pelzl, S. Hüfner and P. Steiner, 1972, Solid State Commun. **10**, 145.
Nowik, I. and J.H. Wernick, 1965, Phys. Rev. **140**, A131.
Nowik, I., 1966, "Mössbauer Studies of Rare Earth Intermetallic Compounds", in: I.J. Gruverman, ed., Mössbauer Effect Methodology (Plenum Press, New York) p. 147.
Nowik, I., S. Ofer and J.H. Wernick, 1966, Phys. Lett. **20**, 232.
Nowik, I. and S. Ofer, 1967, Phys. Rev. **153**, 409.
Nowik, I. and S. Ofer, 1968, J. Appl. Phys. **39**, 1252.
Nowik, I., E.R. Bauminger, J. Hess, A. Mustachi and S. Ofer, 1971, Phys. Lett. **34A**, 155.
Nowik, I., B.D. Dunlap and G.M. Kalvius, 1972, Phys. Rev. **B6**, 1048.
Ofer, S., E. Segal, I. Nowik, E.R. Bauminger, I. Grodzins, A.J. Freeman and M. Schieber, 1965, Phys. Rev. **137**, A627.
Ofer, S., M. Rakavy, E. Segal and B. Khurgin, 1965, Phys. Rev. **138**, A241.
Ofer, S. and E. Segal, 1966, Phys. Rev. **141**, 448.
Klein, U.F., G. Wortmann and G.M. Kalvius, 1976b, J. Magn. Magn. Mater. 3, 50.
Lundin, A.G. and S.P. Gabuda, 1966, Sov. Phys.-Solid State 8, 1495.
Misra, S.K. and G.R. Sharp, 1977, J. Phys. C 10, 897.
Mørup, S. and G. Trumpy, 1970, Phys. Stat. Solids 40, 759.
Mössbauer, R.L., 1965, Pure & Appl. Chem. 11, 297.
Nowick , I., and S. Ofer, 1963, Phys. Lett. 3, 192.

Ofer, S. and I. Nowik, 1967, Nucl. Phys. **A93**, 689.
Ofer, S., I. Nowik and S.G. Cohen, 1968, "Mössbauer Effect in Rare Earths and their Compounds", in: V.I. Goldanskii and R.H. Herber, eds., "Chemical Applications of Mössbauer Spectroscopy", (Academic Press, New York).
Oppelt, A., E. Dormann and K.H.J. Buschow, 1972, Phys. Stat. Sol. (b) **51**, 275.
Orbach, R., 1961, Proc. Roy. Soc. **A264**, 458.
Orbach, R., M. Peter and D. Shaltiel, 1974, Arch Sci. Geneve **27**, 141.
Pelzl, J., 1972, Z. Physik **251**, 13.
Peter, M., D. Shaltiel, J.H. Wernick, H.J. Williams, J.B. Mock and R.C. Sherwood, 1962, Phys. Rev. **126**, 1395.
Petrich, G. and R.L. Mössbauer, 1968, Phys. Lett. **26A**, 403.
Pletnev, R.M., V.N. Lisson and A.A. Fotiev, 1975, Soviet Physics–Solid State **16**, 2397.
Poole, C.P., Jr. and H.A. Farach, 1971, "Relaxation in Magnetic Resonance", (Academic Press, New York).
Poteet, W.H., R.F. Tipsword and C.D. Williams, 1970, Phys. Rev. **B1**, 1265.
Potter, W.H. and H.J. Stapleton, 1972, Phys. Rev. **B5**, 1729.
Pryce, M.H.L., 1950, Phys. Rev. **80**, 1107.
Purcell, E.M., H.C. Torrey and R.V. Pound, 1946, Phys. Rev. **69**, 37.
Quinn, R.K. and H.T. Weaver, 1976, J. Solid State Chem. **16**, 197.
Ramsey, N.F., 1950, Phys. Rev. **78**, 699.
Reese, R.A. and R.G Barnes, 1967, Phys. Rev. **163**, 465.
Reese, R.A. and R.G. Barnes, 1969, J. Appl. Phys. **40**, 1493.
Rehm, K.E., W. Henning and P. Kienle, 1969, Phys. Lett. **22**, 790.
Rettori, C., H.M. Kim, E.P. Chock and D. Davidov, 1974, Phys. Rev. **B10**, 1826.
Rettori, C., D. Davidov, A. Grayevskey and W.M. Walsh, 1975a, Phys. Rev. **B11**, 4450.
Rettori, C., R. Levin and D. Davidov, 1975b, J. Phys. F: **5**, 2379.
Rettori, C., D. Davidov, P. Chaikin and R. Orbach, 1973c, Phys. Rev. Lett. **30**, 437.
Rettori, C., D. Davidov, G. Ng and E.P. Chock, 1975d, Phys. Rev. **B12**, 1296.
Ross, J.W. and J. Sigalas, 1975, J. Phys. F: 5, 1973.
Ruderman, M.A. and C. Kittel, 1954, Phys. Rev. **96**, 99.
Sano, N., S. Kobayashi and J. Itoh, 1970, Progr. Theor. Phys. Suppl. **45**, 84.
Sano, N., S. Kobayashi and J. Itoh, 1970, Progr. Theor. Phys. Kvoto Suppl. **46**, 84.
Sano, N., M. Teraoka, K. Shimizu and J. Itoh, 1972, J. Phys. Soc. Japan **32**, 571.
Sano, N., K. Shimizu and J. Itoh, 1975a, J. Phys. Soc. Japan **39**, 84.
Sano, N., K. Shimizu, Y. Aoki and J. Itoh, 1975b, J. Phys. Soc. Japan **39**, 93.
Saraswati, V. and R. Vijayaraghavan, 1966, Phys. Lett. **21**, 363.
Saraswati, V. and R. Vijayaraghavan, 1967, J. Phys. Chem. Solids **28**, 2111.
Sauer, Ch., U. Köbler, W. Zinn and G.M. Kalvius, 1974, J. de Phys. **35**, C6–269.
Schäfer, W., H.K. Schmidt and S. Hüfner, 1968, Phys. Lett. **28A**, 279.
Schäfer, W., H,K. Schmidt, S. Hüfner and J.H. Wernick, 1969, Phys. Rev. **182**, 459.
Schäfer, W., H.K. Schmidt, B. Elschner and K.H.J. Buschow, 1972, Z. Physik **254**, 1.
Scherg, M., E.R. Seidel, F.J. Litterst, W. Gierisch and G.M. Kalvius, 1974, J. Phys. Collq. **35**, C6–527.
Schmidt, V.H. and E.D. Jones, 1970, Phys. Rev. **B1**, 1978.
Schreiber, D.S. and R.M. Cotts, 1963, Phys. Rev. **131**, 1118.
Schreiber, D.S., 1965, Phys. Rev. **137**, 923.
Scott, P.L. and C.D. Jeffries, 1962, Phys. Rev. **127**, 32.
Schulz, M.B. and C.D. Jeffries, 1966, Phys. Rev. **149**, 270.
Schulz, M.B. and C.D. Jeffries, 1967, Phys. Rev. **159**, 277.
Seidel, E.R., G. Kaindl, M.J. Clauser and R.L. Mössbauer, 1967, Phys. Lett. **25A**, 328.
Seitchik, J.A., V. Jaccarino and J.H. Wernick, 1965, Phys. Rev. **138**, A148.
Seiwa, Y., T. Tsuda, A. Hirai and C.W. Searle, 1973, Phys. Lett. **43A**, 23.
Semin, G.K., T.A. Babushkina and G.G. Yakobson, 1965, "Nuclear Quadrupole Resonance in Chemistry", (John Wiley, New York).
Shaltiel, D., A.C. Gossard and J.H. Wernick, 1965, Phys. Rev. **137**, A1027.
Shamir, N., N. Kaplan and J.H. Wernick, 1971, J. Phys. Collq. **32**, C1-902.
Shen, L., 1968, Phys. Rev. **172**, 259.
Shen, L., J.P. Kopp and D.S. Schreiber, 1969, Phys. Lett. **29A**, 438.
Shenoy, G.K., G.D. Dunlap, G.M. Kalvius, A.M. Toxen and R.J. Gambino, 1970, J. Appl. Phys. **41**, 1317.
Shenoy, G.K., B.D. Dunlap, D.G. Westlake and A.E. Dwight, 1976, Phys. Rev. **B14**, 41.
Shimizu, K., N. Sano and J. Itoh, 1975, J. Phys. Soc. Japan **39**, 539.
Shirley, D.A., 1964, Rev. Mod. Phys. **36**, 339.
Shulman, R.G. and K. Knox, 1960, Phys. Rev. **119**, 94.
Silbernagel, B.G. and J.H. Wernick, 1973, Phys. Rev. **B7**, 4787.
Silhouette, D., 1970, Solid State Commun. **8**, 467.
Sill, L.R., A.J. Fedro and C.W. Kimball, 1971, Int. J. Magn. 1, 319.
Slichter, C.P., 1963, "The Principles of Magnetic Resonance", (Harper and Row, New York).
Smith, J.A.S., 1974, "Advances in Nuclear Quadrupole Resonance", vol. 1 (Heydon).
Smith, W.C., 1971, "High Frequency Nuclear Magnetic Resonance in Thulium Intermetallic Compounds", Ph.D. Thesis, Iowa State University (unpublished).

Petrich, G., 1969, Z. Physik 221, 431.
Schmidt, V.H., 1973, in: C.J. Kevane and T. Moeller, eds., "Proc. 10th Rare Earth Research Conf." Vol. II (National Technical Information Center, Springfield, VA, CONF-730402-P2) p. 1007.
Schrittenlacher, W., K. Baberschke, G. Koopmann and S. Hüfner, 1975, Solid State Comm. 16, 923.
Shulman, R.G., B.G. Wyluda and B.T. Matthias, 1961, Bull. Am. Phys. Soc., 6, 103.
Sharma, V.K., 1971, J. Chem. Phys. 54, 496.

Stachel, M., S. Hüfner, G. Crecelius and D. Quitmann, 1969, Phys. Rev. **186**, 355.
Standley, K.J. and R.A. Vaughan, 1969, "Electron Spin Relaxation in Solids", (Plenum Press, New York).
Stapleton, H.J., C.D. Jeffries and D.A. Shirley, 1961, Phys. Rev. **124**, 1455.
Steichele, E., 1967, Z. Physik **201**, 331.
Sternheimer, R.M., 1966, Phys. Rev. **146**, 140.
Stevens, J.G., J.C. Travis and J.R. DeVoe, 1972, Anal. Chem. Annual Reviews **42**, 384R.
Stevens, J.G. and J.C. Travis, 1974, Anal. Chem. Annual Reviews **46**, 287R.
Stevens, J.G. and V.E. Stevens, 1973, Mössbauer Effect Data Index, (Adam Hilger, London).
Stevens, J.G. and J.C. Travis, 1976, Anal. Chem. Annual Reviews **48**, 232R.
Stevens, J.G. and B.D. Dunlap, 1976, J. Phys. Chem. Ref. Data **5**, 1093.
Stevens, K.W.H., 1953, Rev. Mod. Phys. **25**, 166.
Stevens, K.W.H., 1963, in: G.T. Rado and H. Suhl, eds., "Magnetism", vol. 1 (Academic Press, New York), p. 1.
Stöhr, J. and J.D. Cashion, 1975, Phys. Rev. **B12**, 4805.
Stöhr, J., J.D. Cashion and W. Wagner, 1975, J. Phys. F: **5**, 1417.
Stone, N.J., 1967, "Some Low-Temperature NO Techniques and Applications", in: A.J. Freeman and R. Frenkel, eds., Hyperfine Interactions, (Academic Press, New York).
Streever, R.L., 1969, Phys. Lett. **29A**, 710.
Streever, R.L. and P.J. Kaplan, 1971, Phys. Lett. **35A**, 8.
Streever, R.L. and P.J. Kaplan, 1973, Phys. Rev. **B8**, 3138.
Sugawara, K. and C.Y. Huang, 1975, J. Phys. Soc. Japan **39**, 643.
Sugawara, K. and C.Y. Huang, 1976, J. Phys. Soc. Japan **41**, 1534.
Sweger, D.M., R. Segna and J.J. Rhyne, 1974, Phys. Rev. **B9**, 3864.
Tanner, G., F.E. Wagner, G.M. Kalvius, G.K. Shenoy and K.H.J. Buschow, 1975, in: P.S. Allen, E.R. Andrew and D.A. Bates, eds., "Magnetic Resonance and Related Phenomena", (North-Holland, Amsterdam) p. 87.
Taylor, K.N.R., 1971, Advances in Physics **20**, 551.
Taylor, R.H., 1973, J. Phys. F: **3**, L110.
Taylor, R.H., 1975, Advances in Physics **24**, 681.
Teplov, M.A., 1969, Sov. Phys.-Solid State **10**, 2009.
Townes, C.H., C. Herring and W.D. Knight, 1950, Phys. Rev. **77**, 852.
Toxen, A.M., R.J. Gambino and L.B. Welsh, 1973, Phvs. Rev. **B8**, 90.
Triplett, B.B., N.S. Dixon, P. Boolchand, S.S. Hanna and E. Bucher, 1974, J. de Phys. **35**, C6-653.
Tsai, S.C., K.S.V.L. Narasimhan, C.J. Kunesh and R.A. Butera, 1972.
Tsang, T. and S. Ghose, 1971, Phys. Stat. Sol. (b) **48**, K117.
Turov, E.A. and M.P. Petrov, 1972, "Nuclear Magnetic Resonance in Ferro- and Antiferromagnets", (Halstead Press).
Uhrich, D.L. and R.G. Barnes, 1967, Phys. Rev. **164**, 428.
Uhrich, D.L., D.J. Genin and R.G. Barnes, 1968, Phys. Rev. **166**, 261.
Urban, P., D. Davidov, B. Elschner, T. Plefka and G. Sperlich, 1975, Phys. Rev. **B12**, 72.
Van der Kraan, A.M., P.C.M. Gubbens and K.H.J. Buschow, 1975, Phys. Stat. Sol. (a) **31**, 495.
Van Diepen, A.M., H.W. de Wijn and K.H.J. Buschow, 1967, J. Chem. Phys. **46**, 3489.
Van Diepen, A.M., H.W. de Wijn and K.H.J. Buschow, 1968a, Phys. Lett. **26A**, 340.
Van Diepen, A.M., H.W. de Wijn and K.H.J. Buschow, 1968b, Phys. Stat. Sol. **29**, 189.
Van Diepen, A.M., K.H.J. Buschow and H.W. de Wijn, 1969, J. Chem. Phys. **51**, 5259.
Van Loef, J.J., 1968, J. Appl. Phys. **39**, 1258.
Van Vleck, J.H. and W.G. Penney, 1934, Phil. Mag. **17**, 961.
Van Vleck, J.H., 1939, J. Chem. Phys. **7**, 72.
Van Vleck, J.H., 1940, Phys. Rev. **57**, 426.
Van Vleck, J.H., 1948, Phys. Rev. **74**, 1168.
Vijayaraghavan, R., S.K. Malik and V.U.S. Rao, 1968, Phys. Rev. Lett. **20**, 106.
von Meerwall, E.D., D.S. Schreiber and J.A. Kaeck, 1975, Solid State Commun. **16**, 1219.
Wachter, P., CRC-Critical Reviews in Solid State Sciences **3**, 189.
Wagg, A.R., M.A.H. McCausland and I.S. Mackenzie, 1975, in: P.S. Allen, E.R. Andrew and C.A. Bates, eds., "Magnetic Resonance and Related Phenomena", (North-Holland, Amsterdam), p. 477.
Wallace, W.E., 1973, "Rare Earth Intermetallics", (Academic Press, New York).
Watson, R.E., S. Koide, M. Peter and A.J. Freeman, 1965, Phys. Rev. **139**, A167.
Watson, R.E., A.C. Gossard and Y. Yafet, 1965, Phys. Rev. **140**, A375.
Watson, R.E. and A.J. Freeman, 1967, in: A.J. Freeman and R. Frankel, eds., "Hyperfine Interactions", (Academic Press, New York).
Weaver, H.T., 1972a, J. Chem. Phys. **56**, 3193.
Weaver, H.T., 1972b, Phys. Rev. **B6**, 2544.
Weaver, H.T., 1972c, Phys. Rev. **B5**, 1663.
Weimann, G. and B. Elschner, 1973, Z. Physik **261**, 85.
Weisman, I.D., L.H. Bennett, A.J. McAlister and R.E. Watson, 1975, Phys. Rev. **B11**, 82.
Welsh, L.B., R.J. Gambino and A.M. Toxen, 1971a, J. Appl. Phys. **42**, 1545.
Welsh, L.B., A.M. Toxen and R.J. Gambino, 1971b, Phys. Rev. **B4**, 2921.
Welsh, L.B., A.M. Toxen and R.J. Gambino, 1972, Phys. Rev. **B11**, 4156.
Wertheim, G.K. and J.H. Wernick, 1962, Phys. Rev. **125**, 1937.
Wertheim, G.K., A. Hausmann, 1971, "Electronic Structure of Point Defects Determined by Mössbauer Effect and Electron Spin Resonance", (Elsevier, Amsterdam).
Wickman, H.H. and I. Nowik, 1966, Phys. Rev. **142**, 115.
Wickman, H.H., I. Nowik, J.H. Wernick, D.A.

Welsh, L.B., C.L. Wiley and F.Y. Fradin, 1975, Phys. Rev. B 11, 4156.

Shirley and R.B. Frankel, 1966, J. Appl. Phys. **37**, 1246.
Wickman, H.H. and I. Nowik, 1967, J. Phys. Chem. Solids **28**, 2099.
Wickman, H.H. and E. Catalano, 1968, J. Appl. Phys. **39**, 1248.
Wickman, H.H., J.H. Wernick, R.D. Sherwood and C.F. Wagner, 1968, Phys. Chem. Solids **29**, 181.
Wickman, H.H. and G.K. Wertheim, 1968, in: V.I. Goldanskii and R.H. Herber, eds., "Chemical Applications of Mössbauer Spectroscopy", (Academic Press, New York).
Wilmshurst, T.H., 1968, "Electron Spin Resonance Spectrometers", (Plenum Press, New York).
Wolfe, J.P., 1977, Phys. Rev. **B16**, 128.
Wong, E.Y. and I. Richman, 1961, J. Chem. Phys. **34**, 1182.
Woolum, J.C. and A.J. Bearden, 1966, Phys. Rev. **142**, 143.
Wortmann, G., J. Moser and U.F. Klein, 1976, Phys. Lett. **55A**, 486.
Wybourne, B.G., 1966, Phys. Rev. **148**, 317.
Yakinthos, J.K. and J. Chappert, 1975, Solid State Commun. **17**, 979.
Yoshie, H., M. Matsushima, N. Miyagi, T. Unate, H. Nagai and A. Tsujimura, 1976, J. Phys. Soc. Japan **41**, 481.
Yosida, K., 1957, Phys. Rev. **106**, 893.
Zamir, D. and D.S. Schreiber, 1964, Phys. Rev. **136**, A1087.
Zavoiskiy, E.K., 1945, J. Phys. USSR **9**, 245.
Zener, C., 1952, in: W. Schockley, ed., "Imperfections in Nearly Perfect Crystals", (John Wiley, New York) p. 289.
Zinn, W. and W. Wiedemann, 1968, J. Appl. Phys. **39**, 839.

Handbook on the Physics and Chemistry of Rare Earths, edited by K.A. Gschneidner, Jr. and L. Eyring

Chapter 19

EUROPIUM CHALCOGENIDES: EuO, EuS, EuSe AND EuTe

P. WACHTER
Laboratorium für Festkörperphysik der ETH Zürich, CH. 8093 Zurich, Hönggerberg, Switzerland

Contents

a_0 = lattice constant
b = experimentally determined slope of the temperature dependence of θ
c = velocity of light
c_{11}, c_{12}, c_{44} = elastic coefficients
C_0 = theoretical Curie constant
C_{exp} = experimental Curie constant
C_L = lattice part of the specific heat
C_m = magnetic part of the specific heat
dS = surface element in $\boldsymbol{k}$ space
$d\Delta_{mag}$ = relative volume change due to magnetostriction
D = specific circular dichroism
e, e^- = unit of electric charge
E_c = energy of conduction state
E_v = energy of valence state
E_{ia} = interaction energy between electromagnetic radiation and magnetized matter
E_D = donor activation energy
E_{D300} = donor activation energy at 300 K
E_G = energy gap
F = specific Faraday rotation
F_h = reduced magnetic field
g_J = Landé factor
h = scaled magnetic field
$\hbar$ = Planck's constant
H = magnetic field
$H_{a,ext}$ = applied magnetic field
H_i = internal magnetic field
H_d = demagnetizing field
H_{ex} = exchange energy
$\mathrm{Im}(\sigma_{xy})$ = imaginary part of the off-diagonal optical conductivity tensor
J = total angular momentum
J_z = z-component of total angular momentum
J_{vc} = joint density of states of valence and conduction bands

$J_{i,j}$ = exchange constant between the ith and jth ion site, respectively
J_r = exchange constant between two ions at distance r
$J_{1,2}$ = exchange constant for nearest and next nearest ion interactions, respectively
$\bar{J}_{1,2}$ = effective exchange constant for nearest and next nearest ion interactions, respectively
J_{fd} = intra-atomic exchange energy between f and d electrons
J_{fd}^{inter} = inter-atomic exchange energy between f and d electrons
J_{sf} = intra-atomic exchange energy between f and s electrons
k = absorption index
$\boldsymbol{k}, \boldsymbol{k}'$ = wave vector
k_B = Boltzmann constant
K = absorption coefficient
K_0 = absorption coefficient for $\omega = \omega_0$ in Urbach's equation
l = thickness of magnetized material
L = orbital quantum number
$\frac{L_T - L_0}{L_0}$ = relative change in length due to magnetostriction
m = scaled magnetization
m = mass of the electron
m^* = effective mass of the electron
m_l = orbital magnetic quantum number
M = magnetization
M_0 = saturation magnetization
M_s = spontaneous magnetization of a domain
M^* = reduced mass of two ions
M_{vc} = momentum matrix element of a transition between valence and conduction band
n = refractive index
$n_{r,\ell}$ = refractive index for right and left hand circularly polarized light respectively
$n_{\alpha\uparrow,\beta\uparrow}$ = numbers of occupied initial spin up and empty final spin up states, respectively, per total number of initial and final states, respectively
N = number of particles per volume
$N_{f.c.}$ = number of free carriers per volume
N_{Eu} = number of Eu ions per volume
N_D = demagnetizing factor
$\boldsymbol{p}$ = momentum vector of the electron
P = spin polarization
P_0 = principal value of the Kramers–Kronig integral
q = wave vector of phonons
Q = quantum efficiency
r = spatial vector of a conduction electron
R_n = spatial vector of the nth ion
R = ionic radius
$\mathrm{Re}(\sigma_{xy})$ = real part of the off-diagonal optical conductivity tensor
s_i = spin of the ith electron
$S_{i,j}$ = spin of the ith and jth ion, respectively
S = spin quantum number
t = transfer integral
T = temperature
T_C = Curie temperature
T_N = Néel temperature
T_x = temperature for which the conduction band crosses the trap or donor level
U_m = magnetic energy
U_p = polarization energy
$U_{(p-de_g)}$ = energy difference between p and $5de_g$ states
$U_{(f-dt_{2g})}$ = energy difference between f and $5dt_{2g}$ states
v_s = sound velocity
V = Verdet constant
W = absorption power
x = percentage of dopant
$z_{1,2}$ = numbers of next and next nearest neighbors, respectively
z_r = number of neighbors at distance r
α, α' = critical exponent of specific heat
a_m = magnetic part of expansion coefficient
β = critical exponent of magnetization
β_{lin} = linear coefficient of thermal expansion
γ = critical exponent of magnetic susceptibility
γ_D = coupling constant of donor to conduction band
δ = critical exponent of critical isotherm
$\Delta a/a_0$ = relative change of lattice constant
$\Delta V/V_0$ = relative change of volume
Δ_{CF} = crystal field splitting between $5dt_{2g}$ and $5de_g$ states
ΔE = red shift of the absorption edge
ΔE_B = band width of conduction band
ΔE_{SO} = spin–orbit coupling energy
Δp = pressure difference
ϵ = critical temperature region
ϵ_0 = influence constant

ϵ_1 = real part of the dielectric constant
ϵ_2 = imaginary part of the dielectric constant
ϵ_{opt} = high frequency dielectric constant
ϵ_{stat} = low frequency or static dielectric constant
λ = wavelength of light
∇_k = gradient of energy in k space
∇V = electric field in matter
μ = mobility of charge carriers
μ_B = Bohr magneton
μ_{eff} = effective Bohr magneton
μ = magnetic moment vector
κ = isothermal compressibility
κ_{ad} = adiabatic compressibility
ρ = density of matter
τ = life time of photo excited carriers
τ_{tot} = total scattering time of electrons
τ_{ph} = electron–phonon scattering time
τ_m = electron–magnetic excitation scattering time
τ_{imp} = electron–impurity scattering time
χ = paramagnetic susceptibility
χ_0 = initial paramagnetic susceptibility
χ_{dia} = diamagnetic susceptibility
θ = paramagnetic Curie temperature (temperature dependent)
θ_0 = paramagnetic Curie temperature (temperature independent)
θ_D = Debye temperature
θ_{Delast} = Debye temperature derived from elastic measurements
σ = electrical conductivity
σ_m = reduced magnetization
σ_s = temperature independent part of the reciprocal inclination
σ_p = constant in Urbach's equation
ω = light frequency
ω_0 = frequency corresponding to the energy gap as used in Urbach's equation
ω_p = plasma frequency
ω_R = resonance frequency of inelastic light scattering
ω_{TO} = transverse optical phonon frequency
ω_{LO} = longitudinal optical phonon frequency
$\omega_{+,-}$ = plasmon-LO phonon coupled mode frequency
Ω_0 = LA phonon frequency as used in Urbach's equation

1. Introduction

During the past 15 years the Eu chalcogenides have received tremendous interest by scientists all over the world. One obvious reason was the hope of using these magnetic semiconductors industrially, e.g. in the form of fast, light beam addressable memory systems in computers, as magneto-optical modulators or as magnetic field activated electronic switches.

The hope for applications dwindled when one realized that upon doping the magnetic ordering temperatures could not be raised up to room temperature. Thus all commercial equipment using these materials would have to work at liquid nitrogen temperatures, if not below.

However, the purely academic interest in magnetic semiconductors, especially the Eu chalcogenides, continued to be an enormous driving force, because the materials turned out to be model substances for studying magnetism. In this respect one should not forget that in the mid fifties the existence of a truly *ferromagnetic* semiconductor or insulator was severely disputed by theoretical physicists. Generally speaking, indirect exchange of the RKKY type (*R*uderman and *K*ittel, 1954; *K*asuya, 1956; *Y*oshida, 1957) via polarization of conduction

electrons is absent in magnetic insulators and Kramers (1934) superexchange leads to antiferromagnetic coupling. The double exchange mechanism of Zener (1951) which necessitates cations of different valence and electrons hopping between them could in principle account for the appearance of ferromagnetism. But perovskites like $La_{1-x}Sr_xMnO_3$ (Jonker and van Santen, 1950) or $La_{1-x}Pb_xMnO_3$ (Searle and Wang, 1969) are either ferrimagnetic and semiconducting or ferromagnetic with high conductivity, being proportional to the magnetization. Only the Bloembergen–Rowland (1955) exchange going via the polarization of the valence electrons of an insulator and described by a damped RKKY function could account for ferromagnetism.

The questions regarding the existence of a ferromagnetic semiconductor or insulator were resolved with the discovery of $CrBr_3$ by Tsubokawa (1960). This compound with a Curie temperature of 37 K is transparent for visible light, thus indicating the existence of an energy gap. In the following year Matthias et al. (1961) discovered in the intermetallic compound $EuIr_2$ a ferromagnetic inclusion which they identified as EuO. Electrical conductivity and magnetization measurements classified this material as a semiconductor becoming ferromagnetic at about 70 K. This discovery opened the door also for the other members of the Eu chalcogenide group to become recognized as magnetically ordering semiconductors. (Busch et al., 1962; McGuire et al., 1962; van Houten, 1962). However, it was not until 1964 that Wachter (1964) and Busch et al. (1964a) gave experimental evidence by means of low temperature optical absorption measurements that the Eu chalcogenides remained semiconductors also below their respective magnetic ordering temperatures. These experiments also gave first evidence of a new magneto-optical phenomenon, namely the red shift of the absorption edge of a ferromagnetic semiconductor upon cooling below T_C.

In the mean time a wealth of information has been collected on the Eu chalcogenides and has been described in various review articles (Methfessel, 1965; Busch and Wachter, 1968; Kasuya and Yanase, 1968; Yanase and Kasuya, 1968; Methfessel and Mattis, 1968; Freiser et al., 1968a; Wachter, 1969a; Haas, 1970; Wachter, 1971a and Wachter, 1972). It may very well be stated that there hardly exists a group of compounds so thoroughly investigated in every respect as the Eu chalcogenides. They are considered not only as model substances with respect to magnetism but also as models for ionic semiconductors. It is obvious that this article depends very strongly on previous reviews for the necessary background information. However, emphasis will be put on the new developments in the seventies and well established experiments and theories will be discussed.

2. Crystalline properties

The Eu chalcogenides crystallize in the fcc rocksalt structure. The lattice constant is increasing with increasing anion radius from 5.14 Å for EuO to 6.60 Å for EuTe (see table 19.1). Since the Eu chalcogenides form divalent compounds

TABLE 19.1
Crystalline data of the Eu chalcogenides

	a_0 (Å)	ρ (gr/cm^3)	N ($\times 10^{22}$ mol/cm^3)	κ[a] ($\times 10^{-12}$ cm^2/dyne)	c_{11}[b] ($\times 10^{11}$ dyne/cm^2)	c_{12}[b] ($\times 10^{11}$ dyne/cm^2)	c_{44}[b] ($\times 10^{11}$ dyne/cm^2)	$\theta_{D_{el.}}$[b] (K)	θ_D (K)	$\beta_{lin.300}$[g] ($\times 10^{-6}$ K^{-1})
EuO	5.141	8.20	2.94	1.1 ± 0.2	19.2 ± 0.6	4.25 ± 0.8	5.42 ± 0.13	350	353[b,c]	13.2
EuS	5.968	5.75	1.88	1.8 ± 0.2	13.1 ± 0.5	1.1 ± 0.8	2.73 ± 0.11	276	262[b,d]	12.6
EuSe	6.195	6.44	1.68	1.9 ± 0.4	11.6 ± 0.4	1.2 ± 0.6	2.28 ± 0.09	232	176[e]	13.1
EuTe	6.598	6.45	1.39	2.5 ± 0.2	9.36 ± 0.4	0.67 ± 0.6	1.63 ± 0.07	189	140[f]	13.6

[a]Levy and Wachter (1970); [b]Shapira and Reed (1972); [c]Petrich et al. (1971); [d]Moruzzi and Teaney (1963); [e]White and McCollum (1972); [f]Busch et al. (1964b); [g]Levy (1969).

of the type $Eu^{2+}X^{2-}$ the lattice constant can be computed rather precisely with a hard sphere model by adding the divalent ionic diameters (e.g. Pauling, 1960) of the constituents. From the lattice constant and the molecular weight, the X-ray density, ρ, and the number of molecules/cm^3, N, can be derived and these values are also compiled in table 19.1. Since EuO has the highest density of molecules it will have the lowest compressibility of the series. This is indeed the case if the compressibility measurements are performed correctly. Sources of error are imperfect substances, non hydrostatic pressure and mechanical dilatation of piston displacement machines (Srivastava and Stevenson, 1968). The first reliable value of the compressibility, κ, of EuO has been given by McWhan et al. (1966) using X-ray scattering of EuO powder dispersed in a NaCl matrix and pressures up to 100 kbar. The bulk modulus was then extrapolated to zero pressure. In this experiment hydrostaticity is ensured because at these high pressures nearly every material is plastic. Levy and Wachter (1970) on the other hand developed a very simple device to measure compressibilities on single crystals at low pressures. The crystal is placed in the center of a beryllium washer (0.7 mm thick, outer dia. 4 mm, bore 1.7 mm) which is clamped between two hardened steel blocks. Oil is conducted to the pressure chamber through a thin steel tube and pressure on the oil is exerted by means of an external power press. The pressure cell is mounted on the goniometer table of an X-ray diffractometer and adjusted so that a Bragg reflection enters the slit of the detector head. The angular deflection of the scattered X-ray beam is related to the lattice spacing by the Bragg law. The change of the deflection angle with pressure directly yields $\Delta a/a_0$. The oil pressure is read with a manometer so the compressibility is given by

$$\kappa = -3\Delta a/(a_0 \Delta p) \tag{19.1}$$

and it is also compiled in table 19.1. Also infrared optical data permit the evaluation of the compressibility which agrees with the tabulated values within the given limits of error (Levy and Wachter, 1970). Jayaraman et al. (1974) have recently remeasured the compressibilities and they find practically the same numbers.

Shapira and Reed (1972) measured the sound velocities (v_s between 1.58 and 4.74×10^5 cm/sec) at 77 K of longitudinal and shear waves propagating along the [100] and [110] directions, this temperature being above the magnetic ordering temperatures of the Eu chalcogenides. From the observed directions of ion displacements together with the X-ray density these data permit the calculation of the elastic coefficients of a cubic system, c_{11}, c_{12} and c_{44}. It can be seen from table 19.1 that the Cauchy relations $c_{12} = c_{44}$ are not fulfilled very well. Only for EuO, the most ionic compound of the EuX series, reasonable agreement is observed. Deviations from the Cauchy relations in rocksalt type crystals usually have their reason in a strengthening of the directionality of the binding which becomes more pronounced in the heavier members of the EuX series. However, as a consequence, the adiabatic compressibility $\kappa_{ad} = 3/(c_{11} + 2c_{12})$ computed from only two elastic constants turns out to be somewhat too large compared with the listed values of table 19.1. Since κ will only be temperature dependent in the order of the thermal lattice contraction $d(\Delta V/V_0)/dT \approx 1\%$ (Levy, 1969) no

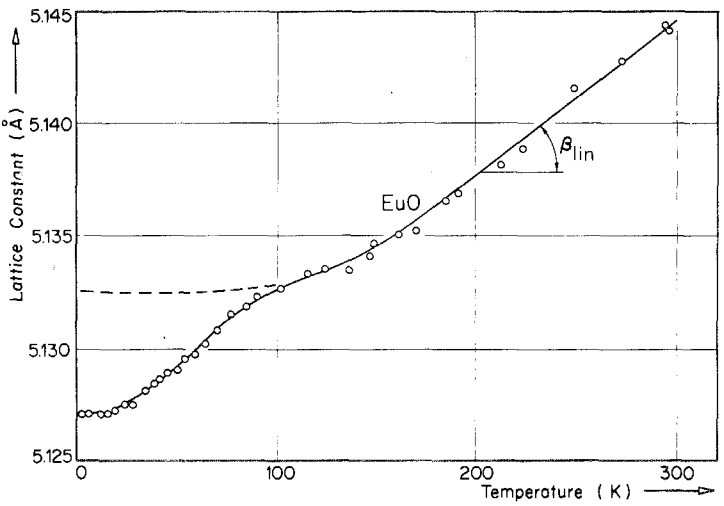

Fig. 19.1. Thermal variation of the lattice constant of EuO (after Levy, 1969). β_{lin} is the linear coefficient of thermal expansion. The dashed line is the expected behavior if there is no magnetic order.

difficulties should arise by comparing compressibilities at different temperatures and also the adiabatic and isothermal compressibility are expected not to differ significantly.

The measurements of the sound velocity at the same time permit the evaluation of the elastic Debye temperature $\theta_{D\,elast.}$, also listed in table 19.1. Using the Debye model one can compute θ_D from specific heat data, correcting for the magnetic contributions. $C_L = 3888(T/\theta_D)^3$ joules/mole degree. Also these Debye temperatures are given in table 19.1 in the case of EuO and EuS using corrections proposed by Shapira and Reed (1972).

The linear coefficient of thermal expansion, β_{lin} has been measured by Levy (1969) using single crystals in an X-ray goniometer in the Bragg configuration. As mentioned already above, the deflection of the X-ray beam is directly related to the lattice constant which then can be observed as a function of temperature. β_{lin} and its temperature dependence is thus obtained above and below the magnetic ordering temperature. The temperature dependence of the lattice constant is displayed in fig. 19.1 for EuO. The values of β_{lin} near room temperature are collected in table 19.1.

3. Magnetic properties

3.1. *Undoped samples*

In the $Eu^{2+}X^{2-}$ series the divalent Eu ion carries the magnetic moment. From the position of the Eu ion in the periodic table it follows that it has in addition to the Xe shell a half filled 4f shell. According to Freeman et al. (1966) the charge

density distribution of these 4f electrons is to a major part inside the filled $5s^2$ and $5p^6$ shell of the Xe configuration. Thus even in EuO which has the lowest Eu–Eu separation of only 3.6 Å, direct overlap of 4f wavefunctions is negligible and 4f electrons are efficiently screened electrostatically against perturbations from e.g. crystalline fields. The spectroscopic ground state of the $4f^7$ electrons is $^8S_{7/2}$, having the highest multiplicity as demanded by Hund's rule and an orbital moment of $L = \Sigma_{+3}^{-3} m_l = 0$.

Early measurements of the paramagnetic susceptibility

$$\chi = C_0/(T - \theta) \qquad \text{with } C_0 = N\mu_B^2 g_J^2 J(J+1)/3k_B$$

have shown that the effective moment of the Eu chalcogenides is close to the theoretical value $\mu_{eff} = \mu_B g_J \sqrt{J(J+1)} = 7.937\ \mu_B$, but usually somewhat larger (see e.g. Busch et al., 1966). Very recent and careful measurements of magnetization and susceptibility for different quality, spherical single crystals by Köbler and Fischer (1975), taking into account also the diamagnetic susceptibility of the ion cores, $\chi = C_{exp}/(T - \theta) + \chi_{dia}$ show consistently that C_{exp} has to be taken between about 3.5% and 7.5% larger than the theoretical value. On the other hand, high quality samples approach the theoretical value of the saturation magnetization (collected in table 19.2) to within some tenth of a percent, although the applied field for ferromagnetic samples had to be as high as 40 kOe. In view of the fact that one observes deviations from the theoretically expected susceptibility it is surprising that the saturation magnetization $M_0 = N\mu_B g_J J$ can be obtained so precisely. Thus the problem rests with the Curie constant C_{exp}. The parameters entering into C_0 are only g_J and J which, however, correspond to the free ion value $^8S_{7/2}$, as has recently been confirmed by precise g-factor measurements of Sperlich and Jansen (1974), yielding $g = 1.993 \pm 0.006$. The question of the enhanced Curie constant will be taken up later.

The paramagnetic Curie temperatures, θ, have recently been remeasured with great accuracy by Köbler and Fischer (1975) and they are also collected in table 19.2. The negative value for EuTe shows that this material is an antiferromagnet. However, a positive θ is not necessarily an indication for ferromagnetism, as demonstrated by the complex magnetic behavior of EuSe. On the other hand EuO and EuS are clear cut ferromagnets. With their highly symmetric rocksalt structure, their spherical symmetric $^8S_{7/2}$ ground state and their negligible magnetic anisotropy (anisotropy constant for EuS less than -5 Oe after Franzblau et al., 1967) these compounds are considered as models for an ideal Heisenberg ferromagnet.

In the Eu chalcogenides the determination of the exact magnetic ordering temperature has always been unsatisfactory. In the early days there was of course the problem of sample quality and calibration of thermometers (see collection of $T_{C,N}$ by Wachter, 1972). But, as pointed out by Schwob (1969), it has not always been realized that the magnetic ordering temperatures should be measured in applied fields appreciably less than the demagnetizing field, $H_d = -\frac{4}{3}\pi M_0$ for spherical probes. Especially for antiferromagnets it turned out best to reduce the applied field to 10 Oe and measure the initial susceptibility. Because

TABLE 19.2
Magnetic properties of undoped Eu chalcogenides

	M_0(theo) (Gauss)	θ[a] (K)	b[a]	$T_{C,N}$ (K)	Magn. Order	$\bar{J}_1/k_B$ (K)	$\bar{J}_2/k_B$ (K)
EuO	24007	79 ± 4	0.075	69.330[b]	ferro	$+0.606 \pm 0.008$[f]	$+0.119 \pm 0.015$[f]
EuS	15346	18.7 ± 1	0.037	16.57 ± 0.02[c]	ferro	$+0.228 \pm 0.004$[f]	-0.102 ± 0.005[f]
EuSe	13720	8.5 ± 1	0.035	4.60 ± 0.1[d]	antiferro I	$+0.073 \pm 0.01$	-0.011 ± 0.01
				2.8[e]	ferri		
				1.8[e]	antiferro II		
EuTe	11356	-4.0 ± 1	0.045	9.58 ± 0.1[d]	antiferro	$+0.043 \pm 0.01$	-0.15 ± 0.01

[a]Köbler and Fischer (1975) (modified); [b]Kornbilt et al. (1973); [c]Berkner (1975); [d]Schwob (1969); [e]Griessen et al. (1971); [f]Dietrich et al. (1975).

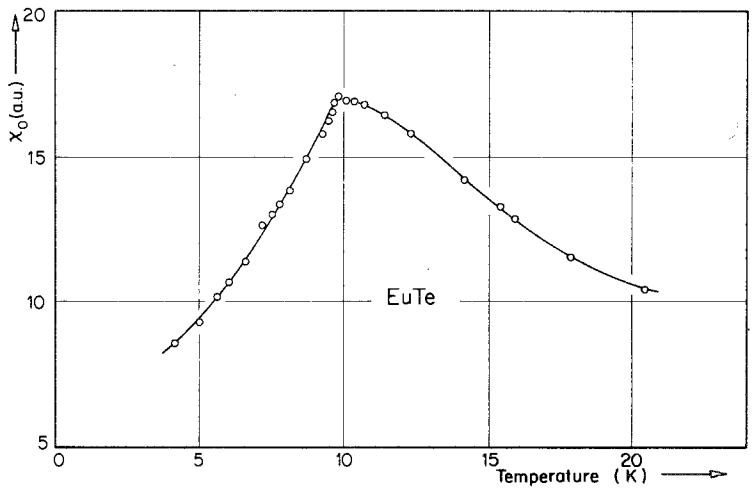

Fig. 19.2. Initial susceptibility of EuTe (after Schwob, 1969).

for $H \to 0$ Fischer (1962) has shown theoretically that the Néel temperature T_N is not at the peak of the initial susceptibility but at the steepest slope of the curve. For EuTe and EuSe the low field susceptibilities are displayed in figs. 19.2 and 19.3, respectively, and the magnetic ordering temperatures of the Eu chalcogenides are collected in table 19.2.

Of further interest are the magnetic structures of EuTe and EuSe. Early neutron scattering experiments by Will et al. (1963) revealed for EuTe antifer-

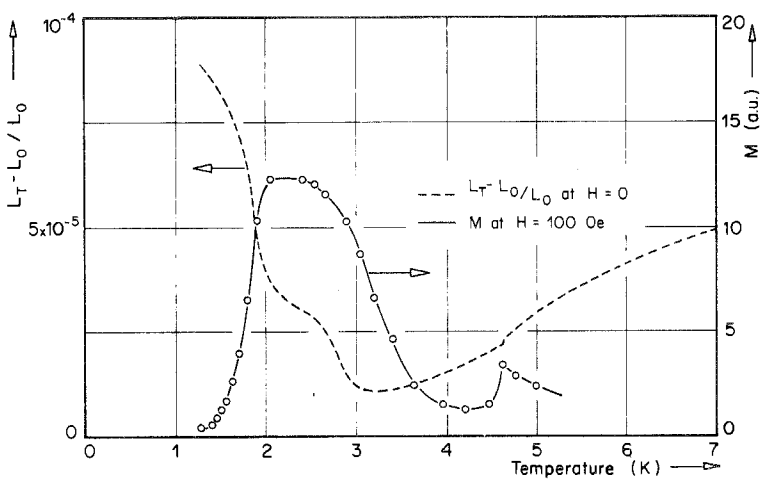

Fig. 19.3. Temperature dependence of the spontaneous magnetostriction of EuSe in the [100] direction and magnetization in a field of 100 Oe. The curves are measured with increasing temperature (after Griessen et al., 1971).

romagnetism of the second kind (MnO structure), with ferromagnetic (111) planes stacked in a NSNS spin sequence. The magnetic structure of EuSe is much more complex. Again, neutron diffraction measurements by Pickart and Alperin (1965 and 1968) have indicated antiferromagnetism below 4.6 K in zero external fields. Successive ferromagnetic (111) planes were supposed to be oriented in a NEWS sequence. However, this spin structure was first questioned by Wachter (1968a), who investigated antiferromagnetic domains with a polarizing microscope and observed magnetically induced optical activity. This necessitates a spiral spin structure, which later indeed has been deduced by Fischer et al. (1969) with a more careful analysis of neutron data. The newly proposed spin structure of this antiferromagnetic I region is NNSS. However, below 2.8 K suddenly a spontaneous magnetic moment appears (Schwob and Vogt, 1966; Busch and Wachter, 1966 and Wachter, 1968a) and the neutron data revealed a mixture of two magnetic phases: NSNS and NNSNNS in a ratio of $\frac{5}{13}$. The magnetic order in zero field is consequently ferrimagnetic with a spontaneous magnetic moment of about 1.7 μ_B. In fig. 19.3 the increase of the magnetization due to the ferrimagnetic order is readily seen, but also in addition a precipitous drop for $T < 1.8$ K, the temperature of the steepest slope. Griessen et al. (1971) proposed for this antiferromagnetic II region a NSNS spin structure. The magnetic transition temperatures of 4.6 K, 2.8 K and 1.8 K have also been confirmed with measurements of the specific heat by White and McCollum (1972). In low applied magnetic fields the two antiferromagnetic regions I and II become also ferrimagnetic in larger fields finally ferromagnetic. Thus EuSe is a metamagnet and the various magnetic phases are displayed in a phase diagram in fig. 19.4.

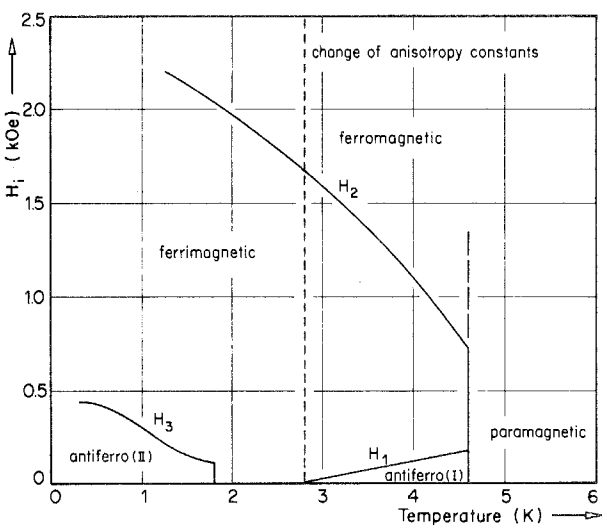

Fig. 19.4. Magnetic phases of EuSe. Hysteresis effects are not shown (after Griessen et al., 1971).

Since the Eu chalcogenides are considered to be models for Heisenberg magnets, the isotropic exchange hamiltonian

$$H_{ex} = -\sum_{ji} J_{ij} \boldsymbol{S}_i \cdot \boldsymbol{S}_j$$

$$= -\sum_{nn} \bar{J}_1 \boldsymbol{S}_0 \cdot \boldsymbol{S}_{nn} - \sum_{nnn} \bar{J}_2 \boldsymbol{S}_0 \cdot \boldsymbol{S}_{nnn} \tag{19.2}$$

can be applied. This yields in molecular field approximation the paramagnetic Curie temperature θ of a ferromagnet

$$k_B\theta = \tfrac{2}{3}S(S+1)(12\bar{J}_1 + 6\bar{J}_2). \tag{19.3}$$

For the ferrimagnetic phase NNSNNS of EuSe Schwob (1969) has derived

$$k_B\theta = \tfrac{2}{3}S(S+1)(3\bar{J}_1 - 3\bar{J}_2), \tag{19.4}$$

assuming, as mentioned above, that about $\frac{3}{4}$ of the spins are in that phase. The Néel temperature of an NSNS antiferromagnet is

$$k_B T_N = \tfrac{2}{3}S(S+1)(-6\bar{J}_2) \tag{19.5}$$

and the one of the NNSS phase of EuSe

$$k_B T_N = \tfrac{2}{3}S(S+1)(+6\bar{J}_1). \tag{19.6}$$

These equations can be easily derived using the spin structures given by the elastic neutron data and the fcc crystal structure of the EuX compounds. $\bar{J}_1$ and $\bar{J}_2$ are the effective exchange integrals of a two parameter solution of eq. (19.2). As pointed out by Zinn (1976) the exchange interactions not only extend over the 12 nearest (*nn*) and the 6 next nearest neighbors (*nnn*) of the Eu^{2+} ions, but further out in a mode determined by the changing covalency of the compounds. Thus $\bar{J}_{1,2}$ are in reality sums over all positive and negative exchange contributions,

$$\bar{J}_1 = \sum_{r_+} (z_r J_r)_+ / z_1 \qquad \text{and} \qquad \bar{J}_2 = \sum_{r_-} (z_r J_r)_- / z_2 \tag{19.6a}$$

with z_1 and z_2 the next and next nearest neighbors, respectively. The individual $J_{1,2}$ may be very different from $\bar{J}_{1,2}$. In addition the measurements of the transferred hyperfine fields of a Mössbauer experiment have given evidence that $\bar{J}_{1,2}$ may also be temperature dependent. For example, considering equation (19.3), this temperature dependence of the exchange constants has in consequence that the paramagnetic Curie temperature θ becomes also temperature dependent. Using only small linear correction terms it can be assumed that $\theta(T) = \theta_0 + bT$. We now have a means of understanding the enhanced Curie constant C_{exp}, described earlier. By inserting $\theta(T)$ into the equation for χ we can see that the experimentally determined Curie constant $C_{exp} = C_0(1+b)$. The relevant b values are also collected in table 19.2. Now the exact determination of the paramagnetic Curie temperature meets criticism and is generally too large. We take this into account by allowing a suitable error limit for θ in table 19.2.

Swendsen (1972) has shown theoretically in a Green's function analysis of a Heisenberg ferromagnet, including also dipolar interactions, that T_C/θ cannot be larger than 0.9. As well for EuO as for EuS the data of table 19.2 show that this ratio is 0.89.

In the case of antiferromagnets $\bar{J}_{1,2}$ can readily be computed from equations (19.5) or (19.6) and (19.3) and these values are also compiled in table 19.2, using $S = \frac{7}{2}$ and θ, T_N from the table. In the case of ferromagnets an analysis of inelastic neutron scattering, magnetic contributions to specific heat and nuclear magnetic resonance (NMR) has to be used to evaluate $\bar{J}_{1,2}$, fitting spin wave theories to the experimental data. While for EuS all experiments yield agreement of the exchange constants to within the given limits of error, specific heat and NMR for EuO have indicated $\bar{J}_2$ to be negative (Henderson et al., 1970 and Boyd, 1966) but inelastic neutron scattering experiments by Passell et al. (1971) have shown $\bar{J}_2$ to be positive.

In a recent critical analysis Dietrich et al. (1975) compare these experiments and argue that specific heat and NMR at temperatures less than about $\frac{1}{4}T_C$ sample only spin waves with low wave vector. In that region the spin wave energy depends only on the stiffness constant, being proportional to the sum of $(\bar{J}_1 + \bar{J}_2)$ and thus $\bar{J}_1$ and $\bar{J}_2$ cannot be determined individually. On the other hand, inelastic neutron scattering determines the dispersion of the spin waves over the entire Brillouin zone and the best fit of spin wave theory to these data yield $\bar{J}_1$ and $\bar{J}_2$ separately and $\bar{J}_2$ is shown to be positive. The recommended values for $\bar{J}_{1,2}$ of EuO and EuS are also collected in table 19.2.

3.1.1. *Critical exponents*

In the preceding subsection we have used simple molecular field theory to describe the magnetic behavior of the Eu chalcogenides. Several objections were made concerning the microscopic exchange mechanisms, e.g. the exchange has long range components, the exchange constants seem to be temperature dependent and dipolar forces may play an appreciable role. The discussion of the temperature region very close to T_C, i.e. the critical region $-0.1 < \epsilon = (T/T_C) - 1 < +0.1$ may shed some additional light on this problem. Near the magnetic phase transition the thermodynamic functions or the corresponding magnetic entities can be described by an asymptotic power law expression (Stanley, 1971) yielding for the

specific heat

$$C_m \sim \epsilon^{-\alpha}, \qquad T \to T_C, \quad H = 0; \tag{19.7}$$

magnetization

$$M(T)/M(0) \sim -\epsilon^{\beta}, \qquad T \to T_C, \quad H = 0; \tag{19.8}$$

initial susceptibility

$$\chi_0 \sim \epsilon^{\gamma}; \qquad T \to T_C, \quad H = 0; \tag{19.9}$$

critical isotherm

$$H \sim M(H)^{\delta}; \qquad H \to 0, \qquad T = T_C \tag{19.10}$$

These equations may be regarded as the definitions of the critical point exponents α, β, γ and δ.

Measurements of the field and temperature dependence of the magnetization have to be performed in the critical region, following certain paths in the $M(T, H)$ diagram: the critical isochore, the coexistence curve (obtained by extrapolation towards zero field) and the critical isotherm. The most recent experiments have been performed by Berkner (1975) and Huang and Ho (1975), using the Faraday rotation of transmitted light in EuS and EuO to determine the magnetization. The analysis in the critical region gave the exponents collected in table 19.3. In addition, measurements of the specific heat and its divergence at T_C exist for EuO (Kornbilt et al., 1973) and EuS (Van der Hoeven et al., 1968). In EuO it could be shown that $\alpha = \alpha' = -0.04 \pm 0.03$ (primed and unprimed parameters correspond to $T < T_C$ and $T > T_C$, respectively) with the identity of α and α' being a postulate of the scaling theory. However, in EuS the specific heat data of van der Hoeven et al. (1968) have been analyzed by Wielinga (1971) to yield $\alpha = -0.04$, whereas $\alpha' = 0.25$ is proposed by Teaney and Moruzzi (1970).

The static scaling law hypothesis (e.g. Griffiths, 1967) provides us with an equation of state in the one phase region close to the critical point which incorporates the power law relations eqs. (19.8)–(19.10):

$$F_h/\sigma_m^{\delta} = h(x) \qquad \text{with} \quad x = \epsilon/\sigma_m^{1/\beta}, \quad \sigma_m > 0 \tag{19.11}$$

where F_h and σ_m are reduced, dimensionless field and magnetization quantities. If this equation of state is correct, then plotting F_h/σ_m^{δ} versus $\epsilon/\sigma_m^{1/\beta}$ should give a universal curve with two branches, one for $T > T_C$ and one for $T < T_C$. This is indeed the case and is shown for 23 isotherms of EuS in fig. 19.5. This experimental verification of the scaling law for EuS (and many other ferromagnets like YIG, $CrBr_3$, EuO etc.) permits us to use also the scaling law for the

TABLE 19.3
Critical exponents exponents of the ferromagnets EuO and EuS

	EuO	EuS	Theory[f]
α	-0.04 ± 0.03[a]	-0.04[c]	~ -0.1
α'	-0.04 ± 0.03[a]	0.25[d]	~ -0.1
β	0.370 ± 0.006[b]	0.335 ± 0.01[e]	~ 0.36
γ	1.30 ± 0.02[b]	1.06 ± 0.05[e]	~ 1.40
δ	4.51*	4.20 ± 0.1[e]	~ 5

*Computed using scaling relations. [a]Kornbilt et al. (1973); [b]Huang and Ho (1975); [c]Wielinga (1971); [d]Teaney and Moruzzi (1970); [e]Berkner (1975); [f]de Jongh and Miedema (1974).

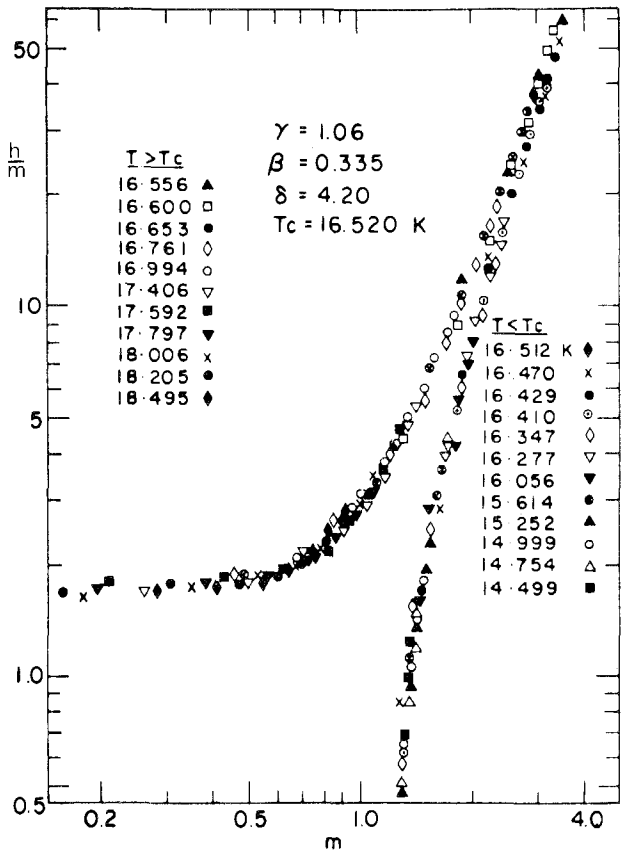

Fig. 19.5. Scaling plot for EuS. The data are plotted as the scaled magnetization $m = (M/M_0)|\epsilon|^{-\beta}$ versus the scaled magnetic field $h = (g_J\mu_B S/k_B T_C)H_i|\epsilon|^{-\beta\delta}$, H_i being the internal field (after Berkner, 1975).

critical exponents

$$\gamma = \beta(\delta - 1) \quad \text{(a)} \qquad \text{and} \qquad \alpha + 2\beta + \gamma = 2 \quad \text{(b)} \tag{19.12}$$

For EuO eq. (19.12b) is fulfilled excellently and from (19.12a) we compute $\delta = 4.51$. For EuS (19.12a) is fulfilled very good and we derive $\alpha = 0.27$ in good agreement with Teaney and Moruzzi's (1970) estimate, but since $\alpha \neq \alpha'$ there is a discrepancy of possibly experimental origin.

The experimental critical exponents of table 19.3 can now be compared with the predictions for 3 dimensional Heisenberg magnets. While the general agreement between theory and experiment is quite good, the exponent γ of EuS is an exception, approaching nearly the molecular field value. As pointed out by Berkner (1975) there is a general trend for low T_C materials to exhibit smaller γ values than theory predicts. On the other hand this is a clear indication that the

microscopic exchange interactions are not understood completely and therefore could not be adequately considered in the theoretical series expansion. More information concerning the temperature and range dependence of the exchange constants is needed.

3.2. *Doped* Eu *chalcogenides*

The room temperature electrical resistivities of the undoped Eu chalcogenides are above 10^6 ohm·cm, so that at the temperature of magnetic order the resistivity for all practical reasons is infinite and no effect of residual free carriers can be expected. In spite of this it must be made clear that this does not mean that the compounds are perfect and stoichiometric. There is always a possibility that Eu^{3+} ions are present which then act as acceptors. If these acceptor states are within kT above the $4f^7$ states or even below the 4f levels we are always left with a hole in the 4f states which remains localized, unless the 4f states are hybridized with other (p) bands and a transfer of holes into these bands is possible.

For n-type doping we must remark that the first incorporated free electrons will be trapped by the ever present Eu^{3+} acceptor states, resulting in an electronically more perfect, compensated material. This effect has not always been realized in the past and therefore doping concentrations in the order of a few percent must be regarded with care, most of the electrons have been lost for compensation. Thus the relevant number in doping experiments is not the concentration of added dopant, but the concentration of free carriers which is related to the concentration of dopant in an unknown manner. In fig. 19.6 we show the absorption coefficient of "pure" EuO I and one observes indeed a rather high residual absorption for wavelengths larger than the absorption edge due to Eu deficiency and formation of Eu^{3+} ions. Heating this same crystal in Eu vapor results in a much more perfect material EuO II with the residual absorption reduced by orders of magnitude. Doping for example with Gd now leads to free carriers and their corresponding additional absorption can be measured.

A further problem which is devaluating the early results of doped or alloyed Eu chalcogenides has been the assumption that the percentage of admixture of dopant in the chemical starting composition is also present in the final composition. But as shown in table 19.4 differences of up to a factor 10 are possible, if as in the case of La the dopant is not dissolved. Besides, it is severely disputed amongst chemists whether e.g. the system EuSe–GdSe forms solid solutions over the whole concentration range, as has been reported for powder material (Methfessel, 1965). Single crystals show phase separations at certain mixing ratios.

Doping can be performed in the cation and in the anion system. If we dope in the cation system we hopefully only substitute some divalent Eu ions with trivalent ions such as Gd, Ho or La and generate free electrons according to Fermi statistics and activation energy of the donor. Gd has been thought of as

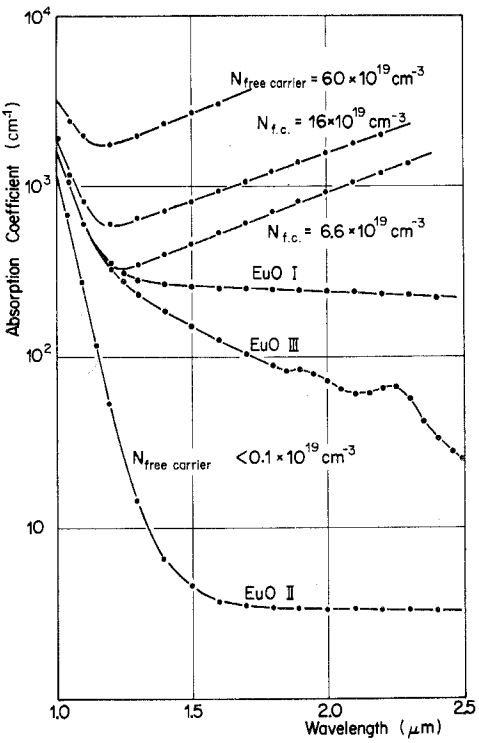

Fig. 19.6. Absorption coefficient of EuO crystals with excess of oxygen (EuO I), nearly stoichiometric EuO (EuO II) and EuO with oxygen deficiency (EuO III) and Gd doped EuO. The Gd doped samples are characterized by their room temperature free carrier concentration (after Schoenes and Wachter, 1974).

TABLE 19.4
Curie temperatures of doped EuO and EuS.

EuO	EuS	Start comp. (mol %)	Final comp. (mol %)	θ (K)	T_C (K)
La		5	0.4	133	132
Gd		5	3.4	137	135
Gd		10	7.8	136	
Ho		5	5.0	136	134
	Gd	5	1	49	30
	Cl		1	56	~55

After Shafer and McGuire (1968).

leaving the spin system undisturbed because of the same spectroscopic ground state $^8S_{7/2}$ of Eu^{2+} and Gd^{3+}. However, the $4f^7$ state of Gd is several eV below the one of Eu. On the other hand doping with La dilutes the spin system. The least disturbance of the spin system is achieved by the incorporation of e.g. Cl in EuS or I in EuTe, i.e. by doping in the anion sublattice.

The general effects of doping the Eu chalcogenides have been extensively discussed in earlier review articles by e.g. Methfessel and Mattis (1968). Since the measurements now bear only qualitative significance for reasons mentioned above they will not be reproduced here. Generally, one observes already for very small concentrations of dopant a drastic increase of θ and T_C and for larger alloying concentrations of about 20% Gd or La, θ decreases again, GdS, GdSe and GdTe being antiferromagnetic metals and LaS, LaSe and LaTe being diamagnetic, even superconducting metals. This behavior of θ has been interpreted as being due to an indirect exchange mechanism of the oscillatory RKKY type. However, this interpretation has been questioned by Bayer and Zinn (1971, 1973) and Güntherodt and Wachter (1974), who showed that the dominant exchange mechanism in the metallic end members of the alloy system, in GdS and GdSe, is fd-superexchange through overlap of p^6 and $5de_g$ antibonding levels.

Since the $4f^7$ states of Eu^{2+} and of Gd^{3+} are at very different positions in an energy level scheme, the microscopic exchange between Gd–Eu ions and Eu–Eu ions may be very different and the question arises whether the spin of the Gd ion is parallel or antiparallel with the neighboring Eu spins. This problem has been investigated for EuO:Gd by Schoenes and Wachter (1974) and for EuS:Gd by Bayer and Zinn (1971, 1973). The latter authors argue if one would have a heterogeneous mixture of $(1-x)$ EuS($\uparrow\uparrow$)$+x$GdS($\uparrow\downarrow$) one expects the gradient $\Delta M_0/\Delta x = -M_0(0) = -15.3$ kG, with $M_0(0)$ the saturation magnetization for $x = 0$. The homogeneous mixture $Eu(\uparrow)_{1-x}Gd(\downarrow)_xS$ with antiparallel alignment of the Eu^{2+} and Gd^{3+} $4f^7$ spins yields $\Delta M_0/\Delta x = -2M_0(0) = -30.6$ kG. The latter value is found to agree with hysteresis experiments, thus establishing that Gd and Eu spins are antiparallel. It is further claimed that each Gd substituent locally distorts the crystal symmetry by disturbing the periodicity. Locally this shifts the energy levels of the Eu ions and modifies the exchange integrals $\bar{J}_1$ and $\bar{J}_2$. Apparently, $\Delta\bar{J}(\text{Eu}) = 12(\Delta\bar{J}_1 + \Delta\bar{J}_2)$ is positive and larger than the negative $J(\text{Gd})$ for x up to about 10%, giving rise to the increase of θ and T_C. The decrease of θ and the appearance of antiferromagnetism for x larger than about 0.5 is due to the antiparallel arrangement of Gd and Eu spins and not to the oscillatory behavior of the RKKY function. Doping with the moment free La can, of course, also increase θ due to local distortions of the 4f states of Eu, but no antiferromagnetism is expected for large La concentrations as is indeed the case. Schoenes and Wachter (1974) showed that also in Gd doped EuO single crystals the Gd spins enter the material antiparallel with the Eu spins. For Gd concentrations of about 0.8% (as measured by microprobe analysis) the saturation magnetization at $T \to 0$ is practically unchanged as compared with the undoped material, however, T_C is increased from 69 K to 83 K. In fig. 19.7 the normalized

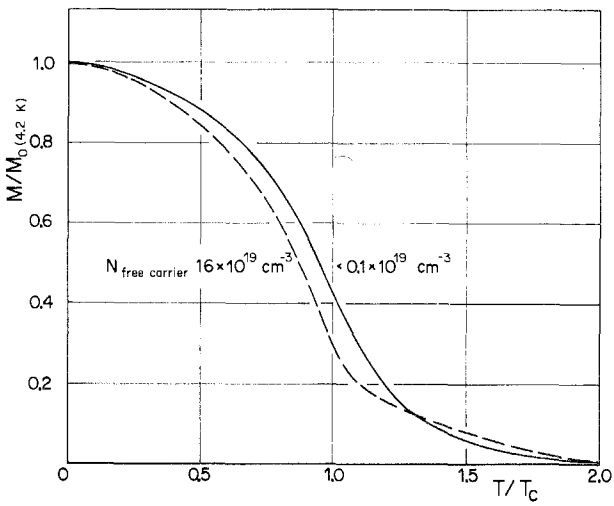

Fig. 19.7. Normalized magnetization of an undoped and Gd doped EuO crystal with 16×10^{19} electrons/cm^3. A magnetic field of 6.7 kOe is applied (after Schoenes and Wachter, 1974).

magnetization of an undoped and Gd doped EuO crystal is shown in an applied field. It is observed that the magnetization of the doped crystal is consistently below the one of the undoped sample indicating that doping makes the sample harder to magnetize. This is also observed in an $M(H)$ plot and has been interpreted with antiparallel Eu–Gd spins and formation of antiparallel Gd clusters.

The formation of chemical clusters of dopants and also of spin clusters (large regions of ferromagnetically aligned Eu spins in a nonferromagnetic matrix) make doped materials inhomogeneous and problems of measuring the Curie temperature must be considered. As can be seen from table 19.4 θ and T_C are close to each other for good quality EuO crystals and $T_C \approx 135$–140 K seems to be the maximum achievable Curie temperature in EuO crystals. However, Ahn et al. (1971) report on Fe doped EuO films with T_C up to 190 K but the magnetization curves show peculiar humps, indicating a two-phase region. The question of measuring T_C becomes acute when seeing specific heat measurements of Moruzzi et al. (1968) on Gd doped EuS which exhibit a very broad peak of the magnetic part of the specific heat, practically excluding a derivation of T_C from these measurements.

In the low doping regime Schoenes and Wachter (1974) have developed a magnetooptical method for the determination of T_C on transparent crystals. T_C is defined in zero magnetic field when magnetic domains appear which depolarize transmitted light due to the Faraday rotation of individual ferromagnetic domains. The precise determination of T_C is of special importance when one wants to make a quantitative comparison with theory of the increase of T_C due to doping. For dopant concentrations less than about 1% most theories (e.g.

Baltensberger and de Graaf, 1960; Karpenkov and Berdishev, 1964) yield an additional ferromagnetic exchange but the most quantitative theory is the "magnetic impurity" model of Kasuya and Yanase (1968). Here the basic idea is that the donor electron with spin s_i, staying in the vicinity of the donor, magnetically polarizes neighboring Eu spins S_n by means of a strong fd exchange interaction (assuming the donor and conduction band to be of d-symmetry) thus creating a giant spin molecule or spin cluster. The additional exchange interaction due to impurity electrons is thus $-2\Sigma_{in} J_{in} s_i \cdot S_n$ and the increase in Curie temperature will be given by

$$k_B \Delta T_C = 2 \sum_{in} J_{in} s_i \cdot S_n \tag{19.13}$$

where n is summed over the number of neighboring 4f spins and i is summed over the number of impurity electrons. This equation can be approximately rewritten in the following form:

$$k_B \Delta T_C \simeq (N_{f.c.}/N_{Eu}) \left(2 \sum_{n} J_n s \cdot S_n\right) \tag{19.14}$$

where $N_{f.c.}/N_{Eu}$ is the relative concentration of impurity electrons. The second term of the right hand side of this equation can be measured directly in an optical absorption experiment and is twice the red shift of the absorption edge, to be discussed in section 7.1. Schoenes and Wachter (1974) have shown experimentally that the exchange splitting of the conduction band due to magnetic order and described by

$$H_{ex} \equiv 2\Delta E = -2 \sum_{n} J_n(r - R_n) s \cdot S_n \tag{19.15}$$

is appreciably reduced upon doping, an effect which has not been realized before. Nevertheless, the right hand part of equation (19.14) is increasing upon doping since the carrier concentration $N_{f.c.}/N_{Eu}$ is increasing more than ΔE decreases, resulting in an increase of T_C. The entities entering into equation

TABLE 19.5

Experimental verification of eq. (19.14) $k_B \Delta T_C = 2(N_{f.c.}/N_{Eu})\Delta E$ for Gd doped EuO. The samples are characterized by their free carrier concentration $N_{\text{free carrier}}$.

Sample	T_C (K)	$N_{\text{free carrier}}$ ($\times 10^{19}$ cm^{-3})	$k_B \cdot \Delta T_C$ ($\times 10^{-4}$ eV)	ΔE (eV)	$2(N_{f.c.}/N_{Eu})\Delta E$ ($\times 10^{-4}$ eV)
0	69	$\ll 0.1$	0	0.270	~ 0
1	80	3.8	9.5	0.236	6
2	80	6.6	9.5	0.224	10
3	83	16	12	0.188	20
4	115	60	40	0.124	50

After Schoenes and Wachter (1974).

(19.14) have been independently measured and are compiled in table 19.5 for undoped and 4 Gd doped EuO crystals. Comparing columns 4 and 6 we realize that equation (19.14) is more or less fulfilled. The physical content of this equation can also be interpreted differently. We realize that the bottom of the conduction band becomes lowered upon magnetic order due to the exchange splitting (see also fig. 19.18). If there are electrons in the conduction band, the lowering of these states represents an increase in energy of the crystal according to column 6 of table 19.5. If all this energy becomes transformed into magnetic energy we find a corresponding increase in T_C. However, we have to draw the conclusion that T_C is not increasing proportionally to the electron concentration, as has been assumed up to now, since the exchange interactions of the impurity electrons are decreasing with increasing concentration. We thus realize that $k_B \Delta T_C$ will not increase without limits, but rather exhibit a maximum for doping in the order of percents, as verified indeed experimentally.

As already mentioned, most theories yield an additional ferromagnetic exchange for doping levels less than about 1%, i.e. for nondegenerate magnetic semiconductors. The idea of the giant ferromagnetic cluster is of course also valid in antiferromagnets like EuTe where these ferromagnetic microregions should be easily detected against the antiferromagnetic background. Vitins and Wachter (1973, 1975a) have made magnetooptical measurements on EuTe doped with iodine in the anion sublattice. Samples No 399 and No 829 with two different iodine concentrations had at 300 K free carrier concentrations of $4 \times 10^{18}\,\mathrm{cm}^{-3}$ and $6 \times 10^{19}\,\mathrm{cm}^{-3}$, respectively. The Néel temperatures remained practically unchanged at $T_N = 9.6$ K but θ was increased from about -4 K for undoped EuTe to $+12$ K and $+14$ K for the two doped samples, respectively. The authors investigated the Faraday rotation and derived from this the net magnetization of the compounds. In addition they discovered a new effect – the exchange resonance on doped EuTe, as manifest by a frequency independent Faraday rotation – FIFR – which depends on the magnetization of only the ferromagnetic spin clusters. This exchange resonance is believed to originate from the magnetic resonance of these spin clusters in the exchange field of the magnetic sublattices of EuTe. The degree of alignment of the Eu spins within a cluster and measured by FIFR in fig. 19.8 is given by the nearest neighbor spin correlation function, which even at 300 K exhibits a nonzero value. However, at low temperatures the spins are parallel aligned within the spin clusters and saturation is practically achieved below about 20 K, i.e. appreciably above $T_N = 9.6$ K. This is shown in the insert of fig. 19.8 where the FIFR, being proportional to the cluster magnetization, is plotted together with the total magnetization of the sample. The latter exhibits a peak at T_N similarly as in fig. 19.2. The insert of fig. 19.8 indicates in addition that with the onset of long range order below about T_N a slight increase in the cluster magnetization sets in. This can be interpreted with an interaction between the clusters (coupling), because such an increase is absent in the weaker doped sample. This interaction between the clusters in the more heavily doped sample also prevails a strictly antiferromagnetic order in the region outside the clusters. The existence of the

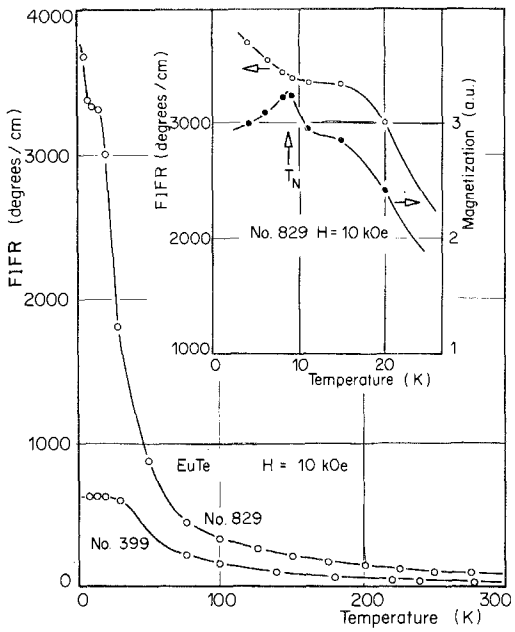

Fig. 19.8. Temperature dependence of the frequency independent Faraday rotation (FIFR) for two doped samples (No. 399 and No. 829) of EuTe: I in an applied magnetic field of 10 kOe. The insert shows the FIFR and the magnetization of the more heavily doped sample No. 829 near T_N (after Vitins and Wachter, 1975).

ferromagnetic spin clusters is also apparent in the field dependence of the magnetization as displayed in fig. 19.9 and compared with an undoped EuTe No 384. Since the slope of the magnetization of the doped samples for low fields corresponds to the demagnetizing factor there exists a spontaneous magnetization for $T < T_N$ even in zero field. This spontaneous moment is found to be $1.2\,\mu_B$/Eu in the heavier doped sample and $0.4\,\mu_B$/Eu in the weaker doped sample. The increase of the total magnetization of the doped samples over the one of the undoped EuTe is exclusively due to the magnetization of the ferromagnetic clusters, which are seen to be saturated at 8 K and fields above 3 kOe.

It is remarkable that a spontaneous magnetization of $1.2\,\mu_B$/Eu ion in the heavier doped sample is caused by comparatively a few electrons namely $6 \times 10^{19}\,cm^{-3}$, only about 0.001 of the atomic density. The ferromagnetic spin clusters comprise therefore a sizable number of Eu ions. If we consider that at low temperatures the number of free carriers is even reduced compared with room temperature (non-degenerate semiconductor), Vitins and Wachter (1975a) estimate the carrier concentration at 10 K to be about $2 \times 10^{18}/cm^3$ and therefore compute that each ferromagnetic spin cluster contains roughly 500 Eu ions. For the weaker doped sample a cluster size of about 2000 Eu ions is derived. As a

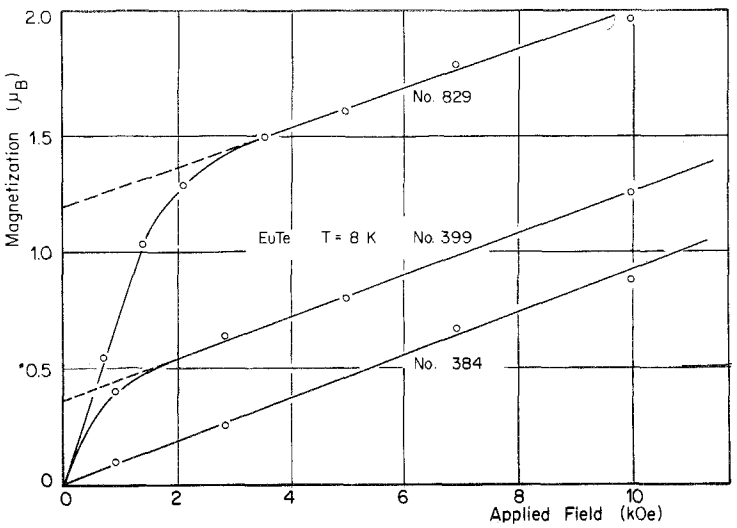

Fig. 19.9. Total magnetization vs applied magnetic field for EuTe: I (No. 399 and No. 829) compared with undoped EuTe (No. 384) (after Vitins and Wachter, 1975).

consequence doped, nondegenerate EuTe must be termed a mixed magnetic material which, at low temperatures, consists of ferromagnetically saturated spin clusters comprising up to 2000 atoms and more or less antiferromagnetic regions outside the clusters.

It is thus established that doping the Eu chalcogenides leads to a much more complex magnetic behavior than has been assumed in the early days of this investigation. Generally speaking, in the low doping regime, Kasuaya's "magnetic impurity" model is quite successful, although modifications, such as f–d exchange (because the conduction electrons have mostly d-character) and a decreasing exchange interaction with increasing electron concentration have to be considered. In the high doping regime or rather with alloy compounds the 4f spins of the dopant (Gd, Ho) enter the material antiparallel with the Eu spins, thus causing a more and more antiferromagnetic exchange until the compounds become antiferromagnets as a whole. In mixed systems there will be chemical clustering besides spin clusters, so additional complications will arise.

4. Electronic structure

4.1. *Estimate of a relative energy level scheme*

It is of considerable interest to get an idea of a relative energy level arrangement of cation and anion derived energy states in order to interpret the optical spectra, which in turn can then be used to obtain the exact electronic

structure. Since one of the decisive factors in the Eu chalcogenides is the position of the localized $4f^7$ states, a treatment using atomic energy levels is more adequate than derivations using plane waves (APW, OPW). The usual procedure assumes that one has formed an ionic compound by transferring electrons from outer atomic shells of cations to anions thus forming completely filled p^6 states.

However, in an energy level diagram one always displays the e.g. $4f^n$ energy states in a $4f^{n-1}$ + electron configuration, meaning that the energy difference which one reads in the diagram represents the energy which one has to supply to the crystal in order to make this transition, for example in an optical excitation. Such excitations can go from anion valence p-bands to cation 5d- or 6s-bands or from $4f^7$ states to 5d–6s conduction bands, duly considering parity and other selection rules for the transitions. An energy level diagram based on such considerations has first been proposed for the Eu chalcogenides by Wachter (1969a) and Kasuya (1970a) making use of the thermochemical Haber–Born process. For EuO and EuTe such an energy level scheme is shown in fig. 19.10a,b. For the anion-cation charge transfer process we use the following equation e.g. for EuO

$$O^{2-}(2p^6) + Eu^{2+}(4f^7) \rightarrow O^{-}(2p^5) + Eu^{+}(4f^7 6s^1) \tag{19.16}$$

For the ionization of an electron from the $4f^7$ states and the formation of an electron and hole the following reaction applies:

$$Eu^{2+}(4f^7) \rightarrow Eu^{3+}(4f^6) + e^{-} \tag{19.17}$$

According to Greenwood (1968) the negative affinity of the second electron of

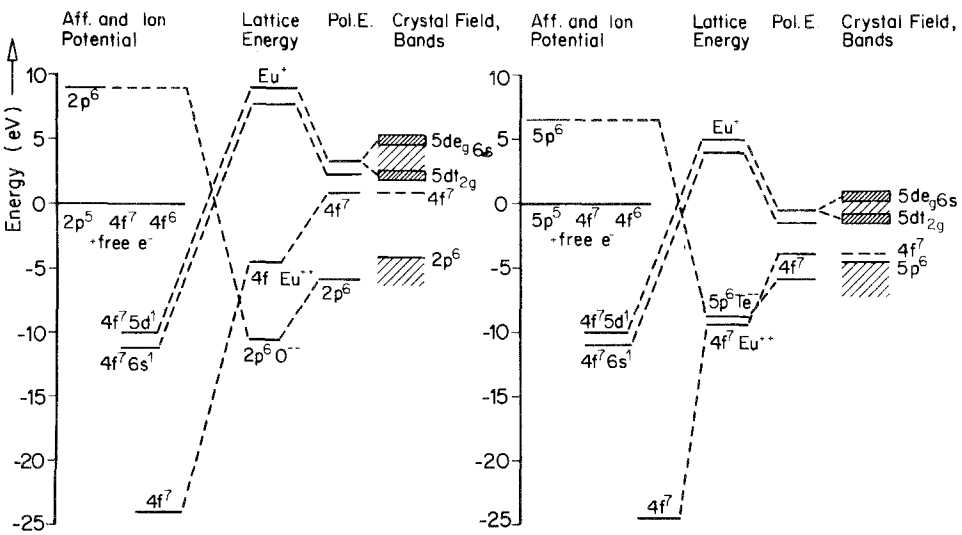

Fig. 19.10. Energy level scheme of EuO (a) and EuTe (b) (in part after Wachter, 1969a).

oxygen ($O^- \rightarrow O^{2-}$) is -8.95 eV and of tellurium -6.5 eV. In fig. 19.10a,b this energy is plotted at the left hand side of the figure, relative to the p^5 state plus a free electron, which serves as the reference level. The second and third ionization energy of Eu are 11.25 eV and 24.92 eV, respectively (Sugar and Spector, 1974) and it is plotted relatively to the $4f^7 + e^-$ and $4f^6 + e^-$ levels, respectively. As a consequence of the Madelung potential of the crystal the Eu^{2+} and Eu^+ levels are enhanced and the O^{2-} and the Te^{2-} level are lowered by the respective amount (19.5 eV and 15.2 eV). This effect is shown in the middle part of fig. 19.10a,b. The process of ionization takes place in a polarizable lattice. Since we only want an estimate of the contribution of the polarization energy we assume that the charges in question are localized in a spherical cavity with radius of the respective ion (Yost, 1933). The polarization energies of holes and electrons have different signs and they are different in size if e.g. holes are in a cation or anion level. The polarization energy is then

$$U_p = (e^2/2R)(1 - 1/\epsilon_{stat}) \tag{19.18}$$

with R the ionic radius and ϵ_{stat} the static dielectric constants. The central part of fig. 19.10a,b shows the influence of the polarization energies. The charge transfer transition anion $\rightarrow$ cation can have as final state a $4f^7 6s^1$ configuration (ionization) or a $4f^7 5d^1$ configuration, the energy of which can be taken from spectroscopic data (Moore, 1965) and is included in fig. 19.10a,b. On the right hand part of fig. 19.10a,b we show the broadening of the p^6 and 6s levels into bands which, of course, can not be included in an atomistic calculation. Now the 5d states will be split into $5dt_{2g}$ and $5de_g$ levels due to the action of the cubic crystalline field. The crystal symmetry is such that the t_{2g} level will be lower in energy than the e_g level, but the splitting, depending on the magnitude of the crystal field, will be so that the energy separation $4f^7$–5d center of gravity will remain about constant in the Eu chalcogenides. The crystal field splitting of the 5d states 10Dq is thus largest for EuO and smallest for EuTe, since the latter compound has the larger lattice constant and in the simple point charge model the crystal field splitting is inversely proportional to the 5th power of the ion distance. If the 5d states have sufficient overlap to form a 5d conduction band, the density of states will be grouped in two maxima which, projected into the center of the Brillouin zone, may be termed t_{2g} and e_g bands.

Without overestimating the simple derivation of this energy level scheme it has a surprising quantitative similarity with the optically measured electronic structure. The latter changes systematically in the Eu chalcogenides and the two end members of the series may serve to elucidate these points. Figure 19.10a,b shows that the energy difference $4f^7$–5d center of gravity practically remains constant in the series. The cubic crystal field acts only on the 5d states and splits them into 6 fold degenerate $5dt_{2g}$ and 4 fold degenerate $5de_g$ levels. Since this splitting is largest in EuO and weakest in EuTe it follows that the energy separation $4f^7$-bottom of the $5dt_{2g}$ conduction band is smallest in EuO and largest in EuTe. If the bottom of the 6s conduction band is higher in energy than the one of the $5dt_{2g}$ band (this will be proven later on) than the $4f^7$–$5dt_{2g}$ energy

separation is also the energy gap of the semiconductors. On the other hand the energy separation p^6–6s or p^6–$4f^7$ becomes reduced from the oxide to the telluride as is usually attributed to covalency effects. However, the energy separation p^6–$5dt_{2g}$ is not very much reduced between EuO and EuTe because, as the p-valence band approaches the 5d-center of gravity, also the crystal field splitting of the 5d states becomes reduced. Comparing fig. 19.10 with fig. 19.14, which shows the optically derived electronic structure of the Eu chalcogenides, the agreement of the atomistic calculation with measured spectra is astonishing. In the meantime, however, these atomic energy level schemes have proved to be powerful tools and they have been applied to NiO (van Houten, 1960; Kasuya, 1970a), GdN (Wachter, 1972) SmS (Kaldis and Wachter, 1972) Eu_3O_4 (Batlogg et al., 1975) and probably many other compounds with great success.

4.2. *Electronic structure and optical transitions*

The electronic structure of a compound can best be obtained from photoemission (UPS, XPS) or from optical reflectivity over a wide photon energy range. Both type of measurements have specific advantages and disadvantages and best results can be obtained if they are used complementary. This has been the case in the Eu chalcogenides. Photoemission usually yields information about occupied electronic states and their density of states can be obtained (Busch et al., 1969; Eastman et al., 1969; Eastman and Kutznietz, 1971; Cotti and Munz, 1974). From reflectivity spectra and their analysis in terms of the dielectric functions one can derive the joint density of states of occupied initial and empty final states and the imaginary part of the dielectric response function is given by

$$\epsilon_2(\omega) = \frac{8\hbar^2\pi e^2}{\epsilon_0 m\omega^2} \int_S (\tfrac{1}{4}\pi^3)\, \mathrm{d}S |M_{\mathrm{vc}}|^2 / |\nabla_{\boldsymbol{k}}(E_{\mathrm{c}} - E_{\mathrm{v}})|_{E_{\mathrm{c}}-E_{\mathrm{v}}=\hbar\omega} \tag{19.19}$$

with

$$J_{\mathrm{vc}}(\omega) = \int_S (\tfrac{1}{4}\pi^3)\, \mathrm{d}S / |\nabla_{\boldsymbol{k}}(E_{\mathrm{c}} - E_{\mathrm{v}})|_{E_{\mathrm{c}}-E_{\mathrm{v}}=\hbar\omega} \tag{19.20}$$

being the joint density of states and $\mathrm{d}S$ a surface element in $\boldsymbol{k}$-space. M_{vc} is the momentum matrix element of the interband transition between states of wave vector $\boldsymbol{k} = \boldsymbol{k}'$. The joint density of states is a strongly varying function of $\boldsymbol{k}$ whenever $\nabla_{\boldsymbol{k}}(E_{\mathrm{c}} - E_{\mathrm{v}}) = 0$ but the matrix element is usually a weakly varying function of $\boldsymbol{k}$, especially for crystal field split d-bands where the density of states is grouped into two rather narrow 5d subbands. It is of special advantage when e.g. the initial state is localized, as is the $4f^7$ state, and thus its density of states practically has no width in energy, because then the imaginary part of the dielectric function will give the density of states of the empty conduction bands alone. However, a problem is inherently connected with optical transitions from localized $4f^n$ states and is manifest in optical absorption as well as in photoemission measurements, it is the excitation of the multi-electron system. In a

$4f^7 \rightarrow$ conduction band transition the remaining 6 electron system $4f^6$ can be left in various excitations, i.e. part of the energy of the incident photon will be used to excite electrons in the ^7F_J multiplet of the $4f^6$ configuration, besides transferring an electron into the conduction band. The width in energy of this ^7F_J multiplet is 0.62 eV and the occupation probability of the various J levels can be computed (Freiser et al., 1968b; Feinleib et al., 1969 and Güntherodt et al., 1971). We thus write an optical $4f \rightarrow 5d$ transition $4f^7(^8S_{7/2}) \rightarrow 4f^6(^7F_J)5dt_{2g}$. If the final 5d state is also sharp and localized the width of an optical absorption peak corresponding to a $4f^7 \rightarrow 5d$ transition will be at least 0.62 eV, according to the width of the ^7F_J multiplet. In such cases also the ladder structure of the transitions to individual J levels of the multiplet can experimentally be observed, e.g. in EuF_2 (Freiser et al., 1968b). If the width of an optical absorption peak of a $4f^7$–5d transition supersedes the 0.62 eV one would attribute the additional width to the distribution of the density of states of the 5d subbands. In this case the band effects are smearing out the transitions to the individual J states and only very careful analysis of optical data at low temperatures can reveal the fine structure (Güntherodt and Wachter, 1973a) or differential measurements like wavelength modulation or electroreflectance (Löfgren et al., 1974).

To obtain the real and imaginary part of the dielectric functions and make use of the density of states argument as discussed above and given in equation (19.19) one has to measure the reflectivity over a very large spectral region in order to perform a Kramers–Kronig (KK) analysis. The KK relation necessitates the knowledge of the reflectivity spectrum between zero and infinite frequencies. Experimentally this is not possible, thus suitable extrapolation procedures must be applied (Güntherodt, 1974). Reflectivities in the far infrared have been

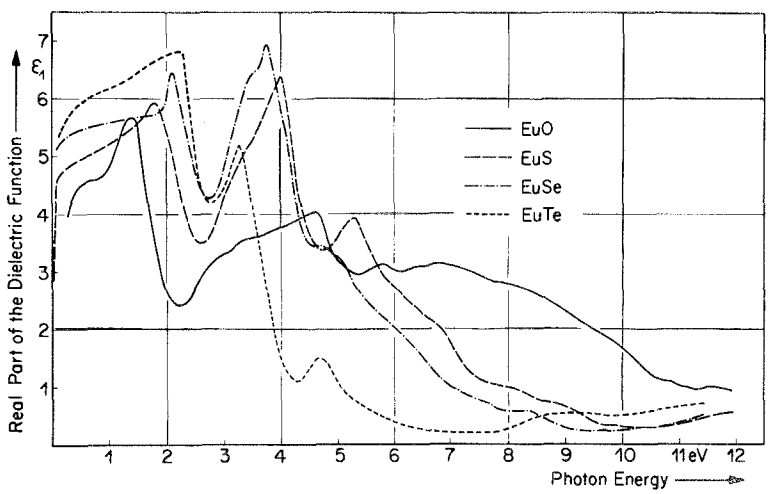

Fig. 19.11. Real part of the dielectric function of EuO, EuS, EuSe and EuTe at 300 K as determined by the Kramers–Kronig relation (after Güntherodt, 1974).

measured by Axe (1969) and Holah et al. (1973) and in the visible and vacuum ultraviolet by Pidgeon et al. (1970) and Güntherodt and Wachter (1973b) and Güntherodt (1974). The reflectivity is thus known from about 6×10^{-3} eV to 12 eV. The analysis in terms of the optical constants has been performed by Güntherodt and Wachter (1973b) and Güntherodt (1974) and the real and imaginary part of the dielectric function for the Eu chalcogenides is shown in figs. 19.11 and 19.12. The figures cover the region of interband transitions. In fig. 19.11 the plateau of ϵ_1 at low energies corresponds to the optical dielectric constant ϵ_{opt}, collected in table 19.6, and in fig. 19.12 the indication of an absorption edge at $\epsilon_2 \to 0$ is visible. However, the position of the absorption edge is more precisely measured by optical transmission on thin single crystalline platelets and its value is also given in table 19.6. Here it should be remarked that the exact value of the absorption edge is somewhat uncertain (±0.05 eV) because it has been shown that the absorption coefficient versus photon energy near the edge is exponential (Freiser et al., 1968a) and its temperature dependence

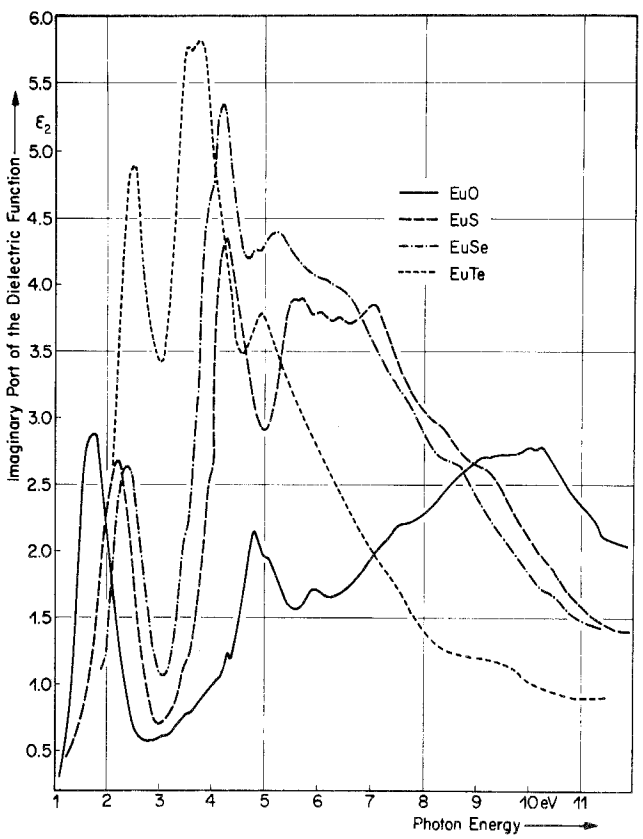

Fig. 19.12. Imaginary part of the dielectric function of EuO, EuS, EuSe and EuTe at 300 K as determined by the Kramers–Kronig relation (after Güntherodt, 1974).

TABLE 19.6
Optical properties of the Eu chalcogenides

	E_{G300}[a] (eV)	Δ_{CF}[a] (eV)	ϵ_{stat}[b]	ϵ_{opt}[b]	$\hbar\omega_p$[b] (eV)	dE_G/dp[c] (meV/kbar)	$\Delta E = (dE_G/dT)_{mag}$[a] (eV)
EuO	1.12	3.1	26.5	4.6	15.6	−4.4	0.27 FM
EuS	1.65	2.2	11.1	4.7	12.5	−7.9	0.18 FM
EuSe	1.80	1.7	9.5	5.35	11.8	−9.3*	0.07 AF I 0.13 FM
EuTe	2.00	1.5	6.9	5.75	10.8	−12.0	−0.03 AF

[a]Wachter (1972); [b]Güntherodt (1974); [c]Wachter (1969b); *Value corrected by Batlogg (1976); $\hbar\omega_p$ is the plasma resonance of the valence electrons.

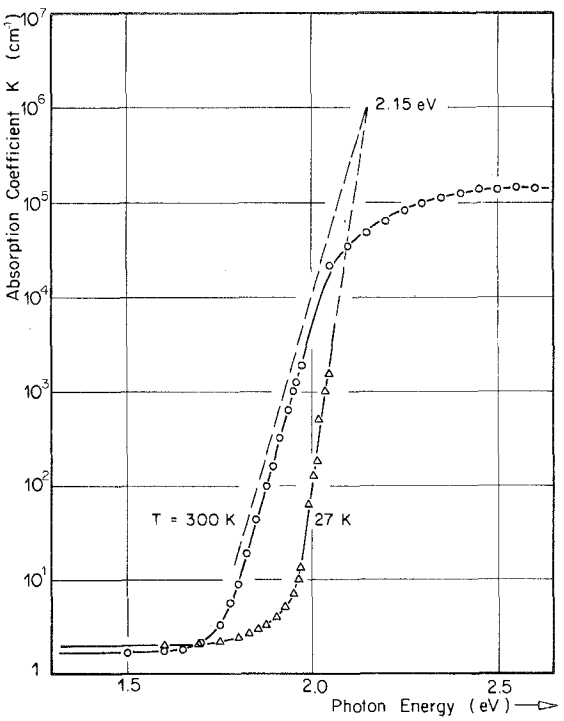

Fig. 19.13. Absorption coefficient of EuSe single crystals ($K < 10^4\ cm^{-1}$) and thin films ($K > 10^4\ cm^{-1}$) at 300 K and 27 K. Verification of the Urbach rule (after Batlogg and Wachter, 1976).

follows the generalized Urbach rule (Batlogg and Wachter, 1976). This is shown in fig. 19.13, where the absorption coefficient of three differently thick crystal plates of EuSe, cleaved from the same piece of crystal, is displayed at different temperatures in the paramagnetic temperature region. It is shown that the generalized Urbach rule (Street et al., 1974)

$$K = K_0 \exp\left(\frac{\hbar(\omega - \omega_0)}{\sigma_s + \sigma_p \coth(\hbar\Omega_0/2k_BT)}\right) \tag{19.21}$$

with $\sigma_s = 11.1$ meV and $\sigma_p = 4.3$ meV and $\hbar\Omega_0$ the energy of a phonon, is fulfilled over at least three orders of magnitude. σ_s is the temperature independent part and $\sigma_p \coth(\hbar\Omega_0/2k_BT)$ is the temperature dependent part of the reciprocal inclination of fig. 19.13. The latter term has been introduced by Mahr (1962). It has been found experimentally that $\hbar\Omega_0$ is 11.2 meV = 130 K and probably corresponds to LA phonons. In fig. 19.13 the shift of the absorption edge due to lattice contraction is also considered using β_{lin} and κ-values of table 19.1. As can be seen from fig. 19.13, K is not always decreasing exponentially with decreasing photon energy but it levels off to a constant value given by residual impurities or lattice imperfections. The intersection of the extrapolated lines can be used as the definition of the absorption edge, although with the above mentioned uncertainty.

It follows from table 19.6 and fig. 19.12 that the absorption edge and thus the energy gap is increasing in energy from the oxide to the telluride. The same trend is given by the lowest energy maximum in ϵ_2 of fig. 19.12. The multiplet structure in this peak as observed by several authors with refined experimental techniques identifies this optical transition as $4f^7 \rightarrow 4f^6(^7F_J)5dt_{2g}$ as already indicated in the energy level scheme of fig. 19.10a,b. However, it can also be seen from fig. 19.12 that the next higher energy prominent peak is closest to the first peak in EuTe and most separated in EuO. Magnetooptical measurements by Güntherodt et al. (1971) and low temperature absorption revealed that this peak corresponds to the transition $4f^7 \rightarrow 4f^6(^7F_J)5de_g$. We thus can obtain from the figures the crystal field splitting 10Dq of $5dt_{2g}$ and $5de_g$ states, compiled also in table 19.6. The decreasing crystal field from the oxide to the telluride is readily explained on the basis of an increasing lattice constant towards the telluride but the power in the simple crystal field point charge model is about -3.5 instead of -5. However, it has been shown by Güntherodt et al. (1971) and Schoenes (1975) that the energy separation $4f^7$–5d center of gravity practically remains constant at 3.1 eV with a very small tendency to increase versus the telluride. Also this behavior has already been deduced in the energy level scheme of fig. 19.10a,b.

Besides the 4f–5d transitions there are also charge transfer transitions from the p^6 derived valence bands to the crystal field split 5d bands and to the 6s band. Due to the crystal field splitting of the 5d states also the p–d transitions must be double and the corresponding absorption peaks should give the same crystal field splitting as for the 4f–5d transitions. Admittedly there is quite a number of structure in a spectrum like in fig. 19.12, but once assigning two peaks or shoulders with the right crystal field splitting to the p–d transitions we also

obtain automatically the energy separation p^6–$4f^7$. This separation can independently be measured with photoemission (Cotti and Munz, 1974) and it is then a check of the assignment. Thus the conditions are very stringent to obtain a selfconsistent scheme for the electronic structure, but for transition energies up to 6 eV the proposed electronic structure is shown in fig. 19.14 (Wachter, 1971a). Here the density of states is plotted versus energy and for simplicity the density of states has been assumed to be parabolic and symmetric to the band center. The width of the valence bands has been taken from photoemission data of Eastman et al. (1969) and Cotti and Munz (1974). The density of states of the crystal field split 5d bands does not have to be zero between the subbands, thus one obtains a total 5d band width of several eV, in agreement with band structure calculations of Cho (1970) and Lendi (1974). Plotting localized and band states into the same diagram always leads to problems because the latter are multielectron states. Therefore, it is best to divide the electronic structure and show initial and final localized states to the left and bands to the right of each diagram. The position in energy of the initial $4f^7$ state cannot be determined with optical means to within the width of the $4f^6$ final state (Wachter, 1971a) and we show it arbitrarily in the middle of the $4f^6$ multiplet.

Comparing now figs. 19.10a,b and 19.14 one must admit that the analysis of the optical transitions has indeed confirmed, even in details, the computations leading to the rough energy level scheme. What remains to be discussed is the position in energy of the bottom of the 6s conduction band. Kasuya and Yanase (1968) have assumed without any proof that the 6s band forms the bottom of the

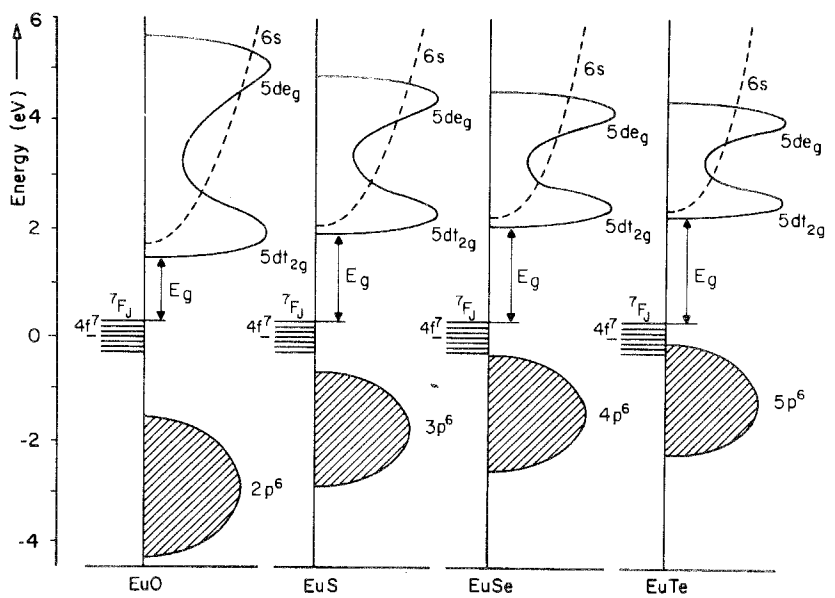

Fig. 19.14. Electronic structure of the Eu chalcogenides.

conduction band and have based their electronic structure and exchange mechanisms on this assumption (Kasuya, 1970b). However, band structure calculations by Cho (1970) using the APW method clearly show that for all Eu cholcogenides the 5d band is lowest at the X-point of the Brillouin zone. The 6s band has a minimum at the Γ-point, but it is higher in energy than 5d at X. Also Lendi (1974) has made band structure calculations using the OPW method and finds in agreement with Cho's derivation that the 5d band is lowest at X, the 6s band being several eV higher in energy at the Γ point. Davis (1971) has made a band structure calculation for the Sm chalcogenides, being isostructural with the Eu chalcogenides, and also computes the 6s band at Γ higher in energy than the 5d bands at X, however, using a Korringa–Kohn–Rostoker calculation. Thus all band structure calculations on the Eu chalcogenides and related compounds show that the 5d band forms the bottom of the conduction bands.

Here we want to collect a few experimental facts to support the conclusion obtained with band structure calculations. We have already established that the optical absorption edge corresponds to the $4f^7$–$5dt_{2g}$ transition which is strongly allowed. As an example we see from fig. 19.13 that after the exponential drop, which forms the edge, the residual absorption coefficient is very small. For all Eu chalcogenides this residual absorption is now about 1 cm^{-1} or less. If the 6s band would be lower in energy than the 5d band there should be a tail of appreciable absorption, because a 4f–6s transition is parity allowed. No such absorption is observed.

All other experimental evidence is based on the comparison of thermally excited electrons, which do not obey optical selection rules, with optically excited electrons, which are subject to selection rules. For example one measures the pressure dependence of the optical absorption edge (Wachter, 1969b) and compares it with the pressure dependence of the electrical conductivity of slightly nonstoichiometric EuO (Oliver et al., 1970a and Sokolova et al., 1971). It is assumed, that under the action of pressure the lattice constant reduces and the crystal field splitting of the 5d subbands increases relative to the center of gravity. Thus the $4f^7$–$5dt_{2g}$ transition energy – the absorption edge – will shift to lower energies. This pressure shift of the absorption edge is also collected in table 19.6. In EuO containing acceptor states, the Fermi level is tied to the $4f^7$ states and in EuO containing oxygen vacancies resulting in deep donor states, the Fermi level is tied at the donor level because of compensation. Since in the latter case the donor level is decoupled from the conduction band (as will be discussed in section 6.3) the bottom of the conduction band shifts under pressure relatively to the donor or 4f states. The pressure coefficient of the electrical conductivity of EuO is with about 5 meV/kbar almost identical with the one of the shift of the absorption edge (table 19.6) since the free impurity electron is sitting in the lowest possible conduction band, equal pressure coefficients can only mean that the bands in question are of the same character; this is a d-band as indicated by the optical transition.

An additional argument is derived from the comparison of the energy of the absorption edge and the thermal activation energy of conductivity in acceptor

doped EuO (Wachter, 1972). Both energies are identically 1.1 eV and since thermal activation of electrons is not governed by selection rules it follows again that the lowest conduction band, at least in EuO, must possess d-character.

In Gd doped EuO the donor level is very shallow (as will be discussed in section 6.2) and coupled very hard to the bottom of the conduction band as it moves nearly concomitant with the conduction band as a function of temperature (Schoenes and Wachter, 1974). Since the Gd donor level is a $4f^75d^1$ state we must conclude again that the lowest conduction band also has d-symmetry.

In the model of the bound magnetic polaron in EuO (Torrance et al., 1972) quantitative agreement with the experiment can only be obtained by assuming the impurity electron to interact with the ion spins by means of a J_{fd} exchange and not a J_{sf} exchange. Thus it seems to be well established that in the Eu chalcogenides and especially in EuO the 6s conduction band is not lower in energy than the 5d band as has been assumed by Kasuya and Yanase (1968). Thus in fig. 19.14 the bottom of the 6s band is shown above the one of the 5d band.

Finally the existence of excitons shall briefly be discussed. Near the absorption edge there is no single sharp absorption line which possibly can be attributed to excitons, neither direct absorption nor modulation techniques gave any evidence. On the other hand one observes photoconductivity in the whole spectral range of the lowest energy absorption peak of fig. 19.12 (Wachter, 1972) and especially at the absorption edge even at 4.2 K. Therefore the entire lowest energy absorption peak of fig. 19.12 cannot be attributed to excitons (Kasuya, 1972) especially, since after the discussion above a possible decay of this 5d exciton into a lower lying 6s band is excluded. On the other hand the existence of an Urbach tail in the optical absorption edge has frequently been used to postulate the existence of excitons. Indeed, from fig. 19.13 it may be deduced that the extrapolation of the Urbach tails to higher energies yields an intersection which could determine the energy of an exciton. This Wannier type exciton has binding energies in the order of a few tenth eV. But the existence of an Urbach tail is inherently connected only with the existence of randomly fluctuating electric fields, so the Urbach tail is conclusive evidence only of the polaronic nature of the Eu chalcogenides.

Mitani and Koda (1974), on the other hand, have measured thermoreflectance of the Eu chalcogenides and interpret a sharp line doublet at about 4 eV photon energy with Wannier excitons associated with the band to band transition p^6–6s. The doublet character is related to spin–orbit splitting just as in the isostructural Ba chalcogenides and below T_C of the ferromagnets EuO and EuS characteristic exchange splittings of these exciton lines can be observed. It is, however, very difficult to decide on the existence of these virtual excitons as they are in the same spectral region and behave the same way with respect to temperature variation as the $4f^7 \rightarrow 4f^65de_g$ transitions and Faraday rotation measurements by Schoenes (1975) in this photon energy region have been interpreted with $4f^75de_g$ fine structure.

To conclude this section we want to remark that the analysis of optical spectra

over a large photon energy range compared with photoemission data has enabled the derivation of the electronic structure of the Eu chalcogenides, which is in agreement with the energy level scheme derived by an ionic model and with basic features of band structure calculations. The existence of excitons at the very absorption edge or preceding the p^6–6s charge transfer transition is possible but the lowest energy absorption peak must consist of delocalized 5d band states because of low temperature photoconductivity and the absence of a decay possibility into a lower lying 6s band.

5. Magnetic exchange mechanisms

5.1. *Antiferromagnetic exchange* $\bar{J}_2$

In this section we want to deal with the question of the systematic change of the exchange integrals $\bar{J}_1$ and $\bar{J}_2$ within the series of the Eu chalcogenides, as manifest in table 19.2. For this purpose we need information on the microscopic magnetic exchange mechanisms which are inherently connected with the electronic structure of the compounds as shown in fig. 19.14.

Starting with the usual Kramers-Anderson 180 degree superexchange for $\bar{J}_2$ one considers a 4f electron to be transferred to another *nnn* (next nearest neighbor) 4f site via the p-bands of the anions thus creating Eu^{3+} and Eu^{+} ions. This process involves the energy differences p^6–$4f^8$ and $4f^7$–$4f^8$. Kasuya (1970b) has given the atomic $4f^8$ level 18.2 eV above the $4f^7$ level, therefore in fig. 19.10a,b the $4f^8$ level appears about 8 eV above the $4f^7$ level, after the Madelung energy and the lattice polarization has been taken into account. Although our estimate of an energy level scheme is somewhat different from that of Kasuya (1970a,b) we come with him to the same conclusion that the Kramers–Anderson mechanism yields a $\bar{J}_2$ of about one order of magnitude too small compared with the value of EuTe as given in table 19.2. The essential reason being that the overlap between p^6 and $4f^8$ states is too small.

On the other hand, if a p electron is transferred to the antibonding $5de_g$ bands of a *nn* (nearest neighbor) Eu ion and polarizes the $4f^7$ spins by means of an fd exchange mechanism, the interaction can be much stronger since the overlap between p and d states is much larger. For this antiferromagnetic coupling Anderson (1963) obtains the following equation

$$|\bar{J}_2| \sim J_{fd}^2 / U_{(p\text{–}de_g)} \tag{19.22}$$

with J_{fd} the intra atomic exchange energy and $U_{(p\text{–}de_g)}$ the energy difference between p and $5de_g$ bands. J_{fd} can be estimated from the difference of the atomic energy levels (Russell et al., 1941) for a 5d electron parallel or antiparallel with the $4f^7$ state, ^9D–$^7D \approx 1$ eV, to be about 0.1 eV and $U_{(p\text{–}de_g)}$ can be taken from fig. 19.14. Kasuya (1970b) estimates this exchange mechanism to be of the correct magnitude and we see from fig. 19.14 that $U_{(p\text{–}de_g)}$ decreases from EuO towards EuTe, thus yielding a larger negative $\bar{J}_2$ in the same sequence. With the exception of EuO, where $\bar{J}_2$ is even positive, the trend is well exhibited in table 19.2.

It is to the credit of Kasuya (1970b) to have been the first to suggest that $\bar{J}_2$ of EuO may be positive, a proposal which later on has been confirmed experimentally by neutron scattering results of Passell et al. (1971). Here a cross term between the Kramers–Anderson and the df exchange is considered with p–d, f–p and d–f transitions involving an inter atomic exchange J_{fd}^{inter}. This inter atomic exchange is estimated to be of the same magnitude as the intra atomic exchange, but with negative sign. So due to the cross term $\bar{J}_2$ may have for EuO a positive sign and it may surpass the negative term of the fd exchange.

In conclusion with respect to the antiferromagnetic exchange interaction $\bar{J}_2$, it may be stated that the fd-exchange interaction via overlap of the antibonding part of the 5d band with the anion p-band seems to be the main mechanism responsible for $\bar{J}_2$, as well quantitatively as qualitatively within the series of the compounds. This interaction necessitates a certain degree of covalency which is also increasing towards the telluride. In EuO the cross term between Kramers–Anderson and fd exchange is dominant, leading to a positive $\bar{J}_2$ and as a whole to a much stronger dependence of $\bar{J}_2$ on the inter atomic distance as has been assumed up to now. Only the $\bar{J}_2$ value of EuSe in table 19.2 seems to indicate some irregularity, which is caused, however, by the complex magnetic structure. The latter is only taken into account by molecular field analysis and no direct $\bar{J}_2$ measurements as in EuO, EuS are available.

5.2. *Ferromagnetic exchange* $\bar{J}_1$

For the ferromagnetic exchange $\bar{J}_1$ Goodenough (1963) has proposed a cation–cation superexchange mechanism based on the Kramers–Anderson theory. Here a 4f electron is transferred to a $5dt_{2g}$ state of a *nn* Eu ion, which then polarizes the 4f spin through the intra atomic J_{fd} exchange. This exchange is ferromagnetic and its magnitude in molecular approximation is

$$\bar{J}_1 = t^2 J_{fd}/2S^2 U^2_{(f\text{–}dt_{2g})}. \tag{19.23}$$

J_{fd} is again the intra atomic exchange of about 0.1 eV, $U_{(f\text{–}dt_{2g})}$ is the energy difference $4f^7$–$5dt_{2g}$ as given in fig. 19.14 and t is the transfer integral being essential due to the inter atomic overlap. The latter, however, is proportional to the band width of the $5dt_{2g}$ subband. Taking into account the considerations of section 4.2 concerning the experimental determination of the $5dt_{2g}$ density of states distribution, we find that the width of the subband decreases from about 1 eV for EuO to about 0.5 eV for EuSe and EuTe (Güntherodt, 1974). If we take $U_{(f\text{–}dt_{2g})}$ from fig. 19.14 or if we identify in agreement with Methfessel (1965) $U_{(f\text{–}dt_{2g})}$ with the energy of the absorption edge, E_G, collected in table 19.6, we realize that $U_{(f\text{–}dt_{2g})}$ increases on going from the oxide to the telluride. The combined effect of the decrease of the transfer integral and the increase of the $U_{(f\text{–}dt_{2g})}$ energy difference is the cause of the decrease of $\bar{J}_1$ from EuO towards EuTe, as manifest in table 19.2.

We even have a means of quantitatively checking equation (19.23) in the series of the Eu chalcogenides, since all the entities entering the equation are known

experimentally but for a proportionality factor. Thus plotting $\bar{J}_1$ from table 19.2 versus $t^2/U^2_{(f-dt_{2g})}$ indeed yields a rather good straight line. Considering just the end member of the compound series, t, (taken from the $5dt_{2g}$ subband width), as well as $U_{(f-dt_{2g})}$ is changing by a factor of two, thus $\bar{J}_1$ should change by a factor of 16, which is the case, consulting table 19.2.

Thus the magnitude and the trend of the magnetic exchange interactions in the Eu chalcogenides are qualitatively and quantitatively well understood with the help of the electronic structure as shown in fig. 19.14.

It should, however, be recalled, that rather narrow $5dt_{2g}$ subbands do not indicate that the total 5d band width is also narrow. Only the density of states is grouped in two rather narrow energy regions, as indicated already in Cho's (1970) band structure calculation. On the other hand tight binding calculations of Khan (1976) for FeS_2, crystallizing also in the cubic structure with Fe distances similar as for EuS, have given $3dt_{2g}$ and e_g band widths of about 1 eV and less, with an optical transparent region for photon energies less than the crystal field splitting (Schlegel and Wachter, 1976). Thus more modern band structure calculations for transition metal compounds yield very narrow d subband widths indeed.

6. Electrical transport properties

6.1. *Undoped* Eu *chalcogenides*

The resistivity of the undoped Eu chalcogenides at 300 K is above 10^6 ohm·cm, thus low temperature measurements exceed very soon the insulation capability of the experimental setup. Since the interesting temperature region is near the magnetic ordering temperature, measurements of photoinduced conductivity are appropriate in the low temperature region, since the generation rate of the photo excited electrons is practically temperature independent. On the other hand the concentration of photoelectrons is about 10^{11} cm^{-3} too small to have any influence on the magnetic properties. Besides, photoconductivity is the only known experimental tool to distinguish between optical transitions into bound electron-hole pairs(excitons) or into extended band like states. The existence of photoconductivity for the same photon energy as the optical absorption, especially at 4.2 K, ensures a transition into a 5d conduction band, if a decay into a lower lying 6s band is excluded. And the arguments given in section 4.2 have made it highly improbable that the 6s band is the lowest conduction band.

In fig. 19.15 we show the photosensitivity (ps) (photocurrent/light intensity) for EuSe at different temperatures in the paramagnetic range. For comparison also the absorption coefficient at 300 K is shown in the same figure. It is observed that the photosensitivity has a rather sharp maximum near the optical absorption edge. On the low energy side of this maximum the photosensitivity edge can be located where the ps has dropped to half its maximum value (Moss, 1952).

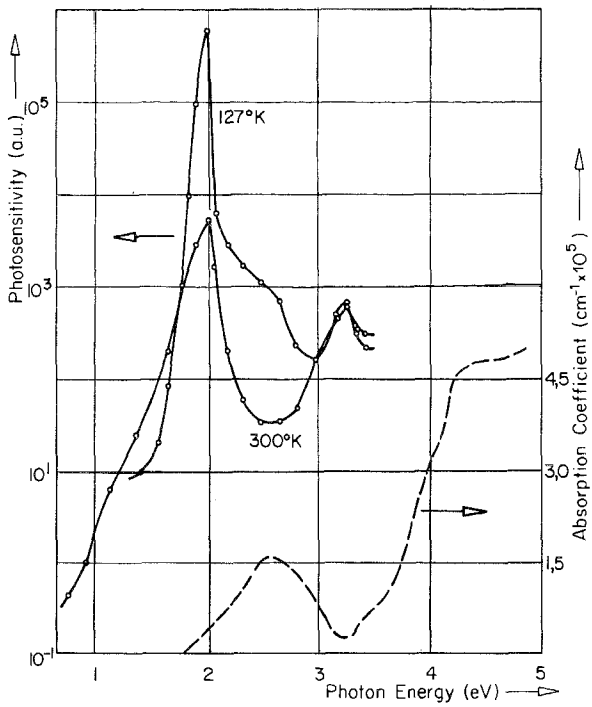

Fig. 19.15. Photosensitivity and absorption coefficient of EuSe (after Wachter, 1970).

This condition holds when the low energy side of the ps follows an exponential law, as in the case of the Eu chalcogenides (note the logarithmic scale for the ps). This photosensitivity edge is observed at exactly the same energy as the optical absorption edge, and this for all temperatures between 4.2 K and 300 K and magnetic fields. Even the paramagnetic blue shift of the absorption edge, demonstrated for EuSe in fig. 19.13, is represented also in fig. 19.15 for the ps edge.

Comparing the photosensitivity spectra of fig. 19.15 with the absorption coefficient it becomes evident that the ps is high for low absorption and vice versa. Since the ps is proportional to the life time of the excited carriers it follows that the life time is low for high absorption or low penetration depth of the light. The general limiting factor on the life time is the recombination probability, being large for high density of electrons and holes, i.e. excitation only in a thin surface sheet. Thus the spectral variation of the ps in fig. 19.15 can be qualitatively understood.

In addition to photosensitivity also photo-emf has been observed at the optical absorption edge, for EuO by Nikolaev et al. (1975) and for EuSe even at low temperatures by Wachter (1971b). Also these data have been interpreted as being due to transitions into a conduction band, since the carriers must migrate to the electrodes.

It is quite interesting to follow the temperature dependence of the photosensitivity near the magnetic ordering temperature of the compounds. For this purpose one measures the intensity of the ps at the lowest energy maximum and follows this maximum at all temperatures and fields. The temperature dependence of the ps is shown in fig. 19.16 with and without a magnetic field. Remarkable are the sharp minima at T_C for the field free case (for EuSe at T_N) and the pronounced influence of a magnetic field. The temperature for minimum ps in an applied magnetic field is by no means an indication of an increased Curie temperature, as T_C is not defined in a magnetic field. Instead the field induced change of the ps is due to an increase of magnetization under the action of the field and corresponds to a negative magnetoresistance.

Now the photosensitivity equals

$$\text{ps} = Q\mu\tau \tag{19.24}$$

with Q being the quantum efficiency, μ the mobility of the excited electron and τ its lifetime in the conduction band. For EuSe it has been shown that the temperature dependence of the ps is the same for excitations in the red or blue maximum displayed in fig. 19.15, thus Q is temperature independent (Wachter,

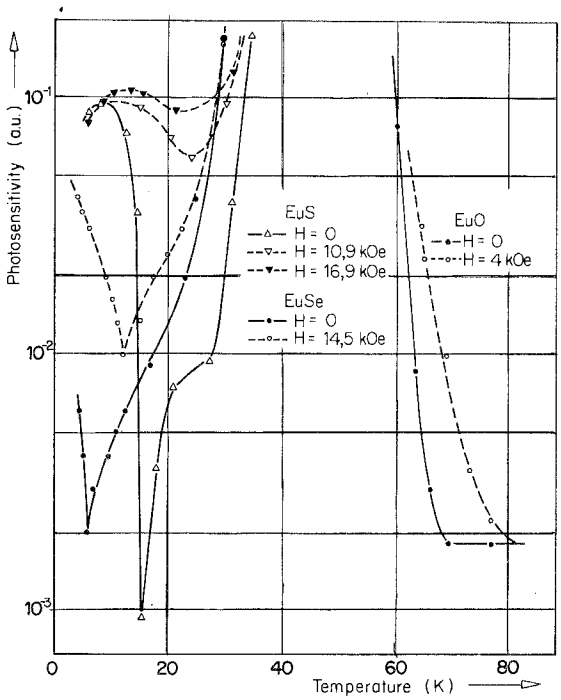

Fig. 19.16. Photosensitivity of EuO, EuS and EuSe near their respective magnetic ordering temperatures. Monochromatic excitation in the maximum of the spectral dependence of the photosensitivity (after Wachter, 1972).

1970). Kasuya and Penney (1970) have shown that also the lifetime τ is temperature independent below about 100 K, so below that temperature the ps is proportional to the mobility $\mu(T)$. Haas et al. (1967) and Haas (1970) have pointed out that spin disorder scattering may lead to a pointed minimum of the mobility at T_C in agreement with the observations in fig. 19.16. However, for the antiferromagnet EuTe no such minimum of the mobility is found, instead a further decrease of μ for $T < T_N$. Thus for this material spin disorder scattering cannot be the dominant scattering mechanism. In the case of EuS it can best be seen that a large enough magnetic field nearly wipes out the anomaly at T_C, but for EuSe a magnetic field still induces an appreciable enhancement of μ even at 4.2 K. This has nothing to do with the temperature being not low enough for magnetic saturation, but at this temperature a magnetic field changes the spin structure form antiferromagnetism to ferromagnetism, as explained in the phase diagram of fig. 19.4. On the other hand it is surprising that the temperature dependence of the ps of antiferromagnetic EuSe in zero field is different from the one of antiferromagnetic EuTe, but this must be due to the complex antiferromagnetic spin structure of EuSe (Wachter, 1972). It is another remarkable fact that the ps of EuO is increasing by five orders of magnitude for temperatures less than T_C and at 20 K it is by 4 orders of magnitude larger than at 300 K. (See fig. 19.17).

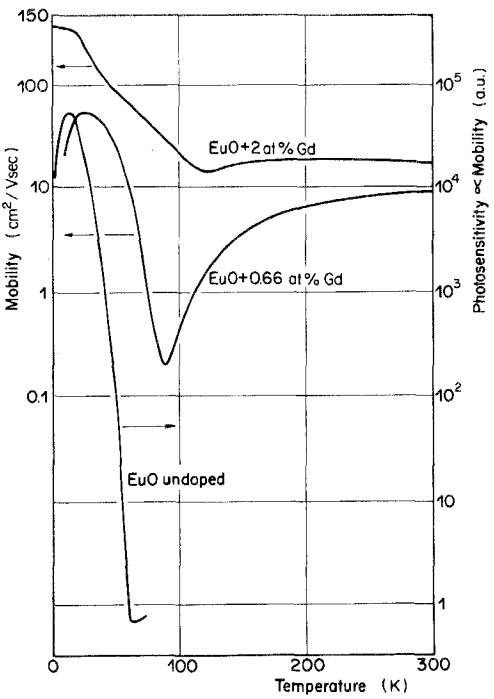

Fig. 19.17. Comparison of the temperature dependence of the dc mobility of undoped and Gd doped EuO crystals. The result of EuO + 2% Gd is taken from von Molnar and Shafer (1970) (after Schoenes and Wachter, 1974).

Also Kajita and Masumi (1970, 1971) have investigated the ps of EuO and EuS and basically find similar results as shown in fig. 19.16. However, their results are much less structured and they observe only a poor minimum at T_C for EuS. These measurements are somewhat invalidated because the light excitation was with filters and the temperature and field variation of the spectral response of the ps (as e.g. collected in Wachter, 1972) could not be followed. Their detection system or sample quality must also be questioned since they were unable to detect ps in EuO at 300 K, were indeed the signals are very strong, as also confirmed by Nikolaev et al. (1975).

The sharp and even exponential decrease of μ with decreasing temperature in the paramagnetic region has been a subject of controversy ever since observed (Wachter, 1970). Several proposals for the underlying scattering mechanism have been made. So von Molnar and Kasuya (1970) propose a magnetic polaron trapped on residual impurities in the material, provoking a hopping of electrons between occupied and empty impurity states. However, the activation energy for hopping as measured by μ in photosensitivity experiments on EuSe and EuTe are the same as the respective activation energies of μ in lightly doped materials (von Molnar, 1970; Vitins and Wachter, 1975a). It is unlikely that in doped compounds the same residual impurity states play the dominant role as in undoped materials. On the other hand an explanation in terms of a self-trapped magnetic polaron has been proposed (Wachter, 1970), but Kasuya (1970c) has stated that the magnetic polaron is large and moves by diffusion and not by hopping. These results are based on his band structure scheme with the 6s band being lowest in energy and an sf exchange. If, however, a highly correlated d band is lowest, as argued in section 4.2, the situation changes, but this possibility has not been explored theoretically. There might still be another assumption in terms of a bound magnetic polaron. Here the electron is bound by Coulomb interactions with the lattice in the sense of a small dielectric polaron. In addition, the interaction with the spin system comes to play, so one has a combined electric and magnetic polaron, which behaves similarly as the impurity bound magnetic polaron. Experimental evidence for this dielectric small polaron may be the fact that for temperatures less than magnetic saturation (e.g. for EuO less than 20 K and EuS less than 6 K) a decrease in ps is again observed just as for μ in lightly doped EuO and EuS (see also fig. 19.17 and Bayer and Zinn, 1971). Such a decrease is absent in higher doped EuO due to the degeneracy of the compound.

Thus the discussion with respect to the mobility of the Eu chalcogenides is still open and further experimental and theoretical work is needed.

6.2. *Doping with shallow donors*

Some of the aspects of doping have already been discussed in connection with the magnetic properties of the compounds. Here we shall be concerned with the electrical transport properties of anion and cation substituted materials. Generally speaking, replacing a Eu^{2+} ion with a R^{3+} ion or a X^{2-} ion with a

halogen (Ha^-) ion will result in shallow donors. When dopant and electron concentration is large, impurity bands will form which eventually merge with the bottom of the conduction band. On the other hand if the impurity concentration is small, the conduction may be due to a hopping process. The critical electron concentration for the semiconductor-metal (Mott) transition can be estimated by using the hydrogen formula in a dielectric medium for the radius of the impurity electron orbit. Overlap of electron orbits and formation of impurity bands occurs for doping levels near 2%. Therefore, one should speak of alloys in cases where the concentration of R^{3+} exceeds the few percentage range.

Here we have to deal also with another, mainly experimental problem. There are many cases reported in the literature where transport properties have been measured on evaporated thin films. However, these results bear only qualitative significance, since usually the vacuum conditions during evaporation are bad, the temperature of the substrate during evaporation is ambiguous, the packing density of the films is less than on single crystals, the films are polycrystalline and doping by coevaporation can result in heterogeneous mixtures. Examples for the influence of these external parameters are given by Bayer and Zinn (1971) for EuS: The resistivity of unannealed EuS films at 300 K is 4×10^{-3} ohm·cm, of annealed EuS 3×10^{2} ohm·cm and of single crystals about 10^{8} ohm·cm. A 4% Gd doped and annealed EuS film has a two orders of magnitude larger resistivity than an only 1% Gd doped EuS single crystal, and even a metallic GdS film has a two orders of magnitude larger resistivity than GdS single crystals (Hauger et al., 1976). In addition there are no control possibilities on the stoichiometry of thin films and so we will refrain describing their electrical transport properties.

Since the electrical conductivity $\sigma = Ne\mu$ one needs Hall effect and conductivity measurements to make significant statements about N and μ. From the experimental point of view the situation is still rather simple when one uses doped single crystals with doping levels of a few percent, because then the Hall effect yields a temperature independent carrier concentration and the conductivity depends only on the mobility. Near the ordering temperature of EuO, EuS and EuSe a minimum in the conductivity is observed which is apparently due to critical scattering by correlated spins. The measurements near T_C resemble the mobility minima deduced from the photoconductivity, but the higher the doping level the more rounded and less pronounced are the extrema and the application of a large enough magnetic field annihilates the mobility anomaly near T_C. Most of these measurements have already been reviewed by von Molnar (1970), and a conductivity curve for 2% Gd doped EuO by von Molnar and Shafer (1970) is reproduced in fig. 19.17. The mobility is proportional to the effective scattering times of the electrons. Since the reciprocals of the scattering times are additive the total scattering time $1/\tau_{tot} = 1/\tau_{ph} + 1/\tau_m + 1/\tau_{imp}$, where individual terms stand for phonon scattering, magnetic scattering and impurity scattering. At temperatures large compared with the magnetic ordering temperatures the phonon and impurity terms are dominant and can well be fitted with conventional theories. For the magnetic term scattering theories of de Gennes and Friedel (1968), von

Molnar and Kasuya (1968) and Haas (1970) have been applied with reasonable success.

Much more ambiguity in the interpretation of experimental results is introduced in the weak doping or semiconducting regime, i.e. for dopant concentrations less than about 1%. Here it seems to be impossible to measure the Hall effect at low temperatures for experimental reasons like contact problems and large magnetoresistive effects. However, it is precisely this weak doping regime where one can speak of magnetic semiconductors, thus different and more adequate experimental methods must be developed and applied. This has been done by Schoenes and Wachter (1974) who used contactless optical methods to evaluate the transport properties. Optical dispersion relations always depend on N, μ and m^*, thus by measuring three related optical quantities such as the free carrier absorption, the free carrier Faraday rotation and the free carrier plasma resonance in function of temperature and magnetic field, the transport entities can be computed. In the case of the mobility one obtains an ac mobility at optical frequencies, but by measuring in addition the frequency dependence of this mobility also the dc values can be extrapolated.

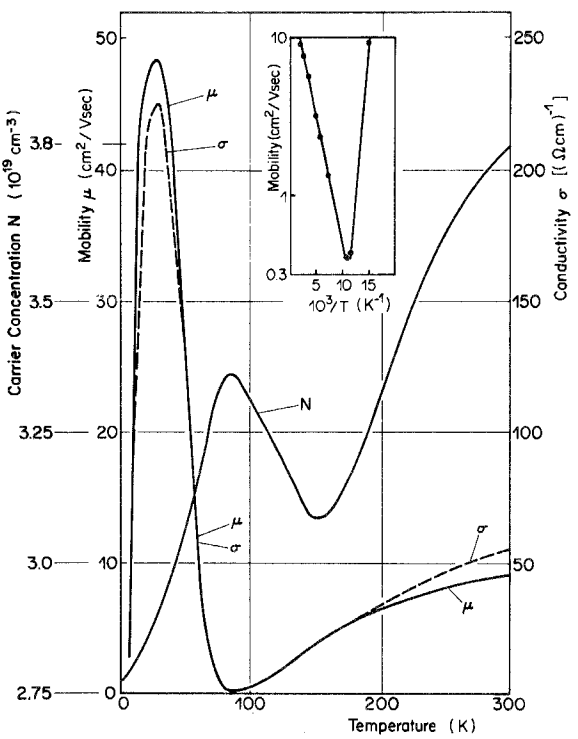

Fig. 19.18. Carrier concentration N, dc mobility μ and dc conductivity σ of a Gd-doped EuO sample, containing 3.8×10^{19} electrons/cm^3 at 300 K (after Schoenes and Wachter, 1974).

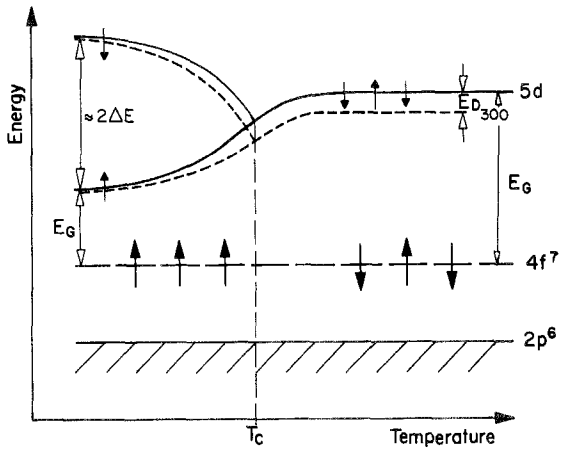

Fig. 19.19. Model of the conduction band splitting of EuO containing shallow donors with activation energy $E_{D_{300}}$ (after Wachter, 1973).

For an EuO crystal with 0.66 at.% Gd we show the temperature dependence of N, the dc mobility and the dc conductivity σ in fig. 19.18. Above about 150 K one observes a decreasing carrier concentration N with decreasing temperature, as typical for a nondegenerate semiconductor. The activation energy in this temperature interval is $E_D = 0.017$ eV and corresponds to a shallow donor. Already appreciably above $T_C = 80$ K, where magnetic short range order commences, an increase of N is observed and with further decreasing temperature N decreases again, but now the activation energy is considerably reduced. However, the material remains semiconducting. We thus observe an exchange induced donor ionization near T_C.

To explain this effect in principle we consider the rough energy model displayed in fig. 19.19. In the paramagnetic temperature range (right hand side) we have the valence $2p^6$ band, at higher energies the localized $4f^7$ states and separated by the energy gap E_G the bottom of the conduction band of 5d character. Some shallow donors with activation energy $E_{D_{300}}$ are indicated. It has first been shown by Vonsovskii and Izyumov (1962) and later by Rys et al. (1967) that the magnetic order splits the conduction band at T_C into spin polarized subbands (left hand side), but short range order lowers the bottom of the conduction band already considerably above T_C. Also the donor will be subjected to an exchange splitting (Haas, 1970), its magnitude depending on the coupling of the donor to its conduction band. Usually the donor wavefunctions are composed from those of the conduction band, especially if like here the donor is a $4f^75d^1$ Gd state and the conduction band has d-character. So the donor is coupled very hard to the conduction band and follows its temperature variation, but independently of the coupling strength the splitting of the donor will always be somewhat less than the one of the conduction band (Haas, 1970). As a consequence we will observe an effective decrease of E_D with decreasing

temperature and near T_C this decrease can be faster than temperature decreases, thus,

$$|\mathrm{d}[E_D(T)/k_BT]/\mathrm{d}T| < 0$$

and

$$E_D(T) = E_{D_{300}} - |(1 - \gamma_D)\langle S_0 S_1\rangle \Delta E/S^2| \tag{19.24}$$

where $E_{D_{300}}$ is the donor activation energy at 300 K, γ_D is the coupling constant, somewhat less than one, and $[\langle S_0 S_1\rangle/S^2]\Delta E$ is the spin correlation function, taken from the red shift ΔE of the absorption edge. ΔE for this compound is found in table 19.5.

Also for other Gd concentrations the temperature dependence of N has been measured. But either N is so large that the compound is already degenerate at 300 K, thus N is temperature independent, or if N is less than given in fig. 19.18 the sample is semiconducting at 300 K and the swing of N near T_C is somewhat larger but N never reaches values higher than at 300 K of fig. 19.18. Thus whenever the doping level is so that the samples are semiconducting at 300 K they remain semiconducting also at lower temperatures.

If we turn now to the dc mobility also shown in fig. 19.18 we find it reassuring that the absolute value at 300 K and at the maximum near 20 K is in reasonable agreement with derivations of the mobility from Hall effect and conductivity of a 2% Gd doped EuO sample at the same temperatures. Again at T_C the mobility displays a pointed minimum due to spin disorder scattering or magnetic trapping effects. The insert of fig. 19.18 shows that the mobility is of the hopping type in the paramagnetic region with an activation energy of 0.035 eV. In fig. 19.18 we also show the conductivity σ composed of N and μ. It is observed that it closely follows the temperature dependence of the mobility, and at 300 K its value has been checked by a four probe conventional conductivity measurement on the same sample. The optically derived and the direct measured conductivity values are in perfect agreement.

It is now instructive to compare the temperature dependence of the mobility of differently doped EuO crystals in fig. 19.17. The degenerate 2% Gd doped EuO displays a one order of magnitude increase in μ below $T_C \approx 123$ K. The 0.66% Gd doped EuO shows already an increase of more than two orders of magnitude below $T_C = 80$ K, but also a decrease of μ below about 20 K, and an undoped EuO exhibits a five orders of magnitude increase below $T_C = 69$ K and also a decrease of μ below about 20 K. Haas (1970) has shown that the spin disorder scattering depends on H_{ex} as given by eq. (19.15). The reduction of the mobility dip at T_C with increasing doping then is a manifestation of a decreasing $H_{ex} \equiv 2\Delta E$ which is given in table 19.5. The decrease of the mobility for temperatures less than about 20 K (for EuS less than about 6 K) i.e. where the spin system is saturated, can be taken as an indication of a hopping mobility due to a small dielectric (Fröhlich) polaron. In degenerate compounds this polaronic effect is absent because of electrostatic shielding.

In EuTe doped with iodine the same optical analysis as for doped EuO has

been performed by Vitins and Wachter (1975a). Also here the mobility is of the hopping type and the activation energy in the paramagnetic region deduced from ps on undoped EuTe, is in perfect agreement with the one of the doped compound.

Thus it is well established that the mobility in undoped and lightly doped, nondegenerate Eu chalcogenides is of the hopping type in the paramagnetic region, with activation energies of about 0.03 eV. Also for very low temperatures, where magnetic saturation is already achieved, a probably activated mobility persists, although with a much smaller activation energy. At the magnetic ordering temperatures of the ferromagnets critical scattering on spin fluctuations is observed (this being also the case for degenerate, metallic compounds). Donor activation energies are around 0.015 eV, usually less than the activation energy of the mobility. Theoretical explanations of these phenomena are not yet very satisfactory, but the solution may be in the direction of a bound magnetic polaron as proposed above. It is important to realize that doping with shallow donors alone does not lead to a semiconductor metal transition near T_C, in spite of the fact that exchange induced ionization of donors is observed.

6.3. *Deep donors: insulator-metal transition*

EuO with O deficiencies shows a completely different behavior than R^{3+} doped compounds. First experiments with this material have been made by Oliver et al. (1970b) who discovered an insulator-metal transition close to T_C. Later on, investigations on this material have been continued by Petrich et al. (1971), Penney et al. (1972), Torrance et al. (1972) and Shapira (1974). In fig. 19.20 we show the experimental results of a typical EuO crystal containing O deficiencies. Remarkable is the 13 order of magnitude increase of the conductivity for $T < T_C$ and the influence of a magnetic field. EuO with oxygen deficiency can e.g. be made by heating stoichiometric EuO in Eu vapor. The optical absorption for such a material is shown in fig. 19.6, labeled EuO III. As new features two absorption peaks at 0.55 eV and 0.65 eV appear, but no free carrier absorption is present in the indicated wavelength range. As a consequence T_C will not be changed compared with the stoichiometric compound and if O deficiencies create a donor level it must be a deep donor. By measuring the temperature change of the conductivity between 125 K and 300 K one finds indeed an activation energy of about 0.28 eV. The presence of compensators pins the Fermi level at these donor levels so that about 0.28 eV is also the donor activation energy. Due to this deep donor the free carrier concentration at 300 K is only $4 \times 10^{13}/\text{cm}^3$ as evident by Hall data. With decreasing temperature the free carrier concentration is rapidly decreasing and between 125 K and 70 K the conductivity is only given by leakage currents. At 5 K on the other hand the carrier concentration has risen to $4 \times 10^{19}/\text{cm}^3$ and is essentially temperature independent near this temperature. It is precisely this large change in the carrier concentration below T_C which permits one to speak of

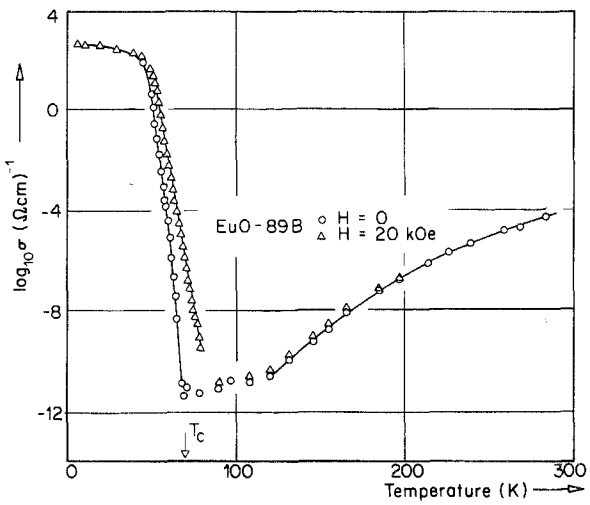

Fig. 19.20. Temperature dependence of the electrical conductivity of an EuO crystal 89B, containing oxygen deficiencies (after Penney et al., 1972).

an insulator-metal transition. However, also the temperature change of the mobility should be taken into account. Only data at 300 K and 5 K are given by Penney et al. (1972) and these values agree which mobilities on other EuO samples as shown in fig. 19.17, but we know from the preceding subsection that the mobility is temperature activated in the paramagnetic range with an activation energy of about 0.03 eV. Since the conductivity will depend on the sum of the activation energies of mobility and carrier concentration the latter will be only about 0.25 eV and this should be the true energy separation donor-bottom of conduction band.

Now an oxygen deficiency in EuO will act like a doubly charged F-center which basically can bind two electrons. For the ground state of these electrons Petrich et al. (1971) have proposed an electron configuration similar as in a He atom with singlet or triplet spin configuration depending on the magnetic order. Later the model of a bound magnetic polaron was forwarded by Torrance et al. (1972) where the spins of the electrons orbiting the vacancy are parallel. Further models have been proposed by Nagaev and Grigin (1972) and Leroux-Hugon (1972). In the model of the bound magnetic polaron the electrons are bound both electrically and magnetically in the paramagnetic region because the electrons, owing to their exchange interaction with the $4f^7$ spins, polarize magnetically the *nn* Eu ions during their orbit around the vacancy. Below T_C the magnetic part of the binding energy gradually disappears and the Coulombic part of the weaker bound electron is not large enough to localize the second electron, thus leading to the metal like conductivity. The model underlying this assumption is basically still the same as the one of Oliver et al. (1970b) and it is shown in fig. 19.21. This figure bears a great similarity with fig. 19.19, but instead of a shallow donor it

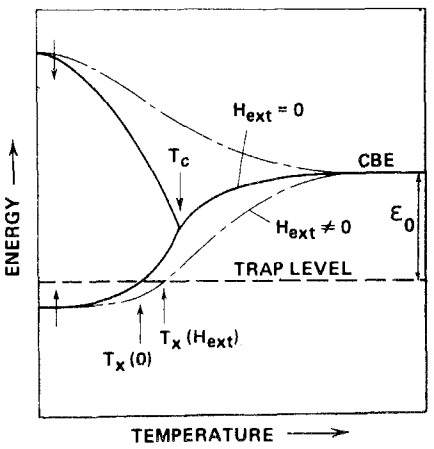

Fig. 19.21. Model of the insulator-metal transition of EuO containing deep traps due to oxygen deficiency. The figure shows the shift and the splitting of the conduction band edge (CBE) for zero and non-zero H_{ext}. The trap level is represented by the horizontal dashed line. T_x is the temperature where the trap level crosses the CBE (after Shapira, 1974).

displays a deep donor. It was the proposal of Oliver et al. (1970b) that this donor is completely decoupled from the conduction band and does not follow the exchange splitting of the latter. Then at a certain temperature $T_x(0)$, the conduction band crosses the donor level, resulting in the delocalization of the trapped electrons. This model is equivalent to the bound magnetic polaron since the magnetic binding energy decreases by the same amount as the conduction band is approaching the donor level.

It is quite obvious, as judged from the model of fig. 19.21 that the donor activation energy $E_D(T)$ will change according to eq. (19.24) with γ_D being practically zero. Thus the change in carrier concentration should follow the short range order given by the spin correlation function. But Penney et al. (1972) argue that the change in the carrier concentration follows the long range order, i.e. the magnetization. Figure 19.20 may indeed look like a magnetization curve for $T < T_C$ and if N follows the spin correlation function it should increase already above T_C. But looking at the conductivity curve of fig. 19.18 one may also get the impression that σ follows the magnetization below T_C, whereas the separate measurement of N and μ has revealed that $N \sim \exp - E_D(T)/dT$ with $E_D(T)$ given by eq. (19.24). We think that also in EuO with O deficiencies the increase of N with decreasing temperature commences already above T_C, but is masked by the decrease of the mobility in that temperature interval and only when N increases substantially below T_C and also μ increases (by about 5 orders of magnitude) the result is a sharp increase for σ. Also from the field variation of the Hall effect for fields up to 130 kOe Shapira (1974) concludes that it is the short range order which determines the change of N near T_C.

EuS with sulfur deficiencies shows a much more complex behavior than EuO

with oxygen deficiencies and it is not clear if an insulator-metal transition has actually been observed. It may very well be that the samples contain other phases or chemical clusters since large hysteresis effects at liquid helium temperature and time dependent decays of conductivity are observed. In any case the conductivity changes due to a possible insulator-metal transition are only about one order of magnitude (Shapira, 1974).

It is thus quite remarkable that R^{3+} doped EuO (shallow donor) and EuO with oxygen deficiencies (deep donor) show such a grossly different conductivity behavior. At first sight the models for both systems are quite similar and the difference in the results is only given by the coupling strength of the donor level to the conduction band.

Finally we want to remark that the situation can be made rather confusing by doping EuO with R^{3+}, e.g. Gd and simultaneously have also oxygen deficiencies (Samokhvalov et al., 1974). In spite of the fact that we have shown that a metal-insulator transition is absent in Gd doped EuO, the presence of oxygen deficiencies nevertheless makes such a transition possible. The situation is similar as in the first attempts of Gd doping of EuO where the compounds were so strongly self compensated that the presence of about 2% Gd in the material could be measured by e.g. microprobe analysis, but neither was their an appreciable change of conductivity or free carrier absorption, nor did the Curie temperature change. Transport properties which depend so strongly on the perfection of the material can only be studied with the most carefully prepared materials. Once the basic effects have been understood with the help of single crystals, thin films may serve to supply additional information.

7. Magneto-optic effects

7.1. *Red-shift of the absorption edge*

The absorption edge of a semiconductor is only weakly temperature dependent and usually a blue shift of the absorption edge with decreasing temperature is observed. This blue shift is caused by the decreasing electron–phonon interaction which changes the self energy of the electron states at the bottom of the conduction band, resulting in a decrease of the width of allowed electron bands. In most materials this blue shift is also larger than a possible red shift due to lattice dilatation effects. In the case of EuSe the influence of both contributions on the optical absorption edge can be seen in fig. 19.13. However, cooling a ferromagnetic semiconductor below its Curie temperature results in a drastically different behavior, as now a large red shift of the absorption edge is observed. This property was discovered in 1964 by Wachter (1964) and Busch et al. (1964a) and is considered a new magneto-optical effect. Since the absorption edge determines the transparent energy gap of a semiconductor the red shift indicates a substantial reduction of the energy gap, which in the case of EuO amounts to 0.27 eV or about 25% of the energy gap (see table 19.6). This reduction in the

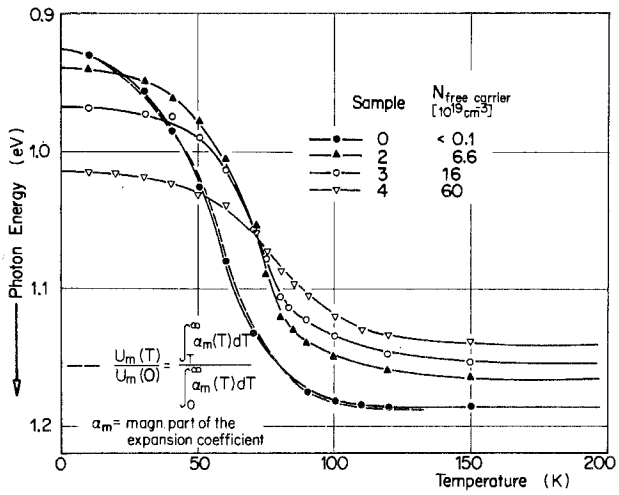

Fig. 19.22. Temperature shift of the absorption edge of undoped and Gd doped EuO crystals. Dashed curve represents the spin correlation function. The samples are characterized by their room temperature free carrier concentration (after Schoenes and Wachter, 1974).

energy gap is a common feature of all known ferromagnetic semiconductors (Batlogg et al., 1975) and in the case of $HgCr_2Se_4$ it is as large as 50% of the gap (Lehmann and Emmenegger, 1969). In fig. 19.22 we show the position of the absorption edge in function of temperature for undoped EuO and three Gd doped EuO samples. For better comparison of the various doped samples the temperature dependence of an arbitrarily chosen, but common absorption coefficient, is plotted. For all samples we observe a red shift of the absorption edge upon cooling below about 150 K. We explain this with the help of fig. 19.19. Above the Curie temperature each state in the conduction band can be occupied by two electrons with antiparallel spin. Below T_C the spin degeneracy is lifted and the bands are split owing to the exchange interaction given by eq. (19.15). For the magnitude of the lowering of the bottom of the conduction band already Vonsovskii and Izyumov (1962) have given an estimate, namely $E_G(M=0) - E_G(M=M_0) = J_{fd}S = \Delta E$. Since $J_{fd} \simeq 0.1$ eV and $S = \frac{7}{2}$, ΔE amounts to about 0.35 eV in agreement with the experiment. However, this number should be considered as the maximum possible value, as will be shown below. The energy gap between $4f^7$ and the conduction band thus becomes reduced, resulting in a red shift of the absorption edge. It is also obvious from fig. 19.19 and has been shown quantitatively by Rys et al. (1967) that the temperature dependence of the absorption edge follows the short range spin correlation function. To demonstrate this we made a fit of the spin correlation function, being proportional to the magnetic energy and thus taken from the magnetic part of the specific heat or the magnetostriction (Argyle et al., 1967), with the red shift of an undoped EuO (dashed line in fig. 19.22). The agreement is excellent.

Considering now that the total red shift of the absorption edge in Gd doped EuO decreases with increasing carrier concentration, we must conclude that the exchange energy becomes reduced in doped materials. The sample with the highest carrier concentration displays a red shift of only 0.12 eV, less than half as much as undoped EuO. The values of the exchange energy, $2\Delta E$, determined by the red shift of the absorption edge are collected in table 19.5.

An external applied magnetic field will have no effect on the red shift for $T \to 0$ and for $T \gg T_C$. Maximum influence is at T_C where the red shift becomes enhanced due to the field induced increase of the magnetization.

Similar effects as for EuO are also observed for EuS and the red shift of EuSe is displayed in fig. 19.23. In the field free case one observes a small peak at $T_N = 4.6$ K just as in fig. 19.3 but already for temperatures just somewhat below T_N, the spin correlation function of the ferrimagnetic phase shows its influence with a further increase of the red shift. A magnetic field at 4.2 K enhances the red shift considerably, because we come into the ferromagnetic phase. The influence of a magnetic field at 4.2 K is thus consistent with the observation of the photosensitivity at the same temperature.

On the other hand antiferromagentic EuTe exhibits a magnetic blue shift of the absorption edge with a kink at T_N. A magnetic field reduces the blue shift until finally, for very large fields, also a red shift is observed. The theory of Rys et al. (1967) just as well contains the blue shift of an antiferromagnet of the second kind because the mere existence of an electron–ion exchange, which is absent in a nonmagnetic semiconductor, already for $T \to \infty$ lowers the bottom of the conduction band by about 0.08 eV. From this new reference level NSNS spin order yields a blue shift and NNNN order a red shift. The spin structure of

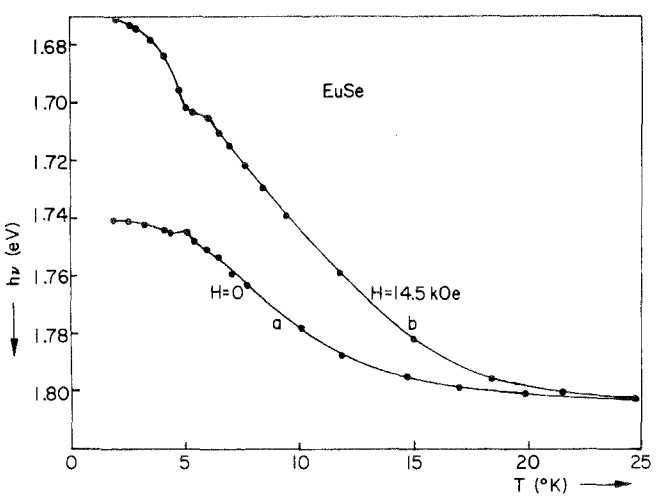

Fig. 19.23. Temperature shift of the absorption edge of EuSe with and without an external magnetic field of 14.5 kOe (after Wachter, 1972).

EuSe, NNSS, on the other hand leads also to a red shift in spite of being antiferromagnetic (Baltogg et al. 1975). In table 19.6 the shift of the absorption edge, ΔE, of the undoped Eu chalcogenides is also collected.

In fig. 19.1 we have shown that EuO (and all the rest of the Eu chalcogenides) makes an isotropic exchange striction for temperatures near and less that T_C. The temperature dependence of this exchange striction follows the spin correlation function (Levy, 1969) and for EuO $\Delta V/V_0 = d\Delta_{mag} = 3\Delta a/a_0 = -3 \times 10^{-3}$ from fig. 19.1. Since we observe also a red shift of the absorption edge with a reduction of the lattice constant or with pressure, we may ask which fraction of the magnetic red shift of the absorption edge is due to the spontaneous exchange striction? The relevant equation is

$$dE_G/d\Delta_{mag} = (1/\kappa)(dE_G/dp) \tag{19.25}$$

with κ being the compressibility of table 19.1 and dE_G/dp the shift of the absorption edge with pressure, collected in table 19.6. We compute $dE_G = 1.2 \times 10^{-2}$ eV which is only about 5% of the observed magnetic red shift of 0.27 eV. (Although the right hand side of eq. (19.25) is measured at 300 K the temperature dependence of this entity is small and of second order). Thus the largest part of the magnetic red shift is due to exchange splitting of the conduction band.

Looking at table 19.6 we realize that the shift of the absorption edge is decreasing from the oxide towards the selenide. We have also seen that the magnetic exchange is splitting the conduction band into spin polarized subbands and is lowering the bottom of the conduction band, which in turn is the reason for the red shift of the absorption edge. Thus we can construct a simple connection between the ferromagnetic exchange integral $\bar{J}_1$ and the red shift of the absorption edge of EuO, EuS and EuSe. We observe with good experimental accuracy that according to Streit (1973)

$$\Delta E \propto \bar{J}_1(E_G)^2 \tag{19.26}$$

Since for EuSe $\bar{J}_1$ is only known in the AF I phase (table 19.2) we should take ΔE from table 19.6 accordingly. If we take for $\bar{J}_1$ eq. (19.23) and use E_G for $U_{(f\text{-}dt_{2g})}$ we find

$$\Delta E \propto t^2 J_{fd}/2S^2 \propto t^2 J_{fd} \tag{19.27}$$

Thus the red shift decreases with decreasing band width of the $5dt_{2g}$ subband (which in turn is proportional to the transfer integral t). The subband decreases from EuO to EuSe by a factor of 2 (see subsections 4.2 and 5.2) thus the spontaneous red shift of the absorption edge is reduced from EuO to EuSe by a factor 4 in agreement with table 19.6. It is of course a trivial consequence that if the final 5d state would also be localized, we would observe no magnetic red shift at all (apart from a possible Zeeman splitting).

Now Kasuya and Yanase (1968) have proposed an explanation of the red shift in terms of the magnetic exciton model and using their formalism we realize that their delocalization factor is proportional to t.

It has also been shown theoretically quite recently by Nolting (1977) that the red shift ΔE of EuO, EuS and EuSe depends only on the band width of the $5dt_{2g}$ conduction band. Also this author deduces that the subband width decreases from EuO to EuSe by a factor 2 in agreement with the expermental results (see above).

So far we have spoken only from the shift of the absorption edge. But it is well known that via the Kramers–Kronig relation a shift of the absorption is connected with a similar change in the refractive index. If one uses wavelengths in the transparent photon energy range of the Eu chalcogenides one can make classical refraction experiments with single crystalline prisms. The temperature and field dependence of the refractive index of three Eu chalcogenides is shown in fig. 19.24 (Wachter 1968b). For the ferromagnets EuO and EuS the field free curves below T_C are only dashed because of a reduced accuracy in the determination of the refractive index due to light scattering on the very small domains (size about 1μm according to Wachter 1968a). There can be no doubt that a change of the refractive index of 0.15 as in the case of EuO is the largest ever observed.

In conclusion of this subsection we want to remark that the magnetic red shift of the absorption edge is the only magneto-optical effect which does not need polarized light. Of course this statement does not exclude that experiments with polarized light have been performed, such as collected by Wachter (1972) or Dimmock (1970), but in view of technical applications it is important to realize that the field induced deflection of a light beam or the intensity modulation of a light beam, using the absorption edge as an optical filter, can be performed with ordinary light. In addition the field direction is largely uncritical since the field

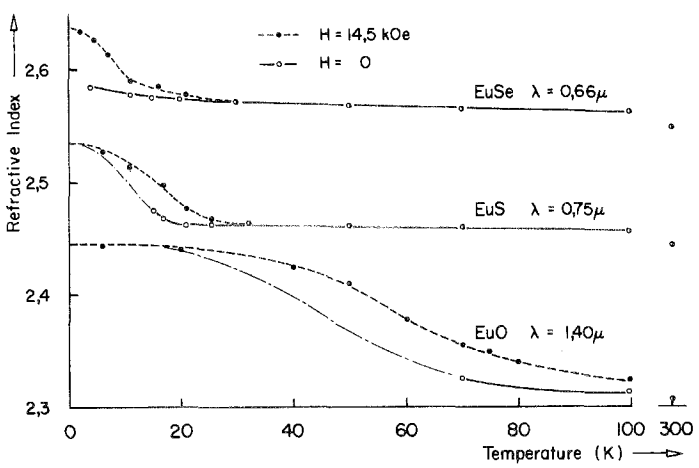

Fig. 19.24. Temperature dependence of the refractive index of EuO, EuS and EuSe prismatic single crystals. In the dash-dotted part of the curves appreciable light scattering due to magnetic domains occurred (after Wachter, 1968b).

serves only to increase the magnetization near T_C. This magnetooptical effect thus is quadratic in magnetic field.

7.2. *Faraday rotation and circular dichroism*

Generally speaking it is understood that magneto-optics describes the interaction of electromagnetic radiation with a magnetized material. The interaction energy is given by

$$E_{ia} \propto \boldsymbol{\mu} \times \nabla V \cdot \boldsymbol{p} \tag{19.28}$$

where ∇V is the electric field in the medium, μ is the magnetic moment and $\boldsymbol{p}$ the momentum of the electron. Therefore, the equation depends on the spin orbit coupling and connects the magnetization with the change of the charge distribution caused by the electromagnetic radiation. Magneto-optical investigations can be performed in various experimental configurations with respect to light propagation, magnetic field and polarization mode of the light. Reflectivity measurements on single crystals comprise observations with right and left hand circularly polarized light (Feinleib et al. 1969, Dimmock 1970), the polar Kerr effect (Suits and Lee, 1971) and magneto-reflectance (Güntherodt and Wachter, 1973a). In transmission experiments on single crystals and thin films the magnetic circular and linear dichroism (Ferré et al. 1972) and the Faraday effect (Busch et al. 1970, Schoenes, 1975) has been investigated. Since the Faraday rotation (FR) and the circular dichroism (CD) are proportional to the magnetization they are of special interest for the Eu chalcogenides and shall be reviewed here. It is worth while noticing that through the FR one may obtain the long range order parameters, while the red shift of the absorption edge gives information on the short range order. These methods therefore are complementary.

One point of interest in magneto-optical spectra arises from the magnitude of the observed effects. Especially for the FR one wants to know the specific FR per cm transmitted material in specific spectral regions at certain temperatures and magnetic fields. Such a dispersion of the specific FR and the CD of the ferromagnet EuS is shown in fig. 19.25 for a temperature below T_C. At full magnetic saturation the FR of the peak at 2.1 eV is 2×10^6 deg. cm^{-1}, in accordance with Tu et al. (1972), but an even larger specific FR is found at 4.3 eV, namely 2.7×10^6 deg. cm^{-1}. Up to now this is the largest FR observed for any material and it is obvious that ferromagnetic semiconductors offer themselves as materials for light modulation techniques, especially since complications due to eddy currents do not exist.

To discuss the spectral dependence of the FR in the range of the $4f^7 \rightarrow 4f^6(^7F_J)5dt_{2g}$ transition ($\hbar\omega < 2.8$ eV), several coupling schemes of the atomic levels have been proposed (Dimmock et al. 1970, Güntherodt et al. 1971, Kasuya, 1972). Here we want to describe the most complete one by Kasuya, valid for $T \rightarrow 0$. The largest effect on the 5d states is the crystal field splitting into t_{2g} and e_g states separated by about 2.2 eV for EuS (table 19.6). The next largest

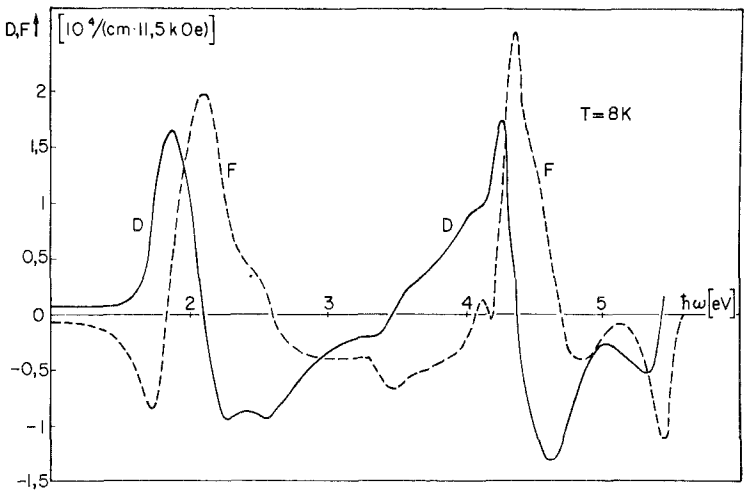

Fig. 19.25. Spectral dependence of the circular dichroism (D) and the Faraday rotation (F) of EuS at 8 K. The dichroism is computed from the Faraday rotation using a Kramers–Kronig relation (after Schoenes, 1975).

interaction is the exchange between an excited $5dt_{2g}$ electron with spin $\frac{1}{2}$ and the remaining $4f^6$ electrons with spin 3, yielding a total spin of $\frac{7}{2}$ or $\frac{5}{2}$, respectively. For EuS this splitting amounts to about $2\Delta E = 0.36$ eV (see table 19.6). Spin orbit coupling with the $4f^6$ electrons results in two multiplets with $J = \frac{1}{2} \ldots \frac{13}{2}$ for $S = \frac{7}{2}$ and $J = \frac{1}{2} \ldots \frac{11}{2}$ for $S = \frac{5}{2}$. Both multiplets overlap and, since spin orbit coupling leaves only J^2 and J_z as good quantum numbers, spin flip transitions are no longer excluded. For such a transition the selection rules are $\Delta L = 0, \pm 1$, $\Delta J = 0$, $\Delta S = 0, \pm 1$ and $\Delta m_l = 0$. The spin flip transitions ${}^8S_{7/2}$ into a $S = \frac{5}{2}$ configuration with $J = \frac{7}{2}$ thus becomes possible and the hump at 2.5 eV in the FR of fig. 19.25 is assigned to this transition. On the other hand, spin conserving transitions with $\Delta J = 0, \pm 1$ from ${}^8S_{7/2}$ into $J = \frac{5}{2}, \frac{7}{2}$ and $\frac{9}{2}$ states are also allowed resulting in a total of 4 transitions up to about 2.8 eV (Schoenes, 1975). In fig. 19.25 the extrema at 1.7, 1.9 and 2.1 eV are assigned to these transitions. The 1.9 eV transition, corresponding to $\Delta J = 0$, could not be resolved in the static FR of fig. 19.25. However, a dynamic FR can resolve all 4 transitions (Schoenes, 1975), just as the magneto-reflectance of Güntherodt and Wachter (1973a). Thus this coupling scheme can indeed describe the observed transitions and give a good hint for the strength of the transitions.

We have mentioned already that the FR and the CD is proportional to the magnetization of the sample. We therefore can write

$$FR = V\mathrm{Ml}, \text{ defining } V = (\omega/2c)(n_r - n_\ell) \tag{19.29}$$

with the Verdet constant, V, and n_r and n_ℓ being the refractive indices for right hand and left hand circularly polarized light. Thus if we observe the temperature

dependence of the FR of e.g. the maximum near 2.1 eV and follow the frequency shift of this maximum (due to the exchange splitting one has a temperature dependence of the spectral position) one obtains a magnetization curve for a large enough magnetic fields. But for fields less than about 2 kOe a sharp kink appears at T_C and a temperature independent FR for $T < T_C$. This effect is due to the demagnetizing field. For the applied field $H_a < N_D M_s$, with N_D the demagnetizing factor and M_s the spontaneous magnetization of a domain, the net magnetization M of the sample is small compared with M_s and the internal magnetic field $H_i \to 0$. Now $H_i = H_a - N_D M$ and it follows for small applied fields that $H_a = N_D M$ and for a constant applied field, $N_D = \text{const} = \text{FR}$. Thus one has the possibility to determine also T_C from FR experiments.

The FR is according to eq. (19.29) a dispersive effect and the CD is an absorptive effect, being proportional to the difference of the absorption indices for right hand and left hand circularly polarized light. Just as in the case of refractive index and absorption index or real and imaginary part of the dielectric function, a Kramers–Kronig relation connects also the FR and CD

$$D(\omega) = -(2\omega/\pi) P_0 \int_0^\infty V(\omega') \mathrm{d}\omega' / (\omega'^2 - \omega^2) \tag{19.30}$$

P_0 is the principal value of the integral. The condition to measure the FR over a very large frequency interval is not very stringent, since positive and negative contributions to the integral lead to a partial compensation of unknown parts of the spectra. The CD in fig. 19.25 has been computed from the FR using relation (19.30). This curve can now be compared with an independent measurement of the CD by Ferre et al. (1972) and one finds indeed an excellent agreement.

It is now of considerable importance to derive the imaginary part of the off-diagonal conductivity tensor σ_{xy} since its integral value

$$\int_0^\infty \mathrm{Im}(\sigma_{xy}) \mathrm{d}\omega \propto \frac{n_{\alpha\uparrow} n_{\beta\uparrow} - n_{\alpha\downarrow} n_{\beta\downarrow}}{n_{\alpha\uparrow} n_{\beta\uparrow} + n_{\alpha\downarrow} n_{\beta\downarrow}}, \tag{19.31}$$

$n_{\alpha\uparrow,\beta\uparrow}$ are the numbers of occupied initial spin up and empty final spin up states, respectively, per total number of initial and final states, respectively (Erskine and Stern, 1973). $n_{\alpha,\beta}$ can be computed from atomic wave functions and with the assumption that the total oscillator strength of an optical transition in the atom remains the same in the formation of bands in the solid, we can compute from the experimental value of $\int_0^\infty \mathrm{Im}\sigma_{xy}\, \mathrm{d}\omega$ the "joint spin polarization" of initial and final states of an optical transition.

The real and imaginary part of the off-diagonal conductivity can be obtained from the FR and CD in conjunction with n and k, the real and imaginary part of the optical constants, (Schoenes et al., 1974).

$$\mathrm{Re}\,\sigma_{xy} = (c/2\pi)(nV - kD) \qquad \mathrm{Im}\,\sigma_{xy} = (c/2\pi)(nD + kV). \tag{19.32}$$

The frequency dependence of FR and CD is shown in fig. 19.25 and the one of n and k is given by Güntherodt et al. (1971), thus $\mathrm{Im}\sigma_{xy}$ and $\mathrm{Re}\sigma_{xy}$ can be

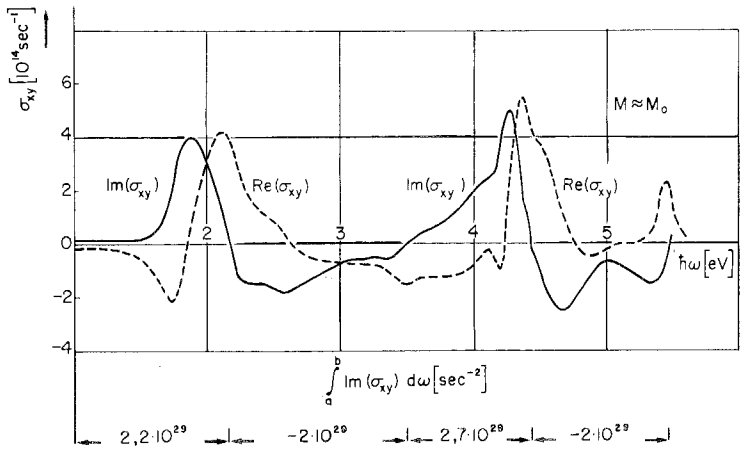

Fig. 19.26. Real and imaginary part of the off diagonal conductivity σ_{xy} of EuS. The numbers at the bottom are the positive and negative integrals of Im σ_{xy} (after Schoenes and Wachter, 1976).

computed and they are displayed in fig. 19.26. To interpret the spectrum of $Im\sigma_{xy}$ one has to know the electronic structure of the material in question as discussed in section 4.2.

In the Eu chalcogenides we expect optical transitions accompanied by large FR going from the localized $4f^7$ states into crystal and exchange split 5d states and also from the p-derived valence band of the anions into the same 5d states (charge transfer). We shortly want to discuss how these transitions will manifest themselves in $Im\sigma_{xy}$. In fig. 19.27a we show schematically the absorption, W, of a solid. The finite band width ΔE_B in the solid and the spin-orbit coupling ΔE_{so} of initial and final states lead to a different absorption W for right- and left hand circularly polarized light. Considering a $4f^7 \rightarrow 5d$ transition, the initial state for $T \rightarrow 0$ is completely spin up polarized. For spin conserving transitions the difference of the two absorption curves yields a non zero contribution to $Im\sigma_{xy}$: positive (negative) for spin up (down) transitions for small ω and vice versa for large ω (fig. 19.27b). An exchange splitting of the 5d states merely shifts the spectrum to lower energies (which is observed experimentally) and does not influence the form and magnitude of $Im\sigma_{xy}$ (fig. 19.27c). It is important to realize that the $4f^7$–5d transitions are symmetric in shape with equal positive and negative areas in $Im\sigma_{xy}$ (full drawn curve in fig. 19.27b, c). In the real crystal there are $4f^7{}_\uparrow \rightarrow 5dt_{2g\uparrow}$ and $4f^7{}_\uparrow \rightarrow 5de_{g\uparrow}$ transitions, separated by the crystal field of 2.2 eV and we must assume that absorptions from other than $4f^7$–5d transitions (namely $3p \rightarrow 5d$ transitions) overlap in $Im\sigma_{xy}$. Therefore, we have to decompose the spectrum of fig. 19.26. Since we know the lowest energy optical transition is $4f^7 \rightarrow 5dt_{2g}$ we construct from the lowest energy positive part of $Im\sigma_{xy}$ in fig. 19.26 an equal negative area as shown by the positively inclined, hatched part of fig. 19.27 and do this also for the $4f^7 \rightarrow 5de_g$ transition. Thus the

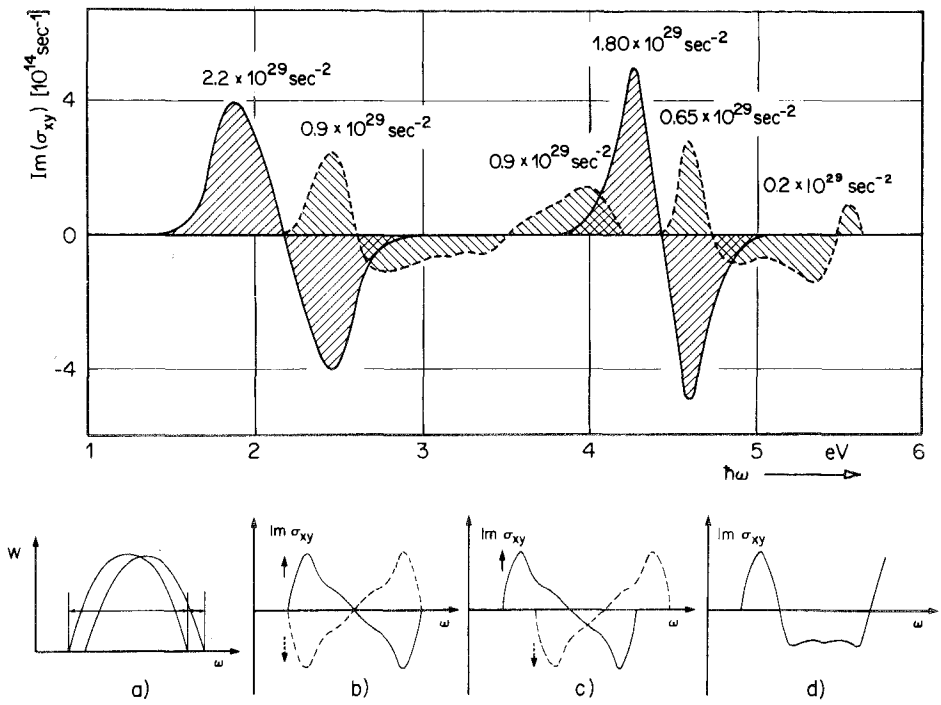

Fig. 19.27. Decomposition of Im $\sigma_{xy}(\omega)$ in two S-shaped curves as expected for $4f_\uparrow \rightarrow 5dt_{2g\uparrow}$ and $4f_\uparrow \rightarrow 5de_{g\uparrow}$ transitions. Insert (a) absorption of right- and left-hand circularly polarized light for spin up states. (b) Im $\sigma_{xy}(\omega)$ for spin up states (solid line) and spin down states (dashed line) without exchange splitting. (c) the same as (b), but exchange splitting included (d) Im $\sigma_{xy}(\omega)$ as expected for $3p \rightarrow 5dt_{2g}$ transitions (after Schoenes et al., 1974).

two positively hatched regions of fig. 19.27 contain all the oscillator strength of the $4f^7$–5d transitions and their areas are in first approximation proportional to the *ratio of spin–orbit splitting to band width* of initial plus final state.

The negatively inclined, hatched regions of 19.27 are the difference between the $4f^7 \rightarrow 5d$ transitions and Imσ_{xy} of fig. 19.26. They are attributed to the $3p \rightarrow 5dt_{2g}$ and $3p \rightarrow 5de_g$ transitions as will be shown below. Transitions from a completely filled valence band into an empty conduction band in the absence of exchange splitting will not lead to a contribution to Imσ_{xy}, as we have equal numbers of electrons with spin up and spin down. Thus, as shown in fig. 19.27b, both curves cancel each other. Only in the presence of exchange splitting (fig. 19.27c) do we obtain contributions to Imσ_{xy} as shown in fig. 19.27d. The shape of this curve is very different from the one of a $4f^7 \rightarrow 5d$ transition (full line fig. 19.27b,c) and is the discriminating property. Indeed, the negatively hatched regions of fig. 19.27 closely resemble the theoretical curves for a $3p \rightarrow 5d$ transition. In the Eu chalcogenides the exchange splitting of the p valence bands is probably negligible compared with the exchange splitting of the 5d bands, so from the areas of

the negatively hatched regions of fig. 19.27 one obtains the *ratio of 5d exchange splitting to band width* of initial and final state.

Now one can insert numbers for the spin–orbit coupling, take the width of the p bands from photo-emission, use for the "apparent" $4f^7$ band width the one of the $4f^6(^7F_J)$ multiplet and derive the exchange splitting of the 5d bands and their band widths (Schoenes et al., 1974, Schoenes, 1975). Surprisingly enough, these numbers are in good agreement with the general knowledge one has collected with other experiments (section 4.2). This also means that the initial assumptions of a completely spin up polarized $4f^7$ state and of a negligible spin polarization of the anion p bands are selfconsistently correct. In other words, the quantitative calculations and their comparison with the experimental $\int \mathrm{Im}\sigma_{xy}\, d\omega$ provide a means to measure the spin polarization. Magneto-optical measurements have this ability in common with the spin polarized photo-emission, to be discussed in section 7.3.1. While magneto-optical measurements are free of problems connected with work functions, escape depth of photoelectrons and their scattering on the way towards the surface, the large amount of theoretical computations necessary to arrive at the spin polarization is a serious drawback, which also manifests itself in a lack of precision ($\pm 20\%$).

On the other hand, such a theoretical analysis of the FR as for EuS is the first analysis of this type to be applied to a semiconductor. Due to the magneto-optical selection rules, pd and fd transitions could be distinguished, however, the FR does not seem to be an adequate tool to obtain information on the density of states. This analysis has also shown that the hump in the FR for EuS at 2.5 eV, which has been attributed to the fd spin flip transition, in part is also due to a superposition of the pdt_{2g} transition.

In conclusion it may be stated that the basic features of the magneto-optical phenomena are understood and further refinement in the analysis will be very complex and ambiguous.

7.3. *Direct observation of spin polarization*

7.3.1. *Spin polarized photoemission*

Electrons emitted from magnetized materials can show a spin polarization because magnetism is due to a parallel alignment of electron spins. Materials like the Eu chalcogenides should be model substances for these experiments, because as we have seen, 100% spin polarized $4f^7$ levels are well separated in energy from other bands and in addition are the highest occupied valence states. If electrons are emitted from the solid by a photoemission process, in which light is absorbed by the 4f electrons, promoting them into a conduction band, they diffuse towards the surface and if they still possess enough kinetic energy to surpass the surface potential barrier, their degree of polarization can be measured by a Mott scattering analyzer. The spin polarization, P, in these experiments is given by a similar formula as eq. (19.31), which represents the "joint spin polarization" of initial and final states, with the difference that now

only the spin polarization of the initial states enters, thus $n_\beta = 1$. P is proportional to the magnetization and it can be measured in function of temperature, field and photon energy. Most experiments dealing with spin polarized photoemission have recently been reviewed by Siegmann, (1975).

In order to observe a net spin polarization of emitted electrons from a multidomain material, a magnetic field perpendicular to the emitting surface must be applied which, in order to achieve magnetic saturation, must exceed $N_D M_0$, with N_D being the demagnetizing factor. In the case of EuO single crystals the demagnetizing factor is about $\frac{1}{3}$, so fields in excess of about 8 kOe should give 100% spin polarization for electrons near threshold with emission of only 4f electrons. However, only a P of about 40% is measured for these fields and even at 40 kOe one achieves only 65% spin polarization (Sattler and Siegmann, 1972). The situation with polycrystalline EuS films ($N_D = 1$) is similar and a maximum polarization of 50% for 30 kOe is observed. (Busch et al., 1971). Thus either the photoemission occurs predominantly from poorly polarized impurity states, which is very unlikely, or a depolarization of photoelectrons occurs in the process of photoemission. Here one must consider a peculiarity of photoemission, namely the escape depth of photoelectrons. Although the penetration depth of the exciting light is several thousand Å, only electrons on their way to the surface, which have not suffered any collisions with phonons or other electrons will have a chance to be emitted. Thus the escape depth of photoelectrons is between 100 Å and a few atomic layers. If the surface layers of a magnetic material are not as completely magnetized as is the bulk, photoemission probes only the surface magnetization. On the other hand, Sattler and Siegmann, (1975) argue that also photoelectrons excited from deep lying 100% polarized $4f^7$ states have a high probability of undergoing spin exchange scattering on a less magnetized surface layer before escaping into vacuum. They estimate that a single non saturated layer at the surface can reduce an initial 100% polarization of deep 4f states to 50%. Thus a more or less paramagnetic sheet is postulated at the surface of EuO and EuS and of possibly the other Eu chalcogenides. It shall also be mentioned that spin polarized photoemission experiments have been performed on EuSe and EuTe and on samples with appreciable structural disorder (Busch et al., 1971).

Spin polarized photoemission has also been investigated on EuO doped with Gd or La (Sattler and Siegmann, 1975) and on EuS doped with Gd. For doped EuO single crystals P is always above the one for undoped material and for EuO doped with La a P of 80% could be measured at 30 kOe. Sattler and Siegmann, (1975) believe that the larger P of the emitted 4f electrons is due to the additional free electrons incorporated by doping. The direct photoemission of these impurity electrons is negligible, but they increase the surface magnetization of the paramagnetic sheet due to a better coupling of the surface to the bulk of the material.

Also from the spectral dependence of the spin polarized photoemission one can draw important conclusions. The photoelectrons emitted with the lowest photon energy will be from always present impurities. A sharp increase of P is

observed when $\hbar\omega$ is large enough to emit 4f electrons, but for still larger $\hbar\omega$ a decrease in P is observed. This is attributed to electrons being emitted from p valence bands which then have to be assumed unpolarized. This conclusion is in agreement with the analysis of the FR given in section 7.2.

Thus spin polarized photoemission has been shown to be a new tool in giving information on the surface magnetization. Besides, efficient sources of spin polarized electrons can be made from e.g. EuO containing a few percent La and degrees of polarization of 80% at 30 kOe have been verified experimentally.

7.3.2. *Spin polarized field emission*

Basically all electron emission experiments, such as photoemission, field emission and thermionic emission are similarly suited also for emission of polarized electrons. Thermionic emission is of course limited to ferromagnets with high T_C and has so far not been used. But field emission is also an efficient source for polarized electrons in the case of the Eu chalcogenides. The first experiments with field emission from EuS have been performed by Müller et al., (1972). The authors use an EuS coated tungsten tip which can be cooled to temperatures below T_C. The tip is in a longitudinal magnetic field of up to 20 kOe and the electric extraction field is 2×10^7 V/cm. After the emission the degree of polarization P is measured in a Mott scatterer.

It is surprising in view of the photoemission results that these experiments yield a P of 90% at a temperature of 14 K, i.e. one may expect 100% polarization for $T \to 0$. Between 2.5 and 20 kOe there is practically no magnetic field dependence. The authors explain this by assuming the emission to come also from the more or less cylindrical shaft of the tip for which the demagnetizing factor may be very small. Using the smallest possible demagnetizing factor, $\frac{1}{4}\pi$, the saturation field for EuS is about 1.2 kOe and at twice this field (2.5 kOe) one observes already 90% spin polarization at 14 K. In contrast for EuO single crystals with twice the saturation field ($\frac{2}{3}$) 24 kOe = 16 kOe the polarization is less than 50% as indicated by photoemission. This was proposed to be due to a paramagnetic surface layer (Sattler and Siegmann, 1975). It is difficult to visualize why such a paramagnetic sheet is not active in the field emission process.

On the other hand it is an interesting question whether the EuS merely acts as a spin filter for the W electrons or whether 4f electrons are tunneling. In the former case exchange splitting of the conduction band and band bending under the action of the electric field are necessary conditions but the spin orbit splitting of the 5d conduction band should not permit a P of 90%. Thus Müller et al. (1972) propose tunneling from 4f states or tunneling assisted by interaction with 4f states. Also Kisker et al. (1976) have performed the same field emission experiments on EuS, but in addition they have obtained the temperature dependence of P in a field of 3 kOe. These authors deduce a T_C of about 50 K, which must be due to an unvoluntarily doping or to incorporation of defects.

Only shortly it shall be mentioned that internal field emission from one metal into another metal via a ferromagnetic semiconductor is also possible. The

semiconductor essentially acts as spin filter with exchange split conduction bands. Temperature and field dependent tunneling is observed, but no information on the degree of spin polarization of the tunneling electrons is obtained. For a review of these effects see Thompson et al. (1972).

8. Phonon modes and inelastic light scattering

In materials with the cubic rocksalt structure one expects from group theoretical considerations only one degenerate transverse optical (TO) phonon mode and one longitudinal optical (LO) phonon mode. Since the inversion symmetric structure is not Raman active in first order, one must depend on far infrared reflectivity studies to obtain the residual ray spectrum. First measurements have been performed by Axe (1969) for EuO, EuS and EuSe and by Holah et al. (1973) for EuTe and for EuO and Gd doped EuO by Güntherodt and Wachter (1973c). The one phonon frequencies at the zone center ($q \approx 0$) are collected in table 19.7. EuO offers some problems because of multiple phonon effects which have been taken into account by Axe (1969) through a fit with a classical oscillator response function and by Güntherodt and Wachter (1973c) with a Kramers–Kronig analysis. The more recent values for the TO and LO modes of EuO of Güntherodt (1974) are used in table 19.7.

The general trend that the wavelength of the phonon modes depends approximately on the reduced mass M^* of the oscillating system like $\lambda \sim M^{*1/2}$ is reasonably fulfilled just as the Lyddane–Sachs–Teller relation, connecting LO and TO frequencies with the optical and static dielectric constants, taken from table 19.6.

Doping EuO has no strong influence on the TO mode, for EuO + 1.26% Gd it shifts to shorter wavelengths by about 10% (Güntherodt and Wachter, 1973c). However, as new effect one observes now a coupling between plasmons and LO phonon modes, resulting in a more phonon like ω_+ mode and a more plasmon like ω_- mode.

TABLE 19.7
Phonon modes of the Eu chalcogenides

	ω_{TO} (cm^{-1})	ω_{LO} (cm^{-1})	ω_R[a] (cm^{-1})	width[a] (cm^{-1})
EuO	182[a]	435[a]	390	—
EuS	178[b]	266[b]	238	24
EuSe	127[b]	182[b]	138	26
EuTe	102[c]	142[c]	129	48

[a]Güntherodt (1974); [b]Axe (1969); [c]Holah et al. (1973); [d]Vitins and Wachter (1976b); "Sharp line" spectra $\omega_R = \omega_{LO}$, half width 7–8 cm^{-1} after Tsang et al. (1974).

It was stated above that due to the inversion symmetric crystal structure of the Eu chalcogenides one does not expect a first order Raman effect. In spite of this, inelastic light scattering experiments in back scattering geometry have been performed with positive results (Ray et al., 1971; Schlegel and Wachter, 1973). Surprisingly enough, the light scattering was found to consist of up to 6 lines shifted by multiples of a basic frequency. As an example we show such a spectrum for EuS at room temperature in fig. 19.28, with Stokes and anti-Stokes lines being observed. The basic frequencies of the Eu chalcogenides, ω_R, are collected in table 19.7 and it can be seen that they are between the zone center LO and TO frequencies. The half width of the lines is between 24 cm^{-1} and 48 cm^{-1} and is considered rather large (broad line spectra) and the polarization of the lines is perpendicular to the laser polarization.

If these lines were due to second order Raman scattering they should exhibit fine structure due to density of states effects as in e.g. NaCl. But the lines for good quality crystals are very simple and smooth. If the first line would correspond already to two optical phonons with opposite wavevector q, there should also exist a line corresponding to 3 optical phonons, to be expected at about 1.5 ω_R which is not observed. Since ω_R is between ω_{TO} and ω_{LO} it cannot be a combination of LO and TO phonons. The intensity ratio of first Stokes and anti-Stokes line is calculated to be 3.3 for EuS with $\omega_R = 238\ cm^{-1}$. Experimentally Schlegel and Wachter (1973) measured 3.5 ± 0.3 and one reads from fig. 19.28 a ratio of 3.2 ± 0.1. Thus it can be stated in agreement with all authors in this field that the inelastic light scattering observed in the Eu chalcogenides is of first order.

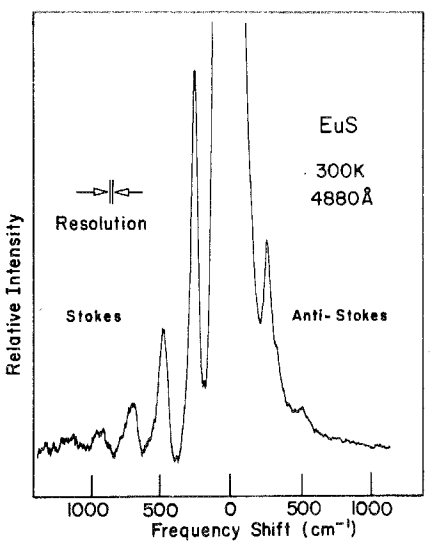

Fig. 19.28. Inelastic light scattering of EuS at 300 K. Excitation with 4880 Å (after Vitins, 1977).

Interpretations in terms of a Raman process are then in conflict with the cubic symmetry of the crystals. Thus alternatives involving defect induced scattering (Schlegel and Wachter, 1973) or spin disorder scattering (Ray et al., 1971; Tsang et al., 1974) have been proposed. While defect scattering has been discarded in later experiments, since no significant variation with doping could be observed (Vitins and Wachter, 1975b) at first sight spin disorder scattering was a promising proposal. Indeed, with increasing spin order, achieved by cooling below T_C, the light scattering became significantly reduced as is shown in fig. 19.29 for EuS. However, the scattering did not go to zero even at 2 K and in fields of 5.3 kOe. In the insert of fig. 19.29 the change of the light scattering with temperature and field has been successfully fitted with a spin correlation function, taken from the magnetic red shift of the absorption edge and indicated by the full and dashed lines.

The interpretation of light scattering with spin disorder was questioned by Vitins and Wachter (1975b), because antiferromagnetic EuTe did not show a decrease of the scattering intensity below T_N, instead even an increase of the intensity. Even more significant, also the diamagnetic YbTe showed the same multiphonon lines as the Eu chalcogenides. In YbS and YbSe a strong temperature dependence of the scattering was observed, increasing for decreasing temperature (Vitins and Wachter, 1976a). All these light scattering experiments had a strong resemblance with the luminescence properties of the Eu chalcogenides, reviewed by Wachter (1972) and Streit (1973). Therefore, Vitins and Wachter (1975b, 1976a,b) proposed for the light scattering mechanism a model based on "hot recombination".

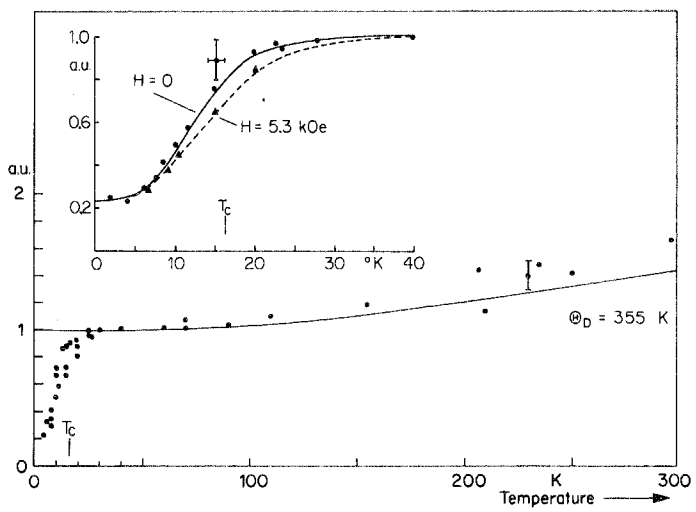

Fig. 19.29. Temperature dependence of the Stokes line of EuS. Theoretical fit with Bose statistics (full line). The insert shows the temperature dependence below 40 K, with spin correlation functions for $H = 0$ and $H = 5.3$ kOe (full and dashed line, respectively) taken from Wachter 1972 (after Schlegel and Wachter, 1973).

Similar as in the "cascade model" of Martin and Varma (1971) the photoelectron is excited into *real* band states from which it decays to the bottom of the conduction band through the successive emission of phonons. At each step of the relaxation process there is a small probability of radiative recombination of the excited, *not yet thermalized* electron with its own hole. This leads to a series of emission lines on Stokes and anti-Stokes side for $T > 0$. In this model the life time of the excited electron is expected to be in the order of 10^{-9} sec. It is well known that the *thermalized* infrared luminescence in the Eu chalcogenides is governed by the polaronic behavior of the excited electron in the 5d band (combined electric and magnetic polaron) (Streit, 1973). Vitins and Wachter (1976a,b) believe that due to its finite lifetime also the *hot* photoelectron is best described by a polaronic behavior. Hence this scattering does not have to follow the usual selection rules and can also occur in crystals with O_h symmetry (Mulazzi, 1970). Just as in the infrared luminescence there is a strong relaxation of the lattice around the localized hole in the 4f shell. Therefore one expects the q-selection rule not to be strictly obeyed and optical phonons (mostly LO) throughout the Brillouin zone can take part in the scattering. This explains the large line width (20–50 cm^{-1}) generally observed in the Eu- and Yb chalcogenides.

In the infrared luminescence of the Eu chalcogenides (Streit, 1973) the thermalized photoelectron recombines with its own localized 4f hole. The recombination probability depends on the overlap of the wavefunctions of both hole and electron, thus the quantum yield depends mostly on the localization of the excited electron, which occurs through a coupling with the phonons and the spin system (electric and magnetic polaron). The same localization mechanism applies also for the "hot recombination" which gives rise to the inelastic light scattering. Hence ferromagnetic order delocalizes the excited photoelectron and quenches the intensity of the inelastic light scattering (see fig. 19.29) (recall that the photoconductivity increases with the appearance of ferromagnetic order) and antiferromagnetic order (EuTe) leads to a small increase of the scattering intensity, as the excited electrons is more strongly localized by the antiferromagnetic order. Of course in the diamagnetic Yb chalcogenides no quenching is expected with decreasing temperature, rather the contrary occurs due to the localization of the electric polaron. Thus the inelastic, broad line light scattering finds its explanation, just as the ordinary thermalized luminescence, in the model of a recombination process.

In addition to this broad line scattering Tekippe et al. (1974) and Tsang et al. (1974) have discovered a sharp line Raman effect in EuS and EuSe. The line is found exactly at the LO frequency and it appears only in the ferromagnetically ordered state, i.e. in EuSe only in applied magnetic fields above 8 kOe. Whereas the excitation frequency dependence of the broad line spectra closely follows the absorption coefficient of the material, the frequency dependence of the sharp line spectra is rather restricted and only near the absorption edge. For example in EuSe maximal scattering intensity is observed for incident photon energies near 2.1 eV, whereas the maximum absorption is at 2.55 eV. It is now quite remarkable that 2.15 eV has been deduced to be possibly the energy of a

Wannier exciton in EuSe, as shown in fig. 19.13 by the intersection of the Urbach lines. It therefore appears possible that the sharp line inelastic light scattering is due to a resonance with this exciton. The temperature dependence and the polarization mode of the sharp line scattering is quite different from the one of the broad line scattering and no conclusive explanation is available as yet. There are, however, indications that sharp line spectra are also present in Yb chalcogenides (Vitins and Wachter, 1976b).

9. Conclusion

Certainly the discovery of ferromagnetic semiconductors opened a new field of physics. In spite of the fact that the Eu chalcogenides have not been the first materials of this kind and are not the only ones, this group of materials is the most investigated one. This is mostly due to the fact that from the magnetic point of view these materials are model Heisenberg magnets and due to their simple cubic structure and strongly ionic bonding they are also model substances in other respects. Quite a number of new and even giant effects have been found in the Eu chalcogenides, such as a splitting of the conduction band upon magnetic order, which in turn is the cause of the magnetic red shift and of the negative magneto-resistance near T_C. Also positive magneto-resistance in the paramagnetic temperature range is observed (Shapira et al., 1974; Vitins and Wachter, 1975a) which is interpreted as being due to the strong exchange interaction of conduction electrons with the 4f spin system. These materials exhibit the largest known magneto-optic effects and a very dramatic shift of the luminescence spectrum upon magnetic order. We think that all described effects in the article, covering experiments and theories made during the last fifteen years, could be explained consistently.

It is quite natural that not all authors and not all papers could be included in this review due to the limited amount of space and capability of the author. But since this article is not the only review and probably not the last one on this topic the problems and materials will always be illuminated from different points of view. With respect to magnetic semiconductors we want to recall that non-rare earth compounds like the Cr spinels (Haas, 1970) offer similar effects as the Eu chalcogenides. Also the group of the RE-pnictides may become ferromagnetic semiconductors with increasing purity and perfection of the samples, but at the moment their conduction mechanism is still in discussion (see also F. Hulliger, vol. 4, ch. 33 of this *Handbook*).

Acknowledgment

The author is most grateful to his coworkers B. Batlogg, G. Güntherodt,* H.v. Känel, A. Schlegel, J. Schoenes, P. Streit** and J. Vitins for significant experi-

*Present address: Max Planck Institut für Festkörperforschung, Stuttgart, Germany.

**Present address: Brown Boveri Forschungszentrum, Baden, Switzerland.

mental contributions to this work and valuable discussions with the author. The technical assistance of J. Müller, B. Naef and H.P. Staub is gratefully acknowledged. The samples and single crystals of the Eu chalcogenides used in recent work in the Solid State Laboratory of ETH have been prepared by E. Kaldis of this laboratory, whose cooperation was very valuable. The author is also greatly indebted to Prof. Dr. G. Busch, for valuable discussions, advice and support. Finally, financial support of the Swiss National Funds is gratefully acknowledged.

References

Ahn, K.Y., K.N. Tu and W. Reuter, 1971, J. Appl. Phys. **42**, 1769.
Anderson, P.W., 1963, Magnetism, Vol. I, ed. G.T. Rado and H. Suhl Academic Press Inc., New York.
Argyle, B.E., N. Miyata and T.D. Schultz, 1967, Phys. **160**, 413.
Axe, J.D., 1969, J. Phys. Chem. Solids **30**, 1403.
Baltensperger, W. and A.M. de Graaf, 1960, Helv. Phys. Acta **33**, 881.
Batlogg, B., E. Kaldis, A. Schlegel and P. Wachter, 1975, Phys. Rev. **B12**, 3940.
Batlogg, B. and P. Wachter, 1977, Solid State Commun. **24**, 569.
Batlogg, B., 1976, private communication.
Bayer, E. and W. Zinn, 1971, Z. angew. Physik **32**, 83.
Bayer, E. and W. Zinn, 1973, JEEE Trans. Mag. **9**, 4.
Berkner, D.D., 1975, Phys. Lett. **54A**, 396.
Bloembergen, N. and T.J. Rowland, 1955, Phys. Rev. **97**, 1679.
Boyd, E.L., 1966, Phys. Rev. **145**, 174.
Busch, G., P. Junod, M. Risi and O. Vogt, 1962, Proc. Int. Conf. on Semiconductors, Exeter, p. 727.
Busch, G., P. Junod and P. Wachter, 1964a, Phys. Lett. **12**, 11.
Busch, G., P. Junod and R.G. Morris, J. Muheim and W. Stutius, 1964b, Phys. Lett. **11**, 9.
Busch, G., P. Junod and O. Vogt, 1966, Proc. Colloque Int. du C.N.R.S. sur les dérivés semi-métalliques, Orsay, p. 325.
Busch, G. and P. Wachter, 1966, Phys. kondens. Materie **5**, 232.
Busch, G. and P. Wachter, 1968, Berichte Arbeitsgem. Magnetismus, p. 1, 1969, Z. angew. Phys. **26**, 1.
Busch, G., P. Cotti and P. Munz, 1969, Solid State Commun. **7**, 795.
Busch, G., J. Schoenes and P. Wachter, 1970, Solid State Commun. **8**, 1841.
Busch, G., M. Campagna and H.C. Siegmann, 1971, J. Appl. Phys. **42**, 1781.
Cho, S.J., 1970, Phys. Rev. **B1**, 4589.
Cotti, P. and P. Munz, 1974, Phys. cond. Matter **17**, 307.
Davis, H.L., 1971, Proc. 9th Rare Earth Conf., Blackburg, Va, pg. 3.
de Gennes, P.G. and J. Friedel, 1968, J. Phys. Chem. Solids **4**, 71.
de Jongh, L.J. and A.R. Miedema, 1974, Adv. in Phys. **23**, 1.
Dietrich, O.W., A.J. Henderson, Jr. and H. Meyer, 1975, Phys. Rev. **B12**, 2844.
Dimmock, J.O., 1970, IBM J. Res. Develop. **14**, 301.
Dimmock, J.O., J. Hanus and J. Feinleib, 1970, J. Appl. Phys. **41**, 1088.
Eastman, D.E., F. Holtzberg and S. Methfessel, 1969, Phys. Rev. Lett. **23**, 226.
Eastman, D.E. and M. Kuznietz, 1971, J. Appl. Phys. **42**, 1396.
Erskine, J.L. and E.A. Stern, 1973, Phys. Rev. **B8**, 1239.
Ferré, J., B. Briat, C. Paparoditis, S. Pokrzywnicki and R. Suryanarayanan, 1972, Solid State Commun. **11**, 1173.
Feinleib, J., W.J. Scouler, J.O. Dimmock, J.O. Hanus, T.B. Reed and C.R. Pidgeon, 1969, Phys. Rev. Lett. **22**, 1385.
Fischer, M.E., 1962, Phil. Mag. **7II**, 1731.
Fischer, P., W. Haelg, W. von Wartburg, P. Schwob and O. Vogt, 1969, Phys. kondens. Materie **9**, 249.
Franzblau, M.C., G.E. Everett and A.W. Lawson, 1967, Phys. Rev. **164**, 716.
Freeman, A.J., J.O. Dimmock and R.E. Watson, 1966, Quantum Theory of Atoms, Molecules, Solid State, O.P. Löwdin Ed. Academic Press, New York.
Freiser, M.J., F. Holtzberg, S. Methfessel, G.D. Petit, M.W. Shafer and J.C. Suits, 1968a, Helv. Phys. Acta **41**, 832.
Freiser, M.J., S. Methfessel and F. Holtzberg, 1968b, J. Appl. Phys. **39**, 900.
Goodenough, J.B., 1963, Magnetism and the Chemical Bond, p. 149, New York, J. Wiley.
Greenwood, N.N., 1968, Ionic Crystals, Lattice Defects and Nonstoichiometry, Butterworths, London.
Griessen, R., M. Landolt and H.R. Ott, 1971, Solid State Commun. **9**, 2219.
Griffiths, R.B., 1967, Phys. Rev. **158**, 176.

Güntherodt, G., P. Wachter and D.M. Jmboden, 1971, Phys. kondens. Materie **12**, 292.
Güntherodt, G. and P. Wachter, 1973a, Surface Science **37**, 288.
Güntherodt, G. and P. Wachter, 1973b, AIP Conf. Proc. **10**, 1284.
Güntherodt, G. and P. Wachter, 1973c, Solid State Commun. **12**, 897.
Güntherodt, G., 1974, Phys. cond. Matter **18**, 37.
Güntherodt, G. and P. Wachter, 1974, Proc. 11th Int. Conf. on Rare Earth Research, Traverse City, p. 820.
Haas, C., A.M.J.G. van Run, P.F. Bongers and W. Albers, 1967, Solid State Commun. **5**, 657.
Haas, C., 1970, CRC Critical Reviews on Solid State Sciences **1**, 47.
Hauger, R., E. Kaldis, G. von Schulthess, P. Wachter and Ch. Zürcher, J. Magn. and Magnetic Materials, 1976, **3**, 103.
Henderson, A.J. Jr., G.R. Brown, T.B. Reed and H. Meyer, 1970, J. Appl. Phys. **41**, 946.
Holah, G.D., J.S. Webb, R.B. Dennis and C.R. Pidgeon, 1973, Solid State Commun. **13**, 209.
Huang, C.C. and J.T. Ho, 1975, Phys. Rev. **B11**, 5255.
Jayaraman, A., A.K. Singh, A. Chatterjee and S. Usha Devi, 1974, Phys. Rev. **B9**, 2513.
Jonker, G.H. and J.H. van Santen, 1950, Physica **16**, 337.
Kahn, M.A., 1976, J. Phys. C: Solid State Phys. **9**, 81.
Kajita, K. and T. Masumi, 1970, Solid State Commun. **8**, 1039.
Kajita, K. and T. Masumi, 1971, J. Phys. Soc. Japan **31**, 946.
Kaldis, E. and P. Wachter, 1972, Solid State Commun. **11**, 907.
Karpenko, B.V. and A.A. Berdishev, 1964, Sov. Phys. Solid State **5**, 2494.
Kasuya, T., 1956, Progr. Theor. Phys. **16**, 45.
Kasuya, T. and A. Yanase, 1968, Rev. Mod. Phys. **40**, 684.
Kasuya, T., 1970a, J. Appl. Phys. **41**, 1090.
Kasuya, T., 1970b, IBM J. Res. Develop. **14**, 214.
Kasuya, T., 1970c, Proc. Int. Conf. Physics of Semiconductors, Cambridge, Mass. p. 243.
Kasuya, T. and T. Penney, 1970, Solid State Commun. **8**, 1547.
Kasuya, T., 1972, CRC Crit. Rev. Solid State Sciences **3**, 131.
Kisker, E., G. Baum, A.H. Mahan and K. Schröder, 1976, J. Magn. and Magnetic Materials **3**, 4.
Köbler, U. and K.J. Fischer, 1975, Z. Phys. **B20**, 391.
Kornblit, A., G. Ahlers and E. Buehler, 1973, Phys. Lett. **43A**, 531.
Kramers, H.A., 1934, Physica **1**, 182.
Lehmann, H.W. and F.P. Emmenegger, 1969, Solid State Commun. **7**, 965.
Lendi, K., 1974, Phys. cond. Matter **17**, 189.
Leroux-Hugon, P., 1972, Phys. Rev. Lett. **29**, 939.
Levy, F., 1969, Physik kondens. Materie **10**, 71.
Levy, F. and P. Wachter, 1970, Solid State Commun. **8**, 183.
Lofgren, K.E., T. Tuomi and T. Stubb, 1974, Proc. of 12th Int. Conf. Physics of Semiconductors, Stuttgart, p. 885, Teubner, Stuttgart.
Mahr, H., 1962, Phys. Rev. **125**, 1510.
Martin, R.M. and C.M. Varma, 1971, Phys. Rev. Lett. **26**, 1241.
Matthias, B.T., R.M. Bozorth and J.H. van Vleck, 1961, Phys. Rev. Lett. **7**, 160.
McGuire, T.R., B.E. Argyle, M.W. Shafer and J.S. Smart, 1962, Appl. Phys. Lett. **1**, 17.
McWhan, D.B., P.C. Souers and G. Jura, 1966, Phys. Rev. **143II**, 385.
Methfessel, S., 1965, Z. angew. Physik **18**, 414.
Methfessel, S. and D.C. Mattis, 1968, Handbuch der Physik, ed. S. Flügge, Springer Verlang, Vol. **18**, p. 1.
Mitani, T. and T. Koda, 1974, Proc. of 12th Int. Conf. Physics of Semiconductors, Stuttgart, p. 889, Teubner, Stuttgart.
Moore, C.E., 1965, Atomic Energy Levels, Nat. Bureau of Standards Circ. No. 467.
Moruzzi, V.L. and D.T. Teaney, 1963, Solid State Commun. **1**, 127.
Moruzzi, V.L., D.T. Teaney and B.J.C. von der Hoeven, 1968, Phys. Rev. Lett. **20**, 719.
Moss, T.S., 1952, Photoconductivity in the Elements, Academic Press, New York.
Mulazzi, E., 1970, Phys. Rev. Lett. **25**, 228.
Müller, M., W. Eckstein, W. Heiland and W. Zinn, 1972, Phys. Rev. Lett. **29**, 1651.
Nagaev, E.L. and A.P. Grigin, 1972, Phys. Lett. **38A**, 469.
Nikolaev, V.I., A.A. Samokhvalov and G.N. Sever, 1975, Sov. Phys. Semicond. **9**, 251.
Nolting, W., 1977, Phys. Stat. Sol. (b), **79**, 573.
Oliver, M.R., J.A. Kafalas, J.O. Dimmock and T.B. Reed, 1970a, Phys. Rev. Lett. **24**, 1064.
Oliver, M.R., J.O. Dimmock and T.B. Reed, 1970b, IBM, J. Res. Develop. **14**, 276.
Passell, L., O.W. Dietrich and J. Als-Nielsen, 1971, AIP Conf. Proc. **5**, 1251.
Pauling, L., 1960, The Nature of the Chemical Bond, Ithaca, Cornell University Press.
Penney, T., M.W. Shafer and J.B. Torrance, 1972, Phys. Rev. **B5**, 3669.
Petrich, G., S. von Molnar and T. Penney, 1971, Phys. Rev. Lett. **26**, 885.
Pickart, S.J. and H.A. Alperin, 1965, Bull. Amer. Phys. Soc. **1032**,
Pickart, S.J. and H.A. Alperin, 1968, J. Phys. Chem. Solids **29**, 414.
Pidgeon, C.R., J. Feinleib, W.J. Scouler, J.O. Dimmock and T.B. Reed, 1970, IBM J. Res. Develop. **14**, 309.
Ray, R.K., J.C. Tsang, M.S. Dresselhaus, R.L. Aggarwal and T.B. Reed, 1971, Phys. Lett. **37A**, 129.
Ruderman, M.A. and C. Kittel, 1954, Phys. Rev. **96**, 99.
Russell, H.N., W. Albertson and D.N. Davis, 1941, Phys. Rev. **60**, 641.

Rys, F., J.S. Helman and W. Baltensperger, 1967, Phys. kondens. Materie **6**, 105.
Samokhvalov, A.A., T.I. Arbuzova, A.Ya. Afanas'ev, B.A. Gizhevsky, N.N. Loshkaryova, M.I. Simonova and N.I. Solin, 1974, Proc. Int. Conf. Magnetism and Magnetic Materials, Vol. V, p. 148.
Sattler, K. and H.C. Siegmann, 1975, Z. Physik **B20**, 289.
Schlegel, A. and P. Wachter, 1973, Solid State Commun. **13**, 1865.
Schlegel, A. and P. Wachter, 1976, J. Phys. C, **2**, 3363.
Schoenes, J., P. Wachter and F. Rys, 1974, Solid State Commun. **15**, 1891.
Schoenes, J. and P. Wachter, 1974, Phys. Rev. **B9**, 3097.
Schoenes, J. and P. Wachter, 1976, IEEE Trans. Mag. **12**, 81.
Schoenes, J., 1975, Z. Physik **B20**, 345.
Schwob, P. and O. Vogt, 1966, Phys. Lett. **22**, 374.
Schwob, P., 1969, Phys. kondens. Materie **10**, 186.
Searle, C.W. and S.T. Wang, 1969, Can. J. Phys. **47**, 2703.
Shafer, M.W. and T.R. McGuire, 1968, J. Appl. Phys. **39**, 588.
Shapira, Y. and T.B. Reed, 1972, AIP Conf. Proc. **5**, 837.
Shapira, Y., 1974, Proc. Int. Conf. on Magnetism and Magnetic Materials, Vol. VI, p. 5.
Shapira, Y., R.L. Kautz and T.B. Reed, 1974, Proc. 12. Int. Conf. Physics of Semiconductors, Stuttgart, Teubner, p. 894.
Siegmann, H.C., 1975, Physics Reports **17C**, 37.
Sokolova, G.K., A.A. Samokhvalov and K.P. Rodionov, 1971, Soviet Phys. Solid State **13**, 1042, Fiz, Tverdogo Tela **13**, 1244.
Sperlich, G. and K. Jansen, 1974, Solid State Commun. **15**, 1105.
Srivastava, V.C. and R. Stevenson, 1968, Can. J. Phys. **46**, 2703.
Stanley, H.E., 1971, Introduction to Phase transitions and Critical Phenomena, Oxford, Clarendon Press.
Street, R.A., T.M. Searle, I.G. Augustin and R.S. Sussmann, 1974, J. Phys. C. Solid State Physics **7**, 1582.
Streit, P., 1973, Phys. kondens. Materie **15**, 284.
Sugar, J. and N. Spector, 1974, J. Opt. Soc. Am. **64**, 1484.
Suits, J.C. and K. Lee, 1971, J. Appl. Phys. **42**, 3258.
Swendsen, R.H., 1972, Phys. Rev. **B5**, 116.
Teaney, D.T. and V.L. Moruzzi, 1970, Colloq. Int. du C.N.R.S. No. 180, Vol. 2, p. 131.
Tekippe, V.J., R.P. Silberstein, M.S. Dresselhaus and R.L. Aggarwal, 1974, Proc. 12. Int. Conf. Physics of Semiconductors, p. 904, Stuttgart, Teubner.
Thompson, W.A., F. Holtzberg, T.R. McGuire and G. Petrich, 1972, AIP Conf. Proc. **5**, 827.
Torrance, J.B., M.W. Shafer and T.R. McGuire, 1972, Phys. Rev. Lett. **29**, 1168.
Tsang, J.C., M.S. Dresselhaus, R.L. Aggarwal and T.B. Reed, 1974, Phys. Rev. **B9**, 984.
Tsubokawa, I., 1960, J. Phys. Soc. Japan **15**, 1664.
Tu, K.N., K.Y. Ahn and J.C. Suits, 1972, IEEE Trans. Mag. **8**, 651.
von der Hoeven, Jr., B.J.C., D.T. Teaney and V.L. Moruzzi, 1968, Phys. Rev. Lett. **20**, 719.
Van Houten, S., 1960, J. Phys. Chem. Solids **17**, 7.
Van Houten, S., 1962, Phys. Rev. Lett. **2**, 215.
Vitins, J. and P. Wachter, 1973, Solid State Commun. **13**, 1273.
Vitins, J. and P. Wachter, 1975a, Phys. Rev. **B12**, 3829.
Vitins, J. and P. Wachter, 1975b, Solid State Commun. **17**, 911.
Vitins, J. and P. Wachter, 1976a, J. Magnetism and Magnetic Materials **3**, 161.
Vitins, J. and P. Wachter, 1976b, AIP Conf. Proc. **29**, 662.
Vitins, J., 1977, J. Magn. Magn. Mater **5**, 212.
von Molnar, S. and T. Kasuya, 1968, Phys. Rev. Lett. **21**, 1757.
von Molnar, S. and T. Kasuya, 1970, Proc. Int. Conf. Physics of Semiconductors, Cambridge, Mass., p. 233.
von Molnar, S., 1970, IBM J. Res. Develop **14**, 269.
von Molnar, S. and M.W. Shafer, 1970, J. Appl. Phys. **41**, 1093.
Vonsovksii, S.V. and Y.A. Izyumov, 1962, Usp. Fiz. Nauk **77**, 377.
Wachter, P., 1964, Helv. Phys. Acta **37**, 637.
Wachter, P., 1968a, Phys. kondens. Materie **7**, 1.
Wachter, P., 1968b, Phys. kondens. Materie **8**, 80.
Wachter, P., 1969a, Habilitationsschrift, Library ETH Zürich.
Wachter, P., 1969b, Solid State Commun. **7**, 693.
Wachter, P., 1970, Solid State Commun. **8**, 473.
Wachter, P., 1971a, Z. angew. Phys. **32**, 171.
Wachter, P., 1971b, unpublished data.
Wachter, P., 1972, CRC Critical Reviews in Solid State Sciences **3**, 189.
Wachter, P., 1973, in Amorphous Magnetism, p. 133, edited by H.O. Hooper and A.M. de Graaf, Plenum Press, New York.
White, H.W. and D.C. McCollum, 1972, J. Appl. Phys. **43**, 1225.
Wielinga, R.F., 1971, quoted in L.J. de Jongh and A.R. Miedema, 1974, Adv. in Phys. **23**, 1.
Will, G., S.J. Pickart, H.A. Alperin and R. Nathans, 1963, J. Phys. Chem. Solids **24**, 1679.
Yanase, A. and T. Kasuya, 1968, J. Phys. Soc. Japan **25**, 1025.
Yosida, K., 1957, Phys. Rev. **106**, 893.
Yost, W., 1933, J. Chem. Phys. **1**, 466.
Zener, C., 1951, Phys. Rev. **82**, 403.
Zinn, W., J. Magn. and Magn. Mater. 1976, **3**, 23.

Handbook on the Physics and Chemistry of Rare Earths, edited by K.A. Gschneidner, Jr. and L. Eyring

Chapter 20

VALENCE CHANGES IN COMPOUNDS

A. JAYARAMAN
Bell Laboratories, Murray Hill, New Jersey 07974, USA

Contents

Symbols

B = bulk modulus
e = electronic charge
e_i = strain
E = energy
E_F = Fermi energy
F = free energy
G = Falicov–Kimball screening parameter
J = total angular momentum
k_B = Boltzmann's constant
m^* = effective mass
n, N = electronic density
T_f, T_{sf} = fluctuation temperature
Δ_w = band width
ΔE_g = 4f–5d band gap
ϵ = fractional time
η = deformation potential
χ = magnetic susceptibility
μ_n = magnetic moment
ω_p = plasma frequency
τ = fluctuation time

1. Introduction

In rare earth systems involving Ce, Sm, Eu, Tm and Yb, the $4f^n5d^x6s^2$ (where $x = 0$, or 1) and the $4f^{n-1}5d^{x+1}6s^2$ configurations are energetically found to be near each other and can be inverted by externally applied or internally generated constraints. Such inversion involves a change in the valence state of the rare

earth ion. The external constraint referred to above is usually pressure or temperature and the internal one is through substitution of a trivalent rare earth ion, or a transition metal ion of higher valency, into the host lattice.

A valence change under pressure was first observed in Ce metal by Bridgman (1927), in his pioneering studies on the effect of pressure on solids. In subsequent studies Ce was found to undergo this so-called γ to α-Ce transition near 100 K at atmospheric pressure and also under the influence of alloying with a quadrivalent metal, such as thorium. The γ to α-Ce transition has proved to be the archetype for the valence changes in rare earth systems. The case of Ce is the subject matter of ch. 4 of volume 1. Also Eu and Yb are discussed in ch. 9.

Among the compounds, SmB_6 has earned a certain notoriety as a system exhibiting a change in the valence state; the Sm ions are largely in the higher valence state at room temperature but change towards the lower state upon lowering the temperature. However, a clear cut valence transition has been found only in SmS, in recent pressure and temperature studies. The first-order character of the transition and the possibility of inducing the same transition by substituting a trivalent rare earth ion has made SmS the focus of attention in much of the recent studies. Many other divalent monochalcogenides have also been studied under pressure and the occurrence of pressure-induced valence changes have been established in them. The important characteristics of the valence transitions in divalent monochalcogenides are: (1) it is an isostructural transition with a striking increase in density, and (2) it is a semiconductor to metal transition, accompanied by a large decrease in resistivity and a dramatic change in the reflectivity. Another very interesting aspect of the valence change in SmS and $Sm_{1-x}R_x^{3+}S$ is the nonintegral valence state. In this state the valence

TABLE 20.1
Rare earth systems in fluctuating valence state

Ambient pressure	High pressure
Ce(α) at $T < 110$ K	
$CePd_3$, $CeSn_3$, $CeAl_3$	Ce(α)
CeN	CeP
CeM_2, (M = Fe, Co, Ru, Rh, Ir)	
Ce–Th	
SmB_6; Sm_4Bi_3	SmS, SmSe, SmTe
$Sm_{1-x}R_x^{3+}S$, $Sm_{1-x}Th_x^{4+}S$	
$SmS_{1-x}As_x$	
$EuCu_2Si_2$, $EuRh_2$, $EuIr_2$	EuO
$Eu_xLa_{1-x}Rh_2$	
TmSe	TmTe
YbB_4, YbB_6, YbC_2	YbS, YbSe, YbTe
$YbAl_3$, $YbAl_2$	
YbCu, YbAg, YbAu	
YbZn, $YbCu_2Si_2$	

is neither 2^+ nor 3^+ but has intermediate values, and the electron is believed to fluctuate very rapidly with time between the $4f^n5d^x6s^2$ and the $4f^{n-1}5d^{x+1}6s^2$ electronic configurations. Hence this state has acquired a special name, the so called Interconfiguration Fluctuation (ICF) state (Hirst, 1975). A number of rare earth alloys and compounds involving Ce, Sm, Eu, Yb and the disilicides, viz., EuM_2Si_2 where M is Fe, Cu or Ag, seem to undergo valence changes with temperature at ambient pressure and exhibit a fluctuating valence state (see table 20.1). Lattice parameter, magnetic susceptibility, X-ray, and ultra violet photoelectron spectroscopic, Mössbauer and other studies have been made on these systems, as well as on the monochalcogenides. More recently the Ce monopnictides have also been shown to be vulnerable to valence changes under pressure. This chapter deals with valence changes in rare earth compounds under the influence of pressure, substitution and temperature and also discusses some of the theoretical ideas that are currently in vogue.

The experimental and theoretical aspects of the valence changes mainly in rare earth monochalcogenides have been reviewed by Jayaraman et al. (1975b), Varma (1976), by Campagna et al. (1976) and by Suryanarayanan (1978) (see also Parks, 1977). In discussing valence changes in rare earth compounds much material has been drawn from the first two reviews.

2. The rare earth monochalcogenides

2.1. *Material preparation*

Details on material preparation have appeared in many papers (Bucher et al., 1975) and only the briefest mention will be made here. Rare earth monochalcogenides have been prepared by reacting appropriate quantities of the chalcogen and the rare earth metal in the form of chips in a sealed evacuated quartz tube at about 600°C for 18–24 hours, followed by further reaction near 900°C for 3–4 hours and repeatedly melting the thoroughly homogenized material in a sealed tantalum tube. Usually, sufficiently large single crystals (0.5 cm in dimensions) appear to result even when the melt is allowed to cool rapidly. Single crystals of centimeter dimensions have also been grown, using a specially shaped sealed tungsten tubular crucible, from melts or by sublimation in the presence of a temperature gradient (Batlogg et al., 1976).

The samples were characterized through lattice parameter, optical absorption, magnetic susceptibility and resistivity measurements. In table 20.2 some relevant data are given. Figure 20.1 shows a plot of the lattice parameter of the rare earth monochalcogenides, wherein the divalent cases are evident. If a transition to the trivalent state were to occur, the lattice parameter should be consistent with that of the other trivalent members shown in the fig. 20.1.

2.2. *Band structure in the lower valence state*

The divalent rare earth monochalcogenides are semiconductors. The general features of the electronic band structure have been deduced from optical

TABLE 20.2
Some properties of divalent rare earth monochalcogenides from Jayaraman et al., 1975 and Bucher et al., 1971.

Compound	Lattice constant a in Å (NaCl type)	Magnetic property χ (Van Vleck)	Resistivity at R.T. (Ω cm)
SmS	5.97	Paramagnetic $\chi(T=0) = 9.47 \times 10^{-3}$	10^{-1}–10^{-3}
SmSe	6.202	Paramagnetic $\chi(T=0) = 7.92 \times 10^{-3}$	10^{3}–10^{4}
SmTe	6.601	Paramagnetic $\chi(T=0) = 7.15 \times 10^{-3}$	$>10^{7}$
EuO	5.14	Ferromag. $T_C = 68$ K	High resistivity
EuS	5.97	Ferromag. $T_C = 16.5$ K	High resistivity
EuSe	6.19	Antiferro. $T_N = 4.6$ K Ferro $T_C = 2.8$ K	High resistivity
EuTe	6.60	Antiferro. $T_N \sim 8$ K	High resistivity
TmTe	6.34	Antiferro. $T_N = 0.21$ K	1–10^{-1}
TmSe	5.35	Complex	10^{-3}–10^{-4}
YbS	5.68	Diamagnetic	High resistivity
YbSe	5.93	Diamagnetic	High resistivity
YbTe	6.36	Diamagnetic	High resistivity
GdS	5.56	Antiferromagnetic	Metallic $\sim 10^{-4}$
YS	5.49	Paramagnetic (Pauli)	Metallic $\sim 10^{-4}$

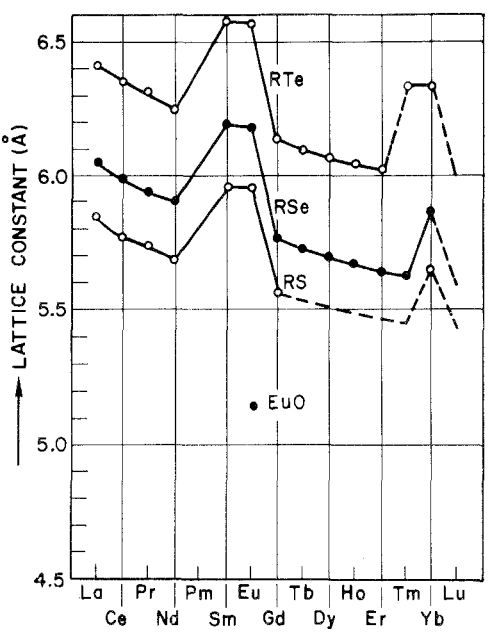

Fig. 20.1. Lattice parameter of rare earth monochalcogenides.

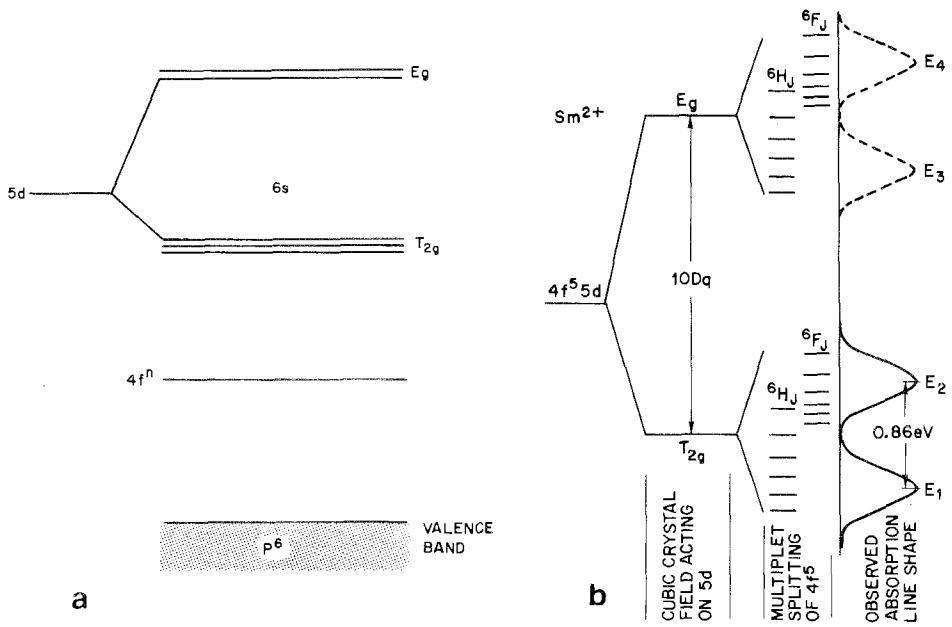

Fig. 20.2. Schematic energy band diagram for rare earth monochalcogenides (Methfessel et al., 1966). On the left the atomic 5d states associated with the rare earth ion is shown. In the crystal these broaden to form the conduction band, the lowest having the T_{2g} symmetry. On the right the multiplet splitting of the $4f^5$ states and its mixing with the crystal field split 5d states are shown. On the extreme right the absorption line shapes that result from 4f to 5d transitions are shown (from Holtzberg and Torrance, 1972).

absorption data and band-structure calculations (Methfessel and Mattis, 1968; Guntherodt et al., 1971; Suryanarayanan et al., 1972; Dimmock, 1970; Chao, 1970; Davis, 1971; Holtzberg and Torrance, 1972; Batlogg et al., 1976) and are shown in fig. 20.2a. The valence band is derived from the anionic P-states and the conduction band is from the 6s–5d of the rare earth ion. The 5d band is split by the crystal field into a T_{2g} and an E_g branch (these are really broad bands in the crystal). The $4f^n$ level lies in the gap, dominating the electrical and optical properties of the material. The features of the band structure for Eu and Sm monochalcogenides (Batlogg et al., 1976) are more or less similar but in the case of Sm monochalcogenides the Coulomb interactions between the excited states of the $4f^5$ electrons give rise to two sets of multiplets, ^6H_J and ^6F_J, which mix with the T_{2g} and E_g branches of the d-states to give four peaks in the density of states at the d-band (see fig. 20.2b). The T_{2g} symmetry bands constitute the lower part of the conduction band. From the point of view of the valence change and the semiconductor to the metal transition, the energy gap between the bottom of the conduction band and the $4f^6$ state is the important parameter.

2.3. *Pressure-induced valence changes*

2.3.1. *Electrical resistivity*

Figure 20.3 shows the pressure dependence of the electrical resistivity of SmTe, SmSe and SmS (Jayaraman et al., 1970a,b; Jayaraman, 1974). The logarithmic decrease in resistivity with pressure is attributed to a decrease in the energy gap between the localized 4f level and the 5d conduction band edge with pressure and consequent exponential increase in the number of electrons excited into the conduction band from the 4f level. Each 4f electron excited into the conduction band should result in the conversion of a Sm^{2+} ion to the Sm^{3+} state, according to the simple semiconductor model. In SmS the resistivity decreases exponentially up to 6.5 kbar and shows an abrupt decrease by about a factor of 10 at that pressure. With further increase in pressure there is a gradual decrease. In SmS after the above first-order transition, and in SmTe and SmSe at pressures above 60 kbar, the resistivities are found to be about $10^{-4}\Omega$cm and the temperature dependence of the resistivity is characteristic of that of a metal. From the pressure dependence of the resistivity it is found that the valence change takes place continuously with pressure in SmSe and SmTe, and through a first-order transition in the case of SmS.

From the resistivity vs pressure data, the pressure dependence of the gap ($d\Delta E_g/dP$), has been obtained by applying simple carrier statistics equations for the electron excitation into the conduction band [$\rho = 1/ne\mu$, $n = n_d \exp\{-\Delta E_g(P)/kT\}$], and the energy gap at atmospheric pressure from the saturation resistivity [$\rho_S = \rho_0 \exp(-\Delta E_g/kT)$], under the assumption that the Fermi level E_F is pinned at the donor level (4f level). The $d\Delta E_g/dP$ values and

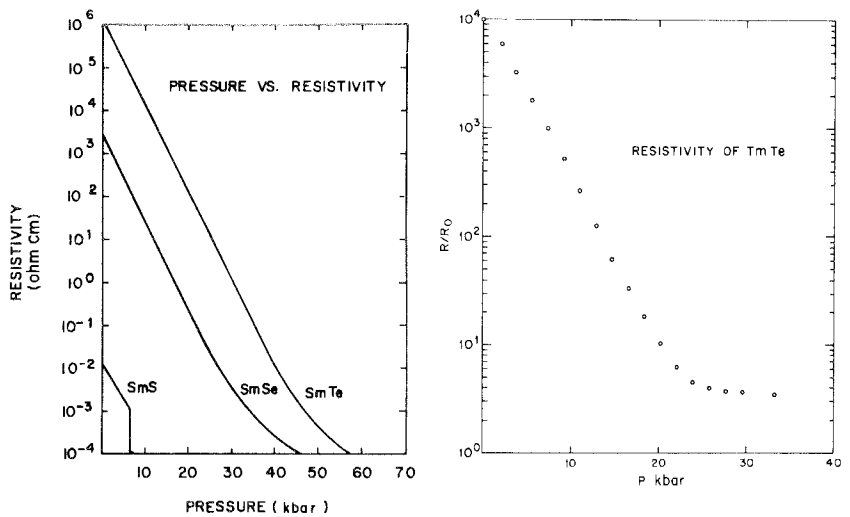

Fig. 20.3. Pressure dependence of resistivity of Sm monochalcogenides (left) from Jayaraman (1974) and of TmTe (right) from Jayaraman et al., 1970c.

the ΔE_g ($4f^6$ to 5d) thus obtained are found to be in good agreement with the values obtained from the optical absorption measurements. With intrinsic materials the resistivity change with pressure has provided strong evidence for the valence change in the Sm monochalcogenides.

In the case of EuO Oliver et al. (1970) have measured the pressure dependence of resistivity up to 10 kbars and find that the $d(\Delta E_g)/dP$ obtained from high resistivity samples agrees well with the pressure coefficient measured from the shift in the optical absorption edge. Francillon et al. (1970) have carried out some resistivity measurements under pressure on YbTe, but the samples used appear to be dominated by extrinsic conduction. In the case of TmTe (Jayaraman et al., 1970c) the resistivity has been shown to decrease by a factor of 10^3 in the 1 to 35 kbar range and saturate thereafter (see fig. 20.3). This pressure variation in resistivity has been attributed to a valence change of the Tm ion from the divalent to the trivalent state. Some resistivity measurements have been made on TmSe as a function of temperature (Bucher et al., 1974) as well as pressure, but the changes are found to be small. From the color and the lattice parameter TmSe appears to be close to being metallic and hence large variations in resistivity are not expected either with pressure or temperature (Bucher et al., 1975).

2.3.2. *Compressibility*

The pressure–volume relationship has been studied in all the Sm, Eu and Yb chalcogenides (Jayaraman et al., 1974, 1975 see also Rooymans, 1966), and TmTe (Jayaraman et al., 1970c; Chatterjee et al., 1972). The data for the Sm chalcogenides are shown in fig. 20.4. For SmTe and SmSe the curves show anomalous regions of compression and for SmS there is a discontinuous volume decrease at about the same pressure, where a sharp drop in resistivity occurs. The crystal structure remains NaCl-type through these anomalies. The abnormal volume changes without any structure change strongly support the occurrence of a valence change of Sm^{2+} towards the 3^+ state. The $P-V$ relationships provide crucial evidence for the valence change in the divalent rare earth monochalcogenides and have shown that the resistivity results are connected with bulk effects and not due to extrinsic impurities. The discontinuity in volume for SmTe near 100 kbar is due to NaCl-to-CsCl structural transition. Among the Eu chalcogenides, EuO is the only case which seems to exhibit a discontinuous volume decrease at about 300 kbars without undergoing any change in the structure (Jayaraman, 1972). This is believed to be an electronic transition involving a change in the valence state of Eu towards the trivalent state. This conclusion is also supported by the vanishing of the energy gap between the 4f level and the conduction band edge at 300 kbars, calculated from the experimentally measured deformation potential of EuO (−4.84 eV) and the relative volume V/V_0 of 0.7 for EuO at that pressure. The volume discontinuity near 400 kbar is due to a phase change of the collapsed NaCl phase to the CsCl-type structure.

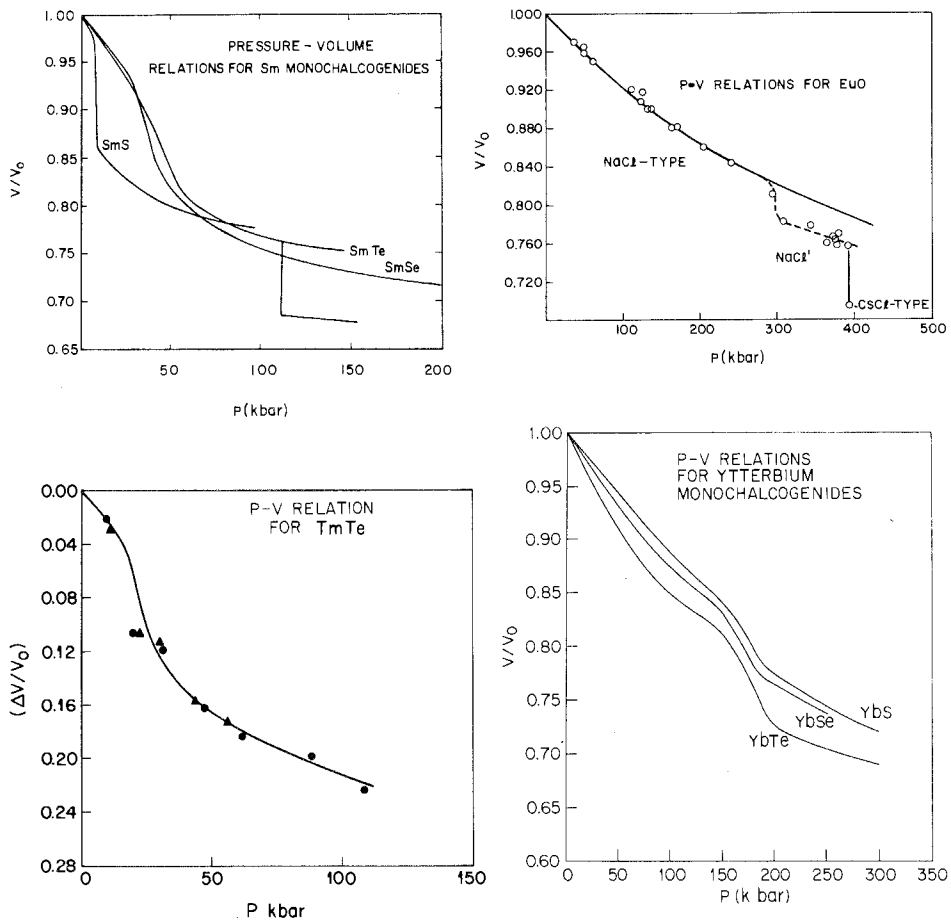

Fig. 20.4. Pressure–volume relationship for rare earth monochalcogenides. The anomalous relationships are due to valence changes of the rare earth ion towards the trivalent state. The discontinuity in SmTe and EuO near 400 k bar are due to NaCl–CsCl transition (from Jayaraman et al., 1974).

Pressure-volume data for the Yb monochalcogenides and TmTe also show anomalous compression regions which have been attributed to a change in the valence state (see fig. 20.4) presumed to take place continuously with pressure (Jayaraman et al., 1975a).

2.3.3. *Optical reflectivity*

The valence change in the rare earth monochalcogenides shows itself in a rather spectacular manner in the optical reflectivity. Samarium sulfide which appears black in the semiconducting state turns brilliant gold in color after the 6.5 kbar transition (Kirk et al., 1972), SmSe a bright copper-like color on

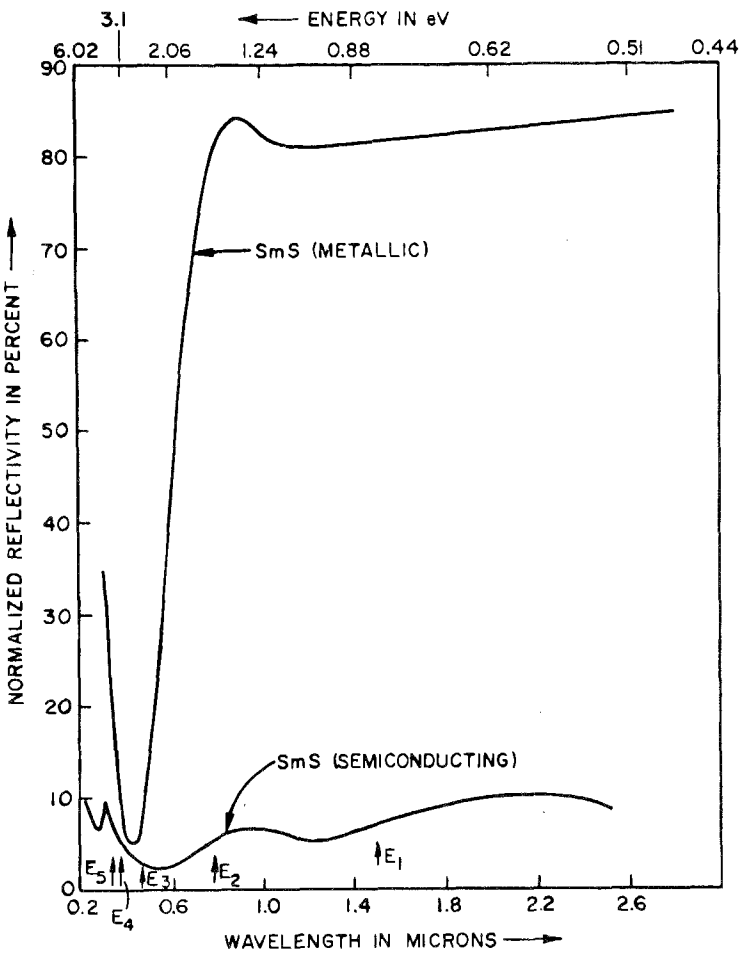

Fig. 20.5. Reflectivity of semiconducting and high pressure metallic phases of SmS normalized to that of Al (from Kirk et al., 1972).

reaching the metallic state and SmTe a deep purple color in the metallic region. (Zhuze et al., (1964) had earlier found that semiconducting SmS when polished acquires a golden color at the surface.) These characteristics in the optical reflectivity seem to be ubiquitous in the metallic rare earth monochalcogenides. Quantitative reflectivity data (Kirk et al., 1972; Batlogg et al., 1974, 1976) have been obtained on the metallic as well as the semiconducting phases of SmS and the curves are shown in fig. 20.5. In the metallic state of SmS the reflectivity increases by an order of magnitude and is found to be comparable to that of Al, in the spectral region above 0.5 micron. The golden yellow color is due to the sharp rise in reflectivity in the 0.5 micron region. The minimum in the reflectivity near 0.4 micron has been attributed to the combined effect of the Drude

TABLE 20.3
Some pressure data of interest (from Jayaraman et al., 1974)

Sub-stance	Energy separation 4f-cond. band edge (eV)	$\frac{d(\Delta E_g)}{dP}$ meV/kbar	Deformation potential Σ (eV)	V/V_0 for $\Delta E_g \rightarrow 0$	Phase transition	ΔV of transition at NaCl–CsCl
EuTe	~2.0[c]	−12.0[a]	−4.8	0.58	NaCl–CsCl ~110 kbar	−11.6%
EuSe	~1.7 1.85[c]	−8.4[a]	−4.37	0.59	NaCl–CsCl ~145 kbar	−12.8%
EuS	~1.64[c]	−7.9[a]	−4.82	0.66	NaCl–CsCl ~215 kbar	−12.5%
EuO	~1.12[c]	−4.4[a]	−4.84	0.77	Electronic Collapse ~300 kbar NaCl–CsCl ~400 kbar	−6.5%
YbTe	~1.80[b]	−11 ± 1[b]	−5.06	0.65	Electronic Collapse 150–200 kbar	—
YbSe	~1.50[b]	−10 ± 1[b]	−6.1	0.75	Electronic Collapse 150–200 kbar	—
YbS	~1.0[b]	−6 ± 1[b]	−4.32	0.77	Electronic Collapse 150–200 kbar	—
SmTe	.70[d]	−11.9[d]	−4.7	0.85	Electronic Collapse Contin. 1–60 kbar NaCl–CsCl (110 kb)	−9.1%
SmSe	.50[d]	−11.0[d]	−5.7	0.92	Electronic Collapse Contin. 1–50 kbar	
SmS	0.065[e](?) ~0.2[g]	−10.0[f]	−4.7	0.98–0.99	Electronic collapse Discont. 6.5 kbar	
TmTe	0.20	−10.0	−4.5	0.95	Electronic Collapse Contin. 1–40 kbar	

[a]Wachter (1969); [b]Narayanamurti et al. (1974); [c]Dimmock (1970); [d]Jayaraman et al. (1970c); [e]Kaldis and Wachter (1972); [f]Jayaraman et al. (1974); [g]Batlogg et al. (1976).

contribution and interband contribution to the dielectric constant. It is believed that the valence band to the conduction band separation is about 2.5 eV in the metallic phase of SmS and this contributes to the dielectric constant, making the substance appear like gold. An analogous situation must be responsible for the characteristic colors of the metallic phases of SmSe and SmTe, and indeed for all the metallic R^{3+} chalcogenides.

Observations under the diamond anvil high pressure apparatus strongly suggests that EuO is metallic above 300 kbar and the high pressure phase has a "silvery" luster (Jayaraman, 1972). The reflectivities of EuTe, EuSe and EuS even up to pressures of 350 kbar do not seem to show any color change which leads to the conclusion that there is no appreciable valence change in them up to 350 kbar.

Similar qualitative observations with diamond anvil apparatus have shown that Yb monochalcogenides undergo the electronic transition near about 200 kbar pressure (Jayaraman et al., 1974). At high pressures YbS acquires a golden yellow color, YbSe a copperish luster and YbTe a purple color, reminiscent of the changes observed in SmS, SmSe and SmTe at high pressure. In table 20.3 data obtained from pressure experiments are presented.

2.4. *Valence change due to cationic substitution*

The rare earth monochalcogenides form solid solutions among themselves over the entire range of composition and have the NaCl-type structure. When a R^{3+} ion replaces the Sm^{2+} ion in SmS, the lattice parameter decreases smoothly first and at a certain critical concentration abruptly contracts to a value close to 5.68 Å, without involving any change in structure (Jayaraman et al., 1973; Holtzberg, 1974; Tao and Holtzberg, 1975; Jayaraman et al., 1975a). The material also changes color abruptly at this point, from black to metallic golden-yellow. In table 20.4 the room temperature lattice parameters for the $Sm_{1-x}Gd_xS$

TABLE 20.4
Lattice constants and color of $Sm_{1-x}R^{3+}_xS$ compounds (NaCl-type structure)(Jayaraman et al., 1975).

Compound	Lattice parameter (Å)	Color	Compound	Lattice parameter (Å)	Color
SmS	5.97	Black	$Sm_{0.75}Ce_{0.25}S$	5.72	golden-yellow
$Sm_{0.95}Gd_{0.05}S$	5.95	Black	$Sm_{0.75}Pr_{0.25}S$	5.71	golden-yellow
$Sm_{0.9}Gd_{0.1}S$	5.925	Black	$Sm_{0.75}Nd_{0.25}S$	5.70	golden-yellow
$Sm_{0.87}Gd_{0.13}S$	5.89	Black	$Sm_{0.75}Dy_{0.25}S$	5.65	golden-yellow
$Sm_{0.85}Gd_{0.15}S$	5.87	Black	$Sm_{0.77}Ho_{0.23}S$	5.67	golden-yellow
$Sm_{0.84}Gd_{0.16}S$	5.68	golden-yellow	$Sm_{0.77}Er_{0.23}S$	5.67	golden-yellow
$Sm_{0.82}Gd_{0.18}S$	5.67	golden-yeltow	$Sm_{0.75}Tm_{0.25}S$	5.66	golden-yellow
$Sm_{0.80}Gd_{0.20}S$	5.66	golden-yellow	$Sm_{0.75}Yb_{0.25}S$	5.89	Black
$Sm_{0.75}Gd_{0.25}S$	5.67	golden-yellow	$Sm_{0.70}Lu_{0.30}S$	5.68	golden-yellow
$Sm_{0.70}Gd_{0.30}S$	5.67	golden-yellow	$Sm_{0.75}Y_{0.25}S$	5.72	golden-yellow
$Sm_{0.5}Gd_{0.5}S$	5.63	golden-yellow	$Sm_{0.70}Y_{0.30}S$	5.68	golden-yellow

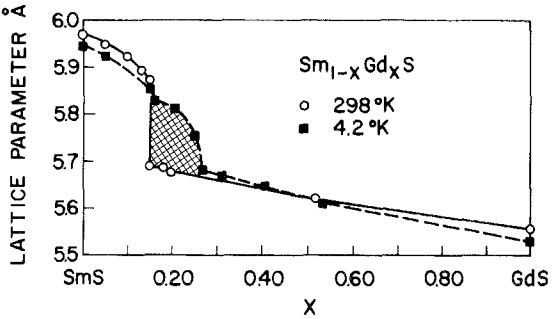

Fig. 20.6. Lattice parameter as a function of Gd concentration x for the system $Sm_{1-x}Gd_xS$. The crossed line region represents the composition over which a first-order transition occurs on cooling the metallic samples (Jayaraman et al., 1975a).

compounds and the observed color of the material are given. In fig. 20.6 plots of the lattice parameter variation with composition for the $Sm_{1-x}Gd_xS$ system at room temperature and at 4.2 K are shown. At room temperature (298 K) the lattice parameter undergoes a discontinuous change near 15 atomic percent Gd. The compound $Sm_{0.85}Gd_{0.15}S$ is black and has a lattice parameter of 5.875 Å. At about 16 atomic percent Gd the sample is metallic golden-yellow in color and the lattice parameter is 5.68 Å. The critical concentration for the lattice collapse in the $Sm_{1-x}Gd_xS$ system at room temperature is between 15 and 16 at.% Gd. At concentrations higher than 16 atomic percent Gd, the a parameter continues to decrease smoothly with increasing Gd content and reaches the value characteristic for pure GdS of 5.56 Å.

An abrupt change in the lattice parameter as well as color (black to metallic gold) at a critical R^{3+} concentration, followed by a smooth decrease in the lattice parameter to the value characteristic of the particular R^{3+} compound is the general pattern of behavior for all the $Sm_{1-x}R^{3+}_xS$ compounds (Jayaraman et al., 1975a) and including Y (the $Sm_{1-x}Y^{3+}_xS$ system has been investigated in detail by Holtzberg, 1974 and Tao and Holtzberg, 1975). With La, however, there does not appear to be any abrupt change either in the lattice parameter or in the color (Holtzberg, 1974; Tao and Holtzberg, 1975; Jayaraman et al., 1975a). Holtzberg (1974) has also investigated $SmS_{1-x}As_x$ system and finds that the valence transition in SmS can be induced by anionic substitution with As.

The abrupt change in the lattice parameter and color that results upon R^{3+} substitution is due to a change in the valence state of the Sm ion. Since R^{3+} ions are substantially smaller than the Sm^{2+}, R^{3+} substitution in the SmS lattice is equivalent to applying pressure. This equivalence has been demonstrated by pressure experiments on $Sm_{1-x}Gd_xS$ compounds (Jayaraman et al., 1975a).

2.4.1. *Metastability in substituted systems*

As noted earlier the valence transition shows a large pressure hysteresis (Jayaraman et al., 1975a). In the case of pure SmS the transition on increasing

pressure occurs at about 6.5 kbar at room temperature, while the reverse transition does not take place until the pressure is down to 1.5–2 kbar. This pressure hysteresis seems to be unaffected over a wide temperature range (130 K to 450 K investigated). Samples containing up to 10 atomic percent Gd reverts when pressure is released, while samples with 13, 14, and 15 atomic percent Gd stay golden-yellow down to atmospheric pressure. The metastable retention of the high pressure phase of the 13, 14, and 15 atomic percent Gd doped SmS samples is because their transition pressures are less than 4 kbar.

2.5. *Valence change due to temperature*

The metallic golden-yellow $Sm_{1-x}R_x^{3+}S$ crystals (R = Ce, Pr, Nd, Gd, Tb, Dy, Ho and Y) near the critical concentration undergo an explosive first-order transition on rapid cooling (immersion in liquid nitrogen) and disintegrate to black powder (Jayaraman et al., 1973; Holtzberg, 1973; Tao and Holtzberg, 1975; Jayaraman et al., 1975a). On warming, the black powder turns golden-yellow in color and this transformation to the metallic state exhibits a marked thermal

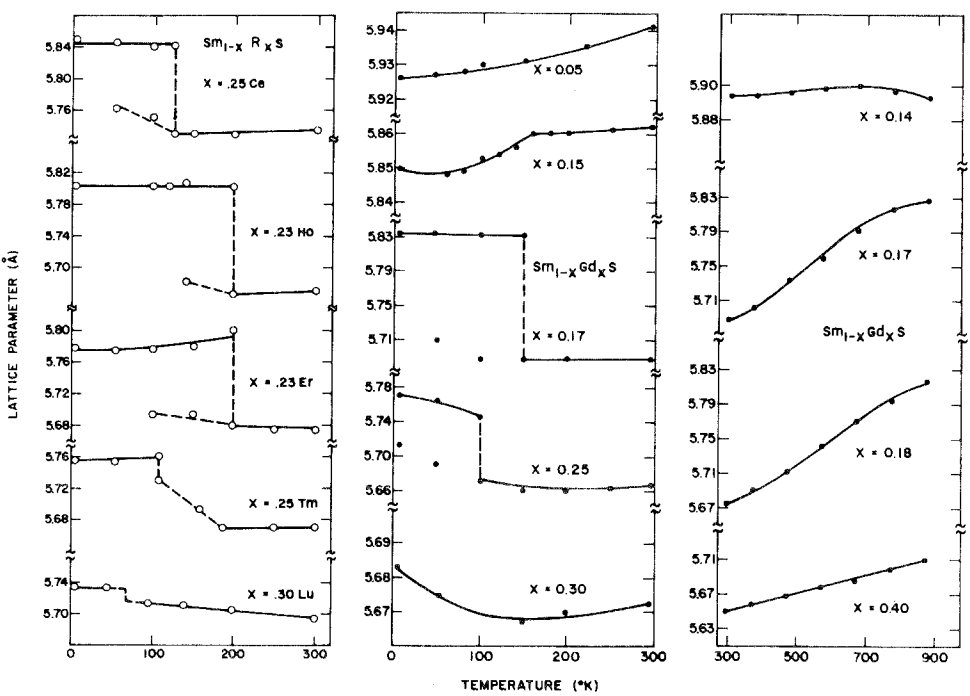

Fig. 20.7. Lattice parameter vs temperature for SmS alloys substituted with different trivalent rare earth ions (left) and for $Sm_{1-x}Gd_xS$ alloys (middle and right). The abrupt changes in the lattice parameter are due to first-order but isostructural phase transition. To be noted is the anomalous thermal expansion (right figure) of $Sm_{1-x}Gd_xS$ alloys (from Jayaraman et al., 1975a).

hysteresis. With Er and Tm substitution (Jayaraman et al., 1975a), the crystals show visible cracks and turn black, but the samples do not appear to disintegrate. Low-temperature X-ray diffraction patterns have shown that the structure remains unchanged as NaCl in the first-order transition in all the compounds, but the lattice parameter undergoes a discontinuous increase in the black phase (fig. 20.7). In fig. 20.7 the lattice parameter variation with temperature for a number of $Sm_{1-x}Gd_xS$ compounds (Jayaraman et al., 1975a) are shown for the range 300 K to 4.2 K. Compounds with nominal concentration in the range $0.15 < x < 0.27$ exhibit the explosive transition mentioned, when cooled to low temperatures. Above ~27 atomic percent Gd, only a smooth variation in the lattice parameter is observed down to 4.2 K (Jayaraman et al., 1975a). The shaded region in fig. 20.6 represents the composition over which the first-order transition is observed. Similar results have been reported for the $Sm_{1-x}Y_xS$ system (Holtzberg, 1974 and Tao and Holtzberg, 1975).

2.5.1. *Lattice parameter*

The lattice parameter is a direct indicator of what is happening at the microscopic level in these systems. It reflects the change in the size of the Sm ion, which in turn is directly related to its valence state. The lattice parameter that characterizes the divalent SmS ($Sm^{2+}S$) and fully trivalent SmS ($Sm^{3+}S$) are respectively 5.97 Å and 5.62 Å. Any lattice parameter intermediate in value suggests an intermediate or fractional valence state for the Sm ion. The lattice parameter data especially as a function of temperature has been very revealing. The abrupt jumps are due to a first-order valence transition.

In fig. 20.7 the lattice parameter variation with increasing temperature (300 K to 900 K) is shown for a few $Sm_{1-x}Gd_xS$ compounds. In the range $0.16 < x < 0.30$ the thermal expansion is unusually large compared to the expansion in samples

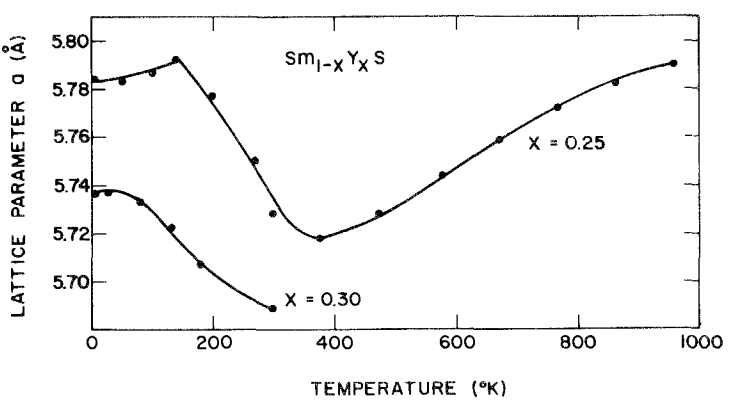

Fig. 20.8. Lattice parameter variation with temperature for two $Sm_{1-x}Y_xS$ samples. The anomalous expansion for $x = 0.25$ without a first-order transition is noteworthy (Jayaraman et al., 1975a).

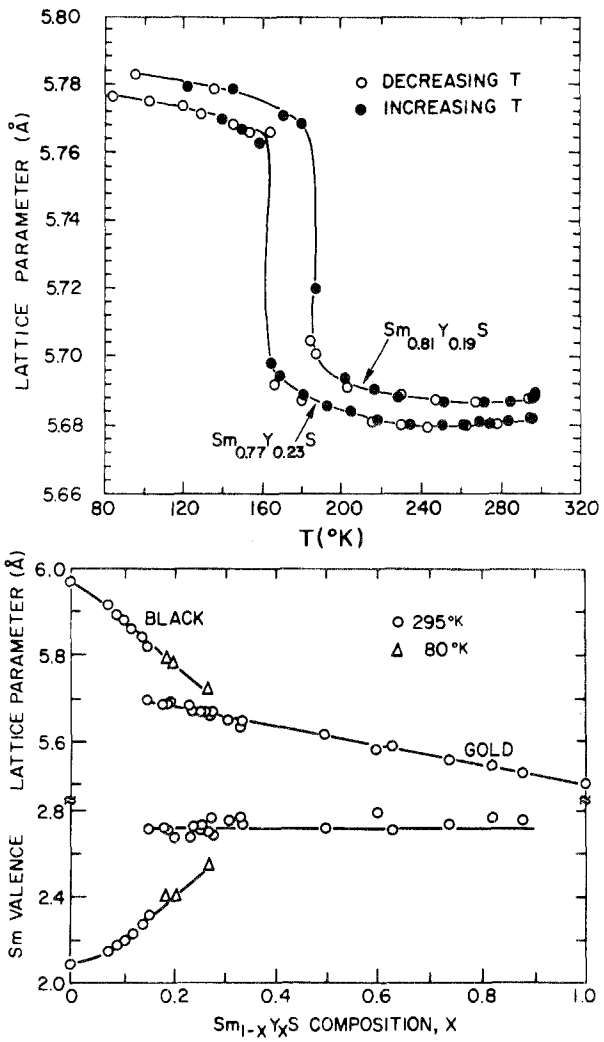

Fig. 20.9. Lattice parameter change with temperature (upper figure) and composition (lower figure) in the $Sm_{1-x}Y_xS$ compounds. The abrupt changes are due to first order isostructural phase transition. In the bottom of lower figure the valence calculated from the lattice parameter is shown (from Tao and Holzberg, 1975).

with $x = 0.40$, or at concentrations less than $x = 0.14$. The thermal expansion of GdS for instance is found to be $\alpha = 12 \times 10^{-6}\,K^{-1}$ (Goryachev and Kutsenok, 1972), whereas the expansion in $Sm_{0.83}Gd_{0.17}S$ is more than three times the above value. The golden phase does not show a first-order phase transition on heating and the X-ray diffraction peaks shift anomalously but continuously with increasing temperature. For the sample $x \sim 0.14$ (black) no evidence for a transition to

the metallic phase is observed in the entire range and the lattice parameter slightly decreases with increasing temperature. In fig. 20.8 the lattice parameter data as a function of temperature from about 1000 K down to 4.2 K are shown for $Sm_{0.75}Y_{0.25}S$ as well as $Sm_{0.70}Y_{0.30}S$. In the case of the former compound the lattice expands anomalously on decreasing and increasing temperature, with the minimum lattice parameter centered around 375 K. This continuous and anomalous expansion behavior suggests, that in the temperature traverse from 4.2 K to 900 K, no first-order transition boundary is intersected in the above compounds and the valence change takes place continuously. Holtzberg (1973) and Tao and Holtzberg (1975) have published lattice parameter measurements for the $Sm_{1-x}Y_xS$ compounds with comparable x, and the low-temperature lattice parameter data is found to be analogous to the curve in fig. 20.8. From the lattice parameter measurements the valence of Sm has been calculated (Holtzberg, 1973) for the $Sm_{1-x}Y_xS$ and this is shown in fig. 20.9. It is clear from the data that in these compounds the valence state of the Sm ion can change continuously or discontinuously with temperature. The existence of intermediate valence states is one of the most interesting aspects of these systems which will be discussed next.

3. The intermediate valence state

The high pressure lattice parameter data on Sm monochalcogenides and magnetic susceptibility measurements (Maple and Wohlleben, 1971) have suggested that the valence change in SmS does not proceed fully to the Sm^{3+} state in the first-order transition at 6.5 kbar; the lattice parameter of ~5.70 Å for the high pressure form of SmS and ~5.68 Å for the metallic $Sm_{1-x}Gd_xS$ and $Sm_{1-x}Y_xS$ alloys (very close to the critical concentration) are to be compared with 5.62 Å expected for $Sm^{3+}S$. In SmSe, SmTe and TmTe the transition proceeds continuously with pressure and hence the valence of Sm or Tm is changing continuously from the 2^+ to the 3^+ state. SmB_6 is also believed to be a material in an intermediate valence state (Nickerson et al., 1971). The nature of the intermediate valence state is one of the central questions in the study of valence changes. There are two ways in which such a state can be pictured: Taking the SmS based system as an example, (1) the Sm ions exist in the material as distinct Sm^{3+} and Sm^{2+} ions (small and large ions) intimately mixed and completely disordered on an atomic scale (spatial mixture). Varma (1976) (see also Wohlleben and Coles, 1973) maintains that the cost in strain energy to sustain a local small volume and distorted structure and the excessive kinetic energy of the conduction electron would rule out this possibility. (2) Every Sm ion in the crystal fluctuates in time between the $4f^65d^0(Sm^{2+})$ and $4f^55d^1(Sm^{3+})$ states on a rapid time scale, the relative time the electron spends in the two configurations determining the extent of the intermediate valence (temporal mixture). This is the fluctuating valence state. The fluctuations are so rapid that the lattice is not able to follow fully the electronic state and all the Sm ions

stabilize at some intermediate size, correlating with the observed intermediate lattice parameter. This dynamic situation has been referred to as Inter Configuration Fluctuation (ICF) state by Hirst (1970, 1974) and homogeneous mixed valence state by Varma (1976). The time scale of the fluctuation is believed to be of the order of $t \approx 10^{-12}$ seconds. The X-ray diffraction measurement cannot differentiate between the above two models and will show only a single characteristic set of diffraction lines appropriate to the NaCl-type structure. However, the magnetic susceptibility measurements and several other measurements have given some insight into the nature of the intermediate valence state and the dynamics of the electronic processes in transitions involving valence changes, not only in the rare earth monochalcogenides but in Ce and other rare earth alloys and compounds (Wohlleben and Coles, 1973; Maple and Wohlleben, 1974; Sales and Wohlleben, 1975; Bauminger et al., 1973; Debray et al., 1976; Andres et al., 1975).

3.1. *Valence change and magnetic susceptibility*

Since the rare earth ions have well-defined magnetic moments associated with the 4f state, the expectation is that any change in the 4f state occupation must involve a distinct change in the magnetic state of the system. Where the rare earth ion is in two integral valence states this expectation is fulfilled. However, in systems where an intermediate valence state prevails the susceptibility behavior is anomalous (see Wohlleben and Coles, 1973; Maple and Wohlleben, 1974). Among the systems showing valence changes, the pressure and temperature dependence of the magnetic susceptibility has been investigated in metallic Ce, in dilute La–Ce alloys and more recently in Sm and Tm monochalcogenides. Also, magnetic susceptibility measurements have been reported in SmB_6 (see Nickerson et al., 1971) and in a number of intermetallic rare earth compounds (Debray et al., 1976) which exhibit valence changes as a function of temperature at atmospheric pressure.

In La–Ce alloys Maple and Kim (1969) found a magnetic to nonmagnetic transition, when the valence state of Ce was changed from 3^+ to the 4^+ state by pressure, and further, this transition restored or enhanced the superconducting T_C of the alloy, depending on pressure or the concentration of Ce in La. In the dilute systems such as the La–Ce system the main interest has been to study the influence of magnetic and nonmagnetic impurities on the superconducting T_C of La, and through these experiments learn about local moment formation and stability. Among the more concentrated rare earth systems, Ce rich alloys and intermetallic compounds involving Ce have been of interest (Van Daal and Buschow, 1970). McPherson et al. (1971) found a discontinuous drop in the magnetic susceptibility in metallic Ce at the γ to α-Ce phase transition at 7 kbar. They also found that the susceptibility of α-Ce had an unusual temperature dependence, which is now attributed to the intermediate valence state of α-Ce. For a detailed discussion on Ce and Ce related systems ch. 4 of volume 1 should be consulted.

Among the rare earth monochalcogenides the Sm compounds have been investigated in detail. In the semiconducting state the Sm monochalcogenides exhibit ionic Van Vleck paramagnetism, with a nonmagnetic ground state (Bucher et al., 1971) consistent with Sm having six 4f electrons. The pressure dependence of the magnetic susceptibility of pure SmS was studied by Maple and Wohlleben (1971). The susceptibility increases slowly at first, drops abruptly in the valence transition at 6.5 kbar and then decreases slowly with pressure. On release of pressure a marked hysteretic behavior is noticed, as in resistivity. The magnetic susceptibility of semiconducting SmS at atmospheric pressure and the high pressure metallic phase of SmS is shown in fig. 20.10 as a function of temperature, taken from Maple and Wohlleben (1971). It exhibits a weak temperature dependence below ~200 K and saturates to a constant value below ~40 K, with no sign of magnetic ordering. The constant low-temperature susceptibility is in sharp contrast to what would be expected if the valence change had proceeded directly all the way to the trivalent state. In pure $4f^5$ configuration (Sm^{3+}) the ground state must be at least a doublet which should result in a low-temperature divergence of the susceptibility, or in magnetic ordering. In the bottom of fig. 20.10 the behavior of the high pressure metallic phase of SmS is compared with materials having typically the $4f^5$ configuration, and SmB_6. The susceptibility behavior of the latter compound is akin to that of the high pressure metallic phase of SmS. The susceptibility behavior for some of the substituted systems are shown in fig. 20.10 (taken from Tao and Holtzberg, 1975) and the similarity with the collapsed phase of SmS is evident. In both SmB_6 and the metallic phase of SmS the valence of the Sm ion is found to be close to 2.7 (from Lattice parameter) and the strange magnetic behavior, or rather the nonmagnetic behavior as Maple and Wohlleben call it, (Maple and Wohlleben, 1971, 1973) is believed to be a special property of the intermediate valence state (see later discussion).

The magnetic susceptibility as a function of pressure has been measured for TmTe (Wohlleben et al., 1972). The latter authors conclude from their data that there are two high pressure electronic phases for TmTe and the transition from one to the other show no hysteretic effects. They believe that in the two magnetically differentiable high pressure phases, the Tm ion is in different intermediate valence states between 2^+ and 3^+. The magnetization curves of the high pressure phases of TmTe according to Wohlleben et al. (1971) are nonlinear, especially at the low-temperature end. TmSe is regarded as a mixed valence material (Campagna et al., 1974a, 1976) although it exhibits interesting magnetic ordering at low-temperatures (Ott et al., 1975). However for Tm both the $f^{13}(Tm^{2+})$ and $f^{12}(Tm^{3+})$ configurations have nonzero magnetic ground state.

The conclusions from the magnetic susceptibility measurements under pressure on the Sm monochalcogenides, TmTe and Ce are, (1) that the valence changes are reflected in the susceptibility behavior, and (2) if the R.E. ion is stable in an intermediate valence state, the low-temperature part of the susceptibility data is anomalous, indicative of nonmagnetic state if for one of the configurations the ground state is nonmagnetic.

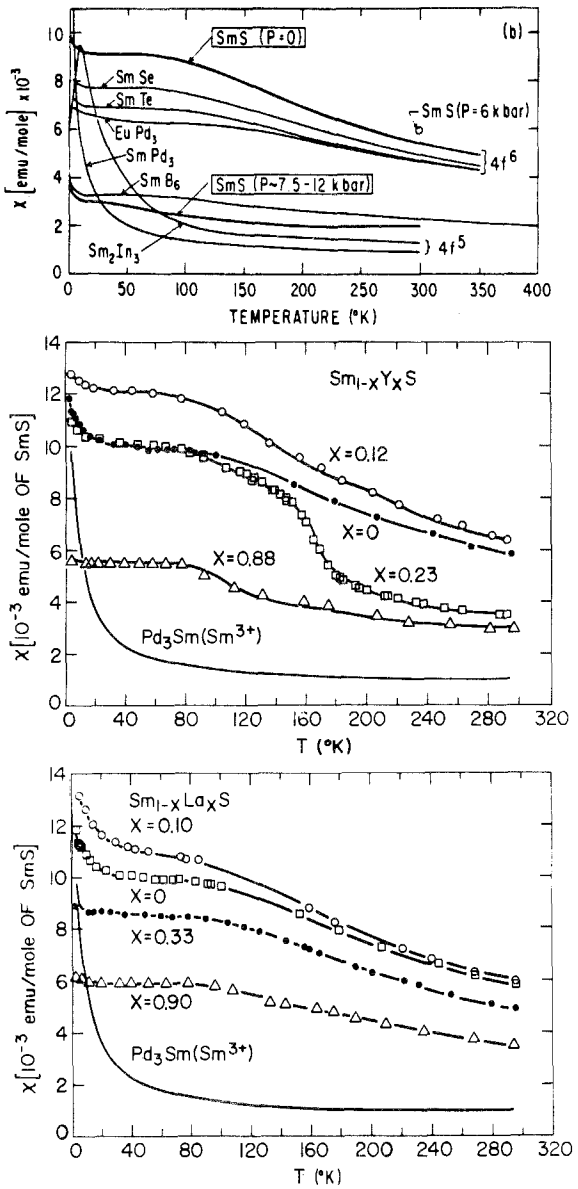

Fig. 20.10. Top figure shows the magnetic susceptibility as a function of temperature for Sm monochalcogenides and a few other compounds. For SmS, data for normal semiconducting phase and high pressure metallic phase are shown. The flat susceptibility behavior in the low temperature region of the high pressure phase of SmS is to be noted and compared with that of $SmPd_3$ and Sm_2In_3 in which the Sm ions are Sm^{3+}. The behavior of SmB_6 is similar to that of the high pressure phase of SmS. In the middle and bottom figures the susceptibility data for substituted systems are shown. The flat susceptibility region and absence of low temperature divergence or magnetic ordering is characteristic of the mixed valence state (from Maple and Wohlleben, 1971; and Tao and Holtzberg, 1975).

Maple and Wohlleben (1971), (1974) claim in their paper that the Freidel–Anderson model as generalized to degenerate states by Coqblin and Blandin (1968, 1971), and by Hirst (1970) (initially developed to account for the local moment formation and the magnetic susceptibility of dilute systems containing rare earth magnetic impurities) can account for the anomalous susceptibility behavior of α-Ce, metallic phase of SmS, SmB_6 and other R.E. compounds exhibiting an intermediate valence state. The basic features of this model seem to be: (1) The electron switches from one integral valence state with (n) electrons on the 4f shell to $(n-1)$ electrons on the 4f shell, with the extra electron going into the conduction band. Incoherent mixing of the electronic states with fluctuation times of the order of 10^{-13} sec broadens the ionic states involved, to a width Δ_w given by $\Delta_w = \langle V_{kl}\rangle^2 \rho(E_l) \approx 10^{-2}$ eV, where V_{kl} is the matrix element for the mixing local and conduction electron states and $\rho(E_l)$ is the density of conduction electron states at the energy of the local (E_l). In the Hirst model the excitation energy E_{exc} between the 4f(n) and 4f$(n-1)$ configuration is very large when the valence states are integral. When this is the case, $E_{exc} > \Delta_w$, the Hund's rule moments are well preserved and the system exhibits a susceptibility behavior reflecting the statistical average of both configurations. However, when the intermediate valence state prevails, $E_{exc} < \Delta_w$, the local state and the conduction electrons are allowed to mix freely, and the system fluctuates with a fluctuation temperature $T_f = \Delta_w/k_B$. The physical explanation why such a situation leads to nonmagnetic behavior according to Maple and Wohlleben is "The Zeeman levels of both configurations undergo the maximum broadening permitted by the uncertainty principle and the Zeeman precession in the external magnetic field is interrupted for each configuration as if there were thermal motion at a temperature $T_f < \Delta_w/k_B$, the spin fluctuation temperature, making it impossible for the system to contribute to the susceptibility, when the temperature is lower than T_f. The temperature dependence of the susceptibility is proposed to be of the form $\chi(T) = \mu_{eff}^2/3k_B(T + T_f)$ with $\mu_{eff}^2 = \epsilon\mu_1^2 + (1-\epsilon)\mu_2^2$ where the μ_i designates the Hund's rule effective moments of the two ionic states, ϵ is the fraction of the time the electron spends in the local shell. At high temperature $(T \gg T_f)$ the susceptibility exhibits a Curie–Weiss law with a Curie constant intermediate between that of the two mixing configurations, because thermal fluctuations caused by T are faster than fluctuations associated with T_f and thus the susceptibility sees both configurations as distinct species. At low temperatures $(T < T_f)$ the divergence of the susceptibility is cut off by T_f and the system exhibits a constant susceptibility $\chi(T) \to \mu_{eff}^2/k_B T_f = \text{const}$. Thus the susceptibility switches gradually from intermediate behavior to a constant value when the temperature is lowered through T_f. These arguments are of a qualitative nature and remain to be proved. According to Maple and Wohlleben (1974) this model developed essentially for dilute systems also holds for the more concentrated systems and the observed susceptibility behavior of SmB_6 and the high pressure phase of SmS exhibit the above characteristics of the model. In α-Ce and $YbAl_2$, T_f is larger than 300 K. In SmB_6 and SmS it is of the order of 50 K and in TmTe and TmSe of the order

of 10 K. Mössbauer experiments (Cohen et al., 1970) and soft X-ray spectra (Vainshtein et al., 1965) of SmB_6 appear to be consistent with the above picture. However it is hard to understand on this basis why TmSe orders magnetically.

The temperature dependence of $\chi(T)$ discussed above is qualitatively similar to that of a magnetic impurity exhibiting the Kondo effect especially when $\epsilon \simeq 1$. For isolated magnetic impurities in metallic systems the problem scales to a strong coupling problem and the local spin is fully compensated by the conduction electrons and the local moment is quenched (see Varma, 1976). A similar situation is envisaged in mixed valent compounds to explain the susceptibility behavior. Varma and Yafet (1976) have taken this view point and have calculated the susceptibility for a two band model (f and d). According to them, for the mixed valent compounds $\chi(T \to 0) = \mu^2/\Delta_w$ where Δ_w is the effective bandwidth as defined earlier. At high temperatures the susceptibility is $\chi = \mu^2/T + \Delta_w$, $T \gg T_f = \Delta_w/k_B$. The calculated susceptibilities qualitatively account for the observed susceptibilities in mixed valent compounds like SmS, $YbAl_3$, $CeAl_3$, etc., and the T_f on this model would be something akin to the Kondo temperature (T_{Kondo}). Varma and Yafet (1976) emphasize that the temperature independent behavior of the susceptibility comes about because the f-levels are very close to the Fermi level and one of the two configurations is nonmagnetic.

3.2. *Fluctuating valence and X-ray, U–V photoelectron and Mössbauer studies*

Ultraviolet, X-ray photoelectron spectroscopic and Mössbauer studies have been carried out on SmS and $Sm_{1-x}R_x^{3+}S$ and TmTe (Freeouf et al., 1974; Campagna et al., 1974a,b and 1975; Pollak et al., 1974; Coey et al., 1975, 1976; see also Campagna et al., 1976). Valence changes have been seen as a large shift in the characteristic K-line of Sm (Shaburov et al., 1973) and in the soft X-ray spectra (Vainshtein et al., 1965). X-ray photoelectron spectroscopic (XPS) and ultraviolet photoelectron spectroscopic (UVS) studies have shown that on the time scale $t \approx 10^{-16}$ second (XPS is believed to have a probing time of 10^{-16} second) Sm^{3+} and Sm^{2+} states are present in the M-phase of $Sm_{1-x}R_x^{3+}S$ compounds; the proportion of the two species is commensurate with the lattice parameter data. The XPS and UVS techniques cannot distinguish between the static and the dynamic situation, if the fluctuation period is orders of magnitude larger compared to the above probing time. However, Mössbauer technique with a probing time of about 10^{-8} second can resolve the problem. In case the static situation prevails, the Mössbauer resonance spectrum should exhibit two isomer shifted lines corresponding to the Sm^{2+} and Sm^{3+}, whereas it is expected to show only a single shifted line, if the ICF state prevails. Unfortunately, the shift in the resonant frequency between Sm^{2+} and Sm^{3+} is only a fraction of the linewidth and hence Mössbauer data leave the question somewhat undecided. However, both in SmB_6 (Cohen et al., 1970) and SmS systems (Coey et al., 1974, 1976) despite the above difficulty, a detailed analysis of the line width appear to be consistent with a fluctuating valence state model rather than the static model.

Coey et al. have concluded from their results that the fluctuation time in metallic SmS must be greater than 10^{-15} second and less than 10^{-9} second.

In this connection Mössbauer studies on $EuCu_2Si_2$ is of interest (Bauminger et al., 1973). The valency of the Eu ions in EuM_2Si_2 (where M = Ag, Fe or Cu) compounds, depends strongly on the interatomic distance. In $EuCu_2Si_2$ the Eu–Cu distance (1.886 Å) indicates that the valence of Eu is intermediate between 2^+ and 3^+. If Eu ions existed as distinct species of Eu^{2+} and Eu^{3+} two resonance lines are expected, since the separation between the two isomer shifted states are clearly resolvable in Eu. However, Bauminger et al. (1973) find only a single line spectrum which moves with temperature, in between the lines characteristic for Eu^{2+} and Eu^{3+}. From this it is concluded that the intermediate valence state of Eu ions in $EuCu_2Si_2$ is a fluctuating state in which the electrons fluctuate with $t < 3.5 \times 10^{-11}$ second between the localized 4f level and the conduction band.

4. Phase stability diagram of the substituted system

Based on the results of low-temperature as well as the high temperature X-ray studies a phase stability diagram (Jayaraman et al., 1975a) has been proposed for the system $Sm_{1-x}Gd_xS$ (see fig. 20.11). The diagram has three phases designated as B for the normal black phases, M for the metallic phase and B′ for the black phase resulting from the first-order transition observed on cooling the M-phase. All the three phases have the NaCl type structure but differ in their valence state and hence in their electronic structure (see later discussion in section 5). The shape of BB′–M phase boundary is a very interesting feature of the phase diagram.

The semiconductor-to-metal transition boundary (B–M) in pure SmS is very steep (~300°/kbar) and has a positive slope (Jayaraman et al., 1975a). If the substitution of Gd is equivalent to positive pressure, the dT/dx phase boundary for the B–M transition in $Sm_{1-x}Gd_xS$ compounds should also be steep and positive. Further, the DTA experiments with samples close to but less than the critical Gd concentration (15 atomic %) have shown that the B → M transition produced by applying pressure is accompanied by evolution of heat (Jayaraman et al., 1975a). From this result the B-phase in $Sm_{1-x}Gd_xS$ compounds has been identified as the higher entropy phase and the dT/dx of the B–M phase boundary as positive.

The following experimental results have led to the identification of the B′-phase as a phase different from the B-phase: (1) the boundary for the first-order transition (M to B′) observed on cooling the M-phase has negative dT/dx, (2) a striking break in slope is seen relative to the M–B boundary, and (3) the transition is accompanied by evolution of heat. Further, experiments with $Sm_{0.85}Gd_{0.15}S$ samples have shown that the metallic phase produced by the application of pressure on them can be retained only when pressure is released

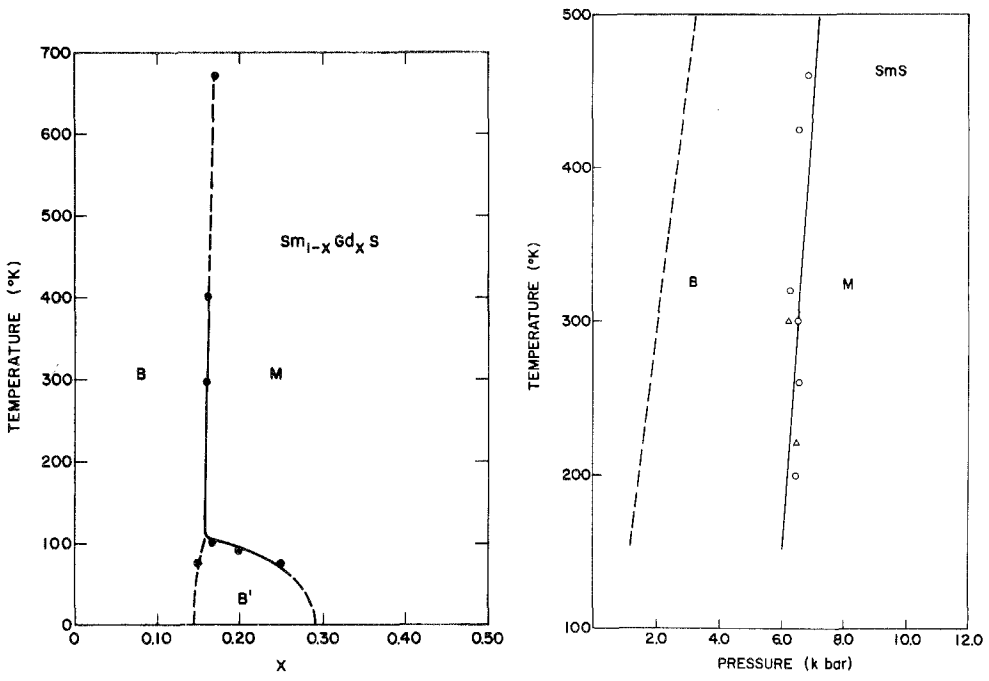

Fig. 20.11. Phase stability diagrams for the $Sm_{1-x}Gd_xS$ system and for SmS. The dashed portion of the B–M phase boundary in the left figure shows the possible location of the solid–solid critical point for the B–M transition. The dashed line in the P–T diagram of SmS shows the hysteresis for the B–M transition (from Jayaraman et al., 1975).

at temperatures above 140 K, suggesting that a different phase boundary is involved in the low-temperature region.

The continuous but anomalous thermal expansion behavior of the golden-phase samples (at compositions close to but higher than the critical concentration) and the absence of any first-order transition on heating are strongly suggestive of the termination of the M–B phase boundary at a critical point (Jayaraman et al., 1975a). Indeed this is to be expected in analogy with the behavior of the valence transition in Ce; in Ce the γ to α-Ce phase boundary has been shown to terminate at a critical point (see ch. 4, section 2.1). Accordingly, in the stability diagram in fig. 20.11 the region in which the critical point could lie is indicated by the dotted line.

From the T–X diagram of the substituted system certain deductions have been made regarding the P–T diagram of pure SmS. In pure SmS a boundary analogous to the M–B′ phase boundary has to exist. There are some indications to this from the low temperature resistivity measurements reported by Bader et al. (1973). However, clear cut evidence for its presence has to be established by performing the experiments using hydrostatic pressures. The B–M boundary in SmS should also terminate at a critical point on the high temperature side.

Tonkov and Aptekar (1974) delineated the S–M phase boundary for SmS from DTA measurements and have predicted a critical point at about 700 C and 7 kbar. This is based on the assumption that the critical point would be situated where the hysteresis interval closes. From the phase stability diagram it is evident that the temperature ordering of the phases is in the sequence B′→M→B with increasing T. It has been argued that this ordering can originate from a delicate balance of a number of physical factors that contribute to the entropy. They are, (1) the electronic contribution, (2) the lattice contribution, and (3) the relative importance of the latter depending on the temperature regime. The B phase with its much larger lattice constant (relative to the M-phase) would have a smaller Debye Θ and hence the lattice contribution to the entropy at high temperature, which would be proportional to $(T/\Theta)^3$, could dominate over the combined electronic and lattice terms of the M-phase. The lower entropy of the B′ phase then is presumed to be due to the absence of the electronic entropy and lowered contribution from the lattice term at low temperatures (see Jayaraman et al., 1975 and Varma, 1976).

5. Electronic structure

Models for the electronic structure diagrams of SmS and its alloys, in the semiconducting and metallic phases have been proposed to explain the phase transitions and the observed properties (Jayaraman et al., 1975; Tao and Holtzberg, 1975; Penney and Holtzberg, 1975; Penney et al., 1976; Batlogg et al., 1976. See also Von Molnar et al., 1976). In fig. 20.12 one such diagram is presented showing the electronic state of B, M and B′ phases of the $Sm_{1-x}Gd_xS$ compound. In the B-phase the Sm ($4f^6$) configuration must lie below the Fermi level E_f, to be consistent with the divalent state of the Sm ion. The $Sm_{1-x}Gd_xS$ (for $x > 0.10$) compounds are degenerate semiconductors when in the B phase but in the above diagram this particular situation (Gd–d–band) is not shown. The 5d band of Sm which constitutes the principal conduction band of the system is largely empty. The 3p states of sulfur constitute the valence band and this is also shown.

In the M-phase on the other hand the Sm ions are nearly trivalent and hence the $4f^65d^0$ configuration must have fewer electrons relative to the $4f^55d^1$ configuration. The way this is realized is through a large reduction in the lattice constant at the transition which lowers the energy of the 5d band and drives it below the $4f^65d^0$ configuration. An approximate calculation shows that for a 10% volume change in going from B to M phase, the 5d-band edge should shift by about 0.5 eV, which was (calculated from the deformation potential of −4.7 eV measured for SmS). Since the system is in the intermediate valence state in the M-phase E_F must be tied to the $4f^6$ state.

The diagram presented in fig. 20.12 is similar to that of Tao and Holtzberg (1975) and that of Penney et al. (1975), but in addition shows the E_F and the Fermi distribution function. The change in the latter function (indicated in fig. 20.12 by dotted line) with temperature is believed to cause changes in the

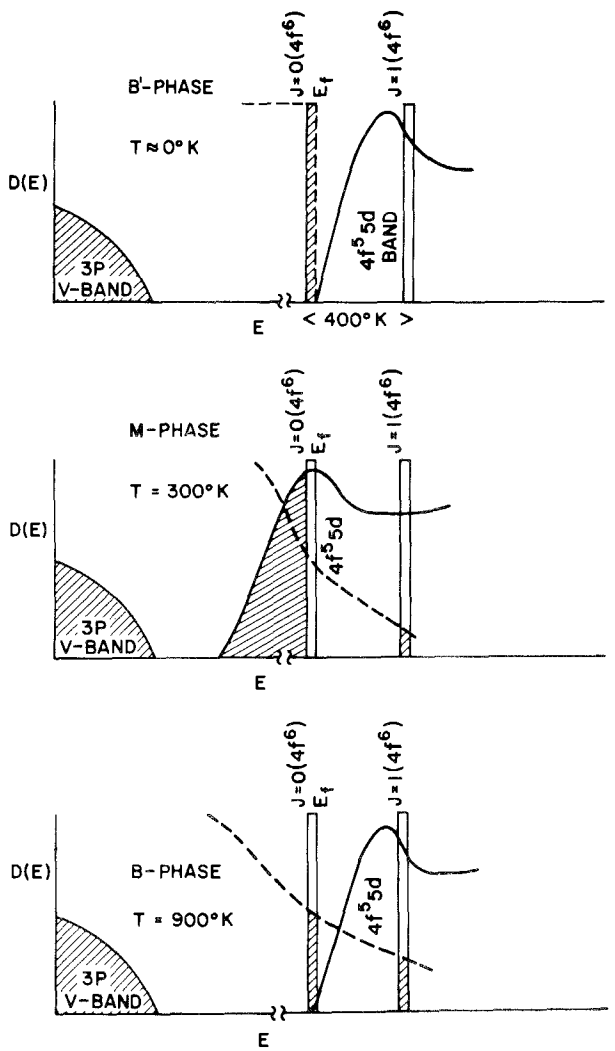

Fig. 20.12. Electronic structure of the B′, M and B-phases in the $Sm_{1-x}Gd_xS$ system. The spin–orbit splitting of the 4f level is shown and this is about 35 meV. The dashed line shows the Fermi distribution function (from Jayaraman et al., 1975a).

occupation probability of the electrons in the various electronic states involved, as temperature is varied, and initiate transitions among the three relevant phases. Although the transitions are electronically driven, it is believed that the particular temperature ordering of the phases as pointed out previously is due to the dominating lattice contribution to the entropy, which makes the B phase as the one stable at high temperatures, the M-phase at intermediate temperatures and the B′ phase at low temperatures.

5.1. *Thermal expansion, resistivity and other measurements and their significance*

5.1.1. *Thermal expansion*

The description of the intermediate valence state in terms of the ICF model and the triggering mechanisms for transitions as a function of temperature stress that the 4f level is tied to the Fermi level in the metallic phase. The strongest evidence for this comes from the anomalous thermal expansion (Jayaraman et al., 1975), the anomalous resistivity behavior (Penney and Holtzberg, 1975) and thermoelectric power (Ramesh and Shuba, 1976) and the anomalous behavior of the bulk modulus (Penney et al., 1975). The anomalous thermal expansion behavior of the M-phase of $Sm_{1-x}Gd_xS$ (especially in samples close to the critical concentration) in the region 300 K to 900 K (see fig. 20.7) must be due to a continuous change in the valence of the Sm ions towards the divalent state and this strongly suggests that in the M-phase the $4f^6$ states lies very close to the Fermi energy (E_F), and become thermally populated with increasing T. At high concentrations of Gd, the $4f^6$ states may be expected to lie too far above E_F, for appreciable thermal excitation to take place, and hence the thermal expansion becomes normal. This is clear from the data shown in fig. 20.7 for $x = 0.40$ Gd. (Even in this case α is still somewhat larger than for pure GdS). Varma (1976) has developed the mathematical expression for the anomalous thermal expansion (see also Jefferson, 1976) based on electron excitation and the strong coupling of the latter to the lattice and has also shown how first-order and second-order transitions can be obtained in the system consistent with the phase diagram of fig. 20.11.

5.1.2. *Resistivity measurements*

Resistivity and Hall effect measurements as a function of temperature (Penney and Holtzberg, 1975) on $Sm_{1-x}Y_xS$ compounds have shown that the E_F and 4f band are tied together in the metallic phase. The resistivity increases (see fig. 20.13) in passing from the black-phase stable at low temperature (B′) to the metallic (M) phase stable at intermediate temperatures. This is a very unexpected and surprising result because the number of carriers increase at the transition as seen in the Hall data, which should result in a decrease in resistivity. This anomalous behavior in resistivity at the transition has been attributed to resonant scattering of electrons from the d-state into the high density of states 4f band, and the conclusion is that in the so-called mixed-valence state (metallic phase), the Fermi level lies at the high density of states narrow 4f band. Farther away from the critical composition, or in YS, no such effect is observed, (Penney and Holtzberg, 1975) since the latter state has moved away from the Fermi level.

5.1.3. *Heat capacity measurements*

The electronic specific heat of the metallic phase of SmS (Bader et al., 1973) and of the Y substituted SmS ($Sm_{1-x}Y_xS$) compounds (Von Molnar and Holtz-

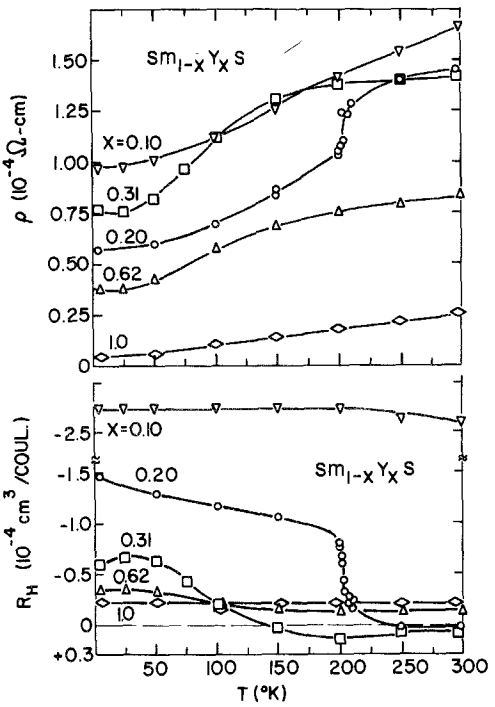

Fig. 20.13. Resistivity and Hall data for some $Sm_{1-x}Y_xS$ compounds as a function of temperature (from Penney and Holtzberg, 1975).

berg, 1976) have been measured. The metallic phases in the mixed valence region have anomalously high values, reflecting an order of magnitude greater electronic density of states in the golden phase compared to the black phase. The low-temperature heat capacity data thus strongly supports the presence of high density of states at the Fermi energy E_F.

5.1.4. *Thermoelectric power*

The thermoelectric power of SmS across the transition and in the metallic phase of the $Sm_{1-x}Gd_xS$ compound with $x = 0.16$ has been measured as a function of pressure and temperature (Ramesh and Shuba, 1976) and are shown in fig. 20.14. The thermoelectric power of SmS changes from a large negative value ($-80\,\mu$V/C) to a positive value ($+1\,\mu$V/C) across the transition and registers a substantial increase with further increase of pressure ($+1$ to $10\,\mu$V/C in the range 7 to 10 kbar) before saturating. With SmS containing 16 atomic percent Gd which is metallic, the thermoelectric power is positive and increases rapidly (from 2 to $15\,\mu$V/C in the range 1 to 15 kbar) with pressure before saturating. In the Gd substituted compound the thermoelectric power decreases with temperature and goes negative when the applied pressure is low. The

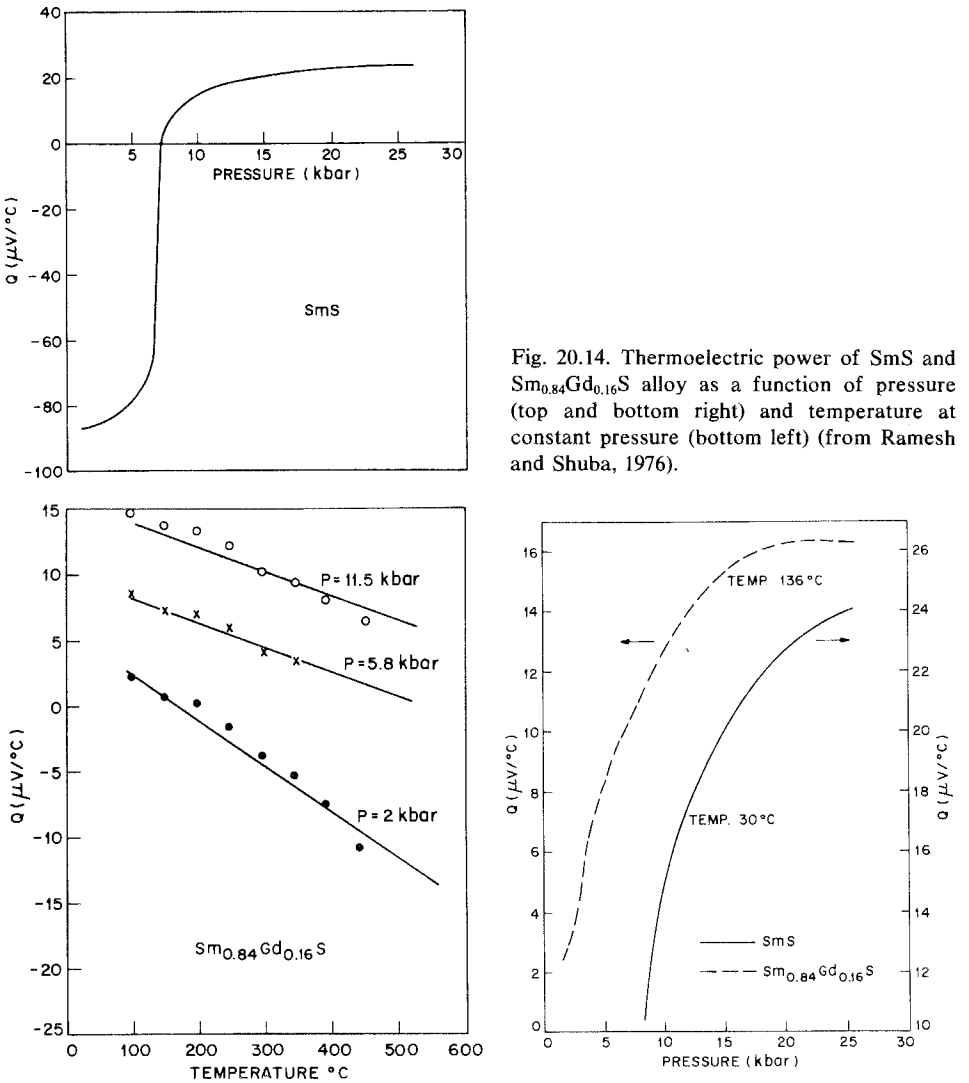

Fig. 20.14. Thermoelectric power of SmS and $Sm_{0.84}Gd_{0.16}S$ alloy as a function of pressure (top and bottom right) and temperature at constant pressure (bottom left) (from Ramesh and Shuba, 1976).

behavior of the thermopower has been interpreted (Ramesh and Shuba, 1976) on the basis that the Fermi level lies within the breadth of the 4f level in the metallic phase.

5.1.5. *Bulk modulus in the mixed valence state*

In a recent study, the elastic constants of pure SmS at ambient pressure and for compounds in the system $Sm_{1-x}Y_xS$ have been measured (Penney et al., 1976). In fig. 20.15 the bulk moduli calculated from the elastic constant data are

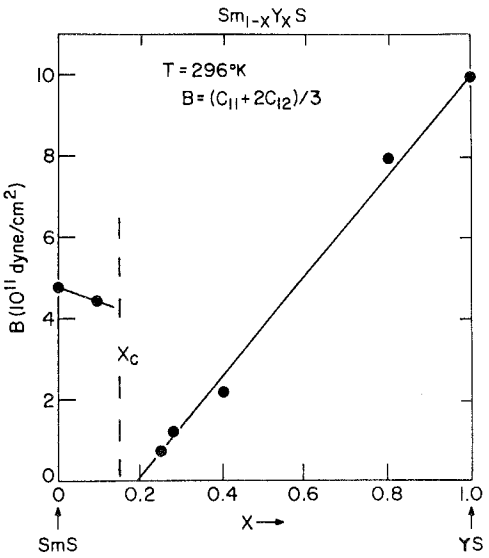

Fig. 20.15. The bulk modulus of $Sm_{1-x}Y_xS$ compounds. In the critical concentration region the bulk modulus undergoes an abrupt decrease indicating extreme softening of the lattice. The bulk modulus calculated from elastic constants obtained from sound velocity measurements on single crystals (from Penney et al., 1975).

shown as a function of x. The interesting point is that in the metallic region very near the critical Y concentration the bulk modulus becomes vanishingly small. According to Penney et al. (1975) in these systems the bulk modulus is given by

$$B/B_0 = [1 - (e_3 - e_2)\eta N]^2 - \eta^2 N/B_0$$

where B_0 is the bulk modulus of SmS and B the bulk modulus of the $Sm_{1-x}Y_xS$ compounds; the strains e_3 and e_2 give the equilibrium volumes of $Sm^{2+}S$ and $Sm^{3+}S$. The two terms which soften the bulk modulus are the electronic term $-\eta^2 N/B_0$ arising from a redistribution of electrons between the two electronic configurations involved, and hence a purely electronic term, and a lattice term $-\eta N(e_3 - e_2)$ resulting from a renormalization of the lattice which is coupled to the electronic energy by η, the deformation potential. When a transition takes place the lattice shrinks, the d-band is lowered and the energy for a d-excitation is reduced (see also the discussions earlier). The softening of the bulk modulus corresponds to the metallic region where the intermediate valence state prevails and this according to Penny et al. is the region of the $f^6 5d^0$–$4f^5 5d^1$ overlap. This is precisely the region where electron transfer and change of valence state can occur continuously until the overlap is removed at high Y concentration. Thus the behavior of the bulk modulus seems to support the model proposed by Penney and Holtzberg (1975) which again has stressed the pinning of the Fermi level E_F at the 4f.

5.1.6. *Other measurements*

Electron paramagnetic resonance experiments (Birgeneau et al., 1972; Walsh et al., 1973, 1974, 1975) have been carried out on SmS and SmS doped systems (with Eu and Gd ions mainly) to gain a microscopic understanding of the electronic interactions in them and the possible significance of these to the valence transition. These experiments have shown anomalous g-shifts which have been interpreted as due to anomalous exchange effects and overlapping 4f electron wave functions. An interesting point is that in Gd-doped samples the EPR signal suddenly vanishes at the valence transition. Further, the EPR measurements appear to have shown that the Sm^{3+} fraction in pure SmS earlier reported was not due to any intrinsic property of SmS itself and is probably due to defects such as the presence of a sulfur vacancy.

As stated earlier, optical reflectivity changes seems to be the most striking effects in these systems. Anomalous thermal expansion is accompanied by a progressive change in color from metallic-gold to copper, bronze, purple, and to black color, due to the localization of the conduction electron on the $4f^6$ states with increase in temperature. This property is related to the shift in the plasma frequency (ω_p) towards the infrared [$\omega_p = (4\pi ne^2/m^*)^{1/2}$] as the number of electrons n in the conduction band changes with temperature. Thus the color of the compounds observed in the reflectivity itself gives a vivid picture of what is happening at the microscopic level.

Reflectivity measurements have been carried out on some members in the $Sm_{1-x}Y_xS$ system and interesting information concerning transport coefficients of current carriers, have been obtained. These measurements again (Guntherodt and Holtzberg, 1975; Suryanarayanan et al., 1976) seem to support the idea of the presence of a virtual bound state due to 4f, near E_f.

6. Theoretical aspects of the transition

Several recent papers (Herbst et al., 1973; Hirst, 1974; Bucher and Maines, 1972; Wio et al., 1974; Anderson and Chui, 1974; Mott, 1974; Coqblin, 1974; Varma and Heine, 1975; Penney et al., 1976; Sicardi et al., 1975; Kaplan and Mahanti, 1976; Coey et al., 1975, 1976; Kanda et al., 1976; Kincaid et al., 1976; Wilson, 1977; Kaplan et al., 1977, 1978; Johansson, 1975; Johansson and Rosengren, 1976) have dealt with the theoretical aspects of the electronic transition in Sm monochalcogenides and the $P-V$ relationships obtained in them. The papers have addressed themselves to the following two major questions concerning the transition: (1) continuous and discontinuous nature of the transition and the triggering and decelerating mechanisms acting, and (2) the fractional valence in the high pressure metallic phase.

The internal energy of the system under consideration consists of contributions from the electronic energy term E_{elec}, the elastic energy term E_{elas}, and other interaction terms E_{int}; E_{elec} includes energy necessary to raise an electron

from $4f^n$ to $4f^{n-1}$ configuration, E_{pr}, and correlation energy E_{corr}. We have therefore for the internal energy or the $T = 0$ free energy, F

$$F(v, z) = E_{elec}(v, z) + E_{elas}(v) + E_{int}, \tag{20.1}$$

where v and z are specific volume and electronic population respectively. In some studies, only E_{elec} was considered while in others all contributions were included. At $T > 0$, F will have entropy terms.

Several years ago, Falicov and Kimball (1969) presented a model to explain metal-insulator transitions in semiconductors which had a localized donor level rather deep below the conduction band. Considering only the electronic term, they showed that the effective gap, ΔE_g(eff.), would go to zero according to the eqn. $\Delta E_g(\text{eff.}) = \Delta E_g - 2Gn$, where ΔE_g is the gap between the donor level and the conduction band, G is the screening interaction parameter and n is the electronic density excited into the conduction band; n increases either continuously or discontinuously depending on the value of $G/\Delta E_g$. Thus the gap would be carrier dependent in this model. Ramierez et al. (1970), Ramierez and Falicov (1971) have developed these ideas further and applied them to the phase transition in Ce metal, which is very similar in character to the transition in SmS. Bucher and Maines (1972) applied this theory to their results on the SmS–SmSe alloy system. According to this, at $T = 0$ the free energy of the system, neglecting the elastic energy contribution is

$$F = \Delta E_g n + an^{5/3} - Gn^2 \tag{20.2}$$

where ΔE_g is the 4f–5d gap, n the electronic density and G is the Falicov–Kimball parameter. The first two terms in the above represent the promotional energy of the 4f electron into the conduction band, and Gn^2 accounts for the gain in the attractive Coulomb energy (the screening term). They showed, that minimizing F with respect to n, and for certain domain of values of G/a and $\Delta E_g/a$, a first-order phase boundary exists; if G/a is greater than $\frac{5}{9}$ the transition is first-order and if less than $\frac{5}{9}$ only second-order. The physical picture is that when the electrons are excited from the 4f level into the conduction band, the hole-states in the 4f shell attract the latter via the Coulomb interaction and this reduces the gap energy ΔE_g in equation 20.2; this is the screening interaction. When the gap is thus reduced, more electrons are promoted, resulting in further reduction of the gap ΔE_g. Provided the strength of the G parameter is sufficiently positive and overcomes the decelerating factors the gap ΔE_g collapses to zero catastrophically. A continuous transition will result if the G parameter is below a critical value and the decelerating factors become dominant. More recently other effects have been included into the Falicov–Kimball Model to explain the discontinuous and continuous transitions (Avignon and Ghatak, 1975; Goncalves et al., 1975; Kanda et al., 1976; Balseiro et al., 1975).

The solutions to eq. (2) obtained by Bucher and Maines are only for pure states $4f^n$ and $4f^{n-1}$. Hirst (1974) has developed the ICF model to take this feature into account. In this model it is emphasized, that in SmS the 4f state

jumps discontinuously at the first-order transition, but locks itself to the E_F, until a pure configuration state namely $4f^{n-1}$ is achieved. In this state the volume could change anomalously but the energy of excitation hardly changes. The 4f level tracks with the Fermi level over a range of pressure until the former is exhausted. Hirst (1974) in his calculations has included E_{elas} and has pointed out that the occurrence of continuous and discontinuous transitions itself is related to various "accelerating" and "decelerating" tendencies that exist in the system. The most important accelerating term, according to Hirst, is the so-called "compression shift mechanism". This originates from the fact that when the lattice is compressed, the d-conduction band edge is lowered with respect to the 4f level, favoring excitation of electrons. Since this in turn will decrease the volume, the d-band will be further lowered. The whole mechanism is therefore accelerating and acts independently of the Falicov–Kimball screening interaction. This will drive the transition discontinuously, provided the lattice compressibility is large. (If the compressibility is small only a continuous transition will result). According to Hirst this compression shift mechanism is more important for SmS, than the Falicov–Kimball screening interaction. The decelerating tendencies arise from the finite density of conduction electron states, and the increase in bulk modulus with pressure. The former causes the Fermi energy to rise as electrons are excited from the 4f into the conduction band, increasing the promotional energy for further excitation. Hirst (1974) has noted that in his primitive model only a discontinuous jump from $4f^n$ to $4f^{n-1}$ can occur, and no choice of parameters leads to a continuous collapse, with the system going to an ICF thermodynamic state. However, he has shown that the situation can be remedied, by using the Birch equation of state for evaluating the volume dependence of the bulk modulus $B(V)$, in his general relationship for the thermodynamic stability condition (Hirst, 1974). What this essentially amounts to is that the increase in $B(V)$ with decreasing volume leads to finite compressibility and this arrests the discontinuous transition, thereby preventing it from running all the way to the pure configuration state. Choice of suitable values for the parameters yields an ICF solution for the whole, or part of the discontinuous transition.

Anderson and Chui (1974) have pointed out that higher order anharmonic strain terms are important and can give rise to continuous and discontinuous transitions. Their model starts from the premise, that replacing Sm^{2+} with Sm^{3+} in the SmS matrix creates a large strain field because of the large size effect involved. This gives rise to sufficiently large anharmonic terms and can dominate the free energy, provided the bulk modulus as well as the electronic promotional energy for $4f^n$ to $4f^{n-1}$ excitations are small.

Thus the elastic energy term E_{elas} is important in calculating the $P-V$ relationship and has been included in several of the recent calculations, including that of Hirst. Using a simple ionic model for the cohesive energy, electronic terms akin to the Falicov–Kimball model, and including entropy terms associated with configuration and spin disorder, Wio et al. (1974) have calculated the $P-V$ isotherms and the phase diagram for SmS. However, agreement with

experiment is not very good. Varma and Heine (1975) have calculated the $P-V$ relationships, using a model in which the promotion of a 4f electron into the d-band is accompanied by a lattice contraction, so that the chemical potential of the d-electron is reduced. The nonlinearities in the lattice contraction apparently give rise to the decelerating factor, restricting SmSe and SmTe to undergo continuous transitions. The principal feature of this model is that it has introduced an explicit volume dependence on the valence in the elastic energy term, in addition to all the other terms that have been considered. Consequently they obtain $P-V$ relationships which are in much better agreement with experiment, than have been obtained in previous studies.

7. Other systems

Some of the other materials known to exhibit valence fluctuations were discussed along with the monochalcogenides, viz.; SmB_6, $EuCu_2Si_2$. There are a number of compounds involving Ce and Yb (see table 20.1) which appear to show properties characteristics of the ICF state (Maple and Wohlleben, 1973; Sales and Wohlleben, 1975; Debray et al., 1976; Andres et al., 1975) namely, temperature independent susceptibility with no evidence of divergence or ordering at low temperature, although one of the 4f configuration has a nonzero J value (in Yb for instance the $4f^{13}$ configuration has $J = \frac{7}{2}$ and $\mu_{\text{eff}} = 4.54\ \mu_B$ from Hund's rule). According to Sales and Wohlleben the susceptibility behavior of these compounds as a function of temperature can be quantitatively given by

$$\chi(T) = N\{\mu_n^2 v(T) + \mu_{n-1}^2[1 - v(T)]\}/3k_B(T + T_{sf}) \tag{20.3}$$

with

$$v(T) = \frac{2J_n + 1}{(2J_n + 1) + (2J_{n-1} + 1)\exp[-E_{ex}/k_B(T + T_{sf})]}, \tag{20.4}$$

where $v(T)$ is the fractional occupation of the state E_n (fractional valence), $E_{ex} = E_n - E_{n-1}$, μ_n and μ_{n-1} are the effective Hund's rule magnetic moments in the two configurations, and $2J_n + 1$ and $2J_{n-1} + 1$ are the degeneracies of the two levels E_n and E_{n-1}. Sales and Wohlleben have calculated the temperature dependence of susceptibility using the above expressions for YbC_2, YbB_4, $YbAl_3$, and $YbCu_2Si_2$ from 0–300 K and have shown that they are in good agreement with experimental values. Further, they have also calculated the valence of Yb in these compounds as a function of temperature. The basis for the above expressions for the susceptibility is again the same as stated earlier in section 3.1 and the cut-off in divergence arising from T_{sf}, the fluctuation temperature. Debray et al. (1976) have measured the susceptibility of Yb–Cu, YbAg, YbAu, and YbZn and have explained the observed constant susceptibility at low temperatures on the basis of ICF model.

Among cerium compounds $CeAl_3$, CeB_4, CeN and a few intermetallic compounds (see table 20.1) are believed to exhibit nonintegral valence state

(Campagna et al., 1974; Andres et al., 1975). Andres et al. (1975) have concluded from very low temperature specific heat and electrical resistivity measurements on $CeAl_3$ that the electrons form virtual bound 4f states and this will be consistent with the mixed valence state that has been proposed for $CeAl_3$. In CeB_4 and CeN the magnetic susceptibility behavior is again suggestive of ICF state (Maple and Wohlleben, 1973). In CeP a valence change near 100 kbar has been reported (Jayaraman et al., 1976).

Among the alloy systems, the $Ce_{1-x}Th_x$ system has become the focus of attention recently (Lawrence et al., 1975; Parks and Lawrence, 1976). With the addition of Th the valence transition in Ce metal (γ to α-Ce) involving $4f^15d^1$ and $4f^05d^2$ configuration (Ce^{3+} and Ce^{4+}) can be investigated at any part of its phase boundary, conveniently at atmospheric pressure. Various properties associated with this transition in the subcritical and supercritical regions are currently being investigated.

8. Concluding remarks

Some of the crucial features (Varma, 1976) associated with the valence change are: (1) pinning of the Fermi level by the f levels, the hybridization of the f and s–d states and the exclusion of states of more than one f-electron per atom (i.e. ionization states higher than +3); (2) large differences between the f-electron and the s–d electron masses and the obeying of atomic spectral rules by the f-electrons; (3) strong coupling of the lattice with the f-electron configuration, preserving the NaCl-type structure symmetry in the phases. These aspects, experimentally well established, have been taken into account in the various models that have been presented. The understanding of valence changes in rare earth systems is by no means complete both from experimental and theoretical view points. Many experiments are yet to be done among which neutron studies would be of much value. Also, diffuse scattering and Debye Waller factor measurements would be revealing. In the latter respect some preliminary studies have been made (Dernier and Weber, 1976). Jayaraman et al. (1975) and Varma (1976) have identified some of the specific questions that are to be answered. To answer them, further experimental clarification and theoretical attempts are necessary. One of the most interesting questions among them is the difficulty of explaining continuous transitions (in SmSe and SmTe) in the framework of Mott's theory (Mott, 1970). This is a fundamental one. In this theory of metal-insulator transition, correlations play an essential role, and in general only a first-order transition can occur because of the long range nature of the Coulomb interaction. Therefore within this framework it is hard to understand the continuous transition in SmSe and SmTe. The behavior of the latter compounds suggests, that for some reason long range Coulomb interactions are not that important compared to other interactions.

The shape of the BB'–M phase boundary (in fig. 20.11) is one of the most interesting features of the phase diagram. A proper theory of this turnover is yet

to be constructed. The theory of the magnetic susceptibility is inadequate and open to question for finite temperatures. Further the theory is quite silent on the issue of resistivity behavior.

Acknowledgment

I am much indebted to Dr. C. Varma for helpful discussions during the writing of some of the theoretical aspects of the valence change. I would like to thank R.G. Maines who helped in many ways during the preparation of this article. My thanks are also due to Drs. T. Penney and L.J. Tao for providing originals of some figures used in this chapter, to H.H. Teitelbaum for his help in the literature survey, and to Mrs. K. Miller for the painstaking effort in getting the article typewritten.

References

Anderson, P.W. and S.T. Chui, 1974, Phys. Rev. B **9**, 3229.
Andres, K., J.E. Graebner and H.R. Ott, 1975, Phys. Rev. Lett. **35**, 1779.
Avignon, M. and S.K. Ghatak, 1975, Solid State Commun. **16**, 1243.
Bader, S.D., N.E. Phillips and D.B. McWhan, 1973, Phys. Rev. B **7**, 4686.
Balseiro, C., M. Passeggi and B. Alascio, 1975, Solid State Commun. **16**, 737.
Barma, M., T.A. Kaplan and S.D. Mahanti, 1976, Phys. Letters.
Batlogg, B., E. Kaldis, A. Schlegel and P. Wachter, 1976, Phys. Rev. **14B**, 5503.
Batlogg, B., J. Schoenes and P. Wachter, 1974, Phys. Lett. A **49A**, 13.
Bauminger, E.R., D. Froinlich, I. Nowick, S. Ofer, I. Felner and I. Mayer, 1973, Phys. Rev. Lett., **30**, 1053.
Birgeneau, R.J., E. Bucher, L.W. Rupp, Jr. and W.M. Walsh, Jr., 1972, Phys. Rev. **85**, 3412.
Bridgman, P.W., 1927, Proc. Am. Acad. Arts Sci. **62**, 207.
Bucher, E., K. Andres, F.J. DiSalvo, J.P. Maita, A.C. Gossard, A.S. Cooper and G.W. Hull, 1975, Phys. Rev. **B11**, 500.
Bucher, E. and R.G. Maines, 1972, Solid State Commun. **11**, 1441.
Bucher, E., V. Narayanamurti and A. Jayaraman, 1971, J. Appl. Phys. **42**, 1741.
Campagna, M., E. Bucher, G.K. Wertheim, D.N.E. Buchanan and L.D. Longinotti, 1974a, Phys. Rev. Lett. **32**, 885.
Campagna, M., E. Bucher, G.K. Wertheim and L.D. Longinotti, 1974b, Phys. Rev. Lett. **33**, 165.
Campagna, M., G.K. Wertheim and E. Bucher, 1975, Spectroscopy of Interconfigurational Fluctuations in Rare Earth Compounds, in: AIP Conference Proceedings, No. 24, pp. 22–26 (Twentieth Annual Conference on Magnetism and Magnetic Materials, San Francisco, 1974).
Campagna, M., G.K. Wertheim and E. Bucher, 1976 "Structure and Bonding", Springer Verlag, Vol. 30, p. 99.
Chao, S.I., 1970, Phys. Rev. B **1**, 4589.
Chatterjee, A., A.K. Singh and A. Jayaraman, 1972, Phys. Rev. B **6**, 2285.
Coey, J.M.D., S.K. Ghatak, M. Avignon and F. Holtzberg, 1976, Phys. Rev. **B14**, 3744.
Coey, J.M.D., S.K. Ghatak and F. Holtzberg, 1975, Semiconductor-Metal Transition in SmS–A^{149}Sm Mössbauer Study, in: AIP Conference Proceedings, No. 24, pp. 38–39 (Twentieth Annual Conference on Magnetism and Magnetic Materials, San Francisco, 1974).
Cohen, R.L., M. Eibschütz and K.W. West, 1970, Phys. Rev. Lett. **24**, 382.
Coqblin, B. and A. Blandin, 1968, Advan. Phys. **17**, 281.
Coqblin, B. and A. Blandin, 1971, J. Physique (Paris), Suppl. 32, C1-599.
Davis, H.L., 1971, Effects of Pressure on the Electronic Structure of the Samarium Monochalcogenides, in: Field, P.E., ed., Proceedings of the Ninth Rare Earth Research Conference, Blacksburg, Virginia. 1971, Vol. I (U.S. Department of Commerce, Springfield, Virginia) pp. 3–14.
Debray, D., B.F. Wortmann and S. Methfessel, 1976 Phys. Rev. **B14**, 4009.
Dernier, P.D., W. Weber and L.D. Longinotti, 1976, Phys. Rev. **B14**, 3635.
Dimmock, J.O., 1970, IBM J. Res. Dev. **14**, 301.
Falicov, L.M. and J.C. Kimball, 1969, Phys. Rev. Lett. **22**, 997.

Francillon, M., D. Jerome, J.C. Achard and G. Malfait, 1970, J. Physique (Paris), **31**, 709.
Freeouf, J.L., D.E. Eastman, W.D. Grobman, F. Holtzberg and J.B. Torrance, 1974, Phys. Rev. Lett. **33**, 161.
Goncalves da Silva, C.E.T. and L.M. Falicov, 1975, Solid State Commun. **17**, 1521.
Goryachev, Yu.M. and T.G. Kutsenok, 1972, High Temp.-High Press. **4**, 663.
Guntherodt, G. and F. Holtzberg, 1975, IBM Res. Rept., No. RZ5253; and, 1975, Optical Studies of Semiconductors to Metal Transition in $Sm_{1-x}Y_xS$ AIP Conf. Proc., 24, pp. 36–37 (Twentieth Annual Conference on Magnetism and Magnetic Materials, San Francisco 1974).
Guntherodt, G., P. Wachter and D.M. Imboden, 1971, Phys. Kondens. Materie, **12**, 292.
Herbst, J.F., R.E. Watson and J.W. Wilkins, 1973, Solid State Commun. **13**, 1771.
Hirst, L.L., 1970, Phys. Kondens. Materie **11**, 255.
Hirst, L.L., 1974, J. Phys. Chem. Solids **35**, 1285.
Holtzberg, F., 1974, Effects of Lattice Pressure on Samarium Valence States in Monosulphide Solid Solutions, in: AIP Conference Proceedings, No. 18, Part 1, pp. 478–489 (Nineteenth Annual Conference on Magnetism and Magnetic Materials, Boston, 1973).
Holtzberg, F. and J.B. Torrance, 1972, Optical Excitations in SmS, SmSe, SmTe and Their Relation to the Semiconductor-Metal Transition, in: AIP Conference Proceedings, No. 5, Part 2, pp. 860–864 (Seventeenth Annual Conference on Magnetism and Magnetic Materials, Chicago, 1971).
Jayaraman, A., 1965, Phys. Rev. **137**, A179.
Jayaraman, A., 1972, Phys. Rev. Lett. **29**, 1674.
Jayaraman, A., 1974, Electronic Phase Transitions in Rare Earth Monochalcogenides Under Pressure and Alloying, in: Haschke, J.M. and H.A. Eick, eds., Proceedings of the Eleventh Rare Earth Research Conference, Traverse City, Michigan, 1974, Vol. II (U.S. Department of Commerce, Springfield, Virginia) pp. 830–839.
Jayaraman, A., E. Bucher, P.D. Dernier and L.D. Longinotti, 1973, Phys. Rev. Lett. **31**, 700.
Jayaraman, A., E. Bucher and D.B. McWhan, 1970c, Pressure-Induced Changes in the Electronic and Lattice Properties of Thulium Monotelluride and Their Significance, in: Henrie, T.A. and R.E. Lindstrom, eds., Proceedings of the Eighth Rare Earth Research Conference, Reno, Nevada, 1970, Vol. I (U.S. Department of Interior, Washington, D.C.) pp. 333–344.
Jayaraman, A., P.D. Dernier and L.D. Longinotti, 1975a, Phys. Rev. B **11**, 2783.
Jayaraman, A., P.D. Dernier and L.D. Longinotti, 1975b, High Temp.-High Press. **7**, 1.
Jayaraman, A., V. Narayanamurti, E. Bucher and R.G. Maines, 1970a, Phys. Rev. Lett. **25**, 368.
Jayaraman, A., V. Narayanamurti, E. Bucher and R.G. Maines, 1970b, Phys. Rev. Lett. **25**, 1430.
Jayaraman, A., A.K. Singh, A. Chatterjee and S. Usha Devi, 1974, Phys. Rev. B **9**, 2513.
Jayaraman, A., W. Lowe, L.D. Longinotti and E. Bucher, 1976, Phys. Rev. Lett. **36**, 366.
Jefferson, 1976, J. Phys. C.; Solid State Phys. **9**, 269–78.
Johansson, B., 1975, Phys. Rev. B **12**, 3253.
Johansson, B. and A. Rosengren, 1976, Phys. Rev. B **14**, 361.
Kaldis, E. and P. Wachter, 1972, Solid State Commun. **11**, 907.
Kanda, K., K. Machida and T. Matsubara, 1976, Solid State Commun. **19**, 651.
Kaplan, T.A., S.D. Mahanti and M. Barma, 1977/78 in Valence Instabilities and Related Narrow Band Phenomena, R.D. Parks, ed. (Plenum Press, New York, 1977) pp. 151 and Proc. Intl. Conf. on High Pressure and Low Temperature Physics (Plenum Press, New York, 1978).
Khomskii, D.I. and A.N. Kocharjan, 1976, Solid State Commun. **18**, 985.
Kincaid, J.M., G. Stell and E. Goldmark, 1976, J. Chem. Phys., **65**, 2172.
Kirk, J.L., K. Vedam, V. Narayanamurti, A. Jayaraman and E. Bucher, 1972, Phys. Rev. B **6**, 3023.
Lawrence, J.M., M.C. Croft and R.D. Parks, 1975, Phys. Rev. Lett. **35**, 289.
McPherson, M.R., G.E. Everett, D.K. Wohlleben and M.B. Maple, 1971, Phys. Rev. Lett. **26**, 20.
Mahanti, S.D., T.A. Kaplan and Mustansir Barma, 1976, Theory of Electronic Properties of SmS, SmSe, SmTe, and SmB_6 in: AIP Conference Proceedings, No. 29, p. 404 (Twenty-First Annual Conference on Magnetism and Magnetic Materials, Philadelphia, 1975).
Maple, M.B., J. Wittig and K.S. Kim, 1969, Phys. Rev. Lett. **23**, 1375.
Maple, M.B. and D.K. Wohlleben, 1971, Phys. Rev. Lett. **27**, 511.
Maple, M.B. and D.K. Wohlleben, 1974, Demagnetization of Rare Earth Ions in Metals Due to Valence Fluctuations, in: AIP Conference Proceedings, No. 18, Part 1, pp. 447–462 (Nineteenth Annual Conference on Magnetism and Magnetic Materials, Boston, 1973).
Melcher, R.L., G. Guntherodt, T. Penney and F. Holtzberg, 1975, Proc. IEE, Ultrasonics Symposium, Cat 75, CHO 994-4SU, p.16.
Methfessel, S., F. Holtzberg and T.R. McGuire, 1966, IEEE Trans. Magnetics, Mag-2, 305.
Methfessel, S. and D.C. Mattis, 1968, in: Fluge, S., ed., Encyclopedia of Physics, Vol. 18 (Springer Verlag, Berlin) p. 389.
Mott, N.F., 1974, Phil. Mag. **30**, 403.
Narayanamurti, V., A. Jayaraman and E. Bucher, 1974, Phys. Rev. **9**, 2521.
Nickerson, J.C., R.M. White, K.N. Lee, R. Bachmann, T.H. Geballe and G.W. Hull, Jr., 1971, Phys. Rev. **3**, 2030.

Holtzberg, F., 1973, AIP Conference Proceedings No. 18, Magnetism and Magnetic Materials, Ed. C.D. Graham and J.J. Rhyne, p. 478.

Oliver, M.R., J.A. Kafalas, J.O. Dimmock and T.B. Reed, 1970, Phys. Rev. Lett. **24**, 1064.
Ott, H.R., K. Andres and E. Bucher, 1975, Low Temperature Magnetic Phase Transition in Thulium Selenide, in: AIP Conference Proceedings, No. 24, pp. 40–43 (Twentieth Annual Conference on Magnetism and Magnetic Materials, San Francisco, 1974).
Parks, R.D., 1977, Ed. Valence Instabilities and Related Narrow Band Phenomena (Plenum Press, New York and London).
Parks, R.D. and J.M. Lawrence, 1976, Thermodynamic Behavior Near Valence Instabilities, in: AIP Conference Proceedings, No. 29, pp. 479–483 (Twenty-First Annual Conference on Magnetism and Magnetic Materials, Philadelphia, 1975).
Penney, T. and F. Holtzberg, 1975, Phys. Rev. Lett. **34**, 322.
Penney, T., R.L. Melcher, F. Holtzberg and G. Guntherodt, 1976, Soft Bulk Modulus at the Configurational Phase Transition in $Sm_{1-x}Y_xS$, in: AIP Conference Proceedings, No. 29, pp. 392–393 (Twenty-First Annual Conference on Magnetism and Magnetic Materials, Philadelphia, 1975).
Pollaček, R.A., F. Holtzberg, J.L. Freeouf and D.E. Eastman, 1974, Phys. Rev. Lett. **33**, 820.
Ramesh, T.G. and V. Shubha, 1976, Solid State Commun. **19**, 591–593.
Ramirez, R. and L.M. Falicov, 1971, Phys. Rev. B **3**, 2425.
Ramirez, R., L.M. Falicov and J.C. Kimball, 1970, Phys. Rev. B **2**, 3383.
Rooymans, C.J.M., 1966, Ber. Bunsengess. Phys. Chem. **70**, 1036.
Sales, B.C. and D.K. Wohlleben, 1975, Phys. Rev. Lett. **35**, 1240.
Shaburov, V.A., A.E. Sovestnov and O.I. Sumbaev, 1973, Trans. of: Jetp Lett. (USA) **18**, 249.
Shaburov, V.A., A.E. Sovestnov and O.I. Sumbaev, 1974, Phys. Letters A **49A**, 83.
Suryanarayanan, R., 1978, Phys. Status Solidi **B85**, No 1.
Suryanarayanan, R., R. Paparoditis, C. Ferre and J. Briat, 1972, J. Appl. Phys. **43**, 4105.
Suryanarayanan, R., I.A. Smirnov, G. Brun and S.G. Shulman, 1976, J. De Physique, Supp. 10, **37**, C4-271.
Tao, L.J. and F. Holtzberg, 1975, Phys. Rev. B **11**, 3842.
Tonkov, E.Yu. and I.L. Aptekar, 1974, Fiz. Tverd. Tela. **16**, 1507.
Vainshtein, E.E., S.M. Blokhin and Yu.B. Paderno, 1965, Sov. Phys. Solid State **6**, 2318.
Van Daal, H.J. and K.H.J. Buschow, 1970, Physica Status Solidi A **3**, 853.
Varma, C.M., 1976, Rev. Mod. Phys. **48**, 219.
Varma, C.M. and V. Heine, 1975, Phys. Rev. B **11**, 4763.
Varma, C.M. and Y. Yafet, 1976, Phys. Rev. **13**, 2950.
von Molnar, S. and F. Holtzberg, 1976, Low Temperature Specific Heat of $Sm_{1-x}Y_xS$, in: AIP Conference Proceedings, No. 29, pp. 394–395 (Twenty-First Annual Conference on Magnetism and Magnetic Materials, Philadelphia, 1975).
von Molnar, S., T. Penney and F. Holzberg, 1976, J. de Physique, **37** C4-241.
Wachter, P., 1969, Solid State Commun. **7**, 693.
Walsh, Jr., W.M., E. Bucher, L.W. Rupp, Jr. and L.D. Longinotti, 1975, Spin Resonance Observation of Sm^{3+} in Semiconducting SmS, in: AIP Conference Proceedings, No. 24, pp. 34–35 (Twentieth Annual Conference on Magnetism and Magnetic Materials, San Francisco, 1974).
Walsh, Jr., W.M., L.W. Rupp, Jr., E. Bucher and L.D. Longinotti, 1974, Evidence for Exchange Enhancement by Impurity-Band Electrons in $Sm_{1-x}Gd_xS$, in: AIP Conference Proceedings, No. 18, Part 1, pp. 535–539 (Nineteenth Annual Conference on Magnetism and Magnetic Materials, Boston, 1973).
Walsh, Jr., W.M., L.W. Rupp, Jr. and L.D. Longinotti, 1973, Pressure Dependent Exchange Couplings in Samarium Monochalcogenides, in: AIP Conference Proceedings, No. 10, Part 2, pp. 1560–1563 (Eighteenth Annual Conference on Magnetism and Magnetic Materials, Denver, 1972).
Wilson, J.A., 1977 "Structure and Bonding" Vol. 32, pp. 58–90 (Springer Verlag Berlin, Heidelberg, New York).
Wio, H.S., B. Alascio and A. Lopez, 1974, Solid State Commun. **15**, 1933.
Wohlleben, D.K. and B.R. Coles, 1973, Formation of Local Magnetic Moments in Metals, in: Rado, G.T. and H. Suhl, eds., Magnetism, Vol. V (Academic Press, New York and London) pp. 3–51.
Wohlleben, D.K., J.G. Huber and M.B. Maple, 1972, Magnetic Properties of Thulium Telluride and the Pressure-Induced Electronic Phase Transition, in: AIP Conference Proceedings, No. 5, Part 2, pp. 1478–1482 (Seventeenth Annual Conference on Magnetism and Magnetic Materials, Chicago, 1971).
Zhuze, V.P., A.V. Golubkov, E.V. Goncharova, T.I. Komarova and V.M. Sergeeva, 1964, Sov. Phys. Solid State **6**, 213; (Fiz. Tverd. Tela. **6**, 268).

Penney, T., R.L. Melcher, F. Holtzberg and G. Güntherodt, 1975, AIP Conference Proceedings No. 29, Magnetism and Magnetic Materials, p. 392.
Sicardi, J.R.I., A.K. Bhattacharjee, R. Jullien and B. Coqblin, 1975, Solid State Commun. 16, 499.

SUBJECT INDEX